Proceedings

ASPE 2013 Annual Meeting

October 20-25, 2013

Crowne Plaza St. Paul - Riverfront
St. Paul, Minnesota, USA

American Society for
Precision Engineering

P.O. Box 10826, Raleigh, NC 27605-0826
(919) 839-8444 | Fax (919) 839-8039

Proceedings of:

The Twenty-Eighth Annual Meeting of

The American Society for Precision Engineering

October 20 to October 25, 2013
Crowne Plaza St. Paul - Riverfront
St. Paul, Minnesota, USA

The American Society for Precision Engineering (ASPE) is a multidisciplinary professional and technical society concerned with research and development, design, manufacture and measurement of high accuracy components and systems. ASPE activities encompass relevant aspects of mechanical, electronic, optical and production engineering, physics, chemistry, and computer and materials science. Membership is open to anyone interested in any aspect of precision engineering.

Founded in 1986, ASPE provides a new focus for a diverse but important community. Other professional organizations have covered aspects of precision engineering, always as a sideline to their principal goals. ASPE is based on the core of generic concepts necessary to achieve precision in any application; independent of discipline, ASPE intends to be the focus for precision technology -- and to represent all facets from research to application.

ASPE -- The American Society for Precision Engineering
301 Glenwood Avenue, Suite 205, Raleigh, NC 27603
P.O. Box 10826, Raleigh, NC 27605
Telephone: (919) 839-8444 Fax (919) 839-8039
http://www.aspe.net

Preface

This book comprises the proceedings of the 28th ASPE Annual Meeting. The contributions reflect the authors' opinions and are published as presented to ASPE, without change. Their inclusion in this publication does not necessarily constitute endorsement by the ASPE, or its editorial staff.

Individual readers of this book and nonprofit libraries acting for them are permitted to make fair use of the material contained in this book to be used in teaching or research; provided they copy said paper in total, as written by the author. Permission is granted to quote excerpts from the scientific or technical works in this book with proper acknowledgment of the source to include: The author's name, the book name, and the ASPE tag line. Reproduction of figures and tables is likewise permitted from the contents of this book, provided that the same acknowledgment of the same source and content is permitted.

Any other type reproduction, systematic copying or multiple reproduction of any material in this book is expressly prohibited except with the written permission of the ASPE editorial staff, addressed to the Society's headquarters.

ISBN 978-1-887706-63-6

2013

American Society for Precision Engineering
301 Glenwood Avenue, Suite 205
Raleigh, NC 27603

Printed in the United States of America

Welcome Note

Welcome to St. Paul and the Twenty-Eighth Annual Meeting of The American Society for Precision Engineering. Precision engineering is important in a wide variety of fields, from manufacturing to microelectronics to basic science. The Society serves as a focus for precision engineers across all of these fields. The Annual Meeting has evolved into an international forum for the exchange of ideas and presentation of research results relating to precision engineering, metrology, controls, and system integration. Precision engineers and scientists from private industry, government laboratories, and universities meet to learn about the latest developments and to exchange ideas about the future directions of these technologies.

The 2013 ASPE Annual Meeting continues the tradition of offering two full days of tutorials presented by some of the foremost precision engineers and scientists in the world. The technical sessions and poster presentations offer the latest research results in the areas of precision engineering advances and challenges, metrology, controls, interferometry, optics, manufacture and metrology of structured and freeform surfaces, precision technologies supporting mass production, design of precision mechanisms, precision manufacturing and assembly processes, measurement uncertainty and nano-positioning and a new standard — methods for performance evaluation of precision positioning systems. The commercial exhibits and commercial session will provide attendees with the opportunity to view and discuss the latest precision engineering equipment, products, and services. Tour state-of-the-art precision engineering technical facilities in the Minneapolis/St. Paul area and if there's time, enjoy the many organized sightseeing tours or explore the Twin Cities area on your own. Many social events including lunches, dinner, breaks and hospitality hours will allow ample time for networking and personal exchanges.

The conference organizing committee is proud to present the program for the Twenty-Eighth Annual Meeting of the ASPE. We welcome your participation and your feedback on how to make future meetings even better.

2013 Organizing & Technical Program Committee

Byron R. Knapp
Professional Instruments Company
Conference Chairperson

Luis A. Aguirre, 3M Company
Marcin B. Bauza, Carl Zeiss Industrial Metrology, LLC
Eric S. Buice, Carl Zeiss Laser Optics GmbH
Benny C.F. Cheung, The Hong Kong Polytechnic University
Thomas A. Dow, North Carolina State University
Jonathan D. Ellis, University of Rochester
Craig R. Forest, Georgia Institute of Technology
Wei Gao, Tohoku University
Kenneth P. Garrard, North Carolina State University
Robert D. Grejda, Corning Tropel Corporation
Liangyu He, University of North Carolina - Charlotte
Jonathan B. Hopkins, University of California - Los Angeles
Bradley H. Jared, Sandia National Laboratories
Eric E. Keller, The Pennsylvania State University
Mark T. Kosmowski, Interdyne Systems
Richard K. Leach, National Physical Laboratory
Don A. Lucca, Oklahoma State University
Stephen J. Ludwick, Aerotech, Inc.
Eric R. Marsh, The Pennsylvania State University
Kate M. Medicus, Optimax Systems, Inc.
Jimmie A. Miller, University of North Carolina at Charlotte
Kang Ni, University of North Carolina at Charlotte
Brian P. O'Connor, Aerotech, Inc.
Robert Matthew Panas, Lawrence Livermore National Laboratory
Robert E. Parks, Optical Perspectives Group, LLC
Antonius T. Peijnenburg, VDL Enabling Technologies Group
Senajith Bandara Rekawa, Lawrence Berkeley National Laboratory
Mark Lee Schattenburg, Massachusetts Institute of Technology
Deming Shu, Argonne National Laboratory
Alexander H. Slocum, Massachusetts Institute of Technology
Mark A. Stocker, Cranfield Precision – Division of Cinetic Landis Ltd.
Pradeep K. Subrahmanyan, KLA-Tencor Corporation
John S. Taylor, Lawrence Livermore National Laboratory
Hans-Jochen Trost, MicroFab Technologies, Inc.
Allen Y. Yi, The Ohio State University

ASPE gratefully acknowledges the time and the effort of the organizing and technical program committee to bring the precision engineering community this program.

2013 Annual Meeting

Contents

Preface ii

Welcome Note iii

Organizing Committee iv

Table of Contents v

2013 Scholarship Recipients and Sponsors vi

Program vii

Keynote Address viii

Technical Exhibitors ix

Open Forum and Best Poster Award x

Sustaining Corporate Sponsors xi

Corporate Sponsors xii

Lifetime Achievement Award xiii

Technical Paper Index . . . . . 2 - 11

Technical Papers . . . . . 15 - 564

Author Index . . . . . 565 - 569

2013 Scholarship Recipients

2013 Carl Zeiss Student Scholarship

Congratulations to **Gelareh Babaie**, University of North Carolina – Charlotte, for being awarded the Carl Zeiss Student Scholarship for 2013. This award includes the ASPE Annual Meeting registration fee and 4 tutorial fees. It also provides for travel and lodging to the ASPE Annual Meeting. Ms. Babaie is the first recipient of the Carl Zeiss Student Scholarship awarded through ASPE. This is truly a great honor.

ASPE gratefully acknowledges Carl Zeiss' five year commitment to provide the student scholarship through ASPE. The scholarship is valued at $5,000 each year.

2013 ASPE Student Scholarships

ASPE is proud to award 4 student scholarships for the 28th ASPE Annual Meeting in St. Paul. The ASPE Student Scholarships include a waiver of the Annual Meeting registration fee and 4 tutorial fees. It also includes an honorarium to cover travel and lodging expenses to the 28th ASPE Annual Meeting in St. Paul. Each scholarship is valued at $2,050. This year's scholarship recipients are as follows:

Sheikh Mashrafi, University of Illinois at Urbana Champaign
Minhao Zhu, University of Rochester
Folkers Eduardo Rojas, Massachusetts Institute of Technology
Vasishta Ganguly, University of North Carolina – Charlotte

ASPE is able to award student scholarships because of the generous contributions from organizations, as well as from many ASPE Members and ASPE supporters. ASPE believes the education and support of the next generation of precision engineers is crucial to the advancement of the field.

2013 ASPE Student Scholarship Sponsors

Program

2013 ASPE Annual Meeting

Time	Sun., Oct. 20	Mon., Oct. 21	Tues., Oct. 22	Wed., Oct. 23	Thurs., Oct. 24	Fri., Oct. 25
8:00	**Registration – Lower Level Lobby**		**Registration – Lower Level Lobby**			Carl Zeiss IMT, Starrett Tru-Stone Technologies and Arc Nano **Technical Tours** Meet in Main Lobby of Crowne Plaza
9:00	**Tutorials***	**Tutorials***	**Technical Session I** Great River	**Technical Session III** Great River	**Technical Session VI** Great River	
10:00			**Break♦**	**Break♦**	**Break♦**	
11:00			**Technical Session II** Great River	**Technical Session IV** Great River	**Technical Session VII** Great River	
12:00			**Lunch and Committee Meetings** Miss. Garden E	**Awards Lunch and Business Meeting** Miss. Garden E	**Poster Award Lunch and Open Forum** Great River	
1:00						
2:00	**Tutorials***	**Tutorials***	**Commercial Session** Great River	**Technical Session V** Great River	**Technical Session VIII** Great River	
3:00			**Break♦**	**Break♦**		
4:00			**Poster Session** Minn. Ballroom	**Poster Session** Minn. Ballroom		
5:00			**Hospitality Hour** Minn. Ballroom	**Hospitality Hour** Minn. Ballroom		
6:00		**Welcome Reception** Miss. Garden	Walk to **Dinner** at the Science Museum of Minnesota See Map in Registration Package			
7:00		**Keynote Address** Great River				
8:00						
9:00						

EXHIBIT OPEN HOURS

Exhibits located in Minnesota Ballroom

*Check hotel event board for exact location of tutorials. Participants of off-site tutorials will meet in Main Lobby of the Crowne Plaza at designated times.

♦Breaks are located in Minnesota Ballroom.

Participants in the sight-seeing tours should meet in the Main Lobby of the Crowne Plaza at designated times.

Keynote Address

Olester Benson, Ph.D.
3M Company

Monday, October 21, 2013 7:00 p.m.
Session chair: Luis Aguirre, 3M Company

Precision Engineering in the Diverse Manufacturing World of 3M

3M is a diversified manufacturer generating $30 billion dollars in sales of products defined by its five major business groups: Consumer, Electronics/Energy, Health Care, Industrial and Safety/Graphics. 3M maximizes its precision engineering infrastructure by designing machine tools and production equipment that combine finely controlled processes with the economic efficiencies of roll-to-roll manufacturing. The result: 3M's performance continues to improve, and product tolerances become smaller and smaller — now on the order of half a wavelength of light for some products. Examples from 3M's product portfolio will be used to highlight the challenges and contributions made by its engineers enabling continual technological advancements.

Olester Benson is currently a Corporate Scientist in the 3M Corporate Research Process Laboratory. Upon completion of his doctoral work in the field of physical organic chemistry at the University of Colorado, he joined 3M in 1988. Dr. Benson has spent his career leading research efforts developing environmentally friendly manufacturing process technologies using 3M's precision engineering infrastructure and high-energy radiation. He has applied these technologies to create products in the medical, safety, traffic safety, renewable energy, aerospace, home improvement, semiconductor processing, and electronic display industries.

Technical Exhibitors

4D Technology Corporation

ABTech, Inc.

Aerotech, Inc.

Alicona

AMETEK - Precitech, Inc.

Arc Nano

attocube Systems AG

Bal-tec

Bilz Vibration Technology

Bruker Nano Surfaces

Carl Zeiss Industrial Metrology

Center for Precision Metrology – University of North Carolina at Charlotte

Chardon Tool

CoorsTek Technical Ceramics

Cranfield Precision, Division of Cinetic Landis Ltd.

cyberTECHNOLOGIES

Delta Tau Data Systems, Inc.

Infinite Graphics

K&Y Diamond

Kaman Precision Products

Lion Precision

Machine Dynamics Research Lab. – Penn State University

Makino

Micro-LAM Technologies

Moore Nanotechnology Systems, LLC

New Way Air Bearings, Inc.

nPoint, Inc.

Optical Perspectives Group LLC

piezosystm jena

Praecis, Inc.

Precision Engineering Center – N.C. State University

Precision Environments, Inc.

Precision MicroDynamics, Inc.

Professional Instruments Company, Inc.

Renishaw

Riverhawk Company

Starrett Tru-Stone Technologies

TRIOPTICS, USA

Trust Automation

VDL Enabling Technologies

Western Environmental Corporation

Zygo Corporation

Commercial Session

Tuesday, October 22, 1:30 - 3:00 p.m.

Session Co-Chairs:

Stephen J. Ludwick (Aerotech, Inc.)

Eric R. Marsh (The Pennsylvania State University)

Company representatives are invited to make brief presentations on their products associated with precision engineering. This provides participants with the opportunity to receive timely information on new technologies that have been commercialized into products and services, as well as information on advances that can be expected in the near future.

Open Forum and Best Poster Award

Thursday, October 24, 2013 12:00 Noon - 1:30 p.m.

Session Chair: Alexander H. Slocum (Massachusetts Institute of Technology)

This session will start off by awarding the Best Poster recipients. Following the award, the floor will be turned over to participants who wish to open discussions on a less formal basis and to promote interaction on a variety of topics. So bring your problems and experiences to this enlightening session of impromptu discussions. There will be sign-up sheets available at the ASPE Registration Desk.

ASPE 2013 Sustaining Corporate Sponsors

3M Company
St. Paul, MN 55144
Phone: (651) 737-3790
www.3m.com

ADCOLE Corporation
669 Forest Street
Marlborough, MA 01752
Phone: (508) 485-9100
Fax: (508) 481-6142
adcole.com

Aerotech, Inc.
101 Zeta Drive
Pittsburgh, PA 15238-2897
Phone: (412) 963-7470
Fax: (412) 963-7459
www.aerotech.com

Agilent Technologies, Inc.
5301 Stevens Creek Boulevard
P.O. Box 58059
Santa Clara, CA 95052-8059 USA
Phone: (877) 424-4536
www.home.agilent.com

Alicona
1261 Humbracht Circle
Suite G
Bartlett, IL 60103 USA
Phone: (630) 372-9900
www.alicona.com

AMETEK-Precitech, Inc.
44 Blackbrook Road
Keene, NH 03431
Phone: (603) 357-2511
Fax: (603) 358-6174
precitech.com

Carl Zeiss Industrial Metrology LLC
6250 Sycamore Lane North
Maple Grove, MN, 55369
Phone: (763) 744-2400
metrology.zeiss.com

Chardon Tool
115 Parker Court
Chardon, OH 44024
Phone: (440) 286-6440
Fax: (440) 286-7165
www.chardontool.com

Cranfield Precision
Division of Cinetic Landis Ltd.
Woburn House
3 Adams Close
Kempston, Bedford, MK42 7 JE
United Kingdom
Phone: +44 (0)1234 312820
www.cranfieldprecision.com

K & Y Diamond
2645 Diab St. Laurent
Quebec H4S 1E7
CANADA
Phone: (514) 333-5606
Fax: (514) 339-5493
www.kydiamond.ca

Lion Precision
563 Shoreview Park Road
St. Paul, MN 55126-7014
Phone: (651) 484-6544
Fax: (651) 484-6824
www.lionprecision.com

Makino
7680 Innovation Way
Mason, OH 45040
Phone: (513) 573-7200
Fax: (513) 573-7360
www.makino.com

Mitutoyo America Corporation
945 Corporate Boulevard
Aurora, IL 60504-9102
Phone: (630) 723-3619
Fax: (630) 978-6471
www.mitutoyo.com

Moore Nanotechnology Systems LLC
230 Old Homestead Highway
Swanzey, NH 03446
Phone: (603) 352-3030
www.nanotechsys.com

nPoint, Inc.
3030 Laura Lane, Suite 100
Middleton, WI 53562 USA
Phone: (608) 824-1770
www.npoint.com

Professional Instruments Company
7800 Powell Road
Hopkins, MN 55343
Phone: (952) 933-1222
Fax: (952) 933-3315
www.airbearings.com

Specialty Components, Inc.
14 Village Lane
Wallingford, CT 06492
Phone: (203) 284-9112
Fax: (203) 672-0371
www.specialtycomponents.com

Trust Automation, Inc.
143 Suburban Road
San Luis Obispo, CA 93401
Phone: (805) 544-0761
Fax: (805) 544-4621
www.trustautomation.com

ASPE 2013 Corporate Sponsors

Contour Fine Tooling, Inc.
143 Jaffrey Road
Marlborough, NH 03455
Phone: (603) 876-4908
Fax: (603) 876-4911
contour-diamonds.com

Center for Precision Metrology
University of North Carolina at Charlotte
9201 University Blvd.
Charlotte, NC 28223
Phone: (704) 687-8499
cpm.uncc.edu

Corning Inc.
Corning, NY 14831
Phone: (607) 974-3842
www.corning.com

Delta Tau Data Systems
21314 Lassen Street
Chatsworth, CA 91311 USA
Phone: (818) 998-2095
Fax: (818) 998-7807
www.deltatau.com

nanoPrecision Products, Inc.
411-B Coral Circle
El Segundo, CA 90245
Phone: (310) 773-3550
nanoprecisionproducts.com

Zygo Corporation
Laurel Brook Road
Middlefield, CT 06455-0448
Phone: (860) 347-8506
Fax: (860) 347-8372
Toll-free: (800) ZYGO-NOW
zygo.com

2013 ASPE Lifetime Achievement Award

W. Tyler Estler

Physicist, National Institute of Standards and Technology (retired)

Tyler Estler is a Charter Member of ASPE, serving as President during 2010. He served two three-year terms on the Board of Directors and is a past Chairman of the Nominating Committee. He has co-taught ASPE tutorials on Self-Calibration/Reversal Techniques and the Fundamentals of Measurement Uncertainty on numerous occasions. He served for thirteen years as Editor-in-Chief of the Society's journal, Precision Engineering, for which he received the ASPE Distinguished Service Award.

Tyler received his B.S. degree, *Summa Cum Laude*, in Physics from Florida Atlantic University in 1966 and his Ph.D. in Physics from the State University of New York at Stony Brook in 1972. He was Associate Professor of Physics at New College of the University of South Florida from 1972 to 1982 and joined the Precision Engineering Division of the National Bureau of Standards (now NIST) in 1982.

Tyler's technical interests include: high-accuracy dimensional metrology of precision machine tools, coordinate measuring machines, and complex workpieces; precision interferometric metrology for displacement, absolute distance, angle, and surface figure measurements; laser alignment metrology; large-scale metrology; refractive index measurements; probability theory and the fundamentals of measurement science and engineering metrology.

Tyler received U.S. Department of Commerce Bronze and Silver Medals for contributions to high-accuracy dimensional metrology, the NIST Allen V. Astin Measurement Science Award for contributions to angle metrology, and the NIST Judson C. French Award for significant improvements in the accuracy of calibration of long standards of length. He received the 2011 SME Albert M. Sargent Progress Award for seminal contributions to advanced manufacturing metrology.

Tyler is a member of the American Association of Physics Teachers and is a Fellow of CIRP, the International Academy for Production Engineering, where served on the Editorial Committee and as Chairman of Standing Technical Committee P on Precision Engineering and Metrology. Tyler also served as a member of the BIPM Director's Advisory Group on Measurement Uncertainty.

ASPE is pleased to present Tyler with the 2013 ASPE Lifetime Achievement Award.

2013 ASPE Distinguished Service Award

Jones Arnold is a Charter Member of ASPE, having served on the Board of Directors and as chairman of the By-laws Committee since the Society's inception. Jones worked in the field of precision machining and metrology for 35 years at the Y12 National Security Complex in Oak Ridge, Tennessee. Jones earned his BS in Math and Science from MTSU and a BS in Mechanical Engineering from the University of Tennessee.

The Society greatly appreciates Jones' sustained, long-term service to ASPE. His contributions are significant to the current functioning and operation of the Society and ASPE honors him with the 2013 Distinguished Service Award.

Technical and Poster Sessions Index

The technical program of the 2013 ASPE Annual Meeting contains 117 papers on precision engineering advances. Papers that lent themselves to significant verbal interaction, concise but important discoveries, or strongly visual or tactile subjects have been selected for the poster presentation. Authors will be in attendance to discuss their work during both poster sessions on Tuesday, October 22 and Wednesday, October 23, from 3:30 to 5:00 p.m.

Session I

Advances in Precision Engineering

Tuesday, October 22, 2013, 8:30 AM - 10:00 AM

Session Chair: Jonathan D. Ellis (University of Rochester) and Bradley H. Jared (Sandia National Laboratories)

1. **Addressing Big Challenges with Precision Symbiotic Systems Thinking**
   Slocum, A. H. (Massachusetts Institute of Technology) 15
2. **Development of Hybrid Nano-Stereolithography System Using Evanescent Light and Propagating Light for High Throughput Fabrication**
   Miyakawa, K.; Matsuzawa, R.; Takahashi, S.; Takamasu, K. (The University of Tokyo) 20
3. **Micro-Laser Assisted Single Point Diamond Turning Feasibility Tests of Single Crystal Silicon**
   Ravindra, D. R. (Micro-Laser Assisted Machining Technologies, LLC); Patten, J. A. (Western Michigan University). 24
4. **Fully-Automated in Vivo Single Cell Electrophysiology**
   Go, J.; Fan, A.; Lu, C.; Kodandaramaiah, S. B.; Holst, G. L.; Stoy, W.; Kolb, I.; Forest, C. R. (Georgia Institute of Technology); Boyden, E. S. (Masachusetts Institute of Technology) 29

Session II

Control of Precision Systems

Tuesday, October 22, 2013, 10:30 AM - 12:00 PM

Session Chair: Luis A. Aguirre (3M Company) and Antonius T. Peijnenburg (VDL Enabling Technologies Group)

1. **Direction Based Filtering of Flexible Modes**
   Groothuijsen, T.; Eisinger, J.; Laro, D. A. H. (MI-Partners B. V.); Hoogendijk, R.; Steinbuch, M. (Eindhoven University of Technology); van Eijk, J. (MICE bv). 33
2. **Friction Modeling and Compensation Using Frequency Domain Parameterization by Dahl Resonance**
   Yoon, J. Y.; Trumper, D. L. (Massachusetts Institute of Technology) 39
3. **Something for (Almost) Nothing: X-ray Microscope Performance Enhancement Through Control Architecture Change**
   Mashrafi, S.; Salapaka, S. (University of Illinois at Urbana-Champaign); Preissner, C.; Zhao, H. (Argonne National Laboratory) 44
4. **Reduction of Residual Vibration of Piezoelectric Actuator Driven by Current Pulse**
   Furutani, K.; Sakata, A. (Toyota Technological Institute) 50
5. **Optimal Damping for the Reduction of Residual Vibrations in Ultra-Precision Manufacturing Machines**
   Lee, J.; Okwudire, C. E. (University of Michigan) 54

Session III

Interferometry, Optics, & Precision Engineering for Large Telescopes

Wednesday, October 23, 2013, 8:30 AM - 10:00 AM

Session Chair: Robert D. Grejda (Corning Tropel Corporation) and
Robert E. Parks (Optical Perspectives Group, LLC)

1. **Precision High Numerical Aperture Scanning System for Femtosecond Micromachining of Ocular Materials Over Large Field**
   Brooks, D. R.; Brown, N. S.; Xu, L.; Savage, D. E.; Knox, W. H.; Ellis, J. D.; (University of Rochester) 58
2. **High Volume Manufacturing of Large Segmented Telescope Mirrors**
   Mueller, U. (L-3 Communications, Tinsley). 63
3. **Visual Inspection of Cosmetic and Functional Defects in a Manufacturing Environment**
   Cilip, C. M.; Pratt, D. S.; Bauza, M. B. (Carl Zeiss Industrial Metrology, LLC) 68
4. **On the Use of Mercury Sessile Drops as Reference Artefacts for the Calibration of Optical Surface Topography Measuring Instruments**
   Chesna, J. W. (University of North Carolina at Charlotte) Schimizu, Y. (Tohoku University); Leach, R.K.; (National Physics Laboratory) 74
5. **Progress on Non-Contact Flattening of Glass**
   Sung, E.; Chalifoux, B.;Schattenburg, M. L.; Heilmann, R. K. (Massachusetts Institute of Technology) 78

Session IV

Manufacture and Metrology of Structured and Freeform Surfaces

Wednesday, October 23, 2013, 10:30 AM - 12:00 PM

Session Chair: Marcin B. Bauza (Carl Zeiss Industrial Metrology, LLC) and
Mark L. Schattenburg (Massachusetts Institute of Technology)

1. **The Tilted-Wave-Interferometer (TWI): A Quick and Flexible Approach to Measure Aspheric and Freeform-Surfaces**
   Baer, G. B.; Schindler, J.; Pruss, C.; Osten, W. (University of Stuttgart) 82
2. **In-Situ Testing of a Freeform Optic with a Chromatic Confocal Sensor**
   Steinkopf, R.; Zwick, S.; Gebhardt, A.; Risse, S.; Eberhardt, R. (Fraunhofer Institute for Applied Optics and Precision Engineering IOF Jena) 87
3. **Round-Robin Measurements of a Toroidal Window**
   Medicus, K. M. (Optimax Systems, Inc.); DeFisher, S. (OptiPro Systems, LLC); Bauza, M. B. (Carl Zeiss Industrial Metrology, LLC); Dumas, P. R. (QED Technologies). 92
4. **High Dynamics Range Enhancement in Digital Fringe Projection Technique**
   Babaie, G.; Abolbashari, M.; Farahi, F. (University of North Carolina-Charlotte) 98
5. **Precision Shaping of Thin Mirror Substrates for X-Ray Telescopes Using Ion Implantation**
   Chalifoux, B; Sung, E.; Heilmann, R. K.; Schattenburg, M. L. (Massachusetts Institute of Technology) 103

Session V

Metrology

Wednesday, October 23, 2013, 1:30 PM - 3:00 PM

Session Chair: Kate M. Medicus (Optimax Systems, Inc.) and Deming Shu (Argonne National Laboratory)

1. **Long-Term Stability of a Moving-Scale Measurement System with Nanometer Uncertainty**
   Bosmans, N.; Qian, J.; Reynaerts, D. (Katholieke Universiteit Leuven). 109
2. **Correction for Amplifier-Induced Phase Lag in Capacitance Gage Measurements**
   Ganguly, V., Schmitz, T. L. (University of North Carolina at Charlotte). 115
3. **Ranging Performance Evaluation of a Laser Scanner**
   Ferrucci, M.; Muralikrishnan, B.; Blackburn, C.; Sawyer, D. S.; Phillips, S. D.; Lee, V. (National Institute of Standards & Technology); Petrov, P.; Yakovlev, Y.; Astrelin, A.; Milligan, S.; (Basis Software, Inc.); Palmateer, J. (Boeing Research and Technology) 121
4. **The Future of Manufacturing Metrology – A Roadmap from the Association of German Engineers**
   Bauza, M. B.; (Carl Zeiss Industrail Metrology, LLC); Imkamp, D. (Carl Zeiss Industrielle Messtechnik GmbH) 127
5. **A High-Accuracy, Multi-Channel, Fiber-Based Displacement/Distance Measuring Interferometer System**
   Badami, V. G.; Wesley, A. D.; Selberg, L. A. (Zygo Corporation) 133

Session VI

Precision Technologies Supporting Mass Production

Thursday, October 24, 2013, 8:30 AM - 10:00 AM

Session Chair: Alexander H. Slocum (Massachusetts Institute of Technology) and John S. Taylor (Lawrence Livermore National Laboratory)

1. **Closed Loop Thermal Control of a Lithographic Optical Component**
   Saathof, R.; Haber, A.; Spronck, J. W.; Verhaegen, M.; Munnig Schmidt, R.-H. (Delft University of Technology). 138
2. **Active Wafer Shape Modulation Using a Multi-Actuator Chucking System**
   Cherala, A.; Choi, B.-J.; Lu, X. (Molecular Imprints, Inc.); Sreenivasan, S. V. (The University of Texas at Austin) 144
3. **The High Dynamic Range Surface Metrology Challenge**
   Leach, R. K.; Jones, C. W.; Sherlock, B.; Krysinski, A. (National Physical Laboratory). 149
4. **Wet Chemical Planarization of Single Crystalline SiC Using Catalyst-Referred Etching**
   Isohashi, A.; Sano, Y.; Okamoto, T.; Sadakuni, S.; Bui, P. V.; Yamauchi, K. (Osaka University); Yagi, K. (Ebara Corporation) 153
5. **Micro-Optic Fabrication for Microsystems-Enabled Photovoltaics**
   Jared, B. H.; Saavedra, M. P.; Anderson, B.; Sweatt, W.; Nielson, G.; Okandan, M. (Sandia National Laboratories) 157

Session VII

Design of Precision Mechanisms

Thursday, October 24, 2013, 10:30 AM - 12:00 PM

Session Chair: Brian P. O'Connor (Aerotech, Inc.) and
Senajith B. Rekawa (Lawrence Berkeley National Laboratory)

1. **Modal Decoupling via Flexure-based Transmissions as Applied to a Micromachined Tuning Fork Gyroscope**
   Thomas, M. A. C.; Panas, R. M.; Culpepper, M. L. (Massachusetts Institute of Technology); DiBiasio, C. M. (Draper Laboratory) 161
2. **Performance of Optimization of Large Stroke Flexure Hinges for High Stiffness and Eigenfrequency**
   Gunnink, K.-J.; Aarts, R. G. K. M.; Brouwer, D. M. (University of Twente) 166
3. **Novel Single-Axis Flexure Mechanism Designs with Improved Bearing Stiffness**
   Awtar, S. (University of Michigan - Ann Arbor) 172
4. **Non-Lithographically-Based Microfabrication of a Hexflex Nanopositioner**
   Panas, R. M.; Nyovanie, P.; Du, L.; Schanne, E.; Szklarzewski, V.; Culpepper, M. L. (Massachusetts Institute of Technology). 176
5. **Design of Multidimensional Flexure Stage System for Hard X-Ray Mirror Focusing at Sub-50-Nanometer Scale**
   Shu, D.; Liu, W.; Maser, J.; Lai, B.; Kearney, S.; Anton, J.; Cai, Z.; Harder, R.; Xu, R.; Assoufid, L.; Vogt, S.; Tischier, J. Z. (Argonne National Laboratory). 182

Session VIII

Precision Manufacturing and Assembly Processes

Thursday, October 24, 2013, 1:30 PM - 3:00 PM

Session Chair: Mark A. Stocker (Cranfield Precision Division of Cinetic Landis Ltd.) and
Pradeep K. Subrahmanyan (KLA-Tencor Corporation)

1. **Graphene Coated Si Mold for Precision Glass Optics Molding**
   He, P.; Li, L.; Yu., J.; Huang, W.; Yen, Y.-C.; Lee, J. L.; Yi, A. Y. (The Ohio State University). 186
2. **Tool Temperature Measurement During DT of Steel**
   Hesler, G. S.; Dow, T. A.; Garrard, K. P.; Kudenov, M. W.; Gettys, T.; Gebb, D. (North Carolina State University). 191
3. **Complex Bore Holes Fabricated by Combined Helical Laser Drilling and Micro Electrical Discharge Machining**
   Uhlmann, E.; Oberschmidt, D. (Fraunhofer Institute for Production Systems and Design Technology (IPK)); Langmack, M. (Technical University Berlin) 195
4. **Developing A Machining Model Database for Hard-to-Machine Materials**
   Tyler, C.; Schmitz, T. L. (University of North Carolina at Charlotte) 200
5. **Self-Tuning Dynamic Vibration Absorber for Machine Tool Chatter Suppression**
   Aguirre, G.; Gorostiaga, M.; Muñoa, J. (IK4-IDEKO); Porchez, T. (Cedrat Technologies) 204

Poster Sessions

Tuesday, October 22, 2013
Wednesday, October 23, 2013

Session Chair: Jonathan B. Hopkins (Lawrence Livermore National Laboratory) and Hans-Jochen Trost (MicroFab Technologies, Inc.)

Advances in Precision Engineering and Nano Technologies

1. **Functional Constraints and the Design of a New Watt Balance**
   Chao, L. S.; Schlamminger, S.; Pratt, J. R. (National Institute of Standards & Technology) 209
2. **Eliminating Parasitic Error in Dynamically Driven Flexure Systems**
   Hopkins, J. B. (University of California - Los Angeles); Panas, R. M. (Massachusetts Institute of Technology) 214
3. **Characterization of Nano-Micro Machining Made by Atomic Force Microscope Scratch on Optical-Fiber End Plane**
   Matsui, S.; Umemura, S. (Chiba Institute of Technology) 218
4. **Objective Functions for Optimizing Resonant Mass Sensor Performance**
   Miller, M. H. (Michigan Technological University) Li, C. (Stanford University) 222
5. **A First Investigation of Green Lasers in Micro-Laser Assisted Scratch Tests on Silicon**
   Mohammadi, H.; Patten, J. A. (Western Michigan University); Ravindra, D. R. (Micro-Laser Assisted Machining Technologies, LLC) 228
6. **Nanocoining Submicrometer Structured Surfaces**
   Nowak, W. J.; Dow, T. A.; Kessing, J.; Garrard, K. P.; Scattergood, R. O. (North Carolina State University) 231
7. **Characteristics of the Brittle Cracking by the Cutting Edge Roughness in the Glass Cutting**
   Ono, T. (Kyushu Sangyo University) 235
8. **Fabrication of Thin Si Crystal for X-Ray Beam Splitter**
   Osaka, T.; Sano, Y.; Matsuyama, S.; Yamauchi, K. (Osaka University); Yabashi, M.; Inubushi, Y.; Sato, T.; Ishikawa, T. (RIKEN SPring-8 Center); Tono, K. (Japan Synchrotron Radiation Institute) 239
9. **Orientation-Controlled Microfabrication of Anode of Solid Oxide Fuel Cells**
   Shinagawa, S.; Nagato, K.; Shikazono, N.; Hamaguchi, T.; Nakao, M. (The University of Tokyo) 243
10. **Laser-Assisted Roller Imprinting of Nanostructures with Real-Time Monitoring of Replication Degree**
    Takahashi, K.; Nagato, K.; Sato, T.; Suehiro, D.; Hamaguchi, T.; Nakao, M. (The University of Tokyo) 247
11. **Ultraprecise Clamping Solution for Diamond Machining – Comparative Characterization of Repeatability**
    Wenzel, C.; Winkelmann, R.; Klar, R. (Innolite GmbH); Arneson, D. A.; Knapp, B. R. (Professional Instruments Company) 251
12. **Continuous and Fast Manufacturing Technique of Ion-Conducting Ceramic Compacts with Oriented Anisotropic Particles**
    Yamauchi, T.; Ikeshima, S.; Nagato, K.; Hamaguchi, T.; Nakao, M. (The University of Tokyo) 256
13. **A 3D X-Ray Microscopy**
    Zou, J. (Tianjin University) Xu, Y. (Sanying Precision Engineering Research Center) 261

Challenges of Precision Engineering for Mass Production & Precision Engineering Supporting the Semiconductor Industry

1. **Scaling and Automating Process Control for Mass Production via Programmable Gauging**
   Emmett, D. H.; Hill, J.; Vasilescu, D. (Renishaw, Inc.) 265
2. **Stable and Precise Mass Production of Milling Parts in Changing Environment Conditions**
   Fritz, M.; Janitza, D. (KERN Microtechnik) 269
3. **Super Precision Turning Center: High Accuracy, Hard Turning, Multi-Tool Machine Tool**
   Kushnir, E. (Hardinge, Inc.) 273
4. **Continuous Feed of an Occluding Medium Into a Flow Stream**
   Rojas, F. E.; Slocum, A. H. (Massachusetts Institute of Technology) 278

Control of Precision Systems

1. **Development of Noncontact Hydrodynamic Micro Handling System**
   Ichinozuka, A.; Toyoshima, A.; Aoyama, H. (The University of Electro-Communications); Qin, Z.; Weijun, H. (South China University of Technology) 282
2. **Practical Controller Design for Precision Positioning of Stages with a Pneumatic Actuator**
   Sato, K.; Sano, Y.; Wang, Y. (Tokyo Institute of Technology) 286

Design of Precision Machines

1. **Design of Vacuum Imprinting System for High Resolution Patterning on Nonplanar Surfaces**
   Chen, J.; Xu, H.; Zhao, N.; Chen, S.-C. (The Chinese University of Hong Kong) 290
2. **Precision Modeling and Measurement of Nut Stiffness in Ballscrews**
   Chung S.-C.; Cao, L. (Hanyang University); Khim, G.; Park, C.-H. (Korea Institute of Machinery & Materials (KIMM)) 295
3. **Design of a Precision Mass Translation System for Gravity Measurements**
   Fitsos, P.; Edson, S.L.; Davis, P. J.; Taylor, J. S.; Libby, S. B.; Johnson, M. A.; Sonnad, V.; (Lawrence Livermore National Laboratory); Loftus, T.; Dubetsky, B. (AOSense, Inc.); Thompson, D.C. (Praecis, Inc.) 299
4. **A Planar Motor with an Active Encoder**
   Gao, J.; Huang, P. (Shanghai Jiaotong University) 304
5. **Design of a New Type Multi Degree of Freedom Spherical Actuator**
   Kim, H.; (Korea Institute of Machinery & Materials); Kim, M.; Gweon, D.-G. (Korea Advanced Institute of Science & Technology (KAIST)) 310
6. **Thermal Analysis of Ballscrew Systems by Finite Difference Methods**
   Kim, M.; Min, B.-K.; Chung S.-C. (Hanyang University) Park, C.-H. (Korea Institute of Machinery & Materials (KIMM)) 314
7. **Heat is the Price You Pay for Spindle Stiffness**
   Liebers, M. J.; Arneson, D. A.; Knapp, B. R.; Oss, D. D.; Bryan, N. (Professional Instruments Company) 318
8. **Design and Optimization of a x-y-θz Cylindrical Flexure Stage**
   Matloff, L.; Telleria, M. J.; Culpepper, M. L. (Massachusetts Institute of Technology) 321
9. **Time Varying Error Behavior in Super-Size Floor Type Boring Machines**
   Min, B.-K.; Chung, S.-C. (Hanyang University) 327

10 **Identification of Thermal Characteristics in the Ballscrew Assembly**
Oh, K.; Min, B.-K.; Chung, S.-C. (Hanyang University); Park, C.-H. (Korea Institute of Machinery & Materials (KIMM)) 331

11. **Development of a Cylinder Type Gas-Liquid Phase-Change Actuator**
Ono, M.; Saito, S.; Kato, T.; Sakamoto, M. (Tokyo Metropolitan College of Industrial Technology) 335

12. **Study on the Impact Load Applied to the Fingers Using A Metal Baseball Bat**
Sakamoto, M.; Ono, M.; Hiroi, T. (Tokyo Metropolitan College of Industrial Technology) 339

13. **Design of Stamping Module to Pattern Alignment Marks for LED Post-Process**
Sohn, Y. W. (3D Plus); Jeon, Y.; Lee, M.-G.; (Ajou University) Cho, H. K. (Andong National University) 343

14. **System Level Optimization of a Cylindrical Flexure for Linear Motion Guidance**
Telleria, M. J.; Culpepper, M. L. (Massachusetts Institute of Technology) 347

15. **A Flexure-Based High-Throughput Roll-to-Roll Printing System**
Zhou, X.; Cheng, J.; Zhao, N.; Chen, S.-C. (The Chinese University of Hong Kong). 353

Interferometry, Optics, & Precision Engineering for Large Telescopes

1. **Piezo VS Voice Coil Modules in the Hybrid Actuator for the E-ELT Telescope**
Glöss, R. S.; Zimmerman, K.; Reith, J.; Haase, T.; Enkrich, C. (Physik Instrumente (PI) GmbH & Co. KG) 359

2. **Application of Wavelet Analysis in Heterodyne Interferometry**
Lu, C.; Tarbutton, J. (University of South Carolina); Gillmer, S.; Ellis, J. D. (University of Rochester); Schmitz, T. L.; Troutman, J. (University of North Carolina at Charlotte) 364

3. **Retroreflector Polarization Model**
Zhu, M.; Ellis, J. D. (University of Rochester); Li, Y. (Tsinghua University) 368

Manufacture and Metrology of Structured and Freeform Surfaces

1. **Adaptive Scanning Control with Optical Probe**
Drescher, J. D. (UTC - Pratt & Whitney); Dow, T. A.; Garrard, K. P. (North Carolina State University). 374

2. **Three Degree-of-Freedom Optical Probe with Fiber Detection Using Carrier Fringe Methods**
Echter, M. A.; Roll, C. D.; Keene, A. D.; Ellis, J. D. (University of Rochester) 378

3. **Suppression of Tool Wear in Diamond Turning by Surface Modification of Steels – Effect of Carbides in Carburized Steels**
Furushiro, N.; Hirooka, D.; Yamaguchi, T. (Kansai University); Terauchi, S.; Iwasa, Y. Matsuda, S. (Osaka Yakin Kogyo Co., Ltd.) 385

4. **DRIE Process Performance for Manufacture of an Artifact for X-ray Phase-Contrast and Micro-CT Characterization**
Thousand, J.; Smith, S. T. (University of North Carolina at Charlotte). 389

5. **Influence of Sensor Sensitivity on Roundness Measurement by a New Successive Three Point Method**
Uda, Y.; Shimada, S.; Iemata, D. (Osaka Electro-Communication University); Kiyono, S. (Precision Measurement Laboratory) 393

6. **Study on High Speed 3D Measurement of Tooth Plaster Model Using 3 Light-Sections Method**
Yazawa, T.; Sakuragi, Y.; Nishiguchi, Y.; Soejima, T.; Kuroiwa, M.; Otsubo, T.; Ougiya, Y.; Kojima, T. (Nagasaki University). . . . 397

7. **High Efficiency Milling of Steam Turbine Blade**
Yuan, X.; Yazawa, T.; Ougiya, Y.; Kojima, T. (Nagasaki University); Maeda, Y. (Toyama Prefectural University); Kogusu, S. (Industrial Technology Center of Nagasaki) . . . 404

Micro and Nano Metrology, Measurement Uncertainty & Nano-Positioning

1. **A Derivative Sampling Calibration Method for Measurement Systems**
Chen, Z.; Huang, P. (Shanghai Jiaotong University). . . . 409

2. **Displacement Measurement Using Speckle Correlation with Reduced Number of Database Patterns**
Farsad, M.; Goch F. G.; Evans, C. J.; (University of North Carolina at Charlotte) . . . 415

3. **An Active Encoder For Precision Position Measurement**
Huang, P.; Tian, K.; Qiang, X. (Shanghai Jiaotong University) . . . 421

4. **Development of Error Budget Software for Machine Tools**
Jadhav, R. D.; Morse, E. P. (University of North Carolina at Charlotte) . . . 427

5. **Development of a Laser-Guided Deep-Hole Measurement System: Adjustment to a Small Size**
Katsuki, A.; Ali, M. D. H.; Sajima, T.; Kurokawa, S. (Kyushu University); Hiroshi, M. (University of Kitakyushu); Ohnishi, O. (Miyazaki University) . . . 431

6. **Synchronous Signal Removal via Wavelet Packets**
Keller, E. E.; Marsh, E. R. (The Pennsylvania State University); Knapp, B. R. (Professional Instruments Company). . . . 437

7. **Electrical Runout Using an Eddy-Current Sensor for Roundness Measurements**
Knapp, B. R.; Arneson, D. A. (Professional Instruments Company); Martin, D. L. (Lion Precision) . . . 440

8. **Accelerometer Assessment of Air Bearing Spindles**
Liebers, M. J.; Arneson, D. A.; Knapp, B. R.; Oss, D. D. (Professional Instruments Company). . . . 445

9. **A Study on the Effect of Noise & High-Order Distortion on a Modulated Encoder**
Makinouchi, S.; Imai, T.; Watanabe, A.; Takasaki, M. (Nikon Corporation); Kohn, C. M.; Ohara, T. (NanoWave Inc.) . . . 448

10. **Spindle Speed and Sensor Bandwidth Requirements**
Martin, D. L.; Kretschmar, M. (Lion Precision). . . . 452

11. **Uncertainty Analysis of Ballscrew Nut Stiffness**
Min, B.-K.; Cho, H.-G.; Chung S.-C. (Hanyang University) Park, C.-H. (Korea Institute of Machinery & Materials (KIMM)). . . . 455

12. **On Performance Verification of 3D Micro Measuring Instrument**
Moroni, G.; Petrò S.; Syam, W. P. (Politecnico di Milano) . . . 459

13. **Volumetric Performance Evaluation of a Laser Scanner**
Muralikrishnan, B.; Ferrucci, M.; Sawyer, D. S.; Lee, V.; Blackburn, C.; Phillips, S. D. (National Institute of Standards & Technology); Gerner, G. (The Pennsylvania State University); Petrov, P.; Yakovlev, Y.; Astrelin, A.; Milligan, S. (Basis Software, Inc.); Palmateer, J. (Boeing Research and Technology) . . . 465

14. **Application of Magnets in Loading Ultra-High-Speed Spindles and Understanding Its Effects on Radial Spindle Error Motions**
Nahata, S.; Ozdoganlar, O. B. (Carnegie Mellon University) . . . 471

15. **Density Measurement of Tantala (Ta2O5) Foams Using X-Ray Radiography**
Seugling, R. M.; Young, P.; Sain, J.; Satcher, J. H. (Lawrence Livermore National Laboratory) 476

16. **Development of a Large-Stroke Piezo-Actuated Stage for Nanopositioning**
Zhang, J.; Huang, P. (Shanghai Jiaotong University) 477

New Standard – Methods for Performance Evaluation of Precision Positioning Systems

1. **Methods for Performance Evaluation of Single Axis Positioning Systems: Point Repeatability**
Brown, N. (ALIO Industries, Inc.) 483

2. **Methods for Performance Evaluation of Single Axis Positioning Systems: Dynamic Angular Performance**
Ellis, J. D.; Gillmer, S. R. (University of Rochester); O'Connor, B. P. (Aerotech, Inc.) 489

3. **Methods for Performance Evaluation of Single Axis Positioning Systems: Move and Settle Performance**
Ellis, J. D. (University of Rochester); Ludwick, S. J. (Aerotech, Inc.). 493

4. **Methods for Performance Evaluation of Single Axis Positioning Systems: A New Standard**
Fesperman Jr., R. R. (National Institute of Standards & Technology); Brown, N. (ALIO Industries, Inc.); Elliott, K. E. (Corning Incorporated); Ellis, J. D. (University of Rochester); Grabowski, A. (Physik Instrmente (PI) GmbH & Co. KG); Ludwick, S. J.; O'Connor, B. P. (Aerotech, Inc.); Maneuf, B. (Newport Micro-Controle Spectra-Physics S.A.S.); Woody, S. C. (InsituTec, Inc.). 498

5. **Methods for Performance Evaluation of Single Axis Positioning Systems: Dynamic Straightness**
Fesperman Jr., R. R. (National Institute of Standards & Technology); O'Connor, B. P. (Aerotech, Inc.); Ellis, J. D. (University of Rochester) 504

6. **Progress on Defining Standard Tests for Quantifying Servo System Tuning**
Ludwick, S. J. (Aerotech, Inc.) 510

7. **Methods for Performance Evaluation of Single Axis Positioning Systems: Incremental Step Test**
O'Connor, B. P. (Aerotech, Inc.); Fesperman Jr., R. R. (National Institute of Standards & Technology); Maneuf, S. (Newport Micro-Controle Spectra-Physics S.A.S.) 512

Precision Manufacturing and Assembly Processes

1. **Hole Sequence Optimization for Minimum Time 5-Axis On-the-Fly Laser Drilling**
Alzaydi, A. A.; Erkorkmaz K. (University of Waterloo); Elfizy, A.; Engin, S. (Pratt & Whitney Canada) 518

2. **Manufacturing Large Ultra-Precision Parts for the New BIPM Watt Balance**
Arneson, D. A. (Professional Instruments Company) 522

3. **Performance Evaluation of a Sessile Drop Deposition Process**
Chesna, J. W.; Rivers, R. I.; Smith, S. T. (University of North Carolina at Charlotte); Samara, A. M. (Intel Corporation). 528

4. **A Study of Modelling and Simulation of Single-Point Diamond Turning of Micro-Structured Patterns on Precision Rollers**
Cheung, C.-F.; Ren, M. J.; Xiao, G. B.; Mak, C. H.; Kong, L.-B.; To, S. S. (The Hong Kong Polytechnic University) 532

5. **Study on Wear of Urethane Polisher Used in Vibration-Assisted Polishing**
Guo, J.; Yamagata, Y.; Morita, S.; (The Institute of Physical and Chemical Research (RIKEN)); Suzuki, H. Y. (Chubu University); Uehara, J. (Nagatsu Precision Mold Co., Ltd.) 536

6. **Study on Surface Processing Process by Using FEMTO-Second Pulse Train Beam with Excitation of Coherent Phonon**
Hayashi, T. ; Michihata, M.; Takaya, Y.; Fukuta, Y. (Osaka University) 540

7. **Investigation of Tooling Effects, Slurry Composition and Workpiece Material in Vortex Machining**
Hunt, J. B.; Howard, S. C.; Mullany, B. A.; Smith, S. T. (University of North Carolina at Charlotte) 545

8. **Relative Axis Error Modeling for Volumetric Errors of Machine Tools**
Hwang, J.; Bui C. B.; Park, C.-H. (Korea Institute of Machinery & Materials (KIMM)) 550

9. **Study on Releasability of Molded Resin from EDM Finished Surface with Metal Powder Mixed Fluid**
Okada, A.; Iwasaki, S.; Okamoto, Y. (Okayama University); Kitada, R. (TOWA Corporation) 554

10. **Machining of Microfluidic Structures for Biotechnological Components**
Uhlmann, E.; Oberschmidt, D.; Hein, C.; Mahr, F. (Fraunhofer Institute for Production Systems and Design Technology (IPK)) 558

11. **High Speed Machining of Semiconductor Products**
van den Hurk, P.; Berkelaar, L. (VDL Enabling Technologies Group) 563

Technical Papers

ADDRESSING BIG CHALLENGES WITH PRECISION SYMBIOTIC SYSTEMS THINKING

Alexander H. Slocum[1]
[1]Department of Mechanical Engineering
Massachusetts Institute of Technology
Cambridge, Massachusetts, USA

INTRODUCTION

Precision deterministic thinking combined with a symbiotic systems approach can help to create viable solutions to the difficult task of supplying the energy we need without crippling civilization. The goal is to identify different problems and potential solutions and then see how the problem of one can be the solution of the other (reversal), and thus by cross pollination create a more cost effective solution. Efficiency and robustness then come from attention to detail that is made so much better through the application of FUNdaMENTAL principals of precision engineering such as reciprocity whereby one system's problem can be another system's opportunity.

The concept of symbiotic design and engineering is perhaps as old as the idea of design itself and is found for example in the phrase "two birds with one stone". More recently, in product design an attemnpt has been made to formalize the process [1]. A strong catalyst for symbiotic design is cost: when the cost is too high for system that seems to be desireable, one should look for whjat else the system can serve as a base for, and then combine functions. An analyagy from control systems is the use of pole-zero cancellation techniques to quell an instability.

This paper draws on past work to emphasize the common thread of symbiotic systems thinking that can help address big issue problems. Examples discussed will include: offshore wind combined with energy storage, fish farms, and/or uranium extraction from seawater; and Direct absorption high temperature salt ponds with energy storage for Concentrated Solar Power stations.

Offshore Wind Energy Platform

An NREL study of US offshore wind resources estimates > 4,000 GW in offshore wind potential, including over 2,400 GW potential in areas with average wind speeds > 7 m/s at water depths greater than 60 m where Floating Wind Turbines (FWTs) are more likely to be deployed. Numerous advantages and challenges for offshore wind are also identified, including proximity to major population centers, greater capacity factors, smoother airflow, and potential for re-building heavy manufacturing industries in coastal states [2].

Energy storage can help address the intermittency problem inherent in wind and reduce the impact of diurnal wind patterns, when high winds/low demand occur at night which can require wind power to be curtailed or thermal power plants idled. Utility-scale energy storage can also help with load-leveling power plants for more efficient fuel use [3].

However, the direct capaital cost of a floating wind turbine is considerably higher than a near shore pylon based unit, especially considering the increased power transmission cable cost. In addition, the maintainance costs of being far offshore will also be substantially more. Both far and near shore wind energy systems could make use of on-shore battery systems for energy storage. Deep offshore FWT could also contain energy sotrage in the form of a pumped hydro system.

To reduce the apparent cost of a FWT farm, one can ask what other things might be located offshore that can utilize the floating platfoirm and not get in the way of the wind turbine? One near term and one longer term opportunity come to mind: 1) fish habitats (including farming) and 2) harvesting uranium from seawater.

Aquaculture

Offshore structures are known to be magnets for wildlife, and in water depths to 300m, common in the Gulf of Maine where FWT farms are likjely, bottom ballast structures could provide safe habitats for fish in various life stages [3]. Near the surface, aquatic tanks could hold farmed species [4,5,6] to avoid polluting

shoreline habitats and reduce the amount of antibiotics needed to farm fish. Although there are issues raised even with offshore fish farms , and these concerns must be addressed [7], the fact remains that the offshore aquaculture will continue to grow as human needs grow and wild fish stocks shrink.

Harvesting Uranium from Seawater[1]

Nuclear power can greatly reduce carbon dioxide emissions from power generation; however, at the current consumption rate the global conventional reserves of uranium (7.1 million tonnes) could be depleted in roughly a century [8]. Uranium is present in ocean water in the form of uranyl ions at a low concentration of 3-3.3µg/L [9]; and the amount of uranium in the ocean is estimated at 4.5 billion tonnes, nearly a thousand times the conventional reserves [10,11]. Uranium adsorption by chelating polymers appears to be the most promising in terms of cost, adsorption capacity and environmental footprint [12,13,14,15].

The process of passively extracting uranium from seawater using adsorbent polymer starts with deploying the adsorbent in seawater. It remains submerged until the amount of uranium captured approaches the adsorbent capacity. During the elution process the adsorbent is immersed in acid solutions of increasing concentration to recover uranium and remove other elements that become bonded to the polymer. After regeneration, the adsorbent can be reused as its functional groups have been freed. The output from the elution process then undergoes the same purification and precipitation that is typical for mined uranium to produce yellow cake.

The second economic strategy is a continuous system, which can deploy and collect the adsorbent continuously, with minimal human intervention. As conceptually and to scale in Figures 1 and 2, it consists of an on-site elution plant and a series of automatic conveying belts suspended from the FWT, which transfer adsorbent between seawater and the elution plant that would be located at the base of the FWT. The system runs automatically for a period of time before a crew is sent to the site to collect uranium and perform maintenance. In addition to reducing the cost of the seawater uranium production, this continuous system can also significantly increase energy production per area of human activity on the ocean. The systems are attached to wind turbines so no new ocean surface area is needed. An additional engineering requirement makes the energy production of this system compelling: the continuous system should produce the same amount of power output, 5 MW, as a 5 MW wind turbine does.

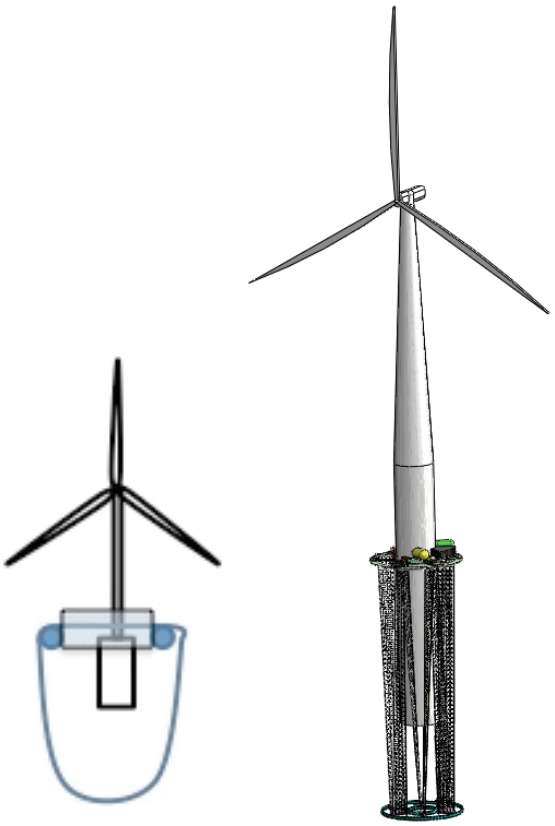

FIGURE 1. Conceptual (L) and to-scale (R) looping cable system to hrvest uranium from seawater.

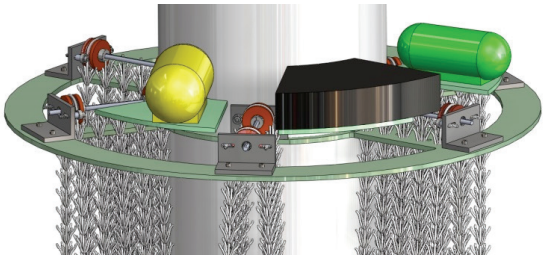

FIGURE 2. Platform configuration.

[1] Paper in progress: "Extraction of uranium from ocean water: design and testing of a symbiotic system" Camille Baelden, Le Chang, Mathieu Picard, You Wu, Alexander H. Slocum

FWT Ballast Strructures for Energy Storage

Fennell Dundar, and Meredith as part of their Master's theses with Prof. Slocum recognized that since FWTs will require significant ballast, and a significant cost of ballast is deploying it; the ballast structures could also function as part of a system for storing energy deep underwater in concrete spheres [16]. Water is pumped out of the spheres to store energy, and allowed to flow back in through a turbine to generate electricity. Figure 3 presents schematic cross-section views of an energy storage sphere as currently envisioned charging (a) and discharging (b). Figure 4 shows a wind farm layout concept.

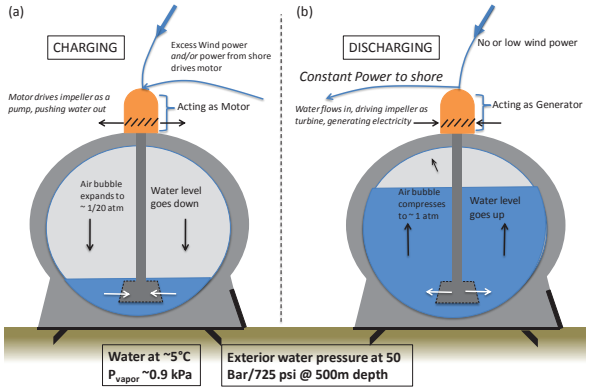
(a)
CHARGING
Excess Wind power and/or power from shore drives motor
Motor drives impeller as a pump, pushing water out
Acting as Motor
Air bubble expands to ~ 1/20 atm
Water level goes down
(b)
DISCHARGING
No or low wind power
Constant Power to shore
Water flows in, driving impeller as turbine, generating electricity
Acting as Generator
Air bubble compresses to ~ 1 atm
Water level goes up
Water at ~5°C
P vapor ~0.9 kPa
Exterior water pressure at 50 Bar/725 psi @ 500m depth

Figure 3. Internal view of ORES concept during charging and discharging operations: The spheres are on the seafloor and water is pumped out to store energy and flows in through turbine to generate electricity.

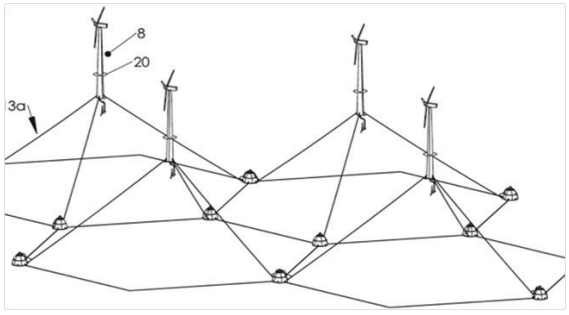

Figure 4. Wind farm layout with energy storage ballast spheres.

In all the above cases, the capital costs are shared as well as the variable costs, for the vessels and people needed to service the industries asscoaited with the FWT can coordinate trips to the site with the maintanance functions to be performed.

Direct Absoprtion Concentrated Solar Power System

Concentrating Solar Power (CSP) systems that use a central receiver with integral thermal energy storage have the potential to produce 24/7 base load and/or peak electric power. Conventional high temperature CSP systems have evolved to use a central tower where a heat transfer fluid circulates through tubes onto which the sunlight is focused. However, maximum allowable fluxes are limited to avoid thermal degradation of the receiver tubing.

Utilizing molten salts as the working fluid enables simple subsequent thermal storage, due to their high heat capacities and wide operating temperatures. Unfortunately, daily receiver filling requires ancillary heaters and presents additional risks should the salt freeze, requiring electric heat tracing on long piping runs, valves and manifolds. To minimize receiver fluid pumping losses and enable alternative receiver designs, beam-down systems have been proposed the light was to be beamed directly into a molten salt/metal filled container [17,18,19]. The Odeillo solar furnace facility uses a north facing parabola focused on a target built into one wall of a building that holds offices and laboratories. 63 south-facing flat mirror heliostats track the sun's movement and focus it down on the north facing parabola [20].

.

CSPonD

D. Codd as part of his doctoral thesis with prof. Slocum created a system in which which uses hillside mounted heliostats to direct sunlight into a volumetric absorption molten salt receiver with integral storage [21]. The concentrated sunlight penetrates and is absorbed by molten salt in the receiver through a depth of 4-5 meters, making the system insensitive to the passage of clouds. The receiver volume also acts as the thermal storage volume eliminating the need for secondary hot and cold salt storage tanks.

A small aperture and refractory-lined domed roof reduce losses to the environment and reflect thermal radiation back into the pond. Hot salt is pumped from the top of the tank through a steam generator and then returned to the bottom of the tank. An insulated barrier plate is positioned within the tank to provide a physical and thermal barrier between the thermally stratified layers, maintaining hot and cold salt volumes required for continuous operation. As a result, high temperature thermal energy can be

provided 24/7 or at any desired time. About 2500 m3 of nitrate salt is needed to operate a 4 MWe steam turbine 24/7 (7 hours sunshine, 17 hours storage), and with a modest heliostat field oversizing to accumulate energy, the system could operate for an additional 24 hours (1 cloudy day). Alternatively, this same storage volume can supply a 50 MWe turbine for 3.25 hours without additional solar input. Accordingly, the system is referred to as Concentrated Solar Power on Demand (CSPonD) and is shown conceptually in Figures 5, 6 and 7

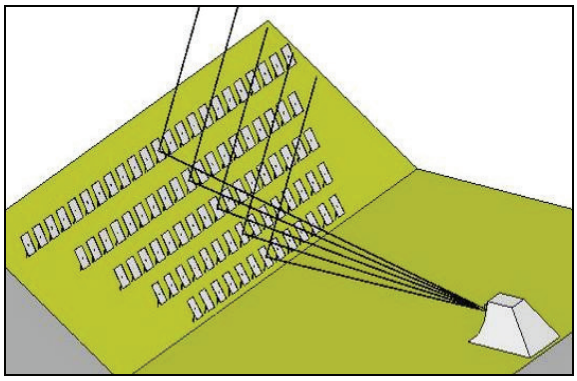

Figure 5. CSPonD concept: heliostats on a hillside reflect sunlight through an aperture into a volumetric molten salt receiver (pond).

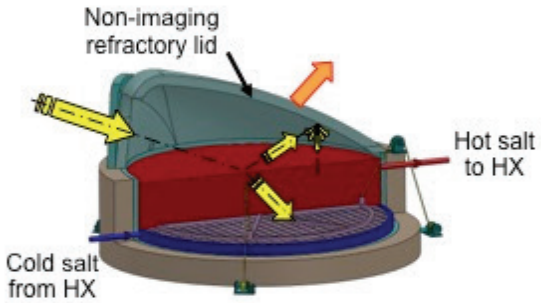

Figure 6. CSPonD concept: end of sunny day and raft is at bottom, system fully charged.

The CSPonD can be placed at the base of a hill, and helioststs on the hillside would then beam the light directly into the salkt. Added cosine losses are incurred, but the reciever simplicity is enhanced. Alternatively, the CSPonD system can be placed at the top of a hill or a tower in a beam up configuration that uses one bounce off of non focussing reflective dome to direct the sunlight from the heliostats into the salt.

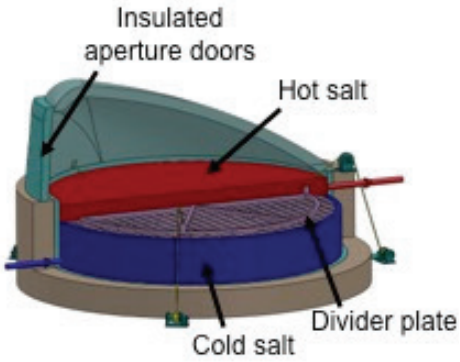

Figure 7. CSPonD concept: after long period of no sun and generating electricity, raft near top.

The raft that seperates the hote (upper) salt from the colder (lower) salt is key. The motion of the raft is controlled so the hot salt is kept at constant temperature which is needed by the heat exchanger for efficient operation.

In either case, the symbiotic nature is that the molten salt cannot be damaged by the sunlight no matter the flux intensity, because the higher the flux the greater will be convection currents that keep the salt mixed due to the penetrating nature of the sunlight. The molten salt then flow directly into the heat exchanger to generate steam for a conventional steam plant. <inimal piping and pumps thereby greatly reduce the risk of freezing salt.

CONCLUSIONS

The systems presented represent simple ways in which renewable energy systems can be mnade more economical by symbiotic design. Combining functions on a single platform will likely be required more and more often as greater industrial efficiencies are sought.

ACKNOWLEDGEMENTS

The development of the energy systems described herein were made possible by generous support of the MIT Energy Initiative (http://mitei.mit.edu).

Many students contributed to the original articles from which material was drawn and referenced for this extended abstract, and Prof. Slocum is very greatful for the excellent work they did. I wish I could list all as authors but then the entire first page would be authors and current affiliations!

REFERENCES

[1] AlGeddawy T.N., ElMaraghy H.A. Symbiotic Design of Products and Manufacturing Systems Using Biological Analysis. Proceedings of the 19th CIRP Design Conference – Competitive Design, Cranfield University, 30-31 March 2009, pp469.

[2] Musial, W., & Ram, B. Large-Scale Offshore Wind Power in the United States: Assessment of Opportunities and Barriers. National Renewable Energy Laboratory. Golden, CO: NREL. Sept 2010.

[3] Eyer, J., & Corey, G. Energy Storage for the Electricity Grid: Benefits and Market Potential Assessment Guide. Sandia National Laboratories. Albuquerque, NM: Sandia National Laboratories. 2010.

[4] Methratta, E. T., & Link, J. S. Ontogenetic variation in habitat associations for four flatfish species in the Gulf of Maine-Georges Bank region. Journal of Fish Biology , pp1669-1688. 2007.

[5] Paquotte P., Pomélie C. de la The experience of offshore fish farming in France. In: Muir J. (ed.), Basurco B. (ed.). Mediterranean offshore mariculture. Zaragoza : CIHEAM, 2000. p. 25-32 (Options Méditerranéennes : Série B. Etudes et Recherches; n. 30).

[6] http://www.thefishsite.com/articles/990/effects-of-offshore-fish-farms-on-wild-stocks

[7] http://www.foodandwaterwatch.org/fish/fish-farming/offshore/problems/

[8] OECD and International Atomic Energy Agency (IAEA), “Uranium 2011: Resources, Production and Demand,” OECD Publishing, 2011.

[9] Oguma K. Suzuki T. Saito K. Determination of uranium in seawater by flow-injection preconcentration on dodecylamidoxime-impregnated resin and spectrophotometric detection. Talanta, vol. 84, no. 5, pp. 1209–1214, 2011.

[10] Tamada M. Current status of technology for collection of uranium from seawater. Japan Atomic Energy Agency, 2009.

[11] Davies R. V. Kennedy J. McIlroy R.W. Spence R. Hill K. M. Extraction of uranium from seawater. Nature, vol. 203, no. 4950, pp. 1110–15, 1964.

[12] Kim J. Tsouris C. Mayes R. T. Oyola Y. Saito T. Janke C. J. Dai S. Schneider E. Sachde D. Recovery of Uranium from Seawater: A Review of Current Status and Future Research Needs. Separation Science and Technology. 2012

[13] Zhang A. Asakura T. Uchiyama G. The adsorption mechanism of uranium (VI) from seawater on a macroporous fibrous polymeric adsorbent containing amidoxime chelating functional group. Reactive and Functional Polymers, vol. 57, no. 1, pp. 67–76, 2003.

[14] Anirudhan T. S. Tharun A. R. Rijith S. Suchithra P. S. Synthesis and characterization of a novel graft copolymer containing carboxyl groups and its application to extract uranium (VI) from aqueous media. Journal of Applied Polymer Science, vol. 122, no. 2, pp. 874–884, 2011.

[15] Seko N. Katakai A. Hasegawa S. Tamada M. Kasai N. Takeda H. Sugo T. Saito, K. Aquaculture of uranium in seawater by a fabric-adsorbent submerged system. Nuclear Technology, vol. 144, no. 2, pp. 274–278, 2003.

[16] Slocum A.H. Fennell G.E. Dundar G. Hodder B.G. Meredith J.D.C. Sager M.A. Ocean Renewable Energy Storage (ORES) System: Analysis of an Undersea Energy Storage Concept. Volume: 101, Issue: 4, Proc of IEEE, April 2013, pp906-924.

[17] Rabl, A., 1976. Tower reflector for solar power plant. Solar Energy 18, 269-271.

[18] Yogev, A., Kribus, A., Epstein, M., Kogan, A. Solar tower reflector systems: a new approach for high-temperature solar plants. International journal of hydrogen energy 23, 239–245. 1998.

[19] Epstein, M., Segal, A., Yogev, A. A molten salt system with a ground base-integrated solar receiver storage tank. Le Journal de Physique IV 9. 1999.

[20] Trombe, F., Le Phat Vinh, A. Thousand kW solar furnace, built by the National Center of Scientific Research, in Odeillo (France). Solar Energy 15, 57–61. 1973.

[21] Slocum, A.H. Codd D.S. Buongiorno J. Forsberg C. McKrell T. Nave J.C. Papanicolas C.N. Ghobeity A. Noone C.J. Passerini C. Rojas F. Mitsos A. Concentrated Solar Power on Demand. Solar Energy 85 (2011) 1519-1529.

DEVELOPMENT OF HYBRID NANO-STEREOLITHOGRAPHY SYSTEM USING EVANESCENT LIGHT AND PROPAGATING LIGHT FOR HIGH THROUGHPUT FABRICATION

Kodai Miyakawa, Ryo Matsuzawa, Satoru Takahashi, and Kiyoshi Takamasu
Department of Precision Engineering
The University of Tokyo
Bunkyo-ku, Tokyo, Japan

INTRODUCTION

In recent years, micro-fabrication technologies have developed dramatically and fabrication methods have become required, by which small devices on the order of micrometer can be fabricated precisely. In particular, methods of fabricating MEMS and microscopic optical devices as typified by a photonic crystal are in huge demand. Micro-stereolithography is a micro-manufacturing method that can fabricate complex 3D microstructures by curing liquid photosensitive resin in a layer-by-layer process [1]. Making thickness of a layer thin is important for high resolution laminating. By this method, small 3D objects with micrometer resolution can be fabricated rapidly.

However, conventional micro-stereolithography method has some technical issues for higher resolution than micrometer. Since it uses propagating light as the exposure energy, surplus growth is generated, which causes a dimension error and makes it difficult to fabricate a complex structure like overhang. Various approaches have been demonstrated to resolve these issues [2][3][4][5].

In this study, we propose a novel stereo-lithography method that uses evanescent light as the exposure energy instead of propagating light [6]. Since an evanescent light energy does not propagate but localizes within the near-field region, no surplus growth is generated. By this unique method, we intend to establish a nano-stereolithography method that can fabricate complex 3D microstructures with a resolution of sub-micrometer.

The purpose of this paper is to develop a hybrid nano-stereolithography system which uses not only propagating light but also evanescent light. This system is capable of exposing resin to propagating light which numerical aperture is controlled. Using this developed system, we carried out experiments in order to examine whether or not the system has fundamental important functions, that is propagating light exposure, evanescent light exposure and lamination.

CONCEPT OF NANO-STEREOLITHOGRAPHY

Evanescent light

When light crosses materials with different refractive indices, the light beam will be partially refracted at a boundary surface, and partially reflected. Assuming that an incident angle is larger than the critical angle, the light beam will totally reflect back internally. Under this optical condition, nevertheless, there occurs partially localized energy at the boundary (FIGURE 1). The energy is called evanescent light and exists in 100 nm scales.

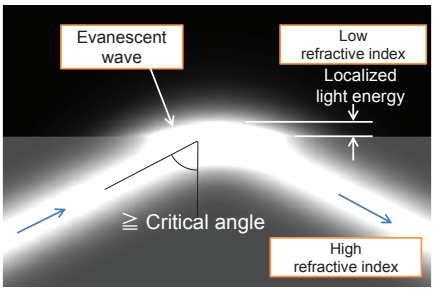

FIGURE 1. Generation of evanescent light.

Nano-stereolithography

FIGURE 2 shows a schematic diagram of the flow of a nano-stereolithography method using evanescent light. First, the incident beam under the total internal reflection condition generates evanescent light at the boundary, which cures liquid photosensitive resin (Figure 2(a)). Next the cured resin adhering on the base rod is lifted and liquid resin is refilled at the boundary surface (Figure 2(b)). Then the evanescent light, which is modulated by a variable mask, exposes and cures a next layer (Figure 2(c)). Doing this loop repeatedly, desired object is fabricated with extremely thin single layer (Figure 2(d)).

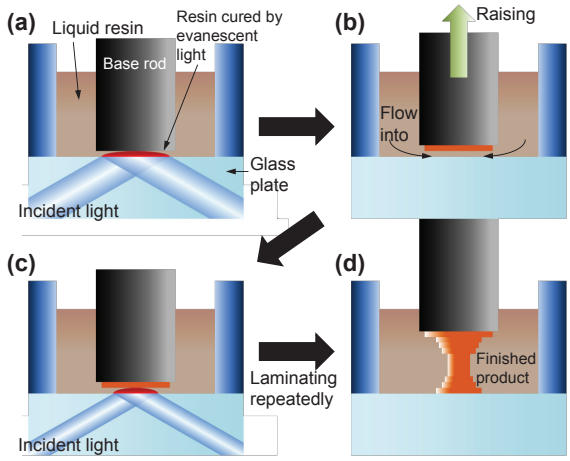

FIGURE 2. Flow of the nano-stereolithography method using evanescent light.

DEVELOPMENT OF A HYBRID NANO-STEREOLITHOGRAPHY SYSTEM

Principles of a nano-stereolithography

FIGURE 3 shows a fundamental optical system of a hybrid nano-stereolithography. It is realized mainly by "image source unit" (Controlling lateral light distribution), "filter unit" (Changing a type of incident light or a numerical aperture of propagating light exposure), and "exposure unit" (Generating an evanescent light). FIGURE 3 means that an image source unit (I) is imaged to an exposure surface (I') and a filter unit is put at the position (F) of a Fourier transform plane of the position (I).

When the controllable filter is set as an annular mode, an evanescent light can be generated at exposure unit. That is because lights within critical angle are cut off. On the other hand, when the controllable filter is set as an aperture mode, the incident light becomes a propagating light. The diameter of the aperture determines the numerical aperture of the propagating light exposure. As mentioned above, the filter unit provides us the method to alter the type of incident light.

The exposure unit needs to generate evanescent wave when the controllable filter is set as an annular mode, that is, an incident light has to be totally reflected. In order to realize this, the refractive indices of the objective lens, the immersion oil and the cover glass are the same and that is higher than the refractive index of a photosensitive resin.

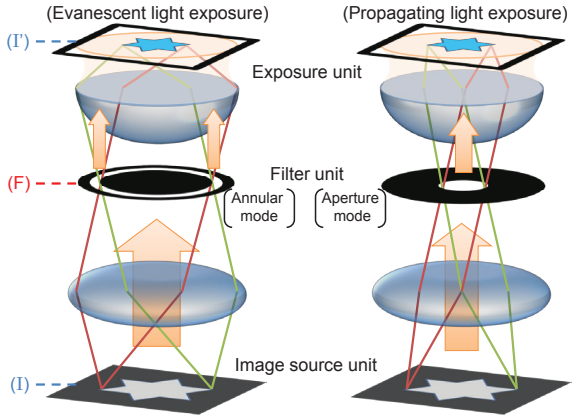

FIGURE 3. Schematic views of the function of controllable filters.

We developed the hybrid nano-stereolithography system shown in FIGURE 4 by installing the fundamental optical system mentioned above. By tube lenses, the image source unit (i) is imaged to the position (i') and (i''), and the filter unit (f) at the position of the Fourier transform plane of (i) is images to (f').

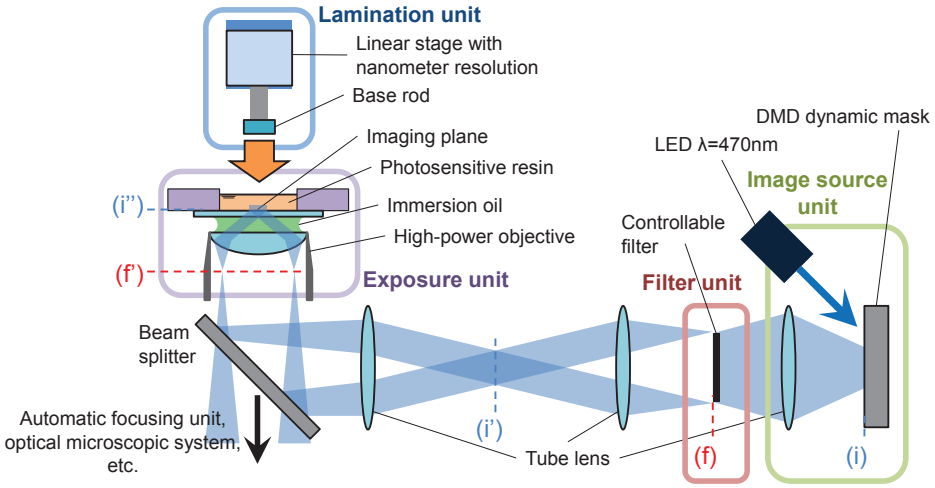

FIGURE 4. Hybrid Nano-stereolithography System Using Evanescent Light and Propagating Light.

The input unit consists mainly of a light emitting diode providing visible at 470 nm as a light source, and a digital mirror device (DMD, mirror size:13.7 μm, 769 x 1024 mirrors) for a mask. This unit provides us the method to control lateral light distribution by using this DMD masks.

The exposure unit consists mainly of a high-power objective and a resin tank located on the objective. A resin tank is a hollow place which bottom is a cover glass. FIGURE 5 is an enlarged view of the exposure unit. The refractive indices of the objective lens, the immersion oil and the cover glass (n = 1.78) are higher than that of a photosensitive resin (n = 1.5). That is the critical angle is about 57 degrees. This unit enables us to generate an evanescent light.

We employed For the lamination unit consists mainly of nano-order resolution linear stage and base rod. This unit provides us the method to laminate extremely thin layers.

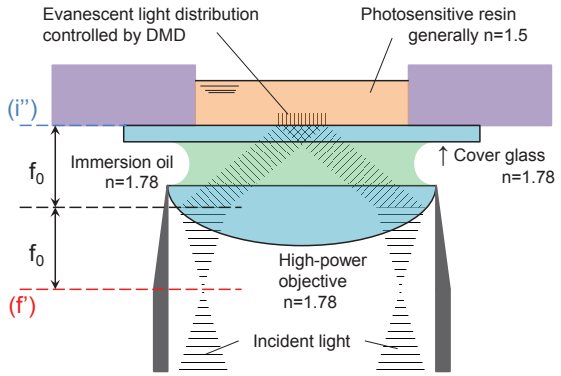

FIGURE 5. Exposure unit consists of solid immersion lens and resin tank.

FUNDAMENTAL EXPERIMENT FOR HYBRID FABRICATION

A hybrid nano-stereolithography needs mainly three important functions, that is propagating light exposure, evanescent light exposure and lamination of cured resin. We examined whether the developed hybrid nano-stereolithography system has these functions. In this experiment, we intended to fabricate a pillar shape by propagating light and a thin layer by evanescent light, and then laminate these cured resins.

Experimental conditions

We employed TMP-A (light acrylate) and Irgacure 784 (photoinitiator) as photosensitive resin. The refractive index of this photosensitive resin is 1.5.

FIGURE 6 shows the procedure of fabrication. First, the photosensitive resin is exposed to propagating light with power of 46.3 mW/cm^2 and numerical aperture of 0.28, for 16 seconds. Then the cured resin is pulled up by base rod and the liquid resin is exposed to evanescent light with power of 503 mW/cm^2, for total 3 seconds.

The lateral light distribution of incident light is generated by the DMD in the image source unit. The masks we used are a star shape for propagating light exposure and a letter shape for evanescent light exposure.

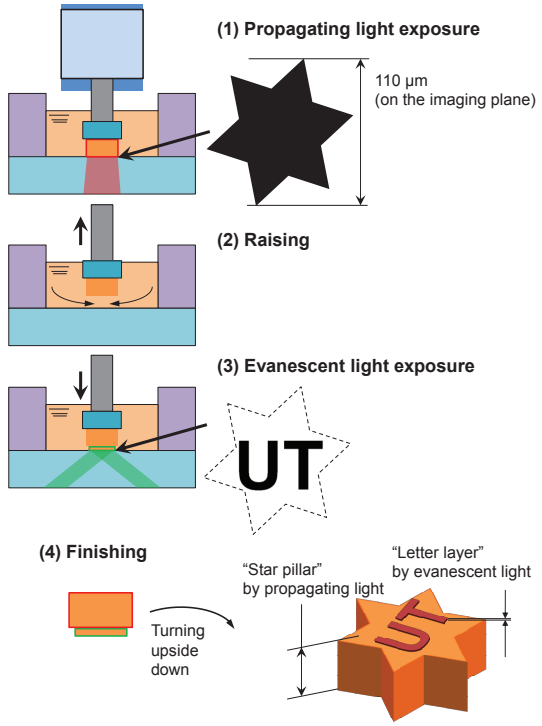

FIGURE 6. Procedure of fabrication experiment.

Results and discussion

Under the experimental condition mentioned above, a micro star pillar is fabricated. FIGURE 7 shows optical microscope images that observed the fabricated object. The star pillar is observed and the height of this pillar is 40 μm. This result shows that we can fabricate a pillar shape by using propagating light exposure.

However the letter layer is not observed in this image. That is because the letter layer is so thin that an optical microscope cannot observe it. FIGURE 8 shows the image of differential interference contrast microscope in order to observe the letter layer. The letter "UT" can be

seen on the top of the star pillar. The thickness of this letter layer is found about 100 nm that is measured by AFM analysis. This result shows that we can fabricate extremely thin single layer with a desired lateral shape by using evanescent light exposure. This result also suggest that lamination of cured resins succeeded.

Therefore it is proved that the developed hybrid nano-stereolithography system has three important functions, that is propagating light exposure, evanescent light exposure and lamination of cured resin.

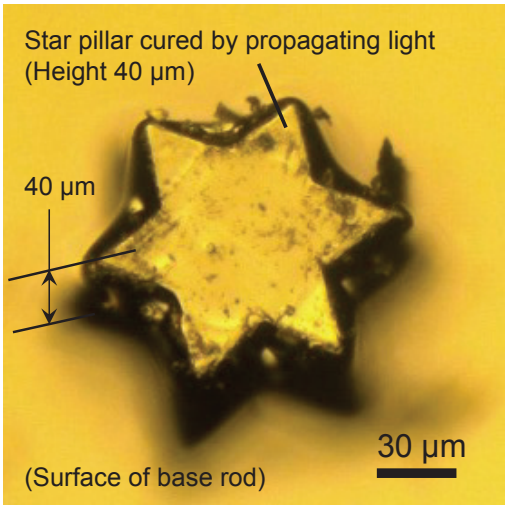

FIGURE 7. Optical microscope image of the fabricated object.

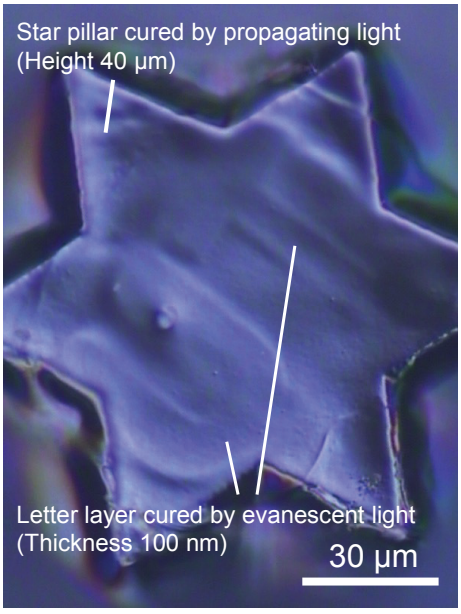

FIGURE 8. Differential interference contrast microscope image of the fabricated object.

CONCLUSION

We developed the hybrid nano-stereolithography system which consists mainly of an input unit, a filter unit, an exposure unit and a lamination unit. The system has three functions, that is propagating light exposure, evanescent light exposure and lamination of cured resin.

In order to verify these functions, we carried out the fundamental experiments that fabricates a lamination of pillar by propagating light exposure and a layer by evanescent light exposure. The pillar of 40 μm height and the layer of 100 nm thickness is fabricated.

This result suggest that a hybrid nano-stereolithography fabrication works well and this system contribute to next-generation nanometer scale fabrication methods.

ACKNOWLEDGEMWNT

This work has been partially supported by JSPS under the Grant-in-Aid for Scientific Research (A) and for Challenging Exploratory Research. The light acrylate is provided by Kyoeisha Chemistry co., ltd.

REFERENCES

[1] Paul F. Jacobs, 1992, Rapid Prototyping & Manufacturing, *SME*.

[2] T. Hayashi, T. Miyoshi, Y. Takaya and S. Takahashi, 2000, Nonlaminate Micro Stereolithography Using TFT LCD, *Proceedings of the 2nd euspen*, 1: 98-106.

[3] S. Kawata, H B. Sun, T. Tanaka, and K. Takada, 2001, Finer features for functional microdevices, *Nature*, 412: 697-698.

[4] S. Maruo and K. Ikuta, 2002, Submicron stereolithography for the production of freely movable mechanisms by using single-photon polymerization, *Sensors and Actuators A*, 100: 70-76.

[5] Kock K. Seet, V. Mizeikis, S. Juodkazis, and H. Misawa, 2006, Three-dimensional circular spiral photonic crystal structures recorded by femtosecond pulse, *Journal of Non-Crystalline Solids*, 352: 2390-2394.

[6] Y. Kajihara, T. Takeuchi, S.Takahashi, and K.Takamasu, 2006, Development of a nano-stereolithography system using evanescent light for submicron fabrication, *Proceedings of ASPE annual meeting*: 111-114.

MICRO-LASER ASSISTED SINGLE POINT DIAMOND TURNING FEASIBILITY TESTS OF SINGLE CRYSTAL SILICON

Deepak Ravindra[1] and John Patten[2]
[1] Micro-LAM Technologies, LLC
Battle Creek & Kalamazoo, MI, USA
[2] Manufacturing Research Center
Western Michigan University
Kalamazoo, MI, USA

ABSTRACT

Semiconductors and ceramics such as silicon, silicon carbide, quartz, etc. are increasingly being used for industrial applications [1]. These materials are hard, inert, light weight and strong. All these properties make them ideal candidates for tribological, semiconductor, MEMS and optoelectronic applications [1, 2]. Manufacturing these material are extremely challenging because of their hardness, poor machinability and brittle characteristics [1, 2]. Due to the low fracture toughness of these materials, severe fracture can be resulted when trying to achieve high material removal rates [1]. In the previous research work, it has been demonstrated that ductile mode machining of semiconductors and ceramics is possible due to the high pressure phase transformation (HPPT) occurring in the material [1]. To study the ductile response of single crystal (100) silicon (Si), a nominally brittle material, single point diamond turning (SPDT) is coupled with the micro-laser assisted machining (μ-LAM) technique.

INTRODUCTION

The patented μ-LAM technology directly heats and thermally softens the workpiece material, in the chip deformation and generation zone, increasing the material's ductility. The fundamental concept of this process is illustrated in Figure 1. Improved ductility that results from reduced material hardness allows for easier chip formation, decreased brittleness and ultimately higher material removal rates, i.e. better tool performance and increased productivity, which leads to lower manufacturing costs.

Ceramics and semiconductors are naturally brittle materials at room temperature and are known for their poor machinability. However, ductile-regime machining is possible under certain conditions (due to the high pressure phase transformation phenomenon). This can be achieved if machining occurs at depths less than the critical depth of cut. Beyond this value, a ductile-to-brittle transition (DBT) occurs and the material behaves in a brittle-fracture manner. One of the initial steps before carrying out any form of ductile mode machining on brittle materials is to define a DBT or critical depth. In previous research work, it has been demonstrated that ductile regime machining of brittle materials is possible due to the HPPT occurring in the material caused by the high compressive and shear stresses induced by the single point diamond tool tip [3,4]. To further augment the ductile response of these materials, traditional single point diamond turning tests are coupled with a micro-laser assisted machining technique.

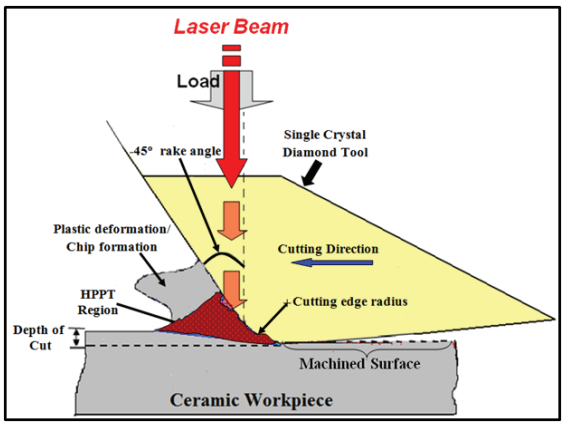

FIGURE 1. Schematic of the μ-LAM process

This paper discusses a study done to analyze and compare machining data from SPDT tests on single crystal Si with varying input parameters such as laser power, cross feed, spindle speed and applied load. A total of 7 regions were machined with different μ-LAM

parameters. For all machined regions, a constant applied load of 100mN is used. The varying machining parameters experimented include three spindle speeds (10, 20 and 30 rpm), three heating conditions (0W, 5W and 10W), and three cross-feed rates (10, 20 and 30 μm/rev).

It is important to note that the process is not speed restricted as μ-LAM speeds of up to 1000 rpm have been achieved on an industrial diamond turning machine (DTM). However, since the current experimental setup relies on a force feedback loop, the cutting process is speed limited to ensure force stability and good uniformity in the cutting process. The purpose was to study the effectiveness of the μ-LAM process and the benefits of the thermal softening effect as a function of cutting speeds, laser power and feeds.

EXPERIMENTAL APPROACH

The Universal Micro-Tribometer (UMT) manufactured by CETR-Bruker Inc. was modified and coupled to the μ-LAM system to perform all of the machining tests (setup shown in Figure 2). A profession instrument (PI) air bearing spindle was integrated in to the system to obtain mirror quality surface finishes. The load controlled UMT was primarily developed to perform comprehensive micro-mechanical tests of coatings and materials at the micro scale [5]. A single point diamond tool with a 1.3 mm nose radius, 45 degree rake angle and 5 degree clearance angle was used for this cutting operation.

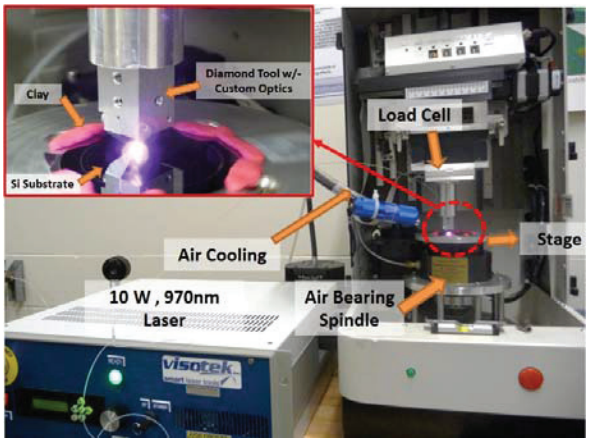

FIGURE 2. Single point μ-LAM setup.

A Visotek infrared diode laser (λ= 970 nm and P_{max}= 10 W) with a Gaussian beam profile of diameter approximately 100 μm is used in this study. The laser beam is guided through a fiber optic cable to an in-built collimator, which is passed through custom optics within the tool assembly. The beam is delivered through an optically transparent single crystal diamond tool and precisely focused at the cutting edge. A scratch/cutting test setup along with the 10W laser powered μ-LAM system used for all the experiments discussed in paper is shown in Figure 2.

All cuts performed in this study were in the ductile regime. The aim was to perform feasibility μ-LAM tests on Si that would be a precursor to scaling up this technique for an actual manufacturing process that involved SPDT. The effects of varying μ-LAM parameters were studied by measuring and analyzing the depth of cuts, cutting forces, surface roughness and tool condition. The depth of cuts and surface roughness of the machined regions were measured using a white light interferometer. The tool condition was periodically monitored using high magnification optical microscopy.

RESULTS SUMMARY AND DISCUSSION

Since the UMT is a load controlled equipment, the desired thrust/applied force is inputted and the resultant depth of cut is measured. This provides the opportunity to maintain the applied force constant for all cut regions and studying the depth of cut effect as a function of laser power, spindle RPM and cross feed. The depth of cut measurement in this case directly corresponds to the thermal softening effect and thus serves as a good measure of the effectiveness of the μ-LAM process.

Figure 3 compares three machined regions where only the laser powers are varied from 0W (room temperature) to 10W. Note that the applied load, spindle RPM and cross feed rates remained constant at 100 mN, 10 RPM and 10 μm/rev respectively.

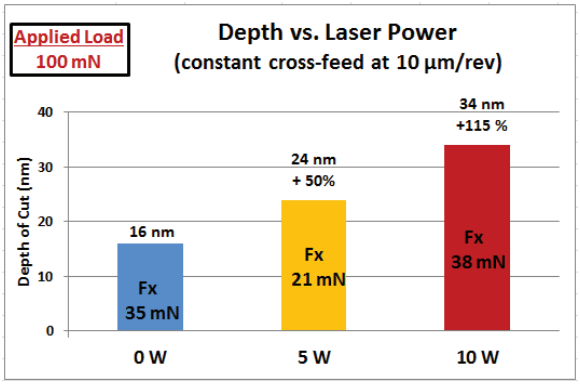

FIGURE 3. The effect of laser power on the depth of cut.

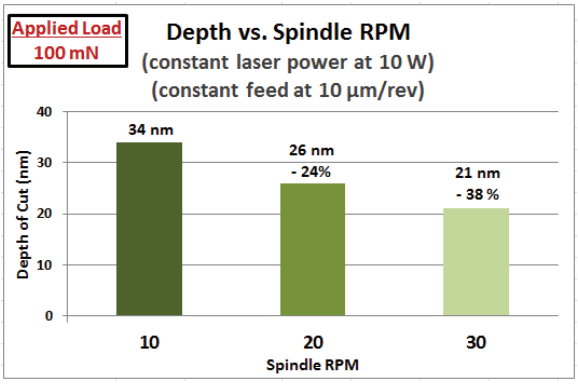

FIGURE 4. The effect of spindle rpm (cutting speed) on the depth of cut.

The results from the analyses suggest that the depths of cuts for all regions with laser are higher than that of no laser power (room temperature). This greater depth directly translates to increased material removal rates and higher productivity while producing a defect free part with no brittle fracture. In addition, the cutting forces for the machined regions with laser are lower suggesting extended tool life for large scale production.

The next analysis carried out was on the cutting speed or spindle rpm. In this set of cuts, all machining parameters such as applied load, laser power and cross feed rate was kept constant. The only parameter altered was the spindle RPM which ran at 10, 20 and 30 RPM. The results in Figure 4 suggest that the cutting speed certainly has an impact on the machined region's depth of cut for an equal applied load (in this case 100 mN) and constant laser power (10W). As the cutting speed increases, depth of cut decreases indicating a decrease in the thermal softening effect. This can be solved by either increasing the laser power proportionately or significantly increasing the spindle RPM to ensure sufficient heat is retained at the tool-workpiece contact spot at each revolution (i.e. at higher RPM's, the Δtemp. required for thermal softening reduces).

The final set of cuts aimed to study the effect of the depth of cut as a function of cross feed rates. Note that all other machining parameters maintained constant for this particular analysis.

From the figure, it is observed that depth of cut significantly decreases as the cross feed increases. This pattern is true even for conventional SPDT as when the cross-feed increases, the width of the tool path and contact area in every subsequent cut decreases causing a shallower depth of cut. This is consistent with the current scientific understanding and it is true for both, 'no laser' and 'with laser' machining conditions [2].

Higher depths were obtained at 10 µm feed than other feeds such as 20 µm and 30 µm. Which represents higher material removal rate or productivity at 10 µm feed. But lowest depth and highest cutting force were obtained with 10 µm feed at 0W cut, it is a good indication that the lack of thermal softening effect due to no laser power.

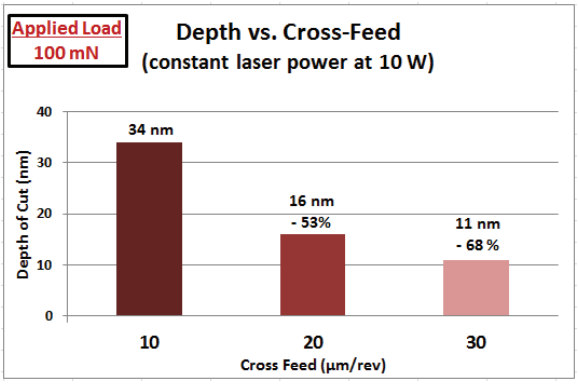

FIGURE 5. The effect of cross feed rates on the depth of cut.

The machined regions were carefully analyzed under a high magnification microscope to detect any possible cracking or fracture behavior. Figure 6 shows a more reflective Si machined surface (than the polished wafer) obtained using the optimized μ-LAM parameters.

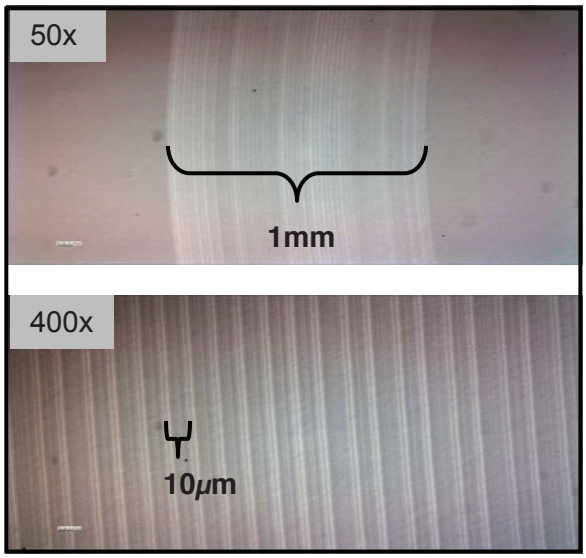

FIGURE 6. Optical microscope images at 50x and 400x magnifications showing the machined region at optimized μ-LAM parameters: 10W, 10rpm & 10 μm/rev feed.

The machined region in Figure 1 indicate no signs of brittle fracture with distinct cross feedmarks, further confirming a purely ductile mode material removal process. It is important to note that the surface finish of the machined regions are either better or comparable to the as received polished wafer surface (Ra < 5 nm). No tool wear was detected in these tests due to small machined areas (short track length covered by the tool), however, more testing will be performed in the future to machine a larger area for tool wear analysis.

CONCLUSION

These results for the feasibility study show that the micro-laser assisted single point diamond turning tests were successful in demonstrating the benefits of the thermal softening effect from preferential laser heating. This also suggests that the μ-LAM technology would be a suitable candidate for manufacturing Si once higher productivity, improved surface finish and lower tool wear can be demonstrated in larger scales. Lower cutting forces obtained from the μ-LAM process are favorable to minimize tool wear while machining hard and abrasive materials such as Si, SiC, sapphire, spinel and more. The results from this study also will benefit the manufacture of brittle materials as laser heating is proven to decrease the brittle response in ceramics and semiconductors, which can result in high productivity rates (i.e. higher material removal rates).

The key to a successful and productive ductile mode machining of brittle materials is understanding the material removal mechanics and optimizing the processing parameters. The findings in this study will lead to the development of improved machining technologies by utilizing the ductile mode material removal mechanism and reduced brittle mode material removal in the manufacture of ceramics and semiconductors.

ACKNOWLEDGEMENTS

The authors would like to thank the National Science Foundation (SBIR Phase I/IB Award #: IIP-1214772) for funding this study. The authors would also like to thank II-VI Foundation for their funding via the block gift program.

REFERENCES

[1] Deepak Ravindra, BogacPoyraz and John Patten. The Effect of Laser Heating on the Ductile to Brittle Transition of Silicon. The 5th International Conference on MicroManufacturing (ICOMM/4M), Wisconsin, USA, 2010.

[2] Deepak Ravindra. Ductile Mode Material Removal of Ceramics and Semiconductors. Ph.D. Dissertation, 2010, Western Michigan University, Kalamazoo, Michigan, USA.

[3] Deepak Ravindra, Muralidhar K. Ghantasala and John Patten. Ductile Mode Material Removal and High-Pressure Phase Transformation in Silicon during Micro-Laser Assisted Machining. Journal of

Precision Engineering (ASPE), Vol. 36, Issue 2, pp. 364-367 (2011).

[4] Deepak Ravindra, H. Bogac Poyraz and John Patten. The Effects of Laser Heating on the Ductile to Brittle Transition of Silicon Carbide. American Society for Precision Engineers (ASPE) 25th Annual Meeting, Atlanta, Georgia (2010).

[5] Deepak Ravindra and John Patten. Ductile Regime Single Point Diamond Turning of Quartz. International Conference on Advances in Materials and Processing Technologies (AMPT2010). AIP Conference Proceedings, Volume 1315, pp.1029-1034 (2011).

FULLY-AUTOMATED IN VIVO SINGLE CELL ELECTROPHYSIOLOGY

Jamison Go[1], Aaron Fan[1], Coby Lu[1], Suhasa Kodandaramaiah[1,2], Gregory L. Holst[1], William Stoy[1], Ilya Kolb[1], Edward S. Boyden[2], and Craig R. Forest[1]
[1]Woodruff School of Mechanical Engineering
Georgia Institute of Technology
Atlanta, GA, USA
[2]Media Lab and McGovern Institute
Massachusetts Institute of Technology
Cambridge, MA, USA

Neurons communicate information through fluctuations in the electrical potentials across their cellular membranes. Although scientists have been recording the electrical activity of neurons for more than a century, it was the advent of intracellular recording technology, or whole-cell patch clamping, which allowed the measurement of neuronal membrane potential that enabled precise characterization of neuronal function, winning Hodgkin and Huxley the Nobel Prize in 1963 and Neher and Sakmann the Nobel Prize in 1991. However, whole-cell patch clamping is something of an art form, requiring great skill to perform and has thus been primarily limited to *in vitro* experiments, a select few *in vivo* experiments, and in very limited applications in the awake brain [1]. Our team has recently developed a robot that *automatically* performs patch clamping *in vivo,* by algorithmically detecting cells through analysis of a temporal sequence of electrode impedance changes. Using it, we have demonstrated good yield, throughput, and quality of electrophysiology recording in mouse cortex and hippocampus [2]. With this autopatching robot enabling routine access to electrical and molecular properties of neurons embedded in intact tissue, systematic and scalable *in vivo* patch clamping experiments have become possible.

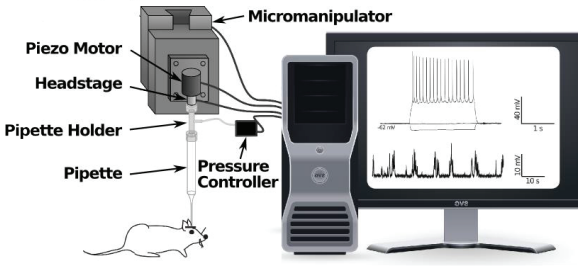

FIGURE 1. The autopatcher: a robot for in vivo patch clamping with representative current clamp traces during whole cell automated patch clamping of a cortical neuron.

This autopatching robot (See Figure 1) utilizes a glass pipette to establish electrical and molecular connections to the insides of single neurons embedded in intact tissue and exhibits excellent signal quality and temporal fidelity, useful for understanding not only how neurons compute during behavior, but how their physiology changes in disease states or in response to drug administration. While this automation is powerfully useful, it still requires manual pipette replacement between each 15 minute single cell electrophysiology experiment. This includes a 3-4 minute preparation process of back-filling the pipette with an ionic fluid, threading a conductive silver wire into the inner diameter of the pipette, and securing the pipette to the headstage. The frequency and duration of pipette swaps thus require constant human supervision of the autopatcher. However, if this automated patch clamp robot were to be integrated with pipette exchange hardware and storage magazine, one could perform *fully-automated* in vivo single cell electrophysiology without human intervention, enabling vastly increased throughput (e.g., hundreds of cells/day) by a single human operator.

DESIGN AND OPERATION

Figure 2 shows the automated pipette exchange robot capable of performing 20 serial electrophysiological recordings without any human interaction. It consists of a pipette storage magazine or carousel, and two motorized linear stages, one oriented vertically and one oriented horizontally. The carousel uses a stepper motor to rotate the pipette into position beneath the collet and detects the

correct position using a photointerrupt sensor that is triggered once the pipette arrives in the correct location. The vertical linear stage raises the carousel to insert the steel pipette holder into the collet.

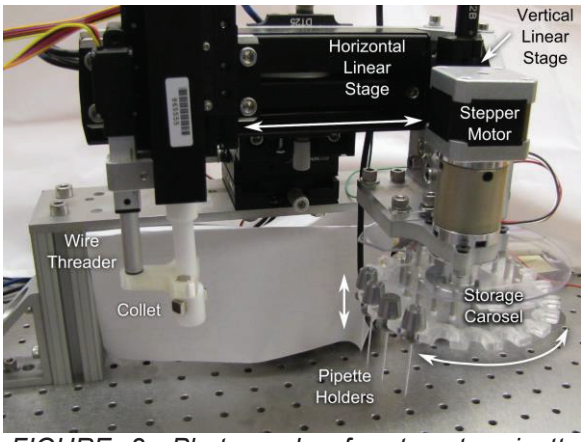

FIGURE 2. Photograph of automate pipette exchange robot. It consists of 2 vertical linear actuators, 1 horizontal linear actuator, a pipette storage magazine, pipette holders, and a restraining collet.

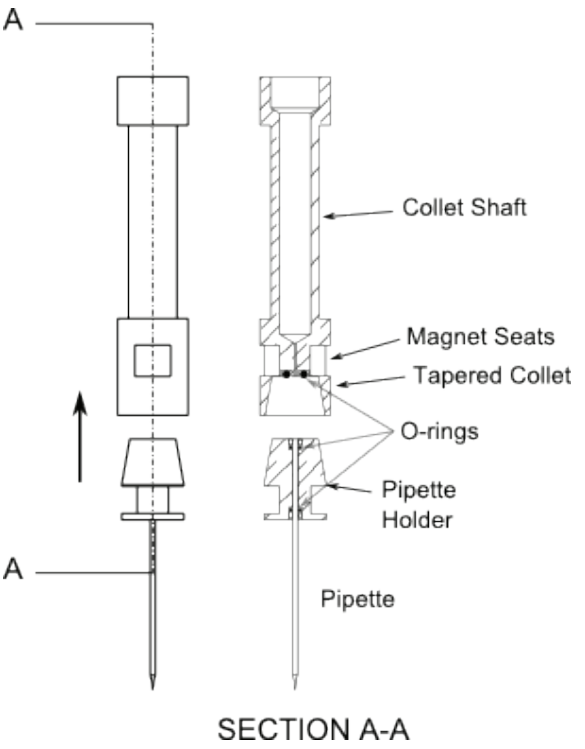

FIGURE 3. Schematic of collet and steel pipette holder. Magnets in the magnet seats retain the steel pipette holder in the collet. The tapered features on the pipette holder and collet align the pipette to the 350 micrometer hole through which the silver wire is threaded into the pipette.

Figure 3 shows a crossection of the steel pipette holder and the collet. The matching tapered features on the pipette holder and collet centers the pipette in the collet and allows for some initial misalignment. The pipette holder uses 2 AS568-001 o-rings to align the 1mm borosilicate pipette to the center of the pipette holder. When the pipette holder is inserted into the collet, it also compresses a larger o-ring between the top surface of the pipette holder and the collet. This seal allows the pressure within the pipette to be controlled which is necessary for obtaining a patch clamp recording. The collet is held inside the collet by two neodymium magnets on either side of the collet. The steel collet is pulled toward these magnets providing a passive retaining force which also compresses the o-ring against the collet. Once the pipette holder is fully seated, another small linear actuator moves two neodymium magnets down along the sides of the collet shaft, which push a steel bead attached to a silver chlorided wire through the 350 micrometer hole in the center of the collet. This threads the electrode wire into the pipette and creates the electrical connection between the Axon Multiclamp 700B amplifier and the ionic solution inside the pipette. This solution and wire conduct the picoamp ionic currents from the neuron to the amplifier.

Once the pipette holder is seated and the wire is inserted, the horizontal linear stage moves the collet to the far left side where the mouse is located. Then the automated patch clamp algorithm activates the piezo motor attached to another vertical linear stage to lower the pipette into the brain to begin searching for cells. Automated control software written in LabView controls the hunt for neurons and handles the recording and stimulation of the cell once a patch has been established onto the cell. Once the recording session is complete, the piezo motor retracts the pipette out of the brain and the horizontal linear stage returns the collet and pipette holder to the carousel. The carousel then descends to extract the pipette holder from the collet. Once it is free, the carousel rotates the next pipette where it ascends to insert the next pipette holder into the collet. This process lasts only 19 seconds compared to the 2-5 minutes required to change it manually and can operate unsupervised.

The traditional manual procedure involves threading the silver wire by hand, securing it to the pipette holder and then aligning and lowering it into the 1mm in diameter craniotomy about 20-50 micrometers above the surface of the brain. This is accomplished with the aid of as stereomicroscope and 3 axis motorized manipulators. This alignment process is time consuming and prone to error as any contact with the 1-2 micrometer tip of the pipette will break or contaminate the precision surfaces used to create the patch on the cell.

POSITIONAL REPEATABILITY

The alignment taper and linear actuators easily align the pipette within the 1mm craniotomy as show in Figure 4. It is critical that the pipettes return to the same location in the brain after the pipette is exchanged so that the recordings are obtained from the correct brain structure. In the somatosensory barrel cortices in mice, for example, structures range in diameter from 150 to 300 micrometers and each correspond to an individual whisker on the snout of the mouse. It is critical, therefore, that the robot accurately positions the pipette above the barrel corresponding to the whisker that is being stimulated by the scientist.

The pipettes all returned to within a 200 micrometer radius after being exchanged. Figure 4b shows a magnified view of the position measurements and shows the systematic error introduced by the pipette holders. The measurements were taken by cycling through the pipette holders sequentially and measuring the position of the pipette after each exchange. It shows good repeatability with each pipette holder suggesting systematic error in the manufacturing of the pipette holders or in the insertion of the pipette itself into the holder.

These measurements were acquired using an automated image acquisition and processing system using two orthogonally oriented microscopes that image the shaft of the pipette when it returns to its position above the craniotomy (see Figure 5). It uses an edge detection algorithm to locate the center of the pipette in the images and then calculates its position using a calibration factor that correlates the number of micrometers per pixel for each camera. Figure 4 shows 104 independent measurements taken using 4 different pipette holders.

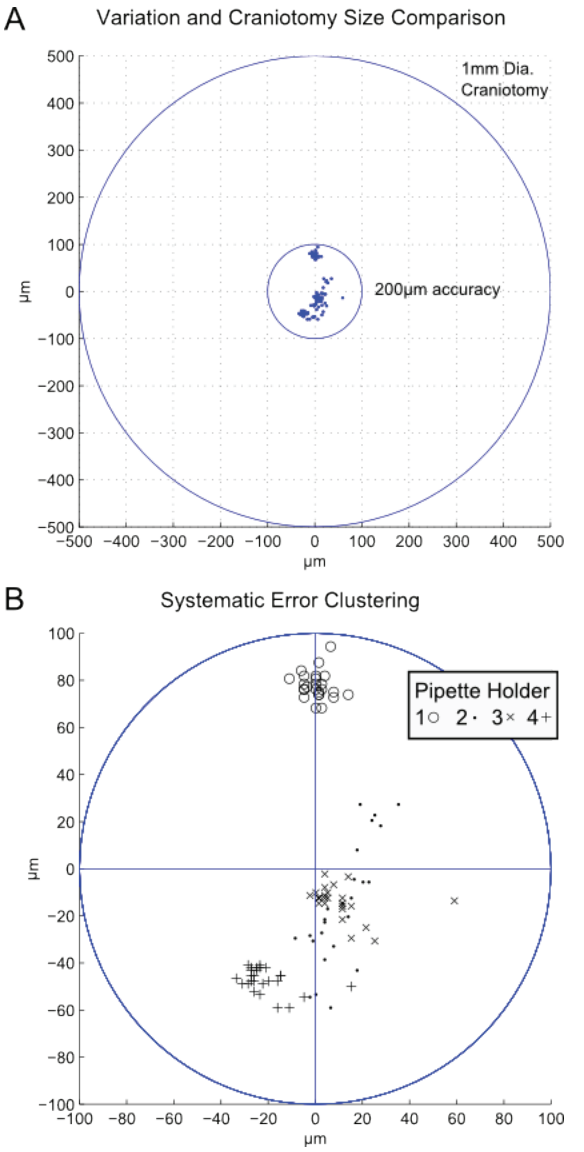

FIGURE 4. Shows the positional variation of the pipette exchange robot. 4a shows the relative size comparison between the 1mm diameter craniotomy and the measured position of 104 position measurements taken after exchanging the pipette. 4b shows systematic due to manufacturing variation in the pipette holders and variation in the manual insertion of the pipettes into the holders.

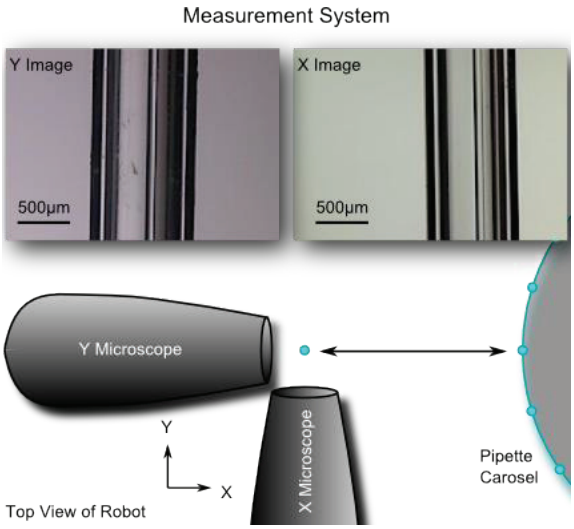

FIGURE 5. Diagram showing the measurement system used to obtain the positional accuracy data in Figure 4. It is a top view of the robot showing the position of the microscopes while imaging the shaft of the pipette. The inset images are representative of the images processed to measure the position data.

CONCLUSIONS

The patch clamp robot combined with this pipette exchange robot have fully automated the art of patch clamping *in vivo*. Because the probability of obtaining a successful patch clamp recording using a single pipette is less than 30%, many pipettes are uses to obtain a few recordings. This robot significantly reduces the time to exchange these pipettes and removes the final manual step in patch clamping. Serial patch clamp recordings can now be performed without any human intervention and allows scientists to spend more time analyzing data rather than performing tedious repetitive tasks. In addition, several experimental setups can now function in parallel with occasional oversight by a technician. This will significantly increase the quantity of data neuroscientists can gather and push the state of the art of patch clamping to a new level.

The current embodiment of the pipette exchange robot shows sufficient positional accuracy and speed. Our future work will focus on reducing the variability between pipette holders and demonstrate the robot performing sequential, fully automated, patch clamp recordings, *in vivo*.

REFERENCES

[1] Poulet JF, Fernandez LM, Crochet S, Petersen CC, Thalamic control of cortical states, *Nat Neurosci.* Vol 22;15(3):370-2.

[2] S. Kodandaramaiah, G. Franzesi, B. Chow, E. Boyden, C.R. Forest, Automated whole-cell patch clamp electrophysiology of neurons in vivo, *Nature Methods.* Vol 9, p. 585–587.

DIRECTION BASED FILTERING OF FLEXIBLE MODES

T. Groothuijsen[1], J. Eisinger[1], R.Hoogendijk[3], D. Laro[1], J. van Eijk[2], M.Steinbuch[3]
[1]MI-Partners BV
Eindhoven, The Netherlands
[2]MICE BV
Eindhoven, The Netherlands
[3]Eindhoven University of Technology
Department of Control Systems Technology
Eindhoven, The Netherlands

ABSTRACT
A method is shown to deal with bandwidth limiting resonance peaks in MIMO (Multiple Inputs Multiple Outputs) control systems by switching from rigid body decoupling to flexible mode decoupling at these resonance frequencies. This method can be used as an alternative to using a notch filter.

INTRODUCTION

Background
A demonstrator setup for demonstrating and studying control of an overactuated, lightweight, flexible 450 mm wafer chuck (*FIGURE 1*) was built at MI-Partners [1]. This setup consists of a glass chuck mounted on a base with flexures, having three rigid body degrees of freedom: displacement Z and rotations R_X and R_Y. The system has four actuators and three sensors, all in Z-direction.

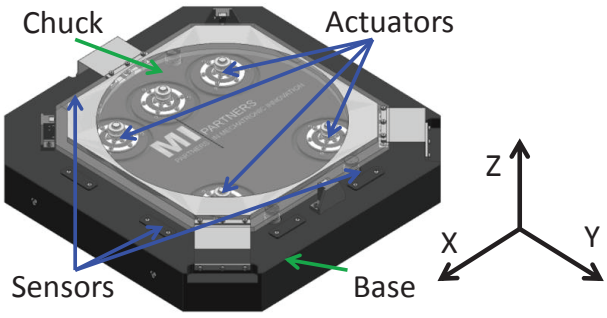

FIGURE 1: System overview.

Control
A decentralized control strategy [2] is used, using static matrices to obtain a diagonalized plant (*FIGURE 2*) for frequencies below the first flexible mode resonance frequency. This strategy results in three decoupled rigid body degrees of freedom. Typically, a PID controller is used for each degree of freedom, with notch filters to supress controller reaction at resonance frequencies.

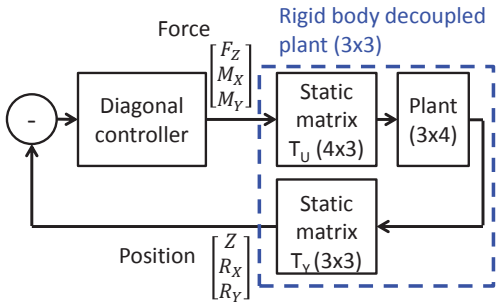

FIGURE 2: Conventional control loop.

Objective
A high control bandwidth of the chuck in Z-direction is desired to suppress low frequency disturbances in Z-direction.

Problem
The idea behind the overactuated design is that the four actuators do not excite the first flexible mode of the chuck (torsion) when exciting the Z, R_X or R_Y directions. This is done in a similar way as described in [3].

In practice, limited excitation of the torsion mode still occurs due to small gain and phase variations between the four actuators. The overactuation leads to a reduction in torsion resonance peak magnitude of approximately 30 dB [1]. However, what remains is a resonance peak with a magnitude of approximately 20 dB greater than the rigid body magnitude at this frequency (*FIGURE 3*).

This remaining resonance peak of the torsion mode of the chuck is limiting the controller bandwidth in Z-direction. This resonance peak is to be handled by the controller.

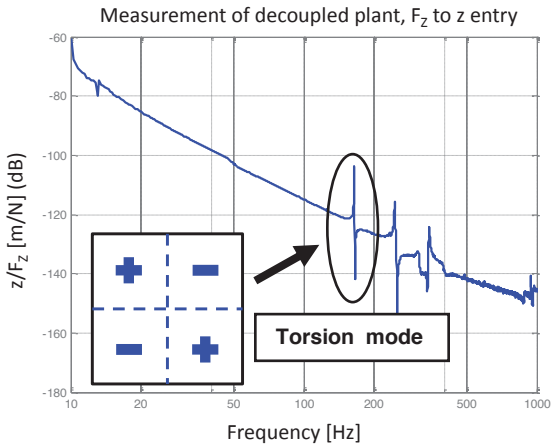

FIGURE 3: F_Z to z entry of decoupled plant, the complete decoupled plant is a 3-by-3 matrix.

Approach

Three examples of how to deal with flexible modes are shown in *FIGURE 4*. The first example is a notch filter, which limits the controller action at a certain frequency. A robust notch filter has to be wider than the resonance peak it is applied to. This results in phase loss, which can also be bandwidth limiting.

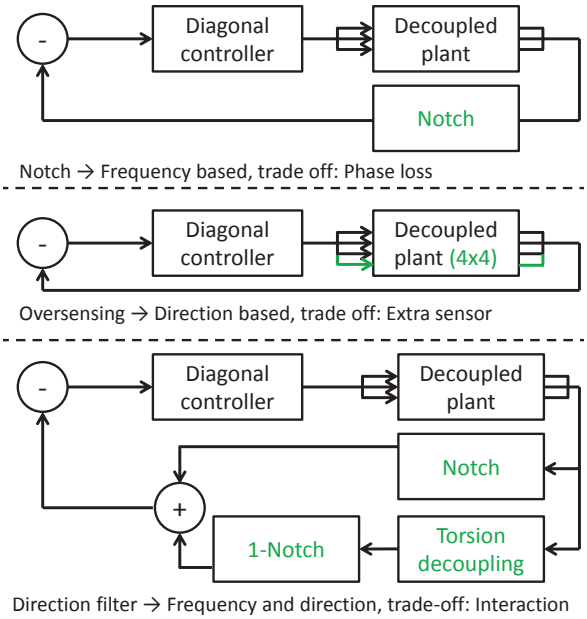

FIGURE 4: Methods to deal with flexible mode.

The second option shown in *FIGURE 4* is oversensing, separating the flexible mode from the rigid body modes on basis of mode shape [4]. The flexible mode will then be unobservable in the rigid body control loops. However, this requires an additional sensor.

The third option from *FIGURE 4* is treated in this text. At the resonance frequency , the coordinate frame in which the controller observes sensor signals is changed to a frame in which the torsion mode is unobservable. The direction filter makes the torsion mode effectively unobservable in the Z-control loop, without phase loss.

Outline

In this text, a dynamic decoupling of sensor signals is used to deal with the torsion resonance peak. Two variants are shown.

The first variant is based on a plant with an equal amount of sensors as it has rigid body degrees of freedom. The main limitations of direction filtering on a conventionally sensed plant are discussed.

The second variant is based on a plant with one more sensor than it has rigid body degrees of freedom. In this case oversensing is used to deal with the first flexible mode, while the dynamic decoupling is used for the second flexible mode.

DIRECTION FILTERING THEORY

Decoupling at plant output

When looking at the frequency response in *FIGURE 5*, it can be split into two frequency ranges. In frequency range A, below the controller bandwidth, rigid body decoupling is preferred. This means that in frequency range A, the Z, R_X and R_Y directions are controlled independently.

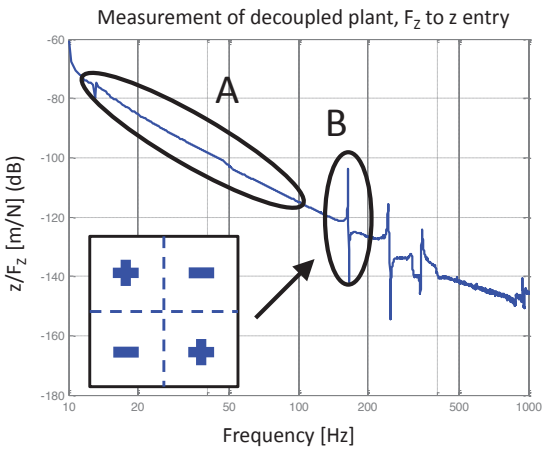

FIGURE 5: Frequency response, force to position in Z-direction.

In frequency range B, it is preferred to make the torsion mode unobservable for stability of the control loop.

Rigid body decoupling

The coordinate frame in which the controller observes sensor signals is defined by decoupling matrix T_Y (*FIGURE 2*). The axes are the sensed components of the eigenvectors of the rigid body modes (Z, R_X and R_Y). With three sensors, these vectors span a three dimensional space.

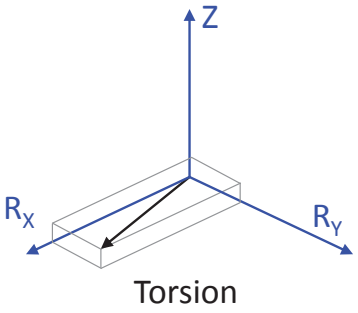

FIGURE 6: Flexible mode eigenvector projected on the decoupled sensor space.

The projection of the torsion mode eigenvector on the decoupled sensor space is shown in (*FIGURE 6*). This torsion vector has a projection on the Z, R_X and R_Y axes and as such, is visible by the controller in all directions. It is not possible to separate four modes on basis of direction when using only three sensors. The projections of eigenvectors on the sensor space will be referred to as 'sensed eigenvectors' for the remainder of this text.

Torsion mode decoupling

It is possible to create a sensor decoupling that filters out all torsion information. This can be performed by passing the sensor signals through a static matrix with the sensed torsion eigenvector in its nullspace. The output of this matrix only contains information in the plane perpendicular to the sensed torsion eigenvector (*FIGURE 7*).

However, this means that the sensed eigenvectors of the three rigid body modes are reduced to a two-dimensional projection on the plane perpendicular to the sensed torsion vector. As such, the output of this matrix contains coupled rigid body information. In the control loop, this two-dimensional projection of three rigid body modes manifests itself as interaction between these rigid body modes.

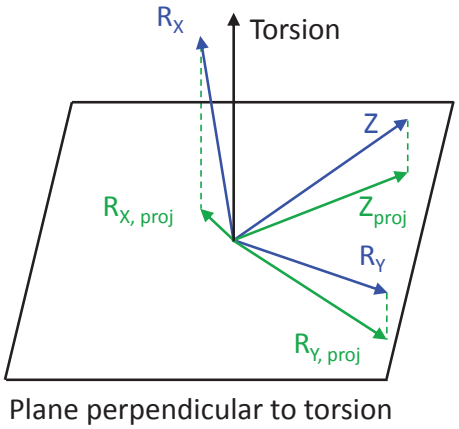

FIGURE 7: Filtering the torsion mode direction.

As such, it is not desirable to use this decoupling over the entire frequency range, but only in frequency range B (*FIGURE 5*).

Dynamic decoupling

In frequency range A (*FIGURE 5*), rigid body decoupling is preferred. In frequency range B, torsion mode decoupling is preferred.

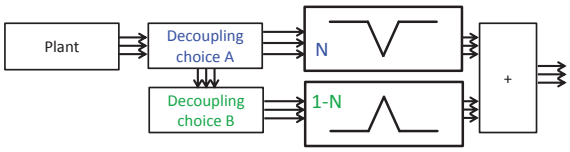

FIGURE 8: Dynamic decoupling.

At the torsion resonance frequency, decoupling choice A is suppressed with a notch filter N (*FIGURE 8*). At this same frequency, decoupling choice B is activated with a '1-N' filter, which resembles a bandpass filter. When these two signals are added up, a dynamic decoupling is obtained. This results in rigid body decoupling for low frequencies and an effectively unobservable torsion mode at the torsion resonance frequency.

Prerequisite: Sensor placement

In *FIGURE 7* one of the prerequisites for using this filter can also be found. This filter can only be used in a direction that is not close to parallel with the mode that is to be filtered out.

In the example of *FIGURE 7*, filtering out the sensed torsion eigenvector also filters out a substantial part of the sensed R_X eigenvector. Amplification of the small amount of R_X information that remains would also results in amplified interaction from Z and R_Y.

To apply the direction filter in the R_X direction, the sensors have to be moved such that the sensed torsion and R_X eigenvectors are closer to perpendicular.

DIRECTION FILTER APPLIED TO SETUP 1: CONVENTIONAL SENSING

Control scheme

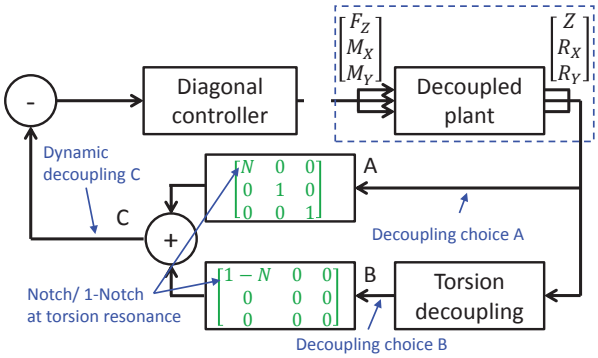

FIGURE 9: Direction based filtering.

The third option from *FIGURE 4* is shown in more detail in *FIGURE 9*. The decoupled plant, the matrix with the sensed torsion eigenvector in its nullspace (torsion decoupling) and the filters N and 1-N are shown. These filters only work in the Z-direction, in the other directions the frequency response is not changed.

The frequency response from the decoupled plant input to various locations in *FIGURE 9* is shown in *FIGURE 10*.

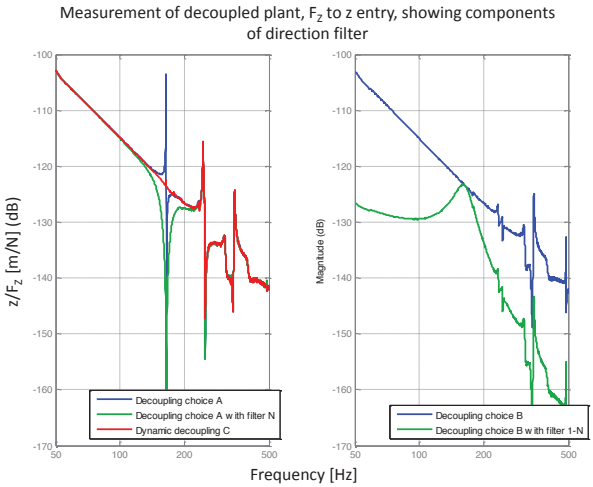
Measurement of decoupled plant, F_Z to z entry, showing components of direction filter
z/F_Z [m/N] (dB)
Magnitude (dB)
Frequency [Hz]
Decoupling choice A
Decoupling choice A w ith filter N
Dynamic decoupling C
Decoupling choice B
Decoupling choice B w ith filter 1-N

FIGURE 10: Showing five different components from FIGURE 9.

The blue line in the left graph of *FIGURE 10* shows the unaltered decoupled system. This is decoupling choice A, for which the torsion resonance peak is present in the transfer.

The green line in the left graph is decoupling choice A with the notch filter N, this would be equivalent to tuning a notch filter in Z-direction.

The blue line in the right graph shows decoupling choice B. The torsion mode is unobservable, but there is a large amount of interaction between the rigid body directions (not visible in figure).

As such, decoupling choice B is not to be used over the entire frequency range, but only near the torsion resonance peak. Decoupling choice B is multiplied with bandpass filter 1-N, resulting in the green line of the right graph.

When the green lines of both the right and left graph are added together, the red line from the left graph is obtained. This represents dynamic decoupling C, which has rigid body decoupling for low frequencies and an effectively unobservable torsion mode near the torsion resonance frequency.

This is not an exact zero-pole cancellation by the controller. If the resonance peak would have small frequency or damping variations, it would still be rendered unobservable by this filter.

Results

The results can be seen in *FIGURE 11*. This figure shows the diagonal term from F_Z to z and the interaction term from M_X to z. The blue line is the original system, the green line is the system with direction filter. The torsion resonance peak is no longer observed in the transfer. As a result, the bandwidth can be increased.

Limitation: Interaction

The drawback, an increase in off-diagonal interaction, can also be seen in *FIGURE 11*. This is because only a two-dimensional projection of the three-dimensional rigid body information is available when using decoupling choice B.

At the resonance frequency, interaction decreases due to a reduction in magnitude of the resonance peak. For other frequencies, interaction increases.

The increase in interaction is present in both off-diagonal entries related to output 'Z' of the decoupled plant (z/M_X and z/M_Y). How the interaction increase is divided over the off-diagonal entries is determined by the choice of the entries of the 'torsion decoupling' matrix (from *FIGURE 9*), as this matrix is not unique.

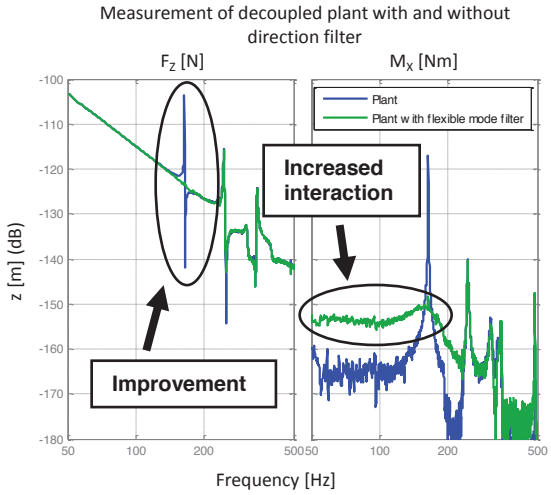

FIGURE 11: Measured plant with direction filter. Only z/F_Z and z/M_X entries are shown.

The entries of the measured plant related to the outputs R_X and R_Y remain unchanged by the direction filter.

DIRECTION FILTER APPLIED TO SETUP 2: OVERSENSING

As seen in the previous paragraph, using a dynamic decoupling to deal with the torsion resonance peak also imposes a limitation: The interaction between the rigid body modes increases. Using this dynamic decoupling with an oversensed setup (*FIGURE 12*), does not have this limitation.

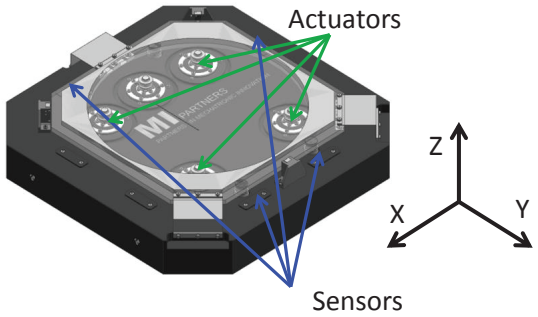

FIGURE 12: Alternative plant configuration as used in current research.

The setup is similar to the one in *FIGURE 1*, but with four sensors instead of three sensors. The sensor space now has four dimensions. This makes it possible to use a static decoupling of four sensor signals to decouple the three rigid body modes and a flexible mode over the entire frequency range.

A such, this additional degree of freedom can make one flexible mode (torsion in this case) unobservable without dynamic decoupling. Dynamic decoupling will be used to deal with the second flexible mode (saddle mode) of this system.

Control scheme

The oversensed plant is shown in *FIGURE 13*. For decoupling choice D the three rigid body modes and the torsion mode are decoupled.

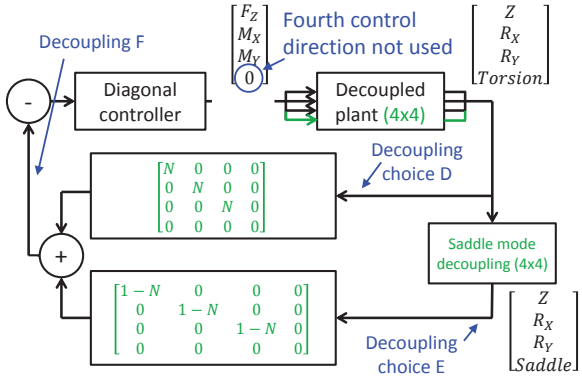

FIGURE 13: Creating a dynamic decoupling to switch between flexible mode decoupling choices.

The block labeled 'Saddle mode decoupling' is a coordinate transformation to a frame where the saddle mode is unobservable. This is decoupling choice E.

At the saddle mode resonance frequency, decoupling choice D is suppressed with the notch filter N and choice E is activated with bandpass filter 1-N. In this setup, the filter is applied in all rigid body directions.

A model of this plant is shown in *FIGURE 14*. The model includes the remaining excitation of the torsion mode. The blue line shows decoupling choice D, the green line shows decoupling choice E.

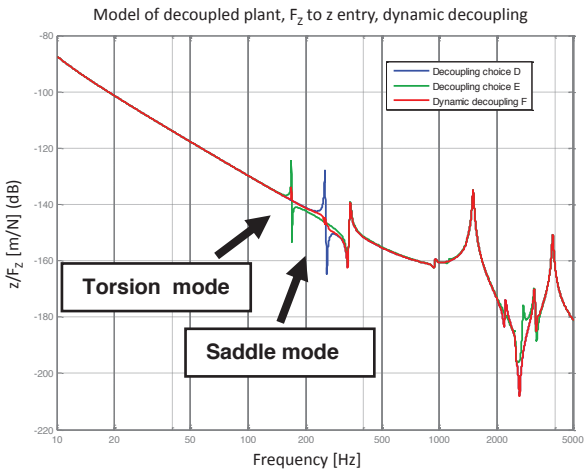

FIGURE 14: The modeled z/F_Z entry of a plant with four actuators and four sensors. The legend refers to FIGURE 13.

Results

The result is also shown in *FIGURE 14.* The red line shows dynamic decoupling F, for which the magnitude of both the torsion and the saddle resonance peaks is strongly reduced.

What can also be seen is that the decoupling quality shown by the red line of *FIGURE 14* is not as smooth as the green and blue line shown in this figure. The cause of this is the limited steepness of the notch filter that is used to switch between the two decoupling choices.

This method can be extended for more modes, using a notch filter to change between different decoupling choices.

The increase in interaction between the rigid body modes, which is present in the setup with conventional sensing, is now no longer present. When changing from decoupling choice D to decoupling choice E at the saddle mode frequency, the magnitude of the interaction terms at that frequency also changes to that of decoupling choice E. This interaction can be either greater or smaller than the interaction for choice D.

This system also has an unused fourth control direction. For other research, this input is used to close a torsion control loop. When looking at the frequency response from the fourth control direction to the rigid body modes, interaction has increased. This is not disadvantageous, as the fourth control direction is not used in this setup.

CONCLUSION

The direction based filtering is performed by using a dynamic sensor decoupling in order to make the controller ignore signals with a certain mode shape in a certain frequency range. From that perspective, the direction filter can be compared to a notch filter, which makes the controller ignore signals with a certain frequency. For this system, the positioning error has little frequency content near the torsion resonance. As such, ignoring this mode is not detrimental to performance.

A notch filter is sensitive to modal frequency and damping variation. The direction based filter is mainly affected by variations in mode shape, similar to an oversensed setup. The direction based filter is made robust to frequency variation of the torsion mode by making the notch filter N wide. However, increased width of the notch filter N comes at the cost of increased interaction between the rigid body modes. The oversensed setup does not have this limitation.

For the demonstrator setup, the mode shape of the torsion mode turned out to be more predictable on basis of a model than its frequency and damping. For this particular system, a filter based mainly on mode shape can be made more robust than a filter based on frequency.

The filter has been successfully implemented on the demonstrator system, which resulted in increased bandwidth and performance.

REFERENCES

[1] Laro, D. Design and control of over-actuated lightweight 450 mm wafer chuck. Proceedings of ASPE 2011 Spring Topical Meeting. 2011.

[2] Vaes, D. Optimal static decoupling for multivariable control design, PhD Thesis, Koninklijke Universiteit Leuven. 2005. p81-84.

[3] Schneiders M, van de Molengraft M, Steinbuch M. Benefits of over-actuation in motion systems. Proceedings of the 2004 American Control Conference. 2004.

[4] Gawronski, W. Advanced structural dynamics and active control of structures, Springer-Verlag. New York: 2004. p16-29.

FRICTION MODELING AND COMPENSATION USING FREQUENCY DOMAIN PARAMETERIZATION BY DAHL RESONANCE

Jun Young Yoon[1] **and David L. Trumper**[1]
[1]**Department of Mechanical Engineering**
Massachusetts Institute of Technology
Cambridge, MA, USA

INTRODUCTION

This paper introduces a frequency domain parameter identification method associated with the Generalized Maxwell-Slip (GMS) friction model [1, 2]. This novel method utilizes Dahl resonances in frequency responses to experimentally obtain friction model parameters, and the identified model can be used to compensate the friction to achieve high accuracy for high-precision applications.

Friction is an inevitable nonlinear factor in servo systems due to the usage of bearings, transmissions, and/or motion guides, and its effects become significant when it comes to high-precision motion control. In order to compensate friction and accomplish better system performance, we need first to understand representative frictional behaviors in both the gross-sliding and the pre-sliding regimes [3]. To this end, we present a case study of motor spin.

Case Study: Motor Spin Free Response

A simple experiment with a servomotor can demonstrate the effects of bearing friction. The servomotor used in the case study is shown in Figure 1, and we use the same setup for the rest of the experiments in the paper.

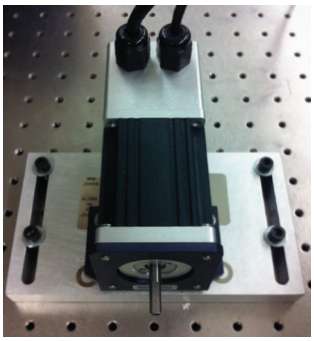

FIGURE 1. Experimental setup of a servomotor with a high-resolution encoder implemented.

The motor is brushless and slotless so that the embedded ball bearing is the major source of friction. An encoder with an interpolated resolution of 10^6 counts per revolution is implemented in the back of the motor to provide the position feedback. In this case study, we spin the motor shaft by hand while reading its position and velocity. The motor coils are open-circuited during the measurement. The resultant free responses are shown in Figure 2. Two spins are measured during a time duration of one second. For both spins, the ball bearing friction opposes the relative velocity and acts as a near-constant drag torque, showing the frictional behavior in the sliding regime. However, as the velocity becomes low, the friction arrives in the pre-sliding regime and shows elastic behavior, which causes oscillation as seen in the magnified view. We also observe that the oscillation period decreases as the motor shaft comes to rest, and this implies that the stiffness of the friction elasticity increases according to the displacement decrease. This result is consistent with the hysteretic behavior of the pre-sliding friction [4].

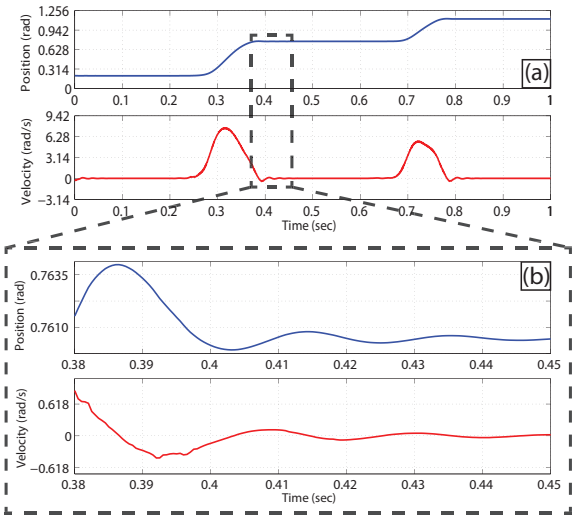

FIGURE 2. Motor spin free responses. (a) Angular position and velocity. (b) Magnified view of oscillation caused by friction as the rotor comes to rest.

FRICTION MODEL

Friction behaves differently according to its regime as illustrated in the simple case study. Therefore, a well-constructed friction model should be able to represent friction in both regimes. First, friction in the sliding regime is well characterized as the Stribeck curve [5] written in the form of

$$F(v) = s(v) + \sigma v$$
$$= sgn(v)\left(F_c + (F_s - F_c)\exp\left|\frac{v}{V_s}\right|^{\delta}\right) + \sigma v$$

where v, F_c, F_s, V_s, δ and σ represent velocity, Coulomb friction, static friction, Stribeck velocity, shape factor, and viscous friction coefficient respectively. Note that the Stribeck curve $F(v)$ consists of a velocity weakening curve $s(v)$ and a velocity strengthening curve σv.

In the effort of incorporating the hysteretic nonlinear elasticity of the pre-sliding friction into the Stribeck curve, many empirical friction models have been introduced in literature including the Dahl model [6, 7], LuGre model [8], Leuven model [9, 10], and Generalized Maxwell-Slip (GMS) model [1, 2]. In this paper, we adopt the GMS model to apply our Dahl resonance identificaiton method and test its performance.

The GMS model uses parallel-connected elementary blocks to simulate the hysteretic behavior of the pre-sliding friction, and imposes slipping dynamics as a weighted stribeck velocity weakening curve to each block to provide smooth transition from the pre-sliding to the sliding regime. The GMS model structure and the behavior of each block are illustrated in Figure 3.

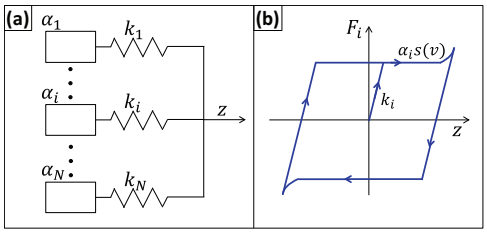

FIGURE 3. Schematic of the Generalized Maxwell-Slip model with stiffness k_i, normalized saturation limit α_i, and friction force F_i. (a) Parallel structure of GMS elementary blocks where z represents the displacement in the pre-sliding regime. (b) Behavior of one GMS block with the slipping dynamics.

Each GMS block either sticks or slips with the threshold of the normalized limit $\alpha_i s(v)$, creating its own hysteretic loop. By superposing N number of blocks, therefore, the GMS model simulates a smooth hysteresis, and it is mathematically represented as

- If stick, $\dfrac{dF_i}{dt} = k_i v$
- If slip, $\dfrac{dF_i}{dt} = sgn(v)C\left(\alpha_i - \dfrac{F_i}{s(v)}\right)$
- Friction, $F_f = \sum_{i=1}^{N} F_i(t) + \sigma v(t).$

Note that Figure 3(b) shows the characteristics of a GMS block exaggerated with a large value of the attraction factor C to illustrate the smooth transition between the pre- and the gross-sliding regimes. The GMS model has advantages of high fidelity and simple implementation for real-time control. However, to guarantee these merits, it requires nontrivial effort to identify many parameters including N number of stiffnesses and saturation limits each.

DAHL RESONANCE METHOD

Here we develop a novel parameter identification (ID) method, which can be conducted solely in the frequency domain. The representative behavior of the pre-sliding friction is the hysteresis, which indicates the change of the friction stiffness. This varying stiffness results in input-amplitude-dependent frequency responses with Dahl resonance, which is the resonance of the spring-like behavior of the pre-sliding friction. We can therefore extract the stiffness information directly from the resonant frequencies of the Dahl resonances. This is the basic principle of, we call, Dahl resonance ID method.

The procedure of this method begins with measuring frequency responses containing Dahl resonances. There are several points to consider in measuring correct Dahl resonances:

1) The low frequency drift needs to be avoided to keep friction in the pre-sliding regime.

2) The applied torque should be controlled to be lower than the static friction torque.

3) The displacement should be constrained within the pre-sliding regime.

The schematic of the measurement setup we suggest to fulfill the conditions above is shown in Figure 4. By closing the loop, we can make the DC gain infinite and eliminate the low frequency drift. We can also control the applied torque to be less than the static friction by using a low-bandwidth controller and adding the dynamic signal analyzer (DSA) excitation to the plant as a disturbance. The control law provided by the low-bandwidth controller would be too small to affect the applied torque τ, thereby meeting both the conditions 2) and 3).

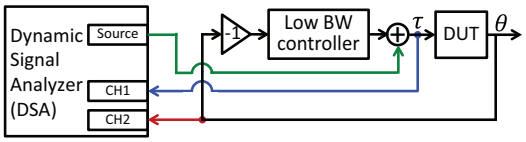

FIGURE 4. Schematic configuration to measure frequency responses of the servo system.

The measured frequency responses of the servomotor setup using the suggested configuration is shown in Figure 5 where the curves are parameterized with the amplitude of the drive current output of the motor drive.

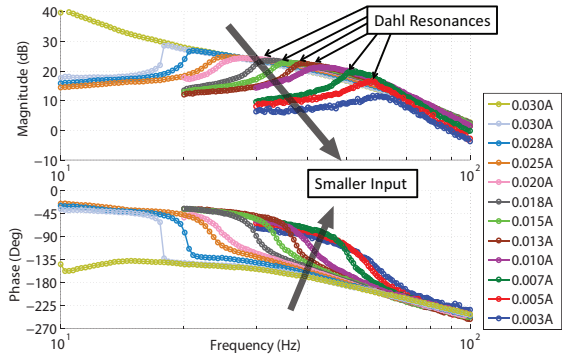

FIGURE 5. Input-amplitude-dependent frequency responses of the open-loop servomotor with Dahl resonances.

From the measurements, the Dahl resonant frequencies f_{D_i} can be used, together with the rotor inertia J, to obtain the input-dependent stiffness K_{tors_i} as

$$K_{tors_i} = (2\pi f_{D_i})^2 \times J \quad [\text{Nm/rad}]$$

where $J = 1.96 \times 10^{-5}$ [kgm^2] is given by the manufacturer. Since we measure the torque as the current command in amperes and the angle in degrees, K_{tors_i} can be scaled to

$$K_{eff_i} = \frac{K_{tors_i}}{K_t} \times \frac{\pi}{180} \quad [\text{Amp/deg}]$$

where $K_t = 0.2$ [Nm/Amp] is the torque constant of the servomotor. This effective stiffness K_{eff_i} is the representative stiffness that the system experiences at each input level and is depicted in Figure 6.

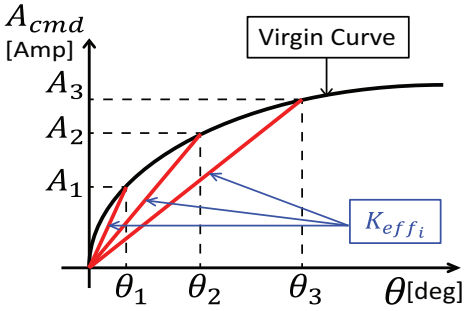

FIGURE 6. Schematic describing the effective stiffnesses K_{eff_i} of the pre-sliding friction relating current command amplitude A_{cmd} in amperes to displacement θ in degrees.

The first effective stiffness K_{eff_1} is the same as the accumulated stiffness K_1 of all N number of elementary stiffnesses. When the first GMS block begins to slip, the next accumulated stiffness K_2 becomes the sum of $N-1$ number of elementary stiffnesses. The first elementary stiffness k_i is then obtained by subtracting K_2 from K_1. Using these steps, we can calculate all k_i's, and the procedure can be summarized as

$$K_1 = K_{eff_1} = \sum_{j=1}^{N} k_j \qquad [\text{Amp/deg}]$$

$$K_{i+1} = \frac{A_{i+1} - A_i}{\theta_{i+1} - \theta_i} = \sum_{j=i+1}^{N} k_j \quad [\text{Amp/deg}]$$

$$k_i = K_i - K_{i+1}, \quad k_N = K_N \quad [\text{Amp/deg}]$$

where $i = 1, 2, ..., N-1$. The saturation limits α_i are then obtained through simple calculation of

$$\alpha_i = k_i \times \theta_i \quad [\text{Amp}].$$

Note that the total sum of the normalized saturation limits should equal one so that the friction smoothly approaches the Stribeck curve $s(v)$ when all the GMS blocks are in the slipping

phase. We use eight blocks ($N = 8$) for our servomotor setup, and the parameters we identified with the Dahl resonance method are organized in Table 1. We utilize these values to complete the GMS friction model and compensate the friction of the servo system.

TABLE 1. Identified parameters through the novel Dahl resonance method for $N = 8$.

i	k_i [Amp/deg]	α_i [Amp]
1	0.0508	0.0306
2	0.0693	0.0767
3	0.0603	0.1134
4	0.0030	0.0123
5	0.0266	0.1686
6	0.0059	0.0525
7	0.0164	0.2196
8	0.0169	0.3264

FRICTION COMPENSATION AND RESULTS

The identified friction model by the Dahl resonance method is used in a simple friction compensation control algorithm as shown in Figure 7. The dashed lines indicate the hardware parts of the system while the solid lines represent the control algorithm in software implemented in the National Instruments real-time controller, PXI-8110. We use a straightforward model-based feedforward compensator so as to better see the performance of the identified model in estimating and compensating the real system friction.

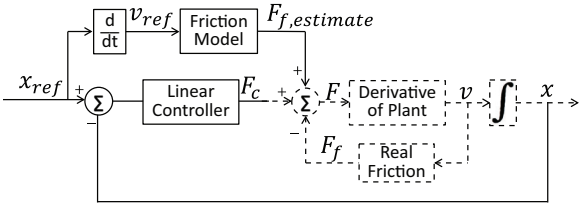

FIGURE 7. Control schematic of feedback position controller and feedforward friction compensator.

We observe the performance results both in the frequency and the time domains. In the frequency domain, the closed-loop frequency responses of the servo system are measured, as shown in Figure 8, to compare the system bandwidth. The uncompensated system shows significant input-amplitude dependency due to the pre-sliding friction, negatively affecting the system bandwidth. For the compensated system, however, we can see that the responses are much less dependent on the input level and the bandwidth are notably improved. These results validate that the novel Dahl resonance ID method provides reasonable values for the parameters of the friction model, allowing the high-fidelity of the identified model.

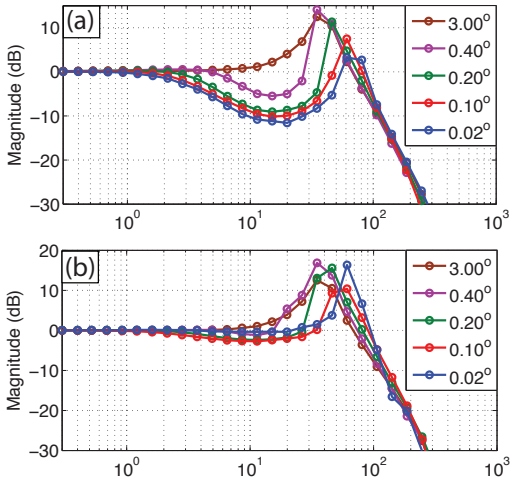

FIGURE 8. System bandwidth comparison in magnitude plots of closed-loop frequency responses. (a) Friction-uncompensated system. (b) Compensated system.

The performance improvement of the compensated servo system is also observed in the time domain in terms of servo tracking. When a control system settles or encounters turnarounds following a commanded position trajectory, it travels the pre-sliding regime and its dynamics becomes dominated by the nonlinear pre-sliding friction. This nonlinearity significantly limits the performance of a linearly controlled servo system, and therefore a proper friction compensation is required for better performance, especially for high-precision applications.

We conduct trajectory following experiments by commanding 0.5 Hz sinusoidal inputs with the amplitudes of 0.12° and 7° for the pre-sliding regime and the sliding regime tests respectively. The resultant tracking errors are plotted in Figure 9 showing significant improvements through the feedforward friction compensation in both regimes. The RMS error in the pre-sliding regime is reduced by 68.0 % and the peak error in the sliding regime by 73.2 %. We compare the peak error reduction in the sliding regime tests because the largest errors occur at the velocity reversals and our friction compensator is designed to reduce these peak errors by eliminating the pre-sliding friction effects. The notable performance

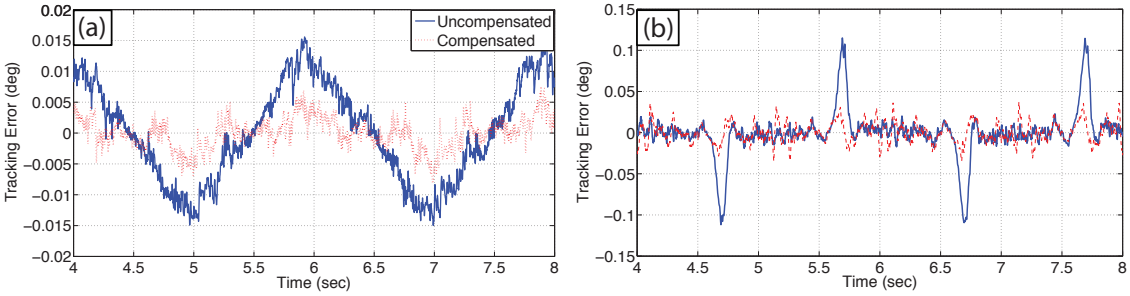

FIGURE 9. Tracking performance comparison in position error between friction-uncompensated (solid blue) and feedforwardly compensated system (dashed red). (a) Pre-sliding regime. (b) Gross-sliding regime.

improvements in the time domain also verify the fidelity of our Dahl resonance ID method.

CONCLUSION

In this paper, we introduce the Dahl resonance method to help identify parameters of the GMS friction model. This method can be conducted solely in the frequency domain, thereby not requiring additional position-controlled experiments. The fidelity of this identification method is validated by the performances of the model-based friction-compensated system in both the frequency and the time domains. The results show promising improvements, indicating this method can be readily used to complete the GMS friction model and compensate friction to achieve higher accuracy for high-precision motion control systems.

ACKNOWLEDGMENT

This work was performed with the support from ASML, Wilton, CT. We appreciate discussions with Ruvinda Gunawardana in particular. We also would like to thank Aerotech for donating the servomotor, and National Instruments for contributing the real-time control system.

REFERENCES

[1] Lampaert V, Al-Bender F, Swevers J. A generalized Maxwell-slip friction model appropriate for control purposes. In: Physics and Control. Proceedings. International Conference. vol. 4. IEEE; 2003. p. 1170–1177.

[2] Al-Bender F, Lampaert V, Swevers J. The generalized Maxwell-slip model: a novel model for friction simulation and compensation. Automatic Control, IEEE Transactions on. 2005;50(11):1883–1887.

[3] Al-Bender F. Fundamentals of Friction Modeling. In: Proceedings, ASPE Spring Topical Meeting on Control of Precision Systems, MIT; 2010. p. 117–122.

[4] Courtney-Pratt J, Eisner E. The effect of a tangential force on the contact of metallic bodies. Proceedings of the Royal Society of London Series A Mathematical and Physical Sciences. 1957;238(1215):529–550.

[5] Stribeck R. Die wesentlichen Eigenschaften der Gleit-und Rollenlager-the key qualities of sliding and roller bearings. Zeitschrift des Vereines Seutscher Ingenieure. 1902;46(38, 39):1342–1348, 1432–1437.

[6] Dahl P. A solid friction model. DTIC Document; 1968.

[7] Dahl PR. Solid friction damping of spacecraft oscillations. DTIC Document; 1975.

[8] Canudas de Wit C, Olsson H, Astrom KJ, Lischinsky P. A new model for control of systems with friction. Automatic Control, IEEE Transactions on. 1995;40(3):419–425.

[9] Swevers J, Al-Bender F, Ganseman CG, Projogo T. An integrated friction model structure with improved presliding behavior for accurate friction compensation. Automatic Control, IEEE Transactions on. 2000;45(4):675–686.

[10] Lampaert V, Swevers J, Al-Bender F. Modification of the Leuven integrated friction model structure. Automatic Control, IEEE Transactions on. 2002;47(4):683–687.

[11] De Moerlooze K, Al-Bender F, Van Brussel H. A generalised asperity-based friction model. Tribology Letters. 2010;40(1):113–130.

SOMETHING FOR (ALMOST) NOTHING: X-ray Microscope Performance Enhancement Through Control Architecture Change

Sheikh T. Mashrafi[1], Curt Preissner[2], Srinivasa Salapaka[1], and Huyue Zhao[2]
[1]Mechanical Science and Engineering
University of Illinois at Urbana-Champaign
Urbana, IL, USA
[2]Advanced Photon Source
Argonne National Laboratory
Argonne, IL, USA

INTRODUCTION

In this paper we demonstrate that simply by changing the controller architecture the nanopositioning performance of an X-ray microscope can be drastically improved. For instance, with our approach we have demonstrated a bandwidth improvement of 193%. Similarly we have shown a resolution improvement of 243% as compared to a traditional proportional-integral-derivative (PID) controller. Both examples are due solely to implementing a new control algorithm on new control hardware. In this paper we present some background and motivation of the application, a summary of our design methodology, sample results, and a discussion.

Current microscopes such as the Hard X-ray Nanoprobe at the Advanced Photon Source (APS) can focus the X-rays to a 30 nm spot size [1]. New microscopes such as the *in situ* Nanoprobe (ISN) will be able to focus X-rays to a 20 nm spot size [2]. The higher X-ray resolution afforded by our approach can enhance the microscope stability during stability-critical applications such as X-ray fluorescence mapping. Likewise the higher bandwidth afforded by our approach can enhance large area scans, either increasing the area scanned in a given time or reducing the time required for a given area as compared to current capabilities. Thus, nanopositioning is an important enabling technology for X-ray microscopes at synchrotrons like the APS. The performance of the current controllers limits the resolution, bandwidth, and disturbance rejection of the microscope system. Improved controller performance can improve instrument performance for the next generation of X-ray microscopes such as the ISN.

Advanced control techniques that improve the precision, accuracy, and bandwidth of nanopositioning systems have seen significant development in the realm of scanning probe microscopes (SPMs). In fact, the area of scanning probe control engineering is extremely active with thousands of papers published in the last two years alone, including well cited review articles [3-5]. This is significant because no comparable body of work exists in the similar yet much smaller field of X-ray optics nanopositioning. While SPMs are much smaller than X-ray microscopes, the design methodologies apply to the larger X-ray microscopes. Thus, we have leveraged the SPM developments to transform the capabilities of one example X-ray nanopositioning device.

The X-ray microscopes in use around the United States and the world are room-sized devices meeting many constraints and incorporating many components, a small portion of which is the nanopositioning system. With such a complex and integrated system any physical change to the nanopositioning mechanics requires a significant investment in effort and money and may have a cascade effect on other systems.

Rather than change the mechanics we have applied the bandwidth-, robustness-, and precision-expanding control algorithms found in the SPM community. Improving performance in this way is not subject to the same constraints and costs less effort and money than would be needed to physically modify the system. Hence our approach does offer something for, when compared to the cost of an X-ray microscope, almost nothing.

The X-ray Nanopositioning Test Bed

We have built a nanopositioning test bed around the Early User Instrument (EUI), prototype for the APS nanoprobe [6, 7]. This instrument was developed in 2004 and was used to test the nanoprobe basic instrument design and produce early science. The EUI was designed to precisely hold and position a diffractive focusing X-ray lens and sample. In experiments on an APS beamline it was shown to achieve a source-size-limited focal spot of 70 nm [7].

The original EUI consisted of a set of coarse motion stages for the sample and a set of coarse and fine motion stages for the X-ray optic. The relative position in two axes was encoded using a multi-reflection laser-based encoding system with subnanometer noise level. The original control system consisted of three industrial PCs running Windows and National Instruments (NI) LabVIEW software. A PID controller was implemented in standard LabVIEW (as opposed to a real-time system), thus in the original implementation (circa 2004) control bandwidth was limited.

For the work described in this paper, we replaced the original EUI control hardware with a system that could allow for reconfigurable controller implementation. This flexibility was enabled by the use of a field programmable gate aray (FPGA). Only the vertical direction motion of the EUI was addressed for this work. The new control hardware consisted of a NI CompactRIO (cRIO) cRIO-9024 Real-Time Controller and a cRIO-9118 Virtex-5 LX110 FPGA Chassis (40 MHz clock), with NI-9223 analog input modules, NI-9402 digital input modules, and NI-9263 analog output modules. The hardware alone was not sufficient to achieve better performance; the performance advantage lies in the control laws or algorithms (controller) that we designed. Each control algorithm that was developed and tested was first discretized and then implemented on the NI FPGA hardware.

The basic layout of the system, including the new FPGA controller is shown in figure 1. The vertical fine motion stage is a flexure-based stage with a 15:1 motion reduction driven by four Physik Instrumente piezo stack actuators.

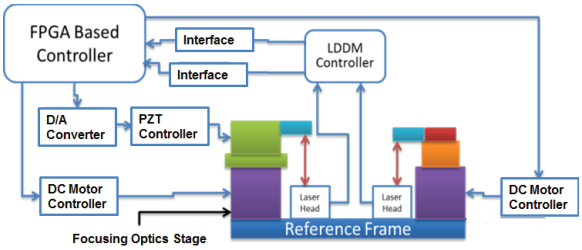

FIGURE 1. A schematic showing the system components. The fine motion stage is part of the focusing optics stack.

CONTROL SYSTEM DESIGN

The design of a new controller for the EUI system followed three basic steps: system identification, control law design, and control law implementation. In system identification experimental measurements were made of the input and output to the system or "plant". A model that captured the significant system dynamics was then fit to these data. Once the plant model had been identified, control design could be carried out. Three different types of control algorithms (controllers) were designed: 1) PID (established baseline performance), 2) Glover-McFarlane (GM), and H_∞ (H infinity). Once a design was run successfully in simulation it was implemented on the NI hardware. We also developed an implementation methodology that overcame unexpected limitations of the NI FPGA software.

System Identification

Data for system identification were generated by actuating the vertical direction piezo with band-limited white noise from 0 to 12.5 kHz. The input signal and the displacement output were measured simultaneously and the frequency response function (FRF) calculated. In order to investigate system variability, the input-output transfer function was measured for a range of RMS noise levels, varying from 50 nm to 1000 nm, spanning the range of operation of the device. Figure 2 shows the measured data.

The system exhibited a softening nonlinearity; as input amplitude increased the system resonances shifted lower in the frequency range. While at this point it is unknown why this behavior manifested, it is this type of variability that can confound standard control techniques and that our approach can address. This plant uncertainty will be addressed through the design of a controller robust to such plant variation.

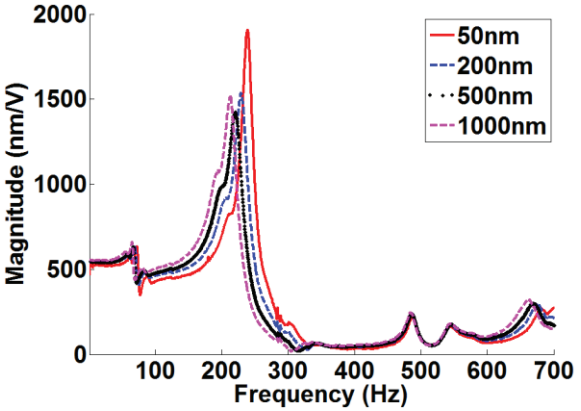

FIGURE 2. Average experimental FRFs for 50 nm, 200 nm, 500 nm, and 1000 nm input amplitudes. The system exhibited a softening nonlinearity.

The 200 nm response was taken to be the nominal experimental result and a single-input single-output transfer function model was fit to these data using identification tools from control systems theory. This resulted in a rather high-order model and a reduction of this plant model through balance realization resulted in a tenth order model. Figure 3 shows the bode plot for the fit model along with the experimentally measured FRF data.

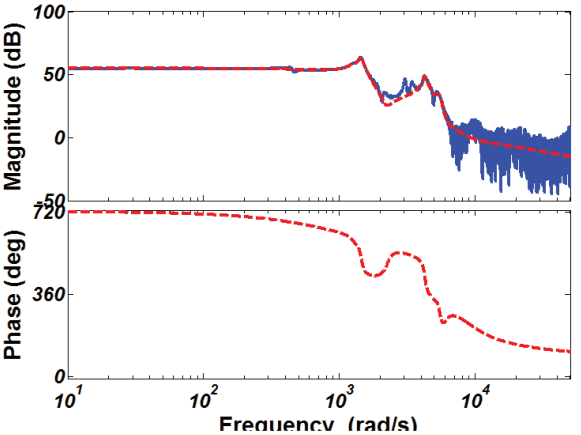

FIGURE 3. Bode plot showing the amplitude and phase plots of the model fit to the 200 nm FRF data along with the measured FRF data.

It is can be clearly seen that the model does not capture the plant dynamics beyond 700 Hz (4398 rad/s), which is acceptable because the instrument operating range is below 200 Hz. This model was used for the subsequent controller design.

Controller Design

As mentioned it can be advantageous to have a nanopositioner that possess high bandwidth (for fast scanning) and high resolution (for stability during long measurements). Our design goals were then to achieve high bandwidth, high-resolution (on the order of nm), and device reliability (meaning here insensitivity to plant variability and environmental noise). Figure 4 shows the block diagram for the typical PID controller.

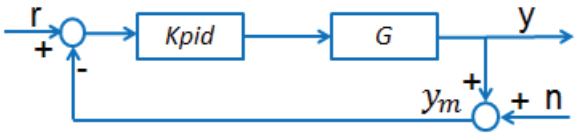

FIGURE 4. Block diagram for the typical PID controller. Symbols are: G = plant, K_{pid} = controller, r = reference signal, y = system output, n = sensor noise, and y_m = noisy measurement signal

These objectives were quantified in terms of the closed loop-system transfer functions—the sensitivity transfer function $S(j\omega)$ that represents the dynamics from the reference signal to the tracking error (r to r-y_m in Figure 4), and the complementary sensitivity function $T(j\omega)$ that represents the dynamics from the reference signal to the displacement output (r to y in Figure 4).

The bandwidth of each controller was taken to be the point at which the magnitude of $S(j\omega)$ exceeds $1/\sqrt{2}$. This represents the frequency range in which the controller could be expected to track the reference (input) accurately. The resolution of each controller was taken to be three times the standard deviation (3σ) of the measured system noise with zero input. The peak-value of S, $|S(j\omega)|$, represents a measure of sensitivity of the closed-loop device and was used to quantify device reliability (how insensitive the system is to plant and model variation).

Controller Implementation

All controllers were implemented on the NI cRIO-9118 Virtex-5 LX110 FPGA using the blocks available in the LabVIEW FPGA software module. The analog signals from the EUI laser encoders were sampled at 25 kHz. Each controller was subsequently discretized for this rate. The original plan was to implement the resulting discrete-time transfer functions by

using the arbitrary transfer function block in the LabVIEW FPGA Module. However, this block was found to be problematic and the controllers implemented this way did not behave as in simulations.

Instead of the transfer function block, the discretized controllers were split into second order sections (biquad sections). These second order sections were cascaded through the use of a loop structure. In addition to enabling the controller implementation, this loop structure conserved resources on the FPGA—any order controller used the same amount of resources as a second order controller.

First, we implemented a PID feedback controller. Then we augmented this designs with a Glover-McFarlane (GM) feedback controller to guarantee better reliability (robustness to plant variability and modeling errors) [5]. We have also designed H_∞ feedback controllers, where the previously mentioned control objectives were cast as an optimization problem and an optimal control law was derived. The control objectives were: low actuator effort, high resolution (noise attenuation), high tracking bandwidth, and high reliability (robustness).

RESULTS

Baseline system: PI controller

As a baseline system a PID controller (second order) with bandwidth of 43 Hz, meeting the robustly stability criteria ($|S(j\omega)|_\infty 2$) was implemented with control law rate of 25 kHz. Figures 5, 6, and 7 respectively show the bode plot, noise histogram and tracking for this controller. It is important to note PID controllers do not account for uncertainty in the plant model and while the controller meets the robust stability criterion for a specific plant model they fail to guarantee robustness for all plant variation (as shown in Figure 2).

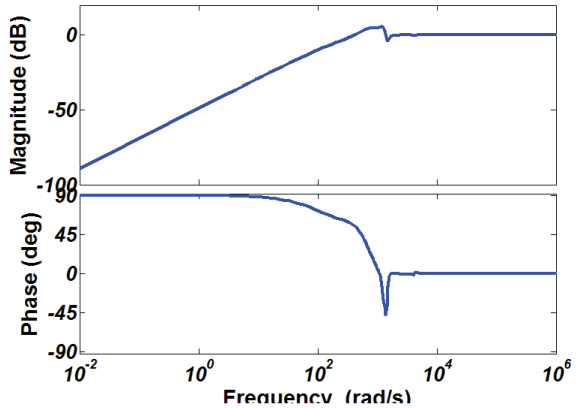

FIGURE 5. Bode plot of the sensitivity transfer function for the system with the implemented PID controller. The magnitude of S exceeds $1/\sqrt{2}$ at 43 Hz (270 rad/s).

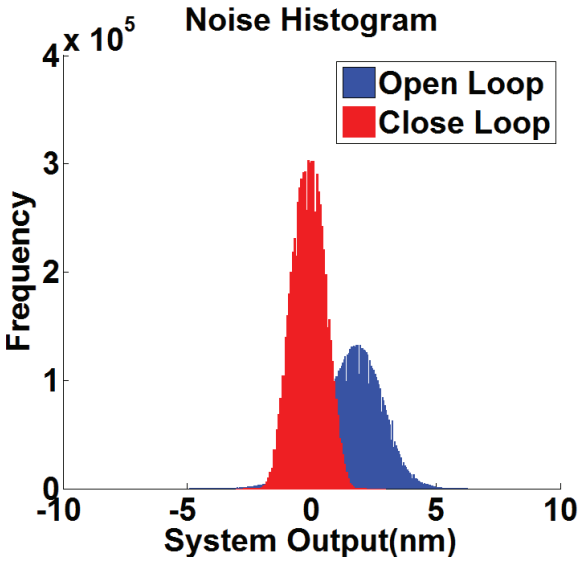

FIGURE 6. Noise histogram for the 43 Hz bandwidth PID controller: Open Loop Resolution = 4.8 nm, Closed Loop Resolution = 1.9 nm

GM based robustification of a PI controller

To address the above mentioned drawback of the PID controller a GM design was developed. The GM control law robustifies an existing PID control law with a small (quantifiable) compromise in performance. This control design accounts for modeling uncertainties and guarantees robust performance by designing for the worst case uncertainty model. We designed and implemented a 7^{th} order GM controller with a 52 Hz bandwidth, which was based on an unstable PID controller with a 76 Hz bandwidth. Figures 8 and 9 show the bode plot and tracking for the GM controller.

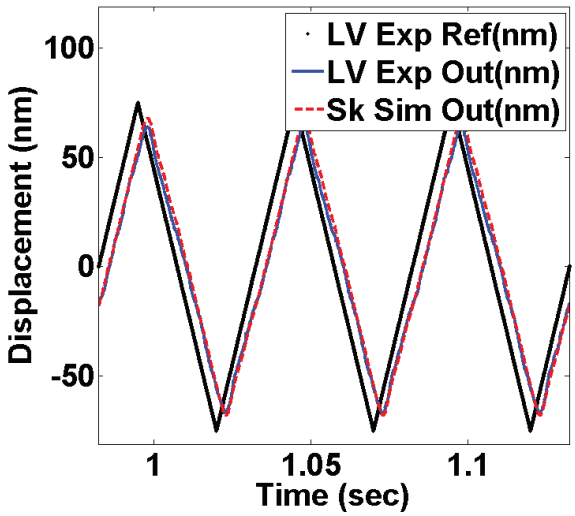

FIGURE 7. Tracking of a 20 Hz triangle wave for the 43 Hz bandwidth PID controller. Note the distortions in both the simulated output (Sim Out) and the experimental output (Exp Out) as compared to the input (Exp Ref).

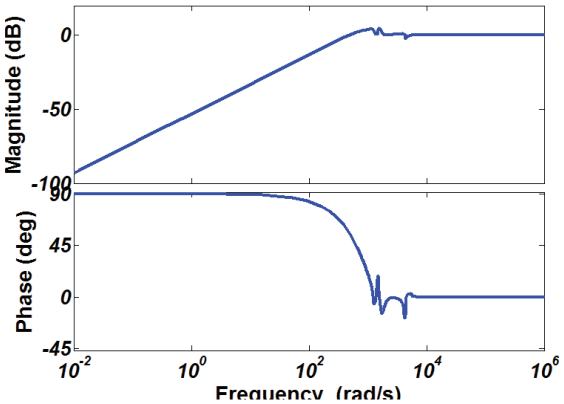

FIGURE 8. Bode plot of the sensitivity transfer function for the system with the implemented GM controller. The magnitude of S exceeds 1/√2 at 52 Hz (326 rad/s). *(Designed based on a 76 Hz unstable PID)*

H_∞ Controller with High Bandwidth

While PID and GM control design performance are limited, H_∞ control law can simultaneously achieve performance and robustness. The bandwidth requirement is met by shaping $S(j\omega)$ and the high resolution requirement is achieved by rolling off of $T(j\omega)$ at high frequencies. Figure 10 describes the H_∞ control problem. Using this approach, we designed a 10^{th} order, 83 Hz bandwidth H_∞ controller, for which the tracking is shown in Figure 11.

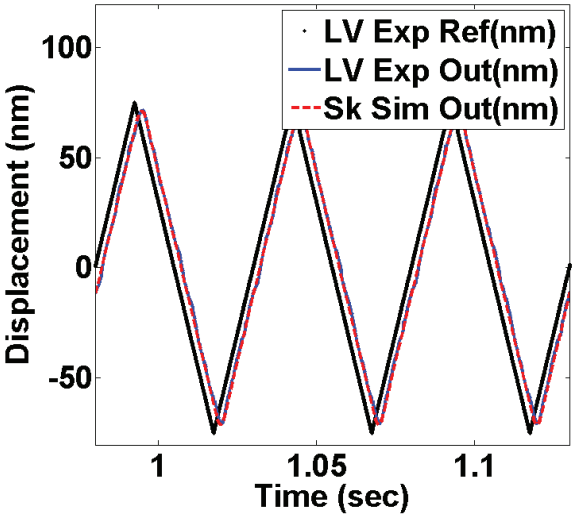

FIGURE 9. Tracking of a 20 Hz triangle wave for the 52 Hz bandwidth GM controller. Note there is less distortion in both the simulated output (Sim Out) and the experimental output (Exp Out) and better amplitude tracking as compared to the PID controller.

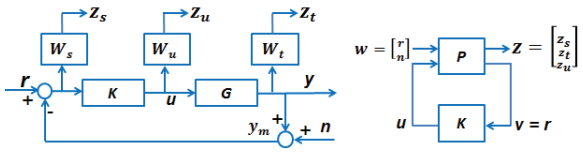

FIGURE 10. Mixed Sensitivity problem for 1DOF control design. The signals z_s, z_t, *and* z_u *represent the tracking error, the noise component in the position signal, and the control signal. The weights* W_s, W_t, *and* W_u *are chosen to reflect the design specifications of tracking bandwidth, positioning resolution, and saturation limits on the control signal. To achieve this objectives, a control design K which minimizes the* H_∞*-norm of the transfer function from w = [r n] to z =[* z_s, z_t, z_u*].*

H_∞ Controller with High Resolution

To address the desire for a high resolution controller the H_∞ control problem of Figure 10 was reformulated to cause $T(j\omega)$ to roll off very early. Because *S* and *T* are not independent, the fast roll off of $T(j\omega)$ causes the magnitude of $S(j\omega)$ to exceed 1/√2 at a low frequency, 30 Hz in this case. Figure 12 shows the tracking performance and noise histogram for a 30 Hz bandwidth H_∞ controller designed for high resolution.

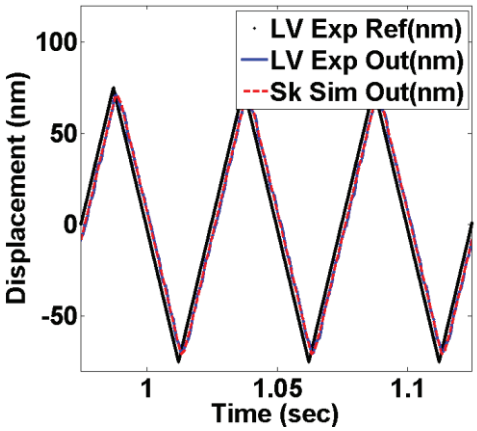

FIGURE 11. Tracking of a 20 Hz triangle wave for the 10th order, 83 Hz bandwidth H_∞ controller. Note the improvement in distortion over the GM and PID controllers.

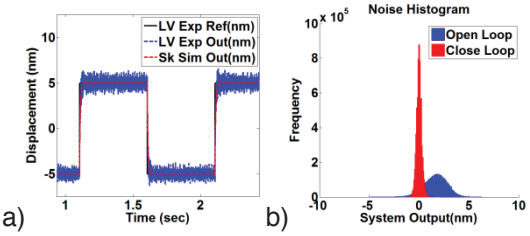

a) b)

FIGURE 12. a) shows tracking of 1 Hz, 5 nm square wave, and b) shows the noise histogram: Closed Loop Resolution = 0.78 nm.

DISCUSSION AND CONCLUSION

We have demonstrated how the H_∞ design process can be used to meet the specific performance constraints of the X-ray nanopositioning problem. Specifically, bandwidth was improved over the PID controller from 43 Hz to 83 Hz and resolution improved from 1.9 nm to .78 nm. Furthermore, these improvements were made without altering the existing mechanics. We have also developed an efficient way to implement arbitrary controller design on a LabVIEW FPGA hardware. This conserves resources and opens up the possibility of multi axis control on a single FPGA.

This work is ongoing and we expect to make additional improvements in both bandwidth and resolution by exploiting multiple-input-multiple-output control and the addition of feedforward control through a two-degree-of-freedom control framework [8].

REFERENCES

[1] R. P. Winarski, M. V. Holt, V. Rose, P. Fuesz, D. Carbaugh, C. Benson, D. Shu, D. Kline, G. B. Stephenson, I. McNulty, and J. Maser, "A hard X-ray nanoprobe beamline for nanoscale microscopy," *Journal of Synchrotron Radiation,* vol. 19, pp. 1056-1060, 2012.

[2] J. Maser, B. Lai, T. Buonassisi, Z. Cai, S. Chen, L. Finney, C. Gleber, C. Jacobsen, C. Preissner, C. Roehrig, V. Rose, D. Shu, D. Vine, and S. Vogt, "A Next-Generation Hard X-Ray Nanoprobe Beamline for In Situ Studies of Energy Materials and Devices," *Metallurgical and Materials Transactions A,* 2013 (in press).

[3] S. Devasia, E. Eleftheriou, and S. O. R. Moheimani, "A Survey of Control Issues in Nanopositioning," *Control Systems Technology, IEEE Transactions on,* vol. 15, pp. 802-823, 2007.

[4] S. O. R. Moheimani, "Invited Review Article: Accurate and fast nanopositioning with piezoelectric tube scanners: Emerging trends and future challenges," *Review of Scientific Instruments,* vol. 79, pp. 071101-11, 2008.

[5] A. Sebastian and S. M. Salapaka, "Design methodologies for robust nano-positioning," *IEEE Transactions on Control Systems Technology,* vol. 13, pp. 868-876, 2005.

[6] D. Shu, J. Maser, M. Holt, R. Winarski, C. Preissner, A. Smolyanitskiy, B. Lai, S. Vogt, and G. B. Stephenson, "Optomechanical design of a hard X-ray nanoprobe instrument with nanometer-scale active vibration control," *Synchrotron Radiation Instrumentation, Pts 1 and 2,* vol. 879, pp. 1321-1324, 2007.

[7] D. Shu, J. Maser, M. Holt, B. Lai, S. Vogt, Y. Wang, C. Preissner, Y. Han, B. Tieman, R. Winarski, A. Smolyanitskiy, and G. B. Stephenson, "Design and test of a differential Scanning stage system for an x-ray nanoprobe instrument," in *Optomechanics 2005*, San Diego, CA, United States, 2005, pp. 1-13.

[8] C. Lee and S. M. Salapaka, "Robust broadband nanopositioning: Fundamental trade-offs, analysis, and design in a two-degree-of-freedom control framework," *Nanotechnology,* vol. 20, 2009.

REDUCTION OF RESIDUAL VIBRATION OF PIEZOELECTRIC ACTUATOR DRIVEN BY CURRENT PULSE

Katsushi Furutani, and Atsushi Sakata
Department of Advanced Science and Technology
Toyota Technological Institute
Nagoya 468-8511 Japan

INSTRUCTIONS

Stacked piezoelectric actuators deform for several tens of micrometers though its resolution is nanometer-order. Hence, they are embedded into magnification mechanisms such as levers and pantographs to enhance the displacement. Because they are basically a hinge structure without damping elements, the residual vibration is frequently a problem in a positioning process. Input shapers have been proposed for voltage drive [1] and they reduce the first mode vibration. The authors have proposed a driving method of a piezoelectric actuator by using current pulses for the high resolution [2]. This has advantages about hysteresis reduction and linearity.

This paper deals with the reduction of the residual vibration by current pulse drive by the adjustment of pulse intervals by a genetic algorithm (GA).

PRINCIPLE OF DRIVING METHOD

Figure 1 shows the principle of the driving method of a piezoelectric actuator by using current pulse [2]. Some current sources and sinks are connected in parallel. The piezoelectric actuator is driven with current pulses. Because the product of current by pulse width is equal to the charge amount, this is a kind of the charge control methods with less hysteresis. Consequently, the displacement can be controlled by counting pulses.

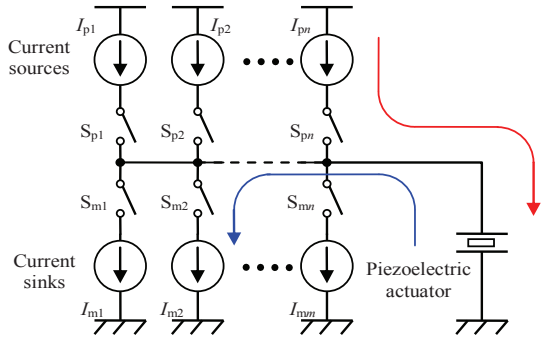

FIGURE 1. Principle of driving method by using current pulse.

Because a series of current pulses is similar to a chromosome, pulse patterns were optimized by a GA. Figure 2 shows phenotype and genotype of pulses. Each current pulse is represented by 2-bit genotype: no pulse (0: 00), charge (1: 01) and discharge (2: 10) ones. The genotype (3: 11) is inhibited.

SIMULATION MODEL OF PIEZOELECTRIC ACTUATOR

By the simulation with Martin's model [3], the displacement was estimated under various pulse patterns. Figure 3 shows a 1st-order simulation model of a stacked piezoelectric actuator. The

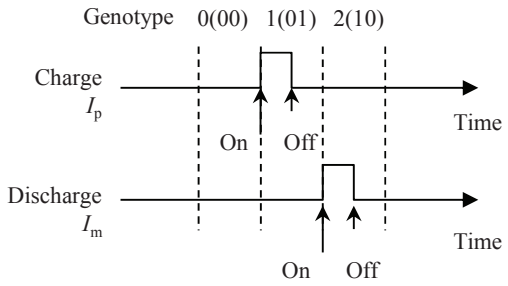

FIGURE 2. Phenotype and genotype of current pulses.

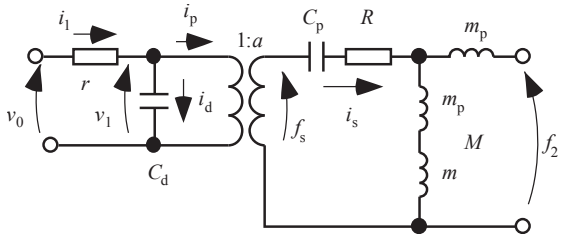

FIGURE 3. Martin's model for simulation.

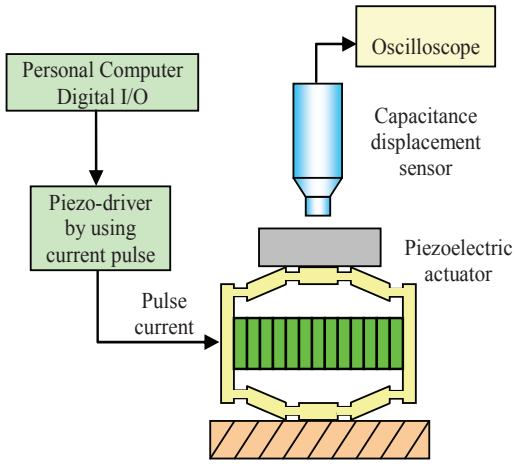

FIGURE 4. Experimental setup.

TABLE 1. Parameters in 2nd order simulation model.

1st mode	Gain K_1	0.830
	Damping ratio ζ_1	9.85×10^{-3}
	Resonance frequency ω_{n1} rad/s	6.19×10^{3}
2nd mode	Gain K_2	0.664
	Damping ratio ζ_2	2.97×10^{-3}
	Resonance frequency ω_{n2} rad/s	1.47×10^{4}
Capacitance C_d F		1.75×10^{-6}
Force factor a N/V		9.18×10^{-2}
Equivalent mass M kg		9.42×10^{-3}

left and right hand sides denote the electrical and mechanical characteristics, respectively. A 2nd-order model was represented by a parallel of two 1st-order models with different resonance frequencies.

$$G_V(s)=\frac{a(K_2g_1+K_1g_2)}{(1+C_drs)Mg_1g_2+a^2rs(K_2g_1+K_1g_2)}$$
$$G_I(s)=\frac{a(K_2g_1+K_1g_2)}{Mg_1g_2C_ds+a^2s(K_2g_1+K_1g_2)}$$
$$g_1=s^2+2\zeta_1\omega_{n1}s+{\omega_{n1}}^2,\quad g_2=s^2+2\zeta_2\omega_{n2}s+{\omega_{n2}}^2 \tag{1}$$

EXPERIMENTAL SETUP

Figure 4 illustrates an experimental setup. The magnification mechanism, in which a stacked piezoelectric actuator was embedded, deformed 35 μm at an applied voltage of 100 V with a hysteresis of 14%. The displacement was measured with a capacitance type displacement sensor with a range of 50 μm, a resolution of 3 nm and a band width of 20 kHz. A personal computer was used for a controller.

Table 1 shows the parameters of the 2nd-order simulation model. They are measured through static characteristics and step response. The frequency components were adjusted by the gains K_1 and K_2.

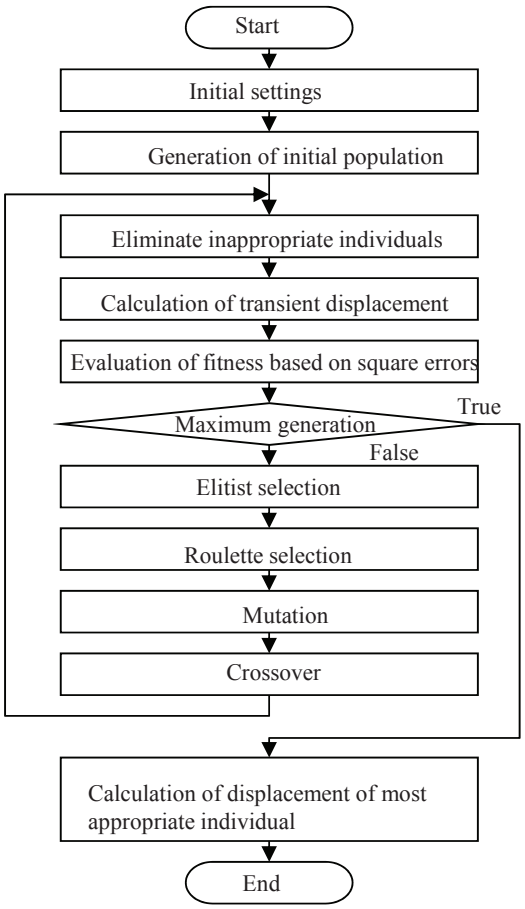

FIGURE 5. Algorithm of generation of current pulse pattern by GA.

GENERATION OF DRIVING PATTERNS

The current or voltage patterns were optimized by simulations before driving in experiments.

Current pattern by GA

Figure 5 shows a flowchart of GA. Firstly, initial individuals are randomly generated. The length of chromosome was 30. Then individuals which do not reach a target displacement were eliminated without the evaluation by a simulation.

TABLE 2. Alternating time in Input shaping.

Time ms	A_i	1st order	2nd order
t_1	+1	0.000	0.000
t_2	-1	0.094	0.036
t_3	+1	0.371	0.253
t_4	-1	0.655	0.330
t_5	+1	0.744	0.498
t_6	-1	–	0.663
t_7	+1	–	0.743
t_8	-1	–	0.956
t_9	+1	–	0.995

The simulated displacement was evaluated based on the integral square error (ISE) criterion. Better individuals were left by the roulette wheel selection. The calculation was terminated when the minimum ISE was not improved even if 50000 individuals (individuals × generations) were tried.

Voltage Pattern by Input Shaping

The actuator was driven by an input shaping method for the comparison. The following simultaneous equations were solved by Newton-Raphson method to extend the unity magnitude zero vibration derivative (UM-ZVD) input shaping:

$$\sum_{i=1}^{N} B_i \cos\varphi_i = 0, \quad \sum_{i=1}^{N} B_i T_i \cos\varphi_i = 0,$$
$$\sum_{i=1}^{N} B_i \sin\varphi_i = 0, \quad \sum_{i=1}^{N} B_i T_i \sin\varphi_i = 0, \qquad (2)$$
$$B_i = \frac{A_i \omega_{nj}}{\sqrt{1-\zeta_j{}^2}} \exp\left\{-\zeta_j \omega_{nj} (T_N - T_i)\right\},$$
$$\varphi_i = \sqrt{1-\zeta_j{}^2}\,\omega_{nj} T_i$$

where j=1, 2 is the vibration modes, ω_{nj} is the resonance frequencies, T_i is the time applying ith pulse, A_{odd}=+1 and A_{even}=-1 are impulse amplitude and $2N$+1 is the number of impulse. Table 2 shows the alternating time for the first and second order models. The applied voltage for the input shaper was determined to equalize the final displacement by the current pulse drive.

COMPARISON OF RESIDUAL VIBRATION

Series of current pulses were generated by the GA. In the current pulse drive, the current peak, frequency and duty factor were 20 mA, 10 kHz and 80%, respectively. The pulses from the source and to the sink were counted as positive and negative, respectively. Then, +10 pulses in total were provided within 2 ms. Figure 6 shows the influence of the number of the individuals generated simultaneously in the GA. The total individuals tried were the same in all cases. The minimum ISE and the convergence speed were better at larger number of individuals generated simultaneously.

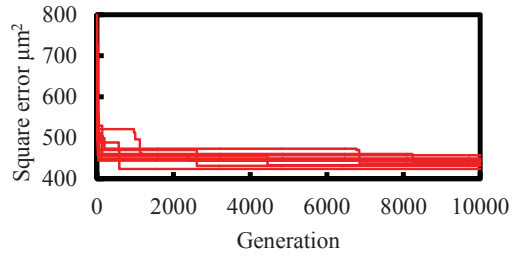

(a) 10 individuals.

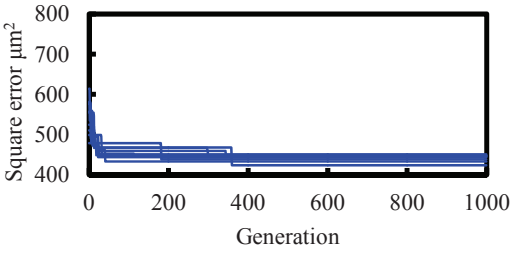

(b) 100 individuals.

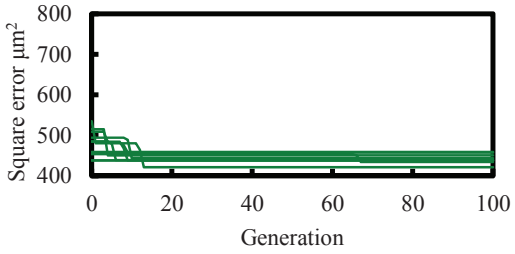

(c) 1000 individuals.
FIGURE 6: Influence of number of individuals on convergence.

Figure 7 shows experimental results of the displacement control. The optimized patterns were applied. While the current pulses optimized by the simulation were provided, the displacement rose smoothly. The residual vibration at higher frequency was observed by the input shaper. Although the voltage is directly proportional to the displacement, the integral of the current pulse decreased higher frequency components. Then the higher harmonics were decreased.

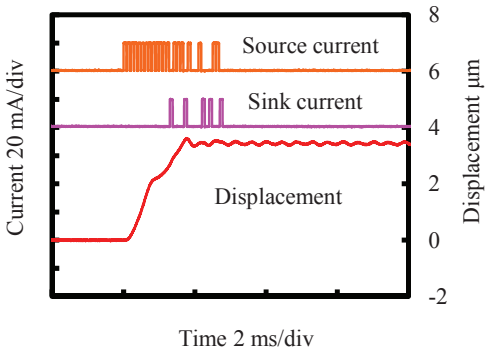

(a) Current pulse.

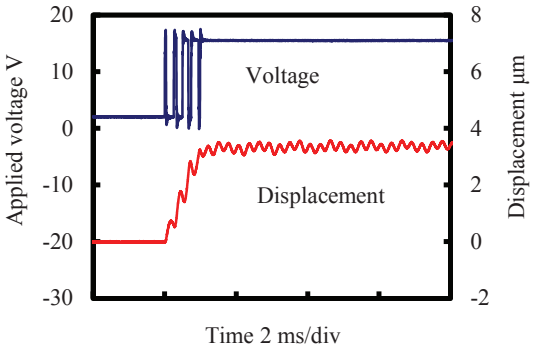

(b) 2nd order input shaper.
FIGURE 7: Positioning performance.

TABLE 3. Comparisons of performance.

	Optimized current pulse	2nd order input shaping
5% settling time ms	1.68	19.30
Overshoot %	4.71	3.78
ISE µm^2	1.53	25.3

Table 3 shows the comparisons of performance. Although the overshoot by the input shaper was smaller than that by the current pulse drive, the residual vibration by the input shaper caused the longer settling time. This allowed the small ISE by the current pulse drive from 10 to 12 ms. The creep of the displacement by the input shaper also deteriorated the settling time.

Figure 8 shows the frequency components of the driving signals. In the input shaping, the components at the 1st and 2nd vibration modes were eliminated. However, a harmonic noise around 3.8 kHz appeared by the alternation. This caused the residual vibration that directly affected the displacement. In the current pulse

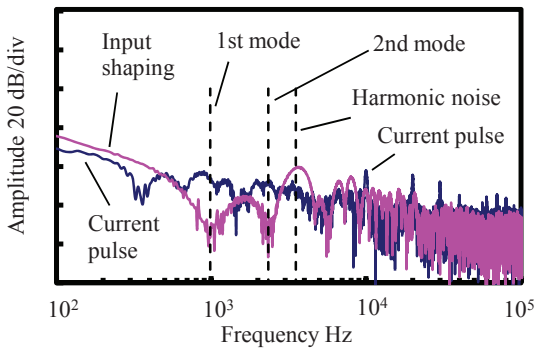

FIGURE 8. Frequency components of driving signals.

drive, a carrier of 10 kHz was observed as well as components at the 1st and 2nd vibration modes. The current pulses were integrated and higher components were reduced at a rate of 20 dB/dec. Therefore, the residual vibration was small. When the input shaper or current pulse pattern for the 1st order model was applied to the 2nd order model, the residual vibration by the input shaper was much larger than that by the current pulse drive.

CONCLUSIONS

In this paper, the intervals of current pulses were optimized by GA. Conclusions can be drawn as follows.

- Although the residual vibrations were almost the same both by the current pulse drive and input shaper voltage drive in the simulations, the current pulse drive allowed smaller vibration in the experiments.
- In the current pulse drive, higher components were reduced by the integration.

REFERENCES

[1] Singhose WE, Seering WE, Singer NC. Time-Optimal Negative Input Shapers. Transactions of ASME, Journal of Dynamics, Systems, Measurement and Control. 1997; 119: 198-205.

[2] Furutani K, Iida K. A driving method of piezoelectric actuator by using current pulse. Meas. Sci. Technol. 2006; 17: 2387-2394.

[3] Furutani K, Furuta A. Simulation of the Performance of a Piezoelectric Actuator Driven with a Current Pulse. Adv. Rob. 2010; 1989: 1945-1961.

OPTIMAL DAMPING FOR THE REDUCTION OF RESIDUAL VIBRATIONS IN ULTRA-PRECISION MANUFACTURING MACHINES

Jihyun Lee and Chinedum E. Okwudire
Mechatronics and Sustainability Research Lab
Department of Mechanical Engineering, University of Michigan
Ann Arbor, MI, USA

OVERVIEW

This paper provides practical guidelines for selecting optimal damping for the reduction of residual (rocking) vibrations in passively isolated ultra-precision manufacturing (UPM) machines. The effects of damping on the residual vibrations of UPM machines are analytically investigated using a planar model with horizontal and vertical damping properties. The analysis reveals that increasing vertical damping always leads to the reduction of residual vibrations. On the other hand, increasing horizontal damping could sometimes be detrimental to residual vibration reduction, particularly when the machine's vibration modes are coupled. A simple objective function is proposed for analytically determining the optimal horizontal damping for a given machine. Simulations using the parameters of a 5-axis ultra-precision milling machine are used for preliminary validation of the findings of the paper. Experiments are planned for future work.

INTRODUCTION

Ultra-precision manufacturing (UPM) machines are designed to fabricate and measure complex parts having micrometer-level features and nanometer-level tolerances/surface finishes [1]. Examples of UPM machines include ultra-precision machine tools, wafer steppers and micro CMMs. UPM machines are often isolated from floor vibrations using passive isolators because they are cost effective, reliable and energy neutral [2][3]. A major problem with the soft mounting provided by passive isolators is that it induces low-frequency residual (rocking) vibrations of the isolated machine base, which degrades the achievable accuracy/speed of UPM machines [2]. A long-standing rule of thumb in isolation system design is to decouple all vibration modes by aligning the isolator mounting locations with the center of gravity (CG) of the isolated machine [4]. In practice, however, many UPM machine designs are mode coupled because it is very difficult to locate the isolators exactly at the CG [3]. Moreover, recent research by the authors has revealed that mode coupling can lead to the drastic reduction of residual vibrations in passively isolated systems [5]. The problem is that mode coupling complicates the damping behavior of the isolated machine compared to decoupling [6]. In decoupled systems, increasing damping always reduces residual vibrations. However, in mode coupled systems, the isolator with the highest damping does not necessarily yield the best reduction in residual vibrations. Methods exist for optimizing the damping of passively isolated systems in other application areas such as vehicle suspensions [7] and dynamic vibration absorbers [8]. However, the existing methods are not readily applicable to UPM machines. Consequently, there is a need to provide machine designers with the analytical tools and practical guidelines to select damping values that provide the best reduction of residual vibrations for mode coupled UPM machines. In this paper, the damping behavior of mode coupled UPM machines is analytically studied using a planar model with horizontal and vertical damping properties. The analysis shows that increasing vertical damping always leads to the reduction of residual vibrations. However, increasing horizontal damping could sometimes be detrimental to residual vibration reduction. A simple method for analytically determining the optimal horizontal damping for a given machine is proposed and validated by simulations using the parameters of a 5-axis ultra-precision milling machine. Experiments are planned for future work.

MODELING AND ANALYSIS

Figure 1 shows a simple model of an isolated UPM machine of mass m and centroidal moment of inertia I about the x-axis. k_y, k_z and c_y, c_z are the combined stiffness and damping constants of the passive isolators in the y and z directions, respectively.

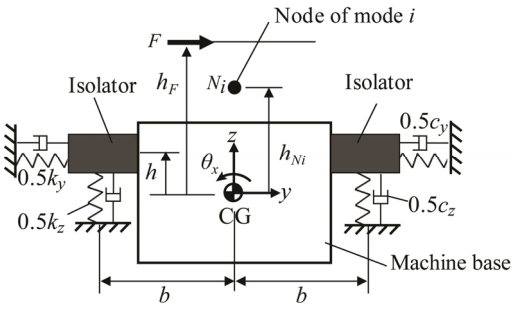

FIGURE 1: Simple Model of Isolated Machine

The vibrations of the machine base are assumed to occur only in the *y*-*z* plane (implying that the machine is symmetrical in the *x*-direction). *h* is the vertical height of the isolator mounting point measured from the CG. Our focus is on the two modes, described by the coordinates *y* and θ_x, which are coupled by non-zero values of *h*, that together contribute to the rocking vibrations of the isolated machine. Therefore, the dynamics in the *z*-direction is not included in the analysis. The free vibrations of the system are described by

$$\mathbf{M}\ddot{\mathbf{u}} + \mathbf{C}\dot{\mathbf{u}} + \mathbf{K}\mathbf{u} = \mathbf{0} \tag{1}$$

M, **C, K** are respectively the mass, damping, stiffness matrices, while **u** is the vector of displacements of the system. They are given by

$$\mathbf{M} = \begin{bmatrix} m & 0 \\ 0 & I \end{bmatrix};\ \mathbf{C} = \begin{bmatrix} c_y & -c_y h \\ -c_y h & c_\theta + c_y h^2 \end{bmatrix};$$
$$\mathbf{K} = \begin{bmatrix} k_y & -k_y h \\ -k_y h & k_\theta + k_y h^2 \end{bmatrix};\ \mathbf{u} = \begin{bmatrix} y \\ \theta_x \end{bmatrix} \tag{2}$$

where $k_\theta = b^2 k_z$ and $c_\theta = b^2 c_z$. The effect of the *y*-axis inertial reaction *F*, at a distance h_F from the CG, on the acceleration of the base in the θ_x direction (i.e., rocking vibration) is represented by the frequency response function (FRF)

$$H = \frac{1}{m\rho}\sum_{i=1}^{2}\left(A_i X_i - B_i\right) \tag{3}$$

ρ in Eq. (3) is the centroidal radius of gyration. A_i, B_i and X_i are dimensionless variables of each mode *i* (*i* = 1, 2). They are given by

$$A_i = \frac{h_F - h_{Ni}}{I_{qi}};\quad X_i = \frac{\omega^2}{-\omega^2 + 2j\omega\zeta_y\omega_{ni}^{\ 2} + \omega_{ni}^2}$$
$$B_i = \frac{X_i}{I_{qi}}\frac{2j\varepsilon\beta\omega\left(A_1X_1 + A_2X_2\right)}{2j\varepsilon\beta\omega\left(X_1/I_{q1} + X_2/I_{q2}\right) + \omega^2} \tag{4}$$

where ω represents the dimensionless excitation frequencies and *j* is the unit imaginary number. ω_{ni}, h_{Ni} and I_{qi} respectively denote the dimensionless natural frequency, node height and modal inertia of each vibration mode *i*. Their expressions are given in Ref. [5]. The variable β is key in determining the damping behavior of the system. It is given by

$$\beta = \zeta_\theta - \varepsilon\zeta_y \tag{5}$$

where

$$\zeta_y = \frac{c_y}{2\sqrt{k_y m}};\ \zeta_\theta = \frac{c_\theta}{2\sqrt{k_\theta I}};\ \varepsilon = \sqrt{\frac{k_\theta}{I}\frac{m}{k_y}} \tag{6}$$

If $\beta = 0$, $B_i = 0$ in Eq.(3) so the coupled system dynamics is proportionally damped. This implies that increasing the horizontal (ζ_y) or rotational (ζ_θ) damping ratios results in the reduction of both resonance peaks in *H*, as shown in Figure 2(a). In most cases, however, $\beta \neq 0$ so the system dynamics is non-proportionally damped [6]. Therefore, the relationship between the magnitude of each resonance peak and the corresponding damping ratios is not as straightforward because of the influence of B_i on *H*. For instance, as ζ_y is increased in Figure 2(b), the amplitude of the first mode initially decreases but beyond a certain value of ζ_y it starts to increase.

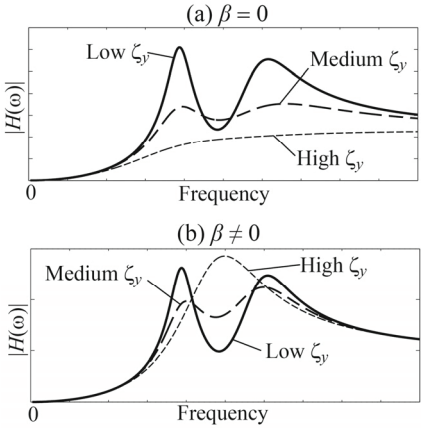

FIGURE 2: Effects of Increasing ζ_y on H for (a) $\beta = 0$ and (b) $\beta \neq 0$. ε, h and h_F are kept Constant

To determine the influence of ζ_y and ζ_θ on each of the two resonance peaks of *H* when $\beta \neq 0$, the partial derivatives

$$P_{yi} = \left.\frac{\partial|H(\omega)|}{\partial\zeta_y}\right|_{\omega=\omega_{ni}};\quad P_{\theta i} = \left.\frac{\partial|H(\omega)|}{\partial\zeta_\theta}\right|_{\omega=\omega_{ni}} \tag{7}$$

are derived and analyzed. $|H(\omega)|$ is given by

$$|H(\omega)| = \frac{1}{m\rho}\sqrt{\frac{Num}{Den}};\qquad Num = N_2\zeta_y^{\ 2} + N_0$$
$$Den = \left(D_{21} + D_{22}\zeta_\theta^{\ 2}\right)\zeta_y^{\ 2} + D_1\zeta_\theta\zeta_y + \left(D_{01} + D_{02}\zeta_\theta^{\ 2}\right) \tag{8}$$

where

$$N_2 = 4\omega^3\left(h_F - h\right)^2;\ N_0 = \omega\left[h_F\omega^2 - \left(h_F - h\right)\right]^2$$

$$D_{21} = 4\omega^2\left[\varepsilon^2 - \left(1+h^2\right)\omega^2\right]^2;\ D_{22} = 16\varepsilon^2\omega^2;\ D_1 = 8\varepsilon\omega^6 h^2$$

$$D_{01} = \left[\varepsilon^2 - \left(1+\varepsilon^2+h^2\right)\omega^2 + \omega^4\right]^2;\ D_{02} = 4\varepsilon^2\left(-\omega+\omega^3\right)^2 \quad (9)$$

The partial derivative $P_{\theta i}$ defined in Eq.(7) is given by

$$P_{\theta i} = \frac{1}{2}\left|H(\omega_{ni})\right|^{-1/2}\left(\frac{-Num\left(2(D_{22}\zeta_y{}^2 + D_{02})\zeta_\theta + D_1\zeta_y\right)}{\left(Den\right)^2}\right) \quad (10)$$

Note that because N_2, N_0, D_{21}, D_{22}, D_1, D_{01} and D_{01} are each always positive, $P_{\theta i} < 0$ always. This means that increasing ζ_θ (for instance by increasing c_z) always reduces both resonance peaks in H, which generally leads to a reduction of residual vibrations.

The situation is different for the partial derivative P_{yi} which is given by the expression

$$P_{yi} = \frac{1}{2}\left|H(\omega_{ni})\right|^{-1/2}\left(\frac{\bar{A}\cdot\zeta_y{}^2 + 2\bar{B}\cdot\zeta_y + \bar{C}}{\left(Den\right)^2}\right) \quad (11)$$

where

$$\bar{A} \triangleq D_1 N_2 \zeta_\theta$$

$$\bar{B} \triangleq \left(N_0 D_{22} + N_2 D_{02}\right)\zeta_\theta{}^2 - \left(N_0 D_{21} + N_2 D_{01}\right) \quad (12)$$

$$\bar{C} \triangleq -D_1\zeta_\theta N_0$$

There is always a value of ζ_y that makes $P_{yi} = 0$, thus yielding the horizontal damping ratios ζ_{y1}^* (at $\omega = \omega_{n1}$) and ζ_{y2}^* (at $\omega = \omega_{n2}$) that minimize each resonance peak in H. They are given by

$$\zeta_{yi}{}^* = \frac{-\bar{B} + \sqrt{\bar{B}^2 - \bar{A}\cdot\bar{C}}}{\bar{A}} \quad (13)$$

ζ_y^*, the optimal horizontal damping ratio, is determined by selecting the $\zeta_{y,i}^*$ value corresponding to the dominant resonance peak in H according to the function

$$\max_{\zeta_{yi}^*}\left(\left|H\left(\omega_{ni},\zeta_{yi}^*\right)\right|\right) \quad (14)$$

SIMULATION RESULTS

Simulations are carried out based on the parameters of Mori Seiki's NN1000 5-axis ultra-precision machine tool [6] whose schematic is shown in Figure 3. Stemming from a granite base supported on four pneumatic vibration isolators, the machine has its x and C axes on the workpiece side and its y, z and A axes on the tool side. The key parameters of the machine used for simulations are provided in Table 1. The machine's isolators are assumed to be located 80 mm above its CG, thus giving a dimensionless h of –0.28 [5]. Similarly, the dimensionless height of the y-axis motor (located 435 mm above the CG) is h_F = 1.53. Using ζ_θ = 0.15, the optimal horizontal damping for the machine is calculated from Eq.(14) as ζ_y^* = 0.1. Figure 4 shows the comparison of the magnitude of the residual vibration FRF (H) obtained using the ζ_y^* = 0.1 and that obtained using the assumed maximum horizontal damping ratio for the machine (ζ_{ymax} = 0.5). Even though ζ_y^* is 5 times smaller than ζ_{ymax}, it gives rise to a 17% reduction in the maximum amplitude of H.

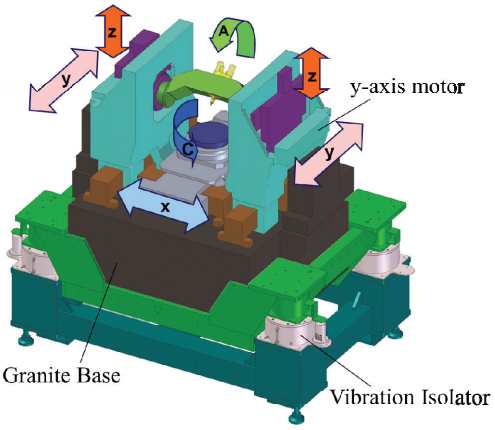

FIGURE 3. Schematic of Mori Seiki's NN1000 5-Axis Ultra-Precision Machine Tool used for Simulations

TABLE 1. Simulation Parameters

Parameter	Value
m [kg]	1,182
I [kg-m^2]	96
k_y [N/mm]	880
k_θ [Nm/rad]	104,430

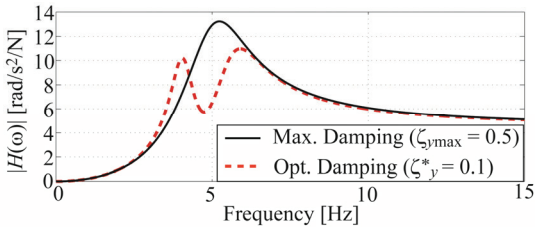

FIGURE 4: Comparison of FRF Magnitude of H for Maximum and Optimized Horizontal Damping Ratios

CONCLUSION

This paper has analytically investigated the effects of damping on the residual (rocking) vibrations of mode coupled, passively isolated ultra-precision manufacturing (UPM) machines. It has shown that higher vertical damping is always beneficial to residual vibration reduction. However, higher horizontal damping may not always be good for residual vibration reduction. A simple analytical method for determining the optimal horizontal damping that minimizes residual vibrations for UPM machines with planar dynamics is proposed. The findings of the paper are validated by simulations carried out using the parameters of a 5-axis ultra-precision milling machine tool.

FUTURE WORK

Figure 5 shows the CAD model of a reconfigurable test bed that has been designed for experimental validation of the work reported in this paper. It consists of a machine base mounted on a foundation by four pneumatic isolators. The array of holes on the base and foundation allow the vertical and horizontal locations of the isolators to be varied. The stiffness and damping of the isolators can be altered by using different isolators. The electromagnetic shaker will be used to provide transient or forced excitations to the machine base in the horizontal and vertical directions. Accelerometers (not shown) will be used to measure the vibrations of the base.

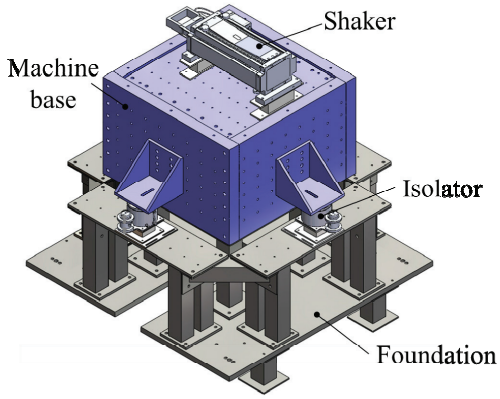

FIGURE 5: CAD Model of Reconfigurable Test Bed Designed for Carrying out Experiments

REFERENCES

[1] Alting L, Kimura F, Hansen H, Bissacco G. Micro Engineering. Annals of the CIRP. 2003; 52: 635-657.

[2] DeBra D. Vibration Isolation of Precision Machine Tools and instruments. Annals of the CIRP. 1992; 41: 711-718.

[3] Rivin E. Vibration Isolation of Precision Equipment. Precision Engineering. 1995; 17: 41-56.

[4] Piersol A, Paez T. Harris' Shock and Vibration Handbook 6th Edition. McGraw-Hill, 2010. 39.13-39.14.

[5] Okwudire C E, Lee J. Minimization of the Residual Vibrations of Ultra-Precision Manufacturing Machines via Optimal Placement of Vibration Isolators. Precision Engineering. 2013; 37:425-432.

[6] Udwadia F E, Esfandiari R S. Non-classically damped dynamic systems: an iterative approach. Transactions of ASME Journal of Applied Mechanics. 1990; 57:423-433.

[7] Li T H, Pin K Y. Evolutionary Algorithms for Passive Suspension Systems. JSME International Journal Series C. 2000; 43(3): 537-544.

[8] Asani T, Nishihara O, Baz A M. Analytical solutions to H∞ and H2 optimization of dynamic vibration absorber attached to damped linear systems. Journal of Vibration and Acoustics. 2002; 124:67-78.

[9] Kim C-J, Padden T, Kim J. Ultra-precision machine tool. US patent # 7,845,257 B2 2010.

ACKNOWLEDGEMENTS

The authors would like to thank DTL Corporation (Mori Seiki) for providing the parameters of their 5-axis ultra-precision milling machine (NN1000 DCG) for the simulations reported in this paper. This work is sponsored by the National Science Foundation's Grant # 1232915.

PRECISION HIGH NUMERICAL APERTURE SCANNING SYSTEM FOR FEMTOSECOND MICROMACHINING OF OPHTHALMIC MATERIALS OVER LARGE FIELD

Daniel R. Brooks[1], Nicolas S. Brown[1], Lisen Xu[1], Daniel E. Savage[1], Wayne H. Knox[1,2], Jonathan D. Ellis[1,3]
[1]The Institute of Optics
[2]Center for Visual Sciences
[3]Department of Mechanical Engineering
University of Rochester
Rochester, New York

BACKGROUND

Femtosecond laser micromachining has been developed for writing custom 3D refractive index modifications into ophthalmic materials [1]. These results can be applied to the development of custom contact lenses, adjusting the refractive corrections in Intraocular lenses (IOLs), or direct writing into the cornea. Recently, a design methodology has been demonstrated for writing lateral gradient index microlenses into hydrogels [2]. The writing process involves a localized material phase change due to accumulated thermal energy when a tightly focused laser beam experiences two-photon absorption in the focal volume. This has now been demonstrated in writing refractive corrections directly into live cornea [3] where it is termed IRIS, for Intra-Tissue Refractive Surgery. Due to the nature of nonlinear absorption, the change in index only occurs in the focal region of the laser and is dependent on the speed the focal region is travelling through the material and laser intensity. In order to write efficiently, it is necessary to be able to reach scan speeds in excess of 200 mm/s with reliable and consistent knowledge of the speed and position. The focal spot volume is on the order of 1 μm diameter, thus high position accuracy is needed to ensure uniformity of the refractive corrections that result. The scanning system must also be able to cover up to an 8 mm range to correct over the entire pupil of the eye. These requirements together put a high demand on the scanning stage and until now, a good solution that could accomplish both the accurate and consistent speed as well the required range has not been available.

In the past, the scanning of the focal region has been achieved by several different scanning methods. Galvanometer based scanning systems using two oscillating mirrors that are imaged into the entrance pupil of a high numerical aperture objective (NA ≥0.7) are able to scan the focal spot rapidly. This method gives very good control and consistency but can only cover an approximately 300 μm scan range when used with high numerical aperture objectives (NA>0.7). Alternatively, a scanning system consisting of two orthogonally stacked piezoelectric stepper stages provide writing with up with ±9 mm travel. In this mode, a sample is attached to the stages and is moved through the focal region, which is stationary. This method of scanning requires the sample to move, which would be inapplicable for clinical settings. We found that the translation speed of these stages was inconsistent, varying up to 20 mm/s from a nominal speed of 100 mm/s. An example scan speed profile is shown in Figure. 1.

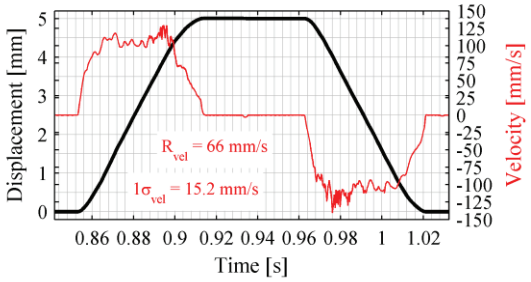

FIGURE 1. Scan speed profile of a PILine® M-663.465 piezo stepper stage with a displacement of 5 mm and a nominal speed of 100 mm/s. Once "constant velocity" is reached, the 1σ standard deviation was 15.2 mm/s with a range of 66 mm/s.

In addition to the variability in the linear scan speed, at higher speeds we observed lateral positional inaccuracies much larger than the linewidths while moving at higher speeds. This can be seen in Figure 2. We believe these to be

caused by straightness and angular errors in the piezo stepper motor.

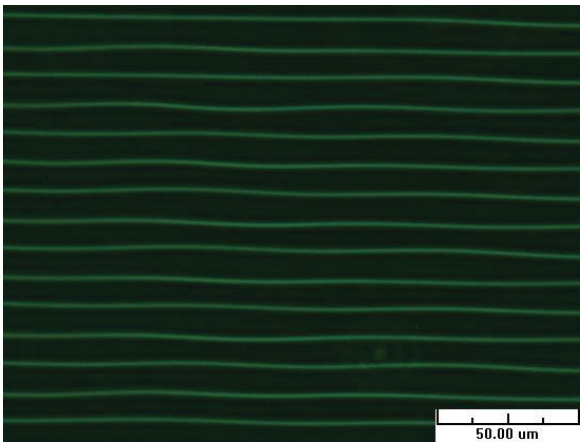

FIGURE 2. Differential interference contrast (DIC) microscope image showing lateral positional inaccuracies in the piezo stage in hydrogel.

These two inaccuracies result in low quality structures that cause significant scattering of the transmitted light. This scattering is unacceptable and leads to difficulties in measuring the refractive corrections created in structures using a wavefront measurement with a Shack-Hartmann wavefront sensor.

After viewing these results it became apparent that new scanning systems are needed to achieve the requirements of high speed, consistent scanning over a large range, when using objectives with NA>0.7.

PROTOTYPE SCANNING SYSTEM

To meet the previously stated requirements, a new scanning system was needed. Previously, a voice coil-based scanner was developed for use in photoacoustic microscopy [4]. To achieve our goals, we have developed a scanning solution in which an objective is attached to an oscillating flexure. The flexure is attached to a z-axis stage which is, in turn, attached to a slower horizontal stage oriented perpendicular to the axis of the translation of the flexure.

First Version

For the first version of this new scanning setup a commercial vibration exciter was used as the oscillating flexure with an NA 1.0 water immersion objective for focusing the light into the sample to be written. This setup can be seen in Figure 3.

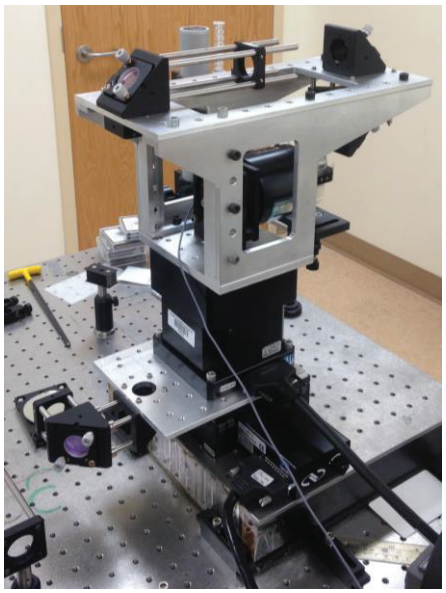

FIGURE 3. First version flexure scanning system using commercial vibration exciter

With the first version of this new stage, we were able to achieve consistent speeds and displacements with up to 2.5 mm of travel range. At higher ranges of motion, there was more variability of the end position which likely means that there was also more variability in the speed across the profile. This can be seen in Figures 4 and 5, which show two examples of structures written using this system in ophthalmic hydrogel polymers (used in contact lenses and intraocular lenses).

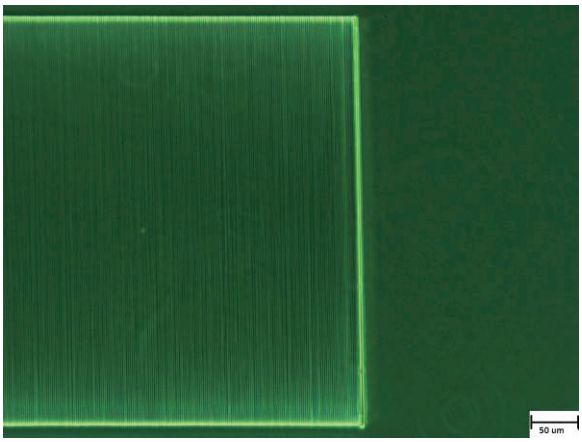

Figure 4. DIC microscope photo of structure written at low speed (24 mm/s in middle, 9 Hz oscillation) in hydrogel. Edges are very consistent.

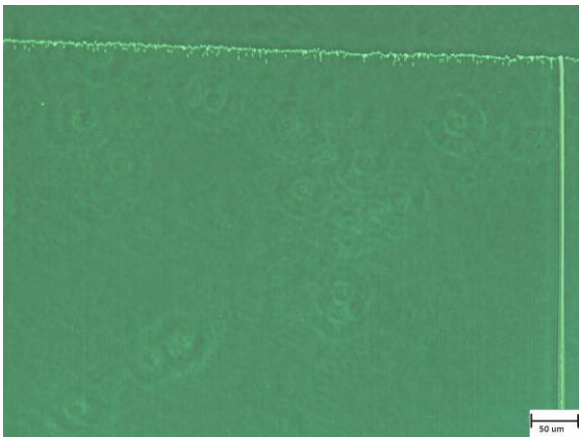

FIGURE 5. Larger structure in hydrogel at higher speed (130 mm/s in middle, 9 Hz oscillation) shows more variability on edges. The total size of this structure is 2.31 mm in the direction of travel of the oscillator.

An example velocity profile using this flexure can be seen in Figure 6.

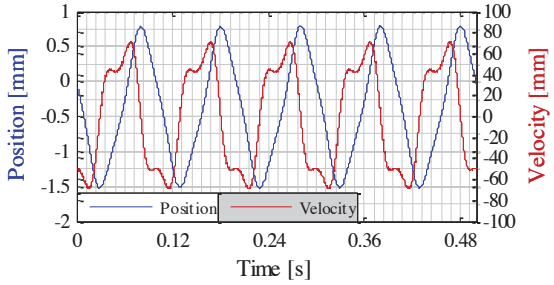

Figure 6. Scan profile of the first version flexure scanning system with a 10 Hz oscillation.

In Figure 6 it can be seen that the velocity profile for the shaker motor is much smoother than that of the piezo stepper stages used previously. While the velocity profile is no longer nominally flat, we find that the much smoother velocity profile and decreased tracking errors leads to significantly less scattering. This decrease in scattering allows us to be able to use a Shack-Hartmann wavefront sensor to measure the optical power of the structures where they could not be measured using devices written with the piezo stepper stages. A comparison of the spots produced by the lenslets in the Shack-Hartmann wavefront sensor from both the piezo stepper stage and the flexure type scanner is shown in Figure 7.

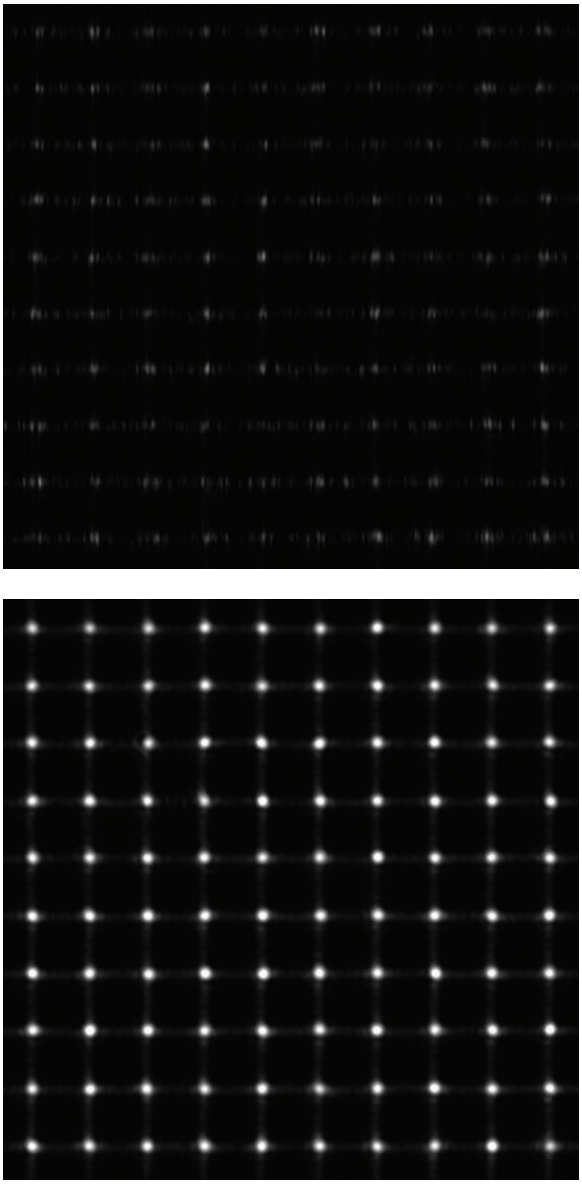

Figure 7. Two images from a Shack-Hartman wavefront sensor demonstrating the dramatic increase in image quality and reduction in scattering using the flexure type scanner as opposed to the piezo stepper stages.

While this version of the flexure scanning system showed significant improvement in velocity and position consistency, there are also a few inherent limitations. One of these is the stroke, which is limited to approximately 2.5 mm. Another is the low frequency response with a resonant frequency of 16 Hz. This low frequency response limits the velocity profile variability that can be achieved. In order to change these limitations a new flexure scanning system was designed.

Second Version

Since the maximum range of the first version of our oscillating scan system was only approximately 2.5 mm, we have designed a new custom flexure system using a titanium flexure excited by four voice coil motors. This new system is designed to produce larger translations along the axis of the flexure, have a higher cutoff frequency to allow for more control over the waveform produced, and allow for closed loop control to ensure that the correct velocity profile is produced. A CAD model of the flexure with voice coil motors is shown in Figure 8.

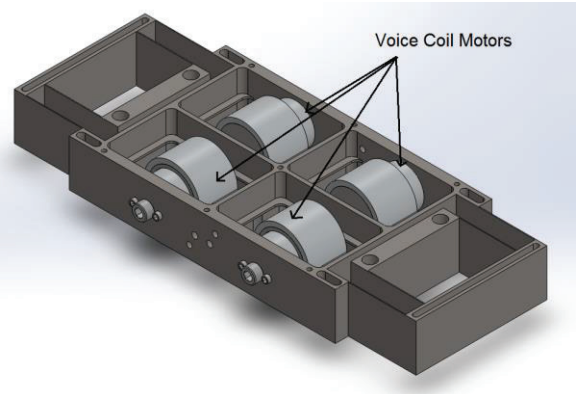

FIGURE 8. SolidWorks model of new flexure with mounted voice coil motors

As shown in Figure 8, the voice coil motors are incorporated into the body of the flexure. Two of the voice coils will be pushing the flexure body while the other two pull so that they all exert force in the same direction. The flexure was designed so that the total force from the four voice coils would produce a maximum displacement of 4 mm in either direction (total stroke of 8 mm). The maximum stress was also designed to be less than one sixth of the yield stress for titanium. The resonant frequencies of flexure with voice coils attached are shown in Table 1.

Table 1. Resonant frequencies of the flexure for second version scanning system

Resonance	Value
1	41
2	192
3	200
4	533

The voice coils are designed to all run off the same signal from an xPC target system with an amplifier to achieve the electrical power necessary.

The flexure and voice coils are mounted to an adapter plate which is mounted to a z-axis stage. This allows us to vary the depth at which we write the structures giving us the ability to write multiple layers if necessary. The z-stage is mounted to another adapter plate which is mounted to a horizontal linear stage to provide what we have termed the slow-axis. The slow axis is translated at the speed necessary for the center line spacing desired (currently 1 μm). The slow-axis stage can either move the flexure across continuously or in discrete steps providing for straighter lines. The laser beam must be aligned to each of the three mechanical axes in turn to prevent drift and changes in the beam through the entire writing process. This is accomplished through kinematic right angle mirror mounts to direct the beam.

This new flexure system should be a significant improvement over the first version. It is designed with a larger stroke which enables writing larger structures. It should also have a higher frequency response which will allow for better control over the velocity profile of the structures. This will enable us to write smooth, high quality structures in both hydrogels and cornea.

ACKNOWLEDGEMENTS

The work has been funded by Bausch and Lomb with support in part by CEIS, an Empire State Development-designated Center for Advanced Technology. The authors are grateful to Dr. Krystel Huxlin and Mr. John Spalding for many fruitful discussions regarding this work.

REFERENCES

[1] Ding L, Blackwell R, Kunzler J, Knox W. Large refractive index change in silicone-based and non-silicone-based hydrogel polymers induced by femtosecond laser micro-machining. Optics Express. 2006; 14: 11901-11909.

[2] Xu L, Knox W. Lateral gradient index microlenses written in ophthalmic hydrogel polymers by femtosecond laser micromachining. Optical Materials Express. 2011; 1: 1416-1424

[3] Xu L, Knox W, DeMagistris M, Wang N, Huxlin K. Noninvasive Intratissue Refractive

Index Shaping (IRIS) of the Cornea with Blue Femtosecond Laser Light. IOVS. 2011; 52: 8148-8155; published ahead of print September 19, 2011, doi:10.1167/iovs.11-7323.

[4] Wang L, Maslov K, Yao J, Rao B, Wang L. Fast voice-coil scanning optical-resolution photoacoustic microscopy. OPTICS LETTERS. 2011; 36

High Volume Manufacturing of Large Segmented Telescope Mirrors

Ulrich Mueller
L-3 Integrated Optical Systems
4040 Lakeside Dr.
Richmond, CA 94806

INSTRODUCTION

Currently there are two extremely large telescopes under design. The European Extremely Large Telescope (EELT) and the Thirty Meter Telescope (TMT). Both are based on large segmented mirrors. They are designed for observations from the near-ultraviolet to the mid-infrared. By design, these telescopes complement the scientific capabilities of the James Webb Space Telescope and the Atacama Large Millimeter Array.

These telescopes will require more than 1200 mirrors combined, which need to be machined from ultra low thermal expansion CTE materials such as Clearceram®-Z or Zerodur™.

FIGURE 1. Artist rendering of the TMT telescope. Source: TMT.org

The 798 segments of the EELT and the 492 segments of the TMT telescope are nearly identical in size which allows for cost savings due to the use of nearly identical tooling. The main difference is that the TMT segments are curved on the backside vs. a flat backside on the TMT segments

The manufacturing of these mirrors has to be carried out over a timeframe of 2-3 years. This assumes the completion of 8-12 segments/week.

Even if this is carried out at several manufacturers it will require a very efficient polishing process.

Description of the Telescope Layout

As an example of a giant telescope the TMT segment configuration is shown in figure 2. There are 82 segment types that repeat every 60-Degrees.

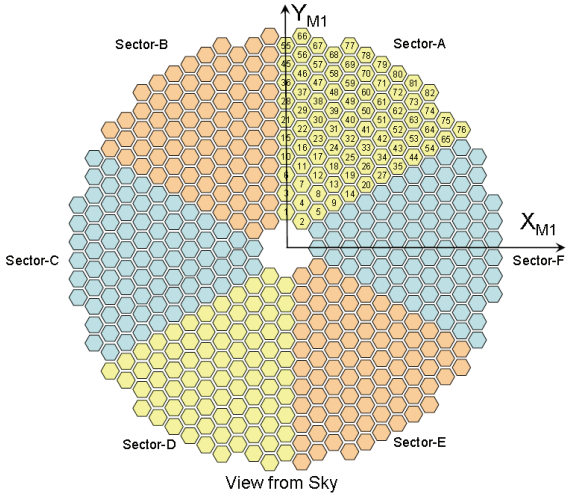

FIGURE 2. Segment layout of TMT. Source: TMT.org

MANUFACTURING PROCESS

The process flow proposed for the stress mirror polishing SMP process is shown in figure 3. The process flow assumes a curve generated roundel as the incoming geometry, and delivers a roundel to the finishing process (IBF, MRF, or other). Most blank manufacturers have Blanchard and curve generation equipment, and it is assumed that overall cost will be lower by using this embedded capacity. The finishing process is assumed to include hexing of the blank. Because the finishing process has an optical test, this test may be able to characterize springing of the material, assuming considerations for a roundel are made in the optical test mount. This was the implementation for the manufacturing of the Keck segments, with hexing occurring at Kodak (now ITT).

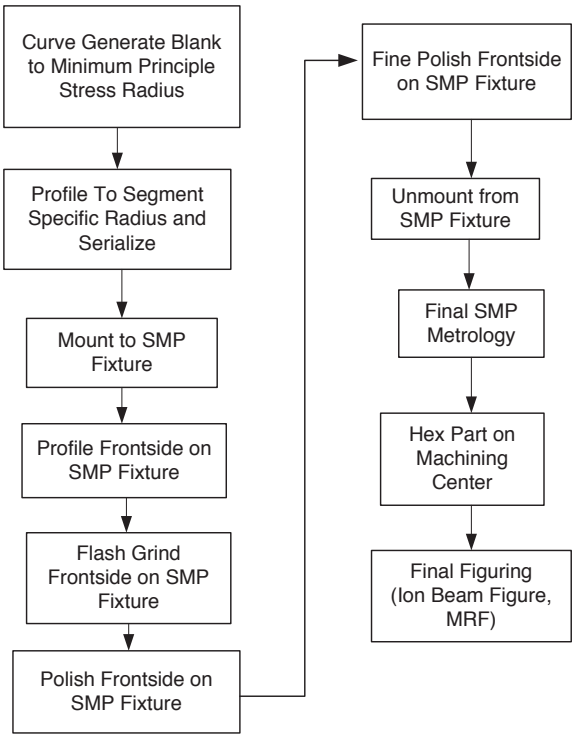
Curve Generate Blank to Minimum Principle Stress Radius
Profile To Segment Specific Radius and Serialize
Mount to SMP Fixture
Profile Frontside on SMP Fixture
Flash Grind Frontside on SMP Fixture
Polish Frontside on SMP Fixture
Fine Polish Frontside on SMP Fixture
Unmount from SMP Fixture
Final SMP Metrology
Hex Part on Machining Center
Final Figuring (Ion Beam Figure, MRF)

FIGURE 3. Manufacturing Process

MANUFACTURING AND METROLOGY INSTRUMENTATION

The two main components besides the well understood curve generating for the blank are the stress mirror polishing and the insitu surface metrology. While it is possible to measure the surface on a coordinate measuring machine CMM it would require either transporting the SMP fixture to the CMM or integrating the CMM with the manufacturing equipment. Instead task specific measurement instruments are being designed.

Stress Mirror Polishing

In order to achieve high removal rates and therefore fast convergence on these large mirrors small tool polishing is not fast enough in terms of throughput. Therefore a large tool process was developed based on the SMP process used in the machining of the Keck telescope segments.

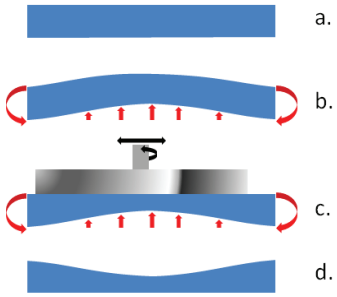

FIGURE 4. Stress Mirror Polishing (SMP)

SMP starts (a) with a plano or spherical form (curvature constant across the surface). A bending fixture applies forces and moments (b) in a controlled manner, causing the surface to assume the inverse of the form desired. The assumed form does not need to be axis symmetric, and in the case of TMT, none are axis symmetric. A large, nearly full size, tool efficiently removes material from the intended surface. Since volumetric removal rates are proportional to tool area, the method assumes most rapid finishing, provided that the final figure can be achieved. Once the mirror has been optically finished to the process goal while held in the bending fixture, it is released from the fixture and (d) will elastically assume the desired form. [1, 2, 3]

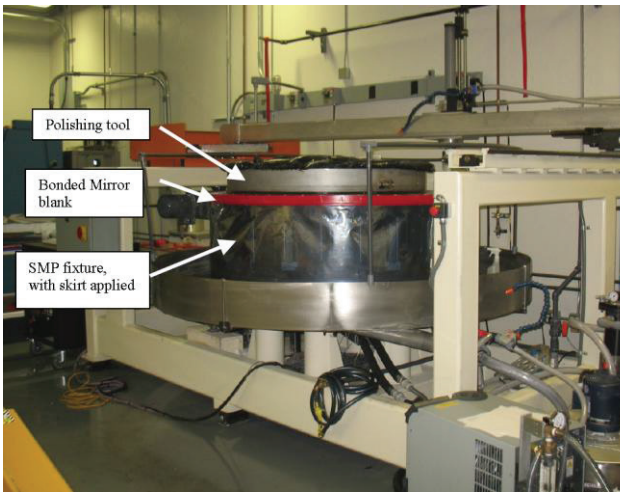

FIGURE 5. Stress Mirror Polishing (SMP) process

Computerized Bending Fixture

The segment must be supported in a manner that allows it to accurately flex to the desired shapes, both during polishing and relaxed (unloaded) for measurements. With 24 arms there are 48 force actuators, two on each lever arm [3].

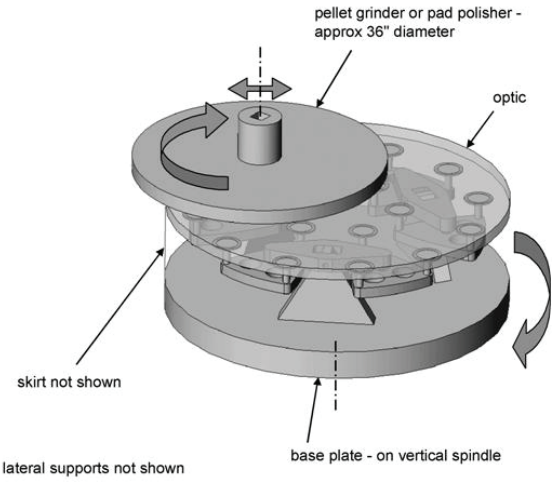
pellet grinder or pad polisher - approx 36" diameter
optic
skirt not shown
base plate - on vertical spindle
lateral supports not shown

FIGURE 6. Stress Mirror Polishing (SMP) Fixture

The force actuators must be very accurate and reliable in a set-and-hold application. A motor driven screw compressing and extending a spring is used with a load cell in series to sense the applied force. The required load range is dependent on the shape of the segments [4, 5].

FIGURE 7. Stress Mirror Polishing (SMP) Fixture

Segment Blank Radius Strategy.

A single blank radius of curvature (ROC) may be used for all the segments. This means a single ROC for the grinding, polishing, and measuring tools. The blank ROC is chosen so that the global maximum bending stress in the segments in minimized. Using this blank ROC the maximum bending stresses in the innermost and outermost segments are equal.

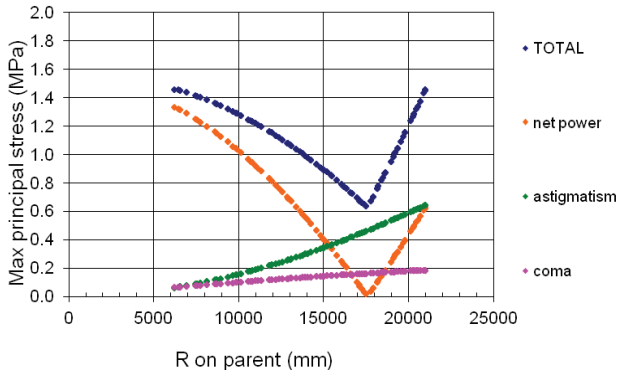

FIGURE 8. Principal maximum stress of EELT segments across the telescope radius.

Comparison of EELT and TMT warping loads

The three major factors that change the required warping loads for EELT vs. TMT are the mirror surface prescription, the segment thickness, and the flat back for EELT versus constant thickness for TMT segments.

Table 1 Warp load differences between TMT and EELT segments

Parameter	TMT vs 69m EELT; (60m/69m)
Warping amplitude ratio vs TMT	0.87
Thickness ratio cubed warp load ratio	1.55
Warping Force multiplier vs TMT	1.35

The EELT mirror surface is flatter than the TMT surface so the amplitude of warping is less for E-ELT segments. The difference is approximately equal to the ratio of base radii, i.e 60,000/69,000, or 0.87. So the warping amplitude required for EELT is ~87% of that required for TMT. However the EELT segments are thicker than TMT segments so more warping load would be required to achieve the same warping amplitude, all else being equal. The EELT segments have a center thickness of 50 mm, edge thickness of ~53.3 mm, and an "effective" thickness of ~52.1 mm which can be used for calculations using classical plate theory. The thickness of the TMT segments is 45 mm and the required warping loads go as the cube of the segment thickness, so the increased thickness of the EELT segments leads to an increase in the required warping loads according to $(52.1/45)^3$, or a factor of 1.55. Combining the above two effects leads to an increase in warping loads required for EELT over TMT assuming classical thin, constant thickness plate

theory. The third factor which influences the required warping loads is the flat back on the EELT segments. The flat back obviously causes a variable segment thickness, which leads to complications and departure from simple warping calculations based on classical plate theory. Essentially, when warping a plate with a curved front surface and a flat back surface, like EELT, higher order surface terms are introduced. These higher order terms can be removed by adding higher order warping, but these additional warping loads add to the required actuator force range. A more detailed discussion of these higher order effects is presented in the following section.

Discussion of flat back warping results

A convenient notation for describing the various Zernike warping terms is Zmn, where m is the order and n is the azimuthal periodicity of the shape. Generally when low order warping is applied to a plano concave plate higher order terms also appear on the surface. Table 2 shows the amount of higher order terms introduced for three low order terms, power, astigmatism and coma. For example, warping in power (20) also introduced some spherical aberration (40) and higher order spherical (60) which needs to be compensated if the magnitudes are significant.

Table 2 Warping terms for E-ELT segments

Term	Description	Warpable by SMP?	Max value [um]	occurs on which segment
Z20	power	yes	-67.2	innermost
Z40	spherical aberration	yes	0.65	innermost
Z60	higher order spherical aberration	no	0.01	innermost
Z22	astigmatism	yes	97.4	outermost
Z42	secondary astigmatism	yes	-0.2	outermost
Z62	higher order astigmatism	no	0.0018	outermost
Z31	coma	yes	2.2	outermost
Z51	secondary coma	no	-0.034	outermost

While the stray terms introduced are not large, the warping loads required to remove them are significant because they add to the required force range of the actuators.

For all but one of the terms of interest, the net actuator forces sum to zero so there is no net upward or downward (or tilting) force on the segment. The exception is spherical aberration, which requires a change in axial support pad pressure for warping. The effect of this is that for spherical aberration the segment is either lifted off, or pushed down onto its support structure to some degree. Removing the stray spherical aberration component requires a certain amount of force. For the innermost EELT segment this would reduce the force applied to its support structure to only about 1/3 of its unwarped value.

Achievable Surface Shape by SMP

Surface shape errors of less than 0.95um over the 1.5m diameter mirror have been achieved for both TMT and EELT demonstration segments. Due to the use of a full size lap a low surface micro-roughness of <8A can routinely be attained [5, 6].

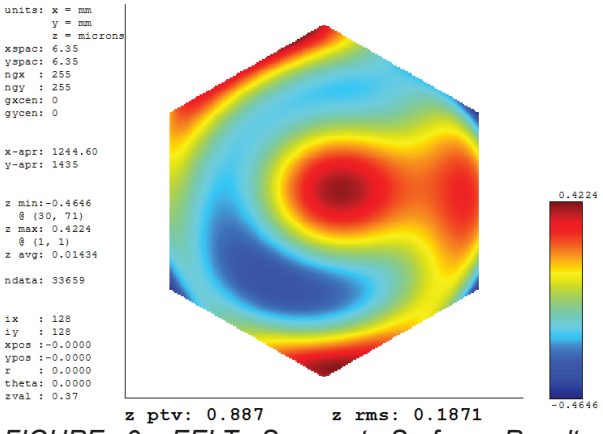

FIGURE 9. EELT Segment Surface Result 0.89um PV

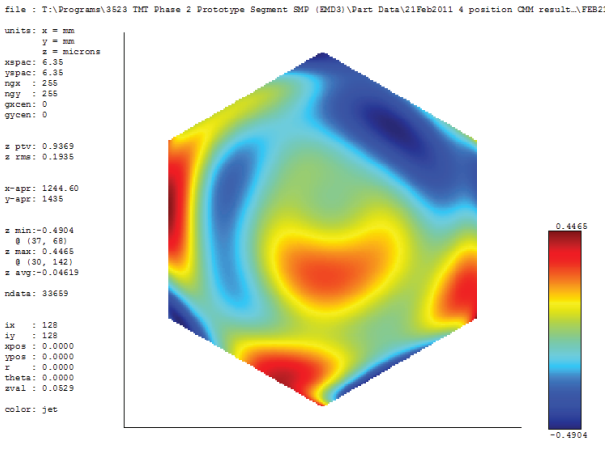

FIGURE 10. TMT Segment Surface Result 0.94um PV

SURFACE METROLOGY

One main benefit of this full aperture machining process is that it will introduce only surface aberrations with a spatial period greater than ~200mm.

In our previous segment manufacturing studies the segments were measured using a sag bar designed under a contract with TMT. The probe array used was a linear array of 9 probes arranged across a diameter of the optic. The array was lifted, rotated, and set 11 times in 36 degree increments to complete a full surface measurement. However for high volume manufacturing a segment surface measurement instrument is under design that measures the segment surface using an array of displacement probes mounted in a sandwich made from composite materials. It is approximately the size of the segment itself. The probes are expensive so it is desirable to find the optimum minimum number of probes.

Mast and Nelson [7] evaluated what probe layout and quantity is needed to limit the residual errors. It is desirable that the probes are more dense with increasing radius and don't overlap for different measurement orientations. Advantages of a full array are the elimination of the rotating lift and set mechanism and faster measurements. For a volume production program where many thousands of measurements will be made over the life of the program, the speed of measurement becomes the dominant factor in minimizing overall program cost.

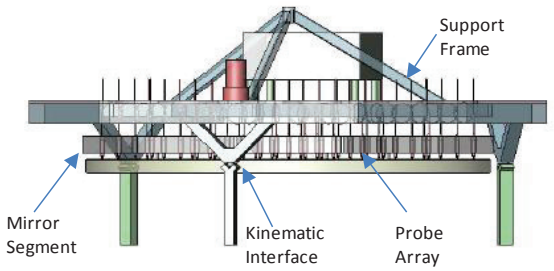

FIGURE 11. Sag-array concept side view

The residual errors of the probe array can be evaluated establishing a vector c that contains all relevant Zernike coefficients and a vector s that contains all probe values. This vectors are related via matrix A where s=Ac. The fitted Zernike vector is $c^*=Bs$ with $B = (A^TA)^{-1}A^T$. The covariance matrix for the fitted c* contains variances that are the square root of the individual errors.

Handoff to Final Finishing

The SMP polish handoff specification is influenced by the process capability of SMP, and by the amount of "springing" or shape change expected in the blank from machining to a hexagon. For the TMT process design, springing in the TMT blank hexing was estimated. An internal stress value of 138kPa was assumed in developing the expected springing. For Zerodur™, values from approximately 70 to 350kPa have been reported. Using a value of 138kPa, springing of 0.1um P-V is estimated. When these values of stress are used in the Keck segment geometry, springing is predicted at 0.2um P-V, or twice the TMT case. For the E-ELT blank geometry, the equivalent amount of springing is expected to be similar to TMT in the order of 0.1-0.2um.

CONCLUSION

An approach for manufacturing and metrology of large segmented telescope mirrors was presented. The finishing capability of the SMP process has previously been presented. The next step is the detail design of the surface measurement probe array as full size segment surface measurement tool.

REFERENCES

[1] Hull, A et al: January 2010: Tinsley Progress on Stress Mirror Polishing (SMP) for the Thirty Meter Telescope (TMT) Primary Mirror Segments; BAAS 42, No. 1, 441.27 (2010)

[2] J. Lubliner and J. E. Nelson, "Stressed mirror polishing. 1: A technique for producing nonaxisymmetric mirrors," Appl. Opt. 19, 2332-2340 (1980)

[3] Pepi, "Delayed Elastic Effects In Zerodur At Room Temperature", Applied Optics, Vol. 31, No. 1, 1 January 1992.

[4] Stephen F. Sporer, "TMT: stressed mirror polishing fixture study" SPIE, Vol. 6267 (2006).

[5] Daniel, Jay; Mueller, Ulrich; Peters, Tracy; Sporer, Stephen F.; Hull, Tony, "Tinsley progress on stress mirror polishing (SMP) for the Thirty Meter Telescope (TMT) primary mirror segments II" SPIE, Vol. 7733, pp. 773328-773328-9 (2010).

[6] Ulrich Müller, Jay Daniel, "Tinsley proves stress mirror polishing for giant segmented telescopes" SPIE, Vol. 8450

[7] T. Mast and J. E. Nelson, Segment Surface Measurement facility" "TMT Report No 86 v39

Visual Inspection of Cosmetic and Functional Defects in a Manufacturing Environment

Christopher M. Cilip[1], Daniel S. Pratt[1], and Marcin B. Bauza.[1]
[1]Visual Systems
Carl Zeiss Industrial Metrology, LLC
Maple Grove, Minnesota 55369, USA.

INTRODUCTION

Often in manufacturing, visual inspectors are relied on to approve the correctness of parts. These inspectors must approve both cosmetic and functional characteristics on shapes ranging from simple geometries to complex free-formed surfaces while also evaluating them by gauging the severity of any irregularity that is found. Human visual inspection is continued because a human's adaptive interpretation allows flexibility where standard vision systems fail, even though the human inspection process remains highly subjective and inconsistent between inspectors. This can be problematic for manufacturing due to the necessity that even the smallest variations in curvature or blemishes can result in a nonfunctional or cosmetically unappealing part [1]. The introduction of phase deflectometry as an optical metrology technique can now give production facilities an objective view of their manufacturing process by imaging irregularities on the surface of free form parts [2]. Additionally, these facilities can achieve peace of mind that the once highly subjective process of visual inspection now has reliable repeatability.

PRINCIPLE OF OPERATION

Phase shifted deflectometry acts on the principle that one is observing the projection of a light pattern on the surface of a test piece instead of focusing on the surface of the part itself. By viewing the pattern, the observer is able to see alternate fringes or sections of the projected pattern while effectively removing the part from the optical system. This differs greatly from technologies such as fringe pattern triangulation which rely on scattering from the surface to obtain depth changes between lateral measurement points and cannot directly view the slope of the measured region but instead have to derive such information. Additionally, by widening the view to the projected pattern, rather than focusing on the measurement point, the system is able to record this detail over a much larger area and perform these observations more quickly.

Phase shifted deflectometry allows for a wide range of surfaces to be evaluated with the main advantage occurring on highly specular or shiny surfaces. This is generally not the case for optical systems which typically have increased difficulty obtaining images as the part becomes more specular, as well as for conventional deflectometry which requires highly specular surfaces (FIGURE 1).

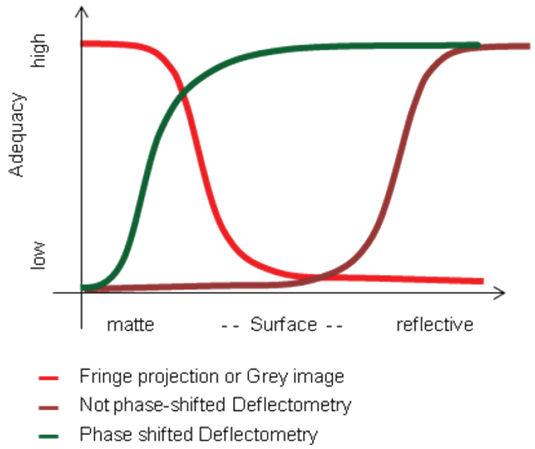

FIGURE 1. Phase shifted deflectometry adequately measures both specular and semi-specular surfaces.

The phase shifted deflectometry system adapted for visual inspection consists of a white light LED array that generates the continuous illumination

patterns which are used to generate the primary images used for defect analysis. Computer numerically controlled positioning stages which move the part under test into optimum fields of view. Various cameras, line and matrix sensor, whose optical resolutions are matched to the limits of the defect sizes being looked for. Finally, a high performance computing cluster is added and scaled accordingly to allow for any evaluation algorithms to be performed at the speed of image acquisition such that evaluation times meet the strict cycle times during production and 100% inspection can be achieved.

The system's white light source produces a series of sinusoidal fringe patterns that are viewed by the cameras as a reflection from the object under test (FIGURE 2). The series of patterns produced by the illumination element are shifted in phase from each other and recorded by the system.

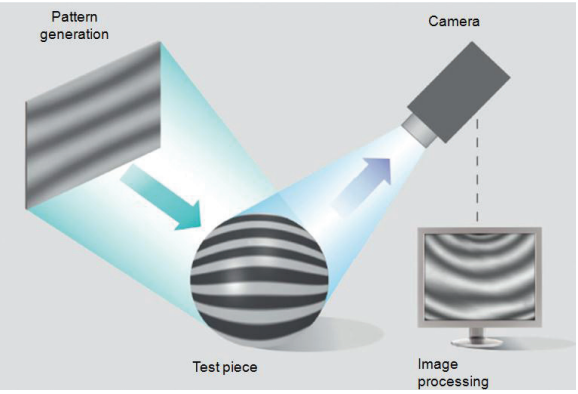

FIGURE 2. Diagram of the phase deflectometry setup.

The resulting images that are acquired are then used to derive three primary images for image analysis; a synthetic grey image, a gloss or shininess image, and a phase or inclination image.

METHODS

The resulting primary images are used to objectify features on the part for inspection tasks such as completeness, position or more importantly, detection of surface irregularities (FIGURE 3) [3].

The first (FIGURE 3a) channel; shows a grey scale image of a polished chrome-coated plastic letter 'Z' under patterned illumination. This is similar to the grey scale images seen from typical vision systems; an image under fixed illumination is viewed from a single vantage point. A large majority of the time the surface defects that are present are very difficult to notice if the surface is not observed from a particular angle. This can result in slippage of a defect; additionally, when the visual inspector mimics this process and is not repeatable in the angles, or vantage points, in which they view the part it is very easy to miss such an irregularity further adding to the subjectivity of the "good or bad" decision process.

A second (FIGURE 3b) channel; the synthetic grey scale image, is a low noise image created by the synthesis of multiple phase shifted images. This image has homogeneous illumination which is widely independent from the shape of the part being tested. This image can be compared to imaging systems which use multiple vantage points to attempt to image irregularities and is a highly useful channel for functions like edge detection, variations in color, optical character recognition and other discrete edge finding characterizations.

A third channel (FIGURE 3c); the gloss image, helps to highlight areas of increased light scattering which are independent of the shape of the part under test. This image gives the distinction of gloss and brightness which is critical for proper detection of cosmetic irregularities, or irregularities which exhibit an increase or decrease in scattering from the nominal surface. In this case the very superficial scratches that change the part's cosmetic appeal are noticeable. This channel is also very useful for tracking changes in polish quality or objectively viewing the surface for any dull spots.

Finally (FIGURE 3d); the inclination image can be obtained from the phase information and used to determine any deviation in the nominal

slope of the part. This image can be highly critical to the evaluation of a functional surface and is necessary when detecting surface irregularities which cause a deviation from the intended spline of the part such as scratches or dents. Additionally, the curvature of the part or any noticed irregularities can be derived from this image providing further analysis of the type of irregularities observed on the surface. These irregularities include indentations, pimples, or other negative and positive irregularities. In this case a linear shaped dent which influences functionality is noticed on the part; this irregularity is very difficult to see in the previous channels due to the specular nature of the dent which resembles characteristics off the surrounding surface finish unlike a typical scratch that has a discontinuity in scattering characteristics from the surrounding surface.

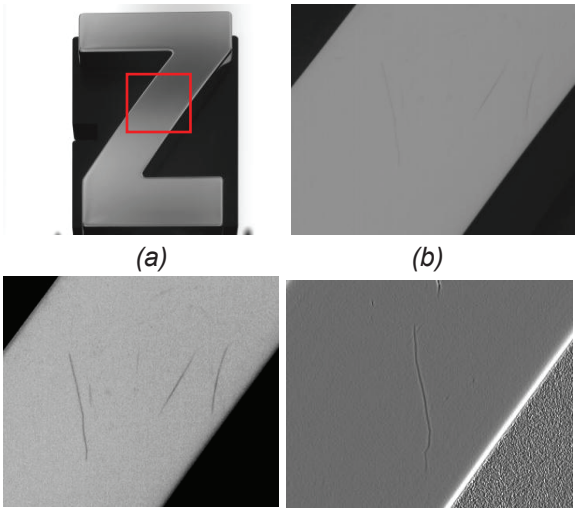

(a) (b)

(c) (d)

FIGURE 3. a) One grey scale image taken during one of the multiple phase shifts. b) Synthetic grey image showing a homogenous illumination of the test part. c) Gloss image showing areas which deviate from the nominal gloss level. d) Inclination image showing deviations in the nominal slope of the surface.

RESULTS

The purpose of this paper is solely to introduce the possibility of surface analysis at high speed with focus on ability to observe defects difficult to observe with classical optical methods. For this reason our results will focus solely on some of the common irregularities seen today in industry and how these irregularities are enhanced and objectified by the channels previously discussed.

Machine chatter continues to be a large concern for manufacturing industry. Detecting this irregularity before it starts to affect the surface topography of the part is critical when optimizing manufacturing processes. Typically, it is most advantageous to view this irregularity by looking for changes in the gloss channel. As the chatter gets more severe it is possible to notice its transition into the inclination image as well. In the image (FIGURE 4a) we can see the regular scratch pattern of chatter along the surface of the part. At this point the chatter has become severe enough to not only be seen as a cosmetic surface irregularity (FIGURE 4b) but additionally it can be noticed as a deviation from nominal spline in the inclination channel (FIGURE 4c). Viewing this process occur over time can help isolate its origin and prevent it in the future.

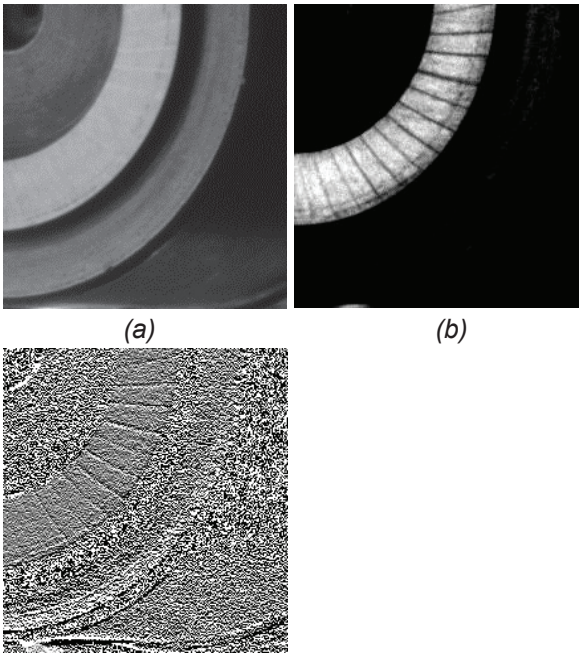

(a) (b)

(c)

Figure 4. a) One grey scale image showing the difficulty in isolating chatter as a defect with typical vision systems. b) Gloss image showing

chatter on the surface. c) As the chatter becomes more severe it is visible in the slope or curvature channel.

Being able to determine gloss levels can be very important when evaluating cosmetic or functional surfaces. When this irregularity occurs it is often difficult for a visual inspector to point it out accurately. Additionally there is a lot of subjectivity involved when inspecting a surface to see if it meets a required gloss level. The under-polished irregularity (FIGURE 5a) is very difficult to notice on a typical grey scale machine however the gloss channel (FIGURE 5b) can regularly show this irregularity. Furthermore, by observing the inclination image (FIGURE 5c) it can be deduced that no actual deviation from nominal form exists for this part and this is purely a cosmetic feature even though the intended use of the part may be purely functional.

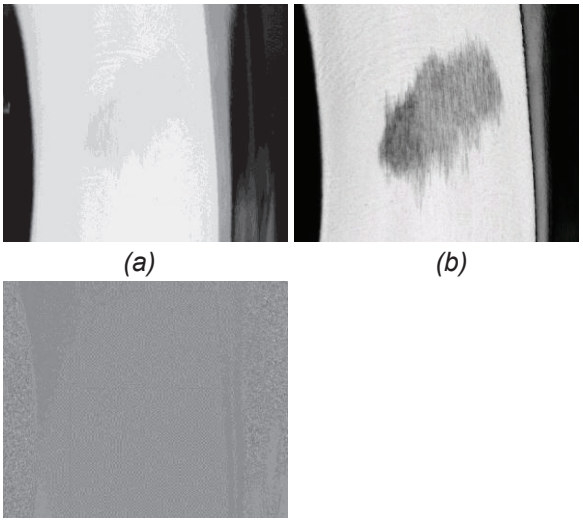

(a) *(b)*

(c)

Figure 5. a) Grey scale image showing a difficult to recognize area where the surface has been under-polished. b) Gloss image of the same area showing a highly identifiable under-polished area. c) Inclination image of the under-polished area showing no topographical information.

Another important aspect of defect detection during manufacturing is the ability to maintain 100% inspection. Fast cycle times are just as critical as the ability to provide quality and robust analysis. One primary benefit of phase-shifted deflectometry is the ability to achieve very fast cycle times while still obtaining enough useful information from the images to make the critical decisions necessary for high quality and robust evaluations. Phase shifted deflectometry can be applied to a variety of product sizes. The acquisition of entire solder bump field (FIGURE 6a) can be performed in a few seconds while maintaining high resolution enabling evaluation of the field for irregular bumps. In addition to the quick evaluation times, the solder bumps which are difficult to analyze from a typical vision system (FIGURE 6b) are now much easier to be analyzed when directly evaluating their slope (FIGURE 6c).

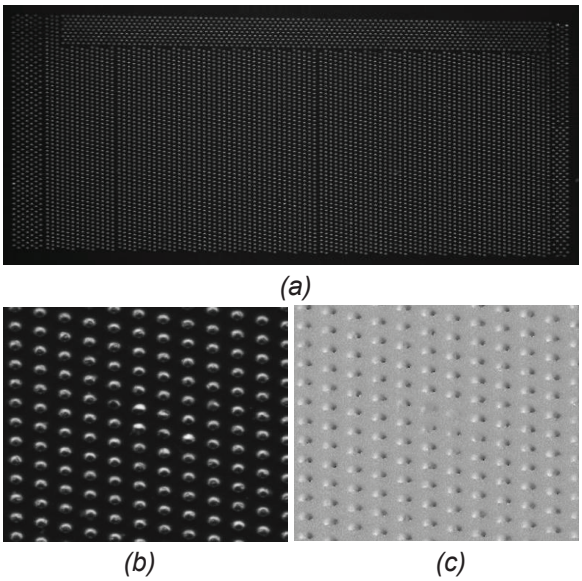

(a)

(b) *(c)*

Figure 6. a) Solder bump field (1.5cm x 3cm) as seen from a line camera acquisition. b) Grey scale image of the solder bump field. c) Inclination image showing same field of view as grey scale image. Irregular shaped bumps are more easily noticed as flat or 'missing' structures even though their shiny nature remains intact.

Versatility across many surfaces allows this technology to be used in a wide variety of applications. While many of the examples and references have pointed to data taken from highly specular surfaces it is possible to take similar data from more diffuse or matte surfaces.

In this case a piece of sheet metal is checked for irregularities prior to being painted (FIGURE 7). Irregularity detection will save time and capital if irregularities are evaluated prior to the process. With phase shifted deflectometry this technique can be modified to inspect a large surface area and keep up with cycle times required in large scale production.

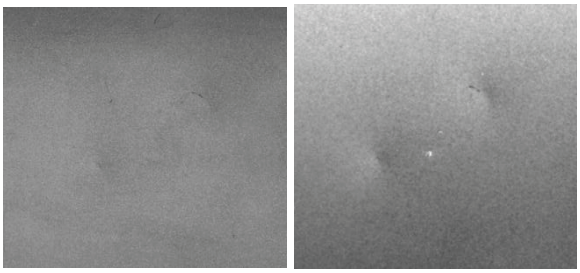

FIGURE 7. a) Grayscale image of sheet metal. Two irregularities are present; however, they appear differently and are difficult to evaluate. b) Inclination image showing two distinct regions with surface irregularities present

Common in almost every manufacturing setting is the creation of unwanted nicks, dings, scratches or other irregularities which gouge or remove material from the surface. These irregularities are perhaps so common due to the fact that they can occur at many stages in the production cycle. While the gloss channel can typically be used to detect these irregularities due to the altered surface finish of the interior of the irregularity, the inclination channel can return much more information. When evaluating these types of irregularities it is typical to consider area, volume, and change in slope of the nominal spline. All of which lead to an indication of how deep the irregularity is from the surrounding surface. For this case a sample coupon was measured at multiple angles of incidence. Twenty measurements were taken at 0, 15 and -15 degrees from incidence and the defect detection repeatability was tested by running the algorithm to identify one structure from the other. The dents were prequalified using a Zeiss F25 micro CMM and found to have maximum depths of *20.1 µm* and *22.7 µm* respectively (FIGURE 8a & 8b). Both dents are visible in the inclination image (FIGURE 8c,& 8d) and when analyzed using defect algorithms it can be shown that each provide an algorithm score which will distinctly identify one from the other (FIGURE 8e).

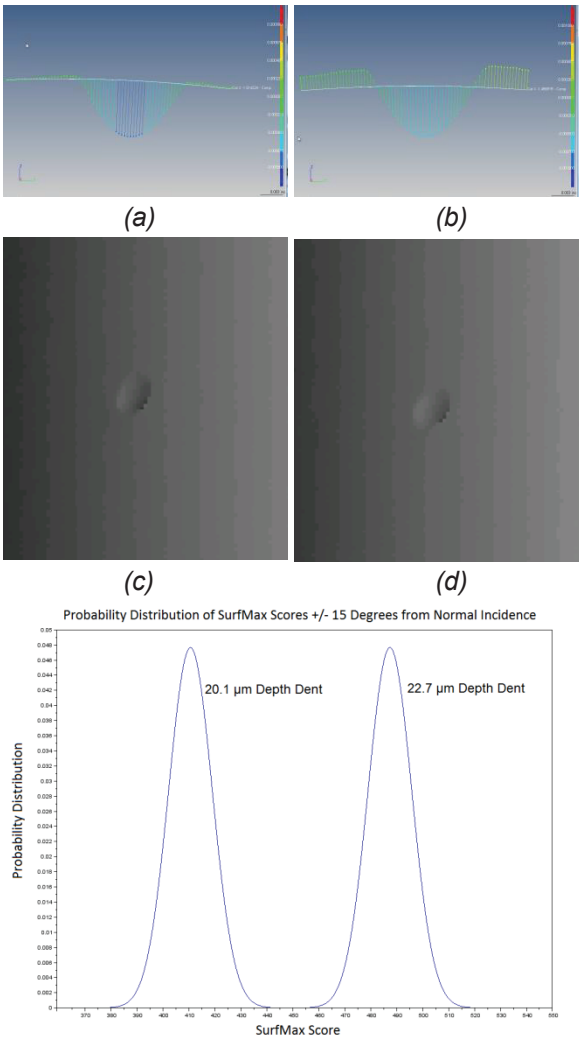

FIGURE 8. a, b) Zeiss F25 micro CMM plots of the two analyzed dents. c) Inclination image showing dent measured at 20.1 µm. d) Inclination image showing dent measure at 22.7 µm. e) Probability distribution graph of 120 random measurements of two parts scored by the software.

CONCLUSION.

Phase shifted deflectometry can be used to automate the visual inspection process and provide traceability for manufacturing processes which might be responsible for defects or

surface irregularities that commonly occur in a precision manufacturing setting. This allows a manufacturer to achieve an objective analysis of defect detection and be confident that his production has minimal overkill or slippage. The ability to maintain low cycle times and keep up with high throughput demand for 100% inspection makes phase shifted deflectometry the next logical solution for enhancing the visual inspection process.

ACKNOWLEDGMENTS

The authors would like to thank Carl Zeiss for the use of the SurfMax 400M throughout the course of this study and Mike Roterdam for the measurements that were taken using the Zeiss F25 CMM.

References

[1] Soren, K. Deflectometric Measurement of Specular Surfaces. IEEE. 2008; 57/04 763-769.

[2] Knauer M, Kaminski J, and Häusler G. Phase Measuring Deflectometry: a new approach to measure specular free-form surfaces. Proc. SPIE 2004; 5457: 366-376

[3] Ballester, A. Mirrored Quality: Deflectometry Opens up Broad Field for Surface Inspection. 2009; 08/09: 30-31.

ON THE USE OF MERCURY SESSILE DROPS AS REFERENCE ARTEFACTS FOR THE CALIBRATION OF OPTICAL SURFACE TOPOGRAPHY MEASURING INSTRUMENTS

Jacob W. Chesna[1,3], Yuki Shimizu[1,2] and Richard K. Leach[1]

[1]Engineering Measurement Division
National Physical Laboratory
Teddington, Middlesex, UK
[2]Department of Nanomechanics
Tohoku University
Sendai, Japan

[3]Center for Precision Metrology
University of North Carolina at Charlotte
Charlotte, North Carolina, USA

INTRODUCTION

Instruments based on coherence scanning interferometry (CSI) are widely used for areal measurement of surface topography [1]. Calibration of these instruments is carried out through the determination of a number of metrological characteristics, which have been listed in draft ISO specification standards [2] and are described elsewhere [3, 4, 5]. However, the metrological characteristics do not take into account the ability of the instrument to measure the local slope and curvature of the measurement surface, which is a major source of error [6]. Some of these errors can be estimated and eventually corrected using knowledge of the optical transfer function [7].

In [7], a method is outlined where measurement of a sphere is used to obtain the optical transfer function of a CSI instrument. It is stated in [7] that a mercury sessile drop of radius less than 25 μm can be considered a reference artifact, with the drop exhibiting a deviation from spherical form that is small enough to enable it to be used to calibrate the slope and curvature measurements of a CSI instrument. The mercury drop will only be used as a reference sphere to calibrate a primary interferometer. The primary interferometer can then be used to calibrate silica spheres which are more practical to be used to calibrate CSI instrument in industry.

In this paper, the form deviations and axisymmetric profile of these mercury sessile drops are theoretically evaluated. A brief comparison of various geometric models is conducted in an effort to verify the suitability of sessile drops as near spherical reference artifacts. In addition, a preliminary study of the temporal stability of the drops is presented.

It will also be shown that a mercury sphere with a diameter of approximately 50 μm may be suitable for calibrating the primary sphere interferometer that is currently being developed at NPL (details of which are to be published at a later date).

HYDROSTATIC DEFLECTION

The degree to which gravity will influence the shape of a sessile drop has been studied for over two centuries [8], and an extensive overview of the axisymmetric drop shape analysis technique was published elsewhere in 1997 [9]. To date, an exact solution does not exist; however, approximations have been developed and optimized *via* the comparison between the approximated profile and goniometric images of actual sessile drops [10, 11]. Typically, sessile drops are not investigated with volumes below 5 mm^3, corresponding to radii at, or just below, 1 mm. The majority of axisymmetric analysis techniques are optimized for larger drops, thus there is a concern regarding the accuracy of scaling current hydrostatic deflection approximations to drops with radii in the tens of micrometres.

The profile of a sessile drop of the size desired here is best approximated by a numerical solution of the pair of first order differential equations [11].

$$\frac{dx}{d\theta} = \frac{\gamma x \cos\theta}{\rho g x z + \Delta P x - \gamma \sin\theta}$$
$$\frac{dz}{d\theta} = \frac{\gamma r \sin\theta}{\rho g x z + \Delta P x - \gamma \sin\theta} \quad (1)$$

Here, x and z are, respectively, the lateral and vertical locations in cylindrical coordinates, with the origin being placed at the apex of the drop, and the positive *z* axis being directed toward the center of the drop. θ is the slope at the point of interest, γ the surface tension of the liquid, ρ is the density of the fluid, g is the local acceleration due to gravity, r is the radius of curvature at the apex, and ΔP is the pressure difference across the fluid interface at the apex.

Given that all current approximations are derived from the various particular solutions of these differential equations (1), and that the computation time with entry level computers can generate a solution in minutes, there is no need to use a complicated polynomial approximation. Therefore the profile generated in this solution is taken as the best estimate for the actual shape of a sessile drop in this research.

APPROXIMATIONS FOR DEFLECTION

While the numerical solution of the differential equations (1) is most likely an accurate representation of the surface, it still does not provide a simple approximation to the magnitude of hydrostatic deflection as a function of drop size. This is due to the solution to the differential equations being for one specific case, *i.e.* one material and one size. For this reason, an approximation to the magnitude of deflection was sought that would provide the capability to parametrically plot an estimate of the maximum deflection for a drop as a function of drop size. This approximation would be most useful for the comparison between different materials and scales and could also be used to predict a range of uncertainties in measurements on sessile drops.

To provide a comparison between models, the parameters for each profile were matched as closely as the equations would allow. To do this: the profiles were calculated using a radius of curvature of 25 μm as an initial condition; the drop being symmetric around the *z* axis; and the profile translated such that the origin be located 25 μm below the apex; and the points in the profile were calculated as a function of the slope at each point of interest, i.e. the angle made between the tangent of the point of interest on the profile and the *r* axis. It was expected that there will be some error in profile comparison between models due to inexact colocation of points in each profile.

The polynomial approximation developed in [10] was evaluated. This work quotes micrometre-level accuracy and was developed for drops with radii of around 1 mm, which for the purpose of this research is inadequate. With this limitation in mind, the results of the Srinivsan approximation (equation's 3 and 4 in [10]) were used as a guide for preliminary investigation. The Srinivsan equation is a parametric approximation, meaning that it can be a function of the radius of the drop, however it is largely complicated and is by no means a fast approximation. For reference, the approximation predicts a 40 nm maximum deviation on a water drop with a radius of curvature of 25 μm at its apex.

An elliptical approximation was used to give a reasonable estimation of the hydrostatic deflection,

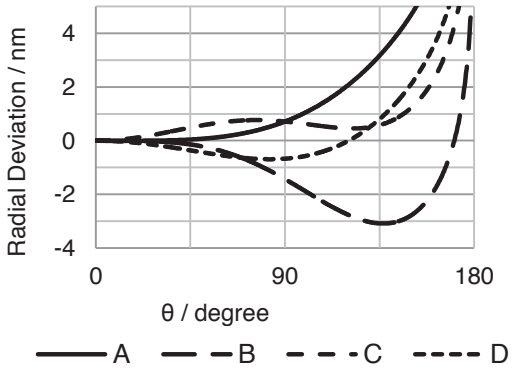

FIGURE 1. The difference between surface profile models of a 50 µm diameter mercury sessile drop. θ represents the slope of the profile, or the angle between the tangent of the surface and the r axis. The four lines show the difference between particular solution of the differential equations and: (A) a sphere whose radius is equal to the radius of curvature at the apex; (B) an elliptical approximation given by equation 3; (C) an elliptical approximation given by equation 4; and (D) a sphere with a radius that results in a minimum least squares deviation.

$$z = \pm \frac{r_w^2}{r_a} \sqrt{1 - \left(\frac{x}{r_w} \right)^2} \qquad (2)$$

where x and z are, respectively, the lateral and vertical coordinates of a point on the surface, r_a is the local radius of curvature at the apex, and r_w is the waist radius of the drop.

To provide a direct comparison with the solution of equations (1), the initial condition of the local radius of curvature at the apex, r_a, was used in equation (3) to calculate the waist radius, r_w, for use in equation (2).

$$0 = \frac{\rho g}{2 r_a} r_w^3 + \frac{\gamma}{r_a} r_w - \gamma \qquad (3)$$

This knowledge of the local radius of curvature at the apex is only practical when making comparisons with theoretical models where it is a given initial condition. A more experimentally practical use for this approximation can be used when the waist radius, r_w, is measured and an approximation to the local radius of curvature at the apex, r_a, is calculated by algebraically rearranging equation (3), to yield equation (4).

$$r_a = \frac{\rho g}{2 \gamma} r_w^3 + r_w \,. \qquad (4)$$

Figure 1 shows a comparison between the particular solution to the differential equation, two cases of the elliptical approximation, one using equation (3), shown as B, and the other using equation (4), shown as C.

SPHERICITY

The deviation of a solution of equations (1) from that of a sphere as a function of profile slope is plotted as line A on Figure 1. For the case of A, the radius of the modeled sphere is set equal to the radius of curvature at the apex of the solution of equations (1).

A more experimentally realistic analysis involves fitting a sphere to the particular solution to (1) using a least squares approach. The difference between a solution to equations (1) and the best-fit sphere is plotted in Figure 1 as line D.

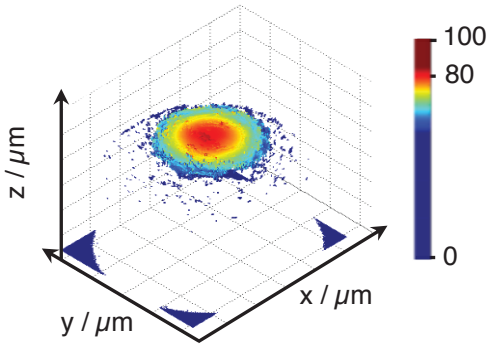

FIGURE 2. The measured surface of a 80 μm diameter silica sphere resting on a glass substrate obtained using a Taylor Hobson Talysurf CCI CSI.

In both cases the difference between the solution to equations (1) and the sphere, within the section of the surface that is measured by the CSI, is sub-nanometer. For reference, the two profiles exhibit sub-nanometer differences up to an angle of about 70 degrees.

TEMPORAL STABILITY

A Taylor Hobson Talysurf CCI CSI instrument was used in a preliminary investigation of the temporal stability of mercury drops, with measurements of three mercury drops being taken over a period of two hours. The radius of the drop was then determined by fitting a sphere to the measured points corresponding to the surface of the drop.

It can be seen from Figure 2, the result of a measurement using this instrument, that only a small portion of the sphere is actually measured; the typical measured area had a diameter of approximately 20 μm when a 53 μm diameter silica sphere was imaged. This restricted view, combined with noise in the measurement, means that there is a variation in the radius of a fitted sphere between measurements even for a solid silica sphere. The standard deviation of the measured radius, calculated using ten measurements on a solid sphere and taken within a few minutes, was 0.9 μm. This large standard deviation is a direct result of the large sensitivity to the calculation of radius from a data set that is within a relatively small solid angle compared to the radial length. More recent measurements completed at NPL suggest that the standard deviation of the measured size of

the silica test spheres taken over a few minutes is closer to 10 nm.

Taking the original experimental standard deviations into account, the measurements of three mercury drops taken over a period of two hours did not show a detectable change in radius. From this, it was concluded that the mercury drops of approximately 50 μm in diameter are stable to better than 1 μm in this period of time. This conclusion may be determined to be conservative as better radial measurement techniques are developed and evaluated for this application.

DISCUSSION AND FUTURE WORK

This work was carried out to assess the possibility of using a mercury sessile drop as a reference sphere for calibrating a primary sphere interferometer being developed at NPL. This preliminary theoretical analysis shows that a mercury sessile drop of appropriate radius may be used for the intended task. However, verification is still required to fully test the theory and the long-term stability of the drops.

ACKNOWLEDGEMENTS

This paper was funded by the UK National Measurement System Engineering & Flow Metrology Programme. Thanks are due to Mr Claudiu Giusca, Mr, James Claverley, Dr Andrew Henning (NPL) and Professor Jeremy Coupland (Loughborough University) for useful discussions.

REFERENCES

[1] De Groot P. Coherence Scanning Interferometry. In: Leach R. K. Optical Measurement of Surface Topography. Springer. Berlin: 2011. Ch 9.

[2] ISO/CD 25178-600 Geometrical Product Specifications (GPS)—Surface Texture: Areal—Part 600. Nominal Characteristics of Areal Surface Topography Measuring Instrument. Geneva: International Organization for Standardization. 2013.

[3] Giusca C L, Leach R K, Helary F, Gutauskas T, Nimishakavi L. Calibration of the Scales of Areal Surface Topography-Measuring Instruments: Part 1. Measurement Noise and Residual Flatness. Meas. Sci. Technol. 2012; 23: 035008.

[4] Giusca C L, Leach R K, Helery F. Calibration of the Scales of Areal Surface Topography Measuring Instruments: Part 2 - Amplification, Linearity and Squareness. Meas. Sci. Technol. 2012; 23: 065005.

[5] Giusca C L, Leach R K. Calibration of the Scales of Areal Surface Topography Measuring Instruments: Part 3 - Resolution. Meas. Sci. Technol. 2013; in press.

[6] Gao F, Leach R K, Petzing J, Coupland J M. Surface Measurement Errors Using Commercial Scanning White Light Interferometers. Meas. Sci. Technol. 2008; 19: 015303.

[7] Mandal R, Palodhi K, Coupland J M, Leach R K, Mansfield D. Applications of Linear System Theory to Characterize Coherence Scanning Interferometry. Proc. SPIE. 2012; 8430: 1-10.

[8] Young T. An Essay on the Cohesion of Fluids. Phil. Trans. R. Soc. Lond. 1805; 95: 65-87.

[9] del Rio O I, Neumann A W. Axisymmetric Drop Shape Analysis: Computational Methods for the Measurement of Interfacial Properties from the Shape and Dimensions of Pendant and Sessile Drops. Jour. of Colloid and Interface Science. 1997; 196: 136-147.

[10] Srinivasan S, McKinley G H, Cohen G H. Assessing the Accuracy of Contact Angle Measurements for Sessile Drops on Liquid-Repellent Surface. Langmuir. 2011; 27: 13582-13589.

[11] O'Brien S B G M, van den Brule B H A A. Shape of a Small Sessile Drop and the Determination of Contact Angle. J. Chem. Soc. Faraday Trans. 1991; 8: 1579-1583.

PROGRESS ON NON-CONTACT FLATTENING OF GLASS

Edward Sung[1], Brandon Chalifoux[1], Mark Schattenburg[2], Ralf Heilmann[2]
[1]Department of Mechanical Engineering
Massachusetts Institute of Technology, Cambridge, MA
[2]Space Nanotechnology Lab
MIT Kavli Institute, Cambridge, MA

INTRODUCTION

This paper reports progress on developing technology for non-contact flattening of thin glass sheets using thermal shaping (also known as slumping). Glass is placed between two horizontal flat air bearings with a gap of 50 microns from each bearing to the sheet. The previously reported method of using shear force via bearing-to-bearing angle to control the position of the glass has been abandoned in favor of tilting the entire bearing assembly to use gravity as an actuation force [1]. The results of high temperature thermal cycling are reported. Figure 1 is a photo of the device that was built and tested.

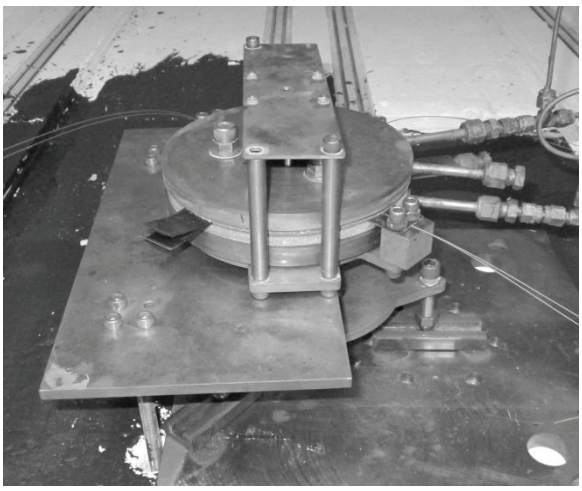

FIGURE 1. Photo of device used to control glass position during thermal cycling.

MOTIVATION FOR DEVELOPMENT

Super-flat glass has many interesting commercial applications including substrates for flat panel displays and disks for hard drives. An important goal of this technology is to shape cylindrical and hyperbolic mirrors for x-ray telescopes. The current solid mandrel slumping method has two main disadvantages in its process. The large coefficient of thermal expansion (CTE) mismatch between mandrel and glass mandates a lengthy cooling process on the order of days. Also, the mandrel itself requires a boron-nitride coating to prevent fusion of glass and mandrel. This boron-nitride coating must be buffed to a uniform thickness, which is a nontrivial task [2]. A non-contact slumping method can bypass both of these issues.

Other applications of this technology include creating flat wafers without any high frequency spatial errors. Glass wafers are typically extruded, which results in large low frequency errors. Glass wafers can be ground flat, but residual stresses result in similar errors as the extrusion process.

SHIFTING TO GRAVITY

A previous device was designed with shear force as the actuation method for glass positioning in the bearing. This used high temperature Inconel bellows that used air pressure to expand and compress. However, the air flow system was much too slow to respond to the movement of the glass. This limited the device to using external (of the oven) actuators that would transmit movement through push-pull rods. Continuing to use shear force meant that the bearing-to-bearing gap would have to be controlled. However, high temperature capacitance sensors used in previous designs were prone to signal cable failure after repeated thermal cycling.

The simplest solution was to clamp the bearings together with shims in between to set the gap. This no longer allowed shear force to be used, and therefore the switch was made to tilting the entire bearing assembly to use gravity to control the movement of the glass.

DEVICE DESIGN

The bearing assembly rests on three Inconel joints that are stiff axially but allow rotation about the x and y axes. One joint is placed in the center and does not move. The other two are placed in-line with the x and y axes and are connected to push-pull rods that extend through the bottom of the oven. The push-pull rods are actuated by

stepper motors. Figure 2 shows a close-up of the bearing assembly.

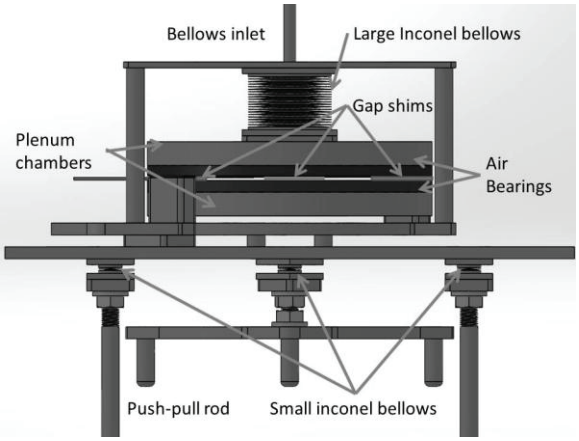

FIGURE 2. Solidworks model of device

A low plenum pressure (0.05 psi) is used to avoid significant deflection of the air bearings. The bearings are made of porous silicon carbide.

To sense the position of the glass, a custom optical sensor is used in which light comes out of a fiber directed normal to the edge of the flat object, is reflected by the edge, and comes back into a second fiber juxtaposed to the first and is detected by a photodiode. The fibers have high temperature silica cores with copper sheaths. Three of these sensors are used; two sensors are for the x and y axes (where z is the vertical axis), and the third is added for redundancy. Figure 4 illustrates the optical setup.

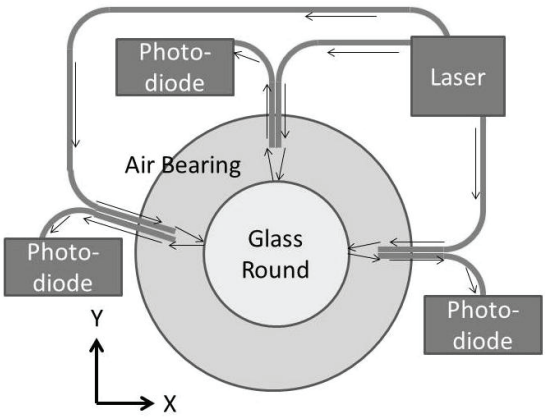

Figure 3. Diagram of optical system in device. Mechanical components not shown.

This optical system has its limitations, which include a high signal noise, a low distance range, and parasitic error between the two axes. The parasitic error is due to the curvature of the edge of the glass, causing the sensor output to decrease as the glass moves off-axis. The redundant sensor helps to mitigate this error.

RESULTS: FIRST ROUND OF SLUMPING

Using the device built, an initial trial of 13 glass wafers were slumped with varying degrees of success. The slumped wafers were measured with the lab's Shack-Hartmann surface metrology tool, which was repeatable to ±0.5 μm P-V during these experiments. Table 1 lists the slumping parameters and results for these samples. During these experiments, the Shack-Hartmann tool was unable to accurately measure samples with greater than 30 μm of distortion. However, the general shape can be ascertained; all of the samples started out with similar cylindrically-curved shapes.

TABLE 1. Results of first slumping round.

#	Gap (μm)	Max temp (°C)	Dwell time (min)	Result P-V (μm) front or front/back
1	>50	600	6	12.3±0.5
2	>50	600	60	>30
3	>50	600	6	5.9/5.2±0.5
4	>50	600	6	14.0/12.6±0.5
5	>50	600	60	>30
6	>50	600	6	4.8/5.1±0.5
7	>50	600	60	>30
8	>50	550	60	>30
9	>50	550	6	6.4±0.5
10	>50	550	6	11.3±0.5
11	36±2.5	550	6	6.7/3.6±0.5
12	36±2.5	550	12	10.1±0.5
13	30.5±2.5	550	6	19.5±0.5

The actual gap for trials 1-10 is unknown. This is because, while the gap was set at 50 μm, there was interference from some sheet metal parts that caused the gap to be somewhat larger than 50 μm. The sheet metal was intended to bend elastically and not interfere with the gap, but was stiffer than anticipated due to repeated thermal cycling. To correct this, more compressive force was added to clamp the two bearings together with shims in between. The shims were measured with a digital micrometer with resolution of ±2.5 μm.

Trials 1-7 were run at 600°C. All attempts with short dwell times (6 minutes) at 600°C were successful, while attempts with long dwell times (60 minutes) failed. It was speculated that this happened because the glass is too soft at 600°C. If the glass is too soft, it may not maintain a flat shape and will instead deform to the confines of the air bearings. During shorter dwell times, the glass might not have had time to actually reach 600°C, thus resulting in a better surface P-V. Other explanations have also been proposed and further research is ongoing.

To confirm that 600°C is perhaps too hot, trials 8-13 were run at 550°C. All samples changed shape significantly, confirming that a lower process temperature is sufficient. In addition, trial 8 was run for a 60 minute dwell time, and also failed, similar to what occurred with 60 minute dwell times at 600°C. This suggests that the process temperature can be lowered even further.

Interestingly, trials 11-13 did not result in significantly better surface P-V, even though the gap was smaller. Trial 13, especially, has the worst P-V of 19.5 μm, but also somehow resulted in a nearly perfectly symmetrical shape, which proves that the glass was floating the entire time instead of getting pinned or stuck on an edge. In addition, the symmetrical shape suggests that the worsened P-V might be the natural mode at steady state instead of being an exception. Further experiments and computer modeling are planned to help elucidate this effect.

RESULTS: SECOND ROUND OF SLUMPING

In a second round of slumping, the primary goal was to evaluate the repeatability of the slumping tool. The glass was slumped below 550°C in order to extend the life of the fiber sensors, and to avoid the instability observed at higher temperatures. Due to the lower temperature, longer dwell times are required in order to allow the glass to reach steady state. The results are shown in Table 2.

Trials 1-3 show that 500°C is not hot enough to slump glass, as the glasses did not seem to reach a steady state (spherical shape) even after 90 minutes of slumping. This is expected since the strain point of the glass is 529°C.

TABLE 2. Results of second slumping round.

#	Gap (μm)	Max temp (°C)	Dwell time (min)	Result P-V (μm) Top side
1	28.5 ± 2.5	500	6	17.6 ± 0.3
2	28.5 ± 2.5	500	30	12.9 ± 0.3
3	28.5 ± 2.5	500	90	12.5 ± 0.3
4	28.5 ± 2.5	550	6	8.5 ± 0.3
5	25 ± 2.5	550	30	10.1 ± 0.3
6	Unknown	529	30	9.2 ± 0.3
7	Unknown	529	30	9.8 ± 0.3
8	Unknown	529	30	9.9 ± 0.3
9	24 ± 2.5	529	30	4.5 ± 0.3
10	25.5 ± 2.5	534	30	6.0 ± 0.3
11	26.5 ± 2.5	534	60	14.5 ± 0.3
12	31.5 ± 2.5	534	60	11.9 ± 0.3
13	Unknown	534	60	13.2 ± 0.3
14	Unknown	534	60	12.6 ± 0.3
15	Unknown	534	60	10.9 ± 0.3

Subsequent trials used 550°C, 529°C, and 534°C with 30 minutes of dwell time. Trials 5-8 were slumped with the convex side of the wafer pointing upward. Trials 9-10 were slumped with the convex side of the wafer pointing downward. Because there was little variation between trials 5-8, but significant variation between the two sets of trials, it was concluded that either a hotter slumping temperature or a longer dwell time was required. Trials 11-15 were slumped with the convex side initially downward, at 534°C for 60 minutes. This resulted in apparently steady-state shapes (spherical). Figure 4 shows the surface mapping of trial 14, which appears to have achieved a steady-state shape.

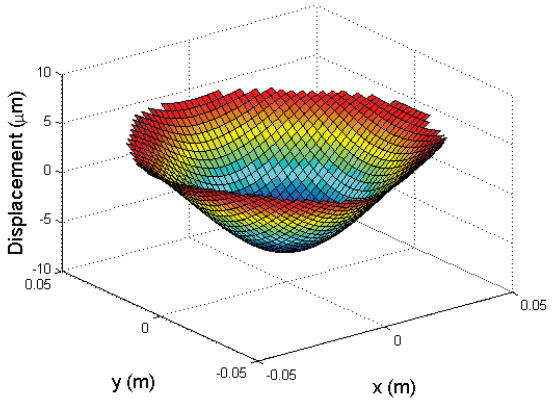

FIGURE 4. Trial 14 surface map.

Wafers G27 and G29 were compared to evaluate the repeatability. Fig. 5 shows the difference between G27 and G29 surface shapes. Over the whole 100 mm wafer, the P-V of the difference between the two wafers is 2.7±0.5 μm and the RMS slope difference is 9.5 arcseconds. In other samples, larger differences from this shape appeared to be due to the center of the spherical shape being shifted slightly. These results are a significant improvement over the previously-reported vertical slumping results [3][4]; when only the center 60 mm is considered (as in the previously-reported results), the difference improves to <1 μm P-V and 5±0.5 arcsec. We judge repeatability to be the most significant performance parameter at this time, since a repeatable error shape (e.g., spherical) could always be ground out of the mandrel set.

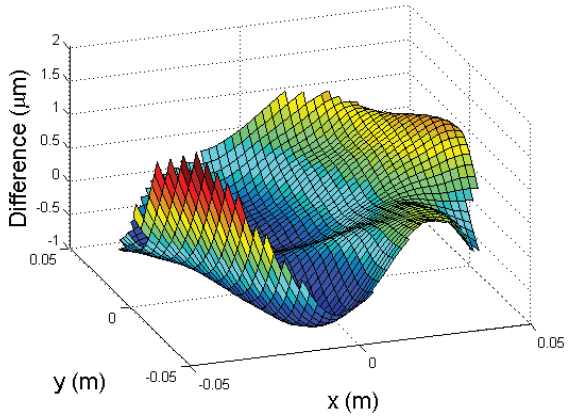

FIGURE 5. Difference between trials 12 and 14 surfaces.

FUTURE WORK

It has been shown that glass can be slumped horizontally, without contact using air bearings, to micron-level precision. The lowest peak-to-valley achieved in the scope of this work was 3.8±0.5 μm. However, this was not the steady state shape of slumped glass. Steady state shapes were found to be symmetrical and spherical with a P-V of about 12 μm. However, this was for a relatively large gap of 36±2.5 μm between bearing and glass. With a smaller gap, the stiffness of the air layer rises as the inverse cube of the gap, and may result in a much lower steady state P-V for the slumped glass.

The repeatability of the slumping process was found to be much improved over the previous vertical slumping method. When aligning the centers of the spherical shapes, the repeatability over 60 mm sections was found to be less than 1 μm P-V and 5±0.5 arcsec, which is challenging to measure with our surface metrology tool. With further development we expect these errors can be reduced.

Additionally, the slumped glass exhibits only low frequency spatial errors, since dust particles are not an issue as they are with traditional methods, and mid-range frequency bearing errors are averaged out by constantly moving the glass within the bearings. We have proposed using a novel technique to remove remaining low-frequency spatial errors via ion implantation (see paper by Chalifoux et al. in these proceedings).

It has been shown that 600°C is not necessary to slump glass using the air bearing method. Lower temperatures, down to 529°C, are sufficient to slump D263 glass, although lower temperatures require longer slumping times since the glass is not as malleable. 534°C was found to provide an adequate balance between slumping time and lower temperature.

Additional work is currently being performed in the form of a new device that does not require an oven. Instead, heated air is blown into the plenum/bearing assembly, which is thermally isolated. This device has the potential to reduce the slumping cycle time to less than 1 hour. Rapid slumping cycles, and potentially cheaper mandrels, should help reduce production costs of high-precision x-ray mirrors.

REFERENCES

[1]E Sung, J Fucetola, M Schattenburg, et al. *Non-contact position control via fluid shear force*. In Proc. 27th Annual Meeting of the American Society for Precision Engineering, 54, p. 245 (2012).

[2] W Zhang, *Next generation x-ray optics: high resolution, light-weight, and low-cost.* In Proc. SPIE 8443, Space Telescopes and Instrumentation 2012: Ultraviolet to Gamma Ray, 84430S (2012).

[3] M Akilian, *Methods of Improving the Surface Flatness of Thin Glass Sheets and Silicon Wafers*. PhD Thesis, Massachusetts Institute of Technology, Sep 2008.

[4] A Husseini, *Design and Modeling of a Third Generation Slumping Tool for X-ray Telescopes Mirrors*. MS Thesis, Massachusetts Institute of Technology, Jun 2011.

THE TILTED-WAVE-INTERFEROMETER (TWI): A QUICK AND FLEXIBLE APPROACH TO MEASURE ASPHERIC AND FREE-FORM SURFACES

Goran B. Baer, Johannes Schindler, Christof Pruss and Wolfgang Osten
Institut für Technische Optik, University of Stuttgart,
Pfaffenwaldring 9, 70569 Stuttgart, Germany

INTRODUCTION

The fabrication of precision optics is always connected to careful optical testing. With the need for better, smaller and lighter optical systems the use of aspheres and also free-form surfaces has become a necessity in modern optics design [1]. New and improved fabrication technologies like ion beam etching or magneto rheological finishing (MRF) have been developed, allowing the flexible polishing of modern aspheric and free-form surfaces. However, for the control of the process it is inevitable to be able to measure the surface. To obtain a highly economic production line it should therefore be the goal to integrate the metrology directly into the fabrication process. Over the past decades the testing of aspheres and more recently also the testing of free-form surfaces has developed from the mere feasibility towards more economic solutions. Flexible solutions without expensive null optics such as computer generated holograms (CGH) have been developed. Different scanning systems have been proposed that either test the surface under test point-wise or patch-wise. However, time sequential scanning leads to comparatively long measurement times. In this contribution we present the principle and recent advancements in what we call the Tilted-Wave-Interferometry. Our goal with the invention of the Tilted-Wave-Interferometer (TWI) was to reduce the measurement time to a minimum while still maintaining a high degree of flexibility [2] [3]. The combination of these advantages makes it a perfect candidate for the integration into a flexible production line for high-quality optical surface fabrication.

STATE OF THE ART IN ASPHERE AND FREE-FORM METROLOGY

In the case of spherical and plane surfaces interferometry is the solution of choice for testing of these objects. Such surfaces can be measured in null-test configuration without the need for compensation optics. When the surface deviated from the spherical form, the rays do no longer impinge perpendicular on the surface. This violation of the null-test condition can lead to vignetting so the surface cannot be measured. Further, since the rays take different paths through the interferometer on their way back, retrace errors are introduced to the measurement [4] [5]. One way to overcome these problems is the use of CGHs. These compensation elements are designed to adapt the wavefront to the surface under test (SUT) and restore the null-test condition, which is the state of the art method in the field of high-accuracy measurement of aspheric and free-form surfaces. The disadvantage here is that for every surface shape, a fitting CGH has to be fabricated, which is very costly. Further the alignment of these elements as well as the SUT is a non-trivial task and can be very time consuming. Different approaches are scanning approaches. Here the null-test condition is locally restored in a small area enabling a sequential measurement. One example for this approach is the scanning Fizeau interferometer [6], where the surface under test is scanned along the optical axis. In every scanning position the center of the surface, as well as an annular region can be evaluated allowing to reconstruct the surface from the combined information from all measurements. The disadvantage of this approach is the - due to the scanning - long measurement time as well as the restriction to rotationally symmetric surfaces. Another non-null approach is stitching interferometry [7] [8]. Here the measurement is divided into several sub apertures and the final result is stitched together from the single measurements. Here again the measurement time is a drawback. Besides the interferometric surface measuring methods also point-wise methods can be used for the testing. These can be divided into tactile contact methods and non-contact methods using optical point sensors. The main disadvantage of all these methods is the long measurement time as well as the low lateral resolution that can be achieved in a reasonable time scale. With tactile methods there is also the risk to damage the object when the stylus probes the surface.

THE TILTED-WAVE-INTERFEROMETER

The basic idea behind the Tilted-Wave-Interferometer is to use the high resolution and measurement speed of full-field interferometry together with a multi beam parallel illumination scheme for flexibility and a sophisticated calibration method to account for retrace errors.The illumination scheme gives the method its name: Tilted-Wave-Interferometry. We illuminate the SUT with a set of discrete wavefronts that are tilted with respect to each other. Thus, for any spot on the SUT, there is a matching wavefront that leads to an interpretable interferogram patch. Light that would produce interference fringes that are not evaluable, is filtered out by the interferometer aperture. This allows in principle to capture the whole SUT in one interferometric measurement. For practical reasons to avoid overlapping of the individual patches only every second wavefront in each direction is switched on. So in practice, four measurements are taken for each SUT, with different wavefronts switched on (see figure 2). The SUT is not moved at all during the measurement. The actual demonstrator setup is capable of measuring aspheres with gradient deviations of up to 10° relative to the best fitting sphere in about half a minute's time. Since the tilting angles of the wavefronts cover angles of 10° in both x and y-direction, the departure from the sphere does not need to be rotationally symmetric but can be an arbitrary free-form.

Setup

In figure 1 the basic setup of the Tilted-Wave-Interferometer is shown. A coherent laser source L is divided into a test and a reference wavefront by a polarizing beam splitter PBS. The light in the test wave is then used to illuminate a micro lens array that is followed by a pinhole array. These two parts serve as an array of point sources for the test wavefronts. The spherical wavefront from each point source is then - after passing the beam splitter BS - collimated by C1 resulting in a set of plane wavefronts with different amounts of tilt [3] [2] [9]. The tilted wavefronts are transformed to spherical wavefronts by the transmission sphere TS to compensate the basic spherical form of the SUT. In the case of surfaces with a best fit sphere of infinite radius no transmission sphere is needed. The wavefronts are then reflected by the SUT and propagate back to the beam splitter, where they are reflected to the camera arm of the interferometer. Here they have to pass an

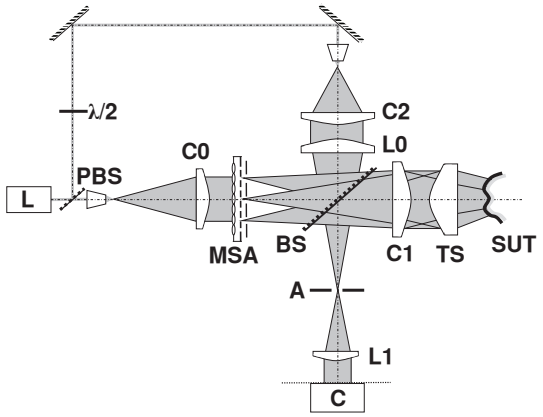

FIGURE 1. Schematic setup of the Tilted-Wave-Interferometer

aperture A that is located in the Fourier plane of the interferometer. The aperture blocks all light, that would generate fringes with a density that violates the Nyquist criterion. After the aperture, the light passes an imaging optics L1 and interferes with the reference wavefront on the camera C. The distance between the sources in the array is chosen to cover the whole surface under test without gaps and a slight overlap. To avoid interference between neighboring sources the measurement is divided into four steps with only every fourth source enabled in each step. The switching between the sources is realized by a simple aperture array that is moved in front of the micro lenses and blocks every second source in each row and column. The main difference of this approach to the scanning type interferometers described in above is that the acquisition of the data is highly parallelized since all the test wave fronts are applied to the surface in only four steps. Further, the SUT does not have to be moved during the measurement process. Both these advantages lead to a very short measurement time of about half a minute.

Calibration

As with all non-null testing methods a major topic is calibration. We use a system of polynomials to describe the aberrations of the interferometer. These polynomials describe not only the wavefront aberrations of the system, but also the field dependency of the aberrations for the tilted wavefronts. The first estimation for the polynomial coefficients is obtained by ray tracing. Since the wavefronts in the real setup deviate from the nominal design of the interferometer, the coefficients have to be adjusted to match the real wavefronts.

As a natural extension from null-test interferometry the calibration is performed using a known reference sphere. This sphere is measured in several positions in the test space of the interferometer. An optimization algorithm using a perturbation method is then used to calculate the coefficients describing the real setup [10]. This black-box model of the interferometer can then be used to calculated all possible rays through the setup. With this information it is now possible to distinguish between retrace errors introduced by the setup or misalignment and aberrations introduced by the surface.

Measurement

The calculation of the surface error is - like for the calibration - performed by perturbation of a polynomial representation of the surface. From this the basic low frequency shape of the surface is obtained.

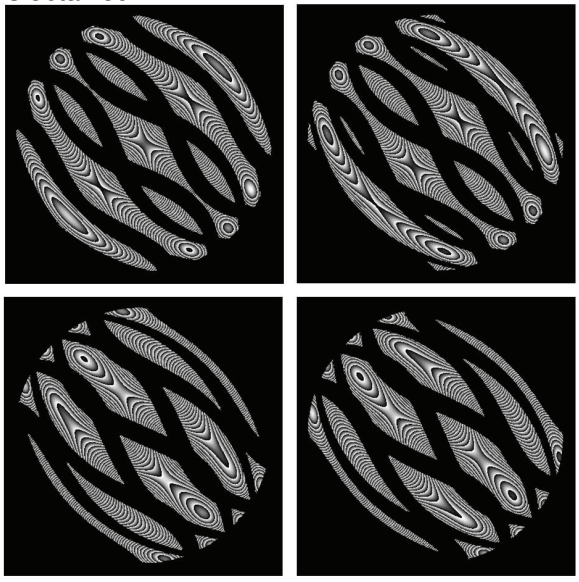

FIGURE 2. Interferometric pattern like obtained in a measurement of a free-form surface. For better visualization synthetic images with a longer wavelength are shown

The polynomial that is used for the surface representation is of finite order and covers the basic shape of the surface under test, but cannot describe the higher frequencies that may also be present in the surface. Since we are also interested in higher frequency errors of the surface which cannot be described by a polynomial of finite order these errors are evaluated in an additional step. The individual patches from the tilted wavefronts, from which each covers a small area of the surface, contain this information. The evaluation is performed in a second step. With the black-boxes obtained by the calibration we are able to calculate all possible rays through the interferometer. With the basic surface shape also known from the first measurement step, we now can calculate the rays from the sources through the interferometer to the surface and from there back to the camera. The difference between the calculated optical path length (OPL) and the measured OPL is the high frequency error that we are searching for. Since not only the OPL but also the exact position on the SUT of the ray is known the high frequency error can now be projected to the measurement. As a final result a reconstruction of the surface including not only the basic shape but also high frequency errors like grooves or tooling footprints is obtained. Some example results of aspheric but also free-from surfaces measured by this method are presented later in the paper.

Alignment

As in all interferometric setups the positioning of the surface under test is important, since a) an incorrectly positioned surface might lead to vignetting and b) it adds alignment errors to the measurement. The TWI with its huge flexibility in terms of aspheric departure offers a unique situation for this problem. Even for a poorly positioned surface under test there will be a signal that helps finding the approximate correct position. In [11] we have demonstrated that the alignment can be automated quite efficiently. With an extension of the algorithm this can be also applied to free-form surfaces [12]. Here we show that this can also be

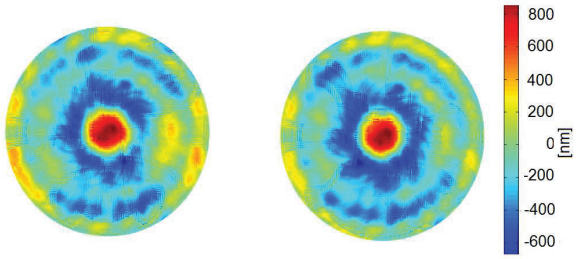

FIGURE 3. Reproducibility measurement of an aspheric surface.On the left with surface perfect aligned, on the right with 20 μm misalignment

done virtually, eliminating the need of doing a fine positioning of the SUT. We have realized an algorithm capable of estimating the correct position of the surface under test. With the position information, we can determine and subtract the alignment errors. As an example, figure 3 shows two measurement results of a surface under test that was

laterally shifted by 20 μm between the two measurements. As can be seen, the algorithm obtains virtually the same measurement result.

MEASUREMENT RESULTS

In figure 4 a measurement of an aspheric surface obtained by the Tiled-Wave-Interferometer is shown. The deviation of the asphere from its best fit sphere is about 600μm and the slope deviation is about 8°. The surface was polished using a MRF finishing technique and footprints from the tool are clearly visible on in the surface reconstruction. As reference to the measurement result the surface was also measured using a tactile Panasonic UA3P coordinate measuring machine. The results of this measurement can be seen in figure 5 The measurement time in case of the TWI was about 30 seconds whereas the tactile measurement took about 40 minutes.

In figure 6 the measurement result of a non rotationally symmetric free-from surface is shown. The surface has a strong astigmatic shape of about 1mm deviation from its best-fit sphere. The finishing of the surface was performed by a diamond turning technique. In the results the grooves from the diamond tool are clearly visible, as well as a central bump which is typical for turned surfaces.

CONCLUSION

The Tilted-Wave-Interferometer is a promising technique for the measurement of aspheric but also free-form surfaces. Its advantage compared to other methods is its high flexibility, allowing measurements with an aspheric departure up to 10° and no requirements for rotational symmetry in the surface. Like all full-field interferometric approaches it has a high lateral resolution compared to tactile methods. Further, no compensation optics like costly CGHs are needed and the measurement time of under one minute is extremely short, compared to scanning approaches. The flexibility can further be used to relax the requirements for the alignment accuracy of the SUT and the process of the alignment can be automated.

ACKNOWLEDGEMENTS

The EMRP is jointly funded by the EMRP participating countries within EURAMET and the European Union. Further we would like to thank the BMBF for funding parts of this work (projects MesoFrei), and the Baden-Württemberg Stiftung for financing part of this work in the project NanoForm.

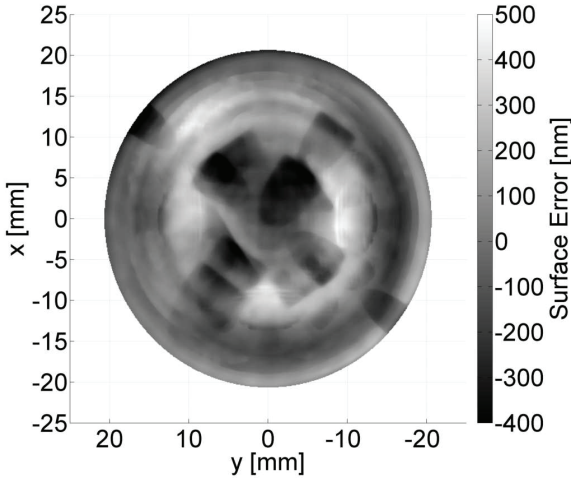

FIGURE 4. Measurement of an aspheric surface including MRF-finishing footprints obtained by the Tilted-Wave-Interferometer

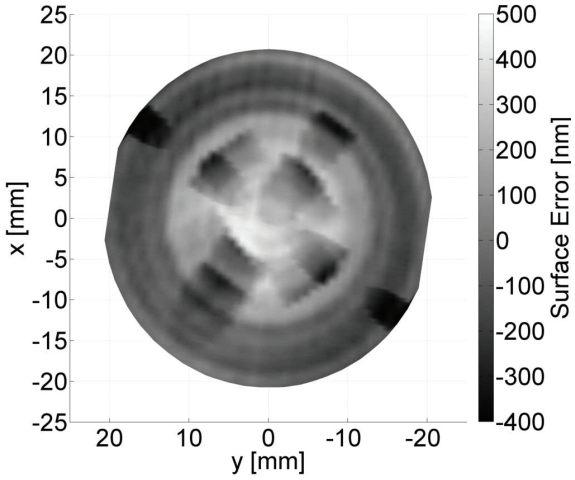

FIGURE 5. Reference measurement of the surface obtained by the a tactile Panasonic UA3P

REFERENCES

[1] Braunecker B, Hentschel R, Tiziani HJ. Advanced Optics Using Aspherical Elements. SPIE Press Monograph PM173; 2008.

[2] Liesener J, Garbusi E, Pruss C, Osten W; Patent DE 10 2006 057 606 A1. Verfahren und Messvorrichtung zur Vermessung einer optisch glatten Oberfläche. 2006;.

[3] Garbusi E, Pruss C, Osten W. Interferometer for precise and flexible asphere testing. Opt Lett. 2008;33:2973–2975.

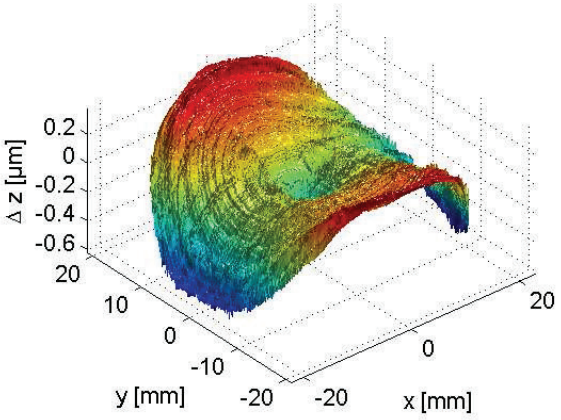

FIGURE 6. Measurement result of a free-from surface with clearly visible grooves from diamond turning.

[4] Evans CJ, Bryan JB. Compensation for errors introduced by nonzero fringe sensities in phase-measuring interferometers. CIRP Annals Manufacturing Technology. 1993;42(1):577–580.

[5] Lowman AE, Greivenkamp JE. Interferometer errors due to the presence of fringes. Appl Opt. 1996;35:6826–6828.

[6] Kuechel MF. Absolute measurement of rotationally symmetric aspheric surfaces. In: Optical Fabrication and Testing (OFT). vol. OFTuB5; 2006. .

[7] Tricard M. Subapertur-Stitching-Interferometrie: Messtechnik füur die Asphären-Präzisionsfertigung. Optics and Photonics News. Photonik;6:38–41.

[8] Murphy P, Forbes G, Fleig J, Dumas P, Tricard M. Stitching interferometry: a flexible solution for surface metrology. Optics and Photonics News. 2003;14:38–43.

[9] Liesner J. Zum Einsatz räumlicher Lichtmodulatoren in der interferometrischen Wellenfrontmesstechnik. PHD thesis Universität Stuttgart; 2006.

[10] Garbusi E, Osten W. Perturbation methods in optics: application to the interferometric measurement of surfaces. Optical society of America. 2009;26:2538–2549.

[11] Baer G, Garbusi E, Lyda W, Osten W. Automated surface positioning for a non-null test interferometer. Opt Eng. 2010;49:095602.

[12] Baer G, Osten W; Patent DE 10 2011 102 196.9. Justage einer zu prüfenden optischen Fläche in einer Prüfvorrichtung. 2011;.

IN-SITU TESTING OF A FREEFORM OPTIC WITH A CHROMATIC CONFOCAL SENSOR

Ralf Steinkopf, Susanne Zwick, Andreas Gebhardt,
Stefan Risse, Ramona Eberhardt
Fraunhofer Institute for Applied Optics and Precision Engineering IOF
Jena, Thüringen, Germany

INTRODUCTION

State of the art machining technologies enable the manufacturing of complex optical surfaces as aspheres and freeforms. To ensure the high quality demands of innovative optical surfaces, correction loops are implemented within the manufacturing process. These loops are based on metrology data. To avoid scratches on sensitive surfaces, non-contact measurements are preferable [1]. The classical approach of non-contact testing of optical surfaces is interferometry. It was demonstrated from a research group of Fraunhofer IPT that *in situ* measurements using a phase shifting interferometer integrated within a diamond turning machine leads to fast and reliable results [2]. However, the testing of freeform elements is complex as Computer Generated Holograms (CGH) have to be used to compensate the wave front differences between reference optic and test part [3]. The results of these measurements are highly accurate, but not flexible and considerably more expensive, since each surface needs its own CGH. *In situ* measurements with alternative non-contact measurement systems could reduce time and costs of the manufacturing process. Besides, tensions from clamping have no influence on the measurement, because *in situ* metrology works without remounting of the work piece.

MEASUREMENT PRINCIPLE

This paper describes a non-contact measurement of a freeform element. The measurement system, a chromatic confocal sensor, is integrated in a diamond turning machine. Basically, the sensor measures the distance between sensor and test surface at different points and generates a 3D map of the optical surface. The sensor setup uses the very accurate axes of the diamond lathe. Thus, the costs of the measurement system are reduced considerably while retaining the measurement accuracy even of complex optical surfaces. The non-contact measurement principle is especially important for the touch-sensitive diamond machined metal optics. In combination with high resolution, which enables a repeatability of +/- 20 nm and measurement rates of 30 kHz and more, fast and accurate measurements are feasible [4]. The limiting fact of this measurement technique results from the decreasing accuracy of the confocal probe with increasing surface slope. Additionally, vibrations of the machine axes reduce the accuracy of the measurement.

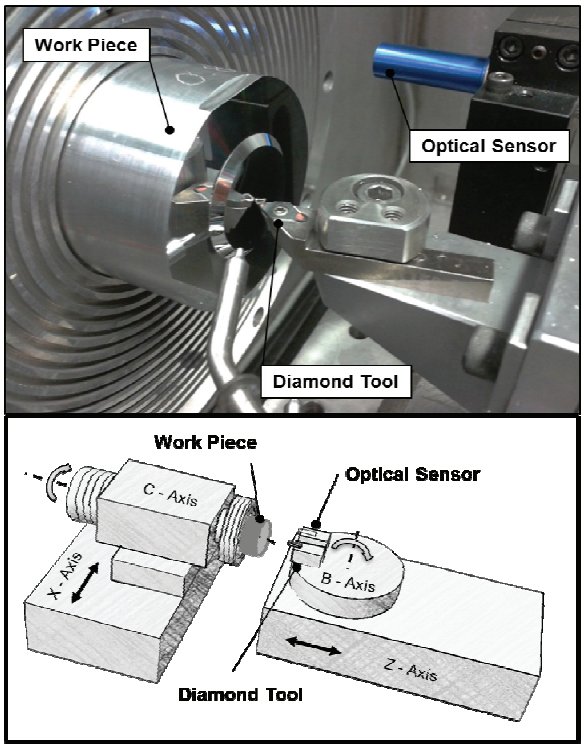

Figure 1: Machine setup of an in situ measurement using an optical sensor integrated in a diamond lathe.

DATA COLLECTING AND DATA HANDLING

The probe moves along the spiral tool path across the optical surface to collect the raw data. The distance between probe and surface as well as the position of the probe in respect to the coordinate system of the diamond lathe are

stored in a point cloud. The data consist of XCZ coordinates of the machine coordinate system and distance values of the sensor. The XCZ position coordinates and the distance values are transformed into XYZ coordinates, with its origin in the center of the optical coordinate system. The XYZ coordinates are used to create a 3D map of the optical surface. The data is further processed with a least square fit and the result is filtered to reduce noise and eliminate outliers of the raw data. The residuals are the form error of the optical surface which becomes negated and added to the original machine path for a correction cut. This technology enables a deterministic procedure to reduce effective surface errors within sub µm range [5].

EXPERIMENTAL SETUP

A diamond turning machine with two linear axes and two rotational axes is used as manufacturing tool. All axes are controlled and can be used in a synchronized operation mode. Thereby, it is possible to use lathes for the manufacturing of freeform elements without rotation symmetry. The two linear axes (X-axis and Z-axis) are orthogonal to each other. On top of the X-axis one of the rotational axes (C-axis) is mounted (Figure 1).

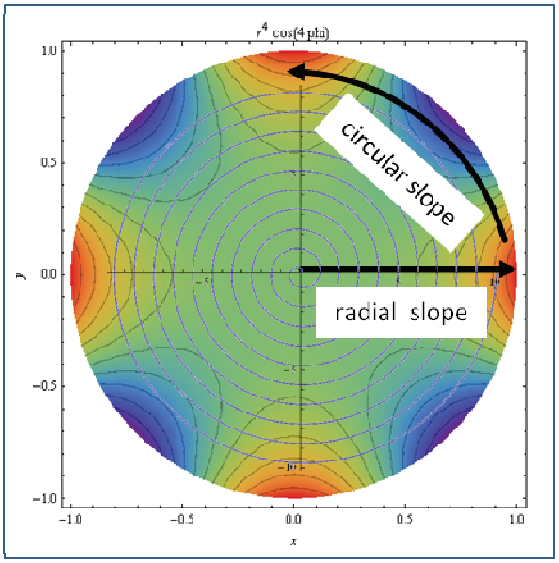

Figure 2: The measurement range of the optical sensor is limited by radial and circular slope.

During manufacturing and measurement, the test part is clamped with a vacuum chuck on the C-axis. The vacuum clamping ensures a low-stress mounting of the part during operation, by distributing the clamping force evenly across the test part. The part itself is thick enough to ensure that the clamping force of the vacuum chuck does not deform the optical surface. The second rotation axis (B-axis) is mounted on top of the other Z-axis. The diamond tool and the optical sensor are positioned on the B-axis. During normal diamond turning operations, the B-axis is not active; it is mainly used as positioning axis. But for some special operations it can be suitable to implement the B axis and use it actively, e.g. in case of parts, where the slope of the optical surface exceeds the slope on the tool. By rotating the B-axis synchronously with the other axes, the maximum workable slope can be increased.

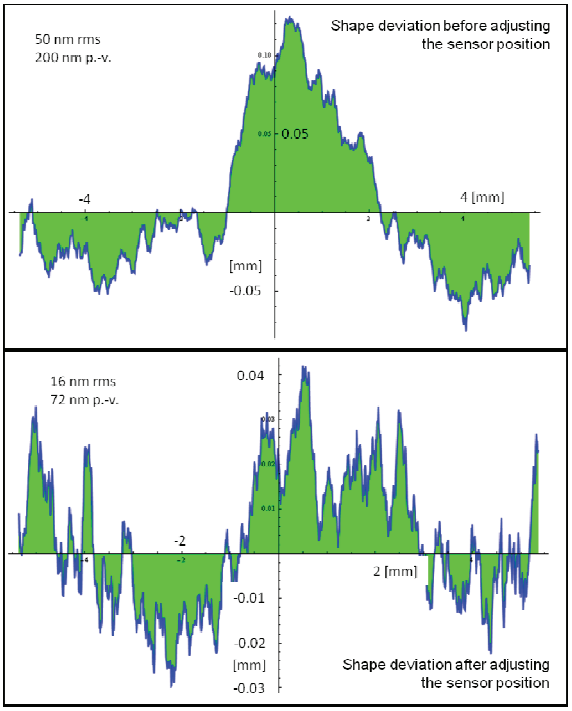

Figure 3: 2d measurement of a reference sphere before and after optimizing the sensor position within the coordinate system of the diamond turning machine. The measurement error could be reduced to 16 nm rms.

The same usage of the B-axis is possible for the optical sensor. The sensor has an operational slope of about 30°. But with increasing slope, the measurement accuracy is decreasing. So, it is possible to minimize the measurement error for large slopes by rotating the B-axis during the measurement in a way that the sensor remains normal to the surface of the part. It is not possible to adapt this rotation to the circular slope (Figure 2), so that the method works well

with large radial slopes. If the measurement accuracy is to be sufficient to measure sub µm shape deviations, the circular slope should not exceed 15°.

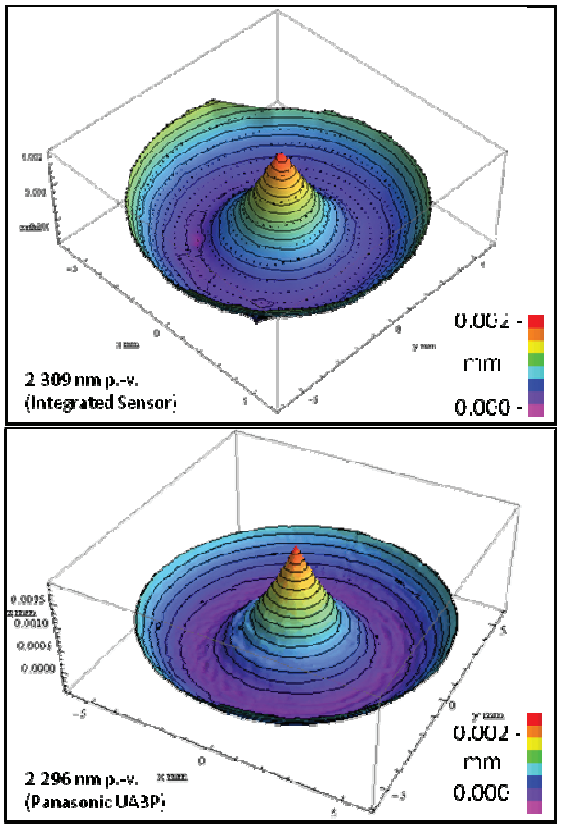

Figure 4: 3D measurements of a test part with a spherical aberration obtained with the tactile measurement system UA3P (Panasonic) and the confocal chromatic sensor.

If tool and sensor are mounted on the lathe, both must be positioned exactly within the coordinate system of the lathe. The positions should be exact within few microns, because increasing position errors are responsible for increasing shape deviations on the part and by testing the part with the integrated sensor for measurement errors, respectively. To reduce these errors, reference parts were cut and measured on the diamond lathe and measured again with an external measurement system for comparison. From the known error pattern of the test parts, it is possible to adjust the position of tool and sensor. Figure 3 shows the difference between measurements of an external measurement system and the integrated sensor, measuring a diamond turned sphere before and after optimizing the sensor height position within the machine coordinate system. The measurements were performed with a 2D contact probe system (FormTalysurf) and the integrated sensor. Subtracting the residuals of both measurements, it can be seen that during the optimization of the sensor position the difference of both measurements could be reduced from 50 nm rms to 16 nm rms.

EXPERIMENTAL RESULTS

To make sure that the 3d measurements of the integrated sensor are comparable with established measurement systems, a sphere was measured with the Panasonic UA3P, a 2½D measurement system as well as with the integrated sensor. Figure 4 shows the spherical aberration of the part. Both systems obtained very similar results, with shape deviations of the spherical surface of approximately 2.3 µm p-v.
To establish the process chain, the measurement and correction loops were carried out with the well referenced Panasonic UA3P before applying the technology on the confocal chromatic sensor.

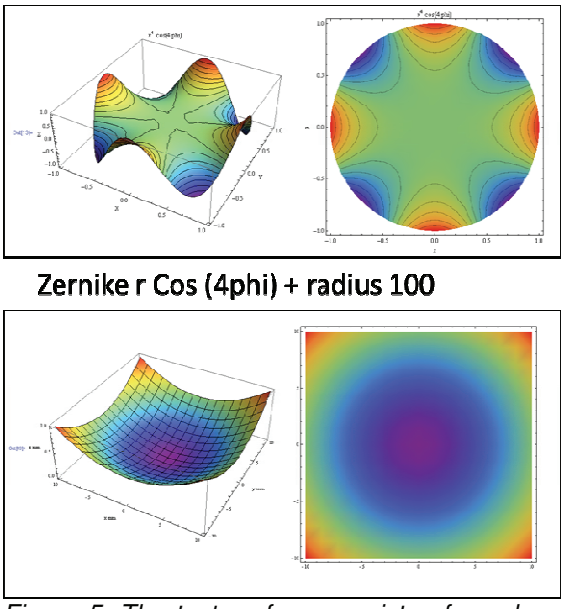

Figure 5: The test surface consists of a sphere which is superimposed with a Zernike freeform.

The test surface is an aluminum part with a diameter of 48 mm. The basic shape consist of a 100 mm radius, superimposed with a Zernike freeform, which is described with the coefficient r*COS(4phi). The slope of the optical part is approximately 25 degree. Implementing the correction cycle, the initial shape deviation could be reduced from 3 µm to 340 nm p-v.

After establishing the process chain with the Panasonic UA3P, the technology was transferred to the integrated sensor.
Due to the measurement principle of the chromatic confocal sensor, the measurement error rises with an increasing slope of the optical surface. To compensate for this systematic error, the slope of the test part was reduced from 25 degree to approximately 5 degree. This was achieved by reducing the diameter of the freeform surface from 48 mm to 25 mm. The sensor is a Precitech Crocodile S with 300 µm measurement range and a sampling rate of 2 kHz. For applying the technology in a production environment, it is recommended to use a sensor with higher sampling rate to speed up the measurement time.
The sensor was selected after detailed verification with sensors from different manufactures. All sensors were tested on a reference sphere. The Precitech sensor was chosen, because it showed the least measurement errors in respect to increasing slopes. The measurement results are shown in Figure 6.

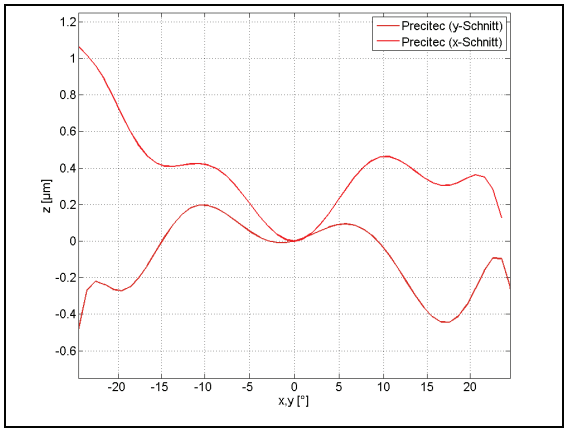

Figure 6: Test measurements show that the chromatic confocal sensor allows measurements up to a slope of 20° within sub µm accuracy.

To cut and measure a freeform surface, the complete surface has to be described. This is a huge difference to rotational symmetric parts and one of the reasons, why it is so difficult to manufacture freeform elements. Classically optics manufacturing benefits from rotational symmetry. It allows for relative simple machine kinematics. Even an asphere is described by a rotating line. Freeforms consist of, however, no rotational axes and must be described completely. The test surface is specified analytically with the Zernike Standard Sag formula, as explained in the user´s guide of the optical design software ZEMAX [6]. The tool path, including the correction of the tool tip, is calculated with the CAM program Diffsys. The result is a point cloud, consisting of CXZ points, which is transferred into the diamond turning machine. The same point cloud is used as the spiral path of the integrated sensor, without tool tip correction. The measurement time depends on the raster, the size of the part and the measuring rate. For parts in the size of Ø 25 mm and the 2 kHz sensor, a reliable measurement is realized in less than 5 minutes. The measurement result, a point cloud again, is transferred to an external computer and further analyzed with a specific algorithm developed on "WolframMathematica®" for fitting, filtering, and correcting shape deviations of optical surfaces. As a result of the analyzing process, the shape deviation after initial cutting is known. The residuals are added to the cutting program and the part is re-cut. This cut-and-measurement loop is repeated until the optical surface reaches the tolerances of the optical surface. In test application, it was possible to reduce the shape deviation from an initial error of approximately 3 microns to 472 nm p-v (c.f. Figure 7).

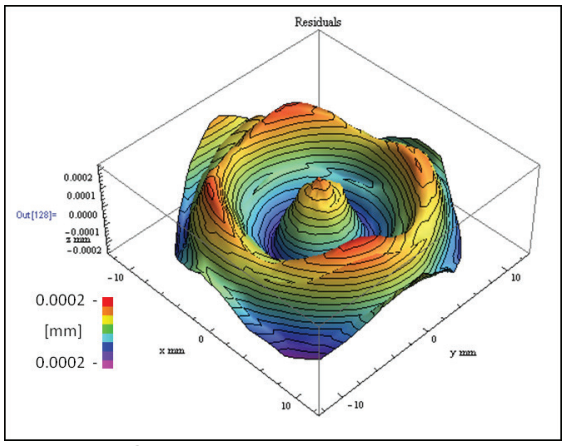

Figure 7: Shape deviation of the freeform part after implementing the measure and correction loop using the chromatic confocal sensor.

CONCLUSIONS

The paper presents an ingenious way of an *in situ* and non-contact measurement method applicable to spherical, aspherical, and even freeform surfaces. A chromatic confocal sensor is integrated into a diamond turning machine and subsequently used for the measurement of a freeform surface. Test measurements on reference parts have shown that sub-micron

shape deviations can be detected and corrected. Due to the measurement principle, the measurement error of the system is increasing with increasing slopes. To enhance the range of the sensor, it is possible to implement a rotary axis to move the sensor in a permanent normal position to the optical surface. So it is possible to measure even steep aspheres and freeforms with steep radial slopes. For freeforms with circular slopes, the work range is limited. Test measurements provide a chart with the accuracy of the sensor in respect to the surface slope. A process chain for analyzing the measurement data and re-cutting the part on the diamond turning machine in a measurement and correction loop was developed. The process chain was implemented and used to correct a freeform surface. The shape deviation could be reduced from initial more than three microns to less than 500 nm p-v. With the aim to increase the measurement range for radial slopes without loss of accuracy, the next step will be the implementation of the B-axis.

REFERENCES

[1] D. Ewert et al., “Integration of an optical Sensor into UPMC”, Proceedings of the 11th euspen International Conference, Como, May 2011

[2] D. Doerner et al., “A new approach to *in-situ* formtest-interferometry”, Proceedings, XVII IMEKO World Congress, June 22–27, 2003, Dubrovnik, Croatia

[3] James H. Burge and James C. Wyant, “Use of Computer Generated Holograms for Testing Aspheric Optics”, Proceedings of the American Society for Precision Engineering Winter Topical Meeting on Free-Form Optics, Design, Fabrication, Metrology, Assembly, 2004

[4] H.-J. Jordan, “Optical chromatic confocal probes”, XII. International Colloquium on Surfaces Chemnitz, January 28/29, 2008

[5] Steinkopf et al., “Data handling and representation of freeform surfaces”, SPIE Optical System Design 2011, September 5-8, 2011, Marseille, France

[6] ZEMAX®, Optical Design Program, User's Guide, May 4, 2009

ROUND-ROBIN MEASUREMENTS OF A TOROIDAL WINDOW

Kate Medicus[1], Scott DeFisher[2], Marcin Bauza[3], Paul Dumas[4]
[1]Optimax Systems Inc., 6367 Dean Parkway Ontario, NY 14519
[2]OptiPro Systems, 6368 Dean Parkway Ontario, NY 14519
[3]Carl Zeiss Industrial Metrology, LLC, 6250 Sycamore Lane N Maple Grove, MN 55369
[4]QED Technologies, Inc., 1040 University Avenue Rochester, NY 14607

INTRODUCTION

Free-form surfaces are quickly becoming a desired and necessary shape for many refractive and reflective optical systems. Some examples of free-form shapes are toroids, ogives, and other conformal windows. A free-form typically means a shape that is not defined by a standard spherical or aspheric (conic) equation. Departures from a best-fit sphere of a free-form surface vary in the range of 1 mm to 10 mm. New and adapted processes have been developed to manufacture these free-form shapes, but without adequate metrology the ability to produce quality surfaces is severely limited.

The purpose of this study is to determine the state of current measurement methods of free-form surfaces. To meet this purpose we have performed a round-robin study measuring the surface irregularities of a free-form shape. In this paper, we review why new measurement methods are necessary for free-form shapes, introduce the methods used to measure the part, review the measurement results, and discuss the variation in the results.

The form of the round-robin study is as follows. First, a design was chosen and Optimax manufactured a toroidal window using grinding and polishing. The surface was polished until free of significant sub-surface damage (gray-free) but the surface was not corrected for surface form error. No specific surface tolerance was used. After manufacturing, the part was measured at Optimax and then the part was mailed to other companies for measurement at their sites. No information was given about the part to each participant other than the nominal shape.

We decided to manufacture and measure a toroidal window for this round-robin study. The nominal concave radii of the toroid are 445 mm and 288.55 mm and the nominal convex radii ate 450 mm and 293.55 mm. A toroid, which has different radii in orthogonal directions, is a good shape for this study because of its highly free-form nature while still being a shape that is easily defined in equation form (as opposed to a cloud of points). As manufactured the toroid is oversize, at 110 mm by 110 mm square and has a manufacturing defect in thickness. Figure 1 shows a picture of the toroid. The window is made of fused silica.

Figure 1: A picture of the toroid.

Desired measurement

The desired measurement is the deviation of the surface from the nominal shape, in a direction normal to the nominal shape. This deviation normal is similar to a typical interferometric measurement of an optical surface. A full surface map has a deviation for each point of an equally spaced grid of x,y points across the surface of the optic. The lateral (x,y) spacing, the mm per pixel, is dependent on the measurement method; no minimum spacing was specified for this round robin test, which in hindsight was a planning error. The needed lateral spacing depends on the manufacturing method and the part's final application. With this full surface measurement, surface corrections and final specification checks are possible.

Why conventional metrology fails

A commercial Fizeau interferometer is the tool of choice for measuring the irregularity of optical surfaces. A Fizeau interferometer measures the difference between the test part and a best fit sphere, normal to the nominal shape. Fizeau interferometers result in a fringe pattern which is the interference between the test and reference

* kmedicus@optimaxsi.com, 585-265-1020 ext. 292

wavefronts. When the differences become large over the same lateral area, the fringes will become very dense. If the fringes reach the Nyquist limit on the camera, the pattern is no longer resolvable. The fringes in the center of the part are resolvable, but quickly become non-resolvable. This is the main reason that the typical optical measurement method, interferometry, fails for measuring free-form optical surfaces. The free-form's high deviation from the spherical reference wavefront results in fringes that are too dense to be resolved.

MEASUREMENT METHODS

Coordinate measuring machine at Optimax

Optimax measured the toroid on a Leitz PMM 866 coordinate measuring machine with certified volumetric accuracy of 1.2 μm + L/400 μm (where L is in mm). The probe is ruby sphere attached to a scanning head which scans at constant force near 0.3 N. The part was held in a vice with minimal clamping force. Each surface of the toroid was measured independently. Each surface was measured with a series of lines. Along the lines (the direction of the scan), the point lateral spacing was approximately 0.5 mm leading to near 17,000 measurement points. The lateral spacing between the lines is approximately 1 mm.

For the measurement, the CMM software uses the surface nominal shape (as a solid model) and user input to approximately locate the shape in space. The surface is then scanned with the probe normal to the nominal shape. The CMM software then performs a best fit operation to fit the nominal shape to the measured shape. This is done to remove misalignments between the nominal shape and the measured shape. The report from the CMM is a set of XYZ points for both the nominal and measured shapes and the IJK vectors normal to the nominal shape. The deviation along the normal vector is then calculated in Matlab, outside the CMM software. This results in an unequally laterally spaced set of normal deviation points. We then fit this set of points to an evenly spaced grid (typically 0.5 mm lateral spacing). This fitting is required for display purposes and for input into typical optical manufacturing equipment. Errors in this fit, from interpolation and from uneven distribution along the slope of the test part are expected to be small compared to the surface form error.

Ultra-Surf at OptiPro

OptiPro Systems has been developing the UltraSurf, a non-contact measuring system using state of the art, air-bearing, precision motion control. The five-axis, non-contact single point measurement is flexible enough to handle common metrology problems such as surface roughness, slope error, and high departure from base radius. UltraSurf measures with sub-micrometer non-contact point sensors to collect surface information. Various sensors are commercially available from multiple companies, each with their own distinct optical measuring technology. An optical sensor using low-coherence interferometry with a near infrared laser was used to measure the inside, outside, and thickness of the toroid at a single point. The probe scanned over the toroid point to point, staying normal to the surface at all times. Taking multiple points on the toroid produced a full 2.5D point cloud for both surfaces along with the material thickness. UltraSurf measures in reflection, so surfaces must be parallel to near 2 degrees total in order to measure thickness. The toroid was measured while sitting on a flat plate, convex side up, secured in place by thin double sided tape. All the data was collected in a single measurement.

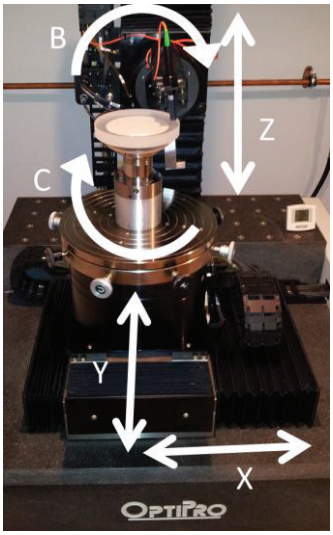

Figure 2: UltraSurf measuring a large radius concave surface, X,Y,C axes move the part under test, B,Z axes move the non-contact probe.

The measured point clouds were best fit to the toroid shape in software. OptiPro used the equation of the toroid to fit lateral translations, rotations, and radius. Optimizing the radius

removes lower order errors from the final data set, and provides the best fit radius that can be used for manufacturing tolerances. In the case of a true freeform, a material offset along the surface normal can be substituted. Both methods are way to separate the shape of the data from the form error. Form error is calculated normal to the surface geometry, which provides a slope insensitive measure of deviation. After form is removed, the datasets are interpolated to a grid using cubic splines. Interpolation accuracy with this technique is on the order of 1000 times less than the input data.

Coordinate measuring machine at OptiPro

OptiPro measured both sides of the toroid with a Zeiss Micura CMM (Figure 3A). The Micura CMM uses a constant force scanning head with less than 200 millinewtons of force to drag a ruby stylus over the surface of the optic. The CMM was qualified to 0.6 micrometers of total accuracy by a Zeiss technician before measurements of the toroid began. The convex and concave sides of the toroid were measured separately. The concave side was measured by placing the toroid on heavy steel v-block, and secured with red wax as shown in Figure 3B. The convex side was measured by directly placing the toroid on the granite base of the CMM and held in place with red wax as shown in Figure 3C. The scanning technique is faster than point to point touch-trigger measurement, although the scan speed should be adjusted to the slope to ensure optimal results. The data was processed and treated in a similar manner to the OptiPro UltraSurf.

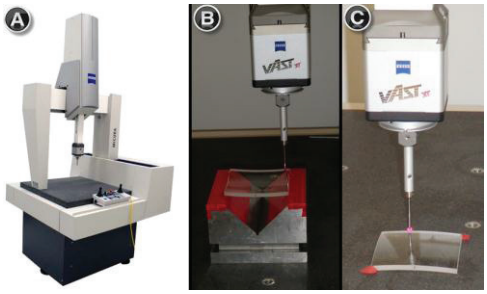

Figure 3: (A) Zeiss Micura CMM, (B) Micura scanning the concave side of toroid, (C) Micura scanning convex side of toroid

F25 coordinate measuring machine at Zeiss

The F25, Figure 4, is a micro-CMM capable of measuring with volumetric accuracy at or better than 0.25 μm + L/666 μm (where L is in mm) and resolution of 1 nm. The probe is a touch stylus with a micro-sphere with probing force down to 0.5 mN/μm. Both surfaces of the toroid were measured with the circular pattern shown in Figure 5. The toroid was set on the three point mount for measurements with the expectation that the low force probe would have no significant effect on the part position. The part was measured in a circular scanning pattern at 0.5 mm per second as shown in Figure 5 with measured point spacing along the circles at 0.5 mm. The data was analyzed in the Zeiss Calypso Software where a best fit analysis was performed to fit the measured data to the nominal shape. Then the deviation between the measured and nominal, normal to the nominal shape, is calculated and reported by the Calypso software. For comparison to the other measurements, this data was fit in Matlab to an equally spaced x,y grid. There are some concerns about the validly of the interpolation in the corner sections where data was not taken as shown in Figure 9b.

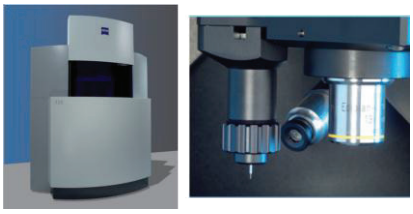

Figure 4: The F25 at Zeiss.

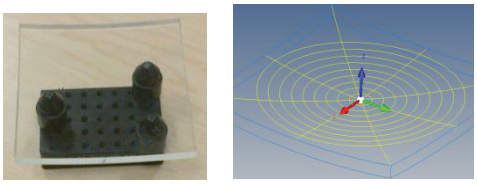

(a) *(b)*

Figure 5: (a) The toroid during the Zeiss measurement and (b) the measurement locations.

Aspheric stitching interferometer at QED Technologies

QED Technologies measured the convex surface of the toroid on the Aspheric Stitching Interferometer equipped with the new QIS™ interferometer. The ASI(Q)™ [1] combines a Fizeau interferometer, an accurate part positioning system, and mathematical stitching algorithms to measure non-spherical and large aperture surfaces. The commercial version of the ASI is used to measure aspheric surfaces, and can measure rotationally-symmetric surfaces with up

to 1000 waves (633 microns) departure from best-fit sphere. For this project, QED extended and generalized portions of the stitch process and developed beta software to allow for a proof-of-concept measurement of the toroid. The departure from best-fit sphere of the toroid is nearly 2.5 times larger than the measurable limit of the current ASI(Q). The intent of QED's measurement of the toroid was to show basic capability and potential, but more development will be needed to fully generalize the measurement process for rotationally-symmetric aspheres to free-form surfaces and improve the accuracy of the low-order figure error.

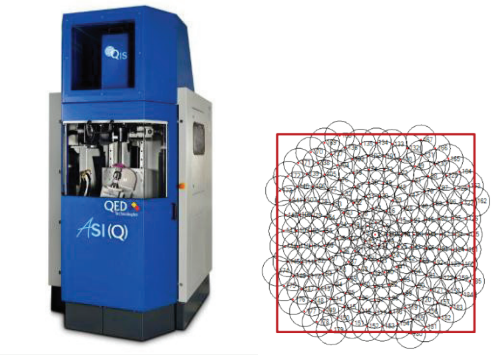

Figure 6: QED Technologies ASI(Q)™ and the lattice of the toroid measurement.

When the toroid is viewed by the stitching interferometer, only a very small portion of the toroid has resolvable fringes. By moving the part relative to the interferometer, different subaperture regions on the part become resolvable. This is a key concept of stitching aspheric or free-form surfaces – in a stitching interferometer, the part is moved relative to the interferometer, and a height measurement of overlapping subaperture subapertures with resolvable fringes is captured. Measuring subapertures (as opposed to the complete full-aperture surface) has the following advantages: it reduces the amount of departure from best-fit sphere in a single measurement, it increases resolution by applying all detector pixels over just the subaperture, and it allows local nulling of fringes through tip/tilt/power adjustments – all reducing the fringe density to be measured and enabling measurements of high-departure surfaces over the full aperture. Using the approximate position, the overlapping areas, and complex algorithms, a final full aperture height map of the surface is calculated. The algorithms take into account removal of reference surface errors, optical retrace errors, and positioning errors of the motion axes. Minimal data processing is required after the stitching process is completed. The measured deviation data is captured and reported normal to the surface.

The concave surface of the toroid was not measured due to time constraints. The full aperture was not measured (the corners are rounded) due to travel limitations on axes that typically are not needed when measuring rotationally-symmetric surfaces. A machine platform specifically designed for measurement freeform surfaces would have appropriate travel limits.

Because high magnification is necessary to resolve the fringes on the toroid, the surface is measured at very high resolution. The actual stitched resolution used for the toroid was 1200 pixels x 1200 pixels – more than enough to highlight the high-frequency features on the surface.

COMPARING THE RESULTS

Measurement results

After measurements, each company sent their measurement data to the other companies for analysis. The data presented here was analyzed by Optimax. We will compare the deviation (along the normal) height maps. This height map is a gird of height points plotted on an equally spaced lateral grid. For some measurements, this grid was found through interpolation. It is expected that any errors in interpolation are small compared to the height errors of the surface. But, we may need to re-examine this assumption in the future. For the comparison, some simple data manipulation was required such as rotating the data to match alignments, inverting to match conventions, and masking to remove some outliers.

First we compared the height maps with piston (the mean value) and tilt (both directions) removed. But, this showed a large variation in the measured heights, especially in the concave surface. To perform a better comparison, we removed power in the x and y directions as shown in Figure 7. Power in the x and y directions (equivalent to power and astigmatism) indicate a radius error in the toroid and/or a measurement misalignment in some measuring methods. As shown, the measurements look very comparable in most cases. While the ASI(Q) excels at measuring the mid to high frequency features of

the toroid, more development is needed by QED to improve the accuracy of the low-order figure error, as evidenced by the data with low-order error included (Figure 7). It is also possible that the difference in low-order error results from mount-induced distortion or differences in the removal of the nominal shape. To look beyond this difference, we removed the general form of that error (Zernike spherical and Zernike 16) on all the datasets as shown in Figure 8. As shown, the comparison improves and may of the measurements look very similar. Removing spherical and Zernike 16 had little effect on the measured data except with QED ASI data.

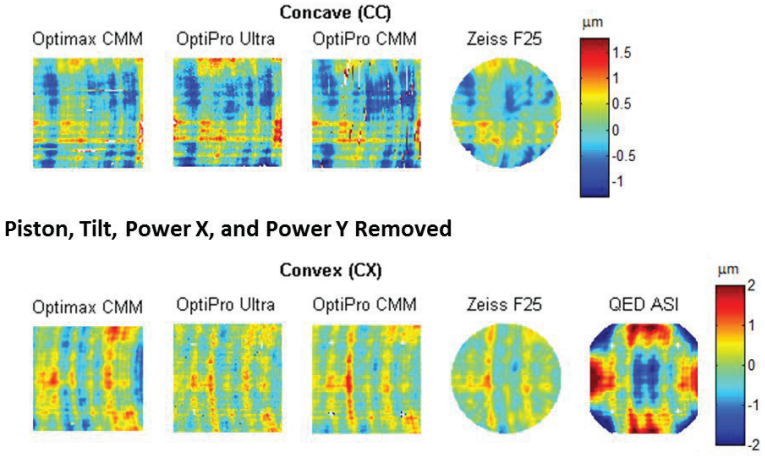

Figure 7: Surface height maps with piston, tilt (both directions), power x and power y (equivalent to piston tilt, power, and astigmatism) removed for all available measurements. Size is 90 mm by 90 mm.

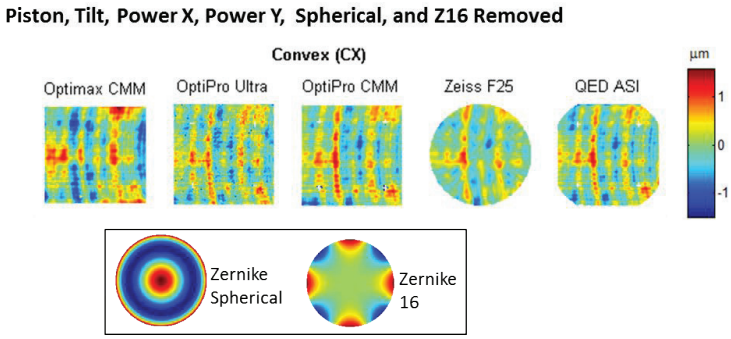

Figure 8: Surface height maps with piston, tilt (both directions), power x, power y, Zernike spherical, and Zernike term number 16 removed for all available measurements. Size is 90 mm by 90 mm.

Figure 9 shows a standard deviation map (0.5 mm per pixel) of the five convex measurements in Figure 8. The rms of this standard deviation map is 0.21 μm. As shown, there is one obvious vertical feature. The 0.21 μm may be approaching the known accuracy of some of the measurement methods presented here. Figure 10 shows the rms (root-mean-square, Sq) of the height maps for the final removal condition. Peak-to-valley was not used due to the large presence of outliers.

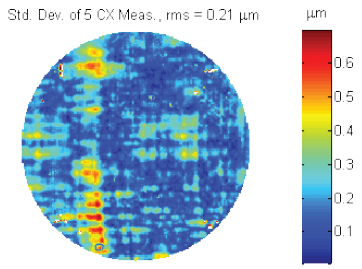

Figure 9: A standard deviation map of the five convex measurements from Figure 8.

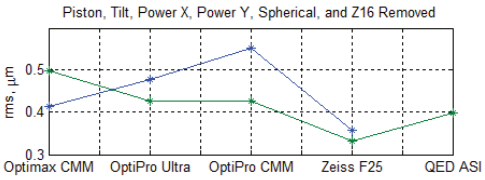

Figure 10: The rms of the surface height maps.

Pixel spacing

The data and measurements presented here vary in the lateral mm per pixel as shown in Table 1. The CMMs show a range of pixel spacing because there is different spacing in the scanning and step-over directions. Clearly, the QED data has a strong advantage in the pixel spacing indicating that much smaller features can be measured. This is shown in Figure 11, the convex measurement by QED with a high pass filter at 2 mm applied. As shown, this measurement is able to pick out the small features. The other measurement methods showed noise at this filter. Analysis is required to determine the required minimum pixel spacing.

Table 1: The measured and presented pixel spacing.

	Meas Pixel Spacing, mm	Presented Pixel Spacing, mm
OM CMM	0.5 – 1	0.5
OP UltraSurf	1	1
OP CMM	0.5	0.5
Zeiss F25	0.25 - 5	0.5
QED ASI	0.08	0.08

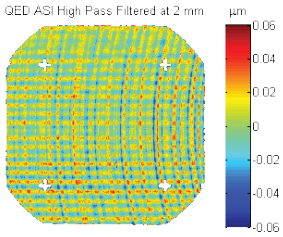

Figure 11: The convex measurement by QED, high pass filtered at a 2 mm cutoff.

CONCLUSIONS

The large variation in the measurements in the 'raw' data is not easily explained. It is possible that the majority of the differences can be explained by differences in the removing the nominal shape. The coordinate measuring methods should all be capable of correctly identifying the low order form error especially. More study should be done to determine why this variation exists, likely investigating misalignment between the nominal and measured shapes.

For the measurements with the low order form removed, we have found that the measurements vary within 0.21 µm rms. This value is approaching the known accuracy of the coordinate measuring machines. This indicates that the measurements compare well. Overall though, we see much promise in using tactile tools, such as CMMs in the free-form manufacturing environment with the hope that stitching interferometry will become fully developed for use in free-forms.

WHERE DO WE GO FROM HERE?

We are open to having more measurements of the toroid performed. Some possible options include a deflectometry system, the Moore M48 CMM at NIST, the GEMM (Geometry Measuring Machine) at NIST[2], and NANOMEFOS[3] at TNO in the Netherlands. We invite any party interested in performing a measurement of this toroid window to contact us.

We would like to use the lessons learned in this study to talk with the community about some of the issues we found. By the community, we mean standards organizations, optical designers, manufacturers, and assemblers. First, specifications on free-form surfaces need to be considered in more detail than a PV specification. How can we easily separate a low-order form error from high order form error for free-forms? Possibly specifications would be Fourier band-pass or Zernike term filtering. In addition, we believe that the community will need to work on references for free-form surface.

REFERENCES

[1] Kulawiec A, Bauer M, DeVries G, Fleig J, Forbes G, Miladinovic D, and Murphy P. "Subaperture stitching interferometry of high-departure aspheres by incorporating configurable null optics," Optifab 2009, Proc. SPIE TD06-44, May 2009

[2] Machkour-Deshayes D, Stoup J, Lu QJ, Soons J, Griedmann U, Polvani P, "Form-Profiling of Optics Using the Geometry Measuring Machine and the M-48 CMM at NIST," J. Res. Natl. Inst. Stand. Technol. 111, 373-384 (2006)

[3] Henselmans R, Cacace LA, Kramer GFY, Rosielle PCJN, Steinbuch M, "The NANOMEFOS non-contact measurement machine for freeform optics," Precision Engineering 35(4), 607-624 (2011)

High dynamics range enhancement in digital fringe projection technique

Gelareh Babaie[2,3],* Mehrdad Abolbashari[2,3] , and Faramarz Farahi[1,2,3]

[1]Center for Optoelectronics and Optical Communications, University of North Carolina, Charlotte, North Carolina 28223, USA
[2]Department of Physics and Optical Science, University of North Carolina, Charlotte, North Carolina 28223, USA
[3]Center for Precision Metrology, University of North Carolina, Charlotte, North Carolina 28223, USA

***gbabaie@uncc.edu**

Abstract
In this paper a new approach to enhance the dynamic range of an imaging system in fringe projection technique is presented. This is done by controlling the intensity of the projection pattern at pixel level based on the feedback from the reflected image captured by the camera.

Introduction
Limited dynamic range of conventional cameras causes difficulties in the metrology of objects with large variation in their optical reflectivity due to either their compositions or forms. For instance, metallic objects with steep slopes have a much higher level of intensity variation in their reflection compared to the 0-255 gray intensity range level of conventional cameras. As a result, reflected patterns captured by conventional cameras lose some information from such surfaces. Therefore achieving a system with high dynamic range is currently a challenge in the field of metrology.
Acquiring 3D topography of objects is a very interesting and active field in both manufacturing and bio-medical imaging. One powerful technique to obtain a 3D profile of an object is the digital fringe projection technique [1-2]. A simple setup to apply fringe projection is to project a light pattern onto the object and capture the image of the illuminated object from another direction. The image includes a deformed fringe pattern, which after some analysis provides the height information of the object. Usually a fringe analysis technique is needed such as a phase-shifting algorithm in order to calculate the phase distribution of the reflected pattern [3]. However, as mentioned above, limited dynamic range of conventional cameras compromises the signal distortion and makes phase recovery a challenge. Several methods have been developed over the years to overcome the limited dynamic range problem of cameras. One proposed technique is to use polarizing filters [4]. This technique drastically reduces the overall intensity of the reflected pattern; therefore, it makes it difficult to derive useful information from the darker areas of the scene, and the complexity of the system increases. Another technique called 'High dynamics range scanning' proposed by Yoshinori et.al [5]. In this technique, a sequence of fringe images was taken from the surface at different exposure times. The images which were taken at low exposure times contained useful information from the area of the surface with high reflectivity, while images taken with long exposure times contained useful information from the area of the surface with low reflectivity. The final image was reconstructed by choosing the brightest but not saturated corresponding pixel from each of the acquired images and combining them. The final image with high dynamic range (HDR) was used for phase retrieving. Recently a HDR imaging technique in fringe projection was proposed by Zhang et al [6]. In this technique a high dynamic range image can be acquired by adjusting the intensity of the projection pattern in different regions based on the feedback from a raw image of the sample. It is claimed that the technique could improve the dynamic range of the system with a single shot; however this

technique for objects with very high variation of reflectivity will be potentially problematic.
In this paper we are proposing a novel technique which can highly improve the dynamic range of a digital fringe projection system. In the experiment, to implement the concept we used a metallic ball as the sample under the measurement. This sample has very high reflectivity at the top of the sphere where light is incident at the ball perpendicularly, and has very weak reflection from the sides due to the steep slopes. Thus, in a reflected projection pattern captured by a CMOS camera, some regions are saturated due to high reflectivity at the top of the sphere, and some regions are underexposed. The system design, the measurement method of the proposed technique, and the experimental results will be discussed next.

System design

A schematic of the experimental system is shown in figure 1.

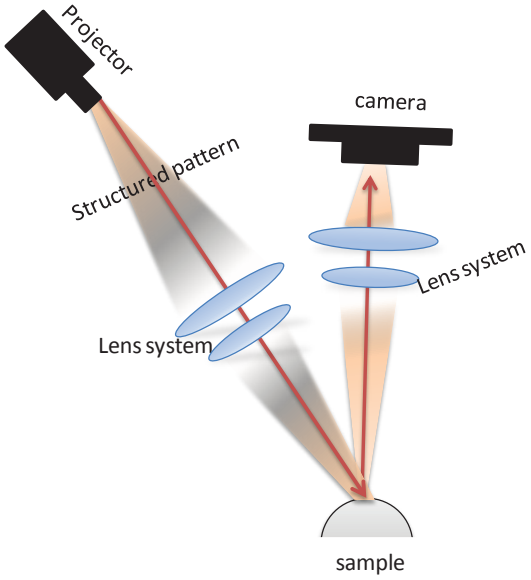

Figure1. Schematic of a system implemented to demonstrate dynamics range enhancement in fringe projection

A pattern, generated by MATLAB code, was projected on the sample at an angle using an AAXA M2 micro projector, native XVGA with 1024x768 resolution. The projected pattern illuminates the sample with an angle. The reflected pattern was captured by an AVT P Guppy F-146 camera with a resolution of 1392 x 1024 along a perpendicular line.
Reflected patterns captured by the camera at two different exposure times from the metallic ball are shown in figure 2. Figure 2(a) shows the reflected pattern with a low exposure time in which only areas with high reflectivity (tip of the metal ball) can be detected by the camera and the rest of the pattern is underexposed. Thus, no information from these areas is attainable. As we increase the exposure time, areas with low reflectivity can be viewed by the camera, while pixels corresponding to areas with higher reflectivity will become saturated. Therefore the corresponding phase and intensity information of those areas (underexposed and saturated) are lost.

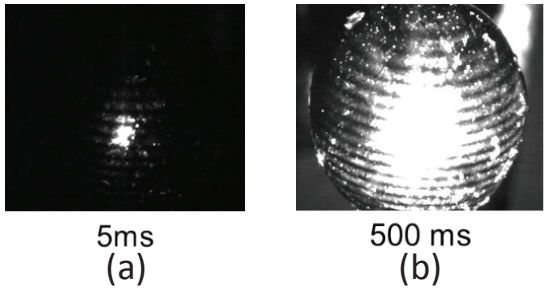

Figure2. (a) Reflected fringe pattern captured by the camera from the metallic ball at exposure time=5ms, (b) reflected pattern of the same sample at exposure time=500ms

In the proposed technique, we have developed a technique called 'spatially varying pixel intensity' (SVPI), which can enhance the dynamic range by adjusting the intensity of the projected pattern at pixel level. This technique can highly improve the dynamic range of the imaging system with no physical modification. The measurement method will be discussed in more detail in the next section.

SVPI measurement method:
Since the proposed HDR imaging is based on adjusting the intensity of the projected pattern at pixel level, a geometrical alignment is essential between the projector and camera's pixels. To geometrically align the system, the system was calibrated by projecting checkerboard pattern on the sample and the reflection pattern was observed by the camera. Corners on the checkerboard pattern were determined in the camera's image plane and the point correspondences between the camera and the projector was calculated considering the linear

transformation at each square, figure 3. From this information the transformation matrix, T_{ij}^{cp} between the camera and projector's pixels was computed. As a result, for each saturated or under-exposed pixel on the camera's plane, C_{ij}, the exact pixel(s) on the projector pattern P_{ij}, will be targeted using equation 1, and their intensities will be adjusted accordingly.

$$P_{ij} = T_{ij}^{cp} \times C_{ij} \qquad (1)$$

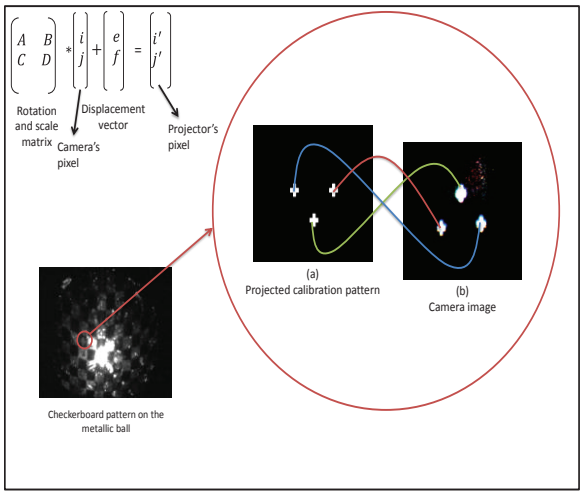

Figure3. Geometrical alignment between camera pixels and projector pixels, a) projected pattern, b) captured image by the camera

After the geometrical alignment is done, the camera gain and exposure time is set to the level where the intensity values of all pixels lie above the dark noise level. In order to satisfy this condition, a sinusoidal pattern is projected to the sample. The reflected pattern is captured by the camera at the lowest possible exposure time and gain. The gain and exposure time of the camera is increased accordingly until no pixel value is below the noise level. We then fix the gain and exposure time for this condition. As the result to improve the dynamic range of the imaging system, only saturated pixels needs to be considered. The reflected pattern is captured by the camera and transferred to the computer for further analysis in MATLAB. All the pixels with values above the saturation level are indicated in the camera's pattern. An intensity mask with the same size as the Camera's pattern is created in MATLAB and scaled using the transformation matrix, T_{ij}^{cp}, and finally multiplied by the initial fringe pattern, considering the geometrical alignment. The intensity mask is created in such a way to reduce the intensity of the structured pattern in pixels which are corresponding to the saturated pixels on the camera. As a result, a new structured pattern with adjusted intensity is created. The modified pattern illuminates the sample and the reflected pattern is captured by the camera for the second time. In order to quantify how effectively this technique improves the dynamic range of the camera, a dynamic range coefficient is introduced as below:

$$K_{DR} = \frac{N_P}{N} \qquad (2)$$

Where N_P is the number of processable pixels in the camera, below the saturation level and above the dark noise level, and N is the total number of camera's pixels.

We can repeat the processes until the entire pixels' values in the camera are less than the saturation level or we reach the limits of the system. Figure 4 shows a flowchart of this process.

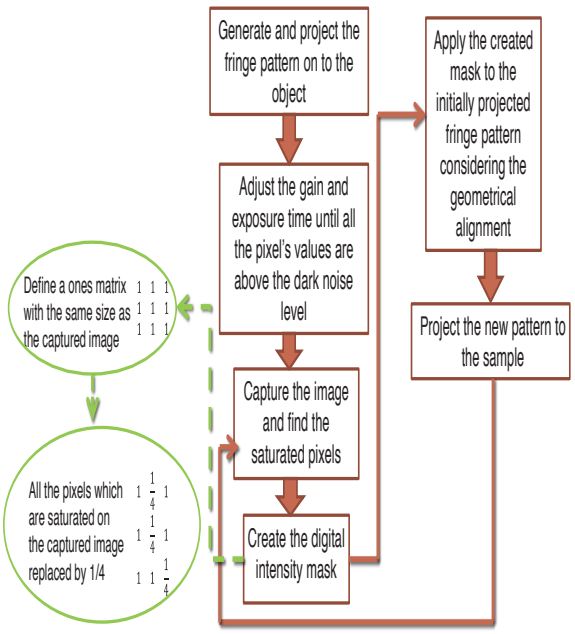
Generate and project the fringe pattern on to the object
Adjust the gain and exposure time until all the pixel's values are above the dark noise level
Capture the image and find the saturated pixels
Create the digital intensity mask
Apply the created mask to the initially projected fringe pattern considering the geometrical alignment
Project the new pattern to the sample
Define a ones matrix with the same size as the captured image
All the pixels which are saturated on the captured image replaced by 1/4

Figure4. Flowchart of HDR using spatially varying exposure in pixel level

The HDR image with the real intensity level can also be reconstructed by multiplying the values of the final image by the reverse values of all the applied masks.

$$\text{HDR\_Image} = \text{final captured image} \times \frac{1}{\prod_{i=1}^{n} \text{mask(i)}} \quad (3)$$

Where "n" is the number of masks which have been applied. By having the HDR image, one can easily find the phase map of the pattern using one of the fringe analysis techniques, such as four-step phase-shifting [7].

Experiment:

The experimental setup used for this new HDR imaging system using the SVPI technique in fringe projection is shown in figure 6.

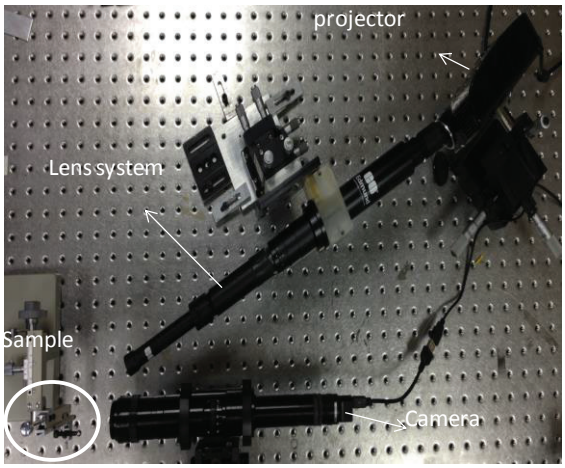

Figure6. Experimental setup for the HDR using spatially varying pixel exposure technique

A geometrical alignment is applied and the transformation between camera's image plane and the projector's image plane, T_{ij}^{cp}, was calculated. The camera exposure time was set for 500ms.The SVPI technique was applied to the reflected pattern captured by the camera. Figure 7 shows a schematic of the process. By comparing the reflected patterns before and after applying the SVPI technique, figures 7a and 7c, it is obvious that the dynamic range of the image is significantly improved by applying the proposed technique. This technique is applied for another time to improve the dynamic range; the dynamic range coefficients for each level were calculated. The results are shown in table 1. Reflected patterns of the metallic ball after one and two times of applying the SVPI technique are shown in figure 8.

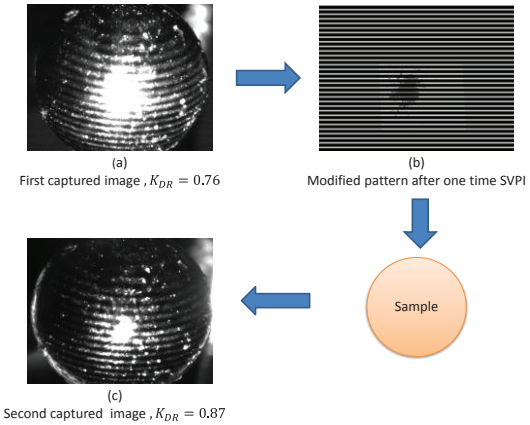

Figure7. (a) First captured image by the camera at exposure time=500ms with $K_{DR} = 0.76$, (b) Modified pattern after SVPI was applied once, (c) Second captured image at exposure time=500ms , $K_{DR} = 0.87$

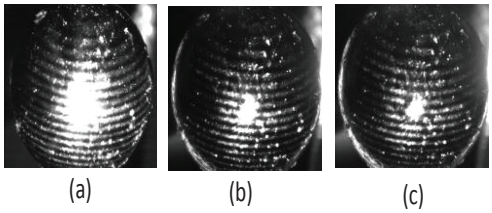

Figure8. (a) First captured image, $K_{DR} = 0.76$, (b) Second captured image, $K_{DR} = 0.87$, (c) Third captured image , $K_{DR} = 0.93$

Table1. Dynamics coefficient of the imaging system increased by SVPI technique at each step of the process

Metallic spherical ball	DR – coeffiecient
Initial fringe pattern (not corrected)	0.76
Modified pattern one time	0.87
Modified pattern twice	0.93

The results show that the dynamic range coefficient of the imaging system is improved by 17%.

In order to calculate the underlying phase of the final captured image, figure 8 (c), a four-step phase shifting algorithm [7] was used and consequently unwrapped using the quality-guided algorithm [8]. The calculated phase and its unwrapped phase are shown in figure 9.

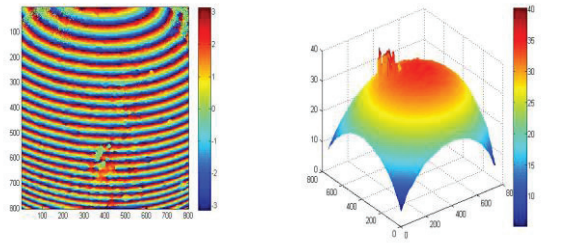

(a) (b)

Figure10. (a) Phase of the metallic ball calculated by the 4-step phase shifting, (b) unwrapped phase map of the sample

In order to translate the phase information into the height information the equivalent wavelength of the system is calculated, λ_{eff}=0.36mm, and thus the height of the semi-spherical ball is 2.3mm

Conclusion:

We developed an HDR imaging system using the fringe projection technique by controlling the intensity of the projection pattern at pixel level. The experimental results verify the proposed technique. The proposed algorithm to achieve HDR imaging system can be applied on any existing fringe projection profilometer without any physical change requirement. The algorithm can repeat as many times as it is needed, therefore this technique is very useful for imaging the objects with very high variation in their reflectivities.

REFERENCES

[1] S. Gorthi, and P. Rastogi, "Fringe Projection Techniques: Whither we are", Optics and Lasers in Engineering, 2010; 48(2):133-140

[2] L. Chen, C. Huang, "Miniaturized 3D surface profilometer using digital fringe projection", Meas. Sci. Techn. 2005;16(5):1061–1068

[3] B.N. Saif, J. Millerd, R. Keski-Kuha, L. Feinberg, and J. C. Wyant, "Instantaneous phase-shifted speckle interferometer for measurement of large structures", Proc. SPIE, 2004; 5494: 152-162

[4] Y. Yoshinori, M. Hiroyuki, N. Osamu, and I. Tetsuo, "Shape measurement of glossy objects by range finder with polarization optical system", Gazo Denshi Gakkai Kenkyukai Koen Yoko, 2003; 200: 43–50

[5] S. Zhang and S.T. Yau, "High dynamic range scanning technique", Opt. Eng. 2009; 48: 033604-033604-7.

[6] Chou, Sen-Yih, et al. "Projection moiré profilometry with high-dynamic range image", Optical Engineering, 2012; 51.2: 021112-1.

[7] K. Creath, "Phase-measurement interferometry techniques", Progress in optics, 1988; 26.26: 349-393.

[8] Zhang, Song, Xiaolin Li, and Shing-Tung Yau, "Multilevel quality-guided phase unwrapping algorithm for real-time three-dimensional shape reconstruction", Applied optics, 2007; 46.1: 50-57

PRECISION SHAPING OF THIN MIRROR SUBSTRATES FOR X-RAY TELESCOPES USING ION IMPLANTATION

Brandon D. Chalifoux[1], Edward Sung[1], Ralf K. Heilmann[2], and Mark L. Schattenburg[2]
[1]Department of Mechanical Engineering
Massachusetts Institute of Technology
Cambridge, MA USA
[2]Space Nanotechnology Laboratory
MIT Kavli Institute for Astrophysics and Space Research
Cambridge, MA USA

INTRODUCTION

The next generation of x-ray telescopes require high-precision, low-cost, thin mirrors to enable high resolution imaging with a large aperture. The x-ray astronomy community has made impressive strides (e.g. [1] [2] [3]) toward high-resolution optics, but further improvement in both cost and performance is required. In order to achieve sub-arcsecond resolution optics, it will be necessary to first fabricate precision mirrors, and follow this with fine shape modification of the mirrors. Ion implantation is a promising method to perform fine shaping of thin mirror substrates.

Implanting high-energy ions into a substrate imparts sub-surface stress, causing a deterministic deformation of the substrate. For example, a uniform implant dose distribution causes a spherical deformation of the substrate; in this case, spherical curvature error can be corrected. Higher-order figure errors can be corrected using non-uniform implant dose distributions on both the front and back surface of the substrates. Ions can be implanted through thin surface layers of even high density, allowing figure correction after a reflective coating has been applied.

Compressive and tensile stress due to ion implantation of various species in different substrates has been measured previously (e.g. [4] [5] [6]). In this work, we have studied the feasibility of using ion implantation for fine figure correction in thin x-ray telescope mirrors.

We measured the stress-dose for three substrates relevant to x-ray astronomy: silicon, BK-7 glass, and Schott D-263T glass. We then demonstrate deterministic correction of both spherical curvature and astigmatism. In addition, we show that ion implantation has no significant effect on thermal stability and surface roughness for these substrates. We show that ion implantation could be an effective and low-cost method for fine figure correction of thin substrates, and could enable thin sub-arcsecond angular resolution x-ray telescope mirrors. Ion implantation could have other applications where thin substrates must have an extremely accurate figure, or where other manufacturing stresses must be removed.

EXPERIMENTAL

Stress Measurement

Wafers were implanted with a uniform dose distribution, and the shape measured before and after implant. The implant stress can be calculated, and the stress-dose relationship determined, from this change in shape.

A total of 107 wafers were implanted with a uniform dose distribution, as summarized in Table 1. All ions were implanted at an energy of 150 keV and a beam current of 60 μA. Doses varied from $1x10^{14}$ ions/cm^2 to $2x10^{16}$ ions/cm^2. CuttingEdge Ions, LLC. performed all implants. The resulting stress as a function of implanted dose is shown in Figures 1 and 2.

TABLE 1. Summary of implanted wafers

Substrate	Species	Number of samples
Silicon	Si^+	36
Silicon	B^+	5
BK-7	Si^+	18
BK-7	Ar^+	15
D-263T	Si^+	24
D-263T	Al^+	9
Total		107

A uniform dose distribution is expected to cause a change in spherical curvature according to Stoney's equation[7]:

$$\sigma t_i = [E h_s^2 / 6(1-v)] [R_1^{-1} - R_0^{-1}],$$

where σ is the in-plane stress, t_i is the implanted layer thickness, E is the substrate Young's Modulus, h_s is the substrate thickness, v is the substrate Poisson's ratio, and R is the radius of curvature. The integrated stress, σt_i, is used instead of σ alone; in part because the implanted layer does not have a well-defined thickness; and because the integrated stress directly affects shape change.

The wafer shape was measured with a Shack-Hartmann metrology system [8] and a low-stress optic mount [9]. The stress measurement is repeatable to $\pm 10^{-6}$ MPa-m.

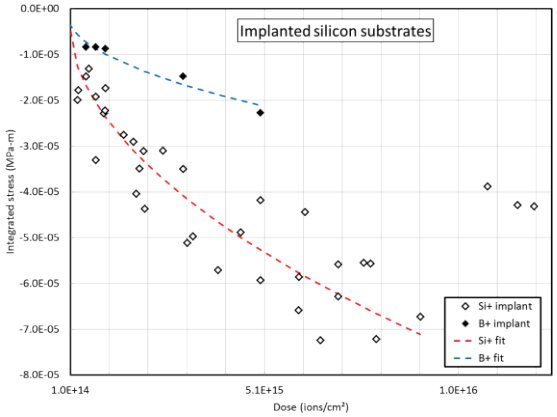

FIGURE 1. Integrated stress from Si^+ and B^+ implanted into silicon wafers. The dashed lines represent quadratic fits to the data.

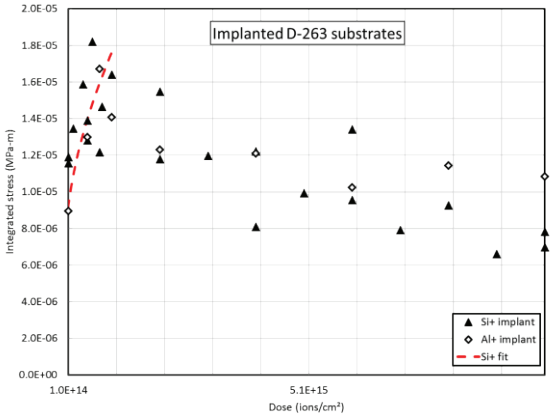

FIGURE 2. Integrated stress from Si^+ and Al^+ implanted into D263 wafers. The dashed line represents quadratic fits to the Si^+ implant data.

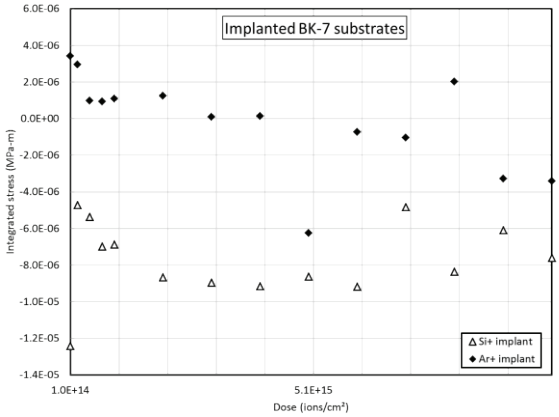

FIGURE 3. Integrated stress from Si+ and Ar+ implanted into BK-7 wafers.

Si+ implanted into silicon shows a monotonic relationship between integrated stress and dose over a large range of doses. Si+ implanted into D-263 and BK-7 also show monotonic relationships between integrated stress and dose, but for lower doses. For fine figure correction, however, the stress generated by the Si+ implants is sufficiently high. Ar+ implanted into BK-7 resulted in stresses below the measurement repeatability at the time.

While the stress in BK-7 and silicon is compressive, the stress in D-263 is tensile. This may be due to the fact that BK-7 and silicon are ground and polished, while D-263 is not. D-263 has an initial compressive surface stress, and if ion implantation relieves some of this compressive stress, this would appear as a tensile stress.

Surface Roughness Measurement

It is important that ion implantation does not roughen the substrate surface, since the surface is used for reflecting x-rays. Implanting ions into a substrate causes damage beneath the surface, but at the energies being used here, sputtering and other surface effects are expected to be minimal. To confirm this, x-ray reflectivity measurements were made before and after ion implantation, for four D-263 samples and one two silicon samples. All samples were piranha-cleaned prior to the reflectivity measurements. BK-7 implanted with Si^+ was not tested.

Figures 4 and 5 show x-ray reflectivity measurements for Si^+ implanted into silicon and D-263, respectively. While models could not accurately be fit to the data, comparing the data

with models that differ only in surface roughness, it is clear that the change in roughness is significantly less than 1Å for all substrates measured.

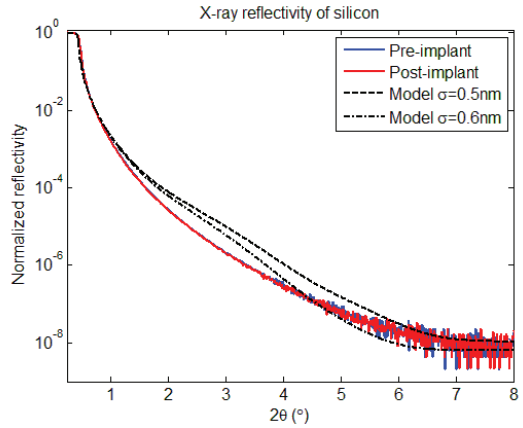

FIGURE 4. X-ray reflectivity as a function of grazing angle for a silicon substrate implanted with Si^+, $2x10^{15}$ ions/cm^2, 150 keV, and 60 μA.

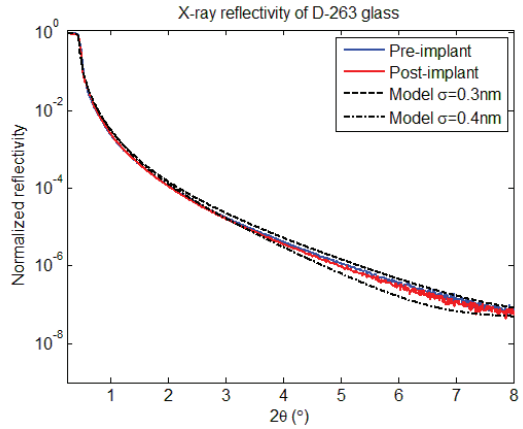

FIGURE 5. X-ray reflectivity as a function of grazing angle for a D-263 substrate implanted with Si^+, $2x10^{14}$ ions/cm^2, 150 keV, and 60 μA.

Thermal Stability

Temporal stability of implanted substrates is of critical importance. Thermal stability at temperatures above the expected operating temperature (20°C) gives an indication of temporal stability at lower temperatures. Stress relaxation of glasses in the solid glassy state follows Arrhenius' equation [10]:

$$K_1 / K_0 = \exp(-E_a/k [1/T_1 - 1/T_0])$$

where K_0 and K_1 are the relaxation rates at temperatures T_0 and T_1, and R is the universal gas constant. The activation energy associated with the relaxation process, E_a, is unknown for implanted D-263, but has been measured to be about 300-500 kJ/mol for relaxation of tempered soda-lime glass [11]. With T_0 = 293K and T_1 = 343K, and using 300 kJ/mol as a conservative measure of E_a, $K_1/K_2 > 10^8$. Thus, exposure for 4 hours at 70°C corresponds to >60,000 years at 20°C. This is sufficient to establish long-term stability of the implanted glass.

Implanted wafers were exposed to successively higher elevated temperatures for 4 hours at a time, and the wafer shapes measured after each time period. The stress relaxation can be calculated from Stoney's equation as above. The results of these experiments are shown in Figure 6.

The range of Figure 6 represents the repeatability of the stress measurement, indicating that there is not significant stress relaxation in either silicon or D-263 implanted with Si^+. BK-7 implanted with Si^+ was not tested.

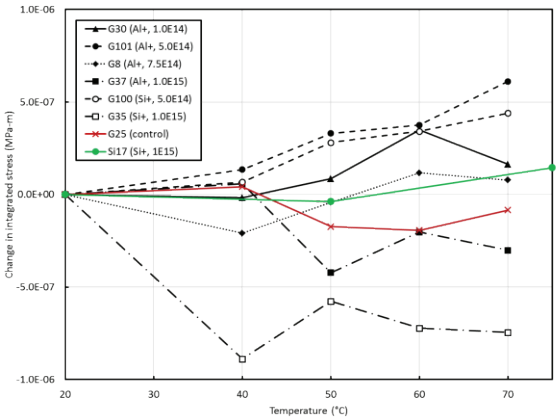

FIGURE 6. Stress relaxation in silicon (prefix Si) and D-263 (prefix G) substrates implanted with Si^+ and exposed to elevated temperatures. The entire range of integrated stress change represents the repeatability of the metrology tool.

Spherical Curvature Correction

The stress-dose relation for Si^+ implanted into silicon was used to correct both spherical curvature and astigmatism in silicon wafers. Correction of spherical curvature required applying a uniform dose over the entire wafer, which is exactly what commercial ion implanters are equipped for. Correction of astigmatism required calculating, then implanting, a non-

uniform dose over the wafer. This was more challenging.

Correction of spherical curvature was quite effective. Figure 7 shows a representative sample, where the power was reduced by more than 10x in a single implant, but where all other figure errors were unaffected. 15 samples were implanted with the intention of eliminating spherical curvature, with a mean reduction of 9x.

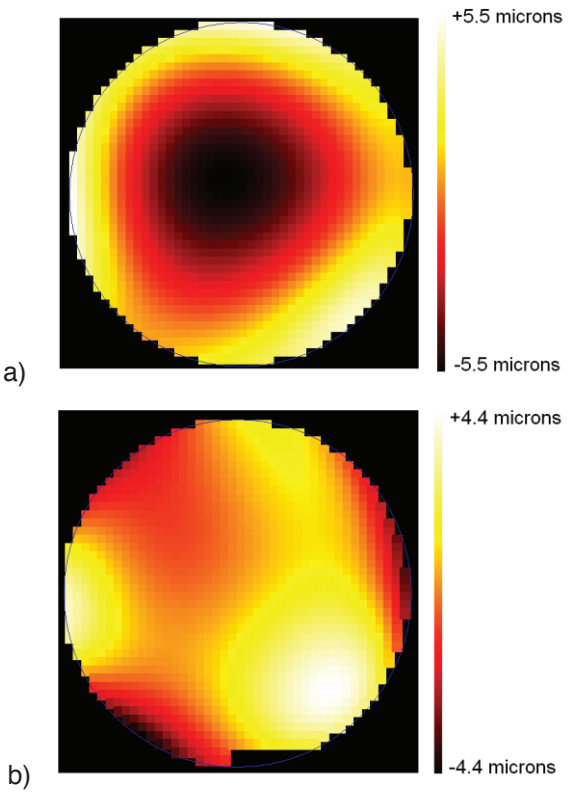

FIGURE 7. Representative silicon wafer shape a) before implant and b) after implant. Spherical curvature has been reduced from 9.2 µm to -0.7 µm in one implantation cycle.

Higher-order Figure Error Correction

In order to correct astigmatism and other higher-order figure errors, a non-uniform dose must be calculated and applied. For flat silicon wafers, a non-uniform dose distribution can be achieved by masking the wafer with photoresist. A 1µm-thick layer of photoresist is sufficient to block Si^+ at 150 keV from penetrating into the silicon substrate. Thus, if there is a layer of photoresist covering some areas of the wafer, it is possible to achieve a non-uniform dose distribution.

It was also necessary to build a model capable of calculating the required implant stress field (and corresponding dose distribution) to achieve a desired change in figure. To solve this problem, we chose to employ a modal decomposition method.

The modal decomposition method involves applying a multitude of test stress fields to a substrate, using the finite element software ADINA, and recording the resulting figure changes as a set of Zernike polynomials. The test stress fields chosen can be described by single Zernike polynomials. In this manner, we build a library of stress responses. Using this library, and the desired change in figure (which can also be described by Zernike polynomials), we can use a least-squares approach to calculate the stress field that gives the best resulting shape.

Using this modal method, we can calculate the dose distribution required to correct the astigmatism error in wafers. The calculated dose distribution for astigmatism correction in the wafer used in this experiment is shown in Figure 8. Using this dose distribution, a chrome photomask was made (shown in Figure 9); it consists of an array of chrome squares of varying area. When the pattern is transferred onto a positive photoresist, the area covered by chrome blocks the implanted ions.

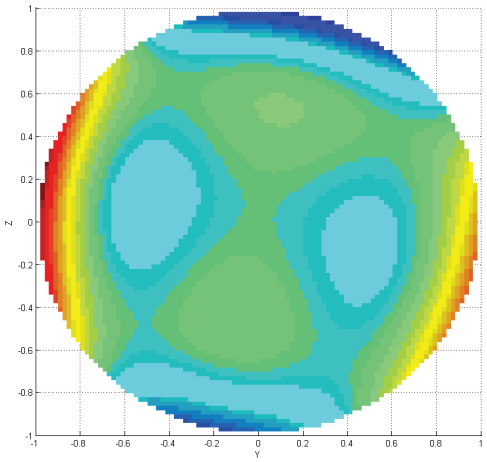

Figure 8. Dose distribution required to correct astigmatism in the wafer tested. Red areas require implantation to the front of the wafer, and blue areas require implantation to the back of the wafer.

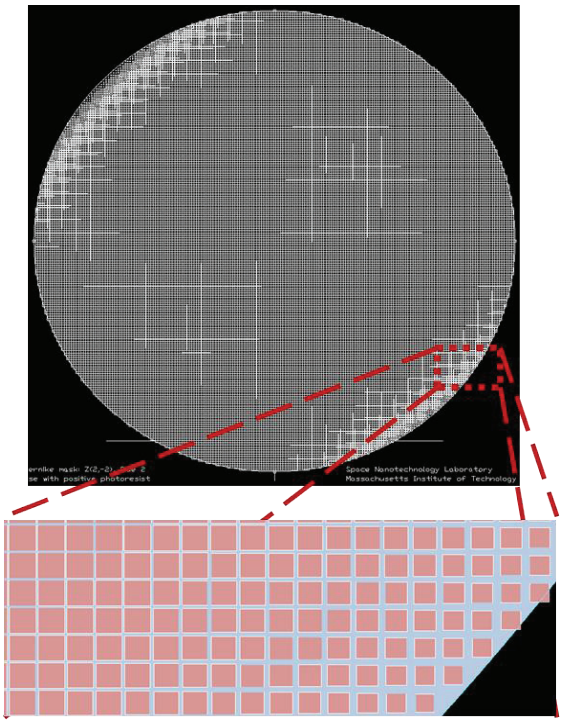

FIGURE 9. Chrome photomask used to correct astigmatism. The pattern is transferred to a positive photoresist on the front and back sides of a wafer.

The result is encouraging. For this wafer, the astigmatism changed, while all other figure errors remained. The change in shape is shown in Figure 10. This wafer was implanted with a dose of $6x10^{13}$ ions/cm^2, which was far too low to correct for the astigmatism present in the sample. It was later determined that this was an error attributed to mis-labeling. Nonetheless, this result is encouraging, and indicates that non-spherical figure errors can be corrected.

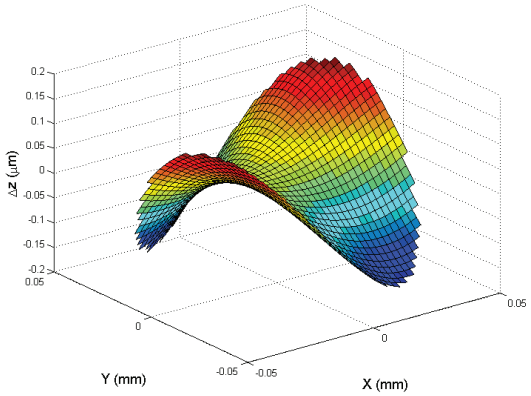

Figure 10. Change in shape of masked and implanted wafer. The shape change exhibits only astigmatism; all other figure errors are unaffected.

MODELING

Extension of the experimental results described thus far for thin flat substrates to near-cylindrical substrates such as Wolter I mirrors for x-ray telescopes requires a custom ion implanter that can implant non-uniform dose distributions and can handle curved substrates. However, the modeling for flat substrates can be extended to cylindrically-curved substrates.

A modal decomposition method very similar to that described for flat substrates is employed. Instead of Zernike polynomials, which are orthogonal over the unit disk, Legendre polynomials are used both to describe applied stress fields as well as describe the resulting changes in figure. Otherwise, the method is identical. This method worked quite well for flat substrates, but while peak-valley errors can be reduced for cylindrical substrates, this method does not result in a reduction of substrate slope error. However, results from [12] indicate that using influence functions rather than Legendre polynomials lead to significantly better results for angular resolution improvement.

CONCLUSIONS AND FUTURE WORK

Ion implantation is a promising method of figure correction of thin x-ray telescope optics. We have demonstrated figure correction of both spherical curvature and astigmatism error, and this methodology could easily be extended to higher-order figure errors. We have also shown that ion implantation is thermally stable, and that there is little effect on surface roughness. Modeling the use of ion implantation for x-ray telescope optics yielded disappointingly small improvement in angular resolution, but it is clear that these results are due to the method of modeling, not a flaw with ion implantation.

Masking a curved glass substrate is impossible with standard semiconductor equipment, so applying ion implantation to x-ray telescope optics requires an ion implanter capable of accommodating curved substrates, and capable of raster-scanning the ion beam. These requirements necessitate building a custom implanter, as commercial implanters only scan the ion beam as evenly as possible. In addition to developing an ion implanter capable of correcting x-ray telescope optics, it will be necessary to improve metrology, to increase our understanding of the implant stress, and to improve our modeling methods.

REFERENCES

[1] Zhang W, et al. Next-generation astronomical x-ray optics: high angular resolution, light weight, and low production cost. Proc. SPIE. 2012; 8443.

[2] Romaine S, et al. Development of a prototype nickel optic for the Constellation-X hard x-ray telescope: IV. Proc. SPIE 2006; 6266.

[3] Wallace K, et al. Silicon-pore optics development. Proc. SPIE 2009; 7437.

[4] Itoh M, Hori M. An ultralow stress tungsten absorber for xray masks. J. Vac. Sci. Technology B. 1991; 9: 165-168.

[5] Burnett P.J., Page T.F. An investigation of ion implantation-induced near-surface stresses and their effects in sapphire and glass. J. Mat. Sci. 1985; 20: 4624-4646.

[6] Misra A, et al. Residual stresses and ion implantation effects in Cr thin films. Nuclear Instruments and Methods in Physics Research B. 1999; 148: 211-215.

[7] Stoney G.G. The tension of metallic films deposited by electrolysis. Proc. Royal Soc. London A. 1909; 82(553): 172-175.

[8] Forest C.R., Canizares C.R., Neal D.R., McGuirk M, Schattenburg M.L. Metrology of thin transparent optics using Shack-Hartmann wavefront sensing. Opt. Eng. 2004; 43(3): 742-753.

[9] Akilian M, Forest C, Slocum A, Trumper D, Schattenburg M. Thin optic constraint. J. Precision Engineering. 2007; 31: 130-138.

[10] Rekhson S. Models of relaxation in glass. J. Non-Crystalline Solids 1987; 95&96: 131-148.

[11] Narayanaswamy O.S. Stress and structural relaxation in tempered glass. J. Amer. Ceramic Soc. 1978; 61(3-4): 146-152.

[12] Aldcroft T.L., Schwartz D.A., Reid P.B., Controneo V., Davis W.N. Simulating correction of adjustable optics for an x-ray telescope. Proc. SPIE 2012; 8503.

LONG-TERM STABILITY OF A MOVING-SCALE MEASUREMENT SYSTEM WITH NANOMETER UNCERTAINTY

Niels Bosmans[1], Jun Qian[1], and Dominiek Reynaerts[1]
[1]Department of Mechanical Engineering
KU Leuven
Heverlee, Belgium

ABSTRACT

To improve the accuracy of normal machine tools, a new concept for placing linear encoders in an Abbe-offset-free configuration is presented. A design for a 1-DOF system has been made and a prototype has been developed. Changes of the environment's temperature and humidity contribute most to the measurement uncertainty. A dedicated measurement setup was built to determine the reproducibility of the moving-scale system for these environmental changes. The uncertainty budget of the setup indicates that the long-term stability can be determined with an uncertainty of 21 nm.

INTRODUCTION

Improving machine tool accuracy has been one of the main drivers of technological evolution for centuries. Taniguchi [1] predicted that machine tools for 'normal machining' will reach accuracies below 0.1 μm by 2020. The largest error sources in current normal machine tools are thermo-mechanical [2] and kinematic errors [3]. Extensive application of two precision design rules, namely Abbe- or Bryan-based metrology [4] and functional separation of the structural and the metrology frame [5] could be used to reduce these errors significantly. Examples of machine tools employing these principles with laser interferometers for position measurement of the stages are [6-8]. A typical, more simplified configuration for coordinate measurement machines with laser interferometers is shown in Figure 1 for two degrees of freedom. Here, two laser interferometers are attached to a stationary metrology frame together with a touch probe. While the workpiece table moves in x-z-direction, the laser beams always cross at the centre of the touch probe, in this way eliminating the Abbe errors. To integrate laser interferometers into the harsh environment of normal machine tools however poses a great challenge since interferometry is highly sensitive to changes in the index of refraction of air. Linear encoders, on the other hand, are far less susceptible to environmental changes, as was already indicated by [9].

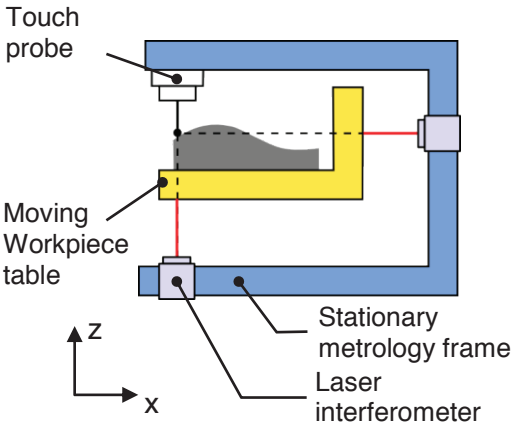

FIGURE 1. Abbe-offset-free configuration of laser interferometers in a CMM.

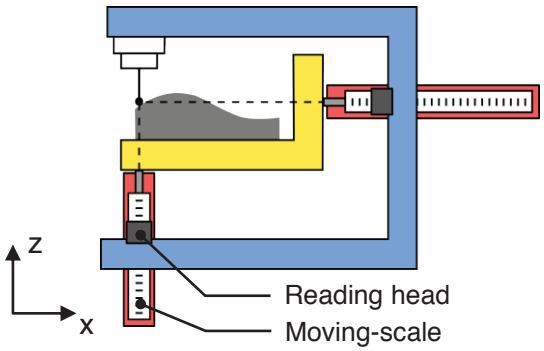

FIGURE 2. Abbe-offset-free configuration of moving linear encoders in a CMM.

Therefore, a new concept for using linear encoders in a similar configuration as laser interferometers was proposed by KU Leuven [10] (Figure 2). In this concept, a linear scale is mounted on a carrier which is driven by a linear motor. A capacitive sensor is located at the end of the carrier and in-line with the scale. The capacitive sensor measures the gap between the sensor tip and a target surface and the linear motor is controlled in such a way that this gap stays within the limits of the capacitive sensor's range. Consequently, the scale follows the

movement of the target surface and the measurement is composed of the long-range measurement of the linear encoder and the short-stroke measurement of the capacitive sensor. This configuration combines both the stability of the linear scales with the possibility of Abbe- and/or Bryan-based metrology. It also incorporates functional separation by mounting the reading heads to the stationary metrology frame and mounting the moving-scales to the base frame. In previous work, the stability of the reading heads and the capacitive sensors was assessed [11]. This paper describes the realization of a 1-DOF prototype and a test setup for determining the long-term stability of the 1-DOF system.

1-DOF MOVING-SCALE PROTOTYPE

Specifications

The objective of this research is to reach an accuracy of machine tools below 100 nm. To reach this, as a rule of thumb, metrology needs to be at least 5 times better, bringing the target measurement uncertainty ($U_{95\%}$) at 20 nm. We assume that the machine tool is in an environment controlled to 20±0.5 °C or that the temperature of the room during production does not change more than 1 °C. Humidity changes should stay within 10 %RH. The layout concept of the moving-scale should allow up to 500 mm of stroke.

Layout

Figure 3 depicts a 1-DOF moving-scale prototype for a measuring length of 109 mm. The linear guide block is mounted to the base frame, together with the stator of the linear motor. The magnet rack and the guide rail are mounted to a moving base which also holds a cable guide for the capacitive sensor cable. A kinematic connection using ball-in-V grooves between the moving base and the scale carrier prevents deformation of the first due to thermal expansion of the latter. Preloading of this connection is done by two springs.

Because the scale (Heidenhain LIP281) and capacitive sensor (Lion Precision C5-D) are in line with each other, the distance between the front end of the scale and the sensor cannot be made zero and measures have to be taken to prevent that thermal expansion of the scale carrier causes measurement errors. One possibility is to produce the entire scale carrier in a low expansion material like Zerodur® or Invar, but then there would be still a difference in thermal expansion between the capacitive sensor, which is made of steel and the scale carrier, causing deformation and stick-slip. Additionally, for a 500 mm measurement length the costs for a Zerodur® scale carrier would be too high. If a practically achievable distance of 45 mm between the sensor tip and the front of the scale would be realized in Invar (CTE = 0.5-2 μm/mK), still a 22.5 to 90 nm thermal expansion would exist for a 1 °C temperature change.

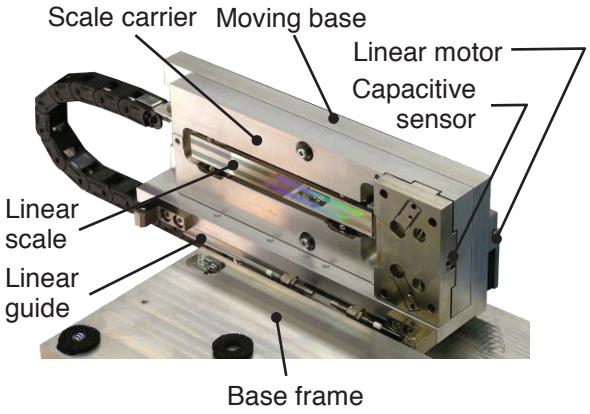

FIGURE 3. Layout of the 1-DOF moving-scale prototype. The reading head is not shown.

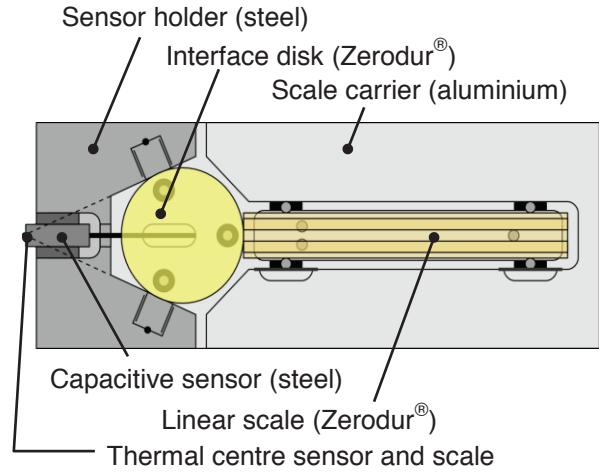

FIGURE 4. Schematic layout of the scale carrier.

It was therefore chosen to apply a thermal centre by preloading a small Zerodur® disk to a wedge in the sensor holder (Figure 4). Both flanges virtually coincide at the centre of the sensor tip and since the sensor holder consists of the same material as the sensor body, uniform expansion of the sensor and holder will not displace the interface disk w.r.t. the sensor tip. The Zerodur® scale is then preloaded to the

TABLE 1. Uncertainty budget of a 109-mm moving-scale measurement system.

Component	U (k=2) [nm]
Affecting reproducibility (for changing environment ΔT=1 °C and ΔRH = 10 %RH)	**13**
Scale expansion (CTE Zerodur® = ±0.1 ppm)	11
Reading head thermal drift	3
Scale carrier assembly thermal drift	4
Capacitive sensor temperature and humidity drift after compensation	3
Other errors due to changes in environmental conditions	3
Dynamic errors	2
Sensor noise	2
Not affecting reproducibility	**12**
Abbe error	4
Cosine error	2
Linear scale calibration error	11
Sensor non-linearity	2
Combined measurement uncertainty [13]	**18**

interface disk, making the thermal expansion between scale and sensor tip virtually zero. Additionally to the connection with the interface disk, the scale is in contact with five precision steel balls in pure rolling contact with scale and scale carrier. The scale is therefore kinematically connected to the scale carrier and will only be deformed or displaced in a minimum way by expansion of the scale carrier. Mounting of the scale in this way will only amount to 4 nm (k=2) thermal drift.

A compensation method for the temperature and humidity drift of the capacitive sensor has been explained in [11], while [12] gives an alignment procedure for reduction of the Abbe offset to attain an Abbe error below 4 nm (k=2) and a cosine error reduction below 2 nm (k=2).

Uncertainty budget

The uncertainty budget for a 109-mm moving-scale system is given in Table 1. For a definition of uncertainty, expanded uncertainty and reproducibility, the author refers to [13]. There has been made a distinction between the error components that require a stable experimental setup that is capable of determining the reproducibility of the measurement system for changing environmental conditions over a long period of time and the error components that can be determined in an experiment by comparison with the length standard over a short period of time. The combined measurement uncertainty would be 18 nm, thereby reaching the 20-nm goal of the measurement system. This paper focuses on the design and prototype development of a setup that is able to check the first part of the error components.

MEASUREMENT SETUP FOR DETERMINING LONG-TERM STABILITY

Design concept

The measurement value of the 1-DOF moving-scale should be compared to a repeatable reference position measurement system operating in a 20±0.5 °C and 45±5 %RH environment. Laser interferometers do not provide enough stability in these conditions unless they are kept in a separate vacuum enclosure [14]. Since the moving-scale system is designed for maximum stability, it is opted to compare position measurements with that of a second moving-scale system, the reference-scale system, placed in line with the first one. The mechanical design of this system is a mirrored version of the one shown in Figure 3, except the capacitive sensor holder is replaced with a target surface. Figure 5 shows a schematic drawing of the measurement setup. The moving-scale system will follow the movement of the reference-scale system. An aluminium metrology frame, kinematically connected to a base frame, holds 3 encoder reading heads. Two are used for detecting the position of the moving-scale and the reference-scale system. A third one is used for correcting the thermal expansion of the metrology frame by

comparison with the other reading head on the reference scale. Since the scale is made of Zerodur®, the measured position difference can be assigned to a uniform expansion of the metrology frame. An approximation of the metrology frame's Biot number gives 0.000371 and for a Biot number smaller than 0.1, the temperature distribution inside an object can be assumed to be uniform.

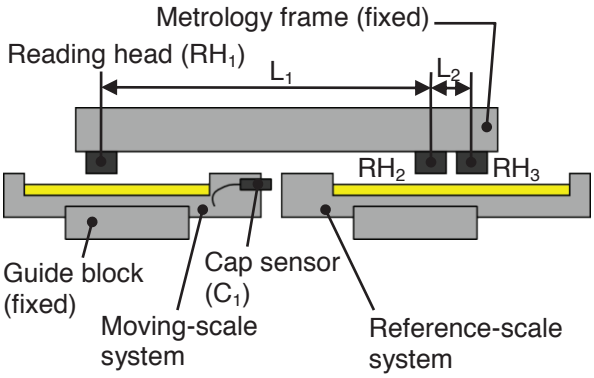

FIGURE 5. Schematic layout of setup for determination of long-term stability in moving configuration.

The two thermal loops for the moving configuration are:

$$e_{drift,\,1} + M_{RH_1} - M_{C_1} - M_{RH_2} = L_1 \alpha_{MF} \Delta T \quad (1)$$

$$e_{drift,\,1} + M_{RH_1} - M_{C_1} - M_{RH_3} = (L_1 + L_2) \alpha_{MF} \Delta T \quad (2)$$

where:
M_i is the measurement of the respective sensor,
L_1 is the distance between the moving-scale reading head and the first reference-scale reading head,
L_2 is the distance between the two reference-scale reading heads,
α_{MF} is the coefficient of thermal expansion of the metrology frame,
ΔT is the temperature change of the environment and
$e_{drift,1}$ is the drift of the whole measurement loop in this configuration.

$\alpha_{MF} \Delta T$ can be eliminated and equation (1) and (2) result in:

$$e_{drift,\,1} = M_{RH_2} - M_{RH_1} + M_{C_1} + \frac{L_1}{L_2}(M_{RH_2} - M_{RH_3}) \quad (3)$$

Calculation of the dispersion of $e_{drift,1}$ from (3) for every position of the scale gives the reproducibility of the combination of measurement setup and moving-scale system for changes in temperature and humidity.

The system could also be configured such that the moving-scale system measures the displacement of a stable stationary target surface (Figure 6). The target surface is fixed to the metrology frame and consists of the same aluminium alloy. The moving-scale is now read by two heads to compensate for thermal expansion of the metrology frame. This configuration allows determination of the stability of solely the moving-scale system, but thermal expansion of the scale or dynamic system performance cannot be evaluated.

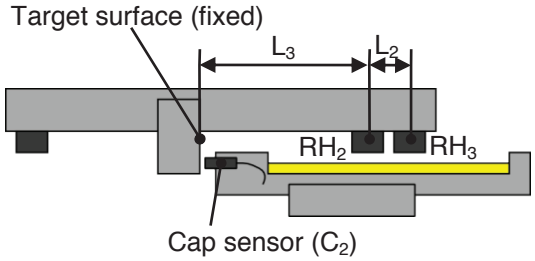

FIGURE 6. Schematic layout of setup for determination of long-term stability in stationary target surface configuration.

Similar equations as (1) and (2) can be found for this configuration to get:

$$e_{drift,\,2} = M_{RH_2} + M_{C_2} + \frac{L_3}{L_2}(M_{RH_2} - M_{RH_3}) \quad (4)$$

where:
L_3 is the distance between the target surface and the first reference-scale reading head and
$e_{drift,2}$ is the drift of the measurement loop in this configuration.

Calculation of the dispersion of $e_{drift,2}$ from (4) gives the long-term stability to environmental changes of a stationary moving-scale system.

Mechanical design

Figure 7 shows the realization of the measurement setup with the moving-scale and the reference-scale system. The guide blocks of both systems are attached to the base frame. The metrology frame is kinematically connected to the base frame with ball-in-V grooves and preloaded with springs. The reading heads are kinematically connected to the metrology frame

in such a way that the thermal centre of the reading head coincides with the thermal centre of the kinematic connection. In this way, thermal drift of the metrology frame assembly will only be due to thermal expansion of the metrology frame itself, and not of the reading heads.

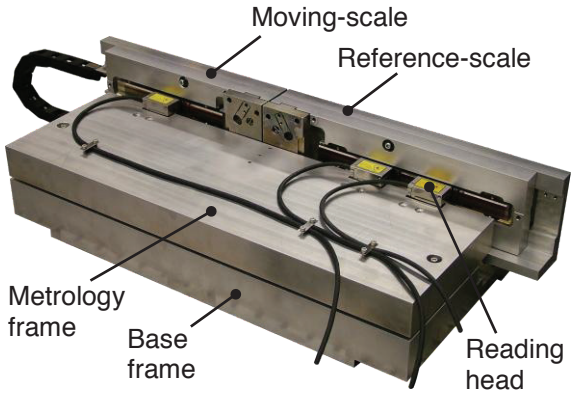

FIGURE 7. Experimental setup for determining the long-term stability of the 1-DOF moving-scale system.

Since this setup measures the drift of the moving-scale system, it is important to calculate the accompanying measurement uncertainty. Table 2 summarizes the uncertainty budget. It shows that for the moving configuration, the long-term stability measurement has a higher uncertainty than the reproducibility of the moving-scale system itself. In the stationary configuration, the measurement uncertainty approaches the reproducibility of the measured system, namely the reference-scale. Therefore, the long-term stability is best determined with the stationary configuration, while the moving configuration can be used for assessing the dynamic performance and the kinematic repeatability.

CONCLUSION

The design and development of a moving-scale measurement system was presented. The system enables the nanometer-accurate position measurement of stages in machine tools by placing the encoders in an Abbe-offset-free configuration. To determine the long-term stability of the measurement system, a dedicated setup has been designed and built and an uncertainty budget has been made. In the future, experiments on this setup should show the feasibility of the moving-scale system for integration in a normal machine tool.

ACKNOWLEDGEMENTS

This work is supported by a PhD grant from the Institute for the Promotion of Innovation through Science and Technology in Flanders IWT/101447, and the EC FP7 FoF collaborative project - “MIDEMMA” (Grant agreement no. 285614).

TABLE 2. Uncertainty budget of the long-term stability measurement setup.

Component	U (k=2) [nm]
Moving-scale reproducibility U_{MS}	13
Reference-scale reproducibility U_{REF}	19
Reading head stability U_{RH}	3
Scale expansion over 55 mm U_{SC}	6
Expansion L_2: $U_{L_2} = \sqrt{2 \cdot U_{RH}^2 + U_{SC}^2}$	7
Expansion L_1: $U_{L_1} = L_1/L_2 \cdot U_{L_2}$	29
Expansion L_3: $U_{L_3} = L_3/L_2 \cdot U_{L_2}$	10
Long-term stability measurement	
Moving configuration U_{MC}	34
Stationary target configuration U_{FC}	10
$U_M = \sqrt{U_{MS}^2 + U_{MC}^2}$	37
$U_F = \sqrt{U_{REF}^2 + U_{FC}^2}$	21

REFERENCES

[1] Taniguchi N. Current Status in, and Future Trends of, Ultraprecision Machining and Ultrafine Materials Processing. Annals of the CIRP. 1983; 32(2): 573-582.

[2] Mayr J et al. Thermal issues in machine tools. CIRP Annals - Manufacturing Technology. 2012; 16: 771-791.

[3] Ramesh R, Mannan M A, Poo A N. Error compensation in machine tools - a review, Part I: geometric, cutting-force induced and fixture-dependent errors. Int. Journal of Machine Tools & Manufacture. 2000; 40: 1235-1256.

[4] Bryan J B. The Abbe principle Revisited: An Updated Interpretation. Precision Engineering. 1979; 1(3): 129-132.

[5] Nakazawa H. Principles of precision engineering. Oxford University Press. New York: 1994.

[6] McKeown P A et al. Ultraprecision, high stiffness cnc grinding machines for ductile

mode grinding of brittle materials, Proc. SPIE. 1990; 1320: 301-313.
[7] Donaldson R R, Patterson S R. Design and construction of a large vertical axis diamond turning machine. Proc. SPIE. 1983; 433: 62-67.
[8] Hemschoote D et al. The use of metrology frames in an ultra-precision 5-axis machine for ELID-grinding. Euspen 6th International Conference proceedings. 2006; 1: 249-252.
[9] Kunzmann H, Pfeifer T, Flügge J. Scales vs. Laser Interferometers Performance and Comparison of Two Measuring Systems. CIRP Annals - Manufacturing Technology. 1993; 42: 753 - 767.
[10] Hemschoote D et al. An Abbe-compliant 3D-measurement concept based on linear scales. Euspen 4th International Conference proceedings. 2004; 1: 336 – 337.
[11] Bosmans N et al. Design of a precision measurement system using moving linear scales. Euspen 12th International Conference proceedings. 2012; 1: 302-305.
[12] Bosmans N et al. Abbe offset reduction for a nanometre accurate moving scale measurement system. Lamdamap 10th Conference Proc. 2013; 1: 91-100.
[13] JCGM. Evaluation of measurement data - Guide to the expression of uncertainty in measurement (JCGM 100:2008). 2008.
[14] Fluegge J, Koening R G. Status of the nanometer comparator at PTB. Proc SPIE 2001; 4401: 275-283.

CORRECTION FOR AMPLIFIER-INDUCED PHASE LAG IN CAPACITANCE GAGE MEASUREMENTS

Vasishta Ganguly and Tony L. Schmitz
Department of Mechanical Engineering and Engineering Science
University of North Carolina at Charlotte
Charlotte, NC, USA

INTRODUCTION

The dynamic response of mechanical structures may be represented by their complex frequency response function (FRF). The FRF is characterized by the frequency dependent magnitude and phase, or real and imaginary parts, which relate the structures response to a force input. The FRF of a structure may be measured using modal testing [1]. In one type of modal testing, referred to as impact testing, an impulse force is applied to a structure and a linear transducer is used to measure the response. The displacement, velocity, or acceleration may be used to identify the FRF.

Capacitance gages and laser Doppler vibrometers (LDV) are non-contact sensors which offer high bandwidth and resolution. These sensors may be used for displacement/velocity feedback, spindle error motion characterization, and frequency response measurements in structural dynamics testing. They employ amplifying electronics to convert the change in displacement/velocity to a proportional voltage which may then be sampled by a data acquisition (DAQ) system. Depending on its design, the amplifier can induce a time delay in the measurement signal, i.e., there is a small time delay between the input displacement/velocity of the target and the output voltage from the amplifier. These time delays lead to frequency dependent phase errors in the FRF. Furthermore, the digital DAQ system may introduce some synchronization errors between the force and response signals.

In this research, an experimental technique to identify the frequency dependent phase error is described. The technique may also be extended to identify synchronization errors due to the DAQ system. A frequency domain approach is proposed to correct the FRF for the phase errors. The method is verified using a standard artifact mounted in a test stand.

EXPERIMENTAL SETUP

Two different methods were employed to evaluate the time delays: a) frequency-sweep test; and b) broadband excitation.

Frequency Sweep Test

In the frequency sweep test, the measurement bandwidth was divided into a number of discrete steps and the phase error was measured independently at each frequency. The amplifier-induced phase error was evaluated by measuring the phase shift between two transducers attached to an oscillating target: a "known" accelerometer and a capacitance gage system. The target was vibrated using a modal shaker (TIRAvib 51075) capable of generating oscillations up to 5000 Hz. A function generator (Hewlett Packard 33120A) was used to drive the shaker at the desired fixed frequency. The target motion was measured using both a low-mass integrated circuit PZT (ICP) accelerometer (PCB 352C23) and a capacitance gage sensor (Lion Precision C23 B). The capacitance gage signal was amplified using a Lion Precision CPL 290 Elite series amplifier. The amplifier bandwidth was set to 15 kHz. Data was acquired at 100 kHz using a NI DAQ card.

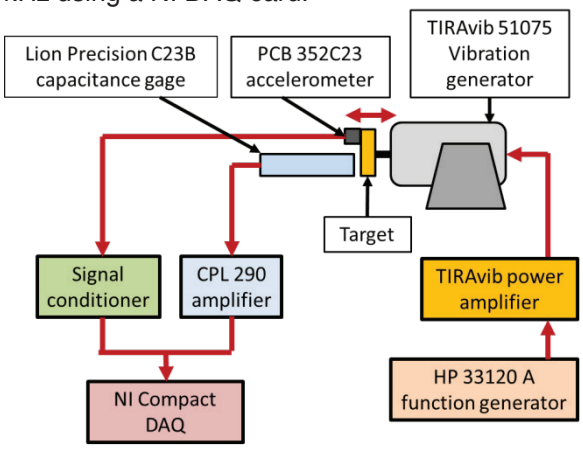

FIGURE 1. Schematic representation of the experimental setup.

Figure 1 shows a schematic representation of the measurement setup. The phase shift, θ, between two time domain sinusoidal signals, x and y, with frequency, ω, may be calculated using:

$$\theta(\omega) = \cos^{-1}\left(\frac{x.y}{|x||y|}\right). \quad (1)$$

Measurements were conducted over a frequency range of 100 Hz to 5000 Hz in 100 Hz increments. The measured data was digitally filtered using a 3rd order band pass filter with a bandwidth of 100 Hz centered at the oscillation frequency. Figure 2 shows the measured phase lag as a function of the oscillation frequency. Within the measured bandwidth, the phase lag changed linearly with respect to the oscillating frequency at a rate of -12.9 deg/kHz, which is consistent with the manufacturer-reported value [2]. Scatter from the best fit line in the 1000 Hz to 2000 Hz range was attributed to compliance in the wax interface between the accelerometer and target, but additional testing is warranted.

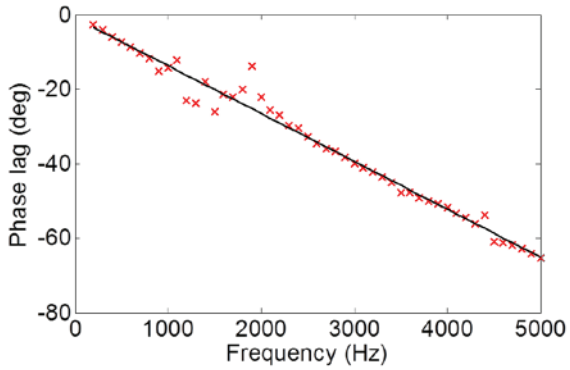

FIGURE 2. Measured phase lag as a function of oscillating frequency.

Broadband Excitation

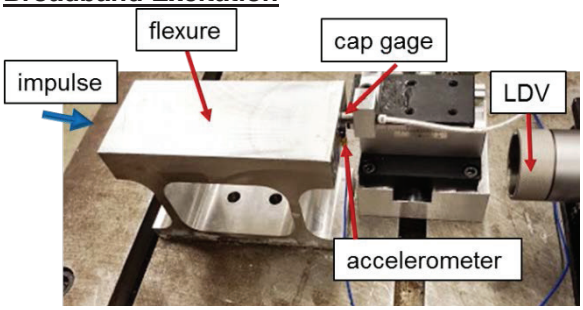

FIGURE 3. Broadband excitation setup.

Figure 3 shows the measurement setup. An impulse force, applied using a modally tuned hammer (PCB 086C04), was used to excite a flexure over a wide frequency range. The response of the flexure was simultaneously measured using an ICP accelerometer (PCB 352C23) which measured acceleration, a LDV (Polytec OFV – 534) which measured velocity, and a capacitance gage (Lion Precision C5 D) which measured displacement. The accelerometer signal was used as the reference signal for the phase error evaluation. The FRF can be expressed in terms of the displacement, velocity, and acceleration signals as:

$$FRF = \frac{X(\omega)}{F(\omega)} = \frac{1}{i\omega}\frac{V(\omega)}{F(\omega)} = -\frac{1}{\omega^2}\frac{A(\omega)}{F(\omega)}, \quad (2)$$

where $X(\omega)$, $V(\omega)$, $A(\omega)$, and $F(\omega)$ are the fast Fourier transforms (FFTs) of the displacement, velocity, acceleration and force signals respectively and ω is the frequency in rad/s. The phase errors introduced by the capacitance gage and LDV amplifying electronics are identified in the frequency domain by comparison with the accelerometer phase.

The excitation bandwidth is inversely related to the impulse period, while the excitation magnitude is directly related to the magnitude of the impulse force. Figure 4 shows a plot of the force FFT magnitude to provide an estimate of the excited bandwidth.

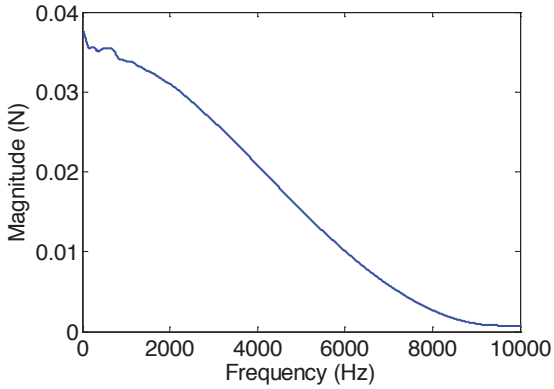

FIGURE 4. Magnitude of impulse force represented in the frequency domain.

Figure 5 shows the first two modes of vibration of the flexure. The three sensors simultaneously measure the dynamics response at different locations on the side of the flexure as shown in Figure 3. The response measured by the three sensors around the first natural frequency (1708 Hz) has the same magnitude and phase. However, for the second (twisting mode) natural

frequency (3400 Hz), the response measured by the three sensors is not necessarily identical. Therefore, the frequency range from 3200 Hz to 3600 Hz was ignored when comparing the phase of the three sensors.

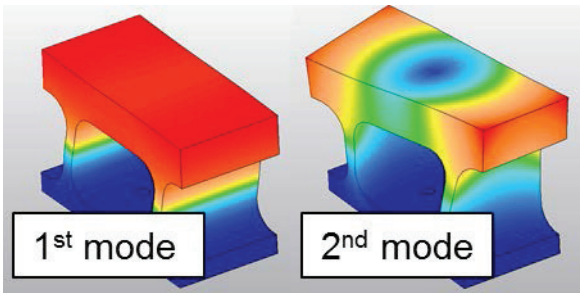

FIGURE 5. First two vibration modes for the flexure.

The coherence of a FRF provides an estimate of the reliability of the measurement [1]. Ideally, the coherence is unity. Figure 6 shows a plot of the FRF coherence for the three sensors. It is less than one at low frequencies for the accelerometer and LDV due to the frequency domain integration. It was also observed that the coherence drops near the second natural frequency. The phase error was only calculated for frequency values where the coherence was greater than 0.95.

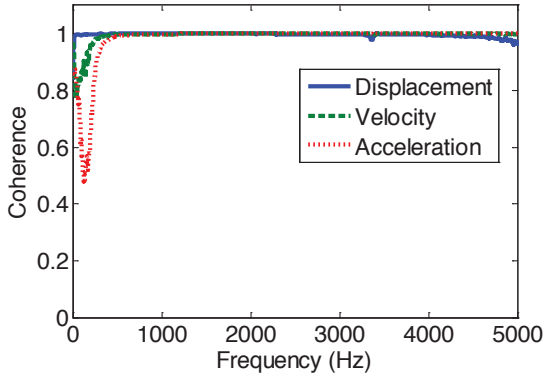

FIGURE 6. FRF coherence: displacement, velocity, and acceleration.

Figure 7 shows the mean phase for the three sensors from 12 repetitions. It is observed that the phase of both the capacitance gage and the LDV lags the accelerometer phase. The frequency dependent phase error is calculated using:

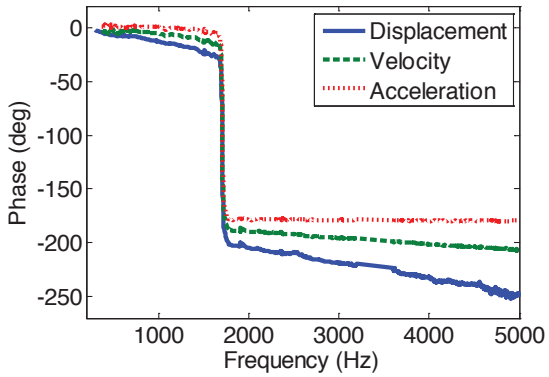

FIGURE 7. FRF phase: displacement (CG), velocity (LDV), and acceleration.

$$\phi_{err_{CG}} = \angle\left(\frac{X(\omega)}{F(\omega)}\right) - \angle\left(-\frac{1}{\omega^2}\frac{A(\omega)}{F(\omega)}\right), \text{ and,}$$

$$\phi_{err_{LDV}} = \angle\left(\frac{1}{i\omega}\frac{V(\omega)}{F(\omega)}\right) - \angle\left(-\frac{1}{\omega^2}\frac{A(\omega)}{F(\omega)}\right), \qquad (3)$$

where∠ represents the FRF phase. Figure 8 shows the frequency dependent phase error for the capacitance gage and LDV measurements. Within the measured bandwidth, the phase error was found to change linearly with frequency. The slope of the linear fit was used to characterize the phase error as shown in Table 1. Note that for the capacitance gage amplifier, the slope derived using the broadband excitation method is 4% higher than that derived using the frequency sweep test. Also note that the capacitance gage phase error is sensitive to the operating bandwidth of the capacitance gage amplifier (CPL 290). In this study, the amplifier was set to a bandwidth of 15 kHz.

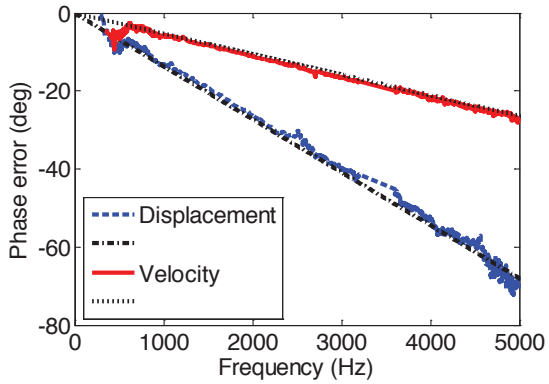

FIGURE 8. Phase error for the capacitance gage and LDV with reference to the accelerometer.

TABLE 1. Slope of frequency dependent phase error.

Instrument	Frequency dependent phase error (deg/kHz)	
	Mean	Standard deviation
Frequency sweep		
Capacitance gage	-12.9	-
Broadband excitation		
Capacitance gage	-13.54	0.165
LDV	-5.47	0.1283

SYNCHRONIZATION ERRORS IN DATA ACQUISITION SYSTEMS

In this study, a National Instrument compact data acquisition system (NI cDAQ 9174) was used to collect the data. Two different cards (NI 9215 and NI 9324) were mounted in the same cDAQ chassis. The NI9215 is capable of measuring a voltage signal within a range of ±10 V at a sampling rate of up to 100 kHz. The NI9324 can measure a voltage signal within the range of ±5 V at a sampling rate of up to 51.2 kHz. The NI9324 also provides the necessary supply current for integrated circuit PZT (ICP) sensors, such as accelerometers and modal hammers. Individually, each card has four channels which are sampled simultaneously. However, the different cards mounted within the same cDAQ chassis are not necessarily synchronized. Synchronization errors between the different channels of the data acquisition system must be taken into account when measuring dynamic response data.

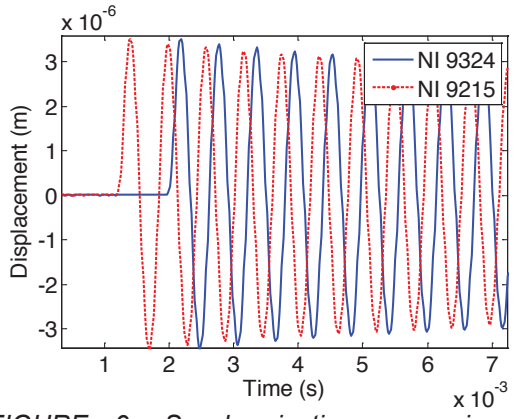

FIGURE 9. Synchronization error in data acquired by two DAQ cards (NI 9215 and NI 9324).

To measure the DAQ system induced synchronization error, the same displacement (response) signal from the capacitance gage was split and was simultaneously collected by both the DAQ cards (NI9215 and NI9324) mounted in the cDAQ chassis. Figure 9 shows a time domain plot of the identical response signal acquired by the two different DAQ cards. The measurement data acquired by the NI9215 card leads that acquired by the NI9324 card. In the frequency domain, the phase delay introduced by the data acquisition system may be estimated as:

$$\phi(\omega) = \angle\left[\frac{X_{NI\,9324}(\omega)}{X_{NI\,9215}(\omega)}\right], \qquad (4)$$

where $X_{NI9324}(\omega)$ and $X_{NI9215}(\omega)$ represent the FFTs of the response signal acquired by the NI9324 and NI9215 DAQ cards, respectively. Figure 10 shows the phase error as a function of frequency. Note that the error is reset to zero each time it is crosses 360 degrees. The NI9324 card lags the NI9215 card.

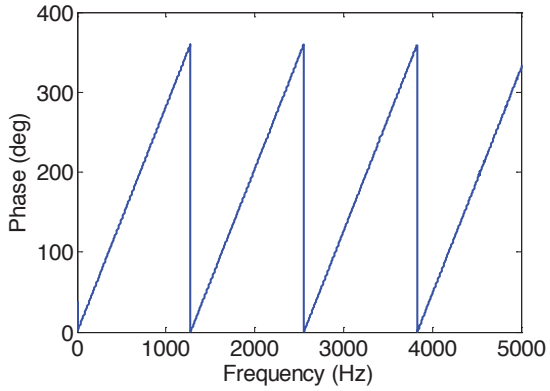

FIGURE 10. DAQ induced phase error.

When measuring the FRF of a mechanical structure, it is necessary to account for the synchronization errors introduced due to the DAQ system as well as the sensor electronics. In this example, the dynamic response of the flexure assembly was measured. The input impulse force signal from the modal hammer was collected by the ICP compatible NI9324 card and the response signal was collected by the NI9215 card. Note that in this case, the impulse data (NI9324) lags the response data (NI9215) which is physically impossible. Also, the capacitance gage amplifier introduced a time delay in the response signal. The phase lag introduced by the capacitance gage amplifier

was smaller than the phase lead introduced by the DAQ system. Both these factors were accounted for when correcting the FRF. Figure 11 shows the net effect of the phase errors introduced by the DAQ system and the capacitance gage amplifier. Figure 12 shows measured and corrected phases for the FRF measurement. Note that the FRF amplitude is constant.

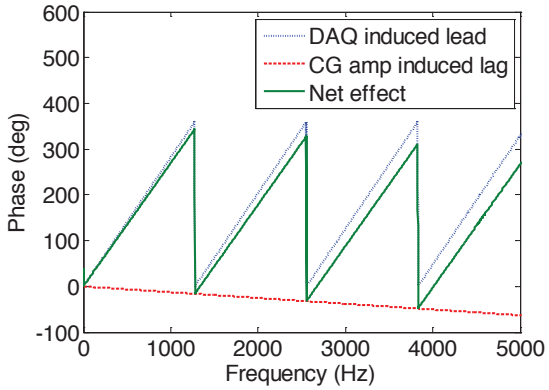

FIGURE 11. Net effect of DAQ and amplifier induced phase errors.

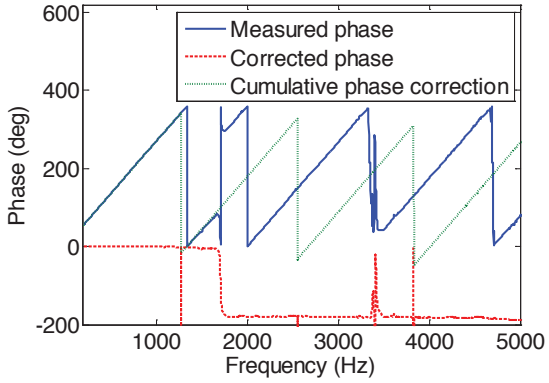

FIGURE 12. Measured and corrected phase of flexure FRF.

CORRECTION FOR FRF PHASE LAG

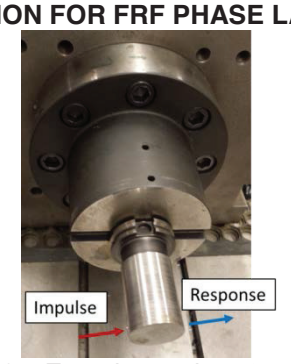

FIGURE 13. Experimental setup to validate phase correction algorithm.

FRF tests were performed at the tip of a standard artifact mounted in a spindle test stand; see Figure 13. A modally tuned hammer (PCB 086C04) was used to apply an impulse force to the artifact and the response was measured using a capacitance gage (Lion Precision C5D), the LDV (Polytec OFV – 534), and an accelerometer (PCB 352C23) sequentially. The data was acquired at 51.2 kHz. All the signals were acquired using the same DAQ card (NI9324) to avoid any DAQ induced synchronization errors. For any FRF, the measured frequency-dependent phase difference between the input force and the output response is:

$$\phi(\omega) = \tan^{-1}\left[\frac{\mathrm{Im}\{FRF(\omega)\}}{\mathrm{Re}\{FRF(\omega)\}}\right], \qquad (5)$$

where Re indicates the real part and Im indicates the imaginary part of the complex FRF. The (linear) phase difference is corrected to account for the amplifier induced phase lag using:

$$\phi(\omega)_{corr} = \phi(\omega)_{meas} - \Delta\theta * \omega, \qquad (6)$$

where $\Delta\theta$ is the rate of change of phase lag with frequency (the slope of the line in Fig. 2).The corrected Re and Im parts of the FRF may then be computed using:

$$\mathrm{Re}(FRF)_{cor} = |FRF(\omega)| * \cos(\phi(\omega)_{corr}), \qquad (7)$$

$$\mathrm{Im}(FRF)_{cor} = |FRF(\omega)| * \sin(\phi(\omega)_{corr}),$$

where $|FRF(\omega)|$ is the FRF magnitude, which is not affected by the phase lag. Figure 14 shows a Nyquist plot of the measured and corrected FRFs obtained using the accelerometer, the capacitance gage and the LDV. In the Nyquist plot, a phase error is manifested as a "rotation" of the Nyquist curve. The corrected curves align with the FRF obtained using the accelerometer. Errors in the magnitude of the real and imaginary parts of the corrected Nyquist plot may be attributed to errors in calibrating the sensor sensitivities.

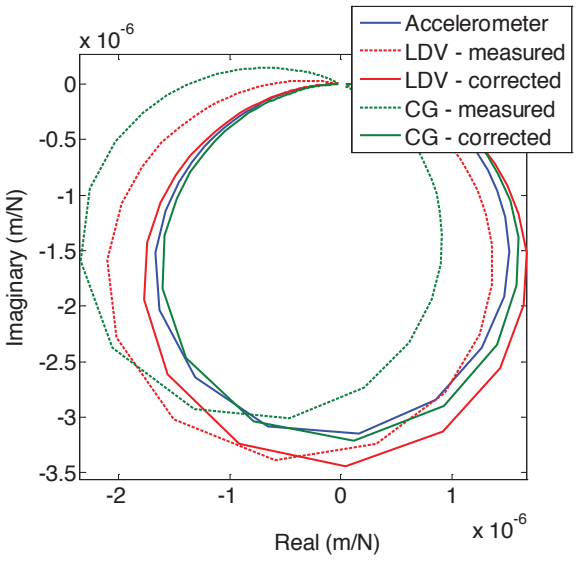

FIGURE 14. Comparison of FRFs obtained using the capacitance gage, LDV, and accelerometer.

CONCLUSIONS

In this study, the frequency dependent phase error induced by the amplifying electronics was identified for a capacitance gage sensor and a laser Doppler vibrometer. Synchronization errors introduced by the data acquisition system was also identified. A frequency domain technique to correct the phase error was described and applied to FRF measurements of a standard artifact in a test stand. The measurements showed that the corrected FRFs agreed with the FRF measured using the accelerometer.

REFERENCES

[1] Ewins D.J, Modal Testing: Theory, Practice and Application, 2nd ed., Research Studies Press LTD, Hertfordshire, 2000.

[2] Lion Precision, TechNote LT03-0031 EliteSeries Amplitude/Phase Frequency Response, 2011.

RANGING PERFORMANCE EVALUATION OF A LASER SCANNER

M. Ferrucci[1], B. Muralikrishnan[1], C. Blackburn[1], D. Sawyer[1], S. Phillips[1], V. Lee[1], P. Petrov[2], Y. Yakovlev[2], A. Astrelin[2], S. Milligan[2], J. Palmateer[3]
[1]Semiconductor and Dimensional Metrology Division, National Institute of Standards and Technology, Gaithersburg, MD
[2]Basis Software Inc., Redmond, WA
[3]Boeing Research and Technology, Seattle, WA

INTRODUCTION

Large volume laser scanners are used for a variety of purposes, including dimensional metrology of large artifacts, digitization and reverse engineering, as well as historical preservation and archiving. These devices have two rotary axes, which scan a single modulated laser beam in the horizontal and vertical planes. The rotary encoders measure the horizontal angle (Φ) and vertical angle (θ) and the modulated laser captures the range information (r), forming a spherical coordinate measuring system.

The design of the scanner used in this study integrates a laser source and a spinning mirror into a rotating head. The scanner head rotates along Φ, while the mirror spins along θ. Range is determined using amplitude-modulation, which is covered in the section on ranging technology.

In evaluating the performance of laser scanners, we seek to understand and quantify how well these instruments can measure geometries of objects in their field of view. A common methodology in evaluating the performance of a particular device consists of comparing its measurement results to those made by a reference instrument. This methodology is applied in the tests described in this study.

Because laser scanners can measure large volumes, the performance evaluation is conducted in two parts. The focus of the first set of tests is purely on the ranging capability of the instrument, while the second set of tests focuses on the volumetric measurement capability. This paper describes the ranging performance tests conducted on a commercial laser scanner. We address the volumetric performance testing of the same scanner in a separate, but concurrent, publication [1].

In subsequent sections, we introduce the reader to the various ranging technologies employed by laser scanners and briefly describe the technology employed by the particular scanner under test. There has been ongoing work within the ASTM E57 committee in the area of range testing, and this will be briefly outlined. We discuss the use of contrast targets and describe the design of our ranging tests. Finally, we present test results and discuss future work. We note that the ranging tests described in this paper are applicable not just to the design considered in this study, but to all opto-mechanical constructions of scanners.

RANGING TECHNOLOGY

There are various methods [2-3] employed by laser scanners to determine range. Time-of-flight works on the principle that light travels at a known speed, given it travels through one medium. The distance traveled by the laser is determined by measuring the time between the laser's emission and its return to the sensor. However, the time-of-flight method is limited by an instrument's ability to discriminate time differences.

Frequency-modulation and amplitude-modulation offer more practical options for range detection with higher accuracies. Commercial systems are available that employ both techniques [3]. In this study, we work with a Surphaser [4] 25HSX-IR_X laser scanner (hereafter referred to as 'Surphaser'), which measures range by amplitude-modulation.

In particular, the Surphaser modulates the optical power of its laser signal at three different frequencies. The lowest frequencies, 9 MHz and 11 MHz, are combined to produce a synthetic half-wavelength (λ/2) of approximately 70 m. The instrument's phase discrimination is constant for all modulation frequencies and, therefore, this long wavelength signal will only allow for coarser range measurements. For the purpose of improving measurement accuracy, a third and higher modulation frequency is

introduced. The Surphaser produces a 660 MHz modulation signal, which translates to a half-wavelength of approximately 20 cm. This shorter wavelength allows for range resolution to be much finer, thus allowing higher precision in range measurement.

ONGOING WORK WITHIN ASTM E57

The ASTM E57.02 working group on 3D Imaging Devices has put forth a document [5] for the ranging performance evaluation of laser scanners using planar targets at two positions along the radial direction. The measured distance is then compared to a calibrated distance made with a reference instrument. This protocol was adopted after considerable discussion over several years to accommodate the testing of a wide variety of ranging technologies. As in the case of any performance evaluation test in a Standard, there is a need to balance the number and rigor of tests against the time and cost to perform them. Our work differs from the scope of the ASTM E57 efforts in that we are primarily focused on understanding ranging errors in our instrument and, if possible, modeling them.

Errors in the measurement of range distances can be a result of the interaction of the laser with the measured surface. Material properties such as color, shape, reflectivity, and surface finish affect the propagation and characteristics of the laser signal, which can ultimately affect the measured range distance. Additionally, ranging errors can be a result of small, but unintended, offsets, tilts, and eccentricities in the mechanical construction and optical alignment of the laser.

Another difference in our testing scheme is the use of contrast targets. Contrast targets are not geometrical targets. This allows us to avoid introducing some of the target object's geometric errors into our range measurements. These targets can be considered 'cooperative,' as they are specially designed to produce highly repeatable position measurements when scanned with the Surphaser. We can, therefore, isolate ranging errors from target induced errors in our tests.

Finally, we evaluate range distances at twelve positions along the radial direction to better understand the scaling of errors as a function of range. It should be noted that, in the testing scheme described in this paper, we borrow the idea of a movable nest assembly that can be re-seated on kinematic plates along the radial direction.

CONTRAST TARGETS

In this ranging evaluation study, we make use of commercially available contrast targets. These targets are rectangular plates with alternating black and white triangles on the front face (Fig. 1a). Mounted on the back of the target is a 38.1 mm (1.5 in) diameter metallic hemisphere, which allows the target to sit on kinematic nests (Fig. 1b). The common vertex of the triangles on the front face is designed to be the center of the partial hemisphere on the back.

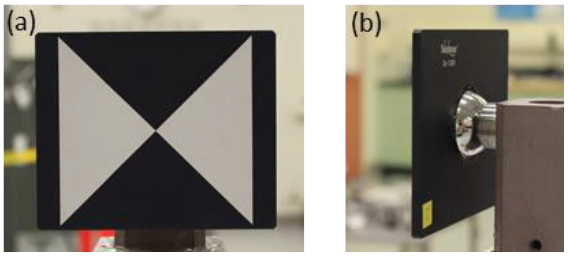

FIGURE 1. Contrast target. (a) The front of the target has alternating black and white triangles whose edges intersect at the center rear mounted hemisphere. (b) A hemisphere mounted on the back allows it to sit on a kinematic nest.

The contrast targets are specially designed to provide repeatable results when used in conjunction with a special target detecting algorithm in the Surphaser software. We verify the repeatability by scanning the contrast target ten times and calculating one standard deviation of the range values. This is performed at various distances from the scanner: 2 m, 4 m, 6 m, and 8 m. We repeat this for two spherical targets as well, a 60.325 mm (2.375 in) Hubbs [4] Precision Sphere and a 101.6 mm (4 in) titanium sphere.

Table 1 clearly shows the repeatability in determining target position along the radial direction is much smaller for the contrast targets. During our ranging tests, we scan each position four times and average the results. This means the repeatability of the mean for the contrast target is 6 μm at a range of 8 m.

TABLE 1. One standard deviation of 10 range measurements to a contrast target and two spheres at multiple range positions.

Range (m)	Repeatability in Range Measurement (mm)		
	Contrast Target	Hubbs Sphere	Titanium Sphere
2 m	0.005	0.010	0.009
4 m	0.005	0.017	0.020
6 m	0.004	0.020	0.043
8 m	0.012	0.058	0.047

The construction of the contrast target allows it to be interchanged with a spherically mounted retro reflector (SMR) on the same kinematic nest. The benefit here is that we can calibrate the nest-to-nest distance using the SMR and a laser tracker – our reference instrument. We can thus evaluate the performance of a laser scanner when it scans the same nest-to-nest displacement with a contrast target. However, the interchangeability between contrast targets and SMRs assumes that the common vertex of the black and white triangles is nominally coincident with the geometrical center of the metallic partial hemisphere. In general, if this condition is not satisfied, the displacement between contrast targets cannot be compared to the calibrated nest-to-nest distances. However, if measurements are conducted using the same target displaced in a purely radial direction, then any offset in coincidence cancels out. Some of the range tests we perform employ targets on both sides (180 degrees opposite each other) of the instrument and are therefore sensitive to target coincidence errors. We address the evaluation of coincidence in the next section.

GEOMETRICAL COINCIDENCE

We define a Cartesian coordinate system that we use to describe geometrical offsets between the common vertex of the triangles and the hemisphere center (Fig. 2). Errors in coincidence would be presented as the offsets in X, Y, and Z, individually.

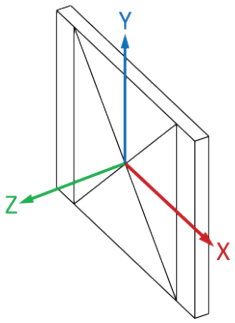

FIGURE 2. To evaluate the coincidence between the vertex and the hemisphere, we establish a Cartesian coordinate system.

We note that, in ranging tests, the contrast targets are positioned along the scanner's radial direction. This is done to minimize errors arising from the opto-mechanical error associated with angle measurements. This also means that offsets in lateral concentricity, i.e., offsets in X and Y (Fig. 3a), produce cosine errors that have a negligible effect on range measurements that are larger than a few millimeters in length. On the other hand, offsets in Z translate directly into offsets in range measurement (Fig. 3b). Thus, we investigate the concentricity along the Z axis.

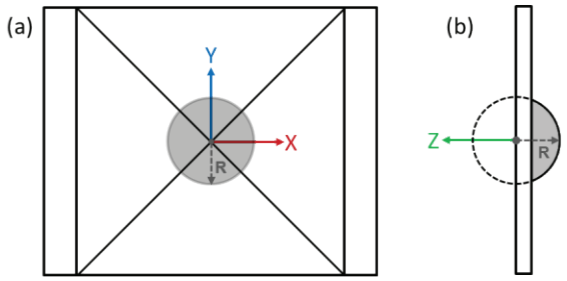

Figure 3. (a) Lateral offsets (X and Y) have a negligible contribution to range measurements. (b) Offsets in Z translate directly to errors in range measurement.

The offset in Z is determined by comparing the center of the contrast target's front face to the center of a 38.1 mm (1.5 in) reference sphere. We perform the measurements on a touch-probe coordinate measuring machine. The reference sphere is seated on a kinematic nest and is probed at 25 points along its top surface. The points are fitted to a sphere, and the coordinates of its center are extracted. We remove the reference sphere and place the contrast target on the same kinematic nest. After ensuring that the contrast target is level, we probe 25 points along a 5 mm by 5 mm square at the center of the front surface. A least-squares plane is fit to these 25 points. The Z offset is thus the orthogonal distance between the previously determined center of the reference sphere and the least squares plane. Measurements are performed on 10 contrast targets, and results are shown in Figure 4.

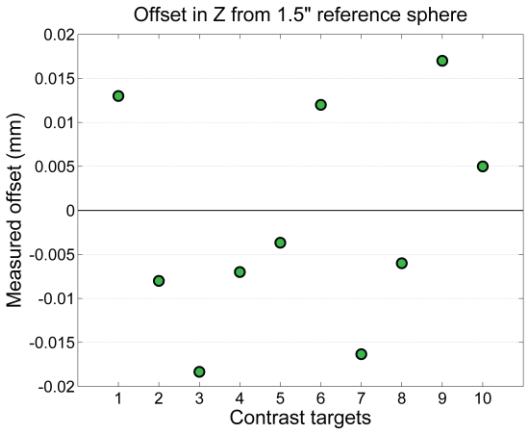

FIGURE 4. The position of a contrast target's center compared to the center of a 38.1 mm (1.5 in) reference sphere. The offset along the Z-axis is shown for 10 different contrast targets.

The plot shows that the offset in Z stayed within 0.02 mm for all the contrast targets that were tested. While 0.02 mm is not negligible, it is small compared to the errors we observe in the scanner's ranging evaluation.

ZERO OFFSET

The zero offset test is intended to detect offsets in the laser scanner's zero position. This involves measuring a nest-to-nest distance from inside the measurement path. In other words, the nests are located on opposite sides of the scanner, roughly 2 m away on each side. The chosen distance corresponds to an observed 'sweet spot' in the scanner's ability to identify the target with high repeatability. The nests are oriented such that the targets are facing inward (Fig. 5). The measured distance is compared to the calibrated distance, which is determined by measuring the same nest-to-nest segment using an SMR and a laser tracker – also positioned within the measurement path. The tracker was compensated using its manufacturer's procedure so that its zero offset, if any, was minimized.

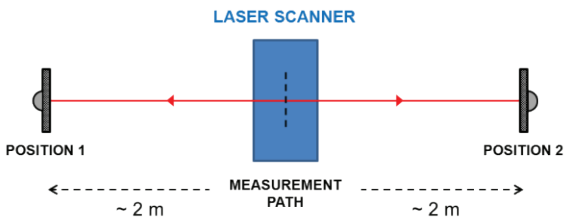

FIGURE 5. The zero offset of a laser scanner can be determined by measuring a length segment from within the measurement path. The measured value is compared to the calibrated value.

The scanner measurements were performed with a single target, which we scan on each nest, consecutively. The target is scanned four times at each position, first using the front face and then using the back face configuration of the scanner. After averaging each set of four measurements, we calculate the distance between them. We then determine the difference in this distance from the calibrated value (determined by the laser tracker) for both the front and back face measurements. The target used in this test was measured to have a +0.005 mm offset in Z. We take this offset into account when determining the difference between the scanner data and calibrated distances. The results from the zero offset test are presented in Table 2.

TABLE 2. The measurement results from the zero offset test in both the front and back face configurations of the scanner.

Error from Calibrated Value (mm)	
Front Face	Back Face
- 0.193	- 0.230

The results show that, despite measuring the same nest-to-nest distance, the scanner reports a shorter length distance by roughly 0.2 mm. This translates to a zero offset of approximately -0.1 mm in each direction. The reason for the 0.04 mm discrepancy between front and back face is not yet clear. We are continuing to investigate this.

RANGE TEST

In performing the range test, the target will remain on one side. We are interested in the scanner's ability to accurately locate a target at increasingly distant positions. By only moving the target along the range, r, we remove any influence that could arise from errors associated with the angle measurement. We constructed a horizontal rail to serve as a straight length segment, on which the target could be positioned (Fig. 6).

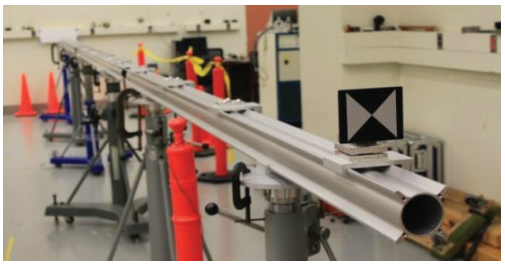

FIGURE 6. A horizontal rail allows the targets to be placed at various positions along a straight line.

Since the same contrast target is used for all positions, the offset in Z is a common mode error and is, therefore, not of concern. We construct a movable nest assembly, similar to that described in the ASTM E57 protocol, which can be moved to various positions along the rail. The assembly (Fig. 7a) consists of a kinematic nest held vertically by a metal block, which is mounted on a horizontal plate. This 'top' plate can be kinematically seated onto a 'bottom' plate. The two plates have opposing magnets built within their centers and thus make up a 'kinematic platform,' designed specifically for highly repeatable seating (Fig. 7b).

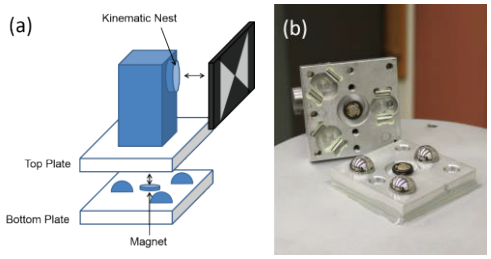

FIGURE 7. (a) The nest assembly allows the nest to be moved to various positions along the rail. (b) The kinematic platform is designed for highly repeatable seating between plates.

Twelve bottom plates are fixed at 1 m intervals along the horizontal rail. These positions are labeled A to L, with A being closest to the scanner (about 1 m away) and L the farthest (about 12 m away). The relative displacement between the positions is measured using a laser tracker placed in line with the rail and an SMR mounted on the nest assembly (Fig. 8a). The laser tracker is then removed and the laser scanner is placed in line about 1 m from position A. The contrast target replaces the SMR on the nest assembly.

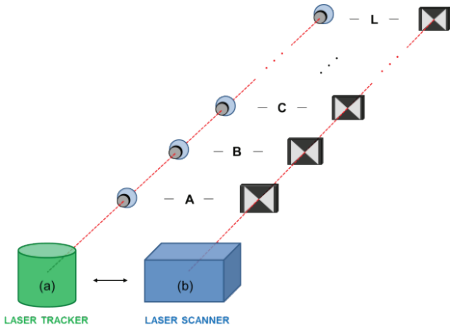

FIGURE 8. (a) The relative displacements between positions are measured by a laser tracker and SMR. (b) The tracker and SMR are replaced by the scanner and contrast target. We place the scanner 1 m from position A.

At each position, we perform four scans and average the point coordinates. The relative displacement between positions is compared to the reference measurements. We choose position B to be the 'zero', from which distances to all other positions are calculated. Position B is located near the previously mentioned 'sweet spot' for the laser scanner, hence will exhibit highest repeatability in target location. The difference in measured displacement is plotted as a function of nominal distance from position B (Fig. 9).

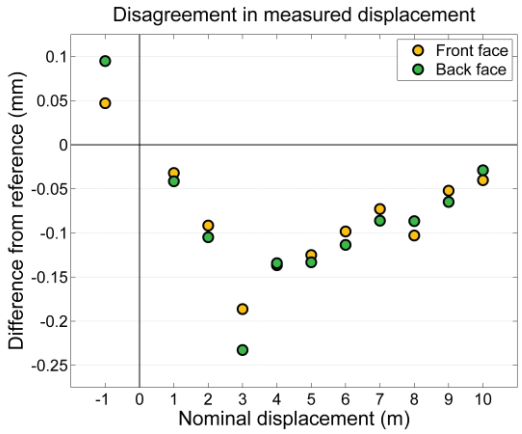

FIGURE 9. The displacement of the contrast target from position B to every other position is compared to reference measurements. The difference is plotted as a function of distance from position B. In this graph, the scanner is located at -2 m.

The ranging test was repeated and the results replicated. We observe that the pattern is not linear. We also note that the largest error

occurred at a displacement of 3 m from position B. This corresponds to a distance of 5 m from the scanner. This is contrary to general expectation that errors would monotonically increase with range. We investigate this behavior by measuring displacements around 3 m at higher displacement density (Fig. 10).

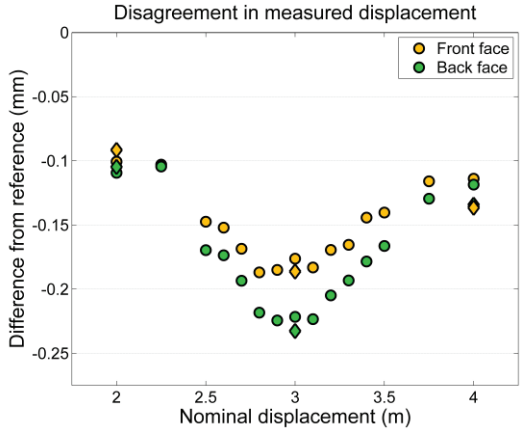

FIGURE 10. We investigate the observed 'dip' in error between scanner measurements and reference measurements. The circles are the new, high density measurements, whereas the diamonds are previous measurements.

The high density data confirms that there is a systematic pattern in ranging errors at a distance of 5 m from the scanner.

We recall the one standard deviation repeatability in detecting range of contrast targets was less than 6 μm and note that the errors observed here are at least an order of magnitude larger and therefore well above the noise floor. We should therefore be able to, in principle, model and remove these errors. We are working with the scanner manufacturer in understating the source of these errors.

The laser tracker employed to calibrate the inter-nest distance has an MPE specification of 4 μm + 0.8 μm/m, which has been independently verified using the NIST laser tracker ranging facility [6]. Hence, the laser tracker's error between the 2 m reference position and the 12 m position is no greater than 12 μm. This value is more than an order of magnitude smaller than the scanner's range measurement capability and is therefore suitable to obtain reference measurements.

CONCLUSIONS

By employing a highly repeatable contrast target and comparing our results to a reference instrument, we were able to design and perform tests that can evaluate the ranging performance of a commercial laser scanner. The results presented in the first part of this study indicate that the scanner has a –0.1 mm zero offset in the ranging direction. The ranging test performed on a long horizontal rail indicates that range errors are not linear. In fact, the largest observed error occurred at a displacement of 3 m from our reference target, which corresponds to a distance of 5 m from the scanner. A higher density range test was performed around this 'dip' in the plot, and the same phenomenon was observed. We also note that there were systematic differences in the measured ranging errors between the front and back face measurements. We continue to investigate this in current and future work.

REFERENCES

[1] Muralikrishnan B., et al., Volumetric performance evaluation of a laser scanner, Proceedings of the ASPE 2013, St. Paul, MN

[2] Blais F., Review of 20 years of range sensor development, Journal of electronic imaging, 13(1), January 2004, p: 231-240

[3] Peggs G.N., et al., Recent developments in large scale metrology, Proceedings of the Institution of Mechanical Engineers, Part B: Journal of Engineering Manufacture 223 (B6) 2009 pp. 571-595

[4] Disclaimer: Certain commercial equipment, instruments, or materials are identified in this paper in order to specify the experimental procedure adequately. Such identification is not intended to imply recommendation or endorsement by the National Institute of Standards and Technology, nor is it intended to imply that the materials or equipment identified are necessarily the best available for the purpose.

[5] MacKinnon D, et al., Proposed E57.02 Test Method to Evaluate the Range Measurement Performance of 3D Imaging Systems in the Medium Range, Proceedings of the CMSC 2013, San Diego, CA

[6] Blackburn C, et al., Common-Path Method for Laser Tracker Ranging Calibration, Proceedings of the CMSC 2013, San Diego, CA

THE FUTURE OF MANUFACTURING METROLOGY – A ROADMAP FROM THE ASSOCIATION OF GERMAN ENGINEERS

Marcin B. Bauza[1] and Dietrich Imkamp[2]
[1]Carl Zeiss Industrial Metrology, LLC
6250 Sycamore Lane N, Maple Grove, MN 55369
[2]Carl Zeiss Industrielle Messtechnik GmbH
73446 Oberkochen, Germany
Member of the Association of German Engineers

This reworked paper is reprinted with permission. This paper is a reworked release of a paper that was published as Berthold, J., Imkamp, D.,: Looking at the future of manufacturing metrology: Roadmap document of the German VDI/VDE society, Journal of Sensors and Sensor Systems (JSSS). The paper is published in the Internet (www.j-sens-sens-syst.net/2/1/2013/jsss-2-1-2013.html) under Creative Commons Attribution 3.0 License.

INTRODUCTION

'Faster, safer, more accurately and more flexibly' is the title of the 'Manufacturing Metrology Roadmap' issued by the VDI/VDE (The Association of German Engineers and Association for Electrical, Electronic & Information Technologies) Society for Measurement and Automatic Control. The document, drawn up by a group of German experts from research and industry, presents a view of upcoming developments in metrology for industrial production over the next ten years. The paper summarizes the contents of the roadmap and explains the individual concepts of 'faster, safer, more accurately and more flexibly' with the aid of examples from the field of dimensional metrology.

METROLOGY AND MANUFACTURING

Measurement is an integral part of modern industrial manufacturing. It forms the basis for the so-called system of interchangeable parts. Such parts are made to a specifications that ensure that they are so nearly identical that they will fit into any assembly of the same type. The definition of the specification is based on a internationally accepted unit system. Machines are required to do manufacturing according to the definition. Furthermore metrology equipment is needed to assure that the manufactured characteristics meet the specification (Figure 1). Therefore trends in manufacturing have a strong impact on manufacturing metrology.

Due to global megatrends manufacturing technology faces a number of challenges. The topics of resource efficiency, of mastering new process technologies, of increasing flexibility and of transparency have a special significance in manufacturing today (Figure 2).

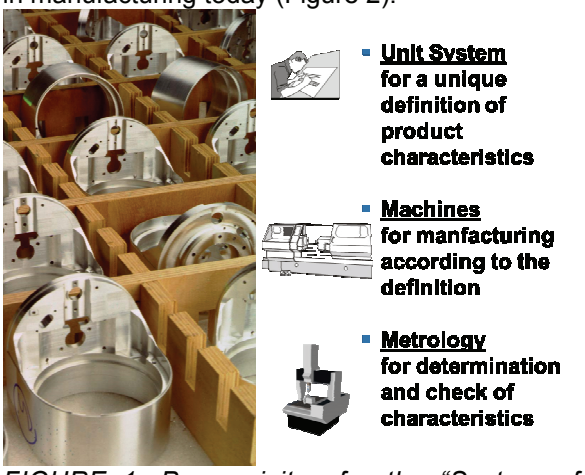

FIGURE 1. Prerequisites for the "System of Interchangeable Parts".

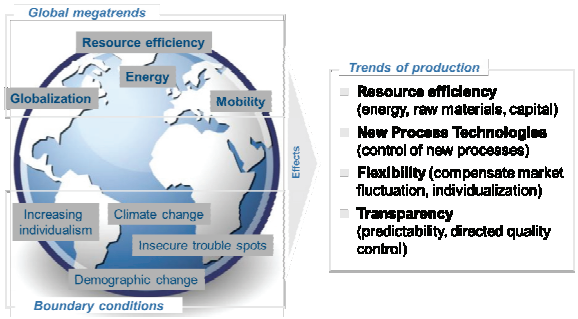

FIGURE 2. Global megatrends and trends in manufacturing technology.

At the same time the trend towards higher product quality continues. Globalization has made it possible for production to be linked up on a worldwide basis and, given this global context, the exchange of information is increasingly more important in securing product

quality. Much of this information, particularly as it relates to the status of products and production processes, is obtained with the help of metrology

Against a background of discussions about the supply of energy and shortages of raw materials, the subject of resource efficiency currently plays an important role in production as well. New methods in manufacturing can contribute to improving resource efficiency. To compile the data needed to evaluate efficiency manufacturing has to rely on measurement technology as well.

Manufacturing technology continues to face challenges arising from the customers' demand for individually designed products, a demand that is fluctuating and therefore requires a greater degree of flexibility. This is accompanied by a considerable reduction in batch sizes which can only be managed by a more intensive use of metrology since lengthy production start-ups and pilot production runs are no longer feasible. At the same time, more and more industry sectors of (such as aviation, medical devices) are calling for a seamless documentation of the conformity assessment for all manufactured products, a task that also relies on a more intensive use of metrology.

These are also examined in the technical committees of the 'Manufacturing metrology' department of the VDI/VDE Society for Measurement and Automatic Control where a work group has been formed which, in the light of the aforementioned trends in manufacturing technology, has set itself the task of producing a forecast for the future of manufacturing metrology, Figure 3.

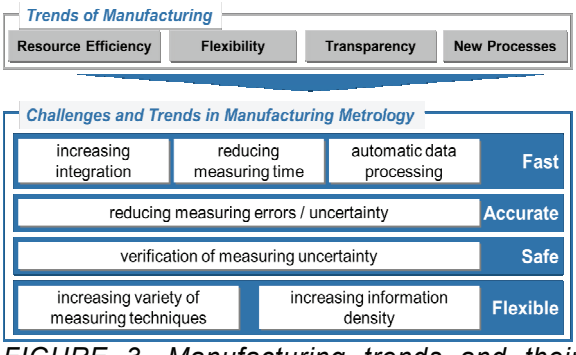

FIGURE 3. Manufacturing trends and their impact on challenges and trends in manufacturing metrology.

The results of this work have been published by the Verein Deutscher Ingenieure e.V. (VDI) under the title of 'Manufacturing metrology 2020: a technology roadmap for metrology in industrial production' [30]. Summaries have been presented nationally [14] and internationally [10, 27]. This present paper sets out the main results of the work.

The challenges and trends in manufacturing metrology can be captured by the terms 'faster', 'safer', 'more accurately' and 'more flexibly'. Particularly the topics of accuracy and speed are of central importance, as other studies of metrology show, such as, for example, the market study on 3D metrology prepared by the Fraunhofer Society [8] and the technology roadmap for process sensors in the chemical-pharmaceutical industry [31].

FASTER

On one hand, speed means the development and application of metrological procedures that allow for timely access to information about product quality. Here it is less a matter of developing procedures from scratch than of adapting a large number of known measurement principles for utilization in production. Optical methods play a significant role here [21], Figure 4.

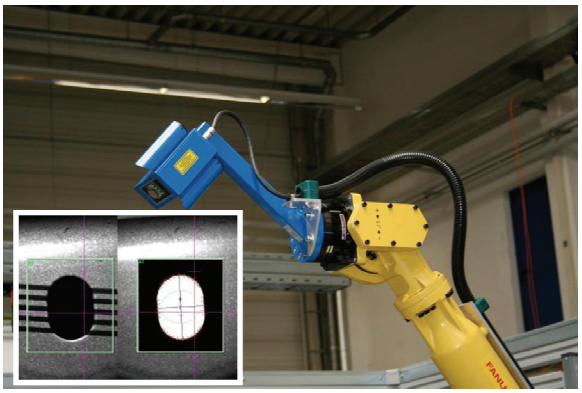

FIGURE 4. Faster metrology by optical capture of position tolerances for stamping holes during inspection of automotive bodywork with multi-line triangulation sensor on robots.

On the other hand, a tighter integration of metrology into production processes, especially by means of automation, will facilitate a faster delivery of measurement results as well as a more efficient use of measurement data.[15]. This integrative approach reduces or even eliminates the time required for product to be transported to the measuring equipment. Figure 5. Furthermore, the information from measurements is directly available in production, thereby allowing for the incorporation of control loops, for example. Regulation by means of an

automated transmission of data can be implemented with a particularly high level of efficiency [11].

FIGURE 5. Faster metrology due to the automated integration of metrology into material flow.

MORE ACCURATELY

Demands relating to the accuracy of measurement technology are also increasing in conjunction with stricter quality requirements. This change affects not only procedures in macrometrology [26] but also the micro- and nanometrology used for capturing product shape [4], Figure 6.

As tolerances become tighter in macrometrology, e.g. for drives in wind power systems [5], greater accuracy of measuring instruments is required. In this context it is worth noting that, in response to the requirements of industrial quality inspection with respect to traceability - to name only one requirement- techniques from geodesy are being used more frequently in manufacturing metrology [12]. Furthermore, progress in optical technology and fast low-cost computation leads to wide-spread application of laser trackers and digital photogrammetry for coordinate metrology [7]. In micrometrology higher levels of accuracy are also required as a result of increasing miniaturization [24]. Figure 7 shows the order of magnitude of these trends.

Demands for greater accuracy are also associated with the measurement of material properties [9] and electrical characteristics [22]. In this context it is not only important to optimize existing procedures but to monitor and correct environmental influences is equally if not more important.

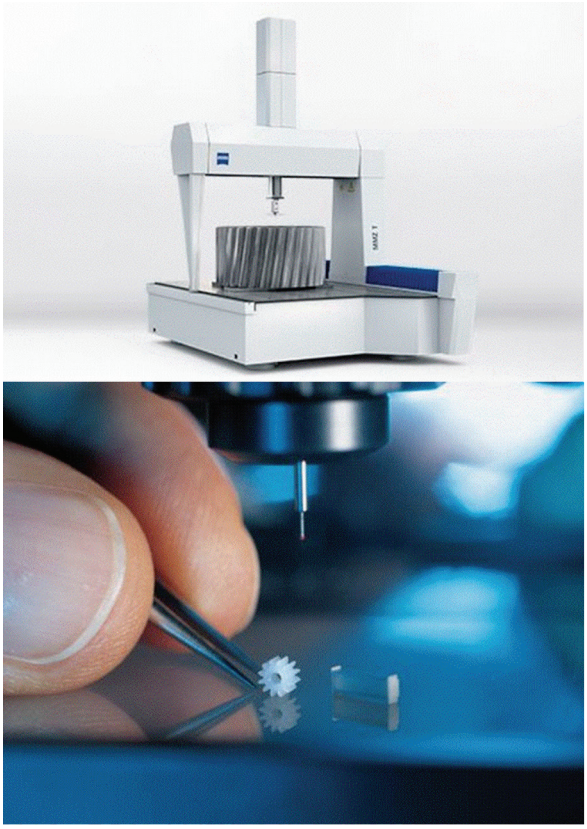

FIGURE 6. Range of gear metrology with coordinate measuring machines from macro-scale gears for wind energy systems [5] to micro-scale gears for watches [24].

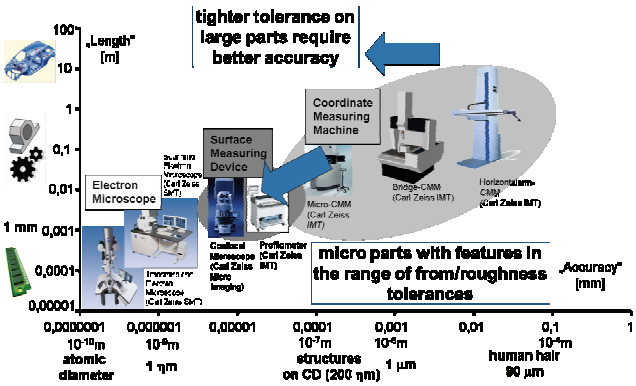

FIGURE 7. Tendencies in the development of accuracy in the case of instruments used in length measurement.

SAFER

It has become increasingly important to consider measurement uncertainty when performing the conformity assessment.

Standardized procedures for determining measurement uncertainty are becoming more

established but they are also readily modified and customized based on the task at hand. A calibration of standards requires an even greater emphasis on determining measurement uncertainty than an inspection of product characteristics. As far as production is concerned, simplified procedures will become the industry standard. Documentation on measurement uncertainty will likely be required for product impacting the overall safety of manufactured goods in industries such as the medical devices and aviation and this practice will drive improvements in safety[16]. In addition, the computer-aided simulation of measurement processes based on the Monte-Carlo method [19] for determining measurement uncertainty will become more important. In the meantime, however, implementations have become available for different measurement methods, in most cases in the form of prototypes [1, 13, 25, 29]. In the field of coordinate metrology, systems already on the market Figure 8 [33] are used specifically in the calibration of individual standards and normative publications are now available [18, 32].

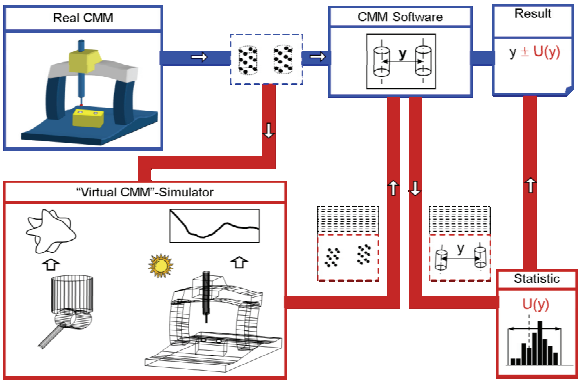

FIGURE 8. Determination of the measurement uncertainty of measurements in coordinate measuring machines by means of Monte-Carlo simulation: 'Virtual CMM' and its connection to the instrument software [33]

MORE FLEXIBLY

The wide variety of measurement methods used in production is increasing and with it metrology is becoming more flexible and adaptable. On one hand, techniques are used which holistically register the shape of a product. These include fringe projection and photogrammetry [2]. With the help of computer tomography it is even possible to register structures not accessible from the outside [3]. Today computer tomography is used to locate defects in castings or for running dimensional plausibility checks, to name only a few applications. Computer tomography systems already attain measurement times which allow for their integration into the clock-pulse controlled production process - in other words, in-line utilization [28].

On the other hand, different methods are often combined into measuring systems that are called multisensor measuring machines [17, 34], Figure 9. The combination of results from several sensors is called sensor fusion [11]. This boosts the flexibility of the systems. It does, however, also increase the complexity of measuring systems and therefore the demands imposed on the user with respect to training and the effort required to prepare for measurements.

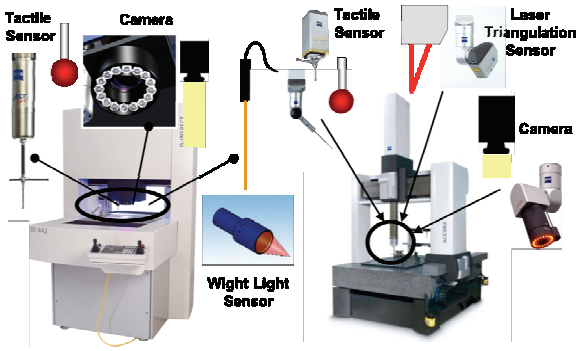

FIGURE 9. Multisensor coordinate measuring machine (left) with parallel sensors and with interchangeable sensors (right).

CONCLUSION

In addition to the technical aspects we have described, the 2020 manufacturing metrology roadmap [30] will include a future reassessment of the economic benefits resulting from metrology applications and the training of metrology equipment operators, not only in institutes of higher education, but also in the commercial sector. This topic is of special importance since the qualifications of measuring instrument operators have, in many cases, direct bearing on the accuracy of results and on their usefulness for driving continuous improvement in production.

Metrology will be increasingly important to industrial production. The enhanced performance capability of metrology is reflected by its greater speed and higher levels of accuracy. At the same time, it is becoming more flexible and able to deliver more data on production processes. Mastering the uncertainty of metrology in production will contribute to making production more efficient and products safer.

REMARKS

This paper is a reworked release of a paper that was published as Berthold, J., Imkamp, D.,: Looking at the future of manufacturing metrology: Roadmap document of the German VDI/VDE society, Journal of Sensors and Sensor Systems (JSSS). The paper is published in the Internet (www.j-sens-sens-syst.net/2/1/2013/jsss-2-1-2013.html) under Creative Commons Attribution 3.0 License.

REFERENCES

[1] Bai, A., Bitte, F., Pfeifer, T.: Der Einsatz von Simulationen zur Bestimmung der Messunsicherheit von Interferometern (English: Assessment of the Measurement Uncertainty of Interferometers by Means of Simulation), in: tm – Technisches Messen, Oldenbourg Industrieverlag, 69 (2002) 5 S. 27-32.

[2] Bauer, N. (Editor): Leitfaden zu Grundlagen und Anwendungen der optischen 3D-Messtechnik, Vision 6, Fraunhofer Allianz Vision, Erlangen 2003.

[3] Benninger, R., Bleicher, M., Berthold, J.: Mit Röntgenblick zum Allrounder - Roadmap Fertigungsmesstechnik 2020 (Teil 6), Qualität und Zuverlässigkeit QZ, 54. Jg., 2009, Nr. 10, S. 44-47.

[4] Bosse, H., Koenders, L., Schmitt, R.: Von Mikro zu Nano - Roadmap Fertigungsmesstechnik 2020 (Teil 3), Qualität und Zuverlässigkeit QZ, 54. Jg., 2009, Nr. 7, S. 28-31.

[5] DeGlee, G.: Measuring for Wind Energy, in: Wind Systems (windsystemsmag.com) OCTOBER 2010, page 42-47.

[6] Dutschke, W., Keferstein, C. P.: Fertigungsmesstechnik, praxisorientierte Grundlagen, moderne Messverfahren, 7. Auflage, Teubner Verlag, Stuttgart 2010.

[7] Estler, W.T., et al.: Large-scale metrology - An update, CIRP Annals - Manufacturing Technology 51(2) (2002) 587-609.

[8] Fraunhofer-Allianz Vision (Editor): Marktstudie 3-D-Messtechnik in der deutschen Automobil- und Zulieferindustrie, Fraunhofer Verlag Stuttgart, Erlangen 2010.

[9] Frenz, H., Schenuit, E.: Sinkende Toleranzschwelle - Roadmap Fertigungsmesstechnik 2020 (Teil 7), Qualität und Zuverlässigkeit QZ, 54. Jg., 2009, Nr. 11, S. 47-49.

[10] Grzesiak, A., Imkamp, D.: Faster, Safer With More Accuracy and Flexibility – The VDI Roadmap Manufacturing Metrology, Xth International Scientific Conference, Coordinate Measuring Technique, 23.-25. April 2012 University of Bielsko-Biala, Poland.

[11] Heizmann, M., Beyerer, J., Puente León, F.: Mehr Wissen durch Fusion von Sensordaten - Roadmap Fertigungsmesstechnik 2020 (Teil 2), Qualität und Zuverlässigkeit QZ, 54. Jg., 2009, Nr. 6, S. 35-39.

[12] Hennes, M.: Potentiale der Ingenieurgeodäsie im Maschinenbau, 3. Dresdener Ingenieurgeodäsietag, Berufliche Weiterbildung (BWB) Industriemesstechnik, TU Dresden, Geodätisches Institut, 1.6. 2007, S. 21-27.

[13] Hiller, J.: Abschätzung von Unsicherheiten beim dimensionellen Messen mit industrieller Röntgen-Computertomographie durch Simulation, Dissertation, Universität Freiburg 2011.

[14] Imkamp, D., Berthold, J.: Road to success – Der Weg der Fertigungsmesstechnik in die Zukunft, in: Qualität und Zuverlässigkeit QZ, 56. Jg., 2011, Nr. 9, S. 26-29.

[15] Imkamp, D., Frankenfeld, T.: Schnittstellen zur informationstechnischen Integration von Geräten der Fertigungsmesstechnik in die automatisierte Produktion, in: Tagungsband zur Automation 2009, 16.-17. Juni 2009, Baden-Baden, VDI Verlag Düsseldorf 2009.

[16] Imkamp, D., Sommer, K.-D.: Für eine sichere Fertigung, Roadmap Fertigungsmesstechnik 2020 (Teil 4), in: Qualität und Zuverlässigkeit QZ, 54. Jg., 2009, Nr. 8, S. 31-33.

[17] Hoben, F., Imkamp, D.: Multi Application Sensor System (MASS) - “Greater than the Sum of Its Sensors”, in: Innovation Metrology Special Nr. 9, Carl Zeiss Industrielle Messtechnik GmbH, Oberkochen, Germany 2007.

[18] ISO/TS 15530-4 Geometrical Product Specifications (GPS) - Coordinate measuring machines (CMM): Technique for determining the uncertainty of measurement - Part 4: Evaluating task-specific measurement uncertainty using simulation Ausgabe: 2008-06.

[19] JGCM 101:2008 Evaluation of measurement data — Supplement 1 to the “Guide to the expression of uncertainty in measurement” — Propagation of

distributions using a Monte Carlo method, JCGM (Joint Committee for Guides in Metrology) 2008 (Internet: http://www.bipm.org/en/publications/guides/gum.html).
[20] Kruth, J. P., et al.: Computed tomography for dimensional metrology, CIRP Annals - Manufacturing Technology 60 (2011) 821–842.
[21] Leibinger, P., Tünnermann A. (Editor): Agenda Photonik 2020 des Programmausschusses für das BMBF-Förderprogramm Optische Technologien, Düsseldorf, November 2010 (Internet: www.photonik2020.de).
[22] Naß, M., Berthold, J.: Basis neuer Messtechnologien - Roadmap Fertigungsmesstechnik 2020 (Teil 8), Qualität und Zuverlässigkeit QZ, 55. Jg. 2010, Nr. 1, S. 53-55.
[23] Pfeifer, T.: Production Metrology, Oldenbourg Verlag, München, Germany 2002.
[24] Porath, M., Seitz, K.: Dimensional Quality Assurance of Micro-mechanical Parts With a Coordinate Measuring Machine, International Conference on Micromanufacturing (ICOMM 2006), University of Illinois, Urbana-Champaign, USA, September 13-15, 2006 .
[25] Schmitt, R., Fritz, P., Jatzkowski, P., Lose, J., Koerfer, F., Wendt, K.: Abschätzung der Messunsicherheit komplexer Messsysteme mittels statistischer Simulation durch den Hersteller, in: VDI/VDE-Gesellschaft Meß- und Automatisierungstechnik –GMA (Hrsg.): Messunsicherheit praxisgerecht bestimmen, Tagungsbericht: 4. Fachtagung Messunsicherheit. 12. und 13. November 2008 in Erfurt, Düsseldorf: VDI Wissensforum, 2008.
[26] Schmitt, R., Jatzkowski, P., Nisch, S., Imkamp, D.: Größer, genauer und integrierter - Roadmap Fertigungsmesstechnik 2020 (Teil 5), in: Qualität und Zuverlässigkeit QZ, 54. Jg., 2009, Nr. 9, S. 31-33.
[27] Schmitt, R., Nisch, S., Heizmann, M., Bosse, H., Imkamp, D.: Production Metrology - Future Trends and Challenges, in: Proceedings of the 10th International Symposium on Measurement Technology and Intelligent Instruments (ISMTII-2011) Daejeon, S. Korea 29th June – 2nd July, 2011.
[28] Schnell, H.: Hochgeschwindigkeits-Computertomografie zur schnellen, zerstörungsfreien und intelligenten Inspektion und Prozessoptimierung von Aluminium-Gussteilen, Dissertation, Universität Erlnagen-Nürnberg, 2011.
[29] Schwenke, H.: Abschätzung von Messunsicherheiten durch Simulation an Beispielen der Fertigungsmesstechnik (Dissertation), PTB-Bericht F36, 1999.
[30] VDI/VDE-Gesellschaft Mess- und Automatisierungstechnik (GMA), Editor: Fertigungsmesstechnik 2020, Technologie-Roadmap für die Messtechnik in der industriellen Produktion, VDI Verein Deutscher Ingenieure e.V., Düsseldorf April 2011 ISBN 978-3-00-034706-1 (Internet: www.vdi.de/44080.0.html).
[31] VDI/VDE-Gesellschaft Mess- und Automatisierungstechnik (GMA), NAMUR (Interessengemeinschaft Automatisierungstechnik der Prozessindustrie) Editor: Prozess-Sensoren 2015+, Technologie-Roadmap für Prozess-Sensoren in der chemisch-pharmazeutischen Industrie, VDI Verein Deutscher Ingenieure e.V., Düsseldorf, NAMUR, Leverkusen, November 2009 (Internet: http://www.namur.de/publikationen-und-news/fachinformationen/roadmap-sensorik/).
[32] VDI/VDE-Guideline 2617 part 7 Accuracy of coordinate measuring machines - Parameters and their checking - Estimation of measurement uncertainty of coordinate measuring machines by means of simulation, April 2006.
[33] Trenk, M., Franke, M., Schwenke, H.: The Virtual CMM, a Software Tool for Uncertainty Evaluation - Practical Application in an Accredited Calibration Lab, ASPE Proceedings, Uncertainty Analysis in Measurement and Design, June 30 - July 1, 2004, The Nittany Lion Inn, Penn State University, University Park, USA, PA2004.
[34] Weckenmann, A., et al.: Multisensor Data Fusion in Dimensional Metrology, CIRP Annals - Manufacturing Technology 58 (2009) 701–722.

A HIGH-ACCURACY, MULTI-CHANNEL, FIBER-BASED DISPLACEMENT/ DISTANCE MEASURING INTERFEROMETER SYSTEM

Vivek G. Badami, Alexander D. Wesley and Lars A. Selberg
Zygo Corporation
Middlefield, CT, USA

INTRODUCTION

This paper describes a high-accuracy, high-stability multi-channel fiber-based interferometer system with compact sensors that combines high-accuracy displacement and absolute distance measuring capability [1,2,3]. This technology distinguishes itself from other fiber sensors in that it addresses applications requiring a relatively large number (up to 64 in a single system, more through synchronized systems) of thermally passive, electro-magnetic interference (EMI) immune, compact sensors with exceptional long-term drift performance and high reliability. Further, this device also provides a large standoff (~mm) and a large measurement range (~mm) with a dynamic range characteristic of interferometric sensors, i.e., this technology is not limited by the range-resolution trade-off characteristic of other sensor types [4].

PRINCIPLE OF OPERATION

This section describes the two operating modes of the sensor: an absolute distance measurement mode that establishes the position of the target relative to the sensor in an absolute sense and a displacement measurement mode that tracks the motion of the target from an initial position.

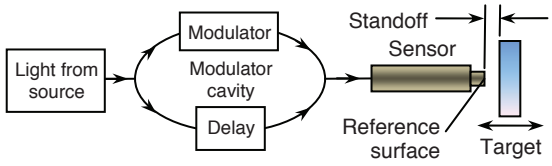

FIGURE 1. Principle of operation

Displacement measurement

In contrast to the absolute distance mode, *displacement* measurement is a relative measurement that tracks the distance moved by a target relative to an arbitrary (often user defined) zero position. This mode is “blind” to the absolute distance of the target. The coupled-cavity arrangement shown schematically in FIGURE 1 forms the basis of this mode operation. A relatively broadband (moderate coherence) source provides the illumination that is split into two paths at the input of the modulator cavity. The coherence length a tradeoff between providing adequate range and eliminating the effect of spurious reflections within the system that may form other cavities. One arm of the modulator cavity modulates the frequency of the light in that arm, while the other arm introduces a fixed phase delay. The modulated and delayed light combines at the output of the cavity. The combined radiation enters a second Fizeau cavity comprised of the sensor reference surface and the target via an optical fiber. Both surfaces reflect portions of the two beams. The portions reflected by the target traverse an additional optical path due to the round-trip to the target. This additional phase delay matches the delay imposed within the modulator cavity. The result is that the optical path lengths traversed by an unmodulated beam reflected from the reference surface and a modulated beam reflected by the target match and interference occurs at the frequency of the modulation. This phase of this frequency modulated AC signal is related to the target displacement, which is extracted using phase measuring techniques. The coherence of the source and delay in the modulator cavity independently determine the measurement range and standoff respectively. This sensor configuration has a number of advantages, including:

- Accessible reference surface to register the measurement datum to a metrologically relevant point in user’s metrology frame
- Independent control of standoff and measurement range
- Large standoff and high dynamic range, i.e., large measurement range with interferometric resolution.
- Elimination of all heat generating components from the sensors

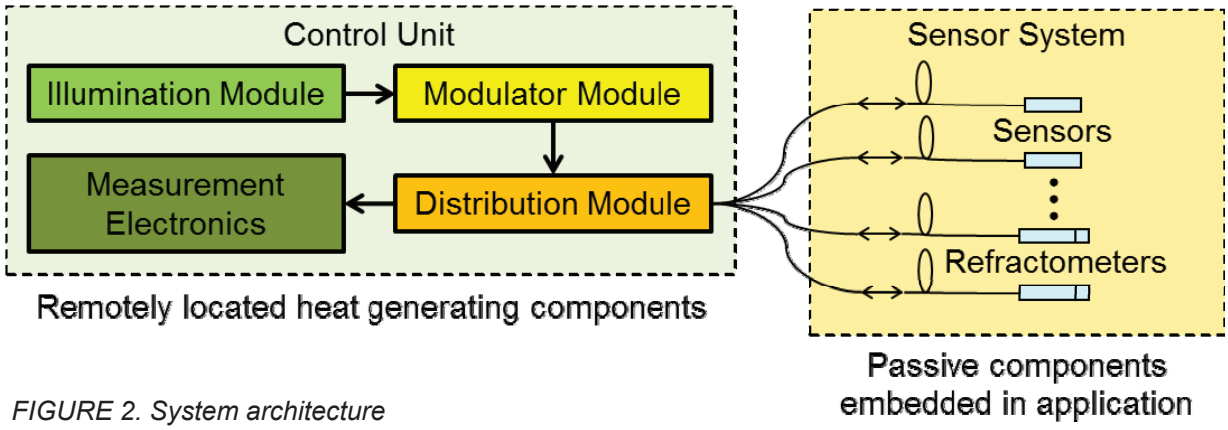

FIGURE 2. System architecture

Absolute distance measurement

The sensor is also capable of measuring the absolute distance of the target from the reference surface. This capability is a natural consequence of the operating principle of sensors such as capacitance gages and triangulation sensors and is typically not available in interferometric sensors due to fringe order ambiguity. In this sensor, the method of exact fractions (due to Michelson and Benoit [5]) forms the basis of this functionality. In this technique, the fringe fraction from the "synthetic wavelength" of (whose length is driven by the maximum distance between the target and the reference surface) provides fringe order information for shorter wavelengths (either a single wavelength or a shorter synthetic wavelength). Two shorter, closely spaced wavelengths generate the synthetic wavelength. Fringe fraction information from the synthetic wavelength resolves the fringe order ambiguity in either of the shorter wavelengths. A combination of the fringe order information from the synthetic wavelength and the fringe fraction from one of the shorter wavelengths enables the determination of the absolute position of the target relative to the reference surface. This capability provides homing capability, i.e., allows the targets to return to known starting positions in the presence of beam interruptions and power cycling. Three wavelengths generate two synthetic wavelengths to establish the absolute position.

A typical measurement sequence starts with the relatively slow (low bandwidth) measurement of the absolute initial position of the target relative to the reference surface while the target is stationary. The system then switches to the displacement measurement mode that tracks the target motion at the full bandwidth of the instrument using a single wavelength.

SYSTEM ARCHITECTURE

The system consists of five functional modules as depicted in FIGURE 2. The control unit contains the illumination, modulator, distribution and measurement electronics modules and is remotely located. This serves to isolate the measurement apparatus from the heat generated by active components within these modules. It also facilitates serviceability by confining components that may require maintenance to an area outside the machine envelope. Embedding only the high-reliability passive sensors within the machine obviates the need for entering the machine envelope for maintenance, thereby minimizing downtime. This arrangement also confines all the electronics to a remote unit, thereby eliminating a potential source of EMI. Optical fibers connect the sensors to the control unit, making it possible to place the sensors at relatively large (tens of meters) distances from the control unit.

Illumination Module

The illumination module provides the moderately coherent (when compared to a laser) radiation at multiple wavelengths, which are used to implement the method of exact fractions for the determination of absolute distance. Displacement measurements rely on a single wavelength.

Modulator Module

The output of the illumination module feeds the modulator module, which imposes the frequency modulation on the incoming radiation and generates a phase delay between the modulated and unmodulated components. This module also contains stable etalons that track any phase drift in the modulator cavity and changes in the calibrated value of the illumination wavelengths.

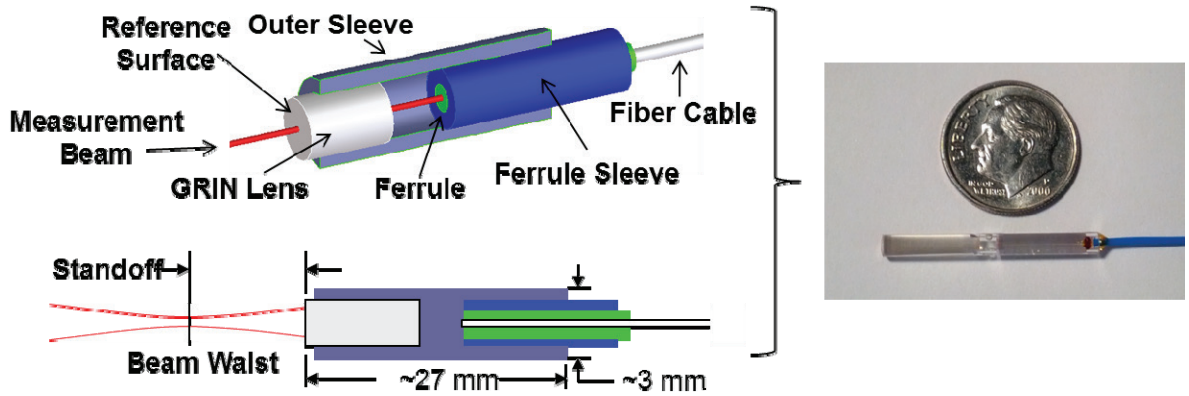

FIGURE 3. Details of sensor construction

Distribution Module

The modulated and phase-shifted output of the modulator reaches the sensors via the distribution module. This module also serves to collect the reflected light from the reference and target surfaces and returns it to the detectors in the measurement electronics.

Measurement Electronics

This module converts the optical interference signal into an electrical signal. The signal from each sensor is processed using phase measuring techniques to extract the displacement. The processing also factors in the refractive index data from the refractometers (specialized sensors that directly measure index of refraction). A high-speed data interface makes the digital position data available to the end-user.

Sensor System

The sensor system is comprised of the sensors embedded in the application. The sensors are constructed from standard telecom fiber components and exploit the reliability of the components and assembly processes developed for this industry. FIGURE 3 shows the details of sensor construction and the approximate dimensions of these extremely compact sensors.

The basic sensor is a fiber collimator, with a gradient index (GRIN) lens serving to collimate the light emanating from the fiber. This lens also couples the reflected light back into the fiber. Sensor reliability stems from the simplicity of the construction and the small number of passive components. The exposed surface of the GRIN lens (the reference surface) reflects part of the incoming light to form the reference beam for the interferometer. This surface provides a well-defined measurement datum, i.e., measurements are made relative this surface. This surface is accessible to the end user to facilitate registration of this datum with the reference frame of the user's metrology system. This in contrast to other displacement sensors of this type where the sensor mount becomes part of the metrology loop thereby making mount instabilities a source of measurement uncertainty.

The collimated beam exiting the sensor has a waist located at the standoff distance of the sensor. This feature provides tolerance to target tilt of a few mrad (to accommodate angular error motions of the mirror, intentional tilts or alignment errors) over the measurement range of the sensor.

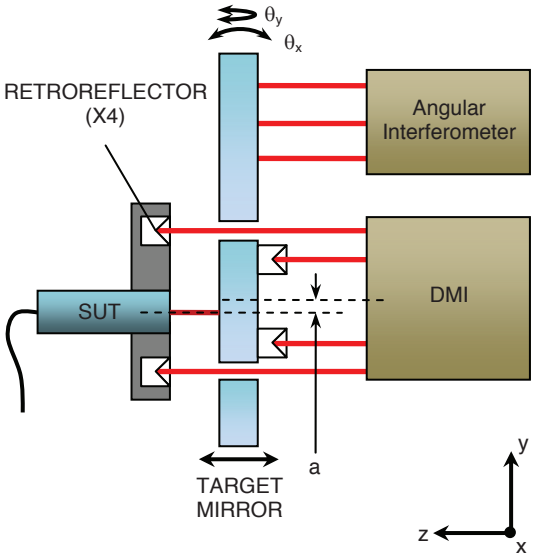

FIGURE 4 Sensor calibration setup

TABLE 1. System specifications

Parameter	Value	Parameter	Value
Number of channels	64	Bandwidth	100 kHz
Measurement range	1.2 mm	Noise over full stroke (3σ)	0.014 nm-Hz$^{-1/2}$
Standoff	3.5 mm	Drift	1 nm/day
Scan-to-scan repeatability	1 nm	Linearity	2 nm

The accuracy of the interferometric measurement depends on knowledge of the refractive index of the medium in which the sensor operates. Index data comes from one or more refractometers that continuously monitor the index. The refractometer is a modified sensor with a built-in etalon of known length whose cavity communicates with the ambient atmosphere. The absolute phase difference between the beams reflected from the two surfaces of the etalon provides a measure of the absolute refractive index. Unlike index measurement methods that rely on the "weather station" approach, this technique can measure the index of any medium, i.e., does not require knowledge of the environmental parameters and the index, and is also sensitive to changes in the composition. High accuracy applications may require several refractometers to mitigate the influence of index gradients.

SYSTEM CALIBRATION

The system is calibrated by comparison against a stabilized He-Ne laser. A custom setup (FIGURE 4) is used to perform the calibration [6]. The arrangement makes simultaneous measurements of displacement of a common target with the sensor under test (SUT) and a differential measurement between the sensor mount and target with a He-Ne based displacement-measuring interferometer (DMI). Errors due to any residual Abbe offset are corrected using information provided by an angular interferometer that monitors the target's angular error motions. This calibration establishes the length metric, i.e., provides a traceable transfer of the unit of length through a NIST traceable standard and establishes the illumination wavelengths and other system parameters.

SYSTEM PERFORMANCE

The system performance as it relates to displacement and distance measurement is evaluated by several different methods. *TABLE 1* summarizes the system specifications and performance.

Linearity & scan-to-scan repeatability

Linearity is measured on the calibration setup and is the deviation from the linear fit that establishes the calibration constant of the system. Multiple scans are performed to establish the scan-to-scan repeatability.

Noise performance & stability

System noise performance and stability are characterized by recording the output of the system over different sampling rates and time scales while monitoring a mechanically, thermally and temporally stable measurement cavity. Coupling the reference surface and the target through a small rigid spacer to form an etalon ensures mechanical stability (eliminates relative vibration between the reference and target surfaces). The optical contacts between the spacer and the two surfaces and spacer ensure temporal stability at a level adequate for this test and the low coefficient of thermal expansion of the spacer material ensures thermal stability. The standard deviation of the data collected at a sampling rate appropriate to the desired bandwidth over a short time period is a measure of the system noise. The maximum variation of sparsely sampled data (in the temporal sense) over an extended period (~10 hours) is a measure of the long-term stability of the system. These data are also a measure of the repeatability associated with the determination of the absolute distance.

SUMMARY

We describe a compact, multi-channel, fiber-based Interferometer system capable of both displacement measurement and absolute distance measurement. This sensor technology offers several advantages over similar displacement measuring technologies, notable among which are the small sensor size, large dynamic range at a large standoff, an accessible measurement datum, low noise and exceptional stability.

ACKNOWLEDGEMENTS
The instrumentation described in this paper represents the work of scientists and engineers in the Precision Positioning and R & D groups at Zygo.

REFERENCES

[1] Badami VG, Deck LL, Fletcher CD, Selberg LA, Winkowski DO, Egashira Y, et al, Compact, multi-channel, fiber-based absolute distance measuring system. In: Proc. of the 24th ASPE Annual Conference; Monterey, CA, Raleigh: ASPE; 2009. p. 67-70.

[2] Deck LL, High-performance, multi-channel, fiber-based absolute distance measuring interferometer system. In: Postek MT, Allgair JA, editors. Proc. SPIE 7405: Instrumentation, Metrology, and Standards for Nanomanufacturing III; San Diego, CA, Bellingham: SPIE; 2009. p.74050E.

[3] de Groot P, Deck LL, Zanoni C, inventors; Zygo Corporation, assignee. Interferometer system for monitoring an object. United States patent US 7,636,166 (2009 Dec 22) and US 7,826,064 (2010 Nov 2). Additional US and foreign patents pending.

[4] Badami VG, de Groot PJ, Displacement measuring interferometry. In: Harding K, editor. Handbook of optical dimensional metrology. New York: CRC Press; 2013. p. 157-238.

[5] Michelson AE, Benoît MR, Valeur du m`etre en longueurs d'ondes, Trav. et Mem. Bur. Poids. et Mes. 1895; 11-1.

[6] Badami VG, Fletcher CD, Validation of the performance of a high-accuracy compact interferometric sensor. In: Proc. of the 24th ASPE Annual Conference; Monterey, CA, Raleigh: ASPE; 2009. p. 112-115.

CLOSED LOOP THERMAL CONTROL OF A LITHOGRAPHIC OPTICAL COMPONENT

Rudolf Saathof[1], Aleksandar Haber[2], Jo W. Spronck[1], Michel Verhaegen[2], Robert H. Munnig Schmidt[1]
[1]Precision and Microsystems Engineering- Mechatronic System Design
[2]Delft Center of Systems and Control
Delft University of Technology, Delft, The Netherlands

Abstract
In EUV lithography the high throughput and high absorption can cause thermal deformation of the mirrors, which induces image distortion. In a previous paper [1] we have presented an actuation mechanism that is suitable to compensate and correct for these thermal aberrations. In this paper we present a closed-loop control strategy to apply it on this actuation mechanism and its application on an experimental set-up.

INTRODUCTION

Three important topics in optical lithography are the simultaneous performance on high throughput, image quality and overlay while it is widely known that these topics have a rather contradictory than a complementary character. In this research project we focus on the compromise between high throughput and image quality, where we look at the optical system. As part of Moore's law with decreasing cost per active element, the cost of ownership of a lithography tool needs to be as low as possible. Amongst others, this can be achieved by tools with a high throughput, realized by fast stages, high transmission optics, high sensitivity resist and high power light sources. Furthermore, Moore's law also drives the improvement of resolution resulting in optical systems with high numerical apertures, enhancing the imaging process using off axis illumination, phase shifting masks and optical proximity correction and decreasing the wavelength [2], which motivates the use of Extreme Ultra Violet (EUV) light [3]. Since EUV light is absorbed by all materials reflective instead of transmissive optics is used. Still, the mirrors absorb radiation, decreasing the optical transmission significantly, which demands an even higher light source power. Additionally, this absorption causes a local increase of temperature of the mirrors, which causes them to deform accordingly. These deformations result in wave-front errors, which can cause image degradation like image blurring and distortion [4].

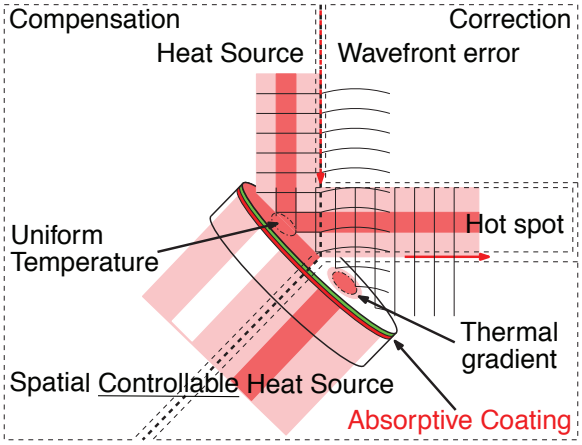

FIGURE 1. Active mirror concept: An absorptive coating absorbs radiation from a spatially controllable heat source. The compensation aspect of this actuation concept exposes an irradiance profile opposing to the heat source profile, creating a uniform temperature. The correction aspect is based on the principle of thermal expansion; thermal gradients cause local deformations. These deformations correct the wavefront error from other components in the optical system.

In this project we aim to correct for these aberrations, by means of an adaptive optics system. In traditional adaptive optics systems, actuators are mounted between a reference frame and the deformable mirror [5]. Because vibrations originating from the environment can excite the mirrors through this reference frame, they have to be avoided. Furthermore, mounting actuators may induce mechanical stresses which can lead to creep. Therefore, we studied a contactless thermal correction mechanism [1], where a radiating heatsource with a spatially distributed irradiance pattern actively heats up and deforms the mirror surface as shown in Figure 1. The first aspect of this active mirror concept is actively applying an irradiance pattern opposing the predicted pattern from the lithographic process. This results in a uniform temperature distribution, which elim-

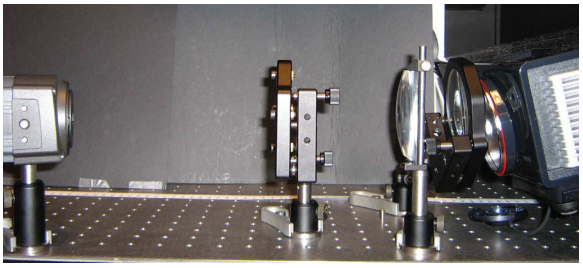

FIGURE 2. The experimental set-up consisting of a thermal camera (left), a glass substrate with an absorptive layer (centre) two lenses to project the irradiance from a projector (right).

inates the aberration caused by this active mirror, defined as compensation. Second, residual wave front aberrations are corrected by using the thermal expansion of the substrate material. By applying local temperature differences, the surface will locally deform, defined as correction. The integration of these two functions is realised by applying an absorptive layer on the mirror substrate, and on top of this layer a reflective coating is deposited. A spatially controllable heat source is used to expose the absorptive layer with a certain desired irradiance pattern. In this manner the actuation can be applied from the backside of the mirror, while influencing the front side of the mirror.

However, previously only open-loop experiments have been done [1], in which only limited accuracy is acquired. Restrictions of the accuracy are first, the thermal conductivity in the substrate material, so the heat input on one point on the mirror substrate is influencing the entire substrate. Second, the prediction of the disturbance caused by the EUV light may have limited accuracy, and its correction may be incorrect. Third, there is disturbance by parasitic irradiance patterns, which consist of a non uniform heat exchange caused by an environment which has a non-uniform temperature distribution. Therefore, we want to apply feedback control on the active component. In this paper feedback control is applied on the thermal distribution and consists of three experiments: the active component is kept at a homogeneous temperature to prove the compensation aspect; a step response is used to see the speed and a thermal profile is imposed to prove the correction aspect of the active mirror.

EXPERIMENTAL SETUP

In order to realise a control strategy in real time, an experimental set-up is built, which is shown in Figure 2. The set-up consists of a BENQ SP870 5000 ANSI lumens video projector, a Bk7 glass substrate of 50×50 [mm], a FLIR A315 thermal camera and a computer. The projector acts as the spatially controllable heat source and has a total maximum optical power of about 1.5 [W] and projects a grey scale Matlab figure. Because the projector has a gamma γ correction, the relation between the grey scale value of the exposed pattern u and the irradiance Q is exponential by $u^{\gamma} = Q$, this non-linearity is compensated by $u = U^{\frac{1}{\gamma}} + 0.5$. In this relation u can vary from 0 to 1.

Two lenses are used to project the irradiance profile on the glass substrate close to the video projector, which results in a smaller picture, but a higher irradiance. The glass substrate has an absorptive coating that absorbs the irradiance originating from the projector. This is a broad-band coating for visible light, which absorbs 96% of the incident light. Before doing experiments, the substrate is brought to a steady state temperature, higher than its environmental temperature by exposing it with half of the power of the projector to enable cooling as well as heating. The temperature of the glass substrate is measured using the thermal camera and its measured data is processed in the computer with Matlab 2011a, using the image processing toolbox.

A checker-board pattern is used as an alignment tool, to align the video projector and the thermal camera. This alignment is done by physically moving the hardware and by adjusting settings in the software. The irradiance pattern exposed to the substrate is a Matlab figure, which can be placed arbitrarily in the projection of the video projector. Furthermore, the area of interest on the thermal camera is 160×160 out of 240×320 pixels, which can easily be shifted over the thermograph. This number of pixels is convenient for choosing different numbers of grid-points, which consist of sectors in the area of interest. In this sense, the size of the exposed Matlab figure is of more importance than the exact location. This flexibility is however limited, since it is desirable to cover the largest possible area of the video projector, since it increases the amount of used power.

The imaging processing is depicted in Figures 3 and 4. First, when the substrate is in its thermal equilibrium as described before, a reference ther-

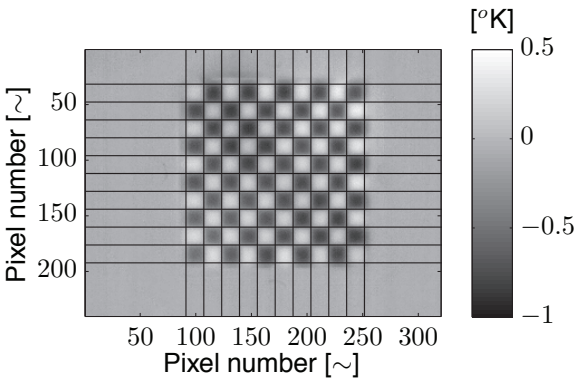

FIGURE 3. A checker-board pattern is exposed to the glass substrate as a tool for alignment. This thermograph is made by the thermal camera. The set-up is aligned, such that a complete picture takes 160×160 pixels.

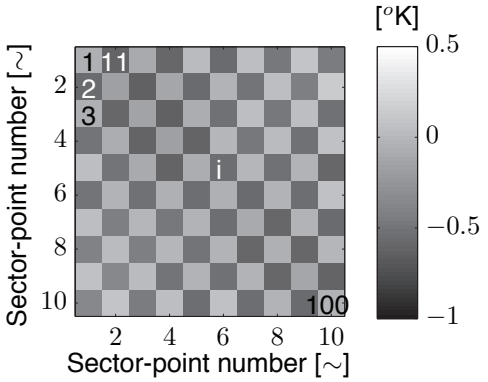

FIGURE 4. The raw data of the checkerboard pattern in figure 3 is processed to obtain this figure. This image is used for determining the contrast, which is the temperature difference between the sectors. These sectors are for control, in which they act as the sensor signal.

mograph is taken, consistent of the mean value of 25 thermographs, which is subtracted from each following measurement. Second, flickering of the whole thermograph is observed. As a stable temperature reference, an aluminium block is placed on the left side in Figure 3, covering the not exposed area between pixel numbers 1 and 50. The average temperature of the aluminium block is subtracted from the total image, which removes the flickering of the thermograph. Third, the area of interest in the thermograph is selected. Fourth, a grid is defined, which is shown by the lines in Figure 3, which defines the sectors of interest. Fifth, the average temperature of the individual sectors are taken, which function as the sensor signals for control. This spatial averaging is used to suppress the noise level of the thermal camera. The result of this image processing is shown in Figure 4.

The control loop is closed according to Figure 5. For this purpose the processed thermograph is compared with the desired image. The difference or error is used to apply the control algorithm as explained in the next section. Then a Matlab figure is projected on the glass substrate, containing the control irradiance, which heats up the substrate. Because the image processing and the control actions must happen within the sample time, we kept track of the time taken by the process. Because the thermal process is slow, the sample time can be chosen low, which is advantageous; imaging processing usually is time consuming. For a grid of 10×10 sector-points pre-processing of the data costs 3 [ms], which mainly consisted of spatial averaging of the thermographic data. The total loop time except acquiring the data, is 15 [ms]; the sampling time itself was 267 [ms]. This indicates that processing time is sufficiently small relative to the sample time to extend the control algorithm, or apply a denser time or spatial sampling.

CONTROL STRATEGY

Consider Figure 5 for the control strategy. By projecting a Matlab figure with the projector, the irradiance distribution Q can be controlled, and is exposed to the glass substrate GS. The irradiance is absorbed by the absorptive layer on the glass substrate, which heats up locally and gets a distributed temperature T. The temperature field causes emittance of infra-red IR radiation, and is captured with the micro-bolometer in the thermal camera. The glass substrate is heating up in a distributed sense; exposure of one point on the glass substrate will influence the entire glass substrate. This influence is weaker for points further away from the exposure of light.

The reason to apply closed-loop control is to reject disturbances d. These are due to the lab environment, which is temperature and moisture controlled, and therefore there is an airflow. Furthermore, the video projector is creating heat, which causes thermal gradients in the air. Additionally, there is a convective heat-flow, caused by the heating of the substrate, that transports heat from the bottom in the x-y plane of the substrate to the top, causing the upper side to be warmer than the bottom. The thermal coupling in the glass substrate is not taken into account; and the intensity

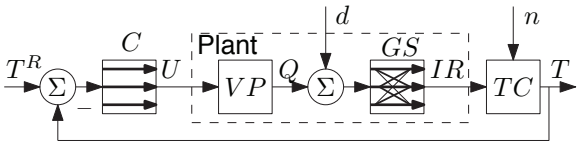

FIGURE 5. The closed loop system schematically. The reference is assigned as T^R, the controller C, which gives the control signal U to the video projector VP, which exposes the glass substrate GS with a irradiance Q and a disturbance irradiance d. This substrate heats up and emits Infra Red (IR) light, which is measured by the thermal camera TC, which has some noise n and is sent to the computer as the output signal T. In the controller and the glass substrate, arrows indicate the coupling: the controller has no coupling, but the substrate has. Three channels are shown; the thicker the line, the stronger the coupling.

of the video projector is not exactly uniform, which also needs to be taken into account. Finally, the performance of the control is limited by the sensor noise n.

To define the control strategy, a control grid has to be defined as shown in Figure 4. For that purpose the glass substrate is partitioned in 100 sectors, assigned with a number, which are Single Input, Single Output (SISO) controlled using Proportional Integral (PI) controllers in Matlab. These controllers have the following form:

$$u_i(t) = k_p e_i(t) + k_i \int_0^t e_i(\tau) d\tau, \qquad i = 1, \ldots, 100 \tag{1}$$

where $u_i(t)$ is the actuator signal at time instance t at the i^{th} sector, $e_i(t) = T_i^R(t) - T_i(t)$ is the error, in which $T_i^R(t)$ is the reference temperature and T_i the measured temperature; k_p is the proportional and k_i the integrative gain. By discretising Equation 1, the discrete-time PI-controller is obtained [6]:

$$u_i(m) = u_i(m-1) + (k_p + k_i T_s) e_i(m) - k_p e_i(m-1), \tag{2}$$

where $i = 1, \ldots, 100, m = 1, 2, \ldots, M$, m is the discrete time instance and M the last time instance.

EXPERIMENTS

In order to choose effective spatial sampling, the first experiments were to determine the noise on the thermal camera and the attainable contrast. The results of these experiments are shown in Figure 6. First, different sample frequencies are used to see whether the noise level is related to the sample frequency of the thermal camera. Furthermore, the spatial sampling is also altered to see the effect of the applied spatial averaging. It is observed that the noise level is lower when less spatial samples are taken, as is expected. Second, the achievable contrast is dependent on the alignment, the power level of the video projector and the uniformity of the video projector over time and space. In this paper the contrast is defined as the temperature difference between neighbouring sectors, when a checker-board pattern is exposed to the glass substrate, see Figure 4. Three levels of contrast were obtained; a minimum contrast, a mean contrast and the maximum contrast. When the noise level of the thermograph is higher than the attainable contrast, the contrast will disappear in the noise. Therefore, this three different contrast values give the realisable contrast using closed loop, and the potential improvement of the set-up.

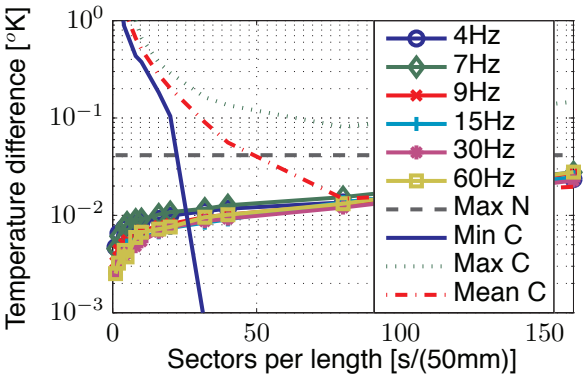

FIGURE 6. This graph is used to determine a suitable number of sectors. The lines with the marks indicate the noise level of the thermal camera. In order to decrease the noise level below the NETD of the camera of 45 [mK], indicated with the dashed line, the thermograph is spatially averaged. This is done for the various sample frequencies of the thermal camera, to see whether the noise is sample frequency dependent. The number of periods is also used to determine the attainable contrast. The contrast is determined, by exposing the substrate with a checker-board pattern and defined as the difference in temperature of neighbouring sectors. The minimal contrast should not be lower than the noise level in order to expose a thermal profile accurately.

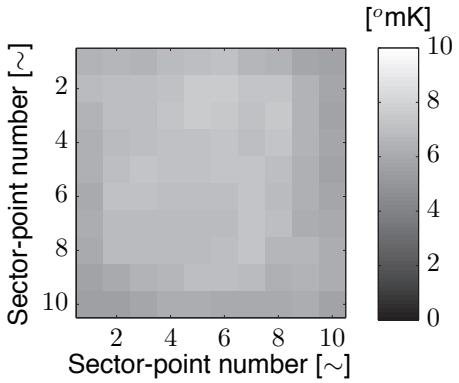

FIGURE 7. The accuracy of the thermal profile is limited by the noise level of the thermal camera. This graph shows the RMS of the residual noise during control of the glass substrate. In this graph the maximum RMS value is 7.6 mK, which corresponds to the measurement presented in Figure 6.

Three different closed loop experiments are carried out: in order to fulfil the compensation aspect of this active mirror concept, the mirror surface is controlled to have a uniform temperature, which reveals the control accuracy. In this experiment the RMS value of the error is observed. Additionally, for the correction aspect the speed of the controlled system and the ability to create a certain distributed thermal profile is relevant. First, the substrate is heated with a spatial distributed irradiance. After 35 [s] of exposure, the substrate is controlled to have a homogeneous temperature. Second, the mirror is controlled to the reference image in Figure 10. This closed loop result is compared with an open-loop experiment as shown in Figure 9, where this reference pattern is directly exposed to the substrate. In all the experiments a k_p and a k_i of 2.5 are used.

RESULTS

First, the performance in therms of static noise suppression is presented. Consider Figure 7, which shows the RMS error during control, over 1024 samples. In this graph the RMS error is 7.6 [mK] with a grid of 10×10 sectors and for a 20×20 sectors the maximal RMS value of the error was 10 [mK]. The residual noise level is equal to the noise level of the thermal camera. So by improving the performance of the thermal measurement, the thermal error can be suppressed further.

Second, the substrate is exposed to a irradiance and cooled down to its equilibrium state with a irradiance pattern as the Reference in Figure 10.

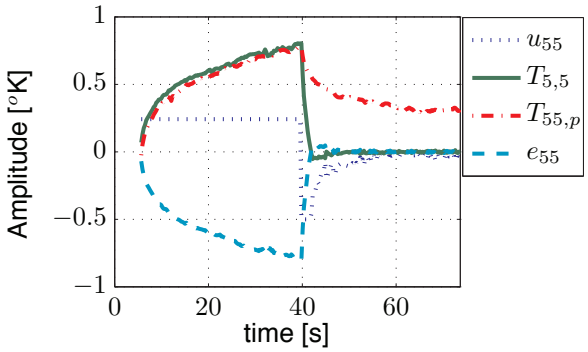

FIGURE 8. This figure shows that the temperature can be rapidly brought to a desired temperature using a PI control strategy. The passive behaviour of heating up and cooling down on sector no. 55 on the substrate is indicated by $T_{55,p}$. In the closed loop experiments, a rapid cooling is shown by T_{55}, u_{55} indicates the input, and e_{55} is the residual error.

Initially, it is heated and cooled down passively, and next actively with the control strategy, to have a fair comparison. Figure 8 shows how the temperature difference develops over time for one sector on the substrate. The passive behaviour is similar to an RC circuit as is expected. By the active control strategy the time constant decreases a factor of 10.

Third, as shown in Figure 9 and mentioned before, disturbances deteriorate the possibility to do open-loop control. The main causes for the errors shown in Figure 9 are the absence of an inverse model, which is still under development; and non-uniform heating, caused by the uniformity of the projector and heat transport caused by convection due to the increase of the substrate temperature. The control of a desired thermal profile, is compared with the current open-loop version. This results in a measured ΔT shown in Figure 9. What is shown in the figure, is that the error is as small as measured before in Figure 7. Furthermore a small gradient shows up in the actuator input. Additionally, in the actuation signal, there is a pattern, which has its similarities compared to the measured temperature in Figure 9, which clearly indicates the need of an inverse model.

DISCUSSION AND CONCLUSIONS

In this paper the feasibility of a feedback control consisting of 100 simultaneous SISO, PI controllers on the thermal distribution on a glass substrate is shown. This is a step in the development of an adaptive optics system suitable for

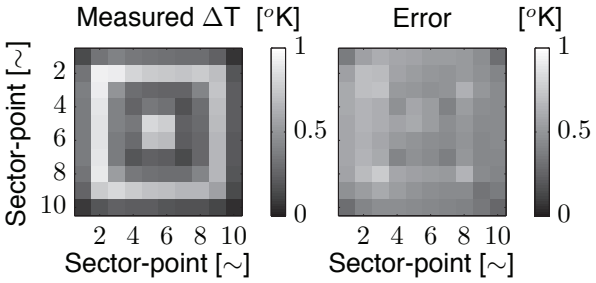

FIGURE 9. This figure shows the open-loop behaviour when the reference of Figure 10 is used as an input. Because of the conductivity of the material, the heat leaks away from one sector to the other. Therefore, we see some typical phenomena in the sectors diagonal to the corners of the squares.

EUV Lithography, to correct for thermally induced aberrations. We proposed an active mirror concept based on the principle of thermal expansion. First, the experimental substrate is controlled to have a uniform temperature, to prove compensation of the thermal impact on the active component itself. In this paper we showed the feasibility of this, by controlling the surface temperature with an RMS of 7.6 [mK]. This level of accuracy is limited by the performance of the thermal thermal camera. Second, we showed that if undesired thermal differences exist, they can be rejected within seconds. The speed of correction is related to the power of the spatially controllable heat-source, the sampling time and feedback gains. And third, we showed that it is possible to accurately control a non-uniform temperature distribution, which corresponds to a certain mirror deformation. In the future course of this project this deformation will be precisely measured.

ACKNOWLEDGEMENTS

The Dutch "Pieken In de Delta" is acknowledged for supporting this research project and TNO for making the absorptive coating.

REFERENCES

[1] Saathof R, Spronck JW, Munnig Schmidt RH. Evolving research on a non-contact adaptive optic actuation method for wavefront correction. In: Proceedings of the 11th euspen International Conference. Como, Italy; 2011. .

[2] Mack C. Fundamental principles of optical lithography: the science of microfabrication. Wiley-Interscience; 2008.

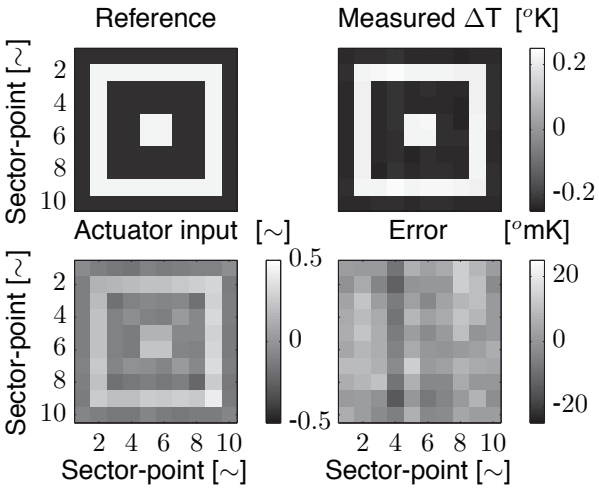

FIGURE 10. Instead of controlling a surface to have no temperature differences, the temperature can also be controlled to a certain desired thermal distribution. This is realised by closing the control loop. This set of figures is obtained in steady state. The measured ΔT is very similar to the Reference, which is also by the error, which shows no clear correlation with the Reference. What is also shown is the actuator input; in order to get the square at a uniform temperature, the lower corner right needs more intensity. This is due to the inhomogeneous irradiance from the video projector.

[3] Bakshi V. EUV lithography. SPIE-International Society for Optical Engineering; 2008.

[4] Spence PA, Gianoulakis SE, Moen CD, Kanouff MP, Fisher A, Ray-Chaudhuri AK. System performance modeling of extreme ultraviolet lithographic thermal issues. Journal of Vacuum Science & Technology B: Microelectronics and Nanometer Structures. 1999;17:3034.

[5] Roddier F. Adaptive optics in astronomy. Cambridge university press New York:; 1999.

[6] Aström KJ, Wittenmark B. Computer-Controlled Systems: Theory and Design. Dover Pubns; 2011.

ACTIVE WAFER SHAPE MODULATION USING A MULTI-ACTUATOR CHUCKING SYSTEM

A. Cherala[†], B.J. Choi[†], X. Lu[†] and S.V. Sreenivasan[‡,†]
[†]Molecular Imprints, Inc., Austin, Texas, USA
[‡]Department of Mechanical Engineering, University of Texas, Austin, Texas, USA

INTRODUCTION

Advanced 193nm immersion (193i) lithography has its resolution limited to approximately 40nm half-pitch. Current production for sub-25nm patterning involves expensive self-aligned double patterning (SADP) techniques that comprise cumbersome processing steps [1] and place constraints on device pattern complexity. While the industry has explored other higher resolution lithography techniques for production including EUV lithography (EUVL) [2] and multiple e-beam lithography (MEBL) [3], these techniques are not ready as significant challenges remain [4]. Imprint technology inherently possesses remarkable resolution having demonstrated sub-3 nm large area patterning in research [5] with the capability to pattern geometries with arbitrary complexity. In recent years, imprint based stepper technology has become commercially mature and a specific form of imprint lithography known as Jet and Flash Imprint Lithography (J-FIL) has been developed and commercialized [6]. J-FIL has recently made significant progress towards addressing defect control [7] and overlay [8] making it an attractive alternative to SADP for manufacturing cost-sensitive semiconductor devices such as advanced memory.

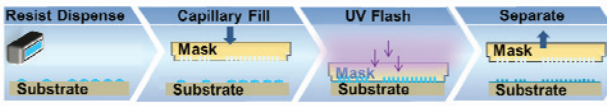

FIGURE 1: Jet and Flash Imprint Lithography.

The J-FIL process uses an *imprint mask* which comprises of nanoscale patterns etched into a fused silica plate. The patterned region (*field*) in a stepper is typically 26mmx33mm. A low viscosity monomer resist formulation is dispensed onto the wafer in an array of drops using an inkjet array. The mask then is brought in contact with the drops and the monomer fills the etched regions of the mask. (See Fig 1). The monomer is then polymerized with a blanket UV cure and the mask separated from the wafer. This process is repeated to cover the entire wafer including 300mm wafer and recently 450mm wafers.

PROBLEM STATEMENT

J-FIL technology uses inkjet arrays to facilitate adaptive deposition of materials so as to match uneven pattern densities in masks. This however requires the imprint tool to create a bubble-free contiguous film from the discrete monomer drops to avoid defects and slow system throughput. A nominal imprinting process will lead to bubbles because the imprint mask and wafer are highly flat and polished surfaces by design for other process requirements. Several approaches such as use of vacuum [9] have been suggested to alleviate bubble problem in imprint lithography. However, these approaches complicate tool design and several advantages of running the tool at atmospheric pressure are lost. Another approach is the control of wafer and mask shape during the imprint process to facilitate the escape of air as the imprint progresses. This can be accomplished by either deforming the mask or wafer or both into a convex shape. This geometry allows the air to be squeezed out more efficiently and reduces the volume of trapped air (Fig 2). It is estimated from previous experiments that an out-of-plane bowing of few microns should be sufficient to observe improved performance. The disadvantage of deforming the mask is that it is typically a 0.25 inch thick plate that cannot be deformed to the required amount without very large forces acting on it. The wafer is typically thinner (700-800 microns) and more easily deformable. The challenge with wafer shape control is that the wafer needs to be held flat and without slippage on a stepper substrate chuck for process requirements. So, the wafer is required to deform only locally and during the imprint process while the rest of the wafer is held flat. The design should also be able to modulate the shape in any part of the wafer depending on the field pattern layout on the wafer. The wafer chuck is held on a linear motor driven precision air-bearing stage that has linear X-Y and rotation

degrees of freedom. Since the precision stage has a large range of motion, only a limited number of cables and pneumatic lines can be routed to the stage from the machine base. Ideally only one vacuum and one pressure line should supply the chuck and the zone selection should happen internally on the chuck.

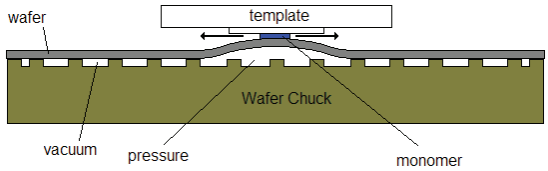

FIGURE 2: Wafer shape modulation schematic

ACTIVE WAFER SHAPE CONTROL CHUCK

To start investigating wafer shape control and its effect on improving throughput, a fixed field layout chuck was first designed. The field size was chosen to be 25mmx25mm. Alternating fields in both directions were connected to the same pneumatic source to minimize the input lines to the chuck. Figure 3 shows one set of fields pressurized with the chuck covered with a thin polymer film to show the bowed regions.

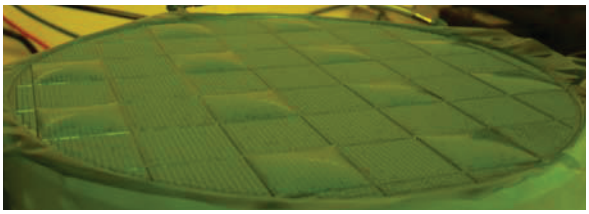

FIGURE 3: Fixed field layout chuck with polymer film showing pressurized fields.

Subsequently a wafer shape control vacuum chuck satisfying all these design requirements was designed to locally modulate the wafer shape while holding the rest of the wafer flat [10]. The concept involves dividing the chuck into a rectangular grid of unit cells (Fig 4). Each cell has two areas, A1 and A2. Each area is independently addressable *via* either a vacuum or pressure source. The two areas and pressures are chosen so that the wafer loses contact with the chuck and bows out only if both areas are under positive pressure.

The size of the unit cell depends on the bowing span resolution required by the process. In the current design, the unit cell is a square of side 5mm. All the A1 areas in a row are connected to the same pneumatic source by cross drills and all the A2 areas in a column are connected to one source by another array of cross drills. Each cell is thus addressable by controlling the vacuum or pressure to the entire row and column of cells. Figure 5 shows the concept's functionality with a polymer film instead of a wafer to exaggerate the deformation.

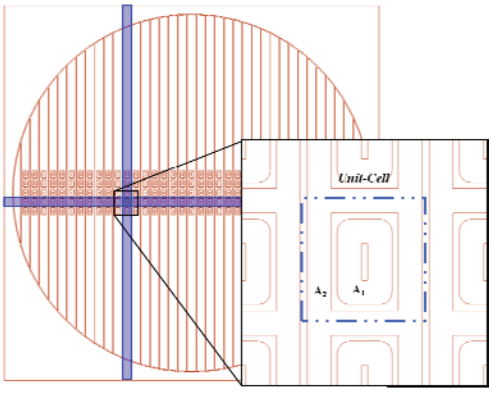

FIGURE 4: Unit-cell design of wafer chuck.

Figure 6 shows a Silicon wafer deformation with 30x30mm span and 10kPa pressure, measured with a Zygo interferometer. The wafer bow magnitude is around 6um.

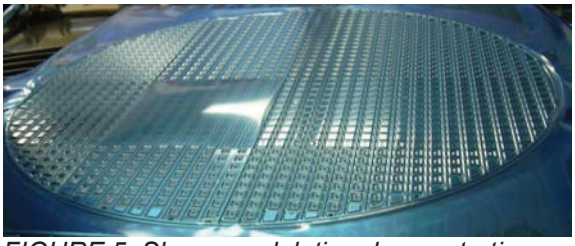

FIGURE 5: Shape modulation demonstration.

When the design of Figure 4 was applied to a 200mm wafer prototype, the 200mm diameter wafer chuck includes about 1250 unit cells with 40 ports on each axis for a total of 80 ports for the entire chuck. As mentioned before, there are only two supply pneumatic lines available, therefore each port is connected to a selection solenoid valve that can connect the port to either supply.

All the solenoid valves are connected to a common manifold with the vacuum and pressure supply. This layout would require eighty solenoid valves to accomplish completely independent selection capability for each cell. The design is somewhat simplified by making use of the fact that the imprinting on CMOS substrates (200mm, 300mm or 450mm) is a step and repeat process with imprinting occurring over a

26mm by 33mm field area (standard photolithography scanner field size). The 200mm wafer chuck prototype was divided into two halves along each axis with two port pairs in each half (total of 20) connected to the same selection valve respectively.

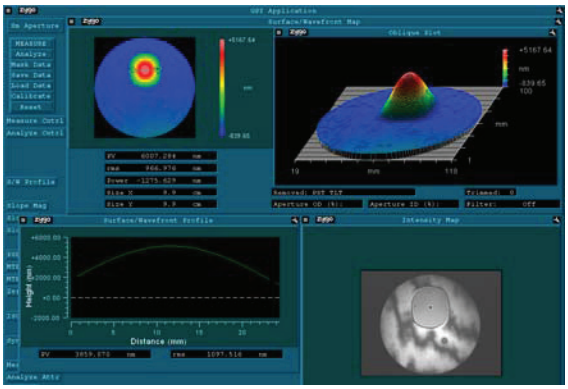

FIGURE 6: Zygo wafer shape measurement over 30mmx30mm span with 10kPa pressure.

Thus the number of valves needed was reduced to around forty. Pneumatic valves are available in miniature sizes and packaging forty valves around a 200mm chuck is feasible. When a certain area on the wafer is selected for bowing, four areas on the 200mm wafer are modulated, but since the areas are sufficiently spaced apart it will not influence the process in the required area. The shape of the bowing can be controlled to be circularly symmetric (Figure 6) or cylindrical in nature. Cylindrical bowing of the wafer requires keeping all the ports on one axis at positive pressure throughout the imprinting process. The magnitude of wafer bow for rectangular spans can be estimated from the following equation [11]

$$y = \frac{\alpha q b^4}{Et^3}$$

Where,
y = maximum deflection
a = span in first direction
b = span in second direction
α = factor to account for a/b ratios
q = load per unit area
E = Young's Modulus
t = thickness of plate

However, the relevant quantity of interest from the perspective of the imprint process is the bowing magnitude only over the size of the field, which is 26mm by 33mm. Figure 7, shows the bow magnitude over 25mm region for different pressures with 30 and 40mm bowing span.

THE BOWED WAFER IMPRINTING PROCESS

The bowed wafer imprinting process is performed as described below. The resist is dispensed by the inkjet dispenser in the required imprint area. Any arbitrary field area (usually square or rectangular shape) that needs to be bowed is fitted to the nearest group of cells and the rows and columns under that group are subjected to positive pressure by appropriate switching of valves. The pressure line is kept at the set point for maximum bow by an electronic pressure regulator. This bows out the required part of the wafer while keeping the rest of the wafer chucked flat.

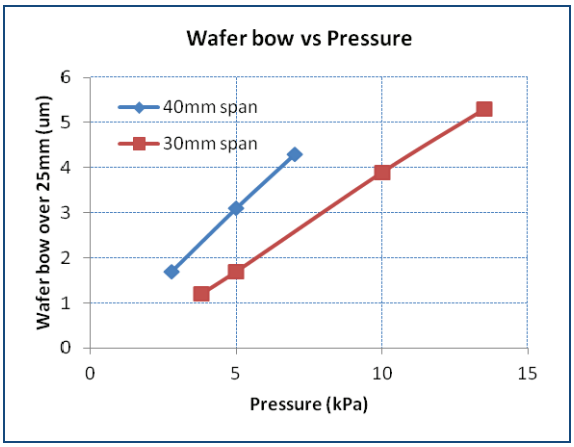

Figure 7: Wafer Bow vs. Pressure for 30mm and 40mm square span

The mask is then brought into contact with the resist drops in the central part of the bow region to create a circular shaped initial spread area. During the imprinting process the imprinting force and wafer bow pressure are controlled to get a smooth initial contact and spread of contact area. This is done by a simultaneous linear tracking control of both the imprint force and pressure. The imprinting process is divided into two phases. In phase 1, the imprint force is increased from about 0 to 10N while the bowing pressure is decreased from 20 to 10kPa. This is done to ensure smooth increase in contact area until the imprint is completes. In phase 2, the imprint force and pressure are both reduced to zero so that the wafer is held flat against the wafer chuck during UV cure step to ensure precision nano-scale overlay. The vacuum supply is usually kept constant during the imprint. The speed at which the entire process occurs is also a function of the wetting characteristics of the resist in the liquid form prior to UV exposure. Typical imprint resists are designed to have a highly wetting interface

between the liquid resist and the wafer (contact angles of <5 degrees) allowing for rapid processes. Figures 8a and 8b show images of the progression of an actual imprint process using wafer shape modulation achieved by tracking control of the chuck pressure trajectory in conjunction with the downward motion of the imprint mask as it makes contact with the resist drops. Figure 8a shows imprinting on a wafer bowed over a square span resulting in a central circular contact area and Figure 8b shows imprinting with a cylindrically bowed wafer resulting in an initial line contact along the cylinder axis. The basic idea is to merge discrete resist drops and convert them to a contiguous film with no bubbles. This requires matching of the mechanical motion controls (that causes increasingly larger number of drops to engage with the mask starting from the center as shown in Figures 8a and 8b) with the inherent wetting characteristics that causes lateral spreading of the drops so as to minimize bubble formation.

EXPERIMENTAL RESULTS

During the imprinting process, resist drops that are initially dispensed spaced apart (gap of ~100um) and are hemispherical shaped will spread due to contact with the mask and neighboring drops merge to trap air bubbles in the interstitial sites between three or four drop locations. The limiting factor that determines speed of imprinting is the dissolution time of these air bubbles. If proper shaped substrate control as discussed above is employed, the size of the bubbles formed is very small (sub-micron), they dissolve rapidly. If on the other hand large bubbles are formed, they can significantly impact throughput.

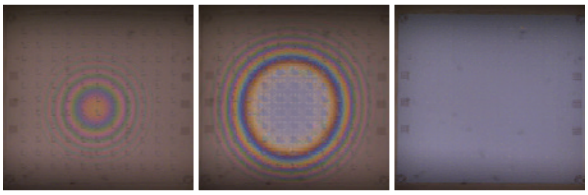

FIGURE 8a: Imprinting on a wafer bowed over square span.

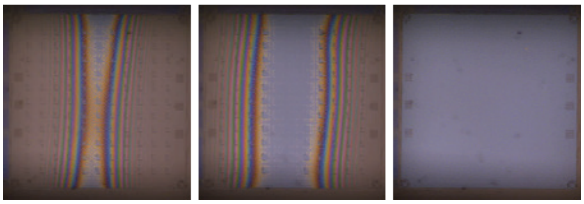

FIGURE 8b: Imprinting on a wafer bowed in cylindrical shape.

Feasibility experiments were conducted to estimate the efficiency of the wafer bow process in eliminating trapped air bubbles by imprinting with a mask pattern that has a square 11x11 grid of large features distributed across the field, that are known to be difficult to fill. The baseline experiment was done with no wafer bow with a spread time of >120 seconds. Spread time is defined as the duration from when the mask makes initial contact with the resist drops up to the start of UV cure. The quality of the fluid filling is determined by inspection of each of the 121 features with an in-tool microscope after the imprint is completed. Any voids or bubbles are counted as defects. Previous work has established that such in-tool microscopes correlate well with high resolution KLA wafer inspection tools in identifying bubble/void defects [12]. The average number of defects with no wafer bow was 12 defects per field. The experiment was repeated with the wafer bow process as described above with 35mm bow span and 20kPa pressure but with spread time reduced to 5 seconds. The average number of defects was 8 defects per field. For imprinting with cylindrical bow, the number was further reduced to 4.5 defects per field. This indicates that the use of active wafer shape modulation can lower bubble/void defects while reducing the spread time by a factor of 24. Further optimization of these processes in conjunction with improvements in resist materials, resist jetting volume resolution, drop placement accuracy, and clean semiconductor grade process protocols have led to spread times of less than 1.5 seconds.

One of the concerns with the process discussed here is that the wafer loses contact locally with chuck during the early phase of imprinting and then gets held back onto the chuck at the end of the imprinting. There is concern that this process may result in the wafer retaining some residual strains or distortions that could affect overlay-alignment. Overlay experiments done with a productized version of the wafer chuck concept described here have shown no significant intra-field distortions. It should also be noted that since the chuck has a large number of addressable zones, the vacuum level under the field being imprinted can be cycled while keeping the rest of the wafer chucked, to allow the wafer to relax and reduce any residual strains without causing any rigid body displacements of the wafer relative to the chuck.

CONCLUSION

An active wafer shape modulation chuck that can address any field size on the wafer while minimizing the number of regulators and valves needed was designed, prototyped and tested. Experiments show that significant (~24X) decrease in spread time and number of filling defects is possible with the active shape modulation imprinting process.

REFERENCES

[1] Lattard, L., et al., "Spacer process and alignment assessment for SADP," Proc. of SPIE Advanced Lithography, Vol. 8326, Optical Microlithography XXV, Paper No. 8326-03, San Jose, CA, February 2012.

[2] Wood, O.R. et al., "Insertion strategy for EUV lithography," Proc. of SPIE Advanced Lithography, Vol. 8322 Extreme Ultraviolet (EUV) Lithography III, Paper No. 8322-02, San Jose, CA, February 2012.

[3] McCord, M.A. et al., "REBL: Design progress toward 16nm half-pitch electron-beam lithography," Proc. of SPIE Advanced Lithography, Vol. 8323, Paper No. 8323-36, San Jose, CA, February 2012.

[4] Kwon, H.J. et al., "EUV mask multilayer defects and their printability under different multilayer deposition conditions," Proc. of SPIE Advanced Lithography, Vol. 8322, Paper No. 8322-08, San Jose, CA, Feb. 2012.

[5] Chou, S., et al. "Nanoimprint lithography," JVST B 14, 4129-4133 (1996).

[6] Sreenivasan, S.V., "Nanoscale manufacturing enabled by imprint lithography," MRS Bulletin, 2008, 854-863.

[7] Ye, Z. et al., "Defect reduction for semiconductor memory using jet and flash imprint lithography", SPIE J. of Micro/Nanolithography, MEMS, & MOEMS, Jul-Sep 2012, pp. 031404-1 to 031404-6.

[8] Higashiki, T., et al., "Nanoimprint lithography for semiconductor devices and future patterning innovation," Proc. of SPIE Advanced Lithography, Vol. 7970, San Jose, CA, February 2011.

[9] Kazuo Itoh et al., "Simple Nanoimprint Lithography with 50 nm Resolution Using Vacuum Packing," 2010, Key Engineering Materials, 459, p. 111.

[10] Cherala, A., Choi, B., Pankaj, L., Shackleton, S., US Patent: 8,033,813, "Chucking System Comprising an Array of Fluid Chambers".

[11] Roark's Formulas for Stress and Strain, 7th Ed., McGraw-Hill.

[12] I. McMackin, W. Martin, J. Perez, K. Selenidis, J. Maltabes, F. Xu, D. Resnick, S.V. Sreenivasan , "Patterned Wafer Defect Density Analysis of Step and Flash Imprint Lithography," J. Vac. Sci. Technol. B 26(1), Jan/Feb 2008, pp. 51-55.

THE HIGH DYNAMIC RANGE SURFACE METROLOGY CHALLENGE

Richard K. Leach[1], Christopher W. Jones[1], Ben Sherlock[1], and Adam Krysiński[1]
[1]Engineering Measurement Division
National Physical Laboratory
Teddington, UK

INTRODUCTION

The rapid rise in consumer and industry demand for low-cost photovoltaic power, novel displays and interfaces, and functional packaging has driven advanced manufacturing progress towards high-throughput production in a large-substrate or roll-to-roll format. The function and reliability of these products is dependent on the efficient management of features and defects in a highly-automated and cost-sensitive production environment. The large disparity between the measurement requirements and techniques associated with the features and those associated with the substrate require a step-change in measurement capabilities based on a combination of new technologies and more intelligent exploitation of *a priori* information.

This new area of metrology, which is divergent from both laboratory-based surface topography measurement and from existing low-resolution inspection methods, we shall call 'high dynamic range surface measurement and inspection' (HDR, see figure 1). Implicit in HDR are the parallel objectives to (1) be able to understand and pare down the exact metrology task associated with a production application; (2) to establish and expand a range of fast, high-resolution and environment-insensitive optical techniques for 2D and 3D surface inspection; (3) to develop novel methods of use for existing techniques that circumvent perceived performance limits; and (4) to make better use of defect information to optimise production and reliability and minimise wastage.

Many structures are being produced on large area substrates (up to metres squared and larger) but with very high feature resolutions (down to micrometres and beyond). This form of 'web-based' manufacturing (also called roll-to-roll manufacturing) throws up a whole range of metrology challenges. For example, the measurement of tiny defects during the manufacture of flat sheets of glass or the measurement of deviations from nominal in laser machined lines for plastic electronics. Inspection techniques in web-based production must be tolerant to continuous substrate motion and flutter, extremely reliable in service and tolerant to environmental variation. Techniques for master stamp drums must be tolerant of large-scale surface form (see figure 2).

Further examples come from the trend to use deterministic surface structuring to produce functional surfaces. The following is a list of a small number of product examples: modern projectors, plastic PV sheets, high-quality paper and packaging, touch-screen devices, back-lighters, vehicle HUDs, displays and HDI electronics.

Associated defects are equally diverse, including randomly-located examples such as pinholes, scratches, organic and process-related contamination as well as more predictable examples such as wear-related form errors and tool misalignment. A typical application may be subject to a large subset of defects, and the functional criticality of each may not be clear.

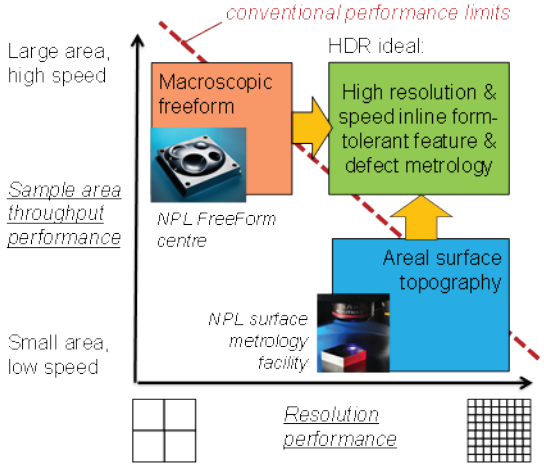

FIGURE 1 Space representing the challenges of high dynamic range metrology.

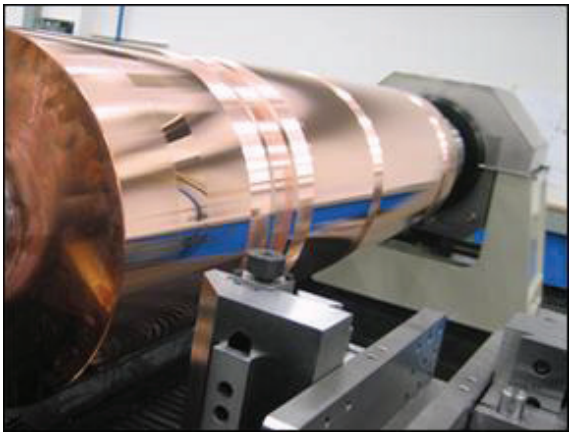

FIGURE 2. A diamond turning application producing a master stamp for micro-optics sheets. The drum length is 1.5 m. Courtesy of Cranfield University.

An additional challenge associated with the move from research production to full supply chain is the significance of defects introduced at each stage in the production process. This not only implies a requirement for inspection at each stage of production but also demands a standardised manner of quality (or defect) classification as a function of location on a roll of functional material.

Recent advances in surface topography measurement provide the starting point for HDR capabilities. The last three decades have seen the development of optical instrumentation, now an established rival to contacting techniques, as well as the development of specification standards for areal topography. There are currently two distinct classes of instrument: 1. those that measure over large areas (metres squared) with tens to hundreds of micrometres spatial resolution (for example, fringe projection, photogrammetry and Moiré interferometry) [1], and 2. those that measure over small areas (up to a few millimetres squared) with spatial resolutions of the order of a micrometre (for example, coherence scanning interferometry (CSI), confocal microscopy and focus variation microscopy) [2]. Essentially, the former class is camera-limited, and the latter is objective-limited. There have been several attempts to try and combine the two classes (see for example [3], [4] and discussion below), but more progress is required before such hybrids can be used in high dynamic range manufacturing.

In this paper, we will attempt to describe some of the areas of research that require further attention if we are to satisfy the metrology requirements for high dynamic range manufacturing. Whilst some of the research being carried out at the National Physical Laboratory (NPL) will be briefly described, the paper will concentrate on generic issues that need to be solved by the community.

FULL-FIELD TECHNOLOGY

There are a number of full-field techniques that can measure surface topography (principally form) over large areas, for example, fringe projection and photogrammetry [1]. However, such techniques do not have the required resolution (axial or lateral) or accuracy for many high dynamic range applications. It is not clear how such techniques could be adapted to increase resolution and accuracy without severely limiting the field of view. Techniques such as digital holography and speckle interferometry have been used to measure topography over large areas to high resolution, but they often have limitations in terms of height range, dynamic range and the need for very stable environments [5].

One potential solution to the high dynamic range challenge is the use of hybrid instrumentation, *i.e.* to detect areas of interest with a relatively low resolution sensor (for example, camera-based sensors), then to “home-in” on the areas of interest using a high resolution sensor (see for example, [4], [6]). Data fusion techniques can then be used to combine the data from the different sensors [7]. In some scenarios the low resolution sensor could use approaches that detect scattering from points of interest, such as defects or scratches, therefore, allowing high resolution detection without the need for imaging. Success in service is dependent on initial investment on defect and defect variation analysis and optimisation of factors such as illumination.

SCANNING TECHNOLOGY

The majority of available surface topography measuring instruments are best suited to the laboratory context, in which a surplus of information is gathered and subsequently analysed in different ways to meet a particular need. In the HDR context, the measurand or measurement output is typically narrowly defined and available instruments will generate a huge information surplus, resulting in very low measurement efficiency. The adaptability of these instruments is constrained both by the

mechanics of integral scanning components and the available choice of scanning patterns

The “brute force” approach to measuring over an area at high spatial resolution is to scan an optical spot over the area in a raster fashion, thus, either measuring height at given (*x*, *y*) co-ordinates or measuring a series of areal maps, which are subsequently stitched together. To build up an areal map usually requires a physical scan though focus at each (*x*, *y*) co-ordinate or for each areal map.

In the point scanning case, the optical instrument acts analogously to a stylus instrument, but often requires a scan through focus to obtain the height data at each (*x*, *y*) co-ordinate, for example confocal and point autofocus instruments [2]. Triangulation instruments do not require an axial scan, but for many applications do not have the required axial resolution. Chromatic confocal instruments are potentially very fast, as they do not require a physical axial scan, but current systems are limited to scanning frequencies of around 70 kHz and their performance suffers as their scan speed increases [8]. All current point scanning instruments are far too slow for many high dynamic range applications that require fast, large area scanning. Line-scanning technology is being developed (see for example [9], [10] and it is feasible to use banks of parallel sensors, but the cost of such systems soon becomes prohibitive. A further alternative is the use of optical scanning, i.e. moving the beam across the surface without the need for physical *xy* scanning, but speeds are still limited (for example, [11]).

In the case of areal sensors, for example CSI, digital holographic microscopy (DHM) and focus variation microscopy [2], there is a trade-off required between the beam coverage area and the numerical aperture (NA) of the objective system. For example, to push the size of the coverage area to a few millimetres squared, NAs of less than 0.3 are used, and the lateral resolution and maximum measureable slope angle tolerance suffer. DHM systems have been shown to scan at several hundred kilohertz [1], [12], but they require multiple wavelength sources to cover the axial ranges needed for many high dynamic range applications. Wavelength scanning techniques are being developed [11] to circumnavigate the need for axial scanning through focus, but the sampling speeds are still not high enough for many high dynamic range applications. Ptychography [13], or lens-less imaging, is a potential candidate technique for high dynamic range sensing, but it has yet to be demonstrated for such high-speed applications.

The simple conclusion of this section is that brute force optical scanning technology is not appropriate for many high dynamic range applications and more research is needed to demonstrate the limits of such technologies – essentially to push them as far as they can go. Research should focus on heavy simplification of the measurement task based on prior analysis of the inspection task.

RESOLUTION ENHANCEMENT

The HDR challenge is essentially a challenge of maintaining high resolution whilst extending range, or bandwidth. Potential solutions may involve the use of a priori information and iterative approaches to extend resolution of far-field optical imaging systems, i.e. super-resolution [5]. Often super-resolution is discussed in the context of imaging systems that are already operating close to their natural resolution limits, i.e. high NA systems. However, it is possible to extend the resolution of low NA systems using a priori information, therefore, extending the dynamic range. In practical terms, smaller features or defects may be resolved without reducing the field of view and throughput of a sensor.

ADVANCED MEASUREMENT AUTOMATION AND OPTIMISATION

The HDR challenge calls for rapid advancements in standardised tools to achieve and automate inline inspection and surface topography measurement, including data handling, defect classification, decision-making and measurement planning, and mixed-sensor coordination. Where two or more sensors are used with different lateral resolutions, data fusion techniques are required to combine the data and to match the co-ordinate systems of the sensors [14]. To reduce scanning times and make full use of all the available information, intelligent sampling techniques will need to be utilised [15]. One relatively promising newcomer to this field is compressed sensing [16], although it has not been demonstrated on high dynamic range applications yet (to the knowledge of the authors). Lastly, methods need to be developed for handling the potentially very large datasets

that will be produced when measuring to high resolution over large areas.

ROLE OF TRACEABILITY IN HDR

Traceability and practical calibration tools will underpin offline defect analysis, objective comparison of potential inspection system components and confidence in accuracy of automated detection. Good practice guidance on the pragmatic use of calibration and functional tests would present opportunities for added product value. Specification and standards for calibrating areal surface topography measuring instruments are only just becoming available [17], [18]. Whether such calibration techniques can be applied for high dynamic range applications remains to be seen. The traditional use of transfer artefacts may need to be re-assessed when such large areas and high speeds are required.

CURRENT PROJECTS AT NPL

NPL is pursuing two approaches to tackle the HDR challenge. 1. Enhancing and extending existing technologies to push them to their limits. 2. Developing novel approaches. In approach 1, we are working with a number of industrial partners to adapt commercially-available instruments to develop inline solutions for current industry applications; we have also developed a platform comprising a simple two-axis roller-bearing slideway and a bridge to support the probe under test. The dynamic performance of a number of sensors will be investigated. For approach 2, we are developing full-field and resolution enhancement approaches [19] that will be reported in future publications.

SUMMARY

As is often the case with new techniques, the metrology for high dynamic range manufacturing is lagging behind the manufacturing capability. We have discussed some of the areas of metrology that need to be developed to address this lag. NPL is currently engaged in projects to develop solutions for high dynamic range metrology.

ACKNOWLEDGEMENTS

This paper was funded by the UK National Measurement System Engineering & Flow Metrology Programme and the FP7 project NANOMend.

REFERENCES

[1] Harding K. Handbook of Optical Dimensional Metrology. Taylor & Francis: 2013.
[2] Leach R K. Optical Measurement of Surface Topography. Springer. Berlin: 2011.
[3] Abolbashhari M, Gerges A S, Davies A. Proc. ASPE, San Diego. 2012; 256-259.
[4] Kayser D, Bothe T, Osten W. Opt. Eng. 2004; 43: 2469-2477.
[5] Osten W, Reingand N. Optical Imaging and Metrology: Advanced Technology. Wiley VCH: 2012.
[6] Manske E, Hausotte T, Mastoylo R, Machleidt T, Franke K-H, Jäger G. Meas. Sci. Technol. 2007; 18: 520-527.
[7] Weckenmann A, Jiang X, Sommer K-D, Neushaefer-Rube U, Seewig J, Shaw L, Estler T. Ann. CIRP. 2009; 58: 701-721.
[8] Nouira H, El_Hayek N, Yuan X, Anwar N, Salgado J. Proc. Met & Props, Taiwan, June. 2013; TS6-01
[9] Chanbai S, Zafarullah I, Wiora G, Wewer L, Roth H. J. Phys.: Conf. Ser. 2011; 311: 021028
[10] Polytec Datasheet. TopLine Quality Control Sensors. 2013.
[11] Jiang X. Phil Tran. Roy. Soc. A. 2012; 370: 4089-4114.
[12] Kim M. SPIE Reviews. 2010; 1: 018005.
[13] Rodenburg J M. Adv. Imag. Elect. Phys. 2008; 150: 87-184.
[14] Lappäniemi J, Mattila T, Kololouma Tm Suhonen M, Alastalo A. Nanotechnology. 2012; 23: 305204.
[15] Wang J, Jiang X, Blunt L A, Leach R K, Scott P J. Meas. Sci. Technol. 2012; 23: 085006.
[16] Baranuik R. Science 2011; 331: 717-719.
[17] Giusca C L, Leach R K. NPL Good Practice Guide 126. National Physical Laboratory, UK. 2013.
[18] Giusca C L, Leach R K. NPL Good Practice Guide 127. National Physical Laboratory, UK. 2013.
[19] Leach R K, Sherlock B. Application of Super-resolution Imaging in the Field of Surface Topography Measurement. Surf. Topog.: Met. Props. to be published.

WET CHEMICAL PLANARIZATION OF SINGLE-CRYSTALLINE SiC USING CATALYST-REFERRED ETCHING

Ai Isohashi[1], Yasuhisa Sano[1], Takeshi Okamoto[1], Shun Sadakuni[1], Pho Van Bui[1], Keita Yagi[2], and Kazuto Yamauchi[1]
[1]Department of Precision Science and Technology, Graduate School of Engineering, Osaka University, Osaka, Japan
[2]Ebara Corporation, Kanagawa, Japan

INTRODUCTION

4H-SiC is an attractive semiconductor material affording excellent physical properties such as wide bandgap, high breakdown voltage, and high thermal conductivity; accordingly, it can find applications in high-power, high-temperature, and high-frequency devices. In order to produce such devices, the preparation of geometrically and crystallographically highly ordered substrate surfaces is critical. However, it is very difficult to realize such surfaces because of the mechanical hardness and chemical inertness of the SiC crystal.

Generally, mechanical and chemical polishing methods are employed to fabricate ordered crystal surfaces. The schematic of the mechanical polishing technique is shown in Fig. 1. Mechanical polishing as typified by lapping using diamond abrasives involves statistically copying the surface shape of the polisher onto the work surface by using the mechanical effect of abrasives [1–3]. During this copying, shape error and the roughness of the substrate surface are selectively removed from the uppermost site. Accordingly, mechanical polishing enables an efficient and rapid preparation of a geometrically ordered surface. However, the introduction of crystallographic damage cannot be avoided because of the removal mechanism employed. The schematic image of the chemical polishing method is shown in Fig. 2. Chemical polishing as typified by wet etching and plasma etching can process the surface without inducing any crystallographic damage. However, the processed surface cannot be smoothened because of the isotropic etching mechanism. The schematic image of the chemical mechanical polishing (CMP) technique is shown in Fig. 3. CMP can be used to copy the surface shape of a polishing pad onto the work surface without inducing any crystallographic damage;

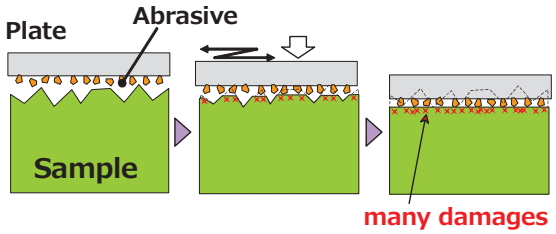

FIGURE 1. Mechanical polishing concept.

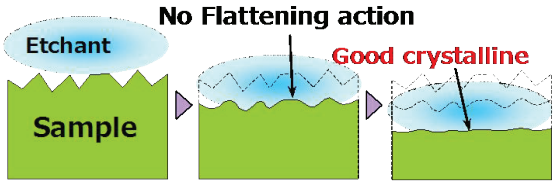

FIGURE 2. Chemical polishing concept.

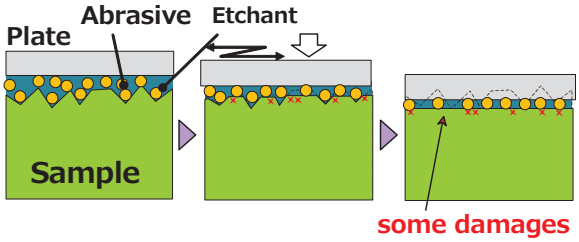

FIGURE 3. CMP concept.

this is achieved using fine abrasives and a soft pad [4–6]. However, this technique cannot perfectly remove the damage because of the persistence of the mechanical effect of abrasives. In addition, the flatness often gets degraded during such processing because of the usage of a critically soft polisher.

We have proposed a novel abrasion-free chemical polishing method, called catalyst-referred etching (CARE) [7]. A schematic image of the etching

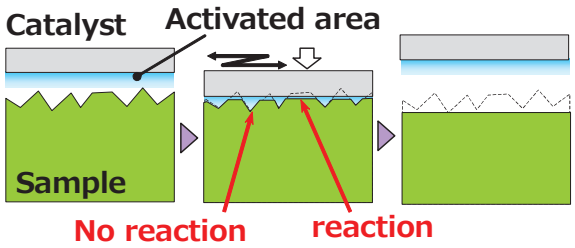

FIGURE 4. The CARE concept.

method is shown in Fig. 4. We use a polishing pad, on which the catalytic material is deposited. The role of the catalyst is to generate species that are reactive against the sample surface, by decomposing molecules that are not reactive themselves. When the lifetime of the reactive species is sufficiently short, the reactive area is limited only to the catalyst surface. Accordingly, only the uppermost sites on the work surface falling within the reactive area are etched. Then, the surface shape of the catalytic pad is statistically copied onto the work surface. Accordingly, CARE can be used to chemically generate geometrically smoothened surfaces without introducing any crystallographic damage.

In this study, we applied the CARE technique to 4H-SiC substrates and analyzed the obtained processed surfaces.

EXPERIMENT

In this study, 2-in n-type 8°-off cut and on-axis cut 4H-SiC (0001) substrates were employed. A schematic of the CARE apparatus is shown in Fig. 5. Wafers were fixed on the sample stage using vacuum and were placed on the catalyst

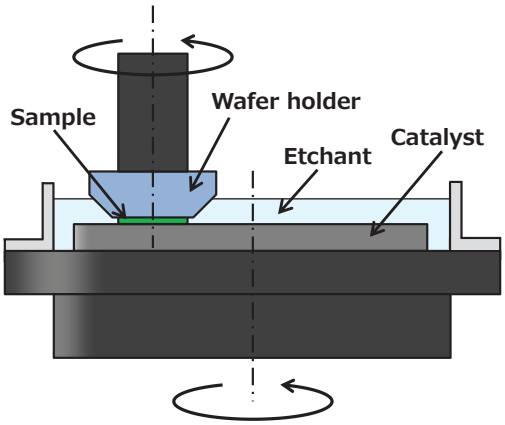

FIGURE 5. Schematic of CARE apparatus.

pad under a controlled pressure of 400 hPa. The substrate was pressed onto the pad surface in the etchant vessel. The workpiece and catalyst pad could independently rotate on each axis. The rotational speeds of the sample and the pad were fixed at 10 and 10.1 rpm, respectively. A thin platinum film was deposited on the rubber pad and then used as the catalyst. The roughness of the pad surface was 0.2 μm (RMS); however, it did not influence the finished surface quality because of the averaging effect induced by the independent rotation of the catalyst pad and the sample. Hydrofluoric acid (25 mol/L) was employed as the etchant. This solution was inert against 4H-SiC in the absence of the catalyst. The processed surface quality was evaluated using the images obtained from an optical interferometer (ZYGO Corp., NewView 200 CHR), atomic force microscope (AFM) (SII Nanotechnology, Inc., SPA400), high-resolution transmission electron microscope (HRTEM), and low-energy electron diffraction (LEED). The removal rates were estimated from the weight loss.

RESULTS AND DISCUSSION

Figures 6 (a) and (b) show the optical interferometer images taken before and after the CARE processing, respectively. The pre-processed surface was prepared using lapping. The measured area was 64 × 48 μm^2. The figure clearly shows that the scratches were removed after the CARE processing. The maximum

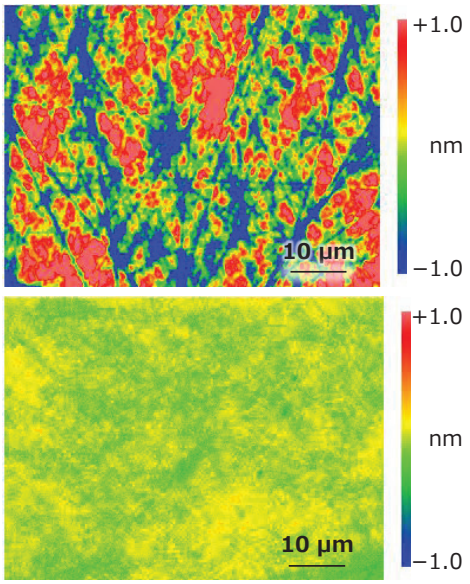

FIGURE 6. Optical interferometer images of 4H-SiC wafers: (a) as-received (after lapping) surface; RMS: 0.732 nm [P–V: 8.078 nm, Ra: 0.581 nm], and (b) CARE-processed surface; RMS: 0.081 nm [P–V: 0.831 nm, Ra: 0.064 nm].

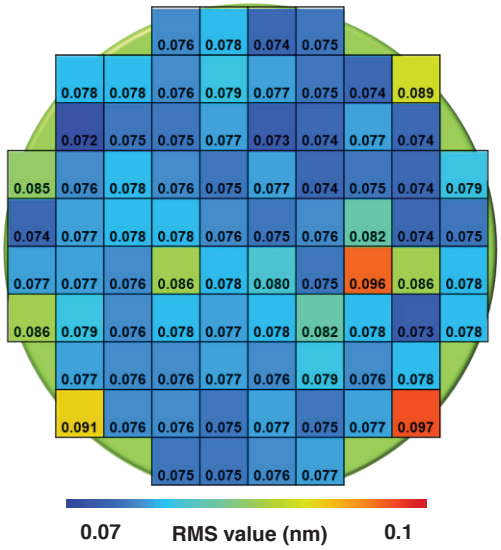

FIGURE 7. Surface roughness (RMS) at each 5-mm interval on the CARE-processed 8°-off cut 4H-SiC (0001) wafer surface (64 × 48 μm²) measured using the optical interferometer.

height of the surface irregularity (PV) and RMS roughness were improved to 0.831 nm and 0.081 nm, respectively. Figure 7 shows the entire area of the processed surface. The RMS roughness was improved to less than 0.1 nm at all points. No scratch was observed even in the wafer-scale measurement.

Figures 8 (a) and (b) show the AFM images of the CARE-processed surfaces for the 8°-off cut and on-axis cut 4H-SiC (0001) wafers, respectively. The measured area was 2 × 2 μm². A step–terrace structure with straight step edges can be observed on the on-axis cut wafer surface with a step height of approximately 0.3 nm, which corresponds to the bilayer step height of the 4H-SiC (0001) surface. Figure 9 shows the AFM images measured at every 10-mm interval on the CARE-processed wafer. The size of each image is 2 × 2 μm². Highly ordered step–terrace structures are observed at all the measured points. The direction and interval of the step edges are different at each point. Such differences were induced by the poor quality of the wafer-slicing process, where the off-angles fluctuate. The removal rate for the 8°-off cut (0001) surface was about 60 nm/h.

Figure 10 shows the cross-sectional HRTEM image of the CARE-processed 8°-off cut 4H-SiC (0001) wafer. The magnifying power was 1,000,000. The surface crystal structure is well

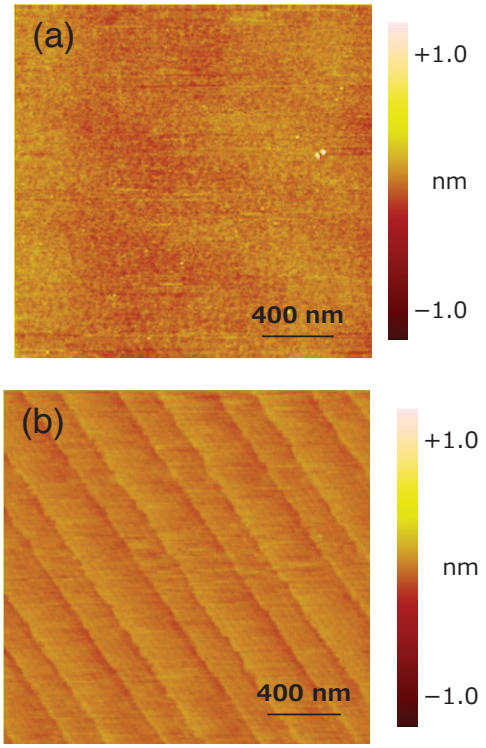

FIGURE 8. AFM images of CARE-processed surface of (a) 8°-off cut 4H-SiC (0001) surface; RMS: 0.082 nm [P–V: 3.559 nm, Ra: 0.059 nm], and (b) on-axis cut 4H-SiC (0001) surface; RMS: 0.106 nm [PV: 1.052 nm, Ra: 0.085 nm] (2 × 2 μm²).

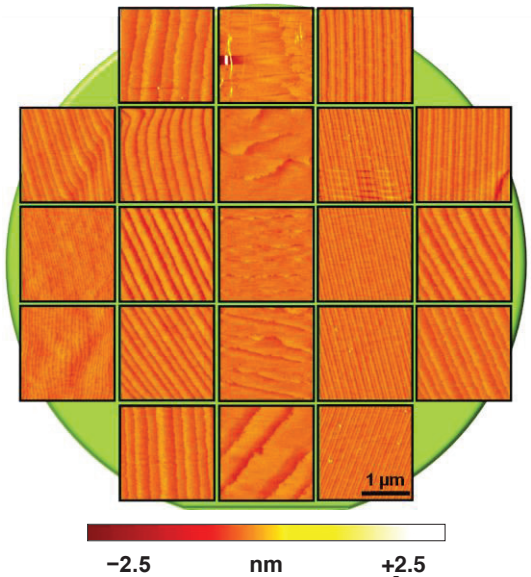

FIGURE 9. AFM images (2 × 2 μm²) observed at 10-mm intervals on the CARE-processed on-axis cut 4H-SiC (0001) wafer surface.

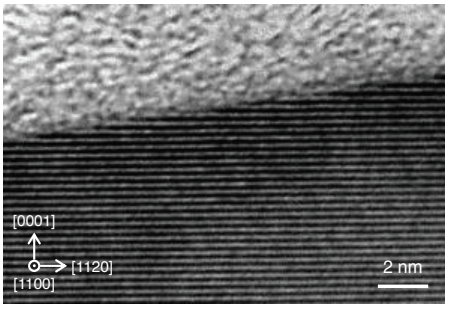

FIGURE 10. HRTEM image of a CARE-processed 8°-off cut 4H-SiC (0001) surface.

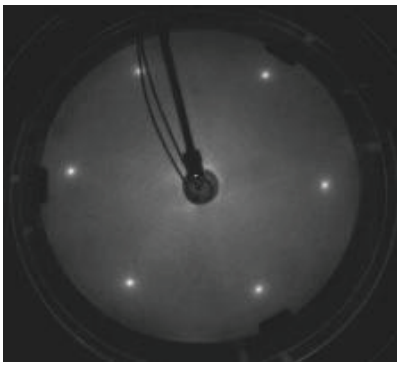

FIGURE 11. LEED image of CARE-processed surface with probe beam of 65 eV energy corresponding to an estimated thickness of 0.4 nm.

ordered up to the uppermost surface, and the processed surface possessed a step–terrace structure with a single-bilayer step height. Figure 11 shows the LEED image of the CARE-processed surface. The probe beam energy was maintained at 65 eV, which corresponds to an estimation thickness of 0.4 nm. The sharp and bright diffraction spots show that the surface exhibits a well-ordered crystalline structure.

In order to reduce the chemically hazardous nature of the CARE process, we used ultrapure water as the etchant (called "Water-CARE"), alternative to the HF solution, based on the viewpoint of the similar reactive characteristics of F and OH. We applied the Water-CARE system to an epitaxially grown 4°-off cut 4H-SiC substrate. Consequently, step bunching observed on the as-received surface was removed, and the surface roughness was improved from 0.167 nm to 0.082 nm. The Water-CARE system has significant potential as an attractive planarization method for SiC device fabrication because of its abrasion-free and environmentally friendly characteristics.

SUMMARY

We proposed a novel abrasive-free polishing method for SiC wafers and applied it to the planarization of 4H-SiC substrates. Crystallographically highly ordered surfaces were observed over the entire area of the treated wafer surfaces. AFM images, cross-sectional HRTEM images, and LEED images of the surfaces revealed atomically flat and damage-free characteristics.

ACKNOWLEDGMENT

This research was partially supported by a grant for the Global COE Program "Center of Excellence for Atomically Controlled Fabrication Technology" from MEXT.

REFERENCES

[1] Qian W, Skowronski M, Augustine G, Glass RC, Hobgood HMcD, Hopkins RH. Characterization of Polishing-Related Surface Damage in (0001) Silicon Carbide Substrates. Journal of Electrochemical Society. 1995; 142: 4290–4294.

[2] Powell JA, Larkin DJ. Process-Induced Morphological Defects in Epitaxial CVD Silicon Carbide. Physica Status Solidi B-Basic Research. 1997; 202: 529–548.

[3] Katsuno M, Ohtani N, Yashiro H, Aigo T, Fujimoto T, Nakabayashi M, Tsuge H, Hoshino T, Tatsumi K, Hirano H. Development of Lapping and Polishing Technologies of 4H-SiC Wafers for Power Device Applications. Materials Science Forum. 2009; 600: 819–822.

[4] Kikuchi M, Takahashi Y, Suga T, Suzuki S, Bando Y. Mechanochemical Polishing of Silicon Carbide Single Crystal with Chromium (III) Oxide Abrasive. Journal of the American Ceramic Society. 1992; 75: 189–194.

[5] Neslen CL, Mitchel WC, Hengehold RL. Effects of Process Parameter Variations on the Removal Rate in Chemical Mechanical Polishing of 4H-SiC. Journal of Electronic Materials. 2001; 30(10): 1271–1275.

[6] White ML, Reggie S, Naguib N, Nicholson K, Gilliland J, Walters A. The Preparation of World-Class Single Crystal Silicon Carbide Wafers using High Rate Chemical Mechanical Planarization Slurries. Materials Science Forum. 2009; 600: 839–842.

[7] Tomoaki H, Fuyuki T, Hara H, Sano Y, Mimura H, Arima K, Yagi K, et al. Reduction of Surface Roughness of 4H-SiC by Catalyst-Referred Etching. Materials Science Forum. 2010; 645: 775–778.

Micro-Optic Fabrication for Microsystems-Enabled Photovoltaics

Bradley H. Jared[1], Michael P. Saavedra[1], Ben J. Anderson[1], William C. Sweatt[2], Gregory N. Nielson[3] and Murat Okandan[3]
[1]Materials Engineering R&D
[2]Thermal, Fluid & Aero Sciences
[3]Microsystems Integration
Sandia National Laboratories
Albuquerque, NM

MOTIVATION

In response to the DOE SunShot initiative to achieve utility scale solar power generation at $1 per watt peak, Sandia National Laboratories is investigating a microsystems-enabled photovoltaics (MEPV) approach that combines the high conversion efficiencies of concentrated photovoltaics (CPV) with the form factor and low system costs of flat panel PV. MEPV combines fully integrated stacked multi-junction PV cells having lateral dimensions smaller than 1 mm with micro-optic concentrators to reduce the use of expensive semiconductor materials and to increase solar conversion efficiency [1]. While existing semiconductor infrastructure is being leveraged for MEPV cell research [2], a parallel effort is underway to develop design and fabrication techniques for MEPV micro-optics.

MICRO-OPTIC DESIGN

A cross-section of an MEPV design, Figure 1, shows that PV cells are mounted onto an electronic substrate that is aligned to lens elements which focus the incident sunlight onto the cell surface. Optical concentration, or magnification, and acceptance angle, or field of view, represent the primary optical requirements for the MEPV optics. While typical CPV systems utilize optical concentrations on the order of 500 to 1000x, MEPV designs are leveraging more moderate concentrations on the order of 50 to 100x based on desired cell designs, manufacturing tolerances and system costs.

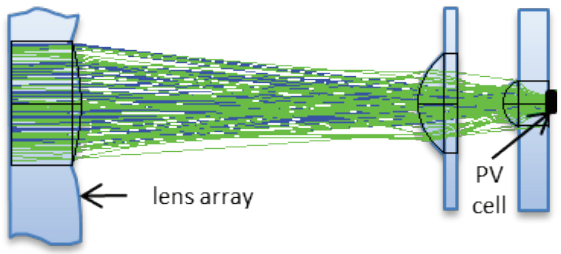

FIGURE 1. First generation MEPV optics.

Initial optical designs sought to maximize the system acceptance angle, but recent work has targeted a ±2° angle based on the performance of tracking systems fielded in current flat panel PV systems. Optical tolerances are roughly 25-50 μm for surface form accuracy and alignment to the PV cell; a common and readily achievable tolerance for single lens train assemblies. Maintaining lens to cell alignment across an array size on the order of tens of cm under temperature extremes approaching -40 to 80°C, however, introduces significant design, fabrication and assembly challenges for a MEPV module. Requirements for a 20 year service life under UV exposure, wind-blown debris, moisture and other environment extremes provide additional constraints to the optical design, predominantly around material selections.

Figure 1 represents the optical design for a first generation prototype that has been used to demonstrate the feasibility of MEPV systems using 720 μm single junction Si cells [2]. The design uses three aspheric PMMA lenses which have an entrance aperture of 3.5 mm, an assembly thickness of 15.1 mm, a magnification of 36x and an acceptance angle of ±4°. Polymer lenses have been primarily considered throughout design evaluations due to their low material costs and amenability to mass production via molding or other replication process. The collection area of the prototype module is approximately 5 cm on a side and includes 216 micro-lens elements in a hexagonal closed pack array to minimize sunlight losses at the entrance apertures. The lens arrays are passively aligned in a pseudo-kinematic manner using dowel pins and machined slots in the optic arrays, Figures 2 and 3. The slots are also positioned in an athermal manner to provide a point of zero thermal expansion at the geometric center of the optic arrays.

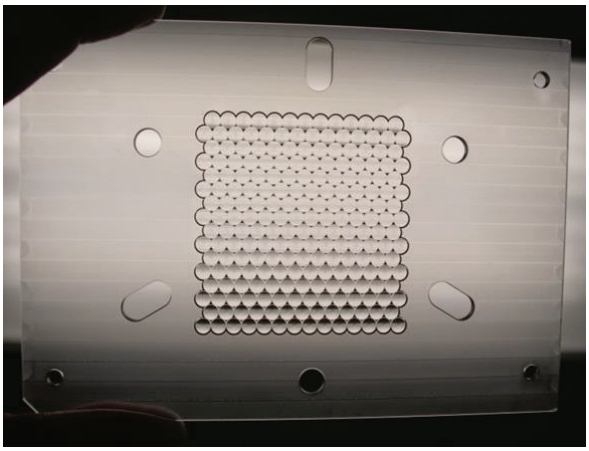

FIGURE 2. First generation front lens array.

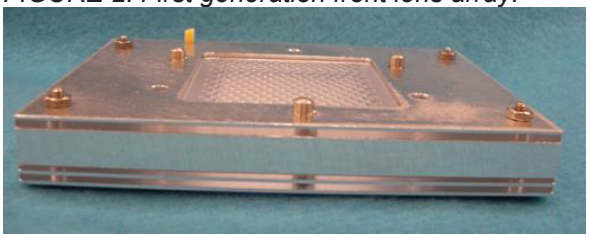

FIGURE 3. First generation optic module.

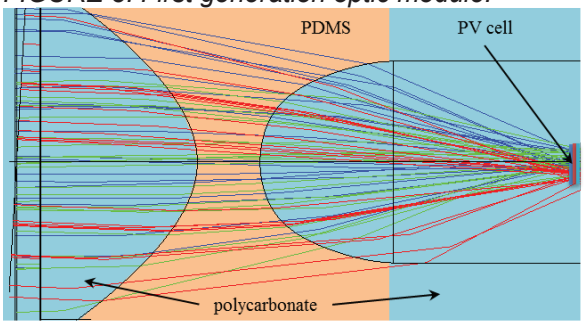

FIGURE 4. Second generation MEPV optical design.

A second generation optical design is in development to improve device performance and to examine the viability of mass producing MEPV at competitive costs. The design provides a 100X magnification with a ±3° field of view, a 2.75 mm entrance aperture, and an exit aperture onto a 250 μm diameter multi-junction PV cell. The lens train incorporates two polycarbonate aspheric lenses with a low index fill of Sylgard®184 PDMS. The thickness of the lens is only 5.30 mm, a 65% reduction from the first generation prototype, and an even greater reduction from traditional CPV systems. The module array arranges 240 elements in a hexagonal closed form across a roughly 40 mm square collection area. The front and rear micro-optic arrays are passively aligned in assembly using pin-in-slot features that are molded into each part, Figure 5. The symmetric geometry of

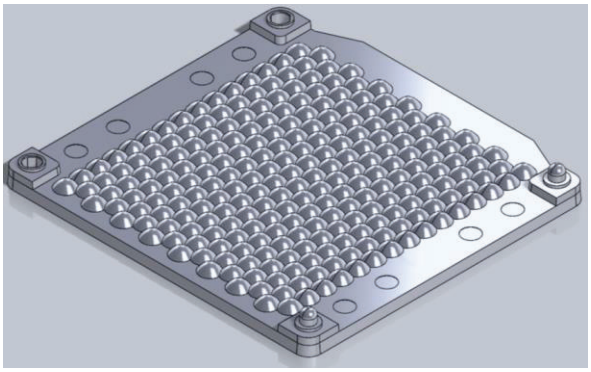

FIGURE 5. Second generation lens array model.

the mating features provides a semi-kinematic, athermal mounting configuration with expected alignment tolerances better than 25 μm. Alignment and assembly of the cell array is also performed passively using monolithic “wedding cake” features in the rear optic array.

FABRICATION

Diamond milling on a 4-axis Moore 350FG was originally planned for fabrication of the first generation prototype. Cost and schedule constraints, however, prompted the evaluation of a faster process based on a 5-axis Yasda YMC-430 micro-machining center. The YMC-430 provides adequate machining accuracy, on the order of 0.5 μm, as optical elements, reference features and mounting holes were all fabricated in a single machining setup, Figure 2. Rough machining with standard carbide micro tools allowed the use of a diamond milling tool for only the final finish pass. As a result, cutting with the diamond was minimized such that appreciable tool wear was not observed after machining in excess of 20,000 individual lens surfaces. The combination of micro-milling with diamond milling also enabled a 2-3x reduction in total machining time which proved critical in meeting project milestones. As expected, excessive surface finish, roughly 100 nm S_a in Figure 6, proved to be the primary drawback of the process producing estimated optical losses of 3% per surface due to scattering.

Fabrication of the second generation prototype optics has investigated techniques amenable to low cost, volume manufacturing. The polycarbonate lens arrays are being injection molded using 6061-T6 aluminum mold inserts that are micro-milled on the YMC-430 using carbide tools for rough figuring. 20 μm of material remains after rough machining which is removed in a single final finishing cut on the

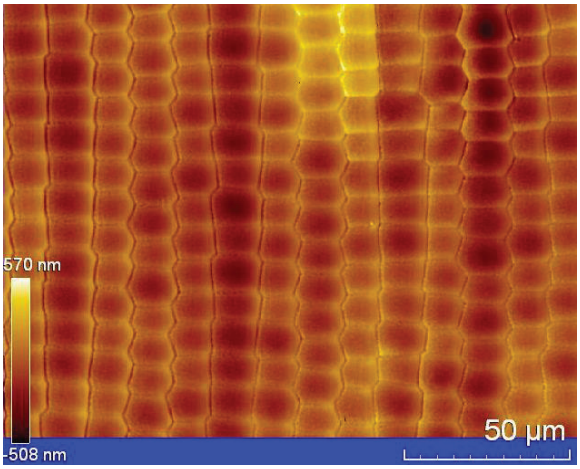

FIGURE 6. PMMA micro-milled surface finish.

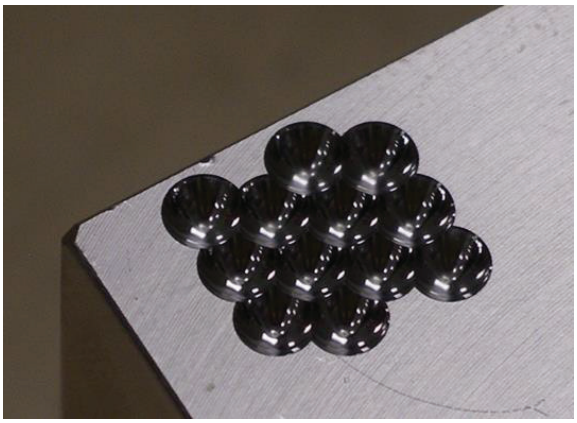
FIGURE 7. 4x4 array test cut in 6061-T6 Al.

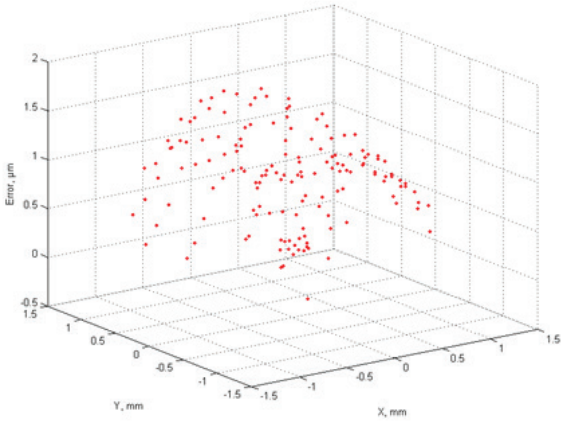

FIGURE 8. Representative test cut 1.5 µm form accuracy.

350 FG using ultra-precision diamond milling. Process development has focused on reducing optic surface finish to improve system efficiency; increasing process throughput to reduce manufacturing costs, and reducing diamond tool wear to minimize performance variations across the lens arrays. Constraints implicit from both machining and molding processes were

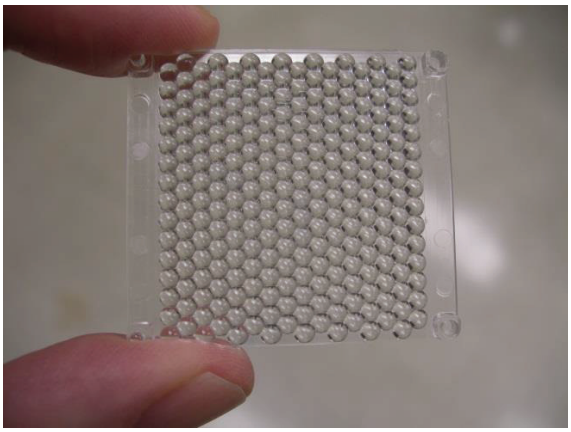
FIGURE 9. Second generation test molded lens array.

incorporated into the opto-mechanical design process. While final insert fabrication remains in process, a 4 x 4 hexagonal test array was produced in 6061-T6 to demonstrate the integrated machining process. Figure 7 shows the machined test part as the form accuracy of the optical elements is roughly 1.5 µm, Figure 8, with a surface finish of 30 nm Sa near the optic apex. Similarly, fabrication of the mold insert for the "wedding cake" features on the rear optic has demonstrated feature dimensional and position accuracies of ±5 µm or better.

Initial optic molding has also been examined by molding a simplified test part, Figure 9. Conventional ball milling was utilized to fabricate the mold insert "optic" array since process development, material shrinkage and array distortion were the metrics of interest; not optic surface finish or form. In-plane material shrinkage across the part was less than 0.2% as the optics were located in X and Y with an accuracy of ±5 µm, Figure 10. Out-of-plane distortion of the entire part, Figure 11, however, approached 100 µm as proper part filling at the corners with minimal distortion has proven difficult. As a result, design changes have been incorporated into the mounting features and part geometry to improve filling and reduce distortion.

FUTURE WORK

Continued work on prototype MEPV systems is focused on increasing collection efficiencies, reducing module size, improving module integration and packaging, and demonstrating cost effective manufacturing strategies. The second generation MEPV system is currently being fabricated and assembled, while a third generation device is being designed.

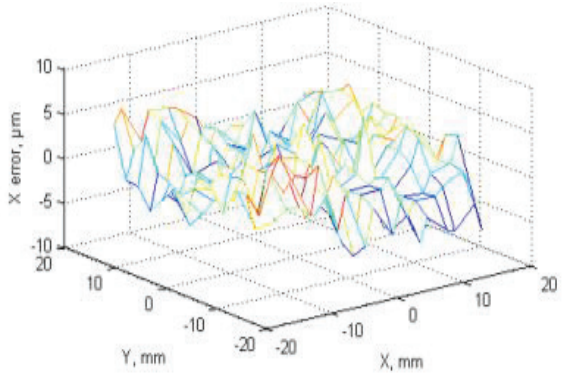

FIGURE 10. Molded test sample in-plane X position errors.

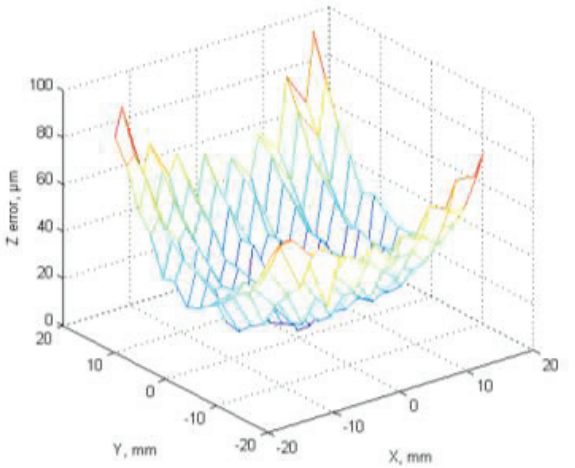

FIGURE 11. Molded test sample out-of-plane Z distortion.

ACKNOWLEDGEMENTS

Sandia National Laboratories is a multi-program laboratory managed and operated by Sandia Corporation, a wholly owned subsidiary of Lockheed Martin Corporation, for the U.S. Department of Energy's National Nuclear Security Administration under contract DE-AC04-94AL85000. This document has been reviewed and approved for unclassified, unlimited release under SAND2013-6466C.

REFERENCES

[1] Gupta V, Cruz-Campa, J, Okandan M, Nielson G. Microsystems-Enabled Photovoltaics: A Path to the Widespread Harnessing of Solar Energy. Future Photovoltaics. May 2010.

[2] Nielson G, et al. Cell Microconcentrator Module with Moderate Concentration, ±4° Acceptance Angle, and 13.3 mm Focal Length. Proceedings of PVSC 2013, Tampa Bay, FL.

Modal Decoupling via Flexure-based Transmissions as Applied to a Micromachined Tuning Fork Gyroscope

Marcel A. C. Thomas[1], Robert M. Panas[1], Martin L. Culpepper[1] and Christopher M. DiBiasio[2]
[1]Department of Mechanical Engineering
Massachusetts Institute of Technology
Cambridge, MA, USA
[2]Hardware Division
Draper Labs
Cambridge, MA, USA

ABSTRACT

Herein, we show that it is possible to decouple the resonant mode shapes of high-performance MEMS tuning fork gyroscopes (TFGs). and to reject linear acceleration disturbances. When properly applied, this leads to (i) increased separation of desired and undesired modes from ~10% to 300% and (ii) decoupled mode shapes. Dealing with (i) and (ii) is important if small-scale solid state gyroscopes are to ever be more than laboratory experiments. They may be used for inertial guidance in aerospace and rollover detection in automobiles. We will present a new design concept, the underlying model, and then demonstrate utility via design of an early meso-scale prototype gyroscope.

INTRODUCTION

TFGs behave according to the following equation 1 and Fig. 1a:

$$\vec{a}_C = 2\vec{\Omega} \times \vec{v} \qquad [1]$$

Proof masses, M_1 and M_2 shown in Fig. 1, are driven by electrostatic comb drives at a velocity v, but in opposite directions. This is called the "drive" mode. The masses experience a Coriolis acceleration, a_C when the system rotates with an angular velocity Ω. The masses are mounted on springs therefore the Coriolis force causes a relative displacement. The mode shape, where one mass moves in the +Y direction and another mass moves in the –Y direction, is called the "sense" mode.

A TFG is driven at or near resonance to minimize energy requirements. Thus, mode ordering is critical to performance. Mode shapes where the proof masses move in the same direction must be >10% from the operating resonance frequency, or they will distort the sensor's signal beyond utility [1].

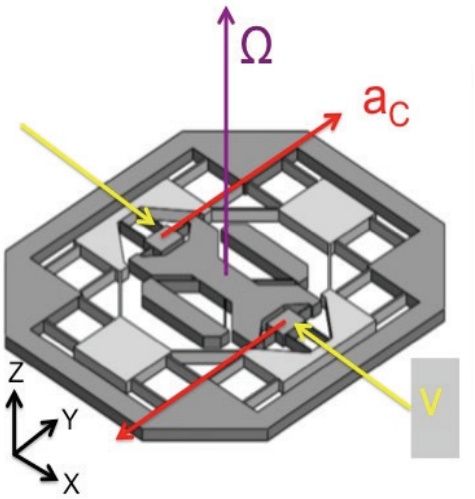

(a)

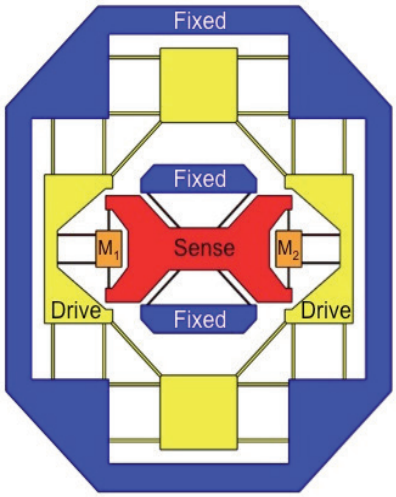

(b)

FIGURE 1. Our TFG. Material in blue is fixed. Flexures (yellow) control the "drive" mode, flexures (red) control the "sense" mode, and material in orange moves in drive and sense.

There are two inherent issues with state-of-the art TFGs that preclude practical use. First, TFGs have undesired modes in close proximity to useful modes with high coupling between desired and undesired modes. Second, TFGs have been designed as 'springs' rather than bearing elements. They are underconstrained, and therefore sensitive to disturbance accelerations and undesired rotations (i.e. rotations about X and Z in Fig. 2.) Useful information can only be obtained if these TFGs are manufactured to tight and expensive tolerances. Several companies have worked for decades, and spent millions of dollars, on gyroscope designs that are inherently coupled and under-constrained [1]. Herein we demonstrate how precision design process/principles [2,3] yield a design without these inherent problems.

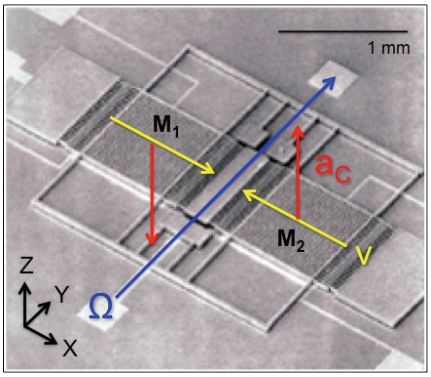

FIGURE 2. Draper-Honeywell TFG [1]

NEW TFG DESIGN

Our TFG is shown in Figures 1 and 3. The motion for the drive and sense mode shapes are kinematically decoupled. If the TFG does not perform as desired, the drive and sense modes may be tuned independently by changing the flexures responsible for their specific kinematics. The drive and sense modes (modes 1 and 2) are shown in Fig. 3.

This design has multiple advantages: (i) increased separation of desired and undesired modes from ~10% to 300% and (ii) decoupled mode shapes. This new TFG may retain a 2½D geometry and may therefore be fabricated via micromilling/EDM (metals) or DRIE (silicon).

The conference paper will lay out the technical details underlying the mechanism design and sensitivity analysis. Data from a meso-scale prototype will be used to compare theory and behavior as well as demonstrate improved performance over current state-of-the-art TFGs.

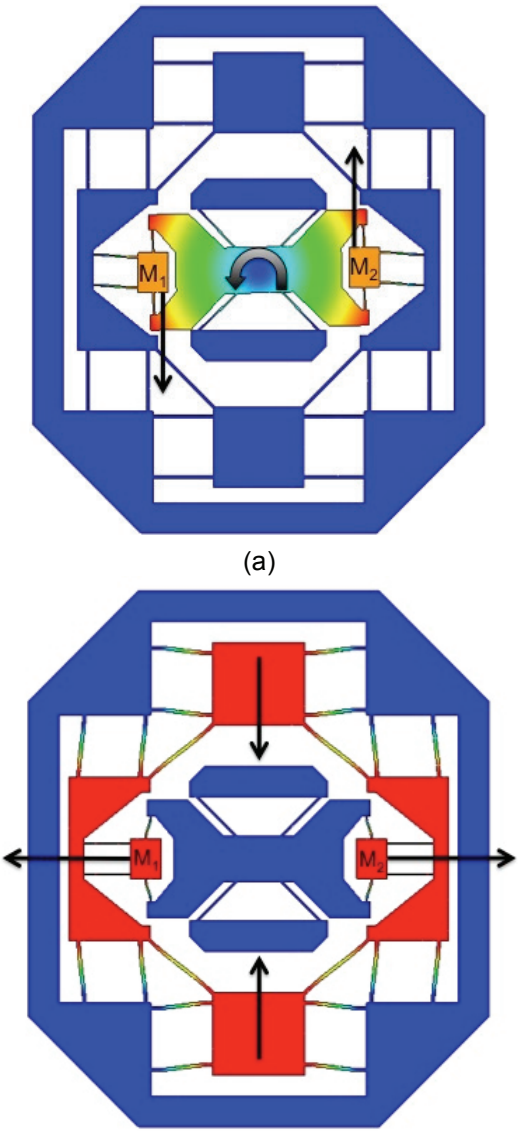

FIGURE 3. "Sense" mode (a), "Drive" mode (b)

DESIGN METHOD

The method of designing this new gyroscope utilizes a combination of FACT [2] and flexure-based transmission mechanisms [3]. The challenges of designing this flexure lies in linking the masses to move in opposite directions, then combining the mode shapes. The abstract idea that forms the basis of the design is shown in Figure 4.

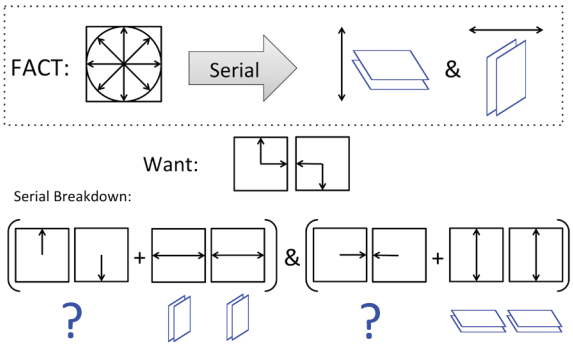

FIGURE 4. Required gyroscope degree of freedom chart.

FACT shows that to obtain a flexure that exhibits 2 DOF translations, the flexure must be composed of two 1DOF translation flexures that are formed by the constraint space of two parallel planes, shown in Fig. 4 [2]. The question marks underneath the opposite motions indicate that there is no constraint space associated with these desired motions. Table 1 introduces the possible motions from screw theory. The "T" represents translations, the "R" represents rotations, and the "S" represents a screw motion. The transmission ratio can also be varied, allowing the linked mass to move by a different amount than the input mass. A negative transmission ratio indicates that the masses can move in opposite directions. The masses can also move along different axes.

Input	Intermediate Stage	Output		
		Type	Transmission Ratio (TR)	Axis
T	T	T	TR = 1	same
R	R	R	0 < TR < 1	
	S		TR = 0	
S	rigid	S	-1 < TR < 0	off
	none	none	TR = -1	

TABLE 1. The possible combinations of motions from screw theory.

The chart allows for the required gyroscope motions by introducing an intermediate stage. There may be a plurality of intermediate stages. Fig. 5 shows design concepts for the drive axis. Fig. 6 shows design concepts for the sense axis. The gyroscope combines the concepts from 5a and 6a because 6a contains flexures that overlap with the drive axis.

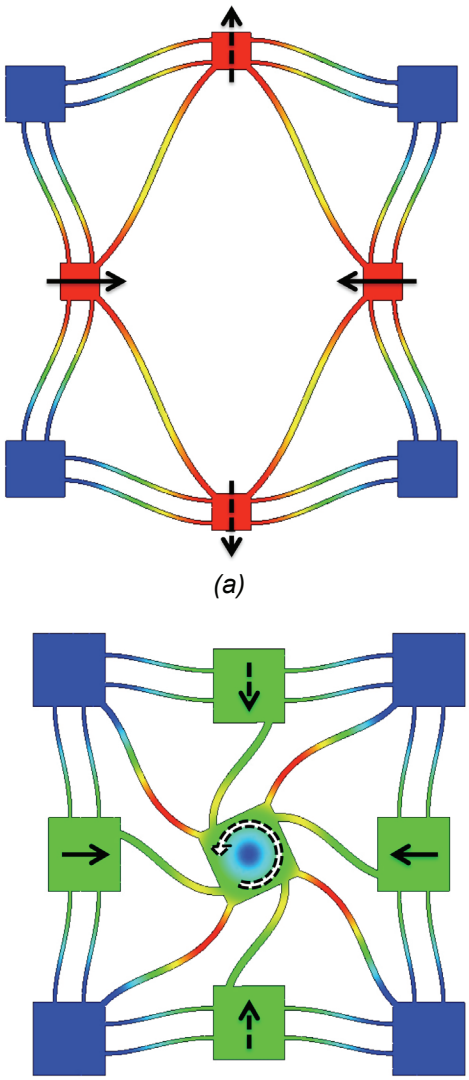

(a)

(b)

FIGURE 5. Concepts for the drive axis. The dashed lines indicate the motions of the intermediate masses. (a) The drive axis concept used in our TFG. The combination from Table 1 is [T,T,T,TR=-1, same]. (b) Another drive axis concept with a different intermediate stage. The combination from Table 1 is [T,T,R,T,TR=-1,same].

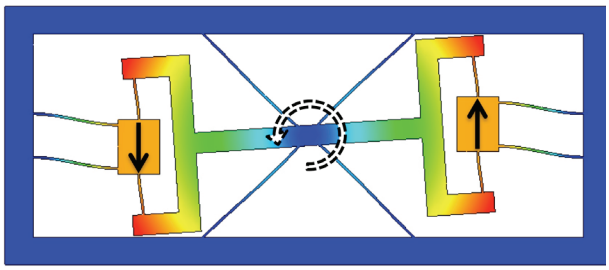

(a)

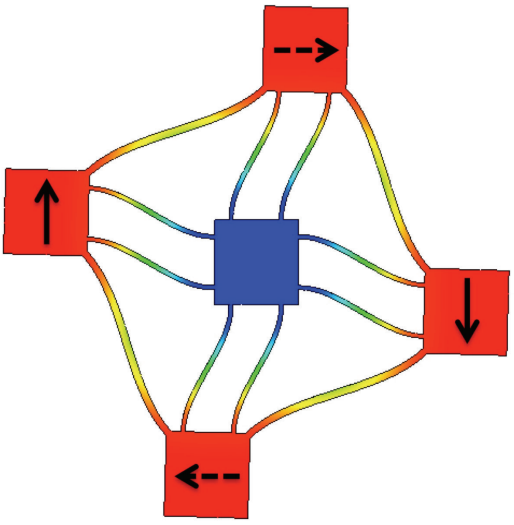

(b)

FIGURE 6. Concepts for the Sense Axis. (a) The concept used in our TFG. The Table 1 combination is [T,R,T,TR=-1,off]. (b) Another sense axis concept with a different intermediate stage. The Table 1 combination is [T,T,T,TR=-1,off].

SENSITIVITY ANALYSIS

TFGs are often trimmed with a laser after they are micromachined to correct for manufacturing errors. However, the head of the laser can be tilted to the side by up to 1 degree. The taper can cause the masses to move out of plane by up to 8% of the in plane motions. Linking the masses can cause a 4x reduction in out of plane motions. An FEA simulation was performed to illustrate how much the masses should move out of plane. The FEA simulation result is shown in Figure 7.

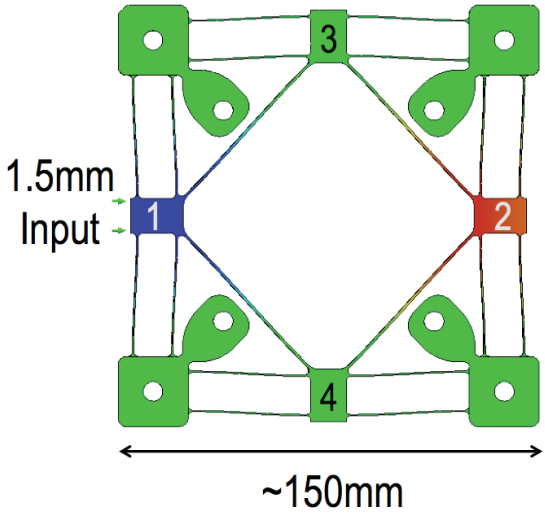

FIGURE 7. FEA simulation including 1 degree of taper. The displacements of masses 1, 2, 3, and 4 are -29, 30, 4, and 4 microns, respectively.

An experiment was performed to measure the out of plane motion of the masses. The masses were actuated in plane by micrometer heads and the out of plane motion was measured with capacitance probes, shown in Figure 8. The data from the experiment is shown in Figure 9.

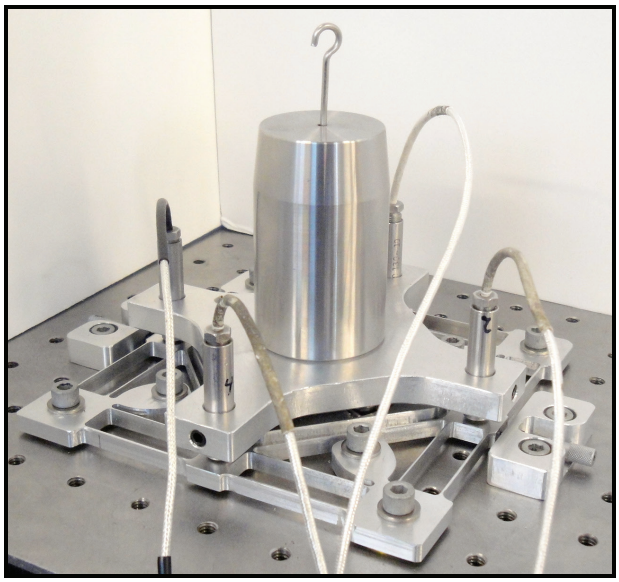

FIGURE 8. Experimental setup. The masses are displaced by micrometer heads and the out of plane motions are measured with capacitance probes.

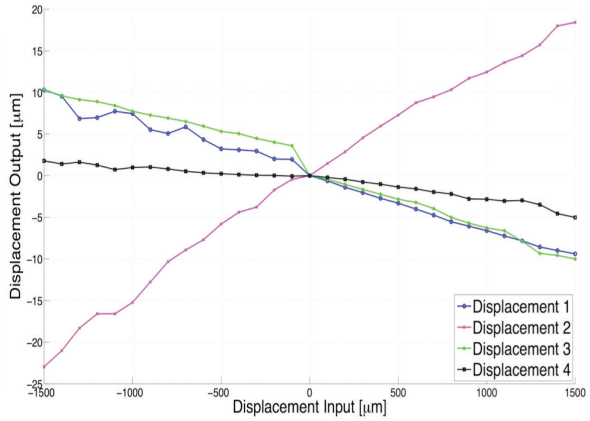

FIGURE 9. Displacement data. The maximum displacement out of plane is -23 microns exhibited by mass 2.

The maximum out of plane motion is -23 microns for a -1500 microns of input. This is less than the FEA predicted, which illustrates that the FEA provides a conservative estimate. The FEA and the experiment both show that the out of plane motion is ~2%, which is four times less than the in plane motion of the current TFG.

REFERENCES

[1] Weinberg M, Kourepenis A. Error Sources in In-Plane Silicon Tuning Fork MEMS Gyroscopes. Journal of Micro-electromechanical Systems. 2006; 479-91.

[2] Hopkins J. Design of Flexure-based Motion Stages for Mechatronic Systems via Freedom, Actuation and Constraint Topologies (FACT), PhD Thesis, MIT 2010

[3] Hopkins J, Panas R. Design of Flexure-based precision transmission mechanisms using screw theory. Prec. Eng. 2013; 299-307

PERFORMANCE OPTIMIZATION OF LARGE STROKE FLEXURE HINGES FOR HIGH STIFFNESS AND EIGENFREQUENCY

K. Gunnink, R.G.K.M Aarts, and D.M. Brouwer
Mechanical Automation and Mechatronics
University of Twente, Enschede, The Netherlands

ABSTRACT

Two flexure hinge types are optimized for high support stiffness and high first unwanted eigenfrequency for two different working ranges, ±5.7° and ±20°. We show how multiple performance specifications lead to different designs with different performance. The optimization uses efficient parameterized non-linear beam-based models. The constraints and load case are taken from an electron microscopy use case.

Optimization results show that the Three Flexure Cross Hinge has the highest first unwanted eigenfrequencies, while the new Infinity Flexure Hinge shows highest support stiffnesses. The design of the optimal geometry is detailed such that a prototype mechanism is manufactured and tested. Experiments show that the first unwanted eigenfrequency is 35 times higher than the first eigenfrequency throughout the working range.

INTRODUCTION

Precision mechanisms often use flexure based hinges for their deterministic behavior and the absence of friction, stiction and backlash. Motion in vacuum is easily enabled without contamination by particles. However, the initially high support stiffness decreases rapidly with deflection. Therefore, sound conceptual designs need to be optimized for stiffness and eigenfrequency over the range of motion with limited stress, actuation stiffness and in a confined volume. The dimensions of the flexures will strongly affect the occurring stresses and performance, making it complex and time-consuming to find the optimal parameters. Chen and Howell [1] proposed a thickness-to-width ratio independent analytical method, but this method is only applied to notch hinges. With more complex shapes, such as the Cross-spring Pivot [2], here called Three Flexure Cross Hinge (TFCH), a numerical method based on a parametric model is preferred to find the optimal design. Boer et al. [3] use a multibody modeling approach, applied to the Curved Hinge Flexure, with which accurate results are obtained for the stiffness characteristics and maximum occurring stresses. Wiersma et al. [4] proposed a method to investigate the performance of several flexure hinge types for large deflection. The new Infinity Flexure (∞-FH, shown in Figure 1) appeared to have the highest first unwanted eigenfrequency over a ±20° range of motion. The compliant actuation direction causes the lowest eigenfrequency. Therefore, the first unwanted eigenfrequency is the second; f_2. However, only one load case with a large moment of inertia and a single optimization criterion, the first unwanted eigenfrequency, were used.

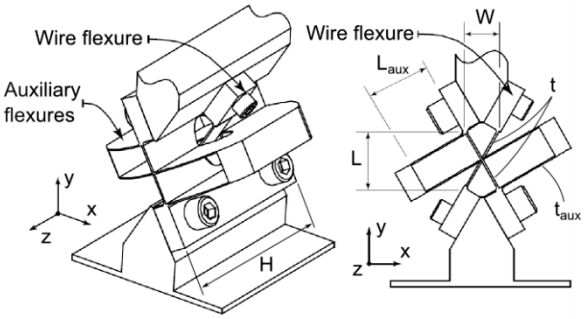

Figure 1. Parameterization of the ∞-FH [4].

This paper extends the method by researching the influence of a different load case, two optimization criterions and the influence of optimizing for different ranges of motion. The TFCH and the ∞-FH, the flexures that showed the best performance [4], are compared.

OPTIMIZATION METHOD

The optimization method starts by defining optimization criteria. Secondly an optimization routine with cost function and constraints should be set-up. Next a sufficiently accurate and fast flexure model is required. The initial geometry is based on sound designs in this case originating from Wiersma [4].

OPTIMIZATION CRITERIA

The optimization criteria are based on an electron microscopy device case. The stiffness at point *T*, Figure 2, and the first unwanted eigenfrequency are of importance. Figure 2

shows a schematic overview of the hinge and load case in undeflected position. The hinge rotates about the origin and is on one side fixed, while on the other side a body is attached. This body is assumed to be rigid and has its center of mass at point *C*. In this point, the mass of the rigid body *m* and inertia, detailed in Table 1, are attached. In point *T*, at a distance *R* = 50 from the origin, a tool can be attached, such that the support stiffness at this location is important. Point *C* is fixed with respect to *T*. The dimensions of the hinge and rigid connection to point *C* can be varied in the optimization. The hinge has Inconel 718 flexures with a Young's modulus of 210 GPa. The hinge orientation line is used to orient the hinge with respect to the load in point *T*, as parameterized by the angle ϕ. Finally, θ is the deflection angle of the hinge.

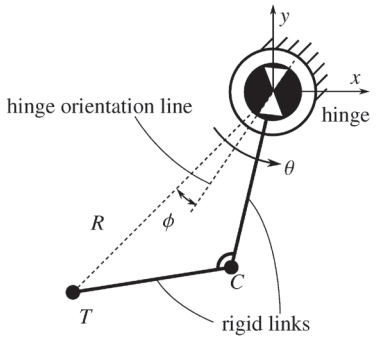

Figure 2. Schematic overview of the mechanism and load case.

Table 1. Loadcase parameters.

Parameter	Value	Unit
m	0.100	kg
J_{xx}	$21.8 \cdot 10^{-6}$	$kg \cdot m^2$
J_{xy}	$-4.88 \cdot 10^{-6}$	$kg \cdot m^2$
J_{xz}	$-3.48 \cdot 10^{-6}$	$kg \cdot m^2$
J_{yy}	$18.0 \cdot 10^{-6}$	$kg \cdot m^2$
J_{yz}	$-3.22 \cdot 10^{-6}$	$kg \cdot m^2$
J_{zz}	$19.8 \cdot 10^{-6}$	$kg \cdot m^2$

OPTIMIZATION ROUTINE

In order to maximize the support stiffness or first unwanted eigenfrequency, two cost functions are minimized in two separate optimization runs. Firstly, the hinges are uni-directionally optimized for stiffness in *z*-direction c_z at point *T*, for the deflection angles +5.7° and +20°. Secondly, for the first unwanted eigenfrequency the hinges are optimized for bi-directional ranges of motion of ±5.7° and ±20°. In order to obtain a manufacturable design with restricted dimensions, the non-linear constraint function includes limits on the Von Mises stress to 600 MPa and the actuation moment to 6 Nm. A lower limit is set for the first unwanted eigenfrequency f_2 > 300 Hz in the full working range. The optimization algorithm needs to deal with non-linear constraints and since the derivatives of the parameter set are unknown a derivative free algorithms is required. A suitable algorithm presented by Nelder and Mead [5] is modified such that the parameter vector is discarded if the constraint function is violated.

FLEXURE MODEL

The optimization requires a parameterized model. In order to keep the computation time within bounds, an efficient modeling approach is required. While Finite Element methods are accurate and widely used, models require large numbers of elements in order to handle the displacements and deformations accurately. Therefore we used models that are based on a flexible multibody approach called SPACAR with non-linear finite beam elements such that it can capture the geometric non-linear behavior with a small number of elements and relatively low computation times [6]. The flexure dimensions (short and wide) do not match well with the assumptions of Euler beam theory, so we modified the torsion stiffness of the beams to account for constrained warping [4]. We used ANSYS APDL and ANSYS Workbench to validate the results from SPACAR. For an experimental validation, a prototype is built. It includes actuators and sensors and has to be vacuum compatible. Measurement data and simulation results are compared in order to verify the optimization and performance of the hinges.

DESIGN 1: THREE-FLEXURE CROSS HINGE

For both hinge types, a suitable parameter vector is presented and parameter bounds are provided, such that the optimal geometry is manufacturable and its volume confined. The parameterized geometry of the TFCH is shown in Figure 3. The parameter vector to optimize is given by {*L w t* h_0 ϕ}, where *L* and *w* are the length and width of the hinge and *t* the thickness of the three flexures. The hinge height *H* is fixed to 54 mm, such that using the outer flexure height h_0 as parameter is sufficient to describe the height of all three flexures. The hinge orientation angle ϕ is the angle between the direction of the outer flexures and point *T*, see Figure 2. The lower and upper parameter bounds, summarized in Table 2, are required in order to obtain a feasible solution.

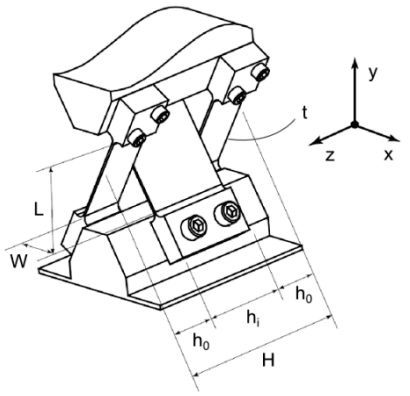

Figure 3. Parameterization of the TFCH [4].

Table 2. Parameter bounds for the TFCH.

Parameter	L mm	w mm	t mm	h_0 mm	ϕ °
Lower bound	10	6	0.2	8	-30
Upper bound	40	15	0.7	15	30

The optimal geometries for the TFCH are determined for highest support stiffness and highest first unwanted eigenfrequency. These geometries are shown in Figure 9. The varying results over the range of motion are shown in Figure 4 and Figure 5. Table 3 summarizes the performance of the optimal hinges. The maximum Von Mises stress showed to be the critical constraint in all cases and is therefore not mentioned. The required actuation moment M is significantly lower for the eigenfrequency optimization at θ_{opt}= 5.7°.This is a result of the shorter and thinner flexures, see Figure 9(b).

Table 3. Performance of the optimal TFCH geometries. M is the actuation moment required for the full stroke θ_{max}, while c_z and f_2 values are measured at θ_{opt}.

Criterion	θ_{opt} °	M Nm	c_z N/m	f_2 Hz
c_z	5.7	1.42	$8.50 \cdot 10^6$	507
f_2	5.7	0.38	$6.81 \cdot 10^6$	1619
c_z	20	1.56	$2.31 \cdot 10^6$	528
f_2	20	1.52	$1.35 \cdot 10^6$	836

DESIGN 2: INFINITY-FLEXURE HINGE

The ∞-Flexure Hinge is shown in Figure 1. The parameter vector describing this hinge is {L w t L_{aux} t_{aux} ϕ}. The hinge orientation angle ϕ is the angle direction of the main flexure and point T, see Figure 2. The parameter bounds for the ∞-FH are summarized in Table 4.

The optimal geometry for the ∞-FH is determined for highest support stiffness and highest first unwanted eigenfrequency. The results are shown in Figure 10 and summarized in Table 5. In order to reduce computation times only several parameters are included in the optimization parameter vector. The auxiliary body height converged to 42 mm. The thickness of the wire flexure t_w was approximately equal to the main flexure thickness t. The wire height h_w was set at 15 mm, which is reasonable compromise between lateral stiffness of the flexure and loss of c_z stiffness due to a hole in the main flexure. The auxiliary bodies of the hinge have a thickness of t_1, which was optimized in a second optimization.

Table 4. Parameter bounds for the ∞-FH.

Parameter	L mm	w mm	t mm	L_{aux} mm	t_{aux} mm	ϕ °
Lower bound	25	10	0.4	20	0.3	-30
Upper bound	45	25	0.7	40	0.7	30

Table 5. Performance of the optimal ∞-FH geometries. M is the actuation moment required for the full stroke θ_{max}, while c_z and f_2 values are measured at θ_{opt}.

Criterion	θ_{opt} °	M Nm	c_z N/m	f_2 Hz
c_z	5.7	2.74	$11.8 \cdot 10^6$	436
f_2	5.7	1.62	$3.5 \cdot 10^6$	542
c_z	20	5.05	$5.6 \cdot 10^6$	327
f_2	20	3.37	$3.8 \cdot 10^6$	438

INFLUENCE OF OPTIMIZATION CRITERIA

Figure 4 and Figure 5 show the support stiffness and first unwanted eigenfrequency respectively, for the full stroke of ±20°. The solid lines correspond with stiffness optimizations, whereas the dashed lines correspond with eigenfrequency optimizations. The influence of the criterion is clearly visible, since the stiffness of an eigenfrequency optimization is significantly lower than for the case when this stiffness was the optimization goal. For example, the first unwanted eigenfrequency f_2 of the TFCH optimized with θ_{opt} =5.7° is about 50% higher for the f_2 optimization over almost the entire stroke.
The results of this research demonstrate clearly that the optimization criterion is of major importance for the resulting optimal geometry. Hence, it should be specified clearly in view of the design requirements.

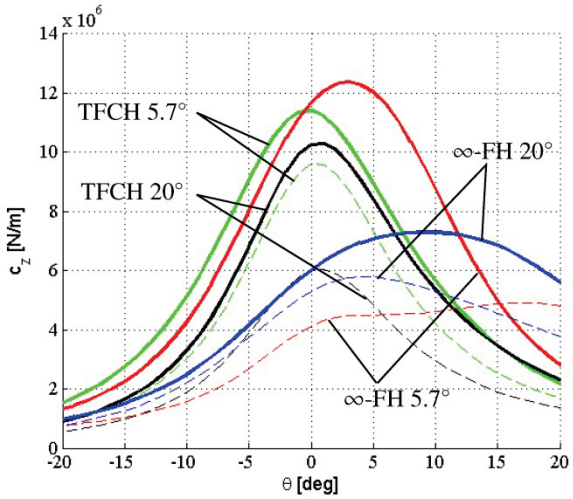

Figure 4. TFCH and ∞-FH stiffness results.

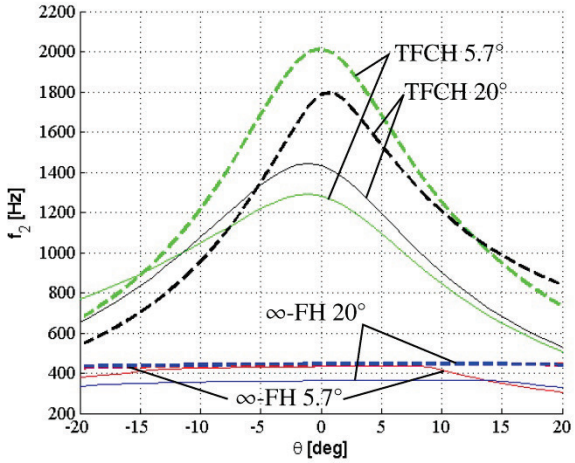

Figure 5. TFCH and ∞-FH first unwanted eigenfrequency results.

With respect to the optimal geometric designs, Figure 9 and Figure 10, we can conclude:
-The optimized geometries of the TFCH are smaller than the ∞-FH.
-The optimization of eigenfrequency leads to smaller designs than the optimization for stiffness
-The point where the stiffness is optimized is close to collinear with the main flexure of the ∞-FH and the outer flexures of the TFCH ($|\phi|<12°$).
-Due to low frequency internal modes of the auxiliary flexures the optimization for eigenfrequency of the ∞-FH leads to smaller auxiliary flexures than optimizing for stiffness. Larger auxiliary flexures allow thicker auxiliary flexures which are crucial for torsional stiffness and therefore for stiffness at $\theta = 5.7°$ or 20°.

- The asymmetric shape of the support stiffness lines of the ∞-FH shows that this flexure can be tuned to a specific load case very well. Alternatively, the TFCH design is less susceptible to optimization criteria changes than the ∞-FH.
-Optimization for stiffness or eigenfrequency leads to local compliance flexure designs as opposed to distributed compliance. This is proven by the fact that none of the optimizations was limited by the upper bound on the length parameter.
-Optimizing for $\theta = 5.7°$ leads to smaller designs than for $\theta = 20°$.

EXPERIMENTAL VALIDATION

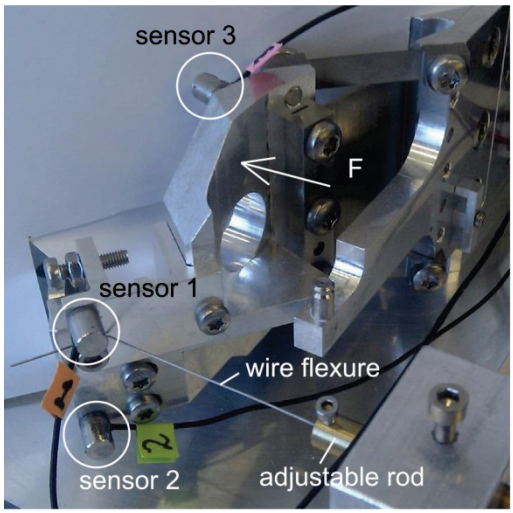

Figure 6. Measurement setup for investigation of the effects of a deflected hinge. The accelerometers are encircled and the direction of the impact force F is shown.

The eigenfrequencies of the prototype were measured in order to verify the simulation results. The prototype was placed on an isolated table and tested using three accelerometers and a small impact hammer. Figure 6 shows the locations of the three accelerometers, which measure the acceleration perpendicular to the face to which they are attached. The location and direction of the impact hammer force is shown as well. The shown wire flexure can be used to constrain the actuation direction, but is not used in this paper. Figure 7 shows the FFT-data of the measurements, from which it can be seen that the actuation frequency and both torsion modes are dominant. The large peak at 50Hz for the hammer data and the small peaks at 150 and 250Hz for the measurement of sensor 3 are artifacts of the AC power supply.

The relative amplitudes and phase data of the sensors match with the predicted eigenmodes. The measured eigenfrequencies are summarized in Table 6. The second column of shows the results from SPACAR. The third column summarizes the ANSYS APDL results based on a model using SHELL 281 elements for the flexures and MPC184 elements for the rigid bodies. The FEM analysis of the detailed design is done with ANSYS Workbench and summarized in the fourth column. The last column shows the experimental results.
The models in SPACAR and ANSYS APDL are limited to the flexure design with rigid load and base. The model in ANSYS Workbench contains the finite stiffness of the base and actuated body, where the confined available volume limits the possibilities to increase the stiffness. This gives rise to an extra mode, Figure 8. Therefore the SPACAR and ANSYS APDL results match, and the experimental results confirm the extra mode predicted by ANSYS Workbench.

Table 6. Comparison of eigenfrequency results (in Hz) at $\theta = 0$

Mode	SPACAR	ANSYS APDL	ANSYS Workbench	Exp.
1	28.0	28.2	27.6	29
2	1996	1636	1196	1040
3	2872	2910	1586	1289

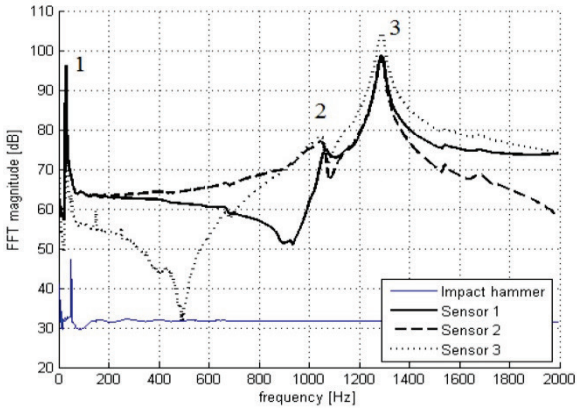

Figure 7. FFT magnitude data. The numbered peaks correspond with the frequencies in Table 6.

CONCLUSION

In this paper, a method is presented for the design and optimization of flexure hinges for large stroke use cases. The influence of the optimization criterion is significant. The trade-off between support stiffness and first unwanted eigenfrequency yields different optimal geometries.

Two hinge types, the Three Flexure Cross Hinge and Infinity Flexure have been analyzed using the presented method. The ∞-FH improves the support stiffness of the system, but a larger volume is required. Furthermore, the internal eigenfrequencies are significantly lower than for the TFCH. The optimization angle can be fine-tuned to perform optimally for specific deflection angles.
Measurements of the manufactured prototype match well with the detailed analysis performed with ANSYS Workbench. Apart from the inherent limitations the modeling and optimization proved to be very attractive for the design of the flexure hinges.

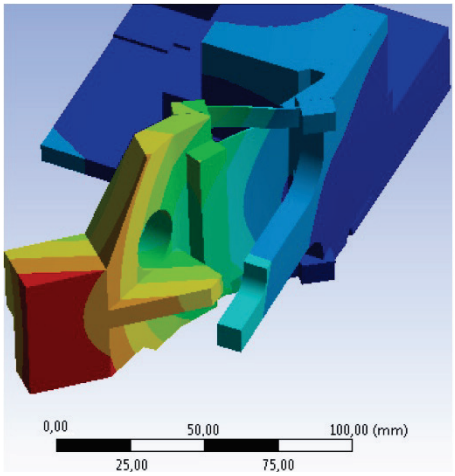

Figure 8. Total deformation plot of the second eigenmode as predicted by the Ansys Workbench analysis of the detailed model.

REFERENCES

[1] G. Chen, L. Howell. Two general solutions of torsional compliance for variable rectangular cross-section… Prec. Eng. 2009; 33: 268-274.
[2] J. Haringx. The cross-spring pivot as a constructional element. Applied Scientific Research. 1949; 1: 313-332.
[3] S. Boer et al. Multibody modelling and optimization of a curved hinge flexure. Int. conf. on multibody syst. dyn. 2010.
[4] D. Wiersma, et al. Performance optimization of large stroke spatial flexure hinges. J. Comp. Nonlin. Dyn. Submitted.
[5] J. A. Nelder, R. Mead, A simplex method for function minimization, The Computer Journal 7 (1965) 308–313.
[6] J. B. Jonker, J. P. Meijaard, Spacar - computer program for dynamic..., in: Multibody Systems Handbook, Springer-Verlag, Berlin, 1990, 1990, pp. 123–143.

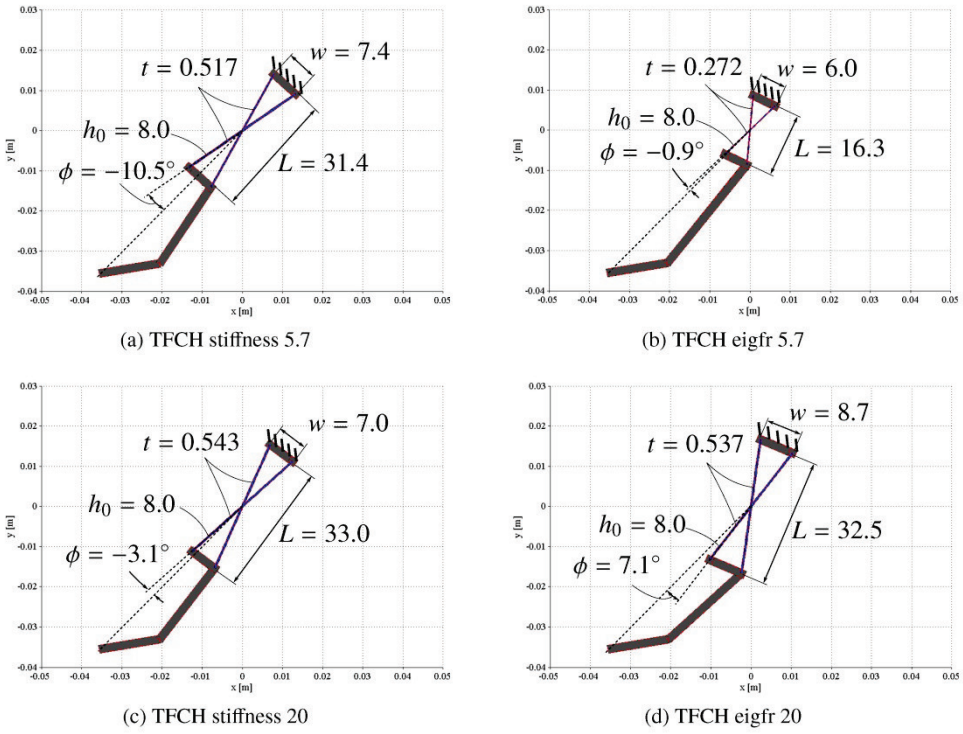

Figure 9. Optimal TFCH geometries for stiffness (left), eigenfrequency (right), 5.7° (top) and 20° (bottom) range of motion. All dimensions in mm. ϕ is the angle between the load and the outer flexures.

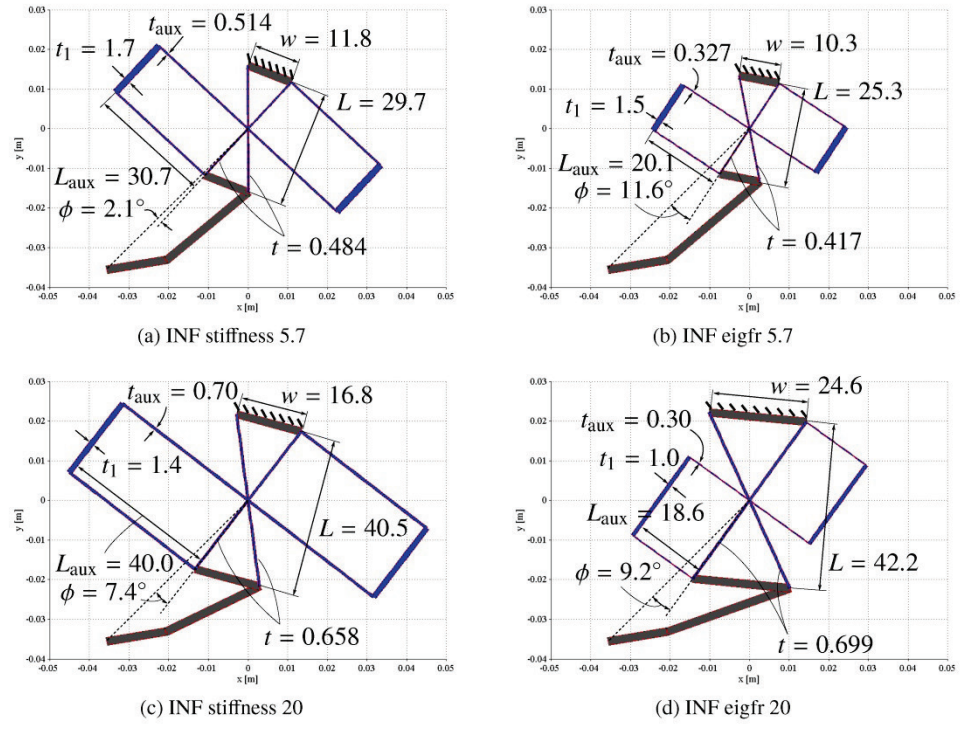

Figure 10. Optimal ∞-FH geometries for stiffness (left), eigenfrequency (right), 5.7° (top) and 20° (bottom) range of motion. All dimensions in mm. ϕ is the angle between the load and the main flexure.

NOVEL SINGLE-AXIS FLEXURE MECHANISM DESIGNS WITH IMPROVED BEARING STIFFNESS

Shorya Awtar (awtar@umich.edu)
Precision Systems Design Laboratory, Mechanical Engineering
University of Michigan, Ann Arbor, MI 48109

INRODUCTION AND BACKGROUND

In this paper, we present two new single-axis flexure mechanism designs that overcome the limitations associated with bearing direction error motion and bearing direction stiffness in the traditional parallelogram and double parallelogram flexure designs, respectively [1, 2].

The parallelogram (P) flexure shown in Fig. 1 provides low motion direction stiffness (K_y), relatively high bearing direction stiffness (K_x), but also exhibits considerable bearing direction error motion (E_x). Assuming the Motion Stage and Ground to be perfectly rigid:

$$K_y = \frac{2EI_1}{L_1^3} k_{11}^{(0)} \qquad \text{Eq. (1)}$$

$$K_x = \frac{2EI_1}{L_1^3} \frac{k_{33}}{\left(1 + k_{33} g_{11}^{(1)} \left(\frac{Y}{L_1}\right)^2\right)} \qquad \text{Eq. (2)}$$

$$E_x = -\frac{k_{11}^{(1)}}{2} \frac{Y^2}{L_1} \qquad \text{Eq. (3)}$$

Here, L_1 is beam length, E is the Young's Modulus, I_1 is the second moment of area in bending, and Y is the motion direction displacement. The non-dimensional coefficients $k_{11}^{(0)}$, $k_{11}^{(1)}$, $g_{11}^{(1)}$, and k_{33} are all functions of the beam shape a_o shown in Fig. 1 and the in-plane beam thickness T_1, as shown in [2]:

$$k_{11}^{(0)} = \frac{6}{\left(3 - 6a_o + 4a_o^2\right) a_o}$$

$$k_{11}^{(1)} = \frac{3\left(15 - 50a_o + 60a_o^2 - 24a_o^3\right)}{5\left(3 - 6a_o + 4a_o^2\right)^2}$$

$$g_{11}^{(1)} = \frac{2a_o^3\left(105 - 630a_o + 1440a_o^2 - 1480a_o^3 + 576a_o^4\right)}{175\left(3 - 6a_o + 4a_o^2\right)^3}$$

$$k_{33} = \frac{6}{a_0 \left(T_1/L_1\right)^2}$$

When a_o = 0.5, which corresponds to uniform thickness beams, these coefficients assume the values of 12, 1.2, 1/700, and $12(L_1/T_1)^2$, respectively. As seen in Eqs. (1) and (2), while K_y remains constant with increasing Y displacement,

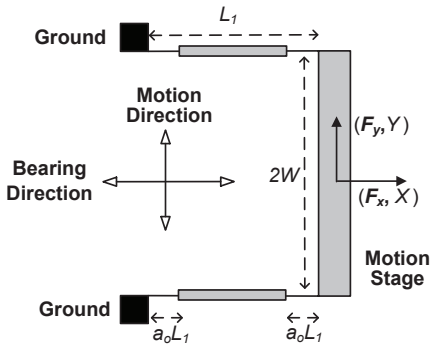

Figure 1. Parallelogram (P) Flexure

K_x gradually drops. This drop is dictated by the elastokinematic effect, which is quantitatively captured by the coefficient $g_{11}^{(1)}$ [1, 2]. This coefficient and therefore the K_x drop can be reduced by optimizing the beam shape via parameter a_o. In general, it is desirable to maximize the bearing direction stiffness (K_x) and minimize the motion direction stiffness (K_y); therefore, the ratio K_x/K_y ratio is plotted in Fig. 2 for a_o = 0.5 and 0.2, with L_1 =1000 μm, T_1 = 3 μm, out-of-plane thickness H_1 = 50 μm, W = 400 μm, and E = 169GPa.

The error motion given in Eq. (3) is fundamental to the kinematics of the P flexure design, causing the Motion Stage to trace a roughly parabolic trajectory instead of a straight line. It arises from beam arc length conservation, which is quantitatively captured by the coefficient $k_{11}^{(1)}$ and cannot be eliminated by beam shape optimization [1, 2]. This

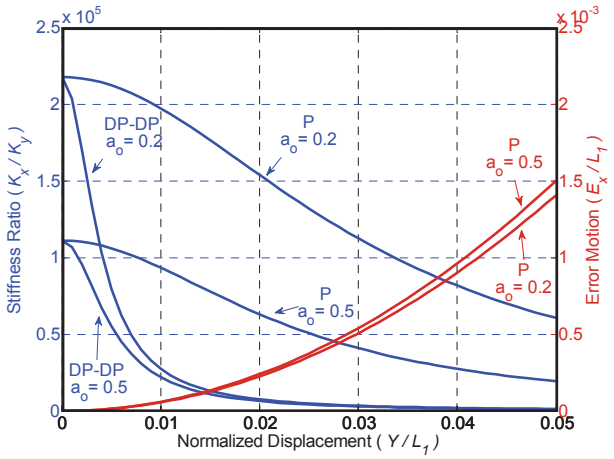

Figure 2. P and DP-DP Flexure Performance

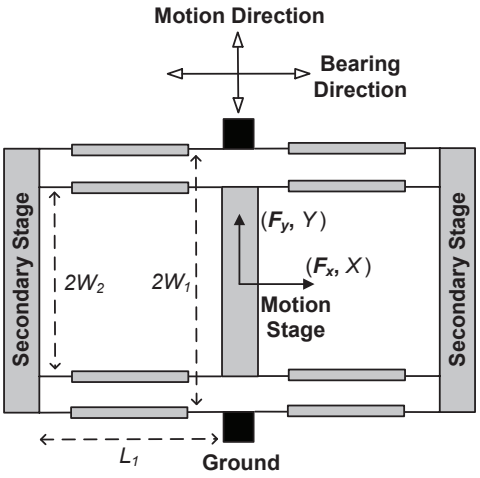

Figure 3. Paired Double Parallelogram (DP-DP) Flexure

error motion is shown in Fig. 2, and proves to be undesirable in certain applications [3].

This error motion is entirely canceled out, in theory, by geometric reversal in the double parallelogram (DP) flexure as well as its paired version (DP-DP) shown in Fig. 3. However, both the DP and DP-DP designs suffer from a precipitous drop in the bearing direction stiffness with motion direction displacement (Y). For the DP-DP flexure design, the bearing direction stiffness is given by:

$$K_x = \frac{2EI_1}{L_1^3} \frac{k_{33}}{\left(1 + \frac{k_{33}\left(k_{11}^{(1)}\right)^2}{k_{11}^{(0)}} \left(\frac{Y}{2L_1}\right)^2\right)} \qquad \text{Eq. (4)}$$

Unlike the P flexure, here the drop in K_x is dictated by the relatively large kinematic coefficient $k_{11}^{(1)}$, which is fundamental to the beam and cannot be reduced much via beam shape optimization. However, the motion direction stiffness (K_y) of the DP-DP flexure remains the same as that of the P flexure, and fairly constant with Y displacement. With the previous dimensions and W_1 = 500 μm and W_2 = 400 μm, the resulting K_x/K_y ratio for the DP-DP flexure is also plotted in Fig. 2 for a_o = 0.2 and 0.5. In the latter case, when going from Y = 0 to Y = 0.01L_1, the K_x stiffness drops by 80% for the DP-DP flexure, compared to 16% for the P flexure.

The large drop in bearing stiffness is explained by the fact that the DP flexure geometry represents a kinematically under-constrained design [1, 2, 4-6]. When its Motion Stage is held fixed at a non-zero Y displacement, its Secondary Stage moves by $Y/2$ but remains kinematically free in the motion direction. Therefore, when a bearing direction force $\boldsymbol{F_x}$ is applied on the Motion Stage, the load-stiffening and load-softening effects in the flexure's constituent beams causes the Secondary Stage to move additionally from its nominal $Y/2$ displacement. This additional displacement of the Secondary Stage leads to a disparity between the geometric contraction of the constituent beams along their length, thus producing an additional displacement at the Motion Stage and therefore an additional compliance in the bearing direction. In the DP-DP flexure, both the Secondary Stages are under-constrained. Upon the application of a bearing force $\boldsymbol{F_x}$, when Motion Stage is displaced by Y, both Secondary Stages move from their nominal $Y/2$ displacement by equal and opposite amounts. An analytical derivation of how this under-constrained behavior affects the bearing direction stiffness is presented in [1, 2].

In this paper, we present two new flexure designs, both based on the DP-DP layout that appropriately constrain the redundant motion of the Secondary Stage, thereby improving the bearing stiffness significantly while maintaining E_x close to zero.

PRIOR ART

The problem of under-constraint in the DP flexure geometry was originally reported by Plainvaux [4] and Jones [5], and subsequently by Awtar [1, 2] and Brouwer [6] among others. While Plainevaux [4] recommended the use of gearing to enforce a 1:2 displacement ratio between the Secondary Stage and Motion Stage of the DP flexure, Jones [6] accomplished this "slaving" of the Secondary Stage via a lever mechanism. A monolithic, flexure-based implementation of this lever solution has been implemented by German [7] and Brouwer [8]. These designs indeed produce the desired improvement in the bearing stiffness of the DP.

A separate approach of pre-tilting or pre-bending the beams of a DP or DP-DP flexure mechanism has been common in the design of MEMS electrostatic actuators [3]. This design variation does not mitigate the drop in K_x stiffness with increasing Y displacement; instead, it shifts the location of the K_x stiffness peak in Fig. 2.

CLAMPED DP-DP FLEXURE DESIGN

In the proposed Clamped Paired Double Parallelogram (C-DP-DP) flexure mechanism, shown in Fig.4, the two Secondary Stages are connected to an external clamp via secondary parallelogram (P) flexures. The high rotational stiffness of these P flexures (provided by an appropriate choice of beam separation W_3) suppresses any relative motion direction displacement between the two Secondary Stages, forcing them to maintain $Y/2$ displacement at all times. This constrains these stages from responding to an $\boldsymbol{F_x}$ force on the Motion Stage. Also, the beam length L_3 and in-plane thickness T_3 in the secondary parallelogram

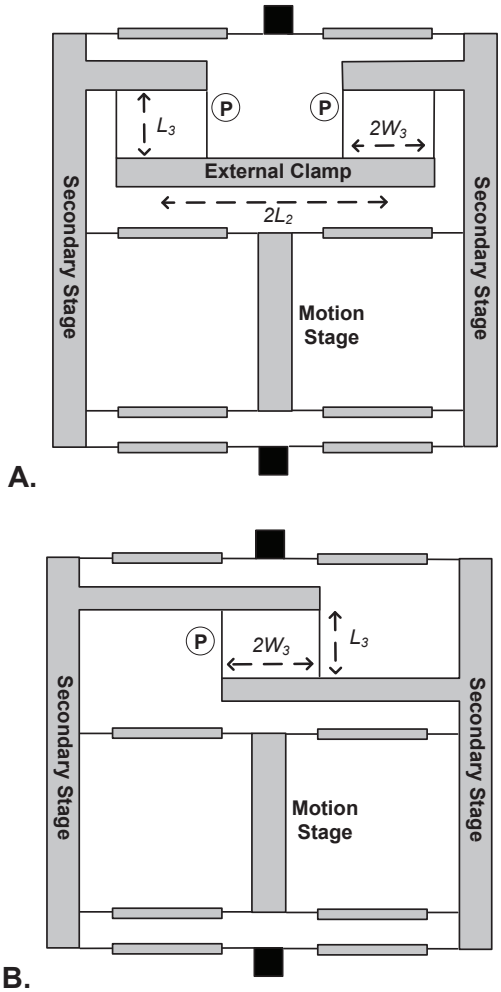

Figure 4. Clamped Paired Double Parallelogram (C-DP-DP) Flexure

flexures are chosen such that they offer minimal resistance to the bearing direction kinematic displacement of the Secondary Stages. This ensures that the motion direction stiffness (K_y) of the C-DP-DP flexure remains the same as that of the DP-DP flexure. However, with the Secondary Stages appropriately constrained, the bearing direction stiffness shows remarkable improvement.

It has been analytically shown that the effectiveness of the clamp is given by the dimensionless parameter η, given by [9]:

$$\eta = \left(\frac{6W_3^2 L_1^3 T_3}{k_{11}^{(0)} L_2^2 L_3 T_1^3} \right)$$

where dimensions are as shown in Figs. 3 and 4. The effect of η on bearing stiffness is shown in Fig. 5 for a_o = 0.5 and other dimensions being same as earlier. When L_3 is sufficiently long (typically within 0.5 L_1) and η is in the range of 100 or greater, the motion and bearing direction stiffness values for the C-DP-DP flexure are given by:

$$K_y = \frac{2EI_1}{L_1^3} k_{11}^{(0)} \qquad \text{Eq. (5)}$$

$$K_x = \frac{2EI_1}{L_1^3} \frac{k_{33}}{\left(1 + k_{33} g_{11}^{(1)} \left(\frac{Y}{2L_1}\right)^2\right)} \qquad \text{Eq. (6)}$$

Thus, the bearing stiffness drop is now dictated by the relatively weak elastokinematic coefficient $g_{11}^{(1)}$, which can be reduced via beam shape optimization (a_o). K_x/K_y stiffness ratio for the C-DP-DP flexure, with η = 575, is plotted in Fig. 5 for a_o = 0.2 and 0.5. In the latter case, from Y = 0 to $Y = 0.01L_1$, the K_x stiffness drops by only 4.5%. E_x in this design remains theoretically zero.

As earlier, the above relations assume that all the components of the mechanism other than the beam flexures are perfectly rigid. Another variation of the C-DP-DP design, shown in Fig. 4b, offers similar improvement in bearing stiffness. Obviously, the C-DP-DP design takes up a larger foot-print, which should be optimized for a given application.

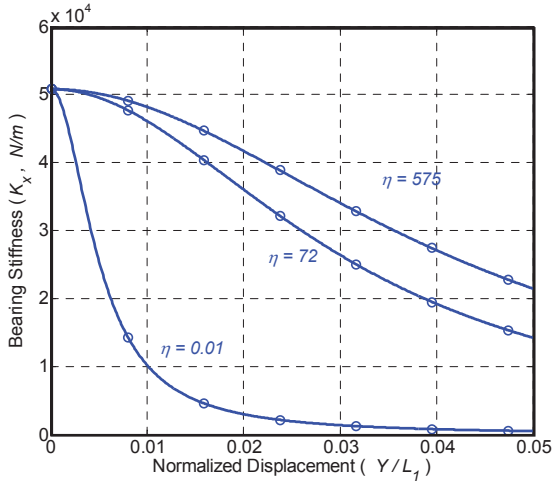

Figure. 5 C-DP-DP bearing stiffness: Analytical results (solid lines) and FEA (circles)

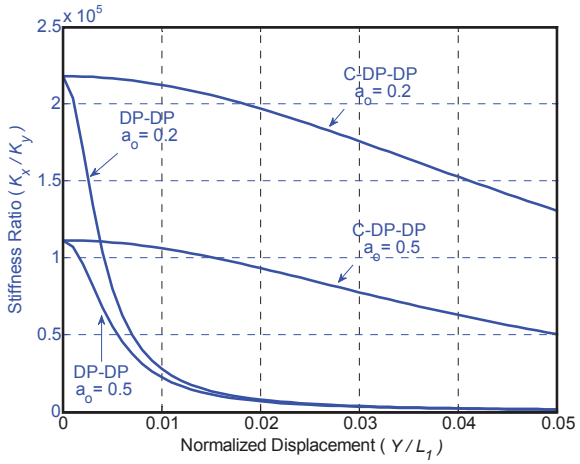

Figure. 6 C-DP-DP Flexure Performance

ASYMMETRIC DP-TDP FLEXURE DESIGN

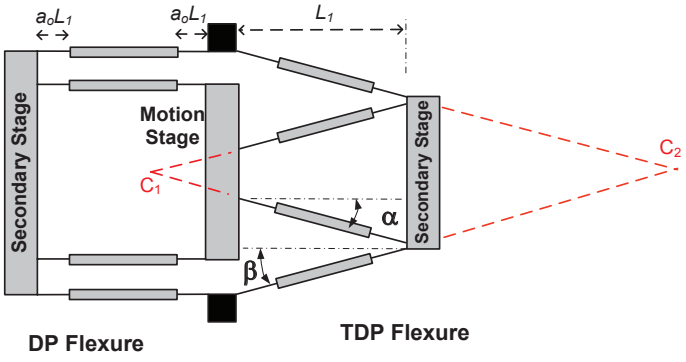

Figure 7. DP-TDP Flexure

The proposed asymmetric Double Parallelogram – Tilted-beam Double Parallelogram (DP-TDP) flexure (Fig. 7) employs a non-intuitive geometric arrangement to kinematically constrain the Secondary Stage of the TDP. The geometry of the TDP module on the right side of Fig. 7 ensures that when the Y and Θ displacements of the Motion Stage are specified, there are two conflicting instantaneous centers of rotation (C_1 and C_2) created for its Secondary Stage. However, for this to happen, the Θ rotation of the Motion Stage has to be specified, ideally to zero. This is not the case for a TDP by itself, which exhibits finite Θ rotation. Therefore, to constrain this Θ rotation to approximately zero, a DP flexure is employed on the left side. Thus, the TDP and DP flexures, when coupled together, serve distinct but highly complementary roles. Even though not good with K_x stiffness, the DP flexure provides a high rotational stiffness which constrains the rotation of the combined Motion Stage. This rotational constraint, in turn, ensures that the Secondary Stage of the TDP is kinematically constrained such that its motion direction displacement remains approximately half that of the Motion Stage. This

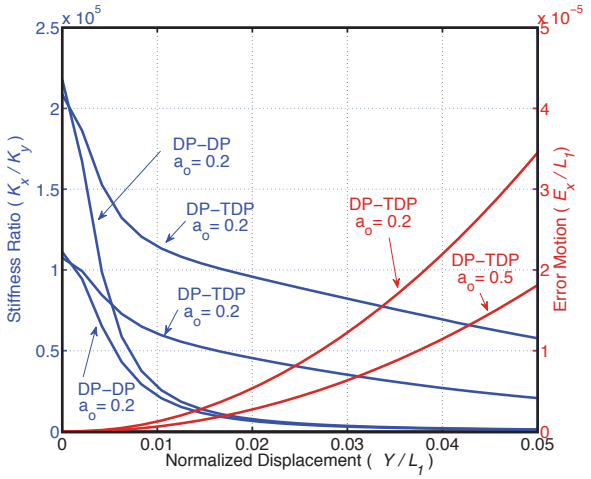

Figure. 8 DP-TDP Flexure Performance

provides the desired improvement in the K_x stiffness behavior of the overall DP-TDP flexure. With suitable choice of angles α and β, the overall K_y stiffness can be maintained at the same level as the DP-DP flexure and the error motion E_x can be maintained close to zero [9]. One optimal combination of α and β is 0.11 and 0.14, respectively.

Closed-form analysis of the DP-TDP design is relatively more complicated. Instead, with same dimensions as earlier, FEA prediction of the K_x/K_y ratio are provided in Fig.8 for a_o = 0.2 and 0.5. In the latter case, from Y = 0 to Y = 0.01L_1, the K_x stiffness drops by 45%. E_x in this design is two orders of magnitude less than the P flexure. The DP-TDP flexure covers approximately the same foot-print as the DP-DP flexure.

RESULTS AND CONCLUSION

All closed-form analytical results presented here have been validated via FEA, which was conducted in ANSYS using BEAM4 elements for the flexures and MPC184 for the rigid stages. Large displacement option (NLGEOM) was turned on. The C-DP-DP and DP-TDP flexures have been separately incorporated within MEMS electrostatic actuators, which experimentally demonstrated large strokes and confirmed the high bearing stiffness. A macro-scale experimental set-up has been assembled to measure the predicted stiffness values, which is work in progress.

REFERENCES

[1] S. Awtar, “Synthesis and Analysis of Parallel Kinematic XY Flexure Mechanisms”, Sc.D. Thesis, Massachusetts Institute of Technology, 2003

[2] S. Awtar, “Characteristics of Beam-based Flex-ure Modules”, *ASME J. Mech. Des.*, vol.129, 2007

[3] J.D. Grade, et al., "Design of Large Deflection Electrostatic Actuators," *ASME/IEEE J. MEMS*, vol.12, 2003

[4] J.E. Plainevaux, “Mouvement Parasite Vertical Dune Suspension Elastique Symetrique a Compensation et Asservissement”, *Nuovo Cimento*, vol.11, 1954

[5] R.V. Jones and I.R. Young, "Some Parasitic Deflexions in Parallel Spring Movements," *J. Scientific Instruments*, vol.33, 1956

[6] D.M. Brouwer, "Design Principles for Six Degrees-of-freedom MEMS-based Precision Manipulators," Ph.D. Thesis, University of Twente, 2007

[7] J.H. Jerman, et al., “Miniature Device with Translatable Member”, US Patent 6664707, 2003

[8] D.M. Brouwer, et al., “Long-range Elastic Guidance Mechanisms for Electrostatic Comb-drive Actuators,” Proc. EUSPEN International Conference, Delft, Netherlands, 2010

[9] S. Sood, “Analysis of Single Axis Flexure Bearings Approaching Ideal Bearing Characteristics”, M.S. Thesis, University of Michigan, Ann Arbor, 2013

Non-Lithographically-Based Microfabrication of a Hexflex Nanopositioner

Robert M. Panas, Prosper Nyovanie, Lucy Du, Elizabeth Schanne, Veronica Szklarzewski, and Martin L. Culpepper
Department of Mechanical Engineering
Massachusetts Institute of Technology
Cambridge, MA, USA

INTRODUCTION

A non-lithographically-based microfabrication (NLBM) process flow has been demonstrated via the fabrication of metal multi-axis MEMS with integrated sensing, in small batches with low average cost. This process [1] allows for low-cost (<$1k) customizable (<1 week fab time) nanopositioning architectures with high performance integrated position sensing (59dB measured, up to 135dB expected at 10kHz bandwidth) to be created for a range of micro-/nano- manufacturing and metrology applications. This is a ≈20x reduction in average cost and time and potentially >30x increase in dynamic range over previous similar nanopositioners [2]. Customized positioning platforms can surmount one of the main hurdles to nanomanufacturing research and development [3], as well as enable further developments in personalized medicine [4] among other applications.

MOTIVATION

A fabrication process for feasible, customizable, meso-scale MEMS nanopositioners must be able to meet several requirements in order to produce a device with integrated sensing: i) bulk micromachining of sub mm-scale mechanical structures out of robust materials like metals, ii) surface micromachining of nm to mm scale electrical structures on the surface of the mechanical structure, and iii) do all of this at low production cost per device.

Currently no fabrication process chain can simultaneously meet all of the requirements laid out above. Traditional fabrication methods can produce mm and larger scale parts, and do so out of many different materials. MEMS microfabrication can produce structures over the correct size scales, however it has significant limitations in the material selection and the cost/time investment are high. A hybrid process, NLBM, has been created to draw from the strengths of each of these approaches in order to make a feasible fabrication process chain.

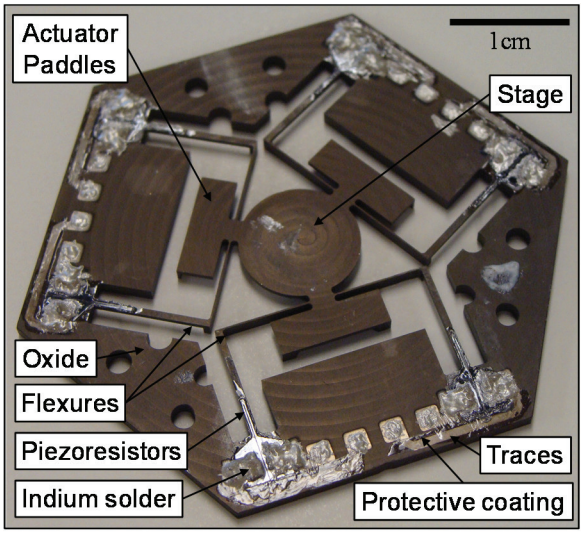

FIGURE 1. Mechanical and electrical structures composing the metal MEMS hexflex nanopositioner.

The NLBM process was driven by a focus on producing a metal MEMS nanopositioner based around the hexflex architecture, shown in Fig. 1. The hexflex architecture is a 6DOF planar flexural nanopositioning platform which is linked to ground via 6 flexural bearings in series, each of which provides a location of integrated strain sensing [2].

NLBM OVERVIEW

The NLBM process has previously been described [1], but the outline of the process will be repeated for clarity. The process, illustrated in Fig. 2, is composed of four steps: i) bulk micromachining, ii) surface micromachining, iii) sensor integration, and iv) circuit bonding. Single crystalline silicon piezoresistors were used for the integrated sensing. A specific process, Thin Film Patterning and Transfer

(TFPT), was developed to fabricate these sensors in a flexible, quick manner.

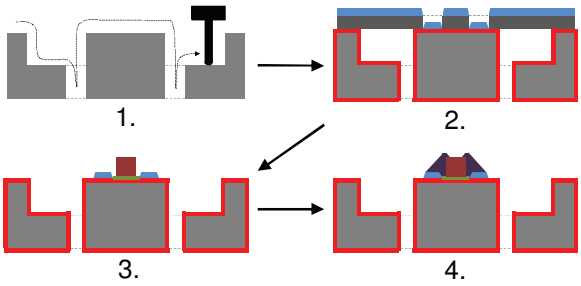

FIGURE 2. Schematic of the NLBM process showing the four main steps.

BULK MICROMACHINING

The bulk micromachining step focuses on the generation of the mechanical structure through conventional milling operations. This forms the outer rigid structure, the center stage and the flexible elements. The milling operation is carried out via a 3-axis Microlution micromill, and only requires about 4 hrs to complete, including stock mounting operations. The completed structure is shown in Fig. 3.

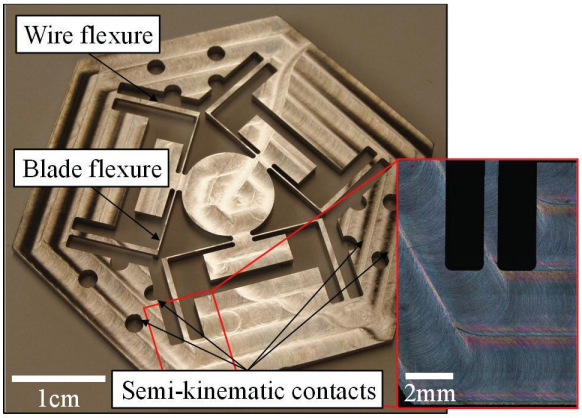

FIGURE 3. Bulk micromachined metal mechanical structure, with closeup on eventual strain sensor location.

The micromilling operation is carried out using a pallet as shown in Fig. 4. This pallet simplifies the process of anchoring the titanium stock via Crystalbond 509-3 adhesive wax. The smaller, removable pallet heats and cools significantly faster (>3x) than the larger structure.

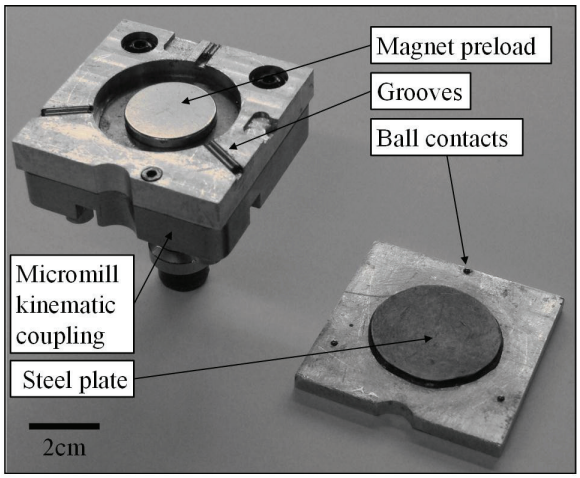

FIGURE 4. Attachment coupling for titanium stock in micromill.

SURFACE MICROMACHINING

The surface micromachining step focuses on the generation of surface electrical features through a combined oxide growth and metal trace deposition process. This results in electrical features that are isolated from the metal body, and thus can be used to form sensor circuitry on the device surface. The oxide generation occurs via a combined anodization and oxidation process, while the traces are deposited via e-beam PVD through a physical shadowmask. The completed features are shown in Fig. 5.

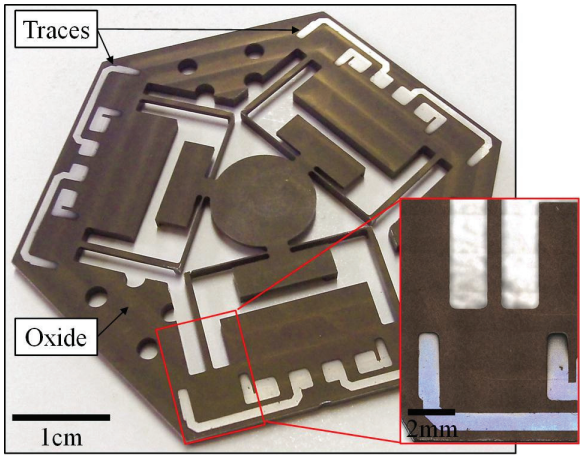

FIGURE 5. Surface micromachined electrical traces deposited on an oxide layer grown over the device.

SENSOR INTEGRATION

The sensor integration step focuses on the fabrication and placement of the device sensors onto the mechanical structure. TFPT is shown schematically in Fig. 6 and is composed of five

steps: i) lamination, ii) laser patterning, iii) etching, iv) transfer, and v) delamination.

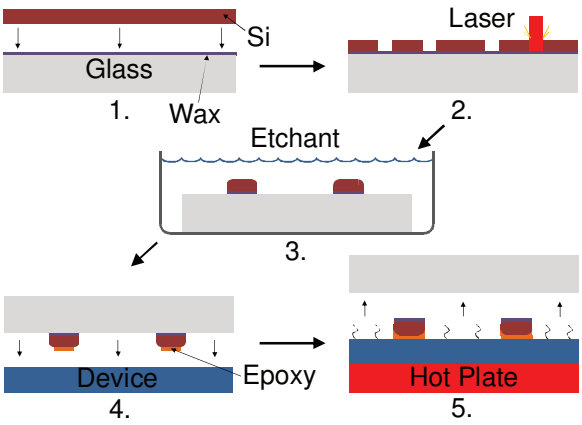

FIGURE 6. Schematic of the TFPT process showing the five main steps.

These five steps produce a sensor structure from bulk single crystalline silicon, and locate this structure at a desired location on the metal structure. The completed device with integrated sensing is shown in Fig. 7.

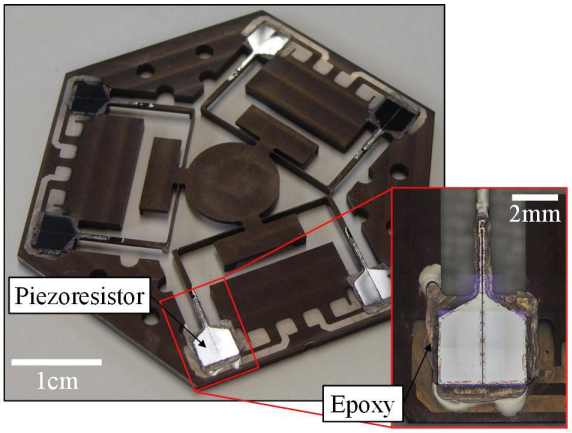

FIGURE 7. Device with silicon sensing integrated onto the structure.

A 50µm p-type doped silicon wafer is diced into stock pieces of about 6x9mm. These pieces are adhered to a borosilicate glass slide via MWM100 etch resistant wax. The wax is wicked under the edges to produce an even film, free of large contaminants. The glass slide is used as it provides a flat handle layer with sharp reference edges (for alignment) that has silicon located in the general area needed for the gages. The resulting structure is shown in Fig. 8.

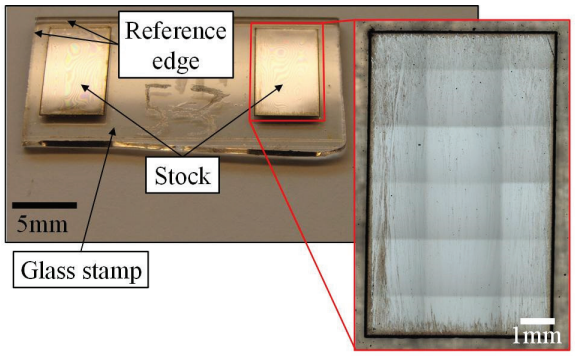

FIGURE 8. Silicon stock attached to the glass slide with wax.

The patterning step requires a specific sequence of cuts, shown in Fig. 9, in order to minimize thermal stress failure on the sensor's fine features. 150µm wide piezoresistor arms (post-etch) were consistently fabricated, with patterning successful down to 25µm final widths.

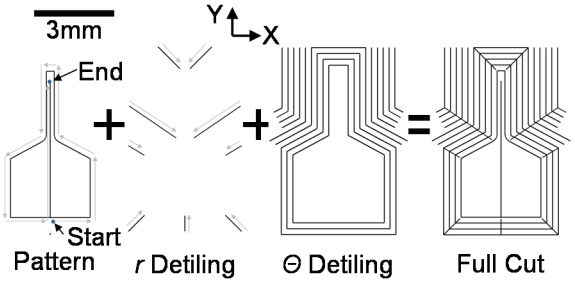

FIGURE 9. Three layers of patterning used to release a functional piezoresistor from bulk silicon stock.

The glass stamp after the patterning step is shown in Fig. 10.

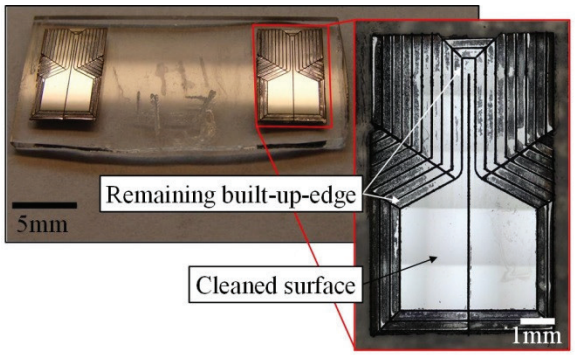

FIGURE 10. Patterned silicon adhered to glass stamp.

The patterned silicon now has the correct geometry and location relative to the reference

edges. The unwanted silicon around the structure is removed with a wax etch that causes the tiled pieces to fall off. The laser cutting damages the silicon, which must be fixed with a silicon etch. A 9:1 mixture by volume of nitric acid to hydrofluoric acid is used to remove the heat-affected zone on the sidewalls of the cut. This rounds out the corners as shown in Fig. 11, bringing the failure strain of the silicon up to around 2500με.

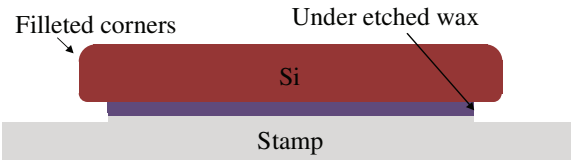

FIGURE 11. Stamp and gages prepared for transfer.

The stamp is prepared for transfer by first reflowing the wax under all parts of the silicon gage. This solidly anchors the gage and protects it from the transfer pressure. The exposed stamp surface is next coated with molybdenum disulfide in order to reduce epoxy adhesion to the glass stamp surface. The prepared stamp is shown in Fig. 12.

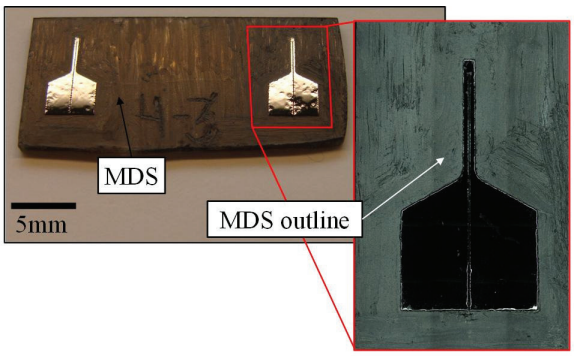

FIGURE 12. Schematic of silicon cross section after wax and silicon etch.

The transfer step must achieve the proper alignment of the sensors relative to the mechanical structure, specifically given the small available area on the thin flexures. This is carried out with an alignment fixture shown in Fig. 13. The sensors have been patterned onto a glass stamp which maintains the coordinate frame of the sensor location. These stamps are placed in 3-pin alignment fixtures and the hexflex is pressed onto these stamps to transfer the sensors to the mechanical structure.

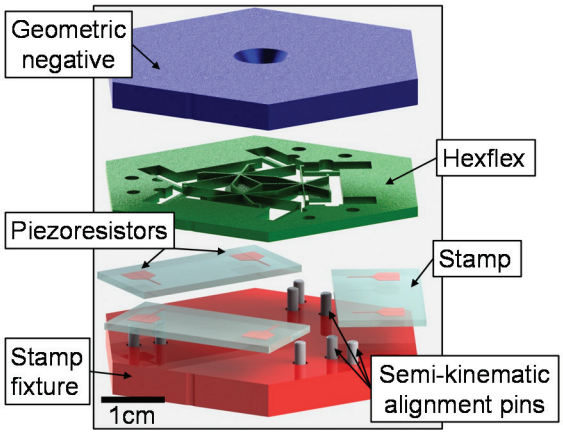

FIGURE 13. The transfer step is carried out via semi-kinematic alignment of the patterned sensors with the mechanical structure

CIRCUIT BONDING

The circuit bonding step attaches the gages to the electrical traces, completing the surface circuitry. Indium solder is used to make an electrical connection to the silicon, while conductive epoxy is used to link from the trace surface to the solder bead. Acrylic paint is finally applied over the surface structures to prevent delamination, reduce noise and protect the features from scratches. The final device appears as shown in Fig. 1.

RESULTS

The alignment capability of the NLBM process was studied in detail for the location of the silicon gage relative to the edge of the wire flexure. This alignment is crucial to ensure the gage is seated entirely on the flexure, but off the center of the flexure. The off-center location allows for the gage to read in-plane motion. The desired gage offset in from the edge of the flexure is 50μm. The variation in the process due to each of the steps is shown in Table 1 below.

Table 1: Sensor integration error budget

Source	Error (±μm) 95%
Micromilling	3
Micromill tooling	4
Pattern calibration	6
Laser and fixture	6
Repair	4
Transfer fixture	3
Cure	25
Sum	27

The dominant error for the sensor alignment is in the cure operation, where the gage is free to shift during the high temperature cure operation. This melts the mechanical anchoring wax, leaving the gage between two liquid films- wax and epoxy. Even application of the epoxy is capable of reducing this error to ≈5μm, however this is difficult in a completely manual process.

The characteristic errors for several of the main features are shown in Table 2. The desired dimension is shown, along with the average error and the variation in the error. The sensor X location is the alignment shown in Table 1. The milled flexures show minimal error, as these are used to calibrate the micromill tooling. The trace width error is largely due to the non-normal alignment of the crucible relative to the face of the device. This means the edges of the mechanical shadowmask obscure the edges of the trace, reducing the generated trace size. This could be solved with sloped shadowmask sidewalls, normal alignment and a thinner shadowmask.

Table 2: NLBM process error

Component	Desired (μm)	Characteristic Error (±μm) 95%
Sensor X location	50	-7±27
PR arm width	150	3±5
Wire flexure width	600	0±4
Blade flexure width	150	6±4
Trace width	800	-55±80
Trace location	1000	30±30

The sensor performance was measured and the out-of-plane gage factor for the gages is shown in Fig. 14.

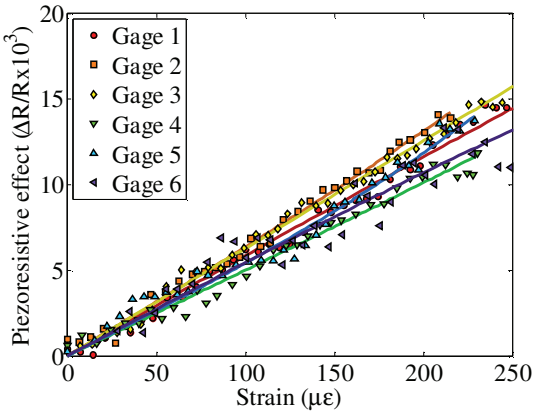

FIGURE 14. Out-of-plane gage factor for the piezoresistive sensors on the Hexflex device.

The average gage factor was measured to be 57±11. This is about 34% of the intrinsic silicon gage factor at the wafer doping level. The attenuation is due to the excess resistance and voltage drop generated via the fabrication process. The sensors were soldered at reduced temperature to minimize chances of damage. An increased solder temperature is expected to bring the gage factor up to around 125.

The present sensor performance is associated with 59dB full noise dynamic range for out-of-plane motion at 10kHz bandwidth. This performance is limited by noise generated at the positive contact to the silicon gages, where a Schottky barrier is formed. The Schottky barrier noise is the dominant source for the sensors, and is sensitive to the silicon surface doping level. Several methods could be used to dope the contact pads, which would result in a performance boost to a predicted 135dB performance limit at 10kHz bandwidth. The silicon stock could be doped using standard techniques prior to attachment to the stock. Spray on dopant [5] could also be used to selectively dope the bond pads without doping the piezoresistive area. Electrical discharge doping of the sensor surface [6] could be done in bench-top conditions on the contact pads after the sensor integration step. These methods should be able to raise the local surface carrier concentration to degenerate levels ($\approx 10^{20} cm^{-3}$), sufficient to lower the Schottky barrier noise to non-dominant status.

CONCLUSION

A new fabrication process is demonstrated that is capable of fabricating metal MEMS with integrated sensing, and doing so quickly (≈1wk), in small batches and at low cost (<$1k). This process is demonstrated with a 6DOF case study flexural nanopositioner based on the Hexflex architecture. The fabrication process is shown to be accurate on the scale of 10's of microns and to be able to produce functional integrated silicon strain sensing. Performance limits are identified of about 135dB full noise dynamic range sensing over a 10kHz bandwidth.

REFERENCES

[1] Panas, R., et al. Non-Lithographically-Based Microfabrication of Precision MEMS Nanopositioning Systems. Proc. 2011 ASPE. 2011, Nov 13.

[2] Lan, H., et. al. Review of the wafer stage for nanoimprint lithography. Microelectronic Engineering, 2007; 84: 684-688.

[3] The Chemical Science and Technology Laboratory. Cross-Industry Issues in Nanomanufacturing. NIST <www.nist.gov/cstl/upload/nano_small_web-3.pdf>, Accessed Jul 13, 2010.

[4] DiBiasio, C.D. Concept Synthesis and Design Optimization of Meso-scale, Multi-Degree-of-Freedom Precision Flexure Motion Systems with Integrated Strain-based Sensors. MIT Doctoral Thesis, Cambridge, MA, 2010.

[5] Silva, J.A., et al. Understanding the sprayed boric acid method for bulk doping of silicon ribbons. J of Crystal Growth, 2011; 327: 221-226.

[6] Dobbs, B.C., et al. Ohmic Contacts on High Purity P-Type Silicon. J Electronic Materials, 1977; 6: 705-716.

DESIGN OF MULTIDIMENSIONAL FLEXURE STAGE SYSTEM FOR HARD X-RAY MIRROR FOCUSING AT SUB-50-NANOMETER SCALE

Deming Shu[1], Wenjun Liu[1], Jorg Maser[1], Barry Lai[1], Steven Kearney[1,2], Jayson Anton[1,2], Zhonghou Cai[1], Ross Harder[1], Ruqing Xu[1], Lahsen Assoufid[1], Stefan Vogt[1], and Jonathan Z. Tischler[1]

[1]**Advanced Photon Source, Argonne National Laboratory, Argonne, IL 60439, U.S.A.**

[2]**University of Illinois at Chicago, Chicago, IL 60607, USA**

INTRODUCTION

The Advanced Photon Source (APS) at Argonne National Laboratory (ANL) is a national user facility for synchrotron radiation research. Mirror-based hard x-ray nanofocusing optics are required for several new flagship beamlines that will be built as part of the APS Upgrade project, specifically the Sub-micron 3-D Diffraction (S3DD) beamline and the In-Situ Nanoprobe (ISN) beamline. The 3-D micro/nano-diffraction beamline is aimed at a spatial resolution of 50 nm with hard x-rays with non-dispersive optics. The ISN beamline is aimed at highest-resolution imaging, spectroscopy, and tomography of energy systems and materials at a spatial resolution of 20-50 nm (baseline) with photon energies between 4 keV and 30 keV [1].

To meet the demanding mechanical specifications for the mirror mounting and manipulating system for the x-ray nanofocusing optics, a multidimensional flexure stage system has been developed. The design specifications, as well as the detailed designs for the individual flexure stages are presented in this paper.

MIRROR BOX FOR HARD X-RAY FOCUSING

As a sophisticated x-ray micro- and nano-focusing tool for synchrotron radiation research, more Kirkpatrick-Baez (K-B) mirrors [2] are being applied in the synchrotron radiation instrumentation. The typical K-B mirror optics for hard x-ray microfocusing is a two-mirror system. Placed orthogonal to each other, each mirror is responsible for a single direction focusing and they both focus to the same focal spot [2]. Its glancing incidence angle is around 3-4 mrad with a metal-coated elliptical profile for a typical x-ray energy range up to 30 keV.

Figure 1 shows a schematic diagram of a prototype of K-B mirror optics for hard x-ray microfocusing. It includes two mirrors mounted in a mirror box operating in a helium environment. Prior to the x-ray alignment, assisted by regular optical alignment tools, manual alignment processes for the two mirrors are performed in the optics laboratory. The motorized manipulations for the K-B mirrors alignment are minimized for the whole of the mirror box (linear motion axes X_b, Y_b, and angular tilting motion axes A_{xb}, A_{yb}) that need to be aligned under x-ray.

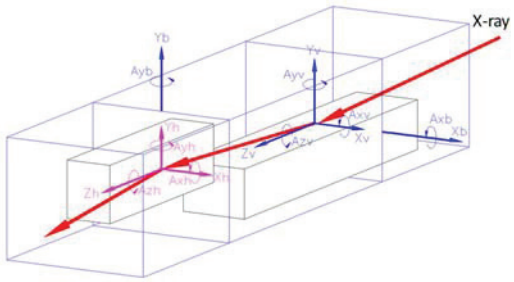

Figure 1. Schematic diagram of a prototype of K-B mirror optics for hard x-ray microfocusing with total degrees of freedom for the two-mirrors alignment. The linear motion axes X_b, Y_b, and angular tilting motion axes A_{xb}, A_{yb} are motorized.

Figure 2 shows a prototype of a mirror-based nanofocusing optics [3,4]. The mirrors are mounted in a helium-gas-filled box with a manual flexure mechanism to adjust the orthogonality between the horizontal and vertical focusing mirrors. The mirror box design is compatible with configurations for both K-B and Montel mirrors for x-ray nanofocusing with focal spot in the sub-50-nanometer scale.

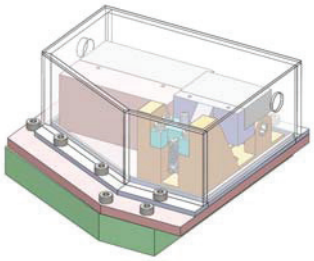

Figure 2. A 3-D model of the prototype of a mirror-based nanofocusing optics.

GENERAL ASSEMBLY OF THE MIRROR BOX MANIPULATING STAGE SYSTEM

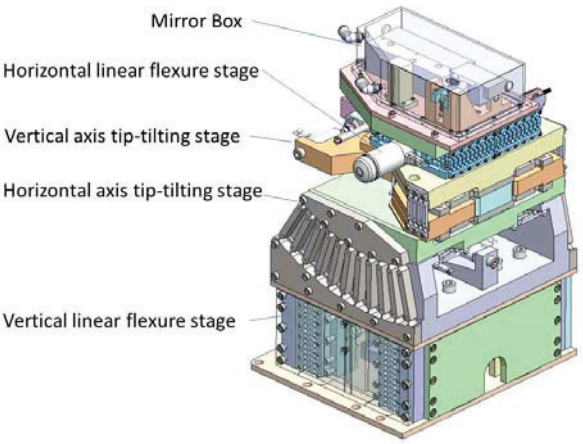

Figure 3. A 3-D model of the assembly of the K-B mirror box manipulating stage system.

As shown in Figure 3, the multidimensional flexure stage system for mirror-based x-ray nanofocusing optics consists of four flexure stages:

- a precision vertical linear flexure stage with 20-kg load capacity and 0.8-mm travel range.
- a horizontal axis tip-tilting stage is mounted on the top of the T8-47 vertical stage.
- a vertical axis tip-tilting stage Z8-5801 is mounted on top of the horizontal axis tip-tilting stage Z8-5802KB with 3-kg load capacity; and
- a precision horizontal linear flexure stage T8-72, mounted on top of the vertical axis tip-tilting stage Z8-5801 that provides 2-kg load capacity.

VERTICAL LINEAR FLEXURE STAGE

The vertical linear stage is a precision flexure stage with 20-kg load capacity and 0.8-mm travel range, as shown in Figure 4. Driven by a piezo linear actuator PZA-12 manufactured by Newport™, and associated with a motion-reduction mechanism, the T8-47 vertical flexure stage provides 10-nm closed-loop positioning resolution with a MicorE™ optical encoder.

The load capacity of the Newport™ piezo linear actuator PZA-12 is 50 N. Since the linear motion reduction mechanism provides a 1:5 motion reduction ratio, the PZA-12 is capable of driving the T8-47 vertical stage to carry a maximum 20-kg load at a speed of 0.04 mm/sec.

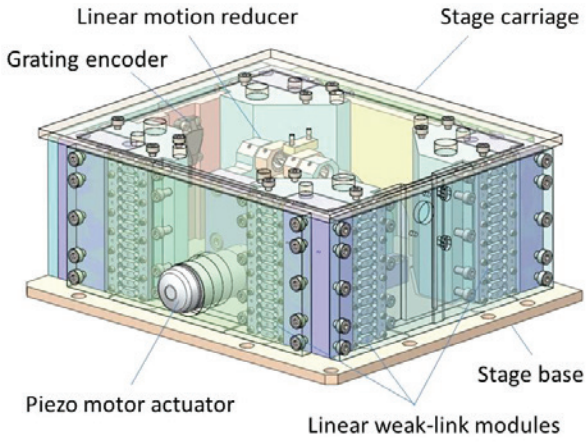

Figure 4. A 3-D model of the T8-47 vertical linear flexure stage.

Figure 5 shows a 3-D model of the linear motion reduction mechanism for the T8-47 vertical stage. The right-angle-tilting-arm is supported by the base structure of the linear motion reducer through a pair of commercial flexural pivots. A ruby ball is mounted on top of the tilting-arm acting as a vertical motion coupling to the carriage of the vertical stage. Table 1 summarizes the design specifications of the T8-47 vertical flexure stage.

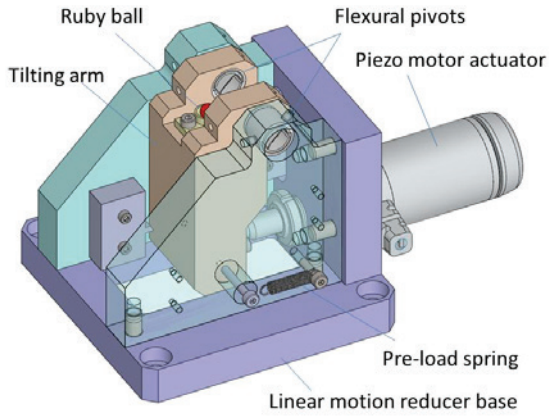

Figure 5. A 3-D model of the linear motion reduction mechanism for PZA-12 piezo motor actuator.

Table 1. Design specifications of the vertical linear stage T8-47

Parameter	*Vertical linear stage T8-47*
Overall dimensions (mm)	162(L) x 188(W) x 75(H)
Travel range (mm)	0.8
Max. load capacity (kg)	20
Min. incremental motion (nm)	10

HORIZONTAL AXIS TIP-TILTING STAGE

The horizontal axis tip-tilting stage is mounted on top of the T8-47 vertical stage. To enhance lateral stiffness, the horizontal axis tip-tilting stage Z8-5802KB is joined to the main high-stiffness weak-link mechanism with a set of four linear weak-link modules as shown in Figure 6. They are mounted between the top plate and the stage base, and are orthogonal to the plane of the main tip-tilting weak-link modules [5]. The rough adjustment is performed by a closed-loop Picomotor™ with a 200-300-nrad step size. A Physik Instrumente™ closed-loop-controlled PZT with strain sensor provides 20-nrad resolution for the fine motion control. Table 2 summarizes the design specifications of the Z8-5802KB vertical flexure stage.

Table 2. Design specifications of the H-axis tip-tilt stage Z8-5802KB

Parameter	*H-axis tip-tilt stage Z8-5802KB*
Overall dimensions (mm)	150(L) x 182(W) x 85(H)
Travel range (mrad)	16
Max. load capacity (kg)	5
Min. incremental motion (nrad)	20

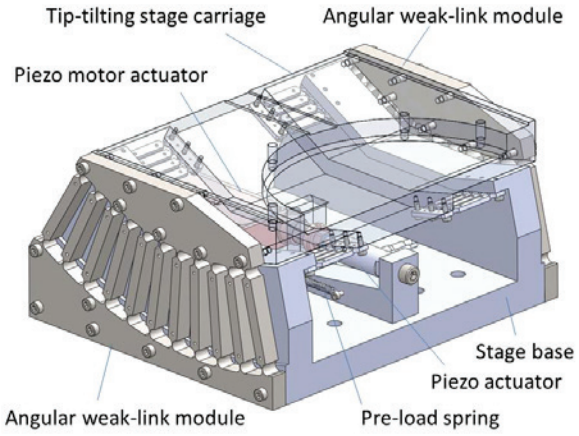

Figure 6. A 3-D model of the horizontal axis tip-tilting stage Z8-5802KB.

VERTICAL AXIS TIP-TILTING STAGE

As shown in Figure 7, the vertical axis tip-tilting stage Z8-5801 is mounted on top of the horizontal axis tip-tilting stage Z8-5802KB with 3-kg load capacity. With the same types of coarse/fine actuators from Picomotor™ and Physik Instrumente™, the Z8-5801 stage is able to adjust the optics with 20-nrad angular positioning resolution in a range of 16 mrad. Figure 8 is a photograph of a prototype of the vertical axis tip-tilting stage Z8-5801. Table 3 summarizes the design specifications of the Z8-5801 vertical axis tip-tilting stage Z8-5801.

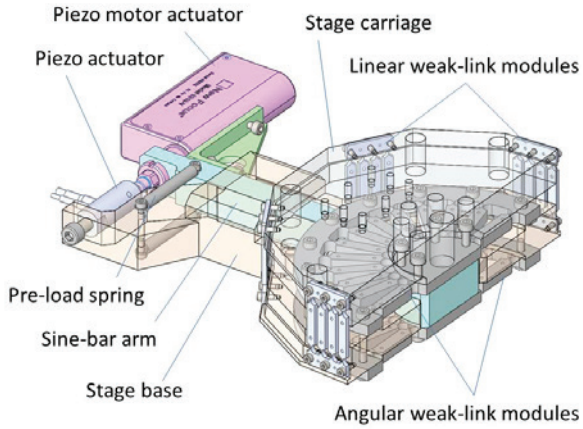

Figure 7. A 3-D model of the vertical axis tip-tilting stage Z8-5801.

Table 3. Design specifications of the V-axis tip-tilt stage Z8-5801

Parameter	*V-axis tip-tilt stage Z8-5801*
Overall dimensions (mm)	182(L) x 154(W) x 50(H)
Travel range (mrad)	16
Max. load capacity (kg)	3
Min. incremental motion (nrad)	20

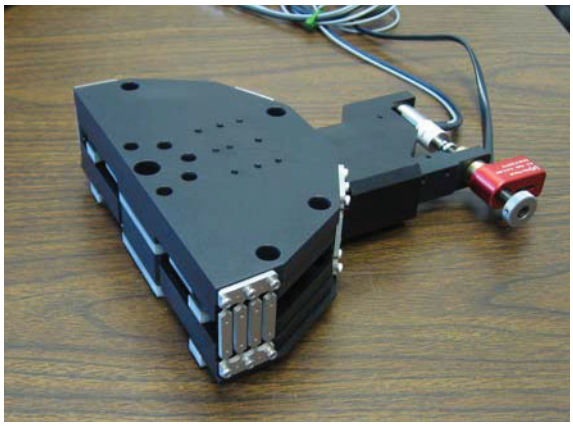

Figure 8. Photograph of a prototype of the vertical axis tip-tilting stage Z8-5801. An open-loop Picomotor™ actuator was mounted on the flexure stage.

HORIZONTAL LINEAR FLEXURE STAGE

Mounted on top of the vertical axis tip-tilting stage Z8-5801, the precision horizontal linear flexure stage T8-72 provides a 2-kg load capacity. The Newport™ PZA-12 actuator

provides a 40-nm closed-loop positioning resolution with a MicorE™ optical encoder. If needed, a Physik Instrumente™ P-840.1 PZT actuator can be added into the stage for a closed-loop fine adjustment with 1-nm resolution as shown in Figure 9 [6]. Table 4 summarizes the design specifications of the horizontal linear flexure stage T8-72.

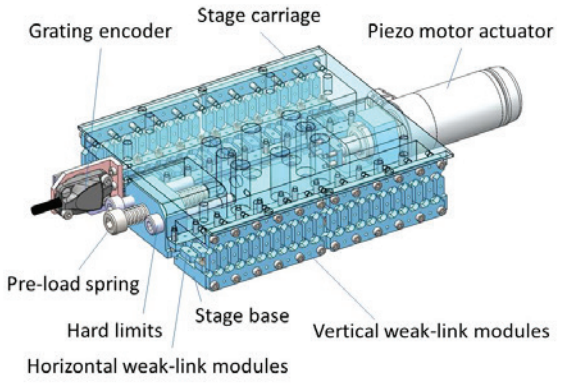

Figure 9. A 3-D model of the horizontal linear flexure stage T8-72.

Table 4. Design specifications of the horizontal linear stage T8-72

Parameter	*Horizontal linear stage T8-72*
Overall dimensions (mm)	152(L) x 88(W) x 25(H)
Travel range (mm)	0.8
Max. load capacity (kg)	2
Min. incremental motion (nm)	40 / 1 (with PZT)

SUMMARY

A multidimensional flexure stage system has been developed to meet the demanding mechanical specifications with 20-nrad tip-tilting resolution for hard x-ray mirror focusing at the sub-50-nanometer-scale. We have presented the design specifications, as well as the detailed designs of the stage system and individual flexure stages. The test of a prototype of the multidimensional flexure stage system is in progress.

ACKNOWLEDGEMENTS

The authors would like to thank C. Jacobsen and G. Pile from ANL for their help in the development of this project. Work at Argonne is supported by the U.S. Department of Energy, Office of Science, under Contract No. DE-AC02-06CH11357.

REFERENCES

[1] http://www.aps.anl.gov/Upgrade/ APS Upgrade project.

[2] Kirkpartrick, P. and Baez, A. V. Formation of Optical Images by X-Rays. JOSA. 1948; 38(9): 766-773.

[3] Liu, W., Ice, G. E., Assoufid, L., Liu, C., Shi, B., Khachatryan, R., Qian, J., Zschack, P., Tischler, J. Z. and Choi, J.-Y. J. Synchrotron Rad. 2011; 18: 575-579.

[4] Liu, W., Ice, G. E., Tischler, J. Z., Khounsary, A., Liu, C., Assoufid, L. and Macrander, A. T. Rev. Sci. Instrum. 2005; 76: 113701.

[5] Shu, D., Lee, W-K., Liu, W., Ice, G. E., Shvyd'ko, Y., Kim, K-J. Nucl. Instrum. Methods A. 2011; 649: 114-117.

[6] Shu, D., Stoupin, S., Khachatryan, R., Goetze, K., Roberts, T. and Shvyd'ko, Yu. Proc. SPIE. 2011; 8125: 812507.

GRAPHENE COATED SI MOLD FOR PRECISION GLASS OPTICS MOLDING

Peng He[1], Lei Li[1], Jianfeng Yu[2], Wenyi Huang[2], Ying-Chieh Yen[2], L. James Lee[2], Allen Y Yi[1]
[1]Department of Integrated Systems Engineering,
The Ohio State University,
Columbus, OH 43210, USA
[2]Department of Chemical and Biomolecular Engineering,
The Ohio State University,
Columbus, OH 43210, USA

ABSTRACT
Despite many attractive properties and well developed micro/nano manufacturing technologies based on silicon (Si) wafers, severe adhesions between Si and glass at high temperature have limited its application as a mold material in precision glass molding. In this research, a coating using carbide-bonded graphene is introduced to build non-stick Si molds for glass molding. The coating has extraordinary mechanical properties and can effectively prevent Si-glass adhesion under high temperature. We demonstrated fabrications of a glass Fresnel lens and glass parts with micron pillars using graphene coated Si molds. This newly developed process enables the use of Si as a mold material to fabricate sophisticated structures with high precision dimensions that was not previously available. This technology will greatly improve precision glass molding process and allow high precision low cost glass optics to be manufactured in large quantity.

INTRODUCTION
Silicon is one of the most widely used materials in micro fabrication because of its material properties, available processing methods, and low manufacturing cost [1]. Various features and structures have been fabricated on Si substrates, such as microlens arrays [2] and optical gratings [3]. On the other hand, these types of features are often encountered in precision glass molding, a net-shaping process for glass optics fabrication by replicating features from precision molds to glass at elevated temperature [4-6]. However, Si cannot be used directly as mold material due to severe adhesions between Si and glass. The adhesions are either caused by anodic bonding or chemical bonding at elevated temperature [7].

A few attempts have been made to use silicon molds for glass molding. For example, Albero et al. demonstrated the molding of glass microlens arrays on a Si mold, which however had to be completely etched after molding to release the glass lens array [8]. This Si-sacrifice molding method consisted of multiple steps and the Si mold could only be used once, thus it is not an economical approach. Hirai et al. used a $Si_3N_3/SiO_2/Si$ mold for imprinting fine patterns to glass surfaces, but the mold had limited feature depth because they were created on a thin layer of SiO_2 instead of directly on the Si substrate [9]. Chen et al. fabricated a micro machined silicon mold for a Fresnel lens glass molding [10], however the process was limited to low glass-transition temperature (T_g) glasses therefore the molded optics had poorer quality as compared to regular glass.

In this research, we developed a technique that can be used to prevent adhesions between Si molds and the molded glass optics by utilizing a thin layer of carbide-bonded graphene, a two dimensional material with extraordinary mechanical properties [11]. The building of a strong graphene coating as a protective layer on silicon substrates [12] provides the surface with a unique combination of many advantages, such as high thermal conductivity, high hardness, and low surface friction. This newly developed technology makes it possible to use micro/nano patterned Si wafers for precision glass optics fabrication in high volume thus result in low manufacturing cost. Although other materials, such as glassy carbon, CVD diamond and nitride ceramics were also used as mold materials [13, 14], most of these materials cannot match Si in terms of versatility of micro/nano scale fabrication, material availability, and manufacturing cost [1].

CARBIDE-BONDED GRAPHENE COATING

In this research, we demonstrated precision molding of glass micro optics with graphene coated Si molds. The coating process requires the heating of high-temperature silicone rubber, a piece of GP-SO_3H nanopaper [15] as well as Si substrates inside a quartz tube. As illustrated in FIGURE 1 (a), at 1,000°C, graphene sheets will exfoliate from the nanopaper and react with thermally activated Si-, SiO- or OSiO-, radicals, and eventually build robust C-Si and C-O-Si bonds between the graphene nanosheets and the substrate and also among graphene nanosheets. The detail coating processes as well as the analysis of the coating are described in [12]. The surface roughness of a uncoated Si wafer and a coated Si wafer were measured using a white light optical profilometer (Wyko, NT9100). As shown in FIGURE 1(b) and (c), no notable difference was found in surface roughness between the uncoated and coated Si wafer.

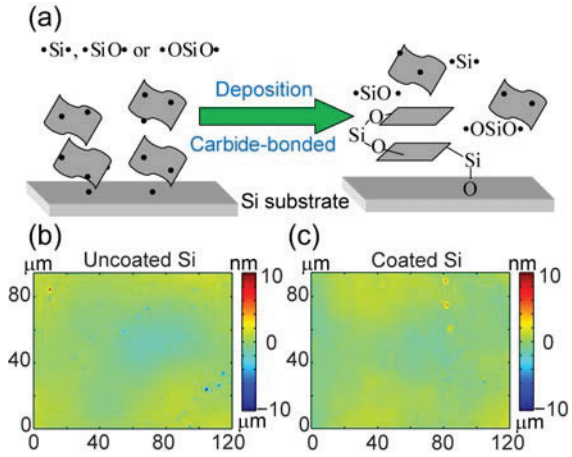

FIGURE 1. (a) Schematic of carbide-bonded graphene coating deposition on the Si substrate using nanosheets. (b) Surface scan of an uncoated Si wafer. Surface roughness was 0.53 nm (R_a). (c) Surface scan of a graphene coated Si wafer, surface roughness was 0.50 nm (R_a).

The carbide-bonded graphene coatings on silicon substrates provide a unique combination of many attractive properties for glass molding. Graphene is an excellent thermal conductor that enhances heat transfer from the Si substrate to glass and also can help generate a uniform temperature distribution during glass molding. The analysis and testing of the thermal conductivity of this carbide-bonded graphene coating will be discussed in a separate paper. The friction coefficient of the graphene coating is found to be only 0.029, which is more than 60% lower than that of a silicon wafer (0.076) [12]. The low friction coefficient can improve the filling ability of glass into small features on molds. The graphene coated Si mold has also greatly increased Young's modulus and hardness that can minimize the wear of molds during compression molding. In addition, the improved anti-scratching performance is also an indicator of a long mold life [12].

PRECISION MOLDING EXPERIMENTS

The graphene coating works as an isolation layer on Si molds to prevent the direct bonding between Si and glass. A few preliminary molding experiments have been conducted to test the performance of graphene coated Si molds. As illustrated in FIGURE 2(a), a glass blank was placed between two Si wafers in a sandwich style. The blank is P-LASF47 (Schott Glass Inc.), a glass formulated for precision glass molding with a T_g of 530°C. Glass blanks were polished into cylinder shape with a height of 5 mm and a diameter of 10 mm. Molding parameters are illustrated in FIGURE 2(b). The glass blank was heated by four 500w Watlow cartridge heaters to 640 °C in vacuum and subsequently compression molded with a molding force of 220 N. After controlled cooling, the molded glass part was released from the Si mold.

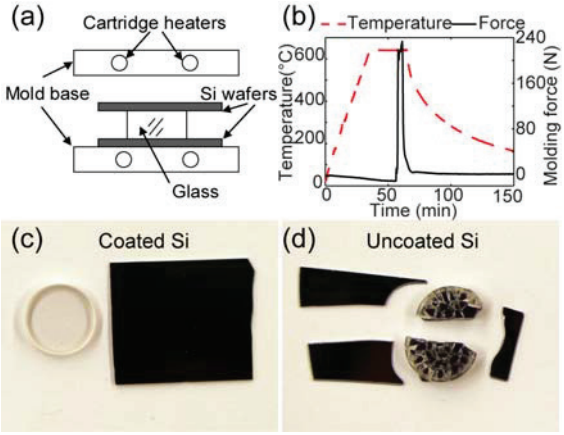

FIGURE 2. (a) Cross-section view of the molding experiment set up. (b) Temperature and load history of glass molding. (c) Glass molding using a carbide-bonded graphene coated Si wafer. (d) Glass molding using a Si wafer without graphene coating.

FIGURE 2(c) and (d) show the glass molding results using a carbide-bonded graphene coated silicon wafer and an uncoated silicon wafer as molds, respectively. As demonstrated in

FIGURE 2(c) and (d), the silicon wafer with carbide-bonded graphene coating has successfully molded a glass part without any contamination and mold/part failure. However, both the molded glass and the uncoated silicon wafer were broken due to thermal stresses from adhesion. After molding, glass blanks were pressed into disks with a height of about 3 mm. The surface roughness of the molded glass in FIGURE 2(c) is about 8 nm (R_a). This experiment demonstrated the effectiveness of graphene coating in preventing Si-glass adhesion.

In order to test the coatings on non-flat surfaces, a Si mold with microwells was fabricated using standard photolithography and inductively coupled plasma (ICP) - reactive ion etching (RIE) method. A thin film graphene coating was applied to the surface of the Si mold. The surface profile of the coated Si mold, which was measured using a Wyko NT9100 optical profilometer, is shown in FIGURE 3 (a) and the scanning electron microscope (SEM) image of the mold is shown in FIGURE 3(b). Each microwell has a width of 11 μm and average depth of 1.5 μm.

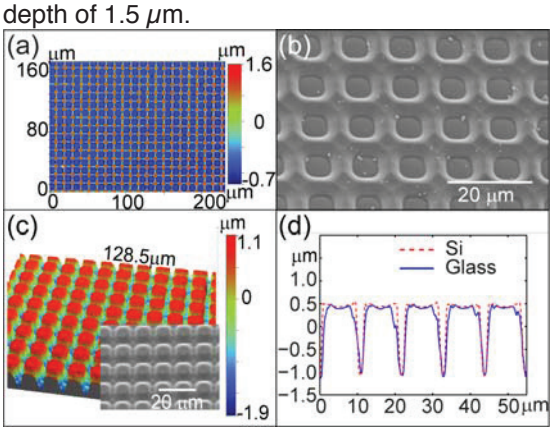

FIGURE 3. (a) Surface profile of a coated Si mold. (b) SEM image of Si mold with microwells after molding. (c) Surface scan of a molded glass with micro pillars. The inset is an SEM picture of the molded glass. (d) Comparison of line scan between the Si mold and the molded glass part (The profile of the Si mold was flipped for comparison).

A glass blank was molded on the coated mold. The replicated features on glass was scanned and shown in FIGURE 3(c). Highly uniformed micron pillars were formed on the glass surface with an average height of 1.5 μm, which matches the dimensions of the microwells on the Si mold. This demonstrated that high precision microfeatures can be successfully transferred to glass surfaces using this method.

The good surface finish on the molded glass indicated that it is possible to fabricate high precision glass optics with graphene coated Si molds. As a proof-of-concept, a glass Fresnel lens was fabricated by precision glass molding using a graphene coated Si mold. For the molding setup, upper mold was a flat Si wafer while lower mold had a Fresnel lens structure, which was fabricated by a combination of ultraprecision diamond turning and reactive ion etching (RIE) [10]. Again, both the upper and lower Si molds were coated with a thin graphene coating.

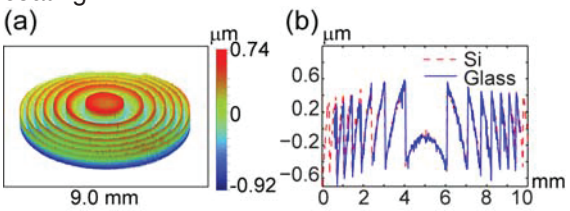

FIGURE 4. (a) Surface scan of the molded glass Fresnel lens. (b) Comparison of line scan between the molded glass lens and the Si mold (The profile of the molded glass lens was flipped for comparison).

The Si mold is a convex Fresnel lens so the molded glass lens is a concave Fresnel. The molded glass Fresnel lens has a diameter of 9 mm and height of the teeth is 1 μm. As shown in FIGURE 4(a), the microstructure of the molded glass lens was again measured using the Wyko NT 9100 optical profilometer. A comparison between the lens surface and the mold surface is shown in FIGURE 4 (b).

The image quality of the molded glass Fresnel lens was tested by using an optical system shown in FIGURE 5(a). Light source was a white light bulb. A light diffuser was used to create a uniform illumination. A target (USAF 1951, 3"x3" negative target, Edmunds Optics) was mounted in front of the light diffuser. Because of the molded Fresnel lens is a concave lens, a standard commercial F/4 lens (Double-convex lens of 25mm diameter and 100 mm FL, Edmunds Optics) was used to form a real image on the CCD. The captured image is shown in FIGURE 5(b). As a comparison, FIGURE 5 (c) is the image of the target using the commercial lens alone. The two images match nicely, demonstrating the imaging quality of the molded Fresnel lens.

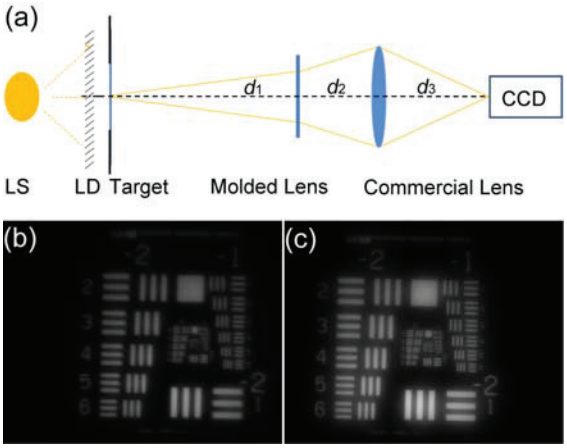

FIGURE 5. (a) Optical setup for testing the imaging quality of molded Fresnel lens. LS: light source, LD: light diffuser, d_1=690 mm, d_2=86 mm, d_3 is about 127 mm. (b) Image of the target with both Fresnel lens and commercial lens. (c) Image of the target on CCD with commercial lens alone. The molded lens was removed and CCD was placed on the focus plane of the commercial lens in this measurement.

DISCUSSIONS

The durability of the carbide-bonded graphene coating was also evaluated. A graphene coated Si wafer has been used for more than 20 times without notable wearing. In the second experiment, a graphene coated Si wafer was repeatedly molded at elevated temperature of 640°C for an extended time (2 hours). After molding, the coating showed no signs of wearing and no changes on surface roughness were found before and after molding. These preliminary experiments have shown that the carbide-bonded graphene has the durability for high precision glass molding applications. A quantitative study on the wear and bonding strength of the carbide-bonded graphene coating will be the focus of a future research.

It is worth to note that the carbide-bonded graphene coating technique is a low cost process compared to other more traditional coating methods. The coating materials are inexpensive and can be obtained rather easily. High-temperature silicone rubber is a standard industrial material and is readily available. GP-SO_3H nanopaper is a newly developed material but can also be fabricated in a cost effective way [16]. The cost of the furnace is much lower compared to other coating equipment. Moreover, the thickness of the graphene coating can be precisely controlled by adjusting the coating time and amount of coating materials, i.e., high-temperature silicone rubber and GP-SO_3H nanopaper.

CONCLUSION

In conclusion, the research for the first time demonstrated the use of carbide-bonded graphene as an effective and high performance coating material for precision glass molding. It was shown experimentally that Si-glass adhesion could be completely avoided by using the carbide-bonded graphene coating on the Si molds. The coating can be applied to Si molds with or without microfeatures. As a demonstration, a glass Fresnel lens was fabricated and the molded Fresnel lens exhibits good optical performance. By using the carbide-bonded graphene coating, we expect to realize the full potential of Si as a mold material to achieve non-adhesion, low friction, uniform temperature distribution, easy to fabricate and demold, with low fabrication cost for micro/nano scale precision glass optical component manufacturing.

REFERENCE:

[1] Franssila S. Introduction to Microfabrication. 2nd ed. Wiley; 2010.
[2] Möller S, Forrest SR. Improved light out-coupling in organic light emitting diodes employing ordered microlens arrays. Journal of Applied Physics 2002;91:3324–7.
[3] Kirakosian A, Bennewitz R, Crain JN, Fauster T, Lin J-L, Petrovykh DY, et al. Atomically accurate Si grating with 5.73 nm period. Applied Physics Letters 2001;79:1608–10.
[4] He P, Wang F, Li L, Georgiadis K, Dambon O, Klocke F, et al. Development of a low cost high precision fabrication process for glass hybrid aspherical diffractive lenses. Journal of Optics 2011;13:085703.
[5] Dambon O, Wang F, Klocke F, Pongs G, Bresseler B, Chen Y, et al. Efficient mold manufacturing for precision glass molding. Journal of Vacuum Science & Technology B: Microelectronics and Nanometer Structures 2009;27:1445–9.
[6] Li L, He P, Wang F, Georgiadis K, Dambon O, Klocke F, et al. A hybrid polymer–glass achromatic microlens array fabricated by compression molding. Journal of Optics 2011;13:055407.
[7] Green K, Burke J, Oreb B. Chemical bonding for precision optical assemblies.

Optical Engineering 2011;50:023401–023401.
[8] Albero J, Nieradko L, Gorecki C, Ottevaere H, Gomez V, Pietarinen J. Si moulds for glass and polymer microlenses replication. Proc SPIE 2008:69920A–69920A.
[9] Hirai Y, Kanakugi K, Yamaguchi T, Yao K, Kitagawa S, Tanaka Y. Fine pattern fabrication on glass surface by imprint lithography. Microelectronic Engineering 2003;67–68:237–44.
[10] Chen Y, Li L, Yi AY. Fabrication of precision 3D microstructures by use of a combination of ultraprecision diamond turning and reactive ion etching process. Journal of Micromechanics and Microengineering 2007;17:883.
[11] Geim AK, Novoselov KS. The rise of graphene. Nature Materials 2007;6:183–91.
[12] Huang W, Jianfeng Y, Kwak KJ, Gallego-Perez D, Liao W, Yang H, et al. Carbide-bonded graphene coating,Manuscripts in preparation,2013.
[13] Takahashi M, Sugimoto K, Maeda R. Nanoimprint of Glass Materials with Glassy Carbon Molds Fabricated by Focused-Ion-Beam Etching. Japanese Journal of Applied Physics 2005;44:5600–5.
[14] Komori M, Uchiyama H, Takebe H, Kusuura T, Kobayashi K, Kuwahara H, et al. Micro/nanoimprinting of glass under high temperature using a CVD diamond mold. Journal of Micromechanics and Microengineering 2008;18:065013.
[15] Huang W, Ouyang X, Lee LJ. High-Performance Nanopapers Based on Benzenesulfonic Functionalized Graphenes. ACS Nano 2012;6:10178–85.
[16] Cabrera E, Ko S, Castro J, Lee LJ. New approach to EMI shielding of plastic parts using in mold coated nanopapers, Unpublished work, 2013.

TOOL TEMPERATURE MEASURMENT DURING DT OF STEEL

G. S. Hesler[1], T A. Dow[1], K Garrard[1], M. Kudenov[2], T. Gettys[1], D. Gebb[1]
[1]Precision Engineering Center (PEC), [2]Electrical and Computer Engineering
North Carolina State University, Raleigh, NC

INTRODUCTION

Diamond Turning (DT) can create a finished specular surface for optical components and molds for optical surfaces. One example is the large drum molds used to transfer μm-scale features to plastic sheets in a process known as micro-replication. These drums are DT to produce high quality, optical molds for reflective tape, infrared motion sensor lenses and laptop screens. As the applications for precision molds have expanded, wear resistant materials such as steel have become more desirable than hard copper or aluminum. However, significant tool wear occurs during the DT of ferrous materials as a result of thermo-chemical effects [1].

Predicting the tool wear is a challenge because it is influenced by both hard abrasive particles in the workpiece and thermal/chemicals effects at the cutting interface. Abrasive wear increases the wear land and tool edge radius leading to a degradation in the surface quality. Chemical wear while machining steel is significantly different and the resulting tool shape is different. The tool wear is not linear; rapid for the first few meters but decreases with distance.

A recently completed NSF project at the PEC documented the wear of a diamond tool machining steel during conventional and vibration-assisted modes [2]. Finite Element Models (FEM) predicted temperatures during the DT of steel. Based on these predictions coupled with the measured wear of the tool, a chemical/abrasive wear model was developed. The result was high wear but the shape of the worn tool was different and the surface finish was better than when machining non-ferrous materials. The key to tool wear is temperature and this paper describes a project to provide temperature, forces and tool wear information during DT of steel and other materials.

EXPERIMENTAL RESULTS

To measure the tool temperature, an instrumented DT lathe shown in Figure 1 was used. The workpiece, a 0.8 mm thick disk, is supported in an air-bearing spindle. The diamond tool is flat and wider than the workpiece so multiple wear experiments can be performed before re-sharpening. The tool is fed into the workpiece at a constant feed to achieve the desired depth of cut discussed. Experiments using 360 brass are illustrated along with the resulting chip geometry, tool forces and temperature predictions.

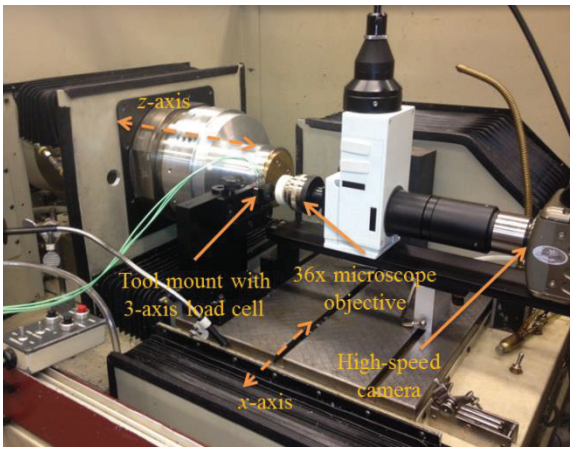

FIGURE 1. Experimental setup for orthogonal DT with high-speed imaging and a dynamometer to measure cutting forces.

High-Speed Chip Image

The high-speed video images of the cutting interface during the DT process were saved at 6000 frames/s with a shutter speed from 1-3 μs. Figure 2 shows images of preliminary experiments with 360 brass at different cutting speeds. The thickness of the chip and the ratio of cutting speed to chip velocity can be determined from the high-speed images to get the shear angle.

Cutting Force

A three-axis tool force dynamometer supports the tool and measures the cutting and thrust forces during machining. Figure 2(b) shows the tool forces measured for the chip images in Figure 2(a).

Tool Edge Shape

A Scanning Electron Microscope (SEM) technique has been developed at the PEC to quantify the shape of the diamond tool cutting edge [3]. A contamination stripe is written across the tool edge with the electron beam then the tool is rotated, imaged and stretched. The result shows the cross section of the cutting edge. This technique has been used to follow the change in the shape of a diamond tool and the radius of the cutting edge at tool wear at nm resolution. The tool can be used in a machining experiment, measured, used again and superimposed to follow its change in shape.

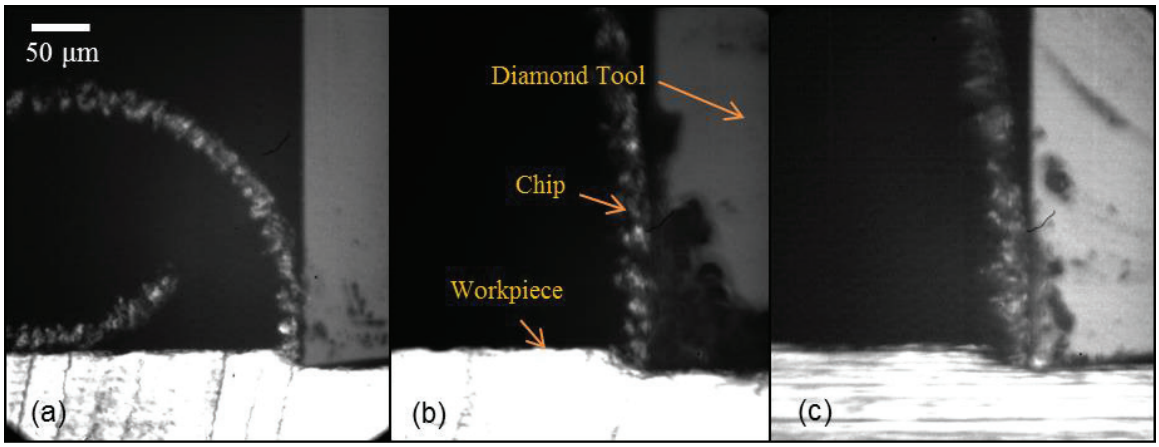

a) High-speed video images for 20 µm depth of cut

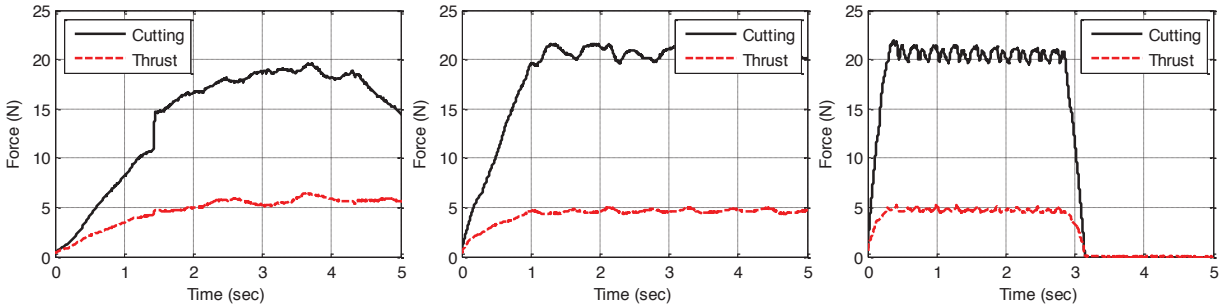

b) Cutting and thrust force for the experiments

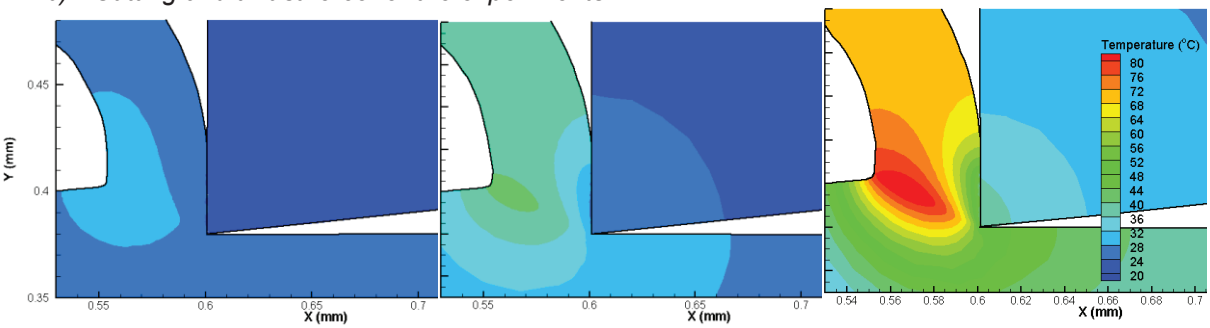

c) Temperature predictions from ThirdWave FEM simulation

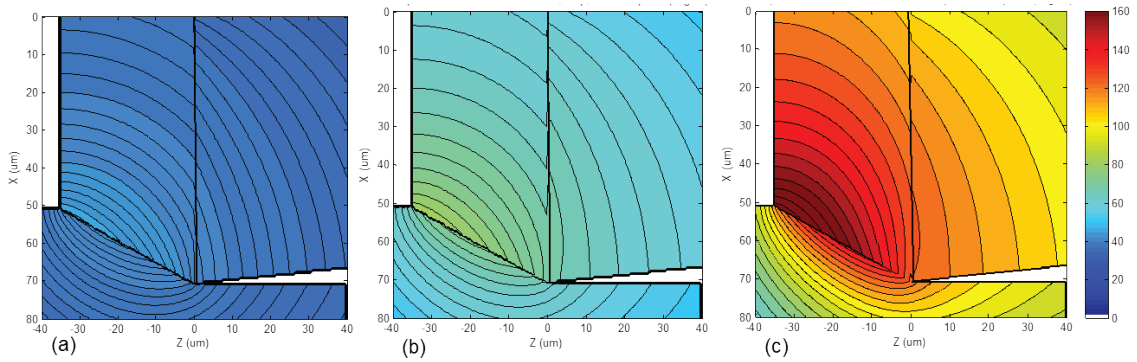

d) Temperature predictions from Heat Transfer model using forces and chip geometry

FIGURE 2. Images of chip geometry, measured forces, FEM and analytical temperature predictions for machining 360 Brass at three cutting speeds: left, 0.1 m/s, middle, 0.25 m/s and right, 1 m/s.

TOOL TEMPERATURE PREDICTION

Two methods have been used to predict the tool temperature and the results are shown in Figure 2.

FE Simulations

The AdvantEdge™ software from Third Wave was used to create a FE model of this orthogonal cutting experiment. A single depth of cut and multiple cutting speeds were simulated and the tool forces were compared to the experimental measurements from the dynamometer in Figure 3. The force results are similar but indicate that a larger friction coefficient should have been selected.

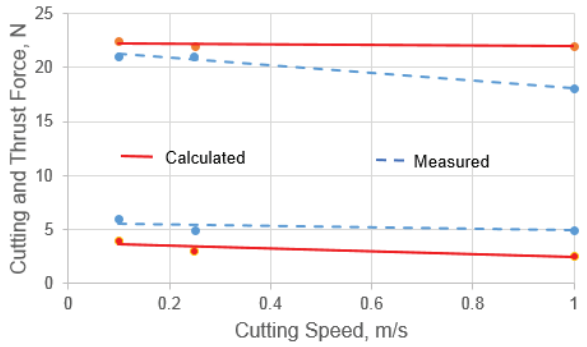

FIGURE 3. Calculated and measured cutting force (top) and thrust force (bottom)

Analytical Model

A heat transfer program was used to calculate the tool and workpiece temperature based on a model proposed by Komanduri [4]. The heat sources are the shear plane and frictional contact between the chip and tool. The inputs are the measured tool forces, chip thickness and chip-tool contact length and the output is the temperatures in the chip, tool and workpiece. Figure 2(d) shows the temperature distribution and Figure 4 compares the two models.

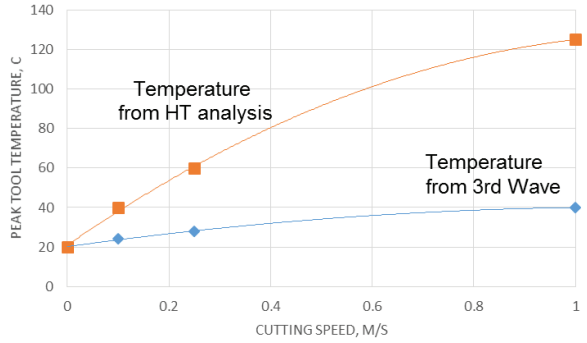

FIGURE 4. Predicted tool temperature with increasing cutting speed from two models.

From these results, it is clear that the predicted peak tool temperature is very different. There are differences in the models such as the size of the tool and the heat partitioning that impact the detailed temperature distribution at the tool-workpiece interface in Figure 2(c) and (d). Additional experimental data is needed is needed to verify the accuracy of the two models.

TOOL TEMPERATURE MEASUREMENT

The models show a large difference in the peak tool temperature which will impact the predicted tool wear in the presence of a carbide former like steel.

Parabolic Tool Shape

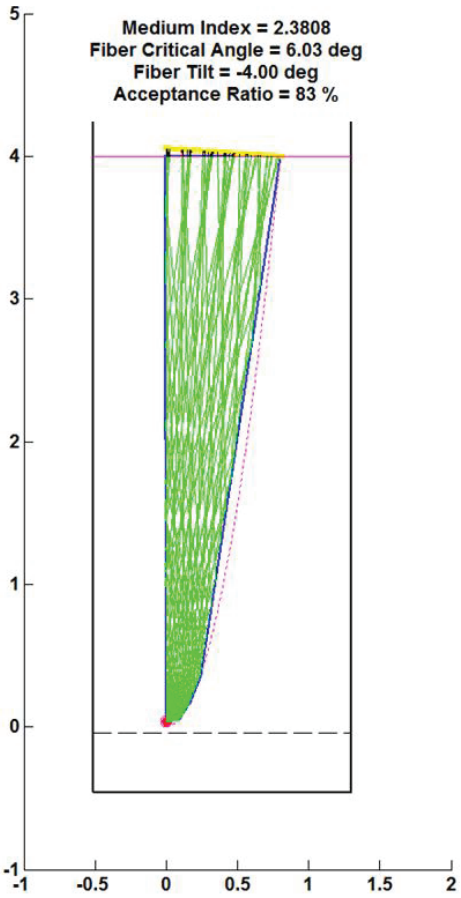

FIGURE 5. Diamond tool is an IR wave guide and improves efficiency to 83% (dimensions mm)

The temperatures predicted by the FE model show peak values less than 100°C using the 360 brass. From an IR perspective, this is a low temperature resulting in low emissions of IR radiation. To overcome this issue, the tool shape was designed to act as a light guide and collect most of the infrared radiation as shown in Figure 6.

The design concept for the diamond tool pyrometer is shown in Figure 7. The diamond tool is optically connected to a chalcogenide optical fiber using an indexing matching fluid. The radiation will be focused onto a cooled, 1 mm InSb infrared detector through a chopper to measure the amplitude of the

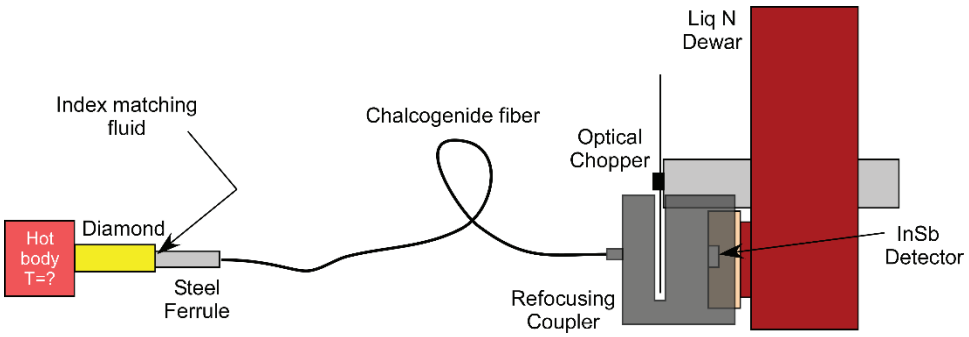

FIGURE 6. Layout of the tool measurement system during calibration of the IR sensor

IR radiation. Figure 6 shows the setup used for the sensor calibration. The emissivity of the diamond peaks in the 4-6 μm range which corresponds to the peak sensitivity for the InSb detector.

Miniature Tool Holder

For the machining experiments, the small diamond tool shown in Figure 5 will be glued/clamped into the tool holder shown in Figures 7 and 8. The end of the diamond tool will be pressed against the fiber through an index-matching fluid to improve the transmission through the interface.

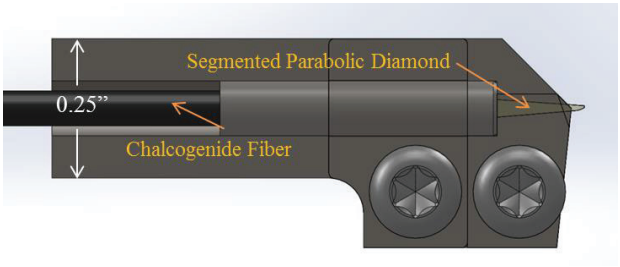

FIGURE 7. Top view of CAD model of diamond tool pyrometer showing fiber connection.

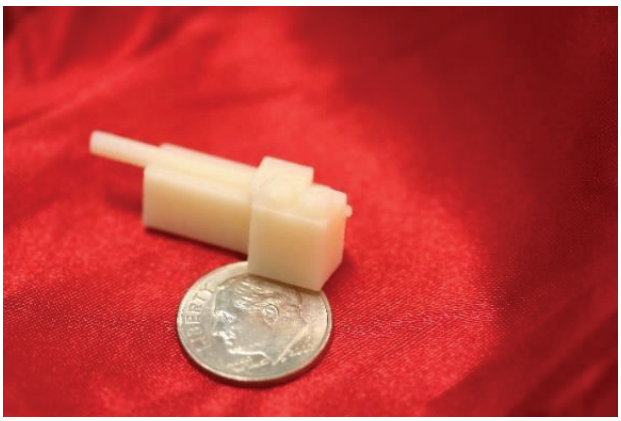

FIGURE 8. Plastic replica showing size/shape of the tool holder/fiber connector.

The cutting experiment will involve simultaneous capture of high-speed video, forces and peak tool temperature. The tool has a flat, 1 mm wide edge and 0.8 mm thick disks of different materials will be machined. The geometry will be the same as in Figure 2 with the tool plunging into the workpiece.

CONCLUSIONS

The wear of a diamond tool while machining a steel workpiece is strongly influenced by the temperature at the tool/workpiece interface. An experimental apparatus has been constructed to provide detailed information on this machining process: from high-speed video of the chip to cutting and thrust forces to peak tool temperature. Experiments are presented that show the response of the diamond tool to a variety of workpiece materials and cutting conditions. The change in shape of the diamond tool is measured using the IBED technique. The tool wear model proposed by Lane using the temperature predictions from the FE model [2] will be extended by using the peak temperatures from the IR measurements.

ACKNOWLEDMENTS

This project was funded by the NSF under contract CMMI-1200318 monitored by Z. Pei. Chardon Tool fabricated the wave guide diamond tool.

REFERENCES

1. Lane, B, Shi, M, Dow, TA, Scattergood, RO, "Diamond tool wear when machining Al 6061 and St 1215", Wear, Vol. 268, p. 1434, (2010).
2. Lane,B.M., Dow,T.A., Scattergood, R.O., Thermo-chemical wear model and worn tool shapes for single-crystal diamond tools cutting steel, Wear, Vol. 300, p216 (2013)
3. Shi, M, Lane, B, Scattergood, RO, Dow, TA, Mooney, C, "Diamond tool wear measurements using EBID", Precision Engineering, Vol.34, Issue 4, p. 717-721, (2010).
4. Komanduri, R, Hou, Z, Thermal modeling of the metal cutting process-Part III: temperature rise distribution from shear plane and the tool/chip friction, Int.J.Mech.Sci. V 43, p 89-107(2001).

Complex Bore Holes fabricated by combined Helical Laser Drilling and Micro Electrical Discharge Machining

Eckart Uhlmann[1], Dirk Oberschmidt[1], and Malte Langmack[2]
[1]Department Micro Production Engineering
Fraunhofer-Institute Production Systems and Design Technology
Berlin, Germany
[2]Department Micro Production Engineering
Institute for Machine Tools and Factory Management
Technische Universität Berlin, Germany

INTRUDUCTION

Precision bore holes of high requirements concerning quality, diameter, and aspect ratio (ratio diameter/depth) are used in a large variety of modern products. Besides applications in the field of automotive and textile industry, such as fuel injector and spinning nozzles, drill holes of complex shapes also come into action as cooling air holes in gas turbine blades within power and installation engineering [1, 2, 3, 4]. Two machining processes mainly used for the production of drill holes with diameters of less than d = 0.5 mm are Micro Electrical Discharge Machining (μEDM) and Laser Ablation.

By facing next generation products requiring a new level of geometrical freedom, precision and efficiency the demand of developing innovative machining processes and machine tools is indispensable. Against this background a novel combined machining system bringing together Laser Helical Drilling (LHD) and Micro Electrical Discharge Machining (μEDM) is introduced in this article. Precise alignment of the EDM and Laser module is provided by a camera device that is integrated in the machine tool. The application area of the machine tool is the fabrication of complex shaped holes with high aspect ratios.

The following paragraphs outline the machine tool set up, its potential and machining results realized by using the combined process. For experiments 18CrNi8, a steel mainly coming into action in the automotive industry, is used as workpiece material.

HYBRID MACHINE TOOL SETUP AND COMPONENTS

The machine tool setup is based on a gantry portal construction. For moving either the μEDM module or the LHD and camera unit two main Z-axes (Z1, Z') are provided (FIGURE 1).

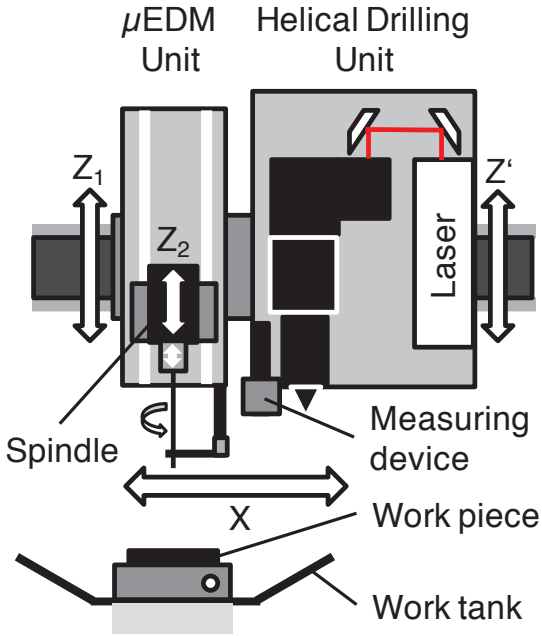

FIGURE 1. Illustration of the Hybrid Machine Tool Setup

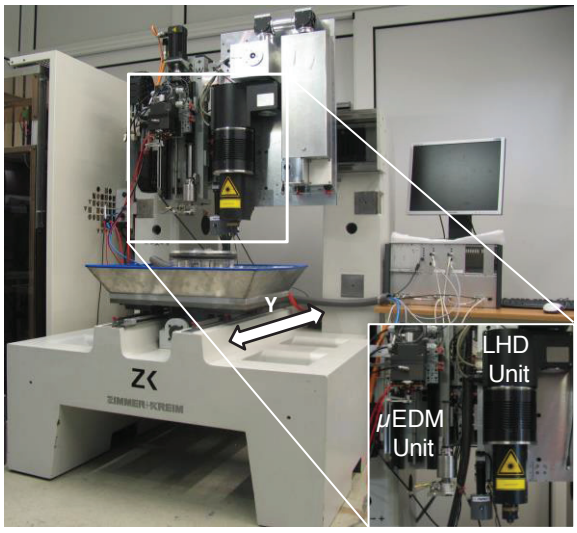

FIGURE 2. Hybrid Drilling Machine Tool

Fast positioning and measuring during combined machining is realized by a linear driven X-axis. Work tank and fixed workpiece are moved by a servo driven Y-axis which is embedded in the machine base (FIGURE 2).

Laser Drilling system

Within the setup of the Laser unit an Edgewave® Innoslab IS4I-E Nd:YVO4 Laser (1064 nm wavelength) with pulse durations from 6 ns to 85 ns and a pulse frequency of up to 50 kHz with 2 mJ/pulse at maximum is used. The output beam is guided into a helical drilling system developed by Fraunhofer-ILT. The core item of the system is a dove prism mounted into a high speed hollow shaft motor to be rotated at different turning speeds. By coupling the laser beam into the rotating prism the beam's axis is turned in itself and across the workpiece (FIGURE 3) [5, 6].

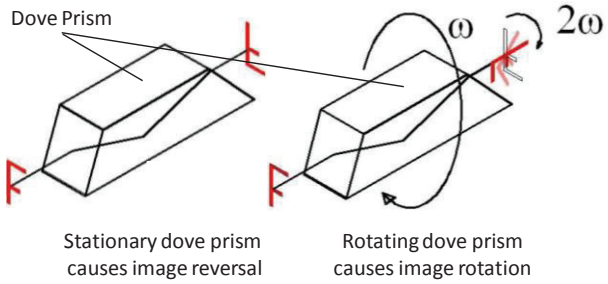

FIGURE 3. Principle of a dove prism´s functionality [6]

Due to the optical properties of the dove prism one turning cycle of the prism effects a double rotation of the output beam (FIGURE 4) [6]. Therefore, a maximal optical beam revolution of 16.000 min^{-1} is possible by turning the hollow shaft motor mechanically only with 8.000 min^{-1}.

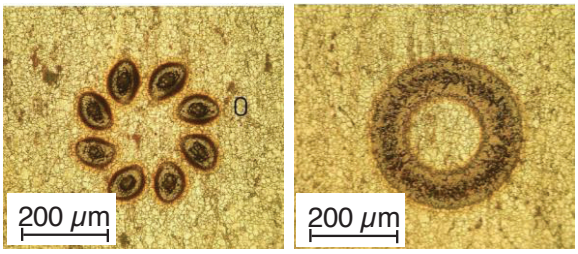

FIGURE 4. Fusion penetrations after manually turning the dove prism at 22.5°-steps (left), rotating the dove prism (right) [6]

Tilting a mirror in front of the rotating dove prism by a defined angle φ causes a variation in diameter of the drill hole (FIGURE 5).

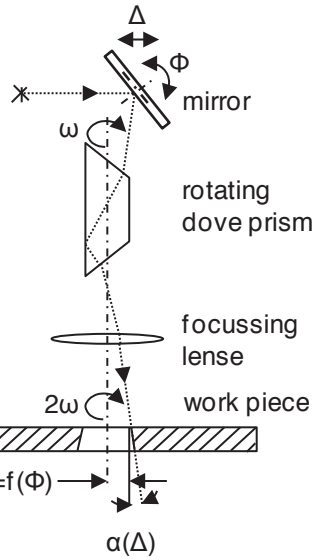

Figure 5. Illustration of laser helical drilling optics [6]

Also drill holes with straight walls or positive and negative taper can be made through a defined displacement Δ of the mirror (FIGURE 6).

Workpiece:	18CrNi8 probe (b_w = 1 mm)
Process gas:	Oxygen
Pulse energy E_p:	0.32 mJ
Pulse frequency f_p:	20.000 Hz
Rotational speed of hollow shaft motor n_{hsm}:	4.400 min^{-1}

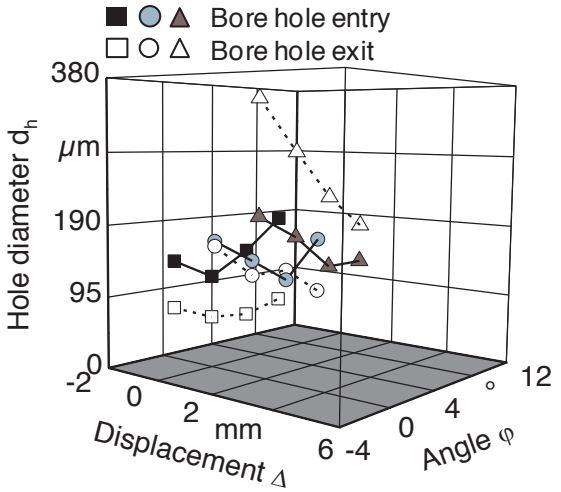

FIGURE 6. Dependence of mirror displacement Δ and angle φ on hole diameter of entry and exit

Displacement Δ and tilt φ are controlled by motors being implemented in the machine´s control.
Besides rotationsymmetric bore holes it is also possible to fabricate nonrotationsymmetric bore holes. For this purpose, the workpiece is moved laterally below the laser beam along a programmed two-dimensional numerically controlled path.
FIGURE 7 shows two machining results for shaped bore holes and gives an overview of the parameters used.

Workpiece:	18CrNi8 probe (b_w = 0.8 mm)
Process gas:	Oxygen
Pulse energy E_p:	0.32 mJ
Pulse frequency f_p:	20.000 Hz
Rotational speed of hollow shaft motor n_{hsm}:	4.400 min^{-1}
Movement speed of the workpiece v_{wp}:	120 $\mu m \cdot min^{-1}$

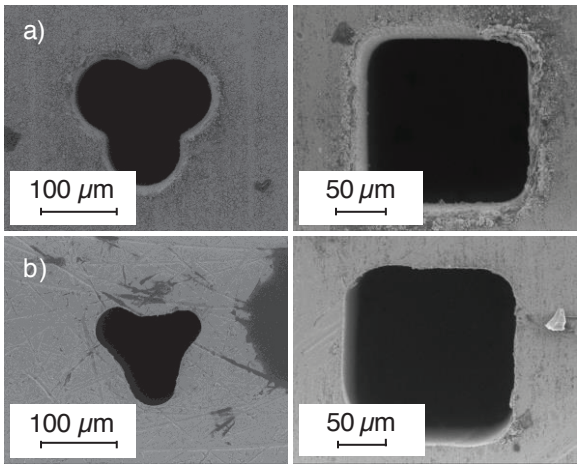

FIGURE 7. SEM-Images of nonrotational-symmetric bore holes fabricated by LHD and lateral movement of the workpiece; a) bore hole entry, b) bore hole exit

µEDM system
The µEDM unit is equipped with an air bearing spindle. For flushing purposes the spindle provides a maximum rotational speed of 3000 min^{-1}. Also the electrode can be indexed at an angle resolution of 0.001°.
For further flushing enhancement two piezo actuators are integrated in the µEDM spindle's body. By oscillating simultaneously they generate an axial vibration of the tool electrode of maximal 150 Hz. Also high pressure flushing of up to 80 bar can be realized when using pipe electrodes.

The spindle is mounted on a double Z-axis unit (FIGURE 1). The main axis (Z1) positions the tool electrode´s ceramic guide above the workpiece. Small lateral or tilting errors of the guide can be adjusted by a precision guide holder.
The secondary Z-axis (Z2) assures a stable control of the working gap and compensates relative frontal tool wear by an adaptive infeed. Worktable and tool electrode are connected to a capacitance-based generator offering minimal discharge energies of $W_e < 1\ \mu J$. To reduce stray capacitances and inductances of the discharge circuit wiring is kept short.
Besides the secondary Z-axis the X- and Y-axis of the machine are controlled adaptively, too. Therefore a µEDM milling process is also possible.
To enhance geometrical flexibility when fabricating complex micro bore holes also a WEDG unit was integrated into the hybrid machine tool (FIGURE 8).

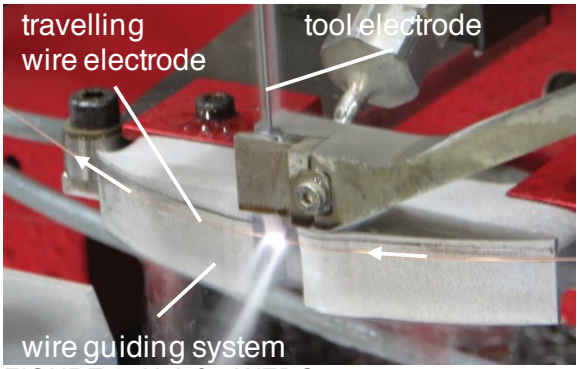

FIGURE 8. Unit for WEDG

Workpiece electrode:	Cemented carbide pin (d = 600 µm)
Tool electrode:	E-Cu 58 wire (d = 100 µm)
Dielectric fluid:	Deionized water
Generator:	Relax. Pulses
Discharge Capacity C_d:	10 nF
Open circuit voltage u_0:	100 V

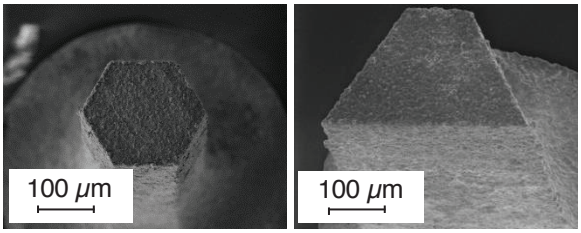

FIGURE 9. SEM-Images of tool electrodes structured by WEDG

Through this, by indexing the tool electrode it can be structured on the same machine by a guided travelling wire with a diameter of d = 100 μm (FIGURE 9).
By applying the structured tool electrode for a following μEDM process complex bore holes can be fabricated (FIGURE 10).

Workpiece electrode:	18CrNi8 probe with b_w = 1 mm
Tool electrode:	Shaped cemented carbide pin
Dielectric fluid:	Deionized water
Generator:	Relax. Pulses
Discharge C_e:	10 / 3.30 nF
Open circuit voltage u_0:	100 V

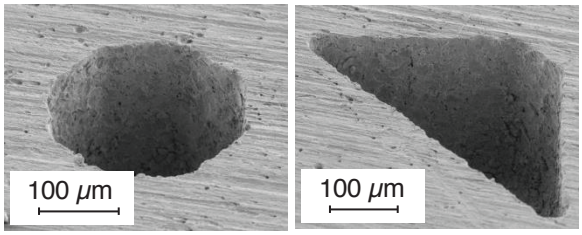

FIGURE 10. SEM-Images of shaped borehole entries fabricated by µEDM

Measuring system
In case of combined machining relative positioning of Laser and μEDM unit towards each other is provided by a camera system mounted close to the laser optics. The system includes a μeye 2240 camera and an objective with a maximal magnification of 10. Fast capturing and analysis of the drill holes´ geometry is realized by a special illumination unit and a recognition-software developed by the Institute of Imaging and Computer Vision/RWTH Aachen.

COMBINED PROCESS AND THE FABRICATION OF COMPLEX BORE HOLES

The combined process starts off with the fabrication of the core hole by using LHD. As shown above.
After laser machining, the bore hole´s entry is structured by μEDM. Depending on the active electrode surface and the volume of the LHD pre-drilled hole enhanced flushing conditions can cause a better debris removal through the pilot hole. This can lead to an increase of the removal rate V_W in comparison to conventional μEDM (FIGURE 11).

Workpiece electrode:	18CrNi8 probe with b_w = 1 mm
Tool electrode:	Cemented carbide
Dielectric fluid:	Deionized water
Generator:	Relax. Pulses
Discharge C_e:	10 / 3.30 nF
Open circuit voltage u_0:	160 V

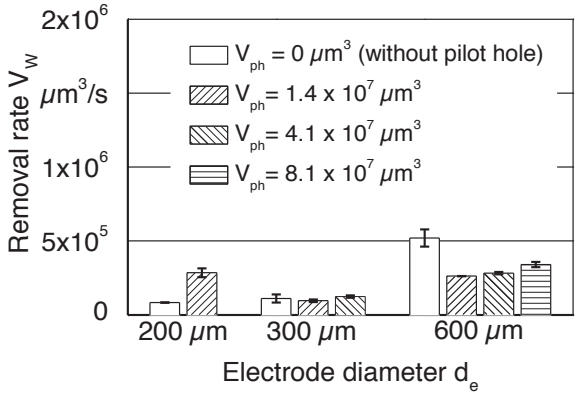

FIGURE 11. Correlation of Removal rate V_w, Electrode diameter d_e and pilot hole volume V_{ph} when machining with µEDM and stationary electrode

For realization of shaped borehole geometries the tool electrode is structured by WEDG before in the way described above. Indexing the tool electrode during the following EDM process gives the possibilty of fabricating complex star- or crosslike shapes with angled sidewalls, too (FIGURE 12).

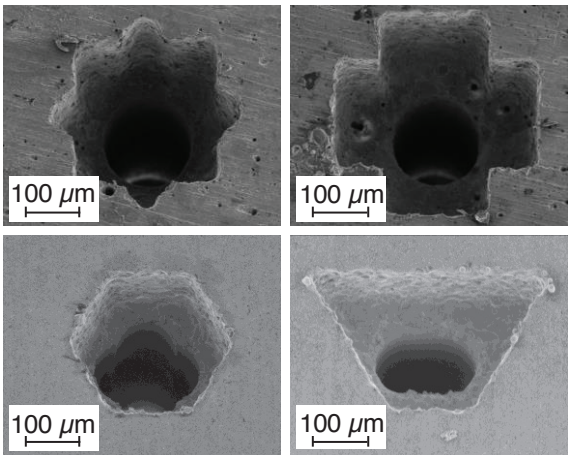

FIGURE 12. Complex Micro Bore Holes fabricated by combined LHD and µEDM process (machining parameters: see FIGURE 7, 9, 10)

SUMMARY AND CONCLUSION

In this paper a novel hybrid machine tool for combined Laser and μEDM machining of micro

bore holes was presented. The machine tool is equipped with a Laser Helical Drilling system for roughing, a μEDM unit for finishing, and an optical measuring device.
The presented study demonstrates the high potential in terms of a wide geometrical freedom and flexibility when bringing both processes on one machine. Through this, rotationalsymmetric and nonrotational-symmetric through holes of different shapes can be manufactured efficiently without unclamping the workpiece.

ACKNOWLEDGEMENT
This research work was sponsored by the German federal Ministry of Economics and Technology (BMWi) under the INNONET program, project „MicroDrill“.

REFERENCES
[1] Diver C, Atkinson J, Helml H J, Li L: Micro-EDM drilling of tapered holes for industrial applications, Journal of Materials Processing Technology. 2004, 149, 1-3: 296-303.
[2] Li L, Diver C, Atkinson J, Giedl-Wagner R, Helml H J: Sequential Laser and EDM Micro-drilling for Next Generation Fuel Injection Nozzle Manufacture, CIRP Annals - Manufacturing Technology. 2006, 55, 1: 179-182.
[3] Liu K, Lauwers B, Reynaerts D: Process capabilities of Micro-EDM and its applications, The International Journal of Advanced Manufacturing Technology. 2009, 47: 11-19.
[4] Uhlmann E, Langmack M, Schimmelpfennig T-M: Novel hybrid machining system for drilling micro holes by Laser Helical Drilling and μEDM, Proc. of the 6th International Conference on MicroManufacturing ICOMM 2011, Tokyo, 2011
[5] Poprawe R, Gillner A, Hoffmann D, Gottmann J, Wawers W, Schulz W: High Speed high precision ablation from ms to fs, Proc. of SPIE, Vol. 7005, 700502, 2008
[6] Wawers W: Präzisions-Wendelbohren mit Laserstrahlung, Dissertation, RWTH Aachen, 2008

DEVELOPING A MACHINING MODEL DATABASE FOR HARD-TO-MACHINE MATERIALS

Christopher Tyler and Tony L. Schmitz
Mechanical Engineering and Engineering Science
University of North Carolina at Charlotte
Charlotte, NC, USA

INTRODUCTION

The analytical stability lobe diagram offers a predictive capability for selecting stable chip width-spindle speed combinations in machining operations. However, the increase in allowable chip width provided at spindle speeds near integer fractions of the system's dominant natural frequency is diminished substantially at low spindle speeds where the stability lobes are closely spaced. Fortunately, the process damping effect can serve to increase the chatter-free chip widths at these low speeds. This increased stability at low spindle speeds is particularly important for hard-to-machine materials that cannot take advantage of the higher speed stability zones due to prohibitive tool wear at high cutting speeds.

The objective of this study is to develop a practical method to identify and model process damping, including a representative database of the process coefficients for hard-to-machine materials in order to accurately predict regenerative chatter in machining operations. This database will include not only process damping coefficients, but also specific cutting force coefficients used to model the forces in milling. The machinability of the materials investigated in this study is generally poor. Therefore, in addition to the process damping and force coefficient database, Taylor-type tool life models are developed for each material.

CUTTING FORCE MODELLING

In metal cutting operations, regenerative chatter is known to be directly influenced by the instantaneous cutting forces during chip generation. The dynamic cutting force, F, may modeled as:

$$F = K_s\, b\{n(t-\tau) \; + \; n(t)\}, \qquad (1)$$

where K_s is the specific cutting force, which depends on the tool-workpiece combination; *b* is the chip width; $n(t-\tau)$ is the vibration amplitude in the surface normal direction from the previous cutting path; and $n(t)$ is the current surface normal vibration amplitude [1].

In addition, the process exhibits additional damping when the cutting speed is low. This is due to interference between the cutting tool's relief face and the undulations left behind on the cut surface. This is known as process damping and it serves as an energy dissipation mechanism which increases stability at low cutting speeds. The dynamic force may be combined with the process damping force, F_d:

$$F_d = -C\,\frac{b}{V}\dot{n}. \qquad (2)$$

The process damping force in the surface normal direction is expressed as a function of cutter velocity, $\dot{n}$, chip width, cutting speed, *V*, and a process damping coefficient, *C* [2].

This process damping force, which depends on both the spindle speed-dependent limiting chip width and the cutting speed, is not included in classic regenerative chatter analytical solutions. Therefore, an analytical solution that includes process damping effects was developed [3]. The process damping coefficient is the only value required to define the process damping model. The following sections describe the procedure for obtaining the process constants, K_s and *C*, for difficult-to-machine materials. Preliminary results for AISI 1018 steel, Ti-6Al-4V, and AISI 304 stainless steel are provided.

EXPERIMENTAL PROCEDURE FOR PROCESS COEFFICIENTS IDENTIFICATION

Tool Life

Tool life is the time required to obtain a predetermined wear level. Depending on the dominant wear mode, options include the flank wear width (FWW), crater depth (CD), and/or notch depth (ND). The Taylor-type tool life equation used in this study relates the tool life to the cutting speed using a power law model [4]:

$$VT^{n_T} = C_T \quad (3)$$

The argument for obtaining tool life parameters for each material in this study is to establish an appropriate cutting velocity range to examine the process damping effect. Even though the tool life parameters are tool/workpiece specific, the tool life models could prove useful in establishing a benchmark range of cutting speeds in other cutting operations.

The workpiece materials were AISI 1018 steel, Ti-6Al-4V, and AISI 304 stainless steel. Down milling wear tests were completed using a 18.54 mm diameter single-tooth indexable square endmill (Kennametal: KICR-0.73-SD3-033.3C). A Kennametal (SDCW090308) TiN coated insert with a 15-deg relief angle, zero rake angle, and zero helix angle was used.

The chip load was 0.05 mm/tooth and the axial and radial depths of cut were 2 mm and 4.6 mm (25% radial immersion), respectively. All tests were performed using a water miscible mist coolant with a flow rate of approximately 15-20 ml/min. The primary mode of tool wear in all tests was flank wear; see Fig. 1. To avoid removing the tool and insert from the spindle, a portable digital microscope was used to record the FWW at regular intervals as shown in Fig. 2.

The tool life, *T*, was defined as the time required to reach a maximum FWW of 0.3 mm. Tests were completed at cutting speeds of {*V* = 29.1, 58.2, and 174.7} m/min, which correspond to spindle speeds of {Ω = 500, 1000, and 3000} rpm. The values for n_T and C_T were identified by curve fitting the (*V, T*) data points.

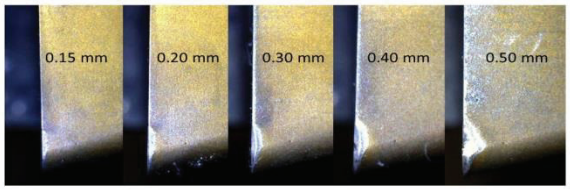

FIGURE 1: Sample measurements of the FWW progression during cutting tests.

Specific Cutting Force

The specific cutting force coefficient, K_s, and average cutting force direction, *β*, were identified from stable milling tests. The tests were performed on a cutting force dynamometer using a single-tooth indexable square endmill; see Fig. 3. Both 11 deg and 15 deg relief angle insert geometries were chosen in order to observe the dependence on tool geometry. The process damping coefficient was sensitive to flank wear. Therefore, cutting coefficients were measured at specific flank wear widths. A linear regression to the mean cutting force over a series of tests at ascending feed per tooth values was used to identify the cutting force model values [1].

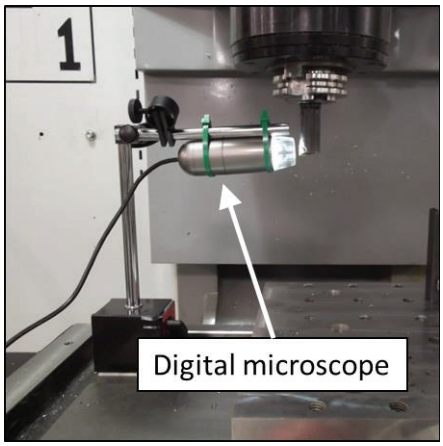

FIGURE 2: Setup for interrupted FWW measurements.

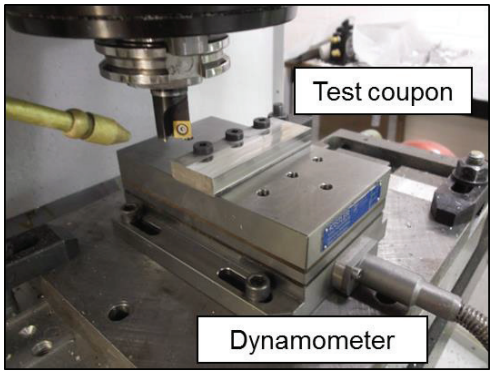

FIGURE 3: Dynamometer setup for cutting specific cutting force coefficient measurements.

Process Damping Coefficient

The process damping coefficient was identified using the flexure method described in ref. [3]. An accelerometer was used to measure the vibration during cutting; see Fig. 4. The frequency content of the accelerometer signal was used in combination with the machined surface finish to establish stable/unstable performance.

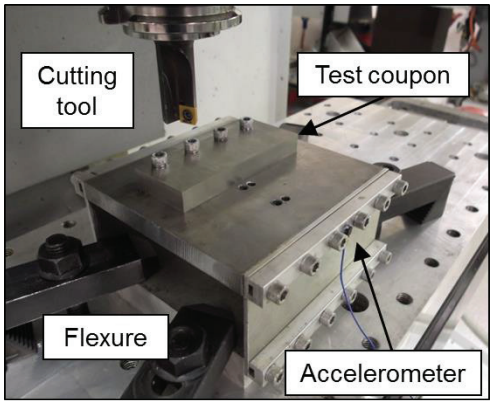

FIGURE 4: Flexure-based machining setup for process damping coefficient measurements.

A grid of stable/unstable test points at low spindle speeds was used to identify the process damping coefficient (via the experimental stability boundary) for each testing condition; see Fig. 5. The coefficient was determined from a least squares fit through the test points.

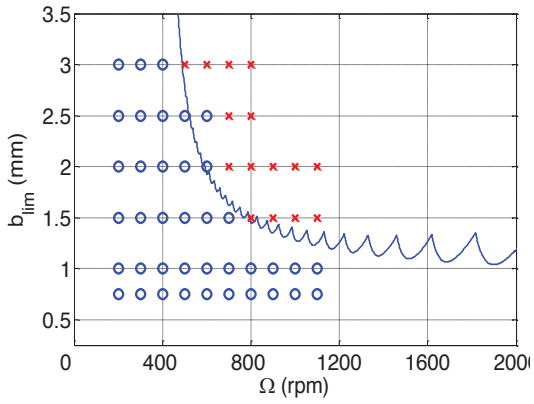

FIGURE 5: Test grid of stable/unstable cutting conditions.

RESULTS

Tool Life

Tool life testing was performed for each material under stable cutting conditions. Figure 6 displays the FWW progression versus cutting time for the specified cutting velocities for titanium. The 'o' symbols represent the intervals at which the FWW was recorded. As expected, the wear rate was found to increase as cutting velocity was increased.

The tool life was then plotted versus the cutting velocity and a power law curve was fit to the data. Figure 7 shows the curve fit through the three data points for Ti-6Al-4V (R^2 = 0.97). It is observed that cutting operations are limited to spindle speeds less than 1000 rpm if a tool life greater than approximately 30 minutes is desired. This range of spindle speeds is used to dictate the operating speeds for process damping characterization. The $\{n_T, C_T\}$ values for the other materials tested are provided in Table-1.

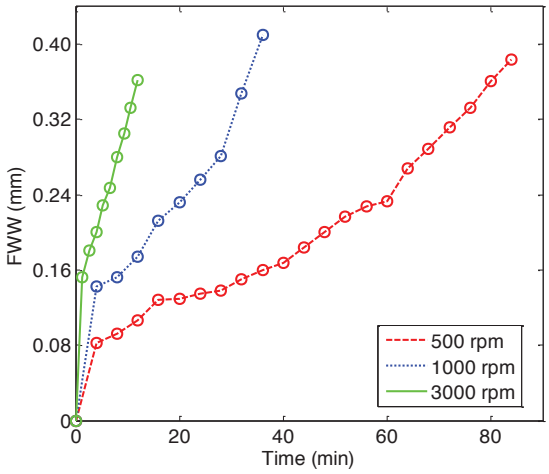

FIGURE 6: Increase in FWW with cutting time at three spindle speeds for Ti-6Al-4V.

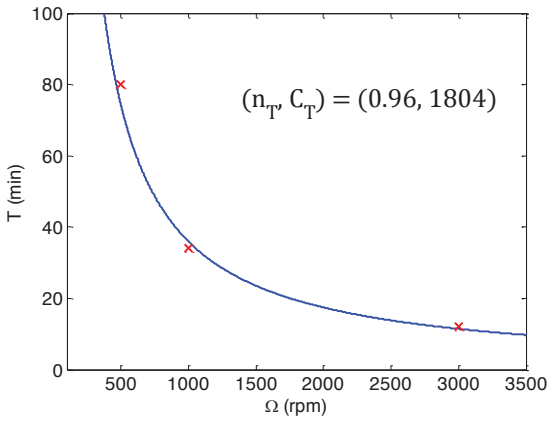

FIGURE 7: Increase in FWW with cutting time at three spindle speeds for Ti-6Al-4V.

TABLE 1: Values for n_T and C_T.

Material	n_T	C_T	R^2
1018 steel*	0.34	649	0.95
Ti 6Al-4V	0.96	1804	0.97
304 SS	0.67	1484	0.98

* Values obtained from testing performed by Karandikar *et al.* [5] using same tool geometry, but uncoated insert.

TABLE 2: Comparison of process coefficients for the 11 deg relief angle tool geometry.

	Low insert wear (FWW < 0.100)			Moderate insert wear (0.150 < FWW < 0.250)		
Material	K_s *(N/mm^2)*	*β (deg)*	*C (N/m)*	K_s *(N/mm^2)*	*β (deg)*	*C(N/m)*
1018 Steel	2531.0	62.0	3.3 x10^5	2550.2	62.0	4.0 x10^5
Ti 6Al-4V	2107.0	66.0	1.7 x10^5	2131.2	60.1	1.8 x10^5
304SS	3318.0	62.5	5.2 x10^5	3517.0	61.0	5.8 x10^5

TABLE 3: Comparison of process coefficients for the 15 deg relief angle tool geometry.

	Low insert wear (FWW < 0.100)			Moderate insert wear (0.150 < FWW < 0.250)		
Material	K_s *(N/mm^2)*	*β (deg)*	*C (N/m)*	K_s *(N/mm^2)*	*β (deg)*	*C(N/m)*
1018 Steel	2359.1	63.5	2.5x10^5	2441.0	63.5	3.0 x10^5
Ti 6Al-4V	2076.3	66.7	1.2 x10^5	2247.2	56.3	1.4 x10^5
304SS	3427.2	63.1	4.1 x10^5	3503.2	61.5	4.5 x10^5

Process Coefficients

The process coefficients for steel (AISI 1018), titanium (Ti 6Al-4V), and stainless steel (AISI-304SS) are provided in Tables 2 and 3. For the tool geometry selected, i.e., zero rake helix angles, there was a moderate increase in specific cutting force coefficient from the new to moderately worn cutting conditions.

In general, there was an observable increase in the process damping coefficient with a relief angle reduction and FWW increase. This serves as an indication that there is an increase in the amount of interference between the cutting edge and the undulations left on the workpiece surface when the tool is worn and/or has a smaller relief angle. Figure 8 illustrates the increase in the stability boundary as the process damping coefficient is increased in the case of 1018 steel.

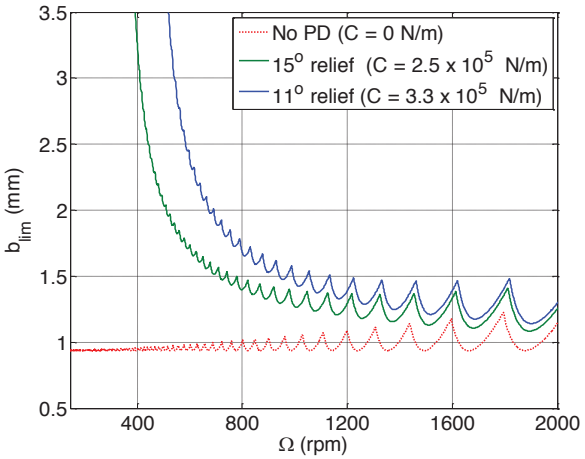

Figure 8: Stability lobe boundary for low wear AISI 1018 steel tests.

CONCLUSIONS

An analytical solution for machining stability while considering process damping was used to obtain process coefficients for hard-to-machine metals. The coefficients, including specific cutting force, process damping, and Taylor-type tool life, were determined experimentally and tabulated for low-speed milling of AISI 1018 steel, Ti 6Al-4V, and AISI 304 stainless steel under various conditions. It was demonstrated that a reduction in the relief angle and an increase in flank wear increased the process damping effect for all materials tested.

Utilizing the effects of process damping can have a significant impact on productivity in machining applications. The effort of cataloging process coefficients could prove to be a practical benefit in today's manufacturing setting.

REFERENCES

[1] T. Schmitz, S. Smith. Machining Dynamics: Frequency Response to Improved Productivity, Springer, New York, NY, 2009.

[2] Y. Altintas, M. Eynian, H. Onozuka. "Identification of dynamic cutting force coefficients and chatter stability with process damping." Annals of the CIRP, 57/1 (2008) 371-374.

[3] C. Tyler, T. Schmitz. "Analytical process damping stability prediction." Journal of Manufacturing Processes, 15 (2013) 69-76.

[4] F.W. Taylor. "On the art of cutting metals." Transactions of the ASME, (1906) 31-248.

[5] J. Karandikar, Abbas, A., Schmitz, T, "Tool life prediction using random walk Bayesian updating." Machining Science and Technology: An International Journal, 17/3 (2013) 410-442.

SELF-TUNING DYNAMIC VIBRATION ABSORBER FOR MACHINE TOOL CHATTER SUPPRESSION

Gorka Aguirre[1], Mikel Gorostiaga[1], Thomas Porchez[2] and Jokin Muñoa[1]
[1]Microtechnology and Ultraprecision
IK4-IDEKO
Elgoibar, Gipuzkoa, Spain
[2]Mechatronic Team
CEDRAT TECHNOLOGIES
Meylan, Isère, France

INTRODUCTION

The current trend in machine tool design aims at stiffer machines with lower influence of friction, leading to faster and more precise machines. However, this is at the expense of reducing the machine damping, which is mainly produced by friction, and thus increasing the risk of suffering from a self-excited vibration named chatter, which limits the productivity of the process. Dynamic vibration absorbers (DVAs) offer a relatively simple and low cost solution to reduce chatter appearance risk by adding damping to the critical vibration modes. The proper tuning of the dynamic characteristics of the damper to the machine/process dynamics is the key for successful implementation.

A new semi-active tuned mass damper concept is presented here, which combines three novelties:

- Automatic in-process chatter detection and optimal tuning frequency calculation by means of dedicated hard/software and embedded accelerometers.
- Automatic in-process tuning of the resonance frequency of the damper to the chatter frequency by means of a variable stiffness spring controlled by a motor.
- Damping is produced by eddy current effect, generated by the vibration of conductor plates within a magnetic field.

Such a damper prototype has been designed and built, with performance, robustness, low cost and compactness as main goals, in order to achieve a system that can be used in real industrial applications. This damper has been designed to fit the requirements of a SORALUCE milling machine at IK4-IDEKO's facilities, which has been used for experimental validation.

The main design and working principles of this damper and the improvement of the machining conditions allowed by the damper will be demonstrated by real milling experiments.

DVA REQUIREMENTS

Dynamic vibration absorbers consist of a mass connected to the machine with a certain stiffness and damping, so that its resonance frequency is tuned to the frequency of the machine mode leading to chatter, by adding damping to it and allowing higher cutting depths [1].

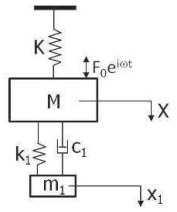

FIGURE 1. DVA concept, m_1 mass connected to machine M with k_1 and c_1

Tunable DVAs are needed because the effectiveness of the damper depends greatly on an accurate tuning of the damper frequency. Furthermore, even within the same machine, chatter frequency can vary with the position in the workspace (due to the variation in the machine stiffness), with the process parameters and with the workpiece mass.

A self-tuning DVA is thus of advantage for ensuring optimal damping in a wider range of working conditions. Such damper needs two main new functions:

- Online chatter monitoring and identification of optimal damper tuning frequency
- Automatic control of the damper resonance frequency to match the monitored one.

DAMPER DESIGN

Following the requirements described above, a new self-tuning DVA concept is presented here. The main novelties of this DVA are (i) online detection of optimal tuning frequency, (ii) automatic control its resonance frequency and (iii) decoupled damping and stiffness generation with linear characteristics. The main design aspects enabling these characteristics are described next.

Stiffness control

The optimal stiffness for the inertial damper is defined by the frequency of the vibration mode leading to chatter, and the inertial mass of the damper. Since the optimal frequency is variable within a machining process, and in order to cover a range of machines and processes with the same damper design, it is of interest to have the possibility of changing the stiffness of the damper.

This is commonly achieved by means of elastomers, which provide required stiffness and damping. Stiffness is then controlled by applying different preloads to the material. An evolution of this principle is the use of magnetorheological elastomers, which change in stiffness when a magnetic field is applied on them [3]. These technical solutions are relatively simple to implement, but are difficult to tune due to the nonlinear behavior of the elastomers. Other authors propose pre-stressable leaf-springs, which offer a more predictable behavior [4].

In this project, a rotary element with variable stiffness in function of the angular direction has been selected. A rotary stepper motor controls the orientation, and thus, the stiffness and frequency. Linearity, predictability and repeatability are the main advantages. A similar concept for variable stiffness was presented in [2], but it has been here improved to enable an easier design and automation. The general design and working principle can be seen in Figure 1. The thickness *a* is used to tune the lower stiffness of the spring, and the thickness *b* for the higher stiffness of the spring.

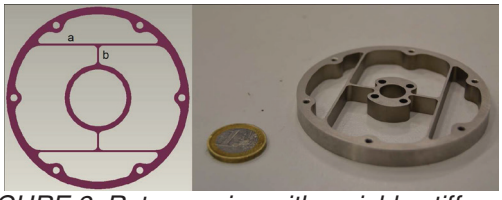

FIGURE 2. Rotary spring with variable stiffness

Eddy current damping

Damping produced by energy losses related to eddy currents is proposed here as an optimal method for generating the damping needed in inertial dampers, since the damping they produce is very close to ideal viscous behavior and it is generated without contact between parts, avoiding, for example, the non-linear effects produced by friction.

When a conductor moves through a static and non-uniform field, eddy currents are induced on it, and they generate a counteracting field which generates in interaction with the original field a braking force, trying to slow down the relative motion of the conductor within the field. Since this force is proportional to the velocity, it can be seen as a damping force. The energy dissipated is converted into heat as Joule's effect losses of the eddy currents on the conductor [5].

The magnet configuration shown in Figure 3 has been selected, in which the poles are arranged in an alternating pattern that increases significantly the damping force and coefficient, and minimizing the required volume. This module design allows fixing the neodymium magnets easily, and then handling and mounting each module in the damper independently.

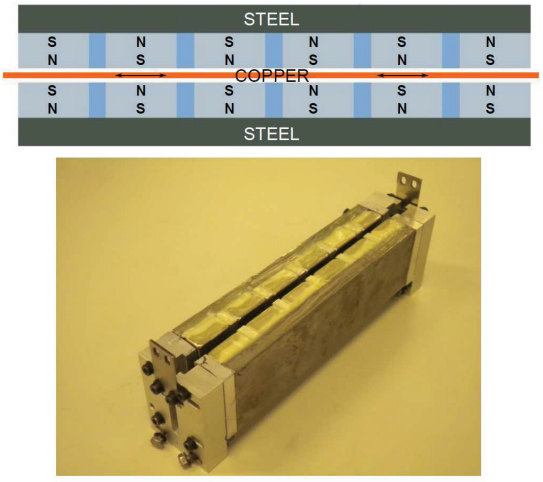

FIGURE 3. Magnet configuration

Self-tuning strategy

The self-tuning requirement aims at ensuring that the damper is always optimally tuned in an automatic way. The first step is to detect whether chatter is occurring or not during the machining process. If it is not occurring, no action is needed. If chatter is detected, the

damper needs to be tuned to the right frequency.

The vibration measured by the accelerometer installed on the structure of the damper is processed in order to find its main frequency components. Here it is important to distinguish between forced vibrations, induced directly by the cutting forces, and chatter, which is an unstable regenerative process generated only under certain working conditions.

Forced vibrations appear at harmonics of the tooth passing frequency, but are stable, and thus are usually not a problem for machining, except in finishing operations where surface roughness needs to be improved. Chatter appears at other frequencies than tooth passing frequencies, and it is an unstable cutting process, meaning that the cutting forces and vibrations increase with time, leading to unacceptable machining conditions, since they produce very bad surface quality and can lead to damage in the machine. The proposed chatter detection and suppression algorithm is presented in the next figure.

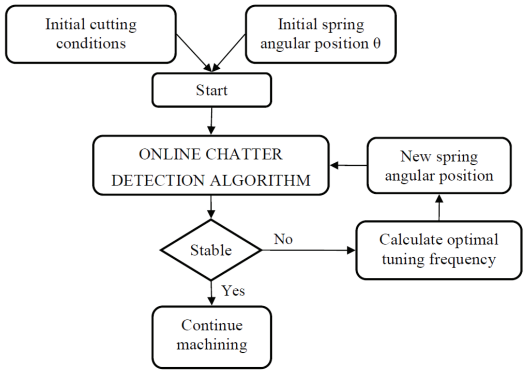

FIGURE 4. Online chatter detection algorithm

This algorithm is implemented on a real-time controller. It is running continuously during the machining process, calculating the spectrum of the measured vibration of the machine, as shown in Figure 5. The algorithm detects the frequency of the maximum vibration peak, and compares it with the tooth passing frequency: if it is an integer multiple of the tooth passing frequency, it is considered a forced vibration, and no corrective action is taken. If it is not an integer multiple, it is considered to be chatter, and the angular position in the damper is modified in order to tune it with the chatter frequency.

It is very important to distinguish clearly chatter from forced vibrations, so that the damper is only tuned to chatter frequencies. Otherwise, once the damper is tuned to the chatter frequency, the vibration level at this frequency will drop, and the algorithm will detect a forced vibration as main frequency. If the damper is tuned to this new frequency, chatter generation could start again, so this needs to be avoided.

In Figure 5, the harmonics of the tooth passing frequency are 66, 100 and 132 Hz. In (a) the highest peak is detected at 96.5 Hz, and it is thus identified as chatter.

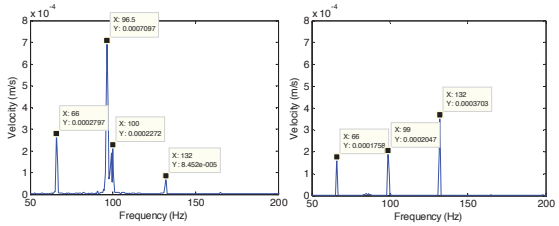

FIGURE 5. Spectrum of measured vibration (a) chatter is detected, 96.5 Hz (b) no chatter is detected

EXPERIMENTAL SETUP

Milling machine

Machining tests have been carried out on a SORALUCE milling machine, mounting the workpiece on a flexible fixture for development and evaluation purposes (see Figure 6). This fixture provides a dynamic response of the machine with a clear and isolated resonance mode, prone to suffer from chatter, and thus of help to avoid other disturbing effects, such us modes at similar frequencies, which would difficult evaluation of the performance of the semi-active damper presented here. Anyway, this is still a realistic test case comparable to many industrial cases.

DVA prototype

A DVA prototype has been built to meet the requirements of this test bench, which shows a critical mode at 94 Hz and 150 kg modal mass. With a moving mass of 7 kg, the DVA can change its main resonance frequency between 65 Hz and 105 Hz, providing an estimated 800 Ns/m damping, values which are in range with the optimal. As it can be seen on Figure 4, the moving mass is formed by the four magnet racks, with the copper plates fixed to the frame, providing thus a very compact system. An accelerometer is placed on the frame to measure machine vibration.

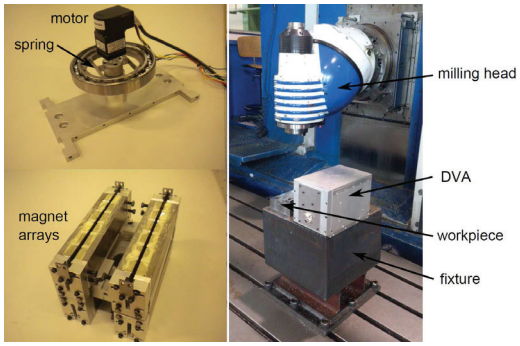

FIGURE 6. Machine tool and DVA setup

EXPERIMENTAL RESULTS

Identification of damper characteristics

In a first step, the dynamic characteristics of the damper have been identified. An experimental modal analysis has been performed on the damper, using a hammer to excite the system and measuring the vibration at different points of the structure. The goal is to check that there is only one resonance mode in the frequency range of interest, and to see how its frequency changes with the angular position of the spring.

Figure 7a shows the variation of the FRF of the damper for different angular positions of the spring. A clear dominant mode is observed, with its amplitude and frequency changes with the spring position. In Figure 7b, the variation of the resonance frequency of the damper in function of the angular position of the rotary spring is shown. The resonance frequency varies between 66 and 105 Hz.

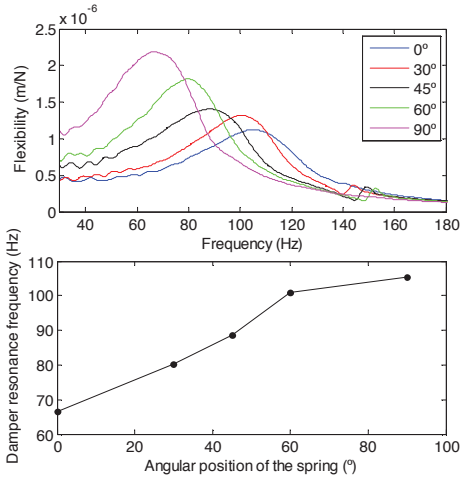

FIGURE 7. Dynamic response of the damper, experimentally measured: a) FRFs for different angular positions b) variation of the resonance frequency with the angular position of spring

These results demonstrate that the damper presented here fits well with the dynamic performance expected from a semi-active damper, with a dominant resonant mode in the direction and frequency range of interest. The results also demonstrate that the frequency tuning capability given by the angular rotation of the spring works well, and that the eddy currents can provide enough damping for this application.

Identification of fixture characteristics

The next test has consisted in testing the influence of the inertial damper on the dynamic characteristics of the workpiece fixture. In Figure 8a, the effect of the damper on the magnitude of the flexibility FRF of the fixture is shown, where the strong reduction of the vibration amplitude due to the damper can be observed, together with its variation with the angular position of the spring.

In Figure 8b, the real part of the FRF is shown for the different angular positions of the spring. This figure is used to find the optimal damper tuning, by minimizing the negative real part of the FRF, as proposed for chatter suppression in manufacturing by [7].

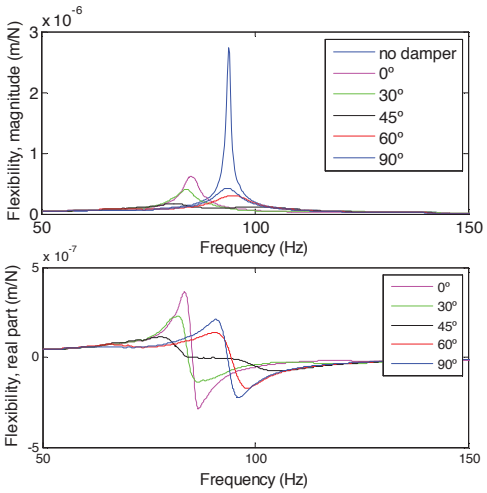

FIGURE 8. Flexibility FRF of the workpiece fixture (a) Magnitude (b) Real part

Machining results

The stability lobes [6] of the cutting process have been calculated by an experimental modal analysis, in order to show the maximum cutting depth that can be achieved without the damper. Machining tests show the validity of this prediction. The DVA was placed on the machine

next, and it was tuned automatically during the cutting process, without using the information from the modal analysis. The process was found to be stable up to the maximum cutting depth defined by the tool (5 mm), compared to the unstable conditions with 1 mm depth without damper. A time simulation [8] of the cutting and tuning process predicts much higher stable cutting depths (see Figure 9), but they cannot be reached due to tool limitations.

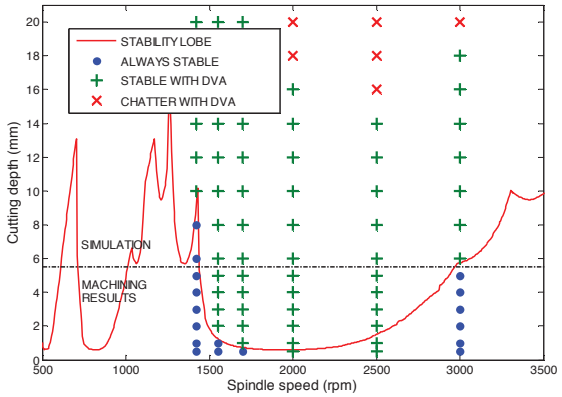

FIGURE 9. Machining stability test and simulation results, with and without DVA

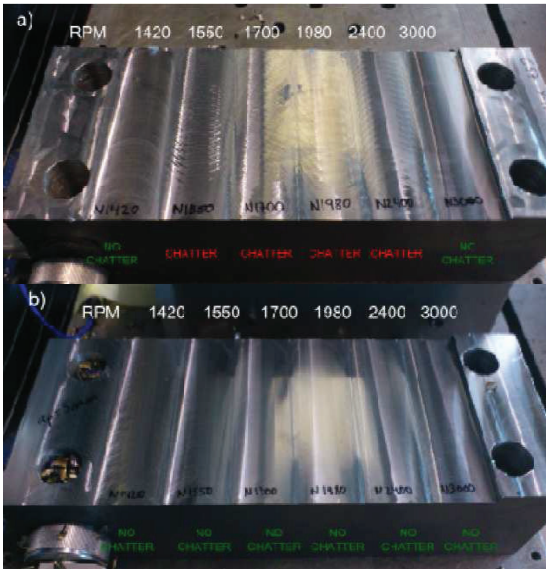

FIGURE 10. Workpiece surface after machining a) without damper, 3 mm depth b) with damper, 5 mm cutting depth

CONCLUSIONS

These results demonstrate the effectiveness of the self-tuning DVA principle presented here, which detects continuously during the machining process whether chatter is happening or not, and automatically tunes itself to the optimal position.

In real applications, productivity improvement will not be as high as the one obtained in this research test bench, but it will outperform existing DVAs by providing a low cost solution that does not require a previous experimental modal analysis and that works in close-to-optimal conditions even when process dynamics change during operation.

ACKNOWLEDGEMENTS

This research was partially supported by the EU FP7 DYNXPERTS (260073/FP7-2010-NMP-ICT-FoF).

REFERENCES

[1] Altintas, Y., M. Weck, Chatter Stability of Metal Cutting and Grinding. CIRP Annals of Manufacturing Technology. 2004; 53, 2: 619 - 642.

[2] A. Olarra, A. L J., G. E, S. M, and C. C, “Aplicación de absorbedores dinámicos sintonizados en máquina herramienta,” presented at the 18 Congreso de Máquinas-Herramienta y Tecnologías de Fabricación, San Sebastián, 2010.

[3] H. X. Deng and X. L. Gong, “Adaptive Tuned Vibration Absorber based on Magnetorheological Elastomer,” Journal of Intelligent Material Systems and Structures, vol. 18, no. 12, pp. 1205–1210, Dec. 2007.

[4] D. Gsell, G. Feltrin, and M. Motavalli, “Adaptive Tuned Mass Damper Based on Pre-Stressable Leaf-Springs,” Journal of Intelligent Material Systems and Structures, vol. 18, no. 8, pp. 845–851, Aug. 2007.

[5] H. D. Wiederick, “Magnetic braking: Simple theory and experiment,” American Journal of Physics, vol. 55, no. 6, p. 500, 1987.

[6] Y. Altintaş and E. Budak, “Analytical Prediction of Stability Lobes in Milling,” CIRP Annals - Manufacturing Technology, vol. 44, no. 1, pp. 357–362, 1995.

[7] Sims, Neil D. “Vibration Absorbers for Chatter Suppression: A New Analytical Tuning Methodology.” Journal of Sound and Vibration 301, no. 3–5 (Abril 2007): 592–607. doi:10.1016/j.jsv.2006.10.020.

[8] Bediaga, I. “Supresión Del Chatter Regenerativo Mediante Variación En Proceso de La Velocidad de Giro.” PhD thesis, Mondragon University, 2009.

FUNCTIONAL CONSTRAINTS AND THE DESIGN OF A NEW WATT BALANCE

Leon S. Chao, Stephan Schlamminger, and Jon R. Pratt
Fundamental Electrical Measurements Division
National Institute of Standards and Technology
Gaithersburg, MD, USA

ABSTRACT
The functional constraints driving the design of the new permanent-magnet driven watt balance (NIST-4) outline the variables and compromises worthy of addressing. Construction according to these design parameters will demonstrate the high precision capabilities of a large complex mass measurement system with overall uncertainties on the order of 3 parts in 10^8.

INTRODUCTION
Redefinition of the SI system is a formidable global undertaking. Of the seven SI units, the unit of mass is the only one still defined via an artifact, a platinum-iridium alloy cylinder casted in 1879 known as the *international prototype kilogram (IPK)* housed in the BIPM in Paris. The two major shortcomings of any artifact standard are replication and stability.

The watt balance, conceived in 1975 by Bryan Kibble, is a weight measuring apparatus that virtually compares electrical power to mechanical power, hence the name watt balance. Recent advancements in quantum physics have helped evolve the watt balance into an instrument capable of realizing the unit of mass.

HOW IT WORKS
The NIST-4 watt balance contains only a few key components. A copper wire coil that is suspended from one side of a diamond turned aluminum wheel balanced on a knife edge along the axle of the wheel (Figure 1). This hanging coil is immersed in a 0.55 Tesla magnetic field (some 10,000 times greater than Earth's magnetic field) generated by a one ton SmCo permanent magnet system. A measurement mass and auxiliary mass hang concentric to the coil on the main mass stirrup (Figure 6). The aluminum ELF (Extremely Large Flexure) is used to precisely locate the moving coil in the X and Y directions.

Theoretically, the instrument operates by linking the unit of mass to Planck's constant, a fundamental constant of nature as demanded by quantum physics. Functionally, the instrument achieves this linkage to quantum physics via indirectly comparing electrical power to mechanical power by toggling between two modes during measurement (Velocity Mode and Force Mode).

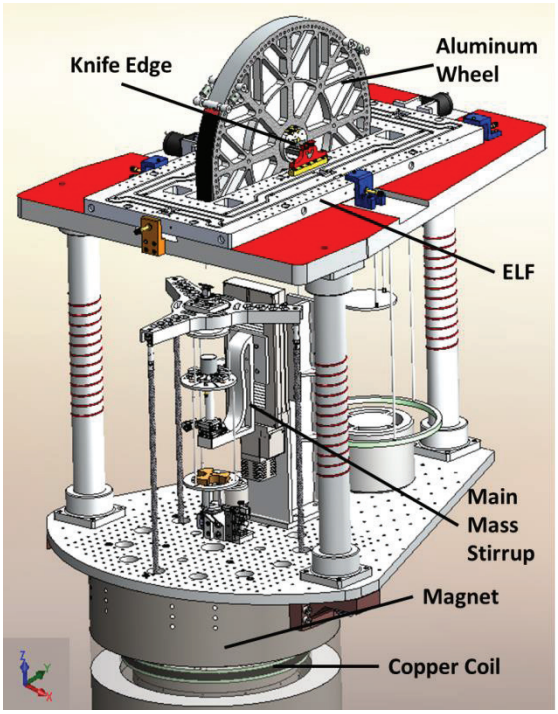

FIGURE 1. Current design phase of the NIST-4 watt balance. The coil and main mass hang concentrically and tangent to the wheel while vertically aligned to gravity.

In Velocity Mode, the coil (wire length L) is moved at a vertical speed, v, through the magnetic field (flux density B) so that a voltage, U, is induced. The voltage is then measured precisely in terms of Planck's constant by comparison to a quantum voltage standard [1].

In Force Mode, the gravitational force of the countermass, $m_2 g$, offsets the weight of the coil and main mass, $m_1 g$. To achieve a balanced state, an upward (or downward if the main mass is unloaded) electromagnetic force, generated by sending an electric current, I, through the coil, levitates the main mass stirrup. Measuring the main mass on the same side as the coil ensures equality in the torque generated by a common lever arm, as long as their centers of mass are vertically aligned to gravity. The current, I, is measured in terms of Planck's constant by monitoring the voltage drop across a known resistor, this time making use of both quantum voltage and resistance standards.

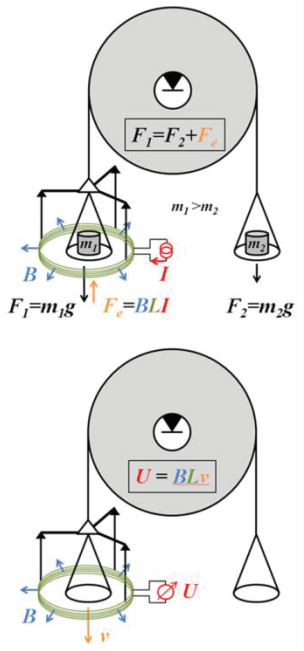

Force Mode: an upward electro magnetic force is generated by the coil to balance the wheel

$$BL = \frac{(m_1 - m_2)g}{I}$$

Velocity Mode: A voltage is induced by moving the coil through a 0.55 Tesla magnetic field

$$BL = \frac{U}{v}$$

FIGURE 2: Force and Velocity Modes

Cancelling out the BL factor common to both equations and rearranging the variables, power is revealed and mass is solved for:

$$BL = \frac{U}{v} = \frac{mg}{I} \quad (scalar\ version)$$

$$Therefore:\ UI = mgv = m\boldsymbol{g} \cdot \boldsymbol{v}$$
$$\therefore\ m = UI/\boldsymbol{g} \cdot \boldsymbol{v}$$

Note that $\boldsymbol{g}$ and $\boldsymbol{v}$ must be parallel vectors (vertical), hinting at the significance of physical alignment during measurement.

Now, $P_{elec} = UI\ and\ P_{mech} = m\boldsymbol{g} \cdot \boldsymbol{v}$, implying the balance of mechanical power and electrical power. However, it is important to recognize that both types of power are "virtual" because they are not directly measured in either mode.

The advantage of a wheel balance over a traditional beam balance becomes apparent when attempting to design for this "virtual" functionality. A watt balance must independently meet two criteria: (1) balance opposing lever arms about the knife edge and maintain equilibrium in the nominal position, and (2) translate the coil in a purely vertical fashion aligned to gravity. Although both balance designs meet criteria (1), the wheel allows pure vertical motion of the coil as it rotates whereas the beam incorporates a parasitic horizontal motion as it pivots.

THE MOVING COIL

The moving coil has six degrees of freedom of motion given by three components (v_x, v_y, v_z) of its velocity $\boldsymbol{v}$ and three components $(\omega_x, \omega_y, \omega_z)$ of its angular velocity $\boldsymbol{\Omega}$ about its center of mass [2]. Additionally, the coil can generate a force $\boldsymbol{F}$ with components (F_x, F_y, F_z) and a torque $\boldsymbol{\Gamma}$ with components $(\Gamma_x, \Gamma_y, \Gamma_z)$. Of the twelve variables that contribute to the virtual mechanical power, F_z and v_z are the only desired components. Note:

$$UI = \boldsymbol{F} \cdot \boldsymbol{v} + \boldsymbol{\Gamma} \cdot \boldsymbol{\Omega}$$
or
$$UI = F_x v_x + F_y v_y + F_z v_z + \Gamma_x \omega_x + \Gamma_y \omega_y + \Gamma_z \omega_z$$

To achieve the precision necessary for realization of mass, the ratio of each off-axis component to $F_z v_z$ must be minimized to 3 x 10^{-9} (ppb). There are essentially three ways to accomplish this: (1) diminish the five off-axis force components, (2) diminish the five off-axis velocity components, or (3) reduce both off-axis forces and velocities to diminish the off-axis product Fv. For example, if

$$\frac{F_x}{F_z} = 10^{-4} \quad and \quad \frac{v_x}{v_z} = 10^{-5}$$

then,

$$\frac{F_x v_x}{F_z v_z} = 10^{-9}\,.$$

The off-axis x and y force and torque components are minimized by concentrically aligning the electrical center of the coil to the center of the radial magnetic field. By doing this, the magnetic flux gradients are balanced on opposing sides of the coil. Compliancy in the

stirrup system, accomplished by small flexure cubes, allows for monitoring of the parasitic forces and torques during Force Mode. However, compliant systems result in amplified parasitic motions.

HIGH PRECISION ALIGNMENT

In order to achieve the required ppb level of uncertainty for mass redefinition, the physical alignment of the moving coil's electrical center to the field's magnetic center is important. These two points must be aligned to sub-micron levels. However, the coil's location traces back to the location of the knife edge whose 35 kg load must be precisely positioned with a device that is both vacuum compatible and nonmagnetic.

An Extremely Large Flexure (ELF) was designed and machined from a monolithic block of 6061 T6 aluminum to adjust the XY position of the knife edge and everything attached. The ELF weighs 33 kg, is 97 x 46 x 3.8 cm, and is mirror symmetric about the x and y axis. The system contains 24 individual flexures measuring 1.8 mm wide and 8 mm long. These flexures allow the movement of the middle plate with respect to the outer ring.

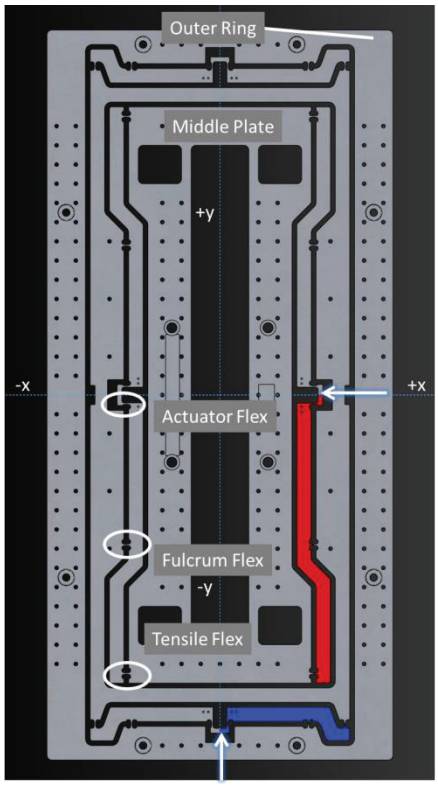

FIGURE 3. Top view of the ELF. Pushing on the tabs indicated by the arrows result in X and Y displacements of the middle plate. Desired displacements = ±0.5 mm in X and Y.

Note the symmetric design and the collinear flexures are significant in removing off axis motions, preserving pure linear motion in X and Y. Focusing only on the shaded vertical beam, one sees three collinear flexures. Pushing on the top actuation flexure in the –x direction pivots the whole beam about the fulcrum flexure, resulting in a pulling force applied to the tensile flexure and displacement of the middle plate in the +x direction. The same is conducted on the bottom shaded beam for displacements in the y direction.

Because maximum actuation force is a design constraint, the flexures were originally designed to be extremely thin, minimizing the spring constant. However, the thinner the flexures, the more sag the middle plate experiences, especially under a 35 kg external load. Optimization of flexure thickness (vertical stiffness) and actuation force can be determined by varying the location of the fulcrum. Longer lever arms amplify the actuation force, allowing for stiffer flexures. In the current design, finite element analysis (FEA) indicates the middle plate should sag approximately 1 mm under a 100 kg load (safety factor = 2.9) while a 50 N X force and 100 N Y force will translate the middle plate by 1 mm.

The force to push the actuator flexures are generated via two stepper motors driving a 1/4-80 adjustment screw. A second benefit of distancing the fulcrum from the actuator flexure is that it increases the resolution of the screw and stepper motor. If the fulcrum is exactly in the middle between the actuator and tensile flexures, the displacement ratio of the actuator flexure to tensile flexure is 1:1. If the fulcrum is shifted such that the new ratio is 10:1, then the actuator resolution also increases by an order of magnitude. A stepper motor with a step size of 1.8 degrees coupled with a 1/4-80 lead screw has a resolution of 1.5 μm. A 10:1 lever arm can magnify the resolution to 0.15 μm. With microstepping techniques, an even finer resolution can be achieved.

CHARACTERIZATION OF ELF

To verify the FEA static loading calculations, the ELF was loaded with 31 kg at the origin. Due to

the limited dynamic range of the dial indicator used in this experiment, it was zeroed in between each incremental loading of 5.5 kg. The total amount measured by the dial indicator summed to 490 μm.

To verify this summed displacement, a flat was bolted to the outermost frame of the ELF and spanned all the way to the middle plate. After loading, the separation displacement between the flat and the middle plate was measured with feeler stock, indicating 508 μm (3.5% disparity between two measurement types).

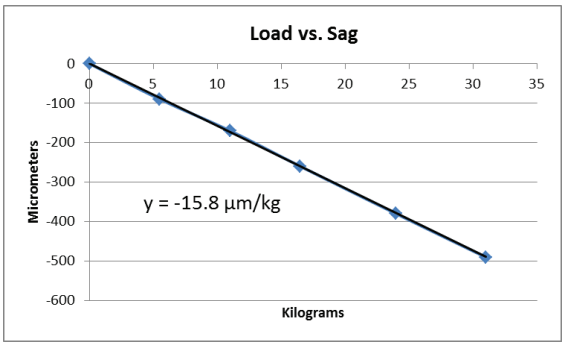

FIGURE 5. A total of 31 kg (incremental masses of 5.5 and 7.3 kg bricks) of load was placed on top of the ELF. This resulted in 490 µm of sag and shows the expected linear trend. Error bars not shown for readability, but commensurate with indicated scatter.

The parasitic motions of roll (rotation about x axis) and pitch (rotation about y axis) during x and y translation were also of concern. Two precision bubble levels were placed on the surface of the middle plate, both with a resolution of 5 arcseconds per division. Each translation direction was independently driven 1.2 mm in 150 micron increments. Under no external load, the pitch had no measurable variation while the roll had a deviation of ± 1.5 arcseconds. Under the full external load, the pitch and roll both had a variation of ± 2 arcseconds.

AUXILIARY MASS

When switching between Velocity Mode and Weighing Mode in the existing watt balance, a ½ kg counter mass is loaded and unloaded from the mass pan hanging from the far side of the wheel. A design flaw is exposed during this process: the knife edge experiences a 1 kg heavier load in Weighing Mode than in Velocity Mode, drastically affecting the hysteresis in the knife edge.

To remedy this issue for NIST-4, the counter mass was replaced with a ½ kg fixed tare mass. A ½ kg auxiliary mass was introduced to the main mass side to serve as the new counter mass. Using its on/off system, the auxiliary mass is removed from the system during Weighing Mode and reinserted during Velocity Mode as a novel way to balance the wheel.

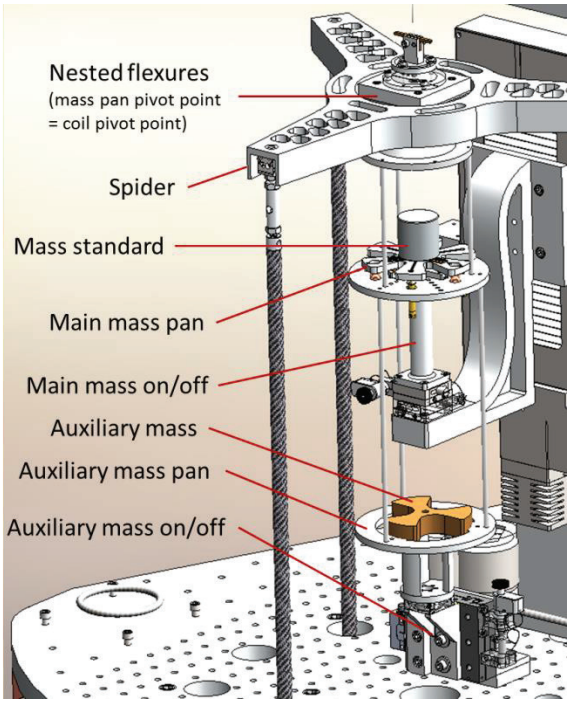

FIGURE 6. Main mass side hanging assembly. The aux mass hangs below the main mass and has its own mass on/off mechanism. It is only loaded on its mass pan during Velocity Mode.

Existing Watt Balance

Mode	F_{coil}	M_{main}	M_{aux}	=	$M_{counter}$	Knife Load
Velocity	0	0	0	=	0	M_{tare} + 0
Weigh (M_{off})	½	0	0	=	½	M_{tare} + 1
Weigh (M_{on})	-½	1	0	=	½	M_{tare} + 1

NIST-4

Mode	F_{coil}	M_{main}	M_{aux}	=	$M_{counter}$	Knife Load
Velocity	0	0	½	=	½	M_{tare} + 1
Weigh (M_{off})	½	0	0	=	½	M_{tare} + 1
Weigh (M_{on})	-½	1	0	=	½	M_{tare} + 1

FIGURE 7. The NIST-4 knife edge load is equal between both modes after introducing the aux mass to the system. This reduces the hysteresis in the knife edge.

When the NIST-4 watt balance is undergoing velocity sweeps, the aux mass is loaded to counterbalance the ½ kg fixed tare mass. Compared to the traditional method of removing the ½ kg counter mass completely, the NIST-4 Velocity Mode has a 1 kg heavier load. However, this 1 kg extra load on the knife edge is now consistent with that of Weighing Mode and should significantly reduce the mechanical hysteresis in the knife edge. Current tests are underway to determine the validity of the auxiliary mass mechanism.

CONCLUSION

NIST-4 will be used to realize the unit of mass once the redefinition of the SI has occurred with uncertainties of 3 parts in 10^8. To disseminate mass with similar uncertainties demands high precision mechanical components capable of sub-micron repeatability and accuracy. The NIST-4 watt balance continues to prove its merit as a great precision engineering experiment.

REFERENCES

[1] Gorman J, Yong-Sik K, Dagalakis N G. Control of MEMS Nanopositioners with Nano-scale Resolution. Proceedings of IMECE2006. November 5-10, 2006.

[2] Rau M, Hayes E. The Principle of the Watt Balance. *Science in School.* Issue 25: Winter 2012. 1, March 2013.

[3] Robinson I A. Alignment of the NPL Mark II watt balance. IOP Publishing, Meas. Sci. Technol. 2012; 23: 17pp.

Eliminating Parasitic Error in Dynamically Driven Flexure Systems

Jonathan B. Hopkins[1]
Materials Engineering Division
Lawrence Livermore National Lab
Livermore, CA, USA

Robert M. Panas[2]
Dept. of Mechanical Engineering
Massachusetts Institute of Technology
Cambridge, MA, USA

INTRODUCTION

The aim of this paper is to guide designers in determining the optimal number and placement of actuators for driving general parallel multi-axis flexure systems at any desired speed. Although the degrees of freedom (DOFs) of a flexure system are largely determined by the location and orientation of its flexure elements, the system's stage will tend to displace in unwanted directions (i.e., parasitic errors) while attempting to traverse its intended DOFs if it is not actuated correctly. The problem of correctly placing actuators is difficult because the optimal location changes depending on the speed with which the stage is driven. In this paper we introduce the mathematics necessary to generate geometric shapes, called dynamic actuation spaces, which enable designers to rapidly visualize all the ways actuators could be placed for driving a general flexure system with minimal parasitic error at any speed without having to move the actuators placed. The theory provided here impacts the design of precision motion stages in that it significantly simplifies their control and increases their bandwidth. Example systems that benefit from this research include flexure-based nano-positioners, high-speed assembly stages, and multi-axis micro-mirrors.

CONTRIBUTIONS

In this paper we *(i)* introduce the concept of dynamic actuation space, *(ii)* provide the complete library of these spaces, *(iii)* provide guidelines for placing the correct number of actuators within these spaces, and *(iv)* introduce the mathematics necessary to generate these spaces as well as calculate the selected actuators' output force magnitudes for driving a system with a desired DOF at a desired speed.

FUNDAMENTAL PRINCIPLES

Consider the steel flexure system in Fig. 1A (E=210GPa, G=79GPa, ρ=7700 kg/m^3). Its four wire flexures guide its T-shaped stage to move with three DOFs—two translations and one rotation. These DOFs may be modeled using twist vectors [1], $\mathbf{T_1}$, $\mathbf{T_2}$, and $\mathbf{T_3}$ (Fig. 1B). If we wish to quasi-statically actuate these DOFs, we could do so optimally (i.e., with minimum parasitic error) by pushing on the stage with two linear forces located in the middle of the flexures

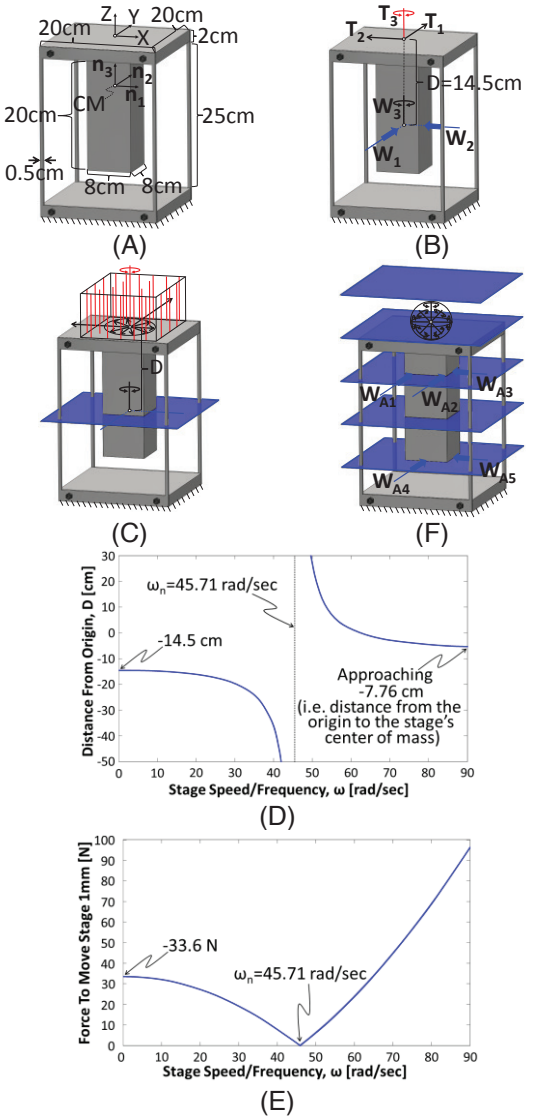

FIGURE 1. Flexure system (A), optimal actuator placement for static actuation (B), freedom and static actuation spaces (C), distance of static actuation space from origin verses stage speed (D), actuator force verses stage speed (E), and dynamic actuation space with five actuators (F)

as shown in Fig. 1B and torqueing the stage with one pure moment respectively. These actuation actions may be modeled using wrench vectors [1], $\mathbf{W_1}$, $\mathbf{W_2}$, and $\mathbf{W_3}$. Their locations correspond with the system's center of stiffness and are shown a distance, *D*, from the origin. As long as the system is not driven with any appreciable speed, these actions will minimize the axial loads in the flexures and will thus produce the corresponding DOFs with minimal parasitic error for small displacements.

Although the stage is capable of moving with three DOFs, it may also move with every combination of these DOFs. These motions are visually depicted by the system's freedom space [2]. Freedom space is a geometric shape that represents all the ways a system may move. The freedom space of this example consists of an infinitely large box of parallel rotation lines (shown red in Fig. 1C) and a disk of translation arrows that are perpendicular to these lines. If $\mathbf{T_1}$, $\mathbf{T_2}$, and $\mathbf{T_3}$ are linearly combined, this freedom space is generated. For the case of quasi-static actuation, the optimal locations and orientations of the actuators that successfully drive all the motions/twists within this freedom space also lie within a geometric shape called a static actuation space [2]. This space results from the linear combination of $\mathbf{W_1}$, $\mathbf{W_2}$, and $\mathbf{W_3}$ and consists of a plane of linear forces (shown blue in Fig. 1C) and an orthogonal moment.

The optimal location of this actuation space will remain at D=14.5cm only if the DOFs in the freedom space are actuated with quasi-static speeds. If, however, we wish to actuate the motions within the freedom space with an increasing sinusoidal frequency of ω, the optimal location of the actuation space will displace downwards until it is infinitely far away when ω reaches the system's first natural frequency (Fig. 1D). As ω increases to infinity above this natural frequency, the planar actuation space descends from positive infinity until it approaches the stage's center of mass. The effect of increasing ω on the absolute value of the actuation force necessary to displace the stage a sustained-amplitude of 1mm is shown in Fig. 1E.

Given these results, one may conclude that the only way to dynamically actuate a stage with minimal parasitic error is to move the actuators according to the desired actuation speed. This is fortunately not the case. If the wrench vectors within every planar actuation space for all values of ω are linearly combined, a new space emerges. This space is called dynamic actuation space. The dynamic actuation space of this example consists of an infinite number of stacked parallel planes that contain linear force wrenches (shown blue in Fig. 1F) and coupled moment/force wrenches as well as a sphere of pure moment wrenches. Unlike the planar static actuation space from Fig. 1C that contains three independent linear forces, the dynamic actuation space of Fig. 1F contains five such forces. Thus, while quasi-static actuation requires only three actuators from the plane of Fig. 1C to drive the system's three DOFs with minimal parasitic error, dynamic actuation requires at least five actuators from the parallel planes of Fig. 1F. As long as these five actuators' lines of action are all independent, like $\mathbf{W_1}$ through $\mathbf{W_5}$ shown in Fig. 1F, their output forces may be combined to actuate any motion within the system's freedom space with minimal parasitic error at any speed without the actuators needing to change locations at any time.

There are a finite number static and dynamic actuation spaces. These spaces are provided in Fig. 2. They are identical to the constraint spaces described in Hopkins [3]. They consist of linear forces depicted as blue lines, pure moments depicted as black lines with circular arrows about their axes, and coupled moment/force wrenches depicted as orange lines. It is not important to the purpose of this paper that the reader understand the details of these spaces. What is important to recognize is that each space is numbered and belongs to one of seven columns. Each column is labeled with the number of independent wrenches (i.e., minimum number of necessary actuators) contained within its actuation spaces. Note that the actuation space of Fig. 1C is the first space in the "3 Actuators" column of Fig. 2 and that the actuation space of Fig. 1F is the third space in the "5 Actuators" column.

Thus, when a system's dynamic actuation space has been determined, Fig. 2 may be used to identify the fewest number of actuators necessary to actuate the systems DOFs with minimal parasitic error. The only actuation spaces that contain enough linear force actuators to achieve all of the system's DOFs are those shown in the pyramid outlined in black (Fig. 2). If the system's actuation space lies outside of this pyramid, it will require at least one

pure moment or coupled moment/force actuator to drive all of the system's DOFs.

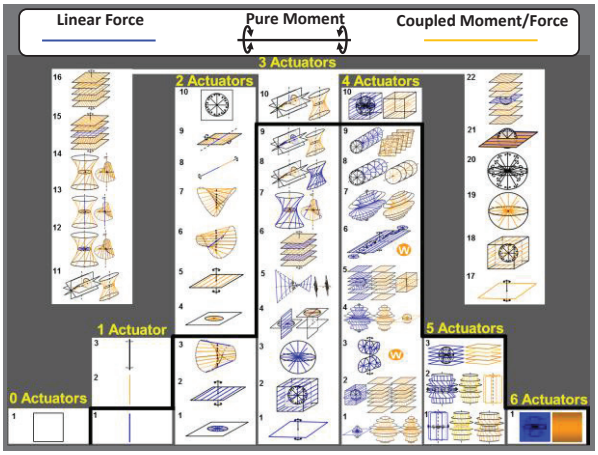

FIGURE 2. Complete library of actuation spaces

MATHEMATICAL TOOLS

This section provides the mathematical tools necessary to *(i)* generate a general parallel flexure system's dynamic actuation space, *(ii)* select appropriate actuators within this space, and *(iii)* calculate the output force magnitudes of the selected actuators for achieving any desired DOF with minimal parasitic error at any speed.

If we wish a general system's stage to move with a twist, $\mathbf{T_i}$, at a speed of ω, the wrench, $\mathbf{W_i}$, required to drive the stage may be calculated using

$$\mathbf{W_i} = \left(-\omega^2[M_{TW}]+[K_{TW}]\right)\mathbf{T_i}, \quad (1)$$

where $[M_{TW}]$ is the system's twist-wrench mass matrix [1] defined by

$$[M_{TW}] = [N][\Delta][in][N]^{-1}, \quad (2)$$

where $[N]$ is defined by

$$[N] = \begin{bmatrix} \mathbf{n_1} & \mathbf{n_2} & \mathbf{n_3} & \mathbf{0} & \mathbf{0} & \mathbf{0} \\ \mathbf{L}\times\mathbf{n_1} & \mathbf{L}\times\mathbf{n_2} & \mathbf{L}\times\mathbf{n_3} & \mathbf{n_1} & \mathbf{n_2} & \mathbf{n_3} \end{bmatrix}. \quad (3)$$

The vector **L** is a 3x1 location vector that points from the system's origin to the stage's center of mass (labeled CM in Fig. 1A), $\mathbf{n_1}$, $\mathbf{n_2}$, and $\mathbf{n_3}$ are 3x1 orthogonal unit vectors, **0** is a 3x1 zero vector, and $[\Delta]$ from Eq. (2) is

$$[\Delta] = \begin{bmatrix} [0] & [I] \\ [I] & [0] \end{bmatrix}. \quad (4)$$

Matrix $[0]$ is a 3x3 zero matrix, $[I]$ is a 3x3 identity matrix, and $[in]$ from Eq. (2) is a 6x6 inertia matrix defined by

$$[in] = diag\,[I_1 \quad I_2 \quad I_3 \quad m \quad m \quad m], \quad (5)$$

where I_1, I_2, and I_3 are the stage's mass moments of inertia (centered about the stage's center of mass) that correspond with the directions of $\mathbf{n_1}$, $\mathbf{n_2}$, and $\mathbf{n_3}$ respectively, and m is the stage's mass. For the plots of the example of Fig. 1, 1/3 of the four wire flexures' mass protruding from the system's stage is considered in the values of Eq. (5). This is done to take the inertia of the moving section of the flexures into account as well as the rigid stage. The twist-wrench stiffness matrix $[K_{TW}]$ in Eq. (1) may be calculated using the theory provided in Hopkins [2]. This stiffness matrix is constructed using information pertaining to the system's flexure element topology as well as geometry and material properties.

The static actuation space of a general flexure system is generated by linearly combining the wrench vectors, $\mathbf{W_i}$, that result from substituting all of the system's DOF twists, $\mathbf{T_i}$, into Eq. (1) for ω equal to zero. The dynamic actuation space of a general flexure system is generated by linearly combining the wrench vectors, $\mathbf{W_i}$, that result from substituting all of the system's DOF twists, $\mathbf{T_i}$, into Eq. (1) for every value of ω. In practice, however, only a few values of ω are necessary to substitute into the equation before a sufficient number of independent wrench vectors are identified that are capable of generating the entire dynamic actuation space.

Once a system's dynamic actuation space has been identified, designers may use the library of Fig. 2 to identify the minimum number of necessary actuators that must be selected from within the space depending on the column under which the space is categorized. This number is never less than the number of system DOFs, nor is it ever more than six. If it equals the number of system DOFs, the system is well designed and requires the fewest number of actuators to eliminate parasitic error for both static and dynamic scenarios. Such systems are generally symmetric and/or possess a center of stiffness that is coincident with their stage's center of

mass. Their static and dynamic actuation spaces are identical. An example of such a flexure system that achieves the same three DOFs as the system from Fig. 1 with minimal parasitic error but with three actuators instead of five is shown in Fig. 3. The system's three actuators are sufficient to drive the stage's DOFs at any speed because the system's static and dynamic actuation spaces are synonymous (i.e., a plane of linear forces and a perpendicular moment).

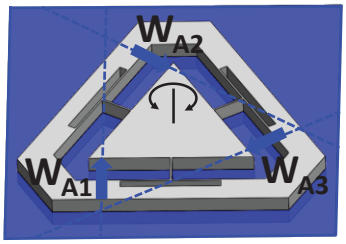

FIGURE 3. Improved flexure system

Once designers know how many actuators to select from the system's dynamic actuation space, they must select them such that their lines of action are independent and correspond with their actuator's type (e.g., blue lines correspond with linear actuators, black lines correspond with pure moment actuators, and orange lines correspond with coupled moment/force actuators). To ensure that the actuators selected are independent, designers may use the concept of sub-constraint spaces described in Hopkins [2-3], or they may apply Gaussian elimination to their actuators' wrench vectors. Actuators should be arranged with as much symmetry as possible and designers should ensure that their lines of action are orthogonal to the stage where they act. Stages should be designed with as few protrusions as possible to minimize inertia and thus increase the system's natural frequencies.

After the actuators have been placed, their 6x1 wrench vectors, $\mathbf{W_{Aj}}$, should be arranged in a matrix $[W_A]$ according to

$$[W_A] = \begin{bmatrix} \mathbf{W_{A1}} & \mathbf{W_{A2}} & \cdots & \mathbf{W_{Aj}} \end{bmatrix}, \quad (6)$$

where the force magnitude of each vector is set to unity and j is the number of actuators placed. If any of these vectors are pure moment vectors, the magnitude of their moment is also set to unity. Note that j is five for the system of Fig. 1F. The actuators' output force magnitudes, F_{Aj}, that are necessary to drive a stage with a desired twist, $\mathbf{T_i}$, at a speed of ω, can be calculated according to

$$\begin{bmatrix} F_{A1} & F_{A2} & \cdots & F_{Aj} \end{bmatrix}^T = \left([W_A]^T \cdot [W_A] \right)^{-1} \cdot [W_A]^T \cdot \mathbf{W_i}, \quad (7)$$

where $\mathbf{W_i}$ is calculated using Eq. (1).

The six mode shapes of a general parallel flexure system are the Eigen vectors of its [*Mode*] matrix defined by

$$[Mode] = [M_{TW}]^{-1} [\mathrm{K_{TW}}]. \quad (8)$$

The natural frequency, ω_n, associated with each mode shape is the square root of the corresponding Eigen vector's Eigen value. The first i mode shapes of a parallel flexure system correspond with the i orthonormal DOF twists that lie within the system's freedom space.

Finally, note that the theory provided in this paper is specific to parallel flexure systems that are not subject to damping or internal losses. Extending this theory such that it applies to more general flexure systems is ongoing research.

CONCLUSIONS

This paper introduces the concept of dynamic actuation space as a geometric shape that guides designers in placing static actuators for driving multi-axis parallel flexure systems at various speeds with minimal parasitic error. A comprehensive library of these spaces as well as the mathematics necessary to generate them, have been provided. This work was performed under the auspices of the U.S. Department of Energy by Lawrence Livermore National Laboratory under Contract DE-AC52-07NA27344. LLNL-PROC-625332.

REFERENCES

[1] Blanchet, P., Lipkin, H., 1998, "Dual Properties for Vibration Analysis Via Screw Theory," Proc. of ASME DETC, Atlanta, GA

[2] Hopkins, J.B., Culpepper, M.L., 2010, "A Screw Theory Basis for Quantitative and Graphical Design Tools that Define Layout of Actuators to Minimize Parasitic Errors in Parallel Flexure Systems," Prec. Eng., 34(4): pp. 767-776

[3] Hopkins, J.B., Culpepper, M.L., 2011, "Synthesis of Precision Serial Flexure Systems Using Freedom and Constraint Topologies (FACT)," Prec. Eng., 35(4): pp. 638-649

Characterization of Nano-micro machining made by Atomic Force Microscope Scratch on Optical-fiber End Plane

Shinsuke Matsui, Shigeru Umemura
Department of Mechanical Science and Engineering
Faculty of Engineering
Chiba Institute of Technology
Narashino, Chiba 275-0016, Japan

INTRODUCTION

Nano-micro scratch machining on the optical fiber end-plane was conducted by Atomic force micro-scope. The machining was done with a AFM tip which can be assumed to a nano-shape cutting edge of an abrasive, and with the machining load which is controlled by the AFM cantilever system [1],[2]. Tip driving by AFM system is enabling to use a well-defined trajectory. This nano-micro machining is thought to reveals the elementary-step of the polishing whose mechanism has not been well-understood yet. The optical fiber for telecommunication used in our experiments is made of silica (SiO_2) glass with high purity. Chemical aspects of polishing also can be investigated by the cutting edge material and the scratching atmosphere changing.

Furthermore in this study the subsurface damage can be estimated optically. By machining to the core part of the optical fiber end-plane, the subsurface machining damage structure can be characterized by the optical-fiber retro-reflection measurement [3],[4]. In this presentation we use diamond and sapphire (Al_20_3) as tip material. The machining depth and subsurface damage change with machining loads and other aspects were revealed. The apparatus for the experiments be reported.

EXPERIMENTS

Fig. 1 shows the AFM scratch machining to the optical fiber end in our experiment. The scratch machining was done to the optical fiber end plane about 20 μm X 20 μm square including the optical core which is located at the center of optical fiber. This core of ten μm diameter is the region of the light signal propagation in single mode optical communication fiber. Fig. 2 shows the experimental set up for our AFM scratching. The AFM (NV2000 made by Olympus Cooperation) was improved to fit our experiment. A cylinder which has a fiber-cord trench is set to the top of the AFM tube scanner. The trench can hold an optical connector ferrule with the optical

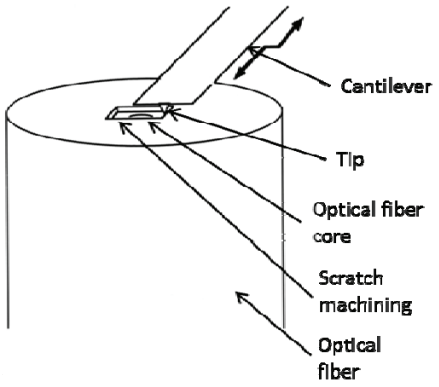

FIGURAE 1. AFM scratch machining to optical fiber end. The region of 20 X 20 μm including optical core are machined.

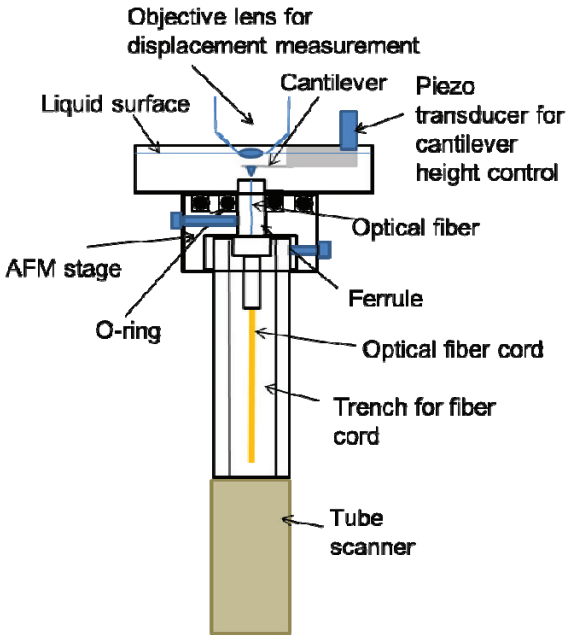

FIGURAE 2. Experimental set up for AFM scratching to the optical fiber end plane. Because it is not necessary to get rid of fiber cord from ferrule, the optical characteristics can be measured after scratching.

fiber cord. The cylinder sustains the AFM stage which has a tray for liquid. The optical connector ferrule inserted to a hole of the AFM stage and the tray. The O-ring prevents liquid from leaking downward. This apparatus enables the AFM scratch machining to the optical fiber end plane in liquid. The scratch machined optical fiber connector ferrule has fiber cord. This enables that optical characteristics of the optical connector end planes are measured before and after the AFM scratch machining. Fig.3 is a photograph of the improved AFM system used in our experiments. A ferrule end inserted to the liquid tray hole can be seen. Through objective lens for displacement measurement, the machining region can be set with the monitor.

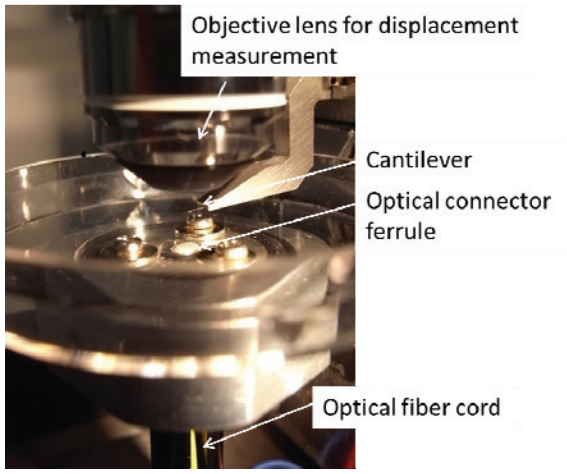

FIGURAE 3. Photograph of the improved AFM system.

The optical return-loss of machined optical fiber end plane was measured. The return-loss indicates retro reflected light amount from polished connector end plane. This optical characteristic reveals the subsurface damage layer. Fig. 4 shows our model of subsurface damage. The uniform high-index mono-layer is estimated for the damaged layer. The silica glass plastic deformation caused by machining with a diamond tip makes high density region in subsurface with residual stress. High density of silica glass makes high optical index.

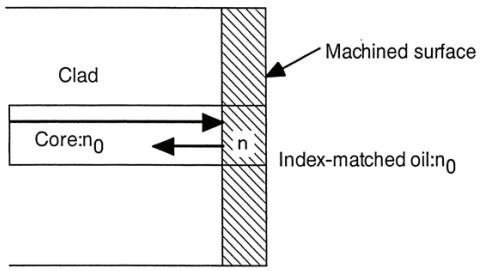

FIGURAE 4. Mono layer model of subsurface damage for return loss calculation.

With this model the return loss is calculated by

$$retrunloss = -10\log_{10}\left\{\frac{r_1^2 + r_2^2 + 2r_1r_2\cos\left(\frac{4\pi nd}{\lambda}\right)}{1 + r_1^2r_2^2\cos\left(\frac{4\pi nd}{\lambda}\right)}\right\} \quad ....(1).$$

Here

$r_1 = \frac{n - n_0}{n + n_0}, r_2 = \frac{n_0 - n}{n_0 + n}$. The return loss is decided with the interference of reflect lights of two planes of the mono layer. Fig. 5 shows the return loss calculation with layer index and layer thickness change. With the fix layer thickness, the return loss decrease as the index increase. The return loss decrease means the retro reflected light amount increase. In the case of a fixed optical index, however, the return loss decrease as the layer thickness increase. By our former study [3],[4] various diameter diamond abrasives increase index of silica glass uniformly. The index increases from 1.45 to 1.53. On the other hand the abrasive diameter increases increase the layer thicknesses. These cause various return losses with abrasive diameter

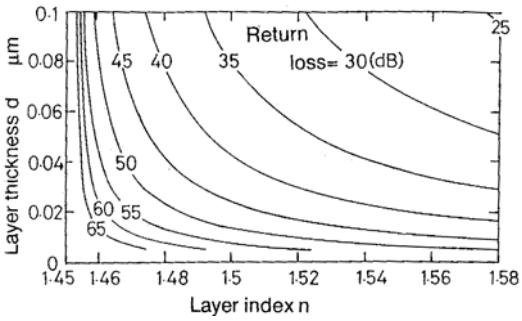

FIGURAE 5. Return loss calculation with layer index and layer thickness changing.

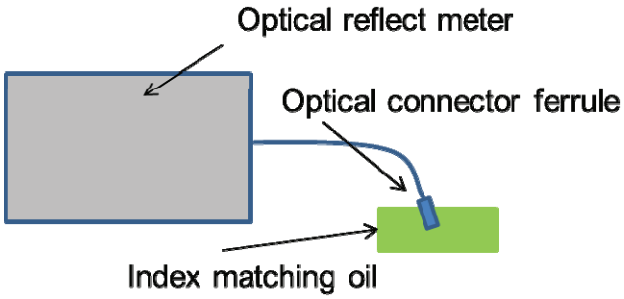

FIGURAE 6. Schematic diagram of return loss measurement. The optical index of oil is the same as the optical fiber core.

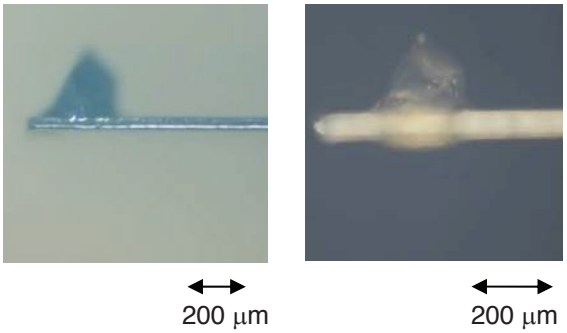

(a) Sapphire tip Curvature radius is 0.2 μm.

(b) Diamond tip Curvature radius is 0.1 μm.

FIGURAE 7. Photos of tips and cantilevers. The cantilevers are made of stainless steel. The width is 200 μm. the thickness is 40 μm.

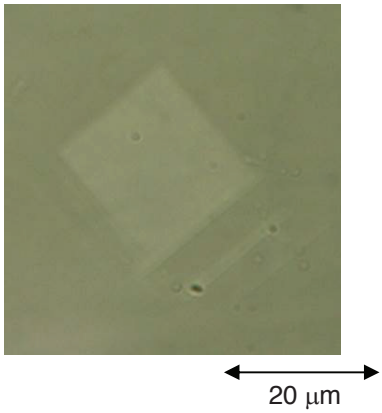

FIGURAE 8. Nano scratch machining to the optical fiber end plane in water (pH=7). The curvature radius of tip was 0.1 mm. The process load is 50 μN.

change. Return loss measurement setup is shown in Fig.6. The optical index of the region contacting with the connector ferrule end plane becomes the same to the undamaged optical fiber core index with the optical index matching oil.

Fig. 7 shows the tips we use in the experiments. We use 0.1- 1.0 μm curvature radius diamond tip and 0.2 μm curvature radius sapphire tip. These tips glued to the rectangular stainless cantilevers with epoxy adhesive. The spring constants were adjusted by changing the cantilever fixed point to the holder. The process loads are in the range of 10 – 300 μN. The scratch machining area is 20 μm X 20 μm as previously stated. The scratch speed was one second for every line. The scanning interval of scratch is 0.04 μm. So, 512 lines of scan traces make a scratch area. Two times of this rectangular scratches were down on the same location. After machining the plane was observed for 50 μm X 50 μm area with the light measurement load or the tapping mode. The pH of liquid was changed from 7 to 12 by KOH dissolving to pure water. Under these conditions the polishing of silica glass by the abrasive of tip-material in the liquid of various pH was simulated experimentally.

RESULTS

Fig. 8 shows the AFM scratch machining to the optical fiber end. The scratch machining trace with diamond tips in the pH7 water can be seen. The curvature radius of tip was 0.1 mm. The process load is 50 μN. The scratch machined plane looks very smooth. By the machining, the optical return-loss decreases from 55 dB to 38 dB on average. Here the initial plane of 55 dB return loss has very little subsurface damage by polishing with silica abrasive. It means that the damage layer was made by the scratching although the surface is very smooth. The scratched depth was 2.6 nm. With the 20 μN process load, the scratch depth becomes shallow. It is 1.2 nm. The return loss indicates 48 dB on average. It is seems that the smaller load causes the shallow machining area and the thinner subsurface damage layer. With the same process load, the machining depth increased as the pH increased. Although the sapphire tip in pH7 liquid could not machine, in higher pH it could machine silica glass. In the latter case the damaged layer was measured optically.

CONCLUSION

AFM scratch machining to the tele-communication optical fiber end plane could be done with newly improved AFM stage. By this machining the local area including optical fiber core could be machined. The scratch machined connector ferrule has the fiber cord. So with the measurement of the return loss of the machined plane, the subsurface damage can be estimated. As a result, the 50 μN machining caused return loss increase to 38 dB which indicates the subsurface damage layer growth.

REFERENCES

[1] Shinsuke Matsui, Fumikazu Ohira, Shigeru Umemura, Kazuo Matsunaga, and Kunio Koyabu : Characterization of Subsurface Damage Made by an Atomic-Force-Microscopy Scratch Test on an Optical-Fiber End Plane, Precision Science and Technology for Perfect surface, (1999) pp. 893

[2] Shinsuke Matsui and Junya Kobayashi : Characterization of damaged layer of optical fiber end by AFM scratch machining, Journal of Abrasive Technology (in Japanese),54 No.10 (2010) pp. 607

[3] Shinsuke Matsui, Fumikazu Ohira, Kazuo Matsunaga, and Yukio Kikuya : Characterization of Process Damaged layers for the Optical Fiber Ends, Proc. of 7th International Precision Engineering Seminar, (1993) pp. 699

[4] Shinsuke Matsui, Fumikazu Ohira, Kunio Koyabu and Kazuo Matsunaga : Characterization of Machining-Damage Layer for Optical Fiber Ends – Relation between Damaged Layer and Return Loss -, Journal of Precision Engineering (in Japanese),64 No.10 (1998) pp. 1467

Objective Functions for Optimizing Resonant Mass Sensor Performance

Michele H. Miller[1] and Chengzhang Li[2]
[1] Department of Mechanical Engineering-Engineering Mechanics
Michigan Technological University
Houghton, MI
[2] Department of Electrical Engineering
Stanford University
Palo Alto, CA

INTRODUCTION

Resonant mass sensors have proven to have high potential for sensing very small quantities of gas vapors [1]. Micro-fabrication technologies provide a way to realize sensitive and inexpensive devices. In particular, MEMS (micro-electrical mechanical systems) offer great promise as chemical sensors. An electrostatically actuated microcantilever with an appropriate coating can serve as a resonant mass sensor for detecting chemical vapors. The ideal resonant mass sensor experiences a large change in resonant frequency in the presence of a small gas vapor concentration.

A number of design variables can be adjusted in an attempt to improve the performance of an electrostatically actuated resonant mass sensor. These include cantilever size, shape and material, gap between cantilever and substrate, actuation voltage, areas and locations of actuation and sensing pads, selection of resonance mode to monitor. During the design optimization process, an appropriate objective function must be selected. The function should capture what good performance is. Because the number of possibilities is so vast, shape optimization can involve extensive computation time. Genetic algorithms are one approach for realizing shapes that improve performance. Given the computation requirements of this type of optimization approach, the objective function needs to be very fast to calculate. In this paper, we evaluate performance measures for resonant mass sensors in terms of their ability to identify the "best" sensor and their computational efficiency.

BACKGROUND

In a sensor, a change in the physical quantity being measured produces a change in the sensor signal. The ratio of the sensor signal change to the physical quantity change characterizes the sensitivity of the sensor. For a resonant mass sensor, the sensitivity is often defined as the ratio of resonant frequency change to mass change. This ratio is referred to as the mass responsivity [2]. If the resonant mass sensor is used to detect chemical vapors, the sensitivity could also be defined as the ratio of resonant frequency change to chemical concentration change.

Another important aspect of sensor performance is detectability. A system with high damping and a flat resonant peak will not be an effective resonant mass sensor. Quality factor (or Q), which is inversely related to damping, can serve as another performance measure [3]. A common approach in optimization work is to combine multiple objectives with weighting coefficients on each such as the following:

$$\text{maximize } \alpha_1 \frac{\partial f}{\partial m} + \alpha_2 Q$$

Chen and Yu [4] choose frequency sensitivity $\partial f/\partial m$ and sensing area as the components of an objective function for optimizing resonant sensor shape. Larger sensing areas are beneficial because they lead to greater mass changes.

The analysis of Ekinci, et al. [2], combined the effects of mass responsivity and quality factor in their expression for the minimum detectible mass change that can be sensed by a nanomechanical resonator:

$$\delta M = \frac{\delta M_{eff}}{\delta \omega_o} \sqrt{\Delta f \frac{\omega_o}{Q}} 10^{(-DR/20)} \qquad (1)$$

where M_{eff} is the effective vibratory mass, ω_o is the resonant frequency of the resonator, $\delta\omega_o$ is the change in resonant frequency caused by the

change in mass, Δf is the measurement bandwidth of the frequency detection circuit, and *DR* is the dynamic range of the resonator taking into account thermomechanical noise. In this case the best sensor would minimize δM.

Motional resistance is another quantity used to characterize detectability. For an equivalent circuit model of an electrostatically driven resonant mass sensor with capacitive gap sensing, the motional resistance is the ratio of the input voltage to the output current [5]. Detectability is inversely related to motional resistance. Thus, detectability relates to the amplitude ratio of the system transfer function with an actuation voltage input and sensing current output. One possible objective function for design optimization is the product of mass sensitivity and motional resistance [6].

Another approach for characterizing resonant mass sensor performance is to calculate the root mean square deviation (RMSD) between the system frequency responses before and after a change in mass. Giurgiutiu and Rogers [7] use it as a damage index in structural health monitoring; it is found by quantifying changes in the electromechanical admittance frequency responses due to damage in a structure. Yan and Chen [8] used an RMSD percentage in structural health monitoring applications, defined as:

$$RMSD\% = \sqrt{\frac{\sum_{i=1}^{N}\left(M_i^1 - M_i^0\right)^2}{\sum_{i=1}^{N}\left(M_i^0\right)^2}} \times 100\% \qquad (2)$$

APPROACH

In this work we attempt to identify an optimization function that identifies the best sensor design. We are interested in a function that is easy to calculate and can be used in finite element or genetic algorithms to quickly provide a metric of performance. Figure 1 shows the frequency responses for two different systems with and without added mass. In the first, the resonant peaks are very sharp and the distance between the resonant peaks is small. The second has damped resonant peaks that are twice as widely separated as in the first plot. The first system has a higher Q while the second has a higher Δf.

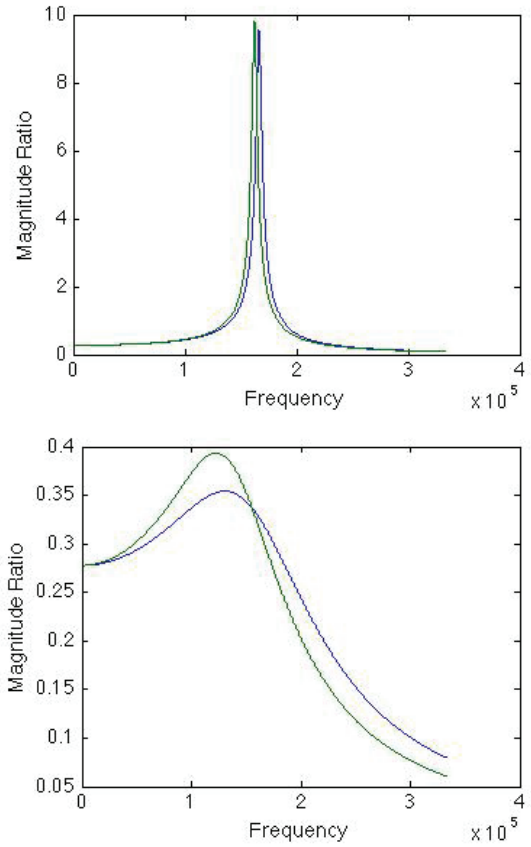

FIGURE 1. Illustration of the tradeoff between Q and $\delta f/\delta m$.

A number of methods have been used to detect a resonant frequency change. In the slope detection method, the cantilever is oscillated near the resonant frequency while monitoring the amplitude. A resonant frequency change leads to a change in the monitored amplitude [9]. A common method is frequency modulation in which the cantilever is actuated at its natural frequency. When the natural frequency shifts due to added mass, a feedback loop adjusts the actuation frequency to maximize the displacement amplitude [3].

To accurately identify the resonant peak frequency depends on the noise level in the measurement system and the amount of time taken to average measurements. The smallest detectable change in mass is proportional to the square root of the measurement bandwidth [2,9].

For the most sensitive nanocantilever mass resonant sensors, noise sources include thermomechanical noise, temperature fluctuation noise, absorption-desorption noise, and momentum exchange [2]. For

micromechanical mass resonant sensors, actuator noise and displacement sensor noise are more significant.

Assuming that noise introduces uncertainty into the resonant peak measurement that is proportional to the DC amplitude of the system, the discrimination of the resonant peaks is a situation that looks like Figure 2. Another possible approach to introducing uncertainty is to define a threshold slope that bounds the uncertainty of the peak detection.

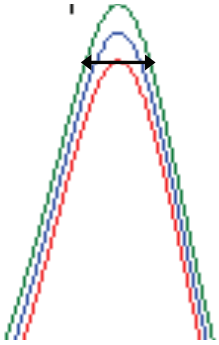

FIGURE 2. Illustration of detectability in the presence of uncertainty.

Given the nature of the noise sources, measurements of resonant frequency will fall into a normal distribution. To conclude that a mass change has occurred and the resonant frequency has shifted, a hypothesis test is used. For 95% confidence and assuming $\sigma_1=\sigma_2=\sigma$ and $n_1=n_2=n$,

$$\frac{\bar{x}_1-\bar{x}_2}{\sqrt{\frac{\sigma_1^{\,2}}{n_1}+\frac{\sigma_2^{\,2}}{n_2}}}=\sqrt{\frac{n}{2}}\frac{\bar{x}_1-\bar{x}_2}{\sigma}>1.96 \tag{3}$$

A higher signal-to-noise ratio would reduce σ, and more measurement samples (and longer measurement time) would increase *n.* Both increase the likelihood of detecting a small change in mass. With this approach, a design that minimizes $\Delta m/m$ (where *m* is the mass of the resonator and is proportional to sensing area) is the best one. The best design according to this approach will serve as the reference against which other approaches are compared.

We compare the utility of three objective functions for optimizing resonator shape. The ability of each objective function to identify the best design is determined by comparing the result to the reference design.

Based on Equation (1) it is desirable to maximize:

$$O_1=\delta\omega_n\sqrt{\frac{Q}{\omega_n}} \tag{4}$$

This is the first objective function. Making use of the RMSD% measure of frequency response change [8], the second objective function to evaluate is:

$$O_2=RMSD\%=\sqrt{\frac{\sum_{i=1}^{N}\left(M_i^1-M_i^0\right)^2}{\sum_{i=1}^{N}\left(M_i^0\right)^2}}\times 100\% \tag{5}$$

where M^0 and M^1 are the magnitude ratio curves for the original system and the one with additional mass, respectively. To simplify further, we introduce a new measure, which is based on just two points of the RMSD%:

$$O_3=\sqrt{\frac{\left(M_{n0}^1-M_{n0}^0\right)^2+\left(M_{n1}^1-M_{n1}^0\right)^2}{\left(M_{n0}^0\right)^2+\left(M_{n1}^0\right)^2}}\times 100\% \tag{6}$$

where n_0 and n_1 are the resonant frequencies of the original system and the one with additional mass, respectively.

RESULTS

We considered the system shown in Figure 3. It is an electrostatically actuated resonator that is a flat plate supported by four leg springs. Half of the plate area is used for electrostatic actuation and half is used for capacitive sensing. The plate is coated with a polymer coating that will accumulate mass when in the presence of a gas of interest. The hole in the center is for the purpose of reducing squeeze film damping.

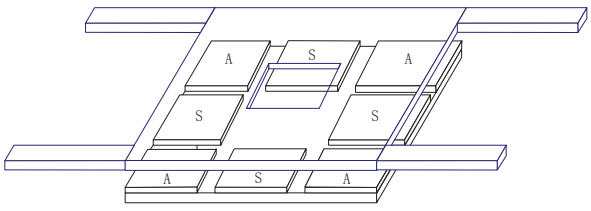

FIGURE 3. Mass resonant sensor with hole.

This system was modeled as a lumped parameter system in which the squeeze film affects the system stiffness and damping. The plate is modelled as eight rectangular sub-elements. The corner elements have venting on adjacent sides while the side elements have venting on opposite sides. The models of Darling, et al. [10] were used to analytically determine stiffness and damping constants for the squeeze film for the two types of elements. These were summed to yield [11]:

$$k_{air} = \frac{32\omega^2 A P_a}{\pi^2 g_o}\left[\sum_{n=odd}\frac{1}{n^2\left(\omega^2+\frac{k_n{}^4}{\alpha^4}\right)}+\frac{8}{\pi^2}\sum_{m,n=odd}\frac{1}{m^2n^2\left(\omega^2+\frac{k_{mn}{}^4}{\alpha^4}\right)}\right] \quad (7)$$

$$b_{air} = \frac{8AP_a}{\pi^2\alpha^2 g_o}\left[\sum_{n=odd}\frac{k_n{}^2}{n^2\left(\omega^2+\frac{k_n{}^4}{\alpha^4}\right)}+\frac{8}{\pi^2}\sum_{m,n=odd}\frac{k_{mn}{}^2}{m^2n^2\left(\omega^2+\frac{k_{mn}{}^4}{\alpha^4}\right)}\right] \quad (8)$$

with

$$\alpha^2 = \frac{12\mu}{g_o{}^2 P_a} \qquad k_n{}^2 = \frac{n^2\pi^2}{b^2} \qquad k_{mn}{}^2 = \frac{m^2\pi^2}{4a^2}+\frac{n^2\pi^2}{4b^2}$$

where *a* and *b* are the element dimensions.

Note that k_{air} and b_{air} are functions of frequency, which makes the system non-linear. Assuming small vibration amplitude relative to the gap, the transfer function between input (actuation voltage) and output (capacitance change) is [11]:

$$\frac{dC}{dV} = \frac{\varepsilon^2 A_s A_a V_o}{\left(g_o - x_o\right)^3\left(g_o - 3x_o\right)}\frac{1}{ms^2+bs+k} \quad (9)$$

where ε is the permittivity of air, A_s is the capacitive sensing area, A_a is the actuation area, V_o is the DC offset of the actuation voltage, x_o is the displacement due to V_o, g_o is the gap between actuator and substrate, *m* is the mass of the plate, *b* is the combined damping of the squeeze film air damping and material damping, *k* is the combined stiffness of the leg springs and air. The optimization problem that was used to test the objective functions is to determine the hole size that gives the best sensor performance. This is a desirable problem because the system includes the non-linear effects of air damping, it is a simple geometry that can be described well with an analytical model, and it has clear tradeoffs. A large hole reduces area for mass accumulation and it reduces the areas for actuation and capacitive sensing. On the other hand a large area increases resonator Q.

Table 1 shows the parameters that are common to all the simulations. Using this analytical model, frequency responses can be quickly computed. The model was validated with Comsol simulation and shown to perform well.

TABLE 1. Parameters used to simulate air damping model for square plate with square hole.

μ	1.862x10^{-5} N-s/m^2
Plate size	200 μm x 200 μm
Plate thickness	3 μm
Gap, g_o	4 μm
Silicon density, ρ	2330 kg/m^3
Air pressure, P_a	101325 Pa
DC offset voltage, V_o	10 V
Stiffness of supporting legs, k_{leg}	50 N/m
Material damping, $b_{mat'l}$	1x10^{-5} N-s/m

Two of the objective functions under evaluation require a frequency response function. They were computed using the model described above.

First, the reference was established. By adding an RMS noise level of 0.1% of the static magnitude ratio, the ability to distinguish a change in resonant frequency was considered. From this the minimum detectable change in mass was determined. Figure 4 shows how this minimum detectable change in mass changes with hole size. The best hole size is 160 μm.

For the same conditions, the three objective functions change with hole size as shown in Figure 5. The Δm/m was set to 0.001 for this case. The best hole size for the three objective functions is 182, 160, and 160 μm.

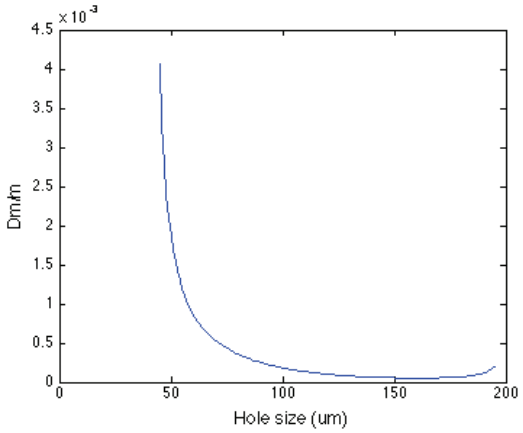

FIGURE 4. Minimum detectable mass change percentage as a function of hole size

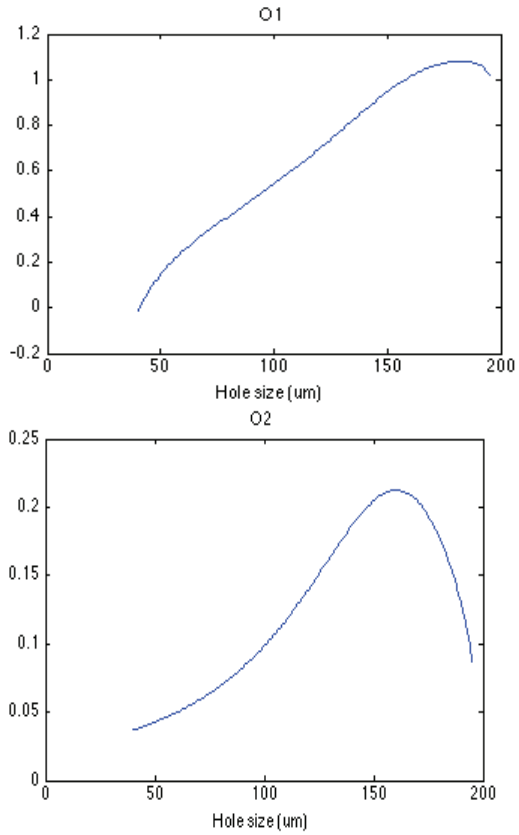

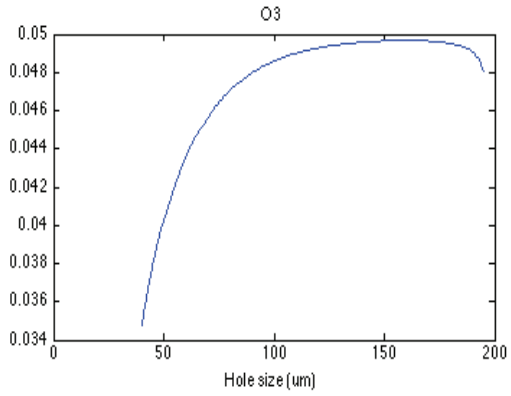

FIGURE 5. Effect of plate hole size on the three objective functions from Equations 4-6.

CONCLUSIONS

This paper describes the evaluation of three objective functions that could be used in the optimization of a resonant mass sensor design. A simple problem was to determine the optimum hole size in a resonator design involving a square plate and square hole. Two of the objective functions (the RMSD% and two point RMSD%) identified an optimum hole size that matched a reference measure. Both would be compuationally efficient if used in a design optmization algorithm.

REFERENCES

[1] Goeders KM, Colton JS, Bottomley LA. Microcantilevers: Sensing Chemical Interactions via Mechanical Motion. Chem. Rev. 2008; 108: 522-542.

[2] Ekinci KL., Yang YT, Roukes ML. Ultimate limits to inertial mass sensing based upon nanoelectromechanical systems. J. Appl. Phys. 2004; 95: 2682-2689.

[3] Albrecht T, Grutter P, Horne D, Rugar D. Frequency modulation detection using high-Q cantilevers for enhanced force microscope sensitivity. Journal of Applied Physics. 1991; 69(2): 668-673.

[4] Yan W, Chen WQ. Structural Health Monitoring Using High-Frequency Electromechanical Impedance Signatures. Advances in Civil Engineering. 2010; 1-11.

[5] Bannon FD, Clark JR, Nguyen C. High-Q HF microelectromechanical filters. IEEE Journal of Solid-State Circuits. 2000; 35(4): 512-526.

[6] DeMartini BE., Development of Nonlinear and Coupled Microelectromechanical

Oscillators for Sensing Applications. PhD Dissertation, UC Santa Barbara, 2008.
[7] Giurgiutiu V, Rogers CA. Recent advancements in the electro-mechanical (EIM) impedance method for structural health monitoring and NDE. SPIE 5th International Symposium on Smart Structures and Materials. 1998; 1-5.
[8] Yan W, Chen WQ. Structural Health Monitoring Using High-Frequency Electromechanical Impedance Signatures. Advances in Civil Engineering. 2010: 1-11.
[9] Martin Y, Williams CC, Wickramasinghe HK. Atomic force microscope–force mapping and profiling on a sub 100-Å scale. Journal of Applied Physics. 1987; 61(10): 4723-4729.
[10] Darling RB, Hivick C, Xu J. Compact analytical modeling of squeeze film damping with arbitrary venting conditions using a Green's function approach. Sensors and Actuators A. 1998; 70: 32-41.
[11] Li C, Miller MH. “Optimization Strategy for Mass Sensor Design in the Presence of Squeeze Film Damping. Micromachines. 2010; 1: 112-128.

A FIRST INVESTIGATION OF GREEN LASERS IN MICRO-LASER ASSISTED SCRATCH TESTS ON SILICON

Hossein Mohammadi[1a], Deepak Ravindra[1b], and John Patten[2]
[1a,2]Manufacturing Research Center
Western Michigan University
Kalamazoo, Michigan, USA
[1b]Micro-LAM Technologies LLC
Kalamazoo & Battle Creek, Michigan, USA

ABSTRACT

Machining of brittle materials such as ceramics and semiconductors in the ductile regime has been a challenge for many years. These materials have many desirable properties, such as being light weight, strong, and hard that make them ideal candidates to use in optics, MEMS and electronic applications. Having a good surface finish, avoiding surface and subsurface damage and at the same time having the highest material removal rate (MRR) is extremely challenging due to their brittle characteristics and poor machinability. Their low fracture toughness makes them very hard and even impossible to manufacture with high MRR without surface and subsurface damage, which needs more post-processes to remove, and this therefore decreases the efficiency of the process. Brittle materials can be machined in the ductile mode due to the high-pressure phase transformation (HPPT) phenomenon during machining, however laser heating can enhance the ductility and reduce the brittleness of these materials.

The novel Micro-Laser Assisted Machining (μ-LAM) technique is a recent development for ductile mode machining of brittle materials. The μ-LAM process utilizes the high compressive and shear stresses induced by the tool tip and laser heating to reduce the hardness and brittleness of the workpiece which increases the MRR, decreases the tool wear, improves the surface finish, and minimizes or eliminates sub surface damage during the machining process.

The amount of laser energy absorption during the machining process will affect the thermal softening of the material. Ceramics and semiconductors in general have different absorptions to various laser wavelengths; therefore finding the most suitable laser wavelength based on the material's optical properties will optimize the process. Also, the cost of laser equipment increases exponentially as the power increases. Thus, it is vital to choose the most appropriate wavelength based on the absorption of the material to maximize the thermal softening effect. If sufficient thermal softening of the workpiece can be successfully achieved, then a low power-low cost laser can be utilized to achieve higher MRRs while significantly reducing the production cost. Additionally, there is always laser energy loss at the tool during machining. Most of this energy causes the temperature of the tool and equipment to rise which has negative effects and can even cause damage while using high power lasers; therefore a lower power laser will be a better option to avoid these kinds of side effects.

One important semiconductor with numerous applications in industry is silicon (Si), which has minimum reflectance (highest absorption) at a wavelength of approximately 590 nm in the atmospheric phase of Si (Si-I) [1]. However, due to the high compressive and shear stresses induced by the tool tip, HPPT occurs and metallic phase of Si (Si-II) forms during machining which has very high absorption (lower but close to Si-I). This means that a laser with a close enough wavelength will have the most efficiency and least energy loss. With the use of a 532 nm wavelength laser, termed "green laser", the reflectivity (Rd) of Si increases slightly from 0.41 to 0.43 (refer to Figure 1).

In previous research, the IR (infrared) laser has been studied and clearly showed that coupling the diamond tool and laser improves the machining process outputs such as MRR and surface finish and even increases the tool life [2, 3, 4]. This study is focused on the first investigation of integrating a green laser in the

μ-LAM process and its effect on thermal softening of single crystal Si during the material removal process. For this purpose, two sets of tests were carried out: with the green laser (532 nm wavelength) and without any laser radiation. The results of these two series of tests are analyzed and compared. The scratch tests were carried out to examine the effect of thermal softening of the high pressure phases via laser heating formed under the diamond tip. The effects are studied based on the measured depth of cut, cutting forces, and machining regime (ductile or brittle). Depths of cuts were measured using a Wyko white light interferometer. Cutting forces were measured in-situ using a dual axis load cell and the regime of machining for each scratch was analyzed using a high magnification optical microscope. The microscope images were used primarily to identify the cut surface conditions and detect any possible scratches or chips.

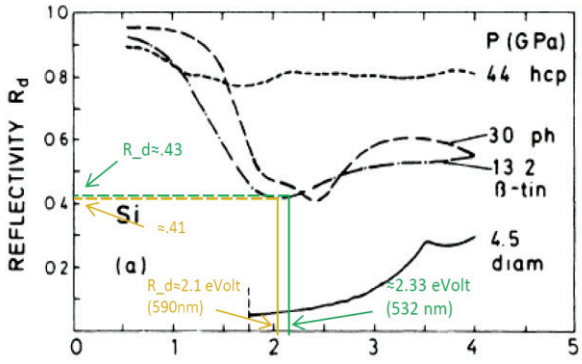

Figure 1. *Reflectivity spectra (Rd) of silicon in diamond, β-tin, primitive hexagonal, and hep phase at 4.5, 13.2, 30, and 44 Gpa, respectively [1].*

The μ-LAM system is coupled to the modified Universal Micro-Tribometer (UMT) to perform all of the scratch tests (refer to Figure 2). The UMT is a load-controlled device where the required thrust force is applied for each test to achieve a desired depth of cut. A load-controlled machine is preferred in this case to study the thermal softening effect. The cutting speed is set constant at 1 μm/sec for all scratches in order to heighten the thermal softening of Si during the material removal process. Based on previous work [2, 3, 4], in order to show a transition from ductile to brittle mode, scratch tests at loads ranging from 10mN to 70mN are ideal. A 5 μm tip stylus, which is coupled to a 10 μm fiber to have maximum density of laser energy and thus maximizing the thermal softening effect, is used.

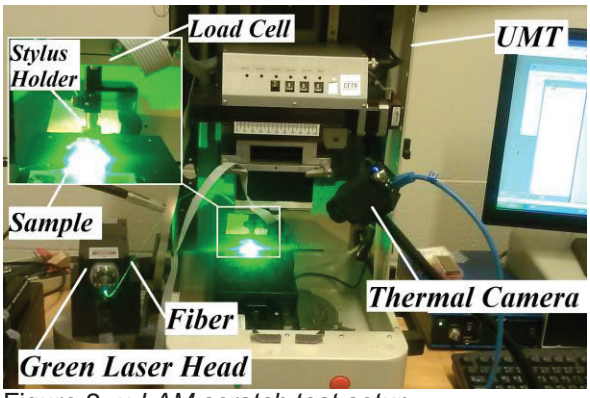

Figure 2. *μ-LAM scratch test setup.*

In the μ-LAM setup, the beam is guided through a 10 μm fiber optic cable to the ferrule, which is coupled to the diamond stylus (refer to Figure 3). In this setup, the laser beam passes through an optically transparent diamond tip (tool) and impinges on the workpiece surface.

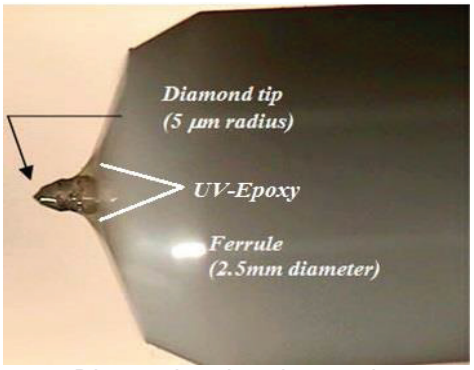

Figure 3. *Diamond stylus tip attachment: 5 μm radius diamond tip attached on the end of the ferrule using epoxy.*

Monitoring the cutting forces during the cutting process is an effective method to detect any occurrence of brittle mode machining. Brittle mode machining can generally be observed in the cutting force data by its unstable behavior which is represented in higher peaks and valleys in the force plot. Another usage of these data is to know how much laser softening decreased cutting forces to achieve similar depths of cuts as that without laser heating. This is crucial as lower forces suggest longer tool life for large scale production.

The results of current research will be very useful for ductile mode machining of Si and these outcomes help to understand the effects (MRR, forces, productivity, etc.) of using a laser wavelength that is highly absorptive by the workpiece material. This research will serve as a

precursor to follow-on studies that will develop an efficient technique to manufacture hard and brittle materials via single-point diamond turning (SPDT).

REFERENCES

[1] Hanfland, M, Alouani M, Syassen K, and Christensen N. E. Optical properties of metallic silicon. Physical Review B 38. 1988; 18: 12864.

[2] Deepak Ravindra, Bogac Poyraz H, and John Patten. The Effects of Laser Heating on the Ductile to Brittle Transition of Silicon Carbide. American Society for Precision Engineers (ASPE) 25th Annual Meeting. Atlanta, Georgia: 2010.

[3] Deepak Ravindra, Muralidhar K. Ghantasala and John Patten. Ductile Mode Material Removal and High-Pressure Phase Transformation in Silicon during Micro-Laser Assisted Machining. Journal of Precision Engineering (ASPE). 2012; 36.2: 364-367.

[4] Deepak Ravindra, Bogac Poyraz H, and John Patten. The Effect of Laser Heating on the Ductile to Brittle Transition of Silicon. The 5th International Conference on Micro Manufacturing (ICOMM/4M). Wisconsin: 2010.

NANOCOINING SUBMICROMETER STRUCTURED SURFACES

John Nowak, Thomas A. Dow, Jonas Kessing, Ken Garrard and Ron Scattergood
Precision Engineering Center
North Carolina State University
Raleigh, North Carolina, USA

INTRODUCTION

Bio-inspired structured surfaces are commonly used in developing coatings that can exhibit a variety of traits, including anti-reflective (AR), superhydrophobic or superhydrophilic qualities. AR surfaces typically mimic moth eye structures and are highly sought after for applications including lenses, solar cells, and photosensitive detectors [1]. Superhydrophobic and superhydrophilic features have applications in antifogging and self-cleaning technologies, as well as biomedical instrumentation applications [2]. These structured surfaces are traditionally generated using lithography techniques, which can be long in duration and suffer from a large number of manufacturing steps [3].

Nanocoining is a novel approach to rapidly create surface structures using a small diamond die (20 x 20 μm) containing an array of nanofeatures formed with focused ion beam (FIB) machining. This die is pressed into a diamond-turned surface, leaving a field of sub-micrometer features. *FIGURE 1* shows a single indentation of the die into the workpiece.

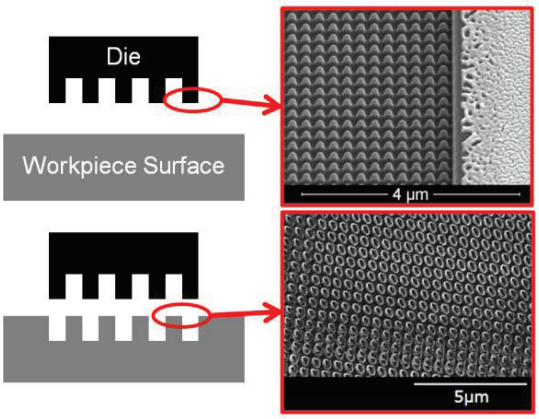

FIGURE 1. Indentation process and SEM image of nanofeatures on die surface.

To create a continuous area of features, the die indents must be tiled together. One way this is done by indenting the surface of a rotating drum on a DTM as shown in *FIGURE 2*. The drum surface speed is created by the spindle speed and the radius of the drum and establishes the upfeed distance (time) based on the size of the die. The crossfeed distance also depends on the die size and the cross feed rate of the linear axis (pass 1 - 2). Some overlap between successive die indents is desirable to avoid regions without features. The die is held by a piezoelectric actuator that moves into and out of the surface with a motion that must be consistent with the surface and crossfeed motions.

Relative motion of the die and workpiece during indentation can cause a distortion of the replicated features on the workpiece. To maximize feature fidelity, the die is moved with elliptical motion to match the surface speed while in contact. This actuator must also be controlled in concert with the machine axes to produce uniform coverage of surface features.

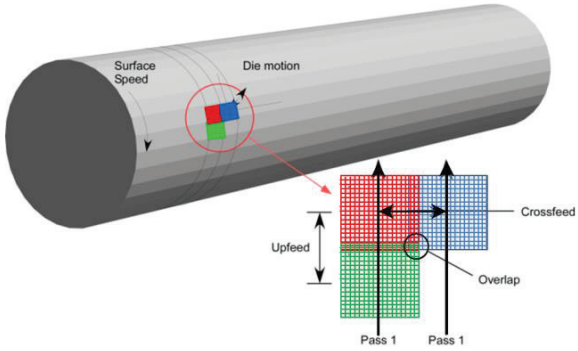

FIGURE 2. Indentation on a large cylindrical surface defining overlap and control problem.

Since the diamond die is small, it must be indented at high speeds (50 kHz) to cover large areas in a reasonable amount of time. This work proposes a system to generate uniform surface features by indentation using a bidirectional resonant actuator at 50 kHz on a diamond turned surface. A control system is implemented to maintain resonant actuation, dynamically synchronize the spindle speed with the actuation frequency, and maintain a constant indent depth.

ACTUATOR DESIGN

A 50 kHz piezo-driven resonant actuator is used for achieving relatively large amplitudes at high frequencies. The design is based on a resonant beam design which is actuated by two piezoelectric elements capable of producing bi-directional motion. The actuator shape is designed such that a longitudinal and bending vibration mode occur at the same frequency, allowing for simultaneous resonant motion resulting in an elliptical motion path. An illustration of the individual mode shapes and combined tip motion is given in *FIGURE 3.*

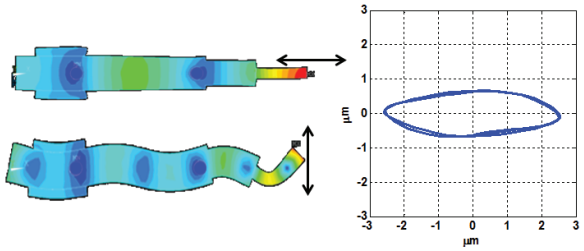

FIGURE 3. Two mode shapes combined to make elliptical path at the tip.

The amplitude of the elliptical tip motion is based on the width of the die in the direction of workpiece motion. The horizontal direction (parallel to the work surface) must be sized to match the surface speed. The vertical dimension of the ellipse (normal to the work surface) affects the time the die is in contact with the surface. A larger ellipse dimension normal to the work surface is desirable to reduce smearing of the features. Smear is due to speed mismatch on the elliptical path during the transition phase of the die entering and exiting the part.

The actuator is mounted at common vibration nodes such that added mount damping does not influence the resonant behavior (*FIGURE 4*).

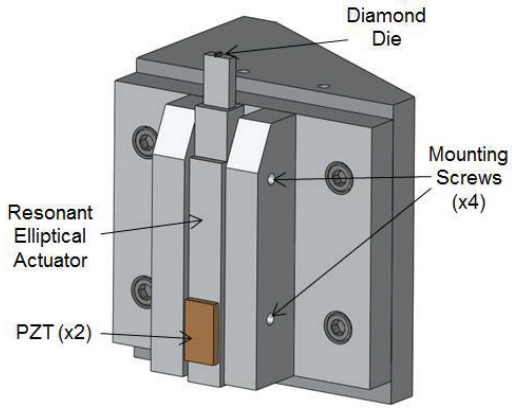

FIGURE 4. Elliptical actuator mounted with diamond die.

PROCESS CONTROL

A controller is needed to maintain resonant operation of the actuator and synchronize this resonant frequency with the machine axes. Producing constant depth features requires amplitude modulation to the drive signal to ensure a consistent indent path, and a surface tracking mechanism to compensate for part and spindle errors in real time (*FIGURE 5)*

Actuator Control

The resonant frequency of the actuator can drift as result of a well-documented phenomenon, typically attributed to self-heating effects in the piezoelectric elements and external loads [4, 5]. This causes a change in displacement at the indenting tip, necessitating a method of following this frequency to ensure steady behavior.

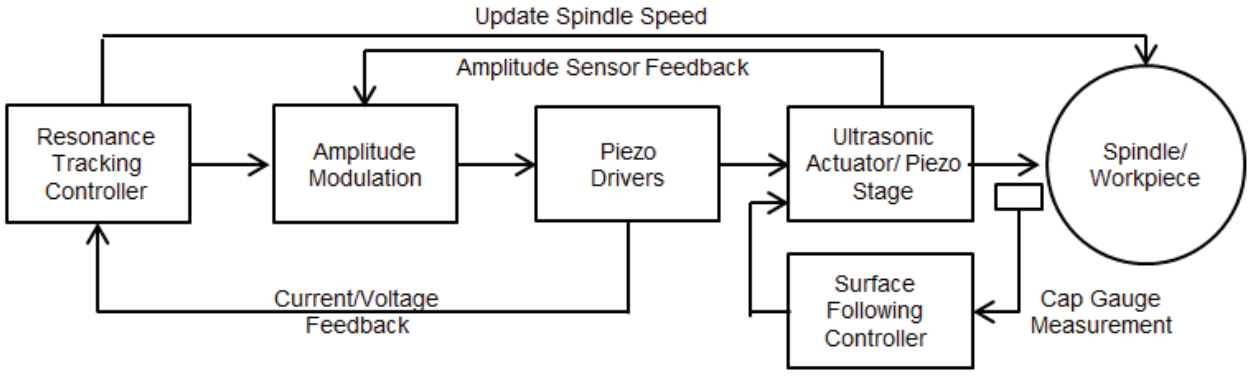

FIGURE 5. Process Control schematic for nanocoining system.

Resonant actuation can be maintained by monitoring the current and voltage across the piezo elements. The configuration of these elements allows simultaneous actuation and sensing. The electrical properties of the piezo are influenced by the mechanical behavior of the assumed mass-spring-damper system to which they are mounted. As the system approaches mechanical resonance, the phase response of the mechanical system physically influences the capacitive electrical system (i.e. piezo). This electrical-mechanical interaction is monitored using the instantaneous phase between the current and voltage, or electrical impedance. As shown in *FIGURE 6*, the point in the frequency response of minimum impedance correlates to mechanical resonance.[6].

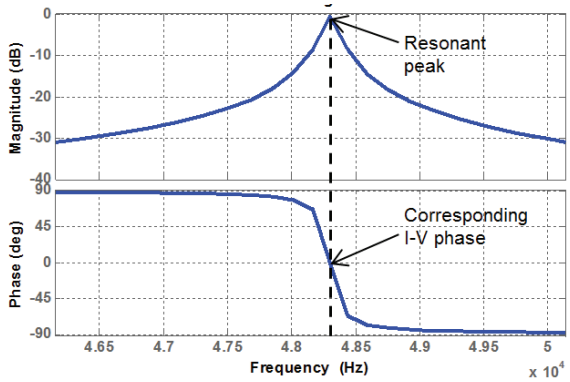

FIGURE 6. Frequency response of an ultrasonic transducer model.

As the system resonance changes, the phase shown in *FIGURE 6* that correlates with resonance changes with the location of the resonant peak (resonance always correlates to a 0° phase angle). Resonant frequency following can be achieved by measuring the phase between the current and voltage and changing the drive frequency to maintain a set phase that corresponds to resonance (*FIGURE 7*).

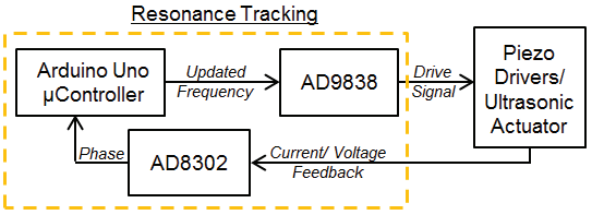

FIGURE 7. Phase locked loop (PLL) based control for resonance tracking.

Depth Control

Compensation for workpiece form and radial spindle error is performed using a second piezo actuator that moves a stage containing the indenting actuator based on a cap gauge measurement. Error in the x-direction along the z-axis is measured and compensated for as shown in *FIGURE 8*. The surface must be tracked to within 50 nm to maintain uniform indentation coverage.

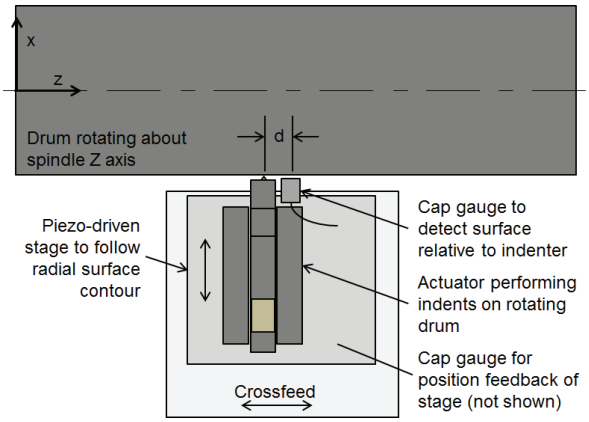
x
z
Drum rotating about spindle Z axis
d
Piezo-driven stage to follow radial surface contour
Cap gauge to detect surface relative to indenter
Actuator performing indents on rotating drum
Cap gauge for position feedback of stage (not shown)
Crossfeed

FIGURE 8. Form error compensation where actuator is traversing rotating workpiece in the z-direction and correcting position in x-direction.

To achieve a higher bandwidth than the DTM axis can achieve, a linear flexure stage was developed to allow for motion in the radial direction relative to the workpiece surface. A piezo stack is used to make position corrections based on an external cap gauge measuring the error in the radial direction. A second cap gauge measures the motion of the flexure stage and forms a closed loop positioning control to track the workpiece measurement based on the external cap gauge. A National Instruments compact RIO (cRIO) platform was used to implement a PID controller via FPGA to position the stage based on the surface measurement (*FIGURE 9*).

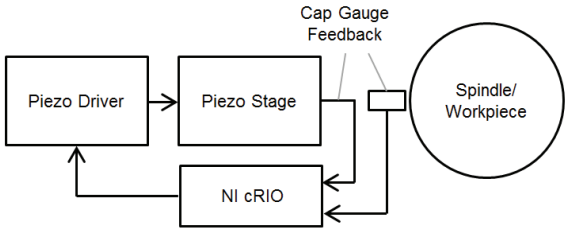

FIGURE 9. Surface following position control.

The bandwidth of the system is filter-limited to 100 Hz. The system is demonstrated using a 1" diameter diamond-turned aluminum cylinder, where a 1 µm off-center error was introduced. While rotating at 500 rpm, once-per-rev errors are compensated which kept tracking errors to within 50 nm (*FIGURE 10*).

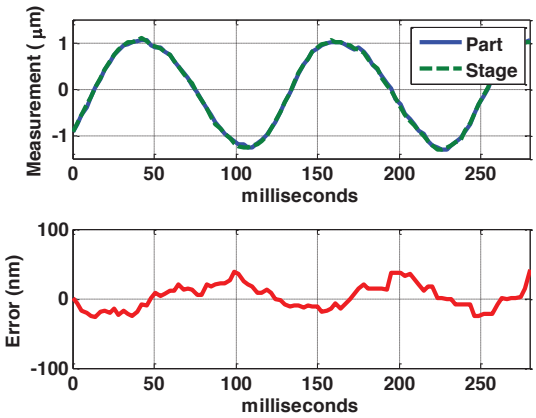

FIGURE 10. Surface tracking of a 1" diameter drum at 500 rpm.

Amplitude Control

Due to thermal effects and other variations in the actuator system, the amplitude does not remain constant while excited at resonance. A method of sensing and controlling the amplitude during indentation is necessary for a constant indent depth. Piezoelectric sensing elements are mounted on opposing sides of the actuator in *FIGURE* 11.

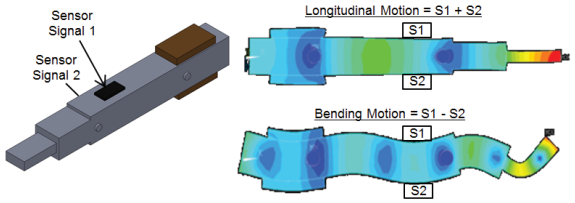

Figure 11. Amplitude sensors on actuator.

The sensors are mounted such that they do not lie on a displacement node in either vibration mode such that sufficient strain is induced to produce the feedback signal. Since they are placed in the same position along the length of the actuator on opposing sides, during combined motion the longitudinal direction can be isolated by adding the signals. The bending motion can be isolated by subtracting the two signals. This feedback method allows the drive signal amplitude to be modulated.

EXPERIMENTAL APPARATUS

The actuator is mounted vertically on a 4-axis diamond turning machine (*FIGURE 12*). A cylindrical workpiece is mounted and finished with a single point diamond tool to produce an optical quality surface finish. The DTM axes are used to bring the die into contact with the workpiece surface. The crossfeed is based on the spindle speed and the die width in the z-direction. Setting a proper crossfeed is critical in generating a uniform array of features. Since the crossfeed is relatively slow compared to the speed of the indents, small changes in actuator frequency have a negligible effect on the indent spacing in the axial direction.

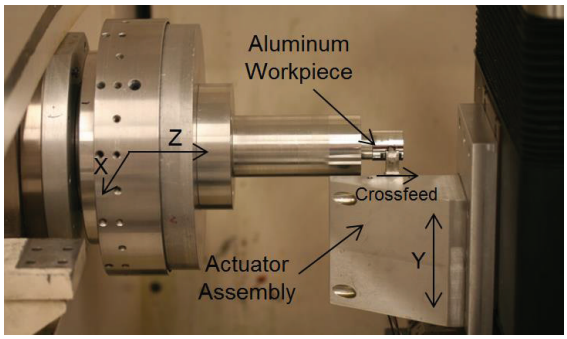

FIGURE 12. Actuator assembly mounted on the DTM with aluminum workpiece.

CONCLUSIONS

Recent developments in the nanocoining system have increased its potential for generating sub-wavelength features. The introduction of the surface tracking system allows for error following within 50 nm which is necessary for indent depths of less than 500 nm. The synchronization of the spindle speed to varying actuator speed also increases the fidelity of the indents by reducing relative velocity between the die and surface speed. A method of amplitude control was proposed which can ensure uniform coverage over large surface areas.

REFERENCES

[1] Guoyong Xie, et al. The fabrication of subwavelength anti-reflective nanostructures using a bio-template. *Nanotechnology 19(9),* pp. 095605. 2008.

[2] J. Drelich, et al. Hydrophilic and superhydrophilic surfaces and materials. *Soft Matter (21),* pp. - 9804.

[3] Erik Zdanowicz, et al. Rapid fabrication of nanostructured surfaces using nanocoining. *Nanotechnology 23(41),* pp. 415303. 2012.

[4] J. L. Pons, et al. Self-tuned driving of piezoelectric actuators: The case of ultrasonic motors. *Journal of the European Ceramic Society 27(13–15),* pp. 4163-4167. 2007.

[5] B. Mortimer, et al. High power resonant tracking amplifier using admittance locking. *Ultrasonics 39(4),* pp. 257-261. 2001.

[6] M. Takasaki, et al. Resonance frequency tracing system for langevin type ultrasonic transducers. Presented at Mechatronics and Automation, 2007. ICMA 2007. International Conference On. 2007.

Characteristics of the Brittle Cracking by the Cutting Edge Roughness in the Glass Cutting

Takenori ONO1
1 Dep. of Mechanical engineering
Kyusyu Sangyo University
2-3-1 Matsukodai Higashi-ku Fukuoka-shi FUKUOKA JAPAN

1. INTRODUCTION

In recent years, the demand of the micro fabrication on brittle materials is increased. For example, a chemical inspection plate is widely used in chemical and pharmacy fields. Optical glasses are typical material to user for these devices because of their excellent mechanical or chemical properties. A micro molding die is used to manufacture micro mechanical components. Tungsten carbides are used for this molding die to replace conventional hard steels because of its high stiffness and low thermal expansion. Generally, these devices are fabricated by the chemical etching or laser milling so far. However, these approaches have some problems. For example, in the chemical etching on glass materials, hydrofluoric acid which is required as the etching liquid has high toxicity. The laser milling induces the thermal deformation and changing the material property on the carbide surface. Also, both manners require the high cost for facilities and the manufacturing.

Based on this background, the author proposes the cutting process on these brittle materials with small diameter carbide ball end mills. The milling process requires only the machine tool and safer cutting fluid (Ex. distilled water) with safer and easier operations. In previous cutting experiments, brittle materials can be machined without brittle cracking on the typical glasses [1]. In another experiments, author tried to cut the glass with a PCD (Poly-Crystal-Diamond) coated carbide milling tool (as shown in Figure 1) to evaluate a tool life. In these tests, this kind tool showed the tool life is 15 times longer than that of the conventional TiAlN coated carbide tools. However, the many small cracks are left on the machined surface. In other experiments, to evaluate an effect of an edge roughness on the brittle cracking, cutting tests are performed by two kinds of PCD coated carbide milling tool they have different coating grain size. As the result,

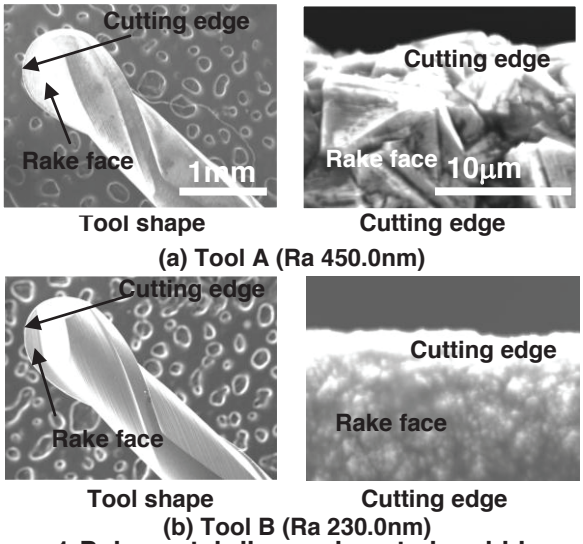

Figure 1 Polycrystal diamond coated carbide ball endmills

Specifications: Material, carbide; radius, 0.5mm; neck length, 2.5mm(a), 2.7mm(b); and helix angle, 25deg.

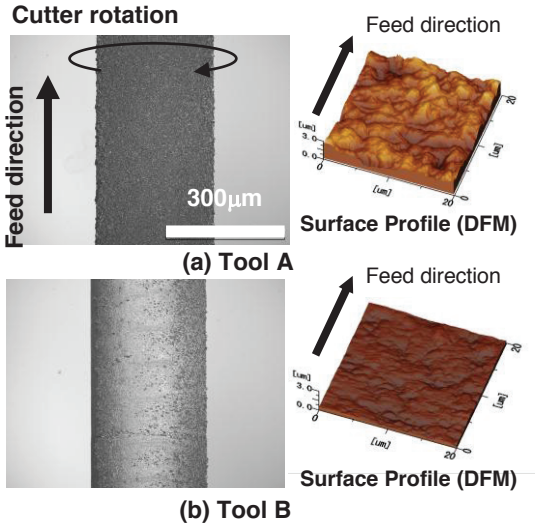

Figure 2 Change in the brittle cracking by edge roughness

Cutting conditions: Tool, R0.5 diamond coated ball endmill; material cut, soda lime glass; feed rate, 0.48mm/min; rotational speed, 20000rpm; feed rate per edge, 12nm/edge; cutting speed, 31.4m/min; depth of cut, 0.05mm; and lubrication, water.

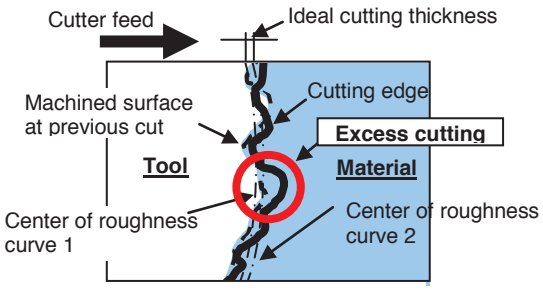

Figure 3. Schematic of the slotting operation

intensity of brittle cracking changes by the grain size as shown in Figure 2 [2].

This problem is regarded that the roughness of the tool edge shape changes the cutting thickness as shown in Figure 3, and the stress distribution at the cutting point is also partially changed. Thus, the brittle cracks leave at the point of excess cutt ing thickness. However, these results were not determined under quantitative conditions. Therefore, this phenomenon must be evaluated with quantitative cutting conditions. Based on this background, the authors have attempted cutting tests to observe the effect of the edge roughness on the brittle cracking in glass cutting. In cutting tests, shaping processes were performed by an edge-shape controlled mono crystal diamond cutting tool. The cutting tool is dressed by a focused ion beam (FIB) machine tool to reform the cutting edge shape as the sine wave curve. The sine wave edge shape is designed to clearly observe the effects of the edge roughness features.

This report discusses about the effect of the wave vertex and inclination angle of oblique cutting on the brittle cracking. Characteristics of brittle cracking are reportedly changed by the distance of adjacent indentations in the indenter testing on the glass due to the tensile stress produced by the stress interference among adjacent indentations[3]. Based on this work, it is expected that the distance between wave vertexes changes the characteristics of brittle cracking in glass cutting. In addition, a typical ball end mill has a helix angle which corresponds to the inclination angle of the oblique cutting in the shaping process. It is well known that the inclination angle changes the directions of the cutting force. Thus, it can be expected that the inclination angle changes the characteristics of brittle cracking in glass cutting. This report shows results of following cutting experiments.

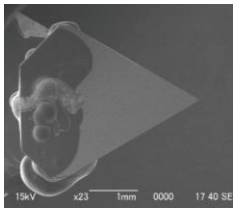

(a) Tool chip

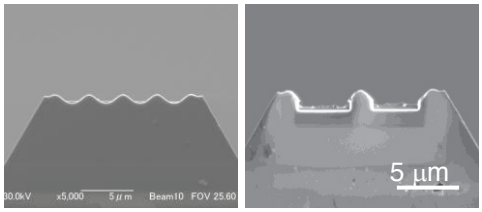

(b) Tool A (c) Tool B

Figure 4. Cutting edge shapes on the diamond tool in cutting tests

Specifications: Material, single crystal diamond; width of main cutting edge, 10 μm; rake angle, 0 deg; and the relief angle of 5 deg.

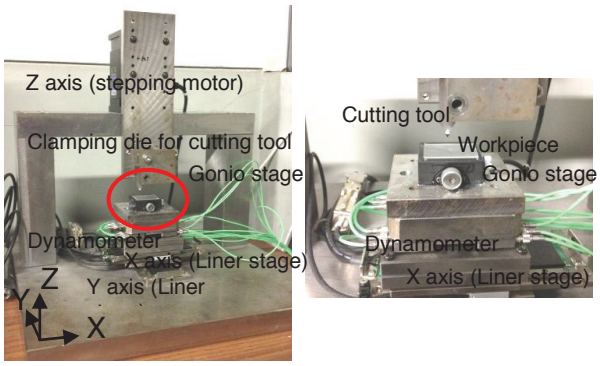

Figure 5. Schematic of the slotting operation

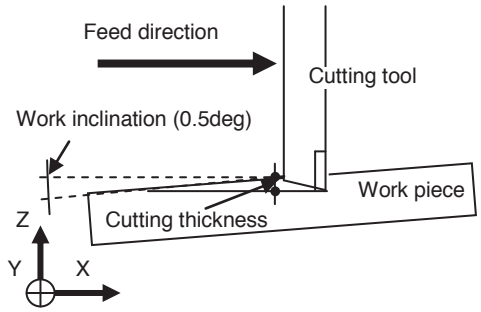

Figure 6. Schematic of the slotting operation

2. CUTTING TESTS

In cutting tests, shaping operations are performed on the substrate of soda lime glass (73% SiO2, 14% Na2O, 9% CaO, 4% MgO, 0.03% K2O) by single crystal diamond tools as shown in Figure 4. As shown in this figure, the vertex angle of 60 degrees and width of flat nose

Table 1. Cutting conditions in cutting experiments

Cutting conditions	
Feed rate μm/sec	100
Cutting length μm	200
Maximum cutting depth μm	2.5
Inclination angle of edge deg.	0, 30
Material cut	Soda lime glass
Cutting fluid	Dry
Cutting tool	
Material	Mono crystal diamond
Vertex angle deg.	60
Width of cutting edge μm	10
Edge roundness μm	< 0.05
Edge shape	Sine wave
Amplitude μm	1
Period	4.5
Number of the wave vertex	5 (Tool A), 3(Tool B)

edge is 10 μm. The nose edge is reformed as the sine wave curves by the FIB machine tool. The reformed cutting edge has 5 (Tool A) and 3 (Tool B) vertexes of the wave and amplitude of 1 μm. After the shaping, the machined surface is observed by the scanning electron microscope (SEM). The shaping was performed by 3 axis machine tool as shown in Figure 5. The machine tool for cutting tests consists of 2 linear motor stages (Nihon Thompson NT80V65) and 1 stepping motor stage (Sigma Kouki PK513PB-C9). The resolution of the linier motor stage is guaranteed at 0.1 μm and stepping motor stage is guaranteed at 0.01 μm as specifiied. These stages are controlled by the motion controller board connected on the PC simultaneously. The workpiece is clamped on the dynamometer via the goniostage to incline 0.5 degrees with respect to the feed direction as shown in Figure 6. The depth of groove increases with cutter feeding at 0.0125 μm (depth / feed). Table 1 shows the cutting conditions in cutting tests. Each cutting tests are performed 3 times to avoid the scattering. In cutting experiments, crack points (larger than 1 μm) on the machined surface are evaluated by observation with SEM images of machined surface.

Figure 7 shows the machined surfaces processed by Tool A in the orthogonal cutting. In these figures, the cutting direction goes from left side to right side. As shown in Fig. 7, large shell like cracks are left from the first cracking point.

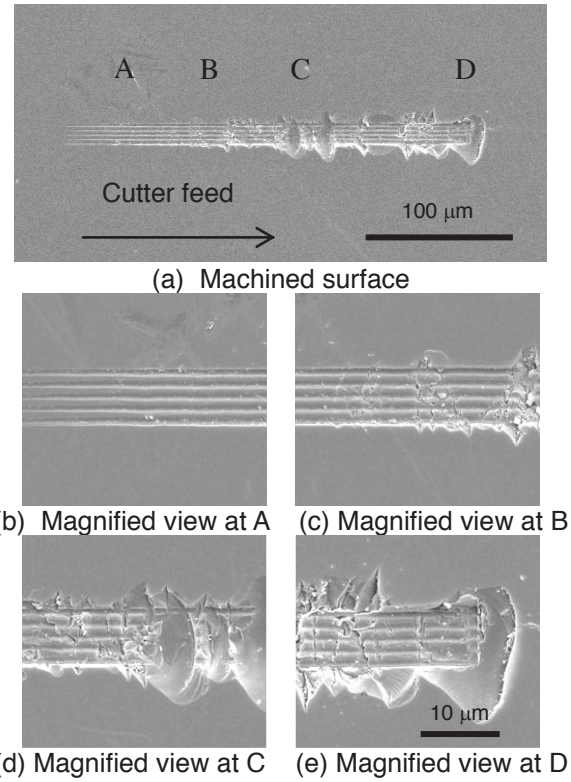

(a) Machined surface

(b) Magnified view at A (c) Magnified view at B

(d) Magnified view at C (e) Magnified view at D

Figure 8. Machined surface in orthogonal cutting by Tool A
Cutting conditions: inclination angle of 0 degree.

Figure 8 shows the surfaces processed by Tool B. As shown in this figure, the large detaching leaves on the center of the cutting groove by Tool B as shown in Fig. 8. Figure 9 shows the machined surface processed by Tool B in the oblique cutting at the inclination angle of 30 degrees. The cracks are left on the above side of the vertex. In general, the crack propagation goes to the orthogonal direction of the inclined tool edge in Fig. 9.Figure 10 shows the mean of measured critical cutting depth of “crack-free” cutting in cutting tests. In this report, “crack-free” means that no brittle cracks are left on the machined surface by the shaping process. In this figure, the error bar is also shown in all plots. The critical depth d_c was determined by the following function.

$$d_c = L \cdot \tan(0.5^\circ) \qquad \text{Eq. 1}$$

In this function, L is the cutting distance between the tool engage point and first cracking point. As shown in Fig. 10, d_c is increased with decrease of wave vertex distance in orthogonal cutting and increase of inclination angle in oblique cutting.

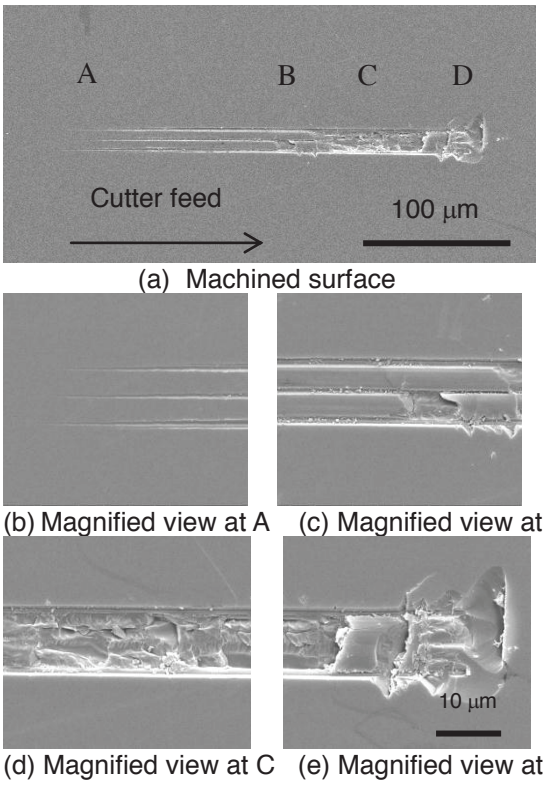

(a) Machined surface

(b) Magnified view at A (c) Magnified view at B

(d) Magnified view at C (e) Magnified view at D

Figure 8. Machined surface in orthogonal cutting by Tool B
Cutting conditions are same as those in Fig. 7.

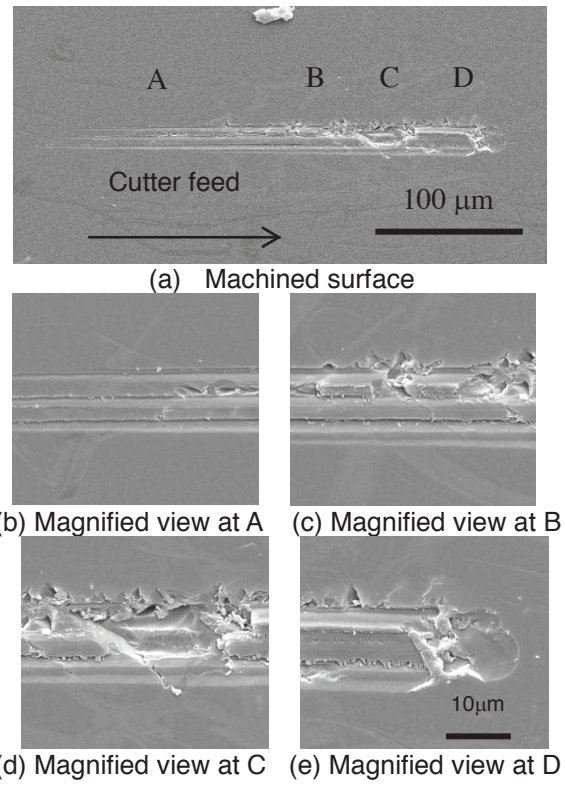

(a) Machined surface

(b) Magnified view at A (c) Magnified view at B

(d) Magnified view at C (e) Magnified view at D

Figure 9. Machined surface in oblique cutting by Tool B
Cutting conditions: inclination angle of 30 degree.

According to these experimental results, it can be concluded that the distance of the vertex of the edge roughness shape and the inclination angle of the cutting edge affect the characteristics of brittle cracking in glass cutting because it changes the stress distribution of the material.

4. CONCLUSION

This report discusses the effects of brittle cracking in glass cutting. In cutting tests, the brittle cracking is changed by the edge vertex distance and inclination angle. The edge vertex distance changes features of brittle cracking and the inclination angle changes the direction of the crack propagation. Based on these results, it is concluded that the distance of the vertex of the edge roughness shape and the inclination angle of the cutting edge affect the characteristics of brittle cracking in glass cutting because it changes the stress distribution of the material.

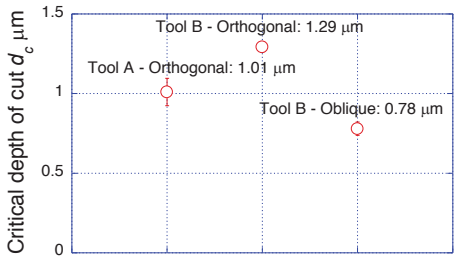

Figure 10. Mean of measured critical cutting depth of "crack-free" cutting in cutting tests

ACKNOWLEDGMENT

This work was supported by JSPS KAKENHI Grant Number (23560145). In addition, the author thanks Dr. Yoshiji Tomokiyo, and Mr. Takeshi Daio, Kyushu University for their valuable comments and assistance.

REFFERENCE

[1] T. Matsumura, T. Ono, Int. J. Machining and Machinability of Materials, Vol.6, Nos. 1/2, 2009, pp.139-158.
[2] T. Ono, Proceedings of NAMRI/SME, Vol. 39 (2011), 4728(CD-ROM).
[3] Z. Bing, et. al, Journal of the Japan Society of Grinding Engineers, 51(9), 2007, pp. 541-546.

Fabrication of thin Si crystal for an x-ray beam splitter

Taito Osaka[1], Makina Yabashi[2], Yasuhisa Sano[1], Kensuke Tono[3], Yuichi Inubushi[2], Takahiro Sato[2], Satoshi Matsuyama[1,4], Tetsuya Ishikawa[2], and Kazuto Yamauchi[1,4,5]

[1]Department of Precision Science and Technology, Graduate School of Engineering, Osaka University
2-1 Yamada-oka, Suita, Osaka 565-0871, Japan
[2]RIKEN SPring-8 Center
1-1-1 Kouto, Sayo-cho, Sayo-gun, Hyogo 679-5148, Japan
[3]Japan Synchrotron Radiation Institute (JASRI)
1-1-1 Kouto, Sayo-cho, Sayo-gun, Hyogo 679-5198, Japan
[4]Japan Science and Technology Agency, CREST
4-1-8 Honcho, Kawaguchi, Saitama 332-0012, Japan
[5]Research Center for Ultra-Precision Science and Technology, Osaka University
2-1 Yamada-oka, Suita, Osaka 565-0871, Japan

INTRODUCTION

X-ray free-electron lasers (XFELs) such as the Linac Coherent Light Source (LCLS) [1] in the USA and SPring-8 Angstrom Compact free-electron LAser (SACLA) [2] in Japan, which provide exceptionally brilliant, spatially coherent, and femtosecond pulses in the hard x-ray regime, have and will open new frontiers in atomic physics [3, 4], structural biology [5, 6], and nonlinear x-ray optics [7]. XFEL technology could also lead to the production of new optical devices. Bragg beam splitters based on ultrathin single crystals operating in the symmetric reflection geometry, which can split an XFEL pulse into two replica pulses with a large reflection angle and have a simple and small impact on the pulse profiles both spatially and temporally, are essential components of a split-delay unit. Such crystal devices can also provide an additional beam branch for beam sharing or photon diagnostics.

To accomplish an ideal Bragg diffraction over various net planes, thin crystals with a wide variety of crystal orientations should be prepared through a purely chemical process. Although near-perfect ultrathin silicon single crystals supported by a thick Si frame across an SiO_2 layers have become available thanks to advancements in silicon-on-insulator technology [8], the difference in the coefficients of thermal expansion and the lattice constants between Si and SiO_2 layer has the potential to cause a critical lattice strain for a high-order diffraction plane such as the (511) with a lattice spacing of less than 1 Å. In the present work, a new technique for fabricating ultrathin all-silicon single crystals based on a reactive dry etching process using atmospheric-pressure plasma has been developed [9]. Here, we present the details of the technique and results ofperforming topographic and high-resolution rocking curve measurements on fabricated crystals at SPring-8 in Japan.

THIN-CRYSTAL PREPARATION

Pre-preparation

A floating-zone (FZ) silicon crystal was used as the crystal of a Bragg beam splitter. A frame-shaped crystal with a thin splitting area 5 mm in diameter supported by a thick frame area (Fig. 1) was mechanically prepared as follows. A tapered hole was introduced at the center of a 2-mm-thick FZ silicon plate of 25 × 25 mm^2. After the surface of the splitting area was polished through a lapping process, the damaged layer was etched with HF and KOH solutions. A chemical mechanical polishing (CMP) process

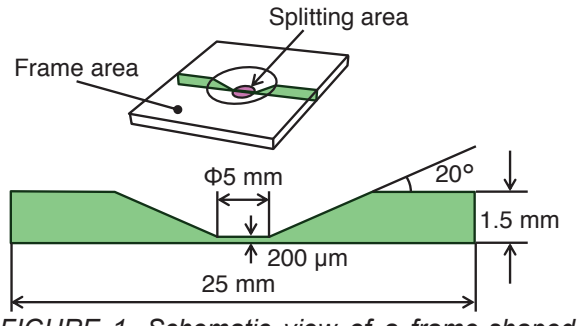

FIGURE 1. Schematic view of a frame-shaped crystal.

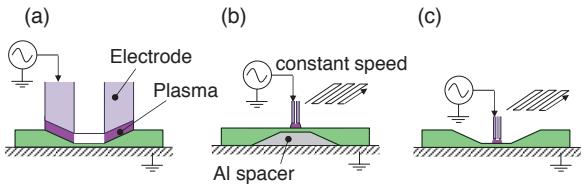

FIGURE 2. Schematic of the procedure with plasma chemical vaporization machining. (a) Step 1, on the tapered area; (b) Step 2, on the rear surface; (c) Steps 3 and 4, on the splitting area.

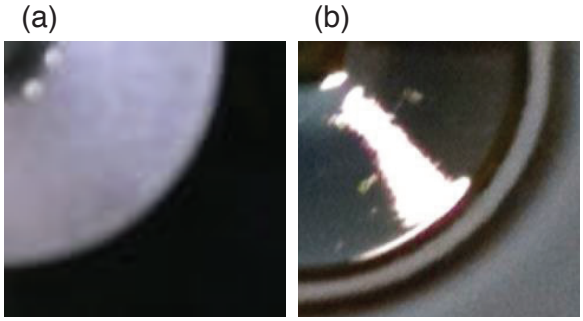

FIGURE 3. Pictures of frame-shaped crystals (a) before; (b) after Step 1.

was performed on both sides to reduce the thickness of the splitting area to 200 μm (thickness removed was approximately 100 μm).

PCVM Procedure

Crystal damage introduced during the mechanical processes was completely removed through a reactive dry etching process using atmospheric-pressure plasma called plasma chemical vaporization machining (PCVM) [10]. In the PCVM process, a high-pressure atmosphere leads to the generation of high-density reactive radicals and ions with low kinetic energies, which cause little crystal damage to the work piece. The high-pressure atmosphere also results in the localization of the plasma at a region where a high electric field is applied. Si atoms on the surface of the work piece react with radicals, and then the products vaporize. By adding fluoride gas as a component of the atmosphere surrounding the silicon crystal, it has been found that the removal rate scarcely depends on the crystal orientation owing to the high reactivity of the F radical. The PCVM technique is also used for damage-free thinning of the splitting area. The PCVM procedure in this work is schematically depicted in Fig. 2.

Tapered Area (Step 1)

First, crystal damage in the tapered area, which is the dominant cause of lattice strain, was removed. In the PCVM process, surface roughness increases on the damaged surface because Si atoms in a damaged area are preferentially removed. After removing the damaged area, the surface gradually becomes smooth. The depth removed should be higher than 10 μm to obtain a damage-free and flat surface at the tapered area. This fact demands that this area should be processed independently of the thin splitting area. This demand was satisfied by localizing the plasma to the tapered area via a tapered-pipe electrode that fits in the frame-shaped crystal as shown in Fig. 2(a). In this step, an atmosphere of He, CF_4, and O_2 with a concentration ratio of 97:1:2 and a flow rate of 10 slm were used. After this step, a smooth surface was obtained at the tapered area, as shown in Fig. 3.

Rear Surface (Step 2)

Second, the rear surface, which included slight damage such as scratches that can cause a critical lattice strain in an ultrathin silicon crystal, was processed through raster scanning with a constant speed of highly localized plasma generated by a fine pipe electrode, as shown in Fig. 2(b). In this step, an atmosphere of He and SF_6 with a concentration ratio of 99.5:0.5 and a flow rate of 90 sccm were applied. Further, an aluminum spacer was used to stabilize the plasma on the silicon-on-nothing structure. The effect of this step on the crystal quality was clearly observed by means of a topographic measurement using coherent x-rays at SPring-8 in Japan (see Ref. [9]).

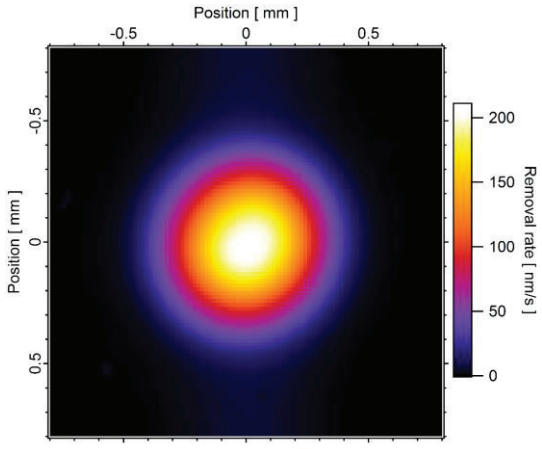

FIGURE 4. Removal rate distribution of highly localized plasma under the conditions of Steps 2–4.

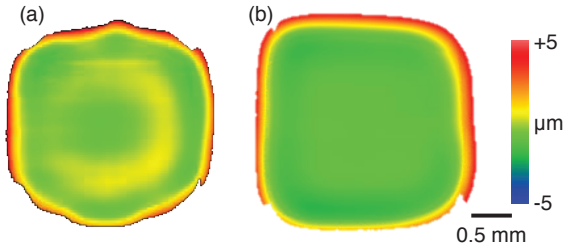

FIGURE 5. Surface profiles of the thinned area, which correspond to the relative thickness distributions, of (a) a (511); and (b) a (110) frame-shaped silicon crystal prepared through the PCVM procedure.

Splitting Area (Steps 3, and 4)

Third, the splitting area was thinned to approximately 20–30 μm at the thinnest point under the same conditions in Step 2. Under these conditions, a high linearity of the removed volume was obtained as a function of the dwelling time of the plasma. Further, a 2D Gaussian-like removal footprint having a full width at half maximum (FWHM) of 300–500 μm corresponding to the removal resolution was also obtained, as shown in Fig. 4. These special features have the potential to precisely correct a residual thickness error with a spatial frequency of up to 2 mm^{-1}. As the final step, thickness correction in the splitting area was performed through computer-controlled machining after calculating a scan speed distribution based on the residual thickness error, which is typically 20–30 μm in P-V, measured by a combination of a 2D thickness determination instrument, a spectral-interference wafer thickness meter (KEYENCE, SI-F80R) with an *X*-*Y* table system (KEYENCE, KS-1100), and a phase-shift interferometric micrometer (ZYGO, NewView200HR).

Fabrication Results

Surface profiles in the thinned area of a (511) and a (110) frame-shaped Si crystals prepared using the above technique are shown in Fig. 5. The size of the uniformly thinned area was approximately 2 × 2 mm^2 because of instability of the plasma around the edge of the splitting area. These profiles correspond closely to the relative thickness distributions of both crystals because the rear surfaces are extremely flat. These crystals, of thickness < 10 μm, were too thin to be measured by SI-F80R, which has a range of 10–300 μm. Further, the finished surface roughness was <0.2 nm root-mean-squared in a measurement area of 64 × 48 $μm^2$.

EVALUATION OF CRYSTAL QUALITY

Methods

To evaluate the quality of the above ultrathin frame-shaped crystals, topographic and high-resolution rocking curve measurements were performed at the 1-km-long beamline, BL29XUL of SPring-8. The x-ray beam from the undulator was reflected by a high-heat-load Si(111) double crystal monochromator. An energy resolution $\Delta E/E = 4.8 \times 10^{-6}$, where ΔE and E are the energy width and the central photon energy of reflected x-rays, respectively, was achieved by using a 4-bounced Si(444) reflection arranged in the (−, +, +, −) geometry positioned in Experimental Hutch 1, which was 52 m downstream from the source. Further, an angular resolution better than 1 μrad was achieved at Experimental Hutch 4 after the 1-km beam transport. The high-resolution x-ray probe was delivered to a sample crystal at a Bragg angle of 45°. The intensities of both the reflected and transmitted x-ray beams were measured by PIN photodiodes, and the reflection topograph was obtained using a CCD camera unit. X-ray probes of 8.39 keV for the (511) crystal and 9.13 keV for the (110) crystal were used to measure the (511) and (440) diffraction, respectively.

Results and Discussions

Measured topographs on the Bragg conditions and rocking curves are shown in Fig. 6. Uniform diffraction profiles were observed in the thinned area. Further, the rocking curves measured at the solid rectangular areas agree well with the calculated ones. The thickness of the (511) and (110) crystals were evaluated as 6.9 μm and 6.4 μm, respectively, from the fringe period of the rocking curves, which could be clearly observed through the high-resolution x-ray probe [11]. These results indicate that the fabricated ultrathin crystals have high crystalline perfection even for high-order diffraction.

Thickness ranges of 6.9–9.0 μm and 6.4–6.8 μm were obtained for the (511) and (110) crystals, respectively. The comparatively large thickness variation in the (511) crystal caused a low contrast on the topograph because the reflection intensity drastically varies at the thickness range. However, the variation leads to a wavefront distortion of <1/10 λ of the transmitted XFEL pulses, which is a negligible value in the case of a wide range of applications.

A wide range of crystal orientations for ultrathin silicon crystals obtained by the PCVM technique enables the provision of two XFEL beams with

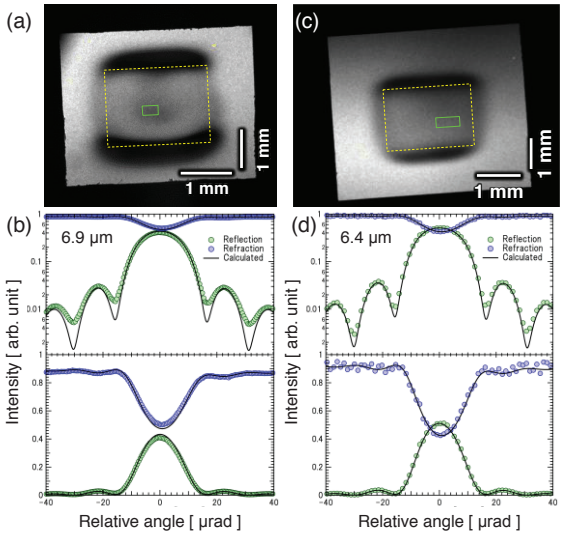

FIGURE 6. Measured topographs and rocking curves for (a) and (b) the (511), (c) and (d) the (440) diffraction. Dashed rectangular area on the topographs corresponds to the thinned area of 2 × 2 mm^2. Upper and lower curves are scaled logarithmically and linearly, respectively. Measured and calculated curves are depicted as symbols and solid lines, respectively.

various features: high flux, high temporal coherence, and high monochromaticity, which are required to perform novel experiments at XFEL facilities.

SUMMARY

Ultrathin frame-shaped Si(511) and (110) crystals with a thickness of <10 μm were prepared through the PCVM technique. The high crystalline perfection of these crystals was verified by topographic and high-resolution rocking curve measurements using coherent x-rays at SPring-8 in Japan. From the fringe periods of the rocking curves, the thickness ranges in the thinned areas were evaluated to be 6.9–9.0 μm for the (511) crystal and 6.4–6.8 μm for the (110) crystal, both of which lead to negligible wavefront distortion of the transmitted XFEL pulses. The PCVM technique, which can be applied to other materials such as diamond enables novel experiments at XFEL facilities and the development of future x-ray sources such as an XFEL oscillator [12].

ACKNOWLEDGEMENTS

This study was partially supported by the Proposal Program of SACLA Experimental Instruments of RIKEN and the Global COE Program from the Ministry of Education, Sports, Culture, Science and Technology, Japan. The use of BL29XUL at SPring-8 was supported by RIKEN.

REFERENCES

[1] Emma P et al. First lasing and operation of an ångstrom-wavelength free-electron laser. Nature Photonics. 2010; 4: 641–647.

[2] Ishikawa T et al. A compact X-ray free-electron laser emitting in the sub-ångström region. Nature Photonics. 2012; 6: 540–544.

[3] Young L et al. Femtosecond electronic response of atoms to ultra-intense X-rays. Nature (London). 2010; 466: 56–61.

[4] Fukuzawa H et al. Deep Inner-Shell Multiphoton Ionization by Intense X-Ray Free-Electron Laser Pulses. Physical Review Letters. 2013; 110: 173005.

[5] Chapman H N et al. Femtosecond X-ray protein nanocrystallography. Nature (London). 2011; 470: 73–77.

[6] Seibert M M et al. Single mimivirus particles intercepted and imaged with an X-ray laser. Nature (London). 2011; 470: 78–81.

[7] Glover T E et al. X-ray and optical wave mixing. Nature (London). 2012; 488: 603–608.

[8] Zhu D et al. A single-shot transmissive spectrometer for hard x-ray free electron lasers. Applied Physics Letters. 2012; 101: 034103.

[9] Osaka T et al. Fabrication of ultrathin Bragg beam splitter by plasma chemical vaporization machining. Key Engineering Materials. 2012; 523–524: 40–45.

[10] Mori Y, Yamamura K, Sano Y. The study of fabrication of the x-ray mirror by numerically controlled plasma chemical vaporization machining: development of the machine for the x-ray mirror fabrication. Review of Scientific Instruments. 2000; 71: 4620–4626.

[11] Osaka T et al. A Bragg beam splitter for hard x-ray free-electron lasers. Optics Express. 2013; 21: 2823–2831.

[12] Kim K-J et al. A Proposal for an X-Ray Free-Electron Laser Oscillator with an Energy-Recovery Linac. Physical Review Letters. (2008); 100: 244802.

ORIENTATION-CONTROLLED MICROFABRICATION OF ANODE OF SOLID OXIDE FUEL CELLS

Shunta Shinagawa [1], Keisuke Nagato [1], Naoki Shikazono [2], Ken Nishibashi [1], Tetsuya Hamaguchi [1], and Masayuki Nakao [1]
[1] Department of Mechanical Engineering, The University of Tokyo, Tokyo, Japan
[2] Institute of Industrial Science, The University of Tokyo, Tokyo, Japan

1. INTRODUCTION

Solid Oxide Fuel Cells (SOFCs) are one of the most promising energy conversion devices because of their high power efficiency. An SOFC consists of three layers: a cathode, an electrolyte and an anode. *Figure 1(a)* shows the structure of the anode, which consists of three phases: Yttria-stabilized Zirconia (YSZ), Ni and pores. In the anode, a chemical reaction occurs at the three phase boundary (TPB). TPB is the point where these three phases come in contact with each other. Oxide ions, electrons and gases pass through in YSZ, Ni and pores, respectively . Our aim is to fabricate an orientation-controlled anode as shown in *Figure 1(b)*. In a conventional anode, the three phases are uniformly distributed and the paths of oxide ions, electrons and gases have high resistance [1]. When Ni and YSZ phases are oriented, the resistances of electrons and oxide ions are reduced and the efficiency is enhanced.

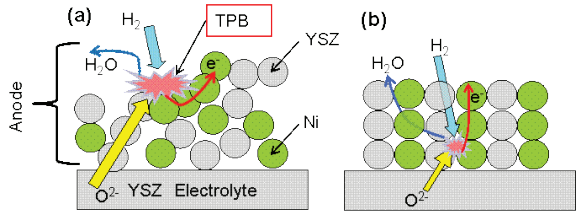

FIGURE 1. Structure of anode of SOFC, (a) conventional anode , (b) oriented anode

In this paper, we report the fabrication of an anode with an oriented microstructure by following two newly proposed methods.

1.1. Applying a Magnetic Field

We have attempted to align Ni and YSZ particles by applying a magnetic field in previous research [2,3]. We previously found that the electric power generation and active TPB were increased by aligning Ni and YSZ in the thickness direction with using a magnetic field. However, evaluation of the orientation of Ni, YSZ and pores upon the application of a magnetic field has not been clarified.

Here, the change in the orientation of Ni, YSZ and pore phases upon the application of a magnetic field was investigated by a reconstruction technique using focused ion beam-scanning electron microscopy (FIB-SEM) and by calculation of the electrochemical reaction and the transfer of matters.

1.2. Laser Processing

An anode with an oriented microstructure was fabricated by laser processing as shown in *Figure 2*. Holes were formed on porous YSZ by laser ablation, then filled with Ni particles. As a result, Ni and YSZ aligned in the thickness direction.

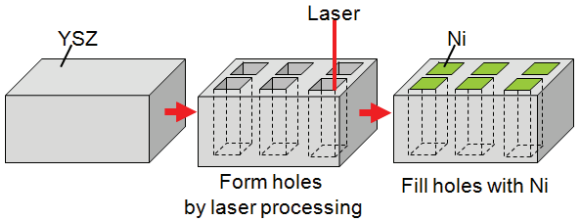

FIGURE 2. Fabrication methods for oriented microstructure by laser processing

2. EXPERIMENTAL

2.1. Applying a Magnetic Field

2.1.1. Preparation of Anode

Ni particles (average diameter: 1 μm) and YSZ particles (average diameter: 1.1 μm) were mixed in a 1:2 volume ratio to obtain a mixed powder. Terpineol and methylcellulose were mixed in a 100:3 weight ratio to obtain a binder. The mixed powder and binder were mixed in an 11:3 weight ratio. The mixture was applied to a YSZ

electrolyte (thickness: 500 μm) using a screen printer to obtain a thickness of 50 μm. A magnetic field (360 mT) was applied to the sample using two magnets located at the top and bottom of the sample. The sample was heated to 300 °C at a rate of 10 °C/min and maintained at 300 °C for 1 hour while applying the magnetic field to evaporate the binder. After the magnets were removed, the sample was heated to 1400 °C at a rate of 10 °C/min and maintained at 1400 °C for 3 hours to sinter Ni and YSZ. Finally, NiO, which was formed during sintering, was reduced to Ni by annealing in H_2 atmosphere.

2.1.2. Reconstruction of Microstructure of Anode

The method used to reconstruct the microstructure of the anode by FIB-SEM was reported by Iwai *et al.* [4] and Shikazono *et al.* [5]. Using this method, we reconstructed the microstructure of the anode as shown in *Figure 3.* From the reconstructed microstructure of the anode, the volume fractions of Ni, YSZ and pores were calculated.

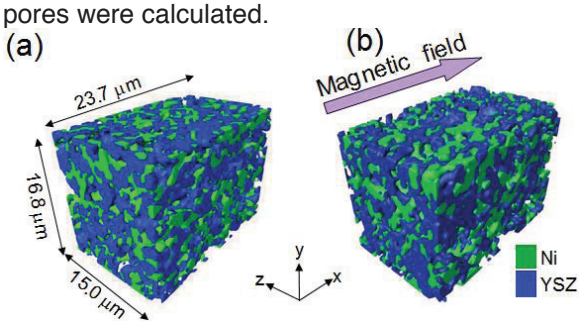

FIGURE 3. Reconstructed microstructure of anode (blue: YSZ, green: Ni), (a) without magnetic field, (b) with magnetic field.

2.1.3. Calculation of Tortuosity Factor

The tortuosity factor τ is defined by the following equations.

$$\tau_{Ni} = \frac{\sigma_{e-}^{eff}}{\sigma_{e-}} \varepsilon_{Ni}$$

$$\tau_{YSZ} = \frac{\sigma_{O2-}^{eff}}{\sigma_{O2-}} \varepsilon_{YSZi}$$

$$\tau_{Pore} = \frac{D_{gass}^{eff}}{D_{gass}} \varepsilon_{Pore}$$

τ : tortuosity factor
σ : conductivity
σ^{eff} : effective conductivity
ε : volume fraction
D : diffusion coefficient
D^{eff}: effective diffusion coefficient

We calculated the tortuosity factors of Ni, YSZ and pores using the method reported by Iwai et al.[3] .

2.2. Laser Processing

2.2.1. Preparation of Anode

YSZ particles and binder were mixed in a 2:1 weight ratio to obtain a YSZ mixture. The YSZ-mixture was applied to YSZ electrolyte with ϕ 10 mm and a thickness of 50 μm using a screen printer. The sample was heated to 1400 °C and maintained for 3 hours to evaporate the binder and sinter YSZ. As a result, porous YSZ was obtained.

Micron-size square holes were formed on the porous YSZ over a 4 mm x 4 mm area using a femtosecond laser. The sizes of the square holes were verified to be 20 μm x 20 μm, 40 μm x 40 μm and 80 μm x 80 μm and the pitches of the holes were 28 μm, 56 μm and 112 μm, respectively. The pitches were designed so that the volume ratio of YSZ to holes was 1:1. The depth of the holes was 30 μm.

Ni particles and binder were mixed in a 1:1 weight ratio to obtain a Ni paste. The Ni paste was applied to the surface of the porous YSZ and the holes were filled with the Ni paste. The sample was heated to 800 °C and maintained for 1 hour.

2.2.2. Evaluation of Microstructure and Power Density

The resulting microstructure of the anode was observed by scanning electron microscopy (SEM).

Lanthanum strontium manganite oxide (LSM) was pasted the opposite side to the anode, as a cathode. The electric potential between the anode and the electrolyte was measured as a function of the current density using SOFC evaluation device (BEL SOFC, BEL Japan, Inc.) at 800 °C. The electric power density was calculated by multiplying the current density by the electric potential. From the relationship between the power density and current density, the maximum power density was determined.

3. RESULTS AND DISCUSSION

3.1. Applying a Magnetic Field

3.1.1. Volume Fractions

The results of the calculation of volume fractions are shown in *Table 1*.

The volume fraction of pores related to that of Ni-YSZ with magnetic field declined to 0.63 times as much as that without magnetic field. Ni particles moved with the magnetic field, and YSZ particles were pushed by the Ni particles to fill the pores. Thus, the volume fraction of pores to Ni-YSZ decreased.

TABLE 1. Volume fractions of Ni, YSZ and pores

	Ni	YSZ	Pores	Ratio of Ni to YSZ	Ratio of pores to Ni-YSZ
With magnetic field	0.21	0.42	0.37	0.50	0.58
Without magnetic field	0.17	0.35	0.48	0.49	0.92

3.1.2. Tortuosity Factor

The results of the calculation of tortuosity factors are shown in *FIGURE 4*. The tortuosity factors of Ni, YSZ and pores in the x-direction with a magnetic field are 0.70, 0.60 and 1.6 times as large as those without a magnetic field, respectively.

The Ni particles were aligned by the magnetic field, and the YSZ particles were moved and aligned by the movement of the Ni particles. The conductivities of electrons and oxide ions were improved.

When the Ni and YSZ particles fill the pores, the volume ratio of pores to Ni-YSZ decreases and the diffusion of gases is impeded.

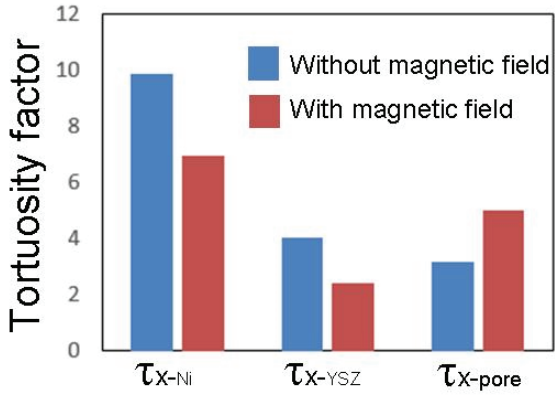

FIGURE 4. Results of calculation of tortuosity factor in x-direction

3.2. Laser Processing

3.2.1. Top View Observation

SEM images of the anode are shown in *Figures 5 (a-1)-(c-2)*. *Figures 5 (a-1), (b-1) and (c-1)* show holes with sizes of 20 μm x 20 μm, 40 μm x 40 μm and 80 μm x 80 μm, respectively. *Figures 5 (a-2), (b-2) and (c-2)* show the holes after they were filled with Ni. An anode in which the Ni and YSZ were oriented was obtained.

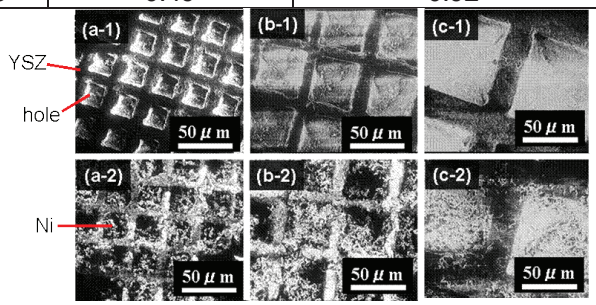

FIGURE 5. SEM images of holes

3.2.2. Examination of Power Density

The relationships between the current density and voltage and between the current density and power density are shown in *Figure 6*. To compare the dependence of the power density on the TPB length, the maximum power densities are plotted as a function of the TPB length ratio in *Figure 7*. TPB length ratio is expressed as a value relative the sample with 80 μm x 80 μm holes.

The TPB length ratio of 20 μm x 20 μm holes, 40 μm x 40 μm holes and 80 μm x 80 μm holes is 4:2:1. The ratio of the maximum power densities for the 20 μm x 20 μm holes, 40 μm x 40 μm holes and 80 μm x 80 μm is 2.7:1.2:1. The maximum power density is positively correlated with the TPB length.

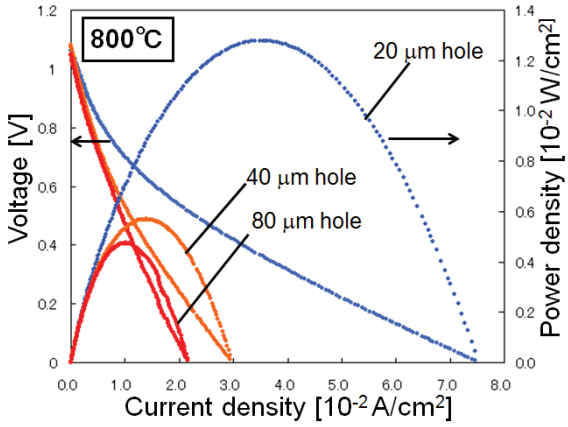

FIGURE 6. Relationships between the current density and voltage and between the current density and power density

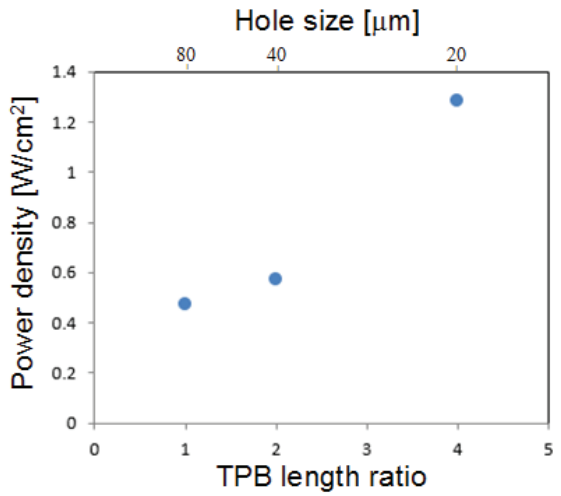

FIGURE 7. Relationship between the TPB length ratio and power density ratio

4. CONCLUSIONS

An anode with an oriented microstructure was fabricated using two different methods: applying a magnetic field and laser processing. The following results were obtained.

4.1. Applying a Magnetic Field

The volume fraction of pores related to that of Ni-YSZ with magnetic field declined to 0.63 times as much as that without magnetic field.

The tortuosity factors of Ni, YSZ and pores in the x-direction with a magnetic field are 0.70, 0.60 and 1.6 times as large as those without a magnetic field, respectively.

When a magnetic field was applied, the conductivities of electrons and oxide ions were improved because the Ni and YSZ particles were aligned, and the diffusion of gases was impeded because the volume ratio of pores to Ni-YSZ decreases.

4.2. Laser processing

The TPB length ratio of 20 μm x 20 μm holes, 40 μm x 40 μm holes and 80 μm x 80 μm holes is 4:2:1. The ratio of the maximum power densities for the 20 μm x 20 μm holes, 40 μm x 40 μm holes and 80 μm x 80 μm is 2.7:1.2:1. The maximum power density is positively correlated with the TPB length.

ACKNOWLEDGMENTS

We would like to thank Mr. Hara and Mrs. Hara at the National Institute for Materials Science (NIMS) for assistance in FIB-SEM. This study was partly supported by JSPS KAKENHI Grant Numbers 24686019 and 24246027 and the Global Center-of-Excellence for Mechanical System Innovation (GCOE-MSI) from the Ministry of Education, Culture, Sports, Science and Technology (MEXT), Japan.

REFERENCES

[1] Kanno D, Shikazono N, Takagi N, Matsuzaki K, and Kasagi N, Evaluation of SOFC Anode Polarization Simulation using Three-Dimensional Microstructures Reconstructed by FIB Tomography. Electrochimica Acta, 2011; 56 (11), 4015-4021

[2] Shinagawa S, Nagato K, *et al.* Enhancement of Power Efficiency of Solid Oxide Fuel Cells by Aligning Microstructure Path of Ion/Electron/Gas in Anode. In: Proceedings of American Society for Precision Engineering Annual Meeting. 2012; 54: 343-346

[3] Nagato K., Shikazono N., Weber A., Klotz D., Nakao M., Ivers-Tiffeé E., SOFC Anode Fabricated by Magnetically Aligning of Ni Particles, ECS Transactions, to be published.

[4] Iwai H, Shikazono N, Matsui T, Teshima H, Kishimoto M, Kishida R, Hayashi D, Matsuzaki K, Kanno D, Saito M, Muroyama H, Eguchi K, Kasagi N, and Yoshida H, Quantification of SOFC anode microstructure based on dual beam FIB-SEM technique, Journal of Power Sources, 2010; 195, 955-961.

[5] Shikazono N, Kanno D, Matsuzaki K, Teshima H, Sumino S, and Kasagi N, Numerical Assessment of SOFC Anode Polarization Based on Three-Dimensional Model Microstructure Reconstructed from FIB-SEM Images, Journal of the Electrochemical Society, 2010; 157 (5), B665-B672.

LASER-ASSISTED ROLLER IMPRINTING OF NANOSTRUCTURES WITH REAL-TIME MONITORING OF REPLICATION DEGREE

Ken Takahashi[1], Keisuke Nagato[1], Toshimi Sato[1], Daisuke Suehiro[1], Tetsuya Hamaguchi[1], and Masayuki Nakao[1]
[1]Department of Mechanical Engineering
The University of Tokyo
Tokyo, Japan

INTRODUCTION

Nanoimprinting lithography (NIL) is a promising technology that is used for the fabrication of micro- to nanometer-scale structures [1]. Since the invention of NIL, many variations have been proposed and developed. Roller nanoimprinting, one of the variations, can be used to fabricate nanostructures continuously with a roller mold. Compared with flat nanoimprinting, roller nanoimprinting has the advantages of being able to pattern large-area substrates in a short time and a lower pressing force [2]. Because of these advantages, roller nanoimprinting is expected to be used for the replication of patterns onto flexible substrates such as thermoplastic films. Flexible substrates with micro- to nanometer-scale patterns can be applied to large-area optical films such as antireflection films and light-excitation films as well as to next-generation flexible displays and sensors.

However, it is generally difficult to replicate patterns completely by conventional roller nanoimprinting. One of the reasons is that a thermoplastic polymer has a glass transition temperature (T_g), below which its viscosity is high and above which it becomes markedly lower. In conventional roller nanoimprinting, a thermoplastic film is fed between a heated roller mold and a counter roller. A reflow process, in which the polymer surface is heated until it is demolded, is carried out, and the nanostructures are destroyed by the surface tension that occurs immediately after demolding.

In this study, we propose and demonstrate laser-assisted roller nanoimprinting. Figure 1 shows a schematic of the system. First, a laser locally heats a nanostructured mold through a transparent glass roller and film in the front half of the area of contact, by which the nanostructures are replicated. Second, in the back half of the area of contact, the film is cooled to below T_g by a cold roller. Finally, the replicated nanostructures are demolded from the mold. Using this method, nanostructures can be completely replicated and demolded.

Furthermore, because the counter roller is made of glass, the real-time monitoring of the replication degree could be carried out. When the mold patterns are irradiated with a laser, the light is reflected and diffracted. The intensity of the diffracted light is monitored during the nanoimprinting process. When the film is filled into the mold patterns, the intensity of the diffracted light changes [3]. By measuring the intensity of the diffracted light, the replication degree can be monitored in real time. This technology enables the replication mechanism to be clarified. By feeding back the signals corresponding to the replication degree, not only the replication phenomena during laser-assisted imprinting but also the optimal parameters for the fabrication can be clarified.

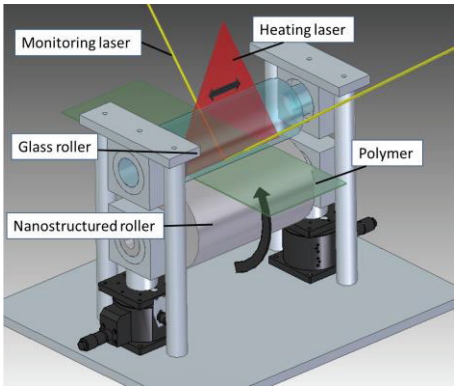

FIGURE 1. Schematic of laser-assisted roller nanoimprinting system with real-time monitoring of replication degree.

EXPERIMENTS AND RESULTS

In this study, we determined the relationship between the size of the replicated area and the laser irradiation time. First, we performed an experiment at which the laser irradiated a thermoplastic film at a spot and measured the size of the replicated area (experiment 1). Second, we scanned the laser one-dimensionally and measured the width of the replicated line (experiment 2). In addition, we compared the result of the line experiment with that of the spot experiment. Finally, we scanned

the laser two-dimensionally, to demonstrate laser-assisted roller nanoimprinting (experiment 3).

Equipment

The experimental setup used in this study is illustrated in Figure 3. We used a Nd:YAG laser (beam diameter: 300 μm, wavelength: 1064 nm) with a laser power set to 4 W. A shutter was placed in front of the laser to control the irradiation time. A galvanometer mirror (Cambridge Technology, 6210HM40) was used to reflect and scan the laser. The galvanometer mirror was driven by signals from a function generator. The signal was a triangle wave. The reflected laser passed through an $f\theta$ lens (Geomatech, FT-100, focal distance: 101 mm, scanning area: ϕ80 mm), a glass roller and a thermoplastic film. The laser irradiated and heated the surface of the nanostructured roller. The nanostructured roller was set on two Z-axis stages. The Z-axis stages and glass roller were fixed on the surface plate. The nanostructured roller pressed the thermoplastic film when the Z-axis stages were moved upward. The pressure was set to about 9 MPa. The nanostructured roller was driven by a motor that was used to feed the thermoplastic film.

The nanostructured roller was manufactured by attaching a flat Ni mold (thickness: 200 μm) onto an Al roller. The mold has 600-nm-pitch line and space (L&S) pattern, and the pattern height was about 230 nm (Figure 2). The flat mold was coated with 100-nm-thick diamond-like carbon (DLC) as a light-absorption layer.

We used a polymethyl methacrylate (PMMA) film (thickness: 75 μm, T_g: 89 ˚C) as a thermoplastic layer. The PMMA film was placed between the nanostructured roller and the glass roller. Figure 3(c) shows a schematic image of the roller-PMMA contact.

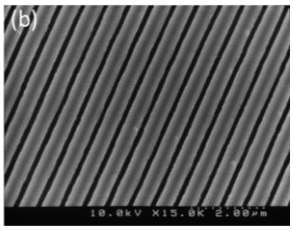

FIGURE 2. SEM image of nanostructured mold pattern.

Experiment 1: Laser Irradiation at a Spot

To examine the relationship between the irradiation time and the size of the replicated area, we performed an experiment in which the laser was irradiated at a spot. In this experiment, the galvanometer mirror and nanostructured roller were not driven.

The steps in the method are described as below;

1. Place a PMMA film between the two rollers and move the Z-axis stages upward to press the PMMA film.
2. Set the opening time of the shutter (initial setting: 0.01 s).
3. Control the shutter and irradiate at a spot.
4. After the shutter has closed, drive the motor a small distance to feed the PMMA film.
5. Change the opening time of the shutter to 0.05 s, 0.1 s, 0.2 s and 0.5 s and repeat steps 3-5 procedures.
6. Move the Z-axis stages downward and remove the PMMA film.
7. Repeat steps 1-6 and prepare three samples.
8. Observe the samples with an optical microscope and measure the size of the replicated area.

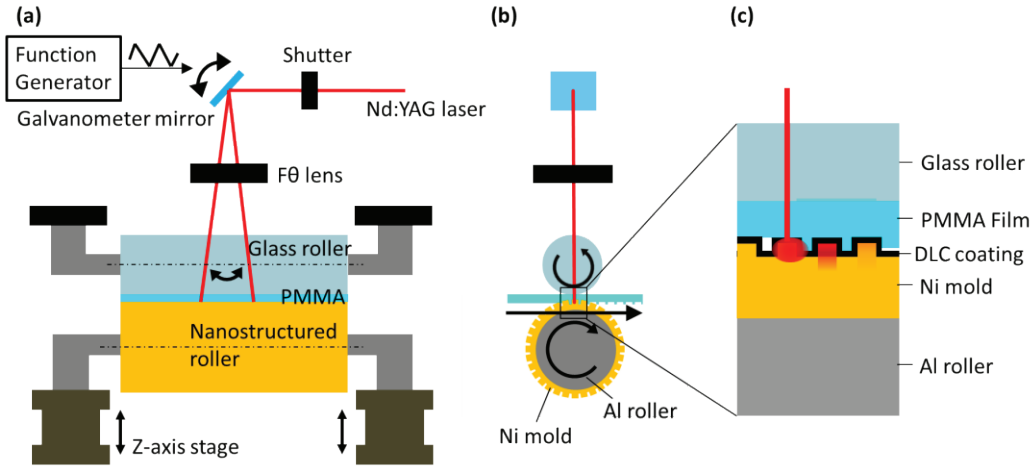

FIGURE 3. (a) Front view and (b) side view schematic images of experimental setup. (c) schematic image of roller-PMMA contact.

Figure 4 shows an image of sample taken with an optical microscope. The blue areas in this image are replicated areas. The blue color is caused by the diffraction of light in the replicated L&S pattern. Figure 5 shows a scanning electron microscopy (SEM) image of the replicated PMMA pattern.

Figure 5 indicates that a larger area was replicated when the laser was irradiated for a longer time. In addition, there was a difference between the length of replication in the axial direction of the roller and in the direction in which the PMMA film was fed. Figure 6 shows the average length replicated in the above directions for each irradiation time

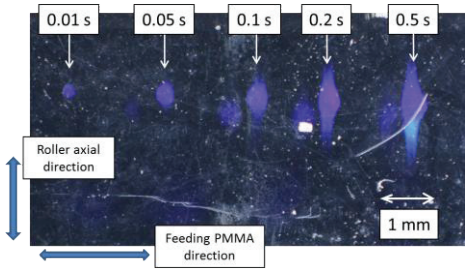

FIGURE 4. Optical photograph of replicated PMMA.

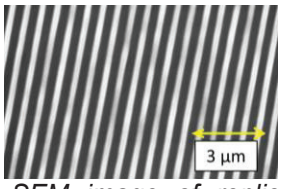

FIGURE 5. SEM image of replicated PMMA pattern.

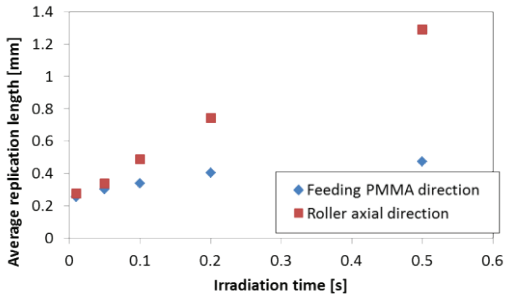

FIGURE 6. Average length of replication in axial direction of roller and PMMA feeding direction for each irradiation time.

Experiment 2: Laser Irradiation in a Line

Next, we examined the case of laser irradiation in a straight line. In this experiment, we drove the galvanometer mirror to scan the laser in a line. To change the irradiation time, we controlled the driving frequency the of galvanometer mirror and changed the scanning speed.

The steps in the method are described as below;

1. Place a PMMA film between the two rollers and move the Z-axis stages upward to press the PMMA film.
2. Set the driving frequency (initial setting: 0.5 Hz).
3. Open the shutter and scan the laser in a line with the nanostructured roller driven quickly so that the laser which turned back does not overlap with the replicated line.
4. Close the shutter and remove the PMMA film.
5. Change the driving frequency to 0.25 Hz and 0.1 Hz and repeat steps 1-4.
6. Observe samples with an optical microscope and measure the width of the replicated line.

The driving frequency of galvanometer mirror was calculated from the result of experiment 1.

The driving frequency *h* [Hz] was calculated from the scanning speed *v* [mm/s] and the one-way scanning length *H* [mm] as

$$h = \frac{v}{2H}.$$

When the radius of the irradiated laser is ω, an irradiation time of t is required to move by a length of 2 ω.

$$t = \frac{2\omega}{v}$$

To determine ω, we use Gaussian beam optics. ω is calculated as follows from the wavelength λ, the incident beam waist radius ω_0, the distance from the point of laser emission to the $f\theta$ lens *d* and the focal distance *f* [4].

$$\omega = \sqrt{\frac{f^2}{z^2 + (d-f)^2}{\omega_0}^2}, \qquad z = \frac{\pi {\omega_0}^2}{\lambda}$$

In this study, we calculated ω to be $\cong 0.635$ mm and set $H = 10$ mm.

Using these parameters, corresponding values of *t* and *h* were calculated as shown in *TABLE 1*. When the driving frequency is set to the value in *TABLE 1* numbers, the irradiation time *t* roughly equals the irradiation time in experiment 1.

TABLE 1. Relationship between driving frequency h and irradiation time t.

Frequency h[Hz]	0.5	0.25	0.1
Irradiation time t[s]	0.127	0.254	0.635

Figure 7 shows an image of the sample obtained at a driving frequency of 0.25 Hz taken with an optical microscope. Because the laser was scanned with the nanostructured roller driven, the replicated line is at an angle to the PMMA feeding direction. Considering the effect of partial contact, we measured the width of the replicated line at three points and calculated the average value (Figure 8).

We compared the result of this experiment with that of experiment 1. In experiment 1, the length of replication the PMMA feeding direction was about 0.255 mm when the irradiation time was 0.01 s. In experiment 2, the width of replication was 0.22 mm when the driving frequency was 0.5 Hz. In addition, the length of replication was 0.30 mm when the irradiation time was 0.05 s, and the width of replication was 0.32 mm when the driving frequency was 0.1 Hz. When the irradiation time was roughly equal, the area of replication upon irradiation at a spot was roughly equal to that of the line.

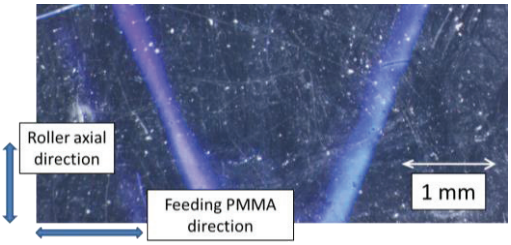

FIGURE 7. Optical micrograph of sample obtained at a driving frequency of 0.25 Hz.

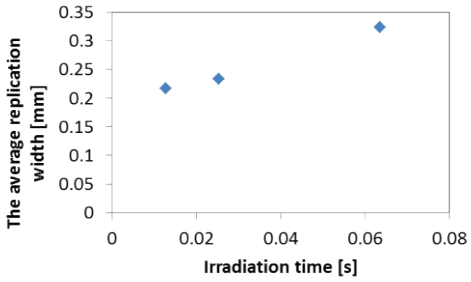

FIGURE 8. Average width of replication for scanning in a line.

Experiment 3: Laser Irradiation in Two-Dimensions

To demonstrate laser-assisted roller nanoimprinting, we performed an experiment in which the laser was scanned in two dimensions by driving the galvanometer mirror and nanostructured roller.

The steps in the method are described as below;

1. Place the PMMA film between the two rollers and move the Z-axis stages upward to press the PMMA film.
2. Set the galvanometer mirror frequency to 0.4.
3. Set the nanostructured roller speed to 0.1 mm/s.
4. Open the shutter and scan the laser.

Figure 9 shows an optical image of the replicated PMMA surface. The replicated area was 21 × 10 mm^2. In this experiment, the replication speed was 10 mm^2/s and it took 1000 s to fabricate the area.

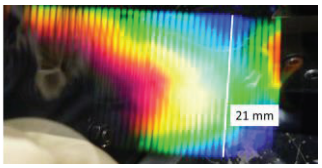

FIGURE 9 Optical image of replicated PMMA surface.

CONCLUSION

In this study, we determined the relationship between the laser power, laser waist size and irradiation time through experiments in which a laser was irradiated at a spot, in a line and in two dimensions. From the experiments at a spot and in a line, we clarified the relationship between the size of the replicated area and the irradiation time. In addition, the result of experiment involving irradiation at a spot can be applied to the experiment involving irradiation in a line. Finally, we replicated PMMA in two dimensions and demonstrated laser-assisted roller nanoimprinting. The laser power was 13 W/cm^2 and the replicated area was 21×10 mm^2 Laser-assisted roller nanoimprinting realizes the high-throughput and low-energy replication of nanostructures. The laser used in this study had a limited power. To achieve higher throughput replication, a higher-power laser should be used with the aim if replication in a shorter time.

ACKNOWLEDGMENT

This study was partly supported by JSPS KAKENHI Grant Number 24246027 from the Ministry of Education, Culture, Sports, Science and Technology (MEXT), Japan.

REFERENCES

[1] Chou S Y, Krauss P R, Renstrom P J. Imprint of sub-25 nm vias and trenches in polymers. Applied Physics Letters. 1995; 67: 3114-3116.

[2] Nagato K, Sugimoto S, Hamaguchi T, Nakao M. Iterative roller imprint of multilayered nanostructures. Microelectronic Engineering. 2010; 87: 1543-1545

[3] Suzuki H, Nagato K, Sugimoto S, Tsuchiya K, Hamaguchi T, Nakao M, Iterative imprint for multilayered nanostructures by feeding, vacuum forming, and bonding of sheets. Journal of Vacuum Science & Technology B. 2008; 26: 1753-1756.

[4] Yariv K, Yeh P. PHOTONICS:OPTICAL ELECTRONICS IN MODERN COMMUNICATIONS, The Oxford Series in Electrical and Computer Engineering, 2006

Ultraprecise Clamping Solution for Diamond Machining Comparative Characterization of Repeatability

Dr. Christian Wenzel[1], Ralf Winkelmann[1], Rainer Klar[1], Dave Arneson[2], Byron Knapp[2]
[1]Innolite GmbH
Aachen, Germany
[2]Professional Instruments
Hopkins, Minnesota, USA

Thanks to the exceptional repeating accuracy of the Nanogrip clamping system, pre-aligned assemblies can be fed into a machine and removed again in minutes. This enables significantly improved machine utilization, reduced down times, and innovative production processes to be achieved.

Ultra-precise cutting with monocrystalline diamond tools is used to produce optical die inserts for plastic injection molding, metal optical systems in laser applications, plastic prototypes and for numerous other applications. While a high level of automation is the norm in conventional series production, the machines and processes used in diamond cutting are largely based on manual activities, and are designed for production of individual parts or small batches.

Work pieces are normally clamped on vacuum chucks at the expense of machine running time and are then aligned manually with a precision gauge and a plastic hammer. Depending on the degree of freedom tolerated in the alignment and the required precision (e.g., adjustment to the center of rotation of a spindle only, or also rotative alignment for overlaid free form surface sections), this alignment process can take up to two hours per component. The tool is also set up manually. Camera systems, individually installed precision gauges and adjustable solid joints assist the operator, particularly when it comes to adjusting the height and angular alignment of the diamond tools. The exact tool position is generally determined by test cuts on sample objects, which are characterized by a microscope. If an appropriate method is used, and the operator is sufficiently skillful, setting accuracies of 1 µm or less are possible. However, this procedure is still performed with full utilization of the machine and can take anywhere between 30 minutes and 2 hours.

The same steps are necessary to change tools or components, especially in mold making. This means that the running and down times for diamond cutting are of similar duration, which result in high costs, minimal parallelization and therefore long processing times. Other characteristics of this procedure include the susceptibility of the activities to error, and the fact that the reproducibility for multiple production of components (e.g., die inserts for 8-piece injection embossing tools) depends on the machine operator.

The increasing spread of LED illuminants makes changes necessary in terms of the efficiency of diamond cutting. Additionally, in order to function properly, most LED require plastic optics with light guidance specific to the application's requirements. As a result the number of die inserts produced by diamond machining is dramatically increasing. As LED are becoming established in industries like automotive production (LED headlights, rear lights, interior lighting), in addition to pure productivity the requirements for process capability and reliability have also increased.

›NANOGRIP‹ – MORE THAN A ZERO POINT CLAMPING SYSTEM

With the development of the ›IL600‹ ultra-precision machining center by Innolite in 2012 clamping systems have been used for the first time for both work piece and tool clamping with a repeating accuracy in the sub-micron range. This milestone has increased the sustainable productivity in diamond cutting and contributed in opening up totally new markets.
Since November 2012, Innolite has been supplying the same clamping technology, successfully used on the IL600, as an independent product range for upgrading existing diamond cutting machines (Figure 1).

FIGURE 1. ›Nanogrip‹ - spindle modules

The focus is on consistent and harmonized solutions ready to be used immediately after installation on the machine. As a result, no additional work is required before production can begin.

When it comes to clamping components on air bearing spindles, various adapters exist to support standard systems. The Nanogrip clamping unit is integrated into those adapters. The vacuum connections for standard vacuum chucks are still available. Depending on the spindle, the clamping unit can be automatically released by applying additional compressed air. If this option is not available on a particular spindle, a compressed air pistol and an integrated valve can be used for unclamping. The clamping unit can clamp pallets over a spring assembly in seconds. Due to the internal clamping ring and the system design, speeds of up to 5000 rpm can be achieved.

The pallets available for setting up and clamping components include simple plates for screwing on components, three jaw chucks, vacuum chucks and fittings for the ›Nanogrip Flex‹. The Nanogrip Flex is supplied as a slotted aluminum or steel plate, into which the negative profile of the component to be clamped is milled. Depending on the clamping situation, the slotted plate has a few millimeters elbow room, allowing complex components to be held with geometric flexibility and excellent precision.

Installing the Nanogrip system on diamond cutting machines enables iterative operations to be carried out extremely efficiently. Cutting, measurement and corrective re-cutting are all performed at high speed. Meanwhile, short handling distances also reduce thermal influences on the component. If multiple machines in a production system are equipped with the Nanogrip system and adjusted to one another (milling machine and lathe for premachining, diamond cutting machine, coordinate measuring machine), there is no need for additional time-consuming and error-prone alignment steps.

In addition to clamping components, the Nanogrip clamping system is also ideal for holding tools. For lathes with only two horizontal axes, pallets with integrated height adjustment unit are available. An optical scale in the height adjustment unit and a digital display enable the tool height to be adjusted with micron accuracy and clamped, despite the system's inherent mechanical tolerance. Machines with a separate vertical axis do not need this mechanism. Both tool change units are available for one or for four tools. Once set up, tools and the associated pallet can be fitted again in seconds. On the four tool module, the indexing allows the tools to cycle through the clamping unit. As a result, Nanogrip-Tool enables diamond tools to be managed efficiently and re-integrated into a machine with sub-micron accuracy (Figure 2). This is particularly beneficial because of tool wear or geometric restrictions for machining with multiple tools. As an alternative to tools, the pallets can also hold various sensors in order to be flexibly incorporated into the production process and used.

PRACTICAL EXAMPLES

To improve quality and productivity, Innolite has been successfully using Nanogrip clamping technology in its own ultra-precision production for more than two years. The system provides major advantages, e.g., in production of an optical eight-section injection molding tool with five individual dies on each side of the mold. For the individual die geometry, four identical fittings are developed, produced, and aligned on pallets. After coating the dies with electroplated nickel, four dies at a time can be fitted, the

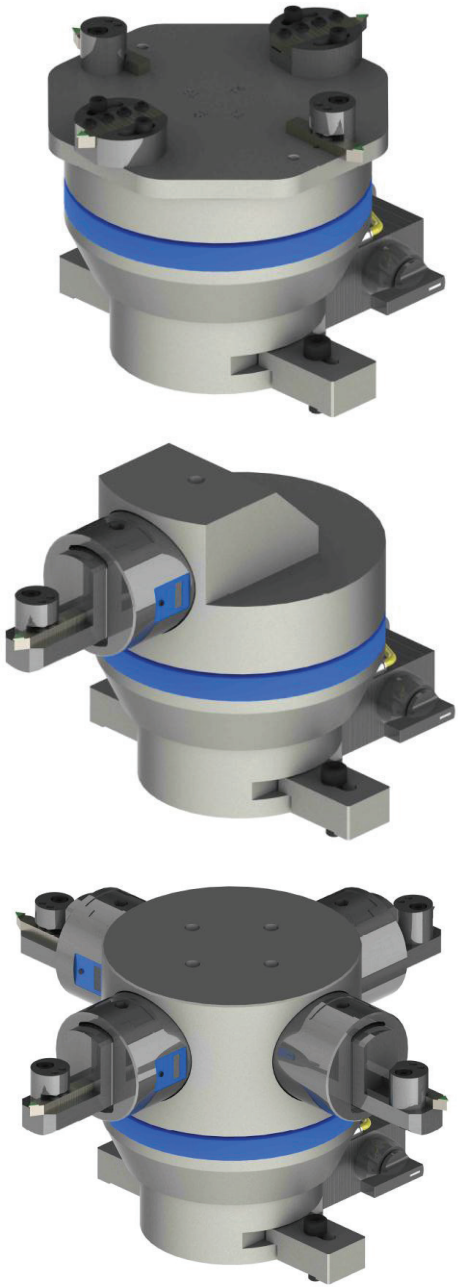

FIGURE 2. ›Nanogrip‹ - tool modules

pallets mounted on a Kern precision milling machine, and trimmed with extreme precision and minimal excess. As an exact transition from the steel core to the nickel layer is essential for the subsequent function, the transition and the functional surface are finished on a diamond cutting machine retrofitted with a Nanogrip clamping system (Figure 3).

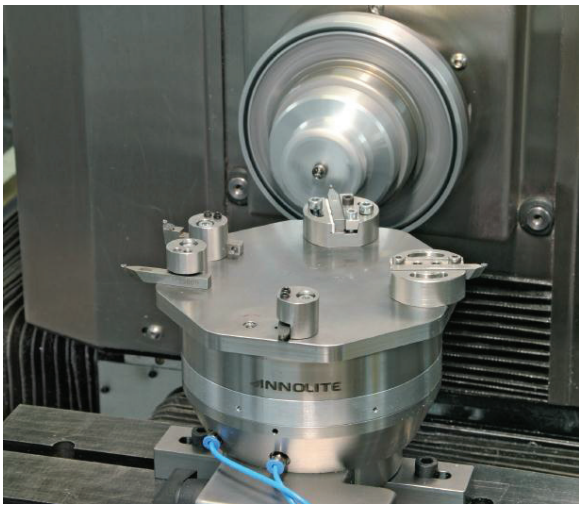

FIGURE 3. ›Nanogrip‹ - spindle and tool upgrade on a diamond cutting machine

Due to the extreme precision of the clamping system, there is no need for manual alignment on the diamond cutting machine after premachining. The tool change system allows a radius tool to be fitted to obtain the exact outer profile of the nickel layer. The five dies differ in terms of micro-structures raised on the front face, which require the use of three additional tools in total. All tools are precisely set up on a pallet and the pallet only has to be advanced by 90 ° for final die machining to select the correct tool. Simultaneously mounting four tools would result in collision between the component and the tombstones.

FIGURE 4. Injection molding die for Alvarez glasses

Alvarez glasses allow different diopter settings to be selected by moving two free form optical elements relative to one another. These free form surfaces have extremely precise tolerances, both for their functional surface and for the outer sections that hold the lenses (Figure 4). Precise pre-machining is carried out on a Kern precision machine. The free form surface, and especially the functional geometry for alignment of the form die in the injection

molding tool, need to be produced with tight absolute tolerances. Without Nanogrip clamping system holding the work pieces, the center of a rotationally asymmetrical work piece would be usually aligned on a standard vacuum chuck on a spindle with a defined rotative position. With tolerances of just a few microns required, this can take up to one and a half hours, even for a highly skilled machine operator. By contrast, the Nanogrip clamping system with adapter plate can carry out the entire operation in around 30 seconds.

IS MECHANICAL CLAMPING ALONE TOO IMPRECISE?

The major argument leveled against the use of high precision zero point clamping systems in ultra-precision engineering is that they are thought to lack precision. When using the systems, it is important to differentiate between the repeating accuracy (one pallet for one clamping system) with fixed indexing, the absolute accuracy when changing the indexing (one pallet for one clamping system) and the system accuracy (one pallet for multiple clamping systems).

For precision applications with iterative corrective machining, and for reloading tools, the repeating accuracy with fixed indexing is critical. To characterize the system, a measuring setup consisting of a confocal sensor (Precitech, ›Chrocodile E‹, measuring range of 2 to 250 µm, resolution 10^{-7} x 250 µm, reproducibility $9*10^{-5}$ x 250 µm) and an air bearing spindle with the Nanogrip clamping system (Figure 5) has been set up.

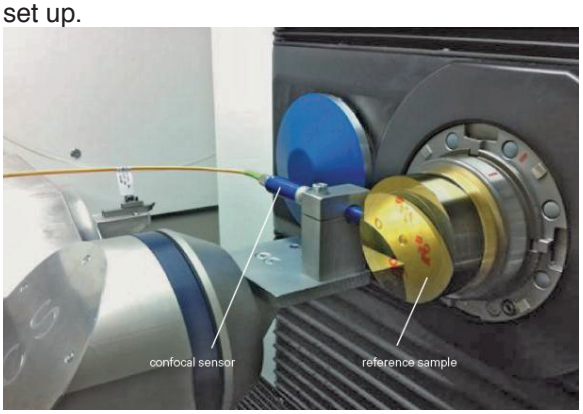

FIGURE 5. Measuring setup for determining the repeating accuracy on the ›IL600‹

A sequence of 60 measurements was performed, with the pallet being removed and fitted manually. In the normal direction to the clamping system, maximum variations of 0.2 µm were established and 0.2 µm in a radial direction, in both cases over the entire measuring series. Innolite specifies a mechanical repeating accuracy of well below 1 µm. To determine the absolute accuracy, two ultra-precision machines with Nanogrip clamping systems were used, each of which with five different pallets clamped and characterized using measuring technology. The system accuracy was less than 2 µm axial and less than 5 µm radial.

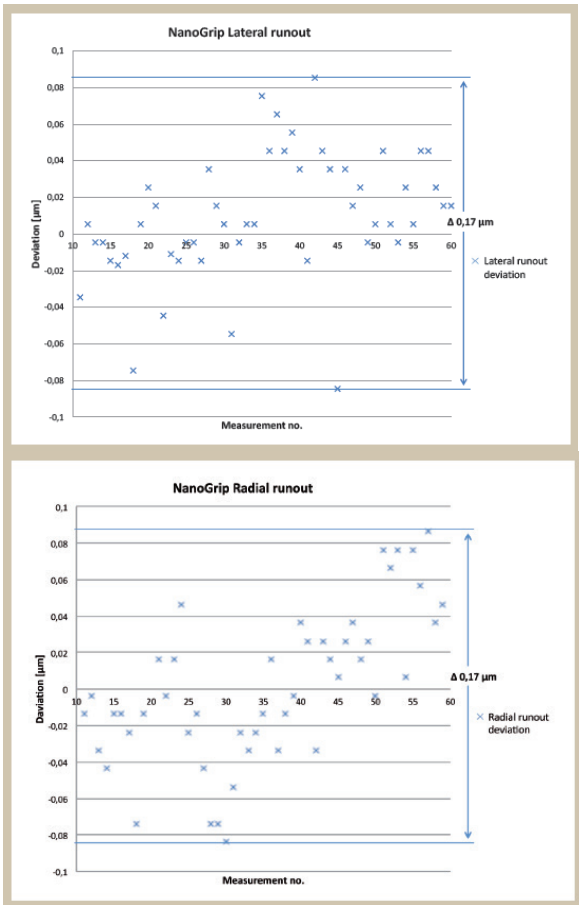

Comparative measurements have been conducted at Professional Instruments in Wisconsin. Using a Lion Precision Spindle Error Analyser measurement setup for spindle run out characterization, 8 characterizations of the run out have been conducted on an ultraprecise air bearing spindle. The probe that is used for the measurements has been attached to a Nanogrip clamping system. In between the measurements the Nanogrip system has been detached and reclamped subsequently. Figure 6 shows a picture of the setup.

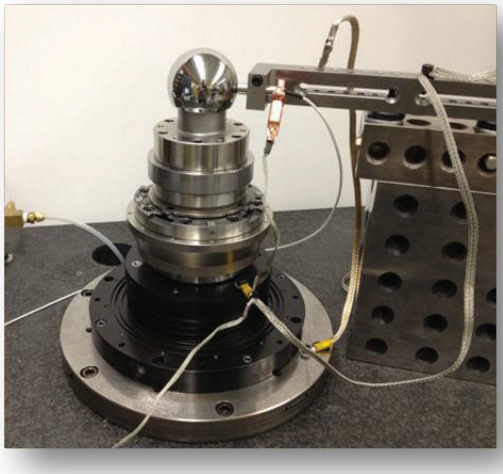

FIGURE 6. Measuring setup for comparative measurements at Professional Instruments, Wisconsin

The documentation of the results is given in Table 1. The achieved repeating accuracy with the Nanogrip clamping system could be documented to be well below 0.5 μm.

Spec/Run	2	3	4	5	6	7	8	9
TIR [nm]	342,68	396,66	472,28	155,37	210,76	212,31	139,14	159,49
SYNCH [nm]	19,43	18,36	17,72	19,10	14,88	14,72	14,25	15,42
ASYNCH [nm]	6,55	6,85	6,64	6,68	6,62	6,61	7,11	6,63
TOTAL [nm]	23,52	23,52	21,93	23,55	19,76	19,65	19,99	19,55
RPM	500	499	501	500	500	500	501	500

TABLE 1. Results of measurements with Lion Precision Spindle Error Analyser setup

Innolite's Nanogrip range enables quality to be improved and raises productivity in ultra-precision production. The key advantage is the reduction of down times on expensive ultra-system's extremely high repeating accuracy, fittings that have previously been aligned can be loaded in the machine and removed again in minutes. This added flexibility can bring considerable improvements in utilization of ultra-precision machines and enables totally new production processes to be implemented.

CONTINUOUS AND FAST MANUFACTURING TECHNIQUE OF ION-CONDUCTING CERAMIC COMPACTS WITH ORIENTED ANISOTROPIC PARTICLES

Takuma Yamauchi[1], Shota Ikeshima[1], Keisuke Nagato [1], Tetsuya Hamaguchi[1], and Masayuki Nakao[1]
[1]Department of Mechanical Engineering
The University of Tokyo
Tokyo, Japan

INTRODUCTION

The orientation of particles in ion-conducting ceramic compacts, such as solid electrolytes, sensors, and piezo elements, is an essential factor for improving their performance. When ions conduct through a ceramic, they have preferential directions of conduction depending on the crystal structure of the ceramic. When an ion conducts through β-alumina, for example, it conducts most easily in the direction normal to the c-axis. Therefore, an electrolyte made of β-alumina in which the c-axis of the particles oriented in the longitudinal direction has a high performance because cations can only be transferred between the layers on the ab-face (*Figure 1*). A technique for manufacturing ceramic compacts consisting of anisotropic particles with their c-axis oriented in longitudinal direction is required. In this study, we selected alumina particles as anisotropic particles.

There are various techniques for manufacturing ceramic compacts consisting of oriented particles such as filtering and slip-casting. However, these techniques are not suitable for manufacturing vertically long ceramic compacts or sheets. We have developed a new technique that enables us to continuously and rapidly manufacture ceramic compacts consisting of oriented particles (*Figure 2*). First, particles are rotated and oriented by the shear flow induced by a rotor. Second, they are allowed to settle and are fixed. Repeating this process by lifting up the rotor and adding slurry, vertically long ceramic compacts with oriented particles are obtained. Our group has already shown that particles are effectively oriented by the Couette flow induced by a rotor [2]. However, we only evaluated the degree of orientation from scanning electron microscopy (SEM) images of cross sections. Moreover, it took a long time to obtain a compact and the process was not continuous. In this study, we evaluated the degree of orientation by X-ray diffraction (XRD), developed a fast process by increasing the settling speed, and demonstrated the possibility of repeating the process continuously.

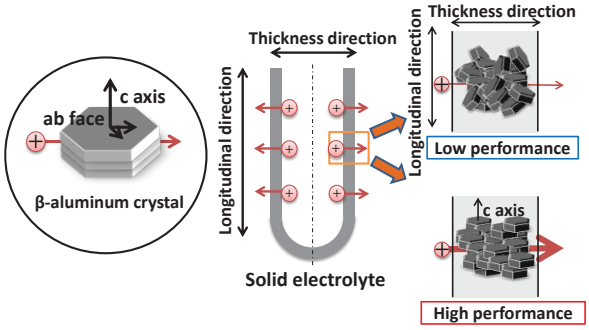

FIGURE 1. Conducting direction of Na ions in β-alumina and ideal orientation for solid electrolyte.

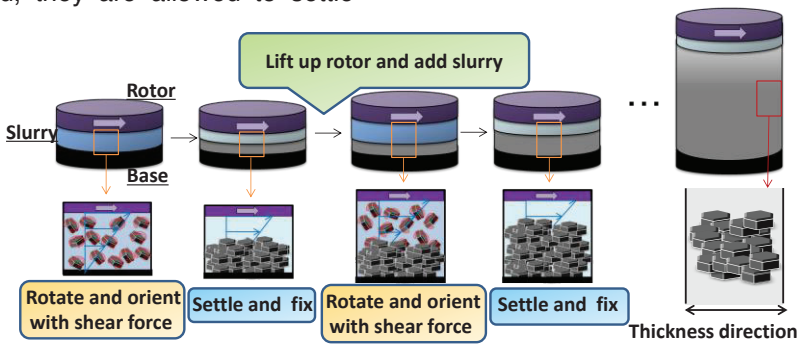

FIGURE 2. Schematic view of our technique.

EXPERIMENTAL

We used α-Al_2O_3 particles (Kinsei Matec Co., Ltd.) with a diameter of about 10 μm and a thickness of 0.3 μm that had a platelike shape.

1. Orientation of Particles by Shear Flow

We induced a Couette flow between the stationary base and the rotor. The volume fraction of particles in slurry used in this experiment was 10 vol%, 15 vol% or 20 vol%. The shear rate was 4.2 s^{-1}, 8.4 s^{-1}, or 12.6 s^{-1}. The particles settled after about 3 h treatment and a compact with a height of 1-2 mm was obtained. We evaluated the degree of orientation from the XRD spectra and SEM images of the cross sections of the compacts.

2. Increasing Settling Speed

The settling speed of particles was very low upon only applying the gravitational force in the above experiment. A centrifugal machine provided a large settling acceleration to particles in the next experiment (*Figure 3*). First, we measured the settling time upon providing a large settling acceleration without a shear flow. We used 0.5 ml of 20 vol% slurry and defined the settling time as the time at which 3 mm of solvent was observed above settled particles, whose observations were made every 5 s. The settling acceleration range was from 6.1x10 G to 6.1x10^3 G. Next, we manufactured compacts while providing a shear flow and a large settling acceleration. The slurry was 10 vol%, the shear rate was 15.7 s^{-1}, and the settling acceleration was 100 G.

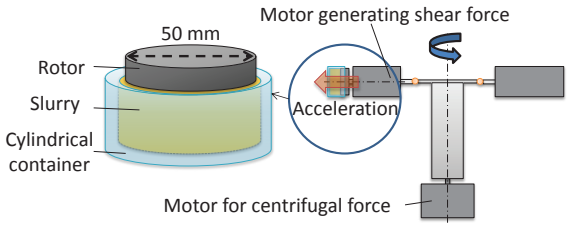

FIGURE 3. Schematic view of the experimental system.

3. Continuous Manufacturing

Continuous control of the orientation of particles is required to manufacture vertically long compacts. In the next experiment, additional slurry was poured on the settled particles after removing the solvent used in the first process, and the settling process was repeated under three different conditions: a wet condition (*Figure 4 (A)*), a dry condition (*Figure 4 (B),*) and a condition in which the slurry was solidified with a hardener (solidified with hardener condition) (*Figure 4 (C)*). Under the wet condition, additional slurry was poured on the settled particles shortly after the solvent above them was removed. Under the dry condition, additional slurry was poured on the settled particles after the solvent above them was removed and the settled particles had been allowed to dry. Under the solidified with hardener condition, a very small dose of a hardener was mixed in the slurry and additional slurry was poured after the solvent above the settled particles was removed.

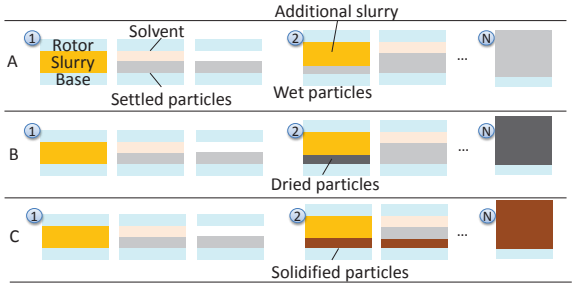

FIGURE 4. Three different conditions.

MODELING

We added two assumptions to general settling theory following Stokes' flow to discuss the settling speed more rigorously. In Stokes' flow, the terminal settling speed u_T is expressed by equation (1), where D is the particle diameter, ρ_p is the density of particles, ρ_l is the density of the liquid, g is acceleration due to gravity, and μ_l is the viscosity coefficient of the slurry.

$$u_T = \frac{D^2(\rho_p - \rho_l)g}{18\mu_l} \qquad \cdots (1)$$

One assumption is that the viscosity coefficient of the slurry $\mu_l(t)$ is proportional to the volume ratio of particles in the slurry $\lambda(t)$.

$$\mu_l(t) = a\lambda(t) \qquad (a = const) \qquad \cdots (2)$$

$\lambda(t)$ is expressed as follows, where h is the initial fluid level.

$$\lambda(t) = \frac{\lambda_0 h}{h - \int_0^t u_T(t)dt} \qquad \cdots (3)$$

The other assumption is that the total force acting on a settling particle is zero. That is, the settling speed $u(t)$ is equal to the terminal settling speed $u_T(t)$. From equations (1) through (3), the settling speed $u(t)$ is expressed as

$$u(t) = gh\frac{D^2(\rho_p - \rho_l)}{18a\lambda_0 h}\exp(-g\frac{D^2(\rho_p - \rho_l)}{18a\lambda_0 h}t) \quad \cdots(4)$$

RESULTS AND DISCUSSION

1. Orientation of Particles by Shear Flow

Figure 5 shows images of the cross sections of compacts after settling with and without a shear flow. The shear rate was 8.4 s^{-1} and the slurry was 20 vol%. Under both conditions, particles are well oriented in the area where the distance from the base is 0 mm. This is because particles are likely to settle with their ab-face parallel to the base. Particles are not well oriented in the areas where the distances from the base are 1 mm and 2 mm without a shear flow, whereas particles are well oriented in these areas with a shear flow.

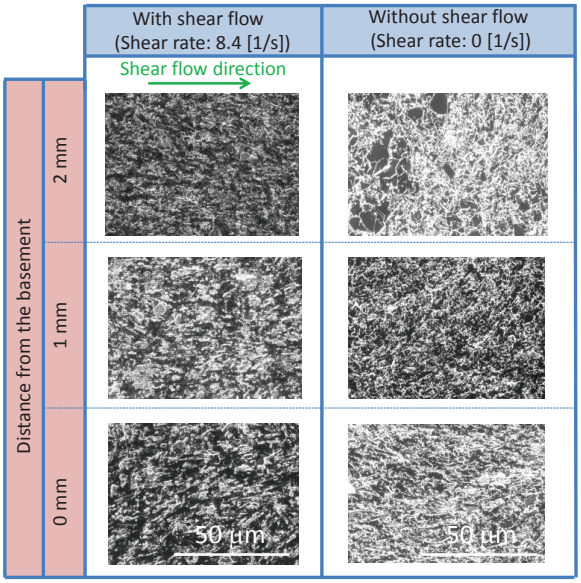

FIGURE 5. SEM images of cross sections of compacts.

Figure 6 shows the XRD spectra of the top plane of the compacts. The (1 1 9) diffraction peak is very large and the 1 1 0) diffraction peak is very small in pattern a. This shows that particles are well oriented in pattern a. On the other hand, the (1 1 9) diffraction peaks is very small and the (1 1 0) diffraction peak is very large in pattern d, which shows that the particles are not well oriented in pattern d. The particles in patterns b and c are more oriented than those in pattern d and less oriented than those in pattern a.

We defined two types of orientation degree. Orientation degree A is the ratio of the number of particles per micrometer in the X-direction to that in the Y-direction in the cross sections of the compacts. Orientation degree B is the ratio of the intensity of the (1 1 9) peak to the intensity of the (1 1 0) peak in XRD spectra.

Figure 7 shows the relationship between the two types of orientation degree and the distance from the base of the compacts. Orientation degrees A and B gradually decrease with increasing distance from base. This is because the base has a large effect on orienting the particles. Orientation degrees A and B at the shear rate of 8.4 s^{-1} are larger than those in the case of no shear flow. This shows that the particles are well oriented by the shear flow.

Figure 8 shows the relationship between the two types of orientation degree and the volume fraction of particles. The figure shows that the volume fraction does not have a large effect on the orientation degree at volume fraction of 10-20 vol%.

Figure 9 shows the relationship between the two types of orientation degree and the shear rate. Orientation degrees A and B at 4.2 s^{-1} are larger than those at 8.4 s^{-1} and 12.6 s^{-1}. This is because the rotor creates a secondary flow in the radial direction when it rotates at a high speed, and the secondary flow disturbs the orientation of the particles.

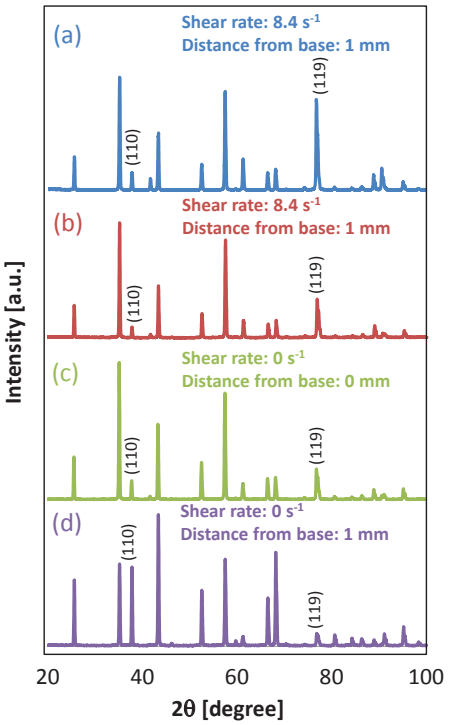

FIGURE 6. XRD spectra of the top plane of the compacts.

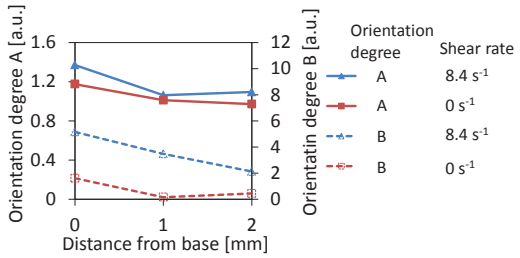

FIGURE 7. Relationship between two types of orientation degree and distance from the base.

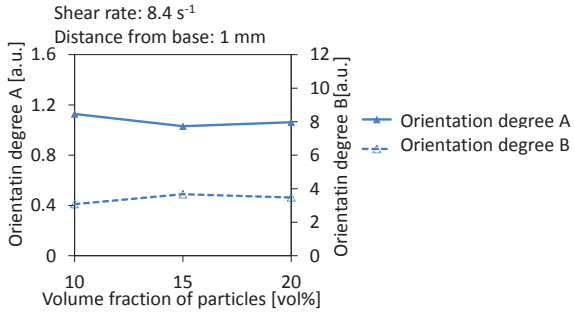

FIGURE 8. Relationship between two types of orientation degree and volume fraction of particles.

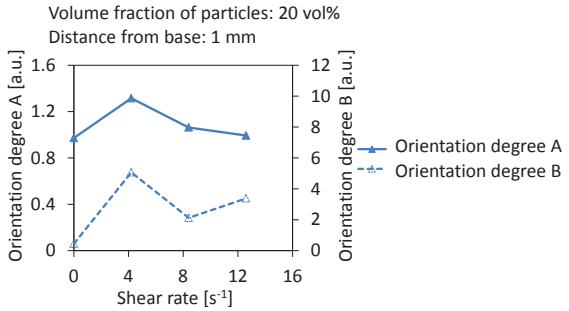
Volume fraction of particles: 20 vol%
Distance from base: 1 mm
Orientation degree A [a.u.]
Orientation degree B [a.u.]
Shear rate [s-1]
Orientation degree A
Orientation degree B

FIGURE 9. Relationship between two types of orientation degree and shear rate.

2. Increasing Settling Speed

Figure 10 shows the relationship between settling acceleration and settling time. The gradient obtained using our theory corresponds well with that of the experimental data under 100 G. The reason why our theory does not correspond well with the experimental data above 100 G is that more time was required to create a larger settling acceleration by the centrifugal machine and it was difficult to measure the exact settling time above 100 G. We obtained a compact successfully with high oriented particles in only 3 min by applying a shear force and a settling acceleration of 100 G.

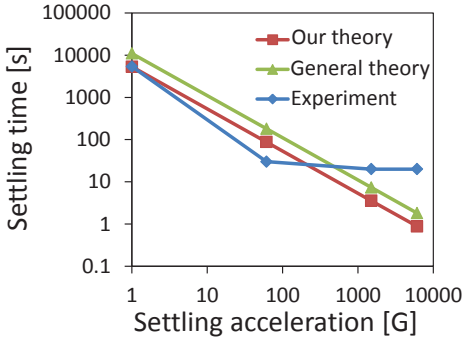

FIGURE 10. Relationship between settling acceleration and settling time.

3. Continuous Manufacturing

In a continuous manufacturing experiment that we carried out, the particles were only successfully oriented under condition C. This was because the pouring of the additional slurry destroyed the particle arrangement under conditions A and B. On the other hand, the particle arrangement was fixed sufficiently strongly not to be destroyed by the pouring of additional slurry under condition C.

CONCLUSION

We have developed a technique that enables us to continuously and rapidly manufacture ceramic compacts consisting of oriented particles by applying a shear flow. We defined two types of orientation degree. Orientation degree A is the ratio of the number of particles per micrometer in the X-direction to that in the Y-direction in the cross sections of the compacts. Orientation degree B is the ratio of the intensity of the (1 1 9) peak to the intensity of the (1 1 0) peak in XRD spectra.

Orientation degrees A and B corresponded well with each other in terms of their relationship with the experimental parameters. Particles were found to be likely to be well oriented near the base, and the volume fraction of the slurry had little effect on the orientation degree for volume fractions of 10-20 vol%. Orientation degrees A and B at a shear rate of 4.2 s^{-1} were larger than those at shear rate of 8.4 s^{-1} and 12.6 s^{-1} because the rotor creates a secondary flow that disturbs the orientation of the particles when it is rotated at a high speed to induce a large shear flow.

The settling speed became markedly increased by using a centrifugal machine to provide a large

settling acceleration. Our settling theory corresponded well with the experimental data well for acceleration of under 100 G.
We also successfully manufactured compacts continuously by repeating the settling process after removing the solvent and solidifying the settled particles with a hardener (condition C).

ACKNOWLEDGMENT
The XRD data were measured using on XRD machine, SmartLab 9kW In-plane, Rigaku Corporation, donated to the Institute of Engineering Innovation of the School of Engineering, the University of Tokyo. This study was partly supported by JSPS KAKENHI Grant Numbers 24686019, 24246027.

REFERENCES
[1] Tsuguto T, Toshihiko T, Yasuyoshi S. Piezoelectric Properties of Bismuth Layer-Structured Ferroelectric Ceramics with a Preferred Orientation Processed by the Reactive Template Grain Growth Method. Japanese Journal of Applied Physics. 1999; 38: 5553-5556.
[2] Shota I, Keisuke N, Takuma Y, Tetsuya H, Masayuki N. Orientation Control of Anisotropic Particle by Shear Force. In: Proceedings of American Society for Precision Engineering Annual Meeting. 2012; 54: 316-319.
[3] Armin D, Andreas H, Andreas R. The Origin of Anisotropic Shrinkage in Tape-Cast Green Tapes. Journal of the American Ceramic Society. 2011; 8: 1312-1319.
[4] Horn J A, Zhang S C, Selvaraj U, Messing G L. Trolier-McKinstry S. Templated Grain Growth of Textured Bismuth Titanate. Journal of the American Ceramic Society. 1999; 82: 921-926.

A 3D X-Ray Microscopy

Jing Zou[2] and Ying Xu[1]

[1]Sanying Precision Engineering Research Center, Dongying ,257000, China
[2]State Key Lab of Precision Measurement Technology and Instruments, Tianjin University, Tianjin, 300072, China

INSTRUCTIONS

In the past decades, the development of microscopy technology has had a tremendous progress. The new technologies has been continuously developed, such as various advanced optical microscopes, SEM/TEM, AFM/STM, etc., which pushes the imaging resolution from micrometer, down to nanometer, or even atomic level. However, all those microscopy technologies can only image the surface (or shallow subsurface) of the samples. A destructive method has to be used to observe the internal micro features of an object. In the paper, a new 3D X-ray microscopy (XRM) is introduced, which can provide a 3D imaging capability with sub-micron spatial resolution for observing the internal micro structures of the samples non-destructively. It provides a powerful tool for scientific research and industrial non-destructive inspection and quality control.

PRINCIPLE OF OPERATION

The imaging principle of the 3D X-Ray Microscopy is based on advanced X-ray computed tomography (CT) scanning technology. The imaging system is composed of a micro-focus X-ray source，a precision sample stage and a lens-coupled CCD detector as shown in Figure 1 and a 3D image is shown in Figure 2. The 3D image is reconstructed with a series of projection images (2D images). The sample is loaded in a rotary sample stage. As the sample stage rotates step by step, a series 2D image is collected by the detector. The CT reconstruction algorithm, filtered-back projection (FBP), requires the projection data acquired within the angular range from 0 to 2pi. Then, those projection images are used to reconstruct a 3D image which is combined by a series of slices. Next, 3D image could be viewed with our 3D Visualization Software Package. Data analysis could be operated to the 3D images for various applications.

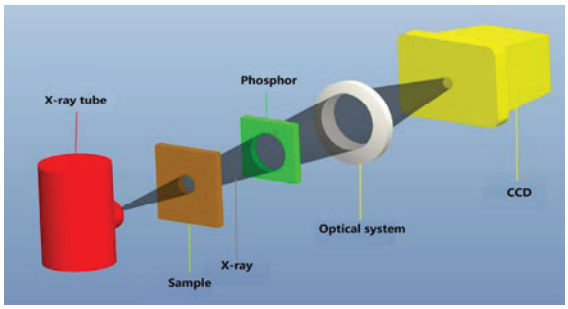

FIGURE1. Schematic of 3D X-Ray Microscopy.

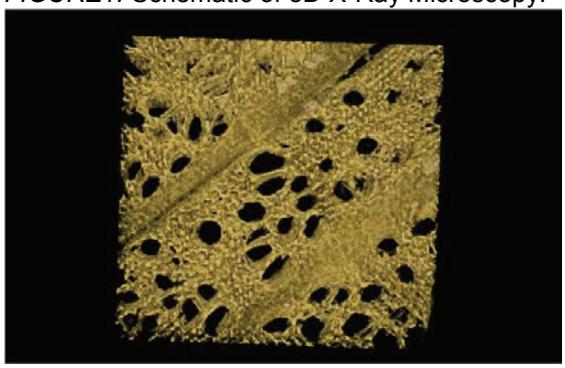

FIGURE 2. 3D image of platanus.

KEY ISSUES

1. To achieve ultra-high spatial resolution

The imaging principle of conventional micro-CT is similar to industry CT, which uses a flat panel detector to collect images. In this case, the spatial resolution of the imaging system is limited by the spot size of the X-ray source, the pixel size on the X-ray detector, and the geometric amplification of the cone-beam projection. To achieve high spatial resolution a lens-coupled detector is used in our system, which is composed of a phosphor, a lens optical system and a CCD. The spatial resolution of the 3D XRM depends on combination effects of the geometric amplification of X-ray cone beam projection and the amplification of the lens optical system. As a result, a 500nm resolution with a multi-scale imaging magnification is achieved.

2. To improve the image quality

The image quality of 3D XRM is generally defined by a few parameters and is influenced by many factors, including spatial resolution, contrast resolution, linearity, noise and artifacts [1]. There are many different types of image artifacts, including noise, beam hardening, scatter, pseudo enhancement, motion, ring and metal artifacts. A few techniques for improving the image qualities are discussed in the paper.

Beam hardening causes the edges of an object in image appearing brighter than the center, as shown in FIGURE3 (left) . Beam filtration and software correction techniques are adapted to improve the image quality. The result is shown in FIGURE3 (right).

Ring artifact is caused by the miscalibration or the defects of detector element, which results in ring artifacts at the center of the images, see FIGURE4 (left). The image is corrected with mechanical dithering and image darnming, as shown in FIGURE4 (right).

Radiant artifact is caused by the scintillation defects of the lens-coupled detector, which lead to radiant artifacts on the image, see FIGURE5 (left). Improved BSCB restore method is applied to correct the radiant artifacts, and the correction image is shown in FIGURE5 (right).

The other techniques for image enhancement and improvement are discussed as well, such as noise reduction, edge and contrast enhancement, etc, see FIGURE6 and FIGURE7.

3. To accelerate image reconstruction

Reconstruction of 3D image is very intensive in computation. So it is very time consuming for image creating. A high accuracy CT reconstruction takes about several hours when single CPU based algorithm is applied. In our system, an efficient GPU based algorithm is developed to accelerate the whole process of reconstruction, which could reduce the time consuming on data read, transfer, storage part and computation part. Now, we could reconstruct a volume image of 1024^3 with 720 projection data of 1024^2 within 5 minutes.

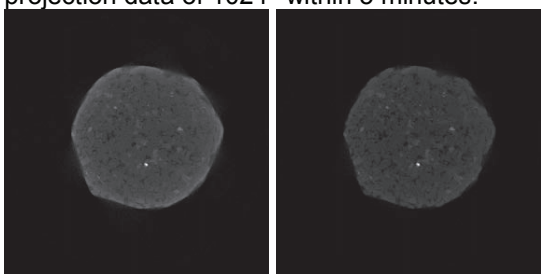

FIGURE3. Cross-section of siltstone with beam hardening effect (left) and corrected image (right).

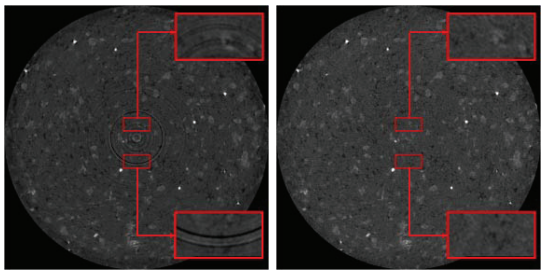

FIGURE4. Cross-section of marlstone with ring artifacts (left) and corrected image (right).

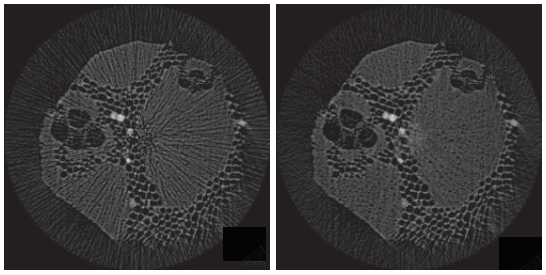

FIGURE5. Cross-section of bamboo stick with radiant artifacts (left) and corrected image (right).

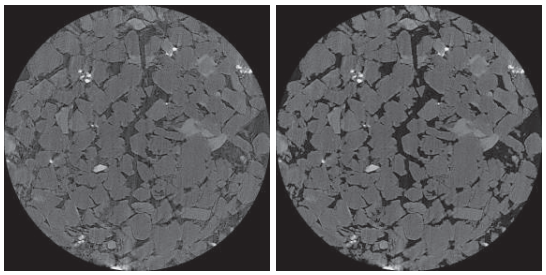

FIGURE6. Cross-section of sandstone without image enhancement (left) and with image enhancement (right).

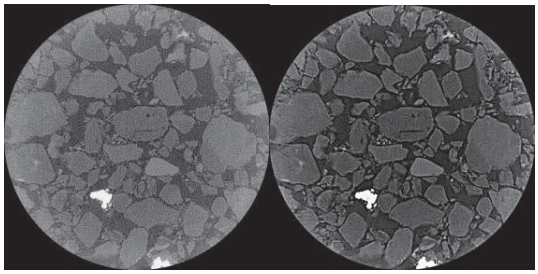

FIGURE7. Cross-section of sandstone without noise reduction (left) and with noise reduction (right).

4. To enlarge field of few of X-Ray Microscopy

The field of view(FOV) in 3D XRM is the area of scan region that is included in the image reconstruction. Normally, the larger the FOV is，the lower the resolution will be. It is desirable for a XRM to have capabilities of imaging with both large FOV and high resolution. Generally speaking, the FOV of 3D X-Ray Microscopy depends on the detector size, the zoom factor and the scanning mode.

A large size flat panel detector can be used in the system to enlarge the FOV. However, the detector is normally selected with the consideration of achieving a high resolution. Different scanning mode can be used to enlarge the FOV. With a wide sample, the well-known half-scan technique is adopted to enlarge the diameter of the horizontal FOV through offset scan. Corresponding half-scanning mode with large FOV is shown in FIGURE8 (right), .and ordinary scanning mode with standard FOV is shown in FIGURE8(left). With a tall sample, spiral scan mode and corresponding algorithm are adopted. The spiral scan mode with large vertical FOV is shown in FIGURE9 (right), and ordinary scanning mode with circular trajectory is shown in FIGURE9(left)

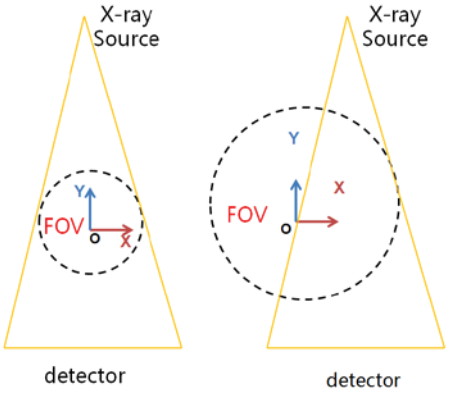

FIGURE8. Ordinary scanning mode with ordinary FOV (left) and half-scanning mode with large FOV(right).

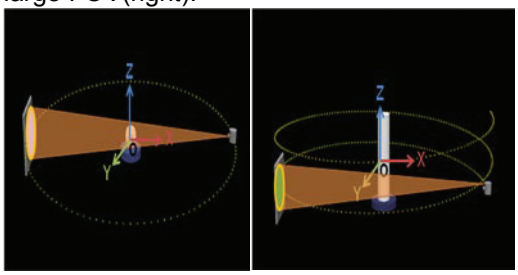

FIGURE9. Scanning mode with ordinary circular trajectory (left) and with spiral trajectory (right).

Also, a small region of interest (ROI) of a large object can be reconstructed reliably through dataset supplement techniques. Therefore, our microscopy fits for imaging various sample sizes from several millimeters to centimeters.

5. To visualize the 3D images

In a wide range of studies, it is highly desirable to visualize 3D images. Therefore , 3D visualization techniques are developed for 3D X-Ray Microscopy. A few techniques for visualize the image are discussed in the paper.

2D cross-sectional display is the most prevailing method to observe 3D data sets, probably due to its simplicity. XY, XZ, and ZY cross-sectional planes can be shown at the same time, see FIGURE10, also, arbitrary 2D cross-sectional display can be operated.

Volumetric rendering and surface rendering are two major rendering techniques, examples of them are shown in FIGURE11 and FIGURE 12.

Pseudo-color processing technique can change the gray level image to color image which is an enhancement technique that accentuates certain features that are essential for a given application. Pseudo-color image is shown in FIGURE 13(right) and original gray level image is shown in FIGURE 13(left) .

In addition, basic techniques of image processing such as interactive rotation, sliding, zooming and cutting are included in our software as well.

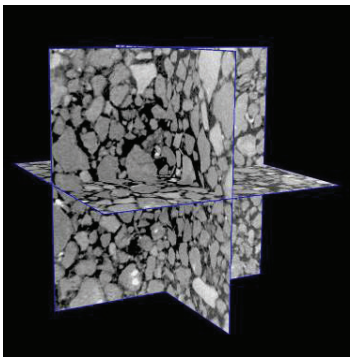

FIGURE10. XY, XZ, and ZY cross-sectional planes.

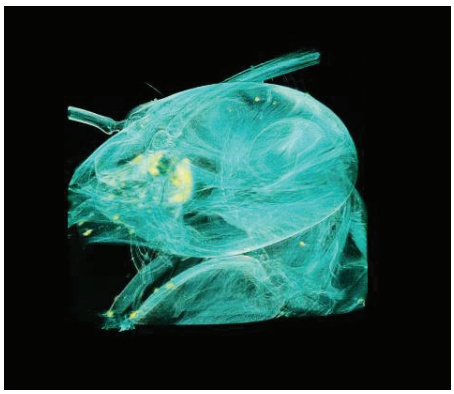

FIGURE11 . Volumetric rendering image of ant.

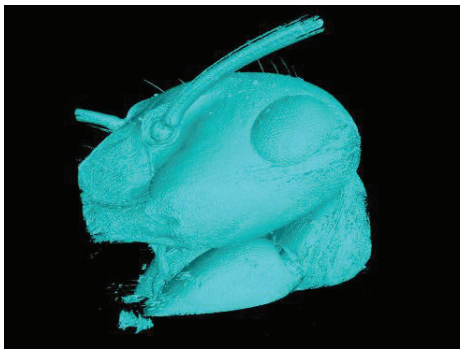

*FIGURE12.*Iso-surface rendering image of ant.

FIGURE13. Gray level image of peanut(left) and pseudo-color image of peanut(right).

Imaging results

3D X-Ray Microscopy provides a powerful tool for scientific research and industrial non-destructive inspection and quality control. It has been widely used in many application fields, such as geology/oil gas, advanced materials, life science, advanced manufacturing and failure analysis. Some typical images are shown in FIGURE14 and FIGURE15. Application analysis software is being developed to extract useful information from the 3D images. For example, in oil geology field, the digital rock analysis becomes a hot technique for oil exploring and development. The rock samples are scanned by high resolution 3D X-Ray Microscopy. The data is analyzed to provide the information of pore size and pore throat distribution in 3D dimension.

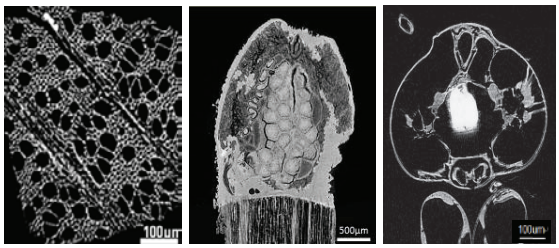

FIGURE14. Platan(left), spider(middle), ant fiber(right).

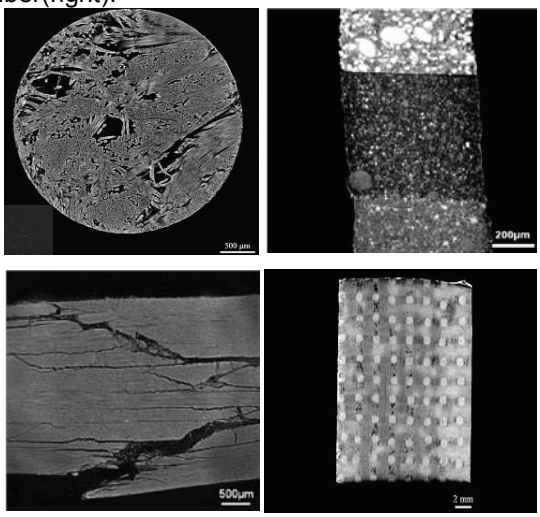

FIGURE15. Carbon-carbon material (top left), high polymer material (top right) , resin base carbon fiber material (bottom left), composite material (bottom right).

ACKNOWLEDGEMENTS

Authors would like to thank Prof Peng Zhang and his team at Capital Normal University for their technical supports in the project, Ministry of Science and Technology of China for funding the project (2011YQ030112), and National Natural Science Foundation of China (61002041).

REFERENCES

[1] Chan MF*, Yang J, Song Y, Burman C, Chan P, Li S. Evaluation of imaging performance of major image guidance systems. Biomed Imaging Interv J 2011; 7(2): e11.

SCALING AND AUTOMATING PROCESS CONTROL FOR MASS PRODUCTION VIA PROGRAMMABLE GAUGING

Dave Emmett, Jim Hill, and Denis Vasilescu
Measurement and Automation Products
Renishaw Incorporated
Hoffman Estates, Illinois

MOTIVATION

The economic forces and events in the aftermath of the 2008 recession have driven U.S. manufacturing towards greater productivity and yield. For high volume applications, incremental improvement in process control comes at the penalty of exponential capital expenditure and personnel investment.

Process capability can be measured and improved using high accuracy, high cost equipment such as coordinate measurement machines (CMMs) which do not economically scale due to low throughput and limited thermal operating range [1].

Hand and custom gauges yield scalable throughput, as they can be used in between operations quickly, and local to the machine tool. However, gauges are susceptible to operator variation which can be reduced through either highly skilled labor or automation. Automated custom gauges are only economically advantageous for rigid designs with long shelf lives [2]. In an increasingly competitive business climate, flexibility in product designs necessitates versatility in gauging.

THEORY OF OPERATION

The principle of the programmable gauge is hardware driven to gauge parts of varying designs through software. Prior attempts at flexible gauging merely retool hardware, e.g. linear differential variable transformers (LVDTs), in order to gauge a family of similar parts [1]; limited flexibility is gained at the cost of significant setup time and lost throughput. A programmable gauge differentiates itself from a retoolable gauge in that reconfiguration for completely different parts is not only possible, but also automated, which vastly reduces setup time.

The Renishaw Equator is a programmable gauge built on a parallel kinematic platform with a tactile scanning probe.

FIGURE 1. Renishaw Equator, a programmable gauge utilizing parallel kinematics.

Gauging and reconfiguration are simultaneously achieved by moving a single sensor around the part, similar to a CMM. The particular features and tolerance dimensions are programmed and operation can be totally automated. Similar to a traditional gauge, it has limited inherent volumetric accuracy, only repeatability. Accuracy is obtained by zeroing a master part's individual touch and scan points to nominal, as if each point was an LVDT in itself.

Unlike traditional gauges which are typically GO/NO-GO or Pass/Fail, quantitative dimensional reporting is readily available due to the nature of software driven inspection. By measuring a master part on a CMM, that CMM's accuracy, and thus process capability potential,

is transferred to the programmable gauge through known offsets. The process control possibilities of one single CMM can be scaled effectively through multiple programmable gauges that offer the cost, robustness, and throughput advantages of traditional gauging.

METHODOLOGY

Implementation of multiple, automated, programmable gauges into mass production lines is developed in this paper.

First, inspection routines are designed based on desired features and geometric dimensioning and tolerancing (GD&T) principles for any and all parts, and programmed into the gauges. Repeatability and reproducibility studies are conducted to validate the programs.

Master parts are then measured on a CMM, usually situated in a temperature-controlled quality room away from, or on the periphery of, the production area, for an accurate reference. The gauges inspect the master parts, and all repeatable error is common mode and can be rejected. Error may be from the gauge, from the part, or from the environment, e.g. temperature [3]. When significant thermal growth from the time of master is deemed to have occurred, the master parts are re-measured in order to obtain relevant offsets.

The programmable gauges are situated next to machine tools and turning centers for in-process metrology. Operators can hand load parts and initiate the gauge through a one-click software button. Alternatively, a work cell can be entirely automated such that parts are loaded and unloaded between machine tools, gauges, and conveyors using robots, and the gauge results are fed back for tool offsets in order to maintain process control [4].

COST ANALYSIS

With the development of new production lines comes the cost of scaling quality to meet production.

In one case study [5], connecting rod manufacturer Kishan Auto Parts Pvt. Ltd. had 360 part variants produced. In-process inspection was done through a set of four air gauges per size range. The average cost per set of gauges to inspect a part was $6,480.

Air gauges can only accommodate a small range of feature size variation, and so does not scale well across a part family with large part variation. Programmable gauges were implemented that could measure 77 of the 360 part variants, eliminating the need for $450,000 of air gauges, at a capital cost reduction of 80%.

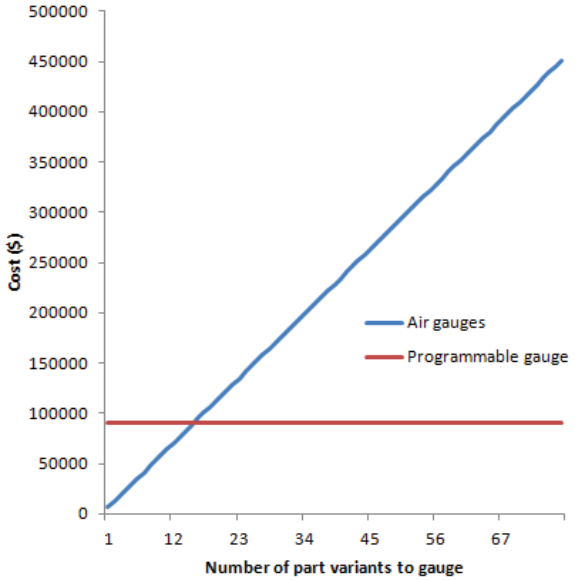

FIGURE 2. Chart of gauging capital costs at Kishan Auto Parts, with air gauges scaling linearly with part variants and programmable gauges as a fixed cost.

If a conventional gauge cannot accommodate a significant number of part variants, the gauging capital costs will linearly scale with the number of variants, whereas programmable gauges are a fixed cost that only need multiply for additional throughput, not for incremental part design differences or changes.

In a second case study [6], the cost of reconfiguring and requalifying a gauge in order to accommodate a design change was quantified. Meyer Tool estimated a design change will result in a gauge change cost of $3,000-$10,000.

This cost applies to over 100 hard gauges at the facility, each costing $10,000-$20,000. Thus it is not just the capital costs that scale linearly with part variants but also the recurring costs of recertification, as well as some non-recurring costs such as design changes.

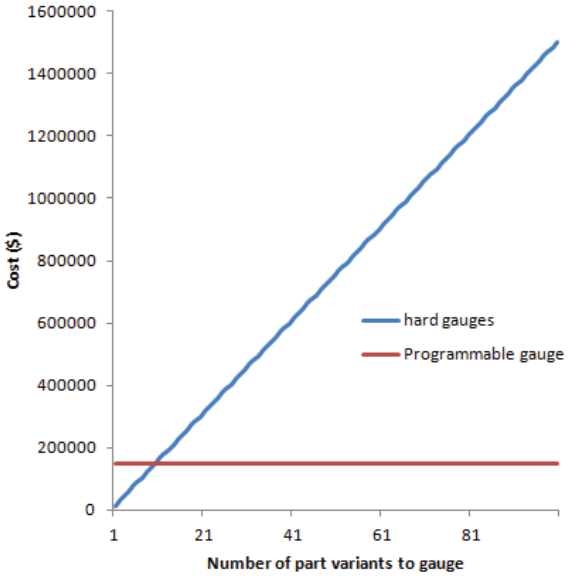

FIGURE 3. Chart of gauging capital costs at Meyer Tool, with hard gauges scaling linearly with part variants and programmable gauges as a fixed cost.

A third case study [7] examined programmable gauges in a fully automated work cell with a dual spindle lathe at Conroe Machine. The total capital cost for an unattended cell containing an Okuma twin-spindle 2SP-250 lathe, a Fanuc robot, two Renishaw Equator programmable gauges, tool compensation software, and packaging automation paid itself off in 18 days of production.

THROUGHPUT

The other factor that is traditionally difficult to scale for further production is throughput. Measurement speed, loading speed, prep time, operator error and operator fatigue are all factors that impact throughput.

In the Kishan Auto Parts case study, the use of air gauges for all the desired features took on average 8 minutes per part, partially due to multiple manual setups. The programmable gauge requires one single loading maneuver and the alignment is done by direct computer control. Total operating time of the programmable gauge was 55 seconds; over 90% time savings compared to the air gauge method.

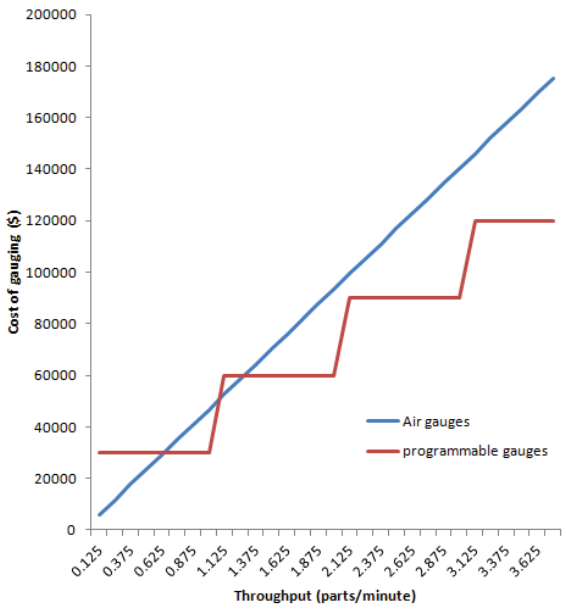

FIGURE 4. Air gauge capital costs outpace those of programmable gauges at higher throughput costs at Kishan Auto Parts.

When compared to a CMM, a programmable gauge can deliver fast measurement speeds without metrology penalty. Although they can be run at fast speeds, CMMs are typically run at conservative speeds for optimal metrology. However, when they are run for optimal throughput the time savings have been shown to be only as much as 27% [8] without statistically significant impact on metrology. For the manufacturing engineer looking to upgrade his process check to a modern shop floor CMM, he may not be able to take advantage of the machine's full speed capability without sacrificing repeatability.

Like all gauges, programmable gauges operate on a principle of comparison to a reference for accuracy; it need only be inherently precise. Dynamic errors associated with high measurement speeds are, by and large, repeatable errors, and are compensated for through the mastering of the gauge, just like thermal error or machine error. In the case of the Renishaw Equator, the programmable gauge has been run as fast as 300 mm/sec positional speed, 300 mm/sec scanning speed, 7 mm/sec touch trigger speed with a 2 mm approach distance, while maintaining the machine repeatability specification of +/- 0.002 mm.

TABLE 1. Measurement range results for a 30 runoff study, on a set of circle features scanned at 300 mm/sec, for a single part re-fixtured using the Renishaw Equator programmable gauge.

Size (mm)	Type	Range (mm)
110	Outer	0.0041
80	Inner	0.0036
80	Inner	0.0037
80	Inner	0.0042
68	Inner	0.0024
68	Inner	0.0035
106.5	Outer	0.0038
110	Outer	0.0027
80	Inner	0.0024
80	Inner	0.0031
80	Inner	0.0030
68	Inner	0.0036
68	Inner	0.0034
106.5	Outer	0.0037

In addition to the measurement time, there are human factors that can throttle the scalability of new production. There are additional personnel and labor costs, but there are less tangible elements such as operator fatigue with manual gauges. In the Conroe case study, previous process checks with gauges and hand instruments were limited by operators producing more measurement errors with additional throughput until the programmable gauge allowed for a completely automated process check.

FIGURE 5. Automated work cell at Conroe with two Renishaw Equator gauges allowing for increased throughput without additional operator fatigue.

SUMMARY

Programmable gauges open new possibilities of process control by offering the versatility and depth of integration of a CMM with the throughput and shop floor robustness of a traditional gauge. The combination of these features allow for both scalability and automation that are necessary for significant productivity and profitability gains in mass production lines.

REFERENCES

[1] Morey, B. The Ins and Outs of In-Line Automated Inspection. Manufacturing Engineering, 2012; 149.1: 97-108.

[2] O'Rourke, K. Versatile Gaging. Quality. 2011; 50.5: 22-23.

[3] Dhokia V, Newman S, Zhu Z, Shokrani A. A Novel Method for Rapid Inspection and Verification. Proceedings of the 11th euspen International Conference. 2011; 340-343.

[4] Allcock, A. Without comparison. Machinery. 2011; 169.4187: 30-32.

[5] "Case story - Kishan Auto - Gauging time and costs cut by 80% and accuracy maintained despite a 21°C range" Renishaw.com. Renishaw PLC, n.d. Web. 1 Aug 2013.

[6] "Case story - Meyer Tool - Aero-engine component maker Meyer Tool "softens" up hard gauge costs with software-driven Equator™ gauge" Renishaw.com. Renishaw PLC, n.d. Web. 1 Aug 2013.

[7] "Equator™ programmable gauges help create the ultimate automation cell for bearing machining and parts sorting" Renishaw.com. Renishaw PLC, n.d. Web. 1 Aug 2013.

[8] Jones, S, Ulsoy A. "An optimization strategy for maximizing coordinate measuring machine productivity. II: Problem formulation, solution, and experimental results" Journal of Engineering for Industry. 1995; 117.4: 610-618

Stable and Precise Mass Production of Milling Parts in Changing Environment Conditions

Matthias Fritz[1] and Dennis Janitza[1]
[1]Research & Development
KERN Microtechnic GmbH
Eschenlohe, Germany

INTRODUCTION

Over the last couple of years the necessity of mass produced high precision milling parts has been constantly increased. These parts are needed in the optical industries, the watchmaking industries, automotive industries, etc.

But transferring the well established processes from laboratories and universities to the industry has been proven to be difficult due to two main reasons. First there are significantly worse environmental conditions in mass production workshops and second the requirements in terms of productivity and cycle times are a lot higher within the industrial enterprises.

ABSTRACT

Concentrating on these two challenges this paper describes an approach to set up a machine tool for a productive, stable and precise mass production.

In the first part of this paper the barriers to transfer the processes form the laboratories to the industry are named and the resulting additional requirement are listed.
The second part deals with the solutions to these problems. The focus is on a new approach to ensure the thermal stability of machine tools.

LIMITING FACTORS IN THE INDUSTRIAL PRODUCTION

There is an enormous pressure in the industrial production to increase the productivity and to decrease the costs. Therefore the business companies try to optimize the run duration of their machine tools. Simultaneously they try to reduce their labor costs. The result is highly automated equipment. A weekly run duration greater than 140 h is an industrial standard. The equipment is operated by only one operator and runs most of the time self-sustaining. At industrial used machine tools the following features are automated: tool change, workpiece change, tool check, tool measurement, disposal of chips and cooling liquid conditioning. The business companies use their equipment very flexible and universal. Different products are fully machined on one machine. The machines are used for roughing and finishing, resulting in a wide range of requirements.
The industrial workshops are often insufficiently air-conditioned. Furthermore daylight shines into the workshops to improve the working conditions for the employees. The resulting environmental conditions are challenging for the machine tool, as they are changing depending on the weather and the daytime.
Another limiting factor is a shortage of skilled employees. The companies have problems to find well educated operators for their expensive and sensitive equipment. According to the demographic trend, this shortage will increase in the industrialized countries

REQUIREMENTS

The requirements for an industrial surrounding are listed in this chapter.

1. The tool holders and the interface to the spindle are standardized in DIN 69893-5 [4] hollow taper shanks or short HSK-E. These are the tool holders for high speed cutting (HSC). For high precision parts the tool change accuracy has to be better than 0.5 μm (circa 2×10^{-5} inch).
2. Due to the skills shortage the machine tool has to be robust against misuse, e.g. collision prevention systems.
3. The chip disposal system has to be automated.
4. The temperature of the cooling liquid has to be controlled in a range smaller than 0.5 K.
5. The tool check and the tool measurement have to be integrated in the machine tool and have to work under the environmental conditions in the working chamber.
6. The spindle must supply a high torque for the roughing as well as high speed and low vibrations for the finish.

7. The machine frame has to be robust against changing environmental temperatures and heat radiation.
8. The machine has to be fast to reach short cycle times.

SOLUTIONS IN KERN MACHINE TOOLS

Tool Changing Accuracy

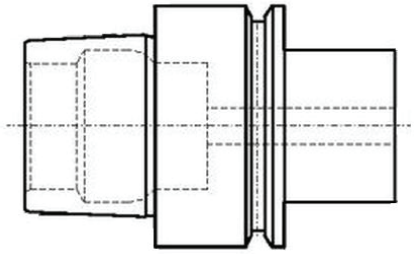

FIGURE 1. Tool holder HSK-E

The established tool holder system for high speed cutting is the HSK-E. The repeat accuracy in the axial direction is smaller than 0.5 μm. This is sufficient for most applications. A problem is the radial runout error. The taper in the spindle and the tool holder have a radial runout error. The angular position between holder and spindle is not fixed. At every tool change there is a recombination of both runout errors under different angular positions, see figure 2.

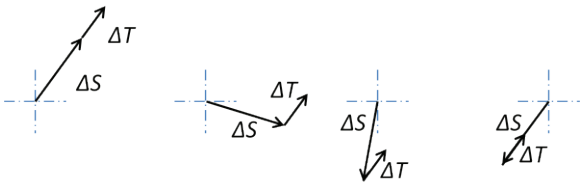

FIGURE 2. Vector addition of radial runout

The result is a change of the actual tool diameter of $2 \cdot \Delta T$. KERN has developed an orientated system which is compatible with the established HSK-E system. With such a system it is possible to keep the runout error of the tool constant.

Robustness against Misuse

The worst misuse might result in a machine crash, the collision between two structure parts of the machine tool. KERN uses a collision monitoring system, which uses a geometric model of the machine tool that checks every NC command line for collision and intervenes before the collision happens.

Automated Chip Disposal

The working chamber of the machine tool is designed in a way that all the chips fall down in the chips disposal. There are no corners where the chips can gather. A compromise is made between the fall of the chips and the abbe error of the machine axis. For the outlet belt it is possible to use commercially available systems. The cooling liquid flows from the outlet belt to the cooling liquid conditioning system. This unit is able to heat and cool the liquid. The high precision temperature management keeps the temperature constant in a range of 0.4 K.

Spindle Technology

In the machine tools of KERN high frequency spindles with a power of 15 kW and a revolution speed of 42 000 rpm are used. These spindles are suitable for high torque roughing tasks in harde~~ned~~ steel and also for fine surface finishing with optical quality. Thus, the spindle meets a wide range of demands. The thermal displacement of the tool is not only controlled by the temperature management system, there is also a model-based compensation for the axial displacement.

Thermal Errors

This point is the focus of the paper. Bryan [1] and Weck [2] claim that up to 70% of today's errors on machined parts are due to thermal effects within and outside of the machine tool, the spindle, the workpieces, the cooling liquid, etc.

As stated above, the environmental conditions in industrial tool shops are changing due to thermal disturbances from other machines and a badly or none-existing air-condition. Combining these two facts, the importance of a thermal stabilization of the used machine tool falls immediately into place. Bryan [1] presented in his work the thermal effect diagram, see figure 3. The diagram shows the factors of influence and their effects of the thermal error. Uniform and non-uniform are treated separately. In experiments at KERN it could be shown that, especially at long and slim structures, the influence of non-uniform temperature changes is much higher than the uniform temperature changes.

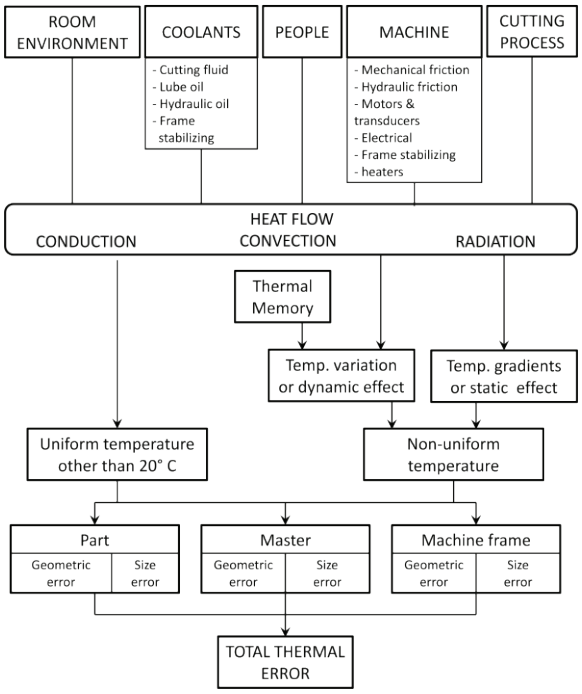

FIGURE 3. Thermal Effect Diagram, Byan [1]

Based on this knowledge Fritz [3] has shown a radical new approach for a machine tool design in order to increase machine dynamics and at the same time decrease thermal errors due to changing conditions. Designing “fast” thermal assemblies with low thermal capacity and high thermal conductivity leads to lightweight constructions with a very short thermal response time. This machine design is based on the following four principals:

- Avoidance of temperature gradients – uniform temperature
- Keeping the uniform temperature constant
- Dissipate the heat where it origins
- Using a closed loop temperature management system

The resulting, dynamic system is characterized by short warm-up cycles and a thermal stable machine frame even in changing environmental conditions.

By actually applying the new design principal to a milling machine tool, it could be shown, that the errors due to thermal influences could be significantly reduced. This leads to two major advantages:

1) The total amount of production uncertainty could be reduced.
2) Stabilization of the process could be achieved.

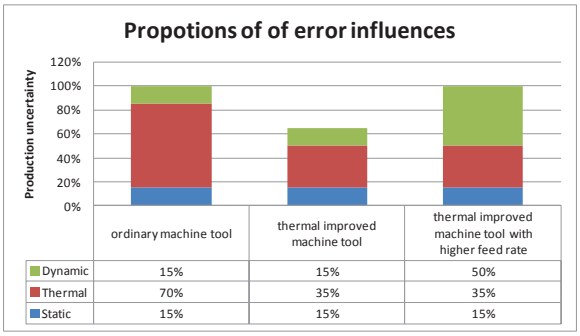

FIGURE 4. Production uncertainty as the summation of different error influences

Why are those two points so important? The key factor to a stable and precise mass production is a reliable and repeatable process. As it is not affordable to do a 100% quality control in mass production, statistical methods are used to ensure the product quality even further reducing the small tolerances of precision parts.

Figure 4 illustrates the advantages of thermal improved machine tool. By reducing the production uncertainty due to thermal effects, a production potential is created that can be used in three different ways:

1) To produce parts with a smaller tolerance in the same quality as before.
2) To increase the c_{pk} - values of the production process in order to reduce quality assurance costs and waste.
3) Increase productivity through higher feed rates, while producing parts in the same quality as before.

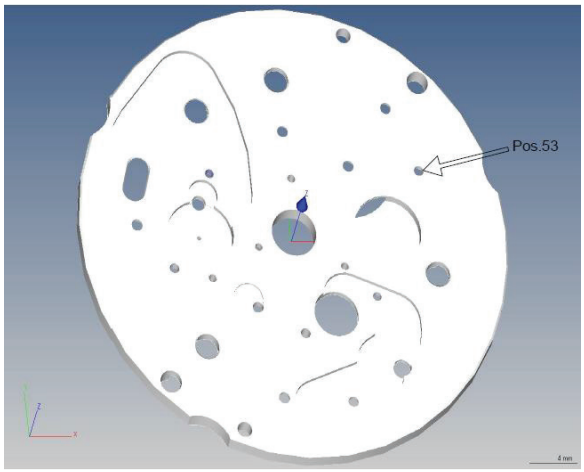

FIGURE 5. Milling part with small tolerances in the positioning of drill holes

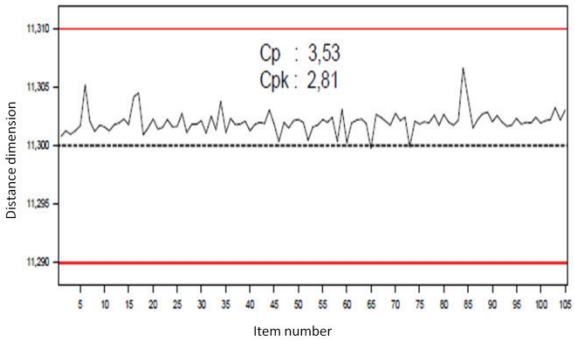

FIGURE 6. c_{pk} - value of the x – position of drill hole #53

Figure 5 and 6 show a typical mass production milling part from the watch industry and a corresponding c_{pk} - value. It can be seen that the used KERN machine tool is capable of achieving c_{pk} - values higher than 2.5 at a tolerance of +/ 10 μm. Industrial standards normally require values between 1.33 and 1.66 so that there is still a high potential for increasing productivity by increasing accelerations and feed rates.

CONCLUSION

This paper deals with the requirements and challenges of transferring laboratory results in machining high precision parts to industrialized processes. Several solutions for these challenges have been presented, having a special focus on the thermal and dynamic behavior of the machine tool. The developed approaches and concepts have been applied to an industrialized series machine tool, consisting of a thermal stable machine frames with a high dynamic capability.

REFERENCES

[1] Bryan J. International status of thermal error research. Annals of the CIRP. 1990.

[2] Weck M, McKeown P, Bonse R. Reduction and compensation of thermal errors in machine tools. Annals of the CIRP. 1995.

[3] Fritz M, Janitza D. A new approach on reducing thermal impacts on high precision machine tools. euspen 12th international conference. 2013.

[4] DIN 69893-5, Kegel-Hohlschäfte mit Plan-anlage, Deutsches Institut für Normung e.V., Berlin, 2006

SUPER-PRECISION TURNING CENTER: HIGH ACCURACY, HARD TURNING, MULTI-TOOL MACHINE TOOL

Emmanuil Kushnir
Hardinge Inc., Elmira, NY, USA

INTRODUCTION

Modern CNC machine tools which use conventional machine elements such as: linear guides, ball screws, and casted structural members - have been steadily improving in the last few decades. Future progress in the accuracy and productivity can be achieved with properly developed design, analysis and manufacturing considered as one continuous process. For example, in the case of turning centers, this approach allows to increase accuracy of a general purpose (GP) machine and close the gap between conventional turning operations and higher precision processes like diamond turning and grinding. Developed by Hardinge Inc super precision (SP) and specially calibrated (SP^2), turning centers can partially substitute or work in synergy with grinding and diamond turning machines (See Fig. 1).

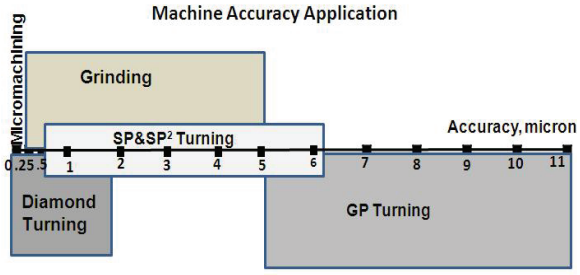

FIGURE 1. Area of manufacturing application of Super Precision Turning Center.

MACHINE TOOL STRUCTURE MODEL DEVELOPMENT

The main functional process performed by the machine tool is the form-shaping process (FSP), which is aimed at form-shaping the surfaces on the part to be machined. Physical implementation of the form-shaping process by the machine tool is carried out by form-shaping system (FSS). The FSS is referred to [1,2] as an ordered aggregate of mechanical components (FSS links), the mutual movements and relative positions of which ensure the specified trajectory of the cutting tool (CT) motion with respect to the workpiece. The FSS theory is used to investigate interrelationships between, geometry & kinematics of the machine tool and, geometry& metrology of the machined part. The basic principles of the FSS theory, its mathematical technique, and applications, are formulated in work [2]. Two well established concepts are applied in this theory: (a) design application of homogeneous vectors and 4 x 4 transformation matrices [3] are used to describe the FSS nominal functions and (b) the terms of spatial errors [4], quasi static errors, and error budgets [5] are used to describe machine accuracy problems.

As it is described in [1], form-shaping function (FSF) is constructed to connect the nominal coordinates of the active points of the CT and motion parameters $q_i (i = 1,..., l)$, with coordinates of the points on the machined surface (MS):

$$\bar{r}_0 = A_{0,l}(q_1, q_2, ..., q_l)\bar{r}_l \qquad (1)$$

where $\bar{r}_0 = (x_0, y_0, z_0)^T$ and $\bar{r}_l = (x_l, y_l, z_l)^T$ are the position vectors of the CT points in two coordinate systems associated with the MS and the CT, respectively; l is the number of the motion drives for the FSS links; $A_{0,l}$ is the 4x4 matrix of coordinate transformation. The vector $\bar{r}_l$ consists of m arguments depending on the dimensionality of the set of active points (SAP) of the CT: m = 0, 1 or 2 if the SAP is the point, line or surface, respectively. Therefore, the form-shaping function (1) comprises $l + m$ arguments, i.e., $\bar{r}_0 = \bar{r}_0(q_1, q_2, ..., q_{l+m})$. The process of the MS processing can be formally interpreted as a mathematical transformation of the equation (1) into the two-parameter position vector of the MS:

$$\bar{r} = \bar{r}(u, v) \text{ , with } \bar{r}_u \times \bar{r}_v \neq 0 \text{ ,} \qquad (2)$$

where u and v are the coordinates of the point of the MS.

Matrix $A_{0,l}$ in Eq. (1) may be represented as a product:

$$A_{0,l} = \prod_{i=1}^{n} A_{i-1,i} \qquad (3)$$

where $n \le l$ is the number of movable links within the FSS; $A_{i-1,i}$ is the 4 x 4 matrix describing the motion of the i-th link with respect to the $(i-1)$-th link. Depending on the value n, the FSS may have two configurations:

-the chain-type FSS when $n = l$. It is the most used and most-known structure in machine tools when its kinematic motion is considered. In this case, product (3) consists of l one-parametric matrices $A_{i-1,i}(q_i)$, where $i = 1,2,...,l$. As known, these factor matrices are of the specific kind: they are either matrix of translation along or matrix of rotations around the coordinate axes.

-the parallel-type FSS when $n < l$. This type of the FSS consists the link(s) with $1 \le N_i \le 6$ degrees of freedom in motion relative to a neighboring link, i.e., the corresponding factor-matrix in product (3) depends on N_i parameters, where $\sum N_i = l$. In general, link i may have more than 1 degree of freedom relative to link $(i-1)$. An example of the FSS having a link with $N_i = 6$ is the hexapod-type machine tool. Another important example is a joint with elastic constraints between the links.

FSF AND MACHINE STRUCTURE DYNAMICS

The form-shaping function was developed to described geometry and kinematics of the machine tool and used to estimate errors of machined part defined by accuracy of the machine components and form shaping process. It may be shown that FSF may be used as a basis to develop equations that will provide a description of the static and dynamic behavior of the machine during cutting or set up motion [6].

The cutting surface, i.e. the surface upon which instantaneous contact of the cutting edge or cutting tool surface with machined material take place in certain moment of time T_0, may be described by radius vector $\bar{r}_{cut}$, which can be found from FSF (1) by substituting into it the appropriate expressions $q_i = q_i(\tau)$, which are depending upon current time τ. As result we obtain:

$$\bar{r}_0 = \bar{r}_{cut}(u,\tau) \qquad (4)$$

-in form shaping with a edge tool, or

$$\bar{r}_0 = \bar{r}_{cut}(u,v,\tau) \qquad (4')$$

- in form shaping with a surface.

From the stand point of theoretical mechanics, the equation (4 or 4') is describing motion of a mechanical system. Since this equation explicitly depends on time, the FSF describes the motion of rheonomous mechanical system for which full variation in any given moment of time T_0:

$$d\bar{r}_0 = \left(\sum_{\mu=1}^{6} \partial\bar{r}_0 \Big/ \partial q_i \Big|_{\tau=T_0} dq_i^{\mu} + \partial\bar{r}_0 \Big/ \partial\tau \Big|_{q_i^{\mu}=q_0} d\tau \right) \qquad (5)$$

where q_i^{μ} (I =1,2,…,I) independent variables by 6 (μ= x, y, z, α, γ, β) in each of the selected local coordinate systems); $d\bar{r}_0 = (dx_0, dy_0, dz_0)$ - differential of radius vector $\bar{r}_0$.

The differential of radius vector $d\bar{r}_0$ may be written in the following form [6]:

$$d\bar{r}_0 = \sum_{i=1}^{l} G_i d\bar{R}_i + \sum_{i=1}^{l} \bar{V}_i d\tau \qquad (6),$$

where: $G_i = \left(A_{0,i-1} D_i^x A_{i,l} \bar{r}_l, ..., A_{0,i-1} D_i^{\gamma} A_{i,l} \bar{r}_l \right)$ - transfer function that is represented by a matrix that transfers displacement in joint i to the cutting zone;

$\bar{V}_i = \dot{q}_i A_{0,i-1} D_i^{\mu} A_{i,l} \bar{r}_l$ - the derivative of time in each moving (mobile) joint, reduced to the cutting zone;

D_i^{μ} - matrix of partial derivatives with respect to the independent variables in each joint [2];

$\dot{q}_i = dq_i / d\tau$ - velocity in the i-th joint

$d\bar{R}_i = (dx_i, dy_i, dz_i, d\alpha_i, d\beta_i, d\gamma_i)^T$ - vector that defines small displacement (dx, dy, dz) and small rotations $(d\alpha, d\beta, d\gamma)$ of the i-th system of coordinate relative to $(i-1)$-th.

Here and below, in the differential relations matrices with omitted 4 (zero) line are used.

Since the number of moving joints is less than l, some of $\bar{V}_i = 0$. Irrespective of this, for convenient writing of the equations, we shall consider all $\bar{V}_i$ $(i = 1,2,...,l)$ to be determined.

The equation (6) expresses the differential relations between the variations in the cutting

zone $d\overline{r}_0$ and the variations of the links relative to each other in the joints $d\overline{R}_i$, with consideration for the velocity error (positioning error). The coefficients of the differentials (transfer coefficients or influencing factors) are functions of the machine tool arrangement and adopted form-shaping laws, i.e. the laws of displacements in the moving joints.

To write down the complete system of the equations of machine tool motion, it is necessary to determine method of calculation of the variations $d\overline{R}_i$ in the generalized joints. In each generalized joint the variations are determined by different factors, including the geometric errors of the joint, the forces causing the contact deformations, kinematic perturbations, etc. It is shown in [2] that the variations of the link, mounted, for example, on the elastic supports which, in turn, have the errors of position relative to the nominal value under the action of the system of the forces applied to the link, may be determined from the following formula:

$$d\overline{R}_i = W_i d\overline{F}_i \qquad (7)$$

The matrix W_i can be real (when solving static problems) or complex (when solving dynamic problems). When solving static problems, the W_i matrix can be, for example, calculated in terms of the compliance matrix of the generalized joint. A variation of load $d\overline{F}_i$ is a vector made up of the differentials of components of the principal moment of the forces acting on the link.

In the form-shaping process, the metal removal occurs and is accompanied by the changes of the cutting force. The change of the cutting force $\overline{P}$ is connected with the change of the relative position of the tool and workpiece by the following relations [7]:

$$d\overline{P} = W_{cut} d\overline{r}_0 \qquad (8)$$

In a general case, W_{cut} is the dynamic characteristic of the cutting process depending on the differential of radius vector of the point of application of the cutting force. It is shown in [7] that W_{cut} can be obtained on the basis of the form-shaping function with the given dependence of the cutting force on the geometrical and kinematic parameters of the cutting process.

Equations (6), (7), and (8) form a complete system of equations of motion of the machine tool as a processing machine relative to the nominal form-shaping motion executed by one cutting element with consideration for the action of the dynamic component of the cutting force, i.e. the working process.

INITIAL STAGE OF TURNING CENTER DESIGN

The equation (6) was obtained at the base of FSF that usually includes moving components of the machine tool, because its goal was to describe kinematic motion of the mechanical system required to produce a certain surface. This approach does not put any limitation on the presentation of FSS links. For example, every movable FSS link may be represented by any number of nonmoving links. These links may be connected the same way that their parent links. It means that FSS may have as many links (or physical) components as it is desired to solve a particular problem. The additive character of the equation (6) allows for an increase or decrease of the machine tool model complexity as it is needed.

At the earlier stage of design of a machine tool, information about its components is uncertain and consists only from general dimensions of the major components, which means that equation (6) shall include just a small number of major components. This limited model will quickly produce results that may be used for a comparison of different layouts of the machine tool and define general requirements and limitations for structure components [8].

For simplicity let's consider only compliance in the X direction (the main direction) for turning operations. Then the equation (6) will include only compliance of these MT components:

G1-spindle, G2- base, G3 – Z axis slide with guides, G4 - X-axis slide with guides, G5 - turret, G6- topplate and coupling, G7-y-axis slide. With simple uniform distribution of compliance in the cutting zone between major structural assemblies, the following compliance distribution (in %) may be considered as starting point: spindle and base assembly -20 %(10%-spindle (headstock), 10%- base); Z axis assembly (slide with guides) -20%; X-axis slide with guides and ball screw-30%; turret, topplate and coupling -15%,Y-axis slide -15%.

Comparison with experimental data for turning centers (Table 1) shows that major components have similar contribution in machines which are considered successful designs.

When machine components are developed to a finer stage, then FEA is used for evaluation of static and dynamic characteristics of the machine tool.

TABLE 1. Contribution of major machine components in turning centers compliance (%).

Components	Theory	Test Data
Spindle	10%	7-11%
Base	10%	8-12%
Z axis assembly	20%	18-27%
X axis assembly (Slide, Linear guides, Ball screw)	30%	25-35%
Turret, Topplate, Coupling	15%	10-13%
Y axis slide	15%	10-15%

SP TURNING CENTER DESIGN

Requirements for the SP turning center design include:

- high accuracy (which means high stiffness), this requirement is very important because SP machines close the accuracy gap between general precision turning machines and diamond turning and at the same time bring turning accuracy in the range usually covered by grinding machine tools. High rigidity is also a necessity for hard turning operations (machining materials with hardness of 55-66 RC, which usually are machined by grinders).
- multi-tool and live tooling capabilities (turret type tooling system) for high productivity;
- Y axis capabilities (to perform off center machining);
- high metal removal rates, and effective chip removal.
- small footprint required for efficient use of customer floor space.

Distances between the X and Z axis rails, slides dimensions, linear ball trucks size, ball screw dimensions, etc. are optimized to provide the required static stiffness and geometrical accuracy of X and Z slides in the cutting point. The optimization process is based at distribution of a lathe's total compliance between its major components (Table1). The compliance of the structure and optimization of components was computed by Excel, based on the above theoretical approach.

The need for multitasking prevents traditional lathe designs from satisfying modern requirements. Contemporary lathes should perform not only turning and drilling operations, but also milling, polygon milling, off center drilling, etc. These operations require not only live tooling but also additional axis movements. This means that a slide has to be added to the structure most often in a direction tangential to the circular turning surface (in Y direction). The addition of an extra slide to a traditional lathe design was done by a slide orthogonal to the X and Z directions. This way, the additional slide has minimum effect on turning center stiffness.

A base with high static torsion stiffness is the key to lathe stiffness in the cutting point. Hardinge Inc. bases for SP machines have the optimal stiffness to mass ratio due to a wide base with stiff inner structure and rigid pockets connected to the outer walls. Modern turning centers are designed as complicated machine tools with two spindles and two or three turrets positioned in different areas. It is important to ensure that the base provides adequate general and local stiffness to deliver the required relative stiffness between components involved in the cutting process.

Static and dynamic torsion stiffness of the base was significantly increased by adding polymer concrete (Harcrete®) to peripheral parts of the base. Polymer concrete was added in cavities, developed by double walls. The analyses and testing showed that filling peripheral areas with Harcrete® affects not only torsion but also horizontal and vertical stiffness. This extra material also increased vibration damping capabilities of the base.

Decisions taken at the earlier stages of design process are checked and verified during the design of machine tool components and full assembly by means of FEA. During this stage, every major machine tool component was analyzed by FEA with the goal to optimize the stiffness to mass ratio. When performing these analyses, the torsion and bending stiffness of every component in two planes was computed. Special attention was given to reduce local deformation and distortion of major castings. These deformations and distortions greatly affect stiffness in the cutting point that is positioned relatively far from components because of machine layout.

GEOMETRY AND CUTTING VERIFICATION

High structural and kinematical stiffness of a SP machine allows successful use of linear scales as position feedback devices. The achievable geometric accuracy (position, straightness, parallelism) of SP turning centers can be compared with the accuracy of diamond turning and grinding machines. For example, results of

the minimum step test (see Fig.2) are comparable with results usually achieved at grinding machines with hydrostatic slides.

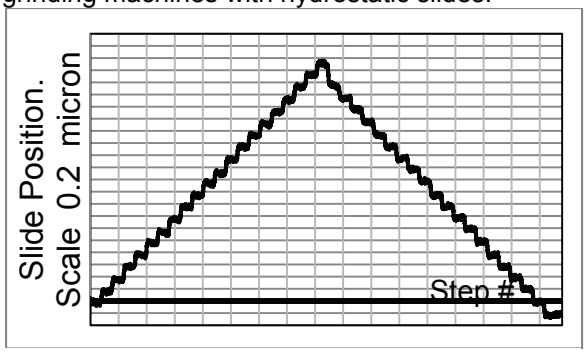

FIGURE 2. SP Turning Center. X-axis slide. Standard minimum step test results (20 steps up and 20 steps down).

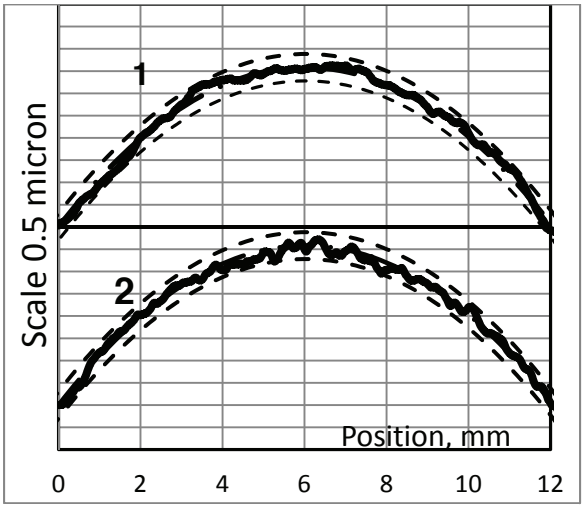

FIGURE 3. Results of cutting a profile with large 5080 mm radii in part with hardness of 62 RC. Curve 1-by SP Turning Center; 2- by Grinder with hydrostatic slides; ----- accuracy range of =+/-0.75 micron.

The contour accuracy of hardened (62RC) parts cut on SP turning center is comparable with accuracy, obtained on very expensive grinding machines (see Fig.3).

Data presented in Fig.2 and 3 came from a production SP turning center that has a main spindle with 42 mm through bar capability, 16 stations top plate with live tools, second spindle, and has 14 inches Z axis and 7 inches X axis stroke. Weight of moving X-axis slide around 1,500 lb, and Z axis slide around 2,500 lb.

REFERENCES

[1] Portman V.T., Sakakura M., Iwatate M. Form- Shaping Systems of Machine Tools: Theory and Applications. Annals of the CIRP, 47/1:329-332.

[2] Reshetov D. N., Portman V. T., Accuracy of Machine Tools, 1988, ASME-Press, NY.

[3] Faux I. D., Pratt M. J., 1979, Computational Geometry for Design and Manufacturing, Ellis, Horwood, West Sussex, UK

[4] Hocken R. J., et al., 1977, Three Dimensional Metrology, Annals of the CIRP, 26/2:339-344.

[5] Donaldson R., 1980, Error Budgets, Technology of Machine Tools, Vol. 5, Livermore, CA.

[6] Kushnir E.F., Portman V.T. Structural Synthesis of Calculation Models of Machine Tool Mechanics. Stanki I Instrument, Vol.62,No.9,pp.9-12,1991 by Allerton Press

[7] Kushnir E.F. Dynamic Characteristics of the Cutting Process and Dynamic Quality of Machine Tool during Multi Tool Machining. Stanki i Instrument, Vol.62,No.4, pp.10-13,1991 by Allerton Press.

[8] Kushnir E., Sheehan T. Development of machine tool structure at the early stages of design process. Proc. of 2003 ASME International Mechanical Engineering Congress and Exposition, November 16-21,Washington

CONTINUOUS FEED OF AN OCCLUDING MEDIUM INTO A FLOW STREAM

Folkers E. Rojas[1], and Alexander H. Slocum[1]
[1]Department of Mechanical Engineering
Massachusetts Institute of Technology
Cambridge, Massachusetts, USA

ABSTRACT

This paper presents experiment undertaken to understand wire entanglement in a cylindrical flow stream. The objective is to develop the theory for a wire feeding machine that feeds a wire (i.e. continuous medium) into a wellbore to form a tangled mass that incrementally obstructs the flow of hydrocarbons in a controlled manner. The experimental data is presented using non-dimensional numbers. The data shows that there are at least three distinct regions: 1) drag flow dominate, 2) wire dynamics dominate, and 3) entangling region. The varying wire entanglement configurations can be altered by varying the stiffness coefficient, entry angles, insertion velocity, etc.

METHOD

The development of the proposed technology required a better understanding of the physics of wire entanglement. Currently, the relation between the critical parameters of the wire (wire stiffness, geometry, feed velocity, etc.) that lead to wire entanglement given the environmental conditions (flow rate, viscosity, operating pressure) is unclear. The approach taken to develop the occlusion generating apparatus was to first perform a series of small-scale experiments to identify the fundamental modes and hence help guide development of an analytical model.

As the wire is exposed to the flow stream, the model behaviour changes based on the stiffness of the wire compared to the flow loading. For a low stiffness wire, where the length of exposed wire is much larger than the wire diameter, the interactions between the surrounding flow and wire can be modelled as a flapping and bending body, similar to that described by Shelley [1]. For high stiffness wires, buckling is induced through the interaction of the wire with the surrounding environment (i.e. casing wall, obstructions, etc.). The critical parameters leading to wire entanglement in the wellbore have been identified as: feed velocity ratio, Reynolds Number, wire stiffness, and entry angles.

EXPERIMENTAL DESIGN

The experimental setup consists of a wire feeding machine submerged in a water tank, powered externally by a ~280 W motor, as shown in Figure 1. Water was chosen as the working fluid and non-dimensional numbers are used for validation. The motor system can be used to vary the feed rate between 4 to 20 cm/sec. The flow is changed from 0.12 to 0.62 L/sec in a 2.54 wellbore diameter. The flow is designed to be fully developed within Reynolds numbers between 6,300 and 30,000, characteristic of blowout conditions in a well.

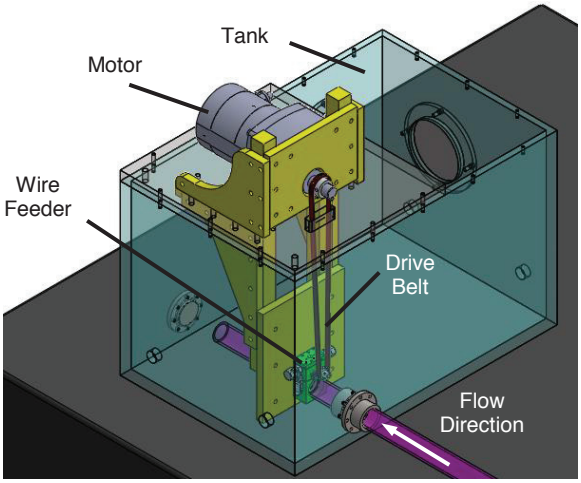

FIGURE 1. Wire entanglement experimental setup.

The wire feeding module is composed of three stages: 1) entry port, 2) drive stage, and 3) closing cap as shown in Figure 2. The three stages of the wire feeding mechanism are designed to connect with a high degree of precision using kinematic couplings [2]. The

result is a highly precise matching between each of the stages, which minimize misalignments that could lead to buckling inside of the machine.

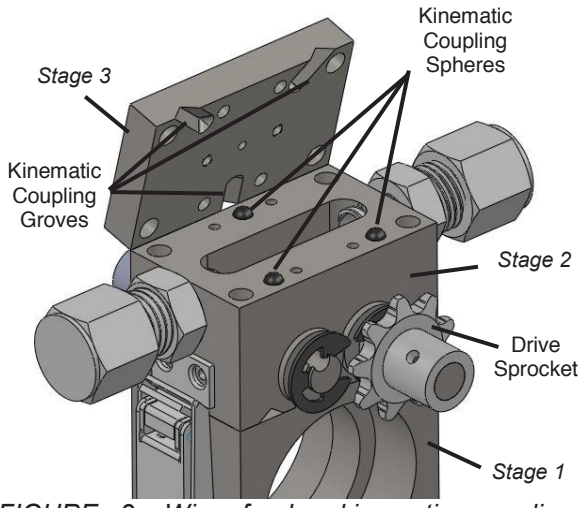

FIGURE 2. Wire feeder kinematic coupling interfaces to minimize alignment errors.

The wire stiffness can be varied by changing the material and wire diameter. The angle of entry can be varied with the use of rotation inserts, as shown in Figure 3. Each rotation insert has a curved channel with varying exit tilt angles ranging from 30 to 70 degrees, where a 90 degree tilt insert consist of a straight channel with no curvature. The use of a 90 degree insert is not a preferred due to the instability at first contact to model buckling behaviour. The top section of the inserts is a twelve sided polygon that allows for the rotation angle to change in increments of 30 degrees. A zero degree rotational alignment with a 45 degree tilt, will feed a wire into the flow stream at a 45 degree angle, whereas a 180 degree alignment with a 80 degree tilt will feed wire into the flow stream direction at almost a perpendicular angle.

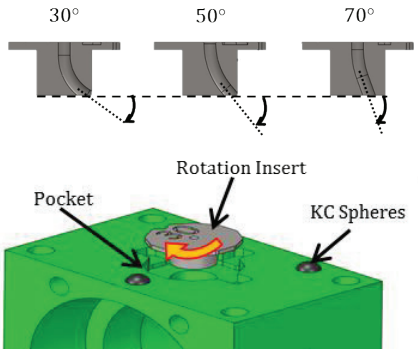

FIGURE 3. Rotation inserts with angular tilt.

THEORETICAL MODELING

As the wire first enters the flow stream it can experience distributive loading from fluid drag, and tangential and axially compressive loading when the wire interacts with the walls channel as shown in Figure 4.

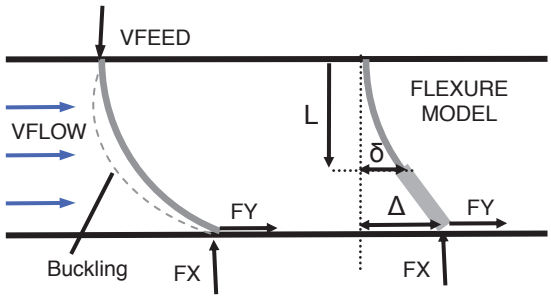

FIGURE 4. Onset of wire buckling analysis.

At low Reynolds numbers (i.e. drag loading small), a flexure analysis can be used to predict the onset of buckling using the flexure stiffness, $k_{\delta yFy}$ [3].

$$\omega = L\sqrt{\frac{F_x}{EI}} \tag{1}$$

$$k_{\delta yFy} = \frac{dF_y}{d\delta_y} = \frac{F_x \cdot \omega}{L \cdot (\tan(\omega) - \omega)} \tag{2}$$

where F_x is the compressive loading, L is the length of the flexure, and ω is the non-dimensional number used to compare normal force F_x to the wire stiffness EI.

When the flexure stiffness goes from positive to negative, the wire will undergo buckling. Since the flexural model is limited to the onset of buckling and ignores drag dynamics a discretized element model needs to be developed.

NUMERICAL MODELING

The foundation of the numerical modeling is based on the formulation for the reverse Spaghetti Problem [4]. The wire entering the wellbore can be discretized into interconnected rigid sections linked by torsional springs as shown in Figure 5.

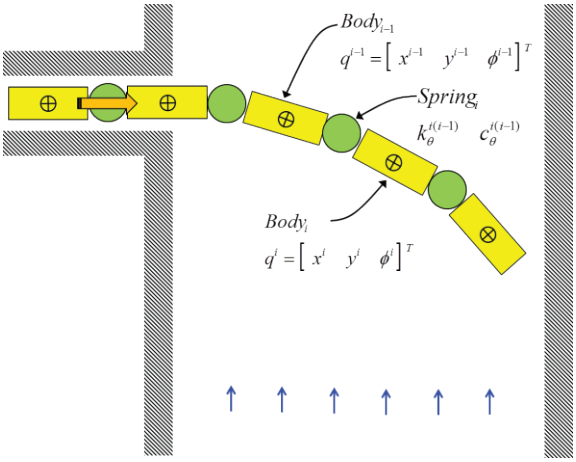

FIGURE 5. Discrete model of wire entering the wellbore.

The loading on each element will depend on the location along the wellbore diameter. For fully developed laminar flows, the drag loading on the wire is a fourth order term.

$$F_{drag} = \frac{C_D \cdot \rho \cdot u_{\max}^2}{R^3} \left\{ x^4 - 4x^3 R + 4x^2 R^2 \right\} dx \quad (3)$$

where R is the radius of the wellbore, C_D is the drag coefficient, ρ is the density of the fluid medium, u_{max} is the maximum fluid velocity, and x is the radial location.

ENTANGLEMENT MODES

Wire feeds below 3 cm/sec and above 15 cm/sec do not lead to entanglement independent of the Reynolds number, for a wire stiffness (EI) 2.33x10^{-3} Nm^2. Inside of the region are three types nest produced, which are arranged by the motion of the system, as illustrated in Figure 6. The preferred configuration is the forward motion nest where the plug incrementally grows and is dragged by the flow stream which corresponds to Δ in Figure 6 and 7.

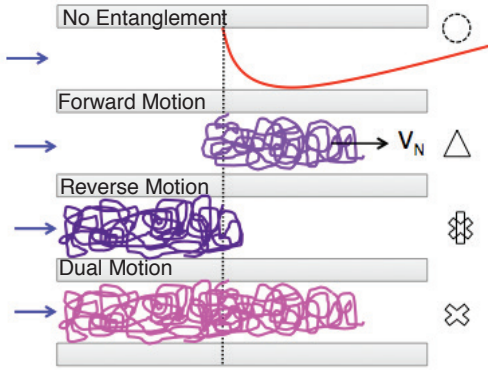

FIGURE 6. Key entanglement configurations observed for aluminum wire.

A plot of entanglement configurations for varying ratios of VFEED/VFLOW and Reynolds number, see Figure 7, shows that there is a band where drag forces and wire inertia forces are comparable and generate entanglement. Additional studies are being done for various wire materials, and tilt entry angles.

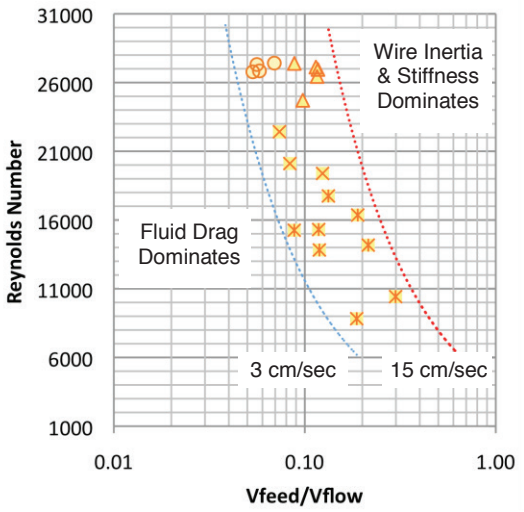

FIGURE 7. Aluminum wire entanglement region for 800 um wire diameter, fed against the flow at a 80° tilt (i.e. almost vertical channel).

The rotation angle can also be used to study the onset of entanglement behavior. As shown in Figure 8, for rotation angles varying from 90 to 180 degrees for aluminum wire. The plot shows how the rotation angle can be used to impart a curl on the wire that will increase anchoring potential.

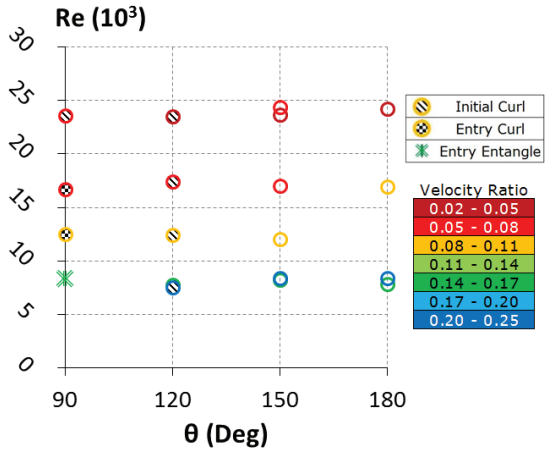

FIGURE 8. Aluminum wire entanglement rotational angular dependence with a 30° tilt. Initial curl is when the wire curls and then taken by the flow stream. Entry curl is when the wire curls and stays in the entry region.

For θ=90° the transition can be observed from a wire that curls on entry at high Reynolds number to a wire that curl and buckles at the entry region. The behavior is changed by the drag forces on the wire.

CONCLUSION

The preliminary data shows that their is a region where wire entanglement is generated, and that by changing the feed velocity ratio and the flow rate we can change the type of entanglement. Similarly, changing the rotational angle on entry can influence the type of entanglement.

FUTURE WORK

The most immediate work ahead is to collect data on varying wire stiffness and entry angle parameters and correlate to the currently under development discrete numerical model with drag loading.

REFERENCES

[1] M. J. Shelley and J. Zhang, "Flapping and Bending Bodies Interacting with Fluid Flows," *Annual Reveiw of Fluid Mechanics,* vol. 43, pp. 449-465.

[2] A. H. Slocum, "Design of Three-Groove Kinematic Couplings," *Jou. Int. Soc. of Precision Engineering and Nanotechnology,* vol. 14, No. 2, pp. 67-76, April 1992.

[3] S. T. Smith, *Flexure Elements of Elastic Mechanisms*: CRC Press LLC, 2000.

[4] H. Sugiyama, N. Kobayashi, and Y. Komaki, "Modeling and Experimental Methods for Dynamic Analysis of the Spaghetti Problem," *Journal of Vibration and Acoustics,* vol. 127, pp. 44-51.

DEVELOPMENT OF NONCONTACT HYDRODYNAMIC MICRO HANDLING SYSTEM

Asa Ichinozuka [1], Aya Toyoshima [1], Zhang Qin [2], Huang Weijun [2] and Hisayuki Aoyama [1]

[1] Department of Mechanical Engineering and Intelligent Systems, University of Electro-Communications, 1-5-1 Chofugaoka, Chofu, Tokyo 182-8585, Japan

[2] School of Mechanical and Automotive Engineering , South China University of Technology Wushan RD.,Tianhe District,Guangzhou,P.R.China,510641

INTRODUCTION

Recently, the demand for fine processing techniques such as micro manipulation and assembly has increased in the fields of not only micro-engineering but also bio-medical applications [1]. Generally, micromanipulation systems can be divided into two categories, physical contact and contact-free. The former is well known as the mechanical contact manipulator for micro-objects by gripper. Alternatively, the contact-free systems can manipulate the target without mechanical contact, reducing the risk of physical damage. There are many types of contact-free handling systems such as focused laser beam and ultrasonic sound waves. The laser micromanipulators are used extensively in biotechnology, and can manipulate micro fragile physical objects. However, the laser beams may cause thermal damage because the near-infrared region of the laser beam corresponds to the absorption band of aqueous media. In this report, contact-free manipulation technique using multiple micro flows is proposed. The principle and the primary experiments are discussed for the feasibility of this idea.

CONTACT-FREE HANDLING SYSTEM USING MULTIPLE MICRO FLOWS

In our group, the micro handling system without mechanical contact using multiple micro flows under an optical microscope has been proposed [2]. This technique can control the position of micro physical object in the working area between several small pipettes with the advantage of holding physical objects without mechanical damage, as only the fluid around the target is manipulated. It employs multiple micro flows and the flow rate from each individual pipette should be controlled precisely. Fig.1 shows the animations of micro flows and the motion of sample. The sample can be positioned around the center of two pipettes with two pipettes arranged in a straight-line and the same flow rate given from the right and left side pipettes. When two pipettes move up and down the sample can be held to move in the same direction with pipettes. The sample can be positioned at the flow force balanced point and rotated by the differential flows.

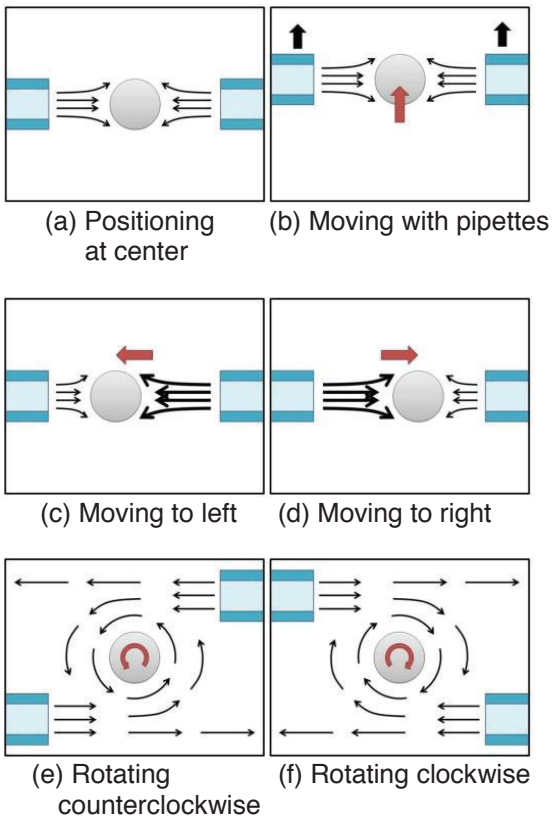

FIGURE 1. Two-dimensional contact-free handling system using two pipettes.

POSITIONING WITH TWO PIPETTES

In the primary experiment of two-dimensional contact-free handling system using two pipettes, two opposite glass pipettes are set up precisely. The movement of fluid flow from two pipettes have been visualized. Fig.2 shows the fluid flow from two glass pipettes inside diameter of 50μm. And the flow rate is 261 [μm/s]. In the center of the work space, it is confirmed that the balance of forces can be produced by two flows. Fig.3 shows the experiment that the inside diameter is 50 [μm] and the flow rate is 58.7 [μm/s]. It is found that the small sample can be held at the center of the working area in this experiment.

ROTATING WITH TWO PIPETTES

In the next, the rotating motion by micro flow was observed. Fig.4 shows the micro flow for rotation. The inside diameter of each pipettes was 50 [μm] and the flow rate was 403 [μm/s]. These results show that the position of such micro sample can be controlled using this system. We carried out the rotating experiment using this system. Fig.5 shows the succeeded experiment. When inside diameter was 50 [μm] and the flow rate was 403 [μm/s], we succeeded in rotating the sample.

DISCUSSION

It is confirmed that the positioning and the rotating can be done using two micro flows. However, the stability and the repeatability of operation is still poor quality. As one of the reasons, the flows that are given in this experiment have pulsation due to the rotary pump. In addition, when two pipettes are employed, it is difficult to put target back into working place.

THREE-DIMENSIONAL CONTACT-FREE HANDLING SYSTEM USING SIX PIPETTES

The contact-free handling system using multiple micro flows is examined. The goal is to reduce the spin-out from the work area of the sample. and the sample should be rotated three-dimensionally for the observation under the microscope. We propose the layout with six micro pipettes. Fig.6 shows the layout of six micro pipettes. Three pipettes is in one side and other three are in the oppose side. Sample which is set in the working area can be manipulated by controlling each flow rate precisely. It is expected that the target can be held and rotated by controlling the flow rate of each pipette as shown in Fig.7.

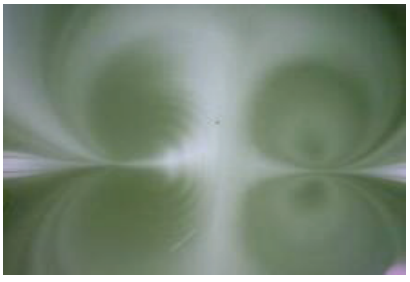

FIGURE 2. Flow visualization from two pipettes.

EXPERIMENT OF PROTOTYPE SYSTEM

We set up the prototype systems of three-dimensional contact-free handling system and carried out several experiments to check the feasibility of micro positioning. Fig.8 shows systems of this experiment. Six micro flows are divided from the rotary pump. In this experiment of prototype system, the size is a little bigger than the final goal system and we used a small paper sheet of 2mmx2mm. In Fig.9,

FIGURE 3. Positioning experiment with two pipettes.

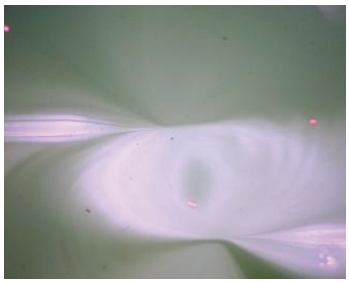

FIGURE 4. Flow visualization of rotational motion.

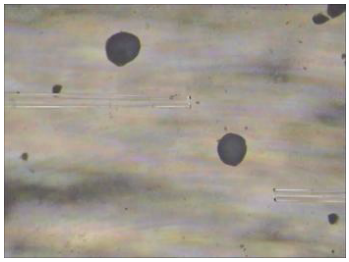

FIGURE 5. Experiment of rotational motion.

the experimental results suggested the possible beneficial effect of three-dimensional contact-free manipulation, when the inner diameter is 500 [μm], diameter of alignment of pipettes is 3 [mm], the distance of between pipettes is 10 [mm], and the flow rate per pipette is 0.007 [ml/min]. Sample can be held around center of working area. However the sample cannot be fixed and oscillated in right and left with rotation. It is considered that the flow fluctuation from the rotary pump causes a pulsation and a force of flows might give the interference to another flows. This indicates that the accurate micro flow control mechanism should be implemented into the system.

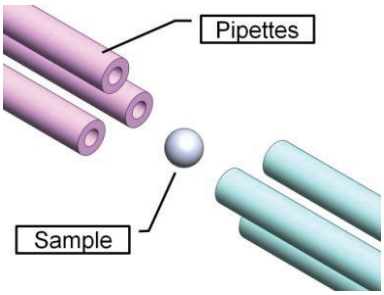

FIGURE 6. Three-dimensional contact-free handling system.

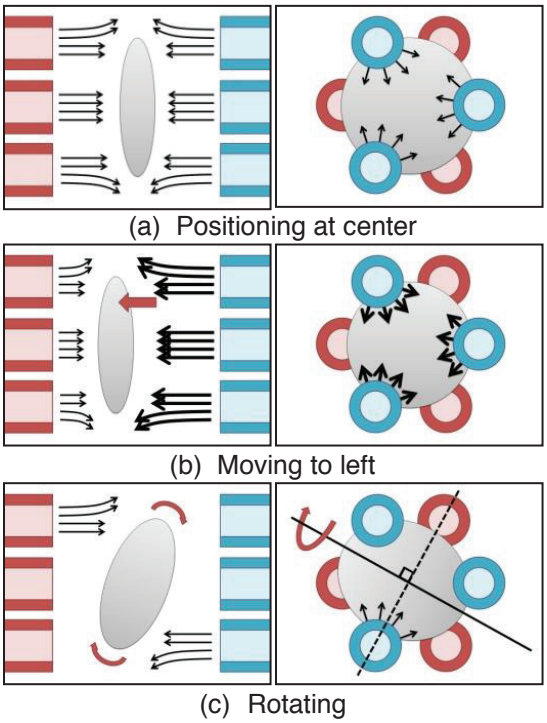

FIGURE 7. Principle of three-dimensional contact-free handling system.

POSITION CONTROL SYSTEM BY USING SIX PIPETTES

We designed the flow paths and the layout of the outlet aperture that solve the problem of explained in the previous section. At first, we discuss about the layout of the outlet aperture. The sample pass out through between the flow and flow from working area is thought to be due to distance between the flow and flow. Therefore, as shown in Fig.10, the six outlet apertures having inner diameter of 300 [μm] at equal intervals in the position of the vertices of the hexagon inscribed in diameter of 500 [μm]. Minimum value of the interval of flow and flow of this model

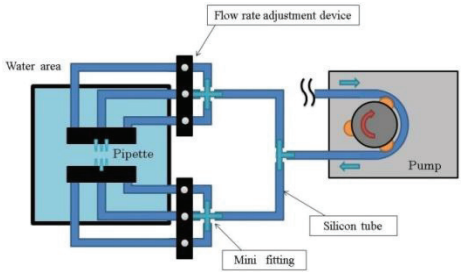

FIGURE 8. Experimental setup.

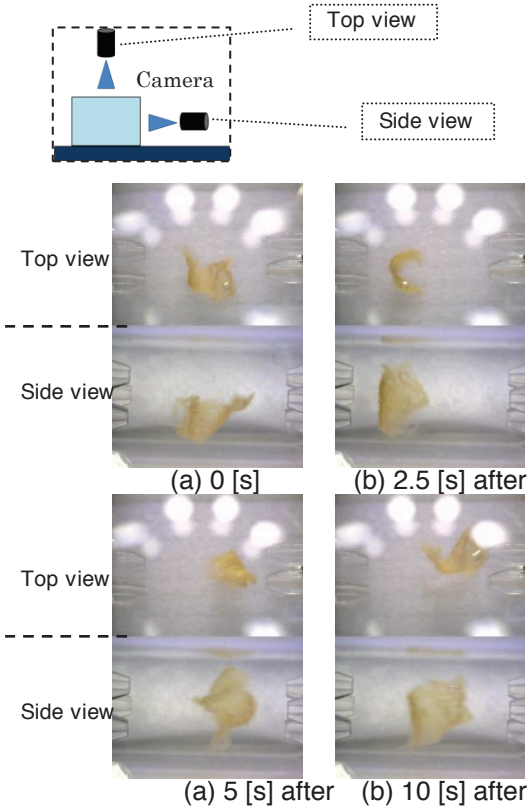

FIGURE 9. Primary result of prototype system.

is 134 [μm]. With these pipettes layout, it is expected that the number of sample escaping from the work area can be reduced when the sample of size larger than the minimum value is used. Fig.11 shows the outlet aperture of real object. In the next, we discuss about the flow control system. We decided the specifications of the fluid control system from the results of experiments of the positioning in the non-contact manipulation system using two pipettes. Maximum flow rate capable of discharging individually from each the output aperture is 14.1 [nL/s]. And the flow rate is set to be a

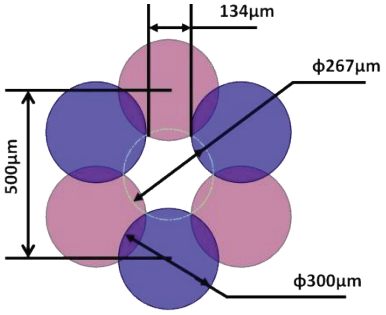

FIGURE 10. Dimension of six outlet apertures.

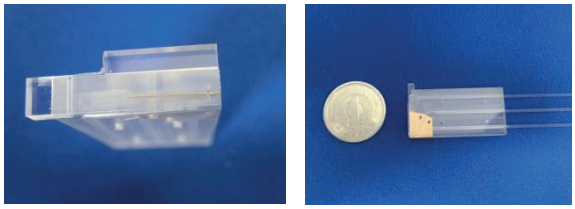

FIGURE 11. Micromachined outlet aperture.

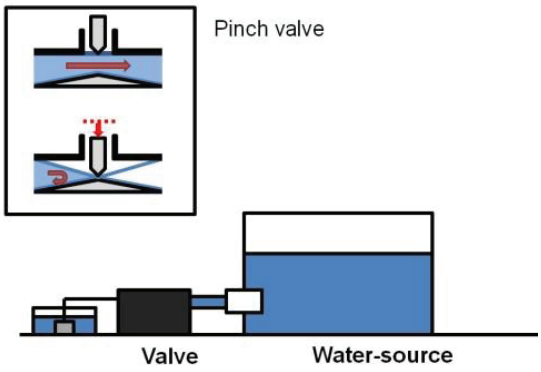

FIGURE 12. Arrangement of the flow control system.

variable from minimum flow rate 0 [nL / s] . It has been shown in the previous studies that pulsating flow from rotary pump greatly influences to the stability of the sample operation. In addition, the possibility of operation using a constant flow to be generated from the injector has been suggested. However, the variation of emissions associated with the change in the volume of injector has also been confirmed. So, a pinch valve is inserted and the controlled constant flow using the atmospheric pressure can be given. Fig.12 shows the arrangement of the flow control system. This water sources is sufficiently larger than the sum total of discharge amount from all outlet aperture. It is also checked that the operability in verification experiments using two kinds of spherical object: diameter of 10 [μm] and diameter of 200 [μm].

CONCLUSION

The principle of contact-free manipulation using multiple micro flows was discussed. The primary experiments of flow visualization with two micropipettes were observed and the feasibility of this system was described. And we proposed the basic principle of three-dimensional noncontact manipulation system using multiple micro flows. The primary experiment results suggested the possibility of three-dimensional noncontact manipulation for micro sample. In addition, system component of verification experiments for system using six pipettes was discussed. In order to improve the operability, the new configuration of the fluid control system and the placement of the outlet aperture was suggested.

REFERENCES

[1] F. Arai, M. Ogawa and T. Fukuda: Non-contact Micromanipulation by Bilateral Control: Control of Micro Tool Using Laser Micromanipulator: Journal of Robotics Society of Japan, 20(4), pp. 417-424 (2002) [in Japanese]

[2] A. Toyoshima, S. Hirata, H. Aoyama, H. Weijun and Z. Qin: Study of a noncontact positioning method with micro countercurrent flows continued report: checking of operation by experiment, Proceedings of JSPE Semestrial Meeting, Spring Conference (2012) [in Japanese]

PRACTICAL CONTROLLER DESIGN FOR PRECISION POSITIONING OF STAGES WITH A PNEUMATIC ACTUATOR

Kaiji Sato, Yusuke Sano and Yuelai Wang
Interdisciplinary Graduate School of Science and Engineering
Tokyo Institute of Technology
Yokohama, Japan

INTRODUCTION

Pneumatic actuators have many advantages such as low-cost, low-heat generation, high power-to-weight ratio, free from magnetic leakage. These advantages give a wide field of application to the actuators. However the compressibility and the nonlinear flow characteristic of the air, the large static and Coulomb friction forces in the pneumatic actuators make it difficult to achieve the precision positioning of stages with the pneumatic actuators [1].

For overcoming the problems and achieving the precision positioning, many challenges have been made. They can be classified into two types: control methods and mechanical methods. For improving the positioning performance of the conventional pneumatic actuators with frictional characteristics, many controllers have been designed based on a wide variety of control techniques and their performances have been examined. In recent year, several complex controllers show high positioning accuracy and the usefulness of pneumatic actuators for precision positioning. The combination of the pneumatic cylinder with the linear guide and the PD/fuzzy controllers with the velocity compensator based on detailed friction model gave the positioning accuracy of 20 nm [2]. The combination of the pneumatic cylinder with slide guide and the adaptive sliding mode controller with the extended observer and the dead bad compensator generally shows the positioning accuracy of 50 nm [3]. However the controller design procedures require detailed information of the mechanism characteristics and sufficient knowledge of advanced control methods.

Systems with conventional pneumatic actuators have several mechanical elements with the friction force which increases the positioning error. The use of non-friction elements is effective to improve the positioning accuracy. The non-contact pneumatic servo system has achieved the positioning error of 20 nm [4]. However the use of non-contact elements significantly increases the cost of positioning systems.

The purpose of this research is to clarify a practical controller design procedure for precision positioning of mechanisms with pneumatic actuators. For this purpose, the nominal characteristic trajectory following controller (NCTF controller) [5] was improved. The improved controller comprises conventional NCTF controller elements and additional three elements. The improved controller can be designed easily as with the conventional NCTF controller. The control system performance was examined experimentally.

EXPERIMENTAL SETUP

Figure 1 shows a positioning stage with a pneumatic cylinder actuator. The overview of the experimental setup including the positioning stage is shown in Fig.1(a). The pneumatic actuator consists of an electric servo valve and a double rod air cylinder for a general-industrial-use. The actuator drives a table. The standard nominal flow rate of the valve is 350 l/min. The cylinder stroke is 150 mm. The table is supported by a linear ball guides comprising two guide rails and four carriages. The mass of the table is 1.66 kg. Its position is measured with a linear encoder of which resolution is 50 nm.

The schematic view of the positioning stage is illustrated in Fig.1(b). The cylinder unit produces the force which is proportional to the difference between the pressure P_1 and P_2. However the characteristics between the input u and the pressure P_1 and P_2 are nonlinear. The stage has friction elements in the guides and cylinder.

Pneumatic actuators with friction characteristics generally have the following problems.
1) Pneumatic actuators have a vibration element resulting from air properties. Since the vibration element has low vibration damping

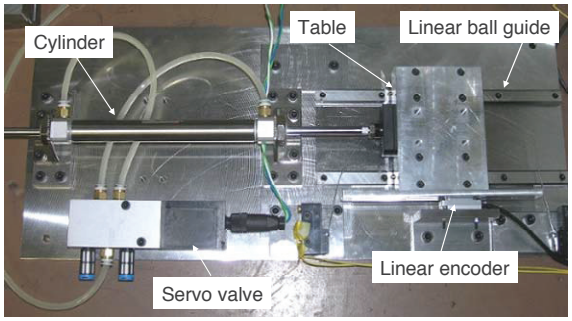

(a) Overall view of experimental setup

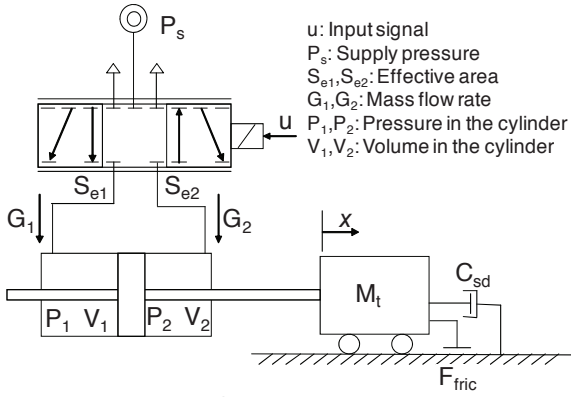

(b) Schematic view

FIGURE 1. Positioning stage with a pneumatic actuator.

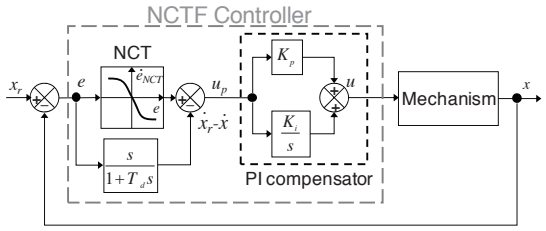

FIGURE 2. Conventional CM NCTF control system.

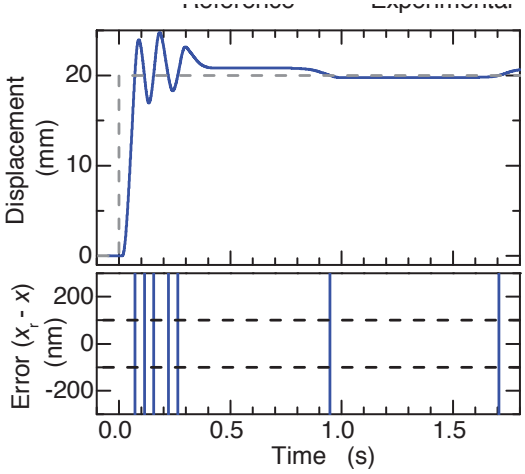

FIGURE 3. Step response of the conventional CM NCTF control system.

characteristics, it is relatively easy to vibrate the table. In the actuators, the difference between the static and Coulomb friction forces often gives an unexpected force to the table and leads to stick-slip phenomena. The combination of the stick-slip phenomena and the low vibration damping characteristics leads to large vibration.
2) Since the friction forces often depend on the table position and change with time, it is not easy to estimate the value exactly.
3) In addition, the friction characteristics depend on the working range and the friction force significantly changes.

CONTROL SYSTEM DESIGN

Figure 2 shows the block diagram of a conventional continuous motion NCTF (CM NCTF) control system. As the common components, the NCTF controllers have a nominal characteristic trajectory (NCT) as the motion reference trajectory expressed on phase plane, and a compensator making the motion reach and follow this trajectory. The NCTF controller makes the object motion quickly reach and follow the NCT. They have been used for positioning mechanisms with electric motors and have given high positioning accuracy easily. However pneumatic actuators generally have lower response than electric motors and several problems deteriorating positioning performance as mentioned previously. Figure 3 shows a step response example of the conventional CM NCTF control system with the pneumatic cylinder actuator. The results indicate that the controller provides low vibration damping characteristics and low positioning accuracy.
In order to easily solve the problems previously described, the NCTF controller is improved. Figure 4 shows the block diagram of the improved CM NCTF control system for the pneumatic cylinder actuator. For pneumatic cylinder actuators, a PI element is replaced with a PD element in the NCTF control system. Similar to electric motors the pneumatic cylinder actuators have the integral property between the

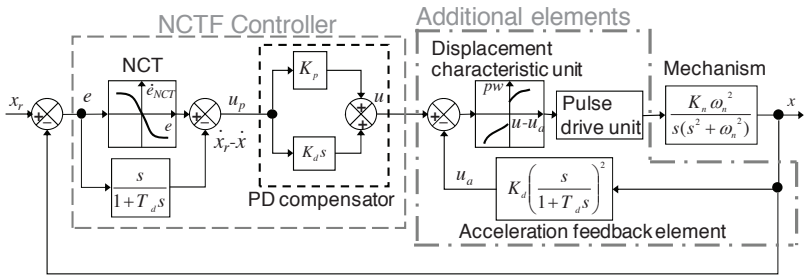

FIGURE 4. Improved CM MCTF control system for pneumatic cylinder actuators.

input signal and the displacement. However the effect of friction force on motion characteristics in the pneumatic cylinder actuator deferent from that in the electric actuator. The PD element is suitable for the pneumatic actuator.

The improved NCTF controller has three additional elements, such as the acceleration feedback element, the pulse drive unit, and the displacement characteristic unit, for overcoming the above problems. The acceleration feedback element acts for increasing the damping effect of the actuator and solving the problem 1). For improving the robustness of the control system to the change of the friction described in the problem 2), the pulse drive unit is added and works like a pulse width modulator. This unit increases the signal amplitude and makes the system insensitive to the change of the friction force. The displacement characteristic unit is a function representing the relationship between the pulse width and the displacement for solving the problem 3). In these elements, the acceleration feedback element and the displacement characteristic unit are determined experimentally.

The improved control system is basically designed according to the following procedure.

(i) Displacement characteristic unit construction: The unit is constructed from the open-loop response to rectangular signal inputs. Figure 5 shows the measured relationship between the pulse width and the displacement

(ii) Acceleration gain determination: The gain K_d is experimentally-determined for sufficient damping characteristics using the mechanism with the pulse drive unit and the range adjustment unit.

(iii) NCT construction: The mono-pulse response of the acceleration feedback system is measured. The NCT is constructed from measured displacement and velocity responses.

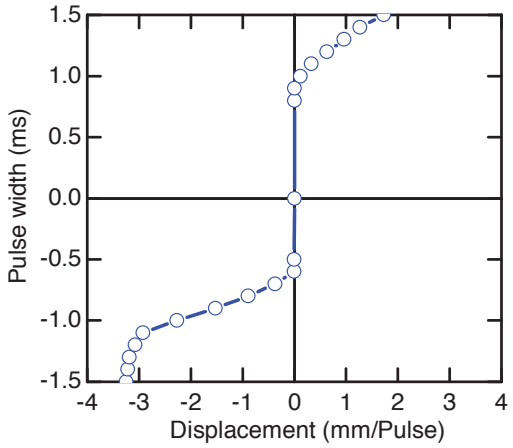

FIGURE 5. Measured relationship between the pulse width and the displacement.

(iv) PD compensator determination: The compensator is experimentally determined.

The acceleration feedback element and the pulse drive characteristic element need be adjusted or measured. However it is easy to determine them. The common components of the NCTF controller can be easily determined as is conventionally done.

EXPERIMENTAL RESULT

Figure 6 shows the response of the control system in Fig.4 to a 20 mm step input. In contrast to the response with the conventional NCTF control system shown in Fig.3, the response in Fig.6 does not vibrate and its overshoot is small. The object motion on the phase plane in Fig.6 follows the NCT. The steady state positioning error is 50 nm, which is similar to the sensor resolution. The same experiment was conducted 20 times. In all the experiments, the positioning errors were kept at

50nm. Under the several conditions, that is, different start positions and many different step heights, the positioning performance of the control system was examined. The results indicate that the control system can show the positioning error smaller than 200 nm.

CONCLUSION

In this paper, the practical controller design method for precision positioning of the stage with the pneumatic actuator was introduced and its usefulness was examined experimentally. The controller design does not require the identified model parameters and can be carried out easily. The experimental results show that the control system has the ability to provide the positioning accuracy better than 200nm.

REFERENCES

[1] G. M. Bone and N. Shu, "Experimental Comparison of Position Tracking Control Algorithms for Pneumatic Cylinder Actuators," IEEE/ASME Trans. Mechatronics, 2007; 12(5): 557-561.

[2] Kei-Ren Pai, and Ming-Chang Shih, Nanoaccuracy Position Control of a Pneumatic Cylinder Driven Table, JSME Int. J. Series C, 2003, 46(3):1062-1067

[3] Yung-Tien Liu, Tien-Tsai Kung, Kuo-Ming Chang, Sheng-Yuan Chen, Observer-Based Adaptive Sliding Mode Control for Pneumatic Servo System, Precis. Eng., 2013, 37; 522-530.

[4] K. Tadano, T. Arai, K.Kawashima, T. Fujita and T. Kagawa, "Precise Position Control of Coarse/Fine Dual Stage Using Pneumatic Actuators, in Proc. of World Automation Congress 2010, 2010; 1-6.

[5] K. Sato and G. J. Maeda, "A Practical Control Method for Precision Motion – Improvement of NCTF Control Method for Continuous Motion Control," Precis. Eng., 2009; 33(2): 175-186.

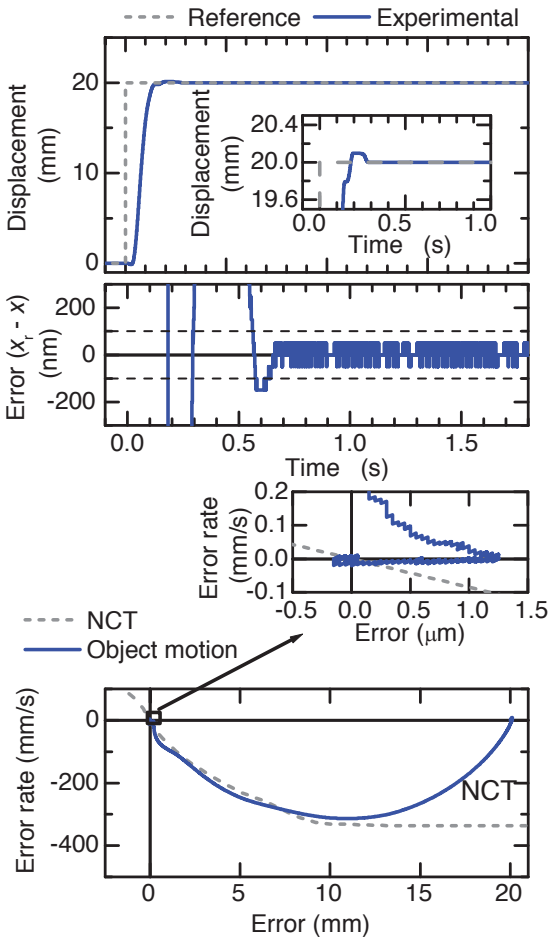

Fig.6 Response of the improved control system to a 20mm step input

DESIGN OF A VACUUM IMPRINTING SYSTEM FOR HIGH RESOLUTION PATTERNING ON NONPLANAR SURFACES

Jianwei Chen[1], Huihua Xu[1], Ni Zhao[2], and Shih-Chi Chen[1*]
[1]Department of Mechanical and Automation Engineering
[2]Department of Electronic Engineering
The Chinese University of Hong Kong
Shatin, N.T., Hong Kong SAR, China
*Email:scchen@mae.cuhk.edu.hk

In this paper, we present the design and development of an automated vacuum micro-imprinting system that enables high resolution 2-D and 3-D patterning on both planar and nonplanar surfaces over a large area, e.g. 4" x 4", in a non-cleanroom environment. This system is applicable to many contact printing processes including microcontact printing (MCP), nano-/micro-imprinting, and micro-molding etc. In this work we selected MCP and UV micro-imprinting to demonstrate the versatility and unique capability of our vacuum imprinting system.

PRECISION CONTACT PRINTING

Many contact printing techniques have been actively researched in recent years as they have the potential to achieve better resolution and lower cost compared to conventional lithographic processes. This is because the resolution of contact printing and imprinting processes is not limited by the diffraction of light; furthermore, without the need of big lenses for the photolithographic system, the overall cost can be significantly lowered.

Figure 1 illustrates a standard MCP process: A soft elastomer, e.g. PDMS, is used as a stamp to bring molecular ink to a surface, where the molecules self-assemble to form a monolayer (SAM) that can modify the properties of the surface. As the resolution is not limited by diffraction, MCP has been demonstrated with a resolution of 30nm and a minimum feature size of 40nm [1]. However, to date all nanometer-resolution prints have only been demonstrated on millimeter scale or chip level. Consequently, MCP and other contact printing or imprinting methods still remain as primarily laboratory-based techniques for academic research. The lack of scalability is mainly attributed to the uncontrolled printing conditions where minor defects on the stamp and small particles in the air prevent high quality large-area prints.

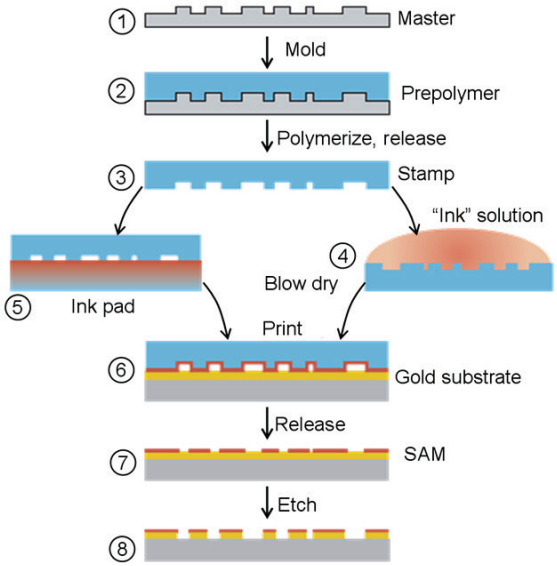

FIGURE 1. Illustration of standard Microcontact Printing (MCP) process to direct the formation of microscale features in gold [2].

REVIEW OF PATTERNING 3-D STRUCTURES ON NONPLANAR SUBSTRATES

Compared to contact printing methods, patterning 3-D structures on nonplanar surfaces is an even more challenging task. One approach is to use the laser lithographic technique that directly writes onto a nonplanar substrate with high-power laser, where the substrate is fixed on a six-axis positioner [3]; however, this technology is costly and time-consuming and only suitable for fabricating micro- and nano-structures in spherical shapes. Another recently developed method for manufacturing micro-structures on nonplanar substrates is to replicate a micro-lens array on a flat PMMA film and subsequently bonds it to a glass substrate by the thermal extrusion process [4, 5]; this process yields high quality micro-lenses, but a planar PMMA film cannot make conformal contact with

curved surfaces; consequently, it is limited to small area patterning.

VACUUM IMPRINTER DESIGN

We have developed a vacuum imprinting system suitable for scaling up various ultra-precise contact printing and imprinting techniques. The concept of the vacuum imprinting system is shown in Figure 2, where an elastomer stamp is installed in the middle of the chamber, separating the room into two independent vacuum chambers (A and B). The substrate (flat or curved) is placed in the bottom chamber. Independent air valves and pressure sensors are used to control the pressure difference between the top (A) and bottom (B) chambers. When a printing process starts, both chambers are vacuumed. Then, chamber A is pressurized to deform the elastomer stamp to make contact with the substrate and perform a controlled printing process with desired pressure and time. Upon completion, the membrane stamp can be lifted by pressurizing chamber B. As shown in Figure 2, the vacuum imprinting system can be used to imprint precision micro-lens arrays with an addition of a UV light module installed above the top chamber.

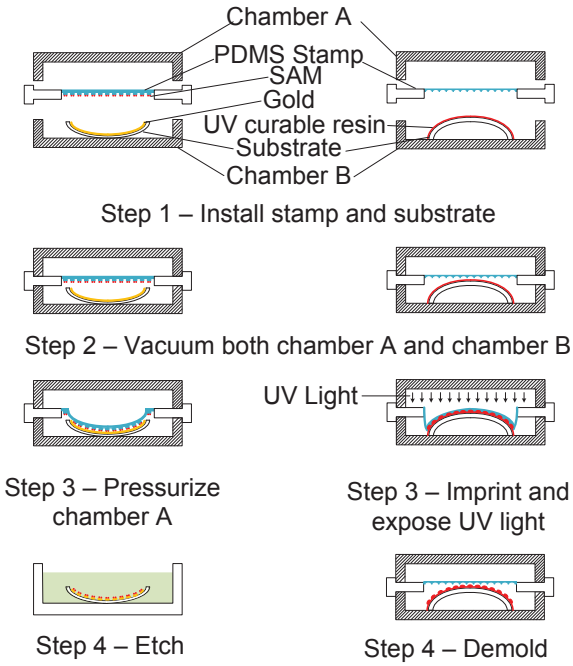

FIGURE 2. Vacuum imprinting system design and its operation for both MCP (left) and UV micro-imprinting (right) modes on nonplanar substrates.

Figure 3 shows the automated vacuum imprinting system. Four valves, two pressure gauges, and a load cell are used to monitor and control the pressure in chamber A and B during operation.

There are a few distinct advantages for performing contact printing with our vacuum system: (1) air-trapping in small pockets of the stamp is minimized, (2) small particles can be largely removed from the bottom (printing) chamber during the printing process, (3) the controlled top chamber pressure on the elastomer stamp may minimize minor defects on the stamp or the particle effect, (4) the printing parameters such as print pressure/force and print time can be precisely controlled, and (5) precision prints can be performed on nonplanar substrates.

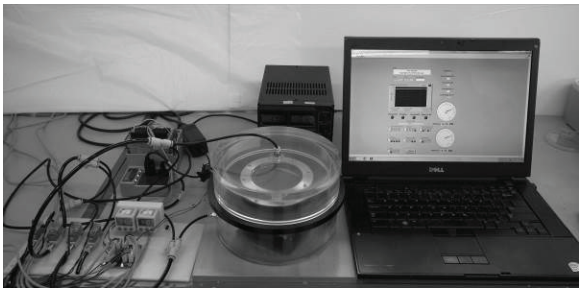

FIGURE 3. Automated vacuum micro-imprinting system.

The printing system enables precise and customizable printing time and pressure. Figure 4 shows the experimental data for a complete printing process: Firstly, both chambers were pumped down to 2 psi. Secondly, the pressure in chamber A was raised to 4 psi, ensuring a controlled contact force, i.e. pressure, and time (60 seconds). Then, the stamp was lifted from the substrate when both chambers were pumped down and reached equal pressure again. Lastly, both chambers were brought back to atmospheric pressure for opening the chamber.

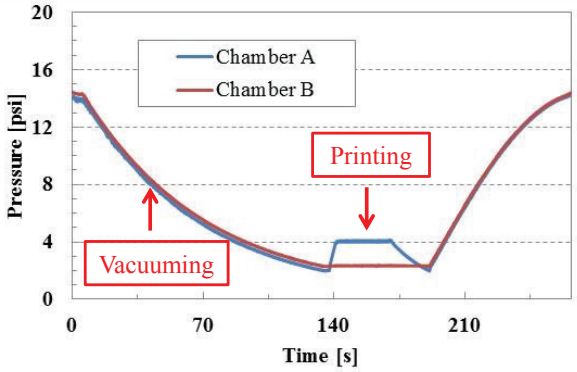

FIGURE 4. Pressure readings from chamber A and B versus time.

PRINTING ON PLANAR AND NONPLANAR SUBSTRATES

One important issue for precision printing is pattern distortion and correction. For example, when printing on a concave substrate (coated with gold or UV curable resin), the membrane stamp will undergo large deformation and consequently patterns in the center region can be two times larger than patterns on the edges. (Actual deformation factor depends on the curvature of the substrate.) To eliminate distortions, distortion correction algorithm has been developed and applied in our mask design by calculating and compensating the extension ratios in longitudinal and latitudinal directions for substrates of specific radius [6, 7]. Two distortion-corrected membranes were used to print/imprint hexagonal grids and micro-lens array on convex substrates respectively. The results are discussed in the next section.

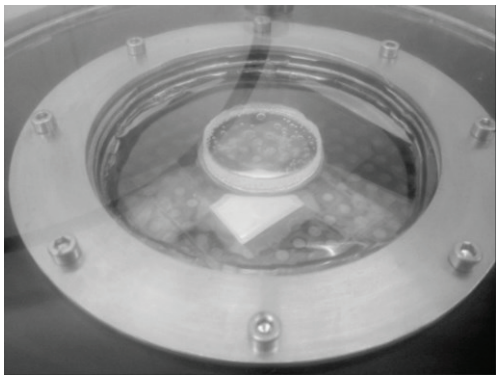

FIGURE 5. Bonded PDMS prevents pattern distortion when printing on flat substrates.

When printing on flat substrates, the stamp deformation issue can be largely controlled by bonding a thick piece of PDMS (e.g. 2 mm) to the back of the membrane stamp. As the thick PDMS can be 20 times thicker than the rest of the membrane, pattern deformation under bonded region will be minimized. Figure 5 shows the thick PDMS bonded to the center region of a membrane stamp in the vacuum system.

CYCLIC PRESSURE VARIATION FOR ENHANCING PRINT QUALITY

Although lowering the pressure in the printing chamber reduces the possibility of air trapping, air trapping can still occur under certain circumstances, including rapid membrane contact motion and the use of concave substrates with high curvature. The trapped air, i.e. air bubbles, has negative effects on transferring of ink molecules and formation of microstructures on thin polymer films during the printing/imprinting processes [8].

To tackle this issue, we developed a cyclic pressure variation technique that can slowly "pump out" the trapped air in the micro-channels. This approach is enabled by our unique vacuum imprinting system, where during the imprinting process the pressure in the top (A) chamber can be increased and decreased in a cyclic fashion. Different pressure loading patterns and frequencies, as shown in Fig. 6, were used to optimize the operating parameters for effective air removal.

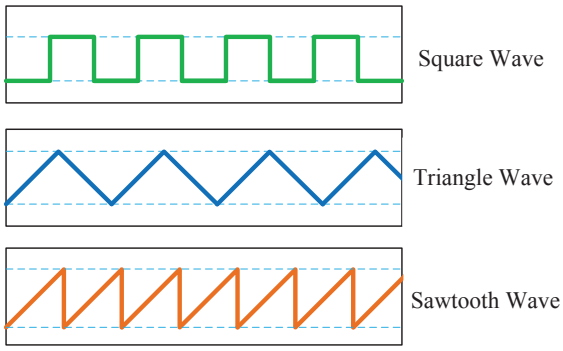

FIGURE 6. Cyclic pressure loading during imprinting processes helps remove air bubbles. Different loading patterns, including square, triangle and sawtooth waves, and frequencies were used to optimize air removing efficiency in our study.

EXPERIMENTAL RESULTS

We used the vacuum imprinting system to demonstrate both the MCP and UV micro-imprinting processes on nonplanar substrates.

In the first experiment, we patterned hexagonal gold grids on a 4" convex glass substrate by the MCP process. Figure 7 shows (1) the image of an SU8 master on a 4" silicon wafer fabricated via standard lithographic processes (top) and (2) the images of patterned hexagonal gold grids on the 4" convex glass substrate (middle/bottom).

The wiggling lines on the SU8 master were due to the limited resolution of the laser transparency mask. By comparing the gold patterns in the center and on the edge of the substrate, we confirmed that our distortion-correction algorithm has effectively removed the pattern distortion effect. And the hexagons in the center and on the edge are only different by a micron (345μm vs. 346μm).

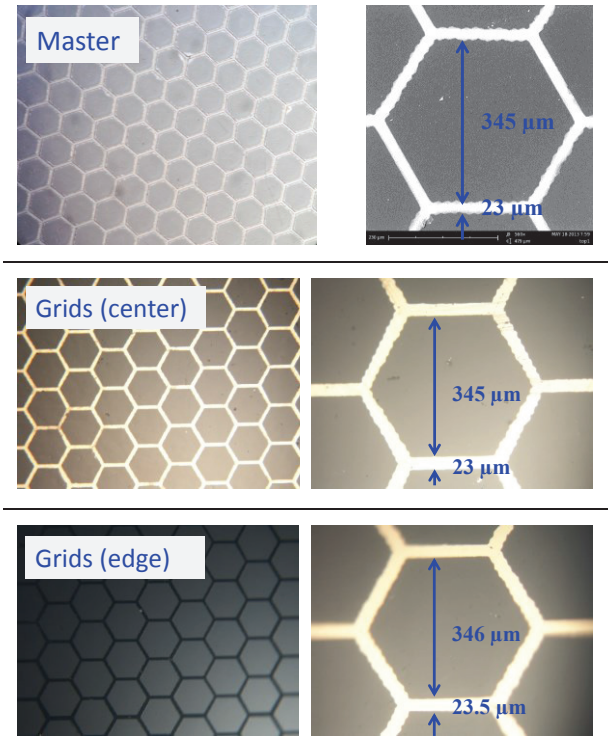

FIGURE 7. SU8 master patterned with hexagonal grids on a 4" silicon wafer with 23 μm line width (top); printed gold grids in the center (middle) and on the edge (bottom) of the convex glass substrate.

In the second experiment, we patterned hexagonal micro-lens arrays on a convex glass substrate by the UV micro-imprinting technique. Firstly, an AZ4620 master was fabricated using standard lithographic processes, followed by a thermal reflow process, shown in Figure 8. The thermal reflow process was used to form the convex lens surface through surface tension. The micro-lens profile is a function of the thickness of photoresist, the size of the hexagonal pattern, and the reflow temperature and time. Secondly, the PDMS mixtures (10:1) were cast to the master to form a 3-D membrane stamp. Thirdly, the UV resin (NOA 61) was spin-coated onto the convex substrate, followed by a 2-minute UV lamp pre-curing process. The pre-curing step serves two purposes: (1) it prevents the UV resin from being absorbed by the PDMS stamp, and (2) it allows pattern transfer with better resolution [9]. After the pre-curing step, the PDMS stamp was brought into contact with the substrate through controlled pressure difference with simultaneous UV light exposure. Lastly, the stamp was removed and the micro-lens array was formed on the convex glass substrate. Figure 8 shows the fabricated master as well as the patterned micro-lens array on the convex glass substrate. The lens array was used to form an image of the character "F", which proves the micro-lens array, including its lens diameter, pitch and focal length, was fabricated with good precision.

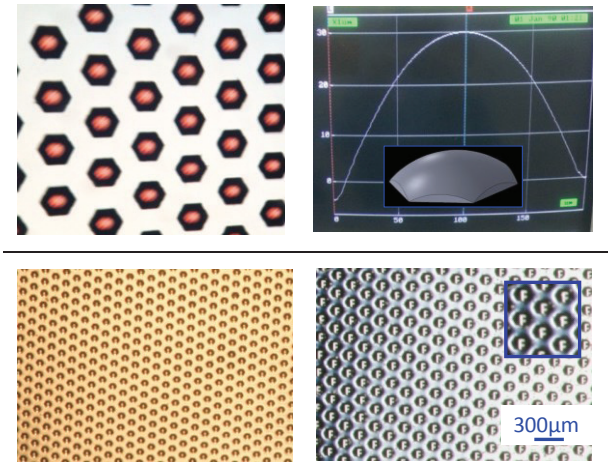

FIGURE 8. The distortion-corrected master (AZ4620) on a silicon wafer through the thermal reflow process as well as profile characterization of an individual lens on the master (top); patterned micro-lens array on a convex glass substrate by UV micro-imprinting technique and the imaging results—character "F" —through the fabricated micro-lens arrays (bottom).

CONCLUSION

We have developed a vacuum imprinting system that enables low-cost, high precision, large-scale (4" to 6") 2-D and 3-D pattern transfer on both planar and nonplanar substrates. This system is

fully computerized and automated with integrated pressure sensors and valves for closed-loop control and can be operated in multiple modes, e.g. contact printing mode or imprinting/molding mode, with minimal modification. Through our distortion-correction algorithm, we have proved the vacuum system can be used to scale up precision contact printing processes including MCP and UV micro-imprinting for patterning precision microscale patterns on 4" convex glass substrates.

ACKNOWLEDGEMENT

This work is supported by the CUHK Direct Grant 4055014: A High-precision Vacuum Stamping System for Printing Flexible Electronics and the HKSAR Innovation and Technology Commission (ITC) Innovation and Technology Fund (ITF), ITS/025/12: Precision Microcontact Printing for Roll-to-roll Fabrication of Flexible Electronics.

REFERENCES

[1] Qin D, Xia Y, and Whitesides GM. Soft Lithography for Micro- and Nanoscale Patterning. Nature Protocols. 2010; 5(3): 491 - 502.

[2] Xia Y and Whitesides GM. Soft Lithography. Annual Review of Materials Science. 1998; 28(0): 153-184.

[3] Radtke D, Duparre J, Zeitner UD, and Tunnermann A. Laser Lithographic Fabrication and Characterization of a Spherical Artificial Compound Eye. Optics Express. 2007; 15(6): 3067-3077.

[4] Chen F, Liu H, Yang Q, Wang X, Hou C, Bian H, Liang W, Si J, and Hou X. Maskless Fabrication of Concave Microlens Arrays on Silica Glasses by a Femtosecond-laser-enhanced Local Wet Etching Method. Optics Express. 2010; 18(19): 20334-20343.

[5] Liu H, Chen F, Yang Q, Qu P, He S, Wang X, Si J, and Hou X. Fabrication of Bioinspired Omnidirectional and Gapless Microlens Array for Wide Field-of-view Detections. Applied Physics Letters. 2012; 100(13): 133701-133701.

[6] Adkins JE and Ronald SR. Large Elastic Deformations of Isotropic Materials. IX. The Deformation of Thin Shells. Philosophical Transactions of the Royal Society of London, Series A, Mathematical and Physical Sciences. 1952; 244(888): 505-531.

[7] Bowen AM and Ralph GN. Fabrication of Flexible Binary Amplitude Masks for Patterning on Highly Curved Surfaces. Advanced Functional Materials. 2009; 19(20): 3243-3253.

[8] Schift H, Heyderman LJ, der Maur MA, and Gobrecht J. Pattern Formation in Hot Embossing of Thin Polymer Films. Nanotechnology. 2001; 12(2): 173.

[9] Moran IW, Briseno AL, Loser S, Carter KR. Device Fabrication by Easy Soft Imprint Nano-lithography. Chemistry of Materials. 2008; 20(14): 4595-4601.

PRECISION MODELING AND MEASUREMENT OF NUT STIFFNESS IN BALLSCREWS

Sung-Chong Chung[1*], Lei Cao[1], Gyungho Khim[2], and Chun-Hong Park[2]
[1]School of Mechanical Engineering
Hanyang University, Seoul 133-791, KOREA
[2] Intelligent Manufacturing System Division
KIMM, Daejeon 305-343, KOREA

ABSTRACT
Ballscrews are precision positioning units applied to industrial machinery and precision machines. As the positioning accuracy of a feeddrive system depends upon ballscrew stiffness, the nut stiffness estimation of ballscrews is important for precision machine design. In this paper, accurate nut stiffness model incorporating Hertzian deformation as well as flexibility of the screw shaft and nut is developed through consideration of contact angle variation of balls in the grooves during loading. Experimental verification of the stiffness model under various loads and assembly conditions has been conducted on the enhanced measurement system.

INTRODUCTION
Total axial stiffness of the leadscrew system depends upon stiffnesses of the nut, screw shaft, supported bearings, and nut bracket. The nut stiffness depends upon screw characteristics, preload and operating conditions. Recalling that the contact deformation of the nut assembly governed by Hertzian contact is affected by the groove shape, preload and thrust force, the nut stiffness of ballscrews should be thoroughly studied according to the contact deformation between the ball and groove.

For stiffness calculation, a rigid model assuming the nut and screw shaft are rigid except for contact points with balls had been used. However, it has been pointed out that the measured stiffnesses are considerably lower than the calculated values obtained using the rigid models [1-3]. They claimed that the calculated stiffness incorporating the flexibility of the screw shaft and nut matched the measured stiffness. However, they did not present explicit theoretical expressions for the stiffnesses of ball screws, which consists of Hertzian deformation and flexibility of the screw shaft and nut. In addition, contact angle variation due to loading changes the nut stiffness [1]. In this paper, calculation of nut stiffness due to the contact deformation between the balls and raceway grooves incorporating contact angle variation and flexibility of the ballscrew nut assembly is studied. To verify the developed explicit nut stiffness model, experimental verification under several loading and assembly conditions are performed in this paper.

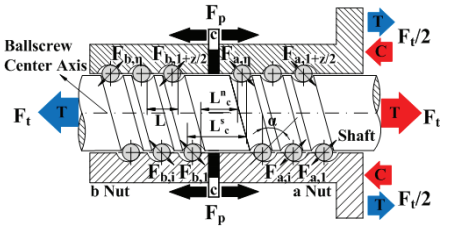

(a) Preloaded Double-nut Ballscrew

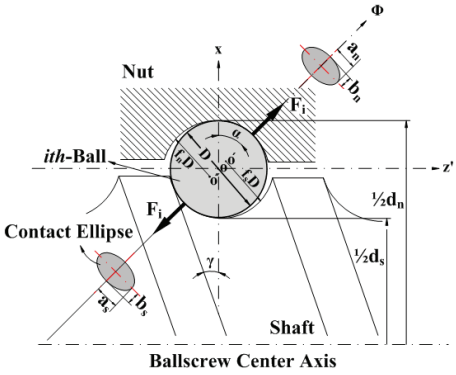

(b) Contact Mechanism

FIGURE 1. Ballscrew and Contact Mechanism.

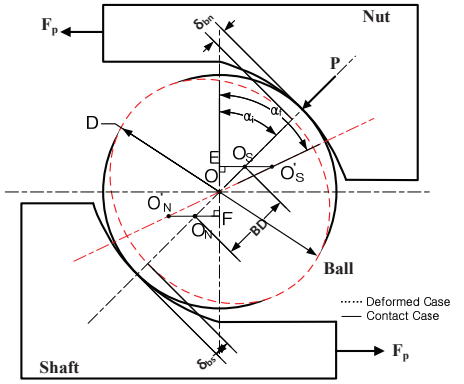

FIGURE 2. Contact Angle Change during Loading.

HERTZIAN AND BODY DEFORMATIONS

Fig. 1 shows cross sections of a double-nut ballscrew subject to thrust force F_t and tension preload F_p in TT (CC) and TC (CT) load conditions. Contact state between the ball and grooves is shown in Fig. 1(b). Assuming the F_p is applied by a spacer and the ball load F_i is equally distributed in the ballscrew, average ball load due to F_p is given by

$$P = \frac{F_p}{Z \sin\alpha \cos\gamma} \tag{1}$$

where Z is total number of loaded balls, α and γ are the contact and helix angles, respectively. According to previous research [1-3], Hertzian deformation constants on the ball and grooves of a ballscrew is given by

$$C_{bs,bn} = \frac{\delta_{bs,bn}^{*} \sum \rho_{bs,bn}}{2} \cdot \left[\frac{3}{2\sum \rho_{bs,bn}} \left(\frac{(1-\zeta_b^{\,2})}{E_b} + \frac{(1-\zeta_{n,s}^{\,2})}{E_{n,s}} \right) \right]^{\frac{2}{3}} \tag{2}$$

Hertzian deformation of nut *a* and *b* parts according to preload and thrust force in the TT (CC) load condition is given by

$$\delta_t^H = \delta_a^H - \delta_p^H = \delta_P^H - \delta_b^H \tag{3}$$

Body deformation of the nut and the shaft with *p* balls is given by

$$\delta_{total}^B = -\sum_{i=2}^{p} \delta_{i-1,i}^s \pm \sum_{i=2}^{p} \delta_{i-1,i}^n \quad \text{for } [\mathrm{TC}(+);\mathrm{TT}(-)] \tag{4}$$

Then, total deformation due to Hertzian and body deformation is given by

$$\delta_{total} = \delta_t^H + \delta_{total}^B \tag{5}$$

Using Eqs. (1), (2) and (5), Hertzian constant of the ballscrew nut assembly is given by

$$C_b = (C_{bn} + C_{bs}) Z^{-\frac{2}{3}} [\sin\alpha \cos\gamma]^{-\frac{5}{3}} \tag{6}$$

According to Eq. (6), it is confirmed that contact angle variation during loading changes Hertzian deformation significantly.

CONTACT ANGLE VARIATION

To derive more accurate stiffness model, the contact angle variation during loading should be included in the previous nut stiffness models [1-3]. Figure 2 shows the contact angle variation during preloading. Initial centers of the shaft and nut grooves O_N and O_S move to $O_N^{'}$ and $O_S^{'}$ after deformation. Length change between final groove centers is given by

$$\overline{O_N^{'} O_S^{'}} = fD + fD - D^{'} \tag{7}$$

where the ball diameter after deformation $D^{'}$ is derived as

$$D^{'} = D - \delta_b \tag{8}$$

Ball deformation δ_b in Eq. (8) is given by

$$\delta_b = \delta_{bs} + \delta_{bn} = \delta_t^H \tag{9}$$

Substituting Eqs. (8) and (9) into Eq. (7),

$$\overline{O_N^{'} O_S^{'}} = fD + fD - (D - \delta_b) = BD + \delta_b \tag{10}$$

where *B* is the total curvature. Considering triangles OEO_S and OEO'_S in Fig. 2, followings are obtained:

$$\overline{OE} = \overline{OO_S} \cos\alpha_i \quad , \quad \overline{OO_S^{'}} = \frac{\cos\alpha_i}{\cos\alpha_f} \overline{OO_S} \tag{11}$$

Diametral deformation of the shaft groove due to loading is given by

$$\delta_{bs} = \overline{OO_S^{'}} - \overline{OO_S} = \left(\frac{\cos\alpha_i}{\cos\alpha_f} - 1 \right) \overline{OO_S} \tag{12}$$

Similarly, diametral deformation of the nut groove is obtained from triangles OFO_N and OFO'_N as

$$\delta_{bn} = \left(\frac{\cos\alpha_i}{\cos\alpha_f} - 1 \right) \overline{OO_N} \tag{13}$$

Substitute Eqs. (12) and (13) into (9), the ball deformation is given by

$$\delta_b = \left(\frac{\cos\alpha_i}{\cos\alpha_f} - 1 \right) BD \qquad (14)$$

Substituting Eqs. (1) and (14) into Hertzian deformation $\delta_b = C_b P^{2/3}$, following relationship between the final and initial contact angles according to preload, number of balls, Hertzian constant, ball diameter, total curvature, *etc.* is obtained:

$$\frac{C_b}{BD}\left(\frac{F_p}{Z\cos\gamma_s} \right)^{2/3} = \left(\sin\alpha_f\right)^{2/3} \left(\frac{\cos\alpha_i}{\cos\alpha_f} - 1 \right) \qquad (13)$$

Considering contact deformation and geometric compatibility when the thrust force F_t is applied as shown in Fig. 1, following relationships are obtained for the working and preload nuts, respectively:

$$\frac{C_b}{BD}\left[\frac{\left(2F_p + F_t\right)/2}{Z\cos\gamma_s} \right]^{2/3} = \left(\sin\alpha_f\right)^{2/3} \left(\frac{\cos\alpha_i}{\cos\alpha_f} - 1 \right) \qquad (14)$$

$$\frac{C_b}{BD}\left[\frac{\left(F_t - 2F_p\right)/2}{Z\cos\gamma_s} \right]^{2/3} = \left(\sin\alpha_f\right)^{2/3} \left(\frac{\cos\alpha_i}{\cos\alpha_f} - 1 \right) \qquad (15)$$

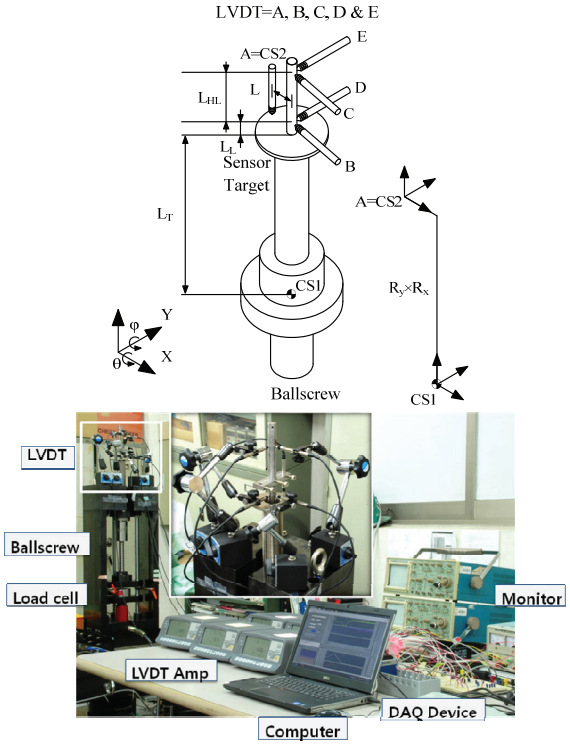

FIGURE 3. Previous Experimental Setup.

EXPERIMENTS

In previous nut stiffness measurements, thrust force was applied through a hydraulic cylinder equipped with a load cell. Measurement was conducted through precision 5 LVDTs with a tilting compensator shown in Fig. 3. However, precise loading and tilting compensation have not been conducted well due to limited number of LVDTs and upper side deformation of the loading mechanism as shown in Fig. 4.

In this paper, to compensator for the uncertainty of the loading mechanism, a screw pump is connected to the previous hydraulic unit for precise loading. New tilting compensator shown in Fig. 5 is applied for accurate measurement of the ballscrew nut deformation. The upper side deformation of the loading unit has been compensated as well. Comparisons of stiffnesses between the improved mathematical model and experiments are performed for several ballscrews, assembly and loading conditions.

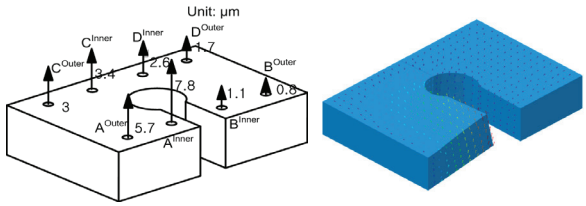

FIGURE 4. Upper Side Deformation of the Loading Unit.

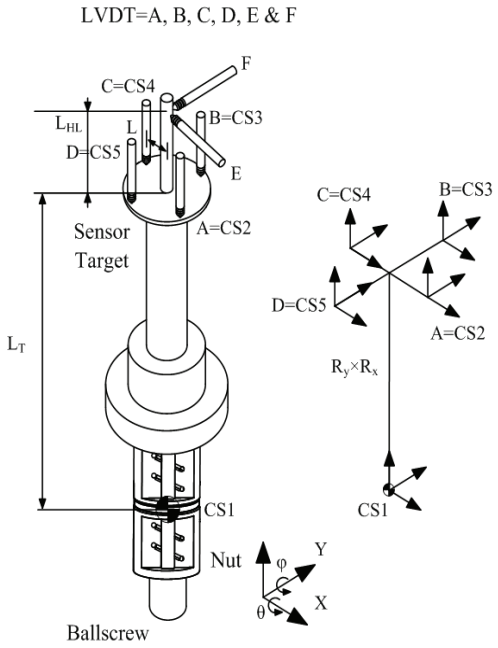

FIGURE 5. New Measurement Setup for Tilting Compensation.

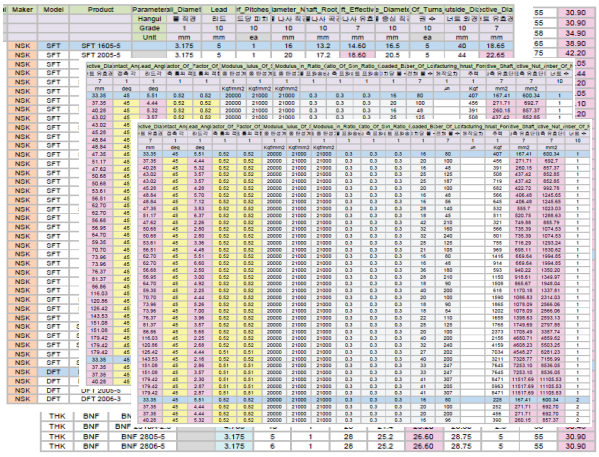

FIGURE 6. Geometric and Material DB of Commercial Ballscrews.

RESULTS AND DISCUSSION

Fig. 6 shows geometric and material DB of commercial ballscrews. Using the updated stiffness estimation models including the contact angle variation effect and the new experimental setup, axial deformation and stiffness according to thrust force in CC (TT) load conditions of THK's BNFN2505-5 have been obtained as shown in Fig. 7. Contact angle during loading is around 43~46°, preload is 129 Kgf, both conformity factors are 0.59. During the experiment, preload is fully released in the *b* nut around 600Kgf thrust force. The stiffness decreases upto this critical load as the thrust force increases. The stiffness increases after passing the critical load. Based on Fig. 7, mathematically obtained axial deformation and stiffness of BNFN2505-5 with 129Kgf preload are 2.53μm and 79.17Kgf/μm at 200Kgf thrust force, respectively. Measured mean deformation and stiffness are 2.56μm and 78.07Kgf/μm at 200Kgf thrust force, respectively. Analytical stiffness at 1000Kgf is 72.07Kgf/μm. Measured stiffness is 71.12Kgf/μm at 1000 Kgf loading. They show that experimental stiffness is around 98.61% and 98.68% of the analytical value at 200Kgf and 1000Kgf thrust force, respectively. It is confirmed that estimated and experimental nut stiffnesses are matched well within 5% in 1000Kgf thrust force loading range. For CT loading case, BNFN2505-5 with preload 129Kgf shows larger deformations and smaller stiffnesses than CC case as shown in Fig. 8. Estimated and experimental nut stiffnesses are within 5% deviation in 1000Kgf loading range as well. For BNFN3610-5 case, estimated and experimental nut stiffnesses are within 8% difference in 2000Kgf loading range as shown in Fig. 9.

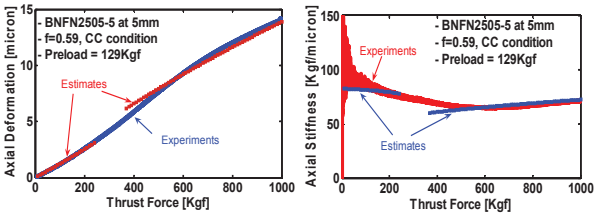

FIGURE 7. Axial Deformations and Stiffnesses of BNFN2505-5 in CC Loading with 129Kgf Preload.

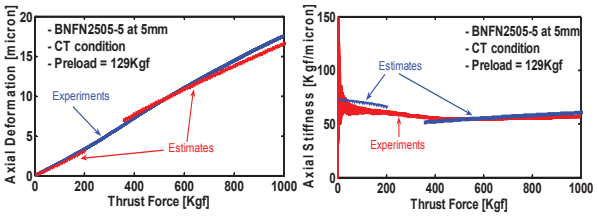

FIGURE 8. Axial Deformations and Stiffnesses of BNFN2505-5 in CT Loading with 129Kgf Preload.

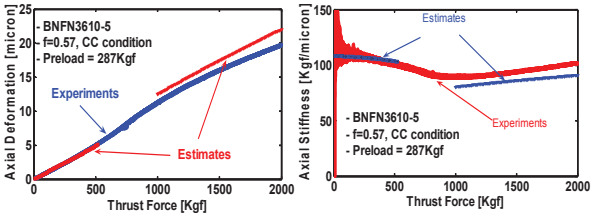

FIGURE 9. Axial Deformations and Stiffnesses of BNFN3610-5 in CC Loading with 287Kgf Preload.

CONCLUSIONS

New stiffness measurement system has been devised for verification of the improved nut stiffness model of ballscrews. It is confirmed that the contact angle variation effect included in the estimation model renders the stiffness estimation correct within 8% deviation

ACKNOWLEDGEMENT

This research is funded by the Ministry of Trade, Industry & Energy, Korea.

REFERENCES

[1] Chung S-C, Park C-H. Analysis of Ballscrew Stiffness owing to Contact Deformation in Leadscrew Systems. Proceedings of the ASPE 2010 Annual Meeting. 2010; 50:160-163.

[2] Chung S-C, Park C-H. Experimental Determination of Nut Stiffness in Ballscrews. Proceedings of the ASPE 2011 Annual Meeting. 2011; 52:295-298.

[3] Chung S-C, Khim G, Park C-H. Precision Measurement of Nut Stiffness in Ballscrews. Proceedings of the ASPE 2012 Annual Meeting. 2012; 54:382-385.

DESIGN OF A PRECISION MASS TRANSLATION SYSTEM FOR GRAVITY MEASUREMENTS

Pete Fitsos[1], Stan Edson[1], Pete J. Davis[1], John S. Taylor[1], Stephen B. Libby[1], Michael A. Johnson[1], Tom Loftus[2], Vijay Sonnad[1], Boris Dubetsky[2], Daniel C. Thompson[3], [1]Lawrence Livermore National Laboratory, Livermore, California, 94550, USA, [2]AOSense, Inc., Sunnyvale, CA, 94085, USA, [3]Praecis, Inc., West Lebanon, NH 03784, USA

INTRODUCTION

Lawrence Livermore National Laboratory (LLNL) and AOSense, Inc. are developing a metrology instrument to be used in conjunction with a high sensitivity cold atom gravity gradiometer to do precision tests of the fundamental nature of gravity [i]. Earlier measurements, both with cold atom sensors [iii] and torsion pendulums, established the feasibility of this type of experiment [ii]. These measurements require very precise control of the absolute strength of the local gravity gradient signal due to a well-characterized proof mass and its geometrical error budget. This paper describes the design, experimental use of the proof mass and motion system and their impact on the accuracy of the instrument. A key feature of this project is calibration using local, controlled variations in the gravitational field caused by the motion of proof masses with known mass distributions. The complete instrument is shown conceptually in Figure 1 with the mass translation system mounted horizontally and the components of the gradiometer mounted vertically.

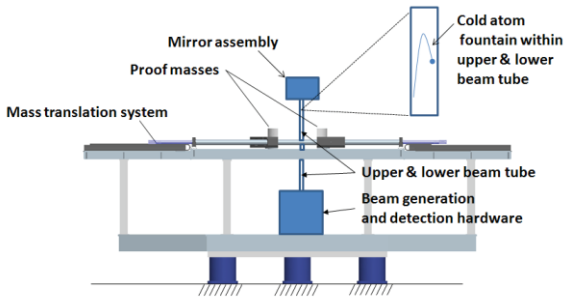

Figure 1. Conceptual design of the gradiometer metrology instrument.

SYSTEM DESIGN

The gradiometer itself is based on atom interferometry [iii] and consists of paired cold atom beam generation (for noise rejection) and detection hardware, a beam tube and mirror assembly. Within the beam tube there are 2 sets of ballistically launched cold atom fountains: one near the proof masses in the upper region of the tube and one set in the lower portion. With proof masses located nominally above the central plane between the two fountains, each set of atoms will be attracted differentially to the proof masses depending on their lateral positions, thus probing the spatial variation and strength of the gravitational force.

This study will require: 1) The repeatable registration of the proof masses center of gravity (CG) with respect to the global coordinate system (CS); 2) The repeatable and accurate linear position of the proof masses with respect to the global CS; 3) An accurate knowledge of the position of the atom clouds within the measurement instrument with respect to the global CS; 4) An accurate measure of the mass of the proof masses.

The support and position of the proof masses will be accomplished with the mass translation system as shown in Figure 2 (gradiometer not shown). The proof masses are identical hemi-cylinders made from sintered tungsten, MT-18C weighing 75 kg each. The proof masses are kinematically supported on carriages using silicon nitride balls in carbide V grooves. The balls are mounted on the proof mass at the plane of the CG to enable a rotation about a horizontal axis so that a vertical reversal test [iv] can be done to separate vertical location uncertainty in the CG from asymmetry in identifying the plane of symmetry between the upper and lower interferometer. The masses can also be exchanged, left for right, to identify lateral uncertainty in the CG location relative to the atom clouds for the respective masses.

At this time, there is no provision for rotating the entire motion system about the axis of the instrument for a more complete exploration of reversal concepts. The proof masses are

supported kinematically by custom balls that have been truncated to allow for a more compact packaging on their V-grooves as shown in Figure 3.

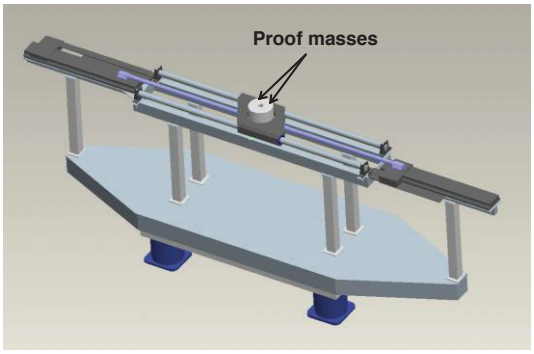

Figure 2. Conceptual design of mass translation system.

The V-grooves are attached to carriages that are kinematically supported by cylindrical air bearing bushings riding on stainless steel rods as shown in Figure 4. The rods are supported by a flexure in the center and a brackets at the ends, which are tied to a sub frame and an isolator supported granite base as shown in Figure 5.

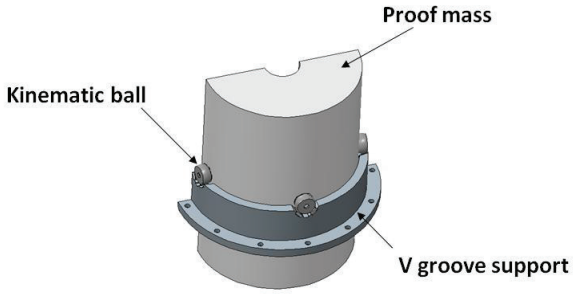

Figure 3. Proof mass and its V-groove support.

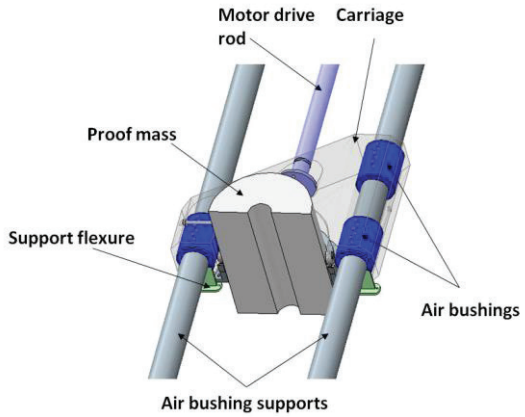

Figure 4. Proof mass assembly supported by air bushings that ride on steel tube supports.

The carriages, driven by linear motors, accurately position the proof masses at various distances from the beam tube as part of the experiment. A rod with flexures at two axial locations connects the proof mass carriage to the driver carriage. Initially, position feedback will be provided by scales within the driver stages, minimizing Abbe offset. Following initial set-up and construction, the stage system with proof masses will be characterized using a CMM to assess repeatability and the precision of mapping the location of the mass CGs to the output of the stage position metrology. Additional concepts developed for position feedback will use either scales directly mounted adjacent to the proof mass carriages or by using displacement measuring interferometers. Both approaches offer advantages, but with space constraints present packaging challenges.

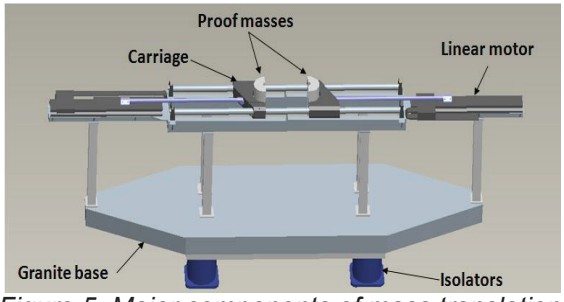

Figure 5. Major components of mass translation system.

ERROR BUDGET

The accuracy will depend on the accurate characterization and position of the center of gravity (CG) for each proof mass. Variation in the inner and outer radius of the proof mass will shift the CG in the horizontal plane, while variation in the height and surface finish will shift the CG in the vertical direction. The variation in the CG due to the accuracy of fabrication and repeatability of the kinematic couplings and the actuator of the proof mass is shown in Table 1.

Table 1. Errors in CG position due manufacturing tolerances and repeatability.

Error Source	lateral (um)	Radial (um)	Height (um)
Δ in radii		26.4	
Δ in height			80.0
Δ in height due to surface finish			1.0
Δ kinematic ball 1	0.062	0.016	0.062

Δ kinematic ball 2	0.060	0.0093	0.045
Δ kinematic ball 3	0.060	0.0093	0.045
actuator precision		0.75	
kinematic coupling	0.50	0.50	0.50
proof mass material homogeneity	TBD	TBD	TBD
SUM	0.68	27.7	81.6
RMS	0.15	7.7	23.1
total= (sum+rms)/2	0.42	17.7	52.4

We believe the material homogeneity of the proof masses is very good but we haven't determined how we will verify it at this time. The overall error for each direction was calculated by taking the average of the sum of errors and the RMS error [v].

In order to accurately capture the gravitational effect of the proof masses, the uncertainty in the CG location must be less than 200 microns in the lateral and radial directions and less than 10 microns in height. Our initial estimate of the geometric error of 52.4 microns is greater than this requirement. This error in the CG will be mitigated by accurately measuring the radii and height of each proof mass and calculating the CG using Finite Element Analysis (FEA). The resulting radial and height errors are expected to be reduced to approximately 1 and 1.8 microns respectively as shown in Table 2 below. This estimate doesn't include the uncertainty in the density of the proof mass material.

Table 2. Errors in CG position after characterizing the proof masses on a CMM.

Error Source	Radial (um)	Height (um)
Variation in radii	1.1	
Variation in height		2.0
FEA error in radii	0.55	
FEA error in height		1.0
Sum	1.65	3.0
RMS of p-v	0.36	0.58
Total (Sum+RMS)/2	1.01	1.79

The revised error budget with this correction is shown Table 3. The total estimated errors in the radial direction are reduced from 17.7 microns to 1.74 and the error in the height is reduced from 52.4 microns to 2.26 microns.

The error due the variation in the position of the kinematic balls was estimated by modeling the coupling triangle [vi] of the ball on the V-groove as shown in Figure 6. The coupling triangle was used to model the kinematics of the errors in the CG due to the variation in the position of the kinematic balls on the proof mass as shown in Figure 7.

Table 3. Errors in CG due to manufacturing tolerances and repeatability with proof mass geometry corrected by characterizing the proof masses on a CMM.

Error Source	lateral (um)	Radial (um)	Height (um)
Δ in radii		1.65	
Δ in height			3.0
Δ in height due to surface finish			
Δ kinematic ball 1	0.062	0.016	0.062
Δ kinematic ball 2	0.060	0.0093	0.045
Δ kinematic ball 3	0.060	0.0093	0.045
actuator precision		0.75	
kinematic coupling	0.50	0.50	0.50
proof mass material homogeneity	TBD	TBD	TBD
SUM	0.68	2.93	3.65
RMS	0.15	0.54	0.88
total= (sum+rms)/2	0.42	1.74	2.26

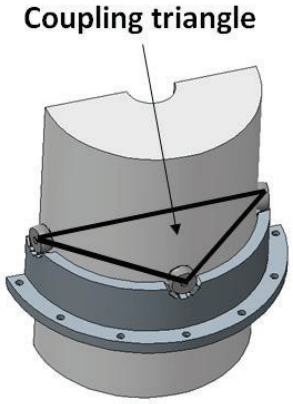

Figure 6. Coupling triangle used to estimate error due to the kinematic ball's position manufacturing tolerances.

The triangle was modeled in Matlab where each vertex of the triangle represented a

kinematic ball position. Changes in the lateral position of the vertex resulted in rotation of the triangle. Vertical variation in the kinematic ball position caused the proof mass to rotate up or down. These kinematics were incorporated into an error matrix for each kinematic ball labeled $\mathbf{E_1}, \mathbf{E_2}, \mathbf{E_3}$. Also included were manufacturing errors in the angle of the respective V-grooves.

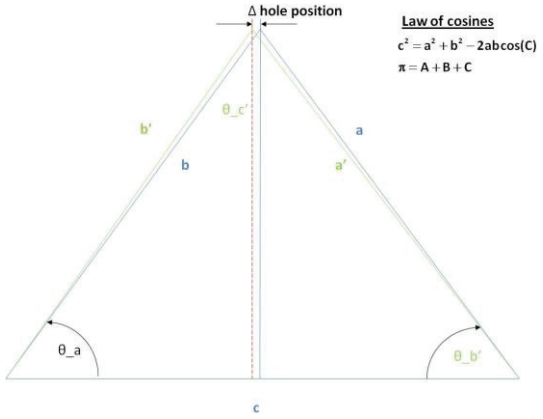

Figure 7. The kinematics of the errors due to changes in the lateral pin hole position of the kinematic ball insert.

Homogeneous Transformation Matrices (HTM) [vi] where used to model position errors by placing coordinate systems on the kinematic balls and the CG and referencing back to a base coordinate system labeled 0 as shown in Figure 8. As an example this approach is summarized in equation (1) where the transformation between coordinate system 0 (CS-0) and CS-1 is multiplied by the error matrix $\mathbf{E_1}$.

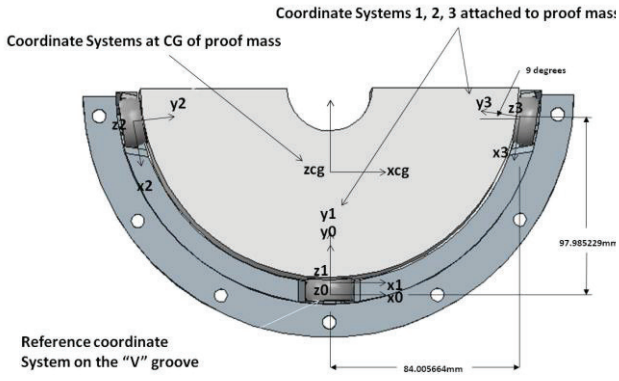

Figure 8. Coordinate systems used with the coupling triangle to estimate errors.

$$\mathbf{T_{0/1}} = \mathbf{M_{0/1}}\mathbf{E_1} \qquad (1)$$

Where:

$\mathbf{T_{0/1}}$ = The transformation between CS-0 and CS-1 including errors

$\mathbf{M_{0/1}}$ = The HTM between CS-0 and CS-1

$\mathbf{E_1}$ = The error between CS-0 and CS-1

The combined matrices that relate the position of the CG back to the base coordinate system is shown below in equation (2):

$$\mathbf{v_0} = \mathbf{T_{0/1}}\mathbf{T_{1/2}}\mathbf{T_{2/CG}}\mathbf{v_{CG}} \qquad (2)$$

Where:

$\mathbf{v_0}$ = The position of the CG in the base coordinate system.

$\mathbf{v_{CG}}$ = The position of the CG in the CG coordinate system.

These errors where subtracted from the ideal position of the proof mass CG when it's seated on the V-grooves with no manufacturing errors to generate the net error as shown below in equation (3):

$$\Delta_{error} = \mathbf{v_0} - \mathbf{v_{0\_ideal}} \qquad (3)$$

The same calculation of error was done for each of the kinematic balls and all of the errors in each direction were added together to give the overall error.

Planned Experiments

Initial experiments will be done by taking gradiometer phase data from three or more mass positions. These will likely be:
1) In the closed position around the beam tube; 2) Separated by the mass translator about 30 cm on each side from the beam tube; 3) Separated about 65 cm on each side of the beam tube. The data will be taken with the mass stationary at each position for about 6 hours because of the sensor stability limits. Then the masses will be brought back to 30 cm and additional measurements will be

taken. The experiment will be run in a cyclic fashion over several weeks. The same experiment will be run with the proof masses exchanged and turned over on the V-grooves.

Another important class of experiments will be to deliberately create asymmetries, such as having the cylinder sections at different distances from the beam tube in order to check our detailed sensor response model, which includes quantum corrections to the basic cold atom trajectories.

This work performed under the auspices of the U.S. Department of Energy by Lawrence Livermore National Laboratory under Contract DE-AC52-07NA27344. The support of LLNL LDRD 12-LW-009 is gratefully acknowledged.

REFERENCES

[i] For example, see: Kapner, D, J., et. al., "Tests of the Gravitational Inverse-Square Law below the Dark-Energy Length Scale," *Phys. Rev. Lett.*, vol. 98, 021101, (2007); Adelberger, E. G., et. al., "Particle-Physics Implication E. G. Adelberger, B. R. Heckel, et. al., "Particle-Physics Implications of a Recent Test of the Gravitational Inverse Square Law," *Phys. Rev. Lett.*, vol. 98 131104, (2007). s of a Recent Test of the Gravitational Inverse Square Law," *Phys. Rev. Lett.*, vol. 98 131104, (2007).

[ii] Fixler, J. B., et. al., "Atom interferometer measurement of the Newtonian constant of gravity", *Science*, vol. 315, 74 (2007).

[iii] M. Kasevich and S. Chu, "Measurement of the gravitational acceleration of an atom with a light-pulse atom interferometer," Appl. Phys. B 54, 321 (1992). Kasevich, M. A., "Atom interferometry in an atomic fountain", PhD Dissertation, Stanford Univ. (June 1992).

[iv] Evans, C.J., Hocken, R.J., Estler, W. T., Self-Calibration: Reversal, Redundancy, Error Separation and "Absolute Testing", CIRP Annals, vol. 45-2 (1996) 617-634.

[v] Shen, Y.L., Duffie, N.A., Comparison of Combinatory Rules for Machine Error Budgets, Annals of CIRP, Vol. 42, No. 1, 1993.

[vi] Slocum, A. H., Precision Machine Desig*n*, Prentice Hall, New Jersey, 1985, p282; the primary reference is Donaldson R. R., "A simple method for separating spindle error from test ball roundness error", CIRP Annals, vol. 21-1 (1972) 125-126.

A PLANAR MOTOR WITH AN ACTIVE ENCODER

Jian Gao and Peisen S. Huang
State Key Laboratory of Mechanical Systems and Vibration
University of Michigan – Shanghai Jiao Tong University Joint Institute
Shanghai Jiao Tong University
Shanghai, China

INTRODUCTION

Planar motion is widely used in various manufacturing applications. In most cases, planar motion is achieved by stacking multiple linear stages together. There are some major disadvantages of such an approach, including error accumulation, increased system complexity, bulky size, and reduced stiffness.

In the past few decades, many researchers proposed ideas of planar motors, which use a single mover to provide planar motions. Trumper and Kim used magnetic levitation to control the mover in an area of 50 x 50 mm [1]. Gao *et al*. developed a planar motor that used air bearings to support the mover and a 3-DOF (degree-of-freedom) surface encoder for position feedback [2]. Lu and Usman extended Trumper and Kim's work by using PCB (printed circuit board) coils, which made long-stroke motion possible [3].

One common problem with all planar motors lies in the position measurement system used. Trumper and Kim's planar motor used a laser interferometer to provide position feedback, which is too expensive and bulky to be integrated with each motor. Gao's planar motor used a surface encoder with a unique angle grating, but the measurement range was limited to 50 × 50 mm. Lu and Usman's planar motor used a 6-DOF stereo-vision based position sensor, which has limited resolutions.

Recently a novel position encoder called active encoder was proposed for nano position measurement [4]. This encoder uses a flat panel display as a grating and a camera as a reading head. Since a flat panel display can be programmed to display any pattern, it is called an active grating and hence the name of the encoder. One important advantage of the active encoder is that it can provide incremental as well as absolute position measurement. The use of a commercial LCD or OLED display also makes simultaneous 3-DOF ($XY\theta_z$) position measurement possible. The experimental system consisted of two industrial cameras with microscope lenses and a flat panel display with a pixel pitch of 26 μm. Experimental results showed that such an active encoder could achieve a resolution of approximately 4 nm for linear displacement and 0.4 μrad for rotational angle measurement. However, the sampling rate, which was limited by the frame rate of the cameras, was relatively low. This makes it difficult for the encoder to be used for dynamic motion control. Besides, the size of the microscope lens was too large to be integrated with a precision motion control system such as a planar motor.

The objectives of this research are two-folds: 1) to develop an active encoder that has a high bandwith and is compact and 2) to integrate the active encoder with a planar motor to demonstrate the feasibility of using the active encoder for position feedback of planar motion control.

For the first objective, we replace the industrial cameras with linear CCD sensors and place them very close to the flat panel display to sense the pattern on the display. Since no lens is needed, the encoder can be made very small. A linear CCD sensor typically has a bandwidth in the KHz range, which is significantly higher than indsutrial cameras. Thus, the bandwith of the encoder can be significantly improved.

For the second objective, we design a meganetically driven planar motor with an integrated active encoder. The planar motor contains three 2-phase synchronous linear motors, which use coil windings as the stators and permanent magnet arrays as the armature. To simplify the control of the planar motor, vacuum preloaded air bearings are used to float the mover at a certain height above the granite base. The active encoder is used to provide positional feedback.

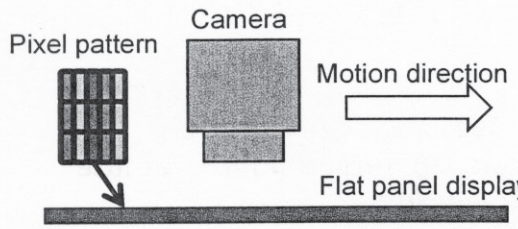

FIGURE 1. Active encoder consisting of a camera and a flat panel display.

The rest of the paper is organized as follows. First, the principle of both the active encoder and the planar motor will be explained. Then the experimental system will be described and some experiemental results of the encoder presented. Finally the paper is concluded with a summary of major findings so far and future work.

PRINCIPLE

Active Encoder

An active encoder consists of a flat panel display and a camera, as shown in Figure 1. The flat panel display is programed to display a perodic pattern, which serves as a grating. The camera captures an image of the pattern, which is then processed by a phase correlation method to obtain position information with high resolution. Since the pattern shown on the display can be changed dynamically, an active encoder allows for absolute positions to be measured with ease. This is the major advantage of an active encoder when compared to conventional encoders.

The resolution of an active encoder is mainly determined by the pitch of the periodic pattern on the display, the resolution of the camera, and the quality of the image captured. The smallest pitch of the display pattern is the pitch of the pixels of the display, which is in the order of tens of microns for commercially available displays. Therefore, to achieve nanometer-order position measurement resolution, a subdivision method is necessary. Previously, a subdivision method based on the phase correlation method has been developed and proven to be effective in subdividing the periodical signal up to 8,000 times.

The phase correlation method detects the change in phase of a periodic signal and use that to measure displacement. Let $x(n)$ be a series of *N* points in the spacial domain, which is a periodic signal obtained from the image captured by the camera. Using DFT, $x(n)$ can be tranformed into the frequency domain as follows:

$$X(k) = \sum_{n=0}^{N-1} x(n) e^{-\frac{j2\pi kn}{N}}, k = 0, 1, \ldots, \qquad (1)$$

where $X(k)$ is a complex number including both the amplitude and phase information. The fundamental frequency in the series $X(k)$ is equal to the pitch of the periodic pattern on the display.

Due to the relative displacement between the camera and the display surface, the phase of the fundamental frequency component will change. Meanwhile, the pitch of the periodic pattern on the display that corresponds to the fundamental frequency of the input signal is fixed. Therefore, the displacement can be calculated from the phase shift of the fundamental frequency component as follows:

$$\Delta d = p\Delta\phi_0, \qquad (2)$$

where Δd is the relative displacement, p is the pitch of the periodic pattern on the display, and $\Delta\phi_0$ is the phase shift of the fundamental frequency component caused by the displacement. By using this phase correlation method, the position information can be obtained from phase information in the frequency domain, which makes it much more sensitive to measure the position information.

If two lines of the image signal at different positions are used, the in-plane rotation angle θ_z can also be measured. Here the phase correlation method can still be used to achieve high resolution. Figure 2 shows the definition of parameters when there is a rotation about the Z axis.

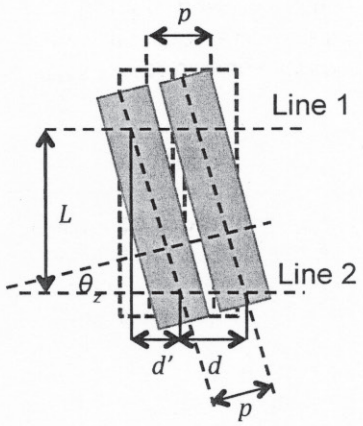

FIGURE 2. Parameter definition for rotation angle measurement.

The blue dashline and shaded rectangles represent the position of the periodic pattern before and after the rotation respectively. Line 1 and Line 2 are two sampling lines of the camera that produce two periodic signals. Their fundamental frequency corresponds to the horizontal distance between two grating lines of the pattern, which is denoted as d. L is the distance between the two sampling lines, d' corresponds to the phase shift $\Delta\phi_0$ of the fundamental frequency between the two sampling lines obtained by the phase correlation method, and θ_z is the rotation angle. Based on the geometric relationship, the following equations can be derived:

$$\Delta\phi = \frac{d'}{d}2\pi - 2n\pi, \tag{3}$$

$$d = \frac{p}{\cos\theta_z}, \tag{4}$$

$$d' = L\tan\theta_z, \tag{5}$$

where n is the number of periods betweent the signals of these two lines and $\Delta\phi$ is in the range $0\sim2\pi$. Substituting Eqs. (4) and (5) into Eq. (3), we obtain the relationship between $\Delta\phi$ and θ_z as

$$\Delta\phi = 2\pi\left(\frac{L}{p}\sin\theta_z - n\right), \tag{6}$$

$$\theta_z = \sin^{-1}\left[\frac{p}{2\pi L}(\Delta\phi + 2n\pi)\right]. \tag{7}$$

From Eq. (7), it is apparent that the resolution of the rotation angle measurement depends on L. The larger the L value, the higher the resolution of rotation angle measurement. The two sampling lines can be from the same camera or from two separate cameras. In the former case, the resolution of rotation angle measurement is limited because L cannot be very large. In the later case, the resolution is determined by the separation distance between the two cameras.

Planar Motor

Figure 3 shows the concept of the planar motor with an active encoder. The coil windings are mounted on a granite base. An LCD display panel (iPhone 4) is mounted at the centor of the granite base. The mover containing three permanent magnet arrays and an encoder reading head is supported by air bearings.

The planar motor is driven by three 2-phase linear motors. The stator has three sets of coil windings while the armature has three permanent magnet arrays. Figure 4 shows the schematic diagram of each linear motor and the geometric relationship between the armature and the stator. With the three linear motors controlled independently, planar motion with three DOFs can be generated.

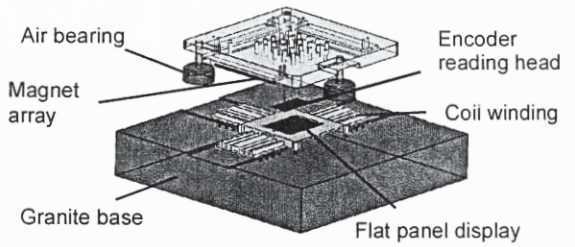

FIGURE 3. Conceptual design of a planar motor with an active encoder.

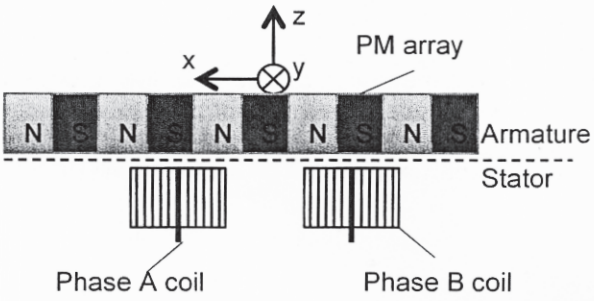

FIGURE 4. Stator and armature of the linear motor.

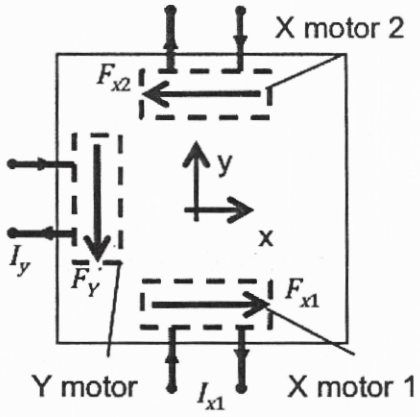

FIGURE 5. Model of the planar motor.

Figure 5 shows the dynamic model of the planar motor. Assume that the thrust force $F(t)$ and the stator coil current $I(t)$ are as follows:

$$F(t) = \begin{bmatrix} F_{x1}(t) \\ F_{x2}(t) \\ F_y(t) \end{bmatrix}, \tag{8}$$

$$I(t) = \begin{bmatrix} I_{x1}(t) \\ I_{x2}(t) \\ I_y(t) \end{bmatrix}. \quad (9)$$

The relationship between $F(t)$ and $I(t)$ is linear and can be represented by

$$F(t) = K_f I(t), \quad (10)$$

where K_f is a force constant matrix defined as

$$K_f = \begin{bmatrix} k_{x1} & 0 & 0 \\ 0 & k_{x2} & 0 \\ 0 & 0 & k_y \end{bmatrix}. \quad (11)$$

Based on the magnetic field distribution of the permanent magnets, a sinusoidal driving current will be produced by the controller to drive the mover and to synchronize the positions of the permanent magnets and the stator coils. A PID controller will be implemented to control the planar motor with position feedbacks from the proposed active encoder.

EXPERIMENTAL RESULTS

Figure 6 shows a diagram of the experimental setup, which includes a planar motor, an active encoder, and an ARM microprocessor as the control unit. The phase correlation algorithm is implemented in the microprocesssor, so is a PID controller.

For the active encoder, a linear CCD sensor is used to replace the camera in the previous system. No lens is used and the sensor is placed very close to the display surface to capture the pattern on the display directly. The signal acquired by the sensor without a lens is blurred. However, since only the fundamental frequency component is needed for the phase calculation, this signal blurring effect is not a problem as long as the signal contrast is sufficiently good.

Use of a linear CCD sensor without a lens has several advantages. First, the device is much smaller in size when compared to a typical camera, which makes it easier to integrate the device with motion control systems. Second, the sampling rate is typically in the KHz range, which is 10 times higher than that for a typical camera. Such a high sampling rate is necessary if the encoder is to be used for motion control. The disadvantage of using a linear CCD sensor without a lens is that the position measurement resolution will be reduced. With a microscope lens, the image can resolve down to the pixel level of the display, which makes it possible to achieve a resolution of a few nanometers. Without the lens, however, the resolving power of the sensor is limited. This means that the the pitch of the line pattern on the display has to be larger, which translates into lower position measurement resolution.

Figure 7 shows the reading head of the active encoder, which consists of 3 identical linear CCD sensors. They are used to measure X and Y displacements as well as rotation angle θ_z. Each sensor has 128 pixels with a pixel size of 63.5 × 63.5 μm and a sampling rate of 2 KHz. Due to the relatively large pixel size and the fact that no lens is used, the pitch of the line pattern on the display cannot be too small. Through experiments, we found the appropriate pitch of the line pattern to be 3 mm. Figure 8 shows the X and Y line patterns used in our experiments. Obviously, these patterns can be easily changed if necessary.

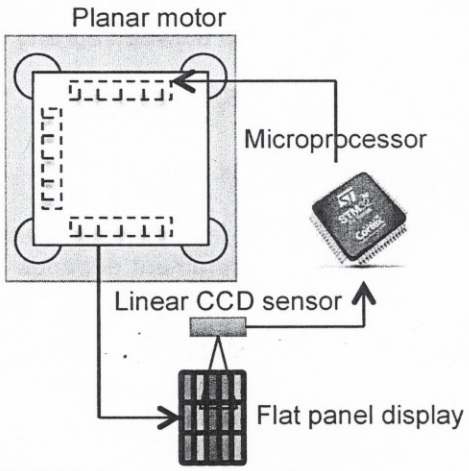

FIGURE 6. Experimental setup.

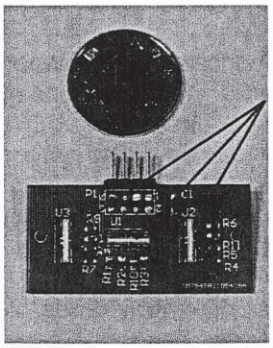

FIGURE 7. Reading head of the active encoder.

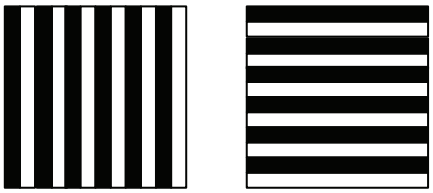

(a) (b)

FIGURE 8. Periodic patterns on the display.

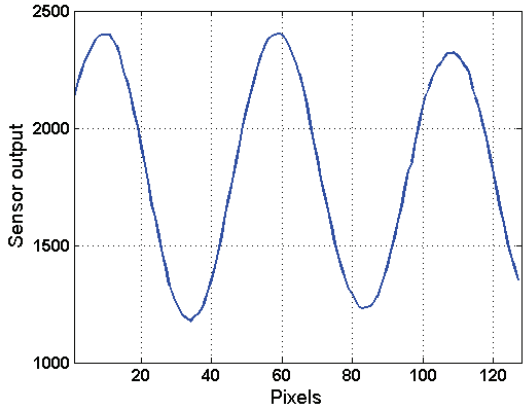

FIGURE 9. Signal from a linear CCD sensor.

Figure 9 shows the signal from a linear CCD sensor, which was placed right above the display with the periodic pattern shown in Figure 8. It can be seen that the signal is a clean sinusoidal signal with low noise. Its modulation depth is approximately 60%. With this signal, we can expect to achieve a high level of subdivision by use of the phase correlation method.

To evaluate the performance of the proposed active encoder with the linear CCD sensors, a multi-axis ($XY\theta_z$) piezo stage with a travel of 100 μm in X and Y directions and ± 1 mrad in θ_z and a closed-loop resolution of 0.3 nm in X and Y directions and ± 0.1 μrad in θ_z direction was used to generate the reference motion. Figure 11 shows the results of the stepping tests in all three directions. The chosen step sizes are 1 μm for displacement in X and Y directions and 50 μrad in θ_z direction. The standard deviations are found to be 0.24 μm in X direction, 0.20 μm in Y direction, and 13.5 μrad in θ_z. These results mean that using the phase correlation method, we were able to subdivide the signal by over 10,000 times, which is quite good. In the future, we plan to use a linear CCD sensor with a much smaller pixel size, which should significantly improve the resolution of the encoder.

Figure 11 is a picture of the prototype planar motor being developed. We are currently at the final stage of assemble the system together and will soon start testing its performance. The results will be reported in the near future.

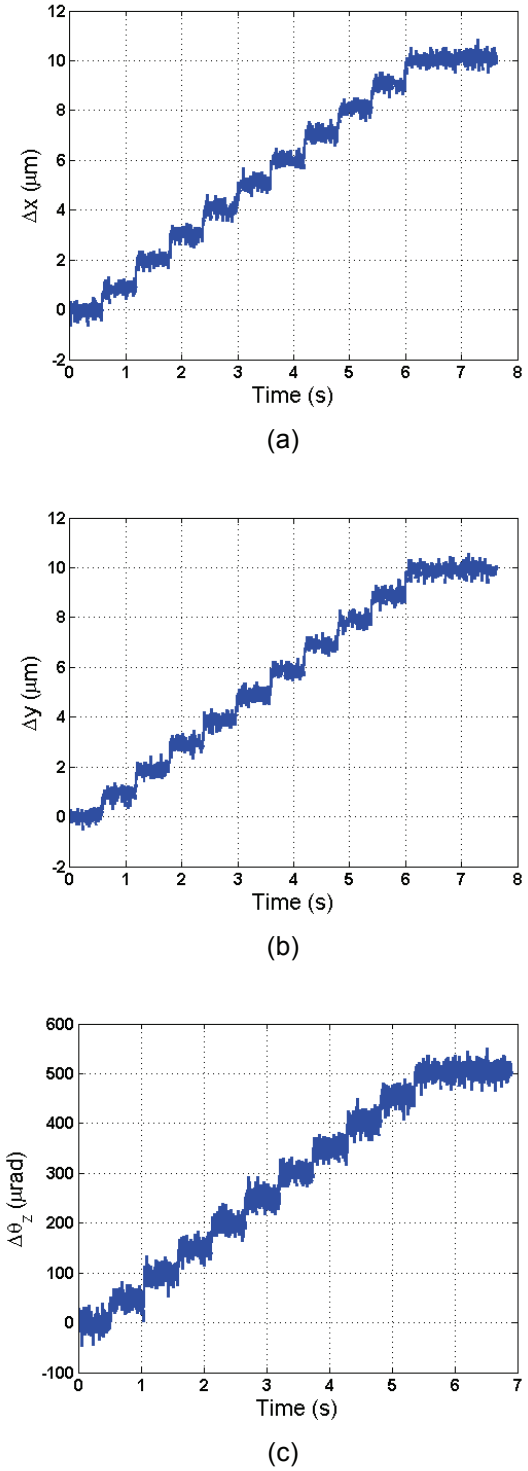

FIGURE 10. Results of the stepping tests. (a) X direction. (b) Y direction. (c) θ_z direction.

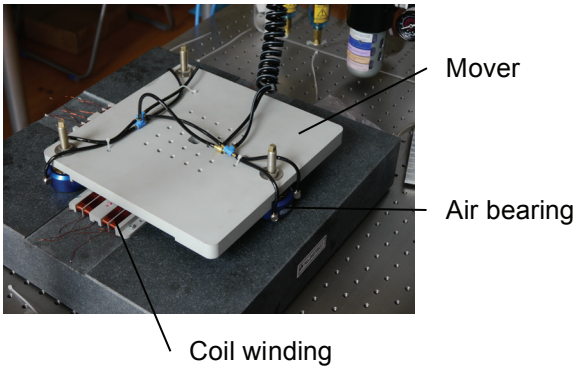

FIGURE 11. Prototype planar motor.

CONCLUSION

In this paper, a planar motor with a novel active encoder for position feedback is proposed. This active encoder uses the LCD display of an iPhone as the grating and three linear CCD sensors as the reading head. The sensors are mounted very close to the display and capture images of the line pattern on the display directly without use of any lens. A phase correlation algorithm is used to process the signals to obtain position information with high resolution. X and Y displacements as well as rotation angle around the Z axis can be measured simultaneously. Since the linear CCD sensors have a high sampling rate, the proposed active encoder has a high bandwidth and is suitable for use in dynamic motion control systems. Experiments with the active encoder demonstrated a resolution of 0.24 μm and 0.20 μm for X and Y displacement measurement and a resolution of 13.5 μrad for rotation angle measurement.

As our future work, we plan to further improve the resolution of the active encoder by using linear CCD sensors with a smaller pixel size and a larger number of pixels as well as micro lenses to improve the quality of the sampled signals. We aslo plan to complete the design and construction of the planar motor and test its motion control performance, especially with position feedback from the active encoder. All the results will be reported in the near future.

REFERENCES

[1] Kim WJ, Trumper DL. High-precision magnetic levitation stage for photo-lithography. Precision Engineering. 1998; 22(2): 66–77.

[2] Gao W, Dejima S, Yanai H, Katakura K, Kiyono S, Tomita Y. A Surface Motor-Driven Planar Motion Stage Integrated with an XYZ**θ** Surface Encoder for Precision Positioning. Precision Engineering. 2004; 28(3): 329–337.

[3] Lu X, Usman I, 6D direct-drive technology for planar motion stages. CIRP Annals - Manufacturing Technology 2012; 61: 359-362.

[4] Tian K. An active encoder for precision position measurement. MS Thesis, UM-SJTU Joint Institute: 2013.

[5] Yasuhito U, Hiroyuki O. A Planar Actuator with a Small Mover Traveling Over Large Yaw and Translational Displace-ments. IEEE Tansactions on Magnetics 2008; 44(5): 609-616.

Design of a New Type Multi Degree of Freedom Spherical Actuator

Hyunchang Kim[1,2], Myeonghyeon Kim[2], and Daegab Gweon[2]

[1]Department of Printed Electronics, Advanced Manufacturing Systems Research Division, KIMM, Jangdong 171, Yuseong-gu, Daejeon, 305-343, South Korea
[2]NanoOptoMechatronics Lab., Department of Mechanical Engineering., KAIST, 291 Daehak-ro, Yuseong-gu, Daejeon, 305-701, South Korea

INTRODUCTION

Recently, the study of single unit spherical actuators that can perform multi degree of freedom movements has increased. The spherical actuator is an electric machine that is able to tilt its shaft on multiple degrees of freedom using electromagnetic force. Various types of spherical motors have been developed. Lee et al.[1-4] devised variable reluctance spherical actuators. They researched the design, sensing, and control of the spherical actuator. Yan et al.[5,6] developed a spherical actuator similar to Lee's; their drive principles are actually synchronous. Tomoaki et al.[7-9] have been studying and developing a wide range of multi degree of freedom drive systems.

In the previous research, spherical actuators have complexity and difficulty in control to accomplish high precision because, to control and drive the actuators, the calculations of the flux density of each driving part according to rotational angle are required. Therefore, an accurate analytic model of flux density is needed. In addition, it has low tilt torque for size.

We propose and design a new type of spherical actuator. The designed actuator has a large tilt angle of ±40°, high tilt torque, and uniform and decoupled torque constant by each coil within a compact diameter of 100 mm.

CONCEPTUAL DESIGN AND PRINCIPLE

The proposed spherical motor purposes to overcome drawbacks of existing development spherical actuator. Therefore, the new concept is derived to solve drawbacks. The new concept is based on voice coil motor (VCM) method. The VCM uses the Lorentz force principle.

Design consideration

Spherical motor has many advantages and potential applications in robotics manipulator and positioning devices. Most of the developed spherical motors are useless in industrial application. Therefore, several considerations for designing a new spherical motor are introduced.

- Large working ranges
- Compact size
- High tilt torque
- Uniform torque constant

Concept of the VCM spherical motor

Figure 1, 2 shows the conceptual design of the proposed new type of spherical voice coil actuator. The proposed spherical actuator is designed to have a large tilt angle of ±40° and out radius of the actuator is 50mm.

It is composed of a stator and a moving coil type rotor. The stator of the actuator has eight permanent magnets and steel yoke for high uniform magnetic flux density. Yoke is divided two parts: outer yoke and inner yoke. The yokes create closed magnetic flux loop. The permanent magnets are attached to outer yoke. There is air gap between inner yoke and outer yoke. The air gap is uniform.

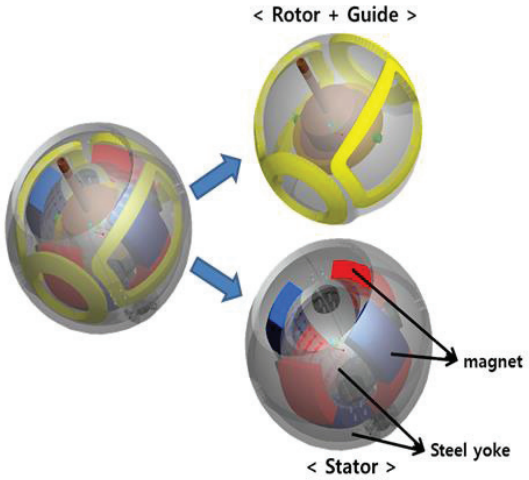

FIGURE 1. Concept of the spherical actuator

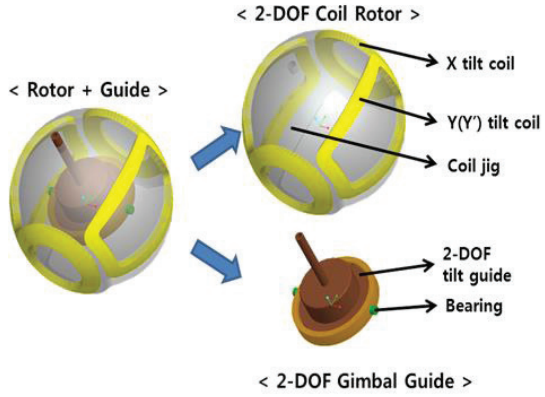

FIGURE 2. Rotor and Guide structure

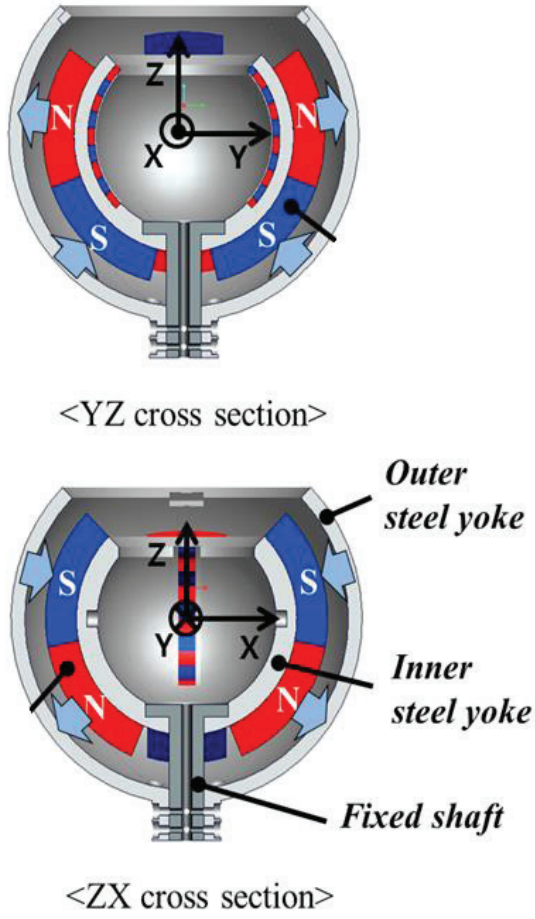

FIGURE 3. Stator part of the proposed spherical actuator

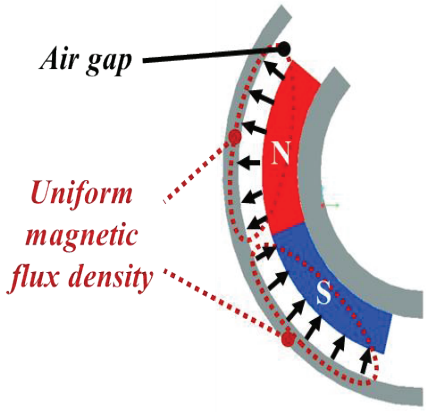

FIGURE 4. Schematic diagram of the magnet and the yoke of the stator

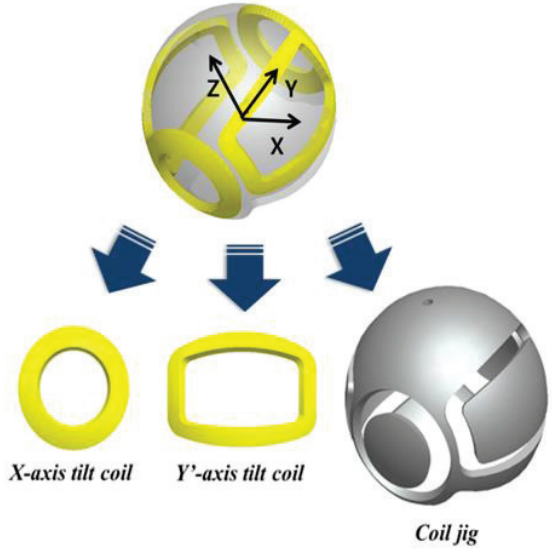

FIGURE 5. Schematic figures of the coil part of the rotor

As shown in figure 3, the stator part is fixed to the base frame. The red colored magnets are polarized along the radially-outward direction, and the blue colored magnets are polarized along the radially-inward direction. The blue-colored arrows represent the flow of the magnetic flux of the stator.

As shown in figure 4, high and uniform magnetic flux density is formed at the air gap between the permanent magnets and the outer steel yoke. There is internal empty space to insert the gimbal guide mechanism for two degree of freedom tilt motion and a one degree of freedom rotational motor.

Figure 5 represents rotor structure. The rotor is composed of a 2-DOF (degree of freedom) gimbal guide mechanism and four coils to drive the tilt motions. There are X-tilt coil and Y'-tilt coil. Two pairs of different shaped coils are used to drive the X and Y'-axis tilt motions. Circular coils generate the X-axis tilt torque and rectangular coils generate the Y'-axis tilt torque. These coils are moved with the gimbal guide mechanism. The coil jig is fixed on the shaft of the gimbal guide mechanism. X-axis means X-directed rotation from global coordinates and Y'-axis from local coordinates.

X-coil is made circular shape in order to getting independence from rotating motion. Therefore, spherical actuator can produce constant torque when it rotates on X-axis. It is also independent of Y'-axis rotation.

The existing spherical actuators have sensing and guide mechanism is outside of actuators. It causes bulk size and unpractical for application. As mentioned before, the proposed spherical actuator has inner guide and sensing mechanism. Guide mechanism is gimbal-guide structure and installed inside of inner yoke. Guide mechanism is easily installed because inside of inner yoke is empty. Gimbal-guide mechanism can guide rotation at specific axis.

Principle of the system

Figure 6 shows the principle of generation of the X and Y'-axis tilt torque. The generation of the tilt torque is based on the Lorentz force. The coils carrying current generate the tangential directional forces that cause the tilt torques. The circular coils always generate the X-axis tilt torque, and the rectangular coils always generate the Y'-axis tilt torque at arbitrary points. For that reason, the X-axis tilt torque and the Y'-axis tilt torque generated by the each coil pair are decoupled. In addition, each axis of the tilt torque generated by each pair of coils coincides with each axis of the gimbal guide mechanism, respectively. Therefore, each torque generated by each actuator can be controlled easily.
Each axis coils are arranged two pairs and one coil creates 40° moving range. In other words, right coil actuates -40° ~ 0° and left coil actuates 0° ~ 40° in figure 6. Also this coil always produce X-axis torque despite the rotor rotate any direction.

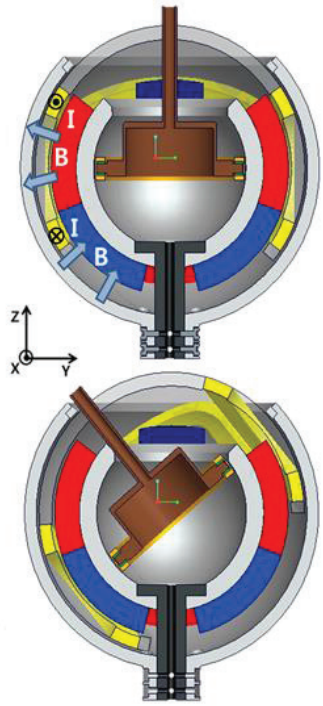

FIGURE 6. Actuation principle of the proposed spherical actuator

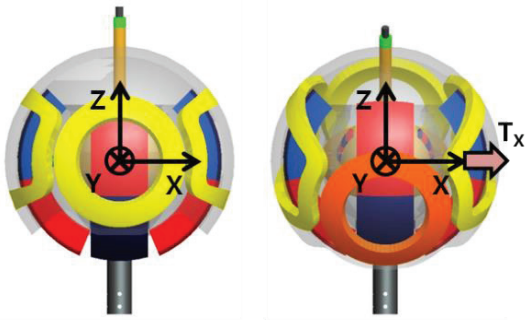

FIGURE 7. Schematic of X-direction torque

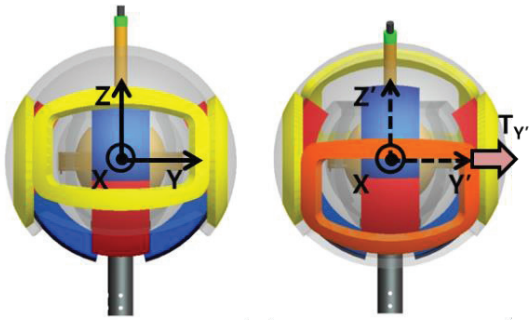

FIGURE 8. Schematic of Y'-direction torque

Figure 7, 8 are schematic of removed yoke for helping understand. The orange color means activating coil. When activating X-coil, spherical actuator rotates X-direction. In all rotation, X-coil always produces X-axis torque at global coordinates. Y'-coil also generates Y'-axis torque at local coordinate in all rotation.

The proposed spherical actuator can produce high constant torque. In addition, direction of torque is always same direction. Therefore, actuator maintains high torque at any position. It is easy to control because the torque constant is uniform in moving range.

CONCLUSION

In this study, a new type multi degree of freedom spherical actuator is proposed and designed. It generate high tilt torque and Outer diameter of the stator of the system is only 100 mm. Future work includes design of a guide mechanism and assembly of the system.

ACKNOWLEDGEMENT

This research was supported by Agency for Defense Development (ADD) grant funded by the Korea government.

REFERENCES

[1] K.-M. Lee and R.A. Sosseh, Proceedings of the 7th International Conference on Control, Automation, Robotics and Vision, Singapore, 2002, p. 384.

[2] K.-M. Lee, R.A. Sosseh, and Z. Wei, Control Eng. Pract. 12, 1437-1449 (2004).

[3] K.-M. Lee and H. Son, IEEE Trans. Magn. 43 3904-3913 (2007).

[4] K.-M. Lee, K. Bai, and J. Lim, IEEE/ASME Trans. Mech. 14 46-54 (2009).

[5] L. Yan, I. M. Chen, G. Yang, and K.-M. Lee, IEEE/ASME Trans. Mech. 11 409-419 (2006).

[6] L. Yan, I. M. Chen, C.K. Lim, G. Yang, W. Lin, and K.-M. Lee, IEEE/ASME Trans. Mech. 13 239-248 (2008).

[7] Y. Tomoaki and S. Takeo, Proceedings of the International Conference on Intelligent Robots and Systems, Lausanne, 2002, p. 1980.

[8] Y. Tomoaki, K. Yoshiaki, S. Toru, and S. Takeo, Proceedings of the International Symposium on Micro-NanoMechatronics and Human Science, 2007, p. 383.

[9] Y. Tomoaki, J. Mech. Sci. Technol. 24 33-36 (2010).

Thermal Analysis of Ballscrew Systems by Finite Difference Methods

Myungjune Kim[1], Bog-Ki Min[1], Chun-Hong Park[2], and Sung-Chong Chung[1*]
[1] Hybrid System Design and Control LABoratory
School of Mechanical Engineering
Hanyang University, Seoul 133-791, KOREA
[2] Intelligent Manufacturing System Division
KIMM, Daejeon 305-343, KOREA

ABSTRACT
To maintain numerical stability and convergence during computation of temperature distribution, alternating direction implicit (ADI) FDM is applied to thermal analysis of ballscrews. Preload change and thermal stiffness are computed from interference change between the screw and nut interface through deformation analysis. Validity of the proposed method is verified through experiments.

INTRODUCTION
Ballscrews have high stiffness, long life, good efficiency, and low driving torque. It is used as a general positioning element in machine tools and precision machinery. To compensate for positioning error, and to predict accuracy of precision machines during the design process, accurate deformation and stiffness estimates of the feed drive system equipped with ballscrews are required. In addition to contact and body deformation occurred in the static state [1], thermal deformation due to friction between balls and grooves degrades accuracy of feed drive systems. To calibrate the thermal deformation error, temperature measurement of the whole ballscrew according to operating conditions is required. However, it is inefficient and almost impossible to acquire the whole temperature distribution by measuring temperatures of every point. Therefore, a thermal model estimating the whole temperature field from mathematical model is required [2-5].

In this paper, contrary to previous researches [4-5], heat generation mechanism of ballscrews and temperature analysis module are more accurately derived through stable numerical analysis of heat transfer. To improve stability and computational efficiency of the finite difference method, temperature distribution is estimated by ADI method. Thermal deformation and interference change is estimated according to the computed temperature distribution. Preload change is estimated from interference change between the nut and shaft. Then, thermal stiffness is obtained by the previously formulated stiffness model [1]. In addition, validity of the developed thermal analysis method is verified through experiments on the ballscrew driven feed drive system under various operating conditions.

THERMAL ANALYSIS
Figure 1 shows a double-nut ballscrew feed drive system. As the ballscrew rotate, heat is generated because of slip between balls and grooves, viscous friction due to shear stress of lubricant, and rolling contact friction. Support bearings generates frictional heat as well. In addition, ambient temperature variation as an external heat source changes temperature distribution of ballscrews.

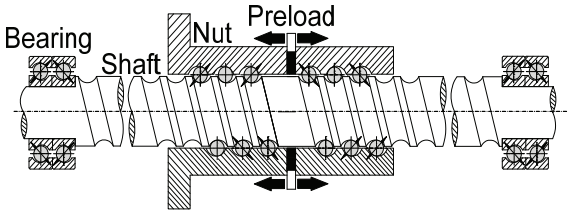

FIGURE 1. Double-nut Ballscrew Assembly.

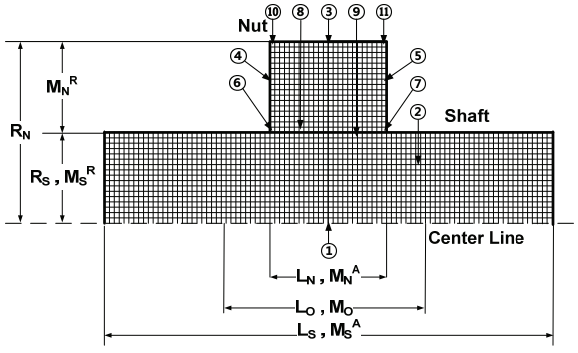

FIGURE 2. Axisymmetric FDM Model.

Alternating Direction Impicit Method

ADI method separates time step from current i to next $i+1$ into two sub-time steps: step 1 from i to $i+1/2$ and step 2 from $i+1/2$ to $i+1$. In step 1, temperature computation is implicit in *z*-direction, and is explicit in *r*-direction. In step 2, *r*-direction is implicit and *z*-direction is explicit. At each nodal point, temperature is computed from neighboring nodal points. Coefficient matrix is tridiagonal. It is solved by Thomas Algorithm. Fig. 2 shows an axisymmetric FDM model with smaller axial and radial differences △z and △r, respectively. Considering heat balance condition, heat conduction in solids, heat convection around surfaces, ambient temperature variation, and frictional heat generation from internal heat sources such as support bearings and contact surfaces between balls and grooves, implicit finite difference equations for the nodes at 11 cases are formulated as follows:

Case 1.

$$step\ 1: {\theta_{m,n}}^{p+1/2} = {\theta_{m,n}}^{p} + \frac{Fo_z}{2}({\theta_{m+1,n}}^{p+1/2} + {\theta_{m-1,1}}^{p+1/2} - 2{\theta_{m,n}}^{p+1/2}) + 2Fo_r({\theta_{m,n+1}}^{p} - {\theta_{m,n}}^{p})$$

$$step\ 2: {\theta_{m,n}}^{p+1} = {\theta_{m,n}}^{p+1/2} + \frac{Fo_z}{2}({\theta_{m+1,n}}^{p+1/2} + {\theta_{m-1,1}}^{p+1/2} - 2{\theta_{m,n}}^{p+1/2}) + 2Fo_r({\theta_{m,n-1}}^{p+1} - {\theta_{m,n}}^{p+1})$$

case 2.

$$step\ 1: {\theta_{m,n}}^{p+1/2} = {\theta_{m,n}}^{p} + \frac{Fo_z}{2}({\theta_{m+1,n}}^{p+1/2} + {\theta_{m-1,n}}^{p+1/2} - 2{\theta_{m,n}}^{p+1/2}) + \frac{Fo_r}{2}(k_1{\theta_{m,n+1}}^{p} + k_2{\theta_{m,n-1}}^{p} - 2{\theta_{m,n}}^{p})$$

$$step\ 2: {\theta_{m,n}}^{p+1} = {\theta_{m,n}}^{p+1/2} + \frac{Fo_z}{2}({\theta_{m+1,n}}^{p+1/2} + {\theta_{m-1,n}}^{p+1/2} - 2{\theta_{m,n}}^{p+1/2}) + \frac{Fo_r}{2}(k_1{\theta_{m,n+1}}^{p+1} + k_2{\theta_{m,n-1}}^{p+1} - 2{\theta_{m,n}}^{p+1})$$

case 3.

$$step\ 1: {\theta_{m,n}}^{p+1/2} = {\theta_{m,n}}^{p} + \frac{Fo_z}{2}({\theta_{m+1,n}}^{p+1/2} + {\theta_{m-1,n}}^{p+1/2} - 2{\theta_{m,n}}^{p+1/2}) + \frac{Fo_r k_3}{2}({\theta_{m,n+1}}^{p} - 2{\theta_{m,n}}^{p}) + \frac{Fo_r \cdot Bi_r \cdot k_4}{2}(\theta_\infty - {\theta_{m,n}}^{p})$$

$$step\ 2: {\theta_{m,n}}^{p+1} = {\theta_{m,n}}^{p+1/2} + \frac{Fo_z}{2}({\theta_{m+1,n}}^{p+1/2} + {\theta_{m-1,n}}^{p+1/2} - 2{\theta_{m,n}}^{p+1/2}) + \frac{Fo_r k_3}{2}({\theta_{m,n+1}}^{p+1} - 2{\theta_{m,n}}^{p+1}) + \frac{Fo_r \cdot Bi_r \cdot k_4}{2}(\theta_\infty - {\theta_{m,n}}^{p+1})$$

•
•
•

case 11.

$$step\ 1: {\theta_{m,n}}^{p+1/2} = {\theta_{m,n}}^{p} + \frac{Fo_z}{2}({\theta_{m-1,n}}^{p+1/2} - {\theta_{m,n}}^{p+1/2}) + \frac{Fo_r k_3}{2}({\theta_{m,n+1}}^{p} - {\theta_{m,n}}^{p}) + \frac{Fo_z \cdot Bi_z}{2}(\theta_\infty - {\theta_{m,n}}^{p+1/2}) + \frac{k_4 \cdot Fo_r \cdot Bi_r}{2}(\theta_\infty - {\theta_{m,n}}^{p}) \quad (1)$$

$$step\ 2: {\theta_{m,n}}^{p+1} = {\theta_{m,n}}^{p+1/2} + \frac{Fo_z}{2}({\theta_{m-1,n}}^{p+1/2} - {\theta_{m,n}}^{p+1/2}) + \frac{Fo_r k_3}{2}({\theta_{m,n+1}}^{p+1} - {\theta_{m,n}}^{p+1}) + \frac{Fo_z \cdot Bi_z}{2}(\theta_\infty - {\theta_{m,n}}^{p+1/2}) + \frac{k_4 \cdot Fo_r \cdot Bi_r}{2}(\theta_\infty - {\theta_{m,n}}^{p+1})$$

where,

$$k_1 = 1 - \frac{0.5}{n},\ k_2 = 1 + \frac{0.5}{n}, k_3 = \frac{4(2n-1)}{4n-1}, k_4 = \frac{8n}{4n-1}, k_5 = \frac{4(2n+1)}{4n+1}$$

$$Foz = \frac{\alpha \Delta t}{(\Delta z)^2},\ For = \frac{\alpha \Delta t}{(\Delta r)^2},\quad Biz = \frac{h \Delta z}{\lambda},\quad Bir = \frac{h \Delta r}{\lambda}$$

$$V_s = \frac{\pi(n-0.25)(\Delta r)^2 \Delta z}{2},\quad V_n = \frac{\pi(n+0.25)(\Delta r)^2 \Delta z}{2}$$

$$T_{fs} = \frac{\dot{Q}_f \Delta t}{c\rho V_s},\ T_{fn} = \frac{\dot{Q}_f \Delta t}{c\rho V_n}$$

TABLE 1. ADI Model Parameters of a Ballscrew.

Shaft Length, L_S [mm]	500
Lead [mm]	5
Total Ball Number, Z	80
Nut Length, L_N [mm]	105
Shaft & Nut Outer Diameter, R_S, R_N [mm]	16
Radial & Axial Difference, Δr, Δz [mm]	1 , 5
Number of Shaft & Nut Meshes in Radial Direction, ${M_S}^R$, ${M_N}^R$	8, 12
Number of Shaft & Nut Meshes in Axial Direction, ${M_S}^A$, ${M_N}^A$	100, 21
Operation Stroke, L_O [mm]	100
Preload, F_p [Kgf]	68
Kinematic Viscosity of Lubricant, v_O [cSt]	32
Ball Screw Rotational Speed, n [rpm]	250~750
Frictional Coefficient, μ	0.003
Specific Heat, Cp [J/Kg℃]	460
Thermal Conductivity, λ [W/m℃]	60.5
Density, ρ [Kg/m^3]	7865

Table 1 describes input parameters for the ADI model of a ballscrew. Comparing with explicit FDM [2,4-5], stability conditions are not required for the model. However, to solve Eq. (1) accurately, frictional heat between the shaft and nut interface as well as convection coefficient around the ballscrew should be inputted to Eq. (1) correctly.

Convection Coefficient

Convection heat transfer coefficients around the screw shaft and nut surfaces depend upon air flow speed as given by Eq. (2).

$$h = c\,\mathrm{Re}^m\,\mathrm{Pr}^{1/3} \quad (2)$$

where Re is the Reynolds number. c and m are subject to Re, and Pr is the Prandtl number.

Heat Generation at the Interface

Frictional torques generated from balls and grooves are calculated by applied load, viscosity and spinning motion [5]. Following equations are applied for better estimation of frictional heat:

$$\dot{Q}_f = \phi T_{fn} \cdot \omega$$

$$T_{fn}: \text{Frictional Nut Torque} \quad (3)$$

$$\phi\ :\ \text{Heat transfer ratio to the Nut}$$

Table 2 shows estimated convection coefficient and frictional torque when $\phi = 0.5$ at the interface according to operating conditions of the ballscrew given by Table 1. Fig. 3 shows temperature distribution of the ballscrew assembly according to time-varying ambient temperature and rotational speeds after 2 hours rotation. On the moving stroke range, temperature of the shaft section is slightly higher than the nut. Due to heat convection to ambient, temperature beside the interface is higher than other region. Although ambient temperature is changing, interface temperature reaches steady state around 120 minutes according to rotational speeds as shown in Fig. 4.

TABLE 2. Estimated Key Parameters.

rpm	$h\ [\mathrm{w/m^2 \cdot K}]$	$T_{fn}\ [\mathrm{N \cdot m}]$
250	5.88	0.09
500	7.46	0.11
750	8.91	0.10

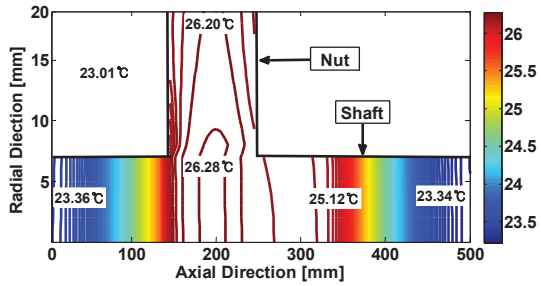

(a) 250rpm, operating time=120 min

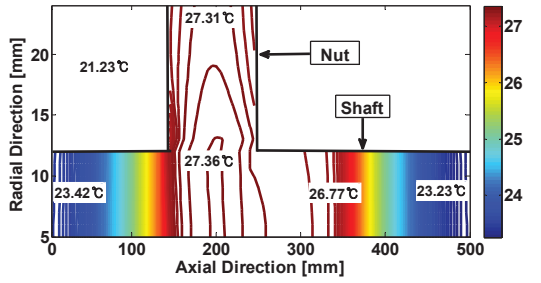

(b) 500rpm, operating time=120 min

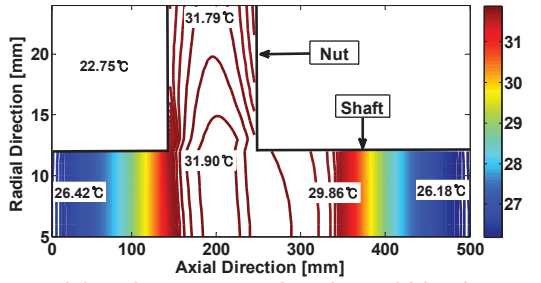

(c) 750rpm, operating time=120 min

FIGURE 3. Temperature Distributions after 1 Hour.

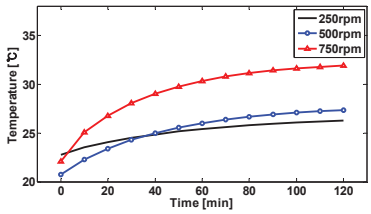

FIGURE 4. Temperature Trends at the Interface.

EXPERIMENTAL VERIFICATION

Fig. 5 shows experimental setup to verify developed thermal analysis ADI module. Fig. 6 shows averaged temperature measurements of #1, #2, #3 and #4 regions at different operating conditions. Through repetitive measurements of frictional torques and ambient temperatures, and applying them to numerical simulations of the ADI model, good boundary conditions has been obtained for the ADI analysis. Fig. 7 shows comparison of averaged nut temperatures with experiments. They confirm that ADI generates good temperature distribution for ballscrews.

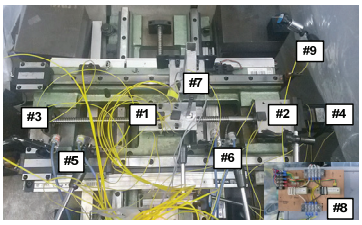

FIGURE 5. Experimental Setup for Verification.

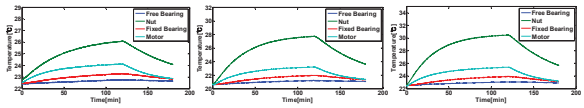

(a) 250rpm (b) 500rpm (c) 750rpm

FIGURE 6. Temperatures vs. Rotational Speeds.

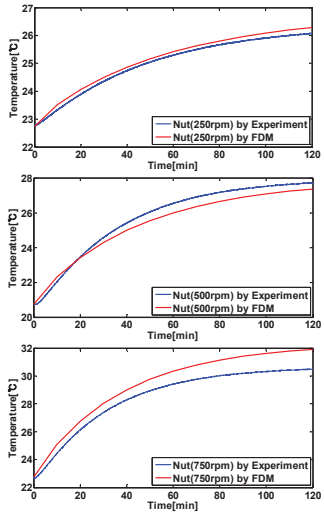

FIGURE 7. Comparisons of ADI with Experiments.

THERMAL NUT STIFFNESS

Thermal expansions in radial and axial direction of the (i, j) nodal point is given by

$$u_{ij} = \alpha \cdot \Delta r \cdot \Delta\theta_{ij} \quad \text{and} \quad v_{ij} = \alpha \cdot \Delta z \cdot \Delta\theta_{ij} \tag{4}$$

Average radial and axial deformations at the interface of the ballscrew is given by

$$u^S_{if,avg} = \frac{\alpha \cdot \Delta r}{m} \sum_{j=1}^{m} \sum_{i=1}^{n} \Delta\theta^S_{ij}$$
$$u^N_{if,avg} = \frac{\alpha \cdot r^N_{if}}{m \cdot n} \sum_{j=1}^{m} \sum_{i=1}^{n} \Delta\theta^N_{ij} \tag{5}$$

$$v^S_{if,avg} = 2\alpha \cdot \Delta z \frac{lead}{m \cdot n} \sum_{i=1}^{n} \sum_{j=1}^{m/2} \Delta\theta^S_{ij}$$
$$v^N_{if,avg} = 2\alpha \cdot \Delta z \frac{lead}{m \cdot n} \sum_{i=1}^{n} \sum_{j=1}^{m/2} \Delta\theta^N_{ij} \tag{6}$$

Interferences at the interface in radial and axial directions are given by

$$u_{\text{interference}} = u^S_{if,avg} - u^N_{if,avg}$$
$$v_{\text{interference}} = v^S_{if,avg} - v^N_{if,avg} \tag{7}$$

According to Fig. 3, temperature of the shaft section on the moving stroke region is slightly higher than the nut section. This generates uniform expansions of the ballscrew. Although significant thermal expansion is observed during rotation, there exists slight interference between the shaft and the nut as shown in Fig. 8. This generates small preload change in the ballscrew [5]. Substituting this small preload change to the static stiffness model [1], ballscrew nut stiffness regarding rotational speed is obtained as shown in Fig. 9. This verifies that there is significant thermal expansion but the interference and the preload change are small. It proves that the thermal nut stiffness of ballscrews does not vary according to the rotational speed.

CONCLUSIONS

Temperature distribution of ballscrews has been conducted well by the ADI Method. This implicit FDM generates numerical stability and convergence during temperature computation. Preload change and interference are estimated through thermal deformation analysis. Validity of the ADI FDM method is verified through experiments. It is confirmed that thermal nut stiffness of ballscrews does not vary according to rotational speed.

ACKNOWLEDGEMENT

This research is supported by Ministry of Trade, Industry & Energy, Korea.

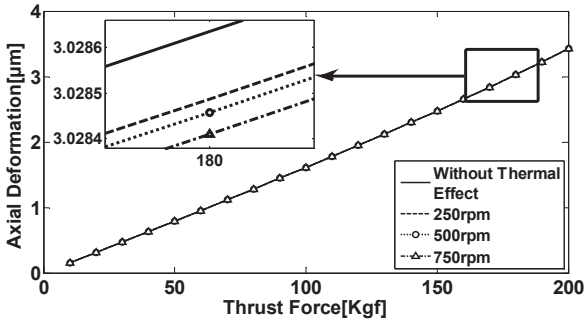

FIGURE 8. Axial Deformation Changes vs. Rotational Speeds.

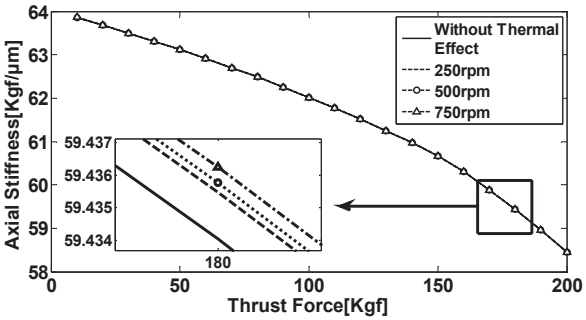

FIGURE 9. Thermal Nut Stiffnesses vs. Rotational Speeds.

REFERENCES

[1] Chung S-C, Park C-H. Analysis of Ballscrew Stiffness owing to contact Deformation in Leadscrew Systems. Proceedings of the ASPE 2010 Annual Meeting. 2010; 50: 160-163.

[2] Chung S-C, Park J-K. Thermal Expansion Analysis of the Ball Screw System by Finite Difference Methods. Journal of the Korean Society of Precision Engineering. 1992; 9: 4: 44-57.

[3] Ahn J-Y, Chung S-C. Real-time Estimation of the Temperature Distribution and Expansion of a Ball Screw System using an Observer. Proceedings of the Institution of Mechanical Engineers Part B, Journal of Engineering Manufacture. 2004; 218: 1667-1680.

[4] Min B-K, Park C-H, Chung S-C. Modeling of Ballscrew Nut Stiffness Including Thermal Effect. Proceeding of the ASPE 2011 Annual Meeting. 2011; 52; 319-322.

[5] Min B-K, Kim M, Park C-H, Chung S-C. Modeling of Thermal Nut Stiffness in Ballscrews. Proceeding of the ASPE 2012 Annual Meeting. 2012; 54; 390-393.

HEAT IS THE PRICE YOU PAY FOR SPINDLE STIFFNESS

Mel Liebers, Dave Arneson, Byron Knapp,
Dan Oss, Nick Bryan
Professional Instruments Company
Hopkins, Minnesota, USA

INTRODUCTION

"Spindle growth" is an unfortunate term which leads down a non-productive path because it's expressed as displacement rather than power (Watts). It's better to consider spindle heating in terms of power required to spin at a given speed because this leads to a deterministic approach to managing the problem.

For spindles in general, whatever you do to increase stiffness - such as increasing bearing diameter or preload - increases the torque required to spin the rotor. (An exception is increasing inlet pressure to air bearings.)

For air bearing spindles, the thickness of the air films affects heating due to shearing, as shown in Figure 1.

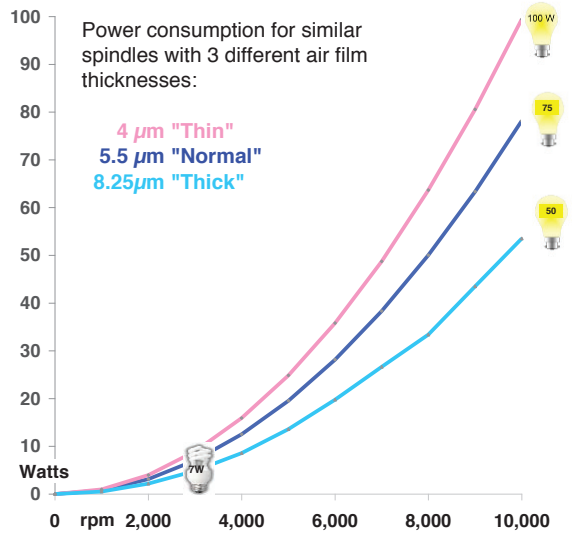

FIGURE 1. Watts generated vs. rpm for three versions of 4R Blockhead air bearing spindles, assembled with different thrust bearing air film thicknesses.

Heat is not a problem at low speed, but above a few thousand rpm the power required to shear the air films rises at an increasing rate.

At 10,000 rpm, heating can be visualized as the effect of a 50, 75, or 100 watt light bulb imbedded in the spindle rotor and this is a useful way to contemplate thermal management.

A DYNAMOMETER SHOWS THE EFFECT

For this test the spindle was arranged in an open-air configuration, with insignificant thermal conduction away from the rotor or the stator.

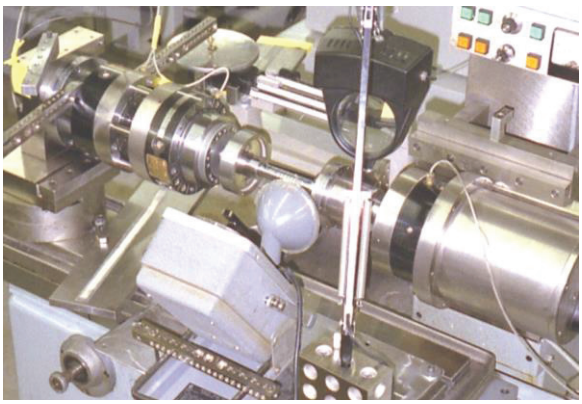

Figure 2. An air bearing dynamometer using a grinder as a base.

Torque from the drive spindle transfers through a coupling to the rotor of the test spindle, which is attached stator-to-stator to the pivot spindle, whose rotor is fixed. Shearing of the test spindle air films rotates the stator of the test spindle, which is connected to the stator of the pivot spindle. Rotation of the pivot spindle stator is restrained by a torque arm pushing down on a triple-beam balance.

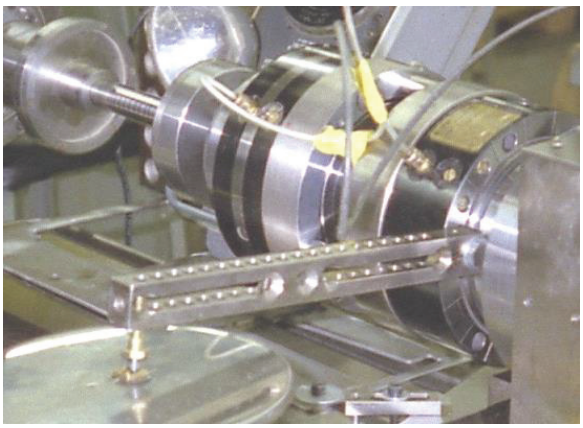

Figure 3. A torque arm from the pivot spindle bears on the balance pan through a diamond indicator tip on a lapped carbide tool bit.

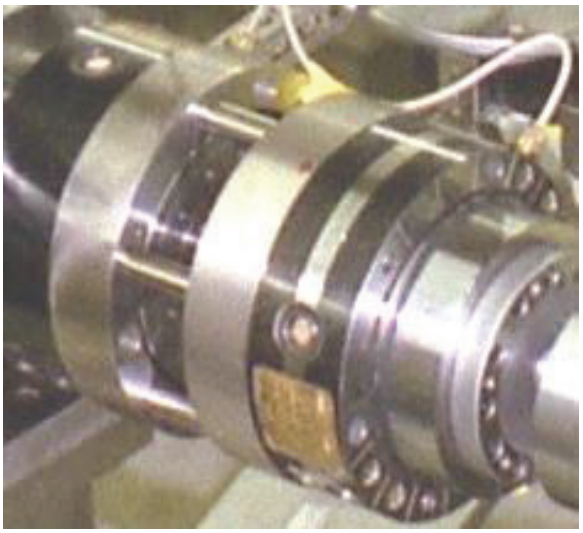

Figure 4. Shows the stator-to-stator arrangement to convey torque from the test spindle to the stator of the pivot spindle.

The test starts by arranging for a 1 gram upward force on the balance and then increasing the speed of the drive motor to just balance the force on the torque arm. One gram at 10.9 inches equals 0.024 pound-inches and this works out to be 390 rpm for the normal-clearance 4R, 240 rpm for the 4R with tight clearance and 570 rpm with extra clearance.

Speed is measured with a strobe light and a magnifier is used to improve the resolution of the pointer position of the triple-beam balance. The 3 spindles are aligned on a common axis to minimize torque variations.

In addition to the three Model 4R spindles with different air gaps, we tested a variety of similar spindles made by other manufacturers to look for the sweet spot for stiffness vs. heat.

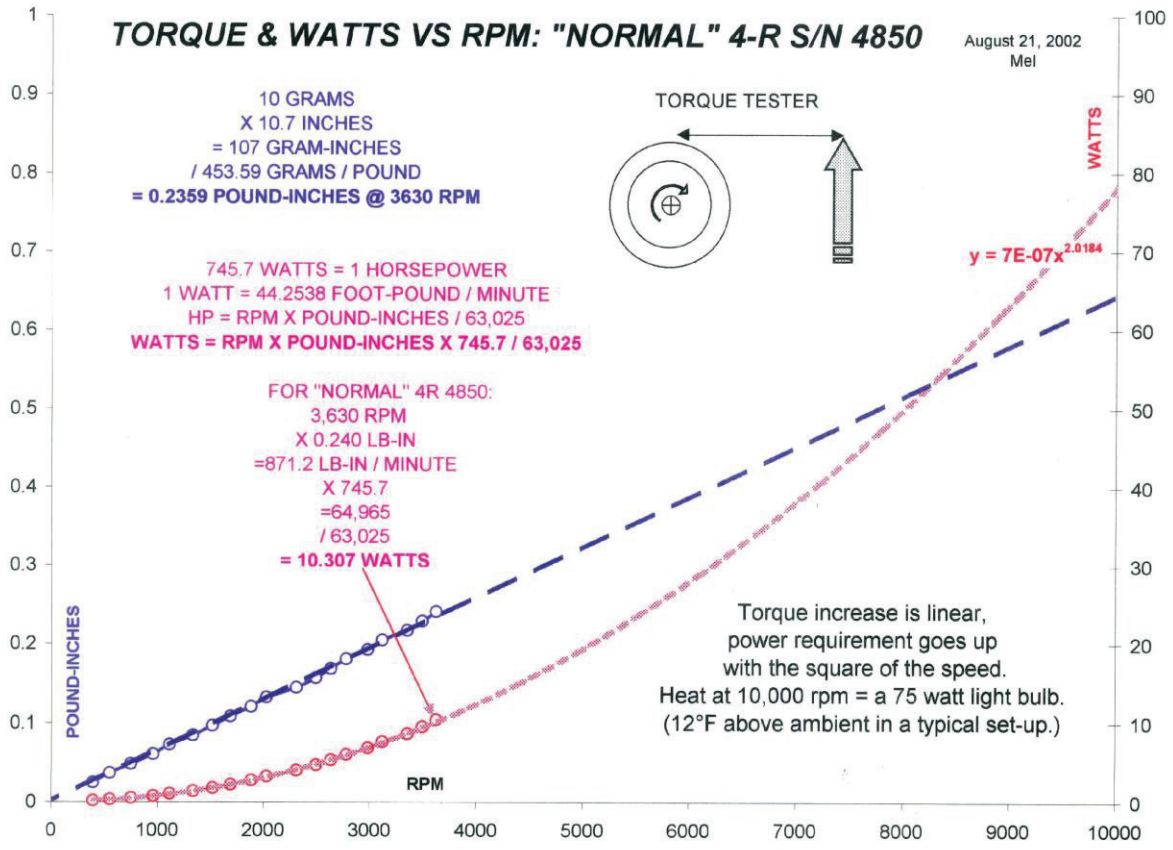

Figure 5. Torque increases at a linear rate and power goes up with the square of the speed; both can be projected to 10,000 rpm as shown here.
For a standard 4R at 3,600 rpm, one needs to deal with 10 Watts of heat.

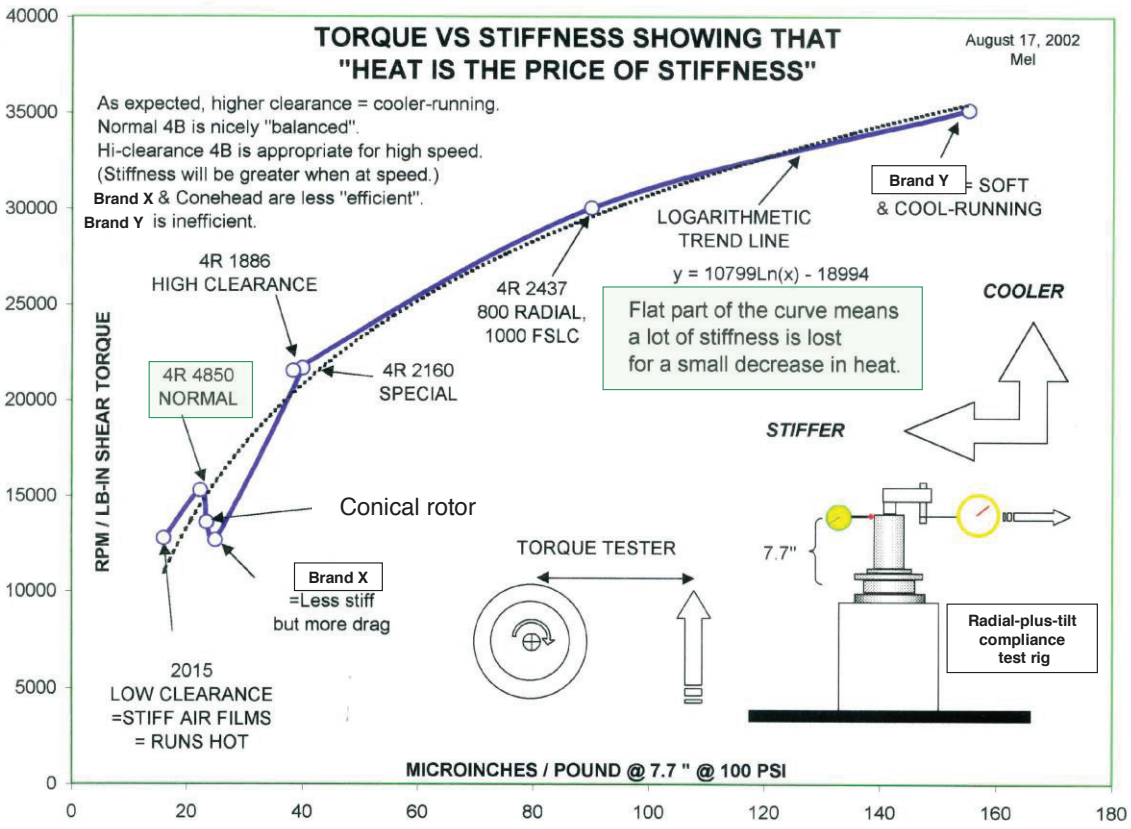

FIGURE 6. Torque vs. radial-plus-tilt stiffness.

Tilt stiffness is an important attribute for machine tool spindles and we constructed the Figure 6 group-graph to visualize a figure of merit for comparing similar-sized spindles. Stiffer spindles are towards the left and cooler-running spindles are towards the top.

Because Blockhead spindles were originally designed for use in machining, tilt stiffness was as important as accuracy; thus they have large thrust plates with thin air films.
This is all very well for workheads but wheelheads need to go fast for efficient grinding.

An experimental spindle with extra clearance for in-house use happened to be available for this test. The tight-clearance spindle was purpose-built for this test.

A few other spindles were available and fit the same tooling so these are included to show the wide range of possible choices.

CONCLUSIONS

Dynamometer testing provides data for a deterministic approach to managing spindle heat. Specifically, knowing the value in Watts enables proper sizing of a cooling system.

REFERENCES

Bryan, Nick, Spindle Torque Experiment, Professional Instruments internal report, July 14, 2002.

Design and Optimization of an X-Y-Θ_z Cylindrical Flexure Stage

Laura Matloff, Maria Telleria, and Martin L. Culpepper
Department of Mechanical Engineering
Massachusetts Institute of Technology
Cambridge, MA, 02139

ABSTRACT

The curved nature of cylindrical flexures (CFs) leads to more complicated kinematics that require additional design rules beyond those that govern straight-beam flexures [1]. The difference in kinematics makes the design of CFs more difficult but also results in an augmented flexure design space, meeting functional requirements that previously could not be met with straight-beam flexures. Unlike the straight-beam counterparts, CF r-compliance blade elements have two DOFs for certain sweep angles, ϕ. When applied to an X-Y-Θ_z stage, this property could be beneficial in reducing space and complexity. In this study CF design rules and models were used to establish the effects of different parameters and to optimize an X-Y-Θ_z stage design for a Dip-pen nanolithography (DPN) application. The design was corroborated using FEA and measurements of the fabricated system. The process of design and optimization shed light on the advantages and disadvantages of using CFs for not only the DPN usage scenario, but also for X-Y-Θ_z stages in general, while also demonstrating the usability of CF design rules [2]. CF design rules greatly informed the design, reducing time spent on FEA by quickly narrowing in on successful designs.

BACKGROUND

Application

Dip pen nanolithography (DPN) technology places chemical compounds on a substrate at the nanoscale resolution. DPN is an analogy to the quill pen where the "nib" is an atomic force microscope cantilevered tip, while the desired chemical compound and substrate act as the "ink" and "paper". A key challenge in DPN is the alignment of the tip with relation to the machine, which needs to be highly accurate and repeatable. A straight-beam flexure system has been previously designed to align and place the tip to the machine [3], but the usage of a CF in this application could provide additional benefits. Alignment of the tip requires that the flexure system allow for an adjustment in ΔX and ΔY of 120μm and a Θ_z adjustment of ± 3°.

r-compliance Cylindrical Flexures

A CF element is described by its radius of curvature, R, sweep angle, ϕ, radial thickness, t_r, and z-axis thickness, t_z. The flexure length is found by multiplying R by ϕ. In r-compliance CF flexures, t_r is the critical dimension, and is generally at least 6 times smaller than t_z. These parameters are illustrated in a generic r-compliant element in Figure 1.

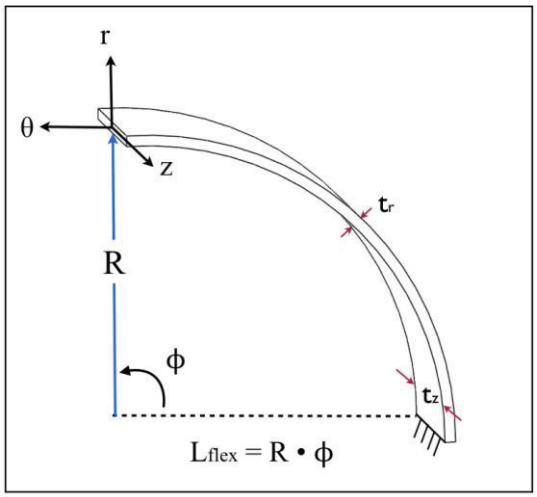

FIGURE 1. General parameters of a CF element include radius of curvature, R, sweep angle, ϕ, radial thickness, t_r, and z-axis thickness, t_z.

The curved geometry of the r-compliance CF blades allows for low stiffness in both θ and r-directions. For certain ϕ the blade will have two-linear DOFs because $K_r \approx K_\theta$. This property makes it possible to use a single flexure blade to guide both *x and y* motions. While this is beneficial for an X-Y-Θ_z stage, a challenge arises because the K_r / K_z ratio also rises quickly with increasing ϕ. Figure 2 plots the r-compliance blade stiffness ratios vs. ϕ.

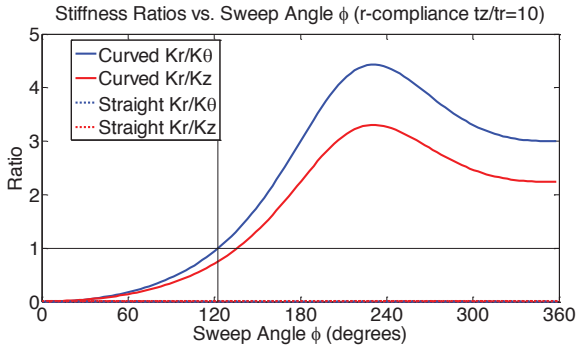

FIGURE 2. Element stiffness ratios (K_r/K_θ and K_r/K_z) for an r-compliance flexure versus sweep angle. Ratios are compared to those of a straight-beam flexure of the same dimensions.

After determining the behavior of a single CF flexure element, multiple elements can be combined into a flexure system model. Modeling flexure systems requires an understanding of the boundary conditions imposed on the elements when they are assembled into the system. CF system coordinates are defined by capital letters while element coordinates are denoted with lower case letters.

DESIGN AND OPTIMIZATION

Design Goals and Functional Requirements

Design parameters and functional requirements were driven by the range of motion required for DPN tip alignment, the force output of the actuators, and a factor of safety of two. The DPN requirements for displacements were determined to be are 272 μm of travel in ΔX and ΔY, and ± 0.1 radians of rotation about the system's z-axis, Θ_z. Compared to the degrees of freedom, the constrained directions must be sufficiently stiff. Stiffness ratios, K_x/K_z and $K_{\theta z}/K_{\theta x}$, should be less than 1/3, and ultimately as low as possible, to ensure proper constraints. Table 1 summarizes the functional requirements for the CF stage.

TABLE 1. Desired DOF stiffnesses and ranges for flexure system.

Max Stiffness	Values	Min Ranges	Values
K_x	2.98 N/mm	ΔX	6.4mm
K_y	2.98 N/mm	ΔY	6.4mm
$K_{\theta z}$	3.18 Nm/rad	Θ_z	0.4 rad

Design Process

Three simple CF element parallel layouts with two, three, and four concentric elements were evaluated. The two-element system could achieve X-Y-Θ_z DOF, but a study of the system showed that it could only attain motion in two quadrants rather than the desired four. The three-element flexure would allow for motion in all quadrants, but the lack of symmetry added unnecessary complexity and off-axis actuation. Figure 3 summarizes the advantages and disadvantages of each design. None of the three designs has a decisive advantage over the others.

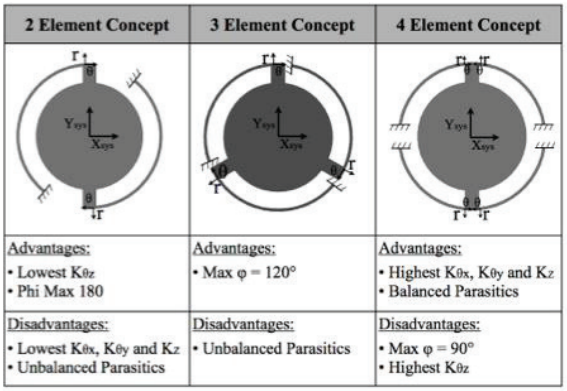

FIGURE 3. A comparison of the advantages and disadvantages of two, three, and four element systems designs. [2]

The four-element flexure was the most promising for balancing parasitic motions and having high $K_{\theta x}$, $K_{\theta y}$ *and* K_z, but had the disadvantages of high θ_z stiffness and limited sweep angles. Figure 4 shows the next design iteration based on a four-element arrangement.

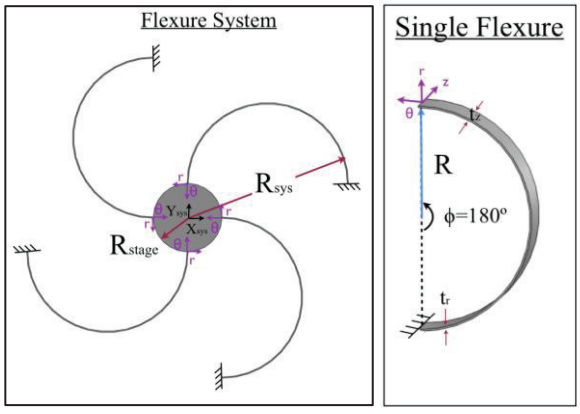

FIGURE 4. Preliminary four-element 180° sweep angle flexure design. Undesired parasitic motions cancel out due to symmetry.

In this design, the flexure elements were rotated so that they all face the same rotational direction, clockwise from tip to ground to reduce the Θ_z stiffness. The elements are also moved off axis so they are no longer concentric with the stage, allowing more room for larger sweep angles.

The design's symmetry also decouples the system's *X* and *Y* motions. Equations (1) through (4) relate element stiffness to the overall system stiffness and were used to model the system, helping to determine the optimal sweep angle and radii for the elements.

$$K_{X-sys} = K_{Y-sys} = 2K_{r-element} + 2K_{\theta-element} \quad (1)$$

$$K_{Z-sys} = 4K_{z-element} \quad (2)$$

$$K_{\Theta z-sys} = 4K_{r-element} \cdot R_{stage}{}^2 \quad (3)$$

$$K_{\Theta x-sys} \approx K_{\Theta y-sys} = 2K_{z-element} \cdot r_{stage}{}^2 \quad (4)$$

With large ϕ, the stiffness in the "constraint" directions ΔZ, Θ_x and Θ_y is reduced because the curved geometry allows the flexure to twist out of plane. The desired operating point for minimizing the stiffness ratios is 60° as depicted in Figure 5.

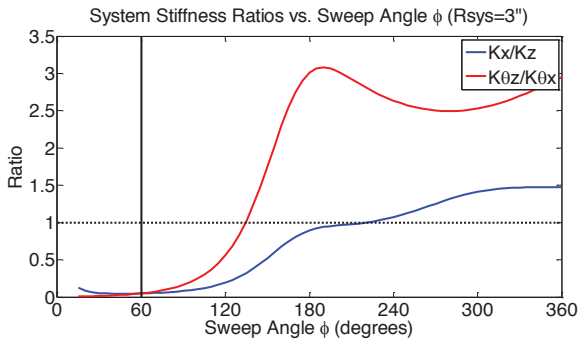

FIGURE 5. System K_X/K_Z and $K_{\Theta z}/K_{\Theta x}$ ratios versus sweep angle. The desired sweep angle for minimizing the stiffness ratios is 60°.

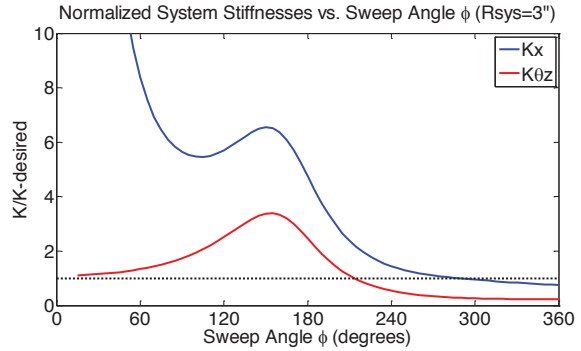

FIGURE 6. System K_X and $K_{\Theta z}$ vs. sweep angle. At 60° the stiffnesses are higher than desired.

Unfortunately, with this sweep angle, the desired stiffnesses are unattainable with the current configuration and volume constraints as shown in Figure 6. Increasing ϕ decreases the stiffnesses, however this also raises the stiffness ratios. Figure 5 shows that for sweep angles greater than 135° the system will not act as an out-of-plane constraint.

The analysis indicates that this design could have more potential as a 6 DOF stage rather than an X-Y-Θ_z stage, with a few adjustments. In order to achieve an X-Y-Θ_z stage that meets the functional requirements outlined earlier, another design needed to be considered. The challenge in designing a CF X-Y-Θ_z stage is to constrain the undesired motions while still achieving a high compliance in the desired directions.

Final Serial Design

To reach the design goals, a more complex design needed to be explored. A serial design approach, shown in Figure 7, with two ϕ=60° beams per arm helps achieve both the desired stiffness ratios and the desired stiffness. To keep the design monolithic the flexures must be connected at an angle, υ, designated as the series attachment angle. The angle between the input-flexure and the stage is given by η, called the stage attachment angle. The effect of υ and η on the performance of the system was analyzed using the CF models.

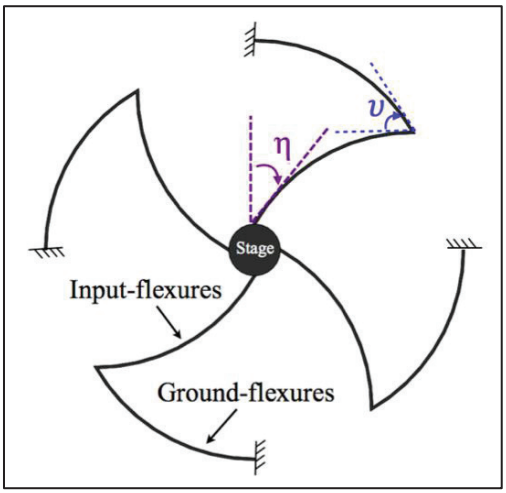

FIGURE 7. Monolithic four-element serial design with 60° element sweep angles. The series attachment angles are denoted by υ and the stage attachment angles by η. The series design achieves desired stiffness with lower stiffness ratios.

The analysis of the serial design requires that the compliance matrix of the ground-flexure be transformed to the input-flexure coordinates. The transformation of the compliance matrix is given in Eq. (5) where *[R]* is the transformation matrix.

$$[R] = \begin{bmatrix} -\cos(\phi+\nu) & -\sin(\phi+\nu) & -R(1-\cos\phi) \\ -\sin(\phi+\nu) & \cos(\phi+\nu) & R\sin\phi \\ 0 & 0 & -1 \end{bmatrix} \quad (5)$$

$$[C_t] = [R][C][R]^T$$

With this CF model, it was determined that the optimal series attachment angle, υ, needed to be as large as possible to lower the stiffness in $K_{\theta z}$ while retaining the same stiffness ratios. Figure 8 plots the relationship between the system stiffnesses and υ. A υ of 60 degrees is chosen since it is the largest attachment angle allowed without changing the system radius.

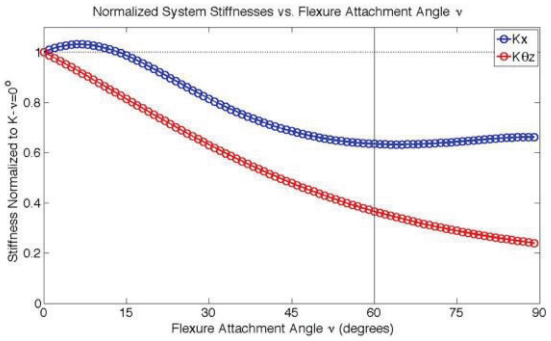

FIGURE 8. Normalized serial four-element system stiffnesses vs. series attachment angle, υ.

FEA Corroborations

Finite element analysis (FEA) was used to verify the predicted system stiffnesses and stiffness ratios as well as to conduct a modal analysis. The CF analytical models reduced the number of FEA runs necessary to drive design optimization. Table 2 summarizes the final parameter values for the system needed to meet the functional requirements.

TABLE 2. Final specifications for CF X-Y-θ_z stage element and system parameters

Parameter	Values
Elemental radial thickness, t_r	0.61mm
System z-thickness, t_z	12.7mm
System radius, R_{sys}	101.6mm
Stage radius, R_{stage}	12.7mm
Element sweep angle, ϕ	60°
Stage attachment angle, η	0°
Series attachment angle, υ	60°
Material	6061-T6 Al

Modal Analysis

The directions with the lowest stiffnesses are traditionally considered degrees of freedom; however the lowest natural frequency modes may also be used in defining degrees of freedom. Modal analysis allows for the comparison of rotational stiffnesses to linear stiffnesses, by finding the lowest natural frequency modes. Modal analysis of the design showed that the first two natural frequency modes of the current design are in *ΔX* and *ΔY* as expected, but the *ΔZ* direction has a lower natural frequency than the θ_z, which is undesirable. Placing mass further away from the center of the stage reduces the natural frequency of the θ_z motion, making it the third lowest mode shape. It should be noted that the additional mass also lowers the natural frequency of the other modes. In the fabricated design, four arms are added to the center of the stage, but the design can be further optimized by placing more weight away from the center of the stage. Figure 9 summarizes the modal analysis for different weight placement configurations.

Original Design			
1st Mode	2nd Mode	3rd Mode	4th Mode
26.7 Hz	26.80 Hz	80.70 Hz	123.75 Hz
Four Arms Added			
1st Mode	2nd Mode	3rd Mode	4th Mode
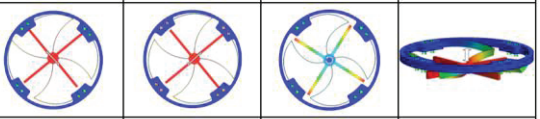			
15.05 Hz	15.09 Hz	24.36 Hz	43.00 Hz
Four Arms with Weights Added			
1st Mode	2nd Mode	3rd Mode	4th Mode
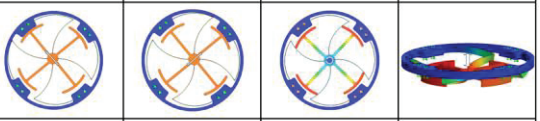			
12.12 Hz	12.14 Hz	14.62 Hz	34.47 Hz

FIGURE 9. The first four frequency modes for the CF Stage with different weight placements.

PROTOTYPE FABRICATION

The final serial flexure design was fabricated from 6061-T6 aluminum using an abrasive waterjet cutting machine. Waterjet machining is beneficial because it places low loads on the flexures and allows for machining in one pass relatively quickly. However, this machining process has the undesirable side effects of a taper angle and a kerf width, which affect the critical thickness, t_r, of the flexure elements. Measurements of the flexure were taken after fabrication, and the prototype flexures were found to be thicker than the original design. The average flexure thickness was 0.0289 inches with a taper angle of about 0.36 degrees. From this result, measured system stiffnesses were expected to be higher than the calculated values from the model. Figure 10 depicts the final fabricated flexure.

FIGURE 10. The CF X-Y-θ_z flexure design machined from 6061-T6 Aluminum.

Measurements were then taken to verify the flexure stiffnesses and parasitic motions. A series of weights and pulleys were used to actuate the flexure while capacitance probes were used to measure the prototype's displacements. Figure 11 depicts the CAD model of the measurement test set up. A measurement stage, placed above the flexure, provides fixturing for the probes and pulleys.

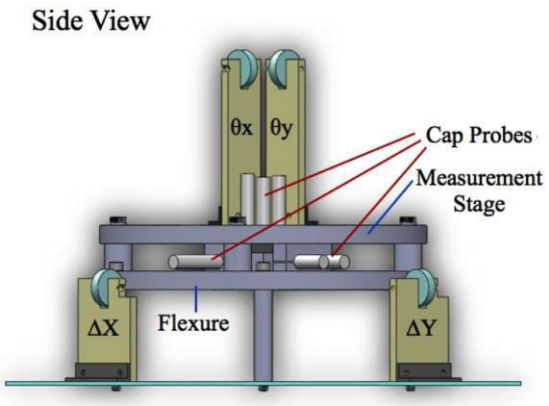

FIGURE 11. CAD model of measurement set up to verify flexure stiffnesses and functionality.

RESULTS AND ANALYSIS

As expected, the measured stiffnesses were higher than as modeled in the original design. Table 3 compares the values of the measured stiffnesses, the FEA modeled stiffnesses and the stiffnesses obtained by the CF model. The higher measured stiffnesses are most likely due

an increase of flexure critical thickness value to 0.03 inches from the modeled 0.024 inches, as well as the introduction of a taper angle, making the flexure thicker at the bottom and thinner at the top. The flexure t_r was increased to ensure successful fabrication.

TABLE 3. A comparison of system stiffness values as determined by CF model, FEA model, and measured fabricated model.

Stiffnesses	Model Value	FEA Value	Measured Value
K_X (N/mm)	0.644	0.612	0.740
K_Y (N/mm)	0.644	0.612	0.877
K_Z (N/mm)	3.43	3.60	5.003
$K_{\Theta x}$ (Nm/rad)	27.7	21.92	27.59
$K_{\Theta y}$ (Nm/rad)	27.7	21.92	29.31
$K_{\Theta z}$ (Nm/rad)	2.09	2.85	5.05

The CF analytical models enabled the design process and efficient optimization of the desired parameters. FEA was only used to verify the predicted system stiffnesses and stiffness ratios. This saved time compared to optimizing through FEA. Without analytical models the effect of the different parameters is unknown, leading to blind optimization. The analytical models reduced the number of FEA runs that were necessary.

CONCLUSIONS

Designing the DPN stage using the CF rules brought forth the advantages and disadvantages of using cylindrical flexures for an X-Y-Θ_z stage and demonstrated the usability of CF rules. This study sets an example for using CF design guidelines to facilitate the effective design of new flexure systems, to expand the design space, and to help others design CFs for other functional requirements.

The final monolithic design allows for easy waterjet fabrication and requires no assembly. However, the r-compliance CF elements have low stiffnesses in the constraint directions so they may be better suited for a six degree of freedom flexure system. Despite this disadvantage, CF X-Y-Θ_z stages are viable and could be used to fill needs that straight-beam flexures cannot. Some of the benefits of a CF stage are larger range to footprint ratios and axial symmetry [1].

REFERENCES

[1] Telleria M. Design Rules and Models for the Synthesis and Optimization of Cylindrical Flexures. Ph.D. Thesis. Massachusetts Institute of Technology; 2013.

[2] Matloff, L. Design and Optimization of an x-y-θz Cylindrical Flexure Stage. S.B. Thesis. Massachusetts Institute of Technology; 2013.

[3] Thomas M, Culpepper M. Design, fabrication and implementation of a flexure-based micropositioner for Dip Pen Nanolithography. S.B. Thesis. Massachusetts Institute of Technology; 2012.

[4] Thomas M, Culpepper M. Design, fabrication and implementation of a flexure-based micropositioner for Dip Pen Nanolithography. S.B. Thesis. Massachusetts Institute of Technology; 2012.

[5] Telleria M, Culpepper M. Element level optimization of cylindrical flexure for linear motion guidance, 2012 ASPE Annual Conference.

TIME VARYING ERROR BEHAVIOR IN SUPER-SIZE FLOOR TYPE BORING MACHINES

Bog-Ki Min and Sung-Chong Chung*
Hybrid System Design and Control LABoratory
School of Mechanical Engineering
Hanyang University
Seoul 133-791, KOREA

ABSTRACT

Time varying 3D volumetric error analysis of a super-size floor type boring machine is conducted through kinematic error modeling of its shape and joint elements. Time constants and gains of deformation transfer functions of them are formulated from CAD and heat transfer information. Using discrete equivalents of the transfer functions, 3D thermal error is estimated regarding environmental and cutting conditions.

INTRODUCTION

Super-size floor type boring machines are applied for milling, boring, drilling and tapping on mega-size parts for the construction, oil field, wind energy, plant, and shipbuilding industries. As the machining parts are too big, machining takes long time. Volumetric errors due to thermal deformation of the shape and joint elements during cutting deteriorate machining accuracy. In previous paper [1], to predict quantity and trend of the volumetric errors of the boring machine, error modeling was conducted by shape and joint transformation matrices. However, time varying characteristics during cutting and idling have not been studied yet [2-3].

In this paper, thermal deformation transfer functions of the shape and joint elements according to internal and external heat sources are formulated for 3D time varying error analysis in a super-size floor type boring machine. Internal heat sources such as motors, bearings, gears, and ballscrews are formulated from power analysis. Room temperature variation is modeled as an external heat source. Heat generation of the cutting process is modeled from cutting conditions. To compute errors from transfer functions, the heat sources are defined as input variables, and the volumetric errors are defined as output variables. Using difference equations obtained from the thermal transfer functions, volumetric error behavior is estimated according to machining conditions and ambient temperature variation.

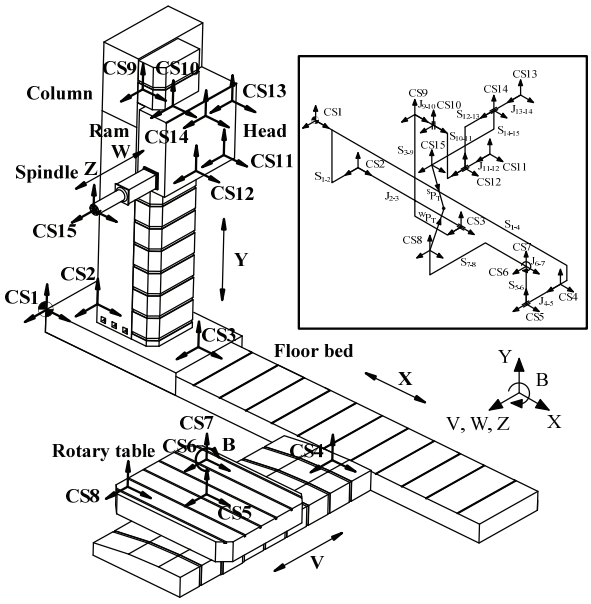

FIGURE 1. Kinematic Chain of a Super-size Floor Type Boring Machine.

TABLE 1. Definition of Coordinate Systems.

Coordinates	Locations
CS1	Reference coordinate
CS2	Rack origin (X-axis)
CS3	Center of pinions
CS4	Ballscrew fixed position (V-axis)
CS5	Ballscrew nut center on rotary table
CS6	Spindle origin in rotary table (B-axis)
CS7	Center of rotary table
CS8	Origin of workspace on the table
CS9	Ballscrew fixed position (Y-axis)
CS10	Ballscrew nut center
CS11	Ballscrew fixed position (W-aixs)
CS12	Ballscrew nut center on the ram
CS13	Ballscrew fixed position (Z-axis)
CS14	Ballscrew nut center in spindle
CS15	Tool center point (TCP)

VOLUMETRIC ERROR MODEL

Fig.1 shows structural configuration and kinematic chain of the super-size floor type boring machine. Table 1 describes coordinate systems for joint and shape elements in the machine tool [1]. Floor bed, rotary table, column, head, ram and spindle are shape elements. Five feed and one rotary joint axes moving by rack and double pinions, ballscrews, and a spindle are joint elements.

Kim and Chung [2-3] modeled volumetric errors due to geometric and thermal deformation errors in small size machine tools. Contrary to small machine tools, the super-sized floor type boring machine is taller, longer and bigger. Ambient temperature difference between factory floor and ceiling generates severe 3D thermal deformation of the column element. Eq. (1) shows shape and joint transformation matrices in X-axis direction with geometric and thermal deformation errors.

$$S_{actual}(t)=\begin{bmatrix} 1 & -\varepsilon_z^S(t) & \varepsilon_y^S(t) & a+\Delta a(t) \\ \varepsilon_z^S(t) & 1 & -\varepsilon_x^S(t) & b+\Delta b(t) \\ -\varepsilon_y^S(t) & \varepsilon_x^S(t) & 1 & c+\Delta c(t) \\ 0 & 0 & 0 & 1 \end{bmatrix} \quad (1)$$

$$J_{actual}(x,t)=\begin{bmatrix} 1 & -\varepsilon_z^J(x,t) & \varepsilon_y^J(x,t) & x+\delta_x(x,t)\pm S+P_x(t)\cdot x \\ \varepsilon_z^J(x,t) & 1 & -\varepsilon_x^J(x,t) & \delta_y(x,t) \\ -\varepsilon_y^J(x,t) & \varepsilon_x^J(x,t) & 1 & \delta_z(x,t) \\ 0 & 0 & 0 & 1 \end{bmatrix}$$

$\varepsilon^S_{x,y\&z}$ and $\varepsilon^J_{x,y\&z}$ are rotational errors of shape and joint transformation matrices. Δa, Δb and Δc are translational errors due to thermal deformation of shape elements. S, δ_x, δ_y and δ_z are squareness, positioning and straightness errors, respectively. P_x is thermal expansions in feed X-axis [1]. Other shape and joint transformation matrices are modeled similarly. Considering dominant thermal error terms only, volumetric errors in X, Y and Z-axis are given by

$$\begin{aligned} dX &= \Delta a_1(t)-\Delta a_2(t)+\Delta a_3(t)-\Delta a_5(t)+\Delta a_6(t)+P_x(t)\cdot x \\ dY &= \Delta b_1(t)-\Delta b_2(t)+\Delta b_3(t)-\Delta b_4(t)-\Delta b_5(t) \\ &\quad +\Delta b_6(t)+\Delta b_7(t)+\Delta b_8(t)+P_y(t)\cdot y \\ dZ &= \Delta c_1(t)-\Delta c_2(t)+\Delta c_3(t)-\Delta c_5(t)+\Delta c_6(t) \\ &\quad +\Delta c_7(t)+\Delta c_8(t)+P_z(t)\cdot z-P_z(t)\cdot v+P_z(t)\cdot w \end{aligned} \quad (2)$$

THERMAL DEFORMATION MODELS

Thermal deformations of each element by external and internal heat sources are modeled as first order systems [2-3]. Input variable is internal or external temperature of the machine element. Output variables are deformations in each direction. Using a discrete equivalent of the transfer function for the *i*-th shape element, its difference equation between the *i*-th heat input and deformation output in X-axis is given by

$$\begin{aligned} \Delta a_i(t) &= \frac{\left(1-\frac{\Delta t}{2\tau^S_{a_i}}\right)}{\left(1+\frac{\Delta t}{2\tau^S_{a_i}}\right)}\Delta a_i(t-1) \\ &\quad +\frac{\frac{K^S_{a_i}\Delta t}{2\tau^S_{a_i}}}{\left(1+\frac{\Delta t}{2\tau^S_{a_i}}\right)}\left[\theta_{i,External}(t-1)+\theta_{i,External}(t)\right] \end{aligned} \quad (3)$$

where $K^S_{a_i}=\frac{\alpha_i\cdot a_i}{h_i\cdot A^{S,S}_{a_i}}$; $\tau^S_{a_i}=\frac{m^S_{a_i}c_{p,a_i}}{h_i\cdot A^{S,S}_{a_i}}$

For the *i*-th shape element, α_i is thermal expansion coefficient, h_i is convection coefficient, $m^S_{a_i}$ is mass, c_{p,a_i} is specific heat, a_i is length in X-axis, and $A^{S,S}_{a_i}$ is surface area. Similarly, other difference equations are formulated as follows:

$$\begin{aligned} \Delta a_i(t) &= \frac{\left(1-\frac{\Delta t}{2\tau^S_{a_i}}\right)}{\left(1+\frac{\Delta t}{2\tau^S_{a_i}}\right)}\Delta a_i(t-1)+\frac{\frac{K^S_{a_i}\Delta t}{2\tau^S_{a_i}}}{\left(1+\frac{\Delta t}{2\tau^S_{a_i}}\right)}\left[\theta_{i,External}(t-1)+\theta_{i,External}(t)\right] \\ \Delta b_i(t) &= \frac{\left(1-\frac{\Delta t}{2\tau^S_{b_i}}\right)}{\left(1+\frac{\Delta t}{2\tau^S_{b_i}}\right)}\Delta b_i(t-1)+\frac{\frac{K^S_{b_i}\Delta t}{2\tau^S_{b_i}}}{\left(1+\frac{\Delta t}{2\tau^S_{b_i}}\right)}\left[\theta_{i,External}(t-1)+\theta_{i,External}(t)\right] \\ \Delta c_i(t) &= \frac{\left(1-\frac{\Delta t}{2\tau^S_{c_i}}\right)}{\left(1+\frac{\Delta t}{2\tau^S_{c_i}}\right)}\Delta a_i(t-1)+\frac{\frac{K^S_{c_i}\Delta t}{2\tau^S_{c_i}}}{\left(1+\frac{\Delta t}{2\tau^S_{c_i}}\right)}\left[\theta_{i,External}(t-1)+\theta_{i,External}(t)\right] \\ P_x(t) &= \frac{\left(1-\frac{\Delta t}{2\tau^J_x}\right)}{\left(1+\frac{\Delta t}{2\tau^J_x}\right)}P_x(t-1)+\frac{\frac{K^J_x\Delta t}{2\tau^J_x}}{\left(1+\frac{\Delta t}{2\tau^J_x}\right)}\left[\theta_{x,Internal}(t-1)+\theta_{x,Internal}(t)\right] \\ P_y(t) &= \frac{\left(1-\frac{\Delta t}{2\tau^J_y}\right)}{\left(1+\frac{\Delta t}{2\tau^J_y}\right)}P_y(t-1)+\frac{\frac{K^J_y\Delta t}{2\tau^J_y}}{\left(1+\frac{\Delta t}{2\tau^J_y}\right)}\left[\theta_{y,Internal}(t-1)+\theta_{y,Internal}(t)\right] \\ P_v(t) &= \frac{\left(1-\frac{\Delta t}{2\tau^J_v}\right)}{\left(1+\frac{\Delta t}{2\tau^J_v}\right)}P_v(t-1)+\frac{\frac{K^J_v\Delta t}{2\tau^J_v}}{\left(1+\frac{\Delta t}{2\tau^J_v}\right)}\left[\theta_{v,Internal}(t-1)+\theta_{v,Internal}(t)\right] \\ P_w(t) &= \frac{\left(1-\frac{\Delta t}{2\tau^J_w}\right)}{\left(1+\frac{\Delta t}{2\tau^J_w}\right)}P_w(t-1)+\frac{\frac{K^J_w\Delta t}{2\tau^J_w}}{\left(1+\frac{\Delta t}{2\tau^J_w}\right)}\left[\theta_{w,Internal}(t-1)+\theta_{w,Internal}(t)\right] \\ P_z(t) &= \frac{\left(1-\frac{\Delta t}{2\tau^J_z}\right)}{\left(1+\frac{\Delta t}{2\tau^J_z}\right)}P_z(t-1)+\frac{\frac{K^J_z\Delta t}{2\tau^J_z}}{\left(1+\frac{\Delta t}{2\tau^J_z}\right)}\left[\theta_{z,Internal}(t-1)+\theta_{z,Internal}(t)\right] \end{aligned} \quad (4)$$

Δa_i , Δb_i and Δc_i are X, Y and Z-axis thermal deformations for the *i*-th shape element, respectively. $P_x(t)$, $P_y(t)$, $P_v(t)$, $P_w(t)$ and $P_z(t)$ are thermal deformation coefficients of each joint. Δt means sampling interval, and t is t-th time step in discrete domain. $K_{a_i}^S$, $K_{b_i}^S$, $K_{c_i}^S$, K_x^J , K_y^J , K_v^J , K_w^J and K_z^J are thermal gains of shape and joint elements. $\tau_{a_i}^S$, $\tau_{b_i}^S$, $\tau_{c_i}^S$, τ_x^J , τ_y^J , τ_v^J , τ_w^J and τ_z^J are time constants of the shape and joint elements. $\theta_{j,Internal}$ and $\theta_{j,External}$ are internal and external temperatures of the *j*-th element, respectively.

ERROR SIMULATION

To simulate quantity and trend of time varying volumetric errors of the super-size floor type boring machine, error database based on previous data [1-3] is applied for the analysis. In addition, powers of spindle and feed motors, frictional information of gears, bearings and ballscrews, as well as cooling jacket and hydrostatic bearing effects supplied by HNK Machine Tool Co., LTD are applied for generation of internal heat inputs. After defining input variables according to the internal and external heat sources, error behavior of each machine tool element is computed according to Eq. (4). To investigate 3D thermal error behavior according to ambient temperature change, seasonal temperature information is collected from weather information. Spring, summer, fall and winter temperatures with minimum and maximum diurnal temperature range are selected as input variables. 3D volumetric errors are estimated by Eq. (2). Fig. 2 and 3 show 3D error behavior of the TCP as output variables for the eight cases. For 24 hours, estimated 3D minimum and maximum errors are 7μm and 130μm, respectively.

Table 2 shows cutting conditions used in boring and milling processes. Fig. 4 shows 3D errors generated in the boring processes with two different ambient temperature conditions. Time varying 3D thermal error behavior with different entry and exit error shapes is observed in two cases. For 10 hours cutting, maximum errors in X, Y and Z directions are estimated 128μm, 77μm and 136 μm, respectively. Fig. 5 shows errors generated in the face milling processes for different ambient temperatures. Two different error vectors are observed as well. Generated maximum error in 80 minutes cutting is 65 μm.

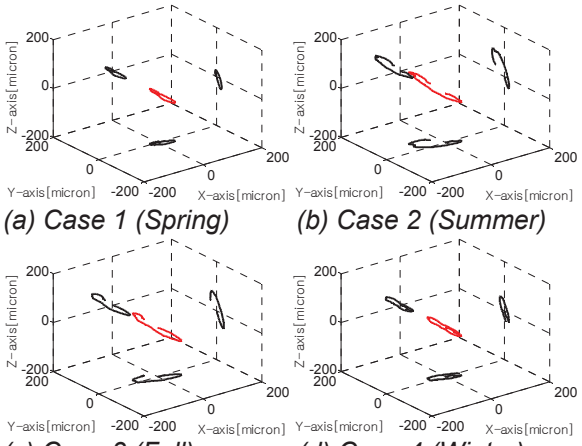

(a) Case 1 (Spring) *(b) Case 2 (Summer)*

(c) Case 3 (Fall) *(d) Case 4 (Winter)*

FIGURE 2. 3D Error Behavior of TCP in Small Diurnal Temperature Range.

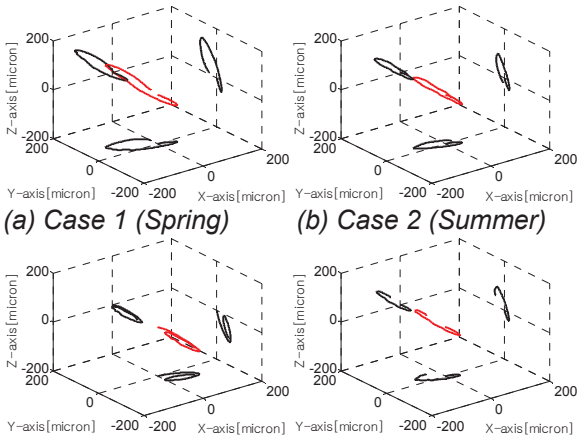

(a) Case 1 (Spring) *(b) Case 2 (Summer)*

(c) Case 3 (Fall) *(d) Case 4 (Winter)*

FIGURE 3. 3D Error Behavior of TCP in Large Diurnal Temperature Range.

TABLE 2. Cutting Conditions.

Boring Process	
Boring Diameter	2000mm
Boring Depth	100mm
Tool Diameter	80mm
Cutting Depth/Stroke	5mm
Cutting Feed Rate	200mm/min
Turnaround Time	600min
Face Milling Process	
Cutting Area	1000(X) x 2000(Y)mm^2
Tool Diameter	250mm
Cutting Width	150mm
Number of Feed	10
Cutting Depth	5mm
Cutting Feed Rate	250mm/min
Turnaround Time	80min

Cutting errors generated in two different processes are quite different owing to ambient temperature changes under the same cutting conditions. These confirm that external heat affect machining accuracy very much in the super-size machine tool.

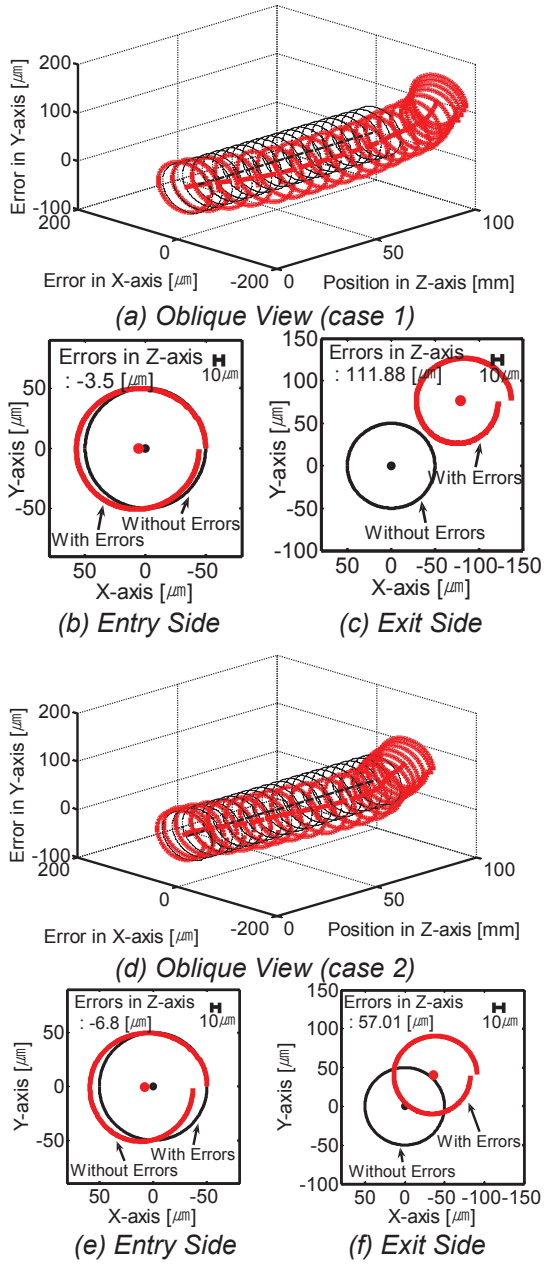
Error in Y-axis [㎛]
Error in X-axis [㎛]
Position in Z-axis [mm]
Errors in Z-axis : -3.5 [㎛]
Errors in Z-axis : 111.88 [㎛]
With Errors
Without Errors
Y-axis [㎛]
X-axis [㎛]
Errors in Z-axis : -6.8 [㎛]
Errors in Z-axis : 57.01 [㎛]

(a) Oblique View (case 1)

(b) Entry Side *(c) Exit Side*

(d) Oblique View (case 2)

(e) Entry Side *(f) Exit Side*

FIGURE 4. 3D Error Maps in Boring Processes.

CONCLUSIONS

Time varying 3D thermal error modeling of a super-size floor type boring machine has been accomplished through kinematic modeling of shape and joint error elements. Thermal deformations of the elements are formulated through discrete equivalents of thermal transfer functions between heat inputs and deformation outputs. Validity of the 3D thermal error modeling is verified in boring and face milling processes. It is confirmed that accuracy of a super-size floor type boring machine depends upon 3D thermal deformation by ambient temperature change very much.

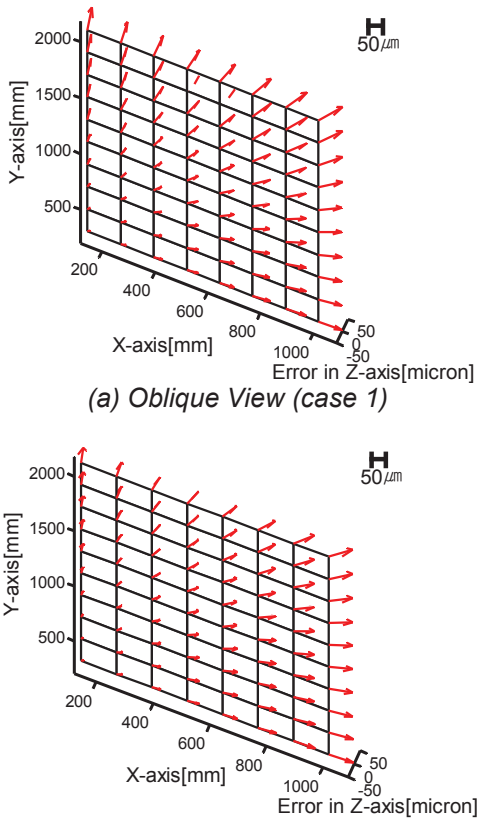

(a) Oblique View (case 1)

(b) Oblique View (case 2)

FIGURE 5. 3D Error Maps in Milling Processes.

ACKNOWLEDGEMENTS

This research is supported by Ministry of Trade, Industry & Energy, Korea and HNK MACHINE TOOL CO., LTD.

REFERENCES

[1] Min B-K, Shin D-S, Chung S-C. Geometric Error Modeling of a Super-size Floor Type Boring Machine. Proceedings of the ASPE 2012 Annual Meeting. 2012; 54: 220-223.

[2] Kim K-D, Chung S-C. On-Machine Inspection System Accuracy Improvement using an Artifact. Journal of Manufacturing Systems. 2004; 4: 299-308.

[3] Kim K-D, Chung S-C. Synthesis of the 3D Artifact for Quick Identification of Thermal Errors in Machine Tools. International Journal of Production Research. 2004; 42: 1167-1187.

IDENTIFICATION OF THERMAL CHARACTERISTICS IN THE BALLSCREW ASSEMBLY

Kwang-Je Oh[1], Bog-Ki Min[1],Chun-Hong Park[2], and Sung-Chong Chung[1*]
[1] Hybrid System Design and Control LABoratory
School of Mechanical Engineering
Hanyang University, Seoul 133-791, KOREA
[2] Intelligent Manufacturing System Division
KIMM, Daejeon 305-343, KOREA

ABSTRACT
A single-input single-output (SISO) thermal system modeling with disturbances is proposed to identify thermal charcteristics in the ballscrew system. Friction torque generated from the ballscrew interface between the shaft and the nut, and convective heat transfer coefficient around the ballscrew are estimated by temperature measurements on and around the ballscrew unit as well as nonlinear least square fitting of the SISO model. Validity of the devised key thermal parameter identification method is verified through experiments.

INTRODUCTION
Precision machinery consists of feed drives and structural elements. In the ballscrew driven feed drive system, its accuracy depends upon thermal and geometric errors of ballscrews. The thermal error is originated from internal and external heat sources. Frictional heat generated from ballscrew nut assembly, support bearings and motors are internal heat sources. Ambient temperature variation is external heat source. To estimate thermal behavior of a feed drive system precisely, heat conduction and convection effect of the ballscrew as well as frictional heat generation between balls and grooves should be modeled and identified accurately [1-3]. Therefore friction torque at the screw interface and the convection coefficient around the ballscrews are key parameters for the identification of thermal characteristics.

In the ballscrew driven precision machinery, to remove backlash and increase nut stiffness, preload is applied to ballscrews through a nut spacer, bigger balls, *etc*. As the ballscrew rotates, heat is generated from slip between balls and grooves, viscous friction due to shear stress of lubricant, and rolling contact friction. Support bearings generates frictional heat as well. In addition, environmental temperature variation as an external heat source changes temperature distribution of the ballscrew.

In this paper, to identify thermal characteristics according to rotational speeds or feedrates, a ballscrew system equipped with thermocouples (TCs), non-contact temperature and current sensors is fabricated as shown in Fig. 1. Considering heat equilibrium for the control volume of the ballscrew nut assembly between two supported bearings, a SISO thermal model with frictional torque as an input and nut temperature as an output is constructed. In this case, heat convection and conduction effects as well as ambient temperature are treated as disturbances for the SISO system. Using CAD data of the test rig as well as averaged temperature measurements of nut, shaft and bearing units, the key thermal parameters are identified regarding rotational speeds through nonlinear least square fitting of the modeled transfer function. Validity of the developed method is verified by experiments.

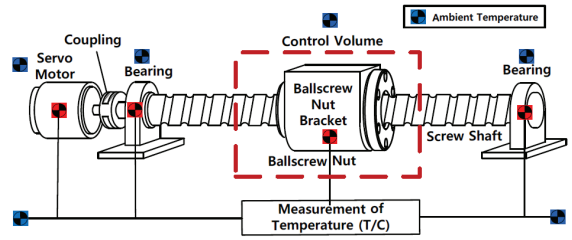

(a) Temperature Measurement Points.

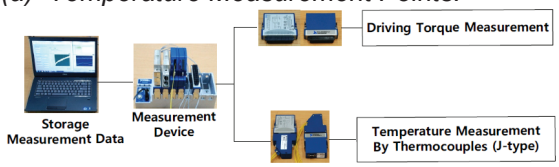

(b) Data Acquisition System Setup.

FIGURE 1. Schematic Diagram of Experimental Setup.

THERMAL CHARACTERISTICS

Assuming temperature of the nut area is uniform, and considering disturbances due to heat convection around the screw and conduction in the ballscrew, heat equilibrium for the lumped control volume of the nut area with input and output heat flow rates is given by

$$C_h \cdot \frac{d\theta(t)}{dt} = \dot{Q}_{in} - \dot{Q}_{conv} + \dot{Q}_{cond} \quad (1)$$

where C_h and $\theta(t)$ are heat capacity and nut temperature of the ballscrew, respectively. Generated heat rate, and in and out heat flow rates across the control surface are formulated as follows:

$$\dot{Q}_{in} = \phi \cdot \omega \cdot T_f = \phi \cdot \left(\frac{\pi N}{30}\right) \cdot T_f$$

$$\dot{Q}_{conv} = hA^s\left[\theta(t) - \theta_a(t)\right] \quad (2)$$

$$\dot{Q}_{cond} = -\lambda A^c\left[\frac{\theta_L(t) - \theta(t)}{\Delta L_L} - \frac{\theta(t) - \theta_R(t)}{\Delta L_R}\right]$$

where N, T_f, h, λ, A^c and A^s are rotational speed, friction torque, convective heat transfer coefficient, thermal conductivity, cross sectional and surface areas of the ballscrew unit, respectively. Left-side and right-side shaft temperatures, θ_L and θ_R, and ambient temperature θ_a are measurable disturbances. ϕ is heat transfer ratio to the nut. In Eq. (2), A^c, A^s, ΔL_L and ΔL_R are given by CAD data. Heat conduction coefficient λ and heat capacity C_h are known physical parameters.

Taking frictional heat rate $\dot{Q}_{in}$ generated by rotational speed N as an input and nut temperature as an output for the thermal system, transfer function of the SISO system is obtained as follows:

$$G(s) = \frac{\theta(s)}{\dot{Q}_{in}(s)} = \frac{1/k}{\tau s + 1} \quad (3)$$

$$\tau = \frac{C_h}{k} : \text{time constant}$$

$$k = hA^s - \lambda A^c\left(\frac{\Delta L_L + \Delta L_R}{\Delta L_L \Delta L_R}\right)$$

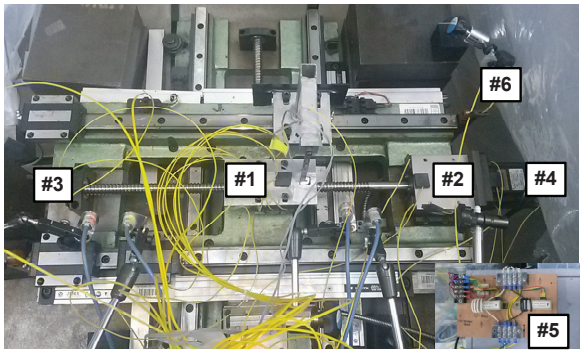

FIGURE 2. Experimental Setup for Identification of Ballscrew Thermal Characteristics.

From Eqs. (1)~(3), nut temperature with respect to the frictional heat input and disturbance temperatures is formulated by

$$\theta(t) = L^{-1}\left\{\begin{matrix} G(s)\dot{Q}_{in}(s) + hA^s G(s)\theta_a(s) \\ -\lambda A^c G(s)\left[\frac{\theta_L(s)}{\Delta L_L} + \frac{\theta_R(s)}{\Delta L_R}\right] \end{matrix}\right\} \quad (4)$$

Discrete equivalent of Eq. (4) with unknown key parameters T_f and h is applied for parameter identification. Implicit estimation of the SISO model is conducted in discrete domain according to rotational speeds through nonlinear least square fitting [4] of the collected temperature data.

EXPERIMENTS

Fig. 2 shows a ballscrew test rig equipped with TCs, non-contact temperature and current sensors. To measure and collect uniform temperatures of the ballscrew units, average temperatures of the nut, fixed and support bearings are measured by TCs of #1, #2 and #3 regions, respectively. TCs of #4 region measure average temperature of the motor. For comparing frictional torque with driving torque, hall sensors are installed for motor driving torque measurement at #5. Averaged ambient temperature is measured by several #6 TCs around the ballscrew. For frictional heating of the system, moving stroke 100mm is selected in the middle region of the shaft. Reciprocation feedrates 1.25, 2.5 and 3.75 m/min are used for heating. Each experiment is performed for 2 hours rotation and then 1 hour rest.

RESULTS AND DISCUSSION

Double-nut ballscrew with shaft diameter 16mm, lead 5mm and preload 670N is applied for

identification experiments. Fig. 3 shows average temperature measurements of the ballscrew system at 250, 500 and 750 rpms for 2 hours rotation and 1 hour rest. Nut temperature increases 8K at 750 rpm for 2 hours rotation. Fig. 4 shows non-contact records of temperature at each side of the ballscrew shaft. Shaft near the nut section increases 7K at 750 rpm for 2 hours. Fig. 5 shows ambient temperatures around the ballscrew system. It varies around 0.5K for 2 hours. Using the collected average nut, shaft and ambient temperatures, a discrete equivalent of Eq. (4) is able to be fitted through a nonlinear least square method [4], the key parameters h and T_f when the heat transfer ratio to the nut $\phi = 0.5$ are identified according to feedrates as shown in Table 1.

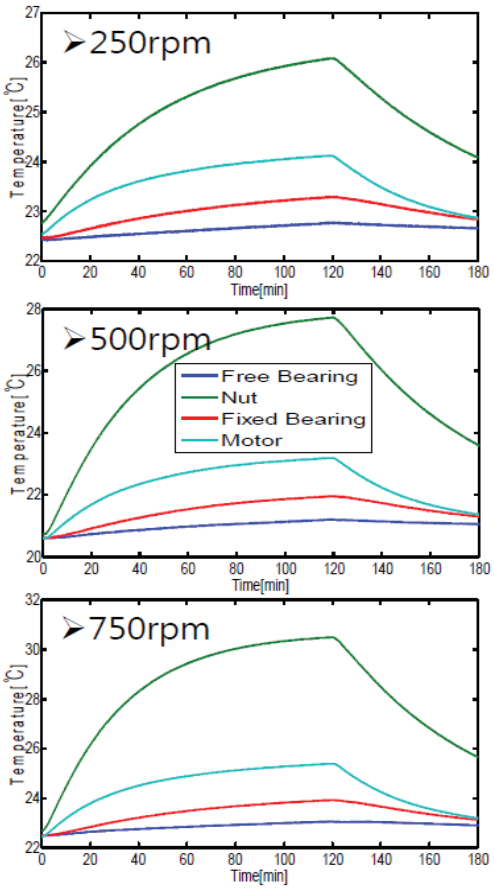

FIGURE 3. Average Nut Temperatures vs. Time.

TABLE 1. Estimated Key Parameters.

Feedrates (m/min)	h[W/m^{2}K]	T_f [Nm]	$\dot{Q}_{in}$ [W]
1.25	5.88	0.09	1.178
2.5	7.46	0.11	2.880
3.75	8.91	0.1	3.927

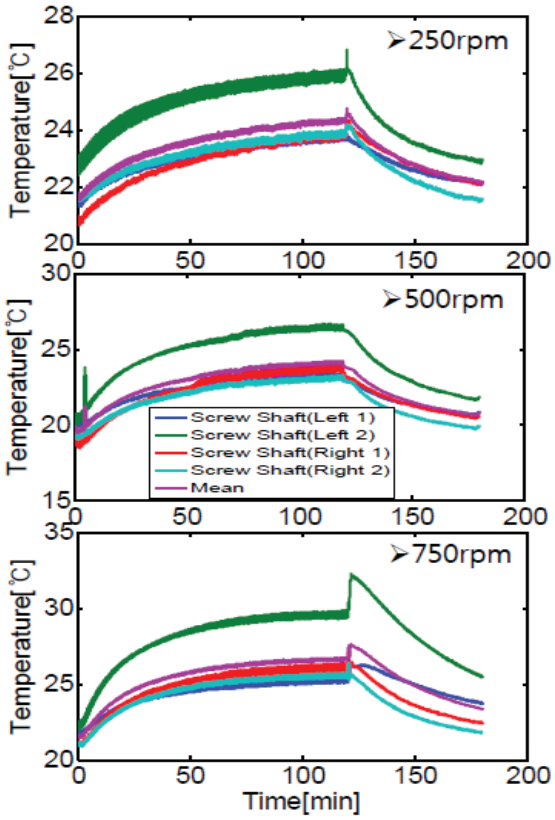

FIGURE 4. Shaft Temperatures vs. Time.

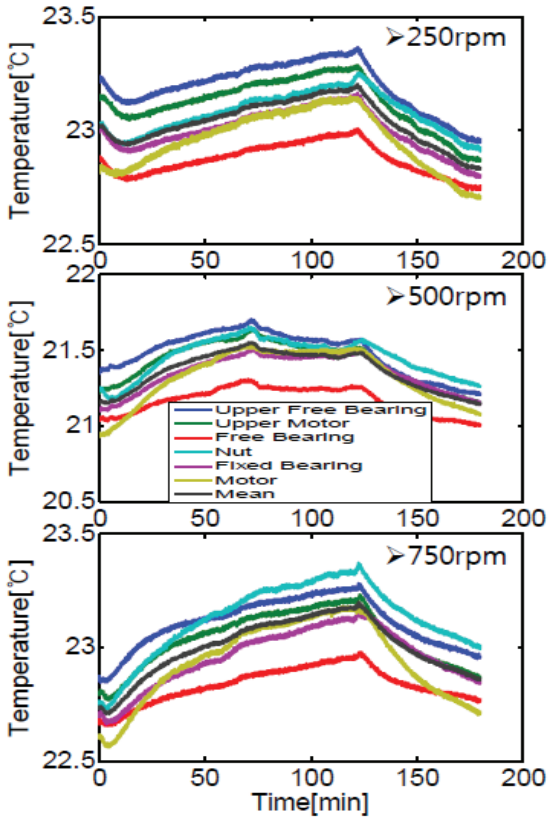

FIGURE 5. Ambient Temperatures vs. Time.

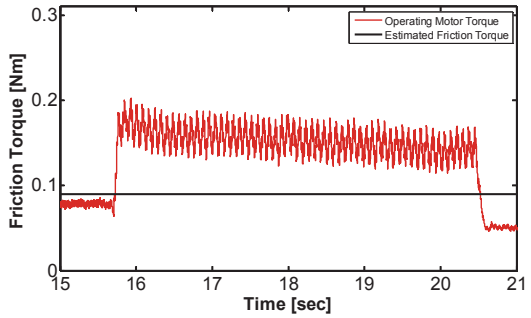

(a) Feedrate 1.25m/min (250 rpm)

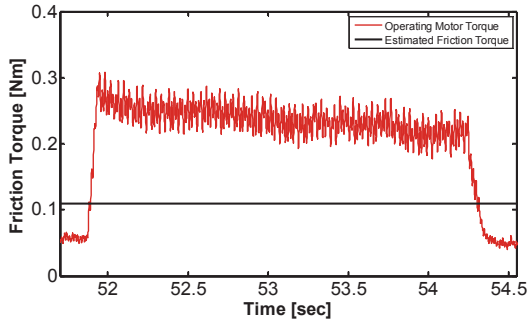

(b) Feedrate 2.5m/min (500 rpm)

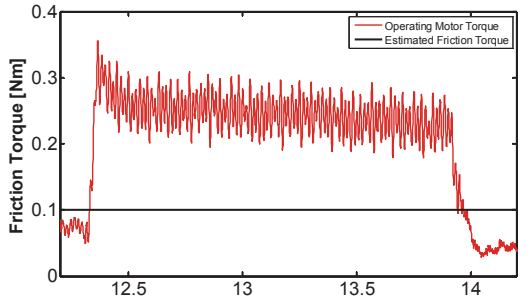

(c) Feedrate 3.75m/min (750 rpm)

FIGURE 6. Torque Comparisons vs. Feedrates.

As the rotational speed increases, the heat convection rate around the ballscrew shaft increases due to air flow speed increase around the screw as shown in Table 1. However, heat input $\dot{Q}_{in}$ due to frictional torque is proportional to the rotational speed N, ballscrew temperature increases as the feedrate increases as shown in Fig. 3 and 4. In addition, temperatures of the shaft near the nut are almost the same as of the nut as shown in Figs. 3 and 4. This effect generates uniform expansions of the screw shaft and the nut as well as makes very small preload change at the screw interface. Thus identified frictional torque at the interface does not change according to feedrates as shown in Table 1.

Fig. 6 shows measured driving torque by hall sensors and estimated fictional torque at the interface. Since the frictional torque is less than the driving torque and does not vary with respect to rotational speed, validity of the developed identification method is verified well. As the viscous friction due to lubricant at the interface decreases along with temperature increase and there is ballscrew installation error, motor driving torque during rotation decreases as shown in Fig. 6. It is concluded that the frictional toque at the ballscrew interface does not vary according to the rotational speed. Estimated key parameters h and T_f shown in Table 1 confirms the validity of the developed implicit identification method.

CONCLUSIONS

Key thermal parameters such as convection heat coefficient and ballscrew frictional torque are identified through the SISO thermal system modeling with disturbances and nonlinear least square fitting of collected temperatures. As the frictional heat input is proportional to rotational speed, units of the ballscrew nut assembly deform uniformly. Very small preload change is generated at the ball screw interface according to rotational speeds. Implicit identification results and experiments confirm frictional torque does not change according to rotational speeds. Identification results also verify that convection coefficient around the ballscrew changes very much according to rotational speeds.

ACKNOWLEDGEMENT

This research is supported by Ministry of Trade, Industry & Energy, Korea.

REFERENCES

[1] Ahn J-Y, Chung S-C. Real-time Estimation of the Temperature Distribution and Expansion of a Ball Screw System using an Observer. Proceedings of the Institution of Mechanical Engineers Part B, Journal of Engineering Manufacture. 2004; 218: 1667-1680.

[2] Min B-K, Park C-H, Chung S-C. Modeling of Ballscrew Nut Stiffness Including Thermal Effect. Proceeding of the ASPE 2011 Annual Meeting. 2011; 52; 319-322.

[3] Min B-K, Kim M, Park C-H, Chung S-C. Modeling of Thermal Nut Stiffness in Ballscrews. Proceeding of the ASPE 2012 Annual Meeting. 2012; 54; 390-393.

[4] Johansson R. System Modeling and Identification. Prentice-Hall International, Inc. New Jersey: 1993.

DEVELOPMENT OF A CYLINDER TYPE GAS-LIQUID PHASE-CHANGE ACTUATOR

Manabu ONO[1] , Shunya SAITO[1],
Taka KATO[1] and Makoto SAKAMOTO[2]
[1]Department of Mechanical System Engineering
Tokyo Metropolitan Collage of Technology
Shinagawa, Tokyo 14-0011 Japan
[2]Department of Production System Engineering
Tokyo Metropolitan Collage of Technology
Shinagawa, Tokyo 140-0011 Japan

INTRDUCTIONS

New microactuators which are used for medical apparatus and inspection microrobots in the human body have been researched. The pneumatic pressure or water pressure have been utilized for microactuators of the in-pipe mobile microrobots[1]-[5]. However, we have noticed a microactuator driven by gas-liquid phase-change phenomenon[6],[7]. When a liquid is vaporized, the volume of the gas produced is more than 100 times that of the liquid. Gas-liquid phase-change microactuators are thermal engines which utilize the large change in volume that occurs during a phase-change.

The actuator of the old model was using the metal bellows for the pressure vessel. A metal bellows type actuator has a high manufacturing cost, and there is a problem which cannot obtain large displacement. We developed the new type gas-liquid phase-change actuator which the improved air cylinder used.

An actuator consists of a cylinder, a heater, a operating fluid, and a control system. The outside diameters of a cylinder are 7 mm, 120 mm in length and 30 mm of the maximum displacement. A cylinder is a product made from stainless steel with high heat dissipation nature. The heater to vaporize the operating fluid is made of a coiled constantan wire which is 0.2 mm thick and 490 mm long. Its electrical resistance is 7.8 Ω.

The operating fluid is non-chlorine per fluorocarbon ($C_5F_{11}NO$), because its vaporizing temperature, though higher than the human body, is still only 323 K at the atmospheric pressure, and its latent heat for vaporization is 104.56 kJ/kg and is only 1/22 that of water. Consequently, the energy needed for vaporization is very low. The operating fluid is high in electrical resistance and very safe because of its incombustibility.

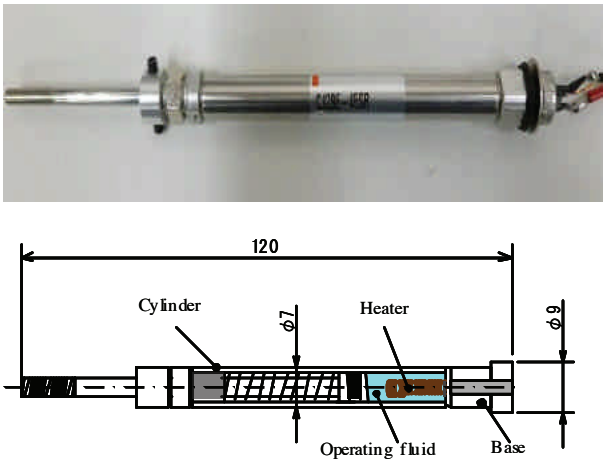

FIGURE 1. Structure of a cylinder type gas-liquid phase-change actuator

We confirmed that the gas-liquid phase-change actuator generated force of 152 N and generated displacement of 2.0 mm at input electric power of 1.92 W.

STRUCTURE OF GAS-LIQUID PHASE-CHANGE ACTUATOR

The photograph and a cross-section of the fabricated cylinder type are shown in Fig. 1. The cylinder is made of stainless steel. Its dimension is 9 mm in outer diameter, 7 mm in inner diameter, and 120 mm long. Operating fluid and a heater are enclosed in the cylinder. The heater to vaporize the operating fluid is made of a coiled constantan wire which is 0.2 mm thick

and 490 mm long. Its electrical resistance is 7.8 Ω. The operating fluid is non-chlorine per fluorocarbon ($C_5F_{11}NO$), because its vaporizing temperature, though higher than the human body, is still only 323 K at the atmospheric pressure, and its latent heat for vaporization is 104.56 kJ/kg and is only 1/22 that of water. Consequently, the energy needed for vaporization is very low. The operating fluid is high in electrical resistance and very safe because of its incombustibility.

THE DRIVE PRINCIPLE OF AN ACTUATOR

The drive principle of an actuator is shown in Fig. 2. Step 1 shows an initial condition. An operating fluid is the liquid phase. At Step 2, it heats by inputting electric power into the heater inside an actuator. In Step 3, a part of operating fluid changes from the liquid phase to the gaseous phase. The rise of the pressure in the cylinder by cubical expansion occurs. With this pressure, force and displacement arise to the rod of an actuator. If the power and displacement of an actuator will be in a thermal equilibrium state, they will be stabilized. In Step 4, the input of the electric power to a heater is suspended and heating is stopped. The phase change of the gaseous phase of an operating fluid is carried out to the liquid phase by heat dissipation from the surface of an actuator. Internal volume is contracted and generative force decreases. Therefore, the force and displacement of an actuator will be in an initial condition.

THE GENERATIVE FORCE MEASUREMENT EXPERIMENT TO AN EQUILIBRIUM SITUATION

The characteristic of the actuator was investigated. The experiment measured the generative force and internal temperature to a thermal equilibrium state. The experimental apparatus used for Fig. 3 is shown. An experimental device consists of direct-current power supply equipment, an ammeter, a voltmeter, an actuator, and a force gauge. Electric power was inputted into the actuator to the thermal equilibrium state. Generative force was measured by the force gauge and internal temperature was measured by the thermo couple. Electric power inputted into an actuator was set to 1.92 W. The interval at the tip of a force gauge and an actuator is called a stroke. The stroke experimented by setting to 2.0 mm.

The generative force and internal temperature to a thermal equilibrium state are shown in Fig. 4.

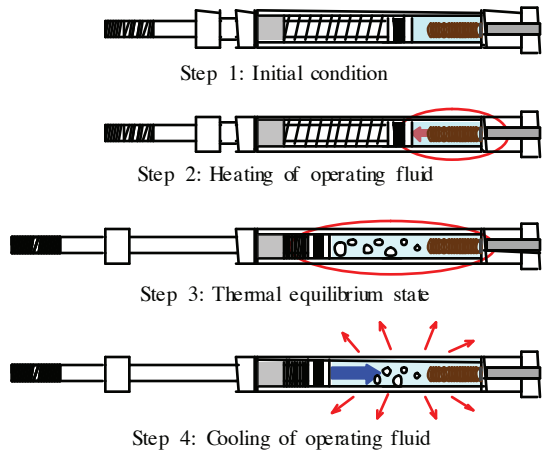
Step 1: Initial condition
Step 2: Heating of operating fluid
Step 3: Thermal equilibrium state
Step 4: Cooling of operating fluid

FIGURE 2. Structure of a cylinder type gas-liquid phase-change actuator

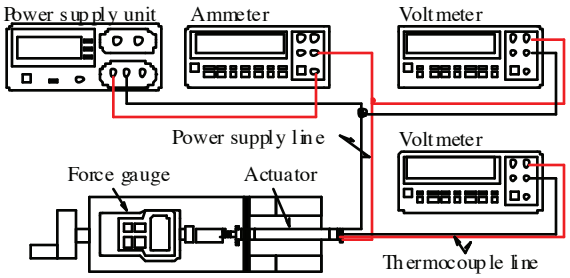

FIGURE 3. Experimental apparatus

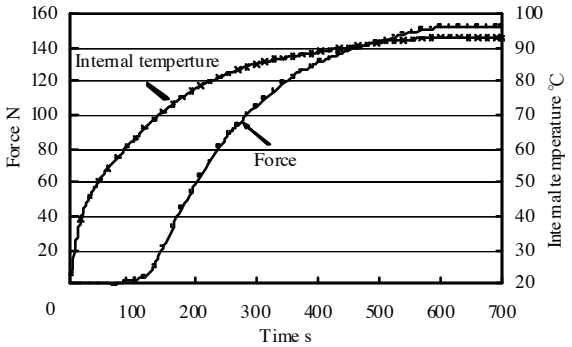

FIGURE 4. Force and internal temperature until thermal equilibrium state

In the thermal equilibrium state, generative force was set to 152.1 N and internal temperature became 93.1 degree Centigrade.

Generative force measured by the force gauge was made into the experimental value. The calculated value was read as pressure using the P-T diagram of a working fluid from internal temperature. The calculated value was obtained from this pressure by taking into consideration the stress area of a cylinder, and the elastic force inside an actuator. The calculated value of generative force was compared from the internal temperature measured by the thermo couple.

The generative force by the thermal expansion of the liquid phase of the working fluid to a thermal equilibrium state is shown in Fig. 5. It turned out that it is the same as that of transition of the generative force by the thermal expansion of the liquid phase of the working fluid of Fig. 5.

We confirmed that the thermal expansion of a working fluid was generative force of an actuator also related besides mind liquid phase change.

IMPROVEMENT OF RESPONSE

If the input electric power to an actuator is constant, it takes time long to a thermal equilibrium state. The speed of response to a thermal equilibrium state has been improved by changing input electric power.

The experimental apparatus added PC and the semiconductor relay circuit to the experimental device shown in Fig. 3. The input electric powers to the actuator were changed because a relay circuit changes the electric power units.

The desired value of generative force was set to 30 N. This value is power acquired when 1.0 MPa which is the maximum pressure of a common air compressor is given to this air cylinder.

Generative force when the generative force of a thermal equilibrium state inputs the only electric power 2.3 W used as a desired value into Fig. 6 is shown. Input electric powers ware changed to 40 W, 20 W, 10 W, and 2.3 W, and the generative force to a thermal equilibrium state was measured. This is shown in Fig. 7.

The time which a desired value takes has been shortened from 458.2 s to 23.9 s. Thereby, the

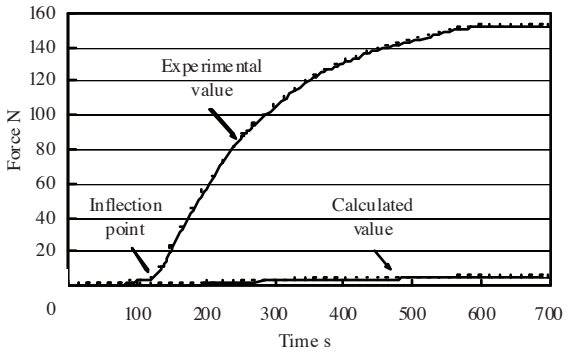

FIGURE 5. Experimental value and calculated value until thermal equilibrium state

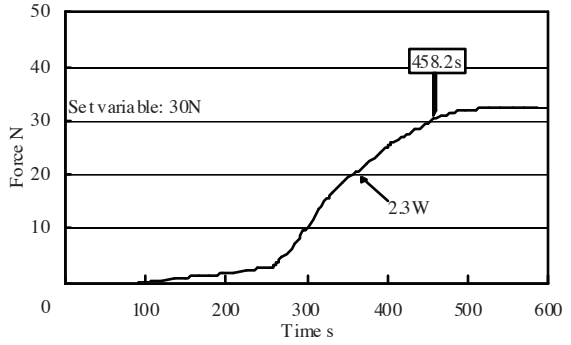

FIGURE 6. Force until thermal equilibrium state in case of a single input power

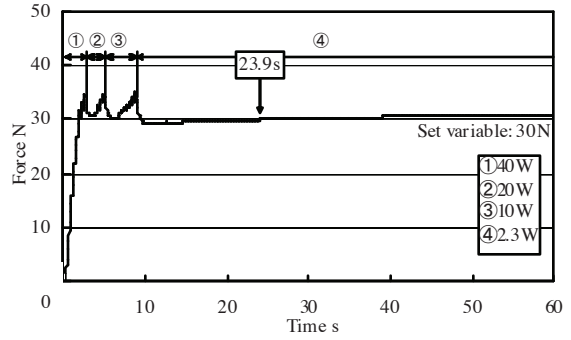

FIGURE 7. Force until thermal equilibrium state in case of relayed input power

improvement of the response was completed when input electric power changed.

APPLICATION TO A ROBOT HAND

The characteristic of this actuator is large and generative force of displacement magnitude is small. Then, the robot hand adapting the reverse principle of the lever which changes power into displacement was made as an experiment. The increase of displacement and the decrement of power were measured by experiment.

The structure of a robot hand is shown in Fig. 8. A robot hand consists of a hand, a mechanism, and an actuator. The robot hand has changed the generative force of an actuator into displacement by the actuator.

The thing up to 22 mm can be inserted into a hand by giving a 5 mm stroke to an actuator. Thereby, it has checked making displacement increase. The pinch force of the hand was measured by the load cell. It turned out that the pinch force of a hand is set to 14.8N 3 seconds after a start.

This actuator is applying the reverse principle of the lever, and using also for the mechanism which needs displacement is possible.

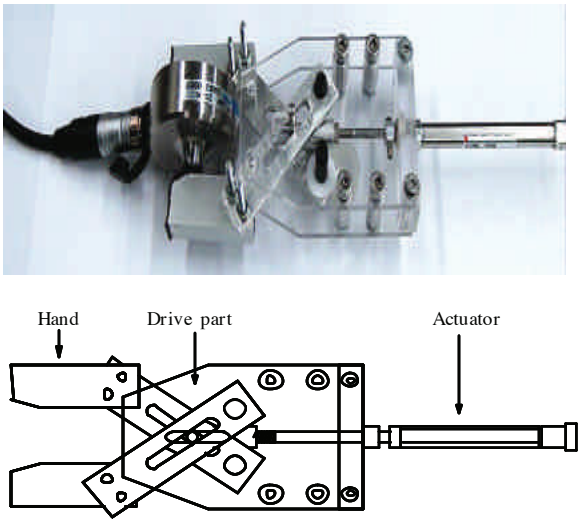

FIGURE 8. Structure of a cylinder type gas-liquid phase-change actuator

CONCLUSIONS

[1] We developed the new type gas-liquid phase-change actuator which the improved air cylinder used. An actuator consists of a cylinder, a heater, the operating fluid, and a control system.

[2] The improvement of speed of response was completed by the change of input electric powers.

[3] We applied the actuator to the robot hand. This actuator is applying the reverse principle of the lever, and using also for the mechanism which needs displacement is possible.

REFERENCES

[1] Yoshida, K., Takahashi, K. and Yokota, S. "An In-Pipe Mobile Micromashine Using Fluid Power," Proc. of JSME centennial Grand Congress, IMPT-100, (in Japanese), (1997), pp. 667-670.

[2] Kato, S., Shirakawa, M., Ono, M. and Tabata, M. " Fabrication of a Microrobot Movable in the Small Intestine of a Pig," (1999), Proc. of American Soc. for Precision Eng. 1999 Annual Meeting, pp. 204-207.

[3] Kato, S., Shirakawa, Akita, H., Miyajima, K., Sugaya, T.and Kasai, Y. " Fabrication of an In-pipe Microrobot Movable in Sheep's Small Intestine," (2000), Proc. of American Soc. for Precision Eng. 2000 Annual Meeting, pp. 341-344.

[4] Phee, L., Stefanini, C., Arena, A., Accoto, D., Menciassi, A. Pernorio, G., Boccadoro, M., and Dario, P. "Mechanical Clamping Mechanisms for Locomotion in the Gastrointestinal Tract," (2001), Proc. of 2nd International Conf. European Soc. for Precision Eng. and Nanotechnology, pp.770-773.

[5] Ono, M., Arakawa, E., Kyomine, S. and Kato, S., "Fabrication of a Microrobot Movable in a Freely Held Pig's Small Intestine," (2001), Proc. of 2nd International Conf. European Soc. for Precision Eng. and Nanotechnology, pp.806-809.

[6] Kato, S., "Modeling of a Gas-liquid phase-change Micro-actuator," (1997), Proc. of 4th Experimental Heat Transfer, Fluid Mechanics and Thermodynamics, pp.465-469.

[7] Kato, S., and Shintani, T., "Fabrication and Thermal Analysis of a Bellows type Gas-liquid phase-change Micro-actuator," (1997), Proc. of American Soc. for Precision Eng. 1997 Annual Meeting, pp. 315-318.

STUDY ON THE IMPACT LOAD APPLIED TO THE FINGERS USING A METAL BASEBALL BAT

Makoto SAKAMOTO[1], Manabu ONO[1], and Tetsumaro HIROI[1]
[1]Department of MONOZUKURI Engineering
Tokyo Metropolitan College of Industrial Technology
1-10-40, Higashiooi, Shinagawa-ku, Tokyo 140-0011, Japan

INTRODUCTION

Use of metal baseball bat was allowed in the Japan high school baseball from 1974. In comparison with the wooden bat, metal bat is hard to be broken. It is mainly used by high-school baseball.

Many researchers [1]-[3] are studied about the properties evaluation of a metal bat. However, discussion of sports injuries such as fractures and discussion of the major impact has not been done very completely imposed on the finger of the batter when using a metal bat.

Then, in this study, the system which measures the impact load applied to a batter's fingers is built. And it aims at clarifying the impact force. After clarifying the impact load, the alarm about use of metal bats is sounded. Moreover, the simulation of a ball and a bat is performed using the finite element method, and it gropes for the method of easing a batter's burden from both sides of an experiment and analysis.

First, a three-dimensional-CAD system is used and design and manufacture of an experimental device are performed. The system by which the impact load applied near the grip of metal bats is measured and evaluated is produced.

EXPERIMENTAL PROCEDURE

Figure 1 is shown the experimental setup which consists of four portions. They are bat support equipment, load cell, data logger, and high-speed digital video camera. A high speed digital video camera is Photron Ltd. FASTCAM SA TM5, which can have the resolution of 1024x1024 pixel, and can record it by 10,000 fps. Moreover, the sampling rate of an attached data logger is 10 kHz. A load cell is LCX-20KN-ID-P of KYOWA Co.. Furthermore, bat support equipment was designed not to break even if it makes with a speed of 40 m/s (about 150 km/h) ball collide with a bat.

The produced experimental device is shown in Figure 2. The baseball bat used for the experiment used the metal bats made from an aluminum alloy used by high-school baseball. Moreover, the ball used the hard ball generally used.

The experiment was conducted in the following procedures. First, a free fall of ball was carried out from a height of 1.5m. Experiments

Multi Channel Data Link

High-speed digital camera

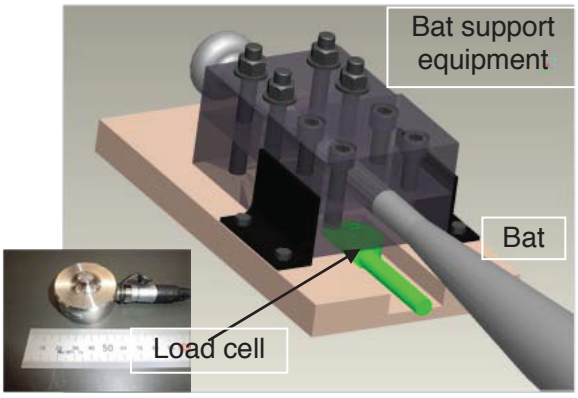

FIGURE 1. The designed an experimental device using 3D-CAD system.

were filmed in the high speed camera. Moreover, the load concerning the grip at that time was measured by the load cell.

The situation of the experiment by free fall is shown in Figure 3. The velocity of the ball just before a collision is 5.41 m/s.

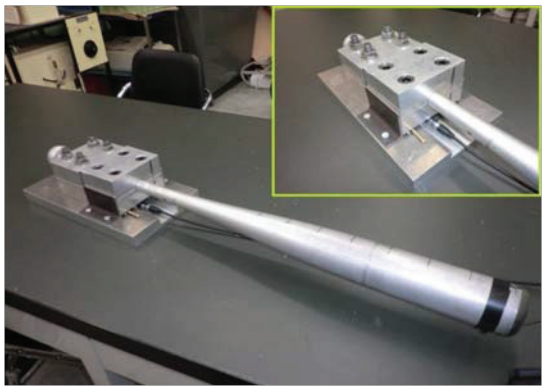

FIGURE 2. Schematic of an experimental device.

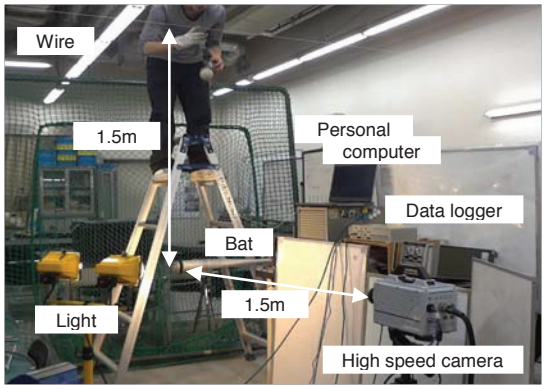

FIGURE 3. Experimental set up (Case of free fall)

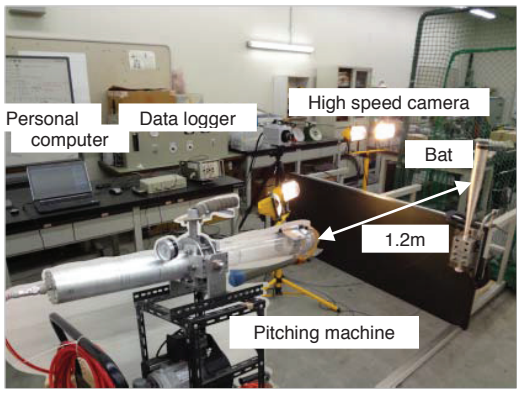

FIGURE 4. Experimental set up (Case of pitching machine)

Second, the experiments were conducted using the pitching machine which was made in our laboratory. It is shown in Figure 4. The velocity of the ball discharged from the pitching machine was about 24.5m/s.

The collision position of the ball was determined by image analysis as shown in Figure 5. The distance from a load cell to the scale of most right-hand side was 288 mm. The distance from the origin of image to a collision point is 130 pixels and to a most right hand point was 744 pixels. An image calibration was hung on this. The image calibration of free fall was 0.471mm/pixel and it of a pitching machine was 0.615mm/pixel.

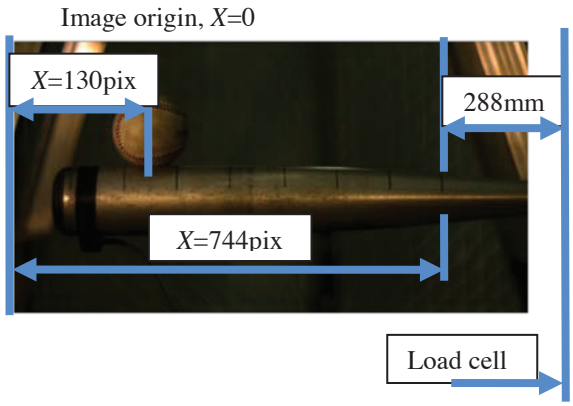

FIGURE 5. Image analysis (collision position)

RESULTS AND DISCUSSION

The situation of a collision of a bat and a ball is shown in Figure 6. It is shown by (a) before the collision. The place which collided exactly is shown in (b). It is detached in 1.5 ms(c). The peak of impact load is recorded in 27.8 ms afterward (d). It turns out that load has risen immediately after a collision. Moreover, the biggest impact load came to the 2nd waves.

The position where a ball collides with a bat is shown in Figure 7. The sweet spot was 488mm from the measurement point.

The impact load measured from the load cell is shown in Figure 8. Impact load becomes large proportionally from root to a sweet spot. This is based on moment. The increase in impact load is small as it goes to top from a sweet spot. In spite of free fall from 1.5m, the impact load which a hand receives is 865N. The intensity of the cortical bone is called about 200MPa. When the foreign material of 2mm^2 existed between a bat and a finger, a cortical bone may be broken.

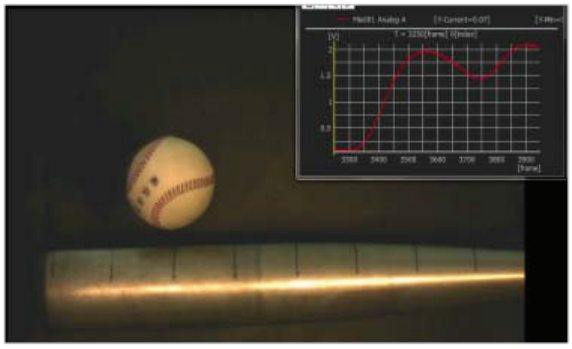

(a) Before a collision

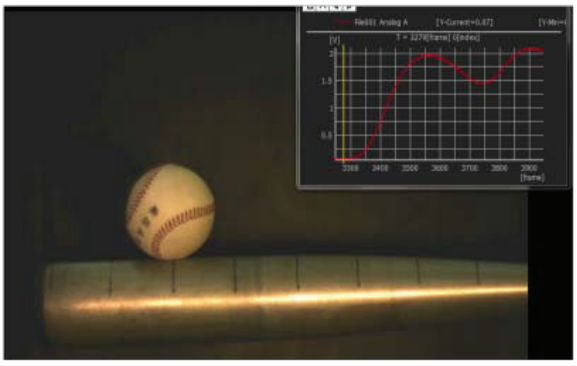

(b) Just a collision

(c) After 1.5 ms

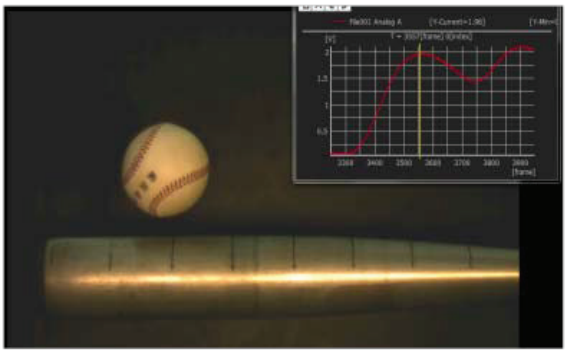

(d) First peek of a load (after 27.8ms)

FIGURE 6. Image analysis

Comparison of the impact load by free fall and a pitching machine is shown in Figure 9. The maximum of impact load was 2.73kN. This value is 3.16 times as large as a free fall's one. Moreover, the inclination from a root to a sweet spot is calculated with 10.5 N/mm. This value is 3.16 times as large as a free fall's.

After a collision, the velocity of the ball was

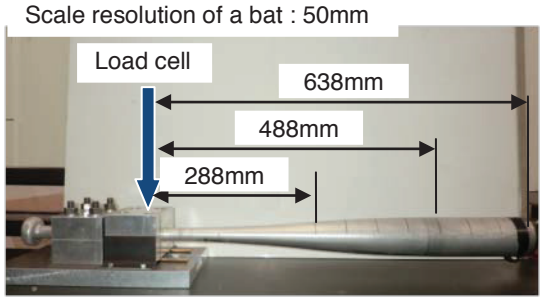

FIGURE 7. The position where a ball collides with a bat

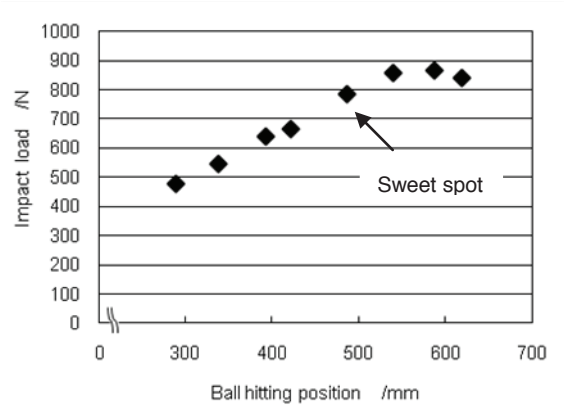

FIGURE 8. Measurement of impact loads

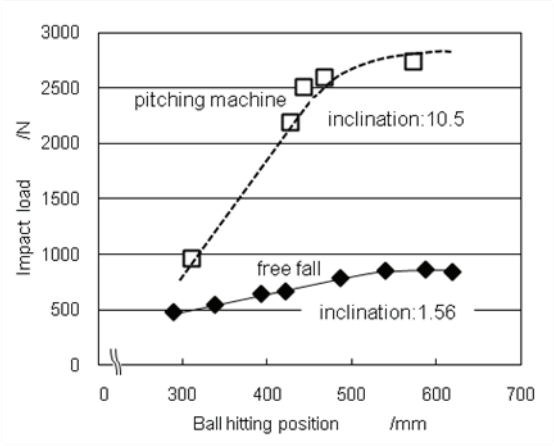

FIGURE 9. Measurement of impact loads in the cases of free fall and pitching machine

calculated by image analysis. The coefficient of restitution is shown in Figure 10. In free fall, a coefficient of restitution becomes small. This is because the velocity after a collision was small, so measurement is difficult. In the case of the pitching machine, the coefficient of restitution is large toward a root to the sweet spot. And at the tip of the bat, it is small.

The characteristic frequency of the bat by free fall and a pitching machine is shown in Figure 11. It was 27.2Hz.

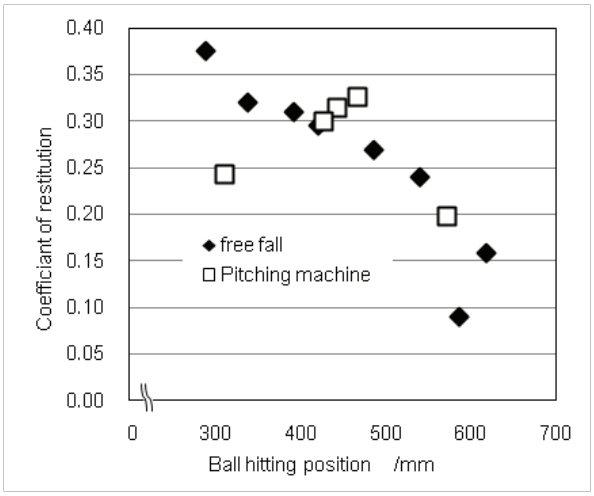

FIGURE 10. Measurement of a coefficient of restitution

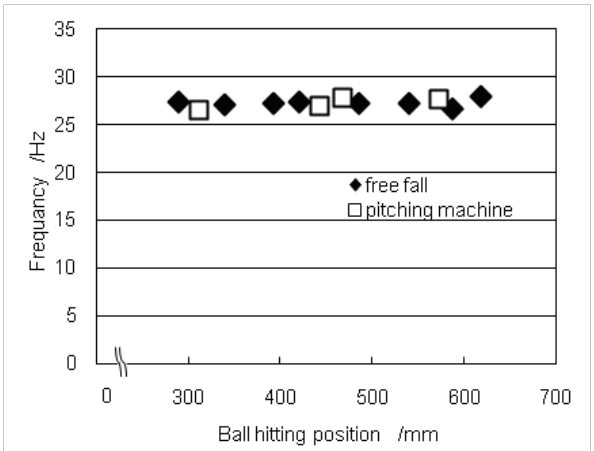

FIGURE 11. Measurement of frequency of metal bat

CONCLUSIONS

In order to measure the impact load concerning a batter's fingers, the experimental device which can measure the impact load of a speed of 40m/s (150km/h) ball was designed and manufactured. The following knowledge was acquired, as a result of also using a high speed camera and measuring a collision phenomenon.

1) Impact load increases as the collision position of a ball goes at a sweet spot. The increase in impact load is small as it goes to top from a sweet spot.
2) In the case of the pitching machine, the coefficient of restitution is large toward a root to the sweet spot. And at the tip of the bat, it is small.
3) The characteristic frequency of the bat is 27.2Hz.

REFERENCES

[1] Tanaka K., Masuda T., Kodama H., High-Speed Impact of Baseball Bats and Balls (1st Report, Impact of Aluminum Alloy Bats and Balls) , J. Soc. Mech. Eng.,58-556, (1992), pp2365-2369.

[2] Tanaka K., Masuda T., Kodama H., High-Speed Impact of Baseball Bats and Balls (2nd Report, Impact of CFRP Cylinders and Balls) , J. Soc. Mech. Eng.,58-556, (1992), pp2370-2374.

[3] Miyazawa T., Shimura M, et al., Batting impact simulation of baseball, J. Soc. Mech. Eng., 77-777, (2011), 135-144.

Design of Stamping Module to Pattern Alignment Marks for LED Post-Process

Young W. Sohn [1], YongHo Jeon [2], Hee K. Cho [3] and Moon Gu Lee [2]
[1]Manufacturing Center
3D Plus Co.
Yongin, Gyeonggi, R. O. Korea
[2]Department of Mechanical Engineering
Ajou University
Suwon, Gyeonggi, R. O. Korea
[3]Department of Mechanical Engineering Education
Andong National University
Andong, Gyeongbuk, R. O. Korea

INSTRUCTIONS

The productivity of the process for light emitting devices (LEDs) is essential to reduce manufacturing cost for flat panel displays (FPDs) because the LEDs are widely applied to the displays as light sources of FPDs' back lightening. [1] The substrate of LED is so expensive sapphire that it should be effectively used to produce LEDs. [2]

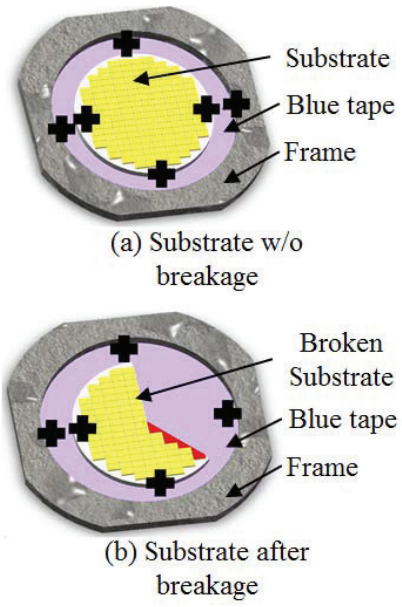

FIGURE 1. Concept of additional alignment-marking on blue tape for productive post-processing: The original '+' and the additional marks are on the substrate and blue table in (a). After partial loss of the original marks, the additional marks on blue tape can be used to the following post-process (b). The marks are exaggerated to show up.

However, the chipmakers have not been able to post-process partially broken substrates because, in part, the breakage results in the loss of alignment marks on the substrates. [3] After the substrate is pre-processed such as lithography, development, and washing, the substrate having LED dies are glued on blue tape, therefore, the dies on remaining area of the substrate after breakage could have the following post-process if additional alignment marks were patterned on the tape. These concepts are presented in Fig. 1.

In this paper, we have focused on two performances. First, we need to know about the positioning repeatability of the module. It is important ability in the precision process module. Second, the durability of the stamping head during over the hundredth stamping process is investigated.

STAMPING MODULE TO PATTERN MARKS

In this work, we proposed and developed a stamping head module that patterns alignment marks on blue tape to maximize usage of the expensive substrate. This can make lower the chip-cost during the post-process such as handling, sorting and dicing

The material for the stamp was stainless mold steel with good hardness, high toughness and sufficient wear resistance. A series of mechanical machining (turning, milling, electro-discharging, heat treatment and grinding) is used to be fabricated the stamp because it is cheaper compared to other alternative process such as electroplating, lithography or etc. On the stamp, the shape of "+" is engraved in relief. It is with the width of 1.5 mm and protrusion of 1.0 mm as shown in Fig. 2.

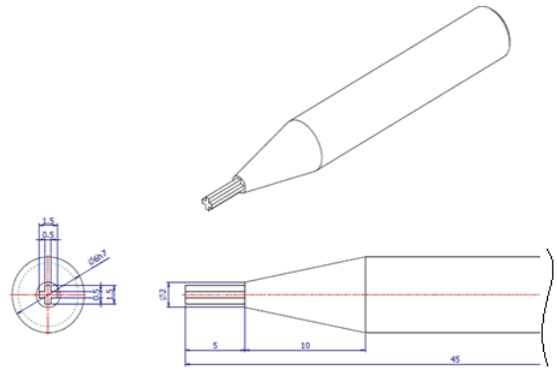

FIGURE 2. Stamp for patterning alignment marks on blue tape: The '+' relief is with the width of 1.5 mm and height of 1.0 mm. It has also a shank to be mounted on stamping module. The stamp is made of stainless steel, SUS430 in JIS. Turning, milling, electro-discharging, heat treatment and grinding are used to fabricate it.

EXPERIMENTAL SETUP

The stamps mounted on the stamping module, as shown in Fig. 3.

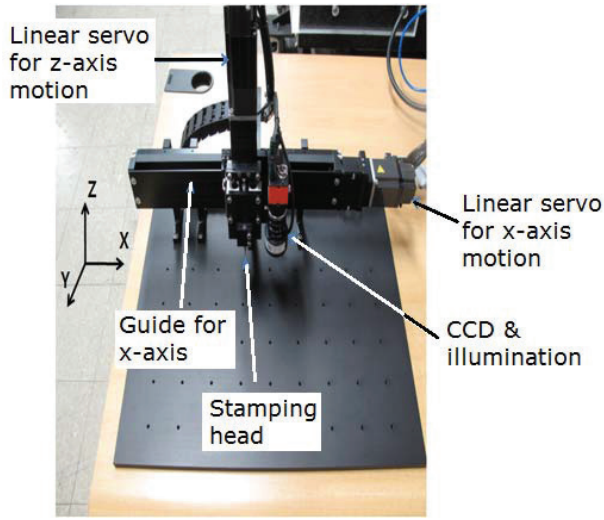

FIGURE 3. Stamping module for patterning alignment marks on blue tape: The stamp is mounted on a positioning linear servo for z- and x- motion. The patterned marks are monitored using CCD and illumination.

For transporting stamping head along x-axis, the module has a servo motor (HF-KP13, Mitsubishi) and single axis linear motion (LM) guide (LX3010C-B1-A3040-350, Misumi). It includes also another servo motor (HF-KPO53B, Mitsubishi) and LM guide (LX2005C-B1-A2040-100, Misumi) for stamping motion along z-axis.

To monitor the stamping, a CCD camera(MV-CV30U, Sony) with an illumination (LED 36ea, ATS Global) are mounted side by the stamp.
The stamping head with the stamp, CCD camera and illumination is to be positioned on the blue tape using the x-axis linear servo. Stamping on the tape is carried out using the z-axis linear servo. All the stamping process is monitored with the CCD camera. The positioning and monitoring is controlled via a PC with controller, image grabber and interface.
The stamp is dipped in a specific ink and then it patterns the marks. The ink was selected taking into account of hydrophobic or hydrophilic properties among ink, blue tape and stamp materials. The combination of the ink, stamp and tape can give fine patterns on the tape without defects.

RESULTS AND DISCUSSION

We measured the positioning repeatability of the module before the stamping experiment. The repeatability is 0.50 μm as shown in Fig. 4. The positioning performance is measured by LDV (Lase Doppler Vibrometer).

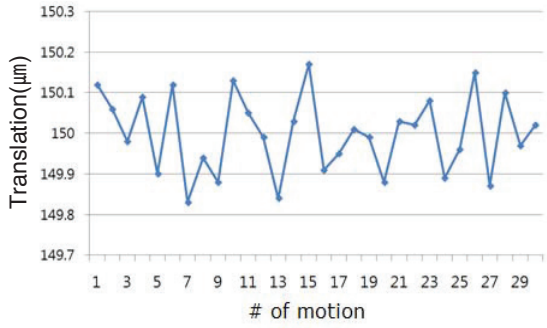

FIGURE 4. Positioning performance of stamping module, measured by Laser Doppler Vibrometer

The stamping head patterns the marks with speed is 0.5 cycle/s. The precision and stamping speed can satisfy the requirements from industry. To asses wear resistance of stamp, the stamp surface was investigated by using an electron microscope after 300 times stamping. The results show there were no significant wear as presented in Fig. 5.

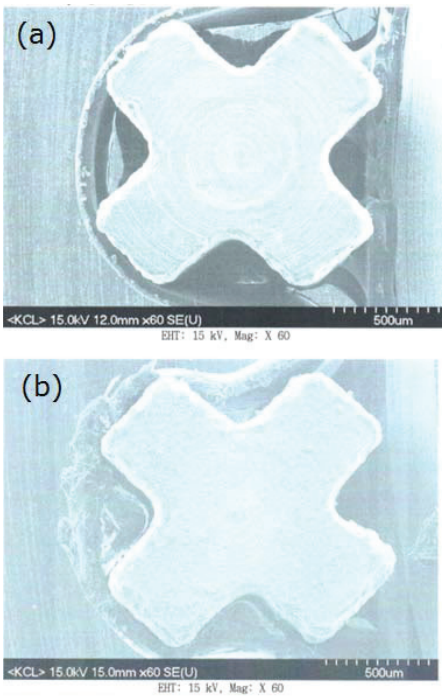

FIGURE 5. Wear resistance of stamping head: Electron microscope image of stamp before stamping, (a) and after 300 times stamping, (b).

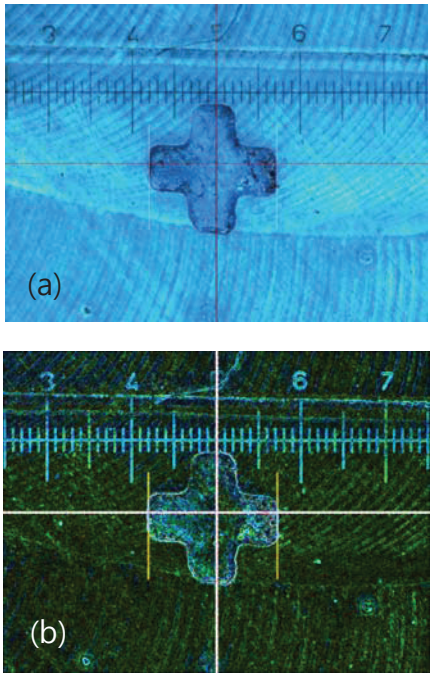

FIGURE 6. One of the stamping mark: Captured after stamping on the blue tape, (a) and post-process to get a center point of the mark, (b)

In order to investigate precision of stamping, a series of experiment repeated 30 times on the blue tape. Every single mark was saved an image file to get a center point of the mark. Then the image files are edited in post-process using image program as shown in Fig 6.

The statistics of the experiments are shown in Fig 7 with the distance of the distribution and the frequency of the stamping position. The mean of stamping position is 453.9 μm and the standard deviation is ±5.23 μm. It is agreed with Gaussian normal distribution except one sample. The requirement of repeatability for the x-axis linear actuator is ±5 μm from industry. When the stamping head is being mark on the blue tape, the z-axis linear actuator has a tiny and parasitic x-axis motion. If we use more advanced control algorithm or an elaborate LM guide, the repeatability of the stamping module could be better than now.

CONCLUSION

We have proposed a stamping module to apply post-process of LED and also demonstrated a precision positioning of the module.

a) The stamp head was made by SUS430 in JIS. It has good hardness and could endure 300 times of stamping experiment and make the pattern as well.

b) The repeatability of the motion of module in measurement is 0.5 μm. It measured by LDV. It has a fine repeatability but the actual stamping mark was different result.

c) The standard distribution of the stamping position in the actual test is ±5.23 μm and one error sample was existed.

This secures it has good wear resistance. Using the module, the pattern could be imaged clearly. When the system is applied to post-process of LED, it is predicted to improve substrate usage up to 30% or reduce cost up to 30%. This can make lower the manufacturing cost and give cheaper LED.

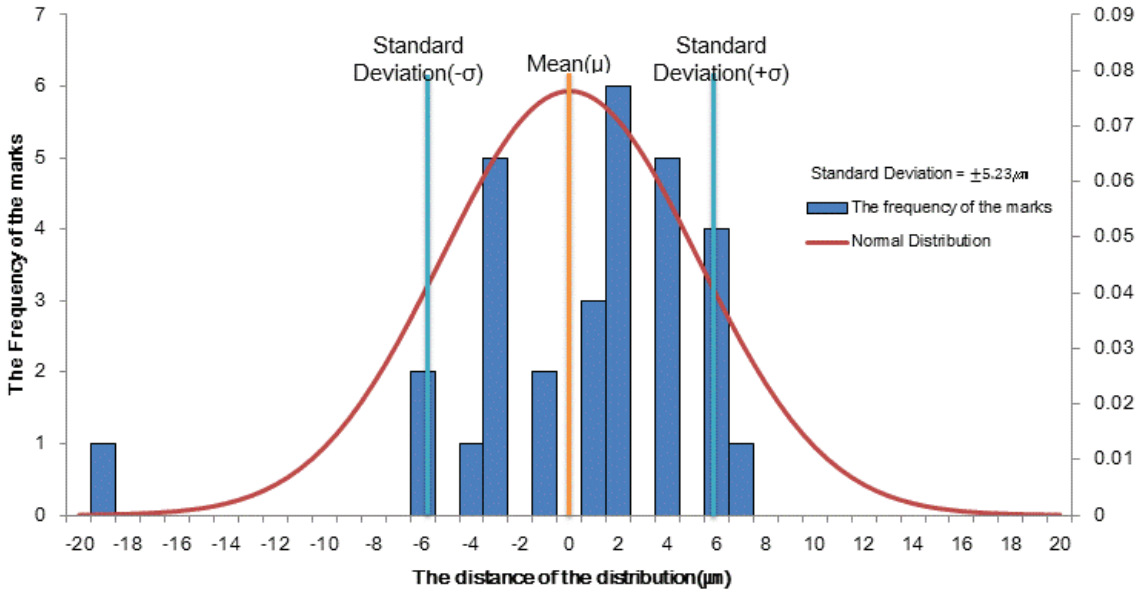

FIGURE 7. Stamping performance of the module and its normal distribution. Average is 453.92 ㎛ standard deviation is ±5.23 ㎛.

ACKNOWLEDGEMENT

This research has been conducted by supporting of "Development project of high energy beam based ultraprecision hybrid machining system" conducted by the Ministry of Knowledge Economy(MKE) of Korea (No.10033350).

REFERENCES

[1] Yamanaka T, Uchida D, Kato N. Display Technology for Passenger Information Display System. Toshiba Review. 2006; 61(9): 42-45.

[2] Wang T, Liu YH, Lee YB, Ao JP, Bai J, Sakai S. 1 mW AlInGaN-based ultraviolet light-emitting diode with an emission wavelength of 348 nm grown on sapphire substrate. Applied Physics Letters. 2002; 81(14): 2508 – 2510.

[3] Lin HT, Shiau GY, Wang PT. Alignment Pattern and Algorithm for Photolithographic Alignment Marks on Semiconductor Substrates. US Patent 5,982,044. 1999.

SYSTEM LEVEL OPTIMIZATION OF A CYLINDRICAL FLEXURE FOR LINEAR MOTION GUIDANCE

Maria Telleria and Martin L. Culpepper
[1]**Department of Mechanical Engineering**
Massachusetts Institute of Technology
Cambridge, MA, 02139

ABSTRACT
Cylindrical Flexures (CFs) may be used to create monolithic, axi-symmetric systems with a smaller volume than their straight-beam counterparts. The kinematic behavior of compliant curved-beam elements differs significantly from that of straight-beams. As a result, current straight-beam element and system models are insufficient for the effective design of CFs. We have previously presented models and guidelines for the element level optimization of curved-beam systems [1]. This paper builds on that work to create system level models and design rules for CFs. The analysis presented is used in the design of a CF linear guide case study. The system and element optimizations led to a 10x improvement in the performance of the linear guide relative to the initial CF concept which was designed using straight-beam models and guidelines [2].

INTRODUCTION

Linear Guide Attributes

The CF linear guides presented were developed for an optical system used in Fourier Transform Spectrometry (FTS). The designs utilize compound four-bars to guide the motion of the stage [2]. The original CF design shown in Figure 1a was conceived as the cylindrical version of two double compound four-bars [3]. This paper utilizes the element and system level models developed by the authors to redesign the CF linear guide to improve its performance [4]. The optimized system is shown in Figure 1b. The two functional requirements of concern were the range of the system, Δz, and its out-of-plane parasitic rotations, α_{tip} & α_{tilt}, as defined in Figure 1b.

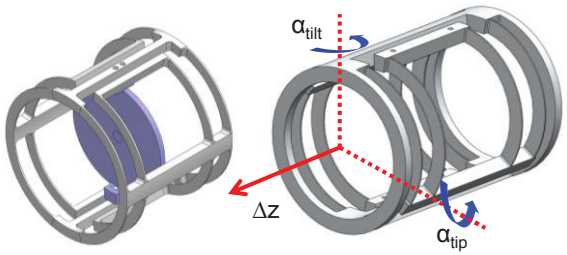

FIGURE 1. A) Original CF linear guide. B) Optimized CF linear guide. Δz is the desired displacement and α_{tip} & α_{tilt} the parasitic rotations.

Compound Four-bar

A straight-beam compound four-bar, shown in Figure 2a, is an example of a parallel and a serial flexure system. The mechanism utilizes two nested four-bar flexure systems to increase the range of the system and mitigate the parasitic displacement, Δy_1, of the input stage [3]. The nesting of the four-bars also reduces the parasitic rotation, α_x, of the input stage. In the curved compound four-bar system, shown in Figure 2b, the floating and input stages are located on different planes due to the curvature of the beams. As a result of the location of the stages, the parasitic displacements, Δr_1 and $\Delta\theta_1$, of the input stage are not directly cancelled by the Δr_2 and $\Delta\theta_2$ of the floating stage.

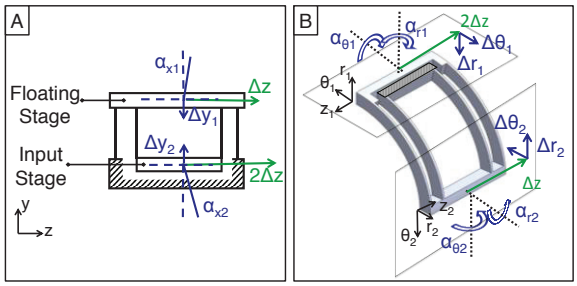

FIGURE 2. A) Straight-beam compound four-bar motions. B) Curved compound four-bar motions.

SYSTEM ANALYSIS

The goal of the CF linear guide optimization was to minimize the mirror's tip & tilt to translation ratio. This optimization requires a model of how the different system and element parameters affect the system parasitics and its range. The analysis was conducted on the curved four-bar which served as the building block for the final compound four-bar design.

Four-bar Parasitic Rotations

In planar compliant mechanisms a four-bar is commonly used to attain an approximate rectilinear motion by using the stage to guide the tips of the flexural elements [3]. Similarly, in the case of the CF four-bar, the stage is used to constrain the two flexure blade's parasitic rotations, $\alpha_{r\text{-}element}$ and $\alpha_{\theta\text{-}element}$. To establish the system parasitic rotations we analyze the effect of these constraints using a force and moment diagram shown in Figure 3. The fixed-guided boundary condition is achieved by applying the necessary M_r and M_θ moments on the flexure blade. Equations (1) and (2) give the moments applied on each element as a function of the element's compliance matrix entries, C_{ij} [4].

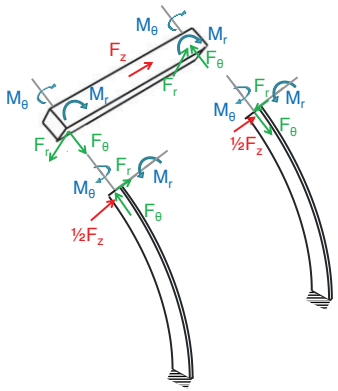

FIGURE 3. Curved four-bar force and moment diagram.

$$M_\theta = F_z \cdot \left(\frac{C_{35} - {C_{34} C_{55}}/{C_{45}}}{{C_{55} C_{44}}/{C_{45}} - C_{45}} \right) \quad (1)$$

$$M_r = -\left(\frac{C_{34}}{C_{45}} F_z \right) \cdot \left(\frac{C_{44}}{C_{45}} M_\theta \right) \quad (2)$$

The stage experiences equal and opposite moments which are balanced by forces on the flexures, F_θ and F_r respectively. The forces lead to displacements along the direction of the force; the displacements are dictated by the element's compliance. The result is two parasitic stage rotations α_r and α_θ, described by Equations (3) and (4) where b is the spacing between the flexures [4]. Figure 4 compares the four-bar parasitic rotation model to the FEA calculated values; the discrepancy between the two values indicates that the model is not complete.

$$\alpha_\theta = -2C_{22} \cdot \frac{M_\theta}{0.5b^2} \quad (3)$$

$$\alpha_r = -2C_{11} \frac{M_r}{0.5b^2} \quad (4)$$

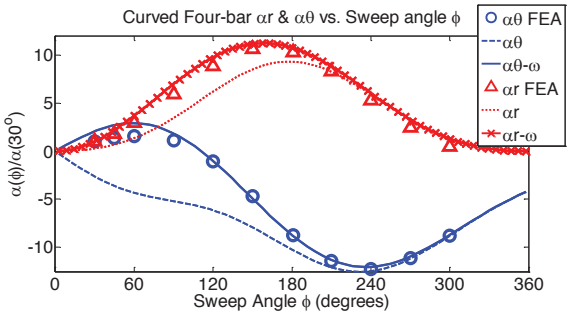

FIGURE 4. Curved four-bar parasitics vs. sweep angle, ϕ. The rotations are normalized using the FEA values for ϕ=30°.

In the previous analysis of the four-bar parasitic rotations it was assumed that the axis of rotation of the stage is dictated by the flexure tip's axes. However, FEA analysis revealed that both the stage length, L_{stage}, and the flexure length, L, to radial thickness, t_r, ratio of the flexures rotate the stage's r-axis away from the axis dictated by the flexure, as shown in Figure 5. The angle between the element's r-axis and the system's is given by ω. A parametric study was conducted to establish the model for ω given in Equation (5) [4]. Figure 4 compares the ω-corrected α_r and α_θ models to the initial model and the FEA results.

$$\omega = \left[.03(L_{stage} - .0019)^{-0.2} \tanh\left(\frac{{L}/{t_r}}{1.7 L_{stage}^{-0.3}} \right) - \frac{(L_{stage} - .0018)^{-0.36}}{120.5} \right] \phi \quad (5)$$

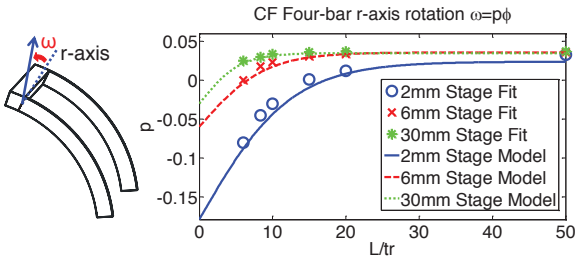

FIGURE 5. The curvature of the beam leads to a difference in length between the inner and outer radiuses. The result is that the r-axis of the four-bar tip is rotated away from its neutral position. The rotation angle is given by ω. Plot shows the ω adjustment vs. L/t_r for three different stage lengths. The chart gives the fitted values for p and the model values. ω is given by pϕ.

Four-bar Range

The parasitic model allows us to optimize the design to minimize the tip and tilt of the mirror. Next an accurate model of the four-bar's stress is required to establish the system's range. The curved-beam element stress model was used as the basis of the four-bar stress model [1]. This CF stress model accounts for the effect of warping due to the torsional moment on the flexures [4]. In the CF four-bar the tips of the flexure elements are constrained by the stage which applies a M_r and M_θ on each flexure tip. The four-bar range model utilizes the presented element stress model, which accounts for the effect of F_z, and superimposes the effect of the two applied moments. These moments are those required to constrain the α_r and α_θ rotations of the element.

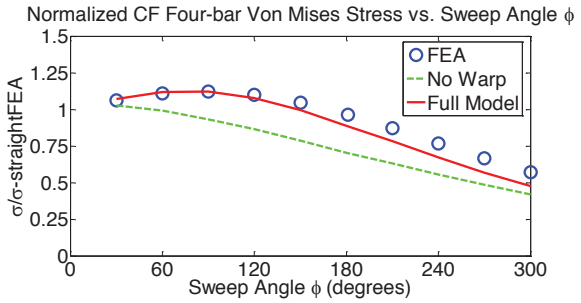

FIGURE 6. Curved four-bar Von Mises stress vs. ϕ. Stress is normalized using the stress of a straight four-bar of the same dimensions under the same load. Plot shows the FEA calculated values, the stress given by a no-warp model and the values given by the full model which includes the warping correction.

Figure 6 shows the effect of sweep angle, ϕ, on the maximum Von Mises stress of a CF four-bar. The plot compares the FEA calculated values to the complete CF four-bar stress model; the plot also shows the values calculated using a stress model that does not account for warping. The complete stress model allows the designer to accurately calculate the elastic range of the system.

CF LINEAR GUIDE OPTIMIZATION

Compound four-bar design

The presented analytical models enable the effective design of a CF system by allowing the designer to quickly analyze the effect of different parameters without having to rely of FEA. The four-bar stress and displacement models developed in this work were used to find the minimum ϕ required to meet the desired FTS range (5mm per four-bar) given the volume, material, z-axis element thickness, t_z, and t_r constraints. The FTS functional requirements limited one of the system dimensions to 70mm [2]. In Equations (3) and (4) it was established that the four-bar's parasitics decrease with the square of the flexure spacing. In order to benefit from the maximum flexure spacing the longest dimension (120mm) was chosen as the constraint for the length of the cylinder. As a result the limit for the diameter of the CF was set at 70mm.

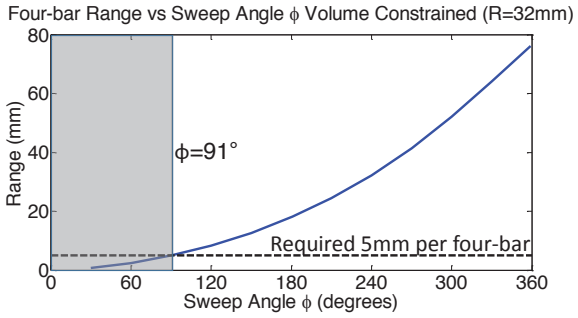

FIGURE 7. Range vs. sweep angle, ϕ, for a 6061-Aluminum four-bar with R=32mm, t_r=6.35mm, and t_z=0.5mm. The minimum range required for the FTS system is 5mm per four-bar, which is achieved for ϕ>91°. An R of 31.75mm corresponds to an outer diameter of 69.85mm.

The range of a four-bar with R=32mm vs. ϕ is presented in Figure 7. The plot shows that for ϕ>91° the four-bars are able to achieve the minimum 5mm range. A safety factor of 1.55

was applied to the range requirement to ensure that the CF system will not fail due to fabrication tolerances. The safety factor brings the minimum ϕ to 115°.

Once the minimum sweep angle required to meet the volume and range constraints was established, the next step was to analyze the design parameters effect on the CF's parasitic tip and tilt rotations. Figure 8 shows how ϕ affects α_r and α_θ of a 6061-Al compound four-bar with the chosen t_r and t_z. In the plot the sweep angles below ϕ=91° have been shaded because these do not meet the minimum range requirement. The model predicts that the parasitic rotations increase with ϕ and therefore a sweep angle as small as possible should be chosen for the design. Considering that with the chosen safety factor the element's ϕ must be at least 115°, Figure 8 shows that a single compound four-bar will not meet the required parasitic ratios. However, by guiding the optic with two compound four-bars spaced 180° apart, the system's parasitic α_{tip} and α_{tilt} are reduced because each subsystem applies equal and opposite moments on the optic. The challenge of joining the two subsystems to create a single cylinder was solved by using two connecting rings to link the two input stages as shown in Figure 9b. The design allows for the floating stages to translate and rotate freely.

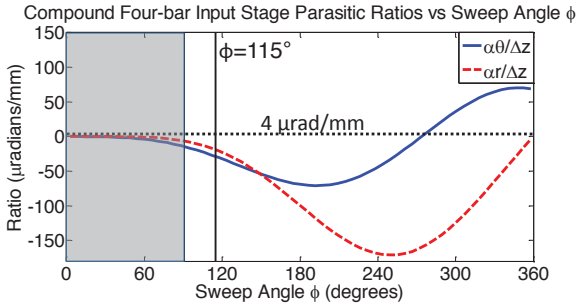

FIGURE 8. Input stage parasitic rotation ratios vs. sweep angle, ϕ, for a 6061 Aluminum compound four-bar with R=32mm, t_r=6.35mm, and t_z=0.5mm. Angles below 91° are shaded because they do not meet the minimum 5mm range constraint. The dotted black line indicates the FTS 5e-4 rad/m parasitic ratio requirement.

FABRICATION AND TESTING

The two CF linear guide prototypes, shown in Figure 9, were fabricated using a Mazak Turning center. The performance of the CF systems was measured using three optical linear encoders with 10nm resolution. Figure 10 shows the setup used to measure the tip & tilt angles of the stage during actuation. The flexures were actuated using a depth micrometer. Figure 11 shows the tip and tilt of the two prototypes vs. Δz displacement.

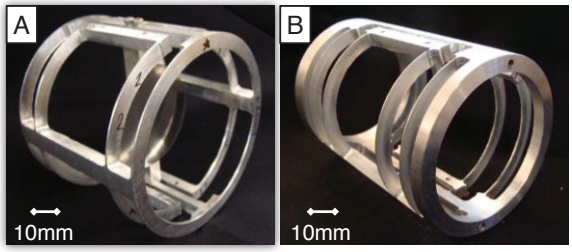

FIGURE 9. Images of the two linear guide prototypes. The original four compound four-bar design is shown in (A) and the optimized design is shown in (B).

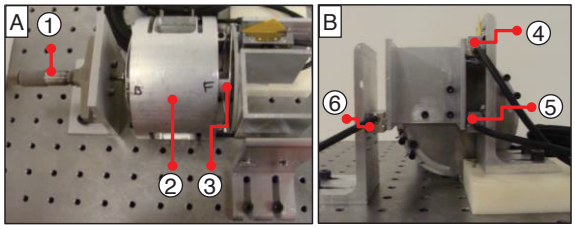

FIGURE 10. Measurement setup: The CF (3) is attached to a grounding cylinder (2) which is then attached to the optical table. The flexure is actuated using a depth micrometer (1) which pushes on a stage attached to the two input stages of the CF. A cap with liner scales was attached to the flexure. The displacements of three points of the CF cap were measured using optical linear encoders: top (4), center (5), and side (6).

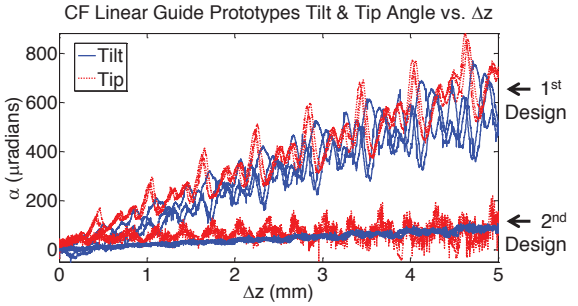

FIGURE 11. CF Linear guide prototypes measured tilt and tip angles vs. axial displacement, Δz.

Figure 11 shows that the optimized guide has approximately an order of magnitude lower stage tip and tilt. The measurements display a cyclic trend approximately every 0.6mm, this trend is caused by to the rotation of the micrometer tip. The cyclic error is not the dominant error for the first prototype; however, it became significant for the second prototype and was removed by actuating the flexure using hanging weights. The performance of the second prototype under the different weights is shown in Figure 12. The flexure was loaded using increments of 50g, which resulted in discreet data points for the tip/tilt error of the system. The plot shows that the tilt error is nearly within the required ±10μradians for the measured 5mm range. The tip error is higher but of the same order of magnitude.

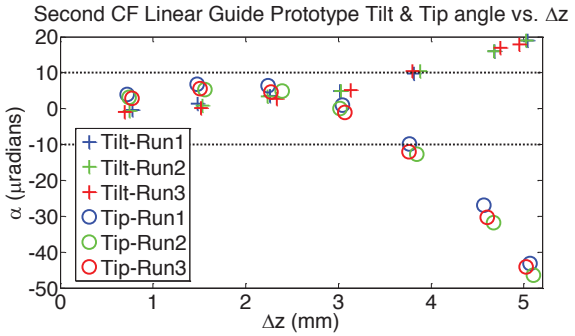

FIGURE 12. Tip and tilt measurements on the same plot.

Table 1 compares the measured performance of the second prototype to the FTS functional requirements as well as the FEA projections. The FEA of the CF predicts a lower tip/tilt error for the design, which suggests that there may be some external sources of error. A mistake was made when machining the prototype which resulted in certain flexures being thinner at their base as shown in Figure 13a. The travel limits of the machine also resulted in one connecting ring being larger than the other as highlighted in Figure 13b. These machining oversights resulted in the design no longer being symmetric. Another possible source of error is the location of the load; FEA shows a tip/tilt error of 9.5 μradians over the 5mm range when the load is applied 1mm off-center. Finally, the measurement setup is also asymmetric; the weight of the u-channel that holds the encoder scales applies a moment on the front of the flexure. This moment may explain why the tip error is larger than the tilt error. FEA predicts a 10 μradian tip angle for a 10 gram (0.1N) mass placed on one of the connecting rings. Table 2 summarizes the possible sources of error.

Table 1. Second CF linear guide performance.
+Error over 5mm range

	Required	Measured	FEA
Volume	12x10x7cm^3	10x7x7cm^3	10x7x7cm^3
Range	10-50 mm	20 mm	20 mm
Tip error	± 10 μrad	45 μrad$^+$	<2 μrad$^+$
Tilt error	± 10 μrad	19 μrad$^+$	<1 μrad$^+$

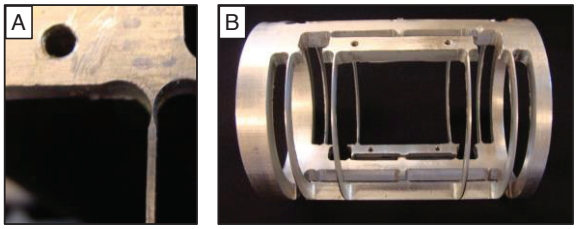

Figure 13: Machining errors: A) Tool lead-in error resulted in some of the flexure elements being thinner at their base. B) The back connecting ring is larger than the front because of the machine's travel limit.

Table 2. Possible sources of tip/tilt error.
+Error over 5mm range

Source	Notes
Machining error	Asymmetric design
Load misalignment	9.5 μrad$^+$ error per 1mm misalignment
Weight imbalance	10 μrad error per 0.1N imbalance

CONCLUSIONS

The guidelines and rules presented in this work were used to create a design with an order of magnitude lower tip/tilt error than the concept created using straight-beam rules and FEA. The CF linear guide performance may be further improved by reducing the sources of error or making the design less sensitive to these errors. The current design should be able to meet the FTS requirements according to FEA if the machining oversights are eliminated, the accuracy of the load location is improved, and the measurement setup is made symmetric such that there is no weight imbalance. Furthermore, the design of the original prototype required months of work because FEA was necessary to establish the range of the system and the effect of different parameters. The analytical models presented made it possible for the linear guide to be designed in a matter of weeks, allowing us to optimize the design without FEA.

REFERENCES

[1] Telleria M, Culpepper M. Element level optimization of a CF for linear motion guidance, 2012 ASPE Annual Conference.

[2] Telleria M, Culpepper M. Design of a monolithic cylindrical flexure for precision motion guidance, 2010 ASPE Annual Conference.

[3] Smith S. Flexures: Elements of Elastic Mechanisms. USA: CRC Press; 2000.

[4] Telleria M. Design Rules and Models for the Synthesis and Optimization of Cylindrical Flexures. Ph.D. Thesis. Massachusetts Institute of Technology; 2013.

A FLEXURE-BASED HIGH-THROUGHPUT ROLL-TO-ROLL PRINTING SYSTEM

Xi Zhou[1], Jiyi Cheng[1], Ni Zhao[2], and Shih-Chi Chen[1*]
[1]Department of Mechanical and Automation Engineering
[2]Department of Electronic Engineering
The Chinese University of Hong Kong
Shatin, N.T., Hong Kong SAR, China
*Email:scchen@mae.cuhk.edu.hk

In this paper, we present the design of a fully automated flexure-based high-throughput, roll-to-roll (R2R) printing system with multiple degrees of freedom (DOF) misalignment correction capability for implementing several nanometer resolution contact printing techniques such as Microcontact Printing (MCP) and Nanoimprint. The completed system can be used to fabricate transparent metal grids as electrodes for organic photovoltaic cells and diffraction gratings with pitches of a few hundred nanometers.

ULTRA PRECISE R2R PRINTING

Although compatibility with R2R processes is the main driving force for many flexible electronics and organic photovoltaic devices (when compared with conventional inorganic semiconductor devices fabricated through lithographic processes), there is a common misperception that this high throughput, low-cost process produces devices of lower resolution and quality. This will not be true if we implement contact printing techniques such as Microcontact Printing [1, 2] or Nanoimprint to properly designed R2R platforms. In fact, the printing resolution can be better than lithographic processes as contact printing is not limited by diffraction. Complex high resolution patterns of tens of nanometers have been repeatedly demonstrated by the aforementioned techniques at laboratory scale [2]. However, it is not practical to directly scale up and apply these techniques to present state-of-the-art R2R systems, e.g. gravure printing and flexographic printing, which have approximately 15 micron print resolution.

To utilize a R2R process for precision printing, we must address the machine's repeatability and accuracy issues. A R2R machine must possess (1) nanometer repeatability, (2) submicron level position control, and (3) better than 0.1 N force control in order to create patterns with submicron resolution. However, current state-of-the-art R2R systems mostly use conventional bearings to guide the printing motion and lack the required repeatability and precision. Additionally, current systems lack alignment features to compensate the "yaw" and "roll" errors (rotational errors in θ_Y and θ_X respectively, shown in Figure 1). This leads to non-uniform distribution of pressure during the printing process and pattern distortions.

A few flexure-based R2R prototypes were developed recently with reasonable success [3 - 5], and some with closed-loop position controls [6, 7]. A complete flexure-based R2R platform that meets all required specifications and precision has yet to be developed.

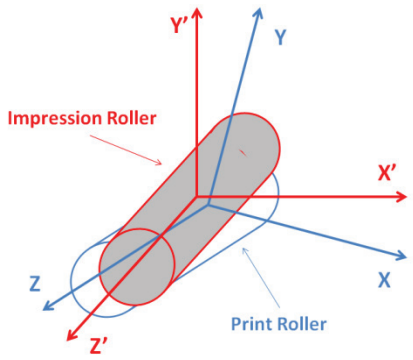

FIGURE 1. Illustration of misalignments between an impression roller and a print roller.

DESIGN CONCEPT

We have been developing a flexure-based R2R printing system for generating submicron resolution metal patterns. This is achieved through precise position control between the web and the print roller that the stamp is attached to. Figure 2 shows a conceptual flexural mechanism design, where two monolithic blocks of compliant mechanisms are

used to support the two ends of the print roller. This arrangement generates 4 degrees of freedom error correction capability, i.e. x, y, θ_X and θ_Y. Each flexure block provides decoupled motion guidance capability in two independent axes. The arrows in Figure 2 indicate the placement locations of four positioning actuators; the stepper motor can be connected to the shaft of the print roller with an elastomeric coupler.

Figure 3 presents simulated results of the monolithic flexure stage subjected to an input displacement of 2 mm in x direction and -2 mm in y direction. By comparing these results, one can conclude that the cross-axis coupling errors are minimized and will be eliminated when manufacturing tolerance is zero.

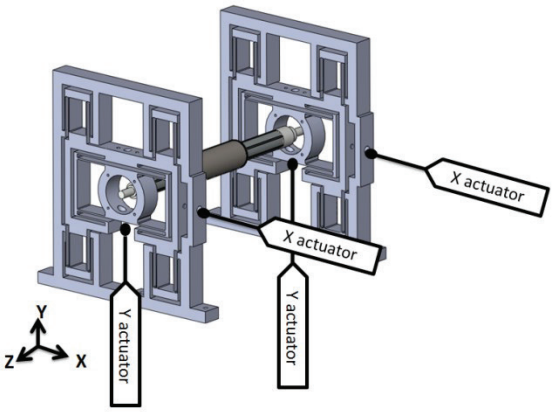

FIGURE 2. Conceptual design of the flexure-based roller positioner.

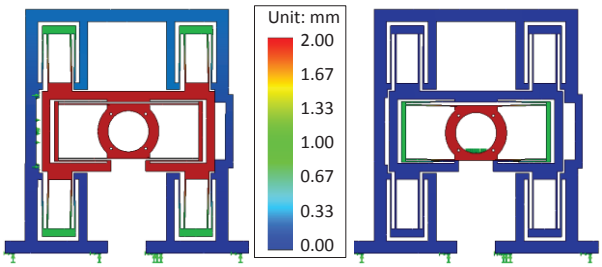

FIGURE 3. Simulated results of decoupled motion generated by the monolithic flexure stage. Motions in X (A) and Y (B) direction.

SYSTEM INTEGRATION

Figure 4 shows the core design of the R2R system (not including collection, intermediate guiding rollers). The two flexure stages are driven by H2W's voice coil actuators in the y direction and PI's stepper motor actuators, i.e. M230.10S, in the x direction respectively. Their positions are monitored by 2 pairs of capacitance probes and eddy current sensors. These sensors provide high bandwidth (15 kHz) real-time position feedback for implementing closed-loop control. In addition, two load cells of 0.05 N resolution (TS-25-PC, MAGPOWR.) are placed at two ends of the impression roller to provide real-time force feedback and control the parallelism between the impression and print rollers.

The lateral position of the web is controlled by a web-guiding module. The module consists of four rollers, and two of the upper rollers are affixed to a rotary stage controlled by a servo motor. The actual position of the web is detected by two infrared edge sensors. When the rollers in the upper frame are rotated, the unbalanced friction force causes the web to move in the lateral (z) direction. This arrangement ensures the web path can be corrected within a short distance with minimized stress in the web.

To ensure stable operation, air bearings are used to guide the motions of both the impression and print rollers. Two load cells are also installed by the print roller to monitor the printing force in real time. Closed-loop web tension control is achieved through the use of a magnetic particle break/clutch and tension sensor.

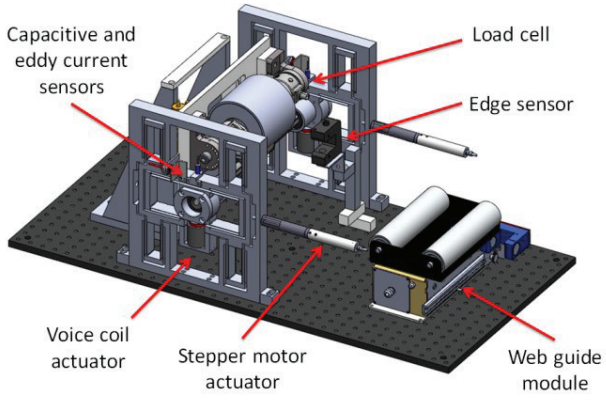

FIGURE 4. CAD model of the partial R2R system; sensors and actuators are implemented for error motion sensing and correction.

To adapt the MCP process for R2R operation, we replace the normal silicon/glass substrates with 4" wide metal coated PET rolls. In the printing process, the web tension, printing load, substrate-stamp wrap angle, and print roller position need to be precisely controlled. For stamp preparation, PDMS stamps are fabricated

by a standard spin-coating procedure, following which the stamp is treated with oxygen plasma and subsequently rolled and securely bonded onto a glass tube. The glass tube is then affixed to the motor-driven print roller through friction generated by the air-expanding unit on the print roller.

MODELING

We derived a parametric model, i.e. stiffness matrix, for the monolithic flexure stage based on beam theory. The monolithic flexure stage consists of multiple thin beams connected in parallel or in series to decouple the in-plane parasitic motions. For each thin beam, a local deformation matrix can be derived by using the force equilibrium condition, as shown in equation (1). In our analysis, *f*, *p*, *m* are exerted loads and *y*, *x*, *θ* are related deflections [8]. By assembling the local matrices, the deformation matrix of the monolithic flexure stage can be expressed as equations (2), (3) and (4).

$$y'' = m + f(1 + \delta_x - x) - p(\delta_y - y) \quad (1)$$

Deformation matrix:

$$y = \frac{2af}{(2a)^2 - (pe)^2} \quad (2)$$

$$x = \frac{p}{2}\left\{\frac{1}{d} + y^2 \frac{r[(2a)^2 + (pe)^2] - 8aei}{(4a)^2}\right\} \quad (3)$$

$$\theta = \left[f_{n1}(p),\ f_{n2}(p),\ f_{n3}(p),\ f_{n4}(p)\right]\begin{pmatrix} f \\ m \\ f^3 \\ f^2 m \end{pmatrix} \quad (4)$$

Kinematic and dynamic models of the system were developed to predict force-displacement and force-acceleration relationships of the stage when a load is applied, as illustrated in Figure 5. The kinematic model is described as equations (5) and (6), and the dynamic model, expressed in state space format, is described as equations (7) and (8). In the model, k_i and c_i are the stiffness and damping coefficients of each monolithic flexure stage (*i* = 1, 2), *m* is the equivalent mass of the shaft and air bushings, and *I* is the inertia of the print roller, air bushings, and all other moving parts of the flexure stage. The model's accuracy was approved by a step response experiment (step size: 116 μm), as shown in Figure 6, where measured displacements were converted to acceleration and plotted to compare with the dynamic model.

$$\begin{bmatrix} y \\ \theta \end{bmatrix} = \begin{bmatrix} 1/2 & 1/2 \\ 1/l & -1/l \end{bmatrix}\begin{bmatrix} y_1 \\ y_2 \end{bmatrix} \quad (5)$$

$$\begin{bmatrix} f \\ \tau \end{bmatrix} = \begin{bmatrix} 1 & 1 \\ l/2 & -l/2 \end{bmatrix}\begin{bmatrix} f_1 \\ f_2 \end{bmatrix} \quad (6)$$

$$\dot{x} = Ax + \begin{bmatrix} 0 & 0 \\ 1/m & 0 \\ 0 & 0 \\ 0 & 1/I \end{bmatrix} u \quad (7)$$

where the coefficient matrix

$$A = \begin{bmatrix} 0 & 1 & 0 & 0 \\ -\frac{k_1 + k_2}{m} & -\frac{c_1 + c_2}{m} & -\frac{l(k_1 - k_2)}{2m} & -\frac{l(c_1 - c_2)}{2m} \\ 0 & 0 & 0 & 1 \\ -\frac{l(k_1 - k_2)}{2I} & -\frac{l(c_1 - c_2)}{2I} & -\frac{l^2(k_1 + k_1)}{4I} & -\frac{l^2(c_1 + c_2)}{4I} \end{bmatrix}$$

$$\mathrm{y} = \begin{bmatrix} 1 & 0 & 0 & 0 \\ 0 & 0 & 1 & 0 \end{bmatrix} x + 0 \cdot u \quad (8)$$

where the state vector, input vector, and output vector are:

$$\mathrm{x} = [y \quad \dot{y} \quad \theta \quad \dot{\theta}]^\top$$

$$\mathrm{u} = [\mathrm{f} \quad \tau]^\top$$

$$\mathrm{y} = [y \quad \theta]^\top$$

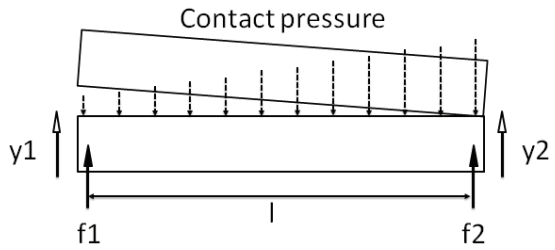

FIGURE 5. Non-uniform contact pressure generated by two misaligned rollers; y1, y2, f1 and f2 are variables used in the model.

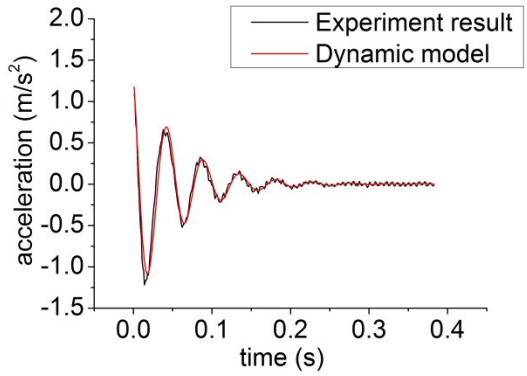

FIGURE 6. Step response: Comparison between the dynamic model and experimental results.

ASSEMBLY AND CHARACTERIZATION

The R2R system consists of four sub-modules: Unwinding module, printing module, web guide module, and rewinding module. A picture of the R2R system is shown in Figure 7.

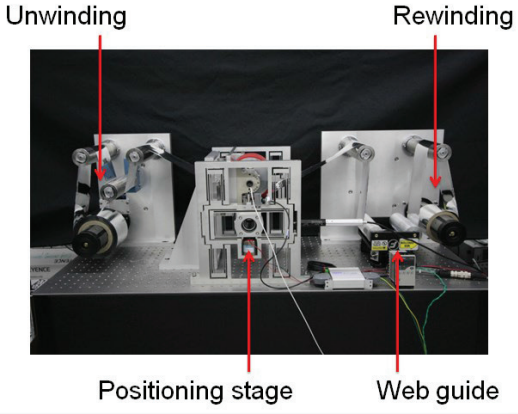

FIGURE 7. Prototype of the multiple DOF flexure-based R2R printing system.

A force-displacement experiment was conducted to validate the stiffness and repeatability of the positioning stage after assembly. The results were compared with the mathematic model. As shown in Figure 8, the mathematic model derived in equation (2) matches the experimental results well with an error of 2.67%. The errors are mainly attributed to manufacturing tolerances of the flexure.

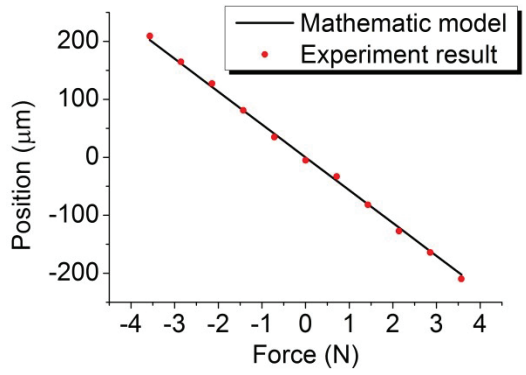

Figure 8. Force-displacement relationship of the flexure stage.

We conducted impulse response and step response experiments to obtain the natural frequency and damping ratio of the positioning stage. These parameters are needed to understand the dynamic behavior of the system as well as for closed-loop control. Figure 9 shows the frequency spectrum of the stage (FFT of the impulse response), where the natural frequency is 21 Hz. Figure 10 shows the step response of the flexure stage, where the damping ratio found through this experiment is 0.2.

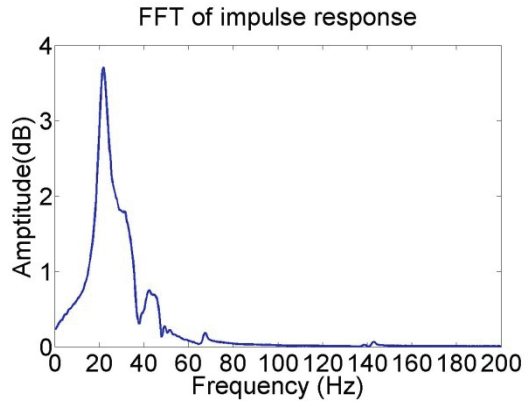

Figure 9. Frequency response of the flexure stage; data obtained through Fast Fourier Transform (FFT) of the impulse response.

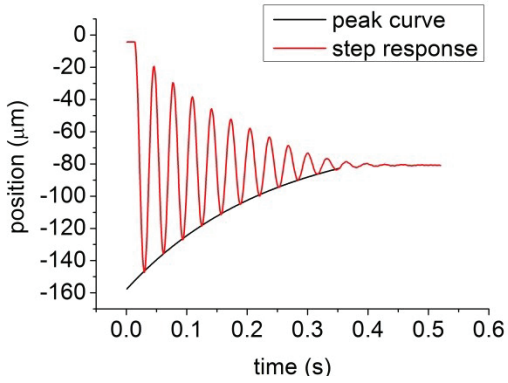

Figure 10. Step response of the flexure stage.

EXPERIMANTAL RESULTS

Three experiments were devised and performed to verify the decoupled position control and force control capability of the R2R system. Based on setups described in the System Integration Section, two PID controllers were developed in LabVIEW to control the position and contact force/pressure between the print roller and impression roller. Note that although the X-Y motion of individual flexure stage is decoupled, motions generated by the print roller positioning system (supported by two flexure stages) are still coupled through the print roller shaft and air bearings. Accordingly, motion decoupling here was achieved through fine-tuning the PID controller.

In the first experiment, the first flexure stage was commanded to move down and up in small steps for -70μm and +70μm respectively in the y direction, while the aim was to remain the position of second flexure stage through closed-loop control. Results are presented in Figure 11 where y motions of stage 2 can be controlled within ±0.5 μm.

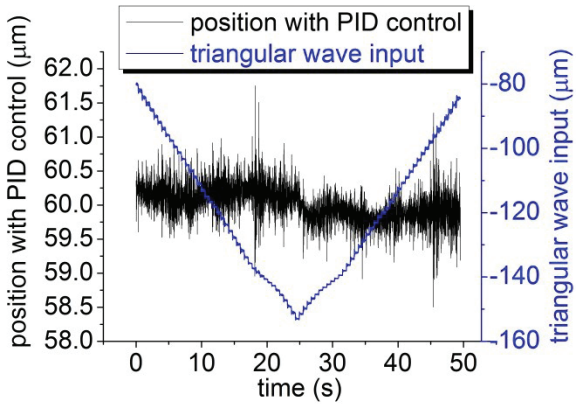

Figure 11. Closed-loop position control under triangular displacement disturbance.

In the second experiment, a disturbance force (±1.5N) was given to the first flexure stage, and the goal was to control the printing force on the second flexure stage to within 16 ±0.05N. The results are shown in Figure 12, where closed-loop (black) and open-loop (blue) data are both presented. From the results, we have verified our R2R system is capable of controlling the printing force within 0.1N, which is the critical contact force for printing submicron features [6, 9]. The first two experiments have validated the decoupled motion and force control between the two flexure stages.

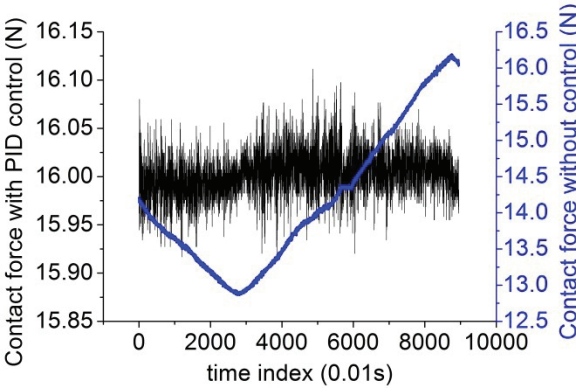

Figure 12. Closed-loop (black) and open-loop (blue) force data of the second flexure stage.

Considering the assembly error, manufacturing error, and eccentricity of both the print roller and impression roller, we'd like to confirm the closed-loop force control system can properly control the variations of printing forces within our target—0.1N. In the third experiment, we set the printing force to be 4.0 N and both closed-loop and open-loop force data were collected when the stepper motor drove the web forward. The results are shown in Figure 13. From the results, we found variations of printing forces can be as large as +3N without control; this force will very likely destroy all submicron features on any elastomer stamps (for MCP). On the other hand, the data also show the printing force can be controlled within 4 ±0.05N with closed-loop control. More experiments indicate slowing down the printing speed can further improve the force and position control accuracy.

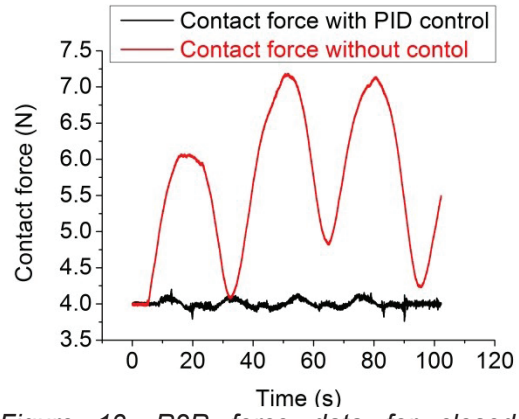

Figure 13. R2R force data for closed-loop (black) and open-loop (red) control at 1 ft/min.

CONCLUSION

We have developed a fully-automated flexure-guided high-throughput roll-to-roll (R2R) printing system. In this paper, we presented the design, modeling, assembly, and characterization of the system, including static and dynamic characteristics of the core flexural positioners. Our experiments indicated the R2R system can control the printing force within ±0.05N and system position within ±0.5μm which make it suitable for adapting precision contact printing techniques, e.g. Microcontact Printing, to this R2R platform for manufacturing submicron precision photonic devices, e.g. diffraction gratings and transparent metal grids, on flexible substrates.

ACKNOWLEDGEMENT

This work is supported by the HKSAR Innovation and Technology Commission (ITC) Innovation and Technology Fund (ITF), ITS/025/12: Precision Microcontact Printing for Roll-to-roll Fabrication of Flexible Electronics.

REFERENCES

[1] Xia Y and Whitesides GM. Soft Lithography. Annual Review of Materials Science. 1998; 28(0): 153-184.

[2] Qin D, Xia Y, and Whitesides GM. Soft Lithography for Micro- and Nanoscale Patterning. Nature Protocols. 2010; 5: 491 - 502.

[3] Krebs FC, Gevorgyan SA et al. A Roll-to-roll Process to Flexible Polymer Solar Cells: Model Studies, Manufacture and Operational Stability Studies. Journal of Materials Chemistry. 2009; 19(30): 5442-5451.

[4] Ahn SH and Guo LJ. Large-area Roll-to-roll and Roll-to-plate Nanoimprint Lithography: A Step Toward High-throughput Application of Continuous Nanoimprinting. ACS Nano 2009; 3(8): 2304-2310.

[5] Søndergaard R, Hösel M, et al. Roll-to-roll Fabrication of Polymer Solar Cells. Materials Today. 2012; 15(1): 36-49.

[6] Petrzelka JE, Contact Region Fidelity, Sensitivity, and Control in Roll-based Soft Lithography. MIT Thesis. 2012.

[7] Petrzelka JE and Hardt DE. Static Load-displacement Behavior of PDMS Microfeatures for Soft Lithography. J. Micromech. Microeng. 2012; 22 (7) 075015.

[8] Awtar S. Synthesis and Analysis of Parallel Kinematic XY Flexure Mechanisms. MIT Thesis. 2003.

[9] Johnson KL. Contact Mechanics. Cambridge University Press. New York: 1987.

PIEZO VS VOICE COIL MODULES IN THE HYBRID ACTUATOR FOR THE E-ELT TELESCOPE

Rainer Gloess, Kurt Zimmermann, Jeremias Reith, Thomas Haase, Christian Enkrich
Physik Instrumente (PI) GmbH &Co. KG, Karlsruhe, Germany

INTRODUCTION

The desire of mankind to explore the mysteries of the universe is unbroken. We want to search for extrasolar planets, extend our knowledge about the universe by looking at the oldest objects in space and seek to discover the remaining secrets of black holes and especially dark matter. For all of the above new telescopes with significantly higher resolution are required.
For ground based astronomy, improvements in optical resolution can only be reached by combining many individual mirror segments a larger one (GMT— 7 Mirrors with 8 meter diameter; TMT and E-ELT with primary mirrors of 30 m and 39 m, respectively consisting of 1.5 m segments). In order to control the overall shape of the segmented mirror, very precise actuators and sensors as well as a highly sophisticated control system are required.

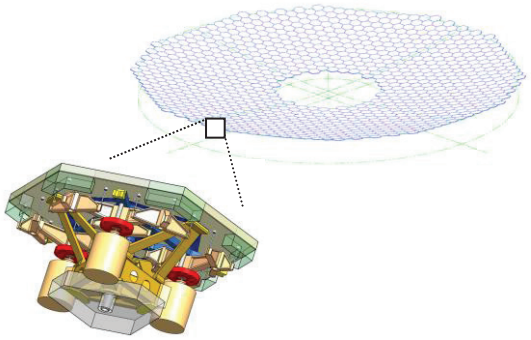

FIGURE 1. Single mirror segment with three actuators (ESO)

The paper describes two different prototype hybrid actuator designs at Physik Instrumente (PI) GmbH for the E-ELT telescope- a 39m diameter telescope, segmented in about 800 hexagonal mirrors. Two concepts are chosen, a very stiff actuator consisting of a roller-screw drive and piezo modules and a soft actuator with based on a roller-screw and a spring/voice coil module.
Both designs achieve similar resolution but with different passive stiffness properties. The soft actuator is better at decoupling vibrations originating from the telescope frame. For stable and hard coupling of the mirror to the frame structure the piezo-hybrid actuator is preferred.

Both actuators meet the same requirements: 15mm travel range and – at the same time – an extremely accurate positioning and tracking performance of better than 2nm RMS. The mass load and the different orientations between zero and 90 degree lead to a resulting force range of zero to 900N.

FIGURE 2. Hybrid actuator prototypes (3 for each mirror elements are necessary)

During observation of stars and extrasolar planets sub-nanometer tracking accuracy is required.

ACTUATOR CONCEPTS

The exact position of the mirror segments is influenced by two error sources: Wind load and distortions from the back structure, mainly caused by vibrations from the cooling system. Both the soft and stiff actuator concept is good at solving one problem, but sub-optimal for the other problem.
The long range motion is achieved by brushless motors with harmonic drive gearheads and a stiff roller screw. Shielded piezo actuator stacks overcome the roughness and stick-slip effects and also meet the high accuracy requirements.
The used PICMA® piezo actuators are encapsulated.

FIGURE 3. Encapsulated PICMA® piezo actuator

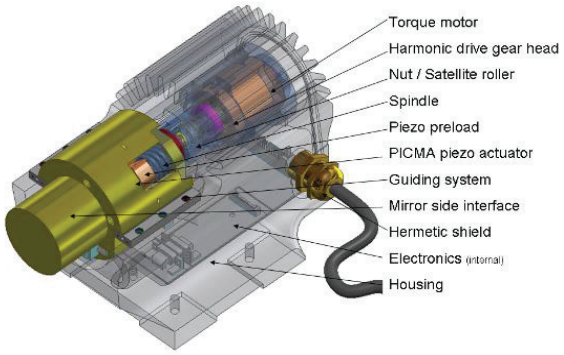

FIGURE 4. M1-Pact prototype actuator is hermetically sealed (piezo hybrid version)

The servo loop is closed via a common high resolution optical sensor. Its excellent amplitude and phase stability allows an interpolation factor of 2000 and results in a resolution of 0.125nm.

PIEZO VS. VOICE-COIL HYBRID DESIGN

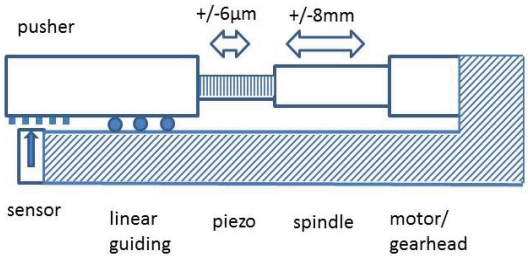

FIGURE 5. Hybrid roller-screw / piezo actuator design

For lifetime and low power dissipation requirements a brushless torque motor was used as well as for the large dynamics range up to 250µm/s. The motor drives a 0.5mm pitch roller screw through a 100:1 harmonic drive, chosen for its constant transmission ratio and - very important— backlash free operation.
Both actuators are self-locking even under high load conditions due to the friction in the screw-drive and the gearhead. Because of the high transmission ratio between the motor and the motion of the pusher the back-driving force on the motor is small enough to be neglected in the servo settings.

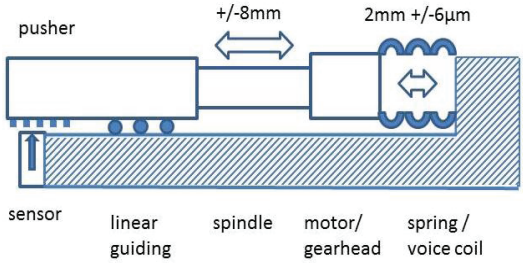

FIGURE 6. Hybrid roller screw / spring-voice-coil combination

Figure 4 shows the spring/voice coil system mounted directly at the end of the screw drive . The voice coil actuator is working parallel to the stiff spring. The challenge is to design a spring with the desired axial stiffness but also very stiff against rotation to prevent any unwanted parasitic motion.

CONTROL ALGORITHMS

The hardware consists of a small embedded PC-platform (QSeven module with Intel Atom 270 processor) and the “OnTime”. real-time operating system with an FPGA for real time and interface access. Within the FPGA hardware-clock-buffered sensor inputs and a synchronized output buffers are implemented.
The same hardware design is used for both actuators. In case of the voice coil fine actuator, the power supply and the current driver is changed.

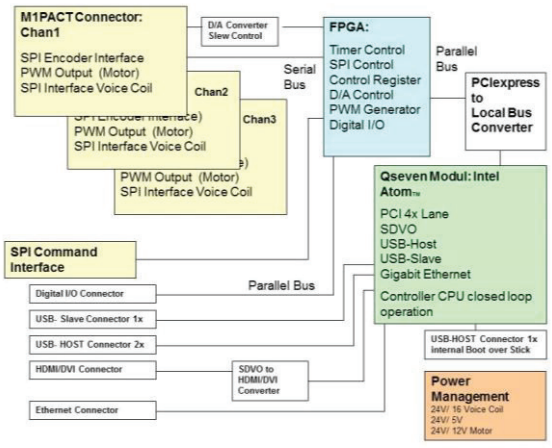

FIGURE 7. Structure of the 3-axes hybrid controller hardware

The servo motor is driven by a PWM signal and the piezo amplifier gets its input from a 24bit D/A converter resulting in a command resolution of less than 1pm (picometer).

The control scheme is based on via two parallel loop structures – one for the torque motor and one for the piezo module and the voice coil module, respectively. The control filter consists of PI, notch and low pass filters for the piezo part and PID, notch and low pass filters for the motor part. The control dynamics will be dominated by the short stroke actuator.
The basic control function of a piezo actuator is more simple than that of a servo motor, because of the constant transfer function up to the resonance peak.
The linearized transfer function of a piezo actuator can be approximated as follows:

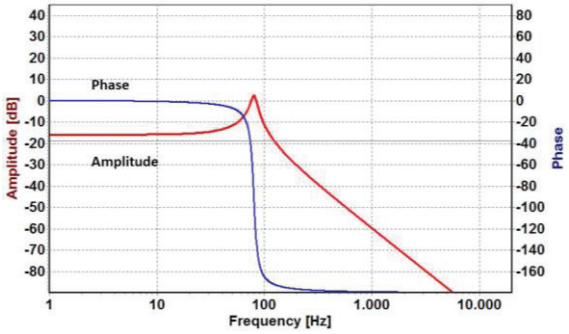

FIGURE 8. Linearized transfer function of the piezo actuator with mirror mass load

$$T_z(p) = \frac{K_p}{1 + 2D\frac{1}{\omega_0}p + \left(\frac{p}{\omega_0}\right)^2}$$

K_p	*gain*	*0.16 [µm/V]*
D	*damping coefficient*	*0.06*
ω_0	*resonant Frequency (with mirror mass)*	*80 [Hz]*

With the Nyquist (fig. 9) criterion it can be shown that a simple PI controller function may be stable but can not provide very high bandwidth. At least a notch filter should be added into the control path, to cancel the resonant frequency peak and improve the stability.

For the voice coil module the PI filter is replaced by a PID filter. No additional integral term is necessary because of the motor transfer function's integral property. The controller behavior was simulated with MATLAB.

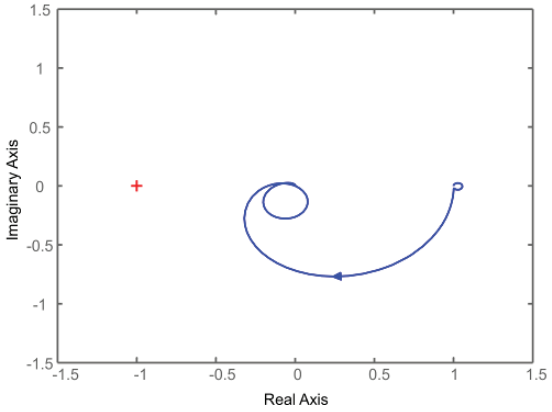

FIGURE 9. Nyquist plot to show the control stability

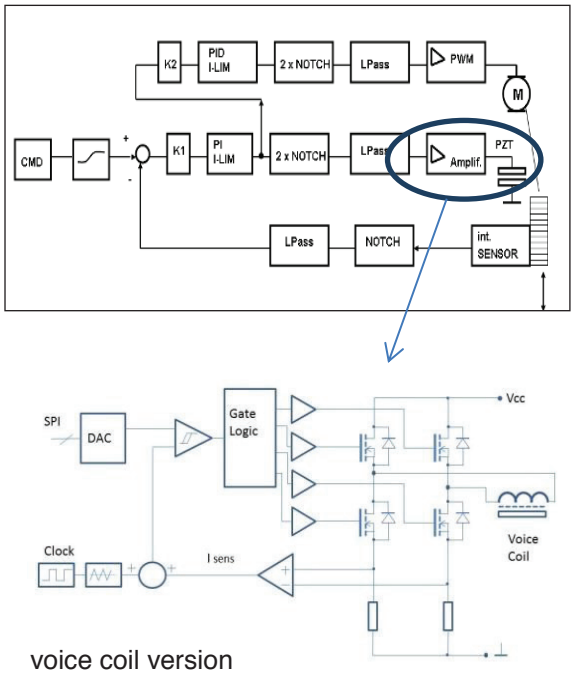

voice coil version

FIGURE 10. Single control loop structure of one hybrid actuator

SYSTEM TEST

During the first few milliseconds after start-up from zero velocity the system will stick for a while and the motion is determined by small vibration due to the roughness of the drive screw and bearings.

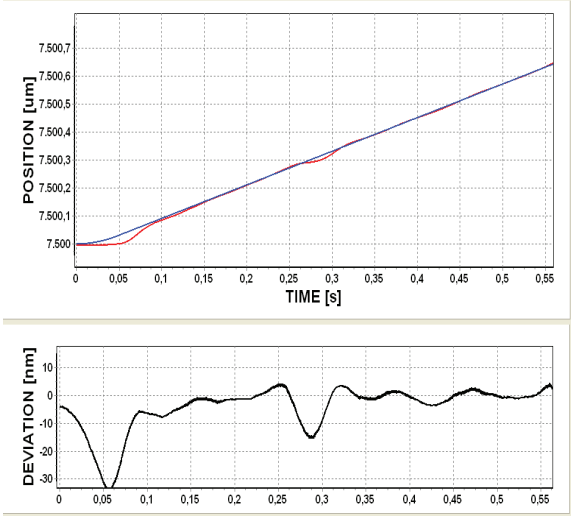

FIGURE 11. Typical system error between trajectory (target) and actual motion of a single motorized system. (Some nanometer wobble and stick slip, Piezo term = off)

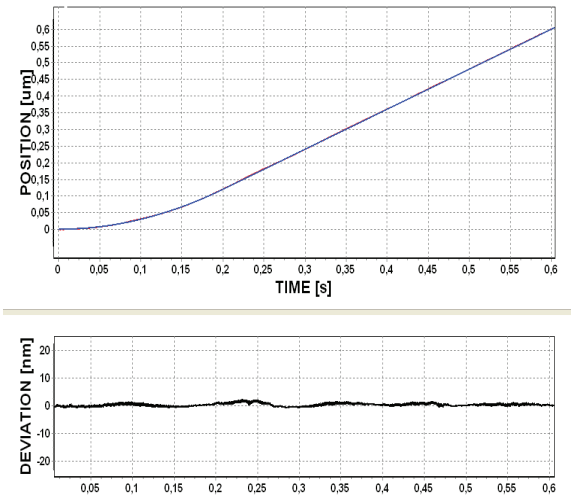

FIGURE 12. Closed loop operation with both hybrid actuator parts active (tracking deviation in laboratory conditions better than 0.8nm RMS).

Because of the ultra-high resolution sensor any disturbance influence from the test equipment and the environment is detected. For long term tests we used “standard measurement” conditions with a wide range of mechanical noise in the nanometer range

An important part of the investigation is to separate the vibration sources from the inner structure.

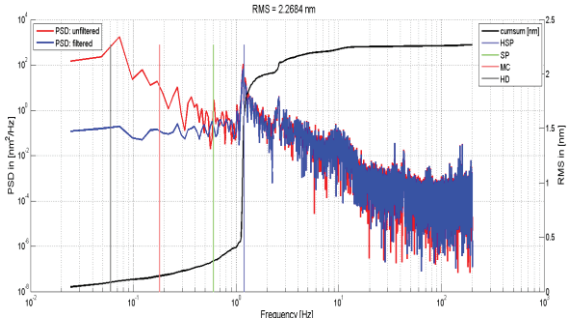

FIGURE 13. Power Spectral Density (PSD) @ tracking velocity v = 0.3µm/s

The aim of the Power Spectrum Density investigation (PSD) is to determine and study the influence of different possible error sources and their contribution to the overall RMS value of a system. A power spectral density illustrates the power of individual frequency components over a specified frequency range. Due to the fact that the integral of the PSD over a given frequency band computes the average power in the signal over that frequency (marked as 'cumsum' in figure 13 and 14) it can be used to analyze the influence of individual frequencies to the overall RMS value of a signal, figure 13.

In addition to the given environmental noise, there are some mechanical and electrical parts of the actuator itself which influence the accuracy of the drive, e.g. the quality of the sensor signal, performance characteristics of the guiding system, natural frequency of the bearings, coupling etc.. Different possible and speed-dependent error sources are shown in figure 13 and 14: HSP (half signal period) and SP (signal period) transcribe the sensor signal quality and its dynamic behavior into the PSD. The influences of the motor cogging (MC) and the harmonic drive gear (HD) are also shown. Figure 13 shows that HSP has a strong influence on the RMS value (2.268nm). Changing the actuator velocity directly affects the influence of the HSP – compare figure 13 and 14.

By way of example, Figure 14 reveals a disturbance at a frequency close to f = 5Hz. After some further investigations it became evident that this disturbance is contributed by the test equipment and will always show up in tracking error measurements made with this set-up. However, it will not exist in the final system.

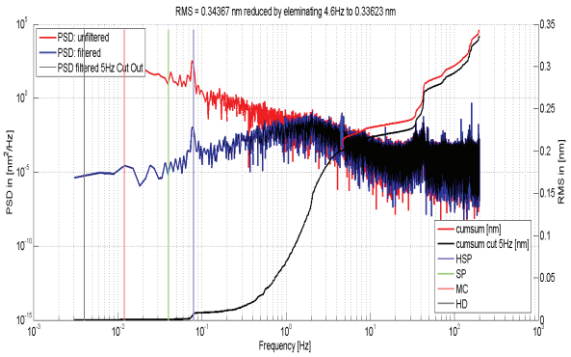

FIGURE 14. Power Spectral Density (PSD) of the Actuator @ tracking velocity v = 20nm/s

Due to the fact that this disturbance is not part of the actuator itself it is permissible to delete its contribution from the overall RMS value, see figure 14. The RMS value changes from 0.34nm RMS down to 0.33nm RMS.

The verification of both principles shows some pros and cons for both versions. The robustness seems to be higher for the voice coil system but it was more sensitive against environmental distortions and shows higher "noise" of these values because of the softness. The non-activated actuator works like a good earthquake sensor.
Because of the longer stroke of a soft actuator the technical effort for the sensor guiding system is higher compared to a stiff piezo-based hybrid system. On the other hand the softer voice coil system provides more freedom for phase compensation of structural vibrations. It would allow the use of an additional force sensor at the tip of the pusher for phase compensation.

	Piezo	Voice Coil
Stiffness of the actuator, during earthquake	+++	+
Robustness against environmental humidity (shielded piezo)	++	+++
Power supply requirements	+	+++
Phase shift for control of back-driving forces	+	+++
Influence on linear guided sensor interface	++	++
Effort on mechanical design	++	++

***Tab. 1:** Verification of piezo vs Voice coil hybrid system (+ less effort, less efficiency*
+++ good efficiency)

SUMMARY

Hybrid actuators, based on a precise spindle drive in combination with a piezo or spring/voice coil actuator combine large motion ranges with ultra-high resolution and tracking accuracy. One common position feedback sensor is used for both sections of the cascade control loop.
Both prototype actuators show similar resolution and can track a position command sequence of 1kHz while reducing the tracking error to less than the required 1.7 nm RMS.

REFERENCES

[1] M. Dimmler, T. Erm, B. Bauvir, B. Sedghi, H. Bonnet, M. Muller, and A. Wallander,E-ELT primary mirror control system, Proc. SPIE 7012-59, 2008

[2] R. Gloess, Sub nanometer precision hybrid positioning systems for vertical inspection tools, ASPE Conference Berkeley 2008

APPLICATION OF WAVELET ANALYSIS IN HETERODYNE INTERFEROMETRY

Chao Lu[1], Steven R. Gillmer[2], Jonathan D. Ellis[2,3], Tony L. Schmitz[4], John Troutman[4], and Joshua A. Tarbutton[1]
[1]Department of Mechanical Engineering
University of South Carolina, Columbia, SC, USA
[2]Department of Mechanical Engineering, [3]Institute of Optics
University of Rochester, Rochester, New York, USA
[4]Department of Mechanical Engineering and Engineering Science
University of North Carolina at Charlotte, Charlotte, NC, USA

INTRODUCTION

Heterodyne displacement measuring interferometry provides important metrology for applications requiring high resolution and accuracy, such as in the semiconductor manufacturing industry and for linear stage calibration. Ideally, the measurement and reference beams in the interferometer completely separate and recombine, where the phase shift is linear with respect to displacement. In practice, however, periodic error exists due to undesirable frequency mixing. Periodic error is non-cumulative and appears as a function of the target displacement. Typically, both 1st and 2nd order periodic errors occur, which correspond to the number of periods (one or two) per fringe displaced, as shown in FIGURE 1. A displacement fringe corresponds to the wavelength divided by the interferometer fold factor which is determined by the interferometer setup. Ultimately, this error can limit the accuracy to approximately the nanometer level.

Many studies have investigated the measurement and compensation of periodic error, including frequency domain and time domain approaches. For frequency domain approaches, the periodic error is measured by calculating the Fourier transform of the time domain data collected during constant velocity target displacement [1]. This method is not well suited to non-constant velocity profiles. An alternate digital algorithm which can be applied in real-time for constant or non-constant velocity motions is also available for measuring and compensating 1st order periodic error [2].

In this work, an analytical wavelet-based technique is used to analyze periodic error for both constant and non-constant velocity motions and also situations where the periodic error amplitude may not be constant, such as interferometers with fiber delivery.

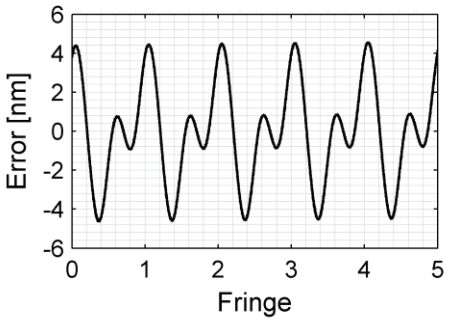

FIGURE 1. Example of 1st and 2nd order periodic error as a function of fringes. Typically, 1st order error has a larger magnitude than 2nd order error.

METHOD

The wavelet transform can be used to analyze time series data that contains non-stationary (variable period) power at multiple frequencies [3]. Wavelet functions refer to either orthogonal or non-orthogonal wavelets. The choice of the appropriate wavelet transform (continuous or discrete) and wavelet function is based on whether the purpose of data analysis is detection or compression [4].

A wavelet function $\psi(\eta)$ is a finite energy function [5] with an average of zero or

$$\int_{-\infty}^{+\infty} \psi(x)dx = 0 \qquad (1)$$

A wavelet family is generated by dilating the mother wavelet via the scale $s > 0$ and translating it via the location $\xi \epsilon R$. This series of wavelets can be expressed as:

$$\psi_{s,\xi}(x) = \frac{1}{\sqrt{s}}\psi\left(\frac{x-\xi}{s}\right) \quad (2)$$

In this research, the continuous wavelet transform (CWT) is used to analyze displacement signals. For a one-dimensional signal $f(x)$, the CWT is

$$W_f(s,\xi) = \int_{-\infty}^{+\infty} f(x)\psi^*_{s,\xi}(x)dx = \int_{-\infty}^{+\infty} f(x)\frac{1}{\sqrt{s}}\psi^*\left(\frac{x-\xi}{s}\right)dx \quad (3)$$

where * indicates the complex conjugate and x represents the time variable.

In practice, EQUATION 3 must be converted from continuous to discrete. For a time series, x_n, with time interval, Δt, where $n = 0 \cdots N-1$, and a wavelet function, $\psi_0(\eta)$, where η is a non-dimensional 'time' parameter, the CWT of a discrete sequence, x_n , is defined as the convolution of this sequence with a scaled and translated version of $\psi_0(\eta)$:

$$W_n(s) = \sum_{n'=0}^{N-1} x_{n'}\psi^*\left[\frac{(n'-n)\Delta t}{s}\right] \quad (4)$$

where s is the wavelet scale. To demonstrate how the wavelet coefficient amplitudes vary with scales and times, the discrete Fourier transform (DFT) can be applied [5]. The DFT of x_n is

$$\hat{x}_k = \frac{1}{N}\sum_{n=0}^{N-1} x_n e^{-2\pi i k n/N} \quad (5)$$

where N is the number of points in the time series [6] and $k = 0 \cdots N-1$ is the frequency index. Also, the function $\psi(t/s)$ becomes $\hat{\psi}(s\omega)$ in the frequency domain. The wavelet transform is the inverse Fourier transform of the product:

$$W_n(s) = \sum_{n'=0}^{N-1} \hat{x}_k \psi^*(s\omega_k)e^{i\omega_k n\Delta t} \quad (6)$$

where ω_k is the angular frequency.

It is complicated to reconstruct the original time series for the CWT, due to the redundancy in time and scale. This redundancy, however, makes it possible to proceed with a completely different wavelet function such as the delta function [4]. By this approach, deconvolution is used to reconstruct the original time series. Comparison is made between the original and reconstructed signal. In this way, a connection between the wavelet function and the output signal is established.

ANALYSIS

Simulated and experimental displacement signals with periodic error were used to assess the validity of the wavelet-based technique.

Periodic Error Reconstruction

The specific wavelet function adopted in this analysis was the Morlet wavelet. The errors were isolated from the displacement signal by subtracting a least-squares best fit polynomial. In FIGURE 2, the simulation results show that the difference between the original and reconstructed periodic error is small, which demonstrates that the signal can be accurately constructed using wavelet analysis. FIGURE 3 shows measurements with periodic (some low frequency drift remained after the least-squares best fit subtraction). The difference during the reconstruction process is still acceptable.

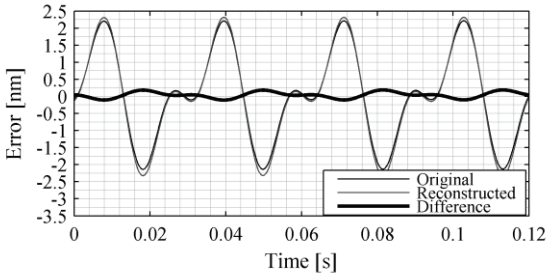

FIGURE 2. The simulated original and reconstructed errors with the difference.

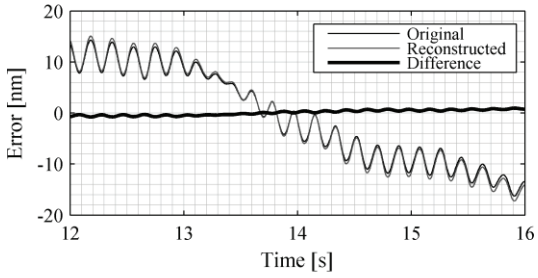

FIGURE 3. The experimental original and reconstructed errors with the difference.

Periodic Error Detection

Here the Haar wavelet was used to detect the periodic errors in the displacement signal. The Haar wavelet is the simplest wavelet and it is not continuous. This property, however, can be an advantage to detect the sudden transitions and sharp rising and falling edges in signals, which is possible in periodic error detection. The signal in FIGURE 4 shows a simulated linear motion

($1.0 \times 10^{-6} m/s$ velocity) with 1st and 2nd order periodic errors.

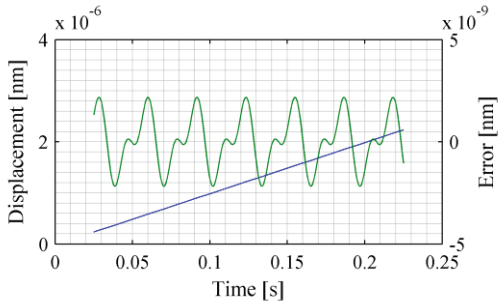

FIGURE 4. The simulated displacement signal with constant velocity and the periodic errors within it.

FIGUREs 5 and 6 give the CWT result with the displacement signal when the peak amplitude of the periodic errors varies.

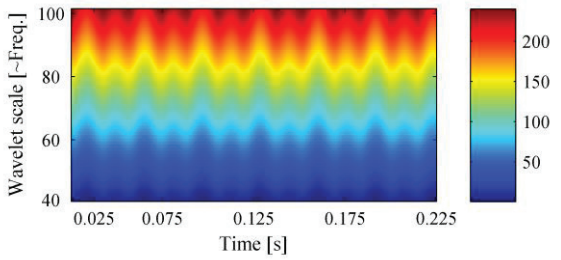

FIGURE 5. The peak amplitudes of 1st and 2nd order periodic errors are $1.28nm$ and $0.95nm$ respectively.

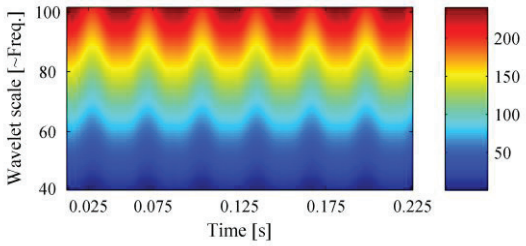

FIGURE 6. The peak amplitudes of 1st and 2nd order periodic errors are $2.99nm$ and $0.37nm$ respectively.

The time intervals between every two closed peaks of the coefficients at the same scale can be used to determine the frequency of the periodic errors. Using the method, the frequency of the periodic error is calculated to be $32Hz$, which matches the simulated frequency value.

The velocity of a measured artifact is linearly proportional to the frequency of the periodic errors. Therefore, through wavelet analysis results the periodic error frequency information as well as the velocity of the original motion can be obtained.

The CWT was applied to a simulated accelerated motion of $2.0 \times 10^{-5} m/s^2$ with periodic errors (FIGURE 7). The result is shown in FIGURE 8. Similar to method described previously, the periodic error frequency is observed to increase from approximately $34Hz$ to $45Hz$ during increasing velocity motion.

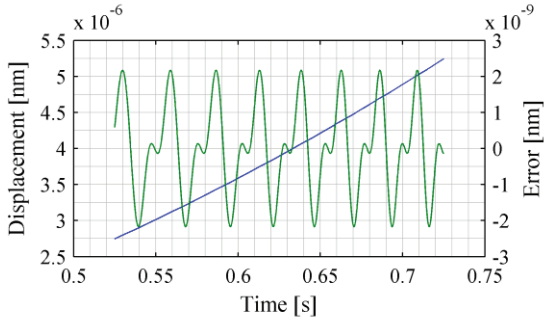

FIGURE 7. The simulated displacement signal with non-constant velocity and the periodic errors within it.

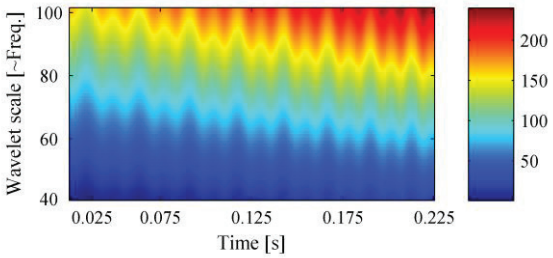

FIGURE 8. The simulated displacement signal with non-constant velocity and the periodic errors within it.

In addition, wavelet analysis was used with experimental data to detect the periodic errors for a heterodyne setup with a sampling rate of $3.2\mu s$. FIGURE 9 shows the displacement and errors.

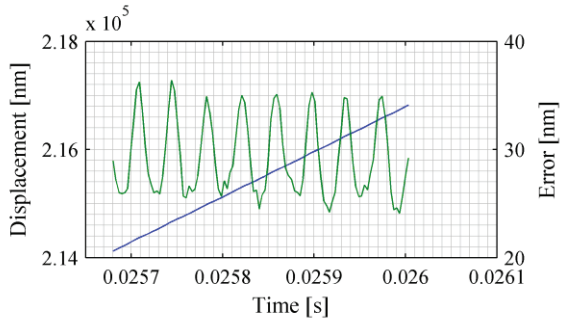

FIGURE 9. The experimental displacement signal with errors.

FIGURE 10 shows the CWT coefficients for the signal depicted in FIGURE 9. FIGURE 11 reveals specific coefficients at scale 10.

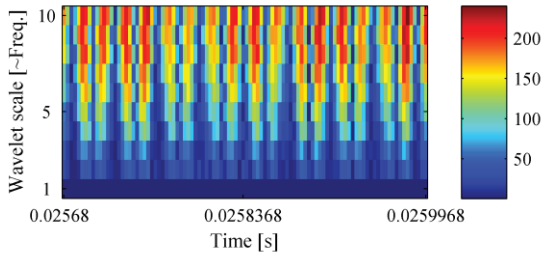

FIGURE 10. The CWT result with the experimental signal.

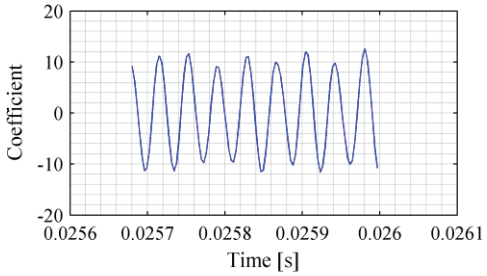

FIGURE 11. The CWT coefficients at scale 10.

Similarly, measuring the average of the time intervals by every two closed peaks, the frequency of the periodic errors obtained here is approximately 26042Hz.

CONCLUSIONS

Wavelet analysis is used in this research to establish an accurate connection between the selected wavelet function and periodic error frequencies/amplitudes in heterodyne interferometer displacement signals. Future work will focus on applying the wavelet analysis in real time and developing an appropriate correction algorithm based on the wavelet coefficients to compensate for periodic errors for both constant and non-constant velocity motion.

REFERENCES

[1] Badami V, Patterson S. A frequency domain method for the measurement of nonlinearity in heterodyne interferometry. Precision Engineering. 2000; 24: 41-49.

[2] Schmitz T, Chu D, Kim H. First and second order periodic error measurement for non-constant velocity motions. Precision Engineering. 2009; 33: 353-361.

[3] Daubechies I. The wavelet transform time-frequency localization and signal analysis. IEEE Transactions on Information Theory. 1990: 36: 961-1004.

[4] Farge M. Wavelet transforms and their applications to turbulence. Annual Review of Fluid Mechanics. 1992; 24: 395-457.

[5] Torrence C, Compo G. A practical guide to wavelet analysis. Bulletin of the American Meteorological Society. 1998; 79: 61-78.

[6] Kaiser G. A friendly guide to wavelets. Birkhauser. 1994; 300pp.

RETROREFLECTOR POLARIZATION MODEL

Minhao Zhu[1,2], Yan Li[1], and Jonathan D. Ellis[2,3]
[1]State Key Lab of Precision Measurement Technology & Instruments
Department of Precision Instruments
Tsinghua University
Beijing, China
[2]Department of Mechanical Engineering
[3]Institute of Optics
University of Rochester
Rochester, NY, USA

INSTRUCTIONS

Retroreflectors have an intrinsic property of retroreflection, which is the reflected light exits the retroreflector at the same angle from which it entered [1]. Retroreflectors are widely used in interferometry [2], enabling compact optical systems and often makes components insensitive to tip and tilt. In many precision interferometry applications, polarization is an important issue that should be considered. Unintended polarization changes can contribute to beam mixing in homodyne or heterodyne displacement interferometers, leading to increased periodic error [3, 4]. In Fabry-Perot (F-P) interferometry, based on laser theory, only laser light with an invariant polarization would stay resonant with folded F-P cavities [5]. Since the incidence upon each reflecting face of a retroreflector is oblique, different input polarizations and misalignments would result in different phase shifts and thus different output polarizations [6]. Each subsequent pass in the interferometer would further shift the output polarization. To get the best multi-interference signals, the polarization properties of the retroreflectors must be analyzed to make sure the laser polarization would remain the same after reflection at the retroreflector. In Ref. [5, 7], eigen polarization states and depolarization effects in retroreflector have been studied using electric field vectors with Jones matrices in these papers. However, all of these are based on normal incidence, which is the ideal situation. In practice, normal incidence is not always achievable and in some situations, the normal angle would even change when, for example, the retroreflector is mounted on a moving stage and the stage has pitch and yaw errors. Thus, it is essential to build a polarization model for retroreflectors under different angular error conditions.

We present a Jones matrix [8] model for describing the polarization changes in a retroreflector as a function of retroreflector pitch and yaw. This model is then applied to solid retroreflectors that use total internal reflection to generate the reflection at the three faces. We developed a Matlab® toolbox for calculating the Jones matrix of a rotated retroreflector to model the polarization changes by the retroreflector under different input polarizations and different misalignments. This polarization model mainly discusses the electric field vector changes of the light after the reflection by the retroreflector. This toolbox can aid in designing heterodyne interferometry systems and in designing folded F-P interferometers and laser cavities. For heterodyne laser interferometers, this Jones matrix model helps assess beam leakage, which is a contributor to periodic error, in interferometer paths, in measurement paths with pitch and yaw errors, and in overall tolerancing for assembly. In F-P interferometers and laser cavities, this Jones matrix model can help assess retroreflector tolerances, coatings, and mounting to ensure the overall design specification is met.

RETROREFLECTOR GEOMETRY

In general, there are two kinds of retroreflectors that generate their retroreflection from three mutually perpendicular faces: solid retroreflectors (SRR) and hollow retroreflectors (HRR). For simplicity, consider a retroreflector as shown in Fig. 1. The three reflecting faces are *AOB*, *BOC*, *COA* respectively. Let *OA*=*OB*=*OC*, so that a cube *OBDCAFGE* can be constructed to help trace the light in the corner cube. The surface *ABC* is the front face through which light enters and exits the retroreflector. The difference between SRRs and HRRs is that for SSRs, refraction occurs at the front face when light enters and exits the retroreflector at non-normal incidence angles. After a laser beam

enters the retroreflector, it reflects at each of the three internal faces sequentially, forming a zigzag beam path in the retroreflector and then hits the front face again (in the case of the SRR), refracting out of the retroreflector. The output beam is always antiparallel with the input beam (within the angular tolerance of the retroreflector). For the purposes of this work, the retroreflector is assumed to have perfectly orthogonal faces. If the retroreflector is oriented normal to input

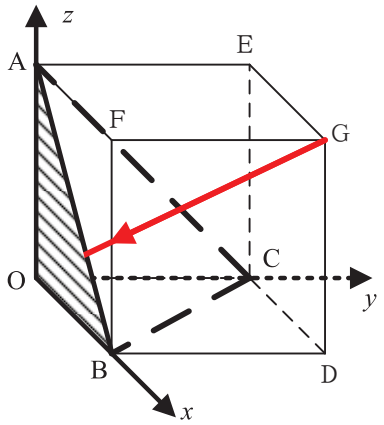

FIGURE 1. Retroreflector viewed in a cube. AOB, BOC *and* COA *are the three reflecting faces mutually perpendicular to each other;* ABC *is the input face through which laser beam enters and exits the retroreflector and where refraction happens for the SRR case.*

face *ABC* and the projected line *O'A* on surface *ABC* is aligned vertically, as shown in Figure 2, a global coordinate system can be chosen for this configuration. There are two reasons for this orientation. First, this orientation is commonly used for plane mirror displacement interferometers. Second, this orientation gives six unique optical paths in the retroreflector which can be distinguished into three different pairs of clockwise (CW) and counter clockwise (CCW) beam paths. As shown in Figure 2 a, the normal orientation to plane *ABC* results in a hexagonal shape to the retroreflector, with vertices described in Figure 1. The solid edges are the vertices of the retroreflector while the dashed lines represent bisecting lines on each of the retroreflector surfaces. The front face *ABC* is divided into six regions by these lines, numbered ①-⑥. Each pair of symbols with the same shape represent the input and corresponding output regions in the front face and a solid (hollow) entering symbol means a CW (CCW) zigzag beam in the retroreflector. For example, if a laser beam enters the retroreflector in the region with

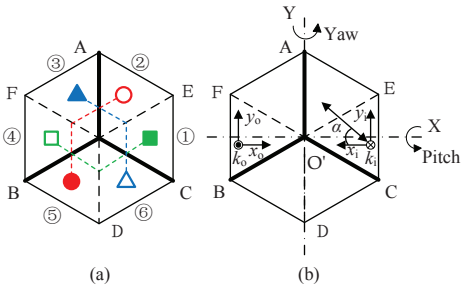

FIGURE 2. View from front face. a) Six regions at the front face of a retroreflector, each pair with the same shape symbol is the input and corresponding output region; Each input region with a solid symbol ends in a clockwise inside beam and hollow symbol ends in a counter clockwise inside beam; b) Definition of the global polarization coordinate system and pitch and yaw axis.

a solid square symbol (Region ①, see Figure 2), it reflects at each face and forms a CW zigzag beam. It exits the retroreflector from the front face region with a hollow square symbol (Region ④, see Figure 2).

Fig. 2 b shows the definition of the global input polarization, which is used to describe the electric field vector component of the input light beam. The input wave vector k_i is perpendicular to the paper plane, which is defined by the vertical and horizontal axes (dotted lines). The polarization state of the input vector can be described using Jones vector in the input polarization system x_i-y_i-k_i, which is defined parallel with the two global axes. When the retroreflector is mounted without pitch and yaw errors, the front face *ABC* coincide with the paper plane and is normal to vector k_i. The projected line of *OA* in the paper plane is parallel with the vertical axis. The angle the retroreflector rotate around horizontal (vertical) axis is called pitch (yaw) angle.

In the simplest case, the input beam is linearly polarized, meaning there is no phase difference between the y_i component and x_i component. The angle between the input beam polarization and the x_i axis is called azimuth angle α. After the interaction with the retroreflector, the light travels antiparallelly back into the output polarization coordinate system x_o-y_o-k_o. Note, all the coordinate systems used in this paper are right handed, thus to compare the output polarization with the input one, coordinate system transformation is required. The whole effect

of the retroreflector and coordinate system transformation can be regarded as a Jones matrix applied to the original Jones vector [8]. The Jones matrix is a function of the pitch and yaw errors for a beam incident at a specific region at the front face. For each of the six numbered incident regions, the function is unique, due to the different incident angle and zigzag optical path. In this work, we outline the formulation of the Jones matrix for each region as a function of pitch and yaw angles.

JONES MATRIX ALGORITHMS

Since the Jones matrix in an SRR is more complicated than that of an HRR due to the refraction in the front face and SRR is often used more in interferometers, the Jones matrix calculation process shown below is for an SRR. The calculation procedure for Region ① is taken as an example. The calculation for all other regions can be achieved by modifying the procedure for Region ①. The input light first refracts into the SSR at the solid square symbol region, then reflects sequentially at the following three surfaces *COA*, *BOC*, and *AOB* (CW). Finally, the light refracts out of the SRR at the hollow square region (Region ④, see Figure 2). Based on this sequence, five steps are needed to calculate the total Jones matrix of the retroreflector. In each step, the main task is to compute the Jones matrix for every single refraction or reflection based on the incident angle, and because the incident plane changes between two consecutive reflections, a rotation matrix is needed to combine all the matrices.

Snell's Law & Fresnel Equations

The reflection and refraction Jones matrix calculation is based on Snell's Law and Fresnel Equations. As shown in Fig. 3, when light passes through a boundary between two different isotropic media with refractive indexes of n_1 and n_2, both reflection and refraction occur. The unit wave vector is $\mathbf{k}$ and the unit polarization vector parallel and perpendicular to the incidence plane are $\mathbf{p}$ and $\mathbf{s}$, respectively. Vectors $\mathbf{p}$, $\mathbf{s}$, and $\mathbf{k}$ form a right handed coordinate system. Snell's Law describes the relationship between the refraction angle and the input angle using

$$n_1 \sin\theta_\mathrm{i} = n_2 \sin\theta_\mathrm{t}, \tag{1}$$

where θ_i and θ_t are the incident and transmissive angles, respectively, relative to the surface normal vector $\mathbf{n}$. The Fresnel Equations describe

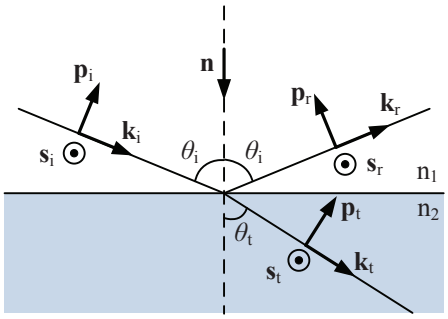

FIGURE 3. Snell's Law & Fresnel Equations.

the fraction of light that is reflected and refracted, and the phase shift of the reflected light using

$$r_\mathrm{s}(\theta_\mathrm{i}) = \frac{E_\mathrm{rs}}{E_\mathrm{is}} = \frac{n_1\cos\theta_\mathrm{i} - n_2\cos\theta_\mathrm{t}}{n_1\cos\theta_\mathrm{i} + n_2\cos\theta_\mathrm{t}}, \tag{2}$$

$$r_\mathrm{p}(\theta_\mathrm{i}) = \frac{E_\mathrm{rp}}{E_\mathrm{ip}} = \frac{n_2\cos\theta_\mathrm{i} - n_1\cos\theta_\mathrm{t}}{n_2\cos\theta_\mathrm{i} + n_1\cos\theta_\mathrm{t}}, \tag{3}$$

$$t_\mathrm{s}(\theta_\mathrm{i}) = \frac{E_\mathrm{ts}}{E_\mathrm{ts}} = \frac{2n_1\cos\theta_\mathrm{i}}{n_1\cos\theta_\mathrm{i} + n_2\cos\theta_\mathrm{t}}, \text{ and} \tag{4}$$

$$t_\mathrm{p}(\theta_\mathrm{i}) = \frac{E_\mathrm{tp}}{E_\mathrm{tp}} = \frac{2n_1\cos\theta_\mathrm{i}}{n_2\cos\theta_\mathrm{i} + n_1\cos\theta_\mathrm{t}}, \tag{5}$$

where E is the electric field, the first subscript indicates incident (i), reflected (r), or transmitted (t), and the second subscript indicates the orientation parallel to incident plane, vector $\mathbf{p}$ (p); or perpendicular to incident plane, vector $\mathbf{s}$ (s). The reflection and transmission Jones matrices can be defined as $\mathbf{T}_\mathrm{r} = \begin{bmatrix} r_\mathrm{p} & 0 \\ 0 & r_\mathrm{s} \end{bmatrix}$ and $\mathbf{T}_\mathrm{t} = \begin{bmatrix} t_\mathrm{p} & 0 \\ 0 & t_\mathrm{s} \end{bmatrix}$, respectively. Both $\mathbf{T}_\mathrm{r}$ and $\mathbf{T}_\mathrm{t}$ can be complex, depending on the refractive index and the incident angle. In each step of the whole calculation, refraction or reflection happens. If the incidence angle is known in each step, all the refraction or reflection Jones matrix can be derived.

Coordinate system transformation

Since the input coordinate system is not coincident with the refraction incidence due to the mount errors of the retroreflector, and the incident plane always changes between two consecutive faces, coordinate system transformation is required all these refraction and reflection matrices [5, 7]. In addition, coordinate transformation can help to determine the incidence angle of each reflection and refraction which is essential in the Jones matrix calculation. Solid geometry is used in developing this retroreflector polarization model to simplify the algorithms. The main *O-xyz* solid coordinate system as shown in Fig. 1

is defined and then each vector and polarization component is calculated with regard to this main solid coordinate system. With the solid geometry, combined with the following intrinsic equations between these unit vectors:

$$\mathbf{k}_\mathrm{r} = \mathbf{k}_\mathrm{i} - 2\mathbf{n}\cos\theta_\mathrm{i}, \quad (6)$$

$$\theta_\mathrm{i} = \arccos\left(\mathbf{k}_\mathrm{i}\cdot\mathbf{n}\right), \text{and} \quad (7)$$

$$\mathbf{s}_\mathrm{i} = \mathbf{s}_\mathrm{r} = \mathbf{s}_\mathrm{t} = \frac{\mathbf{k}_\mathrm{i}\times\mathbf{k}_\mathrm{r}}{|\mathbf{k}_\mathrm{i}\times\mathbf{k}_\mathrm{r}|}, \quad (8)$$

All the rotation matrix between consecutive step can be derived, as well as the incident angle in each step. Finally the whole Jones matrix for input Region ① is derived by cascading all the matrices:

$$\mathbf{J}_{①} = \mathbf{R}_\beta^{(5)}\mathbf{R}\mathbf{T}_\mathrm{t}^{(4)}\mathbf{R}_\beta^{(4)}\mathbf{T}_\mathrm{r}^{(3)}\mathbf{R}_\beta^{(3)}\mathbf{T}_\mathrm{r}^{(2)}\mathbf{R}_\beta^{(2)} \mathbf{T}_\mathrm{r}^{(1)}\mathbf{R}_\beta^{(1)}\mathbf{T}_\mathrm{t}^{(0)}\mathbf{R}_\beta^{(0)}, \quad (9)$$

in which $\mathbf{R}_\beta$, $\mathbf{T}_\mathrm{t}$, $\mathbf{T}_\mathrm{r}$ is the rotation matrix, the transmission matrix and reflection matrix of each step, respectively (the superscript denotes the step) and $\mathbf{R}$ is the reverse matrix $\mathbf{R} = \begin{bmatrix} 1 & 0 \\ 0 & -1 \end{bmatrix}$. Since the value of all the matrices vary with the input pitch (δ_p) and yaw (δ_y) errors, their product, the final Jones matrix of the SRR is also a function of the input pitch (δ_p) and yaw (δ_y) errors. The steps to compute the Jones matrix for Regions ②-⑥, are similar to those for Region ①, except that the sequence of the three reflecting RR faces is different. Modifying the calculation consequence would result in the Jones matrix for all the six regions.

MODELING RESULTS

Using the algorithms described in the last section, a retroreflector, under different pitch and yaw angles, can be simplified as a 'black box' with a Jones matrix of $\mathbf{J} = \begin{bmatrix} J_{11} & J_{12} \\ J_{21} & J_{22} \end{bmatrix}$. (**J** will vary depending on the input regions.) This simplifies studying the output polarization states of different input polarized beams after interaction with an SRR. For every input beam polarization state, the electric field vector can be projected to the global input polarization coordinate system x_i-y_i-k_i, in Fig. 2b. Thus, the input polarization can be expressed as $(E_{x0}, E_{y0})^{\text{-}1}$. After retroreflection, the output polarization state $(E_x, E_y)^{\text{-}1}$ is then obtained as:

$$\begin{pmatrix} E_x \\ E_y \end{pmatrix} = \begin{bmatrix} J_{11} & J_{12} \\ J_{21} & J_{22} \end{bmatrix} \cdot \begin{pmatrix} E_{x0} \\ E_{y0} \end{pmatrix}. \quad (10)$$

In this section, some modeling results are derived using the Jones matrix and input electric field vectors.

Results in global coordinate system

In most retroreflector applications like heterodyne displacement interferometers and folded Fabry-Perot cavities, linearly polarized beams are often used as the light source. This assumes that a linearly polarized beam with an azimuth angle of α (the angle between input polarization and the global x_i-axis) is launched into the SRR. The input polarization vector can be written as $(\cos\alpha, \sin\alpha)^{\text{-}1}$. After the retroreflection, the output polarization $(E_x, E_y)^{\text{-}1}$ is derived using Eq. (10). Both the E_x and E_y components are complex quantities and an additional phase shift φ is introduced between them, making it an elliptically polarized light, as shown in Fig. 4a & b.

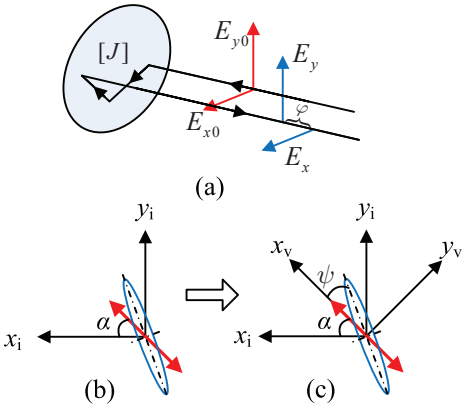

FIGURE 4. Output polarization changes by retroreflector. (a) Input and output polarization state in the original global polarization coordinate system. (b) The output elliptically polarized light viewed in the global coordinate system, in which α is the azimuth angle; (c) A variable coordinate system to account for the polarization changes relative to the input one. The x_v-axis is parallel with the input polarization, α is the azimuth angle and ψ is the main axis angle.

Fig. 5 shows the output polarization states dependence on azimuth angles under normal incidence for each region in a BK-7 SRR. The results are divided into three groups according to the first hitting reflecting faces. For each group, the magnitude of the output x_i-axis component $|E_x|$, y_i-axis component $|E_y|$ and the phase difference between the two components φ are calculated. Since the input horizontal and vertical magnitudes $|E_{x0}|$ and $|E_{y0}|$ change with the azimuth angles, they are also depicted using grey lines in the first two figures of each group. The

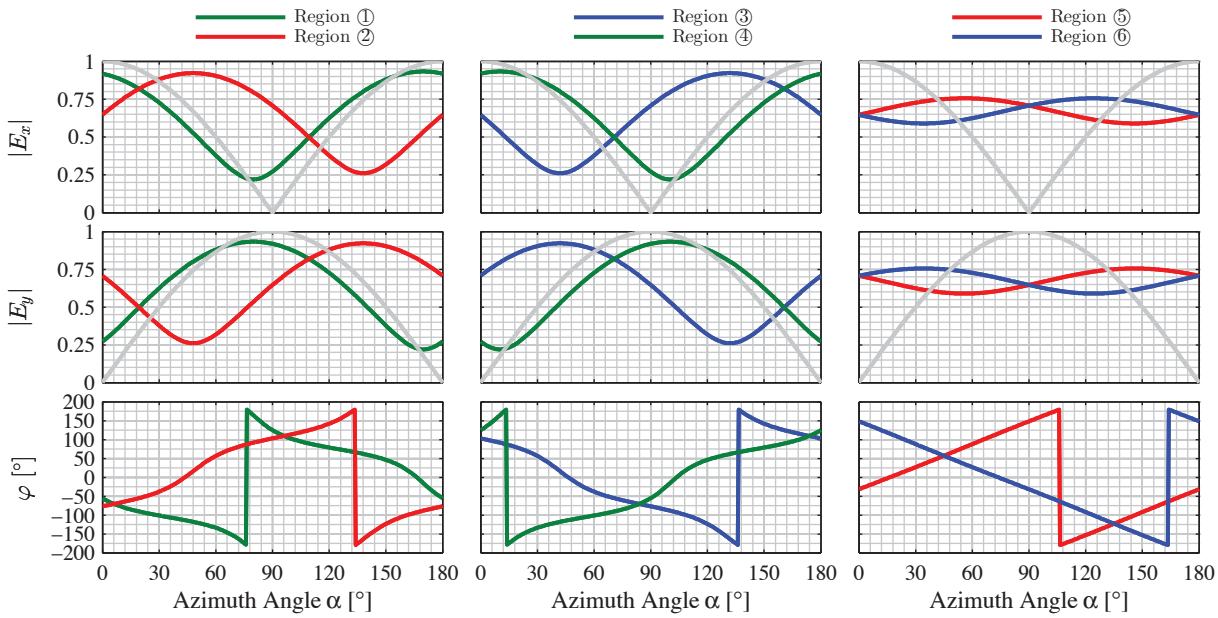

FIGURE 5. Output polarization states comparison between the six different regions when the incident beam is at normal incidence for a BK-7 retroreflector. The results are divided into three groups according to the first hitting reflecting faces. The magnitudes of the input horizontal and vertical components are depicted using grey lines in the first two figures of each group.

$|E_x|$ and $|E_y|$ profiles of the Region ① and ④ match the best with the input profiles among the six regions. For Region ⑤ and ⑥, $|E_x|$ and $|E_y|$ have little dependence on the azimuth angle and is quite significant with respect to the input magnitudes. The output phase difference φ also changes with the azimuth angle. The two φ profiles of each group change reversely with the azimuth angle since they result in CW and CCW beams inside SRR, respectively. For the third group (Region ⑤ and ⑥), φ changes linearly with the azimuth angle.

Results in variable coordinate system

In some applications, the output polarization change relative to the input polarization is often of interest [5]. However, it is difficult to directly describe it in the global polarization coordinate system. Thus, a variable polarization coordinate system x_v-y_v can be created, with its x_v-axis parallel to the original input polarization and y_v-axis perpendicular to it, as shown in Fig. 4c.

In this variable coordinate system, the input polarization vector is always $(1, 0)^{-1}$ while the output polarization vector $(E_{xv}, E_{yv})^{-1}$ is

$$\begin{pmatrix} E_{xv} \\ E_{yv} \end{pmatrix} = \begin{bmatrix} \cos\alpha & \sin\alpha \\ -\sin\alpha & \cos\alpha \end{bmatrix} \cdot \begin{pmatrix} E_x \\ E_y \end{pmatrix}. \quad (11)$$

Define $|E_{yv}/E_{xv}|$ as the magnitude of the polarization ratio, which is a description of the amount of amplitude leakage converted to the orthogonal direction. The phase difference between E_{yv} and E_{xv}, φ_v is a description of the phase delay of the leakage component relative to the original component. To better describe the output polarization, two more parameters are also calculated: the main axis angle, ψ, and the ellipticity of the output polarization, ε, which can be calculated based on the E_{xv} and E_{yv} components.

Fig. 6 shows the output polarization states' dependence on the pitch angle δ_p, yaw angle δ_y, and azimuth angle α for input Region ①. In this figure, yaw is significantly more sensitive than pitch for the same azimuth angle in Region ①. It is possible to have a linearly polarized output beam (where the ellipticity ε is almost 0), however the output polarization is different from the input one, which means linear polarization can never preserve in a SRR. In practical applications in interferometry, for example, light is often reflected to and from a polarizing beamsplitter using a retroreflector. If the polarization properties of that beam must be persevered, the retroreflector prohibits this and causes mixing. After computing

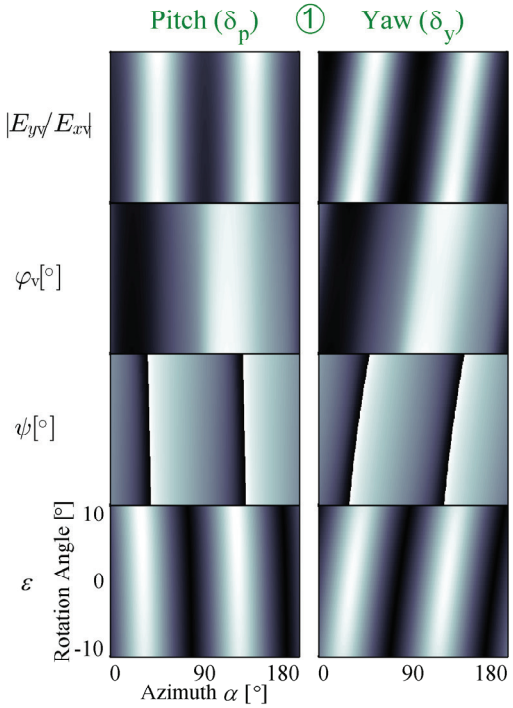

FIGURE 6. Output polarization states' dependence on the pitch angle δ_p, yaw angle δ_y, and azimuth angle α for Region ①. The horizontal axis of each small figure stands for the azimuth angle and the vertical axis stands for the pitch angle. Each parameter dependence is depicted using grey level.

and comparing the output polarization properties for all six regions, the Regions ① and ④ have little dependence on pitch. For all other regions, pitch is slightly more sensitive than yaw for the same azimuth angle although the output polarization states show a dependence on both rotations. In addition, Region ① and ④ have the minimum polarization ratio for vertical and horizontal input polarization states, making these two regions have the best properties for typical interferometry and Fabry-Perot applications. Also, because those Regions have little sensitivity to pitch, the retroreflector can still be slightly misaligned using pitch rotations to prevent ghost reflections from the front surface from interfering with the main optical beams.

CONCLUSION

A theoretical model has been developed to analyze the output polarization state of a solid retroreflector using Jones matrices. The Jones matrices are computed based on Snell's Law, Fresnel Equations and the solid geometry, enabling the output polarization state to be determined as a function of input azimuth angle and retroreflector rotation angle.

Possible applications of this model are to determine the polarization leakages in displacement interferometers and for choosing the configuration of a folded Fabry-Perot cavity. Possible extensions of this work include investigating the polarization effects if the retroreflector is coated or has a hollow architecture and the ideal coating properties to produce the least polarization scrambling in the retroreflector.

ACKNOWLEDGEMENTS

This work was supported by the China Scholarship Council.

REFERENCES

[1] Eckhardt HD. Simple Model of Corner Reflector Phenomena. Appl Opt. 1971 Jul;10(7):1559–1566.

[2] Bobroff N. Recent advances in displacement measuring interferometry. Measurement Science and Technology. 1993;4(9):907.

[3] Quenelle RC. Nonlinearity in interferometer measurements. Hewlett Packard. 1983;34(10).

[4] Hou W, Wilkening G. Investigation and compensation of the nonlinearity of heterodyne interferometers. Precision Engineering. 1992;14(2):91–98.

[5] Shih CC. Depolarization effect in a resonator with corner-cube reflectors. J Opt Soc Am A. 1996;13(7):1378–1384.

[6] Peck ER. Polarization Properties of Corner Reflectors and Cavities. J Opt Soc Am. 1962;52(3):253–253.

[7] Liu J, Azzam RMA. Polarization properties of corner-cube retroreflectors: theory and experiment. Appl Opt. 1997;36(7):1553–1559.

[8] JONES RC. A New Calculus for the Treatment of Optical Systems. J Opt Soc Am. 1941 Jul;31(7):500–503.

Adaptive Scanning Control with Optical Probe

Drescher[1], J., Dow[2],T.A., Garrard[2], K.
[1] United Technologies – Pratt & Whitney, East Hartford, CT, USA
[2] Precision Engineering Center, North Carolina State University, Raleigh, NC, USA

INTRODUCTION

Scanning probes in coordinate metrology have dramatically improved speed compared to point by point touch-trigger methods. However, they are limited to some extent and in some applications by the dynamics of the contact with the work. Higher probe force may improve speed limits but higher force also causes more probe wear and possibly damage to the part. Non-contact sensors are potentially much faster for scanning. A chromatic confocal displacement sensor has been used successfully in scanning on a spherical measuring machine [1-4]. Data acquisition rates, axial resolution, and lateral resolution of this type of sensor support the idea of very fast scanning if the probe is integrated with a good machine. The main problem to be overcome with the confocal probe is the requirement for the axis of the probe to be normal to the surface. Measurement error occurs when the probe axis is not normal to the surface. Limits of the angle may be determined by the manufacturer or by calibration based on an acceptable error. This maximum angle for a given accuracy is usually within the second limit which is the range of operation. Beyond the operating range, the signal simply disappears.

Usually, a workpiece location and shape is known well enough so that a scanning path can be programmed using the constraints for incidence angle limits.

However, there are at least two sets of circumstances where this is not the case and adaptive scanning control is desirable.

- The first is when there is no CAD model of the part such as for reverse engineering applications.
- The second situation includes workpieces on which there may be small features with high curvature whose specifications for form are relatively stringent while their specifications for location with respect to the part coordinates are relatively less stringent. Open loop programming of surface normals from CAD, even when incorporating part alignment algorithms will in these cases be inadequate.

One example of the second case is a blade for an axial compressor in a gas turbine in Figure 1. A blade is typically defined by several sectional profiles at defined planes parallel to the rotational centerline along the blade from root to tip. Each section may have tight tolerances for profile, especially around the leading and trailing edge, while the tolerance for orientation of these section profiles relative to one another (blade twist) is relatively loose. Therefore, for the profile scanning of each cross-section, iterations are needed to establish the location before a non-contact probe can be used to scan in a single continuous sweep while maintaining the incidence angle within operating limits. Because cycle time for these measurements is long, the additional time and expense to locate each section is undesirable.

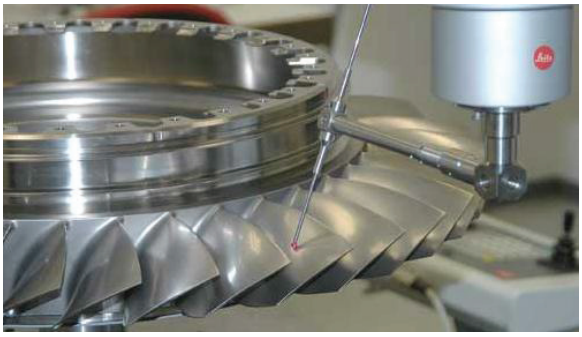

Figure 1: Axial compressor rotor stage measured with a contacting probe (courtesy Leitz)

CONTROL CONCEPT

An adaptive control method is proposed for measurement in circumstances where the surface normal vector is unknown. As a scan occurs, the system automatically collects point data from the surface whose spatial derivative along the scan direction provides slope and curvature of the surface relative to sensor orientation in the plane of the scan profile. This information can be used in real time to maintain the incidence angle near normal depending on the measuring speed and the shape of the surface.

However, finding the general, optimal solution is not trivial. If uniform spatial sampling frequency is desired on the part surface, the control algorithm must take into consideration the acceleration-deceleration limitations of the machine axes, their maximum velocities and the sensor range. Filtering the data during collection is also shown to be important. A short cutoff frequency may lead to unstable behavior due to surface finish or other noise while a long value may lead to a loss in signal if curvature changes rapidly. It is assumed the

slope in the orthogonal direction can be controlled open loop from CAD path generation and part alignment. This would be true except for the case of a small feature such as a sphere having tight form tolerance and loose location tolerance.

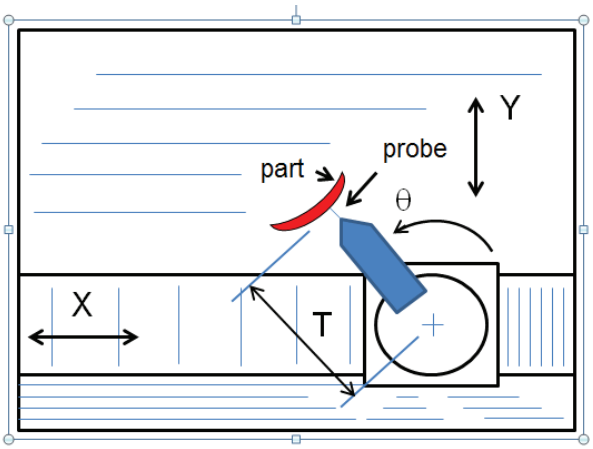

Figure 2: X-Y-θ machine configuration. Part-holding portion is not shown.

Simulations

This paper describes optimization to minimize the measurement time for different theoretical profiles and machine kinematic configurations. A simple, X-Y-Theta machine is illustrated in Figure 2. The probe is mounted to the θ axis with a probe offset defined as a distance, T, from the rotation center with no lateral offset. As a first step, a surface with known profile in the X-Y plane is used to simulate axis control. Equal increments are selected along the profile path, S, and the reverse kinematic model of the simple machine is used to calculate the positions, velocities, and accelerations of the X, Y, and θ axes. This is useful for several things:

- Identification of limitations on surface profiles based on chosen constraints; for example, minimized axis reversals.
- Optimization of the probe offset for different profiles or features within the surface profile.
- Minimization of the inverse kinematic calculation time.
- Investigation of limits on surface scanning speed for various profiles.

The schematic machine of Figure 2 can be controlled to maintain the probe direction normal to the surface and also maintain a fixed probe length as required for a confocal probe operating at a fixed wavelength. This probe offset could be as shown with positive T, zero or negative to minimize axis acceleration requirements. The addition of a redundant, linear R-axis parallel to the probe centerline would allow the probe offset to vary within a measurement to optimize motion as curvature changes. The R-axis could also control a set point for the probe offset and operate on a servo loop at a higher rate than the overall machine control cycle.

Given a surface point coordinate (x_s,y_s) and surface unit normal (i_s, j_s), the inverse kinematics of this simple machine configuration give the target (t) axis coordinates:

$$\theta_t = Atan\left(\frac{j_s}{i_s}\right), x_t = x_s - i_s T, y_s - j_s T$$

The following algorithm can be used to obtain each successive target probe point and the expected normal unit vector at that point from Figure 3:

1. Define a probe coordinate system (PCS). Assuming the current probe orientation is normal to the surface, the X coordinate of the PCS is tangent to the surface in the direction of travel. The Y coordinate is along the probe and into the part surface.
2. Transform the measured point, (X_0,Y_0) and the previous two points, (X_{-1},Y_{-1}) , (X_{-2},Y_{-2}) from machine coordinate system (MCS) to PCS.
3. Fit quadratic equation to obtain the coefficients:

$$\bar{A} = \bar{X}^{-1}\bar{Y}$$

where,

$$\bar{A} = [\boldsymbol{a}\ \boldsymbol{b}\ \boldsymbol{c}]^T, \bar{Y} = [\boldsymbol{y_{-2}}\ \boldsymbol{y_{-1}}\ \boldsymbol{y_0}]^T$$

$$\bar{X} = \begin{bmatrix} \boldsymbol{X_{-2}^2} & \boldsymbol{X_{-2}} & \mathbf{1} \\ \boldsymbol{X_{-1}^2} & \boldsymbol{X_{-1}} & \mathbf{1} \\ \boldsymbol{X_0^2} & \boldsymbol{X_0} & \mathbf{1} \end{bmatrix}$$

4. Using the local quadratic equation, calculate the Y coordinate and slope at the next measurement point which is X_1=X_0+ds with ds equal to the nominal point spacing desired. Note, ds may also be a function of the magnitude of the quadratic coefficient such that point spacing may be efficiently less dense when curvature is small and more dense when curvature is high.
5. Estimate the slope at X_1 as $2aX_1 + b$.
6. Calculate the unit normal as before in the simulation as

$$i_s = -\frac{\left(\frac{dy}{dx}\right)}{\sqrt{dx^2 + dy^2}}$$

$$j_s = \sqrt{1 - i_s^2}$$

7. Transform X, Y, i, j back to machine coordinates

8. Finally, from the same inverse kinematic calculations:

$$\theta_t = \tan^{-1}(j_s/i_s)$$
$$x_t = x_s - i_s T$$
$$y_t = y_s - j_s T$$

where x_s is X_1 and y_s is Y_1.

9. Apply loop gains to the new commanded position

10. Measure next point upon arrival within target window on all axes.

11. Iterate

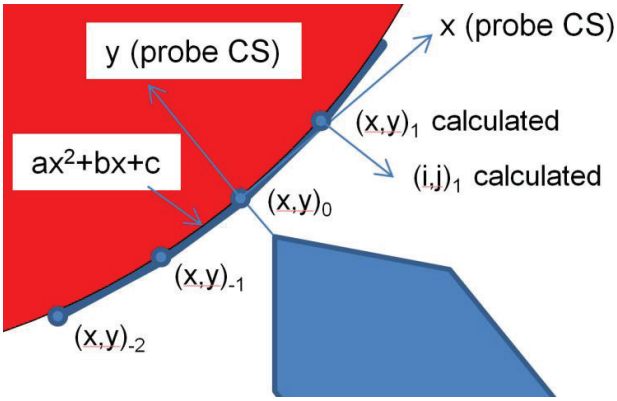

FIGURE 3 Expanded view showing series of measured points and extrapolated target point and surface normal vector

Example

An example surface profile is shown in Figure 4(a). The surface, Z(x) is parallel to the X-axis for a distance of 10mm then becomes a sine function of X with amplitude, A, offset by the 10mm in X.

$$Z(x) = 7 \quad (0< x <10)$$

$$Z(x) = 7 - A\{1 - \cos[2\pi (x - 10)/\lambda]\} \quad (x>10)$$

For a given tool offset, T, the positions and velocities (Figure 4 b.) of x, y, and θ axes are derived from the normal vector of the surface at each measurement point.

$$dZ/dX = -2\pi A \sin[2\pi (X - 10)/\lambda]/\lambda$$

$$i_s = -(dZ/dX)/\mathrm{mag}(dZ/dX),\ j_s = \mathrm{sqrt}(1 - i_s^2)$$

A constant velocity along the surface in the x-direction is assumed. With this simulation established, a probe offset, T=5mm was found to be the maximum length such that x-axis velocity remains positive (no x-axis reversal).

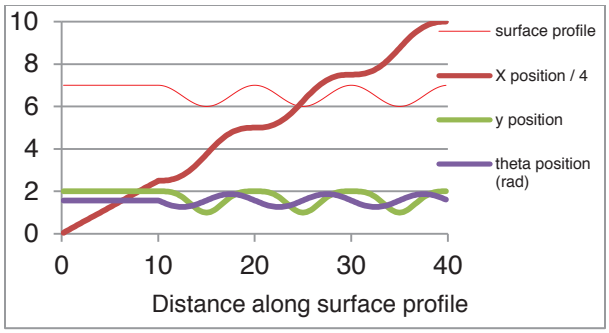

a. Position

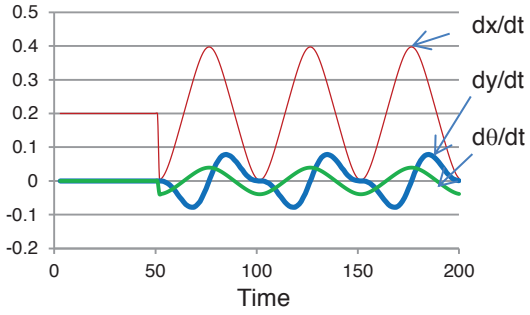

b. velocity

FIGURE 4: Simulation of machine motion to measure a surface profile.

Another interesting case is probe offset, T=0 as shown in Figure 5. This results in constant x-axis velocity while the y-axis simply traces the surface exactly and θ rotates sinusoidally about the starting position of 90deg. Clearly, the ability to change probe offset with the addition of an R-axis as mentioned would add flexibility and ability to optimize a measurement subject to various constraints.

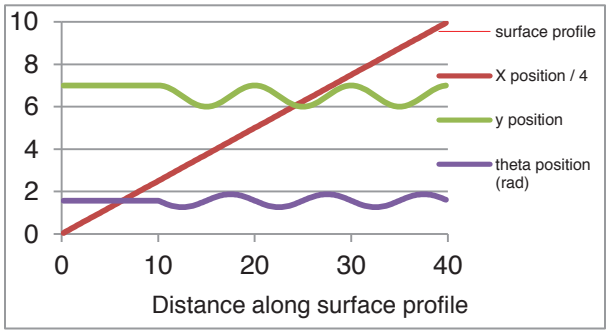

a. Position

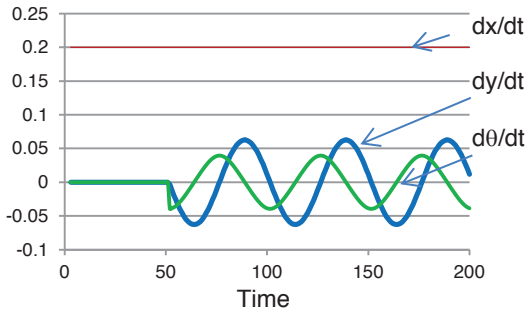

b. velocity

FIGURE 5: Simulation of machine motion to measure a surface profile with zero probe offset

CONCLUSIONS

This paper proposes a novel method for scanning measurements using sensors for which orientation with respect to surface is important. The basics of the idea have been presented with some preliminary discussion on the issues related to optimization and control requirements related to a particular machine configuration. One application is complex shapes such as turbine blades where detailed feature geometry is more important than the actual location of that feature. In this case, following the surface and controlling the angle of the measurement sensor will be necessary to quickly and accurately measure the shape.

REFERENCES

1. Sohn, A, Garrard, K. and Dow, TA, Four-axis spherical geometry measurement of freeform surfaces – Polaris 3D, Proceedings of the ASPE, Vol 511, 2011, pg 38-42.
2. Sohn, A., Garrard, K, Dow, TA, The Spherical Profilometer Polaris 3D, Proceedings of the ASPE, Vol. 47, pp. 43-46 (2009).
3. Polar Coordinate-based Profilometer and Methods, US Patent 6,895,682 B2, May 2005
4. Sohn, A, Garrard, K, Dow, T, "the Polar Profilometer Polaris", *Proceedings of the 2001 ASPE Annual Meeting*, Vol. 25, 2001, pg. 28-31.

THREE DEGREE-OF-FREEDOM OPTICAL PROBE WITH FIBER DETECTION USING CARRIER FRINGE METHODS

Michael A. Echter[1], Christopher D. Roll[1,*], Andrew D. Keene[1], and Jonathan D. Ellis[1,2]
[1]Department of Mechanical Engineering, [2]Institute of Optics
University of Rochester
Rochester, NY 14627 USA

INTRODUCTION

Freeform and conformal optics represent the next generation of optical systems where their utilization leads to more compact, lighter, and higher performance systems for solar collectors, consumer optics, and defense applications [1]. Optical coordinate measuring machines (*e.g.*: [2, 3]) present one option for accurate metrology of freeform components but have two limitations: metrology system errors and optical probe errors. In this work, we are focusing on demonstrating an optical probing technology capable of fiber delivery and fiber detection to remove potential heats sources away from measured optic. In previous work, we demonstrated a bench top proof-of-concept with a displacement resolution below $\pm$10 nm and has a noise floor of approximately $\pm$18 μrad for surface slope in two orthogonal directions. In this proof-of-concept system, the fiber detected version using a fiber bundle had a 50% reduction in angular resolution, which is still acceptable for optical probing applications. In this Proceedings, we briefly discuss our probe concept and the algorithms used for determining the displacement and angle using carrier fringe processing [4].

OVERVIEW OF FIBER OPTIC DMI PROBE

The probe design is based around the operating principles of a Michelson Interferometer as shown in Figure 1 [5]. The light fiber-delivered laser source is collimated and sent to a beamsplitter (BS). One arm transmits through the BS and reflects from the part while the other arm reflects at the beamsplitting surface and reflects from a tilted, fixed reference. On the return trip, both beams interfere in the BS and the interference pattern can be detected through the fourth surface in the BS. Two lines are then digitally masked on the CCD camera and processed using carrier fringe methods [4] to determine the phase and frequency, which are used to track the displacement and angle of the measurement surface. A schematic of the carrier fringe method is shown in Figure 2. The fiber detected

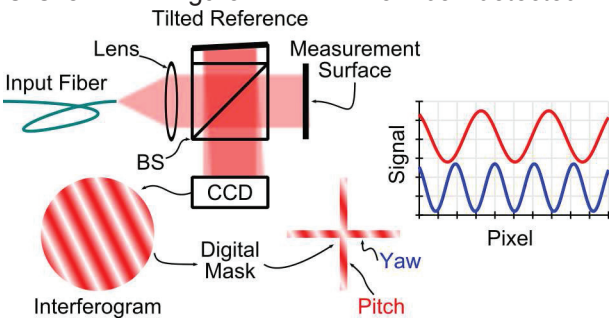

FIGURE 1. Schematic of the optical probe concept using a freespace detection system [5].

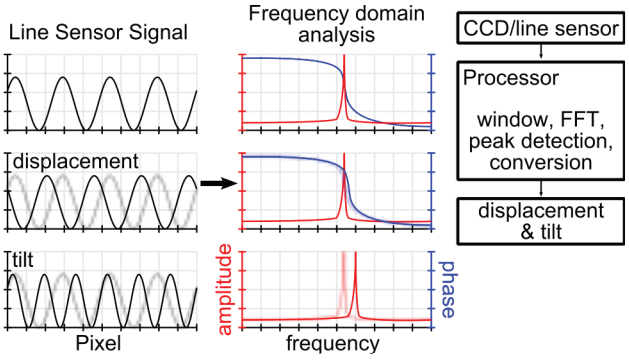

FIGURE 2. Schematic of the carrier fringe processing method [4] to extract the angle and displacement based on changes in the interferogram.

variant of this system is shown in Figure 3. In this case, a fiber bundle is used to transmit the interferogram prior to imaging it on the detector. Two options are possible for detecting and processing. The first method, used in this work, is to acquire the image with a CCD camera, mask the fringes, and determine the information in post-processing. The other method is to split the interferogram and image it onto two orthogonal line sensors that have high bandwidth for closed loop applications. The amount of

*Currently at: MIT Lincoln Laboratory, Lexington, MA 02420

fringes will vary dependent upon the relative tilt of the measurement and reference surfaces. Thus, the masked CCD (or line sensor) will measure a sinusoidal signal proportional to the number of tilt fringes present in the interferogram. This signal is then analyzed in the Fourier domain to determine the peak amplitude, nominal frequency of the fringes, and the phase, as shown in Figure 2. If the slope of the measurement surface changes, then the frequency of the peak location in the Fourier domain shifts while the phase remains constant at that location. If the distance to the measurement surface changes, however, then the relative phase of the signal will also change.

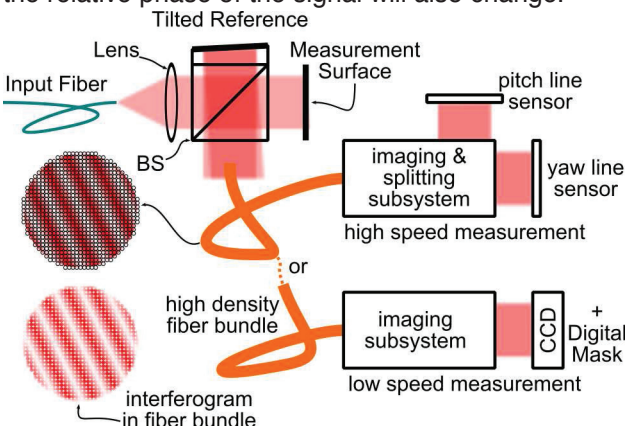

FIGURE 3. Fiber detected variant of the optical probe using a fiber bundle to transmit the interference pattern.

To achieve fiber detection, we employ a fiber optic bundle with approximately 13.5k fibers in a 1.1 mm diameter tube. The ultimate goal of this work is to build a fiber-delivered and fiber-detected system that has a high bandwidth for feedback applications. High speed sensing is achieved through using line sensors instead of CCD or CMOS detectors because their bandwidth can be $>$10 kHz.

LABORATORY DEMONSTRATION

Several bench top setups were explored using a beam splitter and two mirrors on a vibration-isolated optical bench. A fiber coupled laser source (Thorlabs HLS635) at 635 nm was setup as the input to the system via a polarization maintaining (PM) fiber. The free end of the fiber was held fixed by a ferrule clamp and the light was collimated using a 25 mm aspheric lens before traveling to a 50:50 BS. At the BS, the light is split equally, with one arm reflecting from a mirror attached to a fixed surface and the other arm reflecting from a mirror attached to a piezo stage. The collimated beam had a diameter approximately equal to the height of the CMOS sensor used, 5.3 mm. Due to ghost reflections in the BS creating artificial interference patterns, the BS and mirrors were tilted by approximately 5° to remove the undesirable reflections. Additionally, the reference mirror was tilted to create the interference pattern necessary for the carrier fringe detection method. This fringe pattern was then imaged on a CMOS sensor (Thorlabs DC1545M-GL). An example image of the tilt fringes is shown in Figure 4.

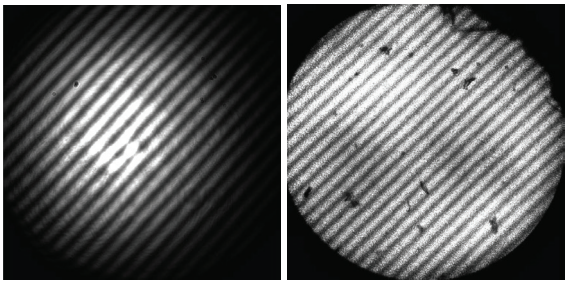

FIGURE 4. Fringe pattern created by the benchtop interferometer projected onto a CMOS sensor (left) and when transmitted through a fiber bundle (right).

To remotely locate the CMOS sensor, a fiber optic imaging bundle was implemented into the system. Fiber bundles are coherent arranged fibers that allow an image illuminated on one end of the bundle to be transmitted to the other end. By using a fiber bundle, a portion of the interferogram could be transmitted to an imaging system and the CMOS sensor away from the probe components. Since these bundles typically have greater than 10k fibers over a 1 mm diameter, there is high resolution both visually and in the Fourier domain.

In order to properly view the interferogram transmitted by the fiber bundle, the surface of the bundle core needed to be imaged onto the CMOS sensor. Numerous imaging systems were tested, however an 18.6 mm Thorlabs Fiber Port and 100 mm plano-convex lens proved to yield the best image for the processing algorithm used. This setup magnified the SCHOTT 1.1 mm fiber bundle core to fill the CMOS sensor as shown on the right of Figure 4. By filling the CMOS sensor there are more sampling points from each interferogram, leading to an increase in accuracy during the FFT calculations.

Individual fibers can be seen on the CMOS

image, however the fiber bundle does still transfer a relatively sharp image of the fringes. The dark spots on the interferogram are caused by damaged cores in the fiber bundle and had minimal impact on the FFT calculations due to their positions. It is very straightfoward to align the probe to the measurement surface due to the clarity of the fringe pattern using a fiber bundle, and demonstrates that fiber optic imaging bundles can be used to successfully fiber couple the interferometer optics to the detector.

ANALYSIS ALGORITHM

Algorithm Background

Measurements were performed on the fringe data using the Fourier techniques described previously. The CMOS camera operated at 16.6 Hz for all testing setups, recording *.avi video files of the changing fringes as the measurement surface was moved. The 16.6 Hz bandwidth proved sufficient for the preliminary testing, however a bandwidth greater than 1 kHz is desired for the final probe. This would likely be achieved by two line scan sensors and an FPGA to perform the data analysis in realtime.

As described previously, several sensitivity tests were conducted by moving the measurement surface in a predictable manner using a piezo stage. As the stage moved the measurement surface, the changing fringe pattern was recorded as an *.avi video file and then imported into MATLAB for analysis. Each frame of the video was saved within a matrix with the values corresponding to the gray value of each pixel in the frame. The matrix size has a number of rows equal to the vertical number of pixels on the sensor, and columns equal to the horizontal number of pixels. To simulate the use of a line sensor, data from only the middle row and middle column of each matrix was selected for analysis. By using two orthogonal line samples, changes in both relative tip and tilt were observed. It was necessary to orient the fringe pattern at 45° to the line samples in order for both the selected row and column to traverse an equal number of multiple fringes. By plotting the gray values of each line sample, a sinusoidal wave with a frequency (scaled relative to the size of the sensor) that is equal to the number of fringes present on the sensor results.

The two line samples were then analyzed in the Fourier domain by taking the FFT of the data sets for each video frame. When the number of fringes changes the frequency of the primary peak in the FFT shifts. The tip and tilt relative to the reference surface is related to the number of fringes by the relationships

$$\Delta x = \frac{\lambda F}{2} - \frac{\lambda F_i}{2} \text{ and} \tag{1}$$

$$\Delta\theta = \arctan\frac{\Delta x}{l}, \tag{2}$$

where F is the number of tip or tilt fringes in the current frame, F_i is the initial number of fringes, λ is the wavelength of the laser source, l is the length of the sensor, and $\Delta\theta$ is the change in relative tip or tilt. This is illustrated in Figure 5. As

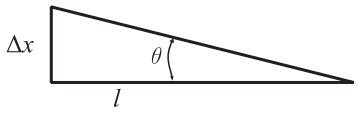

FIGURE 5. A sketch showing the relationship between the number of fringes and the relative tip/tilt angle.

the measurement surface is displaced, the phase at a fixed point in the frequency domain changes. The displacement is related to phase by

$$\Delta d = \frac{\phi}{2\pi}\frac{\lambda}{2} - \frac{\phi_i}{2\pi}\frac{\lambda}{2}, \tag{3}$$

where ϕ is the current phase angle and ϕ_i the initial phase angle. Since the phase is always changing between 0 and 2π, the data must be unwrapped before the calculation can be made correctly. The angle is in radians, and therefore must be converted to displacement based on the wavelength, λ, and the interferometer fold factor, 2 in this case. In addition to calculating the FFT results, we use additional filtering and interpolation methods to improve the frequency resolution.

Zero-Padding

Given that the interferogram is transmitted through a fiber bundle and collected by a finite number of pixels, there are both resolution and noise issues that must be considered. First, the amount of sampling points per image is limited by the number of illuminated pixels on the sensor

(1024 by 1024 pixels). This dimension sets the bin spacing for the FFT algorithm, which gives the frequency resolution in the FFT. Based on the size of the fiber bunle and pixels, the maximum spatial period is about 2 μm. This in turn limits the detection of the number of fringes to approximately half of a fringe, which correlates to about 150 μrad of angular uncertainty over a 1.1 mm fiber bundle. In order to gain a finer resolution of the peak frequency, a zero-padding technique was implemented. Adding a vector of zeros to the end of the data set before running the FFT algorithm allows the program to interpolate between points, creating finer bin spacing. While this technique does not help to resolve multiple peaks spaced very close together, it does interpolate between the points that make up a high intensity individual peak, which is what was desired. Figure 6 shows the result of this technique, with the black line (solid line) demonstrating the improved FFT after zero-padding the data. The raw data is the discrete points. The finely resolved peak has a spacing of approximately 0.01 fringes. Various levels of zero-padding were tested; as the padding increases, the interpolation factor increases as well as the computation time. Currently, a vector with zeros of length 128^2 is being used for analysis.

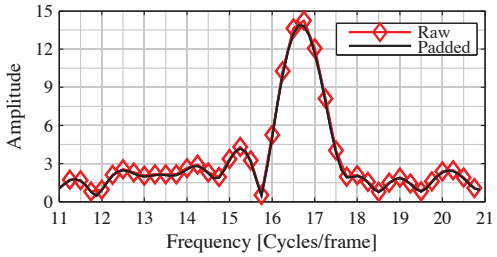

FIGURE 6. Increasing peak detection resolution through zero-padding. The padded data has a significantly increased resolution in bin spacing.

Windowing

In addition to zero-padding, windowing the data can also be used to help provide a well-defined peak and decrease the intensity of side lobes that occur from spectral leakage. This is done by multiplying the data set by a defined function, often smooth and bell-shaped, over a set interval. All of the pre-defined MATLAB windows available were tested on sample data sets. In addition to the pre-defined MATLAB windows, correction scaling factors were applied to the Hamming, Hanning, Blackman, and Blackman-Harris windows as described by Jacobsen and Kootsookos [6]. Many were very comparable, however, the Bartlett window provided the finest peak resolution. Figure 7 demonstrates the effect of windowing the data, shown in blue (solid line). The window decreases the definition of the side lobes compared to the main peak, and with relatively noisy signals windowing was beneficial in creating a more robust algorithm.

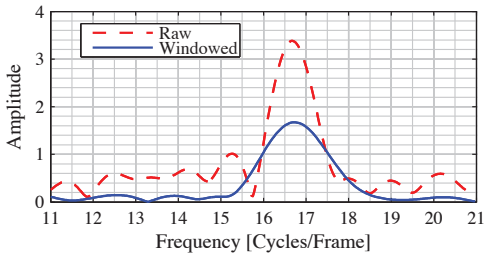

FIGURE 7. The red line (dashed) is a plot of the non-windowed data, and the blue line (solid) represents the data after applying a Bartlett window.

Low Pass Filtering

Another processing technique added to the algorithm was a low pass filter. When projecting the interferogram directly on to the CMOS sensor without the fiber bundle, the data is virtually noise free as seen in Figure 4. However, with the fiber bundle the boundaries of each fiber are seen, which adds noise to the signal. This is easily filtered out with a low pass filter set with a cut-off frequency that correlates to the approximate number of fringes seen by the detector. Also, because there is a lag time before the filter becomes fully effective, the data is zero-padded in front of the data to provide a buffer for the filter to ramp up. Figure 8 demonstrates the effect of the filter as the noisy signal shown in red becomes a relatively clean sinusoidal signal. However, from the analysis of sample data sets, the filter had a negligible effect in aiding the FFT algorithm when computing the fringe frequency.

While the techniques discussed are primarily concerned with improving the resolution of the fringe count, the relative displacement of the measurement surface is found by the phase of the fringe pattern. The phase angle at the peak frequency is determined from the FFT calculation. The phase is recorded as the fringes shift, providing displacement data according to Equation 3. It is important to note that the phase is initially measured at the frequency where the

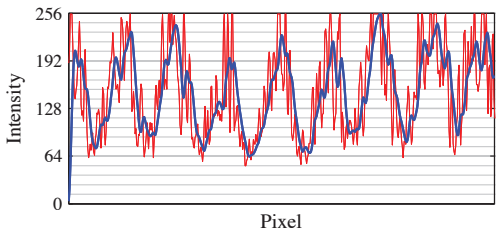

FIGURE 8. The red line represents the unfiltered pixel intensity data, and the blue line the filtered data.

peak amplitude is greatest, then the phase is tracked at this frequency bin even though the peak amplitude may shift bins with tip and tilt.

Parabolic Interpolation for Peak Detection

To further improve the peak detection of the algorithm, a parabolic interpolator was incorporated. The maximum found from the FFT magnitude spectrum calculation, k, is used in conjunction with one value above and one value below it to fit a parabolic curve to as shown in Figure 9.

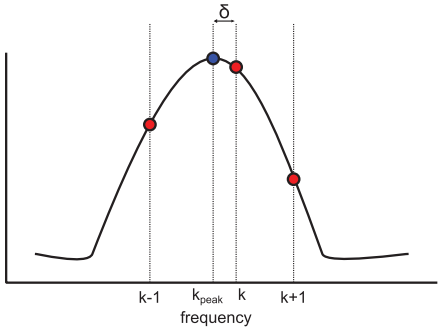

FIGURE 9. The red dots represent the three maximum points from the FFT calculation. By fitting a curve to these three points, a new k_{peak} is found shown in blue.

Using Equation 4, the difference δ from the FFT peak and interpolated curve peak is calculated. This value is added to k from the FFT and used to better predict the actual peak of the FFT for the tip, tilt, and displacement calculations later in the algorithm. When testing the Hamming, Hanning, Blackman, and Blackman-Harris windows, a correction scaling factor Q was also tested as described by Jacobsen and Kootsookos [6] shown in Equation 5.

$$\delta = -Re\left[\frac{(X_{k+1} - X_{k-1})}{(2X_k - X_{k-1} - X_{k+1})}\right] \qquad (4)$$

$$\delta_Q = Re\left[\frac{Q(X_{k-1} - X_{k+1})}{(2X_k + X_{k-1} + X_{k+1})}\right] \qquad (5)$$

By using the parabolic interpolated peak, the tilt and tip resolution improved over using the maximum from the FFT magnitude spectrum. For all calculations of the test videos the parabolic interpolated peak was utilized.

INITIAL TESTING RESULTS

Fiber Bundle Imaging

After developing the algorithm for processing the interferograms, testing began to quantify the resolution of the interferometer. The measurement mirror was mounted to a piezo flexure, allowing for a controlled displacement of approximately 1.25 μm over a 10 s period. The fiber bundle was inserted into the system and coupled to imaging optics and the CMOS sensor for remote imaging. The imaging systems tested were based on a 4F Fourier imaging design, utilizing two or four objectives to manipulate the image. In every setup tested, the first objective was utilized to collimate the light from the fiber bundle. Additional lenses were used to adjust the magnification of the final image, as well as creating the image plane for the CMOS sensor. Both a rotating and stationary diffuser were tested in one imaging configuration in an effort to smooth the interferogram and remove the interstitial boundaries of the fibers.

To determine which imaging system performed the best, the same range of fringe densities were tested for all setups. The standard deviation for each system was calculated for the resolution of the tilt and tip, and were then compared between each system. Using an 18 mm Fiber Port and 100 mm plano-convex for imaging had closely agreeing tilt and tip standard deviations, as well as the lowest average between tilt and tip standard deviation among the imaging systems.

The measurements shown in Figure 10 represent the $max(Data) - min(Data)$ of the tilt and tip measurements in the fiber bundle system, the 'worst case scenario' over the 10 s test. Making the reasonable assumption that the piezo travels in a linear fashion, it can be determined that tilt and tip motions of the measurement mirror in the data are inherent in the system and/or processing. Several fringe densities were tested to determine if there is a trend or an ideal number of fringes for each setup. There was no noticeable

trend over the fringe densities tested, however 16 fringes provided the best agreement between the tilt and tip resolution calculations.

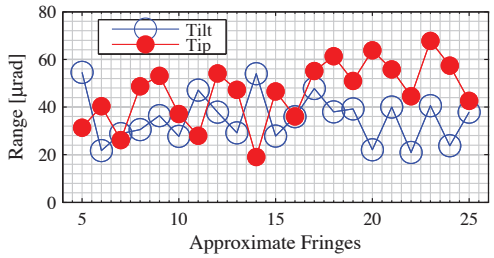

FIGURE 10. Tilt and Tip measurements of a piezo actuated surface with the fiber bundle and 18-100 imaging optics over a range of fringe densities.

Figure 11 shows the tilt and tip data for 16 fringes with the 18-100 imaging system. The tilt data shows a decrease in the position of the amplitude centerline while the tip data remains relatively constant. By using the $max(Data) - min(Data)$ calculation, the tilt resolution was 32.9 µrad and the tip resolution 36.0 µrad, an average resolution of approximately $\pm$ 18.0 µrad.

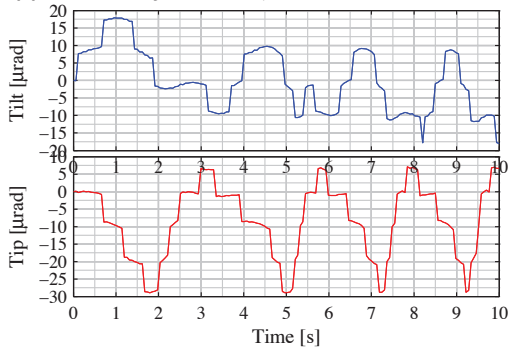

FIGURE 11. Tilt and Tip measurements of a piezo actuated surface with the fiber bundle and 18-100 imaging optics at approximately 16 fringes.

Since the diameter of the fiber bundle was known, the section of the beam measured could be related to the pixel dimension the image of the fiber bundle filled on the CMOS sensor. From this information, the algorithm was able to compute an accurate displacement measurement as previously described in the Analysis Algorithm section. By taking a vertical and horizontal line from the center of the interferogram, a vertical and a horizontal displacement was calculated through the algorithm. These two orthogonal lines, as well as their difference, are shown in Figure 12. The resolution of the displacement calculation is approximately $\pm$10 nm. Barring unwrapping issues, this resolution is consistent for most of the imaging setups.

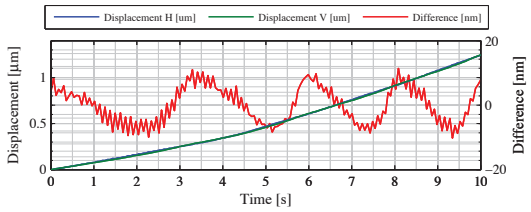

FIGURE 12. Displacement measurements of a piezo actuated surface with the fiber bundle and 18-100 imaging optics at approximately 16 fringes.

CONCLUSIONS

We present a fiber-delivered and fiber-detected, 3-DOF optical probe for measuring optical components in conjunction with an OCMM. The optical probe uses a Michelson interferometer to produce carrier fringes and a high density fiber bundle to transmit interferograms that are recorded away from the probe head. In preliminary testing, the fiber delivered version had displacement errors around 20 nm, which is similar displacement errors as its freespace counterpart, meaning that displacement information is preserved even when detecting through a fiber bundle. The angular error was about $\pm$18 µm. For optical probing applications, assuming the probe is around 25 mm away from the surface, the optical path error for a 20 µrad angular error translates to less than 1 nm of displacement error, which is below the noise level. Thus, for optical probing of freeform optics, where the angular DOFs are only used for continuous contouring, this probing concept would be viable provided it fit the form factor of the OCMM.

ACKNOWLEDGMENTS

The authors would like to thank OptiPro Systems (Ontario, NY) for supporting this work through a NYSTAR STAR fund. Additionally, the authors would like to thank Thomas Brown and Kyle Fuerschbach for many fruitful discussions on imaging systems.

REFERENCES

[1] Thompson, K. and Rolland, J., "Freeform Optical Surfaces: A Revolution in Imaging Optical Design," Optics & Photonics News 23(6), 30-35, (2012)

[2] Henselmans, R., Cacace, L.A., Kramer, G.F.Y., Rosielle, P.C.J.N., and Steinbuch, M., “The NANOMEFOS non-contact measurement machine for freeform optics,” Precision Engineering, 35(4) 607-624 (2011)

[3] DeFisher, S., Bechtold, M., and Mohring, D., “A non-contact surface measurement system for freeform and conformal optics.” Proc. SPIE 8016, 80160W (2011)

[4] Takeda, M. and Mutoh, K., “Fourier Transform profilometry for the Automatic Measurement of 3-D Object Shapes,” Applied Optics, 22(24) 3977-3982 (1983)

[5] Strube, S., Molnar, G., and Danzebrink, H.U., “Compact field programmable gate array (FPGA)-based multi-axial interferometer for simultaneous tilt and distance measurement in the sub-nanometre range,” Measurement Science and Technology 22(9), 094026 (2011)

[6] Jacobsen, E. and Kootsookos, P. “Fast, accurate frequency estimators,” IEEE Signal Processing Mag., 24(3) 123-125 (2007)

SUPPRESSION OF TOOL WEAR IN DIAMOND TURNING BY SURFACE MODIFICATION OF STEELS
– Effect of Carbides in Carburized Steels –

Naomichi Furushiro[1], Daisuke Hirooka[1], Tomomi Yamaguchi[1], Shuntaro Terauchi[2], Yasuhiro Iwasa[2], and Shigetaka Matsuda[2]
[1]Kansai University
Suita, Osaka, Japan
[2]Osaka Yakin Kogyo Co., Ltd.
Higashi-Yodogawa, Osaka, Japan

INTRODUCTION

Severe tool wear occurs when commercial steel alloys are single-point diamond turned (Figure 1(a), Figure 2(a)). Consequently, suppression of tool wear in diamond turning of steels are awaited in the manufacture of molds for high-precision, complex optical components.

In previous papers, we have reported that the formation of small carbon-compound particles that are uniformly dispersed within a continuous α-ferrite matrix suppresses nose wear of diamond tools [1], and also reported that carbon compound precipitation by carburizing and nitride formation by nitriding suppress nose wear of diamond tools [2] (Figure 1(b), Figure 2(b)).

In this paper, wear suppression effect of surface modification (e.g., carburizing) is discussed based on the results of cutting test and metallographic analysis.

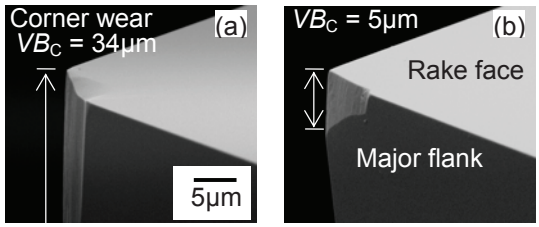

FIGURE 1. SEM micrographs of flank of diamond tools after turning of (a) quenched and tempered JIS SKD61 steel, (b) carburized one. V=3.3m/s, f=3.1μm/rev, d=3.5μm, L=16m.

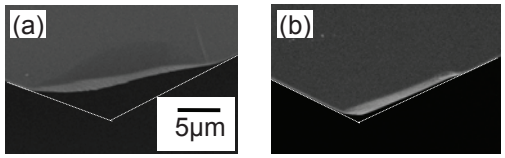

FIGURE 2. SEM micrographs of tool geometry after turning of (a) quenched and tempered JIS SKD61 steel, (b) carburized one. Dotted lines indicate tool geometry before turning.

MACHINABILITY OF STEEL
CARBURIZED STEEL

Figure 3 shows SEM micrographs showing microstructure of carburized hot work die (JIS SKD61) steel in different depth (100μm, 250μm, 500μm, 1500μm, and 2000μm).

Carbon compounds were precipitated in each depth of carburized steel. The number and the size of precipitated carbides decreased in accordance with the depth increased.

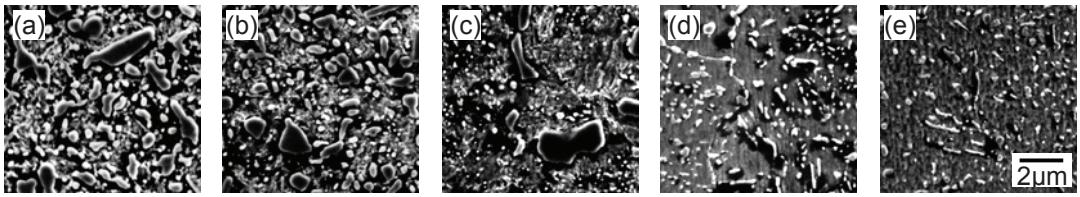

FIGURE 3. SEM micrographs showing microstructures of carburized SKD61 steel in depth of (a) 100μm, (b) 250μm, (c) 500μm, (d) 1500μm, and (e) 2000μm.

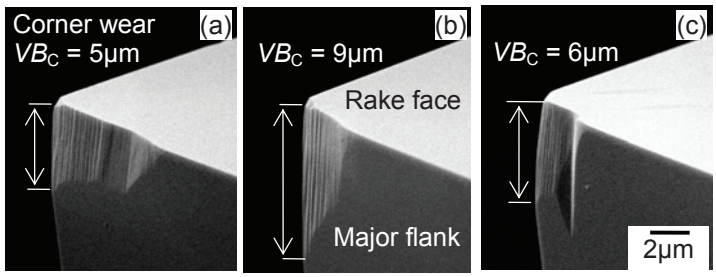

FIGURE 4. SEM micrographs of flank of diamond tools after turning of carburized JIS SKD61 steel in depth of (a) 100μm, (b) 500μm, and (c) 2000μm.
V=3.3m/s, f=3.1μm/rev, d=3.5μm, L=16m.

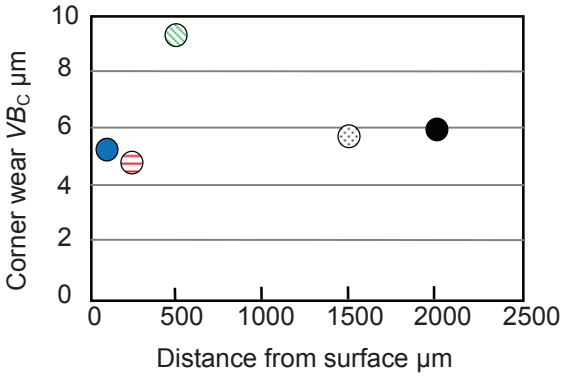

FIGURE 5. Comparison of corner wear of diamond tools after turning of carburized JIS SKD61 steel as a function of distance from surface.

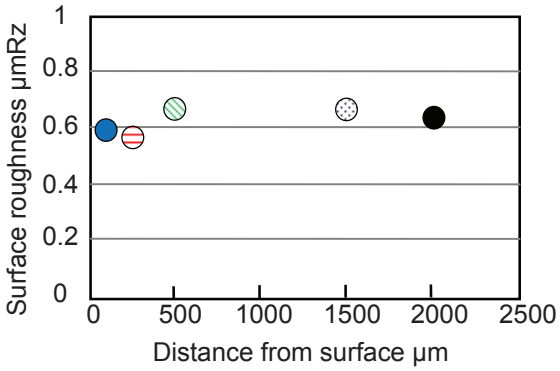

FIGURE 6. Comparison of surface roughness of diamond tools after turning of carburized JIS SKD61 steel as a function of distance from surface.

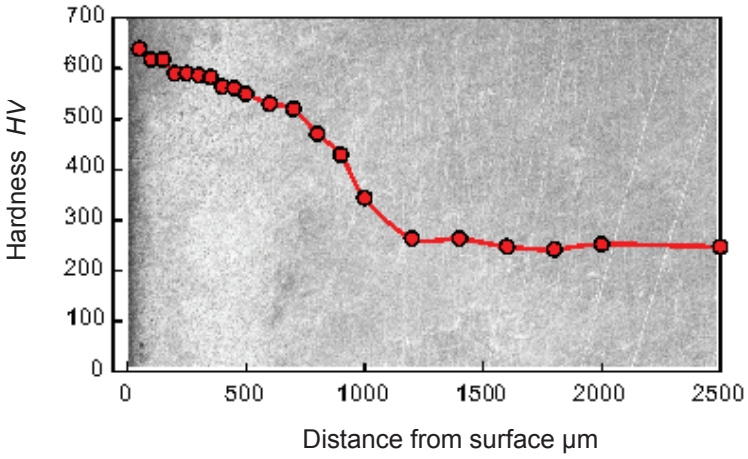

FIGURE 7. Hardness of carburized JIS SKD61 steel as a function of distance from surface.

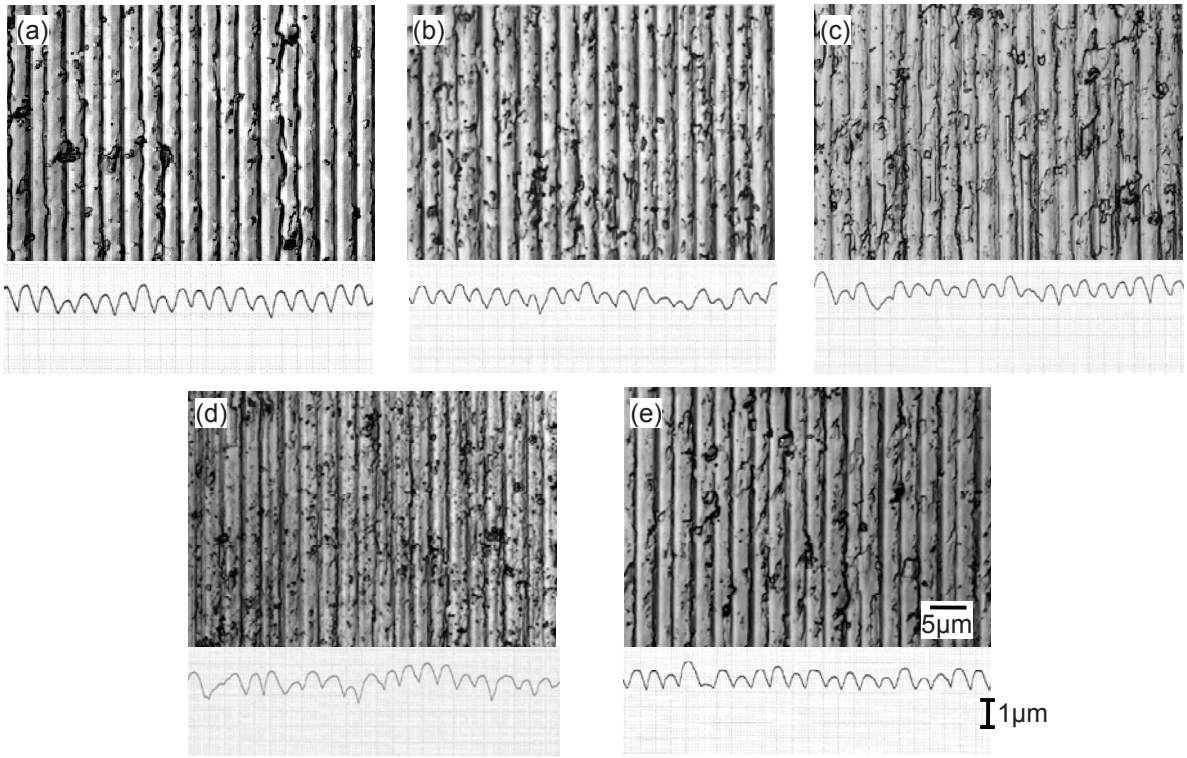

FIGURE 8. Micrographs showing machined surface of carburized SKD61 steel in depth of (a) 100μm, (b) 250μm, (c) 500μm, (d) 1500μm, and (e) 2000μm.

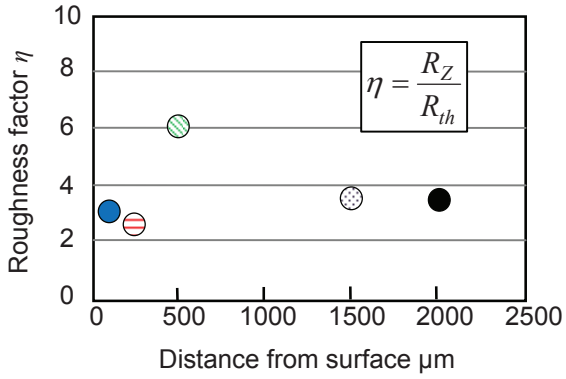

FIGURE 9. Comparison of roughness factor of carburized JIS SKD61 steel as a function of distance from surface.

RESULTS AND DISCUSSIONS

Tool Wear

Figure 4 shows SEM micrographs of flank of diamond tool after turning of carburized JIS SKD61 steel in different depth (100μm, 500μm, and 2000μm)

Maximum wear was observed at the tool nose, and its extent varied with depth.

Figure 5 shows comparison of corner wear of diamond tools after turning of carburized steel in different depth.

These results indicate that carbon compound precipitation by carburizing of steels suppresses nose wear of diamond tools.

Surface Integrity

Figure 6 shows comparison of surface roughness in different depth.

Maximum height surface roughness did not vary with depth.

Figure 7 shows cross-sectional Vickers hardness of carburized JIS SKD61 steel.

The hardness decreases with depth.

Figure 8 shows micrographs of machined surface and their roughness profiles.

Precipitation of large carbides affects surface integrity.

The roughness should be smaller than its theoretical roughness because the edge of the tool was worn out.

To clarify this fact, we calculated roughness factor of each depth.

Figure 9 shows comparison of roughness factors of carburized JIS SKD61 steel.

Roughness factor when turning depth of 500 um was more than 5, whereas those of other depths were 3 to 4.

These results indicate that suppression effect of carburizing depends on microstructural differences.

CONCLUSIONS

- Carbon compound precipitation by carburizing of steels suppresses nose wear of diamond tools.
- Precipitation of large carbides affects suppression of tool wear and surface integrity.

REFERENCES

[1] Furushiro N, Higuchi M, Yamaguchi T, Terauchi S, Matsuda S, Shimada S. Tool Wear in Diamond Turning of Steels. Proceedings of ASPE 2010 Annual Meeting. 2010; 431-434.

[2] Furushiro N, Yamaguchi T, Terauchi S, Matsuda S, Shimada S. Suppression of Tool Wear in Diamond Turning of Steels by Surface Modification–Effect of Carburizing–. Proceedings of ASPE 2011 Annual Meeting. 2011; 345-348.

DRIE Process Performance for Manufacture of an Artifact for X-ray Phase-Contrast and Micro-CT Characterization

Jeffery D. Thousand and Stuart T. Smith
Mechanical Engineering
University of North Carolina at Charlotte
Charlotte, North Carolina, United States

INTRODUCTION

X-ray phase-contrast imaging is performed using a high intensity, collimated X-ray beam and exploiting the diffraction through a single-crystal material. The concept is known as X-ray interferometry and the first example of the interferometer was presented by Bonse and Hart in 1965 [1]. The first X-ray microtomography image of a small snail was developed by Elliott and Dover in 1982. As the method of detection relied on a single detector translated by an XY stage, the scan completed by Elliott took nearly 3 hours to create a 64 x 64 pixel image, with a resolution of 15 μm [2]. By 1994, phase-contrast computer tomography using synchrotron radiation was investigated by Momose at Hitachi's Advanced Research Lab using X-ray sensing pickup tubes and creating 960 x 1024 pixels [3].

An X-ray interferometer is constructed from single-crystal silicon with three parallel blades machined along a specific orientation. For Bonse and Hart, the orientation they utilized was for 220 reflections. The incident X-ray radiation X_i interacts with the splitter S near the Bragg angle θ and is split into two coherent beams.

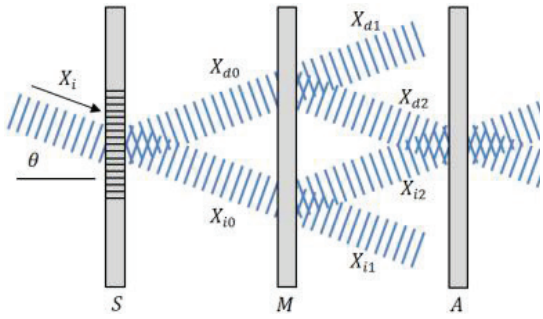

FIGURE 1. Diagram of the interferometer operation showing the beam separation when interacting with the splitter S, mirror M, and analyzer A. Horizontal lines in the splitter represent the planes for reflection.

As beams X_{i0} and X_{d0} draw nearer to the mirror M, the beams are spatially separated. Upon interaction with the mirror, each beam is separated into two additional beams, creating a total of four beams. Beam X_{i0} is divided into beams X_{i1} and X_{i2}, while beam X_{d0} divides into X_{d1} and X_{d2}. Two of the beams, X_{i2} and X_{d2}, converge upon each other at the analyzer A to create a standing wave pattern. A graphical representation of this process is shown in FIGURE 1.

The method for inducing a phase shift is to place an object in a beam's path, such as X_{i0} or X_{i2}, however this will also attenuate the beam's intensity (FIGURE 2). When the phase of one beam is shifted, the end result is a change in position of the standing wave pattern in the analyzer.

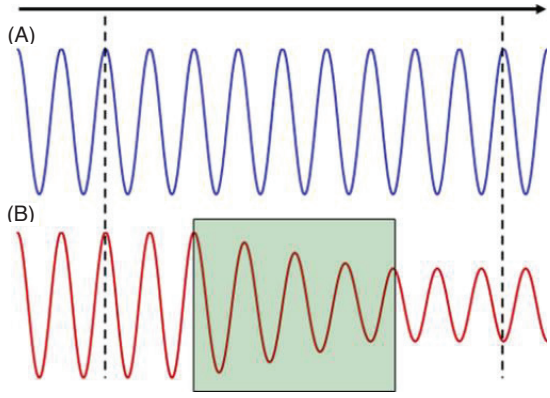

FIGURE 2. Example of a (A) normal beam without an object in its path and a (B) phase shifted and attenuated beam when an object is added.

The benefits of using phase-contrast X-ray imaging over conventional absorption-contrast imaging are: improved signal-to-noise, radiation dosage is lowered, and quantitative information is obtainable [4]. These advantages enable phase-contrast imaging to be used on materials

where absorption-contrast imaging often shows few noticeable details, such as soft-tissue [5,6]. In the manufacturing field, this technology could be used to precisely analyze surface coatings for regions containing impurities, measure the coating thickness, and improve detection of material defects. With the influx of interest in phase-contrast imaging in recent years, there is a need to develop a standard artifact for testing and calibrating such systems. This project investigates the performance of deep reactive ion etching (DRIE) as a method for production of a calibration artifact.

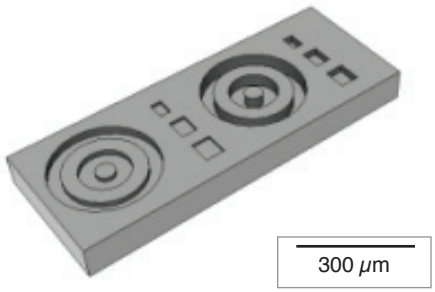

FIGURE 3. Example of potential features with various shapes and dimensions that could populate the calibration artifact.

THEORY

For a homogeneous solid, the dimensions of the calibration artifact are directly related to the phase shift through the material. It is known that the phase shift per unit distance is related to the electron number density of the material and the source wavelength [7]. Thus, the fundamental equation relating material and phase shift is

$$\phi(x,y) = -\lambda r_0 \int_M \rho(x,y,z)dz. \quad (1)$$

Where:

λ is the wavelength of the X-ray radiation
r_0 is the classical electron radius
$\rho(x,y,z)$ is the electron number density

When dealing with material that has a uniform density, such as perfect single-crystal silicon, the electron number density simplifies to Equation 2.

$$\rho_e = \rho_m N_A \frac{Z}{A_r} \quad (2)$$

Where:

ρ_m is the material density
N_A is Avogadro's constant
Z is the atomic number
A_r is the standard atomic weight

Merging Equation 2 with Equation 1 and integrating with respect to the thickness (t) yields the phase shift.

$$\phi(t) = -\lambda r_0 \rho_e t \quad (3)$$

For single-crystal silicon, the electron number density is $6.995 \cdot 10^{29}$ electrons·m^{-3}. Common X-ray targets are Kα copper and molybdenum with λ of 1.54184 Å and 0.71073 Å respectively. To generate a 2π phase shift using a copper target, the thickness of the silicon medium is approximately 20.7 μm and 44.9 μm when using a molybdenum target.

ARTIFACT DESIGN

The X-ray system in this project is fitted with a molybdenum target and can operate up to 50 kV or 2.5 mA at 25 W. The distance between the X-ray camera and the source for the system is 750 mm with a FWHM spot size near 1.8 mm at the detector. As the phase shift using a molybdenum target is less sensitive than copper, feature depths will be based on a copper target. Combining the X-ray system and the phase shift information, design goals are as shown in TABLE 1.

TABLE 1. Calibration artifact feature dimensional range. Dimensions were determined using the phase shift theory and available X-ray system specs.

Dimension	Minimum	Maximum
Lateral	1 μm	300 μm
Depth	1 μm	20 μm

Potential features that will populate the artifact are concentric squares and rings (an example is shown in FIGURE 3), checkerboard patterns, and gratings.

EXPERIMENTAL PROCEDURE

This section outlines the method for manufacture of the features on a silicon wafer surface. As a first step, a 100 mm diameter silicon wafer was cleaned with a piranha etch solution, rinsed with deionized water, and dried using nitrogen and a spin dryer. Shipley 1813 photoresist was spin coated onto the surface at 3500 RPM for 30 seconds to apply a uniform

layer between 140 μm and 150 μm thick, and soft-baked for 60 seconds at 115 ºC. The resist was exposed with a mask containing numerous features of diversified dimensions and the exposed resist was removed using photoresist developer. An aluminium hard mask was sputtered on and the remaining photoresist was removed in an acetone bath agitated by a sonic cleaner. This was followed by a 2 minute methanol bath, rinsed with deionized water, and dried with nitrogen. The thickness of the aluminium mask measured 210 nm. A Surface Technology Systems (STS) Advance Silicon Etch system was used to accomplish the etching. The STS was run with a coil power of 600 W and the plate at 15 W with helium cooling on the backside of the wafer. The etching cycle was ran at 4 second intervals with 13 atm $cm^3 \cdot min^{-1}$ of O_2 and 130 atm $cm^3 \cdot min^{-1}$ of SF_6 before switching to a passivation cycle for 2 seconds at 85 atm $cm^3 \cdot min^{-1}$ of C_4F_8. After completing the etch, the wafer was soaked in deionized water within a sonic cleaner.

Images were taken with an optical microscope before and after etching for comparison. Metrology of the sample was realized using an atomic force microscope (AFM) and a scanning white light interferometer (SWLI). An AFM was chosen to analyze surface roughness line profiles below 10 μm, while the SWLI was used to look at the surface form of the etched area.

RESULTS

To determine the feasibility of using deep reactive ion etching as an artifact manufacturing process, a single wafer was manufactured using photolithography and DRIE to an etch depth of 19 μm. Before measuring the surface, the wafer was examined with an optical microscope. Originally it was thought that the aluminium and silicon surfaces were contaminated; however there was no visible difference after cleaning the surfaces with deionized water in a sonic bath. Therefore, the speckling of the surface seen in FIGURE 4 was produced during the DRIE process.

The surface was measured using an AFM and SWLI. The measured R_q of a single profile scan using the AFM is 26.1 nm. For the SWLI, the R_q pre-filtering is 7.2 nm and when filtered below a wavelength of 8 μm, R_q decreased to 6.5 nm. See FIGURE 5 for an AFM scan and SWLI image.

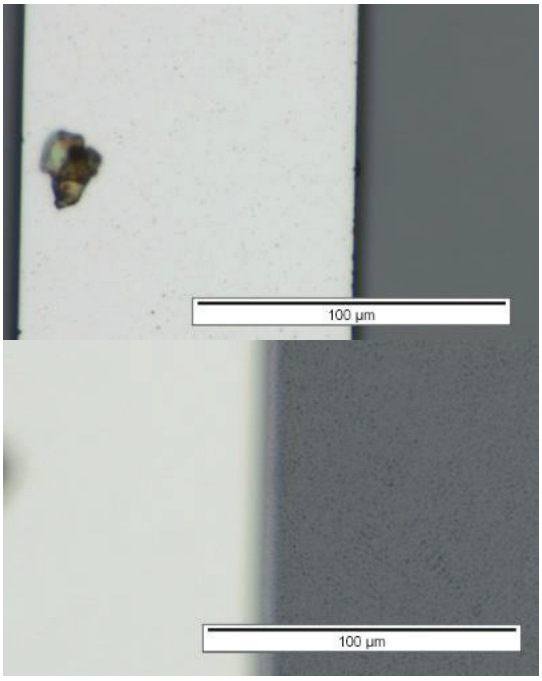

FIGURE 4. Optical images of the wafer after etching showing surface speckling. Top image shows the aluminium in focus and bottom image is focused on the silicon surface.

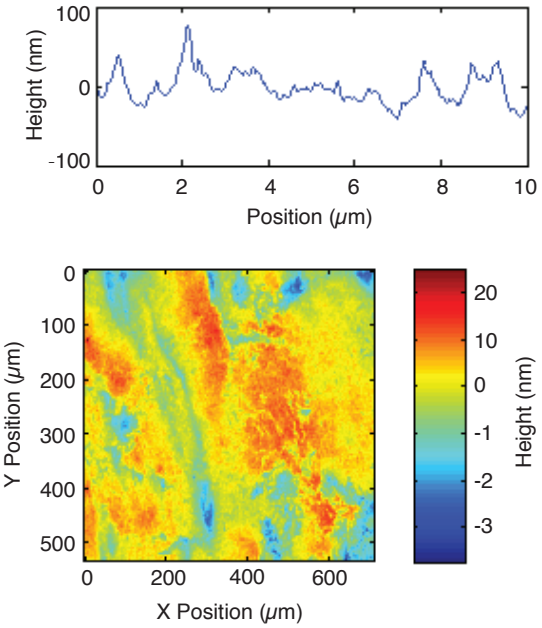

FIGURE 5. AFM scan and SWLI image of the surface after etching to a depth of 19 µm.

Process related problems were encountered during this initial study. These are thought to be

one source of added roughness, with another source being the use of non-optimized etching system parameters. Improvement to the surface quality is expected through further refinement of the process and optimization of the parameters influencing surface roughness during etching.

CONCLUSION

While the DRIE process is capable of producing the feature sizes and depths to make the calibration artifact, most research has focused on the surface roughness of the sidewalls rather than the base surface finish. The groups that have measured the surface finish using different etching techniques show DRIE is capable of providing the nanometer surface roughness sought in artifact development [8,9]. The preliminary results of this study were to assess feasibility of producing roughness below 10 nm to ensure uniform phase variation over the X-ray beam diameter. To verify the performance of DRIE as a manufacturing process, a single specimen was developed measured using AFM and SWLI. The results of the AFM study and SWLI were in the nanometer range and are a positive indicator that DRIE can be used to develop the artifact.

FUTURE WORK

Processing parameters can often vary from machine to machine. To determine the optimal processing parameters to meet the requirements for a micro-CT artifact, additional refinement of our current process is necessary. To address this, silicon wafers have been produced with optimal resist coatings and await the etching and subsequent metrological analysis. A different mask has been chosen for the new batch of wafers that contains more features comparable in size to the requirements of the final artifact design. Another change made to the manufacturing process is eliminating using the aluminium hard mask lift-off process step. Etching the wafers with the photoresist will minimize complication in the process that could introduce errors and reduce production time. Two processing parameters that have been shown to impact topography are the automated pressure control and the etching time [8], and will be the first investigated.

Although the X-ray system that will be utilized for the phase-contrast micro-CT study is in development, multiple silicon interferometer monoliths have been manufactured and the X-ray system is currently able to perform absorption-contrast linear and rotational scanning. Tests will initially be performed on the artifact samples using absorption-contrast prior to implementing the phase shifting interferometry.

ACKNOWLEDGEMENTS

Research funding for this project has been provided by the Center for Precision Metrology's affiliates program at the University of North Carolina at Charlotte.

REFERENCES

[1] Bonse U, Hart M. An X-ray Interferometer. Appl Phys Lett 1965;6:155–6.

[2] Elliott JC, Dover SD. X-ray Microtomography. J Microsc 1982;126:211–3.

[3] Momose A. Demonstration of Phase-contrast X-ray Computed Tomography using an X-ray Interferometer. Nucl Instruments Methods Phys Res Sect Accel Spectrometers Detect Assoc Equip 1995;352:622–8.

[4] Wilkins SW, Gureyev TE, Mayo SC, Nesterets YI, Paganin DM, Pogany A, et al. Hard X-Ray Phase-Contrast Imaging for Medical Applications — Physicist's Dream or Radiologist's Mainstream? AIP Conf Proc 2007;902:33–6.

[5] Diemoz PC, Bravin A, Coan P. Theoretical Comparison of Three X-ray Phase-contrast Imaging Techniques: Propagation-based Imaging, Analyzer-based Imaging and Grating Interferometry. Opt Express 2012;20:2789–805.

[6] Momose A, Takeda T, Itai Y, Hirano K. Phase-contrast X-ray Computed Tomography for Observing Biological Soft Tissues. Nat Med 1996;2:473–5.

[7] Davis TJ, Stevenson AW. Direct Measure of the Phase Shift of an X-ray Beam. J Opt Soc Am 1996;13:1193–8.

[8] Kuo-Shen Chen, Ayon AA, Zhang X, Spearing SM. Effect of process parameters on the surface morphology and mechanical performance of silicon structures after deep reactive ion etching (DRIE). Microelectromechanical Syst J 2002;11:264–75.

[9] Chandrasekaran S, Sundararajan S. Effect of microfabrication processes on surface roughness parameters of silicon surfaces. Surf Coatings Technol 2004;188–189:581 – 587.

INFLUENCE OF SENSOR SENSITIVITY ON ROUNDNESS MEASUREMENT BY A NEW SUCCESSIVE THREE POINT METHOD

Yutaka Uda[1], Shoichi Shimada[1], Daichi Iemata[1] and Satoshi Kiyono[2]
[1]Department of Mechanical Engineering
Osaka Electro-communication University
Neyagawa, Osaka, Japan
[2]Precision Measurement Laboratory
Sendai, Miyagi, Japan

INTRODUCTION

The successive three point method is a useful technique for on-machine measurement of roundness especially at the factory site because of its simple and easy calculation algorithm. However the method has a restriction in detectable spatial frequency. Previously, a new successive three point method, which can evaluates the radial figure without any undetectable harmonic component, using recurrence formula was proposed and the effectiveness of the method is confirmed by numerical simulation by the authors [1]. In this study, the influences of different sensitivities among three displacement sensors on the roundness measurement is investigated by numerical simulations and measuring experiment.

PRINCIPLE OF THREE POINT METHOD FOR ROUNDNESS

The arrangement of three displacement sensors is shown in Figuer 1. φ is the setting angle between the sensors. $f(\theta_i)$ and $m(\theta_i)$ are discontinuous radial figure of the specimen and output of the sensor obtained at equal angular interval of φ along a circumference line of the specimen, as shown in Figure 2. $e_x(\theta_i)$ and $e_y(\theta_i)$ are the error motion of the rotary table. When 2π is not divisible by φ without remainder, the radial figure profile can be evaluated without any undetectable harmonic component. The periodic revolution *M*, which is the number of revolution necessary to obtain date at an identical position along the circumference, is larger than 2. The number of data point *n* within the period can be expressed as Eq. (1).

$$n=2\pi*M/\varphi \quad (1)$$

The output signals of the sensors are expressed in Eqs.(2) to (4).

$$m_1(\theta_i)=f(\theta_{i-1}-\varphi)+e_x(\theta_i)\cos\varphi-e_y(\theta_i)\sin\varphi \quad (2)$$

$$m_2(\theta_i)=f(\theta_i)+e_x(\theta_i) \quad (3)$$

$$m_3(\theta_i)=f(\theta_{i+1}+\varphi)+e_x(\theta_i)\cos\varphi+e_y(\theta_i)\sin\varphi \quad (4)$$

To eliminate the error motion $e_x(\theta_i)$ and $e_y(\theta_i)$, the differential output signals $\mu_1(\theta_i)$ and $\mu_2(\theta_i)$ are calculated as expressed by Eqs.(5) and (6).

$$\mu_1(\theta_i)=m_1(\theta_i) - m_2(\theta_i)\cos\varphi \quad (5)$$

$$\mu_2(\theta_i)=m_2(\theta_i)\cos\varphi - m_3(\theta_i) \quad (6)$$

The second order difference of the output signals $\Delta\mu(\theta_i)$ is expressed by Eq.(7).

$$\Delta\mu(\theta_i)=\mu_1(\theta_i) - \mu_2(\theta_i)$$
$$= f(\theta_i-\varphi) - 2f(\theta_i)\cos\varphi + f(\theta_i+\varphi) \quad (7)$$

Using the Eqs.(5), (6) and (7), the recurrence formula of the radial figure profile is obtained as Eq.(8).

$$f(\theta_i+\varphi)=\Delta\mu(\theta_i)+2f(\theta_i)\cos\varphi - f(\theta_i-\varphi) \quad (8)$$

Eq.(8) shows that the radial figure $f(\theta_i+\varphi)$ can be calculated using $f(\theta_i)$and $f(\theta_i-\varphi)$ with the second order difference of output signals of the sensors #1 to #3. To solve successively the recurrence formula, two initial values of radial figure $f(\theta_0)$ and $f(\theta_1)$ are necessary when the sensors #1 and #2 are at the initial start position, $\theta=-\varphi$ and 0, respectively.

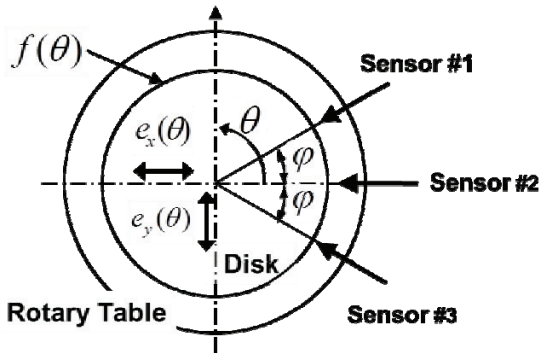

Figure 1 Arrangement of sensors in successive three point method for roundness measurement

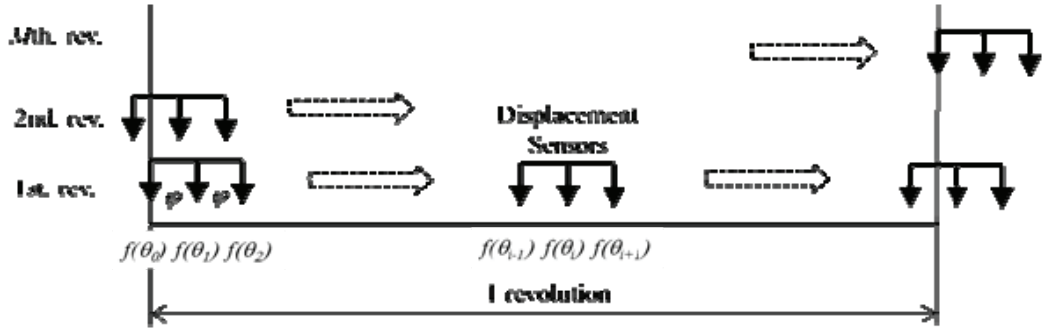

Figure 2. A concept of roundness measurement by successive three point method

NUMERICAL SIMULATION OF ROUNDNSS MEASUREMENT

Generally, in roundness measurement of machine elements, the higher order harmonic components are not considered to influence on mechanical accuracy of the machine. Therefore, the lower components than 10th are investigated in this work. Based on the sampling theory, to measure all of harmonic components lower than 10th, more than 40 measuring points are necessary along the circumference. Therefore, n, M and φ were determined to be 45, 4 and 32 deg., respectively from the Eq. (1). In the simulations, three specimens are measured including individually 3rd, 4th and 9th harmonic components. The roundness of all specimens was supposed to be 10μm as shown by blue dotted line in Figure 3. To investigate the influence of different sensitivities among three sensors on roundness measurement, simulations were carried out replacing the sensor 2 by a sensor with 150% sensitivity of the others.

Measured roundness values of the specimens were magnified to be 145%, 167% and 178%, respectively, of the original values supposed as shown by red solid line in Figure 3. The magnification of roundness is also influenced by the order of harmonic component as shown in Figure 4. The amplitude of higher order component seems to have larger magnification.

To investigate the influence of sensor sensitivity on magnification, the amplitude of radial figure of the specimens with 3rd, 6th and 9th harmonic components were measured, changing the sensitivity of sensor 2 from 50% to 150%. The linear relations are observed between sensor sensitivity and magnification on these three harmonic components as shown in Figure 5(a). However, on the specimens with 10th and 11th harmonic components, the magnification is about 10 times as large as that of lower harmonic components. And the relation between sensor sensitivity and amplitude has a minimum value as shown in Figure 5(b). The results show that the difference in sensitivity should be suppressed within a few percent for reliable measurement. And that the setting angle between sensors may dominant the limitation in measurable order of harmonic component.

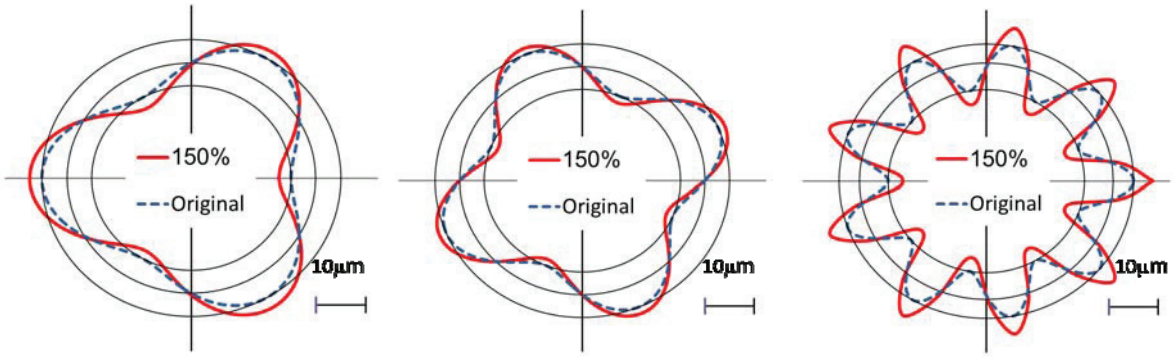

(a) Radial figure of specimen with 3rd harmonic component
b) Radial figure of specimen with 4th harmonic component
(c) Radial figure of specimen with 9th harmonic component
Blue dotted line : radial figure supposed Red solid line : radial figure measured

Figure 3 Influence of sensitivity of sensor 2 on roundness

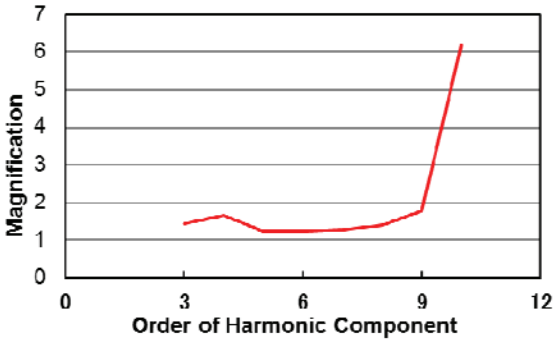

Figure 4 Influence of the order of harmonic component on magnification of amplitude of the individual component when the sensitivity of sensor 2 is 150%

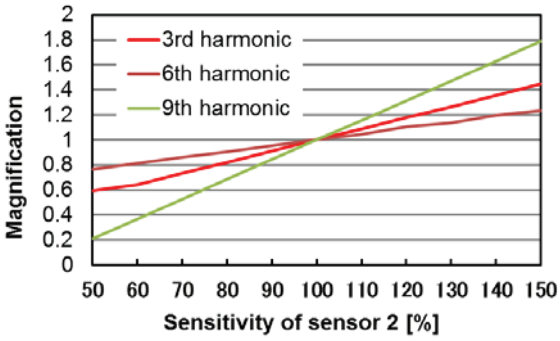

(a) 3rd, 6th and 9th harmonic components

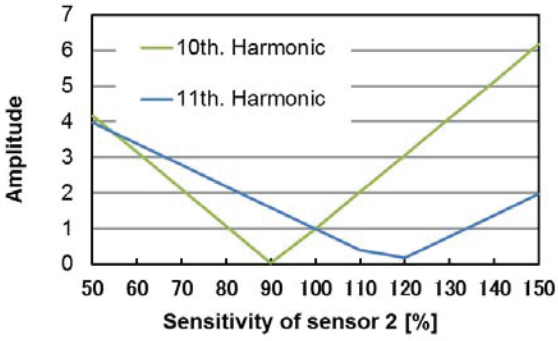

(b) 10th and 11th harmonic components

Figure 5 Influence of the sensitivity of sensor 2 on the magnification of different harmonic components

EXPERIMENT RESULTS

Measuring experiments were carried out replacing the sensor 2 by the sensor with 140% sensitivity of the others. The objective specimen is a disk with remarkably large 3rd harmonic component as shown in Figure 6. The roundness of the disk was 16μm measured by a commercial measuring instrument.

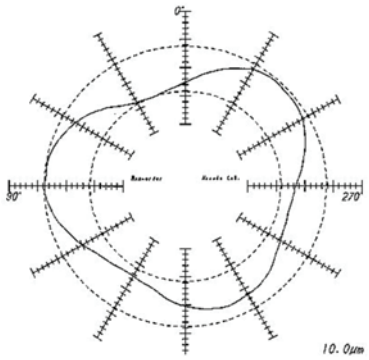

Figure 6 Radial figure of objective disk

The roundness measured was deteriorated to the level more than 10 times worth than the original value and characteristic feature of 3rd harmonic component cannot be observed as shown in Figure 7(a). The error motion of the rotary table cannot be eliminated due to the difference of sensor sensitivity. Figure 7(b) shows the figure profile obtained after the numerical compensation of sensitivity of sensor 2 to 100%.

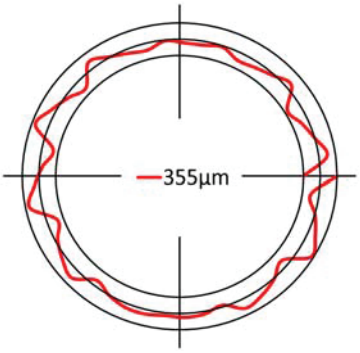

(a) 140% sensitivity

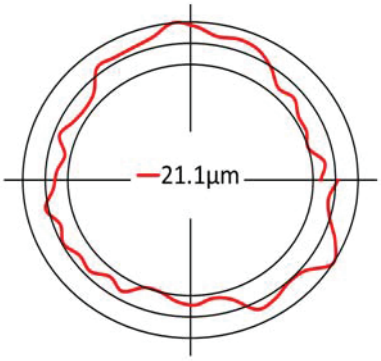

(b) After compensation to 100%

Figure 7 Results of measuring experiments replacing the sensitivity of sensor 2

The figure profile and roundness approaches to the original ones. However, higher order harmonic components than 10 are still remaining. Numerical simulation show that the figure profiles of some higher order harmonic components are not occasionally eliminated depending on the order even when all sensors have identical sensitivity. To detect these higher order components, the number of measuring point and the setting angle between sensors should be determined properly.

Another problem is observed in the figure profile shown in Figure 7. The radial figure profile at the beginning of measurement $f(\theta_b)$ did not coincide with that at the end of measurement $f(\theta_b+2\pi)$.

Figure 8 shows the results of numerical simulation to investigate the influence of error motion of rotary table on roundness measurement, especially in case of the error motion not synchronizing with the revolution of table. In this case, the number of peak of the error motion included in one revolution of rotary table is not expressed by integer. An example is seen in an error motion due to rolling of ball in ball bearing. The rotary table used in the simulation is supposed to have the error motion the number of peak included in one revolution and the amplitude are 8.9 and 50% of the roundness of specimen, respectively. The results show that such kind of error motion causes the discontinuous figure profile when a sensor has different sensitivity as shown in figure 8(a). However, when the sensitivities of sensors are identical, the figure profile can be obtain correctly as shown in Figure 8(b).

The discontinuous figure profiles and remaining high order component observed in the results of measuring experiments in Figure 7 are due to a difference in sensitivity of the sensors caused as a result of alignment error of the sensors.

SUMMERY

Based on both a numerical simulation and a measuring experiment, the influence of sensor sensitivity on roundness measurements is investigated. The difference of sensitivity among three sensors may cause the large measuring error due to magnifying the amplitude of higher order harmonic components. The difference in sensitivity should be suppressed within a few percent for reliable measurement. The setting angle between sensors may dominant the limitation in measurable order of harmonic component. An error motion the period of which is not synchronizing with the revolution of rotary table causes the discontinuous figure profile when the sensitivities of sensors are not identical.

REFERENCES

[1] Uda Y, Shimada S, Kiyono S. “A New Successive Three Point Method Of Roundness Measurements“. 2012; Proc. 27-ASPE Annual Meeting

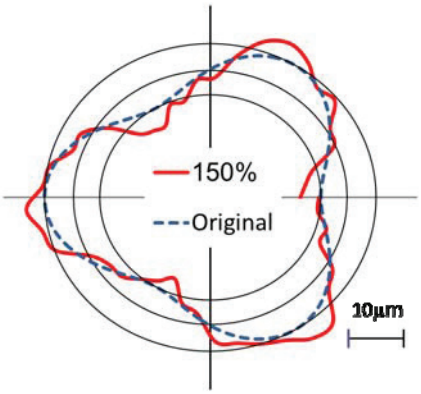

(a) When the sensitivity of sensors 2 is 150% of the others

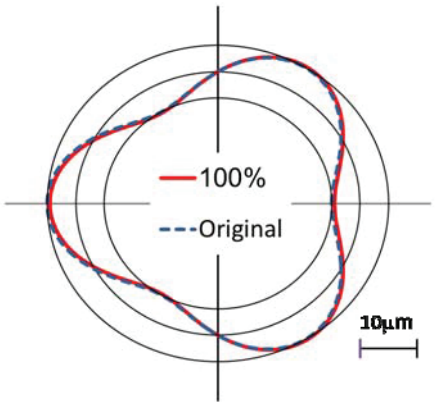

(b) When the sensitivity of all sensors are identical

Figure 8 Influence of error motion of rotary table and difference of sensor sensitivity on roundness measurement. Specimen has 3rd harmonic component the amplitude of which is 10μm. Rotary table has the error motion the number of peak in one revolution and the amplitude of which are 8.9 and 5μm, respectively.

Study on High Speed 3D Measurement of Tooth Plaster Model using 3 Light-Sections Method

Takanori YAZAWA[1], Yutaka SAKURAGi[1], Youichi NISHIGUGHI[2], Tsuyoshi SOEJIMA[1], Megumu KUROIWA[3], Tatsuki OTSUBO[1], Yasuhiko OUGIYA[1] and Tatsuhiro KOJIMA[2]
[1]Graduate School of Engineering
Nagasaki University
Nagasaki City, Nagasaki Prefecture, Japan
[2]Graduate School of Science and Technology
Nagasaki University
Nagasaki City, Nagasaki Prefecture, Japan
[3]Em Laboratory Corporation
Nagasaki City, Nagasaki Prefecture, Japan

INTRODUCTION

Currently, in the dental area, such as skill level evaluation of dental education, 3D tooth figure is measured using a tooth plaster model. However, in the conventional measurement system, the measuring time including the process from getting one image to synthesis of the calculated results is about 2 hours. If it can be shortened to about 10 minutes, the number of measurement and evaluation can be increased significantly, so it can be expected to improve the measurement time for the quality of education and skills. The authors have proposed a new measuring method[1][2][3], which is called 3-lines optical cutting and scanning method, for the above problems. In this paper, the principle of the 3-lines optical cutting and scanning method is explained, calculation process of 3D figure is maintained and experiments are carried out.

PRINCIPLE OF MEASUREMENT

The conventional method to measure 3D figure for the tooth model is the general optical cutting method. Fig.1 (a) shows the schema of this method. The laser line, which is made by a rotating polygon mirror and an f-θ lens in many cases, is irradiated to the tooth model. When the camera is installed on the diagonal of the laser line on the tooth model, the laser line on an image shows cross section of the tooth model under the laser line. The model moves one step about sub mm depending on required resolution perpendicular to the laser line. One surface figure is measured and calculated by moving and imaging are repeated whole of tooth model. In conventional equipment, total moving and imaging time, which is called single measurement time, is about 5 minutes.

Fig.1 (b) shows the principle of the 3-line sections method. In this method, parallel and equal intervals 3 laser lines are used to measure the surface figure. The interval is about 1/3 of maximum length of tooth model. Therefore, 3 cross sections of the tooth model can be obtained at the same time. The imaging is

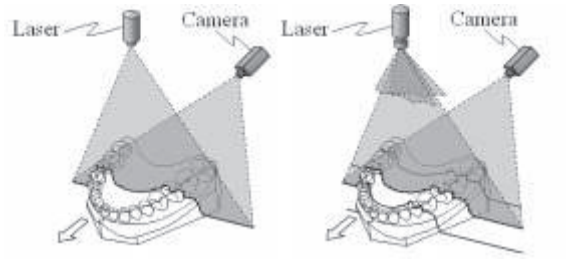

(a) Conventional method (b) Proposed method
FIGURE 1. Principle of 3-line sections method

carried out into scanning instead of stopping and moving. The error generated by scanning is dependent on scanning speed and shooter speed. Comparison of the measurement time of 3-line sections method and the conventional method is shown in Table 1. The main requirement is less than 0.1mm resolution. This table shows that possibility of measurement time is less than 10 minutes.

EXPERIMENTAL AND CALCULATION METHOD

Fig.2 shows the schema of experiments and the experimental conditions are shows in table 2. The 3 parallel lines are made by the diffraction grating, the laser line generator lens (Edmond optics NT43-473) and the cylindrical lens. The scanning speed is 3mm/sec and the shooter speed is 1/1000 sec. The measurement figure and evaluation parameters are shown in Fig.3. Fig.4 shows the flow of image processing to calculate the cross section at the same time. Calibration was performed by moving the pitch 0.5mm up to 25.0mm from the origin for each stage Z-axis should be noted.

TABLE 1. Comparison of measurement time

		Light-section method (conventional method)	line beam sweeping method (3 lines)
Single measurement time		**5 min.**	**17.8 sec.**
Dual partitioning of single face		2 times	2 times
Turn over for complement of blind area	Top surface	5 times	5 times
	Side surface	5 times	5 times
Data acquisition time		**100 min.**	**5 min. 56 sec.**
Data processing time		+20 min.	+4 min.
Total measurement time		120 min.	9 min. 56 sec.

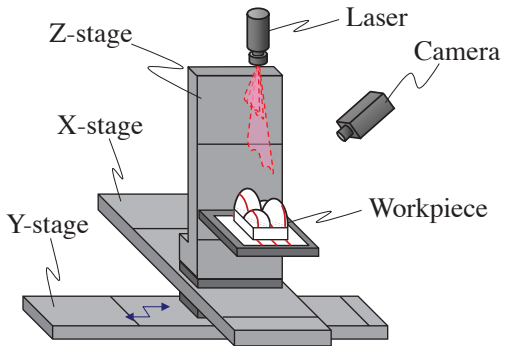

FIGURE 2. Schema of proposal method

EVALUATION OF EFFECTIVENESS ON EXPERIMENTL METHOD

Fig.5 shows example of 3 lines image, Fig.6 shows the side view of each line and synthesizing result and Fig.7 shows 3D view of each line and synthesizing result. It was found in these figures,

(a)Measurement areas of each line are different.

(b)Synthesizing of 3 measuring results can be correction of each non measurement area, but there is blind area of the camera.

To correct of the blind area, the attitude of the measured object must be changed.

In case of two lines overlap as shown in Flg.8, it is difficult to automatically identify whether any line.

TABLE 2. Experimental conditions

Workpiece	Shape	Dome × 4
	Size	30 × 30 × 20mm
	Material	ABS plastic
Camera Device Drivers E!Kit-CAM-USB	Image sensor	1/4 CMOS Color
	Pixel size	2.8 × 2.8mm
	Effective pixels	1280(H) × 1024(V)
	Lens	F=2.8 / f=3.56mm
Laser diode module	Design wave length	635nm
	Output	5mW(Maximum)
	Head type	Multi 3 line
	Angle of between lines	5.0˚
X,Y,Z-stage Sigma Koki SGSP20-85,35	Max displacement	85(X,Y),35mm(Z)
	Accuracy of positioning	0.007mm
	Displacement of each pulse	0.001mm

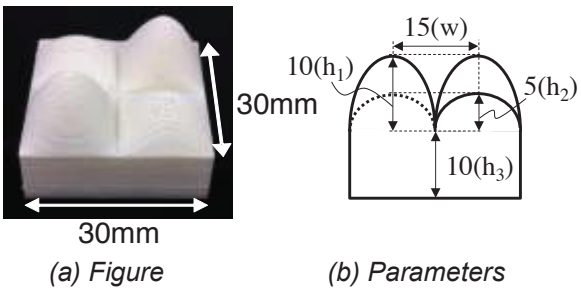

(a) Figure *(b) Parameters*

FIGURE 3. Measurement figure and evaluation parameters

IDENTIFICATION OF 3 LINES

In this paper, 3 lines are identified by a color CMOS camera and three optical lines of different wavelength. The additional conditions of experiment are shown table 3. Fig.9 shows the flow of identification of 3 lines and Fig.10 shows the example of identification. Fig.10 (a) is the binarization image and Fig.10 (b) is identification result using labeling result. These figures show that it was possible to distinguish between overlapping lines.

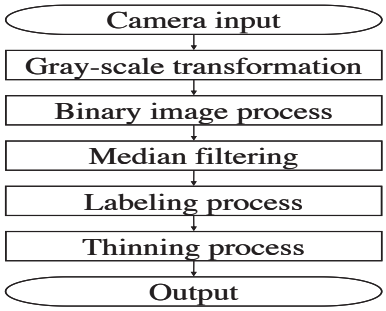

FIGURE 4. Image processing flow

FIGURE 5. Example of 3 lines image

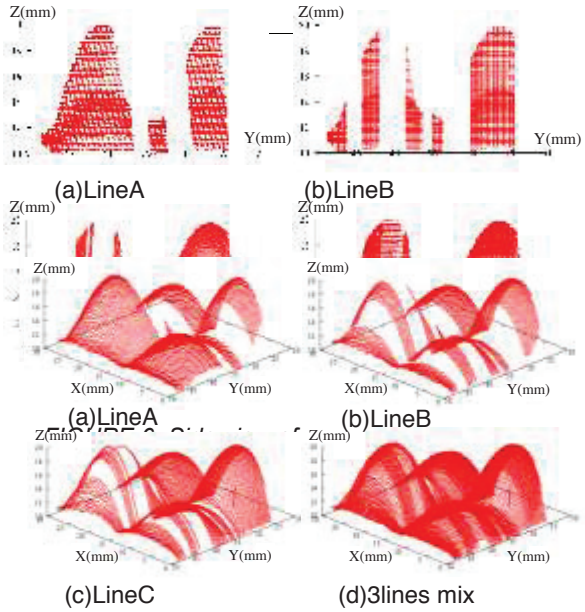

FIGURE 7. 3D view of measurement results of each line

Influence of wavelength on measurement accuracy is shown in Fig.11. Since maximum difference between each wavelength is about 100μm, this method is enabled.

EVALUATION OF MEASUREMENT FOR TOOTH PLASTER USING 3 LIGHT-SECTIONS METHOD

A tooth plaster model, as shown in Fig.12 (a), was measured by 3 light-sections method. The measurements were performed in five portions, which are top right, top left, right side, left side and front. The measurement result of any portion was an average of five times

FIGURE 8. Example image of two lines overlap

TABLE 3. Additional conditions of experiment

Laser diode module	Red laser	Design wave length	635nm
		Output	5mW(Maximum)
	Green laser	Design wave length	532nm
		Output	0.9mW(Maximum)
	Blue laser	Design wave length	405nm
		Output	0.9mW(Maximum)
	Head type		Single line

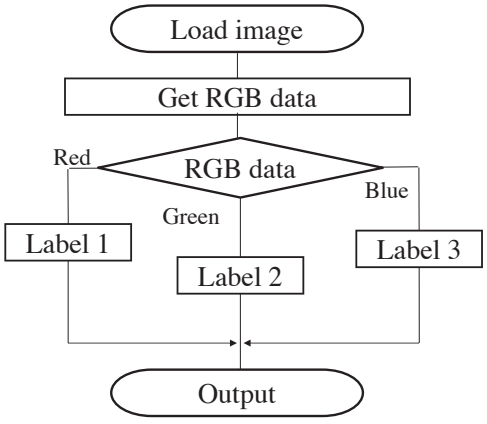

FIGURE 9. Identification flow of 3 lines

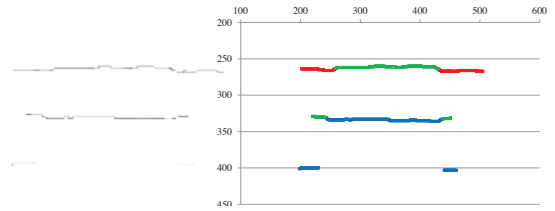

(a) Binarization image (b) Image after labeling

FIGURE 10. Example of identification

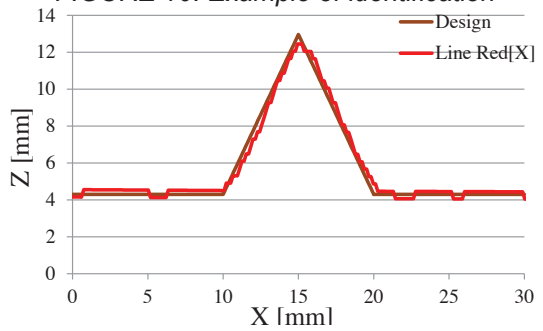

(a) Measurement section by red line laser

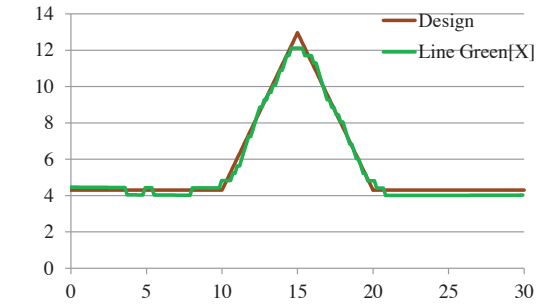

(b) Measurement section by green line laser

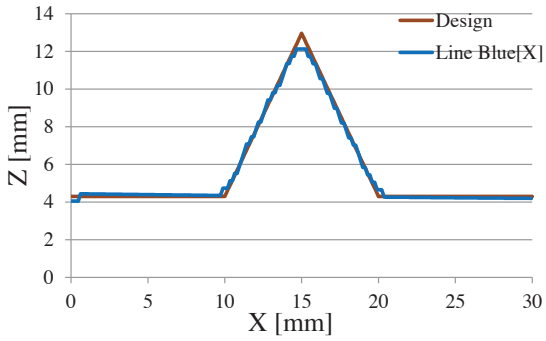

(c) Measurement section by blue line laser

FIGURE 11. Influence of wavelength on measurement accuracy

measurement. Feature point is extracted in order to synthesize the measurement results. Fig.12 (b) shows the synthesize result of measuring the tooth plaster model. One measurement took an average of 26 seconds. The total time concerning posture change, feature point extraction and calculation was 110 seconds. The total measurement time is about 12 minutes 40 seconds. This time is somewhat longer than the target time, but it became shorter about 90% than the time of the conventional method (about 2 hours).

CONCLUSIONS

In this paper, high-speed measurement for the plaster tooth model is objective. We proposed the 3-line sections method. Calculation process of 3D figure was maintained, prototype of this measurement system was made and basic experiments were carried out. 3 lines are identified by a color CMOS camera and three optical lines of different wavelength. Finally, a tooth plaster model was measured by 3 light-sections method. These results introduce the effectiveness in high-speed measurement for the plaster tooth model using proposal method.

REFERENCES

[1] T.SOEJIMA, T.YAZAWA et.al; Study on high-speed contactless 3D measurement for plaster figure of jaw, JSME Kyusyu. No.64 PP283-284 (2011.3) in Japanese

[2]T.YAZAWA, Y.NISHIGUCHI et.al; Study on high-speed contactless 3D measurement for plaster figure of jaw, ABTEC2012. p293-294, (2012.8) in Japanese

[3] Takanori YAZAWA, Youichi NISHIGUCHI et.al; Study on high-speed contactless 3D measurement for plaster figure of jaw, IEEE Xplore of ISOT 2012, p1-2 (2013.1)

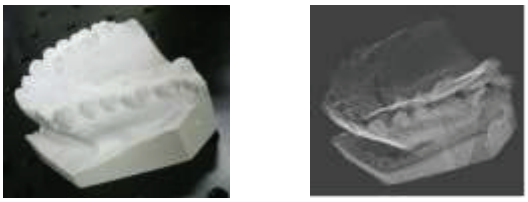

(a)Tooth plaster model (b) Measurement

FIGURE 12. Measurement of model

(a) Conventional method (b) Proposed

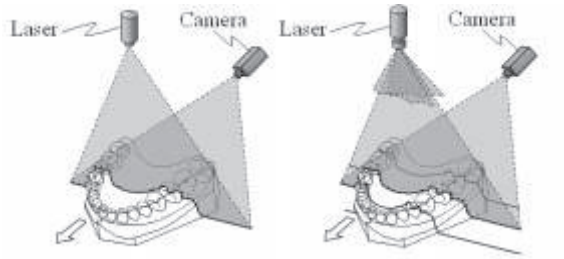

(a) Conventional method (b) Proposed method

FIGURE 1. Principle of 3-line sections method

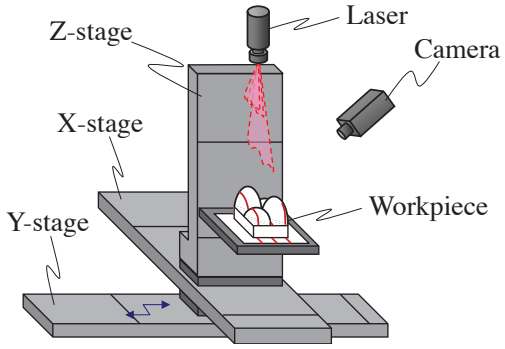

FIGURE 2. Schema of proposal method

TABLE 1. Comparison of measurement time

		Light-section method (conventional method)	line beam sweeping method (3 lines)
Single measurement time		**5 min.**	**17.8 sec.**
Dual partitioning of single face		2 times	2 times
Turn over for complement of blind area	Top surface	5 times	5 times
	Side surface	5 times	5 times
Data acquisition time		**100 min.**	**5 min. 56 sec.**
Data processing time		+20 min.	+4 min.
Total measurement time		120 min.	9 min. 56 sec.

TABLE 2. Experimental conditions

Workpiece	Shape	Dome × 4
	Size	30 × 30 × 20mm
	Material	ABS plastic
Camera Device Drivers E!Kit-CAM-USB	Image sensor	1/4 CMOS Color
	Pixel size	2.8 × 2.8mm
	Effective pixels	1280(H) × 1024(V)
	Lens	F=2.8 / f=3.56mm
Laser diode module	Design wave length	635nm
	Output	5mW(Maximum)
	Head type	Multi 3 line
	Angle of between lines	5.0˚
X,Y,Z-stage Sigma Koki SGSP20-85,35	Max displacement	85(X,Y),35mm(Z)
	Accuracy of positioning	0.007mm
	Displacement of each pulse	0.001mm

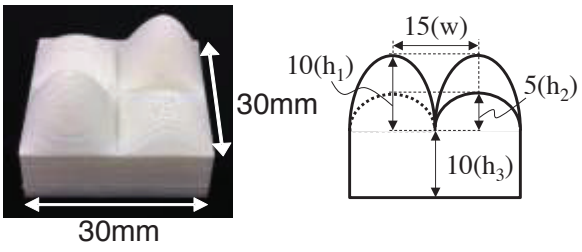

(a) Figure (b) Parameters

FIGURE 3. Measurement figure and evaluation parameters

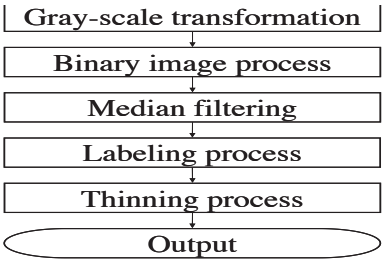

FIGURE 4. Image processing flow

FIGURE 5. Example of 3 lines image

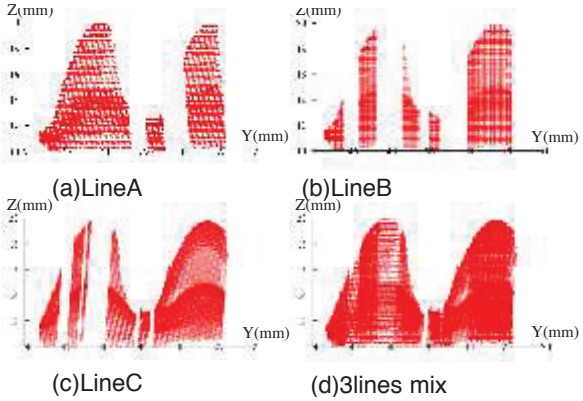

FIGURE 6. Side view of measurement results of each line

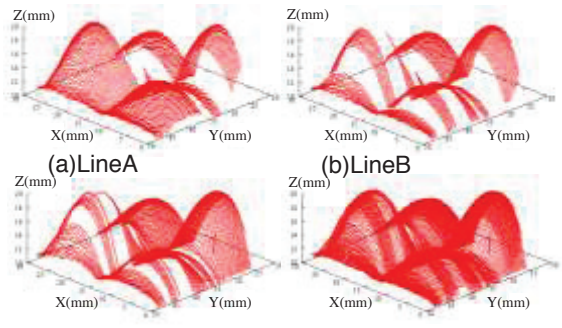

FIGURE 7. 3D view of measurement results of each line

FIGURE 8. Example image of two lines overlap

TABLE 3. Additional conditions of experiment

Laser diode module	Red laser	Design wave length	635nm
		Output	5mW(Maximum)
	Green laser	Design wave length	532nm
		Output	0.9mW(Maximum)
	Blue laser	Design wave length	405nm
		Output	0.9mW(Maximum)
	Head type		Single line

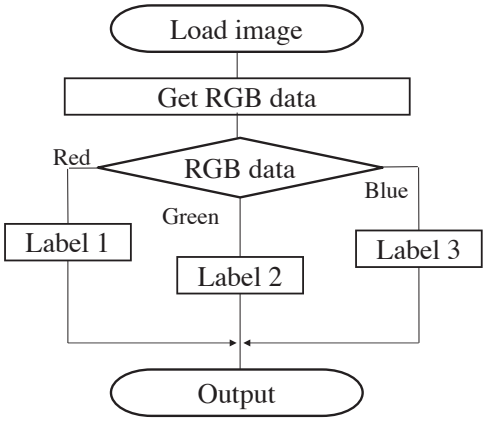

FIGURE 9. Identification flow of 3 lines

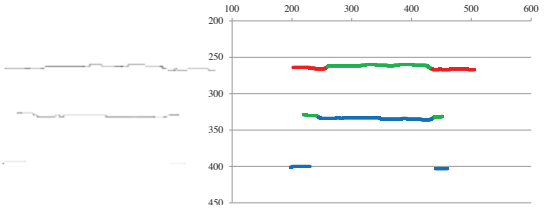

(a) Binarization image (b) Image after labeling

FIGURE 10. Example of identification

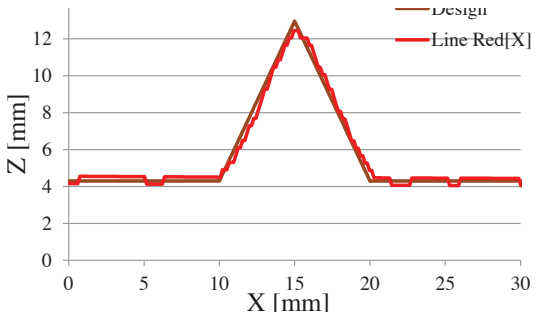

(a) Measurement section by red line laser

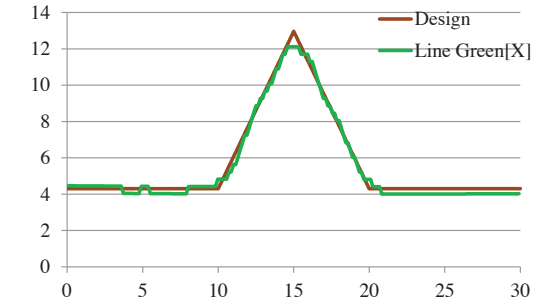

(b) Measurement section by green line laser

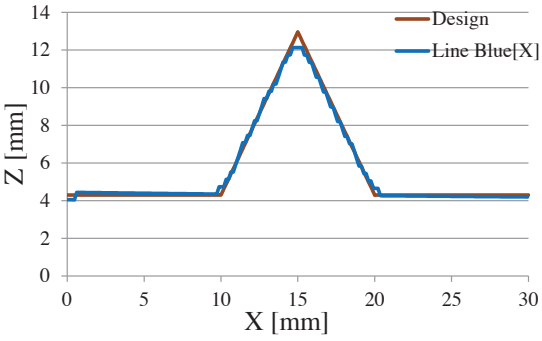

(c) Measurement section by blue line laser

FIGURE 11. Influence of wavelength on measurement accuracy

FIGURE 12. A tooth plaster model

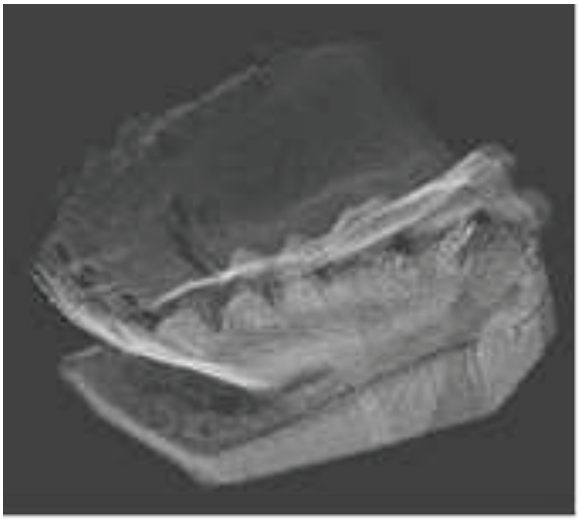

FIGURE 13. Measurement result of the tooth plaster by 3-line sections method

HIGH EFFICIENCY MILLING OF STEAM TURBINE BLADE

Xin. Yuan[1], Takanori. Yazawa[1], Yukio Maeda[2],
Shinichi Kogusu[3], Yasuhiko Ougiya[1] and Tatsuhiro Kojima[1]
[1]Graduate School of Engineering
Nagasaki University
Nagasaki, Japan
[2]Intelligent Stems Design Engineering
Toyama Prefectural University
Toyama, Japan
[3] Industrial Technology Center of Nagasaki
Nagasaki, Japan

INTRODUCTION

Steam turbine blade, which is typically 60 inches in length, has a complex shape and needs to be made out by a material of low thermal conductivity to withstand temperatures above 600 degree Celsius. Since a small ball end mill is often used in conventional method (in Figure 1), it has to choose the small pick feed (*Pf*) to satisfy surface roughness requirement. Moreover, a grinding operation is needed to smooth the machined surface after the milling. Therefore, it has limitations to improve the milling efficiency.

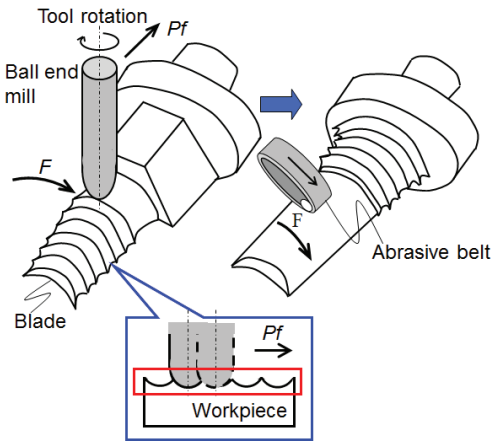

FIGURE 1. Conventional method.

As the solution, authors have proposed a new method Linear Interpolation Milling (LIM) as shown in Figure 2 [1]. In LIM, a special taper end mill is used instead of a small ball end mill and the cutting edge keeps parallel to the pick feed direction. It makes to enlarge the pick feed. Based on the results of validity when milling plane surface, this paper will presents the validity when milling curved surface by modeling experiments.

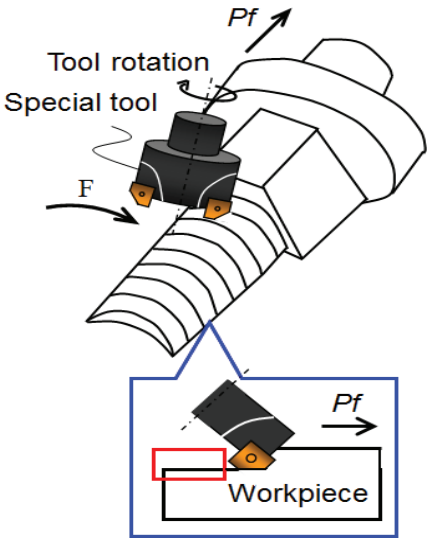

FIGURE 2. Linear Interpolation Mill.

Computer-aided manufacturing (CAM) systems as well as computer numerical control (CNC) machine tools are widely used in today's manufacturing industries [2]. Many research have

done the work to generate tool paths using different approaches [3-6]. However, current commercial CAM is difficult to generate the tool path for the proposed method. Due to this, the objective of this work is to solve it and obtain a high accuracy surface, this paper will present an implementing work in automatic generation of 5-axis tool paths and NC code for the special taper end mill, and then verify the validity through modeling experiments of sphere.

CONCEPTUAL APPROACH

Because the work is the primary stage of special CAM development, it will take no account of tool path optimization. This section will introduce the definitions of the special tool and the parametric surface, and the NC data generation by software MATHEMATICA 9.0.

Tool Definition

Instead of the ball end mill, the propose method uses a taper end mill to machine the steam turbine blade. Tool sectional view in XZ plane as shown in Figure 3, tr is the edge point of top end, $t\theta$ is angle of the taper edge, tp is the point at the cutting edge, v is the length from tr to tp, it is decided according to the defined point. ω is the angle in rotating direction relative to z axis. Eq. (1) represents the coordinate of arbitrary point on the cutting edge for a given tool, *tr* and *tθ* are known quantities.

$$\mathbf{tp}(v,\omega)=\begin{bmatrix}tx\\ty\\tz\end{bmatrix}=\begin{bmatrix}(tr+v\cos(t\theta))\cos(\omega)\\(tr+v\cos(t\theta))\sin(\omega)\\v\sin(t\theta)\end{bmatrix} \quad (1)$$

Tool Path

Before generating the tool path, it has to define the target shape. In order to facilitate the validity evaluation of the developed CAM, here, spherical surface is selected. Its formula is given in Eq. (3). Each point on the surface should own directionality, us and ue represent the start angle and end angle in rotating direction respectively, and vs and ve represent the

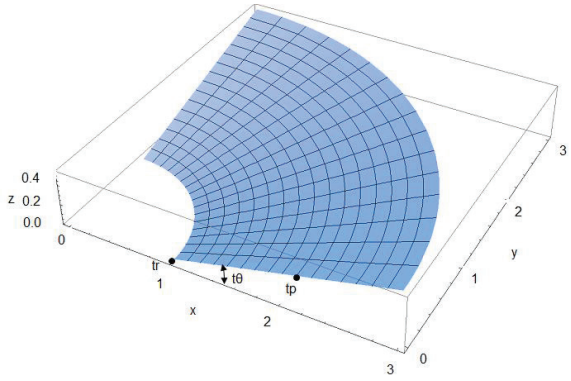

FIGURE 3. Schematic of the defined taper end mill.

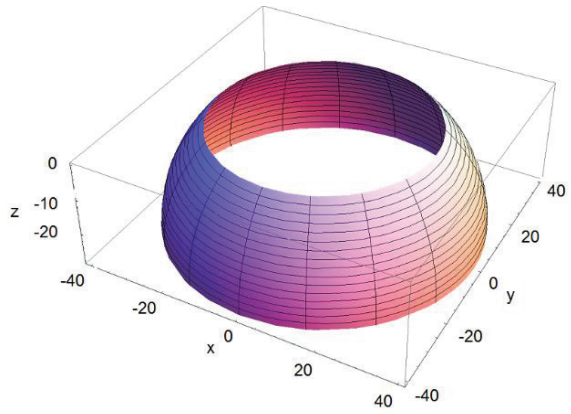

FIGURE 4. Target surface.

start angle and end angle in height direction respectively. Both the start angle is 0 degree, end angle in two direction are -360 degree and 45 degree. The u and v are the parametric variables of sphere, thus, $u \in [\, us, ue\,]$ and $v \in [\mathrm{vs}, \mathrm{ve}]$. When setting the curvature radius r 40mm, the target shape as shown in Figure 4.

$$\mathbf{w}(u,v)=\begin{bmatrix}wx\\wy\\wz\end{bmatrix}=\begin{bmatrix}r\cos(v)\cos(u)\\r\cos(v)\sin(u)\\r\sin(v)-r\sin(ve)\end{bmatrix} \quad (2)$$

Partial derivatives in u and v are calculated respectively. Thus, normal vector $\mathbf{n}\ (u,\ v)$ is the outer product of two tangent vector.

$$\mathbf{n}(u,v)=\frac{\frac{\partial \mathbf{w}(u,v)}{\partial u}\times\frac{\partial \mathbf{w}(u,v)}{\partial v}}{\left|\frac{\partial \mathbf{w}(u,v)}{\partial u}\times\frac{\partial \mathbf{w}(u,v)}{\partial v}\right|} \quad (3)$$

This experiment adopt the Contour machining. Pn is the number of tool path, i is the ordinal number of the tool path. Ps is the start tool path

angle in height direction, so it is equal to ve, Pd is the angle of two adjacent tool paths relative to the center of sphere, therefore, spatial parameter $\mathbf{b}(u)$ of the tool path can be derived. Each tool path formula is denoted as $\mathbf{cp}(u, i)$, as shown in Figure 5. Thus, its tangent vector $D\mathbf{cp}$ can be calculated (see Eq. (7)).

$$\mathrm{Pd} = (\mathrm{ve} - \mathrm{vs}) / (Pn - 1) \tag{4}$$

$$\mathbf{b}(\mathrm{u}) = \begin{bmatrix} u \\ Ps - Pd * i \end{bmatrix} (i \in [0, \mathrm{Pn} - 1]) \tag{5}$$

$$\mathbf{cp}(u, i) = \begin{bmatrix} rcos(Ps - Pd * i)\cos(u) \\ rcos(Ps - Pd * i)\sin(u) \\ rsin(Ps - Pd * i) - rsin(ve) \end{bmatrix} \tag{6}$$

$$\mathrm{D}\mathbf{cp} = \frac{\partial \mathbf{cp}(u,i)}{\partial u} \tag{7}$$

NC Generation

When generating the NC code, it has to take into the structure of the machine tool, here, we adopt the desktop 5-axis machine tool (TAKUMI UNC-100-M5), arrangement of each axis as shown in Figure 6. The L is the distance from pivot point of B axis to the bottom surface of tool, therefore, it includes the tool length, in the experiment, its length subtracts the tool length is 54.939mm. Depth of cut dd can be set according to the machining allowance. All the tool paths start at u is zero. The $\mathbf{cf}$ is the unit tangent vector of the cutter contact (CC) points in feed direction, $\mathbf{cn}$ is surface normal at the point, $\mathbf{cb}$ is their cross product, $\mathbf{ccp}$ (i) is the local coordinate of the starting point (see Figure 7).

$$\mathbf{cf} = \frac{\frac{\partial \mathbf{cp}(u,i)}{\partial u}}{\left|\frac{\partial \mathbf{cp}(u,i)}{\partial u}\right|} \tag{8}$$

$$\mathbf{ccp}(\mathbf{i}) = \begin{bmatrix} \boldsymbol{ccpx} \\ \boldsymbol{ccpy} \\ \boldsymbol{ccpz} \end{bmatrix} = \mathbf{cp}(0, i) \tag{9}$$

Using the calculated cc data, machine coordinate can be deduced to generate the corresponding NC data. At present, coordinate transformations of 5-axis machine tool all adopt 4×4 matrix. Eq. (10) includes all the coordinate information of CC points, Eq. (11) represents the translation in Z direction, Eq. (12) represents the rotation relative to C axis, and Eq. (13) is the rotation relative to B axis. When the tool is rotated relative to B axis, it has to compensate the rotation translation of cutting edge, that because when the tool rotated, the cutting edge cannot contact the target cutting point, so it cannot remove the material enough, as a result, the machining accuracy becomes low. Therefore, the inverse transform of the rotation is compensated. Additionally, $\mathbf{tp}$ in Eq. (13) is the midpoint of the cutting edge to satisfy the proposed method, in a word, the theoretical machining is the midpoint of the cutting edge is exactly at the cutting point.

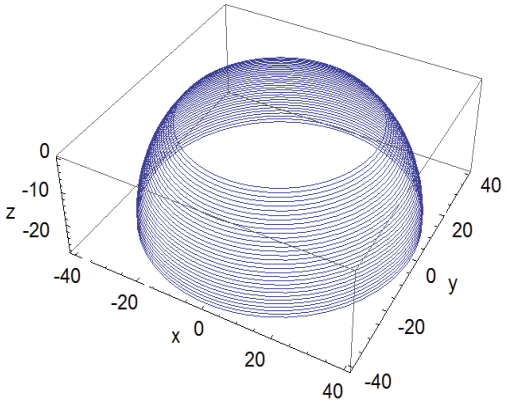

FIGURE 5. Tool path.

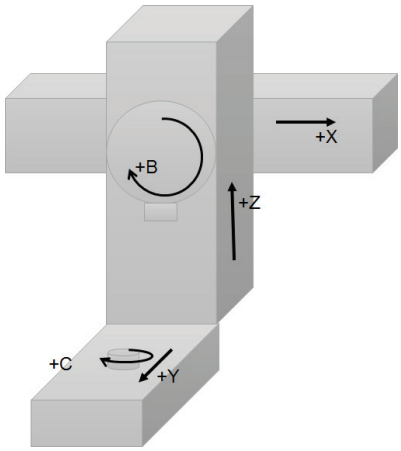

FIGURE 6. Structure of machine tool.

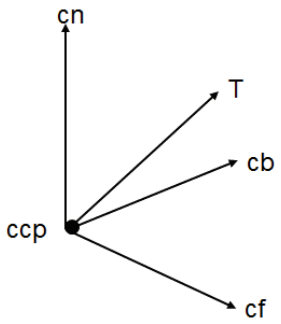

FIGURE 7. Local coordinate system.

$$\mathbf{M0}=\begin{bmatrix} cfx & cbx & cnx & ccpx \\ cfy & cby & cny & ccpy \\ cfz & cbz & cnz & ccpz \\ 0 & 0 & 0 & 1 \end{bmatrix} \tag{10}$$

$$\mathbf{M1}=\begin{bmatrix} 1 & 0 & 0 & 0 \\ 0 & 1 & 0 & 0 \\ 0 & 0 & 1 & dep \\ 0 & 0 & 0 & 1 \end{bmatrix} \tag{11}$$

$$\mathbf{M2}=\begin{bmatrix} \cos(\alpha) & -\sin(\alpha) & 0 & 0 \\ \sin(\alpha) & \cos(\alpha) & 0 & 0 \\ 0 & 0 & 1 & 0 \\ 0 & 0 & 0 & 1 \end{bmatrix} \tag{12}$$

$$\mathbf{M3}=\begin{bmatrix} \cos(\beta) & 0 & \sin(\beta) & -\cos(\beta)\mathrm{tpx}-\sin(\beta)\mathrm{tpz} \\ 0 & 1 & 0 & 0 \\ -\sin(\beta) & 0 & \cos(\beta) & \sin(\beta)\mathrm{tpx}-\cos(\beta)\mathrm{tpz} \\ 0 & 0 & 0 & 1 \end{bmatrix} \tag{13}$$

The $\mathbf{M4}$ is the inner product of the former four matrixes, it represents the overall coordinate transform when tool moves between two cutting points. Eqs. (15) and (16) mean that choose the forth row and third row as **pp** and **qq** respectively. In order to facilitate the calculation, we use px and so on to represent some value of the matrix.

$$\mathbf{M4}=\mathbf{M0}\cdot\mathbf{M1}\cdot\mathbf{M2}\cdot\mathbf{M3} \tag{14}$$

$$\mathbf{pp}=\begin{bmatrix} px \\ py \\ pz \\ 1 \end{bmatrix}=\mathbf{M4}\cdot[0 \quad 0 \quad 0 \quad 1]^T \tag{15}$$

$$\mathbf{qq}=\begin{bmatrix} qx \\ qy \\ qz \\ 1 \end{bmatrix}=\mathbf{M4}\cdot[0 \quad 0 \quad 1 \quad 0]^T \tag{16}$$

Since CL and orientation data are defined with respect to the coordinate system of workpiece, they need converting for machine control commands in machine coordinate system [7]. Each absolute coordinate of cutting points can be calculated by Eq. (17). As the target shape is symmetrical, we just consider the positive direction. Besides, the rotation center of B axis is not the tool end, when B rotating, the x and y coordinate of machine system is changed with it, thus, it also should be taken into consideration.

$$\begin{aligned} \mathrm{bb} &= \arccos(\mathrm{qz})\ (\mathrm{b}\in[0,\pi/2]) \\ \mathrm{cc} &= \mathrm{arcTan}\left(\frac{\mathrm{qx}}{qy}\right) \\ \mathrm{xx} &= \mathrm{px}\cos(\mathrm{cc})+\mathrm{L}\sin(\mathrm{bb})+\mathrm{py}\sin(\mathrm{cc}) \\ \mathrm{yy} &= \mathrm{py}\cos(\mathrm{cc})-\mathrm{px}\sin(\mathrm{cc}) \\ \mathrm{zz} &= \mathrm{pz}-\mathrm{L}+\mathrm{L}\cos(\mathrm{bb}) \end{aligned} \tag{17}$$

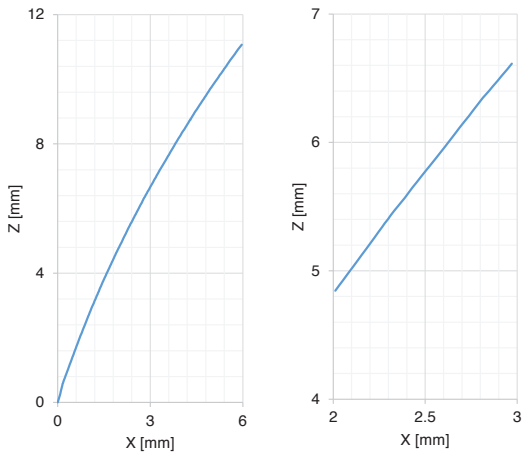

FIGURE 8. Line profile of section.

APPLICATION

Using the generated NC code, an experiment is carried out to examine the validity of the proposed method. The *tr* is 1mm, *tθ* is 15°, and the radius of the tool 3mm. *ve* is set 45°, Pn is set 32, and the depth of cut is 0.4mm. The material is chemical wood, pick feed is set about 1mm. Machined surface was inspected by CMM (Mitutoyo LEGEX9106). In pick feed direction, the proposed method use short straight lines to replace curves, the geometry error cannot be

avoided, however, machining error in feed direction is very little. Therefore, only line profile of section in vertical direction are discussed. Figure. 8a shows the line profile of the section, it appears smooth, and cannot see obvious error, Figure. 8b shows the enlarged part of Figure .8a, it can see that the line keeps straight, therefore, the result identical with expectation, in a word, the validity of the proposed method in the experiments is verified.

CONCLUSION

A special CAM is developed to realize the proposed milling method. The special tool definition and target shape definition were carried out. Moreover, NC generation algorithm was given. From the application example, it knew that thegenerated NC code could be successfully implemented in machining spherical surface.

REFERENCES

[1] X. Yuan, T. Yazawa, N. Baba, Y. Maeda, Y. Ougiya, and T. Kojima. Study on High Efficiency Milling of Steam Turbine Blade. ICRERA2012. Nagasaki, Japan.

[2] Chin-Ching Lo. A new approach to CNC tool path generation. Computer-Aided Design. 1998; 30: 649-655.

[3] Young-Keun Choi, A.Banerjee. Tool path generation and tolerance analysis for free-form surfaces. International Journal of Machine Tools & Manufacture. 2007; 47:689-696.

[4] Nan Wang, Kai Tang. Five-axis tool path generation for a flat-end tool based on iso-conic partitioning. Computer-Aided Design. 2008; 40:1067-1079.

[5] Sergej N.Grigoriev, A.A. Kutin, V.V.Pirogov. Advanced method of NC programming for 5-axis machining. Procedia CIRP. 2012; 1:102-107.

[6] Young-Keun Choi, A. Banerjee, Jae-Woo Lee. Tool path generation for free form surfaces using Bézier curves/surfaces. Computers & Industrial Engineering. 2007; 52: 486–501.

[7] Y.H. Jung, D.W.Lee, J.S.Kim, H.S. Mok. NC post-processor for 5-axis milling machine of table-rotating/tilting type. Journal of Materials Processing Technology. 2002; 130-131: 641-646.

A Derivative Sampling Calibration Method for Measurement Systems

Zonghao Chen and Peisen S. Huang
State Key Laboratory of Mechanical Systems and Vibration
University of Michigan - Shanghai Jiao Tong University Joint Institute
Shanghai Jiao Tong University
Shanghai, China

INTRODUCTION

Calibration is important for all measurement systems. Without calibration one cannot be sure if the output of a measurement system is accurate or not.

The conventional calibration method compares the measurement system being calibrated with a reference measurement system that has a higher accuracy. For example, to calibrate a displacement sensor with an accuracy of 1 μm in the range of 500 μm, the rule-of-thumb is to use a reference sensor with an accuracy of 0.1 μm in the same range. This calibration method is simple to understand and easy to use. However, there is a limitation with this method. What if the accuracy of the measurement system being calibrated is so high that a reference measurement system with a sufficiently better accuracy cannot be found?

Some researchers focused on this problem and proposed the so-called "self-calibration method" [1, 2]. They divided the calibration process into two steps: 1) calibrate the mean sensitivity and 2) determine the nonlinearity error. Instead of using a reference measurement system as in the conventional calibration method, this method uses a small reference to sample the derivatives of the output of the measurement system at discrete points. The nonlinearity error is obtained by integrating the derivatives. Different mechanical configurations were designed to measure the derivative, mainly using piezoelectric actuators.

The authors of the above papers mainly focused on the calibration of specific measurement systems. They did not discuss in details the method itself from a mathematical point of view. They only reported the repeatability of the calibration method in experiments, without analyzing its potential errors. Besides, the authors adopted an integration method that integrates the sampled derivatives directly without using a proper interpolation algorithm, which could potentially lead to a comparatively large calculation error.

The purpose of this research is to generalize the derivative sampling method for measurement system calibration, analyze its potential error sources, and determine through simulation the level of accuracy this method can achieve. The authors hope that this work will serve to make this unique calibration method easier to understand and as a result, help promote its wider acceptance in the field of measurement system calibration.

PRINCIPLE

A measurement system can be represented by a one-to-one relationship between its output x and the physical quantity y to be measured. Such a relationship can be defined as a characteristic function $y = f(x)$. With this relationship, given any output x, we can tell what the measured physical quantity y is. Calibration is to reconstruct this characteristic function as accurately as possible.

As mentioned in the first section, the conventional calibration method compares the output of the measurement system being calibrated with that of a reference measurement system at a series of points within the whole measurement range. Since the reference system has a much higher accuracy, its output can be regarded as true values. This process can be described mathematically as reconstructing the function $y = f(x)$ by first sampling $n + 1$ points (x_i, y_i), $i = 0, 1, 2, 3, \ldots, n$, and then doing interpolation. In this method, the calibration accuracy depends on the accuracy of the reference system and the interpolation method. As long as the reference system is sufficiently accurate, the sampling points are

dense enough and the interpolation method is properly chosen, the calibration accuracy can be guaranteed.

In the derivative sampling calibration method, instead of y, the derivative y' is sampled. To reconstruct the characteristic function $y = f(x)$, $n+1$ points (x_i, y_i'), $i = 0, 1, 2, 3, \ldots, n$, are sampled, and then numerically integrated along the x axis from a starting point (x_0, y_0). As in the conventional calibration method, uniform sampling is not required in this method.

The derivative at each sample point is obtained by calculating $\Delta y/\Delta x$, in which Δy is the value of a small reference, preferably provided by a traceable standard, and Δx is the output of the measurement system corresponding to Δy. Figure 1 shows how $\Delta y/\Delta x$ is calculated. First set the physical quantity to be at a certain value y_{i_l}. The corresponding output of the measurement system is x_{i_l}. Then add the small reference Δy to y_{i_l}, making the value of the physical quantity to be $y_{i\_u} = y_{i\_l} + \Delta y$. The corresponding output is now x_{i_u}. The derivative at $x_i = (x_{i\_u} + x_{i\_l})/2$ is calculated as

$$y_i' \approx \frac{\Delta y}{\Delta x_i} = \frac{\Delta y}{x_{i\_u} - x_{i\_l}}. \quad (1)$$

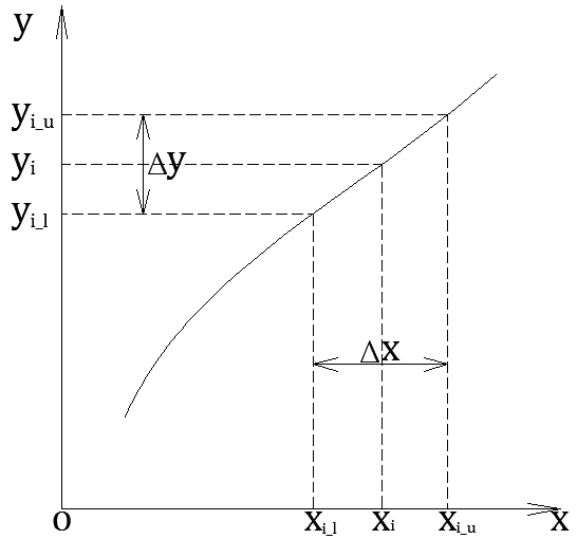

FIGURE 1. Calculation of the derivative.

With this method, only the values of the small reference and the output of the measurement system need to be known, not the values of the physical quantity. Therefore, a full-range reference measurement system is not needed. The major advantages of the derivative sampling calibration method are: 1) a small reference can be more easily and accurately obtained and maintained; 2) the error of the reference will not result in nonlinearity error; 3) the method can potentially be used to calibrate measurement systems with very high accuracy, which is difficult to do with the conventional method because of the lack of appropriate reference measurement systems.

ERROR ANALYSIS

The derivative sampling calibration method will not be usable unless its calibration error can be controlled to an acceptable level.

There are three possible error sources: the sampling error, the differentiation error, and the integration error. Following subsections analyze these error sources in details.

Sampling Error

Sampling error is caused by the inaccuracy of the small reference and the output noise of the measurement system. Since the small reference is the reference for the whole calibration, its accuracy is critical and will determine the final calibration accuracy.

Assume that the small reference has a nominal value of Δy and a true value of Δy_t. Then its error $e_{\Delta y}$ is

$$e_{\Delta y} = \Delta y - \Delta y_t, \quad (2)$$

which is a fixed error. The calculated derivative and true derivative at point (x_i, y_i) are

$$y_i' = \frac{\Delta y}{\Delta x_i + R_{\Delta x}}, \quad (3)$$

$$y_{i\_t}' = \frac{\Delta y_t + R_{\Delta y}}{\Delta x_i + R_{\Delta x}}. \quad (4)$$

where $R_{\Delta x}$ and $R_{\Delta y}$ are the random errors of Δx_i and Δy, respectively. The sampling error of the derivative at point (x_i, y_i) is then

$$y_i' - y_{i\_t}' = \left(\frac{e_{\Delta y} - R_{\Delta y}}{\Delta y}\right) y_i'. \quad (5)$$

With integration, the error of the reconstructed characteristic function can be found as

$$E_s = \frac{1}{\Delta y}\int_{x_0}^{x} (e_{\Delta y} - R_{\Delta y}) y' dx = \frac{1}{\Delta y}\int_{y_0}^{y} (e_{\Delta y} - R_{\Delta y}) dy. \quad (6)$$

The maximum error due to the fixed error $e_{\Delta y}$ occurs at the last sampling point, which is

$$E_{e\_max} = \frac{e_{\Delta y}}{\Delta y}(y_{max} - y_0). \quad (7)$$

If expressed as a percentage of the y range, the normalized maximum error becomes

$$E_{e\_nor} = \frac{|e_{\Delta y}|}{\Delta y} \times 100\%. \quad (8)$$

It can be seen from the above equation that the maximum calibration error due to the fixed error of the small reference is the same as the fixed error of the small reference itself percentage wise.

For easier analysis, the error caused by the random error $R_{\Delta y}$ is rewritten in a discrete form

$$E_{R\_j} = \frac{(y_{max} - y_0)}{n\Delta y} \sum_{i=0}^{j-1} R_{\Delta y}(i), \quad (9)$$

where $j = 1, 2, \ldots, n$. If the random error $R_{\Delta y}$ obeys a normal distribution with an expectation of 0 and a standard deviation of $\sigma_{\Delta y}$, which can be expressed as $R_{\Delta y} \sim N(0, {\sigma_{\Delta y}}^2)$, the above error will have the following normal distribution:

$$E_{R\_j} \sim N\left(0, j\left(\frac{(y_{max} - y_0)\sigma_{\Delta y}}{n\Delta y}\right)^2\right). \quad (10)$$

The distribution at the last sample point is

$$E_{R\_n} \sim N\left(0, \frac{1}{n}\left(\frac{(y_{max} - y_0)\sigma_{\Delta y}}{\Delta y}\right)^2\right). \quad (11)$$

Obviously, the standard deviation at the last point is the largest. Therefore, the last point is more likely to have a larger error. Moreover, since the largest standard deviation is inversely proportional to $\sqrt{n}$, increasing the number of sample points will reduce the calibration error caused by random errors.

Differentiation Error

The derivative of $y = f(x)$ is defined as $\lim_{\Delta x \to 0}(\Delta y / \Delta x)$. Since Δx is not infinitely small, there will be difference between $\Delta y/\Delta x$ and y', which is called differentiation error here. The smaller the Δx or Δy, the closer $\Delta y/\Delta x$ is to y'. However, since the percent error of Δy appears directly in the calibration error, it is more desirable to choose a larger Δy, which can typically lower the percent error of Δy.

To make it possible to choose a larger Δy while keeping the differentiation error small, an iterative error compensation algorithm has been developed. Figure 2 shows the flowchart of the algorithm. Simulation is done using the reconstructed function y_r and Δy to determine the differentiation error E_d. Since the reconstructed function y_r is already close to the original characteristic function, E_d can be considered as an accurate representation of the differentiation error in y_r. By subtracting E_d from y_r, the resultant new function $\hat{y}$ becomes closer to the original characteristic function compared to y_r. The process repeats until $|E_{dn} - E_d| \leq \varepsilon$ where E_{dn} is the new differentiation error and ε is a predefined constant used to judge when to terminate the loop. In most cases, only one iteration is needed.

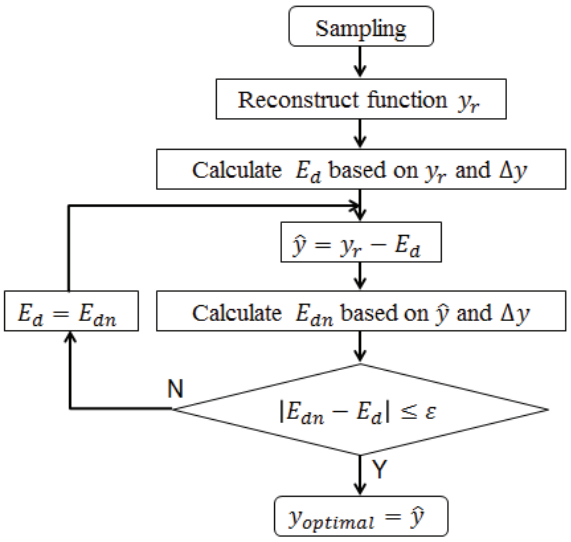

FIGURE 2. Flow chart of the iterative error compensation algorithm.

Integration Error

For better understanding of the integration error, we can regard numerical integration as a two-step process. The first step is to reconstruct the derivative function, $y' = f'(x)$, from a limited number of sample points. The second step is to integrate the reconstructed derivative function from a given starting point (x_0, y_0). In the first step, if the form of the derivative function is known, the derivative function can be obtained by curve fitting. However, in most cases, the form of the derivative function is unknown. In such cases, the derivative function can only be reconstructed by interpolation between sampling

points. The accuracy of integration depends on the accuracy of interpolation.

An interpolation algorithm called Kriging has been used in this research to improve the integration accuracy. Kriging is named after the South African mining engineer Danie G. Krige. He proposed some basic ideas of Kriging in his Master's thesis in 1951, trying to solve problems in geostatistics. Then French mathematician Georges Matheron fully developed the mathematics of Kriging, making it a widely recognized method in the world. Later on, more researchers contributed to improve this method. Kriging has been widely used in recent years for predicting the values of unobserved points based on known information [3].

The basic idea of Kriging is that the value of an unobserved point is the weighted sum of all observed points. Each weighting factor is related to the distance between two points. The longer the distance is, the smaller the weighting factor becomes [4]. By properly choosing the regression model and correlation model, Kriging can usually perform better than other interpolation methods [5]. The error of Kriging interpolation can typically be neglected when compared with other error sources.

After Kriging interpolation, the number of sample points has increased from $n+1$ to $m+1$, where $m \gg n$. In the *j*th integration interval, $y = f(x)$ is fit with a quadratic polynomial. Knowing the point (x_j, y_j), the value of y_{j+1} can be calculated as

$$y_{j+1} = a_j x_{j+1}^2 + b_j x_{j+1} + c_j, \qquad (12)$$

where

$$a_j = \frac{y_j' - y_{j+1}'}{2(x_j - x_{j+1})},$$

$$b_j = y_j' - 2a x_j,$$

$$c_j = y_j - a x_j^2 - b x_j.$$

CALIBRATION PROCEDURE

The calibration procedure for the derivative sampling calibration method is as follows:

1) Select a proper number of sampling points $n+1$ and a small reference Δy.
2) At the *i*th sample point, first adjust the physical quantity to be measured so that the output of the measurement system is roughly $x_{i\_l} = (x_{max} - x_0)(i/n) + x_0$. Then add Δy to the physical quantity and record the output of the measurement system as x_{i_u}. Calculate $\Delta y/(x_{i\_u} - x_{i\_l})$ as the derivative at $x_i = (x_{i\_u} + x_{i\_l})/2$.
3) Use the Kriging method to interpolate and then integrate the sampled derivatives to reconstruct the characteristic function.
4) Use the iterative error compensation algorithm to reduce the differentiation error.
5) If the overall sensitivity of the measurement system is known, use that to eliminate the calibration error due to the fixed error of Δy.
6) Optimize the values of n and Δy based on the reconstructed characteristic function. Then repeat Steps 2 to 5.

SIMULATION

To verify the analysis above, a mathematical model was used to conduct simulation. The shape and nonlinearity error of the characteristic function emulates those of a real angle measurement device [2]. The characteristic function is defined as

$$y = \frac{250}{30}x + 20\sin\left(\frac{2\pi}{60}x + \pi\right), \qquad (13)$$

where x is the output of the angle sensor and y is the angle to be measured, $x \in [-30\%, 30\%]$, $y \in [-250\ \mu\text{rad}, 250\ \mu\text{rad}]$. The nonlinearity of the function is 4%. According to the paper, $\Delta y = 10\ \mu$rad, the number of sample points is 51, and the resolution of the angle sensor is 5 nrad. The error of Δy is unknown. Here we assume that both the fixed error and standard deviation of Δy are 10 nrad.

Figure 3 shows the curve of the reconstructed function obtained by integrating the simulated derivative samples using the Kriging based method, which is very close to the characteristic function defined in Eq. (13). Figure 4 shows the calibration errors of 5 simulations and their average value. The maximum calibration error is approximately 0.1%, which is the same as the percent fixed error of Δy. Therefore, the fixed error of Δy is the main error source in this case. Figure 5 shows the remaining errors after the overall sensitivity is corrected, assuming that y_{max} and y_0 can be accurately determined. The blue solid line shows the error before the iterative error compensation algorithm is applied, which is approximately 0.004%. The green

dashed line shows the same error after the same algorithm is applied, which is approximately 0.006%. Obviously, the iterative error compensation algorithm does not work in this case. In fact, the error actually becomes larger after the compensation. The reason is because Δy is small so that the differentiation error becomes insignificant when compared to errors caused by random noises.

From the discussions in previous sections, we understand that a larger Δy will usually result in a smaller percent error of Δy, and hence a smaller error in the reconstructed function. On the other hand, a larger Δy may incur a larger differentiation error. If we assume the differentiation error can be effectively compensated for by using the iterative error compensation algorithm, then it is more advantageous to select a larger Δy.

To verify the above observation, we increase Δy value to 40 μrad. Figure 6 shows calibration errors of 5 simulations and their average value. It can be seen that the variance is much smaller than that in Figure 4 as expected. The overall error is only slightly larger than that in Figure 4, but now the differentiation error becomes the dominant error source. Figure 7 shows the error before and after the iterative error compensation algorithm is applied. Clearly the iterative error compensation algorithm is very effective in this case, reducing the maximum error from 0.12% down to approximately 0.025%. The remaining error is mainly due to the fixed error of Δy. Since a calibration error of 0.025% is small enough for most calibration applications, this result means that it is feasible to rely only on a small reference to calibrate a measurement system as long as an appropriate Δy is selected. Figure 8 shows that if the overall sensitivity is known, the calibration error can be further reduced from 0.025% to approximately 0.002%.

CONCLUSION

In this paper, a so-called derivative sampling calibration method has been studied to evaluate its performance for measurement system calibration. Compared to conventional calibration methods, this method only requires an accurate small reference instead of a reference measurement system with a significantly higher accuracy in the whole measurement range. The mathematical model of the method is built and

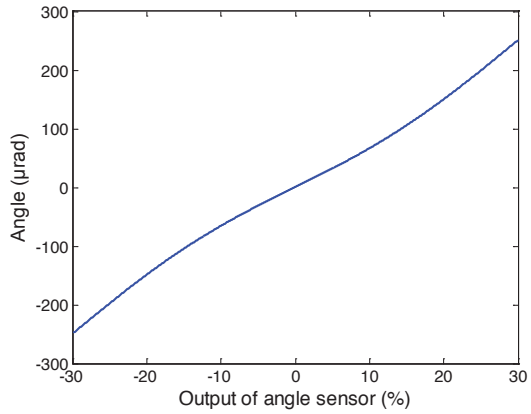

FIGURE 3. The reconstructed function.

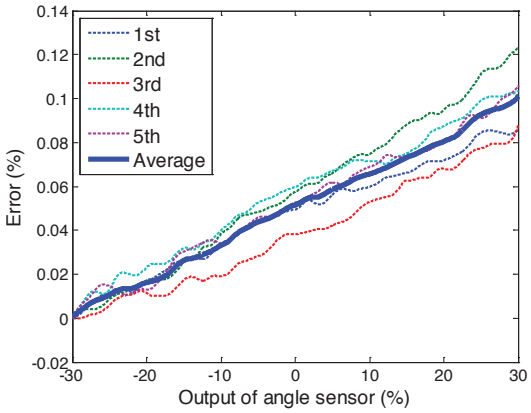

Figure 4. Calibration errors of 5 simulations and their average value. Δy = 10 μrad.

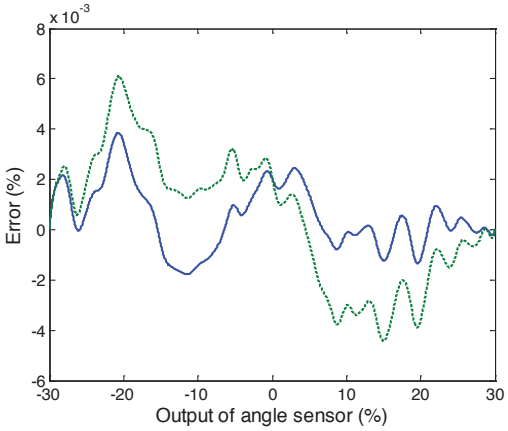

FIGURE 5. Calibration errors after the iterative error compensation algorithm is applied and the overall sensitivity is corrected. Δy = 10 μrad.

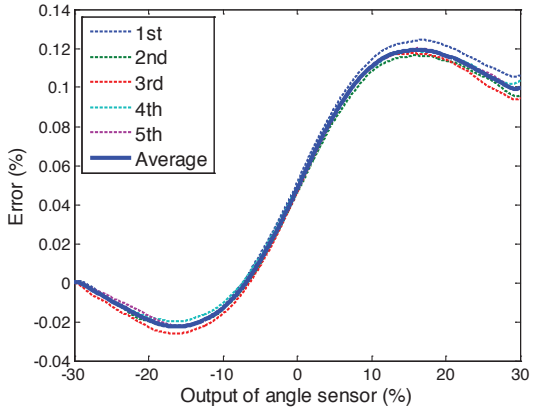

FIGURE 6. Calibration errors of 5 simulations and their average value. Δy = 40 μrad.

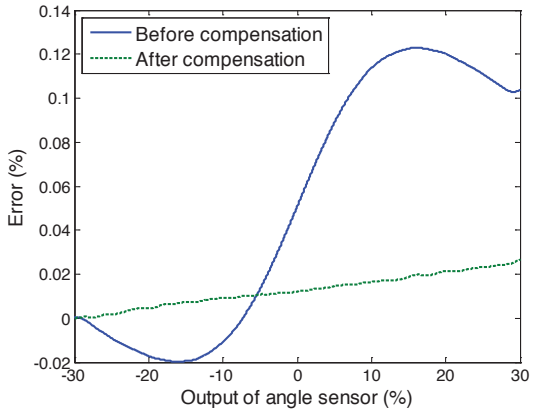

Figure 7. Calibration errors before and after the iterative error compensation algorithm is applied. Δy = 40 μrad.

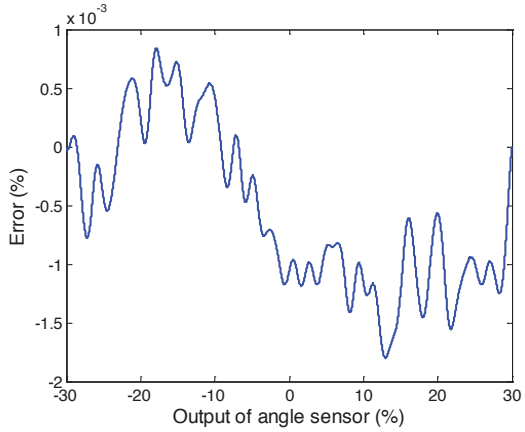

FIGURE 8. Calibration error after the iterative error compensation algorithm is applied and the overall sensitivity is corrected. Δy = 40 μrad.

the error sources are analyzed. The Kriging based method has been developed to reduce the integration error and improve the calibration accuracy. An iterative error compensation algorithm has also been proposed to compensate for the differentiation error to further reduce the calibration error. Simulation results show that the derivative sampling calibration method is robust and accurate. It can be applied to the calibration of any measurement system as long as an accurate small reference can be obtained.

REFERENCES

[1] Zhang S, Kiyono S. An Absolute Calibration Method For Displacement Sensors. Measurement. 2001; 29: 11-20.

[2] Zhang S, Kiyono S, Uda Y. Nanoradian Angle Sensor And In Situ Self-calibration. Applied Optics. 1998; 37: 4154-4159.

[3] Cressie N. The origins of kriging. Mathematical Geology. 1990; 22(3): 239-252.

[4] Oliver M A, Webster R. Kriging: a method of interpolation for geographical information systems. International Journal of Geographical Information System. 1990; 4(3): 313-332.

[5] Lophaven S N, Nielsen H B, Jacob S. A Matlab Kriging Toolbox (version 2.0). Informatics and Mathematical Modeling, Technical Univ. of Denmark, TR IMM-TR-2002-12, Lyngby, Denmark, 2002.

DISPLACEMENT MEASUREMENT USING SPECKLE CORRELATION WITH REDUCED NUMBER OF DATABASE PATTERNS

Mahsa Farsad[1], Gert Goch[2], and Chris Evans[2]
[1] Optical Science and Engineering Graduate program
Center for Precision Metrology
University of North Carolina
Charlotte, North Carolina, USA
[2]Department of Mechanical Engineering
University of North Carolina
Charlotte, North Carolina, USA

INTRODUCTION

Speckle patterns are complex intensity distributions, which occur when an optically rough surface is illuminated with a coherent light. Scattered light waves from illuminated points of the surface, interfere and create the speckle pattern. This phenomenon was known to be troublesome when the laser was first introduced, but later it was discovered to be an opportunity for various measurements.

One of the earliest attempts for measurement using the speckle phenomena goes back to 1970 [1]. This paper uses the speckle pattern correlation to determine surface displacement. Since then, many investigators have applied speckle techniques to displacement, deformation, surface roughness, stress and vibration analysis. The two review articles, [2] and [3] have covered theoretical and practical characteristics of the technique as well as its development over time.

Speckle pattern correlation is one of the applicable methods for high resolution displacement measurement. In [4], it is applied to enable precise alignment of work pieces with minimum relocation uncertainty of 7.6 μm. In [5], the method is used for absolute position measurement with a lateral resolution of less than ± 20 nm. However, this method requires a large number of database patterns. In [4], the largest spacing between the database patterns is one third of the relocation resolution and in [5] the database spacing is one fourth of the displacement measurement resolution. The large number of required database patterns limits the measurement range, especially in two dimensions. This paper describes an improved speckle correlation technique that reduces the number of required database patterns by an order of magnitude and makes it feasible to create an absolute scale for machine tools (Figure 1), inspired by [5].

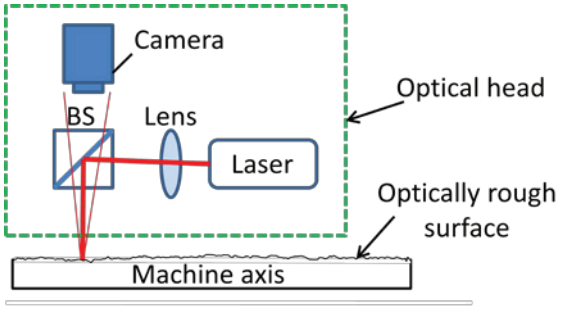

FIGURE 1. Absolute scale based on speckle correlation

Figure 1 shows a coherent light illuminating the surface of the machine axis through a lens and a beam splitter.The speckle pattern is reimaged onto a camera.

Each position on the sample (here the machine's axis) produces a unique speckle pattern. Therefore, the system can be calibrated by shifting the sample or the read head in incremental steps, capturing and storing the speckle pattern at each position. Now the system can make an absolute position measurement.

At any position in the travel of the machine, the system captures the speckle pattern at that point and compares it with the database patterns. The database pattern that has the highest correlation with the randomly selected pattern indicates the position of the sample.

In this paper, we compare three different methods of using the correlation between the speckle patterns to determine the sample position. The target resolution for all the methods is one micron. In the first method, we create one database entry every micron. In the second and third methods, we create one database entry every 10 microns and determine the sample position in between by fitting a curve to the 10 micrometer interval. The curve we use in the second method (the correlation curve) depends on the characteristics of the measurement system and the curve we use in the third method is a second order polynomial. This paper shows that using the curve that depends on system characteristics helps to reduce the number of required database patterns and is more efficient than using a polynomial.

THEORY

The correlation method that we use to compare two speckle images requires that the two images have the same dimensions. We can determine the correlation coefficient (cc) from

$$cc = \sum_{ij}\left(\frac{a_{ij}-\bar{a}}{\sigma_a}\right).\left(\frac{b_{ij}-\bar{b}}{\sigma_b}\right) \quad (1)$$

where a_{ij} and b_{ij} denote the pixel intensities of the two captured patterns, $\bar{a}$ and $\bar{b}$ the mean values of the intensities in the two images and σ_a and σ_b the intensity standard deviations.

Using this definition, Figure 2 shows a typical database of speckle patterns over a 10 micrometer range and how we can determine any position within this range using the database and finding the correlation peak.

If we determine the correlation of one of the database patterns with all the others, we can obtain the correlation distribution at that specific position. From this distribution, we can deduce the sensitivity of the measurement system. A larger correlation drop between adjacent patterns indicates a more sensitive system because the correlation drop is due to the speckle shift. A more sensitive system has a larger speckle shift for a given sample shift.

Using a cubic spline to interpolate the correlation distribution, we obtain the correlation curve. Figure 3 compares a typical correlation curve for the sample position at 10 μm over a 10 μm range to a second order polynomial over the same range. The polynomial shares three points with the correlation curve at sample shifts 0, 5 and 10 μm.

The correlation curve mainly depends on the speckle size and the speckle shift. The spot size controls the speckle size [6] and the wavefront curvature controls the speckle shift [4]. By changing the spot size and the wavefront curvature, we can adapt the correlation curve. Assuming that the correlation curve is constant at each sample position, (which we show experimentally is a valid assumption), then from one database pattern every 10 μm we can determine the two database patterns between which the sample is located. For example, we can determine whether the sample is between 0 and 10 μm, 10 and 20 μm, 20 and 30μm, etc. This is possible if half width of the correlation curve is larger than 10 μm (which is the length of each interval). Figure 4 shows typical correlation curves at sample positions 0 and 10 μm .If the

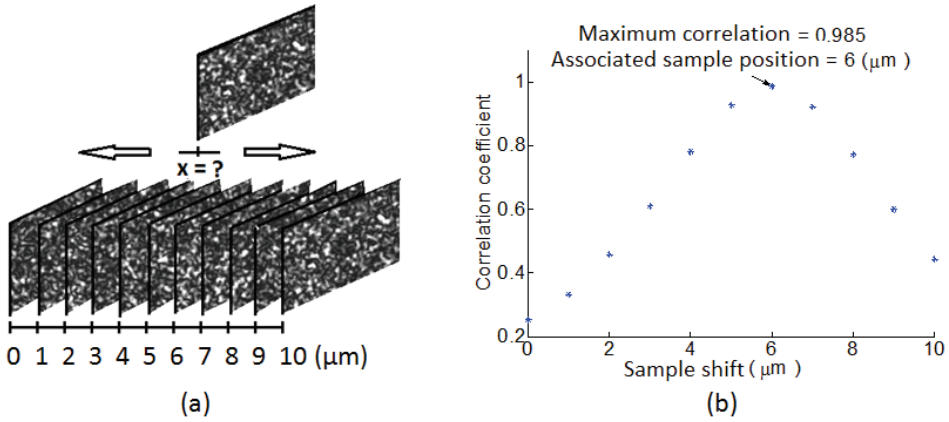

FIGURE 2. Absolute position measurement by speckle pattern correlation. a) The database of speckle patterns and the corresponding sample positions. b) Correlations between the randomly selected position and the database patterns. The correlation peak shows the sample position.

sample is at an unknown position between 0 and 10μm, its speckle pattern would have specific correlations with the database patterns at 0 and 10 μm. Hence, by determining the correlation of the pattern with these two database patterns, we can determine if the sample is between 0 and 10 μm. (If a randomly selected sample position is between 0 and 10 μm, its correlation with the database at 0 μm should be greater than the correlation coefficient at point "b" in Figure 4, which is 0.32, and its correlation with the database at 10 μm should be greater the correlation coefficient at point "a", which is also 0.32 in this example).

Figure 5 shows a situation where half width of the correlation curve is smaller than 10 μm. In this case, we cannot determine if the sample is between 0 and 10 μm by finding its correlation with the databases at 0 and 10 μm. For example, if a randomly selected sample position is in interval "m", we cannot distinguish it from its symmetry about the line "Sample shift = 10 μm", located in interval "n", as both would have zero correlation with the database at 0 μm and the same correlation with the database at 10 μm.

By designing the correlation curve with half width greater than 10 μm, we can determine the two database images between which the sample is located over a large range. For a 100 μm range, we calculate the correlations of the randomly selected sample with all the database patterns (the patterns at 0, 10, 20, ..., 100 μm). The first and the second correlation maximums are the two patterns between which the sample is located. This is illustrated in Figure 6. Based on this figure, the sample is between 80 and 90 μm. Also, because the first maximum is at 80 μm, the sample is closer to this point.

Earlier we assumed that the correlation curve is the same at each sample position. We also determined the two points that the correlation curve at the randomly selected sample position should pass (these two points are the correlation of the randomly selected sample position with the patterns at 80 and 90 μm). This means that if we fit the correlation curve to pass these two points, the peak of the curve would reveal the sample position.

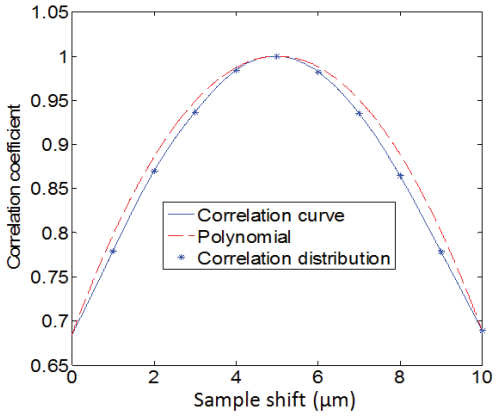

FIGURE 3. Comparing a typical correlation curve with a second order polynomial

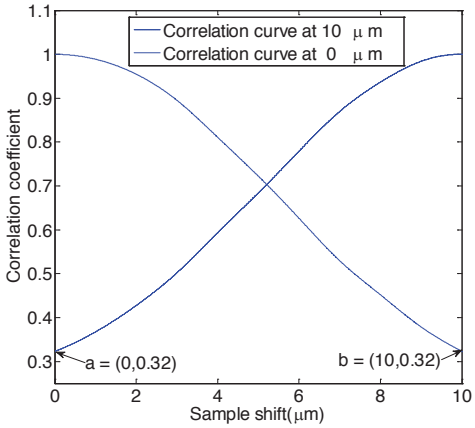

FIGURE 4. Correlation curves at sample positions 0 and 10 μm when the half width of each curve is greater than 10 μm.

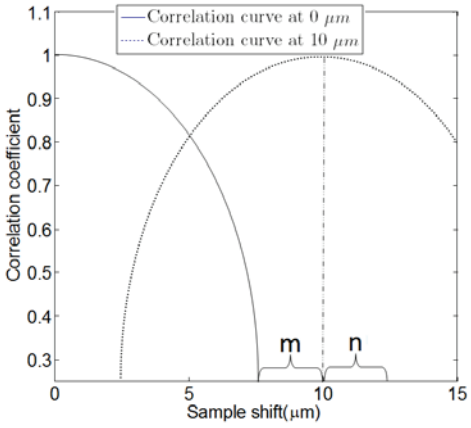

FIGURE 5. Correlation curves at sample positions 0 and 10 μm when the half width of each curve is smaller than 10 μm.

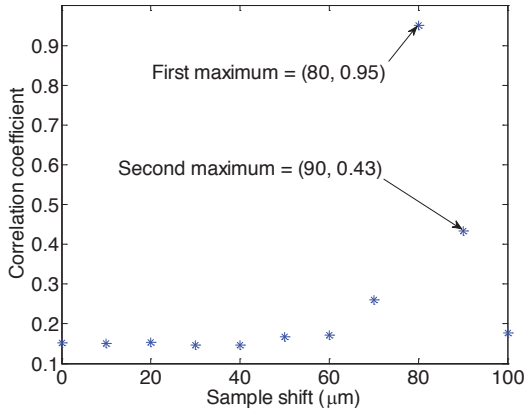

FIGURE 6. The first and second correlation maximums are observed at 80 and 90 μm which shows the sample is between these two points.

EXPERIMENTAL SETUP AND RESULTS

The experimental setup for an absolute position measurement using speckle correlation is shown in Figure 7. A 3mW HeNe laser illuminates an optically rough sample. We adjust the spot size and the wavefront curvature by a laser lens. The CCD screen directly captures the speckle patterns. A motorized stage also shifts the sample perpendicular to the beam direction and we use an attenuator to control the maximum intensity of the speckle pattern.

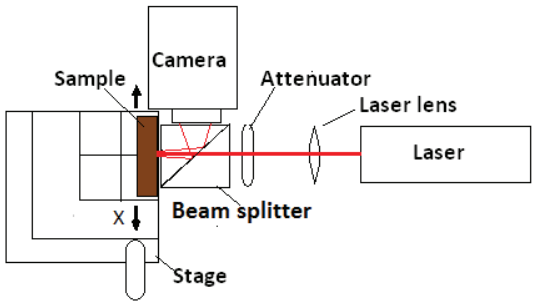

FIGURE 7. Experimental setup of the absolute position measuring system based on speckle pattern correlation

The motorized stage consists of a piezo actuator for fine displacement and a step motor for coarse displacement. In order to capture the data every 0.1 μm over 100 μm (a total of 1001 data), we use the piezo over the first 20 μm range. Than we shift the sample to 20 μm using the step motor and capture the data from 20 to 40 μm using the piezo again. We repeat this process up to 100 μm.

In order to analyze the correlation methods discussed in the introduction, we need to investigate if the sample position that the correlation technique determines matches the sample position that the stage measures. As a result, in the first method, we use the patterns captured every micron (the patterns captured at 0, 1, 2, ..., 100 μm) as the database patterns. Then we select one data randomly from all the data (captured every 0.1 μm) and calculate its correlation with the database. The highest correlation coefficient shows the sample position (Figure 8). Because we designed the system for 1 μm resolution, we expect the system to round the fractions of a micron to the nearest integer. Analyzing the system with the 1001 data we captured earlier shows that the system rounds all the data consistently.

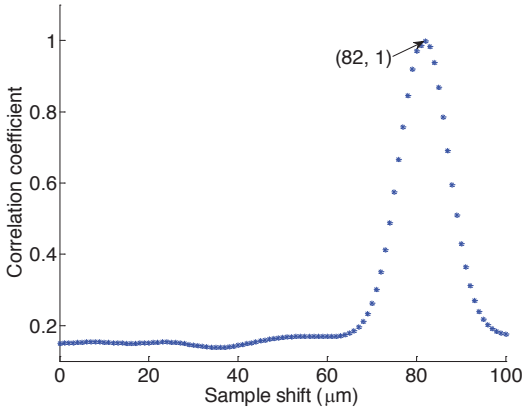

FIGURE 8. Determining the sample position by finding the correlation peak.The stage measures the sample position to be at 82 μm and so does the first correlation technique. This is why the correlation coefficient at 82 μm is equal to 1.

In order to analyze the correlation curve method described above, we use the patterns captured every 10 microns (the patterns captured at 0, 10, 20, ..., 100 μm) as database patterns and we select one position randomly from all the data (captured every 0.1 μm). Next, we determine between which two database positions the randomly selected position is located. For this purpose, we calculate the correlation of the randomly selected pattern with the database. The first and the second maximum show the two database patterns between which the sample is located (Figure 6). In order to determine the sample position with 1 μm resolution, first we need to determine the correlation curve and verify that the curve is the same at different

sample positions. For this purpose, we determine 5 different correlation curves at different sample positions, verify that they are identical and use the average of them as the reference correlation curve. We select the curves at 10, 30, 50, 70 and 90 μm. As mentioned earlier, in order to determine the correlation curveat 10 μm between 0 and 20μm, we determine the correlation distribution every micron and use a cubic spline to interpolate the distribution. Next, we determine the correlation curve at 30 μm between 20 and 40μm. We repeat this process to determine correlation curves at 50, 70 and 90 micrometers. The maximum absolute deviation of each curve from the curve at 50 μm is 0.01, which shows the correlation curves are in good agreement. As a result, we can use the average of these five curves as the reference correlation curve.

At this point we know that the sample is between 80 and 90 μm, we have determined the correlation curve and we know that it is constant at all sample positions. We have also determined the two points that correlation curve at the randomly selected pattern passes, which is 0.95 at 80 μm and 0.43 at 90 μm (Figure 6). Having a higher correlation with 80 μm also shows that the sample is closer to 80 μm. At this point, in order to find the sample position with 1 μm resolution, we fit the correlation curve to the points mentioned above. The peak of the curve shows the position of the sample (Figure 9). Because the correlation curve might not exactly pass the two determined points, one way is to make the curve pass the point with the higher correlation (in this example the correlation is higher at 80 μm). Also, because the resolution of the measurement is 1 μm, we should round the value determined by the peak of the correlation curve to nearest integer.

The polynomial method mentioned in the introduction is similar to the correlation curve method, which means we use the patterns captured every 10 microns as database patterns, select one data randomly from all the data captured every 0.1 μm and determine between which two databases, the randomly selected data is located. However, in the polynomial method we use a second order polynomial (instead of the correlation curve) to pass the two correlation maximums that we have determined in Figure 6.

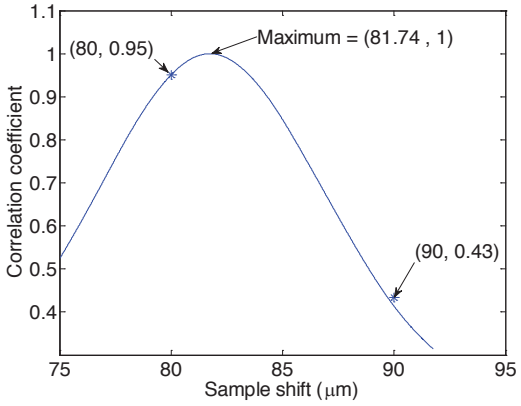

FIGURE 9. Fitting the correlation curve to the first and the second correlation maximums determined in Figure 6. We should round the sample shift associated with the curve's peak to the nearest integer (82 in this example) to determine the sample position.

In order to create a polynomial between 0 and 20 μm, we determine the correlation of the pattern at 10 μm with the patterns at 5, 10 and 15 μm. These three points define the polynomial. In order to determine the polynomial between 20 and 40 μm, we need to determine the correlation of the pattern at 30 μm with the patterns at 25, 30 and 35 μm. However, this polynomial is identical to the one we have determined in the previous interval (between 0and 20 μm). The same condition happens for the remaining intervals (40 to 60 μm, 60 to 80 μm and 80 to 100 μm). As a result, instead of determining the polynomials at different intervals and calculating the mean curve, we use the polynomial we determined in the first interval. We make this polynomial pass the first maximum in Figure 6. The peak of the polynomial shows the sample position (Figure 10). In this specific example the polynomial seems to provide a more accurate result (the actual sample position determined by the stage in 82μm). However, if we determine the average deviation of the sample position determined by polynomial from the position determined by the stage for 1001 data we captured earlier, this number for the method using the correlation curve is 50% less than the method using the polynomial.

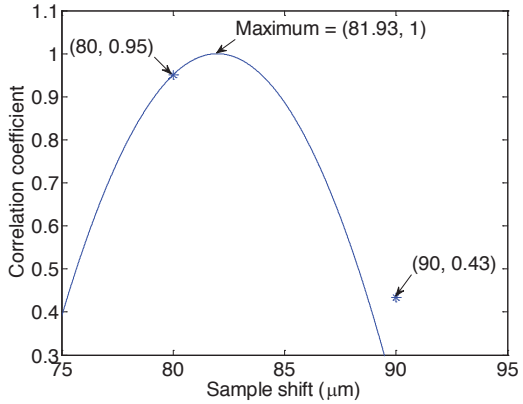

FIGURE 10. Fitting the second order polynomial to the first and the second correlation maximums determined in Figure 6. We should round the sample shift associated with the curve's peak to the nearest integer (82 in this example) to determine the sample position.

SUMMARY

This paper compares three methods of displacement measurement with 1 μm resolution using speckle pattern correlation. It shows to what extent the correlation curvecan be regarded as constant over a 100 μm interval and how it is possible to use this curve to reduce the number of required database patterns. Reducing the required database patterns makes it possible to expand the displacement measurement using speckle correlation to longer ranges and to two dimensions. This may lead to development of a two dimensional absolute scale for machine tools which could be fast and low cost.

REFERENCES

[1] Leendertz J A. Interferometric Displacement Measurement on Scattering Surfaces Utilizing Speckle Effect. Journal of Physics E-Scientific Instruments. 1970; 3(3): 214-8. PubMed PMID: WOS: A1970G439600012.

[2] Jacquot P. Speckle Interferometry: A Review of the Principal Methods in Use for Experimental Mechanics Applications. Strain. 2008 Feb; 44(1):57-69. PubMed PMID: WOS:000252331100007.

[3] Tiziani HJ, Pedrini G. From Speckle Pattern Photography to Digital Holographic Interferometry. Applied Optics. 2012; 52(1): 15.

[4] Goch G, Prekel H, Patzelt S, Faravashi M, Horn F. Precise Alignment of Workpieces Using Speckle Patterns as Optical Fingerprints. CIRP Ann-Manuf Techn. 2005; 54(1): 523-6. PubMed PMID: ISI:000230322000125. English.

[5] Patzelt S, Pils K, Tausendfreund A, Goch G. Optical Absolute Position Measurement on Rough and Unprepared Technical Surfaces. Euspen; June 2012; Stockholm.

[6] Parry G, Dainty J. Laser Speckle and Related Phenomena. Topics in Applied Physics Series (Springer-Verlag, Berlin, 1984). 1975; 9.

AN ACTIVE ENCODER FOR PRECISION POSITION MEASUREMENT

Peisen S. Huang, Tian Kai, and Xuefeng Qiang
State Key Laboratory of Mechanical Systems and Vibration
University of Michigan – Shanghai Jiao Tong University Joint Institute
Shanghai Jiao Tong University
Shanghai, China

INTRODUCTION

Encoders are widely used in machines for precision position measurement and control. Most encoders are incremental encoders that can only measure relative positions. Absolute encoders that can measure absolute positions are available, but they are less well-developed, especially planar absolute encoders.

Gao *et al* and Kimura *et al.* developed novel planar encoders that can measure positions relatively with nanometer level resolution [1, 2]. Their scale patterns are uniform across the scales and thus do not allow for local positions to be uniquely identified. Leviton *et al.* developed a Cartesian absolute planar encoder that used a pattern recognition method to detect the Cartesian code unique in every single position of the scale and achieved a resolution of 5 nm [3]. However, the manufacturing of such scales is complex and expensive.

With the rapid development of digital display technologies, flat panel displays can be used as the scale for planar encoders. These display-based encoders utilize the periodic pattern of pixels in OELD substrate. Position estimation can be achieved by using digital subdivision or boundary detection method [3]. However, the patterns on the display substrate are fixed and cannot be controlled. Therefore, it is impossible to uniquely identify a local pattern to determine the absolute position. As a result, these display based encoders are all incremental encoders.

In this paper, a novel active encoder is proposed for planar position measurement, which uses a flat panel display as its grating scale and a camera to capture the periodic pattern of the display pixels. The display is controlled by a computer program to display desired patterns. This essentially makes the display an active grating. The idea of active encoders has never been proposed and tried before. All existing encoders are passive encoders, meaning that they use scales that are fixed and cannot be controlled during usage. The most important advantage of active encoders is that they can be easily built to measure absolute positions.

The rest of the paper is organized as follows. First, the principle of the proposed active encoder is described. Then a mathematical model of the active encoder is introduced and some simulation results discussed. The experimental results are presented next. Finally, the conclusion of the research work is given.

PRINCIPLE

A new type of position encoder, namely active encoder, is proposed for high precision planar position measurement. This encoder uses a flat panel display as the grating scale and a camera as the reading head. Since every pixel can be uniquely distinguished, an active encoder can easily provide absolute position measurement.

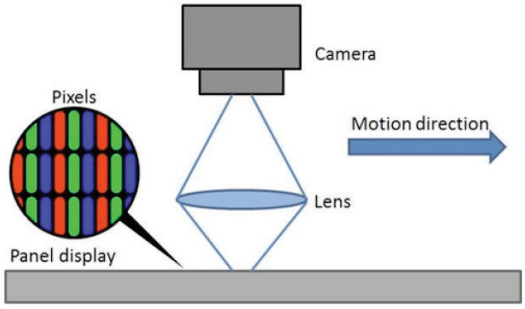

FIGURE 1. Schematic diagram of an active encoder.

Active Encoder

The term active encoder is used to describe an encoder whose grating pattern can be actively controlled. Figure 1 shows the concept of an active encode that uses a flat panel display as the grating.

The flat panel display can be either LCD or OLED. Obviously each pixel of the display can be digitally controlled by software to different levels of brightness. A camera is used to capture the image of the pixels through a microscope

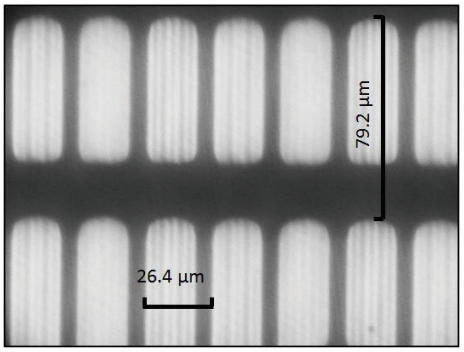

FIGURE 2. Image of the pixel pattern of a flat panel display.

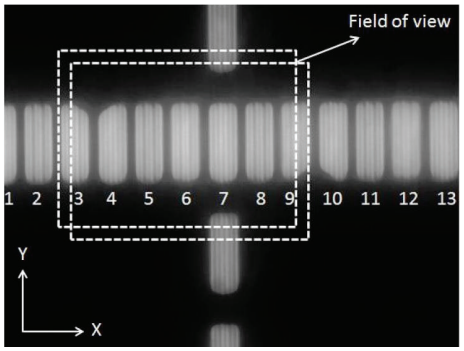

FIGURE 3. Absolute position measurement.

lens (see Figure 2). When there is a relative displacement, rotation, or a combination of the two between the camera and the flat panel display, the camera will capture a slightly different image of the pixels. By analyzing the shift of the pixels in the image, both the displacement and rotation can be determined. Since each pixel can be easily identified by use of a coding method (see the No.7 pixel in Figure 3), absolute position measurement can be made.

Phase Correlation Method

Counting the shift of the display pixels will result in only very limited measurement resolution. For higher resolution, a phase correlation method has been developed to subdivide the periodic pattern, so that nanometer resolution can be achieved in both X and Y directions.

Let $F(x)$ be a periodical discrete function of N points. With Discrete Fourier Transform, $F(x)$ can be expanded to its Fourier series as shown in Eqs. (2.1) and (2.2), where X_k (k = 0 to N) represent different frequency components of the original function $F(x)$. The amplitude A_k and initial phase ϕ_k can be calculated using Eqs. (2.3) and (2.4).

$$F(x) = \sum_{n=0}^{\infty} A_n \sin(2\pi f_n x + \phi_n)\,, \tag{1}$$

$$X_k = \sum_{n=0}^{N-1} x_n e^{-\frac{i2\pi kn}{N}}, \quad k = 0, 1, 2, \ldots\,, \tag{2}$$

$$A_k = \frac{|X_k|}{N} = \frac{\sqrt{\mathrm{Im}(X_k) + \mathrm{Re}(X_k)}}{N}\,, \tag{3}$$

$$\phi_k = \mathrm{atan}\,2(\mathrm{Im}(X_k), \mathrm{Re}(X_k))\,. \tag{4}$$

For better accuracy of phase determination, only the fundamental frequency component F_0 is used, which has the following form

$$F_0(x) = A_0 \sin(2\pi f_0 x + \phi_0)\,. \tag{5}$$

When there is a relative displacement between the camera and display, the phase shift of the fundamental frequency component can be used to calculate the displacement as follows.

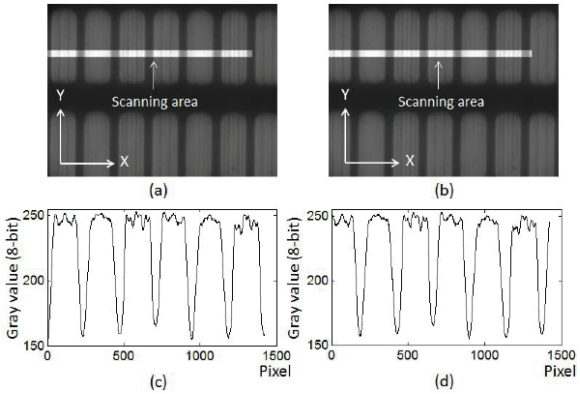

FIGURE 4. Pixel image and intensity profile before and after the displacement.

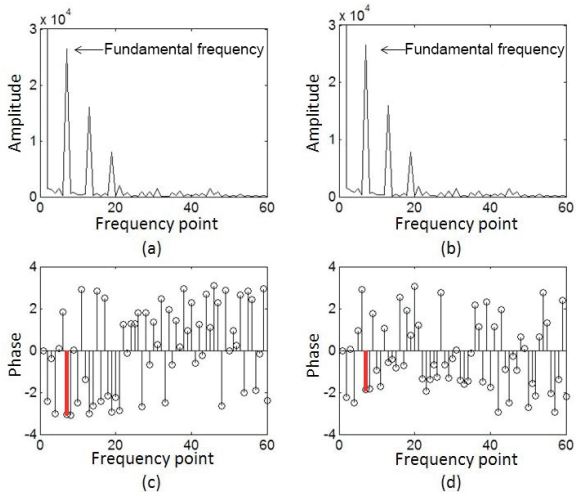

FIGURE 5. Amplitude and phase before and after the displacement.

$$\Delta d = p\Delta\phi_0 \,, \tag{6}$$

where Δd is the relative displacement, p is the pitch of the pixel pattern of the display, and $\Delta\phi_0$ is the phase shift of the fundamental frequency.

Figure 4 shows the pixel images and intensity profiles of the scanning area before and after the displacement. Figure 5 shows the corresponding amplitude and phase plots with the amplitude and phase of the fundamental frequency component indicated.

Rotation angle measurement

Displacement measurement with the proposed method relies on the accurate knowledge of the pitch of the pixel pattern of the display. If the pitch changes due to rotation, then measurement error will occur. Therefore, to guarantee displacement measurement accuracy, it is necessary to measure the rotation angle as well.

In this research, two methods were proposed to measure the rotation angle. First, an image processing method based on Radon transform was developed. In this method, the image is first processed with a boundary detection algorithm, as shown in Figure 6. Then the image is further processed with Radon transform. The result is shown in Figure 7. The bright spots in the image indicate the rotation angle. Experiments with real images demonstrate that this method can achieve an angle measurement resolution of 0.01 deg. This resolution is sufficient for the compensation of displacement measurement errors due to rotation. For measurement of rotation angles at a higher resolution, a two-camera method has been developed, which demonstrated a resolution at the sub-micro-radian level (see the section of Experiment).

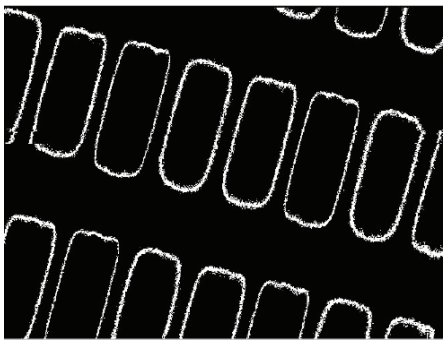

FIGURE 6. Pixel boundary detection result.

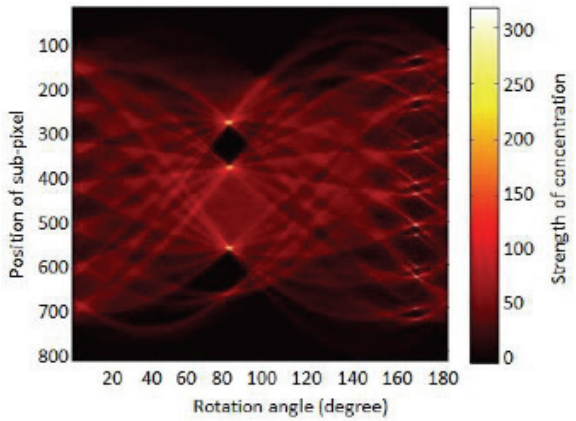

FIGURE 7. Radon transform result.

SIMULATION

To verify the feasibility of the active encoder, a mathematical model of the active encoder has been developed and used to simulate the potential performance of the encoder. Different system parameters and error sources were considered in the simulation, such as camera resolution, noise level, display pixel size and display manufacturing errors. The results can be used to guide the design of active encoders.

Mathematical model

The mathematical model of the active encoder includes three parts: the pixel pattern of the display, the camera sampling process, and the noise. To model the pixel pattern of the display, the intensity profiles of a real image of the pixel pattern are obtained. Then a two-dimensional continuous function, which is a modified Gaussian function, is built to model these profiles and therefore the pixel pattern of the display. The camera is simply modeled as a sampling window. The window size reflects the resolution of the camera. The movement of the sampling window on the display models the camera sampling process. Noise is modeled as Gaussian noise based on the observation of the noise of the real imaging system.

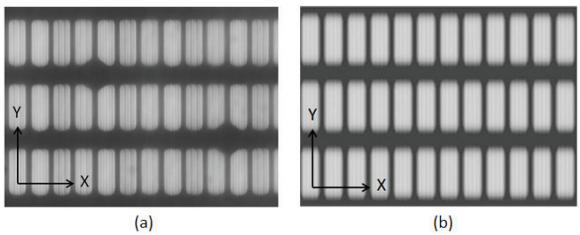

FIGURE 8. Pixel pattern of the display. (a) Real pixel pattern. (b) Simulated pixel pattern.

Figure 8 shows the images of both the real and simulated pixel patterns of the display. It can be seen that the simulated pixel pattern closely resembles the real pixel pattern.

Encoder parameters and resolution

Using the mathematical model developed, the relationship between the encoder parameters and the displacement measurement resolution can be simulated. The general simulation parameters are as follows: 1) the number of display pixels in the field of view is 12; 2) the camera resolution is 1600 pixels; 3) the noise level is 1.6 gray scales; 4) the pixel size of the display is 26 μm; 5) the width of the camera scanning area is 16 pixels.

Figure 9 shows the relationship between camera resolution and displacement measurement resolution. In this simulation, the camera resolution is made to change from 500 to 3000 pixels in X direction. The result shows that the displacement measurement resolution increases with the increase of camera resolution.

Figure 10 shows the relationship between the number of display pixels in the field of view and the displacement measurement resolution. In this simulation, the number of display pixels in the field of view changes from 2 to 50. The result shows that the displacement measurement resolution decreases with the increase of the number of display pixels in the field of view.

Figure 11 shows the relationship between the signal noise level and the displacement measurement resolution. In this simulation, the signal noise level σ^2 changes from 0 to 10. The result shows that noise reduction could dramatically improve measurement resolution.

Figure 12 shows the relationship between display pixel size and displacement measurement resolution. In this simulation, the display pixel size changes from 6 to 400 μm. The result shows that the smaller the display pixel size, the higher the measurement resolution.

With the above simulation results, we can conclude that higher camera resolution, higher lens magnification, smaller display pixel size, and lower noise level result in better measurement resolution.

Effect of display manufacturing errors

Commercial flat panel displays are not manufactured for metrology purpose. Therefore, relatively large manufacturing errors are expected. It is important to find out how these errors will affect the measurement results.

There are mainly three relevant types of manufacturing errors: 1) uneven brightness of pixels; 2) variation of pixel size; 3) deviation of pixel position; and 4) variation of pixel pitch. Since pixel pitch is the reference for displacement measurement here, any variation in pixel pitch will directly cause errors in the measurement result. Therefore, the discussion here will focus on the first three types of manufacturing errors.

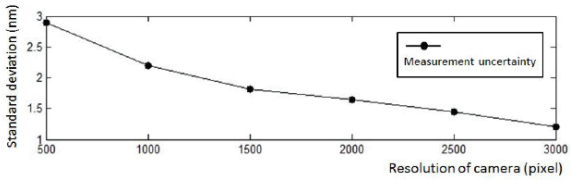

FIGURE 9. Relationship between camera resolution and displacement measurement resolution.

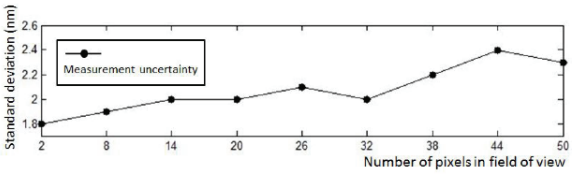

FIGURE 10. Relationship between the number of display pixels and displacement measurement resolution.

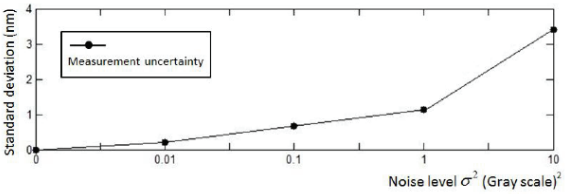

FIGURE 11. Relationship between signal noise level and displacement measurement resolution.

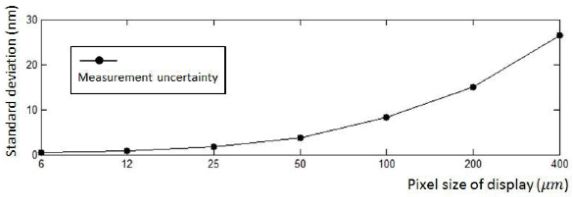

FIGURE 12. Relationship between display pixel size and displacement measurement resolution.

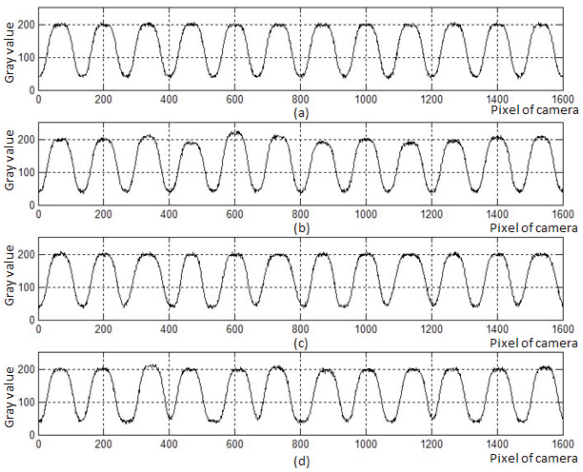

FIGURE 13. Signal profiles with simulated manufacturing error. (a) Perfect display. (b) With uneven pixel brightness. (c) With pixel size change. (d) With deviation of pixel center positions.

Figure 13 shows the simulated signals when (a) there is no manufacturing error and (b)-(d) when there are manufacturing errors of the first three types described above respectively. The level of error is set at approximately 15%, which is larger than typical manufacturing errors for flat panel display products. Using a step test with a step size of 50 nm, the standard deviation was found to be 2.1 nm when there is no manufacturing error and 2.3 nm, 2.2 nm, and 3.2 nm when there are manufacturing errors of the first, second, and third type respectively. Therefore, of the three types of manufacturing errors, the pixel position error affects the measurement result most significantly.

EXPERIMENT

To demonstrate the performance of the active encoder, a prototype planar active encoder has been developed that measures linear displacements in X and Y directions, and angular displacement θ_z. The encoder consists of two black-and-white (B/W) cameras, separated by a distance of 120 mm, and two iPhone4's. Each camera has a pixel count of 1600 x 1200 pixels, a pixel size of 4.4 x 4.4 μm, a frame rate of 28 fps, and a custom-designed microscope lens composed of a 50X microscope objective and a field lens. The LCD display of iPhone4 is the so-called Retina display, which has a PPI (pixels per inch) of 326. The pitch of the pixel pattern is 26 μm in X direction and 78 μm in Y direction. The pitch in X direction is one-third of that in Y direction because in X direction each display

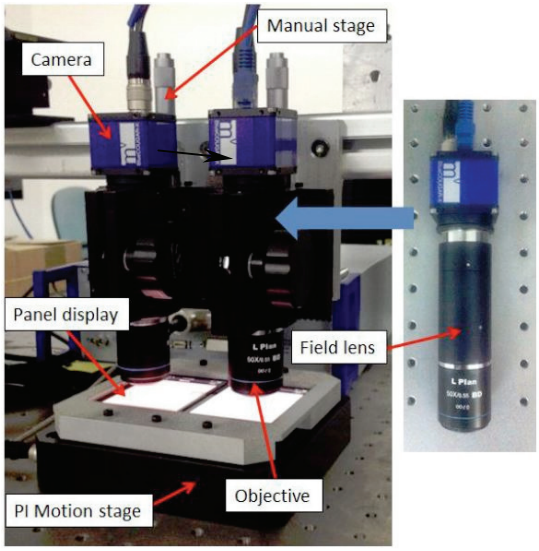

FIGURE 14. Experimental setup that consists of an active encoder and a multi-axis piezo stage.

pixel has three RGB sub-pixels. The images of the display are captured by the cameras and then sent to a PC for processing.

Figure 14 shows the experimental setup, which includes the active encoder and a multi-axis ($XY\theta_z$) piezo stage used to evaluate the performance of the active encoder. The stage has a travel of 100 μm and a closed-loop resolution of 0.3 nm in X and Y directions and a travel of ± 1 mrad and a closed-loop resolution of ± 0.1 μrad in θ_z direction. The stage is controlled by the same PC via a driver.

Before testing the resolution of the active encoder, various measures were taken to improve the quality of the acquired images. First, the brightness of each color pixels was adjusted so that they appear in the B/W camera image with similar gray scale values. Second, the image was captured in a size of 1600 x 16 pixels. The 16 lines of signals were averaged to reduce noise. Third, the image was intentionally defocused to reduce the effect of the high-frequency structures in the pixels of the display. The above measures were experimentally confirmed to be effective in significantly improving the quality of the signal obtained.

To determine the resolution of the proposed active encoder, a step test was conducted using the multi-axis piezo stage described above. The stage was programmed to move in a preset step repeatedly. After each step, the step size was measured by the active encoder. Figure 15

shows the results of the step tests in X direction. The step sizes are 50 nm, 100 nm, 500 nm, and 1 μm. From the results, the standard deviation was found to be 3.2 nm. For step tests in Y direction, the standard deviation was found to be 7.2 nm. Figure 16 shows the step test result in Y direction when the step size is 50 nm. The step test result for angular displacement θ_z is shown in Figure 17. Here the standard deviation was found to be 0.42 μrad.

The above experimental results demonstrate that the active encoder concept is valid and that active encoders have good potentials for precision position measurement at the nanometer level.

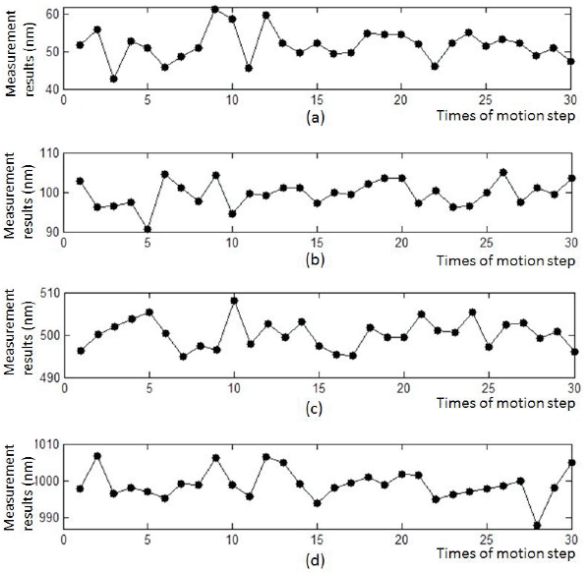

FIGURE 15. Step measurement results in X direction with a step size of (a) 50 nm, (b) 100 nm, (c) 500 nm, and (d) 1 µm.

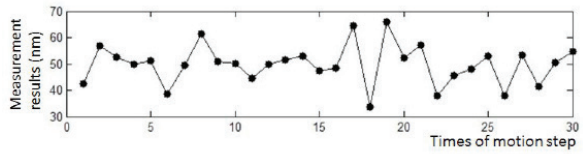

FIGURE 16. Displacement measurement result in Y direction with a step size of 50 nm.

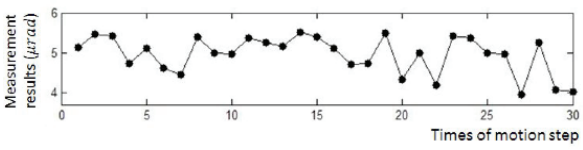

FIGURE 17. Rotation angle (θ_z) measurement result with a step size of 5 µrad.

CONCLUSIONS

A novel active encoder has been developed for planar absolute position measurement with a nanometer resolution. This active encoder uses a flat panel display as the grating scale and a camera as the reading head. The pattern on the display is actively controlled by a computer program. Image processing algorithms based on the phase correlation method have been developed to obtain position information from the display images with high resolution.

To verify the feasibility of the active encoder, a mathematical model of the active encoder has been developed and used to simulate the potential performance of the encoder. Different system parameters and error sources were considered in the simulation, such as camera resolution, noise level, display pixel size and display manufacturing errors. The results have been summarized and used to guide the design of active encoders.

To demonstrate the performance of the active encoder, a prototype planar active encoder has been developed. Experimental results show that the active encoder achieved a measurement resolution of 3.2 nm and 7.2 nm for linear displacement measurement in X and Y directions respectively, and a measurement resolution of 0.42 μrad for angular displacement measurement. These results demonstrate that the active encoder concept is valid and that active encoders can be used for precision position measurement at the nanometer level.

REFERENCES

[1] Gao W, Dejima S, Kiyono S. A dual-mode surface encoder for position measurement. Sensors and Actuators A: Physical. 2005; 117: 95-102.

[2] Kimura A, Gao W, Arai Y, and Jiang Z. L. Design and construction of a two-degree-of-freedom linear encoder for nanometric measurement of stage position and straightness. Precision Engineering. 2010; 34(1): 145-155.

[3] Leviton D B, Jeff K, Luck L. Ultrahigh-resolution Cartesian absolute optical encoder. SPIE proceedings. 2003; 5190: 111-121.

[4] Pieters R, Jonker P, Nijmerjer H. Trajectory generation for 1000 fps direct visual servoing. The 12th IAPR Conference on Machine Vision Applications. Nara, Japan: 2011.

Development of Error Budget Software for Machine Tools

Raunak Jadhav[1], Edward Morse[1]
[1]Center for Precision Metrology
University of North Carolina at Charlotte
Charlotte, North Carolina, USA

INTRODUCTION

For the purposes of this abstract, the term machine tool is used to describe tools that rely on metal cutting to obtain the desired part. Over the past two centuries machine tools have been able to produce parts with greater and greater accuracy. Systematic testing of machine tools and the necessary instrumentation to perform these tests has been progressing at a somewhat slower pace compared to the tolerances being held by most modern machine tools. Standards such as ASME B.5.54 or ISO230-1 provide guidelines for the evaluation of machine tools. An end user cannot directly infer the suitability of a machine to meet the required production part tolerances based on the results obtained through these tests. At the design stage of building a machine tool, an Error Budget can be can be used to help identify the sources of subsystem errors, and improve the accuracy of the machine by focusing resources on the major contributors of error [1]. There have also been attempts to perform such simulations for CMMs [2]

The goal of this research is to develop a software program to predict machine tool performance and compare this to the requirements of parts to be produced on the machine. The software program would be used to determine the suitability of a machine tool for a particular part tolerance requirement. It can also be used in preliminary design stages where a little is known about the subsystem errors but the magnitude of subsystem errors can be estimated based on experience or preliminary design calculations. In this paper two serial kinematic link based machine tools have been considered: a Tool room Mill and a Tool room Lathe. The simulation results obtained from these models can be used as a prediction of possible part outcomes.

CONCEPT

The orientation in space of one axis with respect to another can be represented by a Homogenous Transformation Matrix (HTM). The structure of a machine tool can be modeled by multiplying several of these matrices in the order of occurrence of the stacking of the axes in the serial assembly. The result of this multiplication represents the spatial relationship between the tool and the work piece. [3] An individual axis has 6 parameters which can be used to determine is deviation from ideal path. Thus a 3 axis machine – in general – would have 18 parameters plus 3 squareness parameters.
These parametric errors are measured by instruments to quantify machine tool performance. The nature of these geometric errors of the machine are such that they can be (and often are) simulated through mathematical polynomials. The actual measurements can be somewhat difficult, and are prone to the classical measurement problems of operator error, instrument error and differences between repeated measurements (repeatability).

Using a single polynomial to represent the error of a machine tool axis would be unwise. Low order polynomials do not capture the local deviations well, while higher order polynomials tend to oscillate excessively. As a compromise, each individual axis error is modeled by a sum of Legendre polynomials. By multiplying the coefficients of these polynomials with suitable random numbers a set of errors can be created to simulate the randomness in the measurement process, or the variability between machines with a similar performance specification. With this simulation of "realistic" axis errors, the positioning errors of the tool with respect to the work piece can be predicted.

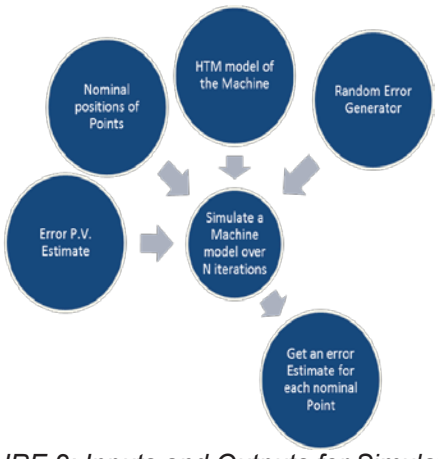
Nominal positions of Points
HTM model of the Machine
Random Error Generator
Error P.V. Estimate
Simulate a Machine model over N iterations
Get an error Estimate for each nominal Point

FIGURE 2: Inputs and Outputs for Simulation of the Machine Tool

An estimate of the distorted geometries can be evaluated by using the nominal workpiece geometry and passing it through the machine tool model. This geometry can further be used for GD&T analysis to estimate the actual values of various tolerance specifications on the distorted work piece. The suitability of a machine tool for a specific part to be produced on the machine can be evaluated in this way.

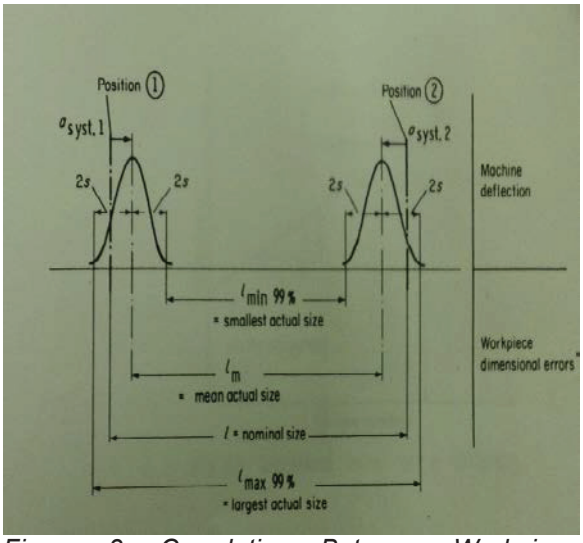

Figure 3: Correlation Between Workpiece Dimensional Errors and Machine positioning Errors [4]

Figure 2, taken from [4], shows how, for a simple tolerance interval, workpiece dimensional errors and conformance to specification can be inferred from the machine tool errors. In the analysis of tolerances, it is common to report the confidence level of the result, in addition to whether the mean value conforms to tolerance or not.

SIMULATIONS

A simulation of a Lathe and a Mill was carried out using assumed peak-to-valley (P-V) ranges for geometric errors of the machine tools. These ranges were used to evaluate the result of machining with these tools. A distribution of the deviations from nominal geometry was found at a number of points on the workpiece surface.

A simple Tool Path containing a taper and a hemisphere, as shown in Figure 3, was chosen as a nominal. This path was discretized at the intervals shown and a simulation was carried out

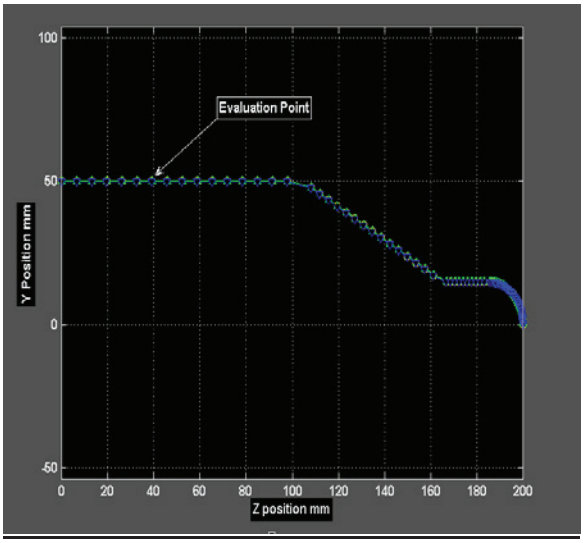

FIGURE 4: Simulated Profile of Tool Path for Haas TL-1 Lathe

By obtaining a Scatter band of width 2s for each position in (e.g. refer Figure 5) in addition to the systematic deviations of the machine in different nominal positions along tool path workpiece Dimensions can be evaluated.

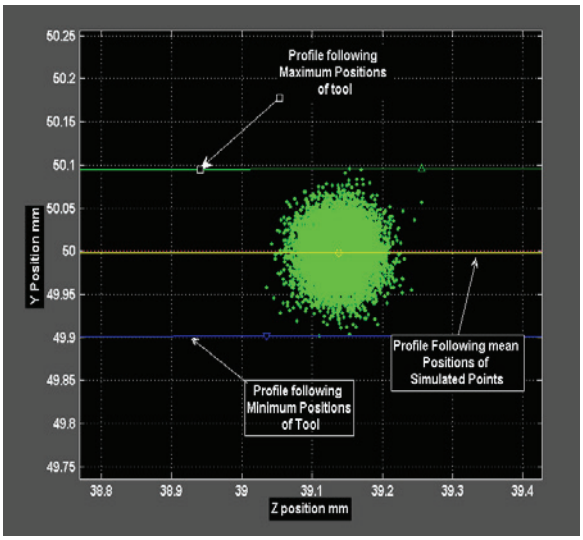

FIGURE 5: A Sample Point and Profiles of Worst Case Scenarios

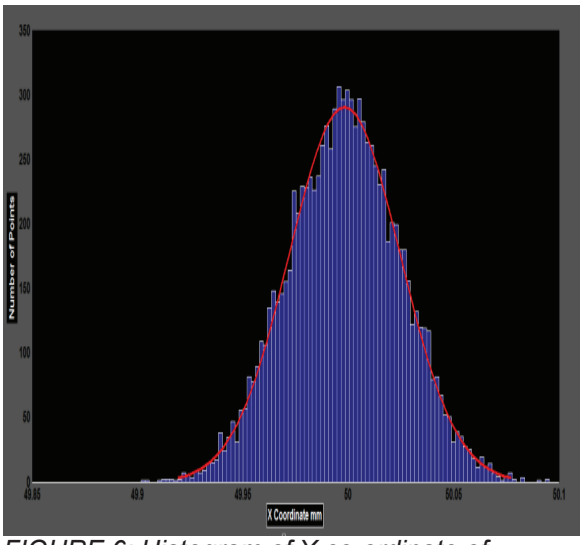

FIGURE 6: Histogram of X co-ordinate of simulated points and their occurrence

A simulation of a Toll room Mill was also carried out using assumed P-V values part chosen for the simulations was a Precision Contouring Test Part Size 1 (approximately 160 mm on a side).

To provide the ability to evaluate any 3-D surface, a common (STL) format was chosen as an input for the software. By converting the 3-D CAD model into the STL format, the 3-D geometry is discretized into triangular facets and the vertices of these facets can be used as nominal points for Simulation of the Machine tool

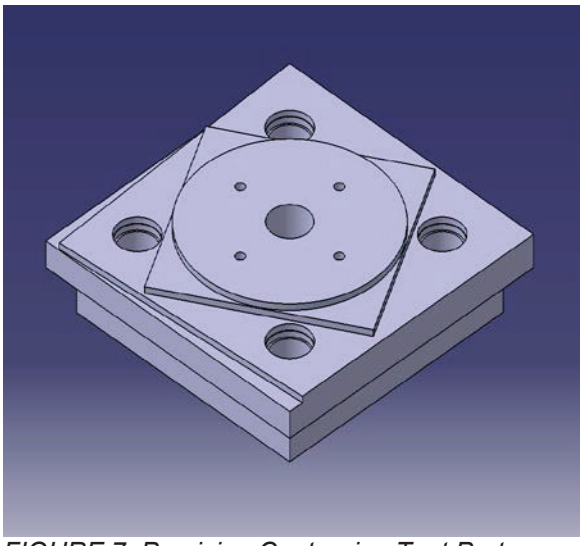

FIGURE 7: Precision Contouring Test Part

The milling test part, commonly know as a circle-diamond-square, is shown in Figure 6, and the predicted geometry of the part manufactured by an imperfect mill is shown below in Figure 7.

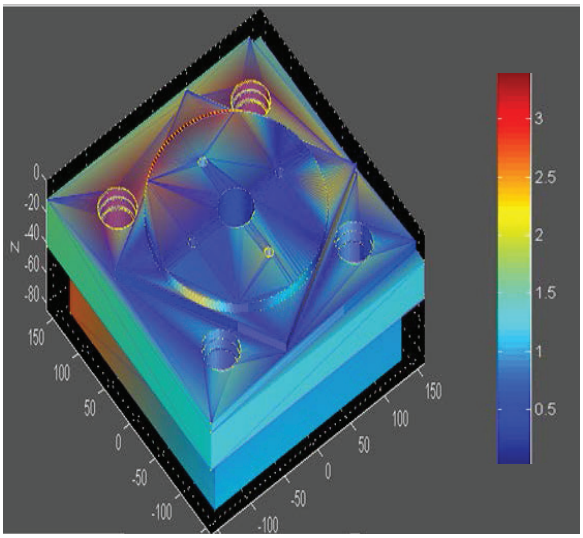

FIGURE 8: A Simulated case of the precision contouring test part

MEASUREMENT OF MACHINE TOOL ERRORS

To validate the results of the error budget simulation, we have begun measurements of machine tool errors so that the geometry of actual workpieces can be compared to the predicted geometry inferred from the machine specification.

FIGURE 9: *Measurement setup using API 6-D laser, X axis measurements*

The HAAS TI-1 lathe errors were measured using a API 6-D laser interferometer system the system is capable of performing straightness and angular errors simultaneously. The parallelism and orthogonality of carriage and cross slide were measured using reversal techniques.

FIGURE 10: Orthogonality Measurement of Crossslide of HAAS TI-1 lathe

The simulation of Lathe using measured data is currently in progress and measurement of Milling Machine errors are also in progress.
To validate the results of the software. CMM measurements of machined workpiece will be compared to the results of the simulated workpiece.

CONCLUSION

The software developed can be used as an error budget tool in the design stage, where P-V estimates of the machine errors are available, in order to determine suitability of machine for a specific part.
If the errors of an existing machine tool are measured, the results of the simulation can be used to provide better estimates of machined workpiece geometry; this information can subsequently be used to evaluate the geometric acceptability of the part to its design tolerances.

REFERENCES

[1] Hale, Layton Carter, *Principles and Techniques for Desigining Precision Machines* (PhD Thesis). Livermore : Lawrence Livermore National Laboratory, 1999.
[2] Eisenbies, Stephen Keeling, *Error Budget by Constraints*, (Master's Thesis), The University of North Carolina at Charlotte, 2001.
[3] Donmez, M. Alkan, *Machine Tool Accuracy Enhancement: Theory, Application and Implemetation*, (PhD Thesis) Purdue University, 1985.
[4] Weck, Manfred, *Handbook of Machine Tools Volume 4*, John Wiley and Sons, 1984.

DEVELOPMENT OF A LASER-GUIDED DEEP-HOLE MEASUREMENT SYSTEM: ADJUSTMENT TO A SMALL SIZE

Akio K.[1], Ali MD Hazrat[1], Takao S.[1], Hiroshi M.[2], Osamu O.[3], and Shuhei K.[1]
[1]Department of Mechanical Engineering, Faculty of Engineering, Kyushu University 36, 744 Motooka, Nishi-ku, Fukuoka 812-8581, Japan
[2]The University of Kitakyushu, Kitakyushu, Japan
[3] Miyazaki University, Miyazaki, Japan

INTRODUTION

Deep holes are bored with the meter-, millimeter-, and micrometer-level diameters in engineering. Their lengths can be several tens of meters to as short as a few micrometers. Examples of holes with large 100-millimeter-level diameters and meter-level lengths are the rotation shafts of jet engines, generators, and high-speed trains; the large cylinder used in plastic injection moulding; the cylindrical liners of ship engines; and cannons. Holes with normal 10-millimeter-level diameters and lengths of several hundred millimeters are used for the main spindles of machines, the small cylinder in plastic injection molding, the tube sheet for heat exchanger, and guns.

Accurate measurement of the diameter, roundness, cylindricity, and straightness of a deep hole is essential for improving the performance of products. However, existing systems have drawbacks to precisely measuring holes with large- length-to- diameter ratios, which require multiple measurement devices. In order to accurately evaluate the parameters of such deep holes with 100-millimeter-level diameters and meter-level lengths, using a single device, a laser-guided deep-hole evaluation probe was developed [1-6].

In this study, the guided system is applied to holes with normal 10-millimeter-level diameters and lengths of several hundred millimeters. A measurement system that can measure a small size hole with a diameter of 17-21 mm and length of 1,000 mm is constructed, and the performance is tested.

MEASUREMENT SYSTEM FOR A SMALL SIZE HOLE

Measurement Probe

Figure 1 shows a measurement probe that can measure a hole with a diameter of 17 - 21 mm and length of 1,000 mm. **Figure 2** shows a measurement unit that consists of a pentaprism, corner cube prism, and stylus. The stylus has a stroke of 2 mm. **Figure 3** shows a sectional view of the probe. The measurement unit is rotated by a DC motor through a reduction gear, coupling, and flange shaft. Parameters of the DC motor: DCSPG10, Cytron Technology Malaysia; gear ratio of 298:1; 45 rpm under no loading; weight of 10 g; current of 30 mA under no loading. At the coupling, a magnet is molded to detect the rotation of the measurement unit using a Hall element (Type SS443A, Honeywell). A collimated laser (Type MLXA, KIKOH GIKEN) is used as a laser diode to detect the probe attitude. In this experiment, the focusing length is 4 m.

Measurement System

Figure 4 shows the deep-hole measurement system for a small size hole. The long measurement bar **3** is a hollow shaft. A deep-hole boring machine is used with one end of the measurement bar fixed by the collet chuck and

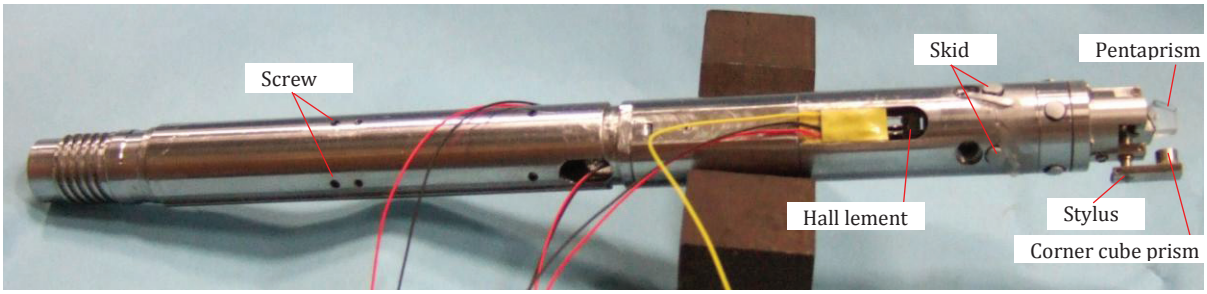

FIGURE 1. *Measurement probe for a hole with a diameter of 17 - 21mm and length of 1,000 mm.*

the other end supported by a pair of skids **10** behind the measurement unit **1**. The workpiece **2** is fixed on a machine table. The hole wall is scanned spirally by rotating the measurement unit and feeding the workpiece along the measurement unit, which is rotated by the gear motor **7**. The up and down movement of the stylus is detected by a laser interferometer **4**, which is placed in front of the measurement unit via the pentaprism **11** and corner cube prism **12**, which are attached to the measurement unit.

The laser diode **8** is located at the back end of

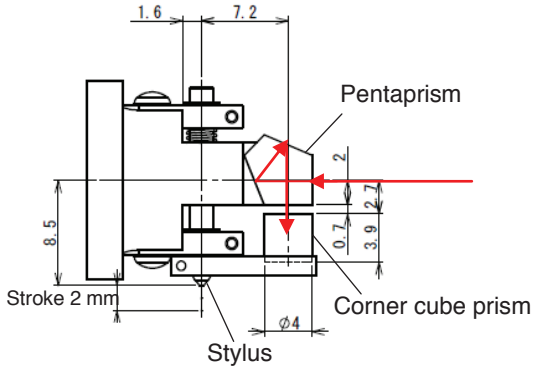

FIGURE 2. *Measurement unit.*

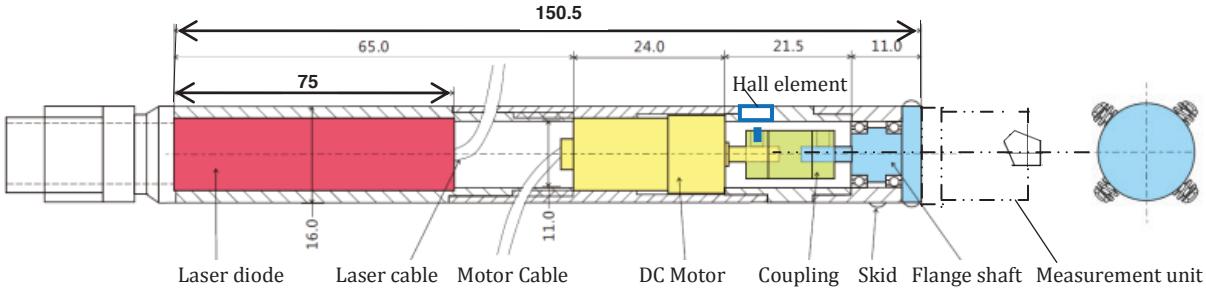

FIGURE 3. *Structure of the measurement probe.*

1 Measurement unit **3** Measurement bar **5** CCDδ **7** DC motor **9** Flange shaft **11** Pentaprism
2 Workpiece 4 Laser interferometer **6** CCD*i* **8** Laser diode **10** Skid **12** Corner cube prism

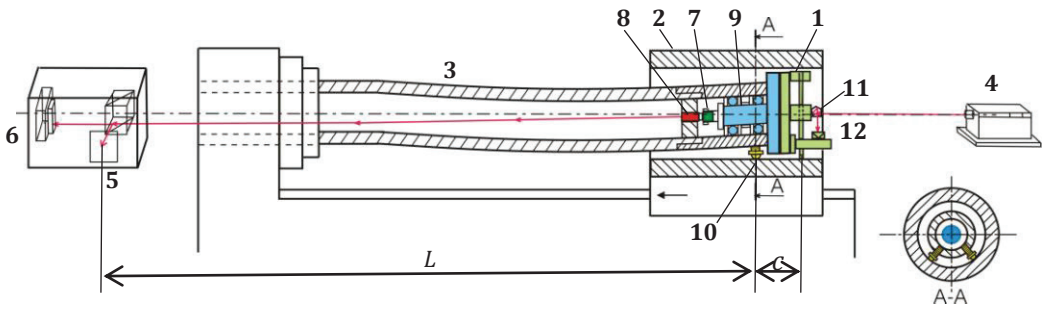

FIGURE 4. *Laser-guided deep-hole measurement system without actuators.*

the measurement probe in order to detect the attitude (position and inclination) of the measurement unit. A laser beam passes through the measurement bar and reaches optical devices CCDδ **5** and CCD*i* **6** to detect the attitude of the measurement unit.

In this measurement system, the laser diode is placed on the measurement axis, which is the center line of the spindle of the headstock, so that the attitude of the measurement unit can be accurately detected. In contrast, the measurement system described in references [2, 3] instead has a laser diode fixed on the measurement probe apart from the measurement axis. Therefore, the rotational deviation of the laser diode due to the rolling of the measurement probe affects the detection accuracy of the probe's attitude [4].

MEASUREMENT PRINCIPLE

Measurement Principle

The optical system consists of a laser interferometer placed in front of the measurement probe, and measurement unit that

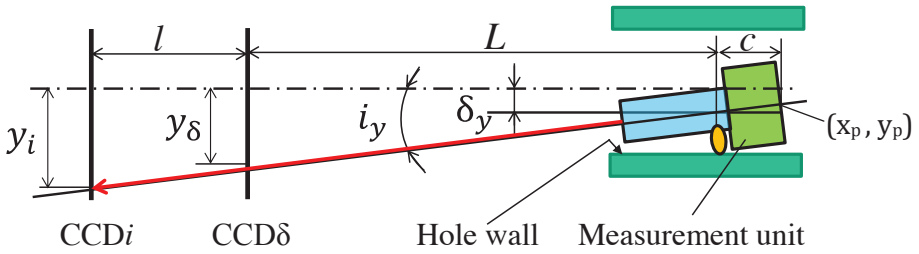

FIGURE 5. *Measurement method of probe position and inclination.*

comprises the pentaprism and corner cube prism (Fig.2). Main structure of measurement unit is similar to a dial gage. Its fabrication error is 0.01 mm. The corner cube prism is fixed to the stylus. The stylus scans the hole wall of a workpiece set on a carriage toward the tangential direction. The pentaprism deviates the input beam precisely by 90°. The corner cube prism reflects the output beam toward the input beam. The laser beam from the interferometer is deflected by the pentaprism to the corner cube prism. Then the returning beam reaches the interferometer along the same path. The movement of the stylus, which is placed perpendicular to the hole wall, is detected by the laser interferometer (Fig. 4).
The measurement length, response speed, and resolution of the laser interferometer are 0 - 10 m, 0 to ±2.0 m/s, and 0.01 μm, respectively.

Detection of Hole Deviation

Hole deviation cannot be detected by the measurement unit, because the measurement unit moves along the hole deviation. Hence, the deviation is detected using CCDδ **5** and CCD*i* **6**. In this experiment, the coordinate of the laser spot of each CCD is stable at the micrometer level.

Figure 5 shows the locations of the probe, CCDδ, and CCD*i* for detecting the probe position and its inclination. The probe position and its inclination are geometrically calculated at the longitudinal skid position from the relationship between the coordinates of laser spots on the two CCDs and the laser source [4]. In the *Y* direction, the probe position δ_y and its inclination i_y at a longitudinal position of skids can be written as

$$\delta_y = y_i - (L+l)\tan(i_y) \quad (1)$$

$$\tan(i_y) = (y_i - y_\delta)/l \quad (2)$$

where *L* = 2,814mm, *l* =1,192 mm, and *c*=22.5mm.

INFLUENCE FACTORS ON DETECTION ERRORS

Deviation of Probe From Hole Center

Figure 6 shows measurement of hole shape. The shape is measured by scanning hole wall circumferentially at intervals of a depth. The locus of the probe center is detected by the CCD cameras **5** and **6**. However the displacement of the probe from the hole center that influences on the detection accuracy is not detected. The displacement can be obtained as following.

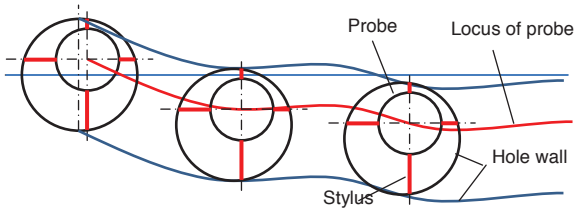

FIGURE 6. *Measurement of hole shape.*

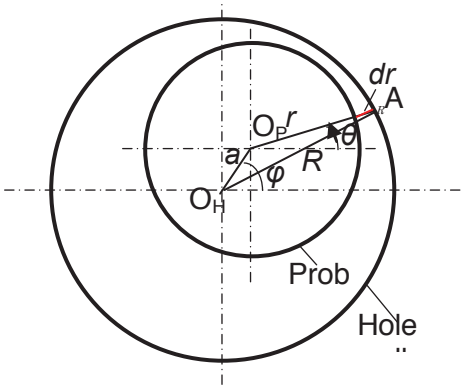

FIGURE 7. *Deviation of probe from hole center.*

In a triangle O_PO_HA shown in **Fig.7**, the following formula can be obtained.

$$R^2 = a^2 + (r+dr)^2 - 2a(r+dr)\cos(\frac{\pi}{2} - \varphi + \frac{\pi}{2} + \theta) \quad (1)$$

$$r + dr = -a\cos(\theta - \varphi) + \sqrt{a^2\cos^2(\theta - \varphi) - (a^2 - R^2)}$$

$$= -a\cos(\theta - \varphi) + R(1 - \frac{a^2}{R^2}\sin^2(\theta - \varphi))^{\frac{1}{2}}$$

$$\frac{a^2}{R^2}\sin^2(\theta - \varphi) \ll 1$$

$$r + dr = R - a\cos(\theta - \varphi) \quad (2)$$

where a and φ are the value and direction of the probe displacement. R and r are radius of hole and distance between probe center and hole wall. θ is rotation angle of stylus. a and φ can be obtained by fitting to the value measured by the interferometer.

Effect of Initial Inclination on Detection Accuracy

In the case of a cantilever with a supported end, an inclination of supported end is shown as:

$$i_0 = \frac{we^2}{48EI} \quad (3)$$

where Young's modulus E=205 GPa and the length between a fixed end of the beam and skids e = 1,025 mm. I is the geometrical moment of inertia. Weight per unit length w is 0.001244 kg/mm. the outside and inside diameters are d_o = 16 mm and d_i = 11 mm, respectively. Calculated inclination angle i_0 is 5.448×10^{-4}. In Fig.5, a point (x_p,y_p) where a center line of measurement head and that of a stylus cross can be arranged on measurement axis (0,0). When the inclination i_0 exists, hole wall is scanned ellipsoidally.

In case of a hole with a diameter of 18 mm, scanning point deviates by maximum $18i_0$ = $18\times5.448\times10^{-4}$ = 9.8×10^{-3} mm in Z-direction (Depth direction). Major axis of the oval is $18/\cos(\tan^{-1}(i_0))$ = 18.00000267 mm, which is larger by 0.00267μm than hole diameter 18 mm. These values are very small. Therefore the effect of scanning deviation due to inclination angle i_0 is negligible.

EXPERIMENTAL PROCEDURE

Measurement is carried out using a deep-hole drilling machine (Fig.4). **Figure 8** shows a shape of a steel workpiece. In this experiment, it is examined whether measurement can be performed accurately even if a hoe length becomes large.

Initial Setting

Optical devices for detecting hole deviation are arranged as follows.

(1) Setting of a laser interferometer
The laser interferometer is set so that its laser beam lies on a spindle axis of a deep hole boring machine using a steel block with a PSD (Position Sensitive Detector) [4]. When the steel block is set on the machine table, a center of the PSD comes to the axis.

(2) Setting of CCD **5** and **6**
CCD cameras **5** and **6** are set so that the laser beam from the laser interferometer comes to their centers

(3) Setting of a laser diode **8**

(4) Attitude of the laser diode is changed using four screws fabricated in the measurement bar so that its laser beam come to the CCD cameras **5** and **6**.

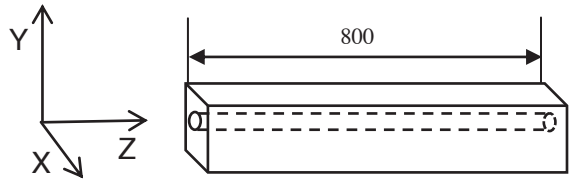

FIGURE 8. *Shape of a workpiece.*

Experimental Procedure

Measurement starts at a longitudinal position where two skids enter a hole. Theoretically a guide bush having a hole with a smaller diameter than workpiece is set on the entrance of measured hole. After that, measurement starts at the hole of the guide bush. The depth of hole is 24 mm. Probe center is put on the hole center by two skids which move radial direction by their screw.

Experiments are carried out under the following conditions.

Hole Deviation

Four hole walls of ±X and ±Y directions are scanned along longitudinal direction *Z*. Measurement unit is not rotated.
Table feed f = 120 mm/min.

Hole shape
Hole shape is measured under the following two conditions.

(1) Spiral scanning:
Rotational speed of the measurement unit N = 6 rpm. Table feed f = 5 mm/rev.
Measurement time t =27 min/800mm.

(2) Intermediate feed and circumferential scanning:
First roundness measurement starts at a depth of 24 mm where two supporting pads enter inside of the hole. Then, measurement is performed every hole depth of 50 mm. Table feed f = 120 mm/min

Roundness
Rotational speed of the measurement unit N = 6 rpm. Table is not moved during measurement.

EXPERIMENTAL RESULTS
The measurement system can measure hole accuracy up to a depth of 1,000 mm.

Hole Deviation
Figure 9 shows hole deviation obtained from CCD δ and CCDi. Hole does not deviate toward Y direction, while deviates by 0.6 mm toward X direction.

Figure 10 shows longitudinal scanning of four hole walls of ±X *and* ±Y. The figures can be obtained from the Y-Z sectional view and X-Z sectional view of the hole shape in the latter Fig.12, respectively.

Hole Shape

(1) Spiral scanning:
Figure 11 shows spirally scanned hole wall from a depth of 24 mm to 49 mm. Influence of probe displacement in the hole is removed.

(2) Intermediate feed and circumferential scanning:
Figure 12 shows circumferentially scanned hole shape every hole depth of 50 mm measured by the laser interferometer **4** shown in Fig.4. Influence of probe displacement in the hole is removed.

Roundness

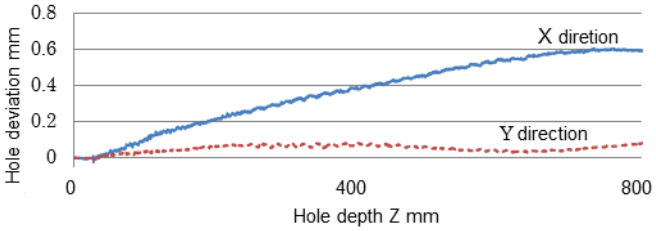

FIGURE 9. *Hole deviation obtained from CCDδ and CCDi .*

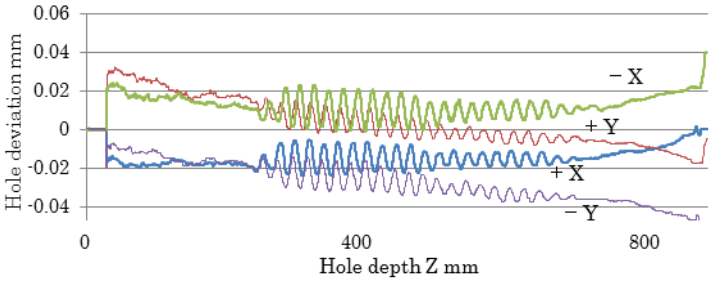

FIGURE 10. *Longitudinal scanning of four hole walls of ±X and ±Y.*

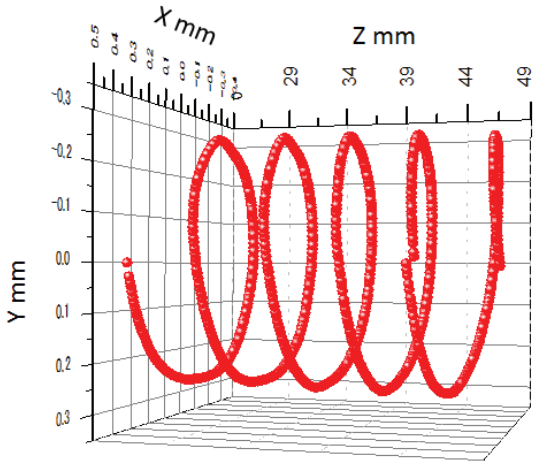

Figure 11. *Spirally scanned hole shape measured by the laser interferometer* ***4.***

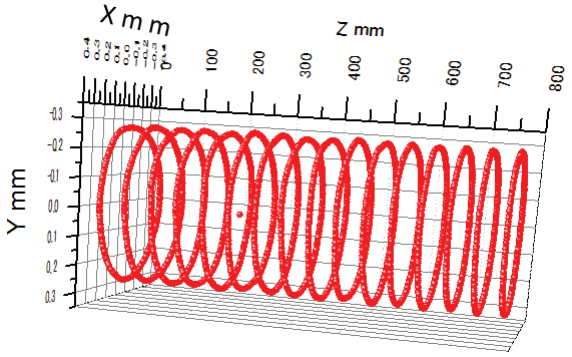

FIGURE 12. *Circumferentially scanned hole shape measured every hole depth of 50 mm by the laser interferometer* ***4.***

Figure 13 shows roundness profile obtained at a depth of 24 mm. This figure is that of a depth of 24 mm in Fig.11. Figure 13(a) shows the measured value and fitted cosine wave; a = 0.07466 mm and φ = 2.924 rad. Figure13 (b) is an original roundness profile. The roundness profile displaces upward due to the probe displacement. In Fig.13 (c), the influence of the displacement is removed. In Fig.13 (d), roundness is corrected as shown in the workpiece coordinate of Fig.8. The stylus is located to the 57° rear from the magnet that works with the hall element for detecting rotation of the measurement unit. If the stylus, the magnet and the hall element are placed on +X axis at the beginning of measurement, the final correction is not necessary.

CONCLUSION

A measurement system that can measure a small hole with a diameter of 17-21 mm and length of 1,000 mm is constructed. As a result of the performance test, it is cleared that it can be used to measure the hole accuracy.

REFERENCES

[1] Katsuki A, et al. Development of a High Performance Deep-Hole Laser-Guided Boring Tool: Guiding Characteristics. Annals of the CIRP. 1997; 46/1:319-323.

[2] Katsuki A, et al. Development of a Laser-Guided Deep-Hole Measuring System: Measurements of the Roundness. Cylindricity and Straightness. LEM 21, Fukuoka, Japan. 2007; 887-892.

[3] Katsuki A, et al. High-Accuracy On-Machine Measurement of Deep Hole with Diameter Varying at Millimeter-Scale. 4th CIRP International Conference on High Performance Cutting, Gifu, Japan. 2010; 2: 239-242.

[4] Katsuki A, et al., Development of a practical high-performance laser-guided deep-hole boring tool: Improvement in guiding strategy. Precision Engineering. 2011; 35/2: 221-227.

[5] Katsuki A, et al., Study on high-speed on-machine measurement of deep-hole accuracy. Journal of the Japan Society for Precision Engineering. 2011; 77/7: 681-687.

[6] Katsuk A, et al. Development of a laser-guided deep-hole evaluating system. Journal of the Japan Society for Precision Engineering. 2011; 77/10: 977-984.

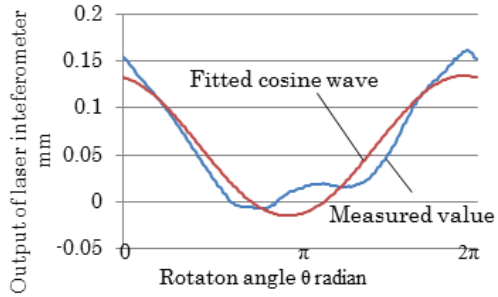

(a) Fitting to measured value

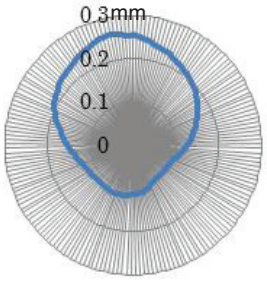

(b) Roundness profile (Before correction)

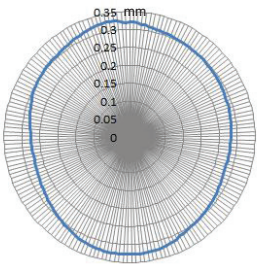

(c) Roundness profile (After correction)

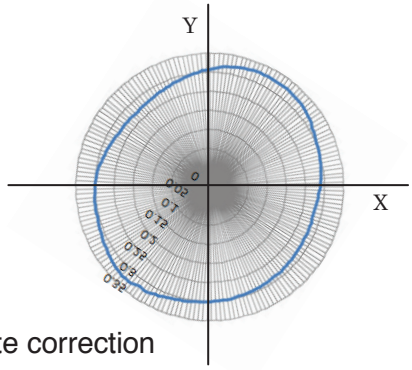

(d) Coordinate correction of rotation sensor

FIGURE 13. *Corrections of measured roundness profile using fitting method, and locational delay of rotation-detection sensor*

SYNCHRONOUS SIGNAL REMOVAL VIA WAVELET PACKETS

Eric E. Keller[1], Eric R. Marsh[1], and Byron R. Knapp[2]
[1]Department of Mechanical and Nuclear Engineering
The Pennsylvania State University
University Park, Pennsylvania, USA
[2]Professional Instruments
Hopkins, Minnesota, USA

INTRODUCTION

One of the fundamental signal processing techniques in spindle metrology is the separation of synchronous and asynchronous parts of spindle motion. While in many cases, the synchronous parts of the spindle motion are more important, there are many cases where knowledge of the asynchronous motion is desired. However, it is common that a time series describing the spindle motion is dominated by the synchronous motion. Applications involving vibration are one area where the desired signal is asynchronous to spindle motion.

Removal of synchronous (or harmonic) signals from a time series is a common problem in science and engineering. An example of this is removing the power line harmonics from low-level sensor signals. The literature regarding harmonic removal is extensive and spans many fields of study.

While standard methods[1] are quite reliable, the wavelet packet method presented here has some advantages. For example, the implementation presented here can be used to produce a time series that is limited to a single band of frequencies, for example to select particular a modal frequency. In addition, there is potential for on-line separation, although this has not been implemented.

WAVELET ANALYSIS

Wavelet analysis is conceptually similar to the Fourier Transform (FT). While it is common to think of the FT as transforming a signal into the frequency domain, it can also be considered as the process of decomposing the signal into frequency components. It is also a projection of the signal onto the frequency domain space. The latter two concepts make more sense in discussing wavelet analysis.

DISCRETE WAVELET TRANSFORM

The method discussed here is fundamentally an application of the discrete wavelet transform (DWT) or Multiresolution Analysis. The DWT is a well-known method of decomposing a signal in a way that preserves both time and frequency localization. The decomposition of a signal involves convolution of the signal with a wavelet, which is a short duration signal of finite energy. This allows a trade-off between preserving the time localization of a signal and the frequency localization of the signal. This contrasts with the Fourier transform, which determines frequencies present in a signal, but destroys the time localization unless extended methods such as the windowed Fourier transform are used.

At each level of decomposition, the DWT projects the signal into what are called the “Approximation” and “Detail” subspaces. The next level of decomposition further separates the approximations into details and approximations. Thus, the final level of decomposition, the signal is fully represented by the last coefficient of the approximation space at that level and the detail coefficients from the lower levels of decomposition. At each level of decomposition, the resulting coefficients are down-sampled by a factor of two. This results in a full decomposition having the same number of data points, only split into the coefficients of the resulting sub-spaces. Thus the method does not create or destroy information and is fully reversible without loss.

DISCRETE WAVELET TRANSFORM

The disadvantage of the DWT method is that the frequency bands that the signal can be decomposed into are limited to a dyadic structure, i.e. the frequencies have a power of two relationship with each other. This often results in a decomposition that is too granular for many applications. One method of solving this issue is the Wavelet Packet Decomposition (WPD). The WPD uses the same

decomposition as the DWT, but has flexibility in which subspaces of the signal that are decomposed. Thus it can be considered as recursively applying the DWT algorithm to subspaces of the orignial signal. Instead of decomposing only the approximation subspace at every level, the user has the choice of leaving the approximation coefficients as they are and decomposing the detail space. Just as with the DWT, the result of a WP decomposition is that there are still the same number of data points as the original signal, but they are split into a set of subspaces.

FILTERING USING WAVELET ANALYSIS

Since the DWT and WP project the original signal onto orthogonal subspaces, one trivial method of filtering is to simply zero out the coefficients of the decomposition that fall in a particular subspace. This removes that subspace from the space defined by the original signal. This is the main technique of bandpass filtering used in the work presented here. Typical applications of the DWT require some form of compression, and so this method is commonly used. It is good practice in sampled data systems to sample at a higher rate than the Nyquist criteria would suggest, and this means that there is no information content in much of the spectrum. This holds true in the wavelet domain as well.

BASELINE SHIFTING METHOD

In many cases, it is desirable to sample spindle motion data synchronized with the spindle rotation using an encoder. This is required for the method presented here to work. If the encoder has N counts, then the sampled data signal can have the synchronous data removed if the wavelet packet decomposition is performed to the $J = \log_2 N$. So for example, a 1024 line count encoder would result in a decomposition to the 10^{th} level. This results in a single point in each coefficient for every complete revolution. Thus, the synchronous portion of the signal is removed by subtracting the average of these points over a number of cycles.

PROBLEMS WITH THE BASELINE SHIFTING METHOD

In real-world data, this fails to satisfactorally remove the synchronous data. The issue is that a sampled data system will spread the spectrum of the synchronous data. The baseline shifting method removes the data at exactly the harmonic frequencies, but leaves significant energy in the surrounding frequencies. In most applications, this is not particularly useful. This work incorporates a high pass filter at the terminal level of decomposition. This reduces the subspace of those terminal levels of decomposition, but there is no theoretical issue with using a time domain filtering technique on the coefficients at this level since they are fundamentally a time domain signal.

IMPLEMENTATION

The modified baseline shifting method was implemented using the Matlab programming language. A graphical user interface was constructed that displays the Fourier domain signal for both the original (red) and filtered (blue) signal. This allows the user to choose the wavelet and filter parameters and assess the results. It is convenient to look at the frequency domain results because it is possible to easily see the effect of the filtering. A comparison in the time domain is very difficult, particularly since this method is most useful in cases where the original signal is dominated by the synchronous element. Both lowpass and bandpass are possible with an option not to remove the synchronous signal which is mostly useful in the bandpass case.

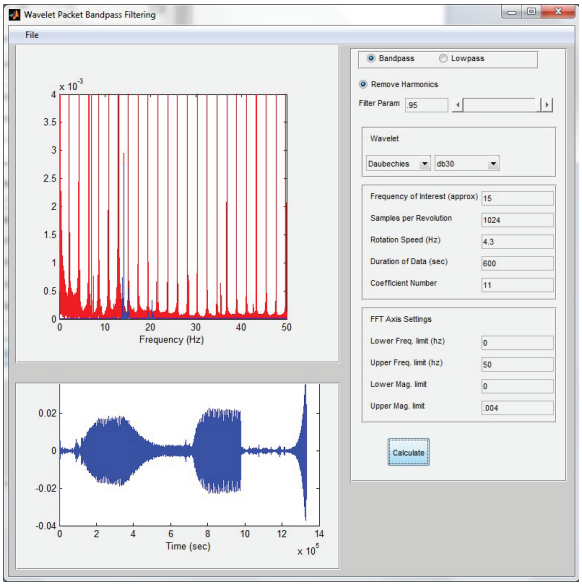

FIGURE 1. The user interface for the wavelet packet filtering program

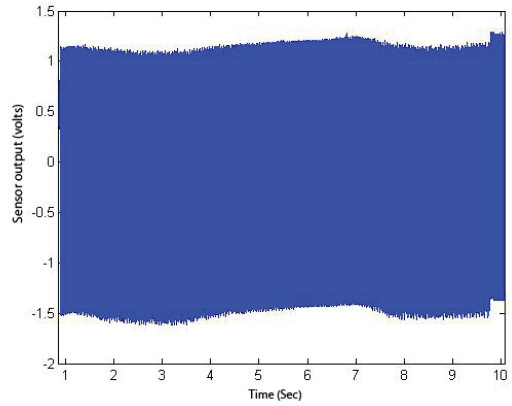

FIGURE 2. The original signal from a grinding operation showing that the signal is dominated by the synchronous signal.

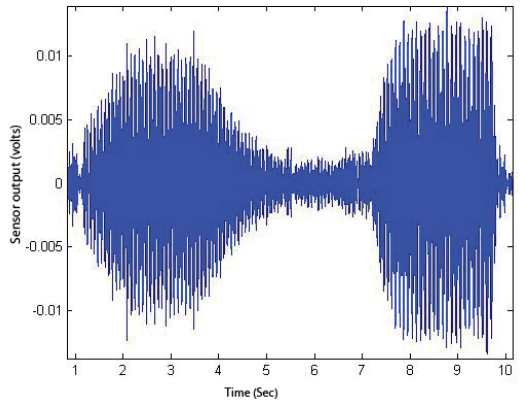

FIGURE 3. The filtered signal from the grinding operation showing the displacements with the synchronous signal removed

EXAMPLE

An experiment with a rotary grinding operation was performed. The machine used is a Moore Nanotech CNC lathe with motorized Professional Instruments air bearing spindles for both the work and the grinding spindles. The work spindle is instrumented with four capacitance displacement gauges arrayed radially around the spindle. Thus, a grinding operation results in displacements of the work spindle. The work piece was a cylinder of tungsten carbide. Grinding was performed using a diamond grinding wheel. The setup is shown in Figure 2.

The work spindle is equipped with a 1024 count encoder, and the capacitance probe signals were sampled using the encoder input as a sample clock.

The experiment consisted of a touch-off pass, a cleanup pass and then a constant infeed grinding pass. The original signal is in Figure 2. Some evidence of the grinding operation is visible in the signal, but it is overwhelmed by the synchronous signal from the bearing end plate surface, which has a known defect. This signal was filtered using the Daubechies 5 wavelet retaining only the 11th coefficient. The 1024 encoder count means that the filtering occurs at the 10th level of wavelet decomposition.

The results of this filtering are shown in Figure 3. The results of the grinding operation can clearly be seen. These results are comparable to ad-hoc filtering techniques previously used.

CONCLUSIONS AND FUTURE WORK

The main advantage of this work is that it can be implemented as a recursive multi-time scale filter. This has not been implemented. Another issue is that wavelet analysis often has issues with transient distortion effects because they are equivalent to very high-order filters. There are methods to reduce these effects, which need to be explored further.

REFERENCES

[1] Marsh E. Precision Spindle Metrology, DEStech Publications, 2009

[2] R. Coifman, Y. Meyer, and M. Wickerhauser, Wavelet Analysis and Signal Processing. Wavelets and Their Applications, eds. Jones andBartlett, pp. 153-178, 1992

[3] L. Xu, “Cancellation of harmonic interference by baseline shifting of wavelet packet decomposition coefcients,” IEEE Transactions on Signal Processing, vol. 53, no. 1, pp. 222–230, 2005.

ELECTRICAL RUNOUT USING AN EDDY-CURRENT SENSOR FOR ROUNDNESS MEASUREMENTS

Byron Knapp[1], Dave Arneson[1], and Don Martin[2]
[1]Professional Instruments Company
Hopkins, Minnesota, USA
[2]Lion Precision
St. Paul, Minnesota, USA

INTRODUCTION

Electrical runout is a commonly used term in the condition monitoring industry. It refers to the apparent displacement of a rotating shaft measured with inductive (eddy current) sensors caused by variations in the material electrical and magnetic properties [1]. Despite this unavoidable error in displacement measurement, inductive sensors remain the best choice when non-conductive contaminants such as dust, water, coolant or oil are present. In this work, actual roundness measured with a capacitance sensor and roundness plus sub-surface variation measured with an inductive sensor are compared for shafts of 6061-T6 aluminum, commercially pure Grade 2 titanium, and case hardened C1117 low carbon steel.

BACKGROUND

The theory behind inductive sensor operation relies on the relationship between electric current and magnetic fields. Inductive probes contain a coil that is excited with alternating current, creating an alternating magnetic field according to Ampère's law.

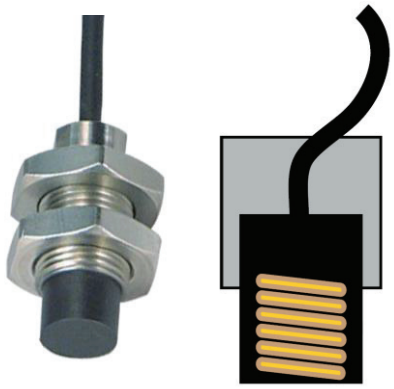

FIGURE 1. Inductive (eddy current) sensor with cross-section showing sensing coil.

According to Faraday, when time-varying magnetic fields interact with a conductive target, electric currents (eddy currents) are induced in the material. The eddy currents in the target create a reaction magnetic field in a direction opposite to the original magnetic field. This principle is known as Lenz's law.

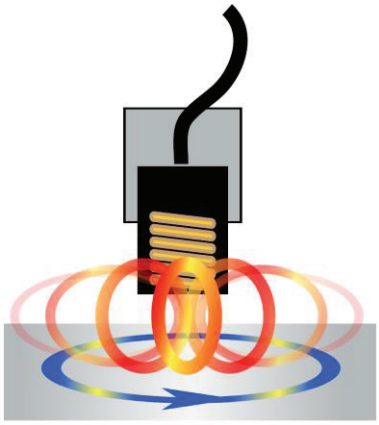

FIGURE 2. Alternating magnetic field produces eddy currents in the conductive target.

In order to maintain the original magnetic field around the sensing coil, the excitation current in the coil is increased to counteract the opposing magnetic field produced by the target. This interaction between the fields is used by the signal processing electronics to generate an output voltage proportional to the gap.

TARGET CONSIDERATIONS

Since the magnetic field of the sensor penetrates the target to induce eddy currents, anything that can disturb the current can cause errors in the gap measurement. The depth of field penetration is dependent on the frequency of excitation. If the target is too thin, the sensor will have reduced sensitivity and increased noise. Furthermore, the magnetic field covers an area on the target that can be 3-5 times larger than the probe tip. As a result, cylindrical targets should be 3-5 larger in diameter than the probe tip.

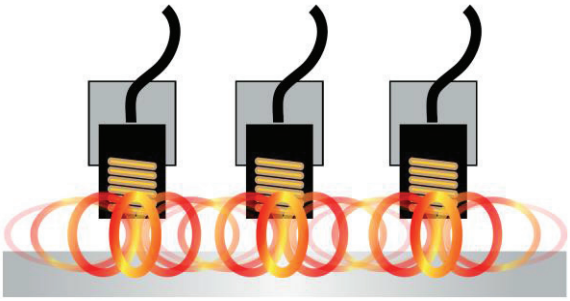

FIGURE 3.The field diameter can be 3-5 times the probe diameter. Multiple probes must be separated to avoid overlapping fields which create cross-talk between probes.

Eddy currents induced in the target are related to the electrical conductivity and magnetic permeability of the material. When calibrating the sensor, the actual material and alloy of the intended target must be used. However, even if the sensor is calibrated for a particular material, attributes such as the grain boundaries, crystal structure, chemical composition, quench profile, surface treatments, machining processes, residual magnetic field, and residual stress can all cause local variations in the material properties [2]. These inhomogeneities result in electrical runout, or measurement errors in target eccentricity and out-of-roundness.

APPROACH

The setup for demonstrating errors in roundness measurement due to electrical runout of various materials is shown in Figure 4. A cylindrical part is mounted to an air bearing roundness tester (Professional Instruments 4R Blockhead) with 512 line count encoder.

TABLE 1. Electrical and magnetic properties of materials used in this work [3].

Target material	Diameter (mm)	Volume resistivity ($\mu\Omega$•m)	Relative permeability
aluminum 6061-T6	38	0.04	1.00002
commercially pure titanium	19	0.5	1.00005
steel C1117	19	0.2	3800

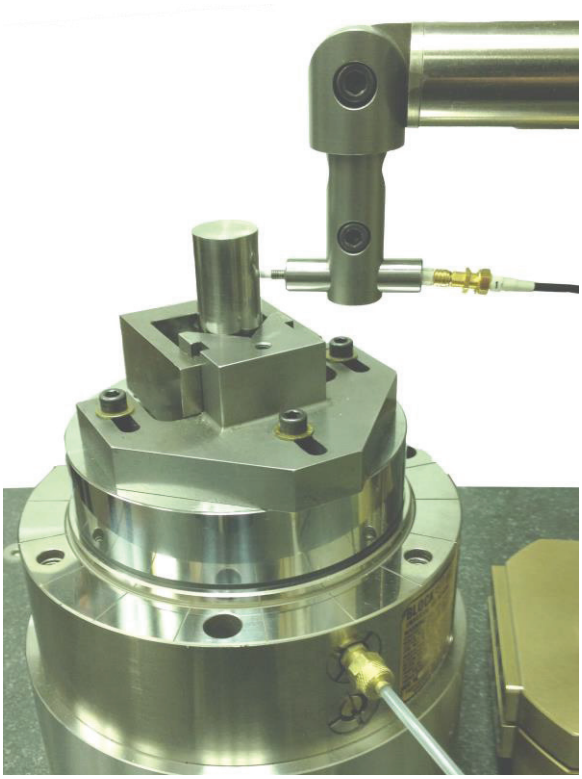

FIGURE 4. Electrical runout test using a Lion Precision U3 inductive sensor and ECL202 driver. The roundness tester uses a Professional Instruments 4R Blockhead air bearing spindle.

An inductive sensor and driver (Lion Precision U3 sensor and ECL202 driver) is calibrated for each of the three materials under test. The apparent out-of-roundness for each target material is measured for 8 revolutions using the inductive sensor at 512 angular locations provided by the encoder. The rotational speed is kept between 95-101 RPM to reduce speed-related variation in target inductance.

In the same setup, the inductive sensor is replaced with a capacitive sensor (Lion Precision C1-C probe and CPL290 driver) to determine the actual roundness using appropriate target corrections [4]. Comparing the two measurements demonstrates the roundness component of electrical runout for each of the three materials.

FIGURE 5. Measurement of the out-of-roundness of an aluminum target using a Lion Precision C1-C capacitive sensor.

RESULTS

The difference between the actual and apparent out-of-roundness shown in the polar plots (Figures 6, 7, and 8) demonstrates the "methods divergence problem" where two different types of displacement sensors produce significantly different results [5]. The divergence occurs because the capacitance sensor only measures the surface out-of-roundness and the inductive sensor measures the surface out-of-roundness and sub-surface material variation. The paramagnetic (small magnetic attraction) aluminum target results in the lowest error while the ferromagnetic steel target is the largest. This is a natural consequence given the differences in the material permeability shown in Table 2. The measurement error between aluminum and titanium is significantly less.

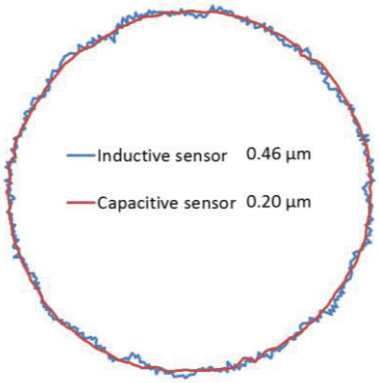

*FIGURE 6. **Aluminum** target out-of-roundness. The 0.26 micrometer difference between the two sensors is attributed to electrical runout.*

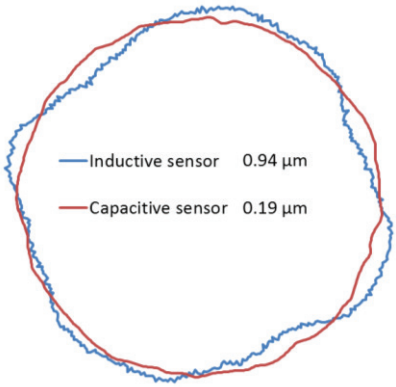

*FIGURE 7. **Titanium** target out-of-roundness. Slightly larger than the effect in aluminum, the electrical runout is 0.75 micrometers.*

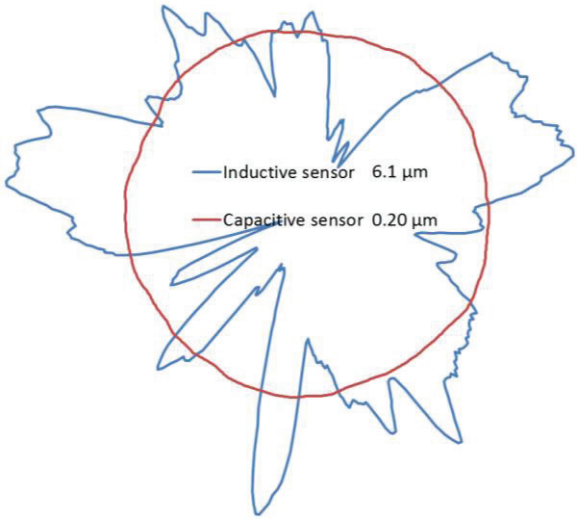

*FIGURE 8. **Steel** target out-of-roundness. The electrical runout in steel is significantly larger at 5.9 micrometers.*

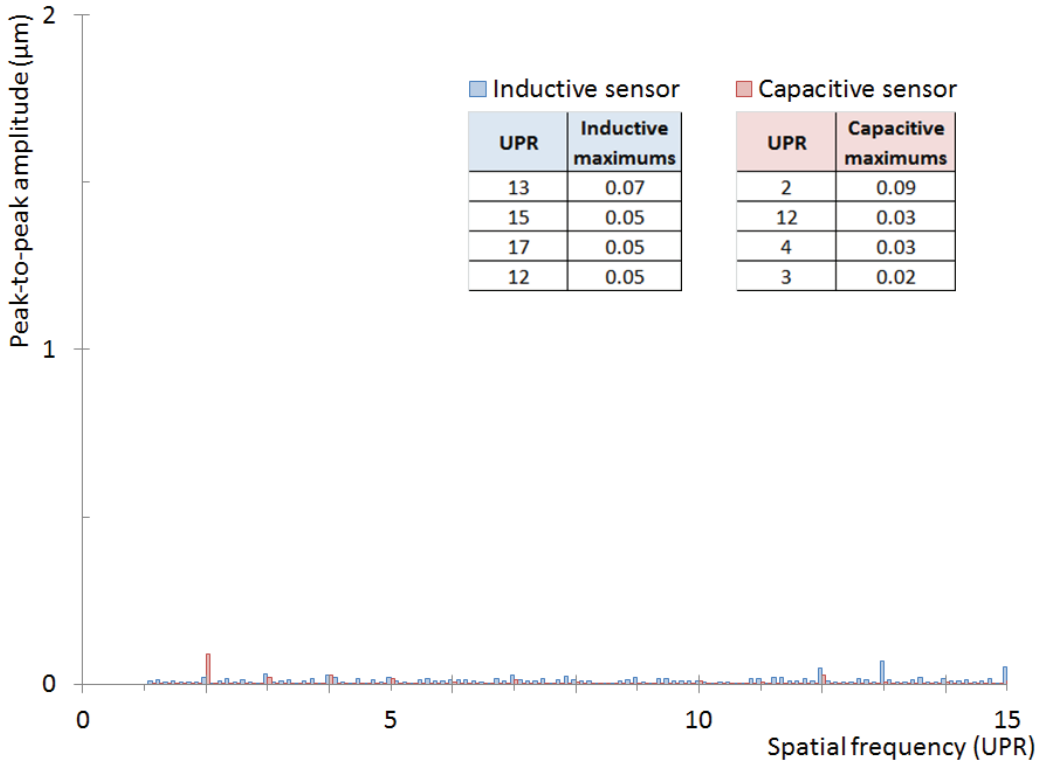

UPR	Inductive maximums
13	0.07
15	0.05
17	0.05
12	0.05

UPR	Capacitive maximums
2	0.09
12	0.03
4	0.03
3	0.02

*FIGURE 9. Frequency content of **aluminum** target out-of-roundness.*

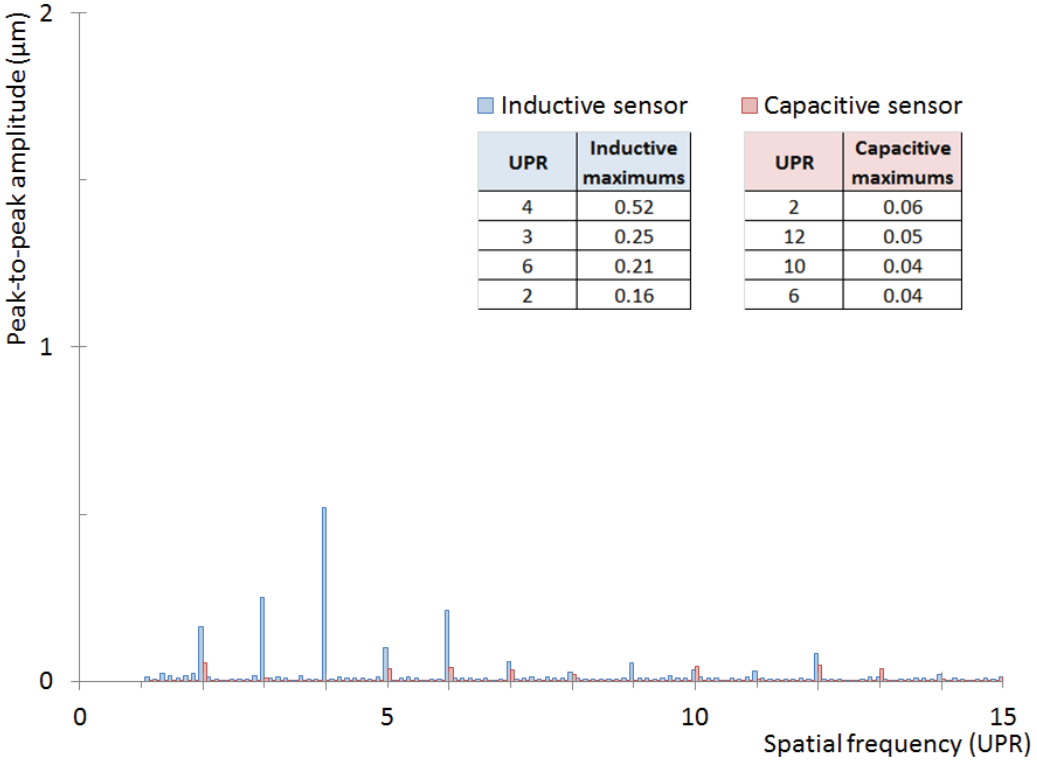

UPR	Inductive maximums
4	0.52
3	0.25
6	0.21
2	0.16

UPR	Capacitive maximums
2	0.06
12	0.05
10	0.04
6	0.04

*FIGURE 10. Frequency content of **titanium** target out-of-roundness.*

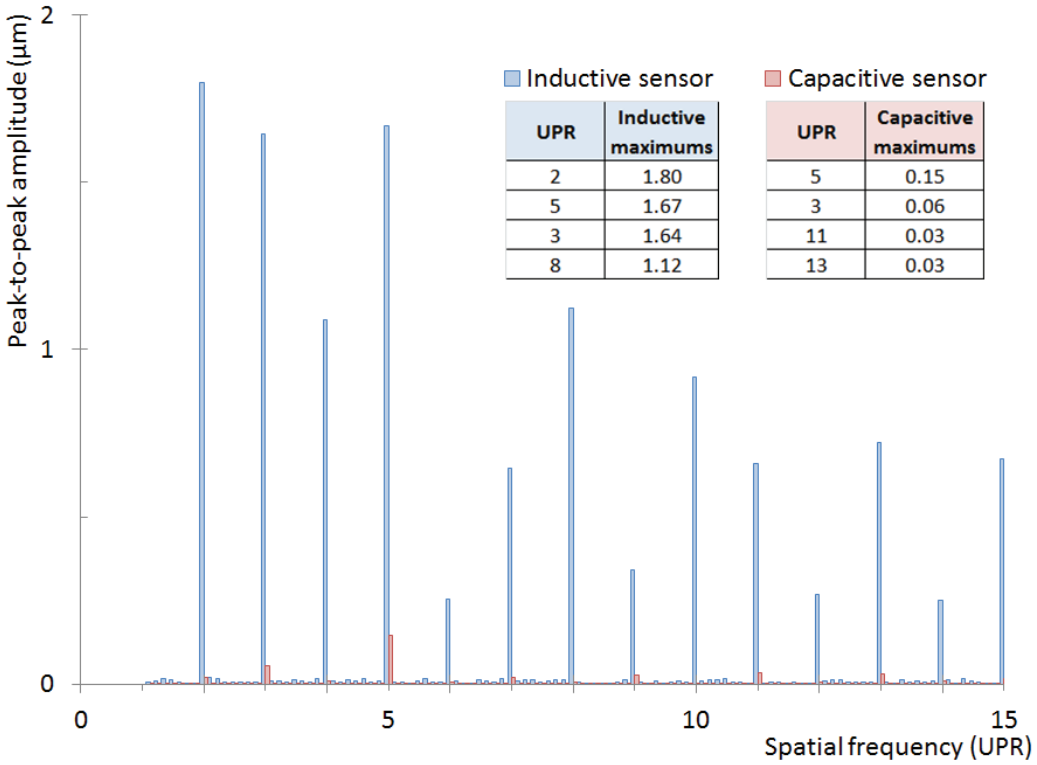

UPR	Inductive maximums
2	1.80
5	1.67
3	1.64
8	1.12

UPR	Capacitive maximums
5	0.15
3	0.06
11	0.03
13	0.03

*FIGURE 11. Frequency content of **steel** target out-of-roundness.*

Figures 9, 10, and 11 show the synchronous and asynchronous frequency content of the out-of-roundness measurement. Content at and below 1 UPR has been filtered out. The asynchronous error is not material dependent and it was approximately 0.6 μm for the inductive measurements and 0.02 μm for the capacitive measurements. It is worth noting that the inductive measurement of the titanium exhibits a strong 4th harmonic not seen with the capacitive measurement. This is a remnant of the forming process and the resulting grain structure.

CONCLUSIONS

Inductive (eddy current) sensors are commonly used for radial vibration condition monitoring of rotating shafts in dirty environments. However, when using inductive sensors with rotating targets, displacement measurement errors exist associated with variations in electrical and magnetic properties of the target. It is demonstrated that measurement errors on the order of 10 μm can exist when using an inductive sensor and a rotating steel target. Aluminum and titanium showed reduced measurement errors on the order of 1 μm. Asynchronous error due the resolution of the inductive sensor was independent of material and was approximately 0.6 μm.

REFERENCES

[1] DeBlock MJ, Wood BM, and McDonnell JW. Shaft proximity probe track runout on API motors and generators. Orbit. 2007;27(2):36-49.

[2] Littrell N. Understanding and mitigating shaft runout. Orbit. 2005;25(3):4-17.

[3] Moosbrugger C editor. ASM Ready Reference Electrical and Magnetic Properties of Metals. Materials Park (OH): ASM International; 2000.

[4] Smith PT, Vallance RR, and Marsh ER. Correcting capacitive displacement measurements in metrology applications with cylindrical artifacts. Precision Engineering. 2005;29(3):324-335.

[5] Phillips SD, Estler WT, Doiron T, Eberhardt KR, and Levenson MS. A careful consideration of the calibration concept. J. Res. Natl. Inst. Stand. Technol. 2001;106(2):371–379.

ACCELEROMETER ASSESSMENT OF AIR BEARING SPINDLES

Mel Liebers, Dave Arneson, Byron Knapp, Dan Oss
Professional Instruments Company
Hopkins, Minnesota, USA

INTRODUCTION

Asynchronous error motion limits the smoothness of diamond-turned finishes and to minimize the problem we search for root causes. This has led us to accelerometer assessment to explore the effect of small disturbances in air flowing though spindle bearings since vibration levels translate into asynchronous error motion. This paper demonstrates the measurement and characterization of these low amplitude vibrations and shows a relationship with asynchronous error motion. This measurement technique is a useful tool for providing rapid feedback in our efforts to minimize asynchronous error.

HISTORY

A number of years ago reports from the field described surface finish improvements by reducing inlet air pressure for certain spindles under particular conditions. Efforts to minimize asynchronous error motion led to our development of a test to measure spindle vibration acceleration because at that time displacement indicators lacked nanometer-level resolution. Also, acceleration measurements are easy and convenient to conduct on a production spindle before motorization. The results are used to provide immediate feedback to the manufacturing processes and to evaluate design modifications and improvements. By comparison, error motion tests are typically performed as the final step in lengthy production process making them less useful for timely feedback.

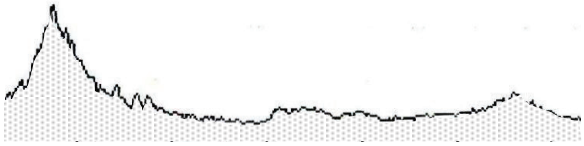

Figure 1. Shows typical accelerometer results.

DESCRIPTION

The spindle being tested rests on a soft support and a radial/axial accelerometer detects broad-range vibration which relates to nanometer-level asynchronous spindle error motions. The size, shape, and location of peaks may be of interest but for our purposes we lump everything together and record a single value that we call AUC for Area Under the Curve.

AUC is a composite value encompassing a wide variety of influences:

- Air film thicknesses at both thrust bearings and both radial bearings.
- Four sets of flute patterns, including uniformity of cross-section and length.
- Roundness, alignment, and taper for radial bearings on the rotor shaft and in the stator housing.
- Circular flatness, parallelism, taper, and perpendicularity of the rotor and stator thrust surfaces.
- Inlet air pressure.

All these factors have to be right to achieve low AUC and low asynchronous error motion.

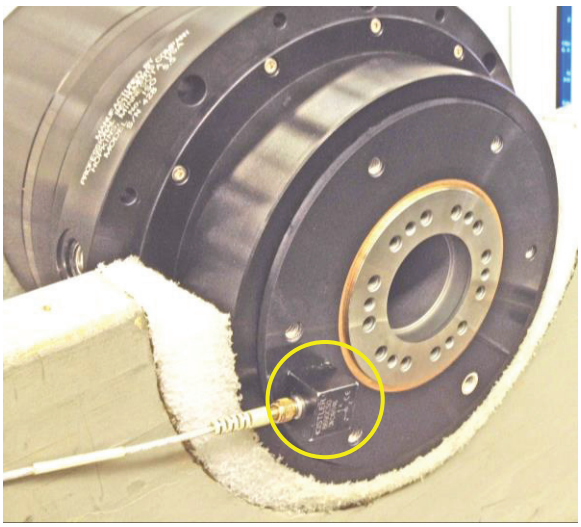

Figure 2. A Kistler Piezobeam triaxial accelerometer detects the effects of air flowing though the bearings.

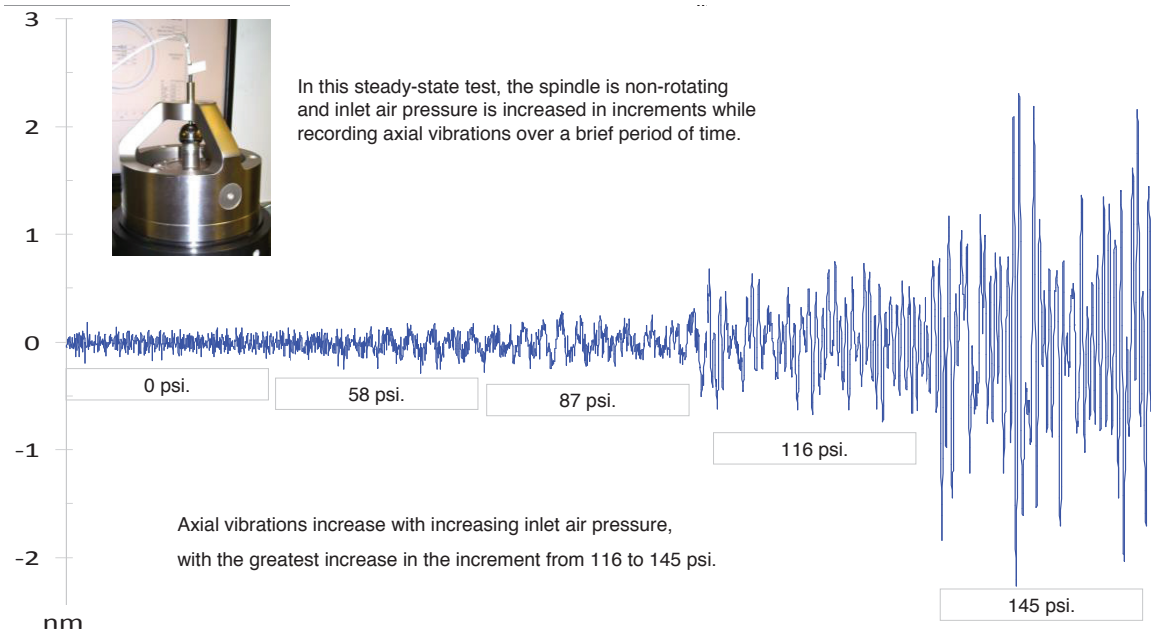
3
2
1
0
-1
-2
nm
In this steady-state test, the spindle is non-rotating and inlet air pressure is increased in increments while recording axial vibrations over a brief period of time.
0 psi.
58 psi.
87 psi.
116 psi.
145 psi.
Axial vibrations increase with increasing inlet air pressure,
with the greatest increase in the increment from 116 to 145 psi.

Figure 3. Zero rpm axial motion increases with increasing air pressure. This illustration shows brief steady-state readings at 5 different pressures, with disproportionate increases at higher pressure.

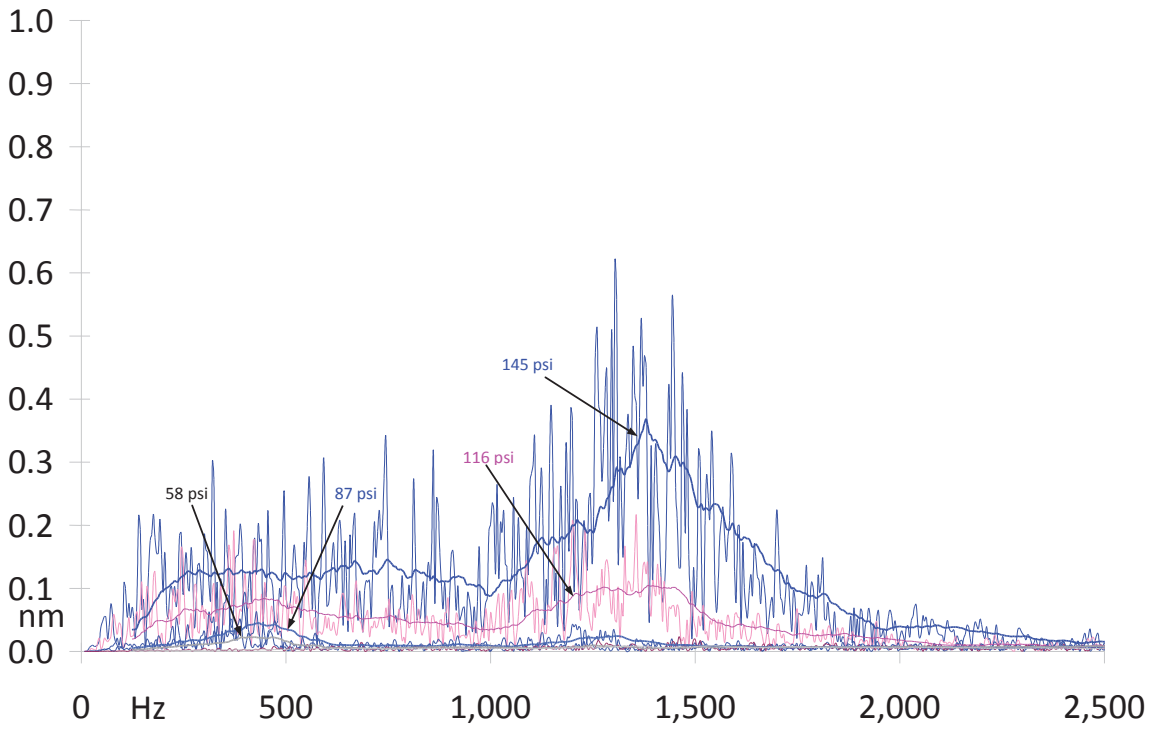

Figure 4. Shows broad-spectrum changes in axial displacements as inlet pressure rises.

AUC AND ERROR MOTION

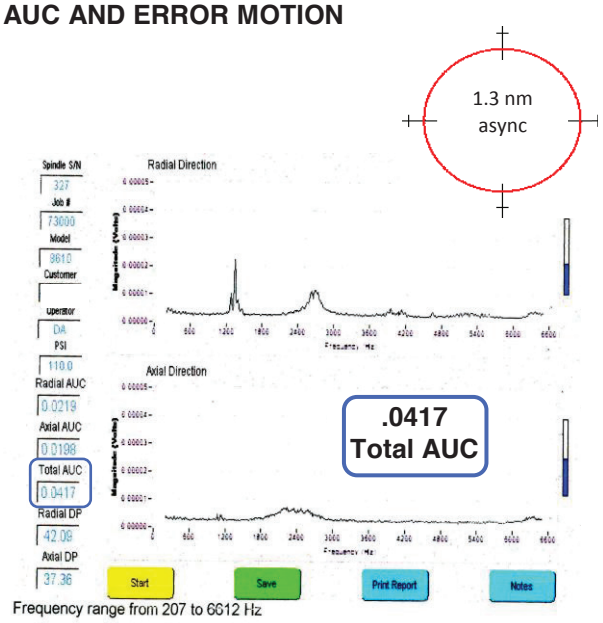

Figure 5. Axial error motion plot and acceleration spectra of a spindle with 1.3 nm asynchronous axial error motion and 0.0417 AUC.

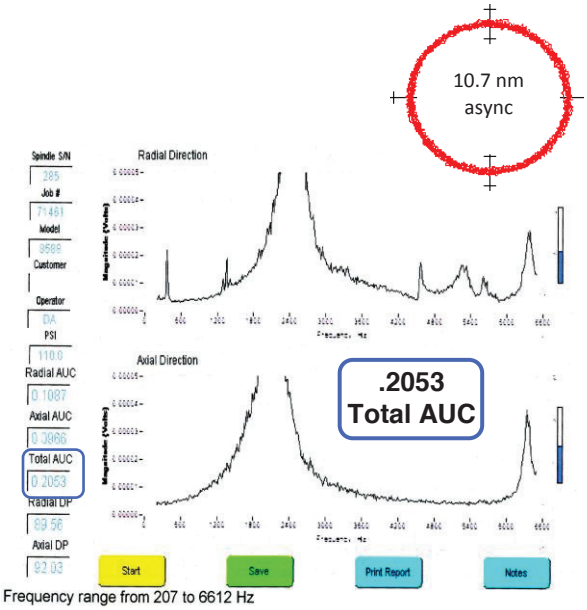

Figure 6. Axial error motion plot and acceleration spectra of a spindle with 10.7 nm asynchronous axial error motion and 0.2053 AUC.

AUC IS NOT A SUBSTITUTE FOR ERROR MOTION RESULTS

There is an obvious relationship between the asynchronous error and AUC but they do not track one-for-one:

- AUC values represent external motions of the stator whereas spindle error motions are relative displacements between the rotor and the stator.
- Total AUC combines radial and axial measurements.
- AUC does not include drive influence.
- AUC is typically measured at zero rpm.

CONCLUSIONS

We find that acceleration vibration measurement is an essential tool for building air bearing spindles. It can be used to find problems before investing time in motorization, balancing, and error motion testing.

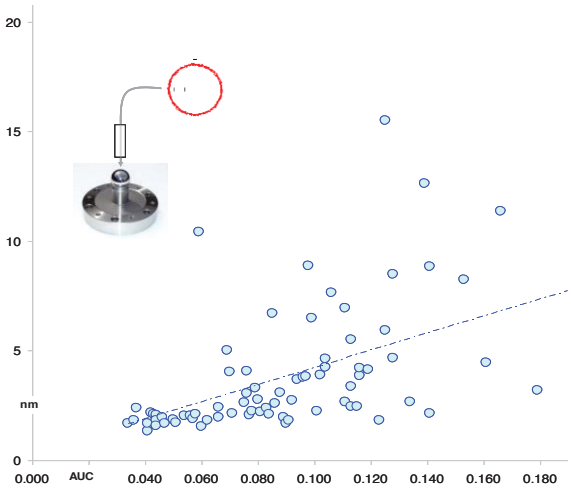

Figure 7. Axial asynchronous error motion tends to rise with increasing AUC but there are many exceptions.

REFERENCES

Knapp BR, Oss DD, Arneson DA, Liebers MJ, and Marsh ER. Vibration Spectra and Asynchronous Error Motion of Ultra-Precision Air Bearing Spindles. Proceedings of the ASPE Topical Meeting: Precision Engineering and Mechatronics Supporting the Semiconductor Industry. Berkeley, CA. 2012.

A STUDY ON THE EFFECT OF NOISE & HIGH-ORDER DISTORTION ON A MODULATED ENCODER

Susumu Makinouchi[1], Toru Imai[1], Akihiro Watanabe[1], Masahisa Takasaki[1], Charles M. Kohn[2] and Tetsuo Ohara[2]
[1]Business Development Headquarters
Nikon Corporation
Shinagawa, Tokyo, Japan
[2]NanoWave, Inc.
Sutton, Massachusetts, USA

INTRODUCTION

Interpolation error is usually regarded as the most important performance parameter of precision encoders. In conventional encoders, actual interpolation performance may be influenced not only by gain and offset, but also by system noise on the analog signals and by errors in the scale performance, caused by such things as manufacturing imperfections or environmental effects including oil on the scale. Sensitivity to these aspects of real-world performance is very important in using the encoders from the perspective of the users, yet we rarely find this topic discussed.

We have developed a new interpolation method for precision encoders with extremely low interpolation error, even in real-world conditions. The new method consists of an optical modulator and phase-locked-loop decoder [1]. This paper compares the performance of our modulated technique to the conventional sin/cos technique, with respect to sensitivity to noise and sensitivity to real-world defects that can modify the performance of the scales.

INTERPOLATION ERROR

Figure 1 shows a configuration of a conventional optical encoder, which has two-phase sinusoidal signals and an arctangent interpolator. Major causes of the interpolation error in the conventional method are amplitude imbalance and voltage offset between the two signals. Figure 2 shows the theoretical interpolation error caused by amplitude imbalance and voltage offset, assuming a 2μm encoder signal pitch.

Figure 3 shows the configuration of the modulated encoder. The novel encoder cannot be sensitive to signal offsets or imbalances because it has only one output signal. In addition, the modulated encoder is far less sensitive to distortion in the sinusoidal signal produced by the photo-detector looking at the scale. Such signal distortion is mainly caused by optical imperfections, due to imperfect blocking of zero-order light or unbalanced diffraction, caused by variation in the manufacturing process, misalignment between the head and the scale or environmental defects such as oil on the scale. Thus, some of causes are unavoidable in industrial usage.

The distorted sinusoidal signal can be

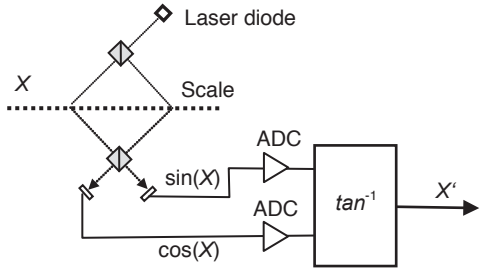

FIGURE 1. Configuration of a conventional optical encoder, X: the scale position, X': measured position.

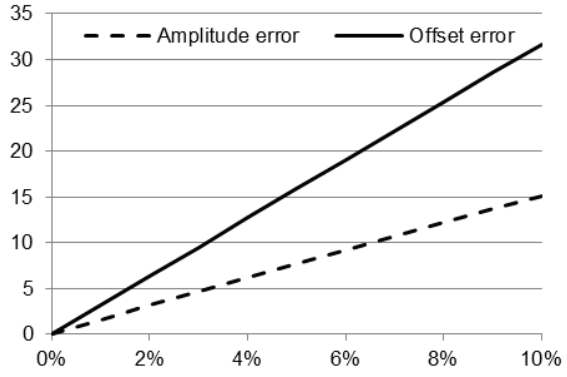

FIGURE 2. Interpolation error of a conventional encoder, with 2µm signal pitch.

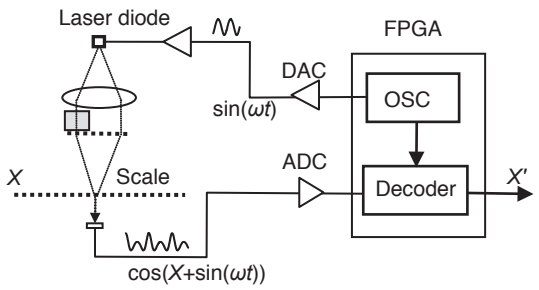

FIGURE 3. Configuration of modulated encoder, X: the scale position, X: measured position, ω: the angular frequency of the modulation, t: time.

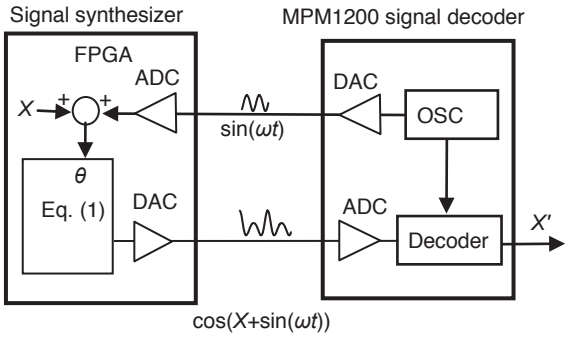

FIGURE 4. Interpolation error test setup, X: the scale position, X': measured position, ω: the angular frequency of the modulation, t: time.

described by Equation (1).

$$E = A_1 \cos\theta + \sum_{n=2}^{\infty} A_n \cos(n\theta + \Delta\theta_n) \quad (1)$$

where A_1 is the amplitude of the fundamental grating frequency, θ is the phase angle, A_n is the amplitude of n^{th} order harmonic distortion, and $\Delta\theta_n$ is the phase offset of n^{th} order harmonic distortion.

Figure 4 shows the configuration of the test tool for determining the effects of the signal distortion in the modulated encoder. The distorted signal, represented by Eq. (1), is generated inside of the signal synthesizer FPGA. The scale position X and the modulation signal sin(ωt) from the MPM1200 signal decoder (manufactured by NanoWave Inc.) are summed and input to the block Eq. (1), where ω is the angular frequency of the modulation and t is time. Then, the modulated encoder signal, cos(X+sin(ωt)), comes back to the decoder.

Figure 5 shows some of the results. The analysis of the error in the conventional encoder, with 2μm signal pitch, was done by simulation, .i.e., $X' = \tan^{-1}(\sin(X)/\cos(X))$. Table 1 shows the comparison of the effects of the distortion signal with different harmonic orders, amplitudes and phases.

POSITION NOISE

Position noise of precision encoders is also important performance because it dominates the short-term repeatability of the encoders. The position noise is caused by electrical noise from the photo sensors and system electrical noise coupled to the encoder circuits. Noise can often be reduced by a low-pass filter (LPF), when high bandwidth performance is not required. The modulated encoder technique uses synchronous detection of the modulation frequency and its harmonics and therefore achieves an advantage with regard to position noise.

Figure 6 shows the setup of the noise test tool. A noise-generator in the signal synthesizer generates white-noise. The noise is generated with a 1.25MHz clock, which means the noise includes frequencies 0-1.25MHz. The amplitude of the noise is controlled as the percentage of the encoder signal. Figure 7 shows the noise signal and the encoder signal of the modulated encoder. We observed the output position signal X' of the MPM1200 signal decoder, and calculated the standard deviation (sigma) of the signal..

TABLE 1. The interpolation error caused by harmonic distortion of the signal on the modulated encoder and the conventional encoder, with 2μm signal pitch.

n	A_n	$\Delta\theta$ [rad]	Interpolation error [nm p-p]	
			Modulated interpolator	Conventional (simulation)
2	0.01	0	1.0	8.8
2	0.01	π	1.0	8.8
2	0.02	0	1.8	18
2	0.04	0	3.4	35
3	0.01	0	0.45	6.3
3	0.01	π	0.78	6.3
4	0.01	0	0.48	8.1
4	0.01	π	0.52	8.4

(1) $E=\sin\theta+0.01\sin 2\theta$, *i.e., 1% 2nd harmonic distortion*

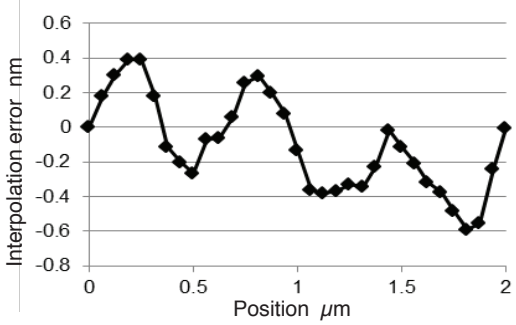

(a) Modulated encoder

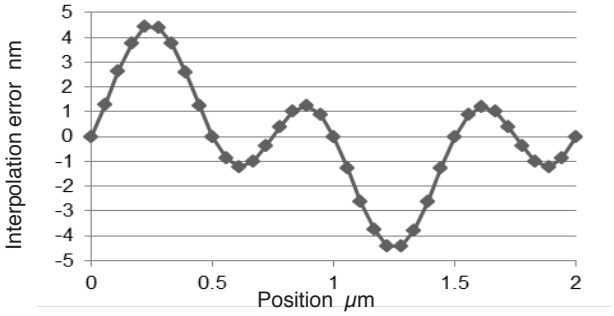

(b) Conventional encoder

(2) $E=\sin\theta+0.01\sin 3\theta$, *i.e., 1% 3rd harmonic distortion*

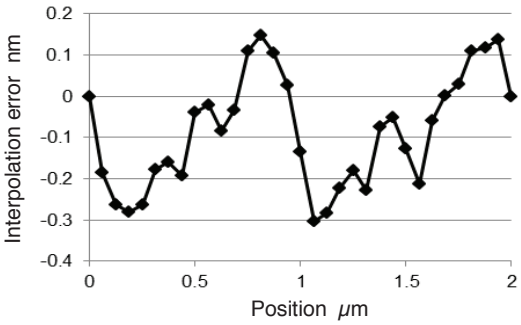

(a) Modulated encoder

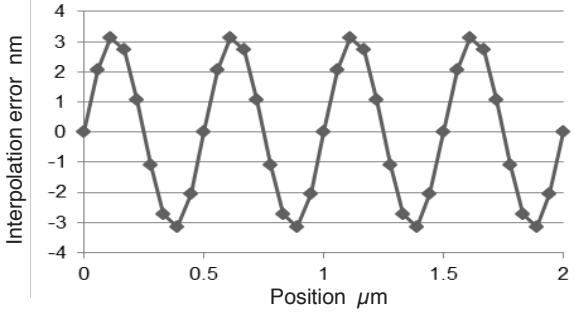

(b) Conventional encoder

FIGURE 5. The interpolation error waveforms of the modulated encoder and the conventional encoder.

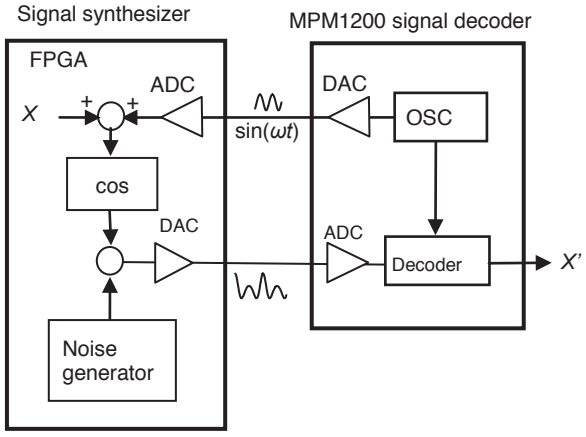

FIGURE 6. Noise test tool setup. X: the scale position, X': measured position, ω: the angular frequency of the modulation, t: time.

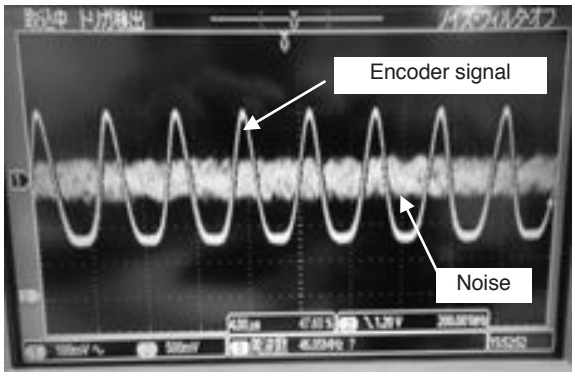

FIGURE 7. Noise-test signals

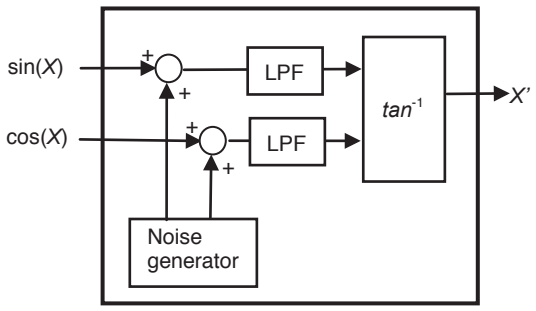

FIGURE 8. Noise evaluation diagram for a conventional encoder, X: scale position, X': measured position.

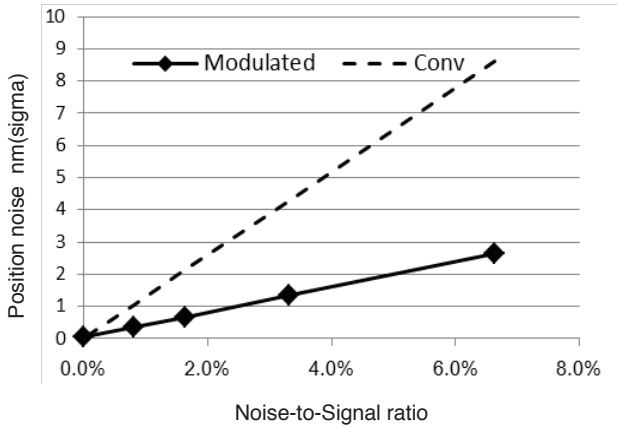

FIGURE 9. Position noise vs. signal noise

Similarly, we evaluated the noise effect on conventional encoders. In the conventional encoder we limited the bandwidth of the two-phase encoder signal via a LPF. We assumed a maximum velocity of 500mm/s and a 2μm signal pitch, so the frequency of the LPF was set to 250kHz. Figure 8 shows the noise calculation diagram for the conventional encoder.

Figure 9 shows the comparison of the position noise evaluation for the modulated encoder and the conventional encoder.

CONCLUSION

The interpolation error created by harmonic distortion is approximately ten times less in modulated encoders than in conventional two-phase interpolation encoders. The position noise performance under a signal noise condition is approximately three times less in modulated encoders than in the conventional encoders.

REFERENCES

[1] Makinouchi S, Watanabe A, Takasaki M, Ohara T, Ong J, Wakui S. An evaluation of a modulated laser encoder. Precision Engineering. 2011; 35. 302-308.

[2] Makinouchi S, Watanabe A, Takasaki M. An interpolation error measuring system using a tuning fork stage. Proceeding of 11th international conference of the European society for precision engineering and nanotechnology. 2011; 1. 62-65.

[3] Ohara T, Youcef-Toumi K. Real-time sub-nanometer position sensing with long measurement range. IEEE Robotics and Automation. 1995; 369-374.

SPINDLE SPEED AND SENSOR BANDWIDTH REQUIREMENTS

Don Martin, Mark Kretschmar
Lion Precision
St. Paul, MN USA

SPINDLE MOTIONS

Spindle error measurements are usually made with sensors in multiple axes. To understand how those measurements are made, consider just one of those sensors. A single noncontact sensor measures displacements of a rotating target in one axis as the target moves toward and away from the sensor. The bandwidth of the measurement system must be capable of measuring the frequency of motion of the spindle in that axis. Even for very high-speed spindles, these frequencies are usually well within a measurement system's capabilities (Figure 1).

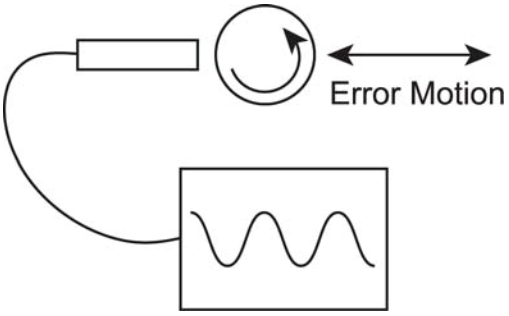

FIGURE 1. A noncontact sensor measures error motions of a rotating spindle in one axis. The frequency of motion in that axis determines the sensors needed bandwidth.

BANDWIDTH OF SENSORS

A typical capacitive sensor used in spindle measurement is "flat" to about 10 kHz, meaning that measurements of targets moving at 10 kHz are accurate[1].

While they are flat to 10 kHz, the "bandwidth" is higher, perhaps 15 kHz. It is critical to understand that the bandwidth specification of any sensor is the frequency at which the output voltage is reduced to 70.7% (-3 db) of lower frequency (or DC) output levels. This means that a target moving at 15 kHz with a displacement of 10 μm will only be measured as 7 μm (Figure 2).

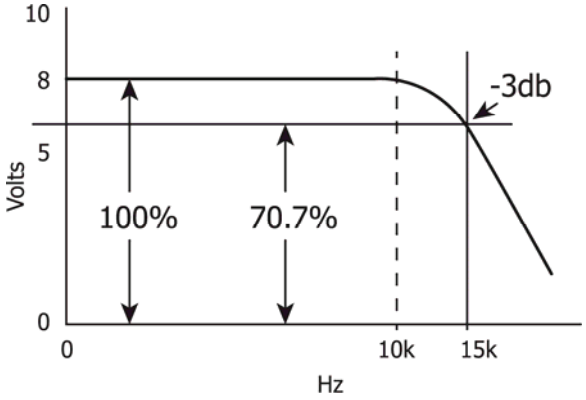

FIGURE 2. With a 15 kHz bandwidth, sensor output is reduced to 70% at 15 kHz. Frequency response is flat until about 10 kHz.

THE FUNDAMENTAL FREQUENCY

Due to eccentricity, all rotating targets will exhibit one cycle of error motion per revolution. This establishes a "fundamental frequency" and it is always:

Fundamental Frequency (in Hz) = RPM/60

A sensor that has a flat frequency response to 10 kHz can accurately measure fundamental motions of targets at speeds up to 600,000 RPM. A standard 15 kHz bandwidth sensor can reliably and repeatedly measure rotational speeds of 900,000 RPM although at 70% of actual amplitude.

NONFUNDAMENTAL FREQUENCIES

The frequency of all other error motions can be measured relative to the fundamental frequency. For example, a frequency that is twice as high as the fundamental frequency is simply labeled as "2." This permits discussions of a general case rather than resorting to examples at specific frequencies that may not be relevant to an individual case.

Frequencies other than the fundamental frequency are also present in the error motions of a spindle. Imperfections in bearing components, mounts, motors, drives, structural

vibration, and other factors each contribute a unique frequency. These error motions occur at integer and noninteger multiples of the fundamental frequency (Figure 3).

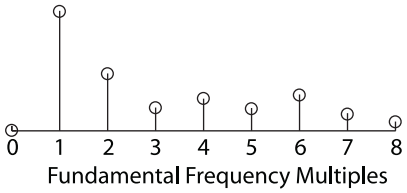

FIGURE 3. Typical frequency distribution of synchronous error motions. Synchronous error motions occur at integer multiples of the fundamental frequency[2].

SYNCHRONOUS ERROR MOTIONS

Error motions which are integer multiples of the fundamental frequency are said to be "synchronous" as they repeat at the same angular location with each rotation of the spindle. Synchronous errors are the result of rotor and stator imperfections, mounting stresses, and other sources affecting the shape of the rotor or stator.

Stator and Rotor Shape Errors

Stators and rotors are not perfectly round. These imperfections create additional frequencies in the spindle motion which are always synchronous with the fundamental frequency. Two- and three-lobe shapes are common out-of-roundness errors (Figure 4). These form errors create spindle motion frequencies two and three times higher than the fundamental frequency.

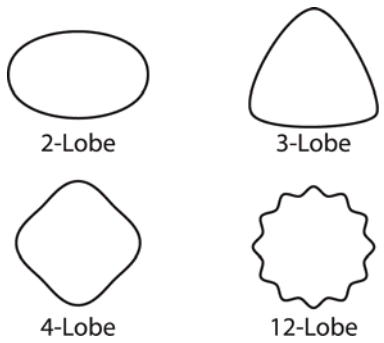

FIGURE 4. Synchronous error motions create "lobed" patterns. Higher numbers of lobes require higher bandwidth for accurate measurement.

A three lobe error would be accurately recorded at speeds up to 200,000 RPM by a flat-to-10 kHz system.

Mounting Induced Errors

Mounting of the spindle can create stresses in the bearing structure resulting in slight deformities. These create synchronous error motions and are essentially the same as stator and rotor shape errors, but the shape errors are introduced by the mounting stresses. These errors can occur at the fundamental frequency or higher. Theoretically, each mounting fastener could add another lobe to the synchronous error motion.

Motor Pole Print-Thru

The magnetic poles in motors create a normal force on the motor's rotor that is different at the poles than between the poles. This varying force cycles on every rotation. Depending on the stiffness of the spindle bearing, this changing force can appear as error motions in the spindle. This motion is synchronous with the fundamental frequency.

The number of poles in the drive motor determines the shape of the print-thru error. For example, an eight-pole motor creates an 8-lobe pattern and would be accurately measured at speeds up to 75,000 RPM by a flat-to-10 kHz system. A typical drive motor has 4, 6, or 8 poles. Very large motors may have more poles, but due to their size they turn at much slower speeds keeping the error motion frequencies comparatively low.

ASYNCHRONOUS ERROR MOTIONS

Some error motions occur at frequencies that are non-integer multiples of the fundamental frequency. While these errors may have a repeating cycle, they do not repeat at the same angular location of spindle rotation; they are not synchronous with the fundamental frequency.

Structural Vibration

The machine structure itself will have natural resonant frequencies that can appear in the spindle motion. Because of the size and mass of the machine structure, these frequencies are usually low (10-30 Hz) and may or may not be synchronous with the fundamental frequency. Because of their low frequency, they are easily measured by the sensors.

Rolling-Element Bearings (Asynchronous Error)

Rolling-element bearings have four basic components: the rolling element itself (ball or

roller), the inner race, the outer race, and the cage (Figure 5). As the bearing turns, these elements interact mechanically; their inherent imperfections cause deviations in bearing forces and the axis of rotation which result in spindle error motions.

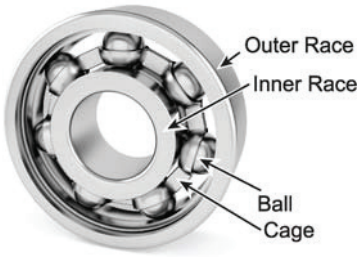

FIGURE 5. Each bearing component has a unique diameter which creates a unique frequency of error motion.

Each bearing component has its own shape errors which produce error motions in the spindle. The ratio of the diameters of the bearing components, as well as the contact angle of the rolling element, determine the relationships to the fundamental frequency. To prevent resonances within the spindle, bearings are intentionally selected so that these frequencies are not synchronous with the spindle rotor; therefore, these errors occur at non-integer multiples of the fundamental frequency.

Bearing Frequencies

The frequency distribution in Figure 6 shows where a typical ball-bearing's bearing frequencies occur. The ball bearings turn on the inner race (ballpass) with a frequency just above 2 times the fundamental frequency. The cage frequency is a little less than half the fundamental frequency.

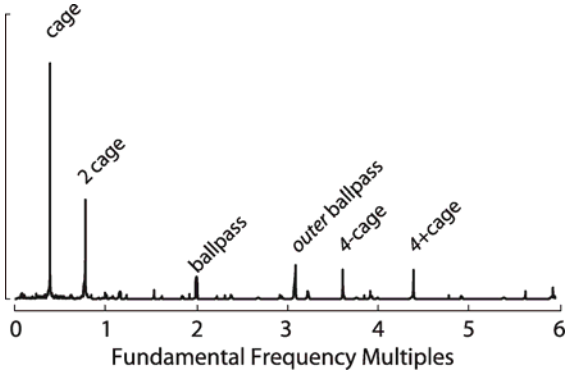

FIGURE 6. Typical frequency distribution of asynchronous error motions occurring at "bearing frequencies." Most of the distribution is below 4.5 times the fundamental frequency[2].

Harmonics occur at 4 ± the cage frequency, and the outer race is seen at just over 3. There is very little activity above 4.5 times the fundamental frequency. Accurate measurements can be made of these error motions on spindles up to 130,000 RPM by a flat-to-10 kHz system.

Table 1 shows another example of typical bearing frequencies shown as multiples of the fundamental frequency[3]. Here the highest frequency is 8.32. Accurate measurements can be made of these error motions on spindles up to 70,000 RPM by a flat-to-10 kHz system.

TABLE1. Typical bearing frequencies for a rolling element bearing.

			Frequencies			
Number of Balls	Ball Diam.	Pitch Diam.	BallPass Outer	BallPass Inner	Cage (FTF)	Ball Spin
15	0.312"	2.854"	6.68	8.32	0.45	4.52

CONCLUSION

While spindle speeds have increased dramatically over the years, the error motion frequencies generated by the spindles are still within the measurement capabilities of a sensor system with 15 kHz bandwidth.

REFERENCES

[1] Lion Precision [Internet]. St. Paul, MN: Lion Precision. CPL190 Capacitive Sensor. Available from: http://www.lionprecision.com/capacitive-sensors/cpl190.html

[2] Marsh ER. Precision spindle metrology, Lancaster, PA: DesTech Publishing; 2008.

[3] NTN Bearing Corporation [Internet]. Mount Prospect, IL: NTN Bearing Corporation. Bearing Frequencies. Available from: http://www.ntnamerica.com/website/documents/brochures-and-literature/tech-sheets-and-supplements/frequencies.pdf

UNCERTAINTY ANALYSIS OF BALLSCREW NUT STIFFNESS

Bog-Ki Min[1], Hyun-Gwang Cho[1], Chun-Hong Park[2], and Sung-Chong Chung[1*]
[1] Hybrid System Design and Control LABoratory
School of Mechanical Engineering
Hanyang University, Seoul 133-791, KOREA
[2] Intelligent Manufacturing System Division
KIMM, Daejeon 305-343, KOREA

ABSTRACT
Uncertainty occurs in the evaluation process of ballscrew nut stiffness through mathematical or experimental procedure. Monte Carlo Method (MCM) and GUM (Guide to the expression of uncertainty in measurement) have been used for analytical and experimental uncertainty analysis. In this paper, uncertainty estimation of ballscrew stiffness is conducted in several types of ballscrews. GUM results obtained from the improved test rig and MCM estimates verify validity of the improved stiffness estimation model including contact angle variation effect.

INTRODUCTION
Fig. 1 shows a preloaded double-nut ballscrew subject to TT(CC) or TC(CT) loading by thrust force F_t. Positioning accuracy is subject to its nut stiffness. Hertzian deformation of balls and grooves as well as body deformation of screw shaft and nut according to thrust force, preload and groove characteristics degrade positioning accuracy [1]. Fig. 1 shows contact state of the *i*-th ball and grooves. α represents the contact angle of the ball and groove, *D* is ball diameter. F_i denotes ball contact load, *etc*. Using the given parameters, Hertzian deformation constants between balls and grooves are derived through elliptic integrations. Applying for compatibility and force equilibrium conditions, body deformation [1] is estimated according to the assembly and load conditions. However, variation of conformity factors affects the contact deformation significantly. Fluctuation of the contact angle generates uncertainty of contact deformation estimates [2-3]. In addition, it is difficult to measure the axial stiffness accurately because of loading unit, measurement, material, and geometric uncertainties during experiments.

To perform uncertainty estimation of the nut stiffness in the analytic process, MCM based on previous analytic models has been conducted according to Fig. 2 [3]. GUM evaluation of stiffness measurement has been accomplished under various loading conditions [2-3]. In this paper, to improve uncertainty estimation accuracy through the MCM process, more accurate stiffness model considering contact angle variation between balls and grooves is applied for the analytic estimation. New loading and amended measuring units for experimental stiffness verification are applied for uncertainty evaluation by GUM. Uncertainty verification between the improved mathematical model and new experiments are conducted for several ballscrews, assembly and loading conditions.

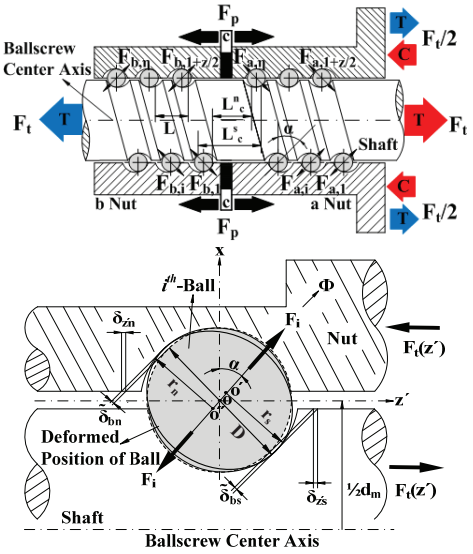

FIGURE 1. Double-nut Ballscrew and Contact Mechanism.

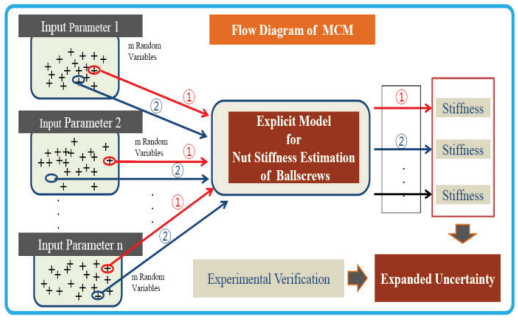

FIGURE 2. Uncertainty Estimation by MCM.

UNCERTAINTY ANALYSIS BY MCM

To account for uncertainty generated in the stiffness estimation, more accurate stiffness model including the contact angle variation effect is adopted for MCM simulation according to Fig. 2.

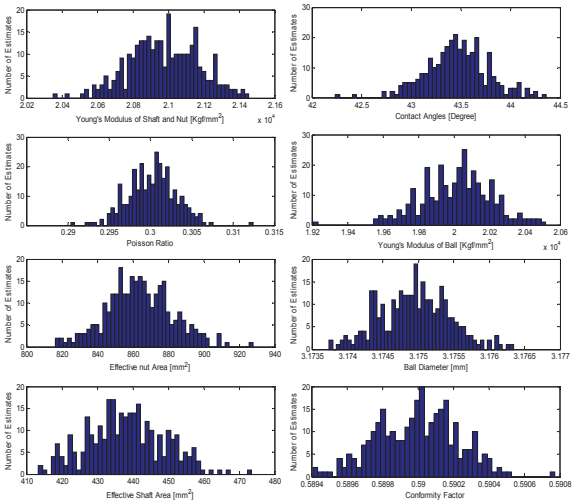

FIGURE 3. Uncertainty Factors for Stiffness Estimation through MCM.

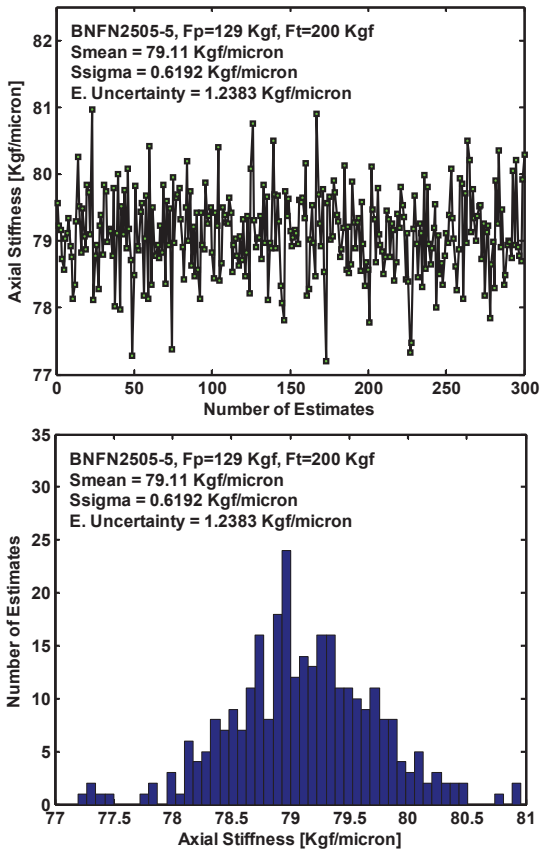
BNFN2505-5, Fp=129 Kgf, Ft=200 Kgf
Smean = 79.11 Kgf/micron
Ssigma = 0.6192 Kgf/micron
E. Uncertainty = 1.2383 Kgf/micron
Axial Stiffness [Kgf/micron]
Number of Estimates
BNFN2505-5, Fp=129 Kgf, Ft=200 Kgf
Smean = 79.11 Kgf/micron
Ssigma = 0.6192 Kgf/micron
E. Uncertainty = 1.2383 Kgf/micron
Number of Estimates
Axial Stiffness [Kgf/micron]

FIGURE 4. Estimated Uncertainty of Stiffness through MCM.

THK's double-nut BNFN2505-5 with tensile preload 129Kgf and CC assembly condition is selected for stiffness estimation. Uncertainty factors such as contact angle α, ball diameter d, conformity factor $f_{s,n}$, effective area $A_{s,n}^{eff}$ of the screw shaft and the nut, elastic modulus, *etc.* are selected for MCM stiffness estimation. Fig. 3 shows histograms of uncertainty factors as input parameters. Fig. 4 shows 300 times of MCM uncertainty estimation results of the nut stiffness at 200Kgf thrust force. Mean stiffness of 79.11 Kgf/μm is obtained at 200 Kgf thrust force. Expanded uncertainty is obtained between 77.87 and 80.35 Kgf/μm with 95.46% confidence.

FIGURE 5. Measurement Setup for CC and CT Load Conditions.

EXPERIMENTS

Fig. 5 shows new stiffness measurement system. To generate precise loading, a screw pump is added to the previous hydraulic unit [3]. Load cell attached to the loading unit is used for thrust force measurement. Six LVDTs are applied for tilting compensation of the previous loading mechanism [3] as shown in Fig. 6. CC and CT types of ballscrews are used for experiments. In the CC type assembly condition, the Hertzian contact and body deformation of a ballscrew nut assembly is measured directly from the stiffness measurement system. However, in the CT assembly case, upper frame of the loading unit deforms according to the thrust force. To compensate for this deformation, the new measurement setup shown in Fig. 6 is devised.

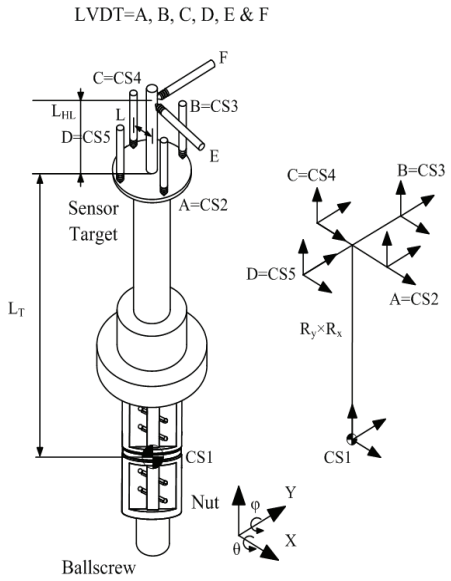

FIGURE 6. New Measurement Setup for Tilting Compensation.

Figs. 7 and 8 show 30 measurements of axial deformations and stiffnesses of BNFN2505-5 in CC and CT conditions, respectively. Fig. 9 shows them of BNFN3610-5 in CC condition.

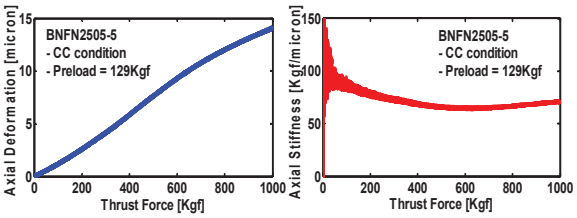

FIGURE 7. Axial Deformation and Stiffness of BNFN2505-5 in CC Condition.

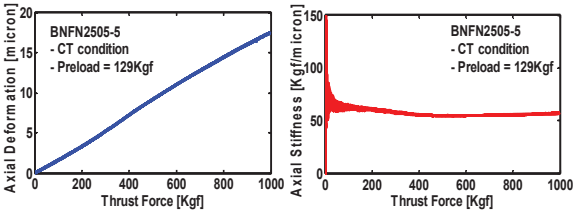

FIGURE 8. Axial Deformation and Stiffness of BNFN2505-5 in CT Condition.

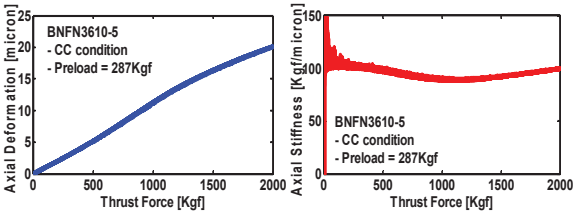

FIGURE 9. Axial Deformation and Stiffness of BNFN3610-5 in CC Condition.

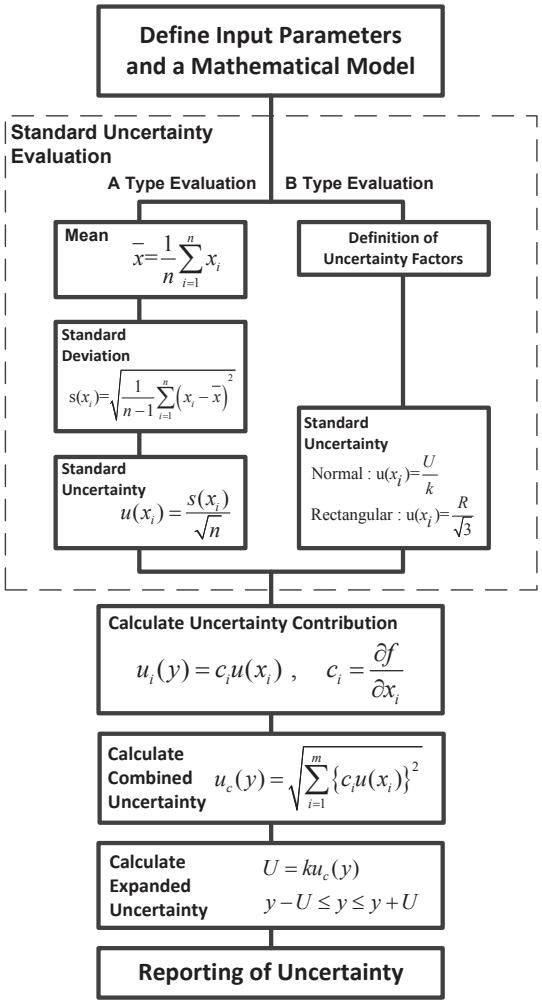

FIGURE 10. Uncertainty Evaluation by GUM.

UNCERTAINTY ANALYSIS

There are many uncertainty factors in the stiffness measurement system. To obtain reliable results, experiments should be conducted in perfect conditions with good ballscrews, sensor and instrument, loading unit, linearity, resolution, repeatability, bandwidth, *etc*. Experts should perform experiments. Although these conditions are satisfied all in experiments, there could remain uncertainty. Evaluation of uncertainty according to Fig. 10 procedure is required to get reliable stiffness information [3-4].

Standard uncertainty is classified as A and B types. A type is statistical evaluation of repeated measurements by *t*-distribution. Thrust force and ballscrew deformation measurements are A type factors. Resolutions of load cell and LVDTs, sensor setup errors, distortion of loading unit, and thermal errors due to ambient temperature are B type factors. Fig. 11, Tables 1 and 2 show

uncertainty evaluation results of the stiffness measurement by GUM. Stiffness uncertainty estimates by MCM proposed in the previous section exist in the confidence interval range of experimental uncertainty results obtained by GUM. It is confirmed that improved loading mechanism, measurement setup and tilting compensation method generate good stiffness measurement results. Uncertainty estimation through MCM verifies that the improved stiffness model including contact angle variation effect estimates correct ballscrew stiffnesses under various loading and assembly conditions.

CONCLUSIONS

Improved stiffness measurement unit equipped with 6 LVDTs and loading unit with additional screw pump render uncertainty factors of the stiffness measurement small. Uncertainty estimation through MCM proves that the improved stiffness model including contact angle variation effect estimates correct ballscrew stiffnesses.

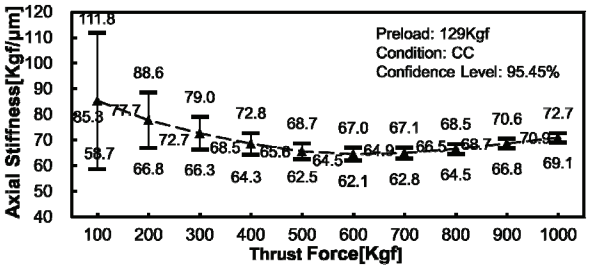

(a) BNFN2505-5(A), CC Condition

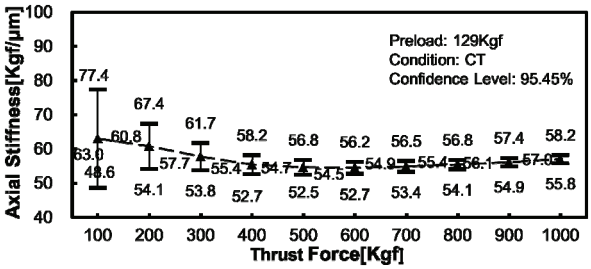

(b) BNFN2505-5(A), CT Condition

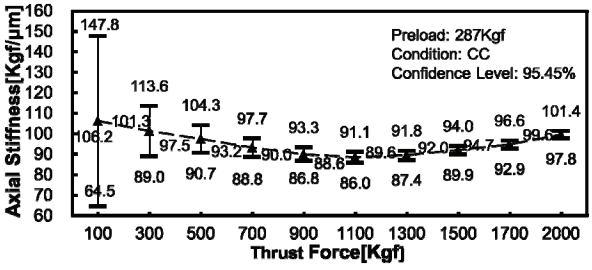

(c) BNFN3610-5(A), CC Condition

FIGURE 11. Measured Stiffness Uncertainties obtained by GUM.

TABLE 1. Stiffness Uncertainty Measurements of BNFN2505-5 in CT Loading Case by GUM.

Thrust Force [Kgf]	Commbined Uncertainty u_C[Kgf/μm]	Expanded Uncertainty U[Kgf/μm]	Confidence Interval [Kgf/μm]
100	14.4	28.8	48.6≤63.0≤77.4
200	6.65	13.3	54.1≤60.8≤67.4
300	3.95	7.9	53.8≤57.7≤61.7
400	2.75	5.5	52.7≤55.4≤58.2
500	2.15	4.3	52.5≤54.7≤56.8
600	1.75	3.5	52.7≤54.5≤56.2
700	1.55	3.1	53.4≤54.9≤56.5
800	1.35	2.7	54.1≤55.4≤56.8
900	1.25	2.5	54.9≤56.1≤57.4
1000	1.2	2.4	55.8≤57.0≤58.2

TABLE 2. Stiffness Uncertainty Measurements of BNFN3610-5 in CC Loading Case by GUM.

Thrust Force [Kgf]	Commbined Uncertainty u_C[Kgf/μm]	Expanded Uncertainty U[Kgf/μm]	Confidence Interval [Kgf/μm]
100	41.65	83.3	64.5≤106.2≤147.8
300	12.3	24.6	89.0≤101.3≤113.6
500	6.8	13.6	90.7≤97.5≤104.3
700	4.45	8.9	88.8≤93.2≤97.7
900	3.25	6.5	86.8≤90.0≤93.3
1100	2.55	5.1	86.0≤88.6≤91.1
1300	2.2	4.4	87.4≤89.6≤91.8
1500	2.05	4.1	89.9≤92.0≤94.0
1700	1.85	3.7	92.9≤94.7≤96.6
2000	1.8	3.6	97.8≤99.6≤101.4

ACKNOWLEDGEMENT

This research is funded by Ministry of Trade, Industry & Energy, Korea.

REFERENCES

[1] Chung S-C, Khim G, Park C-H. Precision Measurement of Nut Stiffness in Ballscrews. Proceedings of the ASPE 2012 Annual Meeting. 2012; 54:382-385.

[2] Min B-K, Park C-H, Chung S-C. Uncertainty Modeling of Ballscrew Nut Stiffness. Proceedings of the ASPE 2011 Annual Meeting. 2011; 52:326-329.

[3] Min B-K, Cho H-G, Park C-H, Chung S-C. Modeling and Uncertainty Estimation of Ballscrew Nut Stiffness. Proceedings of the ASPE 2012 Annual Meeting. 2012; 54:394-397.

[4] Guide to the Expression of Uncertainty in Measurement, International Organization of Standardization (1995).

ON PERFORMANCE VERIFICATION OF 3D MICRO MEASURING INSTRUMENT

Giovanni Moroni[1], Stefano Petrò[1], Wahyudin P. Syam[1]
[1]Department of Mechanical Engineering
Politecnico di Milano,
Milano 20156, Italy

INTRODUCTION

Quality is a key factor in any manufacturing system. High quality products can be sold with higher profit margin. Often quality is linked to immaterial properties of the product, but where possible a quantification of quality should be looked for. To quantify quality, measurement of some key characteristics of the product is required. These key characteristics directly affect the product performance. Verifying these key characteristic are equal in any manufactured part, and conforming to project tolerances, is the aim of any quality system.

A key factor of devices performing measurements for quality is traceability. According to the VIM [1] metrological traceability is the "property of a measurement result whereby the result can be related to a reference through a documented unbroken chain of calibrations, each contributing to the measurement uncertainty". It guarantees the measurement of the same measurand with different instruments gives compatible results.

In the field of mechanical engineering, recent years have seen an increasing diffusion of micro- and nano-components. These parts propose new measurement challenges [2]. Contact measurement is in general not possible for them. The current solution consists in a series of measuring principles which were originally developed in the field of areal texture measurement [3]: at present their application for geometric measurement is being studied. Nowadays, several non-contact measurement methods like coherence scanning interferometry, confocal microscopy, and focus variation are available. These optical measuring devices can yield a nanometric resolution, but at present guaranteeing their traceability is not easy [4]. In geometric metrology traceability is usually guaranteed by initial performance verification as well as by periodic instrument testing to understand the condition of the instrument itself after some period of usage. Nevertheless, achieving traceability for optical instruments by means of performance verification is often difficult. The factors influencing their performance are quite different from those influencing contact devices (for which well-established performance verification protocols are available), including all the optical properties of the measured surface. Currently a gap exists in the traceability of contact measurements to micro optical measurements.

The purpose of the study is to design and manufacture an artifact for performance verification of a 3D micro measuring instrument. The instrument is an optical measuring device based on focus variation [7]. The artifact will comply with the recommendation in the ISO 10360 series of standards. Initial data will be proposed on the applicability of the artifact and on the system performance.

ARTIFACT DESIGN AND CALIBRATION

The key to traceability is calibration [4]. A traceable measurement is a critical aspect in global manufacturing, where parts come from different suppliers, different countries, and of course, measurement conditions are different. A traceable measurement is needed to assure accuracy and consistency of the measurement. Even if optical metrology instruments have recently seen a wide diffusion, a unified calibration procedure, and especially a unified calibration artifact for micro-geometric measurement, is still lacking [5]. In an optical measuring device, two calibrations are required: a calibration of the optical sensor, and a calibration of the stage which is usually associated to the sensor to move the part to measure. Here, we will focus on this second issue, in in particular on the verification of the effectiveness of calibration to reach traceability.

A reference artifact is a fundamental element to achieve instrument traceability by performance

verification. The main purpose of performance verification is the evaluation of the instrument volumetric error in terms of Maximum Permissible Error of Length measurement (MPE_L) and Maximum Permissible Error of Probing measurement (MPE_P). Hiersemenzel et al. [6] have recently published their works related to the design of a reference artifact to assess these volumetric errors. Their artifact design consists of a multi-diameter cylinder. On each step of the cylinder a circular pattern of concave half-sphere is machined. The spheres centers relative coordinates can be measured to perform both distance and diameter measurement.

In our proposed artifact, the whole volumetric error assessment is considered. The artifact consists of precision balls supported by rods of different length. A square steel plate is used as base. Figure 1 shows the side and top view of the artifact. The size of the artifact is 100x100x100 mm, coherent with the measuring volume of the instrument, so that the volumetric error can be comprehensively taken into account. The selected balls are grade G10 steel balls [8], characterized by a roughness tolerance on Ra of 20 nm and form and diameter tolerance both equal to 250 nm. The balls grade selection is relevant since G3 grade balls, which present the smoothest surface, cannot be measured by a focus variation instrument. As explained in Leach [7], focus variation needs certain level of roughness such that the focus of a point relative to its neighbors can be differentiated. Otherwise, no point can be captured on the surface of the part. The minimum roughness required for point sampling is 10 nm.

The key idea of the artifact design is the selection of ball diameter and location. Balls were selected characterized by two differing diameters, which are 2 mm and 5 mm shown in blue and red respectively in figure 1. Spheres of 2 mm diameter have been selected such that they can be measured with only single image field by using a 5x magnification lens. 5 mm diameter balls are used so that multiple images stitched together will be needed to capture the surface of the sphere. Therefore, the performance verification considers the stitching procedure of the obtained surface to have a comprehensive evaluation.

Finally, the balls reciprocal locations were designed in order to be as coherent as possible

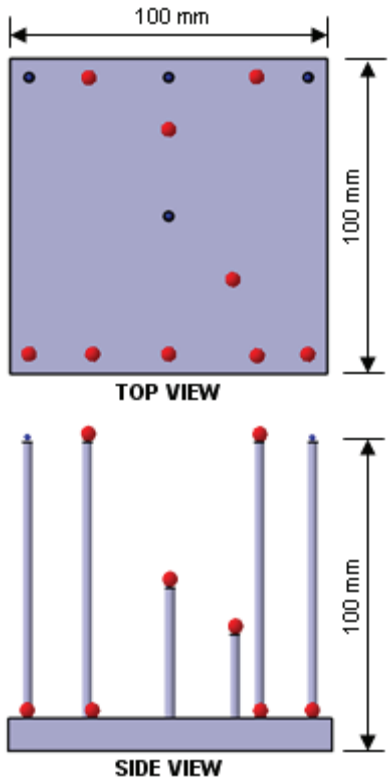

FIGURE 1: Design of the calibration artifact for performance verification.

with the ISO 10360 standards series [9] for performance verification of tactile CMM. for series of balls are present in the artifact, each one characterized by differing configuration: three inline configurations at constant height (0 mm, 50 mm, and 100 mm) and one diagonal configuration. By 90^0 rotating the artifact, all positions configuration for performance verification stated in ISO 10360-2 can be yielded. Based on this, the volumetric measurement error can be assessed. In each configuration, either inline or diagonal, there are four spheres which have different reciprocal distances. Thanks to this configuration, 5 different length measurements can be carried out by defining a series of ball couples. Beside, these configurations have a minimum number of spheres making the artifact easier to manufacture and calibrate. In this study, only two configurations were used: in-line configuration with height of 50 mm and diagonal configuration. This in-line configuration was rotated to evaluate the x- and y-axis distance measurement. The five nominal lengths of these configurations are 26 mm, 42 mm, 45 mm, 71 mm, and 87 mm. For diagonal type, the five distances are 46 mm, 74 mm, 79 mm, 107 mm,

and 153 mm. Metal glue was used to paste the spheres on the rods. Glue was chosen to avoid mechanical deformation of the spheres by e.g. welding or screwing. Figure 2(a) shows the manufactured calibration artifact.

The artifact calibration was carried out according to a multiple strategies measurement. This procedure does not require a reference artifact. Instead, uncertainty is determined by varying the orientation of the artifact as the calibration is carried out. The idea of this procedure is to carry multiple different strategies to measure the artifact such that volumetric error of the CMM can be taken into account in the calibration uncertainty. This allows the calibration of unique artifacts.

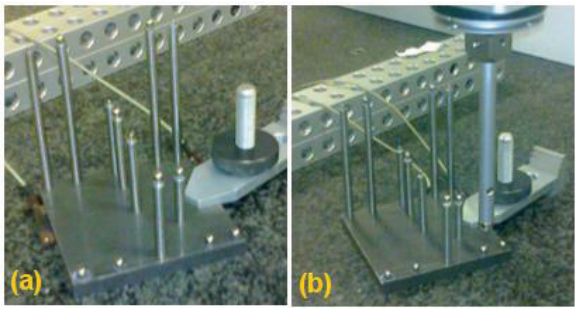

FIGURE 2: (a) The manufactured calibration artifact, (b) Artifact calibration with contact-CMM.

Four different orientations were selected. On each orientation, five measurement repetitions were carried out to be able to evaluate the repeatability contribution to the total calibration uncertainty. A tactile CMM with $E_{0,MPE}$ = 2 + L/300 μm (where L is the measured length in mm) was used. The calibration was carried out to determine the reciprocal location of the spheres. After the locations of the spheres are calibrated, the distance between two sphere can be calculated. For each of the four (three in-line and one diagonal) series of four balls, five reciprocal distances were considered, by coupling different balls. Thus, in total twenty distances relative distances have been calibrated. The relative distances are derived from the measurement of the coordinates of the center of the spheres obtained by fitting the points measured on the spheres themselves.

The artifact calibration process is shown in figure 2(b). The selection of the four different positions should be carefully addressed since in each position the locations of all spheres should be different. Thus, the configuration is skewed to comply with this requirement. The calibration uncertainty obtained is between 300 nm and 800 nm (depending on the considered length).

PERFORMANCE VERIFICATION

The performance verification is applied to a non-contact instrument based on focus variation. This performance verification focuses on the evaluation of the instrument's moving stage, shown in figure 3. The objective lens used for this performance evaluation has a 5x magnification such that the largest field of view (FOV) can be obtained. Since the surface is specular, polarized light was used. Vertical resolution of the z-stage was not maximized since what we are interest in is the form rather than the surface roughness, so the acquisition time can be reduced. To measure the 2 mm spheres a single image is sufficient to catch the whole sphere surface, so there is no stitching to capture the sphere itself. On the contrary, stitching of four images was used when measuring 5 mm diameter spheres. Therefore, the stitching process is taken into account in the evaluation of the center of the spheres.

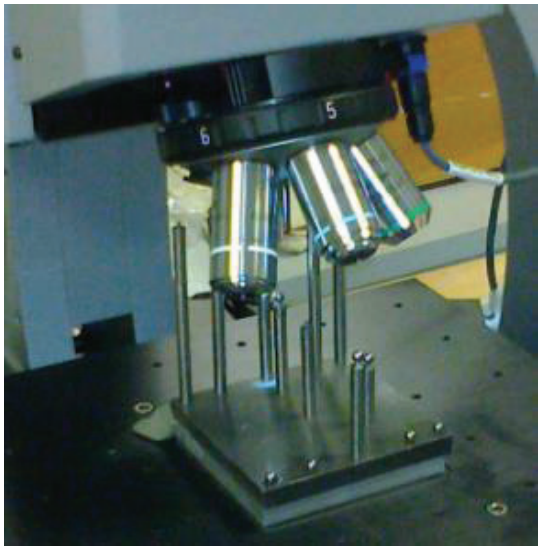

FIGURE 3: Performance verification for focus variation instrument.

The points of the spheres are supposed to be independent. Since there is no intersection between the clouds of points describing each sphere, the calculated locations and distance among the spheres depend only on the stage accuracy, without any stitching between different spheres contribution. Three repetitions for each

length measurement were carried out. The length is defined as the distance between the two centers of the specified spheres. Figures 4, 5 and 6 show the result of the errors obtained from the length measurement in X-direction, Y-direction and diagonal-direction respectively. The errors were obtained by calculating the difference between the measured length and the calibrated length.

As it can be observed, the maximum error of length measurement is approximately 13 μm. This error occurred in the diagonal direction. This can be caused by the combination all the three axis imperfections (volumetric error) contributing in the diagonal length measurement. Beside, the spread of the measurement error is still considerably large. The largest spread (in term of the range) of the error obtained is around 9 μm. This was observed in the measurement in X-direction.

There is an assignable result for the length measurement error in X-direction (figure 4). In this measurement, at the third length, there are two errors are almost identical while the other error (in the same third length) is significantly different. In figure 5, an incremental pattern is apparent. An incremental pattern is typical in the case in which the axis presents a scale error, This suggests that at least the y axis requires a calibration to adjust the scale factor.

A final, relevant note regards temperature compensation, which was not applied. This contributes to the measurement error, but not very significantly, because the artifact is quite small, and the environment temperature was controlled (20±0.5° C). In addition, a possible factor which contributes to the errors is the surface fitting algorithm, which depends on a series of operator defined parameters.

CONCLUSION

Driven by the micro scale products, micro geometric measurement is becoming very important for the quality control of these products. Non-contact geometric measurement systems are the most suitable solution since contacting a micro part or a micro feature of a larger part by tactile CMM is very difficult. Various types of non-contact measuring methods exist. But there is a gap in the verification of their performance. Performance verification is fundamental to assure the traceability of the instrument.

In this paper, a performance verification methodology is proposed for non-contact 3D measurement instruments based on focus variation. In principle, the methodology can be extended to any other similar instrument. A specifically designed artifact was proposed and performance verification was carried out. The artifact is designed to comply with the existing tactile CMM performance evaluation method described in ISO10360-2. According to these initial test results, the stage error is still considerably large. An improvement for the X-Y stage is needed, especially to support the measurements of a geometric feature of a part rather than micro parts. A complete performance verification test has also to be performed, especially for all four diagonals. Finally, the procedure to perform the performance verification is to be further investigated.

AKNOWLEDGEMENT

Financial support to this work has been provided by Regione Lombardia – Fondo per la promozione di Accordi Istituzionali istituito con d.g.r n° 5200 del 2 Agosto 2007 e integrata con d.g.r n° 8545 del 3 Dicembre 2008., as part of the project REMS - Rete Lombarda di Eccellenza per la Meccanica Strumentale e Laboratorio Esteso, CUP: D81J10000220005.

REFERENCES

[1] ISO/IEC. ISO/IEC GUIDE 99:2007(E/F): International Vocabulary of basic and general terms in Metrology (VIM). Geneva, Switzerland; 2007.

[2] Hansen HN, Carneiro K, Haitjema H, De Chiffre L. Dimensional Micro and Nano Metrology. CIRP Annals - Manufacturing Technology. 2006;55(2):721–743.

[3] ISO. ISO 25178-6 Geometrical product specifications (GPS) - Surface texture: Areal - Part 6: Classification of methods for measuring surface texture. Geneva, Switzerland; 2010.

[4] Phillips S, Krystek M, Shakarji C, Summerhays K. Dimensional measurement traceability of 3D imaging data. In: Proceedings of SPIE - Three-Dimensional Imaging Metrology. vol. 7239. San Jose, CA; 2009. pp. 72390E–72390E–7.

[5] Acko B, McCarthy M, Haertig F, Buchmeister B. Standards for testing freeform measurement capability of optical and tactile coordinate measuring machines. Measurement Science and Technology. 2012;23(9):094013.

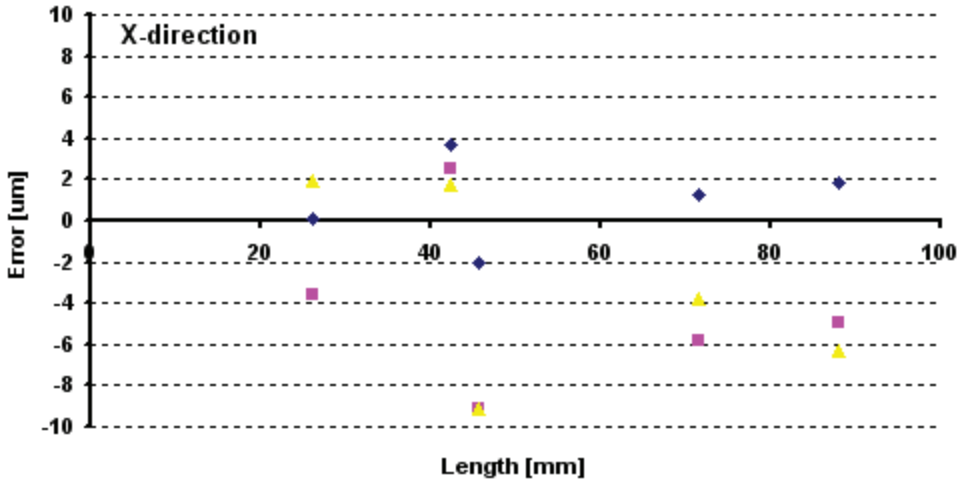

FIGURE 4: Length measurement errors in X-direction.

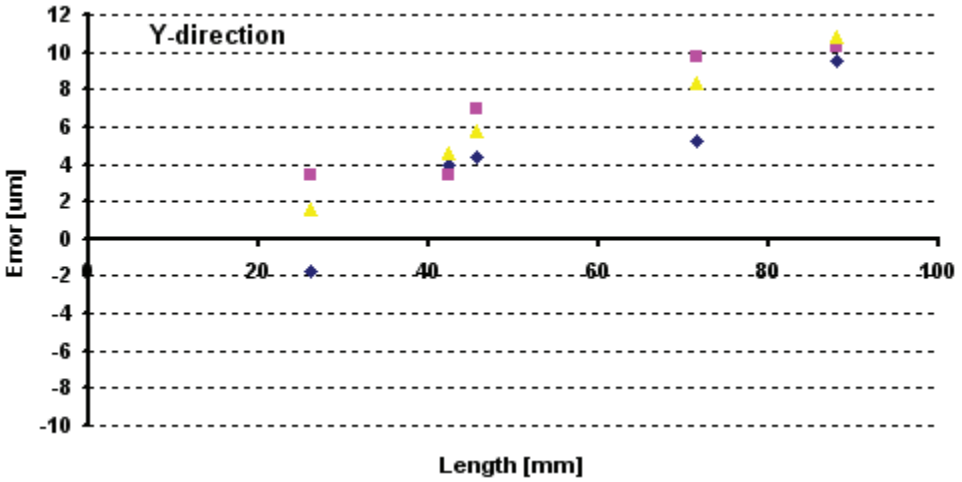

FIGURE 5: Length measurement errors in Y-direction.

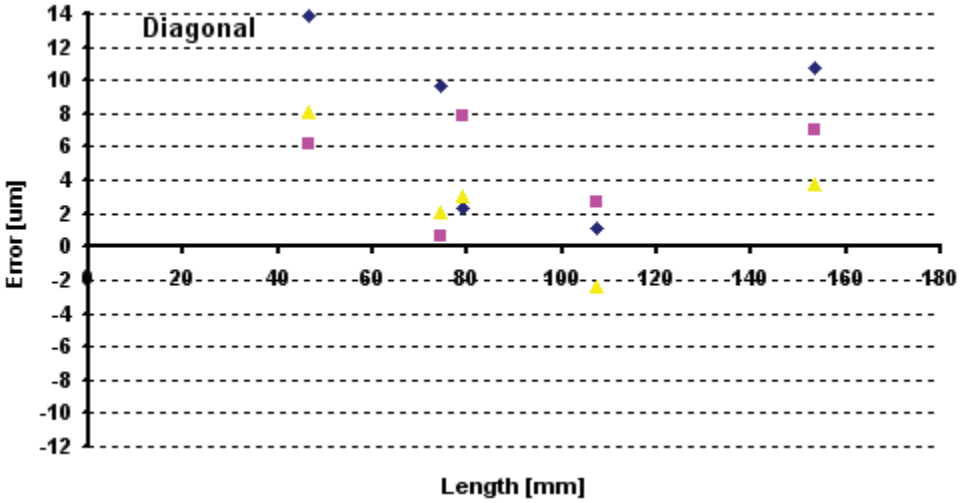

FIGURE 6: Length measurement errors in diagonal-direction.

[6] Hiersemenzel F, Claverley JD, Singh J, Petzing JN, Helmli F, Leach RK. ISO Compliant reference artifacts for the verification of focus variation-based optical micro-co-ordinate measuring machines, In: Proceeding of the 13th euspen International Conference. Berlin, Germany: EUSPEN, 2013.
[7] Leach RK (Ed.). Optical Measurement of Surface Topography. Springer Verlag: Berlin.2011.
[8] ISO 3290-1: Rolling bearings-Balls. Part 1: Steel balls. Geneva, Switzerland; 2008.
[9] ISO 10360-2: GPS-Acceptance and re-verification tests for CMM-Part 2: CMMs used for measuring linear dimensions. Geneva, Switzerland; 2007.

VOLUMETRIC PERFORMANCE EVALUATION OF A LASER SCANNER

B.Muralikrishnan[1], M.Ferrucci[1], D.Sawyer[1], G. Gerner[2], V. Lee[1], C. Blackburn[1], S. Phillips[1], P. Petrov[3], Y. Yakovlev[3], A. Astrelin[3], S. Milligan[3], and J. Palmateer[4]
[1]National Institute of Standards and Technology, Gaithersburg, MD
[2]The Pennsylvania State University, Erie, PA
[3]Basis Software Inc., Redmond, WA
[4]Boeing Research and Technology, Seattle, WA

INTRODUCTION

There are several sources of error in a laser scanner measurement [1, 2]. The optical and material properties of the target, the shape, form, surface texture, color, reflectivity, and orientation of the target in space, environmental effects, etc., all contribute to measurement errors. In this abstract, we address a particular source of systematic error arising from geometric misalignments within the system that result in errors in the measured point coordinates.

We describe the different sources of misalignment for one mechanical design and present a geometric error model. Using a manufacturer recommended contrast target, we present results from experiments that demonstrate clear systematic errors. We present possible explanations for the observed errors using the terms from our model. Finally, we discuss arrangement of targets in space that can be employed for the performance evaluation of this scanner.

INSTRUMENT GEOMETRY

For this study, we consider a design of a laser scanner in which the laser source and a spinning prism mirror are mounted on a platform that can rotate about the vertical axis, as shown in Fig. 1. The laser emanates from the source, strikes the spinning mirror at *O*, and is directed to the target *P* with the return signal traversing the same path. The coordinate system *XYZ* is fixed to the base. The measured angles *Hm* and *Vm* are shown in the figure.

In an ideal construction, the horizontal (*AT* in Fig. 1) and vertical (*OZ*) axes are orthogonal and intersect at point *O*. The source is coincident with the horizontal axis and the laser thus strikes the mirror at *O*. The angle encoders are mounted collinear to their respective axes. The mirror is mounted so that it reflects the beam in the plane *OPN*, which is orthogonal to the horizontal axis *AT*. In a practical realization, any or all of these conditions may be violated, resulting in unintended offsets, tilts, and eccentricities.

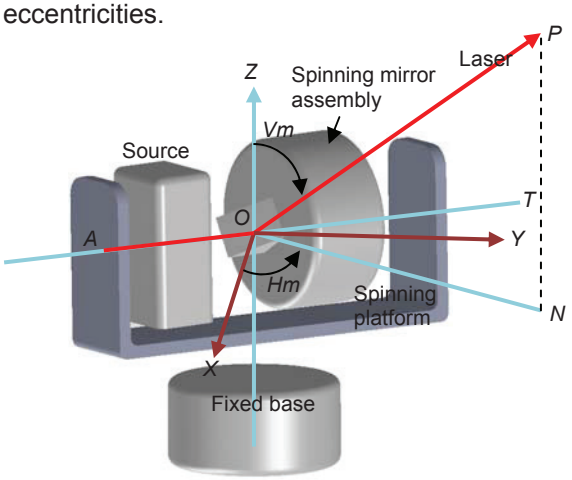

FIGURE 1. Coordinate system definition

TARGET AND REPEATABILITY

The contrast target is a rectangular plate with four alternating black and white triangles on the front face and a partial hemisphere on the back face. The common vertex of the triangles (which is also the intersection of the diagonals of the rectangle) on the front face of the plate is designed to be the center of the hemisphere.

We inspected these targets for eccentricity, but this characteristic is of no consequence to the two-face experiments described in this abstract. Two-face measurements involve the determination of a coordinate of a target in the front face and again in the back face of the instrument. The apparent distance between the two coordinates is a measure of geometric misalignments within the instrument.

From repeated measurements of a contrast target located 4 m away, we estimate the one standard deviation repeatability in determining the coordinate to be generally smaller than 30 µm. This is notably better than the

repeatability of determining the center of matt finish sphercial targets, which have at least a 40 µm standard deviation. By averaging measurements from 4 scans on contrast targets, we reduce the repeatability of the mean to less than 15 µm.

TWO-FACE MEASUREMENTS

Eight contrast targets are mounted on a vertical rail as shown in Fig. 2. The laser scanner is placed approximately 2 m (near position) from the vertical rail. Each target is measured in the front face and in the back face. This process is repeated four times. The front face and back face measurements are averaged separately. We then calculate the difference between the front and back face horizontal angle (*dHm*) and the difference between the front and back face vertical angle (*dVm*) for each target. We then rotate the laser scanner in increments of 45º (clocking angle) from 0 through 360º and repeat the measurements. We move the laser scanner to approximately 4 m (far position) from the rail and repeat the procedure.

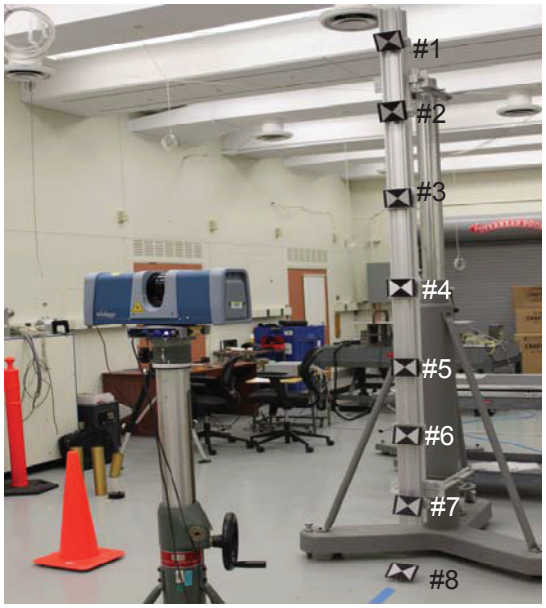

FIGURE 2. Contrast targets are mounted on a vertical rail. Targets are labeled in the image[1].

[1]**Disclaimer**: Commercial equipment and materials may be identified in order to adequately specify certain procedures. In no case does such identification imply recommendation or endorsement by the National Institute of Standards and Technology, nor does it imply that the materials or equipment identified are necessarily the best available for the purpose.

The measured differences between the front and back face angles, *dHm* and *dVm*, are shown in Fig. 3 for the 0 and 90º clocking angles for the near and far positions. Figs. 3 (a) and (b) show that both *dHm* and *dVm* exhibit clear dependence on the nominal vertical angle *Vm*. That is, the observed errors are a function of the height of the target with respect to the scanner. There does not appear to be any dependence on the nominal horizontal angle *Hm*, that is, the clocking angle.

It is important to note that the overall magnitude of the observed errors *dHm* and *dVm* are on the order of 200 µrad to 400 µrad, which is an order of magnitude larger than the repeatability in the determination of the coordinate. The data clearly suggests that this error may be modeled and removed; in fact, predictions from our model (discussed later) are also shown in Fig. 3 as the solid black line. We present the terms of the error model next.

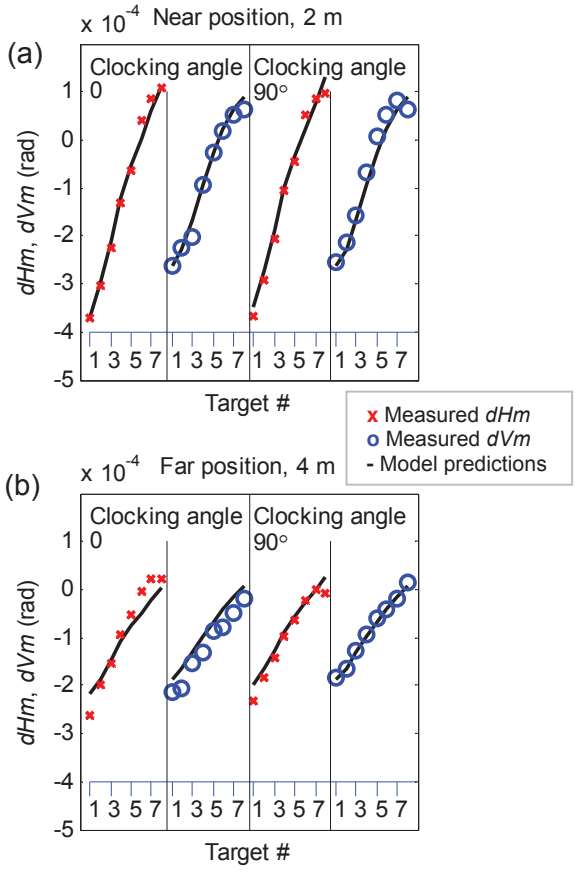
(a)
x 10^-4 Near position, 2 m
Clocking angle 0
Clocking angle 90°
dHm, dVm (rad)
1 0 -1 -2 -3 -4 -5
1 3 5 7 1 3 5 7 1 3 5 7 1 3 5 7
Target #
x Measured dHm
o Measured dVm
- Model predictions
(b)
x 10^-4 Far position, 4 m
Clocking angle 0
Clocking angle 90°
dHm, dVm (rad)
1 0 -1 -2 -3 -4 -5
1 3 5 7 1 3 5 7 1 3 5 7 1 3 5 7
Target #

FIGURE 3. Measured differences between front and back face angles and model predictions at (a) ≈2 m (b) ≈4 m

MODEL PARAMETERS

There are several sources of offsets, tilts, and eccentricities that may produce the observed errors shown in Fig. 3. We describe them here. Note that we use the notation *dHm* and *dVm* to denote the difference between front and back face angles (measured or model predictions), and ΔHm and ΔVm to denote the model based corrections to the measured angles *Hm* and *Vm*. For a term that is sensitive to two-face testing, the front face to back face difference *dHm* (*dVm)* will be twice the correction ΔHm (ΔVm) because the corrections reverse in sign in the back face. Due to space restrictions, equations are simply stated without derivation.

Beam offset (x_{1n} and x_{1z}): The beam originating from the source may be displaced from its ideal position *A* by a constant offset (x_1) to emerge from *A*', as shown in Fig. 4. The offset may be resolved into two components, x_{1n} along the *ON* direction, and x_{1z} along the *OZ* direction. Both components produce an error in both the measured vertical and horizontal angles. From the geometry shown in Fig. 4, the corrections to the measured front face angle can be derived as

$$\Delta Hm_1 = (x_{1n} \sin Vm)/(Rm \sin Vm) = x_{1n}/Rm$$
$$\Delta Hm_2 = (x_{1z} \cos Vm)/(Rm \sin Vm)$$
$$= x_{1z}/(Rm \tan Vm)$$
$$\Delta Vm_1 = (x_{1n} \cos Vm)/Rm$$
$$\Delta Vm_2 = (-x_{1z} \sin Vm)/Rm$$

where *Rm* is the measured range. It should be noted that x_{1z} is sensitive to two-face testing along the horizontal angle direction but not along the vertical angle direction while the reverse is true for x_{1n}. Therefore ΔHm_2 and ΔVm_1 reverse in sign in the back face but ΔHm_1 and ΔVm_2 do not. Two-face sensitivity arises from the geometry of the construction, not from the functional form of the equations. We note that x_{1z} is a candidate that may explain the observed *dHm* dependence on *Vm* while x_{1n} is a candidate that may explain the observed *dVm* dependence on *Vm* in Fig. 3.

Transit offset (x_2): In the presence of a transit offset x_2 (see Fig. 5), the beam is directed to *P'* instead of to *P* when the measured vertical angle is *Vm*. When the beam is subsequently directed to the target at *P*, the measured vertical angle and range will be smaller than the true angle and range respectively. The corrections are given by

$$\Delta Vm_3 = (x_2 \cos Vm)/Rm$$
$$\Delta Rm_1 = x_2 \sin Vm$$

These terms are sensitive to two-face testing. We note that x_2 is another candidate that may explain the observed *dVm* dependence on *Vm.*

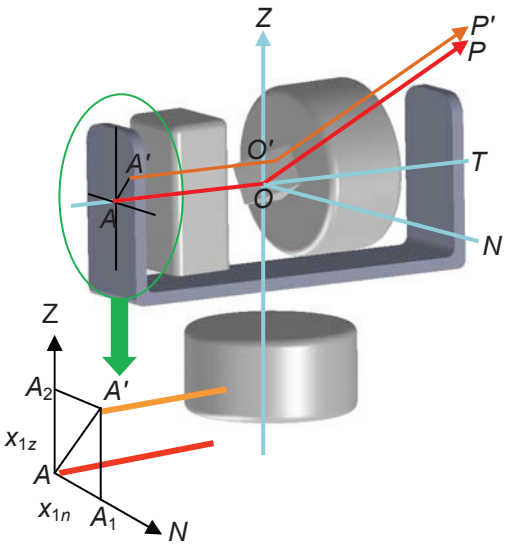

FIGURE 4. Geometry of beam offset

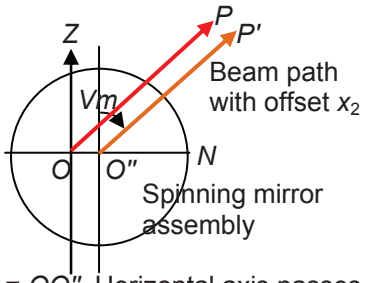

Offset $x_2 = OO''$. Horizontal axis passes through *O''* and into the plane of the paper.

FIGURE 5. Geometry of transit offset

Mirror offset (x_3): If the plane of the prism mirror is offset but parallel from its ideal position in space by an amount x_3, the measured horizontal angle will be in error. The correction to the front face horizontal angle is given by

$$\Delta Hm_3 = -x_3/(Rm \sin Vm)$$

Mirror offset is sensitive to two-face testing. Mirror offset can account for some of the bias (note that the majority of the errors are negative instead of being symmetrically located) in the observed *dHm* errors in Fig. 3.

Vertical index offset (x_4): A shift in the zero of the vertical angle, x_4, from the pole results in a constant error in the measured vertical angle. Vertical index offset is sensitive to two-face testing. Because the error is identical for all targets, this term can account for the bias in the

observed *dVm* errors in Fig. 3. The correction is given by

$$\Delta Vm_4 = x_4$$

Beam tilt (x_{5n} and x_{5z}): In addition to an offset, the laser emerging from the source may also suffer from a tilt. Fig. 6 shows the laser emerging from point *A*' to intersect the mirror at point *O* (note that if the beam does not intersect the mirror at *O*, that effect is modeled by the beam offset term described earlier). The tilt in the laser can be resolved into two components x_{5n} and x_{5z} as shown in Fig. 6. Although shown in Fig. 6 as an offset, beam tilt is the offset per unit length and is therefore expressed in units of angle. For positive offsets, as shown in Fig. 6, the corrections are given by

$$\Delta Hm_4 = (x_{5n} \sin Vm)/\sin Vm = x_{5n}$$
$$\Delta Hm_5 = (x_{5z} \cos Vm)/\sin Vm = x_{5z}/\tan Vm$$
$$\Delta Vm_5 = x_{5n} \cos Vm$$
$$\Delta Vm_6 = -x_{5z} \sin Vm$$

As in the case of beam offset, ΔHm_5 and ΔVm_5 reverse in sign in back face, but ΔHm_4 and ΔVm_6 do not. We note that x_{5z} is another candidate that may explain the observed *dHm* dependence on *Vm* while x_{5n} is a candidate that may explain the observed *dVm* dependence on *Vm* in Fig. 3.

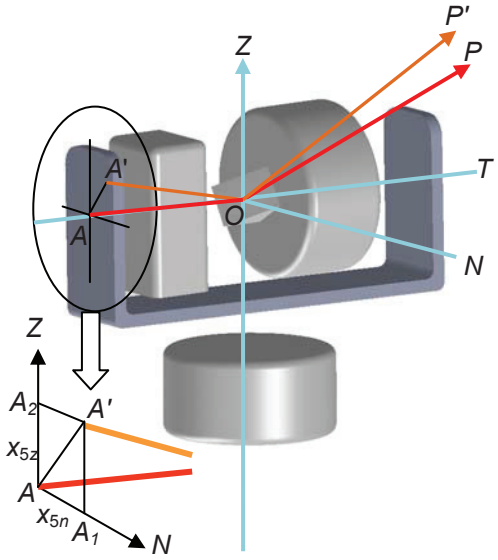

FIGURE 6. Geometry of beam tilt

Mirror tilt (x_6): The plane of the mirror is ideally oriented so that the reflected beam is orthogonal to the incident beam. If the mirror has a small tilt, the measured horizontal angle will be in error. This term is similar to the well-known collimation error [3] in theodolites and beam tilt in certain types of laser trackers. The correction is given by

$$\Delta Hm_6 = -x_6/\sin Vm$$

This term is sensitive to two-face testing, that is, the sign of ΔHm_6 reverses in the back face. This term provides a possible explanation for the bias in the observed *dHm* errors in Fig. 3.

Transit tilt (x_7): The transit axis, although intersecting the standing axis, may be tilted (thus making the two axes non-orthogonal) relative to the standing axis. This lack of squareness between the axes is referred to as transit tilt [3] and is also a common theodolite error source. Again, as in beam and mirror tilt, the parameter x_7 is a ratio of offset per unit length and is expressed in units of angle. Lack of squareness between the two axes produces an error only in the measured horizontal angle. The correction is given by

$$\Delta Hm_7 = x_7/\tan Vm$$

Transit tilt is sensitive to two-face testing. We note that x_7 is also a candidate that may explain the observed *dHm* dependence on *Vm* in Fig. 3.

Encoder eccentricity (x_8 and x_9): The horizontal and vertical angle encoder eccentricities also contribute to error in the measured angles. Resolving the horizontal angle encoder eccentricity along *X* and *Y*, and the vertical angle encoder eccentricity along *N* and *Z* axes, we have

$$\Delta Hm_8 = x_{8x} \cos Hm$$
$$\Delta Hm_9 = x_{8y} \sin Hm$$
$$\Delta Vm_7 = -x_{9n} \cos Vm$$
$$\Delta Vm_8 = x_{9z} \sin Vm$$

It should be noted that ΔVm_8 does not reverse in sign in the back face, while ΔHm_8, ΔHm_9, and ΔVm_7 do. Also, we note that x_{9n} is a candidate that may explain the observed *dVm* dependence on *Vm* in Fig. 3.

Bird-bath or zero-offset (x_{10}): The correction due to the constant error in range is given by

$$\Delta Rm_2 = x_{10}$$

This term is not sensitive to two-face testing.

Second order scale error (x_{11} and x_{12}): The corrections due to the second order scale error in the encoders are given by

$$\Delta Hm_{10} = x_{11a} \cos 2Hm$$
$$\Delta Hm_{11} = x_{11b} \sin 2Hm$$
$$\Delta Vm_9 = x_{12a} \cos 2Vm$$
$$\Delta Vm_{10} = x_{12b} \sin 2Vm$$

These terms are not sensitive to two-face testing.

MODEL

Combining the corrections ΔHm_i, ΔVm_i, and ΔRm_i, the error model for the scanner is given by

$$\Delta Rm = k(x_2 \sin Vm) + x_{10}$$

$$\Delta Hm = k\left[\begin{array}{l} \dfrac{x_{1z}}{Rm\tan Vm} - \dfrac{x_3}{Rm.\sin Vm} + \dfrac{x_{5z}}{\tan Vm} - \dfrac{x_6}{\sin Vm} \\ + \dfrac{x_7}{\tan Vm} + x_{8x}\cos Hm + x_{8y}\sin Hm \end{array}\right]$$

$$+\left[\frac{x_{1n}}{Rm} + x_{5n} + x_{11a}\cos 2Hm + x_{11b}\sin 2Hm\right]$$

$$\Delta Vm = k\left[\begin{array}{l} \dfrac{x_{1n}\cos Vm}{Rm} + \dfrac{x_2.\cos Vm}{Rm} + x_4 \\ + x_{5n}\cos Vm - x_{9n}\cos Vm \end{array}\right]$$

$$+\left[\begin{array}{l} -\dfrac{x_{1z}\sin Vm}{Rm} - x_{5z}\sin Vm + x_{9z}\sin Vm \\ + x_{12a}\cos 2Vm + x_{12b}\sin 2Vm \end{array}\right]$$

where k is +1 for the front face and -1 for the back face.

PARAMETER ESTIMATION

While the model above has 18 parameters, only 12 are sensitive to two-face testing and we therefore only fit those to the data. The parameter values from the least-squares fit are shown in Table 1.

In Fig. 7, we plot the relative contributions of each of the model terms determined by the fit (i.e, the values shown in Table 1) to the *dHm* and *dVm* model predictions for the eight targets. We show the results only for the first clocking angle (horizontal angle of zero) and at the near position. While the plot is informative in that it suggests likely candidates that may explain the dependance of *dHm* and *dVm* errors on *Vm* and the bias in the data, caution must be exercised prior to forming conclusions.

For example, the plot suggests that the leading contributors to the *dHm* errors (that explain the dependance of *dHm* on *Vm*) are the transit tilt (x_7) and beam tilt along OZ (x_{5z}) axis. However, it should be noted that these two terms have the same functional form and are therefore indistinguishable as far as two-face testing is concerned. This is reflected in Table 1 as well, where the two parameters have equal values. Additional length tests in front face are necessary to separate the two terms before we can determine which of these two terms (or a linear combination) is in fact present in our system.

Table 1. Model parameters for the scanner affecting two-face measurements

Parameter	Description	Value
x_{1n}	Beam offset along *n*	0.012 mm
x_{1z}	Beam offset along *z*	0.015 mm
x_2	Transit offset	0.012 mm
x_3	Mirror offset	-0.033 mm
x_4	Vertical index offset	0.000049 rad
x_{5n}	Beam tilt along *n*	0.000062 rad
x_{5z}	Beam tilt along *z*	0.000067 rad
x_6	Mirror tilt	-0.000041 rad
x_7	Transit tilt	0.000067 rad
x_{8x}	Horizontal angle encoder eccentricity along *x*	0.000006
x_{8y}	Horizontal angle encoder eccentricity along *y*	-0.000005
x_{9n}	Vertical angle encoder eccentricity along *n*	-0.000062

Similarly, the plot suggests that the leading contributors to the *dVm* errors are the beam tilt along the *ON* (x_{5n}) axis and the vertical encoder eccentricity along the *ON* (x_{9n}) axis. Again, these two terms have the same functional form and are therefore indistinguishable as far as two-face

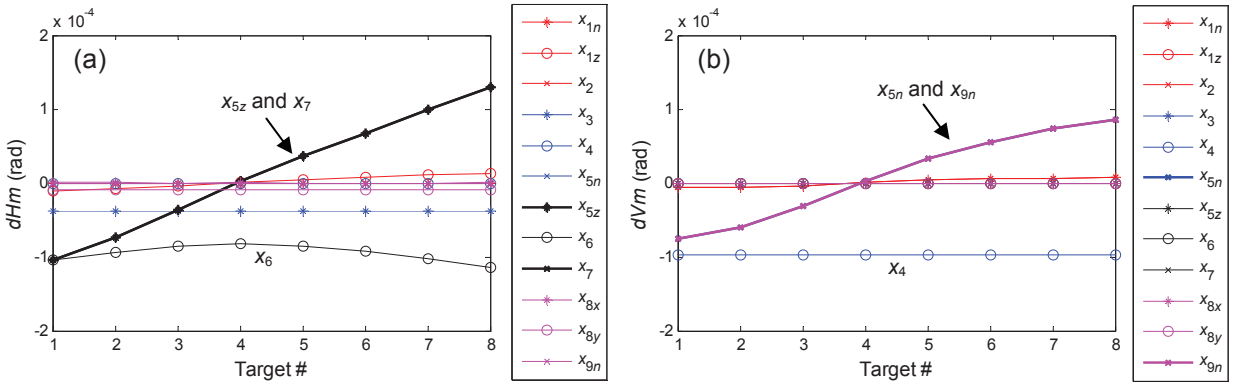

FIGURE 7. Relative contributions of the different model terms to (a) *dHm* (b) *dVm*

testing is concerned. This is reflected in Table 1 as well, where the two parameters have equal values.

PERFORMANCE EVALUATION

The purpose of performance evaluation testing is to evaluate a device through preferably a minimal collection of tests (two-face and volumetric length) that are sensitive to all known sources of error. In order to determine suitable placement of targets for the purpose of performance evaluation, we have studied sensitivity of different length/two-face tests to model parameters through numerical simulations, similar to that reported earlier for laser trackers [5]. Based on these simulations, we show one possible scenario for the placement of targets in space in Fig. 8. The inter-nest distances are assumed to be calibrated using trackers.

The grid comprising 11 targets is scanned from four scanner positions *P*, *Q*, *R*, and *S* as shown in Fig. 8 in both the front and back face of the scanner. Two clocking angles are suggested for scanner positions *Q* (0 and 90º), *R* (0 and 90º) and *S* (0 and 30º), while one is sufficient for *P*. Simulations suggest that these measurements would provide a collection of two-face and length tests that would be sensitive to all model parameters. For example, lengths *CG* and *AI* are the left and right symmetrical diagonals that are sensitive to transit tilt (squareness), *MN* from position *S* is sensitive to the second order scale error, length *BH* from position *P* is sensitive to the zero-offset in ranging, etc.

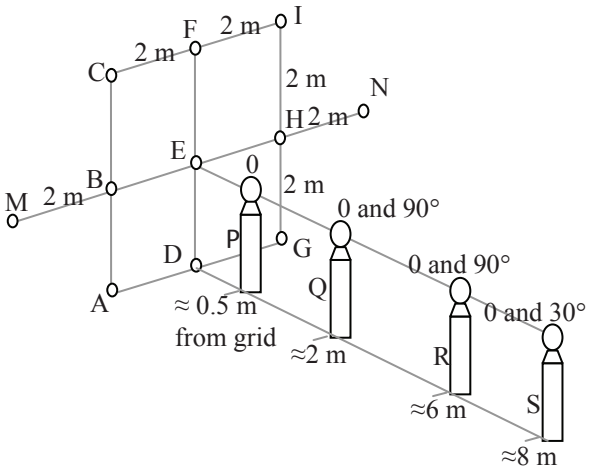

FIGURE 8. Target and scanner placement for performance evaluation

We are currently in the process of constructing this grid. It should be noted that the choice of target is crucial in the performance evaluation of laser scanners; keeping target-induced errors to a minimum is critical in isolating the errors from the geometry of the instrument. We are currrently working with contrast targets and plan on incorporating them as part of the grid as well. We eventually plan on transitioning to spheres or other dimensional targets in the future because contrast targets may not be applicable to all systems.

CONCLUSIONS

We describe a geometric error model for a large volume laser scanner that employs a spinning prism mirror mounted on a rotating head to direct the laser to the target. We demonstrate the presence of clear systematic errors through several two-face tests. We estimate the parameters of our model through least squares fitting on our test data. Finally, based on simulation studies, we present a possible placement of targets in space for the purpose of evaluating the performance of these instruments. As future work, we plan on performing volumetric length measurements to provide a better estimate of some of these parameters.

REFERENCES

[1] Nguyen T. T., Liu X. G., Wang H. P., Analysis of error sources in terrestrial laser scanning, Proceedings of the Joint ISPRS Workshop on 3D City Modelling & Applications and the 6th 3D GeoInfo Conference, Wuhan, China, 2011

[2] C. Coşarcă, A. Jocea, A. Savu, Analysis of error sources in terrestrial laser scanning, RevCAD – Journal of Geodesy and Cadastre, 2009

[3] Fritz Deumlich, Surveying Instruments, Walter de Gruyter, Berlin/New York (1982)

[4] B. Muralikrishnan, C. Blackburn, D. Sawyer, S. Phillips, and R. Bridges, Measuring scale errors in a laser tracker's horizontal angle encoder through simple length measurement and two-face system tests, Journal of Research of the NIST, 115 (5), 2010

[5] B. Muralikrishnan, D. Sawyer, C. Blackburn, S. Phillips, B. Borchardt, W. T. Estler, ASME B89.4.19 performance evaluation tests and geometric errors in laser trackers, Journal of Research of the NIST, 114 (1), 2009

APPLICATION OF MAGNETS IN LOADING ULTRA-HIGH-SPEED SPINDLES AND UNDERSTANDING ITS EFFECTS ON RADIAL SPINDLE ERROR MOTIONS

Sudhanshu Nahata[1] and O. Burak Ozdoganlar[1]
[1]Department of Mechanical Engineering
Carnegie Mellon University
Pittsburgh, PA 15213

INTRODUCTION

The objective of this work is to understand the effects of external loading on radial error motions of an ultra-high-speed (UHS) micromachining spindle. Micromachining utilizes miniature cutting tools as small as 10μm in diameter to produce micro-scale features. To attain effective material removal rates while using micro-scale tools, miniature UHS (>40,000 rpm) spindles are used. Accurate rotational motion of the micro-tools is critical to satisfy absolute accuracy requirements of micro-scale features, which partly depends on the accuracy of axis of rotation provided by the spindle. An ideal spindle should rotate only along its axis of rotation but due to a number of unavoidable factors (e.g. manufacturing defect in bearings, misalignment during assembly, thermal fluctuations, and environmental effects etc.); it exhibits motion in remaining five degrees of freedom. These motions are undesired and are termed as spindle error motions (see [1, 2, 3] for detailed description) which are amplified when the cutting tool encounters forces while micro-machining. Therefore, it becomes necessary to understand this change in spindle behavior and characterize error motions under different loading conditions.

For macro-scale spindles, use of master axis for characterization of spindle error motions under load has been prescribed by [4]. ASME standards [5] also dictate to use master axis method for dynamic compliance measurement by applying load to the master axis stator. In case of UHS spindles, this method is not suitable as the dynamic axial and radial stiffness values of these spindles are very low and ambiguous. Even a slight misalignment with the master axis would cause permanent damage to the spindle.

In order to provide loading to the spindle, a non-contact loading approach is demonstrated in this work with the help of permanent magnets and Direct Current (D.C.) electromagnets. The major part of this work involves exploring different types of magnets, their geometry and loading capabilities to apply suitable static (constant magnitude) loads in axial and radial directions.

During micro-machining processes, e.g. micro-milling, tool-tip experiences dynamic forces in all three orthogonal directions as indicated in Figure 1 below. In general, the peak force magnitude of these dynamic forces in each direction falls between 0.2 - 5 N assuming commonly used materials and machining conditions [6]. We believe that, even the application of static force with similar magnitudes might result in different error motions. Therefore, we intend to apply forces in both axial and radial directions through the use of magnets when the spindle is rotating at its operational speeds. This force will be applied to the cylindrical artifact, attached to the spindle which acts as a dummy tool.

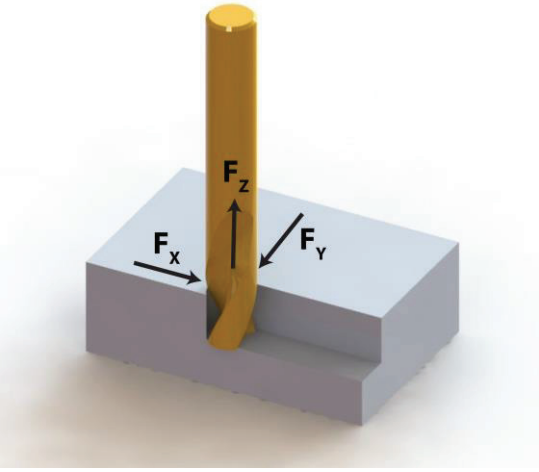

FIGURE 1. Schematic of axial (normal, F_Z) and radial (feed, F_X and transverse, F_Y) forces encountered during micro-milling operations.

In this work, artifact form is not separated from the measured radial motions. Therefore, the experimental data presented here will contain contributions from the surface profile of cylindrical artifact in addition to the spindle error motions.

MAGNETS

We explored two different classes of magnets for providing required force magnitudes: (1) Permanent magnets, and (2) D.C. electromagnets. Permanent magnets are available in a variety of materials, e.g. Alnico, ceramic, rare-earth etc. We chose magnets made from sintered Neodymium (rare-earth) because of their higher magnetic strength amongst all. These magnets come in different grades ranging from N27 to N52, where increasing numbers denote higher energy product (BHmax). Out of these, magnets made from N50 grade are commercially available in a variety of shape and sizes which we have explored in this work. On the other hand, D.C. electromagnet is a standard product which consists of thin insulated copper wires wound around a soft iron core. We chose the largest D.C. electromagnet which we could use with the maximum artifact overhang length (15 mm) as prescribed by the spindle manufacturer (Fischer-Precise). Figure 2 compares the attractive forces as a function of air-gap between the magnet and the cylindrical artifact attached to the spindle. From the comparison, permanent magnet is a clear choice for static force applications due to higher forcing capability.

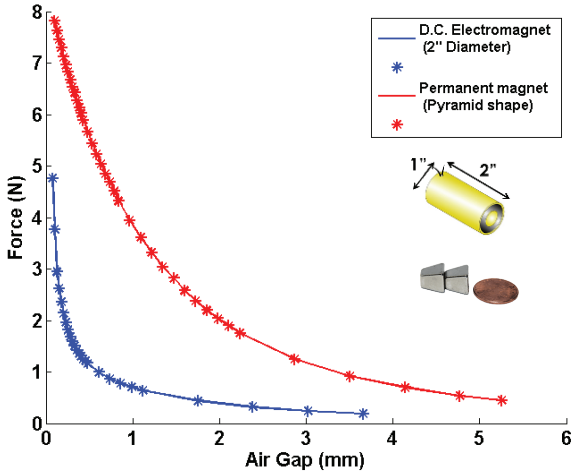

FIGURE 2. Plot of attractive force v/s air-gap (between magnet and cylindrical artifact) for D.C. electromagnet and permanent magnet. Image courtesy: www.supermagnetman.com and www.electromechanicsonline.com.

EXPERIMENTAL SETUP

The experimental setup consists of an UHS spindle under testing, a static loading setup and a laser Doppler vibrometer (LDV) to measure displacements from the surface of the rotating artifact. An exploded view of the static loading setup is presented in Figure 3. It consists of a precision XYZ stage, a high accuracy load cell to measure forces and a magnet on top which applies non-contact forces. This set-up can be used for both axial and radial loading of the spindle. Suitable magnets can be selected and attached at top of the setup based on the type of loading required for different applications. The load cell used here can measure +/- 5 lbs force with an uncertainty of 0.3% full scale output.

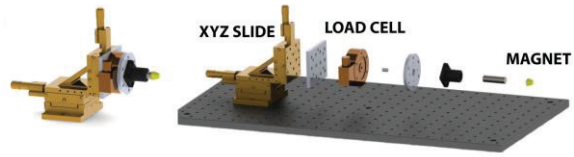

FIGURE 3: Loading setup which includes precision XYZ stage, a high accuracy load cell and a magnet attached at the tip.

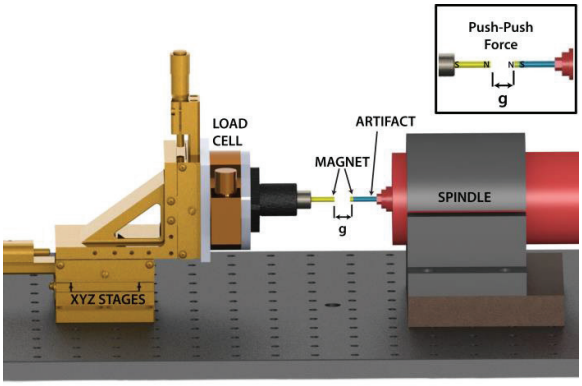

FIGURE 4. Details of axial loading setup to apply a push-push force with the help of two 1/8" diameter cylindrical N50 neodymium magnets.

Axial Loading

For emulating normal forces (F_Z) experienced by the cutting tool during micro-machining operations, a push force is required against the artifact. For this purpose, we used a pair of cylindrical magnets with same poles facing each other creating a push-push force (see Figure 4). One of the magnets is attached to the loading setup and other is attached to the cylindrical artifact. The diameter of the cylindrical magnet is equal to the diameter of artifact (1/8"). By varying the air-gap (g) between the magnets, the force magnitude can be varied. The maximum force that can be generated with this method is 3 N. The peak force is restricted by the size of the magnet attached to the artifact.

Radial Loading

We can emulate forces in feed (F_X) and transverse (F_Y) directions by applying a single, resulting force in radial direction. For this purpose, we are using a permanent magnet in a configuration described in Figure 5. A variety of magnets were tested (including D.C. electromagnet) and based on the higher force magnitudes, a pyramid shaped N50 neodymium magnet is finalized. Pyramid shaped magnets provide concentrated flux at the tip portion which results in a stronger attractive force maintaining a small profile. Through the use of pyramid magnet we can apply a maximum force of 6 N by varying air-gap (g) between the artifact and the magnet.

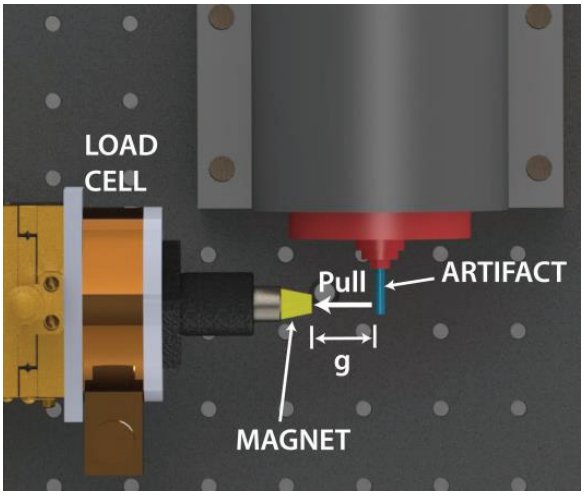

FIGURE 5. Details of radial loading setup to apply a pull force with the help of pyramid shaped N50 neodymium magnet.

RESULTS AND DISCUSSION

Experiments were performed at various spindle speeds and at multiple axial and radial loading magnitudes to explore its effects on spindle error motion. Displacement data is measured with the help of LDV from the tip of the artifact from radial direction and is separated into various components (synchronous and asynchronous error motions) by following the process as described in [3]. These experiments were performed on a Fischer-Precise motorized air-bearing spindle, ASC-200. The spindle has an axial failure load specification of 180 N and a radial failure load specification of 90 N. The cylindrical artifact is kept at 15 mm overhang length for all the experiments.

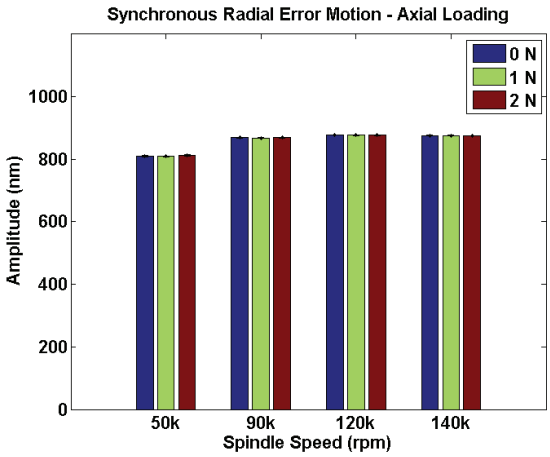

FIGURE 6. Synchronous radial error motion at different spindle speeds for variable axial loading.

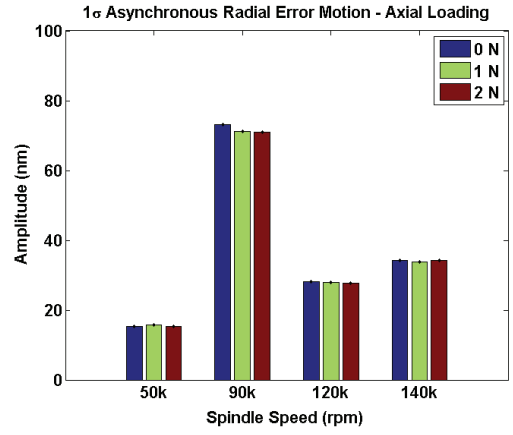

FIGURE 7. 1-σ of asynchronous radial error motion at different spindle speeds for variable axial loading.

Figure 6 and Figure 7 plots the effect of variable axial loading on radial spindle error motions. It is observed that both the synchronous radial error motion and 1-σ of asynchronous radial error motion undergoes marginal change on application of an external load up to 2 N. One of the reasons for this behavior could be related to the high axial failure load limit of the spindle. Applying 2 N (~ 1% of failure load limit) might not be sufficient to see considerable variations in the behavior of the spindle.

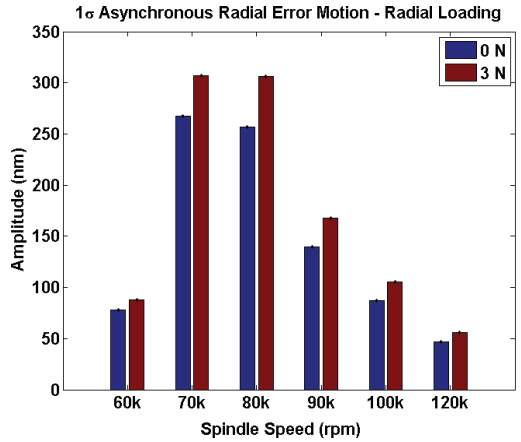

FIGURE 8. 1-σ of asynchronous radial error motion at different spindle speeds for variable radial loading.

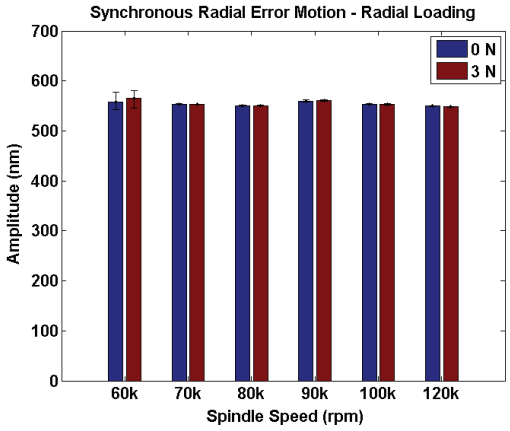

FIGURE 9. Synchronous radial error motion at different spindle speeds for variable radial loading.

In case of radial loading up to 3 N, the spindle shows a significant increase in 1-σ values of asynchronous radial error motion at all the tested spindle speeds, as seen in Figure 8. The synchronous radial error motion (see Figure 9) shows small variation at certain rotating speeds. There could be various reasons to why the asynchronous radial error motion exhibits considerable increase in 1-σ values. The external forcing on the rotating artifact tends to increase the eccentricity of the artifact (w.r.t axis of rotation of the spindle) which may excite the dynamics of the spindle due to rotating unbalance type loading [7]. The overall trend of the asynchronous radial error motion across different speeds is due to the presence of first natural frequency of the spindle system - around 1200 Hz.

CONCLUSION

Use of permanent magnets for applying static axial and radial loading to UHS spindles have been explored in this work. Although the magnitude of static forces that we can apply at this point is limited due to various factors such as small size of artifact, limited overhang length etc. We could still see the effects of loading on the radial spindle error motions. In most cases, asynchronous error motion component was found to be largely affected by the application of external load.

ACKNOWLEDGEMENTS

This work was supported by the NIST award #70NANB12H208 (Ozdoganlar). The authors wish to thank Dr. Alkan Donmez, Dr. Shawn Moylan, Dr. Gregory Vogl and Dr. Ronnie Fesperman for their constant guidance throughout this work. The authors also thank Fischer-Precise USA for providing UHS spindle for testing purposes.

REFERENCES

[1] ISO 230-7:2006 Test Code for Machine Tools. Part 7: Geometric Accuracy of Axes of Rotation. 2006.

[2] Anandan K P, Tulsian A S, Donmez A, Ozdoganlar O B. A Technique for Measuring Radial Error Motions of Ultra-High-Speed Miniature Spindles used for Micromachining. Precision Engineering. 2012; 36: 104-120.

[3] Anandan K P, Ozdoganlar O B. An LDV-based Methodology for Measuring Axial and Radial Motions when using Miniature

Ultra-High-Speed (UHS) Micromachining Spindles. Precision Engineering. 2013; 37: 172-186.

[4] Marsh E, Gredja R D. Experiences with Master Axis Method for Measuring Spindle Error Motions. Precision Engineering. 2000; 24: 50-57.

[5] ANSI/ASME B89.3.4M. Axes of Rotation: Methods of Specifying and Testing. 2010.

[6] Camara M A, Rubio J C C, Abrao A M, Davim J P. State of the Art on Micromilling of Materials, a Review. J. Mater. Sci. Technol. 2012; 28(8): 673-685.

[7] Bibler J E. Effects of Imbalance and Geometric Error on Precision Grinding Machines. PhD Thesis. MIT: 1997.

Density Measurement of Tantala (Ta_2O_5) Foams Using X-Ray Radiography

Richard M. Seugling, Peter Young, John Sain and Joe Satcher
Lawrence Livermore National Laboratory
Livermore, CA 94551

Abstract

Successful High Energy Density Science experiments at the National Ignition Facility (NIF) require that millimeter-scale targets are fabricated, aligned, and measured with micrometer-scale tolerances. In addition to the stringent dimensional requirements, inherent bulk properties such as density need to be understood to the %1.0 level. LLNL has used the combination of dimensional metrology, chemical analysis and x-ray radiography to meet this specification for Tantala (Ta_2O_5) foams.

In the case of targets containing low density materials, such as 500 mg/cc Tantala (Ta_2O_5) being discussed in this paper, density variation due to the bulk material manufacturing and/or machining processes is a critical element of the experiment. In general, density variations such as voids or inclusions can occur during material synthesis or during machining operations and often have the most direct impact to the experiment. However, contaminants like absorbed and adsorbed moisture from the environments seen by the sample as it goes through a number of process steps can also have a large effect on the experiment depending on the material chemistry.

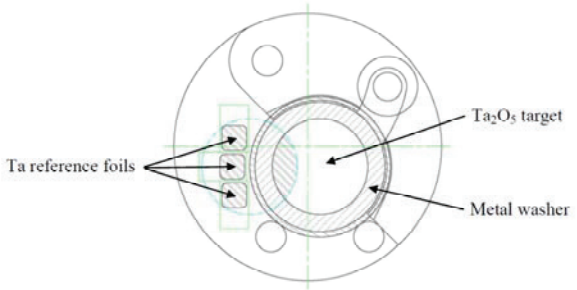

FIGURE 1. Illustration of the test sample in a fixture within the x-ray system. Three calibrated reference foils are used insitu as a baseline for the intensity map generated by the CT system.

To quantify the density of these Tantala samples to the %1.0 level a combination of dimensional measurement, chemical analysis and x-ray radiography techniques have been developed to verify the integrity of the samples before being used in an experiment. The configuration being used for measuring density variation across the sample surface is shown in Figure 1. A set of calibrated reference foils are used in conjunction with the sample under test to compare x-ray transmission intensity while under the same environment in a single set-up. Figure 2 shows an image of the sample foam part. The variation in intensity across the area illustrates density variations.
LLNL-ABS-535812

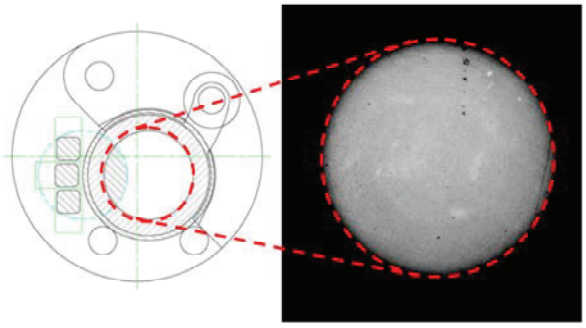

FIGURE 2. Example radiograph showing foam sample. Variations in intensity represent voids or inclusions throughout the bulk of the sample.

The focus of this paper will be to describe the uncertainty and error sources related to determining 500 mg/cc Tantala foam density by combining dimensional metrology, chemical analysis and x-ray radiography.

This work was performed under the auspices of the U.S. Department of Energy by Lawrence Livermore National Laboratory under Contract DE-AC52-07NA27344.

DEVELOPMENT OF A LARGE-STROKE PIEZO-ACTUATED STAGE FOR NANOPOSITIONING

Junbin Zhang and Peisen S. Huang
State Key Laboratory of Mechanical Systems and Vibration
University of Michigan – Shanghai Jiao Tong University Joint Institute
Shanghai Jiao Tong University
Shanghai, P. R. China

INTRODUCTION

The demand for nanopositioning systems is growing rapidly in many modern industrial and scientific applications, particularly in semiconductor manufacturing and micro/nano fabrication. These applications usually require that nanopositioning systems have a high positioning resolution and accuracy as well as a large motion range.

Various nanopositioning systems have been developed so far. Typical actuation methods include electromagnetic planar motors [1,2], ultrasonic motors (USM) [3,4], elastic deformation [5], "stick-clamping" [6], and "stick-slip" effect [7].There are some disadvantages with the aforementioned actuation methods. Electromagnetic planar motor needs complex dynamic motion control. Ultrasonic planar motors require complex dynamic analysis of the actuation and expensive friction material. Nano-positioning stages utilizing elastic deformation for actuation have small motion volumes even when flexure-lever mechanisms are used. Stages based on the "stick-clamping" method have a limited velocity because the clamping action in each step stops the stage. Stages actuated based on the "stick-slip" effect have a limited frictional driving force and suffer from severe wear due to the existence of slipping.

To overcome some of the drawbacks of the nanopositioning systems described above, a novel large-stroke piezo-actuated stage for nanopositioning is proposed. The stage is actuated by four piezo legs with three operation modes, the skiing mode, the stepping mode, and the tilting mode. The skiing mode is a high-speed actuation mode. The stepping mode provides high-resolution positioning capability. The tilting mode allows for fine adjustment of the stage in its final position with the highest resolution.

In this paper, the mechanical design of the stage and legs are first introduced. The working principles of the three operation modes are then discussed in the following section. The control system and experimental setup of the stage are described in the next two sections. The paper is concluded with a summary of major conclusions and a discussion of future work.

DESIGN OVERVIEW

As shown in Figure 1, the proposed stage has four piezo legs located at each corner of the stage. A vacuum preloaded air bearing is positioned in the center, which provides a supporting and clamping force for the stage. Pitch and roll angles of the stage platform can be adjusted by three micro adjustment screws evenly distributed around a flexure hinge that connects the air bearing and the stage platform. Two 3DOF (degree-of-freedom) piezo legs, each providing three DOFs ($\theta_x\theta_y Z$) of motion at the tip of the leg, are mounted at two diagonally opposite corners of the stage, as illustrated in Figure 2. Two 1DOF piezo legs providing one DOF (Z) of motion at the tip of the leg are mounted at the other two corners, as illustrated in Figure 4. The stage has three DOFs ($XY\theta_z$) and omni-directional motility at any instant with four piezo legs operating cooperatively with different operation modes.

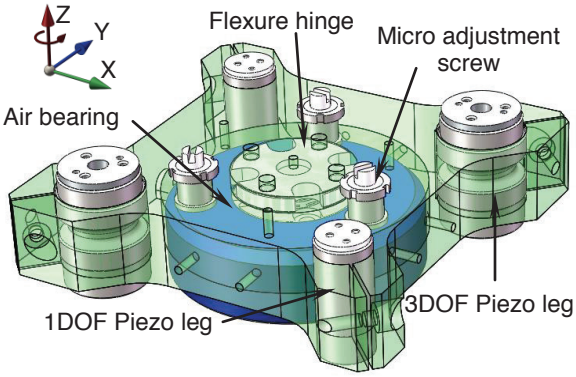

FIGURE 1. Piezo-actuated stage designed for nano-positioning

PIEZO LEGS

3DOF piezo leg

Figure 2 shows the mechanical design of the 3DOF piezo leg. Three piezo actuators, each with a displacement range of 15μm, are mounted inside the leg and distributed evenly along a circle of 5-mm radius. Two disc springs are stacked together to provide a large preload force for high-speed motion of the motion head. The motion head consists of two components, the main body made by light-weight aluminum and the tip made by a wear-resistant material. These two components are assembled together by glue.

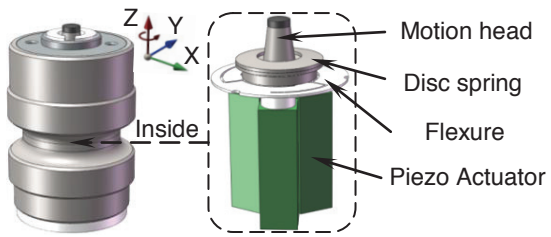

FIGURE 2. Mechanical design of the 3DOF piezo leg

A specially designed flexure provides low structural stiffness in Z direction and high structural stiffness in X and Y directions. With this design, the motion head fixed on the flexure will have three intended DOFs of motion: Z displacement, pitch and roll. High stiffness in X and Y directions will reduce the effect of external vibration. Low stiffness in Z direction allows the displacement range of the piezo actuators to be maintained. Figure 3 shows simulation results of the structural deformations with an external force of 1N applied in different directions. The results show that the stiffness in X or Y directions is almost 100 times larger than that in Z direction.

1DOF piezo leg

Figure 4 shows the mechanical design of the 1DOF piezo leg, which is used to provide linear motion in Z direction. The motion head is preloaded by two disc springs. The preload force can be adjusted by an adjustment screw. A piezo tip is fixed on the piezo actuator to make sure that the force from the piezo actuator is applied to the motion head along exactly the axial direction. When the piezo actuator extends, the tip of the motion head will be in contact with the base plate of the stage, providing the braking effect.

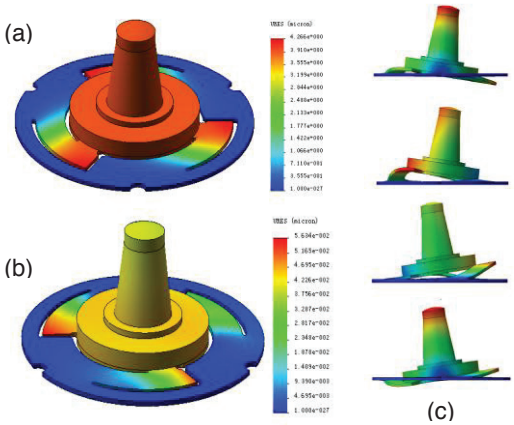

FIGURE 3. Structural simulation result of the flexure fixed with the motion head. (a) Z-direction displacement under a force of 1N. (b) X-direction displacement under a force of 1N. (c) Motion simulation result of the motion head magnified by 150 times.

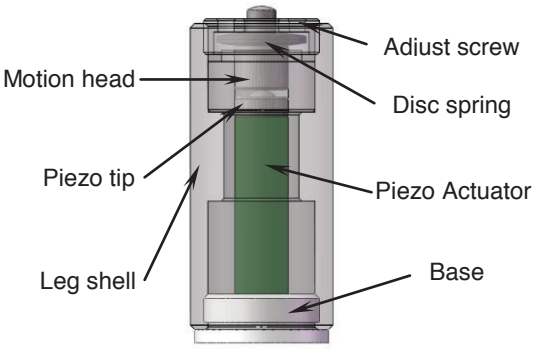

FIGURE 4. Mechanical design of the 1DOF piezo leg

OPERATION MODES

Three operation modes can be implemented in the proposed stage, the skiing mode, the stepping mode, and the tilting mode. The skiing mode can be used to achieve high speed. The stepping mode allows for the stage to be actuated with high resolution. With the tilting mode, the stage can be stabilized and fine adjusted in its final position with the highest resolution. These three operating modes are introduced in more details as below.

Skiing mode

In the Skiing mode, two 1DOF legs are raised up while two 3DOF legs move simultaneously to generate the frictional driving force. Under the frictionless condition provided by the air bearing, the velocity of the stage can be high with the successive repetition of steps similar to skiing. In this mode, wear of the leg tip and the base plate

maybe severe if slippage exists. To reduce the slippage, the acceleration of the stage must be controlled within a range to keep the actuation force less than the maximum friction force. This operation mode can be used to move the stage to the target area at the maximum speed. The operation mechanism is shown in Figure 5.

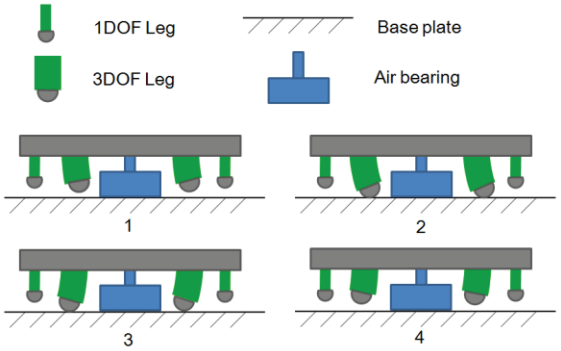

FIGURE 5. Skiing-mode operation mechanism

Stepping mode

In the stepping mode, the stage moves step by step as shown in Figure 6. Two 1DOF legs are used to clamp the stage to the base plate to brake the stage while the 3DOF legs are raised up. When 1DOF legs are raised up, the 3DOF legs are actuated to move the stage. This mode has a limited velocity because the clamping of 1DOF legs in each step prevents the stage speed from building up. However, the stepping mode can achieve higher positioning accuracy compared to the skiing mode because the stage is always in contact with the base plate.

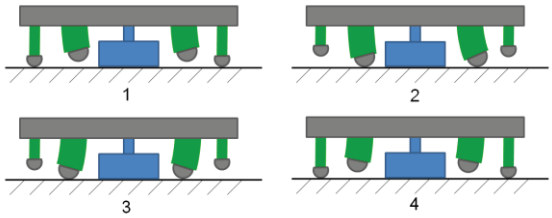

FIGURE 6. Stepping-mode operation mechanism

Tilting mode

In the tilting mode, the two 1DOF legs are raised up while the tips of the 3DOF legs stick to the base plate. To adjust the position of the stage with a high resolution, the tips of the 3DOF legs are tilted in the desired direction. Then the two 1DOF legs are extended to brake the stage for stability. Pitch and roll angles of the stage can also be adjusted via changing the displacement of four legs. This mode aims to complete a final adjustment of the stage to the desired position with high accuracy. It can be used for mask alignment in the stepper system before the photolithography process starts.

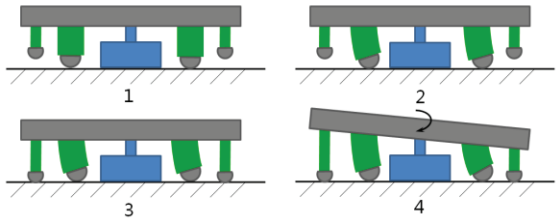

FIGURE 7. Tilting-mode operation mechanism

LEG AND STAGE CONTROL

The kinematics of the 3DOF piezo legs and the whole stage is described in this section. The displacement control of the eight piezo actuators given the motion of the stage and the operation mode is also discussed.

Leg Control

Control of the 1DOF legs is simple because the legs provide only one DOF motion. On the other hand, control of the 3DOF legs is significantly more complex because the legs are each driven by three piezo actuators and their motion trajectories are more complex. Here the discussion will be focused on the control of 3DOF legs.

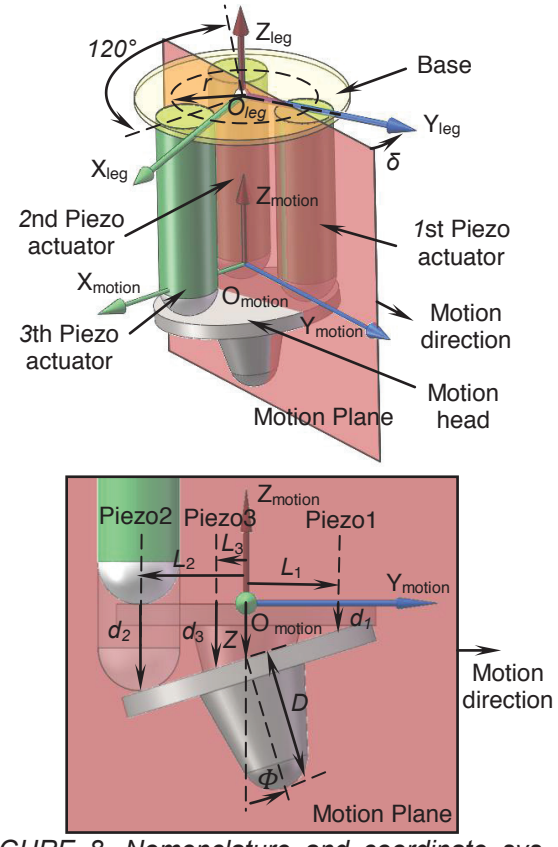

FIGURE 8. Nomenclature and coordinate systems of the piezo leg

Figure 8 shows the coordinate systems and parameter definitions of the 3DOF piezo leg. The O_{leg} coordinate system is attached to the base of the piezo leg, whose XY plane is defined to coincide with the base and its origin is at the center of the base. The Y-axis coincides with the center of the 1st piezo actuator. The motion plane coordinate system O_{motion} of the 3DOF leg is defined such that the motion head rotates in the YZ plane when motion direction is determined. The origin of O_{motion} coincides with the center of the top surface of the motion head when the displacements of the three piezo actuators are zero. Y-axis is pointing at the desired motion direction of the leg. The motion direction angle δ is defined as the angle between Y_{leg} and Y_{motion} in Z_{leg}. The coordinate system O_{motion} is static on the leg when δ is determined.

The motion head has three DOFs including the motion direction angle δ, and linear displacement Z of the motion head and the rotation angle Φ in the motion plane. The angle δ is fixed when the motion direction of the stage is fixed. Z and Φ in the motion plane define the motion trajectory of the motion head. The projection distance L_j between the origin O_{motion} and the axis of the three piezo actuators in the motion plane can be calculated as

$$L_j = r\cos(120°(j-1)-\delta), j = 1,2,3. \quad (1)$$

Given the motion direction angle δ, motion head angle Φ and motion head motion in Z direction, the displacement d_j of the piezo actuator in the 3DOF piezo leg can be obtained

$$d_j = Z - r\cos(120°(j-1)-\delta)\Phi. \quad (2)$$

Stage control

Figure 9 shows the definition of the stage coordinate systems O_b, O_s, O_1, O_2, which are attached to the base plate, stage, 1st 3DOF leg, 2nd 3DOF leg respectively. Two 3DOF legs are mounted such that the coordinate systems of the 3DOF legs have the same X- and Y-axis directions with the stage coordinate systems. Given the desired velocity of the stage and operation mode, the desired velocity of the piezo legs and the final control equation of the motion head can be derived. The nomenclatures used in the following formulations are explained in *TABLE 1.*

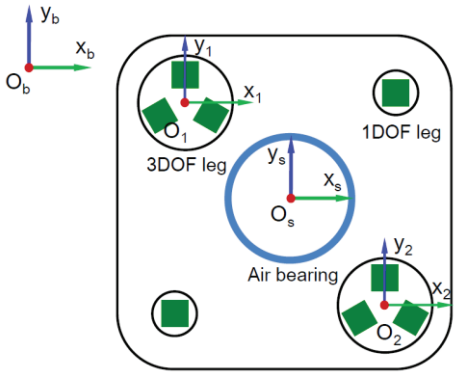

FIGURE 9. Definition of the stage coordinate systems

TABLE 1. The term definition

i	Index of the 3DOF piezo leg, $i = 1,2$
δ_i	Motion direction angle for the *i*th leg
Φ_i	Rotation angle of the motion head in X_{motion} direction for the *i*th leg
f	Stepping frequency in the stepping mode
D	Length of the motion head measured from the center of the bottom surface to the top of the tip
$\mathbf{P}_n^m$	Position vector of coordinate system O_n's origin with respect to coordinate system O_m
$\mathbf{R}_n^m$	Rotation transformation matrix from coordinate system O_n to coordinate system O_m
x_n^m	X component of the position vector of coordinate system O_n's origin with respect to coordinate system O_m
y_n^m	Y component of the position vector of coordinate system O_n's origin with respect to coordinate system O_m
θ_s^b	Rotation angle from coordinate system O_s to O_b in *z* direction
$\mathbf{V}_i$	Desired velocity of the *i*th piezo leg with respect to coordinate system O_i in XY plane
$\mathbf{V}_s$	Desired linear and angular velocities of the stage with respect to coordinate system O_b
$\mathbf{T}_i$	Desired tilting displacement of the *i*th piezo leg with respect to coordinate system O_i in XY plane
$\mathbf{J}_i(\theta_s^b)$	Velocity Jacobian for the *i*th piezo leg

The desired velocity $\mathbf{V}_s$ of the stage with respect to the coordinate system O_b at any instantis defined as

$$\mathbf{V}_s = [\dot{x}_s^b \quad \dot{y}_s^b \quad \dot{\theta}_s^b]^T. \quad (3)$$

The current position of the *i*th leg in coordinate system O_b is

$$\mathbf{P}_i^b = \mathbf{P}_s^b + \mathbf{R}_s^b \mathbf{P}_i^s. \quad (4)$$

Take the derivative of Eq.(4) and transform the desired velocity of the *i*th leg to coordinate system O_i.Then the desired control velocity of the *i*th leg with respect to the coordinate system itself can be obtained

$$\mathbf{V}_i = \mathbf{J}_i(\theta_s^b)\mathbf{V}_s, \quad (5)$$

where

$$\mathbf{J}_i(\theta_s^b) = \begin{bmatrix} \cos\theta_s^b & -\sin\theta_s^b & -y_i^s \\ \sin\theta_s^b & \cos\theta_s^b & x_i^s \end{bmatrix}. \quad (6)$$

The motion direction angle δ_i of the *i*th piezo leg can be derived as

$$\delta_i = \text{atan2}(\mathbf{V}_i). \quad (7)$$

In the skiing mode, the angular speed of the tip of the motion head is

$$\dot{\Phi}_i = -\frac{|\mathbf{V}_i|}{D}. \quad (8)$$

In the stepping mode, when the stepping frequency f is given, the angular step $\Delta\Phi_i$ of the tip of the motion head in each step is

$$\Delta\Phi_i = -\frac{|\mathbf{V}_i|}{Df}. \quad (9)$$

In the tilting mode, given the desired stage adjustment distance $\Delta\mathbf{P}_s^b$, the tilting displacement of the piezo leg $\mathbf{T}_i$ is

$$\mathbf{T}_i = \mathbf{J}_i(\theta_s^b)\Delta\mathbf{P}_s^b. \quad (10)$$

The motion direction angle δ_i and adjustment angle $\Delta\Phi_i$ of the motion head is

$$\delta_i = \text{atan2}(\mathbf{T}_i), \quad (11)$$

$$\Delta\Phi_i = -\frac{|\mathbf{T}_i|}{D}. \quad (12)$$

The proposed stage can operate with a high-precision position-measuring sensor, such as an interferometer or a planar encoder, to achieve high positioning accuracy. The velocity feedback from the sensor can be used to control the velocity of the two legs in order to avoid the slippage so that wear of the motion head can be minimized. To drive the piezo actuators, eight precision high voltage amplifiers are designed using power operational amplifier chips.

EXPERIMENTALSETUP

The experimental setup is shown in Figure 10. It includes an air supply system, the piezo-actuated stage, a granite platform, and a position feedback system. The 3DOF ($XY\theta_z$) active encoder developed by Tian and Huang [8] is used as the feedback system here. An iPhone with a grating pattern displayed is mounted on the stage. A camera with a zoom lens captures images of the pattern on the screen. A phase correlation algorithm converts the image information into accurate position signals with nanometer resolution for feedback control of the stage. The motion range of the stage is currently limited by the area of the iPhone screen. In the future, a larger display screen will be mounted on the granite platform to increase the motion range of the stage. A miniature camera will be mounted on the stage to capture images of the display screen. With this design, the stage can have a very large stroke while maintaining nanometer order positioning resolution.

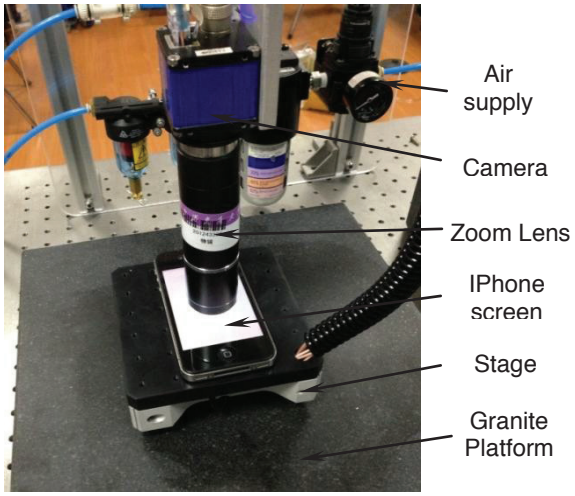

FIGURE 10. Experimental setup

The control system diagram of the stage is shown in Figure 11. The host PC obtains the target position from the encoder and calculates the desired velocity and motion direction of each piezo leg. Any of the three operation modes, the skiing mode, the stepping mode, and the titling mode can be selected to actuate the stage. The user can also select an automated mode, in which the stage will choose appropriate operation modes based on the current stage condition and motion requirements. The FPGA control card (NI-7852) uses information from the host PC to calculate the necessary motion of each piezo actuator in each leg. The control signals are magnified by power amplifiers before sending to the piezo legs to control the stage. The image from the camera is sent to the host PC for processing. The obtained position information is displayed in a graphical user interface (GUI) and used for feedback control.

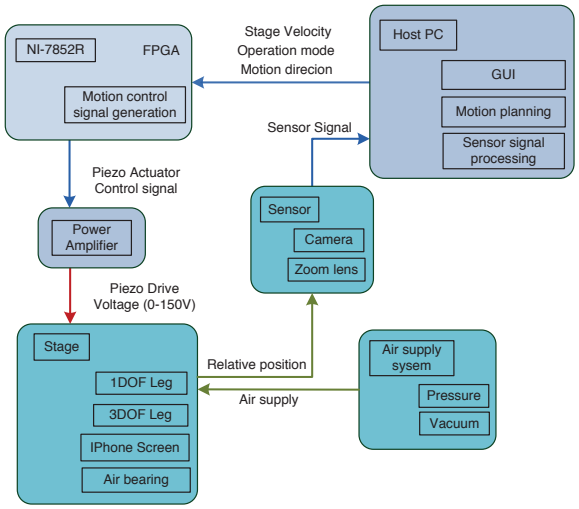

FIGURE 11. CONTROL SYSTEM DIAGRAM

CONCLUSION AND FUTURE WORK

In this research, a novel large-stroke piezo-actuated stage is proposed for nanopositioning applications. The stage uses an air bearing with vacuum preload to reduce friction while maintaining high stiffness. It uses four piezo legs to drive the stage with a positioning resolution up to the nanometer level. The stage can operate in three modes: the skiing mode, the stepping mode, and the tilting mode. In the skiing mode, the stage can move in high speed, which is suitable for large distance movements. In the stepping mode, the stage walks step by step in a resolution that is adjustable and can be up to the nanometer level. However, the motion speed is relatively low because of the stepping nature of the operation mode. In the tilting mode, the piezo legs do not move at all. Instead, they tilt to fine adjust the position of the stage. This operation mode provides the most stable and highest resolution positioning control. The above three operation modes can also be combined to achieve both a high positioning speed and a high positioning resolution. One major advantage of the proposed stage is that the motion range is limited only by the measurement range of the sensor. Omni-directional motility is another advantage of the stage.

The stage has been built and is currently being evaluated for positioning resolution, accuracy, and speed under each of the three operation modes. The experimental results will be reported in the near future.

REFERENCES

[1] W. J. Kim and D. L. Trumper, High-precision magnetic levitation stage for photolithography. Precision Eng. 1998; 22 (2), pp. 66–77.

[2] W. Gao, S. Dejima, H. Yanai, K. Katakura, S. Kiyono, and Y. Tomita, A Surface Motor-Driven Planar Motion Stage Integrated with an XYZ_θ Surface Encoder for Precision Positioning. Precision Engineering 2004; 28(3): pp.329–337.

[3] L. Yan, Y. Hu, H. Lan, N. Yao, Z. Jiao, and I-M. Chen. A Novel Two Degree-of-freedom Ultrasonic Planar Motor Driven by Single Stator. Industrial Informatics, 2012 IEEE International Conference 550-553.

[4] S. J. Shi, J. K. Liu, W. S. Chen, and Y. X. Liu, Development of a 2-DOF planar ultrasonic motor using longitudinal-bending hybrid transducer, IEEE International Symposium on the Applications of Ferroelectrics, pp. 1-5, 2009.

[5] Q. Yao, J. Dong, and P.M. Ferreira. A novel parallel-kinematics mechanism for integrated, multi-axis nano-positioning Part 1. Kinematics and design for fabrication. Precision Engineering 32 (2008) 7–19.

[6] S. W. Lee, K. G. Ahn, and J. Ni. Development of a piezoelectric multi-axis stage based on stick-and-clamping actuation technology. Smart Mater. Struct. 16 (2007) 2354–2367.

[7] L. Juhasa, A. Vujanićb, N. Adamovićb, L. Nagyc, and B. Borovac. A platform for micro-positioning based on piezo legs. Mechatronics 11 (2001)869-897.

[8] K. Tian and P. S. Huang, An active encoder for precision position measurement, Proc. 28th ASPE Annual Meeting.

METHODS FOR PERFORMANCE EVALUATION OF SINGLE AXIS POSITIONING SYSTEMS: POINT REPEATABILITY

Nathan Brown
ALIO Industries.
Wheat Ridge, CO, USA

INTRODUCTION

Precision motion systems are used in a variety of industry applications varying from metrology, nano-machining, laser marking, photonics, and manufacturing. The selection and use of a specific precision motion system is dependent on the ability of the system to meet the performance required for the application. With the advancement of application requirements, including increasing levels of precision and introduction of new performance metrics, both the stage technology and testing methodology have evolved to be able to meet and prove these performance requirements. As a result, many motion system manufacturers have developed their own testing definitions and procedures [1,2,3,4]. This leads to confusion in industry as test results, which are used for comparison and qualification, are not based on a consistent set of principles.

Repeatability of a functional point attached to a linear or angular motion axis is commonly specified as a one-dimensional linear measurement. However, the three-dimensional repeatability of a functional point (linear, straightness, and flatness repeatability) is critical for many applications, such as those listed above. Characterizing the repeatability of a functional point in three-dimensional space at specified target positions can be achieved using existing methods and equipment, for example: 6D laser measurement system, laser tracker, straightedge, angular interferometer, etc. However, the measurement uncertainty may be too high, the equipment may be too expensive and too large, and with some methods and equipment, it may be too time consuming to measure the repeatability in three directions.

This paper defines “point repeatability” as a measure of repeatability in three dimensional space and presents a simplified method for quickly characterizing this repeatability in three directions (X,Y,Z) using displacement sensors [5]. The method enables characterization of repeatability of target positions at the nanometer level with appropriate uncertainty ratios. Test setup and equipment are common, cost effective, and can quickly be setup to test high precision angular and linear axes.

While this method is presented for single axis systems, the potential application to multi-axis systems is discussed because this method captures statistically significant repeatability errors that are often neglected when a multi-axis system is characterized on a per axis basis.

This proposal is presented in conjunction with the preliminary work conducted by a working group of Technical Committee TC52 (ASME B5/TC52) tasked with developing and drafting a new performance standard for characterizing single axis, high precision motion systems.

REPEATABILITY DEFINITIONS AND IMPORTANCE OF POINT REPEATABILITY

Per ASME B5.54-2005, repeatability is "a measure of the ability of a machine to sequentially position a tool with respect to a work-piece under similar conditions. Repeatability is defined on a per-axis basis [6]." A similar definition is in ISO 230-2:2006(E) [7].

Existing Definition: Linear Repeatability

Per test procedures and calculations in ASME B5.54-2005, motion system manufacturers specify linear repeatability as a single number representing the variation in linear displacement. The one-dimensional nature of the test means that each test position measured can be conceptually viewed as the intersection of a plane with the axis, see Figures 1 and 2. The test does not tell us any information about the pitch, yaw, or roll of this conceptual plane and we do not know where our actual test point is located horizontally or vertically on the plane. We only know one piece of information, where the assumed orthogonal plane is along an assumed perfectly straight axis, the linear positioning repeatability.

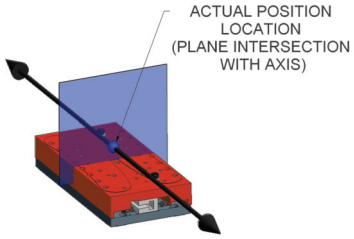

FIGURE 1. The intersection of a plane (fixed to a moving carriage) along an assumed perfect axis is a positional data point used in traditional repeatability testing.

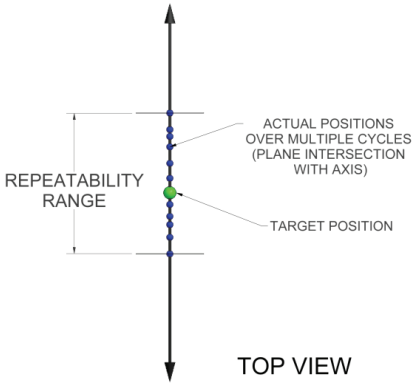

FIGURE 2. One-dimensional linear repeatability is a range of points along an axis.

Existing Definition: Rotational Repeatability

Rotational repeatability is defined as the angular repeatability of a point as it rotates around an axis. This definition only describes one (rotational) degrees of freedom of the repeatability error, see Figure 3. It does not account for radial runout, axial runout, or angular affects such as wobble, all of which will affect the repeatability of a functional point.

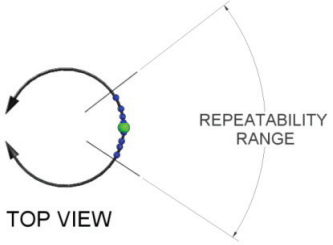

FIGURE 3. One-dimensional rotational repeatability is a range of points along an axis.

Three-Dimensional Repeatability Importance

A motion axis has errors in six degrees of freedom: X,Y,Z, pitch, yaw, and roll, see Figure 4. Each of these error sources will affect the three-dimensional repeatability of a functional point attached to a stage. Current standards include methods to test these multiple repeatability error sources. However, there is no clear terminology or requirement for specifying repeatability as a multi-dimensional performance metric that accounts for all error sources.

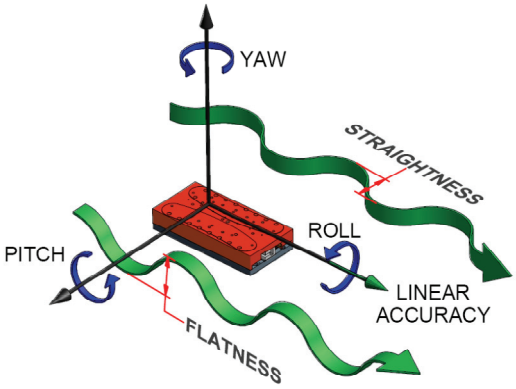

FIGURE 4. The six degrees of freedom of errors of a motion axis.

By definition, the point repeatability methodology will characterize all repeatability error sources. For example, Figure 5 is a real world representation of Figure 2, which includes straightness repeatability error in the two dimensional distribution of points. For each example, the linear (one-dimensional) repeatability along the axis is equivalent. However, the often unmeasured straightness repeatability perpendicular to the axis of travel varies between the two situations. The point repeatability characterization will quantitatively capture these differences.

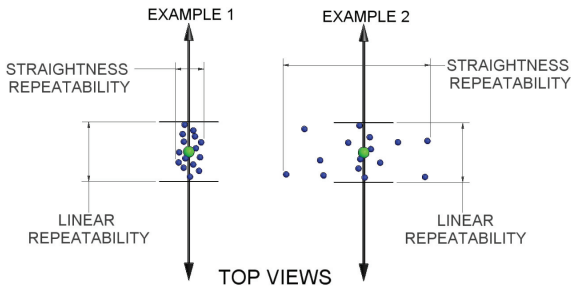

FIGURE 5. Two independent representations of repeatability of a linear axis in a 2D plane.

Angular repeatability error effects on a functional point are captured by linear positioning measurements because the angular errors result in linear translations of the functional (test) point. For example, linear (or axial) repeatability will capture the pitch and yaw repeatability effects for each test point. The location of the functional point relative to the stage is critical to the measurement result in that different functional points will result in different repeatability results.

Figure 6 shows an example of the effects of pitch repeatability error's affect on two different functional points. The point repeatability test is dependent on and only valid for the functional point tested.

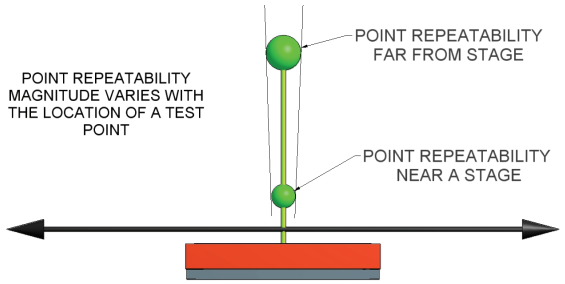
POINT REPEATABILITY FAR FROM STAGE
POINT REPEATABILITY MAGNITUDE VARIES WITH THE LOCATION OF A TEST POINT
POINT REPEATABILITY NEAR A STAGE

FIGURE 6. A visual representation of the impact pitch repeatability will have on actual point repeatability magnitude recorded.

Defining Point Repeatability

Each axis of a motion system has errors in six degrees of freedom, and all error sources are statistically significant when characterizing the repeatability of a point in three-dimensional space [5]. The test method is designed to be a simplified method focused on collecting the X, Y, and Z distributions of the repeatability data of a few target positions of a functional point attached to a stage, see Figure 7. ***Point repeatability is a measure of the ability of a motion system to sequentially position a functional point fixed to a stage to a target position with respect to a fixed three-dimensional reference frame.*** Point repeatability is specified on a per system basis.

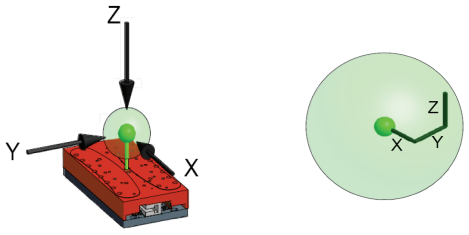

FIGURE 7. A representation of (a) X, Y, and Z repeatability components of a functional point attached to a motion carriage and (b) the conceptual three-dimensional tolerance zone.

Over many cycles, the test point locations will create a three-dimensional distribution of points and the shape of the distribution will vary from stage to stage or manufacturer to manufacturer. ***The point repeatability tolerance zone is the three dimensional tolerance zone characterized the X, Y, and Z components of the repeatability performance around a target position of a point repeatability test.*** The X, Y, and Z components are all presented so the actual tolerance zone geometry and distribution is known.

We also use two other terms that will be used throughout this document. Per ISO 230-1, "***the functional point is the position of a tool when a moving component carries the tool [8]***." The functional point is defined relative to the motion system's moving carriage and there are an infinite number of possible functional points. It should be defined to coincide with the process location specified by the end user. ***The target position is a position to which the moving functional point is commanded.*** There are also an infinite number of possible target positions and the target positions selected for the test will depend on the end use application.

Prior Work

The point repeatability concept has been previously used in prior forms to document repeatability in three-dimensional space. This proposal's goal is to standardize definitions and procedures of this prior work. For example a similar procedure is referenced in ASME B5.54-2005 in reference to tool change repeatability where three-dimensional repeatability is measured with a three sensor nest, see Figure 7.43 in ASME B5.54-2005 [6].

IMPORTANCE OF POINT REPEATABILITY

Existing methods and equipment can be used to calculate the multi-dimensional errors presented above. However, in many situations the equipment may be very expensive, may have large uncertainties, or may require time consuming setup to collect the necessary data.

Importance: Test Efficiency

For example, the use of a rotary stage as part of a pick-and-place operation may require quantified repeatability performance in three-dimensional space of the pick or place location. A runout test paired with an angular repeatability test (i.e. interferometer or auto-collimator) will provide this data but requires multiple pieces of test equipment and multiple test setups. The point repeatability test methodology enables the characterization of the pick and place repeatability with one set of test equipment.

Importance: Uncertainty

Furthermore, for high precision motion systems it is common to require repeatability

uncertainties in the nanometer range. Existing test equipment may have large uncertainties that result in invalid test to uncertainty ratios [4]. The capacitive gauge test equipment proposed enables uncertainties in the single or double digit nanometer level [9].

Importance: Multi-Axis Systems

Lastly, this methodology provides an accurate representation of repeatability performance for multi-axis systems. By definition, ASME B5.54-2005 defines repeatability on a "per axis basis." It is common practice for manufacturers to present "per axis" data (for individual axes of a multi-axis system) as the system level performance. Furthermore, typically only the one-dimensional linear repeatability is presented and other errors are neglected, see Table 1. This is an inaccurate representation of system level performance. As an example, for an XYZ stage, the X direction repeatability is not just a function of the X axis linear repeatability but also a function of the Y axis straightness repeatability and the Z axis straightness repeatability. In fact to fully characterize the repeatability, all error sources must be examined for each axis – 6 degrees of freedom of errors of 3 axes for a total of 18 error sources, see Table 1.

TABLE 1. A table showing the 18 error sources for repeatability of an XYZ stage with the three linear repeatability error sources highlighted.

	Error Degrees of Freedom					
Axis	Linear in X	Linear in Y	Linear in Z	Theta in Z (Yaw)	Theta in Y (Pitch)	Theta in X (Roll)
1	✓	?	?	?	?	?
2	?	✓	?	?	?	?
3	?	?	✓	?	?	?

While all this data can be collected with existing equipment, it would not be efficient to do so while maintaining uncertainties at the nanometer level. Furthermore, there is no consensus procedure for combining all this "per axis" data into a representation of what the performance is at the functional point for the system. The point repeatability test methodology can record the X, Y, and Z repeatability components for a functional point with two setups with all axes moving bidirectionally as a system during the test. Thus the error data collected will capture the impact of all error sources at once. All error sources shown in Table 1 are accounted for which represents the true system performance.

TEST METHODOLOGY

The following methodology outlines the process for analyzing X, Y and Z repeatability components of a functional point and using that data to calculate the point repeatability.

Define Functional Point and Target Positions

The tester must define the functional point fixed to the motion system carriage and the target position along the axis of travel to which this test point will be sequentially positioned during test measurement. Primarily, the functional point and target point locations should be agreed upon with the customer or user to coincide with the process/application. Additionally, the tester must define if the functional point is moving to different target positions or if the target position is moving to different functional points. Both setups are valid and are used in end user applications.

Test Setup

This test methodology is mainly focused characterizing the X, Y, and Z repeatability component datasets of a functional point. This methodology proposes that one and two sensor nests be used with a displacement (capacitive gauge, white light sensor, probe, etc.) to collect repeatability data for X or Y and Z repeatability components respectively, see Figure 8. These sensor nests can be easily and cost effectively procured and configured to test any motion system geometry. The one sensor nest is used to collect axial repeatability data. One point to note is the motion displacement towards the sensor will typically be limited due to target and sensor interference. However, many high precision axes only require displacement of 10's or 100's of microns bidirectionally in order for bidirectional errors to be included in the characterization. The two sensor nest is used to collect repeatability data perpendicular to the axis of travel so bidirectional moves can be performed.

Motion Cycle

The main requirement of the motion during testing is that the target position be approached bidirectionally to collect a total of 20 data points. If it is agreed upon with the user, the motion cycle may be truncated to a uni-directional test. Just as the functional and target points are defined per application usage, the motion cycle should also coincide with actual usage.

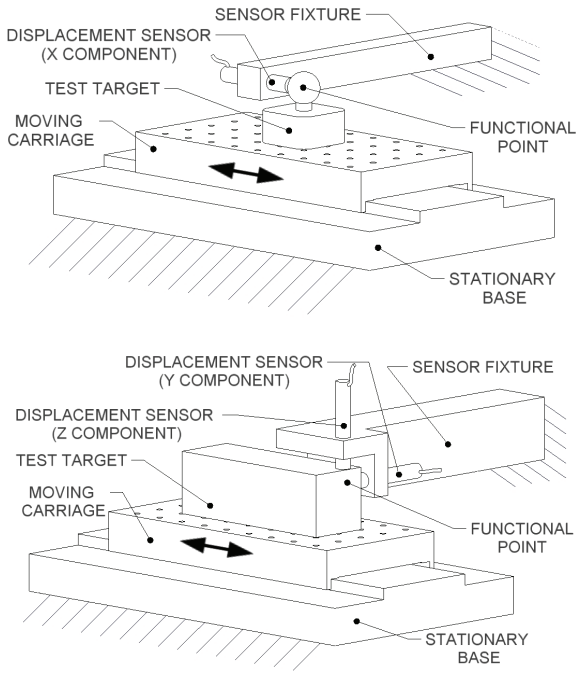

FIGURE 8. Example of one and two sensors nests for respective X (axial) or Y (straightness) and Z (flatness) repeatability component testing.

Data Analysis

For each target point there will be three arrays.

$Ex_{i,j}$ X directional repeatability data
$Ey_{i,j}$ Y directional repeatability data
$Ez_{i,j}$ Z directional repeatability data

where for all presented equations,

i = test point along the axis of travel
j = data point (1,2,3,...) at each test point
$n = j_{max} = 20$

The mean position is defined as follows.

$$\bar{E}x_i \uparrow\downarrow = \frac{1}{n}\sum_{j=1}^{n} Ex_{i,j} \quad \text{(Eqn. 1-a)}$$

$$\bar{E}y_i \uparrow\downarrow = \frac{1}{n}\sum_{j=1}^{n} Ey_{i,j} \quad \text{(Eqn. 1-b)}$$

$$\bar{E}z_i \uparrow\downarrow = \frac{1}{n}\sum_{j=1}^{n} Ez_{i,j} \quad \text{(Eqn. 1-c)}$$

The mean is assumed to be the target position as the data models a normal distribution. The error of each data point from the mean is:

$$E'x_{i,j} = Ex_{i,j} - \bar{E}x_i \uparrow\downarrow \quad \text{(Eqn. 2-a)}$$

$$E'y_{i,j} = Ey_{i,j} - \bar{E}y_i \uparrow\downarrow \quad \text{(Eqn. 2-b)}$$

$$E'z_{i,j} = Ez_{i,j} - \bar{E}z_i \uparrow\downarrow \quad \text{(Eqn. 2-c)}$$

For these adjusted data sets the mean position deviation is zero.

$$\bar{E}'x_i \uparrow\downarrow = 0 \quad \text{(Eqn. 3-a)}$$

$$\bar{E}'y_i \uparrow\downarrow = 0 \quad \text{(Eqn. 3-b)}$$

$$\bar{E}'z_i \uparrow\downarrow = 0 \quad \text{(Eqn. 3-c)}$$

The estimator of the bidirectional standard uncertainty of the X, Y, and Z components at the test point is:

$$Sx_i \uparrow\downarrow = \sqrt{\frac{1}{n-1}\sum_{j=1}^{n}(E'x_{i,j} - \bar{E}'x_i \uparrow\downarrow)^2} \quad \text{(Eqn. 4-a)}$$

$$Sy_i \uparrow\downarrow = \sqrt{\frac{1}{n-1}\sum_{j=1}^{n}(E'y_{i,j} - \bar{E}'y_i \uparrow\downarrow)^2} \quad \text{(Eqn. 4-b)}$$

$$Sz_i \uparrow\downarrow = \sqrt{\frac{1}{n-1}\sum_{j=1}^{n}(E'z_{i,j} - \bar{E}'z_i \uparrow\downarrow)^2} \quad \text{(Eqn. 4-c)}$$

The repeatability X, Y, and Z components, at a test point are the deviation from the target position derived from the expanded uncertainty of positional deviations at a position using coverage factor of two.

$$Rx_i \uparrow\downarrow = \pm\ 2Sx_i \uparrow\downarrow \quad \text{(Eqn. 5-a)}$$

$$Ry_i \uparrow\downarrow = \pm\ 2Sy_i \uparrow\downarrow \quad \text{(Eqn. 5-b)}$$

$$Rz_i \uparrow\downarrow = \pm\ 2Sz_i \uparrow\downarrow \quad \text{(Eqn. 5-c)}$$

When a motion system is analyzed the point repeatability of the system is presented as the maximum of the X, Y, and Z expanded uncertainty of positional deviations of all test points.

$$Rx \uparrow\downarrow = Max\ (Rx_i \uparrow\downarrow) \quad \text{(Eqn. 6-a)}$$

$$Ry \uparrow\downarrow = Max\ (Ry_i \uparrow\downarrow) \quad \text{(Eqn. 6-b)}$$

$$Rz \uparrow\downarrow = Max\ (Rz_i \uparrow\downarrow) \quad \text{(Eqn. 6-c)}$$

EXAMPLE TEST DATA

The following example presents data for a 700mm linear travel air bearing linear stage. Target points were defined every 100mm of travel (total of 8 target points) and a bidirectional pendulum test motion cycle was used at each target position. The functional point was defined at the front centered location (50mm height) of the mounting carriage (offset 200mm from the center of the carriage) to match the end user process location. The sensor nest was moved to the new target position for each point tested. The raw repeatability charts and tables for point, i = 5 (see Figure 9 and Table 2) as well as intermediate calculations of the point repeatability are shown. The point repeatability of this linear axis is shown in the last row of Table 3.

FUTURE WORK

The proposed point repeatability terminology and test method is a starting point for discussion with industry and academia. Future work will lead to discussion of the principles put forth above as well as the following.

- Further development of uncertainty calculations.
- Investigation of planar and volumetric geometric arrangements of target points.
- The addition of thermal compensation.

(a)

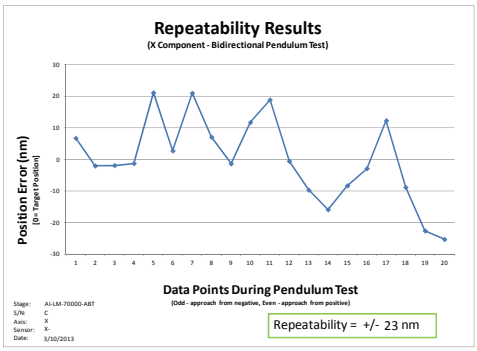
Repeatability Results
(X Component - Bidirectional Pendulum Test)
Position Error (nm)
(0 = Target Position)
Data Points During Pendulum Test
(Odd - approach from negative, Even - approach from positive)
Repeatability = +/- 23 nm

(b)

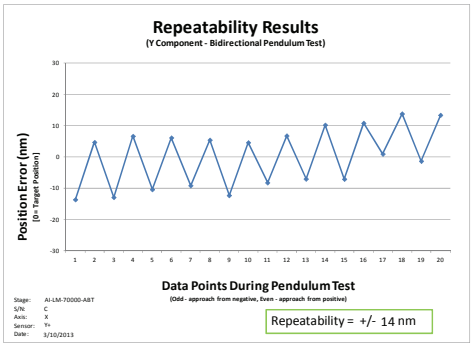
Repeatability Results
(Y Component - Bidirectional Pendulum Test)
Position Error (nm)
(0 = Target Position)
Data Points During Pendulum Test
(Odd - approach from negative, Even - approach from positive)
Repeatability = +/- 14 nm

(c)

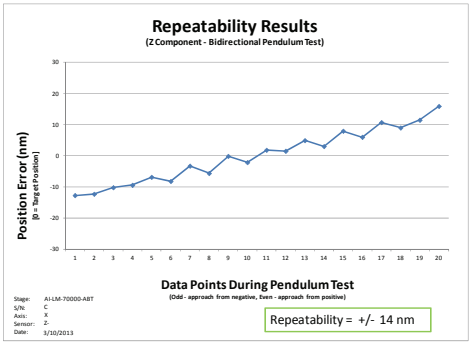
Repeatability Results
(Z Component - Bidirectional Pendulum Test)
Position Error (nm)
(0 = Target Position)
Data Points During Pendulum Test
(Odd - approach from negative, Even - approach from positive)
Repeatability = +/- 14 nm

FIGURE 9. The (a)X, (b)Y, and (c)Z components of the raw repeatability for target point, i = 5.

TABLE 2. Tabulated data for target point, i = 5.

Target Point, i = 5			
Tolerance Zone Component	X Component	Y Component	Z Component
units	nm	nm	nm
Variable (Equation 2)	$E'x_{(5,j)}$	$E'y_{(5,j)}$	$E'z_{(5,j)}$
j = 1	6.7	-13.7	-12.8
j = 2	-2.1	4.6	-12.4
j = 3	-1.9	-13.0	-10.3
j = 4	-1.3	6.6	-9.5
j = 5	21.1	-10.5	-6.9
j = 6	2.7	6.1	-8.3
j = 7	20.9	-9.2	-3.3
j = 8	7.0	5.3	-5.7
j = 9	-1.4	-12.4	-0.2
j = 10	11.7	4.5	-2.2
j = 11	18.8	-8.3	1.8
j = 12	-0.6	6.7	1.4
j = 13	-9.7	-7.1	4.8
j = 14	-16.0	10.2	3.0
j = 15	-8.4	-7.1	7.9
j = 16	-2.9	10.7	5.9
j = 17	12.2	0.9	10.6
j = 18	-8.9	13.7	8.9
j = 19	-22.7	-1.4	11.4
j = 20	-25.3	13.3	15.8
Standard Deviation			
Units	nm	nm	nm
Variable (Equation 4)	$Sx_4 \uparrow\downarrow$	$Sy_4 \uparrow\downarrow$	$Sz_4 \uparrow\downarrow$
i = 5	13.2	9.3	8.5

TABLE 3. The X, Y, and Z point repeatability components for all target points.

2 Sigma Component Repeatability (+/-)			
Tolerance Zone Component	X Component	Y Component	Z Component
units	nm	nm	nm
Variable (Equation 5)	$Rx_i \uparrow\downarrow$	$Ry_i \uparrow\downarrow$	$Rz_i \uparrow\downarrow$
i = 1 (@ -350mm)	25.7	19.1	7.0
i = 2 (@ -250mm)	25.7	11.3	5.1
i = 3 (@ -150mm)	32.1	13.9	5.0
i = 4 (@ -50mm)	29.0	26.2	9.5
i = 5 (@ +50mm)	26.4	18.7	17.1
i = 6 (@ +150mm)	30.0	4.6	12.8
i = 7 (@ +250mm)	35.8	13.4	13.6
i = 8 (@ +350mm)	24.6	12.6	3.6
Point Repeatability of all Test Points			
Units	nm	nm	nm
Variable (Equation 6)	$Rx \uparrow\downarrow$	$Ry \uparrow\downarrow$	$Rz \uparrow\downarrow$
Point Repeatability	**35.8**	**26.2**	**17.1**

CONCLUSIONS

Existing terminology and test methodology for quantifying motion system repeatability remain valid and useful but have the inherent weakness in that they may include expensive equipment, time consuming setup or tests, or invalid test to uncertainty ratios. The proposed point repeatability methodology is the framework for characterizing the repeatability of a functional point in space while accounting for all error sources in three dimensional space. This methodology can be used to efficiently characterize point repeatability of selected target positions with readily available test equipment.

REFERENCES

[1] Fesperman et al, Methods for Performance Evaluation of Single Axis Positioning Systems: A New Standard, Proceedings of the ASPE Annual Meeting, 2013.

[2] Fesperman R, Donmez M, Moylan S, Ultra-precision Linear Motion Metrology, Proceedings of the ASPE Summer Topical Meeting, 2010; 49: 103-108.

[3] Fesperman R, Donmez M, Moylan S, Ultra-precision Linear Metrology of a Commerically Available Linear Translation Stage, Proceedings of the ASPE Annual Meeting, 2011; 52: 81-84.

[4] Khanam, S.A., Morse, E., Test Uncertainty and Test Uncertainty Ratio (TUR), Proceedings of the ASPE Annual Meeting, 2008.

[5] Brown N L, A New Way of Analyzing Motion System Repeatability for Nanometer Precision: 6-DOF Point Repeatability, ASPE Annual Meeting, 2011; 52, 85-86

[6] ASME B5.54-2005, Methods for Performance Evaluation of Computer Numerically Controlled Machining Centers, 2005

[7] ISO 230-2:2006(E), Test Code for Machine Tools - Part 2: Determination of Accuracy and Repeatability of Positioning Numerically Controlled Axes.

[8] ISO 230-1:1996(E), Test Code for Machine Tools - Part 1: Geometric Accuracy of Machines Operating Under No-Load or Finishing Conditions.

[9] Brown N, Point Repeatability: Proposal of Concepts and Test Methods, ALIO Industries Internal Report.

METHODS FOR PERFORMANCE EVALUATION OF SINGLE AXIS POSITIONING SYSTEMS: DYNAMIC ANGULAR PERFORMANCE

Jonathan D. Ellis[1,2], Steven R. Gillmer[1], Brian O'Connor[3]
[1]Department of Mechanical Engineering, [2]Instute of Optics
University of Rochester, Rochester, New York, USA
[3]Aerotech Inc., Pittsburgh, PA, USA

INTRODUCTION

Many new ultra-precision linear and angular positioning systems with exceptionally long ranges of motion on the order of tens of millimeters and degrees with positioning resolutions on the order of a nanometer and a micro-radian are finding their way into emerging global technologies. Measuring and certifying the performance of these systems with off-the-shelf instrumentation and test methods suggested by existing machine tool standards can be very challenging, if the test uncertainty ratio (TUR) is to be greater or equal to 4:1 [1]. Static/quasi-static angular error measurements and specifications are well-defined processes described in existing performance standards [2, 3]. A standard test method for characterizing and specifying angular errors for single axis linear positioning systems does not currently exist. As a result, many manufactures and users of linear positioning systems have developed their own internal methods and standards, which have led to customer confusion and ambiguity.

Members from industry, academia, and government are working to develop a new positioning performance standard [4] that includes a new test method for characterizing angular errors of a linear positioning system under dynamic conditions. In this paper, we discuss a test method for characterizing *dynamic angular errors*. Descriptions of measurement setups, measurement and analysis procedures, and suggestions for reporting dynamic angular results are presented.

ANGULAR ERRORS

The angular errors of a linear positioning system are characterized by measuring the motions of the carriage about the three axes of the stage coordinate system. Based on the coordinate system shown in Figure 1 with the main travel axis aligned to the X-axis, the rotational errors about the Y-axis, E_{BX}, are commonly referred as pitch. Similarly, rotations about the Z- and X-axes are E_{CX} and E_{AX}, and are commonly referred to as yaw and roll, respectively [3].

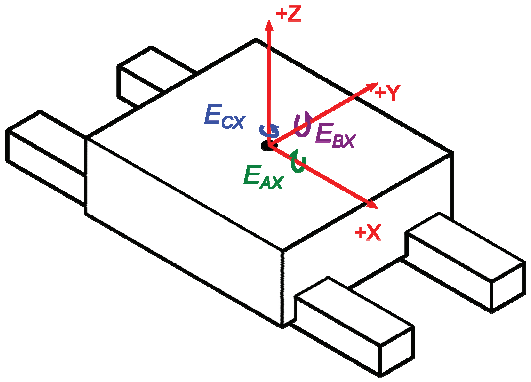

FIGURE 1. A schematic identifying the angular errors of a linear positioning system traversing in the X-direction. E_{BX} (pitch), E_{CX} (yaw), and E_{AX} (roll) are the angular errors about the Y-, Z-, and X-axes, respectively.

The stage's performance during acceleration, deceleration, and constant velocity scanning (CVS) may be of interest to the user, depending on the specific application. Thus, it is important to establish a motion profile that takes into account the intended application. Depending on the angular degree of freedom, the angular error present may vary as a function of the stage dynamics. For example, dynamic loading from the motors and frame distortions may lead to increased pitch errors when the acceleration/deceleration rate is increased. As with dynamic straightness characterization [5], velocity (or motion) profiles used for driving positioning systems can vary with different influences on the functional point. The selection of the transition regions from acceleration to constant velocity (if any) can affect angular errors through dynamic forces changing with the positioning system.

Identifying the transition regions requires detailed information about the motion profile and its parameters (e.g., drive forces, accelerations and time constants). Most modern controllers

allow access and exporting of motion profile data. Alternatively, the profile data can be provided by the manufacturer or it can be determined by characterizing the positioning system following standard test methods such as the Feedrate and Acceleration method described in ASME B5.54 [1]. Similar test methods are being considered for inclusion in this new standard [4].

General Measurement Setup

Common methods for measuring angular errors differ depending on the desired measurement degree of freedom. For example, pitch and yaw errors can be measured with an autocollimator, angle interferometer, two linear interferometers with a known offset, or two displacement sensors and a reference straightedge [2, 3]. Roll, however, is more commonly calibrated using a differential level or two displacement sensors with a straightedge [2, 3], although optical methods do exist [6, 7]. The differences in measurement methods may lead to different measurement uncertainties and must be considered in the overall uncertainty budget. Unlike static/quasi-static measurements, the mass and location of the measurement artifact, mirror, angle optics, level, etc., can have a large impact on the dynamic performance. This is particularly the case when the stage to be assessed has a limited payload capacity. The equipment and method chosen should reflect the expected performance of the positioning system and the results of a test uncertainty evaluation [8, 9].

System Condition

Prior to commencing measurements, the positioning system should be exercised to thermally stabilize the system. At minimum, axis warm-up should include five back-and-forth movements between the first and last target points. The velocity/motion profile and payload employed should be the same profile and payload used for the angle measurement. If deemed necessary, controller tuning in response to the measurement payload should be considered acceptable as long as the payload is closely related to the payload of the application.

Dynamic Angular Test Procedure

The test should be conducted at a programmed feedrate, acceleration/deceleration rates, and load that best replicates the conditions of the application in which the positioning system is intended to be used. If the positioning system is to be used as a general purpose system or a predefined programmed velocity is not available then three different tests should be conducted at 10%, 50%, and 100% of the maximum programmable feedrate (velocity). The default traverse distance should consume the maximum allowable distance for the positioning system. A trigger or digital marker should be used to initiate or mark the measurement at the beginning of both positive and negative directions of motion. Any dwells added to the motion profile should be documented.

Procedure

1) Align the measuring equipment such that the intended degree of freedoms are measured and sensitivities in other degrees of freedom do not affect the measurement. Ensure the measurement equipment used has the anticipated measurement range needed for the measurement.
2) Exercise the positioning system following the recommendations described in System Condition.
3) Program the positioning system to continuously move the carriage with the predetermined velocity profile.
4) Set the data acquisition system sampling rate to accurately capture and detect the acceleration and deceleration regions. Ensure aliasing and filtering rolloff are considered. For example, heavy filtering can cause significant lag in the measured signal when the stage is positioning with high accelerations.
5) Document all test parameters.
6) Perform five sets of bidirectional or unidirectional measurements for each angular degree of freedom. Record time, axis position, and the corresponding raw readings for angular error.

Dynamic Angular Error Analysis

If post-process filtering or other data manipulation is performed on the raw measurement data and the type of filter (e.g., low-pass 4^{th}-order Butterworth filter) and cutoff frequency should be reported. Additionally, the raw data should be presented alongside or superimposed behind the filtered data or be made available upon request.

Full Travel Angular Error Analysis

Full travel angular error can be reported as either bidirectional or unidirectional error. For each set of measurements, the angular error is then reported as the peak-to-peak (pk-pk) of the data over the full positioning range of the stage (no post-processing other than filtering should be done). This is illustrated in Figure 2. The averages of the five angular error values and the expanded measurement uncertainty are reported as the full travel angular error of the axis for the specified velocity profile, filter condition, and angular degree of freedom.

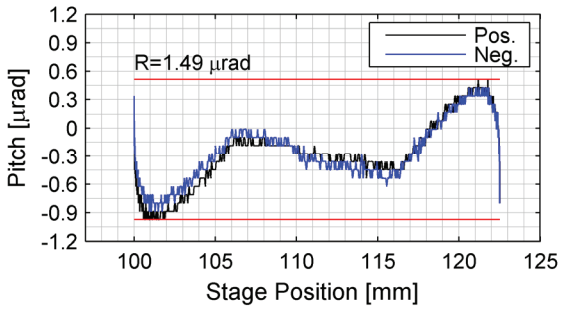

FIGURE 2. Measurement of dynamic pitch errors of a small air bearing stage for bidirectional dynamic angular error. The large pitch swings in the beginning and end are caused during the acceleration and deceleration regions.

Constant Velocity Angular Error Analysis

Constant velocity angular errors can be reported as either bidirectional or unidirectional. For each set of measurements, the pk-pk error corresponding to the raw or filtered constant velocity data is calculated and reported as the pitch error. The average of five angular error values and the expanded measurement uncertainty are reported as the constant velocity angular error.

Reporting and Presentation of Results

Dynamic angular errors of a positioning system should be identified as either the angular error of full travel for a defined motion/velocity profile or the angular error over a constant velocity region. For either case, a velocity profile plot identifying the acceleration regions should be provided along with a plot of dynamic straightness. In addition, settling times and regions for constant velocity measurements should be identified. A dynamic straightness plot should contain the average of the five measurement runs and the two parallel lines that envelope the straightness data. The angular error values, the filter parameters, the load, and location of the measured point should be reported. An example of a dynamic angular error report for constant velocity angular error due to stage pitch is provided as Figure 3.

COMMENTS

A new standard test method for characterizing and specifying the dynamic angular error of linear positioning systems was presented. The work is ongoing and the robustness of the method is being evaluated by characterizing the dynamic straightness for a variety of single axis positioning systems.

ACKNOWLEDGEMENTS

The authors would like to thank Ronnie Fesperman, Nathan Brown, Kevin Elliot, Axel Grabowski, Steve Ludwick, Serge Maneuf, Shane Woody, and the ASME B5 Technical Committee (TC52) for many fruitful discussions regarding this research.

REFERENCES

[1] Fesperman R, Donmez M, Moylan S, Ultra-precision Linear Metrology of a Commercially Available Linear Translation Stage, Proceedings of the ASPE Annual Meeting, 2011; 52: 81-84.

[2] ASME B5.54-2005, Methods for Performance Evaluation of Computer Numerically Controlled Machining Centers, 2005.

[3] ISO 230-1:2012, Test code for machine tools – Part 1: Geometric accuracy of machines operating under no-load or finishing conditions, 2012.

[4] Fesperman R, Brown N, Elliott K, Ellis J, Grabowski A, Ludwick S, Maneuf S, O'Connor B, Woody S, Methods for Performance Evaluation of Single Axis Positioning Systems: A New Standard, Proceedings of the ASPE Annual Meeting, 2013.

[5] Fesperman R, O'Connor B, Ellis J, Methods for Performance Evaluation of Single Axis Positioning Systems: Dynamic Straightness, Proceedings of the ASPE Annual Meeting, 2013.

[6] Patterson SR and Schmidt DM, Precision roll measurement using a polarization reference, Proceedings of the ASPE Annual Meeting, 1994; pp. 80-83

[7] Kroll JJ, Six degree of freedom optical sensor for dynamic measurement of linear axes, PhD Thesis, University of North Carolina at Charlotte, 2003.

[8] ISO/TR 230-9:2005E, Test code for machine tools – Part 9: Estimation of measurement uncertainty for machine tool tests according to series ISO 230, basic equations, 2005.

[9] JCGM 100:2008, Evaluation of measurement data – guide to the expression of uncertainty in measurement, 2008.

Dynamic Angular Error Test Report

Date: 8/5/2013 Time: 17:00 Test ID: T1000

Purpose: Acceptance_Vendor

Positioning System Identification

Manufacturer: XYZ Model: BFG5000 Serial Number: LMNOP

Test Setup

Direction of Motion:	X
Measurand:	B
Equipment Class:	Laser_Interferometer
Payload:	75 grams(angle optics)
Filter Type:	None
Measurement Point:	(0,0,25) mm

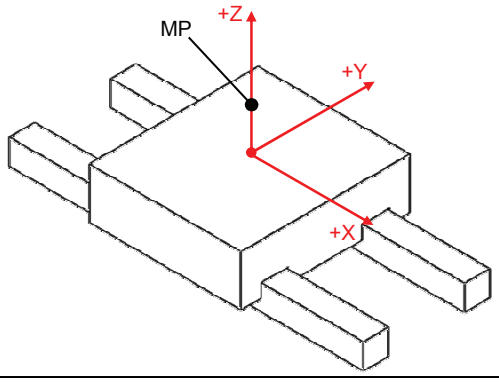

Programmed Velocity Profile
Type: Constant Velocity
Travel: 10 mm
(during constant velocity)
Acceleration: 200 (mm/s^2)
Velocity: 50 (mm/s)
Closed loop control

Filter Type: none Bandwidth: none

Results

Constant Velocity Angular Error

$E_{BX(\uparrow)}$	±	0.44	µrad
$E_{BX(\downarrow)}$	±	0.61	µrad
$E_{BX(\uparrow\downarrow)}$	±	0.61	µrad

Velocity: 50 ± 0.02 mm/s

#	time	position
1	0.29	100.0 mm
2	0.51	106.2 mm
3	0.71	116.2 mm
4	0.95	122.5 mm

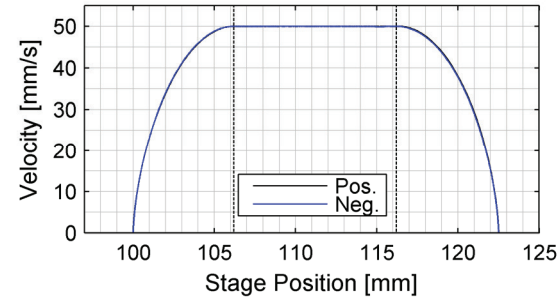

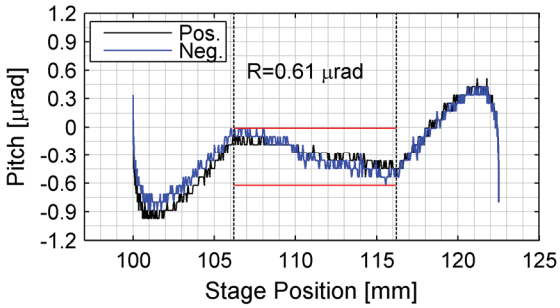

Figure 3. Example report of a dynamic angular error test for pitch measurements during constant velocity.

METHODS FOR PERFORMANCE EVALUATION OF SINGLE AXIS POSITIONING SYSTEMS: MOVE AND SETTLE PERFORMANCE

Jonathan D. Ellis[1,2], Stephen Ludwick[3]
[1]Department of Mechanical Engineering, [2]Institute of Optics
University of Rochester, Rochester, New York, USA
[3]Aerotech, Inc, Pittsburgh, PA USA

INTRODUCTION

Many new ultra-precision linear and angular positioning systems with exceptionally long ranges of motion on the order of tens of millimeters and degrees with positioning resolutions on the order of a nanometer and a micro-radian are finding their way into emerging technologies. Measuring and certifying the performance of these systems with off-the-shelf instrumentation and test methods suggested by existing machine tool standards can be very challenging, if the test uncertainty ratio (TUR) is to be greater or equal to 4:1 [1]. In addition, accepted methodology and terminology do not account for or accurately represent error sources and uncertainties that become contributing factors as motion system requirements become more precise. Many manufactures and users of these systems are recognizing this challenge and have begun to develop their own internal methods and standards for characterizing these systems. Performance specifications based on these diverse and independent methods leads to customer confusion and ambiguity. For these reasons, members of industry, academia, and government have stressed a need for new or improved standards and measurements that specifically address this class of positioning systems.

This work is a subset of the scope of a new standard for evaluating the performance of single axis positioning systems [2]. In this manuscript, we will present potential performance evaluation methods to assess a stage's performance during a Move and Settle operation, and the associated timing uncertainty and displacement uncertainty.

MOVE AND SETTLE ASSESSMENT

The traditionally quoted "settling time" on stage specification sheets leads to ambiguity because the parameters that adequately describe just the settling time depend on deciding the point at which the stage is no longer moving but rather trying to settle. Additionally, nonlinear frictional effects apparent at sub-micrometer displacements prevent a straightforward application of classical "time-constant" type estimates for settling time, as shown in Figure 1 and discussed in [3]. To remove this ambiguity, we are proposing a combined Move and Settle assessment approach where the move size and profile is considered in conjunction with the settling time. The move profile can be a step function, ramp, impulse, or a specified profile that is closely related to the intended application. For example, if the desired function of the stage to rapidly reposition from one location in the work volume to another, a step function may not be the quickest method for driving the stage nor may it be the most accurate method because excessive oscillations may occur.

In this Proceedings, we are not explicitly proposing methods that can achieve the desired 4:1 TUR. Rather, the goal of this work is to discuss some analysis techniques and assessments that can be used to establish potentially useful performance metrics.

METHOD

Real-time feedback and offline processing present two distinct options for analyzing move and settle performance. Offline processing can use the whole data set whereas real-time processing can only use past data. This is critical specifically when the stage controller must deem the stage as "settled" for triggering other serial processes. In those instances, the stage must be in a certain state (i.e., stationary, past a certain location, etc.) in order for the controller to initiate the next process. Using a defined timing window, the positioning error can be quantified using three different metrics [4], that can take into account the differing needs of assessments based on post-processing and/or real-time data.

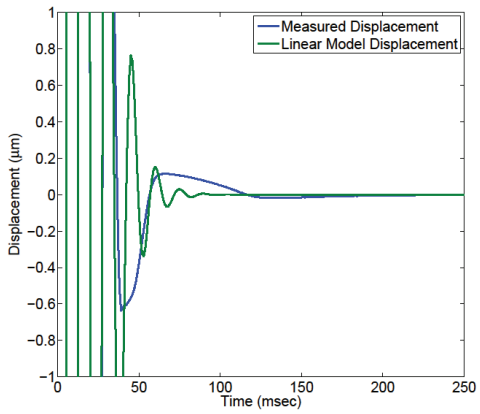

FIGURE 1. Linear displacement model and measured displacement showing nonlinear friction, increasing the settling time. (From Ref. [3])

The three different metrics are:

$$MAE(t) = \frac{1}{T}\int_{\tau=t-T/2}^{t+T/2} e(\tau)\,d\tau \quad (1)$$

$$MSD(t) = \sqrt{\frac{1}{T}\int_{\tau=t-T/2}^{t+T/2} \left(e(\tau) - MAE(\tau)\right)^2 d\tau} \quad (2)$$

$$MPE(t) = \max\left(|e(\tau)| : t - T/2 < \tau < t + T/2\right) \quad (3)$$

where MAE is the moving average of positioning error signal e over temporal window T, MSD is the moving standard deviation, MPE is the maximum positioning error, and τ is the time during the window. In Equations 1-3, the window is assumed centered, however, for real-time applications, it is useful to use a single sided window using only the past data. This can be implemented by changing the limits of integration, resulting in the error assessment shown in Figure 2.

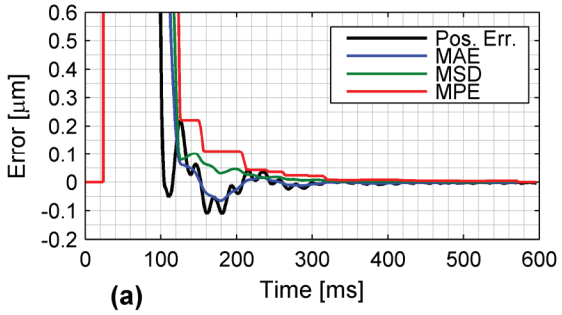

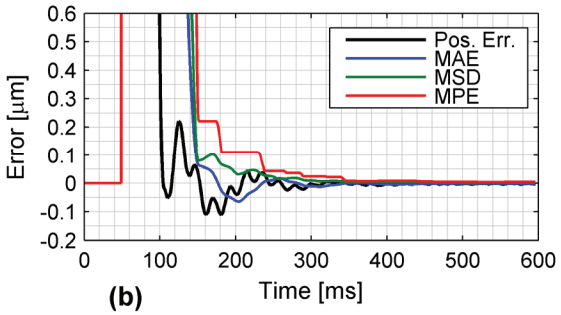

FIGURE 2. (a) Position error and error metrics using a centered window. (b) The same position error using a single sided window of the past data. Using the past metrics increases the apparent delay, adding a safety factor which is useful to ensure the stage is settled for triggering other chained processes.

ANALYSIS

Three analysis specifications are needed to assess the stage's move and settle performance: timing specifications, settling specifications, and the move profile. The timing specifications are the temporal window used and the duration that the stage must be "settled" within to determine that it is settled. The settling specifications determine the error threshold where it is acceptable to consider the stage as settled and the window type (MAE, MSD, MPE) used. For example, the temporal window could be a centered, MPE 50 ms window where the stage error is less than 150 nm for at least 30 ms, as shown in Figure 3.

Another example, shown in Figure 4, uses different analysis specifications. For example, a centered 50 ms MSD window is used where the stage error is less than 90 nm with no delay. Here, the stage meets that threshold at 124 ms although the stage exceeds that threshold at 135 ms due to stage oscillations. Because the delay was specified at zero seconds, the stage appears to move and settle within 100 ms, although the actual recorded error shows differently. Thus, it is critical that the error signal and the move and settle analysis specifications be reported to alleviate confusion between the user and supplier. This effect can be mitigated by specifying a delay for which the stage error must be held within that threshold. For example (also Figure 4), if the delay selected was 25 ms, the oscillation in the error can be seen in the new settled time, which is after 150 ms. Note, the absolute value of the error is still greater than the threshold.

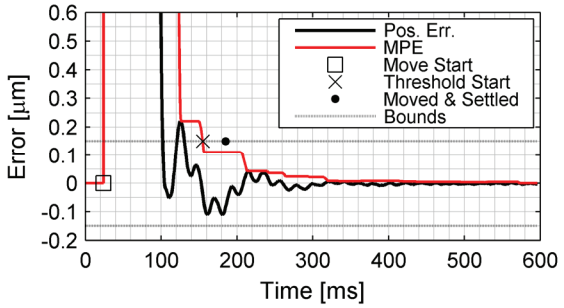

FIGURE 3. Stage is moved and settled after 161 ms, assuming a 50 ms centered MPE window, a threshold of 150 nm, and a delay of 30 ms. The dashed lines show the bounds, which the stage is within.

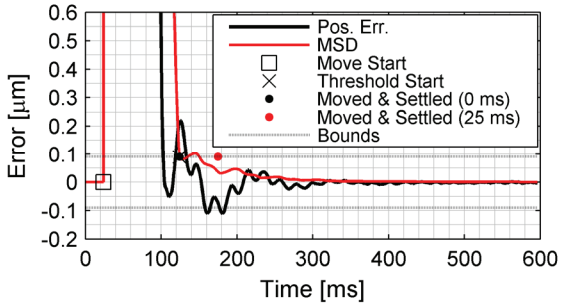

FIGURE 4. A centered, 50 ms MSD window with 90 nm bounds without a delay on the same error signal shown in Figure 3. While the analysis appears that the stage has moved and settled, the positioning error is still outside the bounds. Even with a 25 ms delay added, the stage is still outside of the 90 nm bounds.

The move profile is the function the stage should exhibit, whether it is a step, ramp, impulse, etc. For example, different step sizes will have different move and settle times because the stage may take longer to physically travel the distance and the dynamics of moving further may cause the stage to exhibit different settling characteristics. Other move profile considerations include the stage load and position within the work volume.

Selection of the timing window duration, type, threshold value, holding duration (the duration the stage must be within the threshold values) and move profile should all be specified and agreed upon by the user and supplier. When reporting move and settle performance, it is recommended that both the raw error signal and the metrics used in the analysis be reported.

ASSESSMENTS

Once analysis specifications are determined and agreed upon by the user and supplier, there are five different assessments that can be performed. Each of these different assessments provides slightly different information about the stage performance.

Assessment 1: Internal Timing

The internal timing assessment is blind to the external world and solely comprises the stage and its controller. Once the analysis specifications are determined, multiple tests are performed to determine the variation in the move and settle time. As this assessment is blind to external systems, it is recommended that only single sided (past) information be used in the windowing characteristics. For example, Figure 5 shows three separate data sets using a 50 ms single sided MPE window and a 200 nm error bound with no holding duration for a 10 mm step. The move and settle time is 195±3 ms.

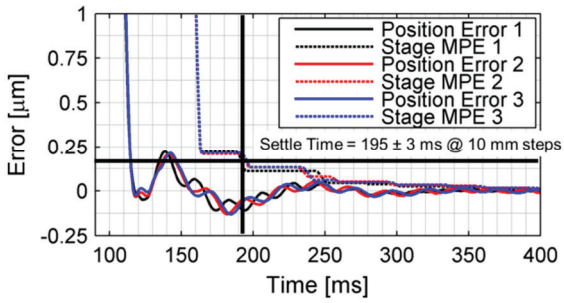

FIGURE 5. Internal timing assessment that is blind to external sensors. Based on the analysis specifications, the move and settle time for a 10 mm step is 195±3 ms.

Assessment 2: External Timing

The external timing assessment is a secondary verification that the stage has moved and settled within the specific time period and positioning error window. This assessment is performed in a similar manner to the internal time assessment but only looks at an external sensor to assess the stages performance. The analysis metrics used for the external timing assessment should match the metrics used in the internal timing assessment. An example of this is shown in Figure 6.

The issue of timing, synchronization, and bandwidth of the external sensor should be explicitly discussed in the uncertainty budget. For example, sensors with a lower bandwidth

may cause effects that appear as heavy filters and/or delays, which can affect performance. Also, the external sensor may be subjected to additional error sources that the internal sensor mitigates (or vice versa), and these differences should be reflected in the uncertainty analysis. The external sensor should be placed to record the position at the desired functional point [2], which may include the influences of Abbe errors, straightness errors, and angular errors.

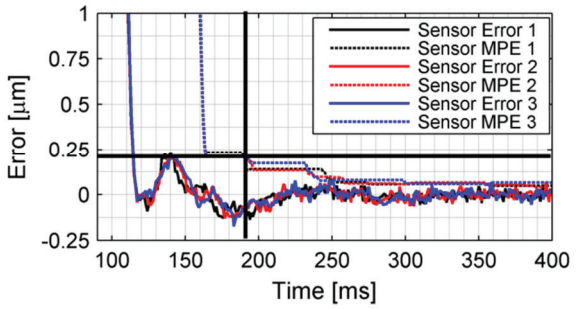

FIGURE 6. External timing assessment that only uses an external sensor and a trigger sent from the stage to assess the performance. The sensor error is the measured positioning error using an external sensor and the sensor MPE is the calculated MPE of the sensor error using windowing parameters.

Assessment 3: Move Size Settle Time

In addition to assessing the performance of a single move repeatedly, random moves of random sizes with different analysis metrics can provide valuable information on the variability in the settling time. For example, if the analysis bound is shifted from 100 nm to a 10 nm window, the move and settle time has more variability, as shown in Figure 7.

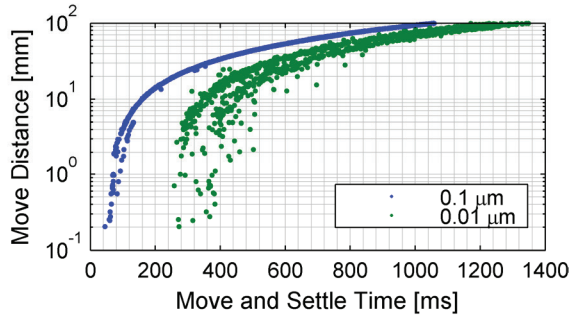

FIGURE 7. Move and settle time variability for different move sizes for two different bounding windows. The 100 nm bound has significantly less variability than the 10 nm bound.

Assessment 4: Likely Error Estimation

The previous three assessments are focused on the timing metrics associated with the move and settle performance. However, the positioning performance is also critical. The likely error estimation is an assessment that describes the variation in the positioning error. First, the analysis specifications for the internal timing assessment are used. Then once a move and settle time is determined, a two-sided window centered ($\pm\tau$) on the data is used and the MSD is calculated for each point in that window. Then the mean and standard deviation of the MSD values for that window are computed. The mean MSD value gives an estimate of the average deviation for that specified temporal window. The standard deviation of the MSD values gives the variability, as shown in Figure 8.

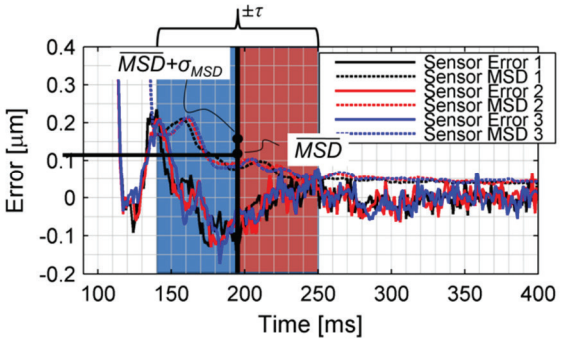

FIGURE 8. Likely error estimation using an external sensor to assess the mean MSD and standard deviation of the MSD over a centered, two-sided window.

If tight tolerances are specified in the timing and window requirements with minimal delay are chosen for the analysis specifications, the standard deviation of the MSD values for the window will exhibit high variability. However, if the analysis specification values are chosen with loose tolerances or significant safety margin, the stage will likely have moved and settled for a longer duration and exhibit less variability. This assessment can be viewed either from an internal perspective (*i.e.,* blind to external sensors) or using external sensors at the functional point.

Assessment 4: Work Volume Bias

The third assessment is used to quantify different move and settle times within the work volume for different move sizes. However, it is important to assess the position uncertainty as a function of volume to quantify any biases that

may be present. The likely error estimation technique can be used, along with the positions from the move size settle time assessment to quantify the errors for random moves of random sizes in the work volume. Figure 9 presents 50 random moves of random sizes based on the starting position and step size. The internal timing assessment is used to select the time at which the stage has moved and settled. The likely error estimation is then computed with the mean MSD plus standard deviation of the MSD for the selected window. This value then represents the positioning variation throughout the work volume.

If there are biases present due to work volume location or move size, the error bars in Figure 9 would be larger to reflect those biases. However, if they are nominally uniform, then little bias is present due to move size or work volume position. As with the likely error estimation, this can be either from the internal stage sensor or an external sensor.

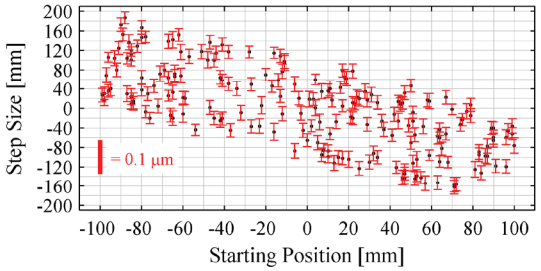

FIGURE 9. Work volume bias using the likely error estimation for random move sizes and positions within the work volume. The error bars represent likely error estimation computed from each move and settle step with the 100 nm error bar size indicated.

One limitation that is not represented in this figure is the different move and settle times as it is likely the case that larger moves will take longer to achieve the settling metric. However, lateral error bars can be added to Figure 9 to reflect the different move and settling times. This gives an overall snapshot of a stage's performance in a single figure.

MOVE AND SETTLE CONCLUSIONS

The proposed metrics for assessing a stage's *Move and Settle Performance* have been presented. Three different analysis methods have been proposed to use with a series of five different assessments to quantify a stage's move and settle performance. The five proposed assessments quantify the timing metrics and positioning metrics of a stage's performance during a move and settle operation.

The work presented in this paper is the view of the authors and is being presented to this community for feedback on the proposed test methods.

Future work

Work is ongoing by the authors to test a variety of positioning axes using the methods described in this paper. In addition, detailed uncertainty analysis methods are being developed for this test to aid the users and suppliers of positioning equipment in quantifying the measurement uncertainty.

ACKNOWLEDGEMENTS

The authors would like to thank Ronnie Fesperman, Nathan Brown, Kevin Elliot, Axel Grabowski, Serge Maneuf, Brian O'Connor, Shane Woody, and the ASME B5 Technical Committee (TC52) for many fruitful discussions regarding this research.

REFERENCES

[1] Fesperman R, Donmez M, Moylan S, Ultra-precision Linear Metrology of a Commercially Available Linear Translation Stage, Proceedings of the ASPE Annual Meeting, 2011; 52: 81-84.

[2] Fesperman R, Brown N, Elliott K, Ellis J, Grabowski A, Ludwick S, Maneuf S, O'Connor B, Woody S, Methods for Performance Evaluation of Single Axis Positioning Systems: A New Standard, Proceedings of the ASPE Annual Meeting, 2013.

[3] B.A. Bucci, J.S. Vipperman, D.G. Cole, S.J. Ludwick, Evaluation of a servo settling algorithm, *Precision Engineering* 2013; **37**(1): 10-22.

[4] H. Butler, Position Control in Lithographic Equipment, *IEEE Control Systems Magazine* 2011; 28-47.

METHODS FOR PERFORMANCE EVALUATION OF SINGLE AXIS POSITIONING SYSTEMS: A NEW STANDARD

R. Fesperman[1], N. Brown[2], K. Elliott[3], J. Ellis[4], A. Grabowski[5], S. Ludwick[6], S. Maneuf[7], B. O'Connor[6], S. Woody[8]

[1]National Institute of Standards and Technology (NIST)*, Gaithersburg, MD, USA
[2]Alio Industries, Wheat Ridge, CO, USA
[3]Corning Inc., Corning, NY, USA
[4]University of Rochester, Rochester, NY, USA
[5]Physik Instrumente (PI) GmbH & Co. KG, Karlsruhe, Germany
[6]Aerotech Inc., Pittsburgh, PA, USA
[7]Newport Corp., Beaune-la-Rolande, France
[8]InSituTec, Concord, NC, USA

INTRODUCTION

Many new high-precision linear and angular positioning systems with exceptionally long ranges of motion on the order of tens of millimeters and degrees with positioning resolutions on the order of a nanometer and a micro-radian, respectively, are finding their way into emerging global micro- and nanotechnology applications. Application areas include photovoltaic manufacturing, semiconductor manufacturing, life sciences, and telecommunications, which are four of many examples existing in a very broad positioning system industry. Some systems are designed and manufactured for specific applications while many others are modular in design to provide customers with the flexibility to integrate positioning systems with existing industrial applications and equipment.

Accurate knowledge of positioning performance is critical when selecting the appropriate positioning system(s) for an application. However, a dedicated standard for evaluating and certifying the performance of single axis positioning systems does not currently exist. Additionally, measuring and certifying the performance of high-precision systems with off-the-shelf instrumentation and test methods suggested by existing standards can be very challenging, specifically because the positioning performance of this class of positioning system is approaching the uncertainty of the measuring devices [1, 2]. Similarly, commonly used measurement methodologies and terminologies do not always account for or accurately represent error sources and uncertainties that contribute to positioning system performance as requirements become more precise. Many manufacturers and users of these systems are recognizing this challenge and have begun to develop their own internal methods and standards for characterizing these systems. Performance specifications based on these diverse and independent methods is leading to customer confusion and ambiguity. Members of industry (manufacturers and consumers), academia, and government have recognized this challenge and the need for a new standard for measurement methods that specifically address single axis positioning systems.

Performance standards provide a common infrastructure that improves communication, efficiency, innovation, and interoperability through the standardization of terminology, measurement methods, analyses, and data formats. The benefits of performance standards have been demonstrated over the past several decades by the advancements in the performance of computer numerically controlled (CNC) machine tools. Performance tests described by existing machine tool standards [3-5] have been used to characterize the performance of single axis positioning systems with success and limitations.

Recently, a group of volunteers from industry,

* No approval or endorsement of any commercial product by the National Institute of Standards and Technology is intended or implied. Certain commercial equipment, instruments, or materials are identified in this report in order to facilitate understanding. Such identification does not imply recommendation or endorsement by the National Institute of Standards and Technology, nor does it imply that the materials or equipment identified are necessarily the best available for the purpose. This publication was prepared by United States Government employees as part of their official duties and is, therefore, a work of the U.S. Government and not subject to copyright.

academia, and government re-evaluated and thoroughly discussed the use of machine tool standards for characterizing single axis positioning systems having high-precision positioning performance. The group concluded that there is a need for a new standard that addresses the performance evaluation of single axis positioning systems. In addition to addressing static/quasi-static positioning performance, a new standard should also address dynamic positioning performance, test uncertainty, and the instrumentation and techniques required for low uncertainty measurements. With this in mind, a draft scope and outline for a new standard was generated and the American Society of Mechanical Engineers (ASME) B5 Technical Committee TC52 was chosen as the Standards Developing Organization [6].

In this abstract, we discuss factors affecting the accurate characterization and communication of positioning system performance. The scope for this new standard is presented and the new test methods being considered for inclusion in the standard are briefly described.

POSITIONING PERFORMANCE

There are many factors that contribute to the accurate characterization and communication of positioning system performance. Many users are not aware nor understand the importance of the contributors and select systems based on specifications (e.g., positioning resolution) that do not completely or accurately describe positioning performance. One goal for this standard is to emphasize and clearly describe these contributors and enhance communication.

Measurement Points and Coordinate System Location

Linear errors of positioning systems (e.g., linear positioning and straightness) are normally characterized by measuring the trajectory of a measured point (MP) that is rigidly attached to the moving element (e.g., linear axis carriage) of a positioning system, as seen in Figure 1. Furthermore, linear errors are affected by the angular error motions of a positioning system and thus, have different magnitudes along different point trajectories. The differences in magnitude are related by the offset distance (d) between points (Abbé Offset) and the angular error motions of the positioning system. These concepts are known as the *Abbé* and *Bryan Principles* [7].

Theoretically, the measured point can be located anywhere around the positioning system. To better understand the effects of the errors on the intended application, the measured point should, ideally, coincide with the functional point (FP) of the application [5], as seen in Figure 1. Unfortunately, spatial constraints may limit the ability to measure linear errors at the functional point and the reported errors may not truly represent the magnitudes of the errors affecting the application. However, if the location of the measured point with respect to the axis coordinate system is known (i.e., well documented). then the linear errors can be transformed to estimate the magnitude of the errors at any functional point in the work volume.

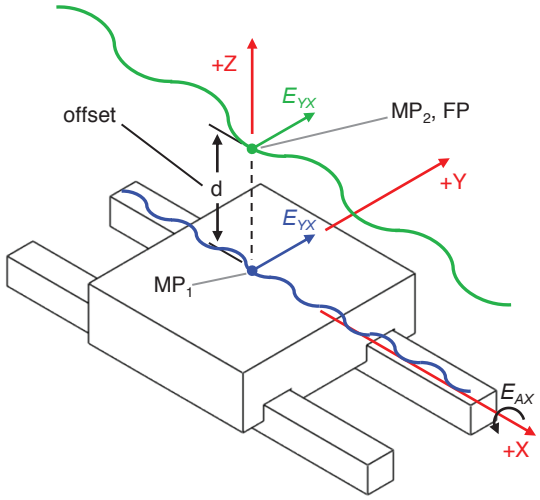

FIGURE 1. A schematic illustrating different straightness errors, E_{YX}, along different measurement points.

In current practices, the location of the measured point is usually not well documented or published and the methods for describing the location of the measured point are inconsistent between manufacturers, users, and metrologists. This makes it a challenge to perform direct comparisons of positioning system performance based on published performance data. Additionally, the locations of the axis coordinate systems vary between the various positioning systems available and the locations are usually vaguely described. Direct performance comparisons and error transformations can benefit from a well-defined and accurate method for describing the location and orientation of the axis coordinate frame and measured point.

To emphasize these principles and to enhance communication, the standard being developed will provide a method for identifying and describing the location and orientation of a positioning system's coordinate frame and the position of the measured point with respect to the coordinate frame. In addition, a guideline for estimating the error at different functional points by performing error transformations will be provided as an appendix. Standard nomenclature for representing the error motions of a positioning system will also be provided.

Static/Quasi-Static Performance

Many robust test methods for characterizing static/quasi-static positioning performance (e.g., linear positioning, straightness, and angular deviation) are well defined by existing machine tool standards [3-5] and have been thoroughly tested and implemented by industry. This standard will reference and describe many of these methods with appropriate examples and suggestions for implementation on single axis positioning systems. Both unloaded and loaded conditions will be considered, as well as rigid body and non-rigid body assumptions. In addition to existing methods, two new test methods for characterizing incremental positioning performance [8] and point repeatability [9] are also being considered for inclusion in this standard.

Dynamic Performance

During static/quasi-static conditions, the positioning errors are nominally the result of the geometric errors of the positioning system. During dynamic conditions, positioning errors are additionally affected by the forces and moments inherent in the dynamic system, e.g., drive forces occurring during acceleration and deceleration [10]. As a result, positioning errors can change and lower modes of vibration of the positioning system can be excited during static to dynamic transitions. Standard methods for characterizing the dynamic positioning performance do not currently exist. This standard seeks to establish a set of methods that can be used to characterize dynamic positioning error, dynamic straightness error, and dynamic angular deviation. In addition to these dynamic tests, this standard will also seek to develop standard methods for measuring the characteristics of the positioning system's servo control, e.g., dynamic response, settling times, etc.

Test Uncertainty and Test Uncertainty Ratio

Many users of high performing positioning systems (e.g., nano-positioners) are unaware of the challenge to accurately characterize their performance [11]. At a minimum, accurate characterization is limited by the uncertainty of the instrumentation and/or artifact(s) used during measurement. However, other influences associated with the test method affect the overall measurement uncertainty and the uncertainty of the calculated performance parameters. Examples include, but are not limited to, the influence of the metrologist, the test procedure, placement and alignment of the test equipment, the repeatability of setting up the test equipment, and the compensation of environmental effects on the measurement.

A measure of the quality of the test, taking into account all the influences, is known as *Test Uncertainty* [12]. An additional measure used to assess the ability of a particular test to evaluate a particular performance parameter is known as the *Test Uncertainty Ratio* (TUR) [12], which is the ratio of the specified performance parameter to test uncertainty. Historically, the general rule for an appropriate ratio was 10:1, but because of higher performing equipment, the current TUR suggested by ANSI Z540.3 is 4:1 [13]. Measuring and certifying the positioning performance of current nanopositioners with off-the-shelf instrumentation suggested by existing performance standards can be very challenging if the TUR is to be greater or equal to 4:1. In some instances the ratio is closer to 1:1 [2]. For this reason, it is important that this standard appropriately and clearly addresses test uncertainty and the TUR.

One goal for this standard is to provide a general guideline for formulating the test uncertainty for positioning performance measurements. This guideline will be similar to the guideline described by ISO 230-9 [14] and will be an essential tool for evaluating test setups and identifying areas of improvement. Examples of test uncertainty calculations for many of the test methods included in the standard will be provided, as well as a list of associated measurement technologies, uncertainty contributors, and limitations. Where necessary, uncertainty analyses for evaluating associated measuring technologies will be described, contributors to the measurement uncertainty listed, and uncertainty limits declared. When possible, existing guidelines for

estimating measurement uncertainty (e.g., ASME B89.1.8-2011 [15]) will be referenced. Most importantly, the expectation is that the provided set of uncertainty tools will make the consumer/user aware of the level of uncertainty and setup scrutiny necessary to characterize precision positioning performance.

Environmental Conditions and Testing

Environmental conditions can affect the positioning systems' performance and the measuring instruments and setups used to characterize positioning system performance, especially as positioning performance specifications become tighter and approach the uncertainties of evaluation methods. Unfortunately, these effects are often misunderstood and contribute to uncertainty in the measurement. This standard will provide a set of guidelines for specifying acceptable environments for performance testing and for high-precision positioning system operation. Standard test methods for characterizing the environment and the thermal characteristics of positioning systems will also be provided. Additionally, methods for characterizing the uncertainty in environmental measurements and a list of the uncertainty limits due to traceability will be included.

Recording and Reporting Performance

When users of positioning systems go through the process of selecting off-the-shelf positioning systems for their application, they, in part, rely on published performance data for making decisions. Published data, however, may not truly represent the performance of the positioning system in the way in which it is intended to be used. Additionally, comparing the performance of similar positioning systems produced by different manufacturers can be challenging due to inconsistencies in the performance information published. Thorough and direct comparisons can be better achieved if a minimum set of test metadata, error results, and error parameters are provided. This data may then be used to predict the performance for a specific application. To help eliminate this challenge, this standard will provide suggested methods for reporting the performance determined by the standard test methods. The method of reporting will identify a minimum set of measurement parameters and encourage use of common units.

Performance data can have many purposes. It may be used for error compensation, vendor specification, customer acceptance, interim evaluation of the condition of a system, estimating performance at different functional points, and for simulating its effects on the performance of a larger machine [16] consisting of a collection of multiple positioning systems. Accurate implementation of data can be enhanced by standard electronic data formats and information models designed to facilitate the collection, archiving, and exchange of measurement and machine performance data [17, 18]. ASME B5.59-1 [17] and ASME B5.59-2 [18] provide such formats for machine tools. It is envisioned that this standard will support the format described by ASME B5.59 by providing additional elements used to describe the properties of single axis positioning systems and performance tests. These elements may be provided in an appendix and may include, but may not be limited to, the location and orientation of coordinate systems, the position of measurement points, the parameters used to describe motion/velocity profiles, and the contributors to test uncertainty.

STANDARD SCOPE

The planned scope for this new single axis positioning performance standard is as follows.

1) The standard will establish a methodology for specifying and testing the performance of precision positioning systems. It will address both single axis linear and angular (rotary) positioning systems with travels ranging from micrometers to meters and millidegrees to continuous rotation, respectively.

2) The standard will seek to highlight the importance of understanding measurement uncertainty, test uncertainty, and the test uncertainty ratio by providing methods for estimating the test uncertainty and the uncertainty of positioning performance parameters.

3) The standard will describe equivalent test methods and instrumentation described in existing machine tool standards [3-5] and additional methods and instrumentation used for the characterization of positioning systems having a relatively high positioning performance when compared to standard machine tool performance.

4) The standard will facilitate performance comparisons between systems by unifying terminology, general system classification, the treatment of environmental effects, the treatment of measurement uncertainty, and the treatment of performance data.

5) The intended use of the tests described by this standard will be for acceptance testing of new and reconditioned positioning systems and verifying continued capability of systems, already in operation, through periodic testing.

NEW TEST METHODS

In addition to describing equivalent test methods described in existing machine tool standards, this standard will also include additional tests for both static and dynamic conditions. Some of the additional tests being considered for inclusion are:

a) *Incremental Step Test*. A test that quantifies the ability of a positioning system to reliably perform a commanded step. The test will also provide a procedure to quantify *minimum incremental motion* (mechanical resolution) that a positioning system is capable of performing [8].

b) *Three Dimensional Point Repeatability*. A test that characterizes a positioning system's ability to repeatedly return to a defined target position(s) in three-dimensional space [9].

c) *Dynamic Positional Accuracy, Straightness [19], and Angular Deviation*. A series of tests designed to characterize the positional accuracy, straightness, and angular deviation of a linear axis for specified motion/velocity profiles.

d) *In-position Jitter*. A test that quantifies the motion of an axis at a functional point while no commanded motion is occurring [8].

e) *Move and Settle*. A test designed to quantify the time required for a servo-controlled axis to move a particular distance and settle to a predefined position error tolerance [20].

f) *Servo Characterization*. A test that uses frequency response techniques to quantify the performance and stability of closed-loop feedback control [21].

COMMENTS

An effort to draft a new standard for the performance evaluation of single axis positioning systems has been introduced and is under way. Members of the working group are actively working to evaluate the robustness of the new standard test methods by measuring the performance of various types of single axis positioning systems. It is expected that this standard will provide the foundation for an additional standard for the performance evaluation of multi-axis positioning systems.

REFERENCES

[1] Fesperman R, Donmez M, Moylan S, Ultra-precision Linear Motion Metrology, Proceedings of the ASPE Summer Topical Meeting, 2010; 49: 103-108.

[2] Fesperman R, Donmez M, Moylan S, Ultra-precision Linear Metrology of a Commercially Available Linear Translation Stage, Proceedings of the ASPE Annual Meeting, 2011; 52: 81-84.

[3] ASME B5.54-2005, Methods for Performance Evaluation of Computer Numerically Controlled Machining Centers, 2005.

[4] ASME B5.57-1998, Methods for Performance Evaluation of Computer Numerically Controlled (CNC) Lathes and Turning Centers, 1998.

[5] ISO 230-1:2012, Test code for machine tools – Part 1: Geometric accuracy of machines operating under no-load or finishing conditions, 2012.

[6] ASME B5 Standards Committee, B5 Machine Tools – Components, elements, performance, and equipment, www.asme.org.

[7] Bryan J B, The Abbé Principle Revisited: An Updated Interpretation, Precision Engineering, 1979; 1: 129-132.

[8] O'Connor B, Fesperman R, Maneuf S, Methods for Performance Evaluation of Single Axis Positioning Systems: Incremental Step Test, Proceedings of the ASPE Annual Meeting, 2013.

[9] Brown N L, A New Way of Analyzing Motion System Repeatability for Nanometer Precision: 6-DOF Point Repeatability, ASPE Annual Meeting, 2011; 52, 85-86.

[10] Miller J, Hocken R, Ramanan V, Feng Q, Foundation of Dynamic metrology of Machine Tools, Proceedings of the ASPE Annual Meeting, 1999.

[11] Personal communication by the authors with their respective customers.
[12] Khanam S A, Morse E, Test Uncertainty & Test Uncertainty Ratio (TUR), Proceedings of the ASPE Annual Meeting, 2008.
[13] ANSI Z540.3, 2006, Requirements for the calibration of measuring and test equipment, 2006.
[14] ISO/TR 230-9:2005, Test code for machine tools – part 9: Estimation of measurement uncertainty for machine tool tests according to series ISO 230, basic equations, 2005.
[15] ASME B89.1.8-2011, Performance Evaluation of Displacement-Measuring Laser Interferometers, An American National Standard, The American Society of Mechanical Engineers, 2011.
[16] Fesperman R, Moylan S, Donmez A, A Virtual Machine Tool for the Evaluation of Standardized 5-axis Performance Tests, Proceedings of the ASPE Annual Meeting, 2012; 54: 484-487.
[17] ASME B5.59-1, Information Technology for Machine Tools Part 1: Data Specification for Machine Tool Performance Tests, 2006; 10a.
[18] ASME B5.59-2, Information Technology for Machine Tools Part 2: Data Specification for Properties of Machine tools for Milling and Turning, draft standard. 2008; 13b.
[19] Fesperman R, O'Connor B, Ellis J, Methods for Performance Evaluation of Single Axis Positioning Systems: Dynamic Straightness, Proceedings of the ASPE Annual Meeting, 2013.
[20] Ellis J, Ludwick S, Fesperman R, Methods for Performance Evaluation of Single Axis Positioning Systems: Move and Settle Performance, Proceedings of the ASPE Annual Meeting, 2013.
[21] Ludwick S, Fesperman R, Progress on Defining Standard Tests for Quantifying Servo System Tuning, Proceedings of the ASPE Annual Meeting, 2013.

METHODS FOR PERFORMANCE EVALUATION OF SINGLE AXIS POSITIONING SYSTEMS: DYNAMIC STRAIGHTNESS

R. Fesperman[1], B. O'Connor[2], and J. Ellis[3]
[1]National Institute of Standards and Technology (NIST)*, Gaithersburg, MD, USA
[2]Aerotech Inc., Pittsburgh, PA, USA
[3]University of Rochester, Rochester, NY, USA

INTRODUCTION

Many new ultra-precision linear positioning systems are finding their way into emerging technologies that are requiring exceptional straightness performance during both static/quasi-static and dynamic positioning conditions. A few examples of these technologies include photovoltaic panel scribing, wafer dicing, and laser machining. Measuring and specifying static/quasi-static straightness is a well-defined process described in existing performance standards [1, 2]. A dynamic straightness test for identifying the amplitude of vibration during the acceleration and deceleration of machine tool axes is provided by ISO 230-8 [3]. However, a standard test method for characterizing and specifying dynamic straightness for single axis linear positioning systems does not currently exist. As a result, many manufacturers and users of linear positioning systems have developed their own internal methods and standards, which have led to customer confusion and ambiguity.

To help mitigate confusion, members from industry, academia, and government are working to develop a new positioning performance standard [4] that includes a new test method for characterizing straightness of a linear positioning system under dynamic conditions. In this paper, we discuss a test method for characterizing *dynamic straightness*. Descriptions of measurement setups, measurement and analysis procedures, and suggestions for reporting dynamic straightness results are presented.

STRAIGHTNESS

Straightness of a linear positioning system is characterized by measuring the motions of the carriage in the two directions orthogonal to the nominal direction of motion, see Figure 1. Under static and quasi-static conditions, the straightness errors are nominally the result of the geometric errors of the positioning system components. During dynamic conditions, straightness errors can be additionally affected by the forces and moments inherent in the dynamic system, e.g., drive forces occurring during acceleration and deceleration [3, 5]. As a result, straightness errors can change during static to dynamic transitions.

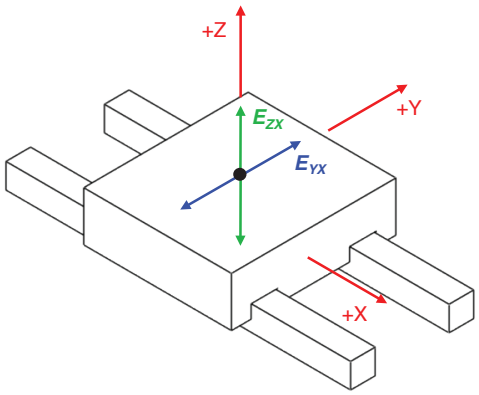

FIGURE 1. A schematic identifying the straightness errors of a linear positioning system traversing in the x-direction. E_{YX} *and* E_{ZX} *represent the straightness error motions in the y- and z-directions, respectively.*

Applications in which linear positioning systems are used vary widely and the acceleration and deceleration regions differ for each. This diversity creates a challenge for specifying dynamic straightness. In some applications, such as constant velocity scanning (CVS), the process (e.g., manufacturing or measurement) may only occur during the constant velocity region of the velocity profile and therefore may

* No approval or endorsement of any commercial product by the National Institute of Standards and Technology is intended or implied. Certain commercial equipment, instruments, or materials are identified in this report in order to facilitate understanding. Such identification does not imply recommendation or endorsement by the National Institute of Standards and Technology, nor does it imply that the materials or equipment identified are necessarily the best available for the purpose. This publication was prepared by United States Government employees as part of their official duties and is, therefore, a work of the U.S. Government and not subject to copyright.

not be affected by the acceleration and deceleration regions. Characterizing straightness over the acceleration and deceleration regions may be impractical when specifying and/or selecting positioning systems for CVS applications. However, other applications that include motions such as raster scanning and circular contouring, are affected by the acceleration and deceleration regions. Including these regions in the characterization and specification of dynamic straightness may be beneficial for these and similar applications. For these reasons, it may be important to consider the velocity profile for a given dynamic condition when characterizing and specifying dynamic straightness.

VELOCITY PROFILES

Velocity (or motion) profiles used for driving positioning systems can vary in form. Profiles can range from the most common and simplest profiles such as triangular or trapezoidal to more complex profiles that control the level of jerk (e.g., S-curve). Each profile differs by the method used to transition (e.g., time rate of change) from one commanded velocity to another. The smoothness of the transitions can affect straightness by introducing unwanted forces and moments on the moving element of the positioning system. Accurate characterization and a detailed understanding of dynamic straightness performance may be enhanced by the identification of the transitions regions. Identifying the transition regions requires detailed information about the velocity profile and its parameters (e.g., drive forces, accelerations and time constants). Most modern controllers allow access and exporting of profile data. Alternatively, the profile data can be provided by the manufacturer or it can be determined by characterizing the positioning system following standard test methods such as the Feedrate and Acceleration method described in ASME B5.54 [1]. Similar test methods are being considered for inclusion in the new standard.

STRAIGHTNESS MEASURMENT

Normally, straightness errors are characterized by measuring the trajectory of a point that is rigidly attached to the moving element (e.g., carriage) of a linear positioning system. Furthermore, straightness errors (i.e., straightness measurement results) are also affected by the angular motions/errors of the positioning system and thus have different magnitudes along different point trajectories, as shown in Figure 2. The differences in magnitude are related by the offset distance between points (Abbe' Offset) and the angular motions of the positioning system. This concept is known as the *Bryan Principle* [6].

Theoretically, the measured point can be located anywhere around the positioning system. Because the magnitude changes with point location, it is recommended that the location of the measured point correspond to the location of the functional point [2], i.e., the point where work for the intended application is occurring. However, spatial constraints may limit the ability to measure straightness errors at the functional point. For this reason it is recommended that the measured point be located as close to the functional point as possible, with the point's location with respect to the axis coordinate frame being well documented [4] and measurements made of the relevant angular

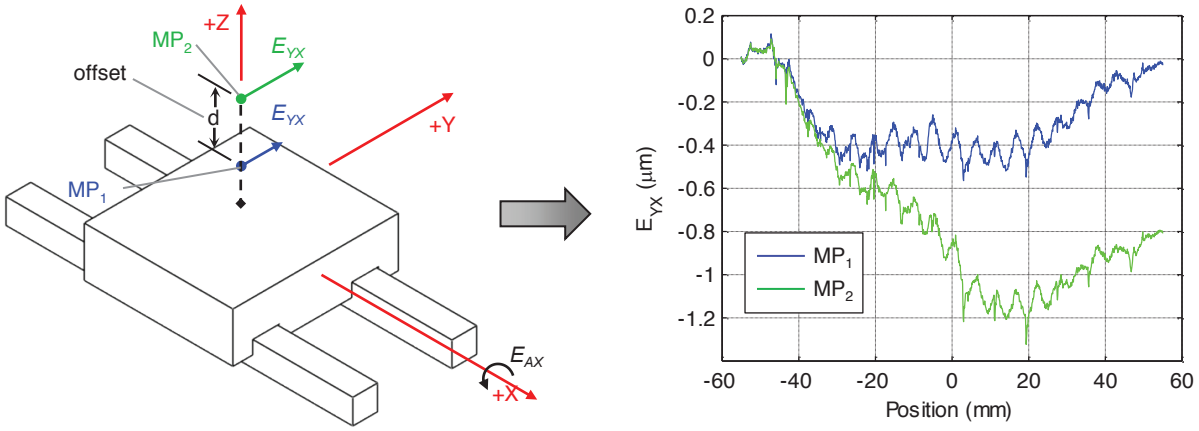

FIGURE 2. Straightness errors of a linear positioning system at two measured points (MP).

errors. Resulting measurement data should then be transformed to represent the straightness errors at the functional point of the intended application.

Representing the straightness of a single axis positioning system as the measured motion of a point rigidly attached to the moving element (i.e., constant with respect to the axis coordinate frame) may be beneficial for the user when comparing positioning systems. Such available data can be employed by the user to simulate the straightness performance for different applications having different functional points.

General Measurement Setup

The two most common methods for measuring straightness include measurement of a straightness reference (straightedge) by a displacement sensor (e.g., capacitance sensor) and use of a laser straightness interferometer consisting of a Wollaston prism and a straightness reflector. The equipment and method chosen should reflect the expected performance of the positioning system and the results of a test uncertainty evaluation [7]. Reversal procedures can be used to further limit the uncertainties due to straightedge errors. With either method, straightness can be determined by measuring with a fixed or moving sensor setup (Figures 3 and 4). Ideally, the setup chosen should reflect how the positioning system is used in the final application.

Moving Sensor Setup

In moving sensor setups (Figure 3), the displacement sensor or prism is attached to the traversing element of the positioning system (e.g., carriage) and measures with respect to a stationary straightedge or straightness reflector fixed to the base of the positioning system. With these types of measurements, the location of the sensor (i.e., sensing surface) or prism represents the location of the measured point. Throughout the measurement, the location of the measured point with respect to the axis coordinate frame is constant and the resulting measurement data represents the straightness of the point's trajectory. It should be noted that displacement sensors with sensor cables attached may experience false readings due to cable movements. Cable management should be considered or a fixed sensor setup eliminating cable movements may be used.

Fixed Sensor Setup

In fixed sensor setups (Figure 4), the displacement sensor or prism is held stationary (fixed to the base of the positioning system) and measures against a traversing straightedge or reference reflector attached to the moving element of the positioning system. With this type of measurement setup, the location of the measured point with respect to the axis coordinate frame is not constant and varies as a function of axis position. If the user wishes to represent the measured data as the straightness of a single measurement point (i.e., identical to the moving sensor measurement), then a transformation must be performed on the data. A transformation, in turn, requires an additional measurement of the appropriate angular positioning errors.

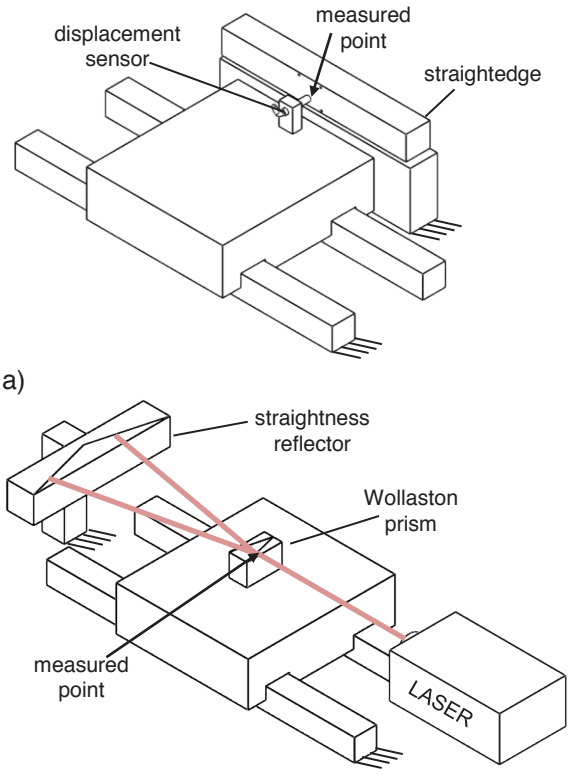

FIGURE 3. A schematic illustrating moving sensor measurement setups; a) displacement sensor measuring against a straightedge artifact b) straightness interferometer using a Wollaston prism.

With either measurement setup, the straightedge should be aligned to the axis motion within an appropriate level of alignment

uncertainty and should be supported to minimize deformations along the functional surface.

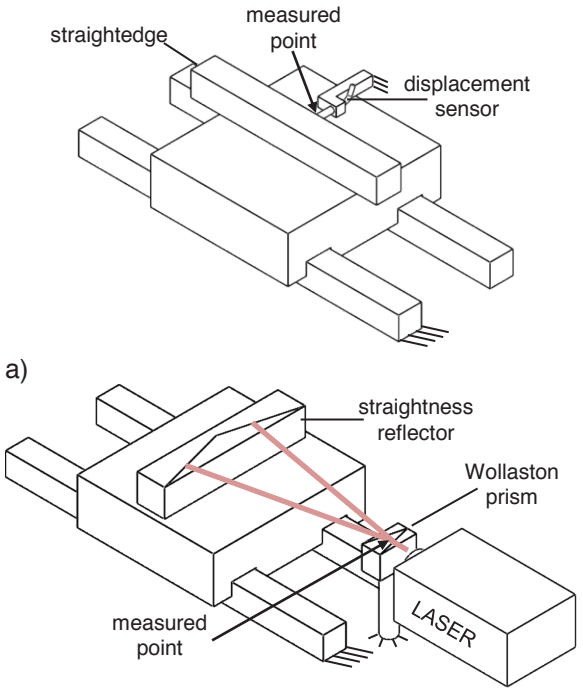

FIGURE 4. A schematic illustrating fixed sensitive measurement setups; a) displacement sensor measuring against a straightedge artifact b) straightness interferometer using a Wollaston prism.

Dynamic Considerations

Because accelerations and decelerations (i.e., drive forces) can affect the dynamic straightness error, the velocity and acceleration regions of the positioning profile should be identified. These regions may be identified by recording the position of the axis encoders during the straightness measurement, directly measuring the position of the axis or measured point with an external sensor, or performing a separate velocity and acceleration measurement for the programmed motion profile. In addition to drive forces, straightness errors may also be affected by gravity or the mass of the payload that the positioning system is intended to carry. For these reasons, the positioning profile, payload mass, and center of payload mass that best represents the intended use of the positioning system should be considered and applied during dynamic straightness measurements.

System Condition

Prior to commencing measurements, the positioning system should be exercised to thermally stabilize the system. At minimum, axis warm-up should include five back-and-forth movements between the first and last target points. The velocity/motion profile and payload employed should be the same profile and payload used for the straightness measurement. If deemed necessary, controller tuning in response to the measurement payload should be considered acceptable as long as the payload is closely related to the payload of the application.

Dynamic Straightness Test Procedure

The test should be conducted at a programmed feedrate and load that best replicates the conditions of the application in which the positioning system is intended to be used. If the positioning system is to be used as a general purpose system or a predefined programmed velocity is not available, then three different tests should be conducted at 10%, 50%, and 100% of the maximum programmable feedrate (velocity). The default traverse distance should consume the maximum allowable distance for the positioning system. A trigger or digital marker should be used to initiate or mark the measurement at the beginning of both positive and negative directions of motion. Any dwells added to the motion profile should be documented.

Procedure

1) Align the measuring equipment with the trajectory of the measurement point under evaluation.

2) Exercise the positioning system following the recommendations described in System Condition.

3) Program the positioning system to continuously move the carriage with the predetermined velocity profile.

4) Set the data acquisition system sampling rate to accurately capture and detect the acceleration and deceleration regions.

5) Document all test parameters.

6) Perform five sets of bidirectional or unidirectional measurements. Record time, axis position, and the corresponding raw displacement readings for straightness.

Dynamic Straightness Analysis

Measurement data should be processed using software. Post-process filtering should be performed on raw measurement data and the type of filter (e.g., low-pass 4th-order Butterworth filter) and cutoff frequency should be reported. All transformations should be performed before straightness calculations.

Full Travel Straightness Analysis

Full travel straightness can be reported as either bidirectional or unidirectional. For each set of measurements, the best-fit line corresponding to the raw or filtered data is calculated using the least-squares method over the full positioning range of the stage. For bidirectional measurements, the best fit line is calculated for either the positive or negative direction of travel, but not both. The minimum distance between two lines enveloping the straightness data (unidirectional or bidirectional) and parallel to the least-squares best-fit line is the straightness value for the measurement and filter condition. See Figure 5. The averages of the five straightness values and the expanded measurement uncertainty are reported as the full travel straightness error of the axis for the specified velocity profile and filter condition.

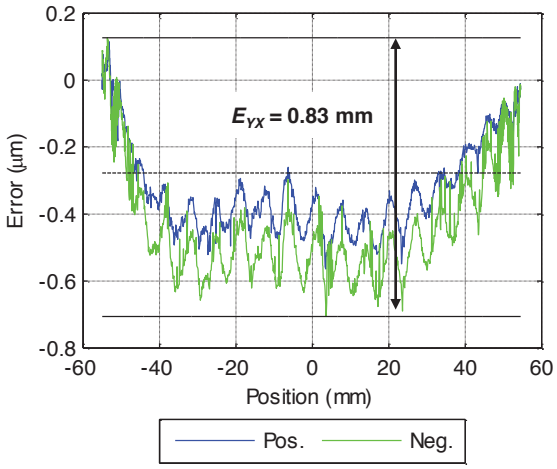

FIGURE 5. Illustration of a unidirectional dynamic straightness plot.

Constant Velocity Straightness Analysis

Constant velocity straightness can be reported as either bidirectional or unidirectional. For each set of measurements, the best-fit line corresponding to the raw or filtered constant velocity data is calculated using the least-squares method. For bidirectional measurements the best fit line is calculated for either the positive or negative direction of travel, but not both. The minimum distance between two lines enveloping the constant velocity straightness data (unidirectional or bidirectional) and parallel to the least-squares best-fit line is the straightness value for the measurement and filter condition. The average of five straightness values and the expanded measurement uncertainty are reported as the constant velocity straightness.

Reporting and Presentation of Results

Dynamic straightness of a positioning system should be identified as either the straightness of full travel for a defined motion/velocity profile or the straightness over a constant velocity region. For either case, a velocity profile plot identifying the acceleration regions should be provided along with a plot of dynamic straightness. In addition, settling times and regions for constant velocity measurements should be identified. A dynamic straightness plot should contain the average of the five measurement runs and the two parallel lines that envelope the straightness data. The straightness values, the filter parameters, the load, and location of the measured point should be reported. An example of a dynamic straightness report for constant velocity straightness is provided as Figure 6.

COMMENTS

A new standard test method for characterizing and specifying the dynamic straightness of linear positioning systems was presented. The work is ongoing and the robustness of the method is being evaluated by characterizing the dynamic straightness for a variety of single axis positioning systems.

REFERENCES

[1] ASME B5.54-2005, Methods for Performance Evaluation of Computer Numerically Controlled Machining Centers, 2005.

[2] ISO 230-1:2012, Test code for machine tools – Part 1: Geometric accuracy of machines operating under no-load or finishing conditions, 2012.

[3] ISO/TR 230-8, Test code for machine tools – Part 8: Vibrations, Technical Report, 2010.

[4] Fesperman R, Brown N, Elliott K, Ellis J, Grabowski A, Ludwick S, Maneuf S, O'Connor B, Woody S, Methods for Performance Evaluation of Single Axis Positioning Systems: A New Standard, Proceedings of the ASPE Annual Meeting, 2013.

[5] Miller J, Hocken R, Ramanan V, Feng Q, Foundation for Dynamic Metrology of Machine Tools, Proceedings of the ASPE Annual Meeting, 1999.

[6] Bryan J, The Abbe' Principle Revisited: An Updated Interpretation, Precision Engineering, 1979.

[7] ISO/TR 230-9:2005E, Test code for machine tools – Part 9: Estimation of measurement uncertainty for

machine tool tests according to series ISO 230, basic equations, 2005.

Dynamic Straightness Test Report

Date: 8/5/2013 Time: 17:00 Test ID: T1000

Purpose: Interim

Positioning System Identification

Manufacturer: ABCD Model: N200 Serial Number: 12345

Test Setup:

Direction of Motion:	X
Measurand:	Y
Measurement Type:	Fixed Sensor
Equipment Class:	Straightedge
Payload:	375 g
Measurement Point (MP):	(0,0,25) mm

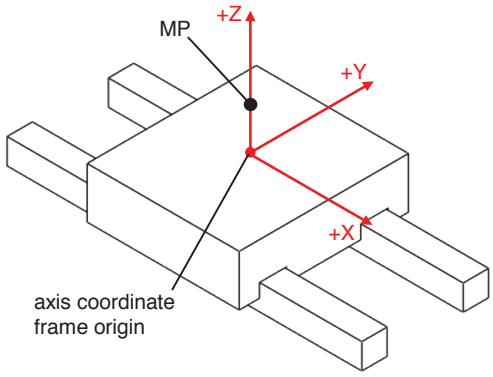

Programmed Velocity Profile

Type: Trapezoidal Acceleration: 25 (mm/s^2) Velocity: 25 (mm/s)
Travel: 110 mm

Analysis
Filter: Yes Type: Low Pass 4th-order Butter Bandwidth: 100 Hz

Results

Constant Velocity Straightness

$E_{YX}(\uparrow)$	345	±	55	nm
$E_{YX}(\downarrow)$	449	±	55	nm
$E_{YX}(\uparrow\downarrow)$	486	±	55	nm

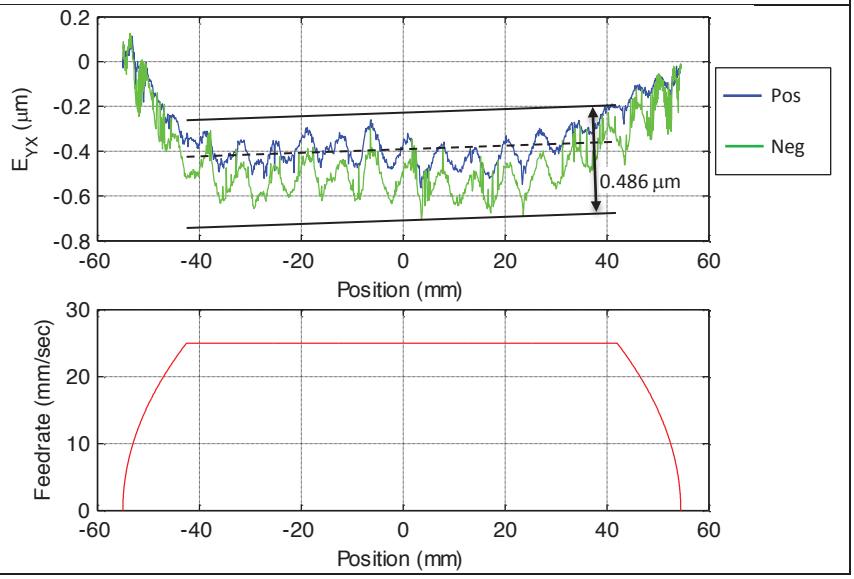

Velocity: 25.0 ± 0.1 mm/s

#	Time (sec)	Position (mm)
1	1.00	-55.0
2	1.00	-42.5
3	4.40	42.5
4	5.40	55.0

FIGURE 6. Example of a dynamic straightness report.

PROGRESS ON DEFINING STANDARD TESTS FOR QUANTIFYING SERVO SYSTEM TUNING

Stephen J. Ludwick[1]
[1]**Aerotech, Inc.**
Pittsburgh, PA, USA

INTRODUCTION

This document proposes standard tests for quantifying servo system behavior in motion control systems. It is part of a larger body of work under consideration for use in a new standard for the performance evaluation of precision positioning systems. Point-to-point positioning times, in-position jitter, and dynamic stiffness are all directly influenced by servo tuning algorithms. In addition, servo system robustness to parameter changes is critical in practice, but not always quantified. Users and Suppliers may discuss *bandwidth,* but this is an ill-defined term as a complete servo system can have multiple values for the bandwidth depending whether one is looking at the ability to follow a reference trajectory or the ability to reject disturbances.

TECHNICAL BACKGROUND

The proposed tests are based on well-established frequency response techniques. These are already extremely popular, well-suited to experimental implementation, allow an end-user to tune a system without having an underlying parametric model, and provide quantitative performance and robustness parameters, namely *crossover frequency, phase margin, and gain margin* [**?**]. There are limitations however. These techniques assume a *linear, time-invariant* system. While this is a useful approximation, most systems are not linear over their entire range of operating parameters. Frequency response techniques become unwieldy (but certainly not impossible) to apply with multivariable systems when several different inputs affect several different outputs simultaneously. Regardless of the limitations, frequency response techniques are useful enough to rely on as a standardized testing technique.

Dynamic systems are often described by the number of inputs and outputs they contain. A motion stage with one motor and one position sensor is described as a single-input, single-output (SISO) system. An active vibration isolation system controlling a payload in six degrees of freedom may have six (or more) actuators, and a dozen or more sensors. This is properly described as a multiple-input, multiple-output (MIMO) system. In many cases, a coupled multivariable system like this can be mathematically reduced through appropriate coordinate transformations to appear as a series of SISO systems. This is quite often the case in practice, and allows familiar single-input, single-output techniques to be applied just as readily to complex systems as to simple ones. The techniques described in this Standard apply most directly to single-input, single-output feedback systems, or to those MIMO systems that can be transformed into SISO equivalents via an appropriate coordinate transformation.

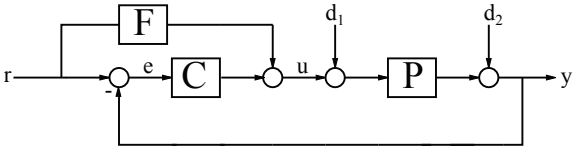

FIGURE 1. The basic control scheme uses by many single-axis positioning systems includes a plant P, a feedforward controller F, and a feedback controller C.

Many single-axis servomechanisms can be adequately represented by three interconnected systems. The *plant* is generally understood to be the mechanics and actuators, the *feedback controller* is the algorithm that modifies the control effort in response to measurements, and the *feedforward controller* applies control effort solely in response to known changes in the reference profile. Figure 1 shows a block diagram of this setup, often called a two degree of freedom controller - as the servo system designer has the ability to modify two different algorithms in order to meet the overall requirements. From this basic block diagram, we will define several useful systems that transform input to output signals.

FREQUENCY RESPONSES

Loop Transmission

The *loop transmission* is the combined response of all systems in a path around the feedback

loop. This measurement captures the response of each system in the chain from an actuator command through the plant response, the state measurement, feedback control algorithm, and finally back to new actuator command. This can be expressed as

$$L = -CP \tag{1}$$

where L denotes the loop transmission in our basic control scheme example. It is likely the single most important measurement to take, as this frequency response is used to quantify stability metrics. In addition, the loop transmission defines the poles (an indicator of dynamic response) for all other closed-loop systems. The loop transmission is closely related to the *open-loop transfer function*, but differs in the important point that measuring the frequency response while the system is under closed-loop control also captures any time delays in the complete feedback loop.

Output Sensitivity

The *output sensitivity* shows the closed-loop servomechanism response to a disturbance added at the output of the plant. This may include floor vibrations. These disturbances cannot be known in advance (as the reference position can be) and so the control algorithm can only respond after the disturbance occurs. The output sensitivity is defined as

$$S = \frac{1}{1 + CP} \tag{2}$$

where again C represents the feedback control algorithm and P is the plant.

Process Sensitivity

The *process sensitivity* shows the closed-loop servomechanism response to a disturbance at the input of the plant. Some examples of these disturbances include noise in the power electronics, cutting forces, or bearing friction. To the extent that these disturbances can be economically modeled and corrected for via feedforward, they should be. However, the process sensitivity characterizes the response to the remaining inputs that are not known in advance. The process sensitivity is defined as

$$S_p = \frac{P}{1 + CP}. \tag{3}$$

Complementary Sensitivity

The *complementary sensitivity* shows the output response to a reference input under only feedback control. Feedforward control is not active in this case. Defining complementary sensitivity as

$$T = \frac{CP}{1 + CP} \tag{4}$$

we can see that the output sensitivity and complementary sensitivity are related through

$$S + T = 1. \tag{5}$$

Closed-Loop Response

The closed-loop response shows the output response to a reference input including both feedback and feedforward control algorithms. It is defined as

$$G = \frac{FP + CP}{1 + CP}, \tag{6}$$

and notice that with perfect (but practically unobtainable) model matching, we can set $F = P^{-1}$ and arrive at $G = 1$ for all frequencies.

FREQUENCY RESPONSE MEASUREMENTS

Most Users and Suppliers will measure the frequency response of a system using commercially-available tools. This could be a standalone *dynamic signal analyzer*, but increasingly takes the form of a software-only tool provided by the manufacturer of the motion controller. The software-only tool may be a necessity as an overwhelmingly digital network may not have available analog inputs to allow a standalone device to be used. The particular tool used to measure the frequency response should be mutually agreed upon between the User and Supplier. Frequency response measurements are part of a rich field of study called system identification, and the interested reader is referred to [**?**] and [**?**] for lower-level details.

REFERENCES

[1] Skogestad S, Postlethwaite I. Multivariable Feedback Control. John Wiley & Sons, Inc.; 1996.

[2] Pintelton R, Schoukens J. System Identification: A Frequency Domain Approach. New Jersey: John Wiley & Sons, Inc.; 2012.

[3] Ljung L. System Identification: Theory for the User. New Jersey: Prentice-Hall; 1999.

METHODS FOR PERFORMANCE EVALUATION OF SINGLE AXIS POSITIONING SYSTEMS: INCREMENTAL STEP TEST

Brian O'Connor[1], Ronnie Fesperman[2], and Serge Maneuf[3]
[1]Aerotech, Inc.
Pittsburgh, PA, USA
[2]National Institute of Standards and Technology (NIST)*
Gaithersburg, MD, USA
[3]Newport Micro-Controle Spectra-Physics S.A.S
Beaune-la-Rolande, France

INTRODUCTION

Many new ultra-precision linear and angular positioning systems are finding their way into emerging technologies. Applications such as semiconductor wafer inspection, laser micromachining, medical device fabrication, and micro assembly all are requiring tighter tolerances and improved positioning performance over previous generations of tools and processes. Measuring and certifying the performance of these types of systems with existing test methods, instrumentation, and standards is challenging at best [1, 2].

Many of these applications rely on a linear or rotary positioning axis to make small incremental moves to perform a task in a process. Currently, no standard test method exists that defines pass/fail criteria for determining the ability of the positioning system to perform these small commanded motions. Furthermore, no standard tests exist that helps quantify the smallest (or minimum) incremental move that a positioning axis is capable of performing. ASME B5.54-2005 outlines a *Least Increment Test* where small steps are performed to illustrate a machine tool's ability to make small incremental moves [3]. However, a quantitative treatment of what constitutes the smallest positioning increment is lacking.

As a result, many suppliers and users of positioning systems have developed their own internal methods and standards for characterizing the smallest increment of movement. In order to address the widespread use of "internal test methods" and "vendor-specific test methods and vocabulary", an effort is underway by members of government, industry, and academia to develop a new positioning standard [4].

This paper will discuss one test that is being proposed as part of this new standards effort – the *Incremental Step Test*. In addition, a proposed procedure for measuring and calculating the *Minimum Incremental Motion* performance parameter or smallest increment that a positioning axis is capable of achieving is also described.

INCREMENTAL STEP TEST

The proposed *Incremental Step Test* is designed to characterize a single axis positioning system's ability to reliably perform a commanded step. The step size is normally relatively small (e.g., 10 nm) and usually reflects the requirements of the precision application in which the axis is intended to be used. During the test, the axis is commanded to perform a series of either unidirectional or bidirectional steps. Based on a given set of criteria (described herein), the axis either passes or fails the test.

General Measurement Setup

An example measurement setup for a linear positioning axis is shown in Figure 1. In this setup, a fixed linear displacement sensor is used to measure the displacement of a target that is rigidly attached to the moving element of the positioning system. The measurement point, ideally, should occur at a point that corresponds to the functional point [5] or location of work of the intended application. The displacement

* No approval or endorsement of any commercial product by the National Institute of Standards and Technology is intended or implied. Certain commercial equipment, instruments, or materials are identified in this report in order to facilitate understanding. Such identification does not imply recommendation or endorsement by the National Institute of Standards and Technology, nor does it imply that the materials or equipment identified are necessarily the best available for the purpose. This publication was prepared by United States Government employees as part of their official duties and is, therefore, a work of the U.S. Government and not subject to copyright.

sensor (e.g., laser interferometer, capacitance sensor, etc.) should be chosen to have adequate resolution, accuracy/linearity, and bandwidth to measure the expected displacements with a low measurement uncertainty. Measurement fixturing should be designed to have a natural frequency (lowest mode) higher than the desired measurement bandwidth.

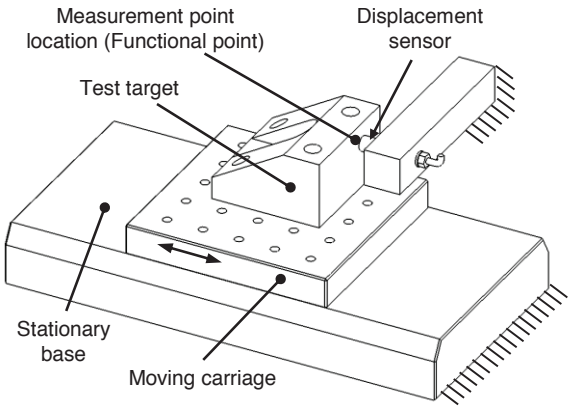

FIGURE 1. Example measurement setup for a linear axis step test showing the measurement of displacement at the functional point.

Incremental Step Test Procedure

As a default, the positioning axis is commanded to perform a minimum of ten positive (forward) and then ten negative (reverse) steps with a constant dwell period at each step. Additional steps may be commanded if deemed necessary to better reflect the end application. Measurements should be performed at a minimum of three locations within the travel range of the positioning axis (e.g., the two extremes of travel and the middle of travel for a linear positioning axis). An example displacement versus time plot for an *Incremental Step Test* performed on a linear positioning axis with a 2.5 nm commanded step size is shown in Figure 2.

Incremental Step Test Analysis

Quantitative step analysis uses performance parameters and variables determined from additional performance tests being developed as part of this standard development effort. These tests include the *In-position Jitter Test* and the *Move and Settle Test* [6]. For the purposes of this paper, these tests and parameters will be briefly described to help aid in the explanation of Incremental Step performance.

In-position Jitter

The proposed definition of *In-position Jitter* is the amount of motion, measured at the functional point, of a positioning axis when no motion is commanded to the axis. The ability of a positioning axis to perform steps that are smaller than the axis *jitter* is of little value to most applications. As a result, the *In-position Jitter* of a positioning axis under servo control must be considered when quantifying the small-step capability. The measurement is performed in the direction of travel while under servo control and employs the same measurement setup as the incremental step test (see Figure 1).

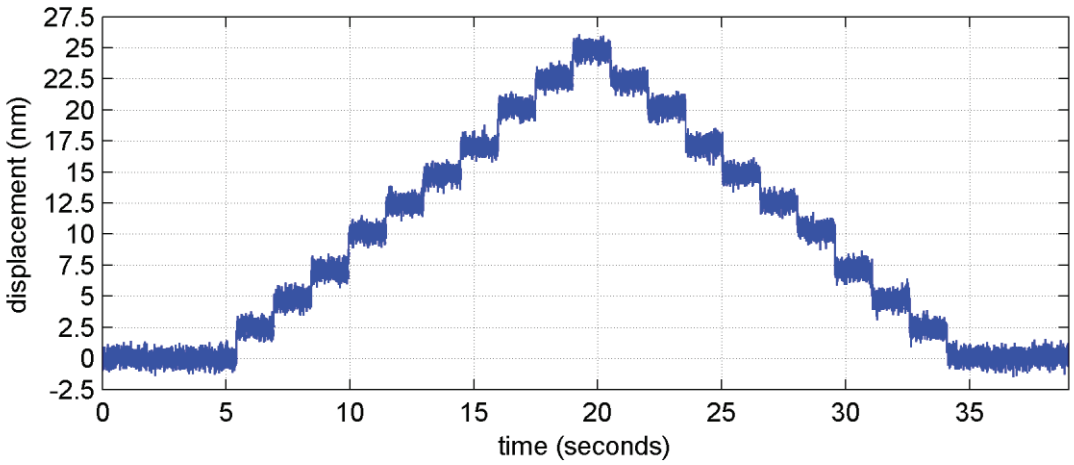

Figure 2. Example time verses displacement plot for an Incremental Step Test performed on a direct-drive linear positioning axis with a 2.5 nm commanded step size.

An example of the results obtained for an *In-position Jitter* measurement of a direct-drive linear stage is shown in Figure 3. The top plot shows the displacement versus time and the bottom shows the cumulative root-mean-square (RMS) value versus frequency of the measured data. In this example, the cumulative RMS value increases rapidly near 500 Hz due to a mechanical resonance present in the positioning axis.

In-position Jitter is reported as a standard deviation, s_{InPos}, over a given time period and measurement bandwidth. The selection of the measurement bandwidth is critical to ensure that the desired dynamics of the positioning axis are adequately captured in the measurement. Also, most measurement and feedback sensor noise increase with increasing measurement bandwidth. Therefore, it is necessary to use only as high as a bandwidth as necessary to capture critical application-specific process dynamics and to keep sensor noise to a minimum.

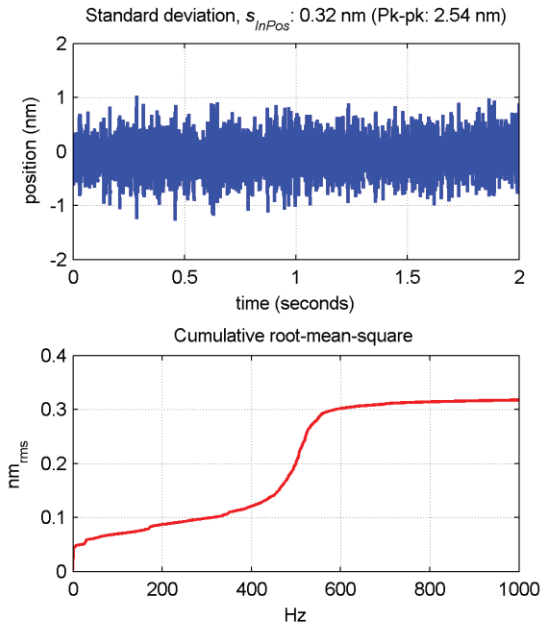

FIGURE 3. Example In-position jitter measurement results for a direct-drive, linear positioning axis.

Because applications can be vastly different, we propose that no single default measurement bandwidth be defined as part of this standard. Instead, it is recommended that the user of the positioning equipment determine and specify a measurement bandwidth based on the sensitivity of the application to motion over a specified spectral range. If the application is unknown or not specified, a measurement bandwidth that adequately captures the dynamics of the stage under test should be used. Such information should be provided by the manufacturer.

In addition, we recommend that the same measurement bandwidth be used for both the *Incremental Step Test* and the *In-position Jitter Test*. The exact details for how the *In-position Jitter* results are used in determining the step capability is defined later in this paper.

Move and Settle Variables

Two temporal variables, the move-and-settle time, t_{ms}, and the average time, t_{ave}, must be defined in order to perform data analysis. The move-and-settle time, t_{ms}, is the amount of time the positioning axis takes to make the commanded step and settle to within a predefined window. Definition of standard move and settle test criteria is currently underway as part of this standards effort [5]. Work performed as part of that effort will be used to define t_{ms}.

An illustration of these two test variables is shown in Figure 4. In order to obtain adequate data at each incremental step, the average time, t_{ave}, shall be at least two times larger than the move-and-settle time, t_{ms}.

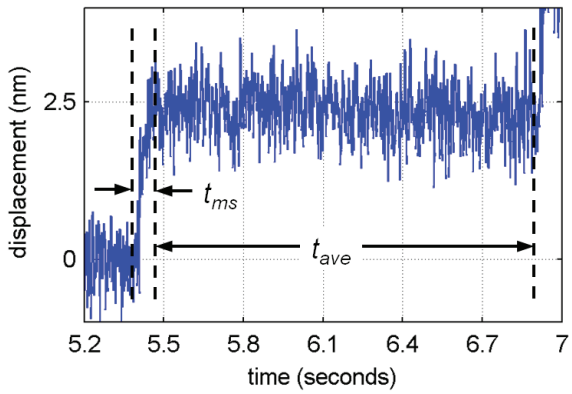

Figure 4. Illustration of the move-and-settle time, t_{ms}, and the average time, t_{ave}.

Incremental Step Test Calculations

In order to analyze the measurement data obtained from the *Incremental Step Test*, a few variables first need to be defined.

The incremental step size, $X_{inc,i}$, is defined as follows:

$$X_{inc,i} = \bar{X}_i - \bar{X}_{i-1} \quad (1)$$

where

$\bar{X}_i$ = mean step position of the *i*th step,
$\bar{X}_{i-1}$ = mean step position of the *(i-1)*th step.

The mean step positions are obtained by averaging the data over time period, t_{ave}. The sample mean, $\bar{X}_{inc}$, and sample standard deviation, s_{inc}, of the incremental step sizes are calculated for the forward (↑) and reverse (↓) directions as follows:

$$\bar{X}_{inc}\uparrow = \frac{1}{N}\sum_1^N X_{inc,i}\uparrow \quad (2)$$

$$\bar{X}_{inc}\downarrow = \frac{1}{N}\sum_1^N X_{inc,i}\downarrow \quad (3)$$

$$s_{inc}\uparrow = \sqrt{\frac{1}{N-1}\sum_1^N\left(X_{inc,i}\uparrow - \bar{X}_{inc}\uparrow\right)^2} \quad (4)$$

$$s_{inc}\downarrow = \sqrt{\frac{1}{N-1}\sum_1^N\left(X_{inc,i}\downarrow - \bar{X}_{inc}\downarrow\right)^2} \quad (5)$$

where

N = number of steps performed in each direction = 10 as default

The sample mean and sample standard deviation of the combined forward and reverse steps are calculated as follows:

$$\bar{X}_{inc} = \frac{1}{N_T}\sum_1^{N_T} X_{inc,i} \quad (6)$$

$$s_{inc} = \sqrt{\frac{1}{N_T-1}\sum_1^{N_T}\left(X_{inc,i} - \bar{X}_{inc}\right)^2} \quad (7)$$

where

N_T = total number of steps performed in the test, $N_T = N\uparrow + N\downarrow$

The calculated incremental step sizes, X_{inc}, for the 2.5 nm Incremental Step Test data example (shown in Figure 3) are shown in Figure 5. Other variables used in the analysis for the 2.5 nm step example are shown in Table 1.

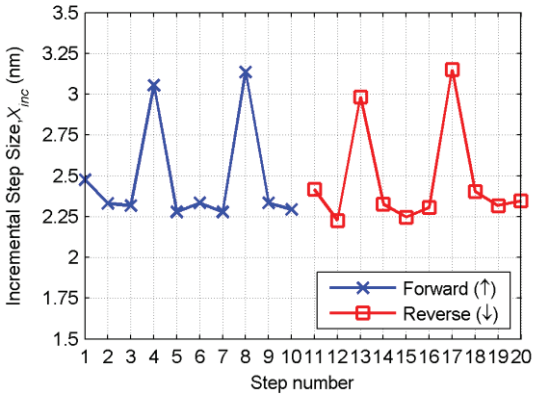

Figure 5. Incremental step sizes, X_{inc}, calculated from the 2.5 nm commanded incremental step test example.

TABLE 1. Step variables calculated from the 2.5 nm incremental step data shown in Figure 3.

s_{InPos}	0.41 nm
$\bar{X}_{inc}\uparrow$	2.48 nm
$s_{inc}\uparrow$	0.33 nm
$\bar{X}_{inc}\downarrow$	2.48 nm
$s_{inc}\downarrow$	0.32 nm
$\bar{X}_{inc}$	2.48 nm
s_{inc}	0.32 nm

Unidirectional Incremental Step Criteria

In order to determine if the axis is capable of performing the commanded step in a unidirectional manner, the following pass/fail criteria is proposed:

Criterion A1 – Four times the standard deviation of the In-position Jitter must be less than the commanded incremental step size:

$$4 \cdot s_{InPos} < X_{CS} \quad (8)$$

where X_{CS} is the incremental commanded step size. For this test criterion, the In-position Jitter is measured for a minimum of 250 msec and a maximum of 2 seconds.

Criterion A2 – The difference between the sample mean of the forward direction incremental step sizes and the incremental commanded step size must be less than 5% of the incremental commanded step size:

$$\frac{|X_{CS} - \bar{X}_{inc}\uparrow|}{X_{CS}} < 0.05 \quad (9)$$

Criterion A2 ensures that the average of all steps taken is reasonably close to the commanded step size.

Criterion A3 – Four times the standard deviation of the forward direction incremental step size must be less than the incremental commanded step:

$$4 \cdot s_{inc} \uparrow < X_{CS} \qquad (10)$$

Criterion A3 ensures that the measured incremental step sizes are bounded. Figure 6 shows a generic illustration of a unidirectional incremental step test that passes both Criteria A2 and A3.

Bidirectional Incremental Step Criteria

In order to determine if the axis is capable of performing the commanded step in a bidirectional manner, the following pass/fail criteria is proposed:

Criterion B1 – Same as Criterion A1.

Criterion B2 – The maximum sample mean of the forward and reverse direction incremental step sizes compared to the incremental commanded step size must be less than 5% of the incremental commanded step:

$$max\left[\left(\frac{|X_{CS}-\bar{X}_{inc}\uparrow|}{X_{CS}}\right),\left(\frac{|X_{CS}-\bar{X}_{inc}\downarrow|}{X_{CS}}\right)\right] < 0.05 \qquad (11)$$

Criterion B3 – Four times the maximum standard deviation of the forward and reverse direction incremental step sizes must be less than the incremental commanded step:

$$4 \cdot max(s_{inc}\uparrow, s_{inc}\downarrow) < X_{CS} \qquad (12)$$

If the measured results meet the unidirectional criteria and do not meet the bidirectional criteria, an additional unidirectional test is performed in the opposite direction as the first test to ensure that the unidirectional criteria are met in both directions when the axis is free from any backlash or machine hysteresis.

One likely cause of failure to meet the bidirectional criteria is the presence of a reversal error caused by backlash or hysteresis in the drive mechanism. This reversal error can be very large compared to the commanded step size and would require many steps in the reverse direction to completely eliminate the error. Therefore, a test is proposed that will attempt to quantify this reversal error. This test is proposed as the Incremental Step Reversal Error Test.

Incremental Step Reversal Error Test

To determine the Incremental Step Reversal Error, alternating successive steps starting at a step size much larger than the commanded incremental step are performed as illustrated in Figure 7.

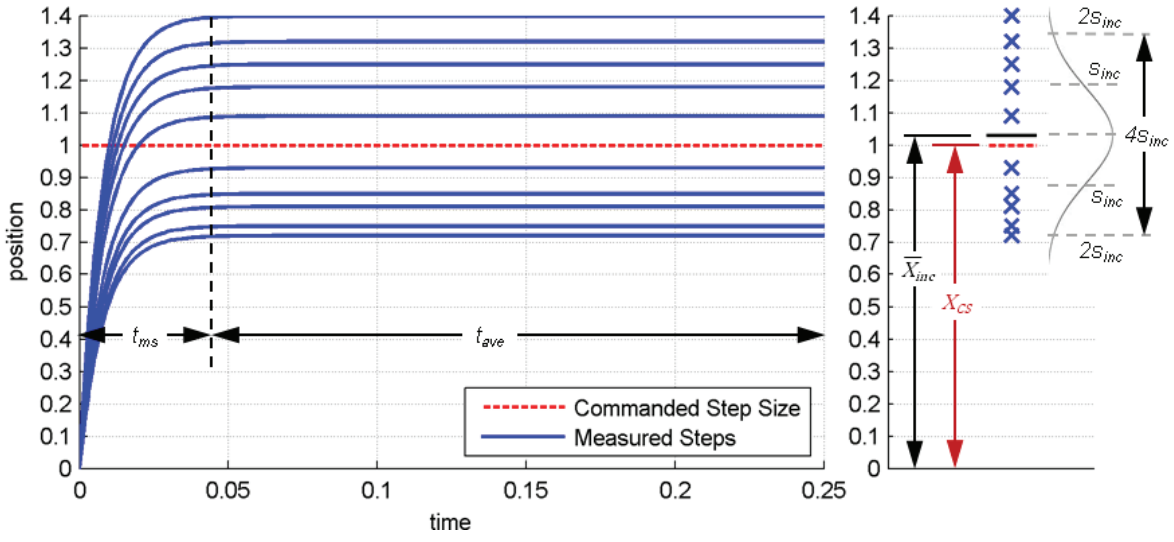

*Figure **6**. Illustration of Criterion A2 and A3 for determining if a positioning axis passes or fails an Incremental Step test.*

Theoretically, the measured position will differ from the commanded position by the reversal error value. However, due to hysteresis and other nonlinearities that could be present at these small step amplitudes, the reversal error must be carefully defined. In order to deal with these other error sources, the Incremental Step Reversal Error, B_{inc}, is proposed as ½ of the commanded incremental step size for which the step error equals 50% of the commanded incremental step size:

$$B_{inc} = \frac{X_{CS,i}}{2} \text{ when } \frac{|X_{CS,i} - X_{inc,i}|}{X_{CS,i}} = 0.5 \qquad (13)$$

where $X_{CS,i}$ is the commanded incremental step at the i^{th} step.

Upon analysis of the results of this test, if the relative step error is greater than 50% for all steps taken, then the starting step size chosen was not large enough. The starting step size is increased and the test repeated until a step error of 50% of the step size is achieved.

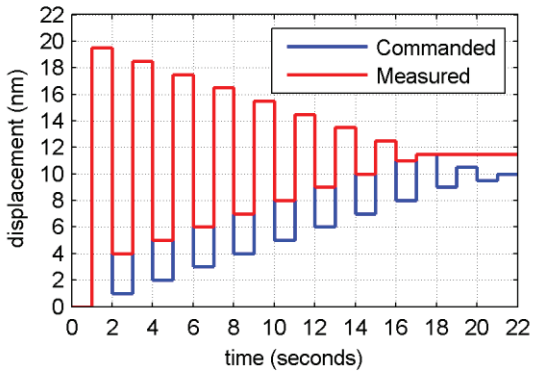

Figure 7. Successively alternating, decreasing steps used to measure the Incremental Step Reversal Error.

MINIMUM INCREMENTAL MOTION

The proposed definition for *Minimum Incremental Motion* is "the smallest mechanical incremental step that a positioning axis is capable of reliably performing" and is determined using the same criteria outlined earlier in this paper (A1-A3, B1-B3). Bidirectional Incremental Step tests are performed starting at the machine resolution or $2 \cdot s_{InPos}$, whichever is greater. The step size is increased until the Unidirectional Criteria (A1-A3), at a minimum, are met.

The results of the test are reported as one of the two following scenarios:

1. Unidirectional Minimum Incremental Motion of XX units with an Incremental Step Reversal Error of YY units (where units are the positioning axis units of nm, um, arc-seconds, etc.)

2. Bidirectional Minimum Incremental Motion of XX units (where units are the positioning axis units of nm, um, arc-seconds, etc.)

CONCLUSIONS

This paper presents proposed test methods for quantifying the small step capability of a positioning axis in order to encourage feedback from interested parties.

FUTURE WORK

An effort is underway to test a variety of positioning axes using the methods described in this paper. Future work consists of continued testing to support the methods and criteria presented.

In addition, detailed uncertainty analysis methods are being developed for this test to aid the users and suppliers of positioning equipment in quantifying the measurement uncertainty.

REFERENCES

[1] Fesperman R, Donmez M, Moylan S, Ultraprecision Linear Motion Metrology, Proceedings of the ASPE Summer Topical Meeting, 2010; 49: 103-108.

[2] Fesperman R, Donmez M, Moylan S, Ultraprecision Linear Motion Metrology of a Commercially Available Linear Translation Stage, Proceedings of the ASPE Annual Meeting, 2011; 52: 81-84.

[3] ASME B5.54, 2005, Methods for Performance Evaluation of Computer Numerically Controlled Machining Centers, 2005.

[4] Fesperman R, Brown N, Elliott K, Ellis J, Grabowski A, Ludwick S, Maneuf S, O'Connor B, Woody S, Methods for Performance Evaluation of Single Axis Positioning Systems: A New Standard, Proceedings of the ASPE Annual Meeting, 2013.

[5] ISO 230-1:2012, Test code for machine tools – Part 1: Geometric accuracy of machines operating under no-load or finishing conditions, 2012.

[6] Ellis J, Ludwick S, Fesperman R, Methods for Performance Evaluation of Single Axis Positioning Systems – Move and Settle, Proceedings of the ASPE Annual Meeting, 2013.

HOLE SEQUENCE OPTIMIZATION FOR MINIMUM TIME 5-AXIS ON-THE-FLY LASER DRILLING

Ammar A. Alzaydi[1], Kaan Erkorkmaz[1], Amr Elfizy[2], and Serafettin Engin[2]
[1]Mechanical and Mechatronics Engineering, University of Waterloo
Waterloo, Ontario, Canada
[2]Pratt & Whitney Canada, Longueuil, Quebec, Canada

INRODUCTION

On-the-fly laser drilling offers advantages over percussion drilling. In percussion drilling, a series of shots are fired to generate each hole while the part is stationary, followed by repositioning. During on-the-fly drilling, the part is in continuous motion while the laser fires one shot at a time at each hole and the motion repeats until all holes are formed. This results in:

- Better material properties and feature quality; due to reduced thermal loading;
- Smoother axis motion, which reduces vibrations induced onto the laser optics;
- Less downtime for optics realignment;
- Higher productivity, as motion 'smoothness' can be translated into higher process speed.

Our earlier work had focused on developing time-optimal trajectories for 5-axis on-the-fly laser drilling, with application to gas turbine combustion chamber panels [1 - 3]. The machine tool; and hole locations and orientations for a sample part, are shown in Figure 1 and Figure 2. For a pre-defined hole sequence [4], trajectories were computed that minimize the constant laser pulsing period (T), while ensuring that the axis velocity, acceleration, and jerk limits are limited. The orthogonal component of the part velocity with respect to the beam, at the drilled hole location, was also limited, in order to contain the hole elongation (Figure 3).

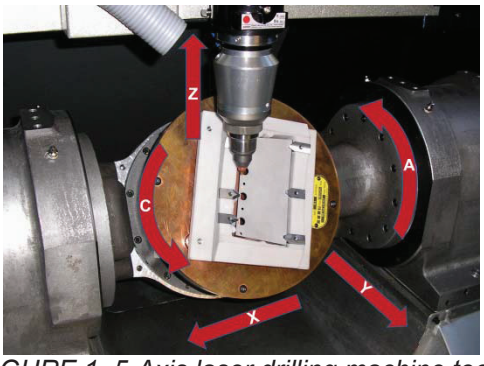

FIGURE 1. 5-Axis laser drilling machine tool.

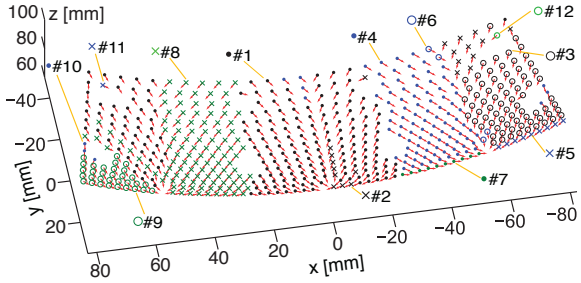

FIGURE 2. Hole locations and orientations.

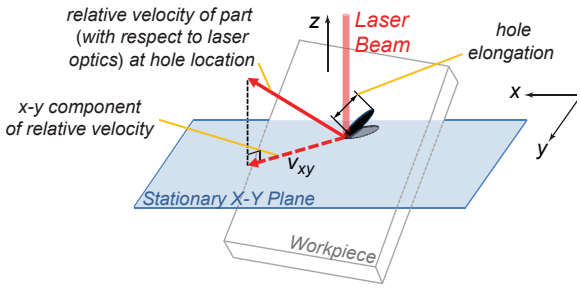

FIGURE 3. Hole elongation due to part motion.

It was determined that improving the sequence at which the holes are drilled is crucial to achieving further productivity. For a part with M holes, this means $M!$ combinations, which becomes very difficult to compute after $M > 11$. While there is some similarity to the 'traveling salesman' problem, the objective here is not to minimize the total travel distance, but rather the achievable laser pulsing period, T'. Hence, the temporal nature of the 5-axis trajectory, and also the machine kinematics, need to be considered in evaluating the objective function.

PROPOSED SOLUTION

For a candidate sequence with N holes, the proposed solution uses a closed curve cubic spline to approximate the potential final trajectory, which would be optimized according to [1, 2]. Simulation studies conducted for large random sets have shown strong correlation between the two trajectories, with the final optimized profile achieving 20-30% shorter time.

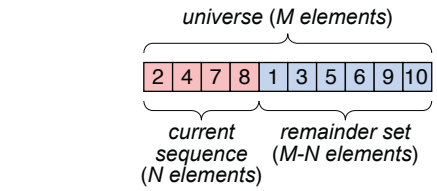

FIGURE 4. Data structure (for M = 10 points).

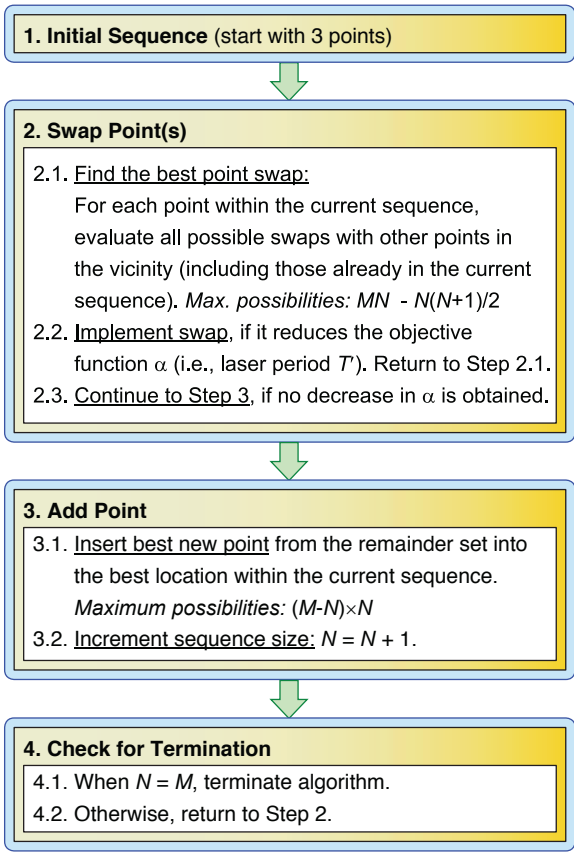
1. Initial Sequence (start with 3 points)
2. Swap Point(s)
2.1. Find the best point swap:
For each point within the current sequence, evaluate all possible swaps with other points in the vicinity (including those already in the current sequence). Max. possibilities: MN - N(N+1)/2
2.2. Implement swap, if it reduces the objective function α (i.e., laser period T'). Return to Step 2.1.
2.3. Continue to Step 3, if no decrease in α is obtained.
3. Add Point
3.1. Insert best new point from the remainder set into the best location within the current sequence.
Maximum possibilities: (M-N)×N
3.2. Increment sequence size: N = N + 1.
4. Check for Termination
4.1. When N = M, terminate algorithm.
4.2. Otherwise, return to Step 2.

FIGURE 5. Proposed optimization algorithm.

Thus, the cubic can be used as a good initial guess. It is C^2 and is solved by initially assuming a unit laser pulsing period (T = 1 s); resulting in a system of N linear equations. The actual achievable laser period T' is then computed by scaling the spline in time by α, so that all 5-axis constraints for velocity, acceleration, jerk, and hole elongation hold, and at least one of the kinematic profiles reaches its limit once.

IMPLEMENTATION RESULTS

Considering the data structure in Figure 4, the sequence optimization algorithm has been developed as shown in Figure 5. While the global optimum is not guaranteed, a local optimum is. The implementation was tested for several hole patterns, including those found in combustion chambers. An intuitive example is shown in Figure 6, which demonstrates the cycle time improvement for a simple grid.

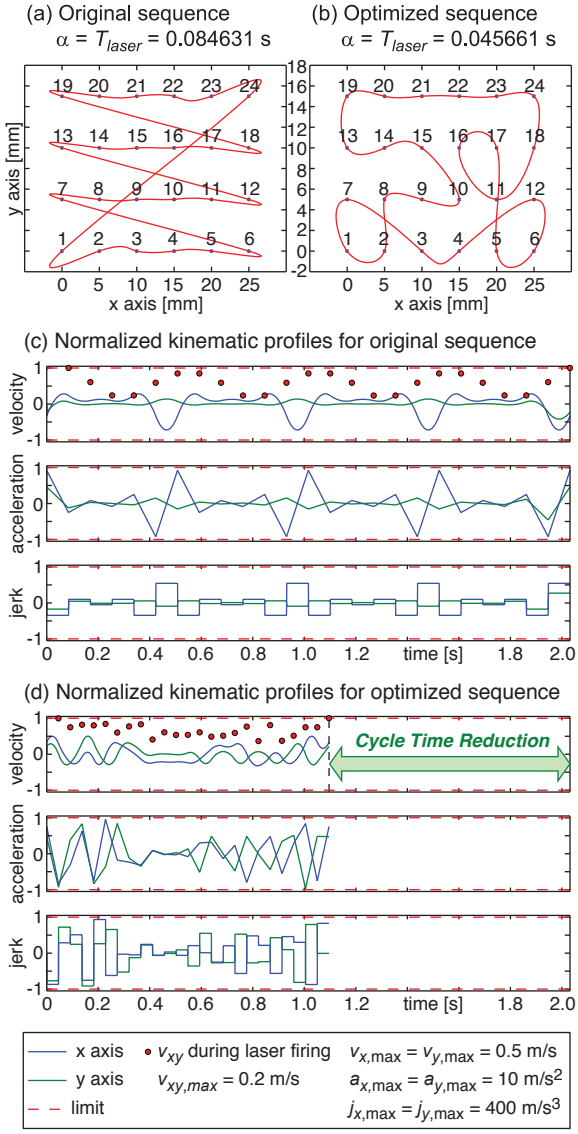

FIGURE 6. Sample implementation result.

This algorithm has been extended to use open cubic splines as well as closed curves. Results for a turbine engine combustion chamber panel with M = 270 holes, sequenced as an open cubic spline, is shown in Figure 7. It should be noted that the machine kinematic limits considered and process cycle times are different than those of the real process, and result presented is only exemplary for demonstrating the potential improvement that can be gained through better hole sequencing.

It is apparent that the sequencing algorithm produced an optimized (cleaner) trajectory

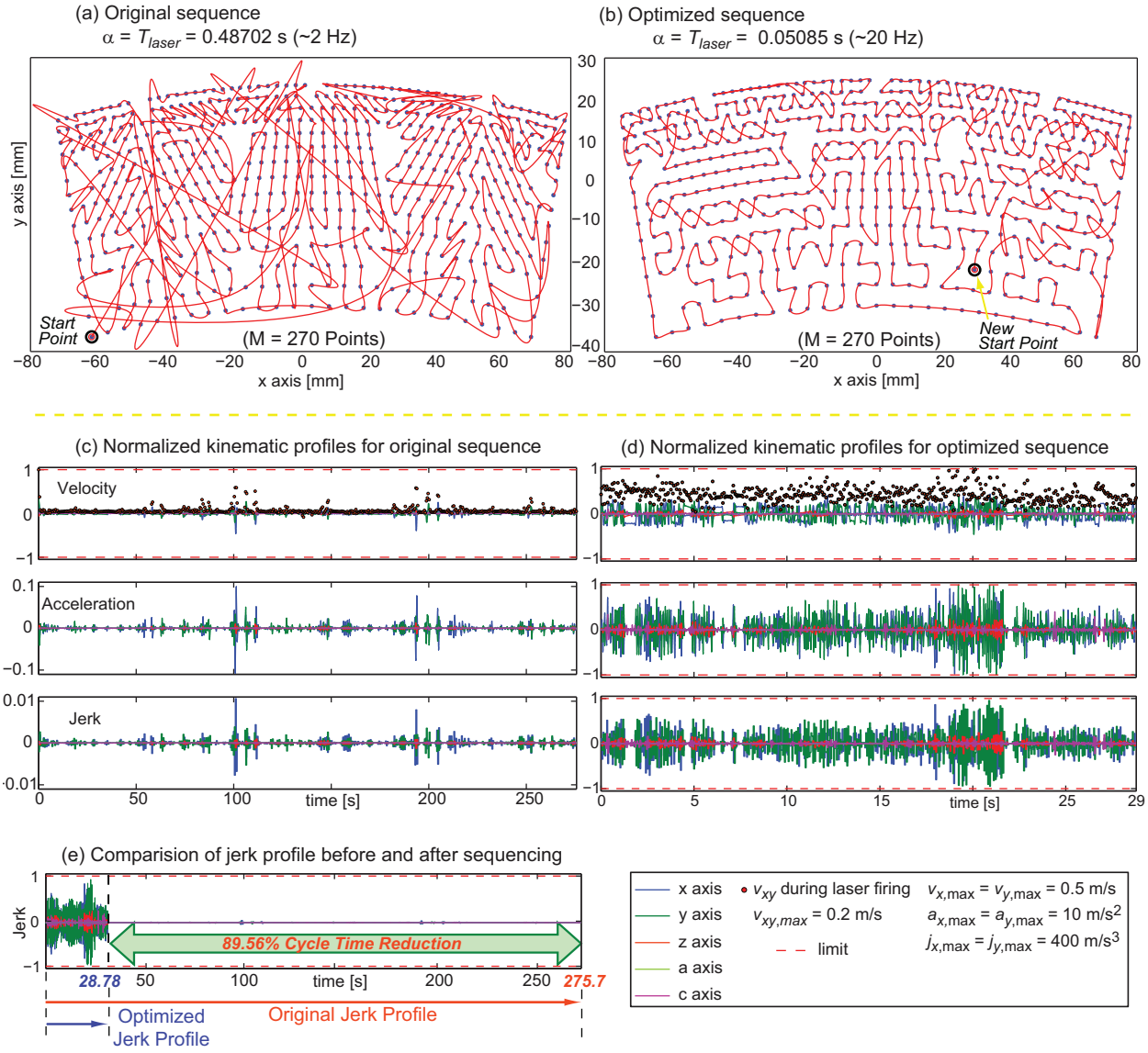

FIGURE 7. Actual turbine engine combustion chamber panel implementation result.

through the set of given holes. The new starting point is different. The total cycle time reduction is from 275.70 to 28.78 seconds (nearly 90% improvement). This would allow the laser drilling frequency to increase from 2 Hz to approximately 20 Hz. This optimized sequence is then to be used as an initial guess for even further cycle time reduction, using the method in [2].

Although the algorithm proved to be very quick and efficient when computing optimized sequences for simple parts with <50 points, longer periods of computation time were required for larger sets of points. The total duration of sequence optimization for the simple grid of 24 points in Figure 6 was 1.46 minutes, compared to 535.36 minutes (8.92 hours) for the actual combustion chamber part used in Figure 7, which contained 270 points. The simulations were conducted using a 2.50 GHz processor. Future research focuses on improving the computational speed of the sequencing algorithm through additional heuristic rules.

REFERENCES

[1] Alzaydi A, Erkorkmaz K, Elfizy A, Engin S, 2010, Time-Optimal Trajectory Generation for Laser Drilling, Proc. 25th ASPE Annual Mtg., Atlanta, GA, Oct 31-Nov 5.

[2] Erkorkmaz K., Alzaydi A., Elfizy A., Engin S., Time-Optimal Trajectory Generation for

5-Axis On-the-Fly laser Drilling, CIRP Annals – Manufacturing Technology, Vol. 60, Issue 1, 2011, P. 411-414.
[3] Elfizy A., High Speed Laser Drilling Machine and Method, US Patent No US7,538,296 B2, May 26, 2009.
[4] Elfizy A., Method for Drilling Holes According to an Optimized Sequence, US Patent 8,362,392 B2 Jan. 29, 2013.

Manufacturing large ultra-precision parts for the New BIPM Watt Balance

Dave Arneson
Professional Instruments Company
Hopkins, Minnesota, USA

ABSTRACT
Because of our unique set of skills and equipment we've developed over the past 60 plus years we were asked recently to manufacture some of the critical parts for the new BIPM Watt Balance currently being built by the Fraunhofer Institute in Aachen.

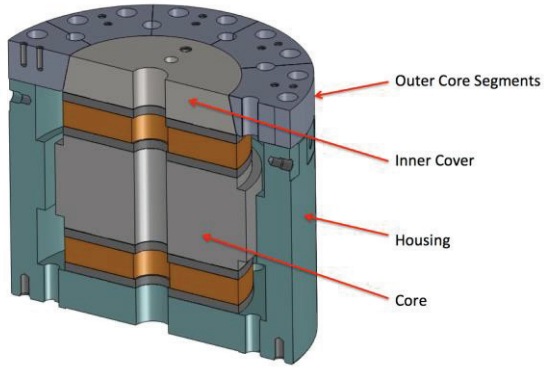

FIGURE 1. BIPM magnet assembly

MACHINING
One of the biggest challenges this job came from the large size and substantial weight of some of the parts. Fortunately, we have an extensive job shop background and so are well equipped to handle the machining of such large pieces.

FIGURE 2. The nature of the project required us to do some of the rough machining ourselves. Here we are roughing out the Housing on a large Monarch engine lathe

FIGURE 3. Our largest CNC machining center, a Haas VF-3, was used to machine details on the outside of the Housing.

FIGURE 4. Our SIP 6A was required to machine some of the features on the inside of the Housing.

GRINDING

We originally developed air-bearing spindles for our own manufacturing, and now use them extensively in our shop. Most of our grinders have been retrofit with our spindles and therefore are capable of achieving extremely high accuracies. The parts for the Watt Balance were some of the most challenging we have ever attempted because of the material, (Supra-50), the size and the precision required.

FIGURE 5. Grinding the Outer Core segments in our Moore #3 Jig Grinder using a belt driven oil hydrostatic Block-Head spindle on a large sine table

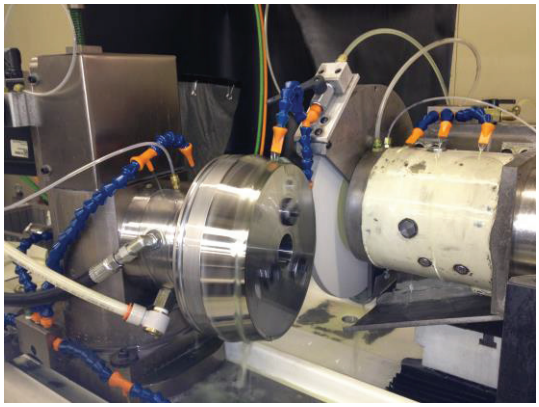

FIGURE 6. Angled section of the Inner Core being ground on our Parker Liberty, CNC cylindrical grinder, equipped with an oil hydrostatic work spindle and an air bearing wheel spindle.

FIGURE 7. Roto-grinding the Housing on a 10R Block-Head in a Brown & Sharpe surface grinder we retrofitted with an air bearing wheel spindle.

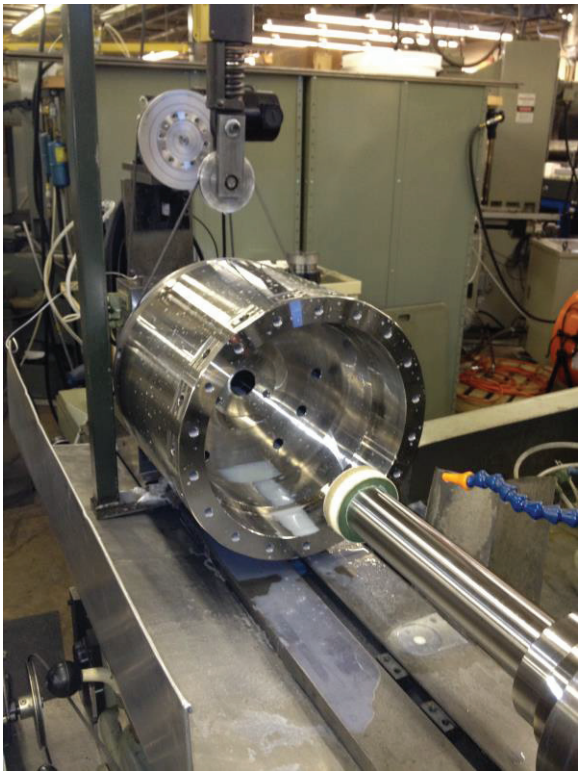

Figure 8. ID grinding the Housing in an old Landis 12x36 cylindrical grinder, we retrofitted with an air bearing wheel spindle and a 10B Block-Head work spindle with a belt lift to allow us to grind the "Housing" which weighs a whopping 91 kg.

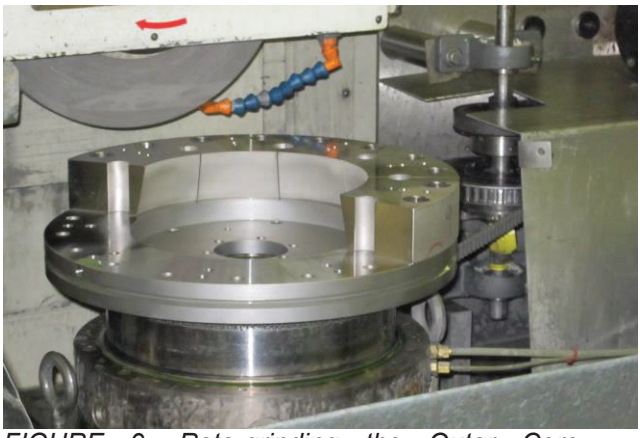

FIGURE 9. Roto-grinding the Outer Core segments on a 10R Block-Head spindle in an Okamoto 1224 DX surface grinder

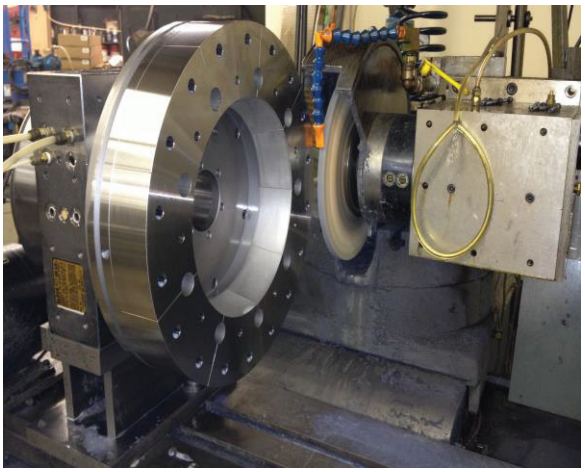

FIGURE 10. Outer Core segments being ground on a Brown & Sharpe #2 cylindrical grinder with air bearing work and wheel spindles

INSPECTION

It is one thing to make the parts right, but inspecting such large precise parts is also quite difficult. We continue to upgrade our inspection capabilities, so we can continue to be able to take on tough jobs such as this one.

FIGURE 11. Inspecting the Outer Core segments in our Zeiss Contura CMM.

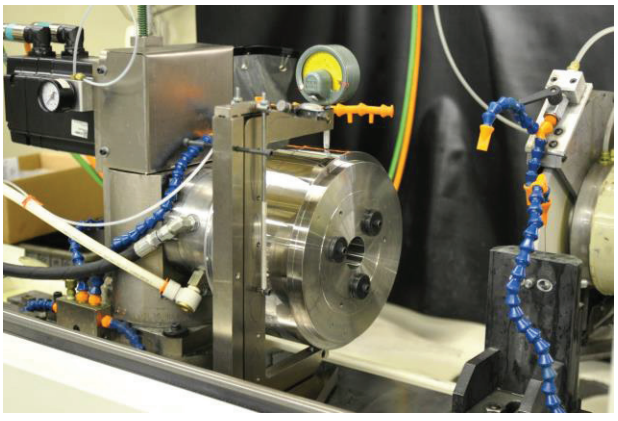

FIGURE 12. Measuring the size of the Core while it is still in the grinder. Using one of our Reed-Mik Comparators and a CEJ ¼ Micron resolution Mikrokator

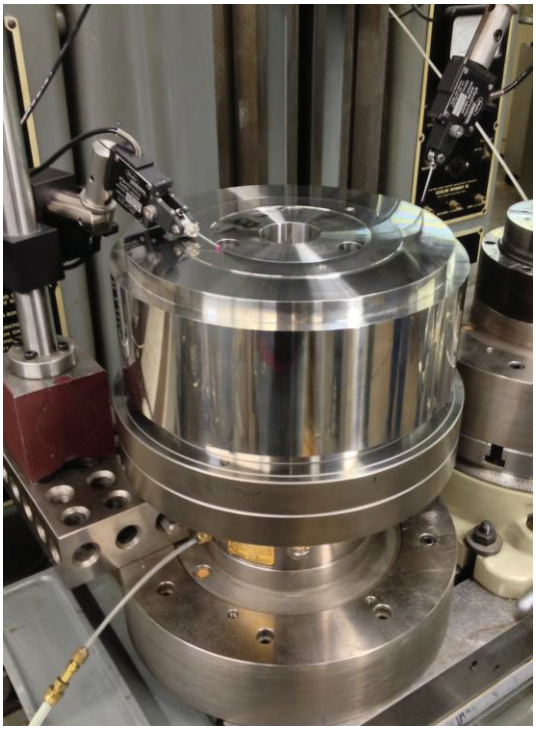

FIGURE 13. Inspecting the Core in our Moore #3 UMM equipped with 4R Block-Head roundness tester using software developed at Penn State's Machine Dynamics Research Laboratory by Professor Eric Marsh and his graduate students

FIGURE 14. Measuring roundness and squareness on the Housing using a Moore UMM equipped with a 4R Block-Head roundness tester and Penn State developed software.

FIGURE 15. To measure the bore diameter of the Housing we used our Zeiss Contura CMM with a VAST XT probe.

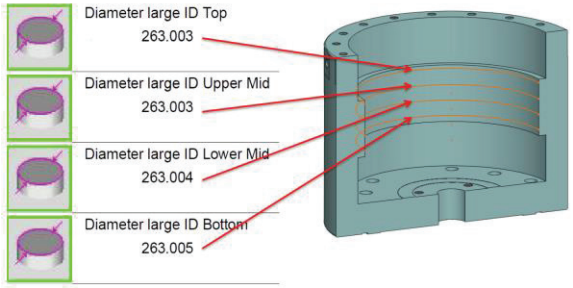

FIGURE 16. Diameter measurements of the Housing from our Zeiss Contura CMM

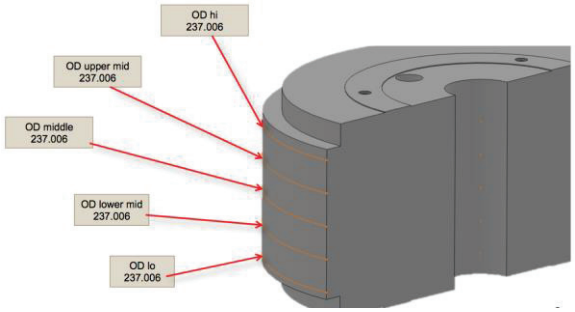

FIGURE 17. Diameter measurements of the Core from our Zeiss Contura CMM

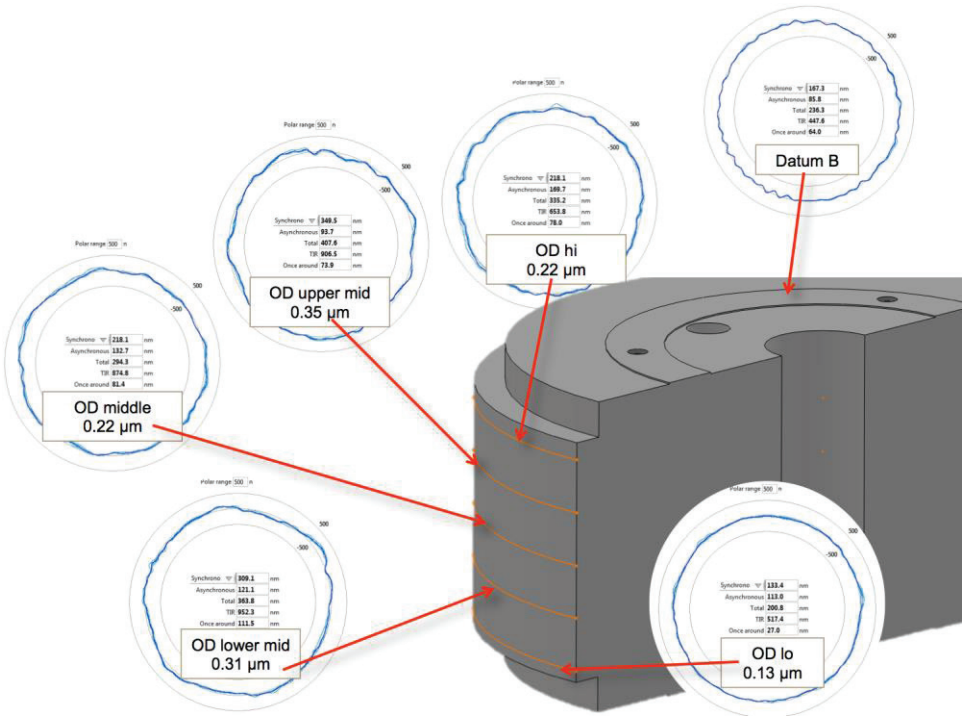

FIGURE 18. Roundness traces at different heights on the outside diameter of the Core. Note that they are all better than 350 nanometers.

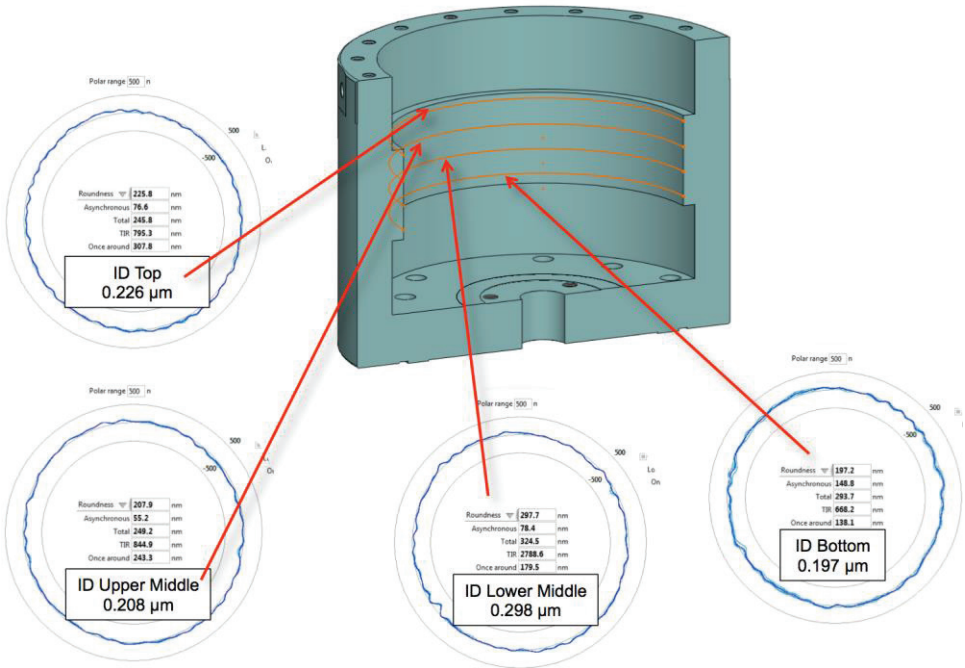

FIGURE 19. Roundness traces at different heights on the inside diameter of the Housing. Note that they are all better than 1/3 of a micron.

CONCLUSION

Parts of this size represent a unique challenge for traditional manufacturing techniques and equipment. Fortunately at Professional Instruments we are used to getting more out of our equipment than it was originally built for. These kind of jobs are very important to take on from time to time as they help us develop new skills and techniques that will help us in our core business; making ultra-precision air bearing spindles. This particular job pushed us to the limit of what is possible but given the great importance of the project it was worth the extra effort.

REFERENCES

[1] Rachel Courtland. (May 2012). The Kilogram, Reinvented. Available from: http://spectrum.ieee.org/consumer-electronics/standards/the-kilogram-reinvented/0

[2] Brumfiel, G. Kilogram Adjustment Courts Controversy. Nature. January 2011.

[3] Weighing a Kilogram. Economist. January 2011.

PERFORMANCE EVALUATION OF A SESSILE DROP DEPOSITION PROCESS

Jacob W. Chesna[12], Ryan I. Rivers[1], Stuart T. Smith[1], Ayman M. Samara[2]
[1]Center for Precision Metrology
University of North Carolina at Charlotte
Charlotte, North Carolina, USA
[2]Assembly and Test Technology Development, Intel
Chandler, AZ, USA

INTRODUCTION

A research platform has been implemented to study the impact of the deposition process on the equilibrated shape of sessile drops. The performance of this platform has been characterized and the results discussed herein. An evaluation of an optimized deposition process will be discussed in the future.

Applications of the study of wetting systems *via* sessile drops include: investigations of face-specific surface chemistry of crystallographic compacts in the pharmaceutical industry [1]; the calibration of optical surface topography measurement instruments [2], the evaluation of adhesion strength in epoxy systems [3], and the study of evaporation characteristics in heat transfer systems [4]. While the impacts of changes to the wetting system on sessile drop shape are typically studied, it is often taken for granted that the sessile drop deposition process has little impact on the measurement of the sessile drop.

For liquid volumes in the milliliter range, the relative influence of changing deposition process parameters are masked by the effects of hydrostatic deflection. However, as the droplet reduces in volume to below the microliter range, the sessile drop deposition process becomes a major influence on subsequent sessile drop shape [5]. To further complicate matters, triple-line pinning can also can also introduce an unpredictable influence on sessile drop shape. Typically dynamic contact angle *via* advancing and receding contact angle experiments are carried out to measure the limits of triple line friction [6]. These methods are often employed by inflating and deflating the drop with a needle, or by tilting the surface on which the drop is deposited. These methods become difficult as volumes reduce below the microliter scale. In the case of the inflation and deflation of the droplet, even the smallest needle that is commercially available approaches the diameter of the sessile drop making the release of the drop from the needle difficult. In the case of tilting the surface, the critical ratio of surface tension and inertial mass approaches the point where deflection due to gravity is negligible leading to unacceptable measurement uncertainty [7].

It is these reasons that, as scales of sessile drops reduce below microliter volumes (or millimeter diameters), the deposition process becomes a major influence on subsequent drop shape. A review of the theoretical considerations in sessile drop deposition has been outlined in the previous work on this project [5].

RESEARCH PLATFORM OVERVIEW

For these studies, a 3-axis positioner has been outfitted with two optical breadboards, one on the *z* axis and one on the stacked *xy* axes that are used to configure subsystem components for process development. A labeled photograph of the machine is shown in *FIGURE 1*.

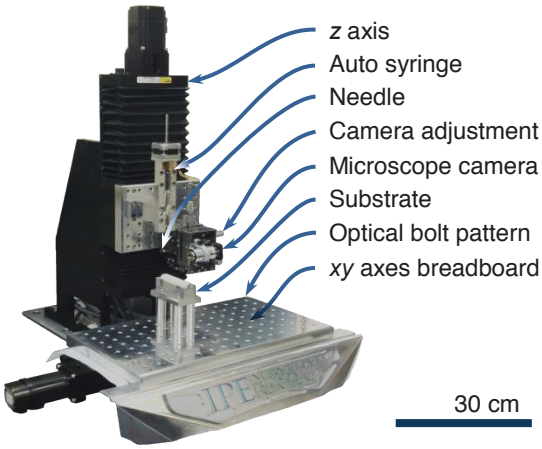

FIGURE 1. Apparatus for the investigation of sessile drop deposition.

Bolted onto the *z* axis breadboard is a custom designed automated syringe, a 3-axis camera adjustment stage, and a microscope camera. Bolted to the *xy* axes breadboard is a specimen platform for the substrate to be affixed.

POSITIONING SYSTEM

The *x, y,* and *z* axis translation stages are Parker model 0816132, 98060210601, and 081-6107-REVD respectively. The axes are driven by Yaskawa Sigma II servo motors and AC motor drivers, models SGMAH-01BAF41 and SGH-02BE respectively. Each motor is close loop controlled *via* a 13 bit AB encoder.

Each axis of the positioning system was evaluated using a LabVIEW™-based control system with synchronized data acquisition. The position of each axis was commanded using the digital IO port of a National Instruments PCI card, model PCI 6052E, and the position of each of the axes was measured using an Optodyne Laser Doppler Displacement Meter (LDDM), model P-210-IATC.

To characterize the performance of the *z* axis, a complex trajectory was commanded, shown in *FIGURE* 2 as "Demand", and the resulting machine position was measured, shown in *FIGURE* 2 as "Measured". As shown, a series of moves was commanded, each with a settling period between each move and each successive move decreasing in length. The objective of this test was to preliminarily characterize a variety of parameters (velocity, acceleration, range and accuracy) in one test.

The data was analyzed and the difference in commanded and measured position after a 1 second settling period was plotted in

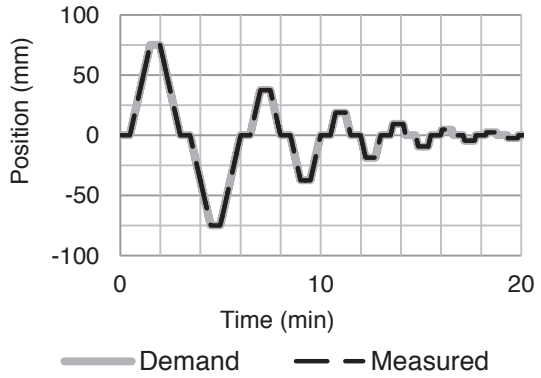

FIGURE 2. Trajectory that was commanded during the characterization of the z axis, and the resulting machine position.

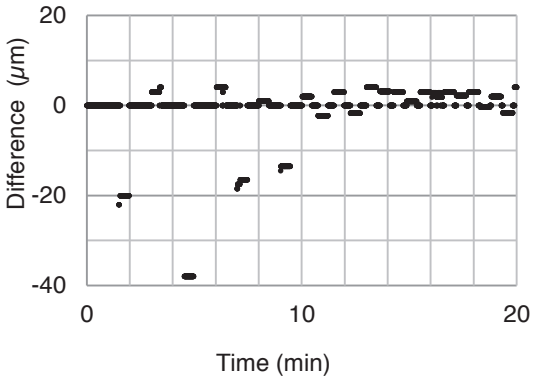

FIGURE 3. Static difference in commanded position and measured position of the z axis.

FIGURE 3. As shown, the maximum static deviation was just less than 40 μm from the commanded position, and the standard deviation of all static data points was calculated to be 9.06 μm using 3836 points distributed over the 28 static locations.

Since the deposition process relies on dynamic positioning in addition to static positioning, all differences between commanded and measured during motion of the stages were recorded. A plot of the difference including all points is shown in *FIGURE* 4. As shown, the dynamic controller error increased as the test progressed. It is not possible to determine the source of the error from this test alone, however the difference is hypothesized to be a result of one of two contributing factors, error due to the servo controller heating up and changing its response characteristics or the result of a less aggressive control response from the servo controller as a result of a lesser change in commanded position. In either case, it is necessary to characterize the dynamic positioning capabilities

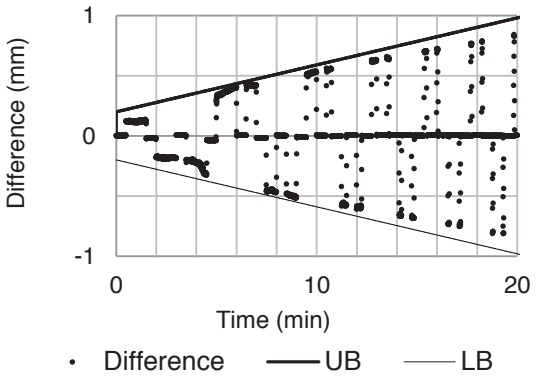

FIGURE 4. Difference in commanded position and measured position of the z axis during characterization test.

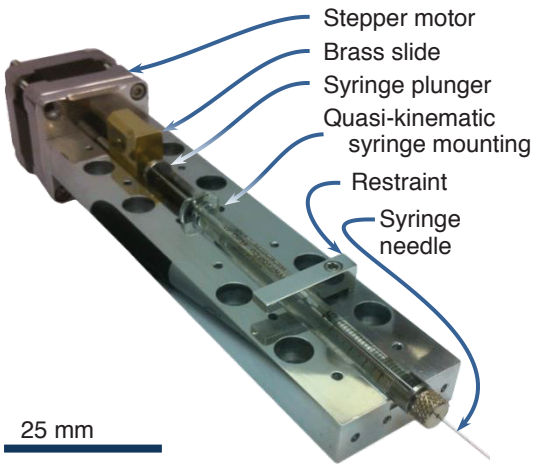

FIGURE 5. Custom auto-syringe for the controlled extrusion and deposition of sessile droplets.

of this machine. From this result, and further testing, the deposition process developed on this machine will account for the errors encompassed within the bounded regions shown in *FIGURE* 4 as "UB", pertaining to the upper bounding of error, and "LB" representing the lower bounds of the measured error.

Being responsible for the approach and retraction of the syringe needle positioning of the *z* axis, is critical to the deposition process. The position of the *x* and *y* axes, only impacting the location of the drop on the substrate, the performance of the *x* and *y* axes is not functionally important and therefore is not discussed.

AUTO-SYRINGE

The auto syringe is comprised of an aluminum body with a dovetail brass slide that is driven with a stepping motor (1 mm pitch and 200 steps/rev). The brass slide has a magnetic

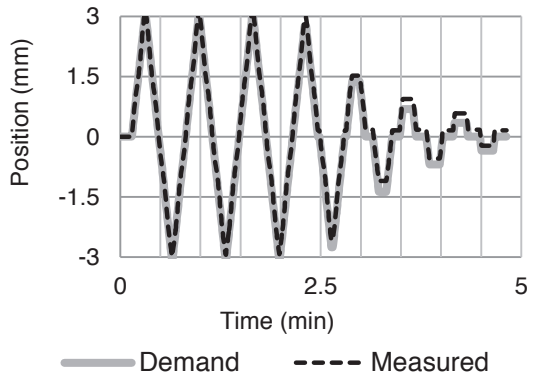

FIGURE 6. Trajectory commanded during the characterization of the auto syringe.

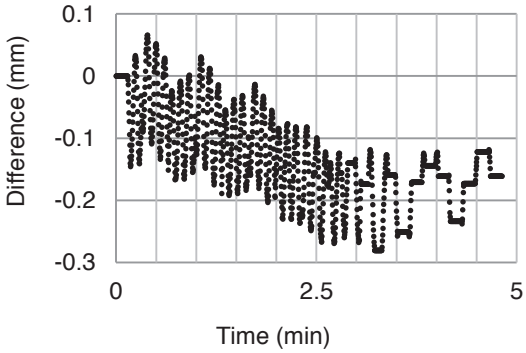

FIGURE 7. Difference in commanded position and measured position of plunger.

interface to fasten to the plunger of the syringe. Syringes are mechanically clamped into a quasi-kinematic mount enabling simple replacement and relocation as necessary. A labeled photograph of the auto-syringe is shown in *FIGURE 5*.

The auto-syringe is controlled using step and direction signals from the control system. The signals are converted into step logic with a Big Easy Driver board, model ROB-10735.

To evaluate the positional control, a retro-reflector was mounted to the syringe plunger and the position was measured with a laser interferometer (Optodyne LDDM). To characterize the positioning capabilities of the plunger the trajectory shown in *FIGURE* 6 as "Demand" was commanded and the resulting position measured, shown in *FIGURE* 6 as "Measured".

FIGURE 7 plots the difference between the commanded position and the measured position. Given that the auto-syringe is driven by a stepper motor with negligible load, the results of the error analysis were as expected with a relatively constant backlash of 0.11 mm and drifts on the order 0.2 mm for the 3 mm scan reversals. For small motion controls, toward the end of this testing, the drift had reduced substantially. This main objective of this test was to confirm the linearity of the system and to determine the minimum incremental movement.

Using the 1441 data points from the 5 minute test, the standard deviation of the difference between the commanded position and the measured position was calculated to be 74.8 μm. Additionally the minimum incremental movement was conservatively estimated to be

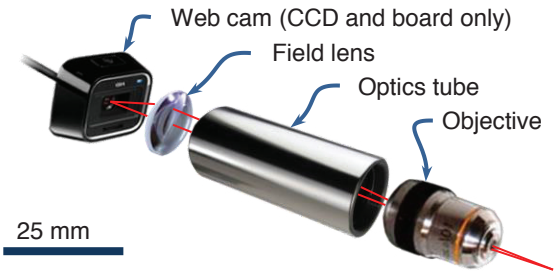

FIGURE 8. Custom microscope camera.

75 μm. Using a Hamilton 2.5 μl syringe, model #62, and using the calculated standard deviation of the error motion as an estimate of uncertainty, both a volumetric deviation and a minimum incremental volumetric change of 9.5 nl can be expected.

IMAGING SYSTEM

A custom microscope camera was developed to enable high magnification with the lens being on a relatively short extension tube. A schematic of the system is shown as *FIGURE 8*. This consists of a Microsoft HD5000 CCD camera (1920×1080), a field lens from a microscope eyepiece (10x), an optics tube, and a microscope objective (typically 20x/0.4 or 40x/0.45).

Using this imaging system a standard deviation of 0.19 degrees. This number was obtained from 5 measurements of the same droplet image with geometry fitted to 20 selection points both on the droplet and its reflection. Due to configuration dependent differences, predominantly, the relative angle between the camera and the plane of the specimen surface, the ability to resolve the contact angle will differ, therefore a more detailed characterization of system performance for geometric measurement has been undertaken and will be reported along with the results from individual data sets.

CONTROL SYSTEM

The main control system for generating translation stage trajectories uses EMC2 software [8], running on a Ubuntu 10.04 operating system. This software interprets G-code, and provides the outputs (direction and step signals) to each of the 4 motion axes. Currently the camera control and image analysis is automated in LabVIEW™ on a separate Windows based computer.

ACKNOWLEDGEMENTS

The Center for Precision Metrology (CPM) for funding this research, and the CPM affiliates for supporting this research.

REFERENCES

[1] Muster T H, Prestidge CA. Application of time-dependent sessile drop contact angles on compacts to characterise the surface energetics of sulfathiazole crystals. Intr. Jour. of Pharm. 2002; Vol **234**, Issue 1-2: 43-54.

[2] Mandal R, Palodhi K, Coupland J, Leach R, Mansfield D. Applications of linear system theory to characterize coherence scanning interferometry. Proc. Os SPIE. 2012; **8430**: 1-10.

[3] Turunen M P K, Laurilla T, Kivilahti J K. E valuation of the surface free energy of spin-coated photodefinable epoxy. Journal of Polymer Science Part B: Polymer Physics. 2002; Vol **40**, Issue 18: 2139-2149.

[4] Mollaet R, Sefiane K, Christy J R E, Veyret D. Experimental and Numerical Investigation of the Evaporation into Air of a Drop on a Heated Surface. Chemical Engineering Research and Design. 2004; Vol **82**, issue 4: 471-480.

[5] Chesna J W, Rivers R I, Smith S T, Her T-H, and Samara A M. Reducing uncertainty of wettability measurements through controlled sessile droplet deposition: Current issues. Annual Proceedings of American Society for Precision Engineering (ASPE) Conference; 2012: 472-475.

[6] Lam C N C, Wu R, Li D, Hair M L, Neumann A W. Study of the advancing and receding contact angles: liquid sorption as a cause of contact angle hysteresis. Advances in Colloid and Interface Science. 2002; Vol. **96**, Issue 1-3: 169-191.

[7] Srinivasan S, McKinley G H, Cohen G H. Assessing the Accuracy of Contact Angle Measurements for Sessile Drops on Liquid-Repellent Surface. Langmuir. 2011; Vol **27**, No. 22: 13582-13589.

[8] Shackleford W P, Proctor F M. Use of open source distribution for a machine tool controller. Proc. SPIE 4191, Sensors and Controls for Intelligent Manufacturing. 2001; **4191**: 19-30.

A STUDY OF MODELLING AND SIMULATION OF SINGLE-POINT DIAMOND TURNING OF MICRO-STRUCTURED PATTERNS ON PRECISION ROLLERS

C.F. Cheung, M.J. Ren, G.B. Xiao, C.H. Mak, L.B. Kong and S. To
Partner State Key Laboratory of Ultra-precision Machining Technology, Department of Industrial and Systems Engineering, The Hong Kong Polytechnic University, Hung Hom, Kowloon, Hong Kong, China

INTRODUCTION

Micro-structured surfaces, such as V-grooves and microlens arrays, are widely used in high value added optical products for enhancing the optical performance of the products, such as collimation, diffusion, focusing, re-direction, brightness enhancement and out-coupling [1]. Rolling imprint lithography is an enabling technology for the mass production of the micro-structured surfaces. For rolling technology, the quality of the manufactured surfaces relies heavily on the geometrical precision of the master roller drum which is normally required to be fabricated with sub-micrometre form accuracy and surface finishing at several nanometers level [1].

Single point diamond turning (SPDT) is an enabling machining technology for the fabrication of micro-structured surfaces [2]. In SPDT, the micro-structures can either be machined by precision replication of the shape of the cutting tool on the workpiece, or cutting by Fast Tool Servo (FTS). However, the machining of the micro-structures on cylindrical surfaces by SPDT is different from traditional face turning. This has imposed a lot of technical challenges in machining. This is particularly true for the large micro-structured rollers of which dimensions are up to 1 meter long and 0.5 meter in diameter. Although much research has been conducted on this subject in recent decades and some commercial roller machining equipments are available in the market [3], research work on the modelling and simulation of the roller machining process is still far from complete.

As a result, this paper presents a study on the modeling and simulation of the micro-structured roller machining process by SPDT. The study is based on the development of a virtual SPDT machine which is able to simulate the machining process. This allows an investigation of the influence of the machining strategy (e.g. the tool path planning, spindle speed, etc.), the geometric error of the machine tool, etc. Based on the extensive computer simulation experiments, the results can be used to optimize the machining strategy in actual machining so as to achieve a good balance between the machining efficiency and the surface quality of the precision rollers. A pilot experimental study has also been conducted to demonstrate the effectiveness of the proposed method.

METHODOLOGY

The proposed study is based on the development of a virtual SPDT machine to simulate the machining process. The virtual SPDT is developed based on a kinematic model and a geometrical error model of the machine tool. It takes into account of the tool path and processing parameters as input to simulate the machining process while the 3D topography of the machined surface is generated by incorporating the influence of the geometrical error of the machine tool and the effect of material swelling of the workpiece. Figure 1 shows a schematic diagram of the conceptual virtual machine.

For machining a specific micro-structured roller, a series of machining strategies are designed in the machining strategy module. For a machining strategy, corresponding NC code and cutting parameters are determined and they are entered into the motion control module so as to generate the trace of the cutting tool. The position of the cutting tool is determined by the kinematic model and the geometrical error model of the machine tool. The 3D surface topography of the machined surface is then generated in Workpiece cutting module. A Finite Element Method (FEM) cutting model is used to estimate the material swelling effect of the workpiece. Finally, the error of the workpiece is determined by comparing the measured results with the designed surface. In this way, an optimal machining strategy can be determined by taking into consideration of machining

efficiency and the surface quality of the machined surface as criteria.

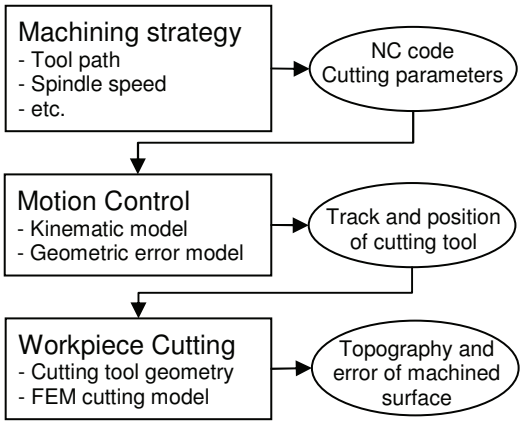

Figure 1: Schematic diagram of the development of the virtual machine

STUDY ON A THREE AXIS DIAMOND TURNING MACHINE

In the present study, the Nanotech 350 SPDT from Moore Ltd. from USA is used to machine the micro-structured roller. Figure 2 shows the schematic diagram of the machine structure of Nanotech 350 SPDT which is composed of three translational stages, i.e. X, Y, and Z stages, and a spindle.

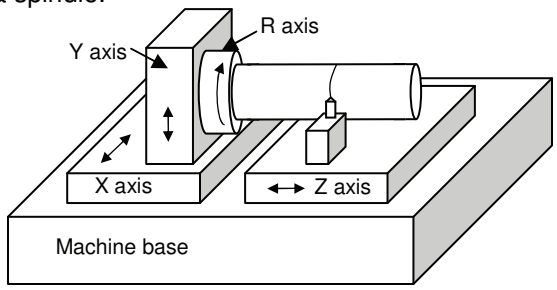

Figure 2: Schematic of the machine structure of Nanotech 350 SPDT

Kinematics Model

As shown in Figure 3, a total of five coordinate frames are constructed to describe the kinematics structure of the machine tool. $C_W=\left[\vec{X}_W,\vec{Y}_W,\vec{Z}_W\right]$ is the world coordinate frame embedded in the machine bed; $C_X=\left[\vec{X}_X,\vec{Y}_X,\vec{Z}_X\right]$ is the moving coordinate frame embedded in the X stage; $C_Z=\left[\vec{X}_Z,\vec{Y}_Z,\vec{Z}_Z\right]$ is the moving coordinate frame embedded in the z stage; $C_Y=\left[\vec{X}_Y,\vec{Y}_Y,\vec{Z}_Y\right]$ is the moving coordinate frame embedded in the Y stage; $C_R=\left[\vec{X}_R,\vec{Y}_R,\vec{Z}_R\right]$ is the moving coordinate frame embedded in the movement of the spindle.

In the present study, the homogeneous coordinate transformation matrix (HCTM) as given in Eq. (1) is used to describe the relative motion between different coordinate frames [4].

$$T=\begin{bmatrix} c(\beta)c(\gamma) & s(\alpha)s(\beta)c(\gamma)-c(\alpha)s(\gamma) & c(\alpha)s(\beta)c(\gamma)+s(\alpha)s(\gamma) & a \\ c(\beta)s(\gamma) & s(\alpha)s(\beta)s(\gamma)+c(\alpha)c(\gamma) & c(\alpha)s(\beta)s(\gamma)-s(\alpha)c(\gamma) & b \\ -s(\beta) & s(\alpha)c(\beta) & c(\alpha)c(\beta) & c \\ 0 & 0 & 0 & 1 \end{bmatrix} \quad (1)$$

where $s(\ )$ and $c(\ )$ are the abbreviation of sine and cosine function; a, b, and c are translational offsets in three axes; α, β, and γ are rotational angles along three axes. Hence, a kinematics model of the machine tool in the machining process can be established by the relative motion between the cutting tool and the workpiece which can be represented by Eq. (2):

$$T_{ZR}=(T_{WZ})^T T_{WX}T_{XY}T_{YR} \quad (2)$$

where $T_{*,**}$ is the HCTM from C_{**} to C_*.

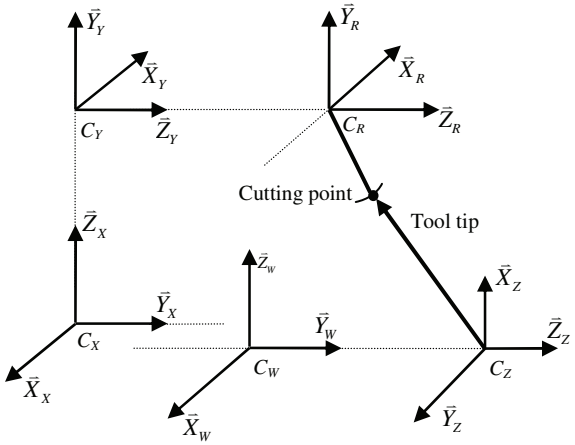

Figure 3: Coordinate frames of the machine tool

Geometrical Error Model

The error of a machine tool is the relative error motions between the cutting tool and the workpiece which can be described by the geometrical error of the moving components in the machine tool. For linear movement, i.e. the three translational moving stages of Nanotech 350, the geometrical error can be divided into six components, including positioning error, two straightness error motions, roll, pitch, and yaw error motions [4]. By taking X stage as an example, with the consideration of geometrical error, the actual HCTM from C_X to C_W can be given by Eq. (3) as follows:

$$RT_{WX}=T_{WX}ET_X^W \quad (3)$$

where

$$ET_X^W = \begin{bmatrix} 1 & -\delta\gamma(x_X) & \delta\beta(x_X) & \delta x(x_X) \\ \delta\gamma(x_X) & 1 & -\delta\alpha(x_X) & \delta y(x_X) \\ -\delta\beta(x_X) & \delta\alpha(x_X) & 1 & \delta z(x_X) \\ 0 & 0 & 0 & 1 \end{bmatrix}$$

$\delta*(x_X)$ is a function which represents the relationship between the error components and the displacement of the X stage.

For rotational movement, i.e. the spindle, the geometrical error can also be described by 6 error components including two radial error motions, one axial error motions, the angular position error , and two tilt error motions. With the consideration of the geometrical error, the actual HCTM from C_X to C_W can be given by Eq. (4) as follows:

$$RT_{YR} = T_{YR} ET_R^Y \quad (4)$$

where

$$ET_R^Y = \begin{bmatrix} 1 & \mathrm{s}(\tilde{\alpha})\delta\beta(\alpha) - \mathrm{c}(\tilde{\alpha})\delta\gamma(\alpha) & \mathrm{c}(\tilde{\alpha})\delta\beta(\alpha) + \mathrm{s}(\tilde{\alpha})\delta\gamma(\alpha) & \delta x(\alpha) \\ \delta\gamma(\alpha) & \mathrm{c}(\tilde{\alpha}) & -\mathrm{s}(\tilde{\alpha}) & \delta y(\alpha) \\ -\delta\beta(\alpha) & \mathrm{s}(\tilde{\alpha}) & \mathrm{c}(\tilde{\alpha}) & \delta z(\alpha) \\ 0 & 0 & 0 & 1 \end{bmatrix}$$

$\tilde{\alpha} = \alpha + \delta\alpha$

Hence, the geometrical error model of the Nanotech 350 machine tool can be established based on the kinematics model and the model equation can be given by Eq. (5) as follows:

$$e = \left| P_{tt} - (T_{ZW} E_{ZW})(T_{XW} E_{XW})^T (T_{YX} E_{YX})^T (T_{RY} E_{RY})^T P_{ct} \right| \quad (5)$$

where P_{ct} and P_{tt} are intended cutting point and the real location of the cutting tool tip.

FEM Cutting Model

Once the position and the orientation of the cutting tool is determined by the geometrical error model, FEM based cutting model is used to generate the topography of the machined workpiece. In the present study, the elasto-plastic FEM simulation are performed. The simulation type is set as Lagrangian incremental, and the Johnson-Cook model is adopted as constitute law [5]. The tool is assumed to be a rigid body while the heat exchange between the cutter and the workpiece is not considered in the present study for simplicity. Two boundary conditions are set during the simulation, including a fixed boundary and a fixed temperature boundary (20°C in this study) in the bottom of the workpiece.

Virtual Machine Tool

Figure 4 shows the virtual machine which is developed based on the kinematic model and geometrical error model of the Nanotech 350 SPDT. The virtual machine is composed of 4 moving components, including 3 translational stages along X, Y, and Z axis, and a rotational stage. It makes use of the NC code such as tool path as input to simulate the motion of each components of the machine tool so as to determine the position and orientation of the cutting tool relative to the workpiece and hence generate the 3D topography of the machined workpiece. Finally, the quality of the workpiece is examined by comparing the simulated results with the design specifications.

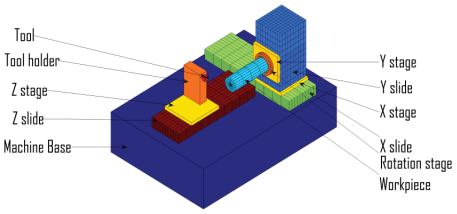

Figure 5: Virtual machine for Moore Nanotech 350 SPDT

EXPERIMENTAL VERIFICATION

To evaluate the validity of the developed virtual machine tool in simulating the surface topography of the micro structured surfaces, a micro V-grooved roller made by Aluminum 6011 is machined by Nanotech 350 ultra-precision machine tool (see Figure 6).The specification of the V-grooves is given in Figure 7.

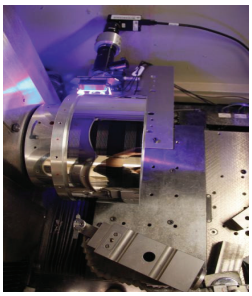

Figure 6: Machining and measurement of micro V-grooves on Nanotech 350.

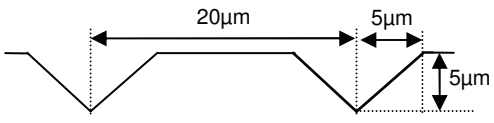

Figure 7: Specification of the micro V-grooves

Due the time consumption in operating the FEM cutting model, a preliminary study has been conducted on the adopted material to establish a relationship between the material swelling effect and the depth of cut. An example of simulated cut surface is shown in Figure 7. The geometrical errors of the X stage and Z stage of the machine tool are modeled by means of

Fourier series [6] for given Maximum permissible error (MPE) provided by manufacture.

Figure 8 shows the simulated 15 micro-V grooves which is generated by the virtual machine. By comparing with the given specification, an estimate of the machining error of the workpiece can be made, as shown in Figure 9. The actual measurement of the machined workpiece is carried by a developed CCD-based 2D measuring system as shown Figure 6 [7]. The average width and pitch error of the machined workpiece is found to be 0.67μm and 0.34μm. It is interesting to note that the results of the actual measurement are found to well agree with the estimated results given by developed virtual machine tool.

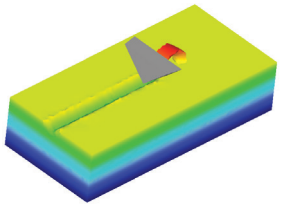

Figure 8: 3D topography of a cut workpiece generated by FEM cut model

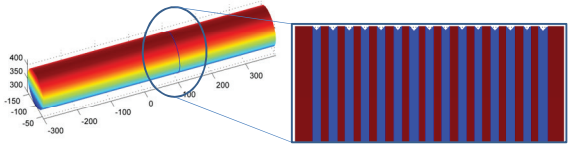

Figure 9: Generated 15 micro-V grooves

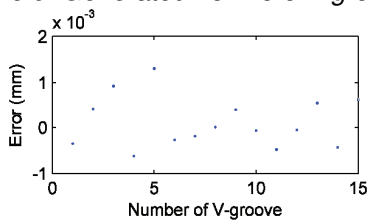

(a): Error of width

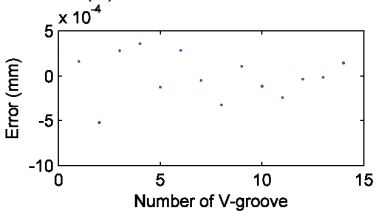

(b): Error of pitch

Figure 10: Estimated error of the cut V-grooves

CONCLUSION

This paper presents a study on the modeling and simulation of the micro-structured roller machining process by SPDT. A virtual machine tool is developed to simulate the machining process for investigating the influence of the machining strategy and the geometrical error of the machine tool. Based on computer simulation, the proposed method is found to be able to optimize the machining strategy in machining the targeted micro-structured roller striking a good balance between the machining efficiency and the surface quality of the precision rollers.

ACKNOWLEDGEMENT

The authors would like to express their sincere thanks to the Innovation and Technology Commission of the Government of the Hong Kong Special Administrative Region (HKSAR) and the Research Committee of The Hong Kong Polytechnic University for the financial support of the research work under the projects nos. GHP/045/10SZ, RTK7, respectively. The work described in this paper was also partially supported by a grant from the Research Grants Council of the Hong Kong Special Administrative Region, China (Project No.: PF10-12032).

REFERENCES

[1] Jiang X. In situ real-time measurement for micro-structured surfaces. Annals of CIRP, 2011; 60: 563-566.

[2] Lee W, To S, Cheung C. Design and Advanced Manufacturing Technology for Freeform Optics, The Hong Kong Polytechnic University, Hong Kong, 2005.

[3] Moriya T, Nakamoto K, Ishida T, Takeuchi Y. Creation of V-shaped microgrooves with flat-ends by 6 axis control ultraprecision machining. CIRP Annals-Manufacturing Technology, 2010; 59:61-66.

[4] Johnson G.R., Cook W.H., A constitutive model and data for metals subjected to large strains, high strain rates and high temperature, Proceeding of the seventh international symposium on ballistics, Haque, Netherlands, Apr. 1983, 541-547.

[5] Schwenke H., Knapp W., Haitjema H., Weckenmann A., Schmitt R., Delbressine F., Geometric error measurement and compensation of machines-an update, CIRP Annals – Manufacturing Technology, 2008, 660-667.

[6] N.V. Gestel, Determining measurement uncertainties of feature measurements on CMMs, Katholieke Universiteit Leuven, Leuven, 2011.

[7] C.F. Cheung, M. Ren, et al., On-Machine Measurement and Characterization of V-Groove Structure Pattern on Precision Rollers, Key Engineering Materials, 2012, 552: 567-574.

STUDY ON WEAR OF URETHANE POLISHER USED IN VIBRATION-ASSISTED POLISHING

J. GUO[1*], H. SUZUKI[1, 2], Y. YAMAGATA[1] S. MORITA[1] and J. UEHARA[3]

**[1] Ultrahigh Precision Optics Technology Team,
RIKEN Center for Advanced Photonics (RAP),
Wako, Saitama, Japan
[2] Department of Mechanical Engineering,
Chubu University,
Kasugai, Aichi, Japan
[3] Nagatsu Precision Mold Co., Ltd.,
Kawasaki, Kanagawa, Japan**

INSTRUCTIONS

Recently, vibration-assisted polishing has been proposed and applied to finish micro-optic molds with low surface roughness and high form accuracy [1-4]. During polishing process, wear of polisher occurs while material is removed, and according to Preston's equation [5], the material removal rate will be changed as wear persists. So as well as parameters such as relative velocity, polishing pressure and polishing time, the situation of polisher also takes a great effect on the polishing performance. To well control the polishing process, the evaluation of polisher's wear becomes quite necessary.

From the view of tribology, loose abrasives polishing can be characterized as abrasion caused by loose or fixed abrasives as a result of their motion relative to the workpiece and polisher [6-9]. Material can either be displaced or removed by two-body abrasion when abrasives become embedded and slide over the surface, or detached by three-body abrasion when abrasives become freely rolling abrasives. Surfaces worn by two-body abrasion exhibit parallel grooves while micro-indentation are generated by three-body abrasion [10].

The Archard wear equation is a simple model based o the theory of asperity contact used for determining the amount of wear. The equation predicts that the abraded wear volume V_w is directly proportional to the normal load F_n and the sliding distance s and inversely proportional to the hardness H of the abraded surface [11]

$$V_w \equiv K\frac{F_n s}{H} \tag{1}$$

where K is the wear coefficient. As mentioned above, wear caused by abrasives does not only happen on the workpiece, but also on the polisher. So Eq. (1) could be used to describe the wear on both of the workpiece and polisher just with different values of parameters.

Additionally, wear rate of polisher equals the value of polisher's wear volume divided by total removed material. It could be expressed as

$$P_{pw} \equiv \frac{V_{wp}}{V_{ww}} \tag{2}$$

where V_{wp} is the wear volume of polisher, V_{ww} is the wear volume (amount of removed material) of workpiece, and P_{pw} is wear rate of polisher.

By following the equations of Archard wear and wear rate, this paper presents some preliminary investigation on the wear of urethane polisher used in vibration-assisted polishing for micro-optic mold. The fabrication process of polisher is firstly introduced. Then the wear behavior is observed through measuring wear diameter on the head of polisher since wear volume of polisher is quite difficult to be precisely obtained in direct due to the small size and hard-to-wear nature of polisher, after that through some polishing experiments, the effect of wear diameter change of polisher on material removal depth is revealed, and a wear map of polisher is obtained.

FABRICATION PROCESS

The polisher used in the micro-optic polishing experiments is made of Polyurethane. It is a kind of soft material which is easy to change its shape but hard to wear so that super-smooth surface roughness could be obtained. It has a international rubber hardness degree (IRHD) of 90. The polisher has a small size and the shape accuracy on its top head is required to be precisely performed. So the main fabrication process of polisher is followed by Phenol resin gluing, precision cutting and urethane-coating. Among them, precision cutting plays a key role to dominate the form shape of polisher. Fig. 1(a), 1(b), 1(c) and 1(d) show some photographs of cutting path planning, cutting experimental setup, view by a microscope and fabricated polyurethane polisher.

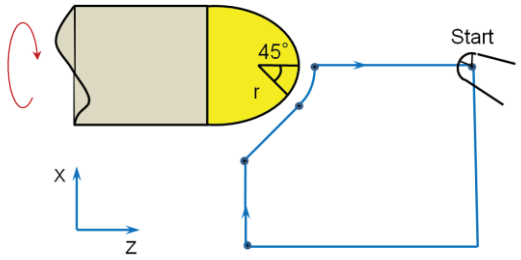

(a) Planning of cutting path

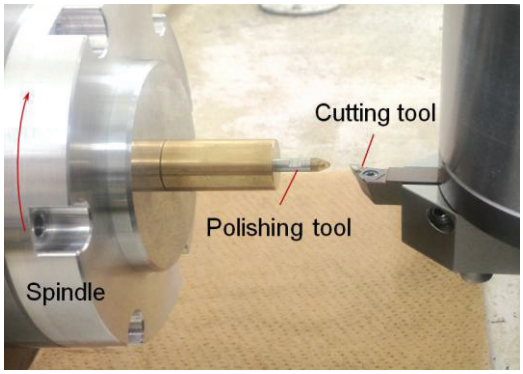

(b) Cutting experimental setup

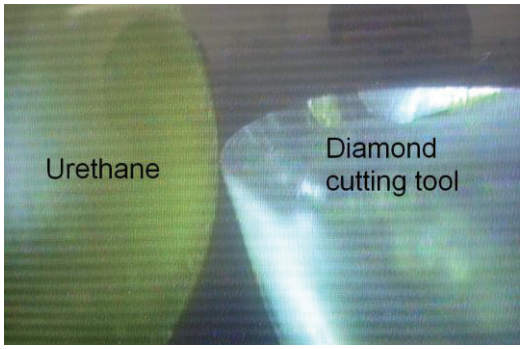

(c) View by a microscope

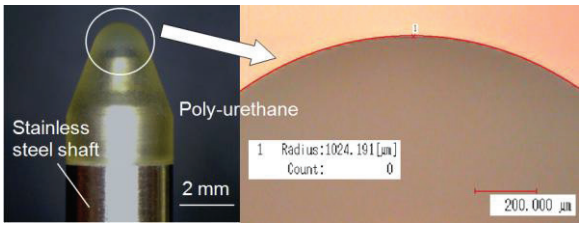

(d) Fabricated polyurethane polisher

Fig. 1 Some photographs of cutting path and cutting process

WEAR BEHAVIOR OBSERVATION

In vibration-assisted polishing by loose abrasive, the wear rate of polisher is correlated with vibration amplitude and frequency, material and concentration of slurry and polishing pressure. During polishing process, the polisher wears on the top of head where it contacts with the workpiece, and the head becomes flat gradually. since wear volume of polisher is quite difficult to be precisely measured, we observe the wear diameter on head of polisher. Fig. 2 shows shape change on polisher's head before and after polishing, and Fig. 3 gives the surface changes on top of polisher's head before and after polishing by a microscope. A measurement result by using NH-3N is shown in Fig. 4, the wear diameter of polisher is defined as *d* for the following investigations.

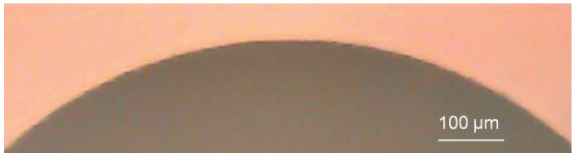

(a) Before polishing

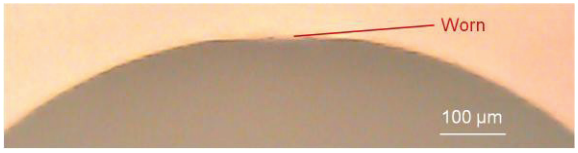

(b) After polishing

Fig. 2 Shape change on polisher's head

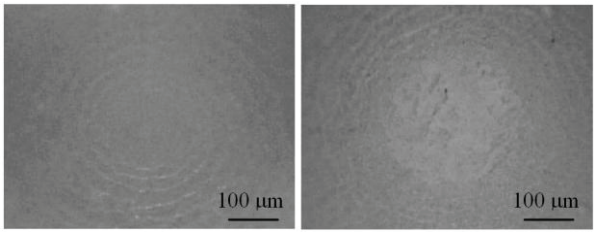

(a) Before polishing (b) After polishing

Fig. 3 Surface changes on polisher's head

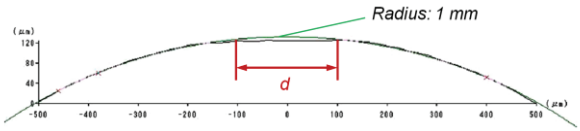

Fig. 4 Wear diameter *d*

EXPERIMENTS

To evaluate the effects of polisher's wear on material removal depth, some polishing experiments are conducted. The experimental conditions are summarized in Table 1. The workpiece is made of tungsten carbide which can withstand high temperature and pressure conditions and is usually used to do the hot-press molding to replicate glass lenses. It is lapped prior to polishing on a lapping machine. The polisher has a radius of 1 mm while the diamond slurry with grain size of 0.1 μm is adopted. The polisher vibrates in a circular vibrating motion under a constant pressure and scans a zigzag scanning path on the surface of workpiece as shown in Fig. 5. The experiment with same conditions is repeated 11 times with the change of polishing areas on workpiece surface.

Table 1 Main experimental conditions

Workpiece material	Tungsten carbide
Polisher head Radius Hardness	Polyurethane 1 mm IRHD 90
Abrasive Grain size Density	Diamond slurry 0.1 μm 1 wt%
Tool dwell time control method	Zigzag scanning
Polishing scope (*L*×*L*)	400 × 400 μm^2
Scanning speed	3.5 mm/min
Scanning pitch size (c)	20 μm

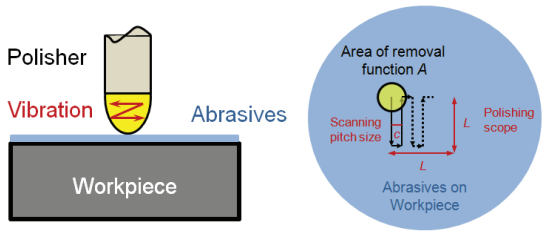

(a) Cross-section (b) Top-view

Fig. 5 Zigzag scanning on workpiece surface

After the experiments, material removal depth is measured by NewView 6000 while shape form of polyurethane polisher is observed by NH-3N (Mitaka Kohki Co.,Ltd.) as shown in Fig. 6.

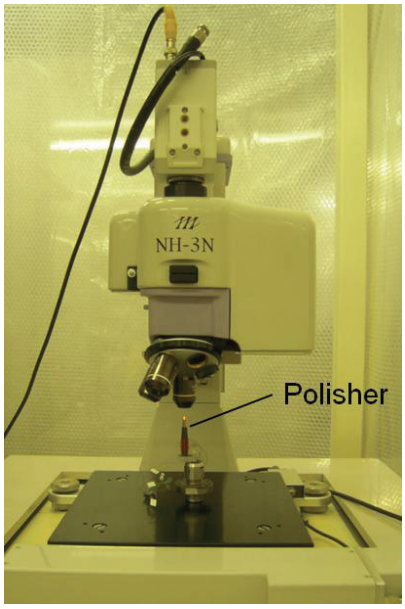

Fig. 6 Measurement by NH-3N

According to the experiment results in Fig. 7, it is found that the wear process is almost divided into three steps. During the 1st step (*d* < *50* μm), both of wear diameter and material removal depth increased, and material removal depth goes to a maximum. At the 2nd step (*50* μm ≤ *d* ≤ *300* μm), the polisher wears proportional to the number of experiment, but the material removal depth keeps almost constant just with a little decrease. From the 3rd step (*d* > *300* μm), the polisher's wear speed reduced while the material removal rate decreased dramatically and after that shows a tendency to a constant value.

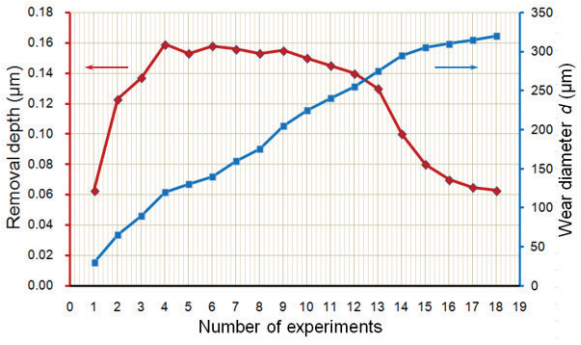

Fig. 7 Wear map of polisher

The reason why material removal depth reduces when d > 300 μm could be explained through observing the shapes of material removal functions in some extent. Fig. 8 shows the comparisons of material removal functions under the conditions of d ≤ 300 μm and d > 300 μm under polishing force of 20-40 mN. When d ≤ 300 μm, the shape of removal function shows center-concave and symmetric which is near to the ideal model of removal function. But when d > 300 μm, the acting polishing abrasives becomes difficult to reach the contact-center of polisher and workpiece, so the material in the center of removal function is left and the removal depth reduces.

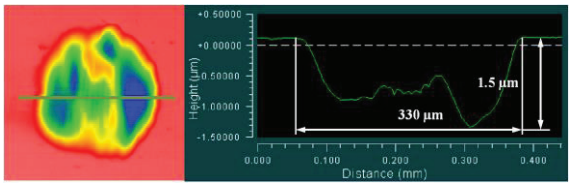

(d > 300 μm)

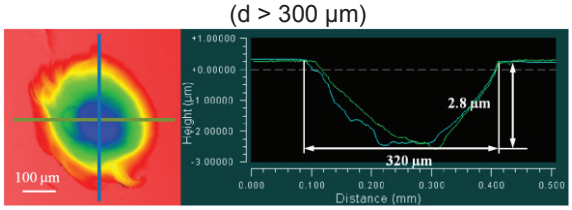

(d ≤ 300 μm)

(a) Polishing force: 20 mN

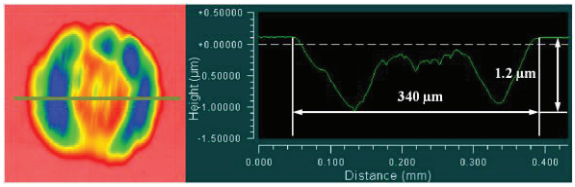

(d > 300 μm)

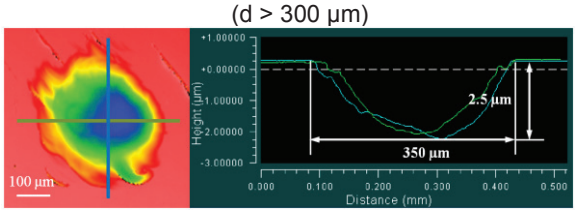

(d ≤ 300 μm)

(b) Polishing force: 30 mN

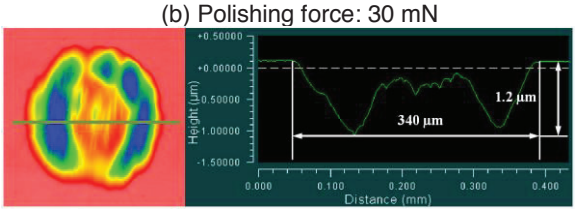

(d > 300 μm)

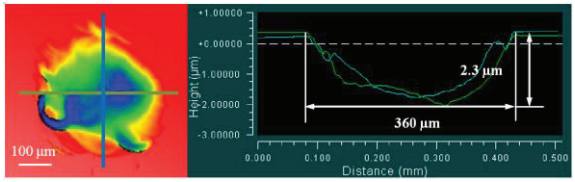

(d ≤ 300 μm)

(b) Polishing force: 40 mN

Fig. 8 Comparisons of material removal functions

SUMMARY

In this paper, the wear characteristics of polisher is investigated and a wear map is obtained. However, the theoretical principle of the wear mechanism is still not understood. Further investigations will be focus on the analysis of contact mechanism of polisher and workpiece.

REFERENCES

[1] Suzuki H, et al., Development of Ultrasonic Vibration Assisted Polishing Machine for Micro Aspheric Die and Mold. 2006, Annals of the CIRP 55(1):385–388.

[2] Suzuki H, et al., Ultraprecision finishing of micro-aspheric surface by ultrasonic two-axis vibration assisted polishing, Annals of the CIRP, 2010, Vol. 59/1, pp. 347-350.

[3] Guo, J, et al., Ultra-Precision Finishing of Micro-Aspheric Mold Using a Magnetostrictive Vibrating Polisher, Annals of CIRP, 2012, Vol.61/1, pp. 371-374.

[4] Guo J, et al., Development of micro polishing system using magnetostrictive vibrating polisher. Precision Engineering, 2013, Vol. 37/1, pp. 81–87.

[5] Preston FW, The theory and design of plate glass polishing machines. The Journal of the Society of Glass Technology, 1927, Vol. 11 pp. 214–56.

[6] Gahr K-HZ. Wear by hard particles. Tribol Int 1998;31(10):587–96.

[7] Williams JA. Wear modeling: analytical, computational and mapping: a continuum mechanics approach. Wear 1999;225–229:1–17.

[8] Trezona RI, et al.. Transition between two-body and three-body abrasive wear: influence of test conditions in the microscale abrasive wear test. Wear 1999;225–229:205–14.

[9] Adachi K, et al.. Wear-mode mapping for the micro-scale abrasion test. Wear 2003;255:23–9.

[10] Brinksmeier E, et al., Finishing of Structured Surfaces by Abrasive Polishing. Precision Engineering, 2006, Vol. 30/3, pp. 325–336.

[11] Archard JF. Contact and rubbing of flat surfaces. J Appl Phys1953;24:981–8.

STUDY ON SURFACE PROCESSING PROCESS BY USING FEMTO-SECOND PULSE TRAIN BEAM WITH EXCITATION OF COHERENT PHONON

Terutake Hayashi[1], Masaki Michihata[1], Yasuhiro Takaya[1], and Yusuke Fukuta[1]
[1] Graduate School of Engineering, Department of Mechanical Engineering
Osaka University
Yamadaoka 2-1, Suita, Osaka, Japan

INTRODUCTION

Ultra short laser pulses processing of materials, especially metals and semiconductors have developed rapidly over last decades. Several review articles are available on femtosecond lasers [1,2] and surface micromachining [3,4] and the history of femtosecond laser micromachining [5]. Ultra short pulses offer many advantages such as precise ablation of materials without significant heat affected zone, ablation of large band-gap materials including insulating ceramics [6] and fluoropolymers [7], ablation of high reflectivity materials [8], smaller and more precise fluence for ablation, avoidance of plasma absorption effects, and low amounts of redeposition [9].

The femtosecond laser processing is the local processing with little heat diffusion and little thermal damage. The laser creates more precise, lower threshold fluence of ablation. The ablation with fluence far above the ablation threshold continue to create unwanted thermal effects within the materials, due to the ultrafast time scales. These effects lead to cleaner, more precise micromachining processes.

In this paper, we propose a novel femtosecond pulse ablation process with oscillation of the coherent phonon by femtosecond pulse train in order to improve the productivity for the processing using the femtosecond laser pulses.

When a laser pulse interacts with metal or semiconductor target, the coherent phonon, which is the coherent motions of lattice and molecule vibrations in solids, is excited by the interaction of electrons and high latitude electric field [10]. It has unique properties of decaying in approximately several picoseconds and substance specific frequency.

The generation of coherent phonon is attributed to a mechanism called displaced excitation of coherent phonon [11-13]. During the laser interaction with materials, the laser energy is initially coupled to electrons; the excited electrons then transfer partial energy to lattice through electron-phonon coupling. The excited electrons will alter the equilibrium position of ions, inducing the ions to coherently oscillate around the new equilibrium position.

When the coherent phonon is excited, electron excitation and diffusion, electron-hole recombination, electron-phonon coupling, and coherent phonon generation is occurred. All of these processes except diffusion increase the temperature of lattice at surface. After the amount of energy coupled from the excited electrons to coherent phonon vibration, the lattice temperature rises. The material removal rate for the ultra short pulse processing is then considered to increase due to raising the lattice temperature.

PULSE TRAIN BEAM PROCESSING

The coherent phonon oscillations enable to activate the lattice motion on the sample surface. The target is ablated efficiently without thermal damage.

Figure 1 shows single pulse oscillation process for the lattice. Pulse interval of femtosecond Ti: Sapphire laser (repetition rate: 80 MHz) is 12.5 nanosecond. The coherent phonon, which is stimulated by single femtosecond pulse, is dumped before the next pulse irradiation. Figure 2 shows the pulse train oscillation process with repetitive oscillation in single pulse train. The coherent phonon is repetitively amplified by using pulse train beam whose decay is within a few picoseconds.

When the first pulse is oscillate coherent phonon, the interval change of double pulses caused the change of the timing of coherent phonon oscillation.

When the timing of the amplification is matched, the amplitude of the coherent phonon is increased. In this case, the exceeding the ablation threshold is easily occurred and the ablation rate is expected to be increased.

Furthermore, the phase of the phonon is matched in the area where the coherent phonon is generated. In this case the energy transfer from free electron to lattice vibration (phonon) is unified. It has advantage to decrease the validation of processing volume.

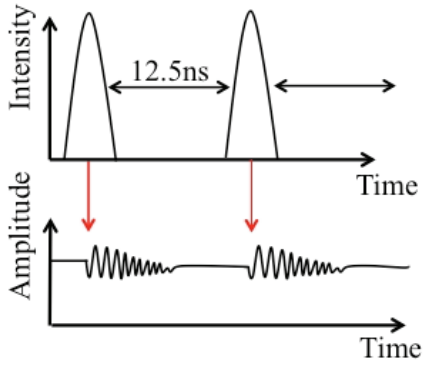

Figure 1 Single pulse oscillation

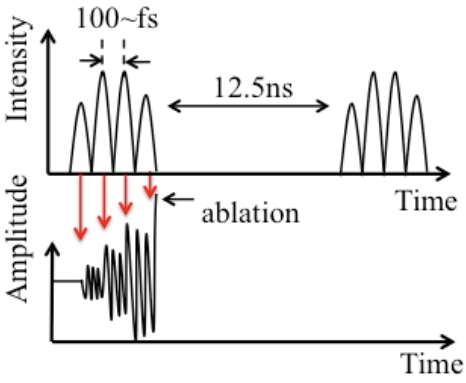

Figure 2. Pulse Train beam oscillation

SHAPING OF FEMTOSECOND PULSE TRAIN

To control the number of pulses and irradiate coherent phonon with its continuously, it is necessary to shape femtosecond pulse train, which has several large peaks of almost the same energy. So in this section, the method of femtosecond pulse shaping is described. The phase control system to shape the pulse train beam in time domain is reported by e.g. Hase and Weiner[10,14]. Figure 3 shows the phase control system for pulsed beam to achieve the pulse shaping in time domain. The pulse train is shaped by using spatial light modulator (SLM), which shift the phase of the passing light.

The system consists of a pair of gratings and lenses and liquid crystal spatial light modulator (LC-SLM) arranged in a configuration known as a zero dispersion pulse compressor, and a pulse-shaping mask. The individual optical frequency components contained with an incident pulse are spatially dispersed by the first grating and lens. Spatially patterned phase masks (LC-SLM) are placed midway between the two lenses at the point where the optical spectral components experience the maximal spatial separation.

After a second lens and grating recombine all the frequencies into a single collimated beam, a shaped output pulse is obtained, with the output pulse shape given by the Fourier transform of the pattern transferred by the masks onto the spectrum. Each element is placed on the focal distance of lens, and Fourier transform plane is formed in left side of SLM and inverse Fourier transform plane is formed in right side. That is, each lens performs a spatial Fourier transform between the plane of the grating and SLM. SLM consists of many liquid crystal and they perform a maximum 2π phase change of incident pulses by electric field control in modulator.

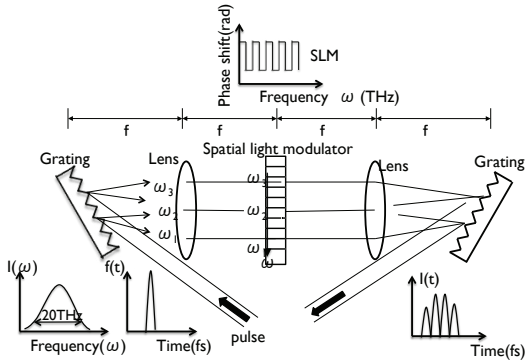

Figure 3 Schematic of femtosecond pulse shaping

PULSE SHAPE EVALUATION IN TIME DOMAIN

In order to perform fundamental laser processing experiment by using pulse train beam, we need the system to evaluate the pulse shape in time domain. Figure 4 shows the pulse shaping system with the pulse shape measurement setup. A single pulse is split into two pulses for pulse shaping and sampling. The shaped pulse and reference pulse is passing

through the second harmonic generation by using BBO crystal. The SHG auto-correlation method is used as pulse measurement method [15].

The pulse shape are measured by intensity cross correlation $X(\tau)$ as shown in Eq. (1) [15,16,17]. The technique has been used for measuring shaped pulses.

$$X(\tau) \propto \int I_R(t-\tau) I_{Pulse}(t)\, dt \qquad (1)$$

The intensity cross correlation $X(\tau)$ can be obtained by measuring the average second harmonic power generated through the interaction of two pulses with intensity profiles I_R and I_{Pulse} in a second harmonic generation crystal as a function of the relative delay τ . When I_R is a reference pulse with short pulse width , and I_{Pulse} is a shaped pulse significantly longer than I_R, then the cross-correlation signal $X(\tau)$ provides a good approximation to the shaped intensity profile in time domain. The pulse shape is then measured by using cross-correlation method by using femto second reference pulse. We integrate the system as shown in fig. 4. We change the optical path by using beam splitter (BS).

When input sine wave phase pattern as shown in figure 5 to SLM for femtosecond pulse shaping, the result is shown in figure 6. Several peaks in time domain can be observed with in the 10 ps range. The pulse width is 12ps for the shaped pulse. The widths of central two peaks are 650 fs (FWHM) and 800 fs (FWHM), and their interval: 1.3ps).

SURFACE PROCESSING USING FEMTO PULSE TRAIN BEAM

Figure 7 shows the experiment setup. A pulse train beam is formed and incident in the objective lens with high NA of 0.95. The beam is focused on the sample. The sample is N-type doped Germanium [100] and surface roughness is better than 1 nm. The thickness is 0.5 μm. The pulse energy is 2.6 nJ/pulse. The fluence is 52 kJ/cm^2. The spot size is 2.1 μm.

Figure 8 shows AFM image of the processing result for the Germanium [100] surface with pulse train beam as shown in fig. 6.

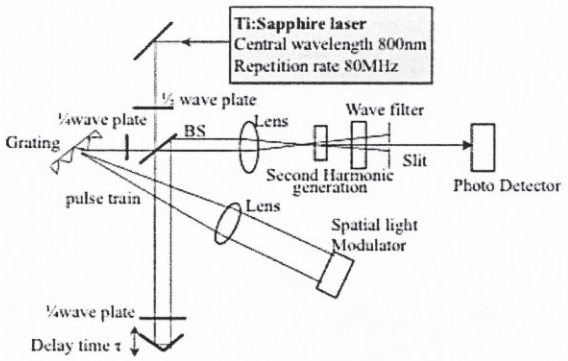

Figure 4. Experiment setup of femtosecond pulse shaping and measurement

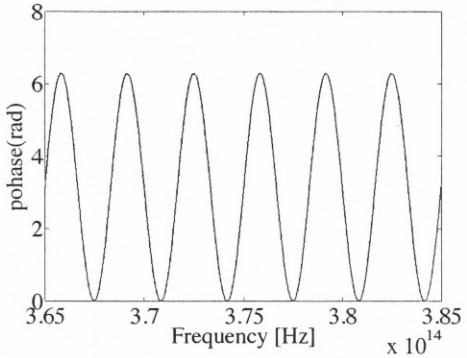

Figure 5. Projected phase pattern on SLM

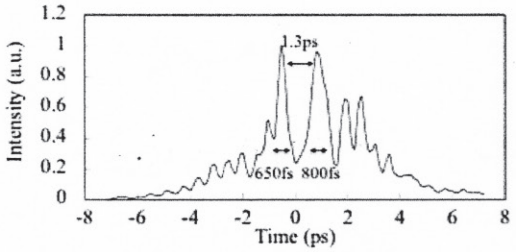

Figure 6. Shaped pulse by using SLM

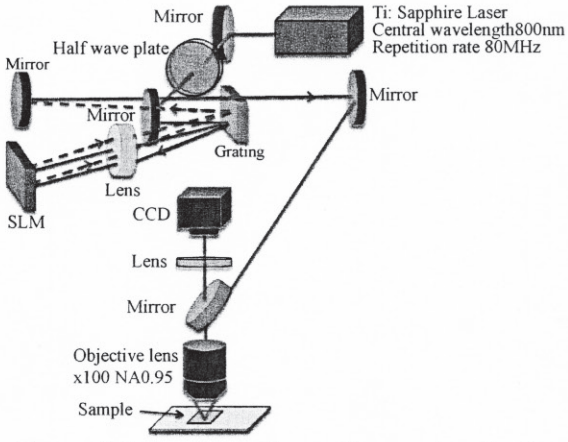

Figure 7 Pulse Train Beam Processing System

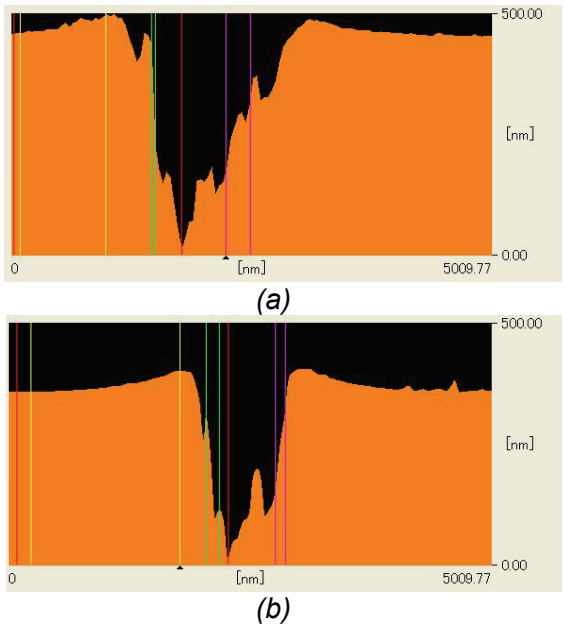

Figure 8 AFM Images of Surface Processing (a) single pulse (b) pulse train beam

Figure 8 (a) shows the processing result of Ge by using single pulse beam. The width of the whole is 1.7 μm and the depth 420 nm. The ripple texture can be observed in the whole.

The width of the whole is 1.4 μm and the depth 330 nm. The ripple texture can be observed in the pulse train beam processing results. The ripple texture is also observed in the whole.

The heat affected zone is so small to avoid heat to be conducted into the Ge and cause undesirable effects such as splatter and re-solidification of melted material. The debris is also reduced due to the size of the heat affected zone.

For ultrashort pulse laser processing (pulse durations of 10^{-12} seconds and below), the duration of the laser pulse is shorter than the time required for energy to be transferred to the surrounding area of the laser interaction volume, or transferred from electrons to atoms, when the initial incident light is absorbed by electrons.

However, it is difficult to determine the effect of the repetitive irradiation of femto second pulse in ps of time duration. We need further experiments to investigate the processing property by using pulse train beam.

SUMMARY

We proposed a novel laser processing method by using coherent phonon oscillation. In this paper, we test and evaluate the pulse shaping system and pulse shape measurement system in time domain, and integrate them to the laser processing system. It is possible to process the Ge surface by using pulse train beam, which repeats pulse irradiation in the duration with 1.3 ps. We will investigate the processing property by using pulse train beam as compared to the single femto-pulse processing results.

ACKNOWLEDGEMENT

This research was supported in part by a Grant-in-Aid for Scientific Research from the Ministry of Education, Culture, Sports, Science and Technology of Japan (Grant-in-Aid for Exploratory Research 25289017).

REFERENCES

[1] Backus, S., Durfee III, C. G., Murnane, M. M. & Kapteyn, H. C. High power ultrafast lasers. Rev. Sci. Instrum., 1998; 69, 1207–1223.

[2] Keller, U. Recent developments in compact ultrafast lasers. Nature, 2003; 424, 831–838.

[3] Kruger, J. & Kautek, W. in Polymers and Light, 2004; 168, 247–289 (Springer, Berlin).

[4] Dausinger, F., Lichtner, F. & Lubatschowski, H. Femtosecond Technology for Technical and Medical Applications (Springer, Berlin, 2004).

[5] Bloembergen, N. A brief history of light breakdown. J. Nonlinear Opt. Phys., 1997; 6, 377–385.

[6] B. C. Stuart, M. D. Feit, A. M. Rubenchik, B. W. Shore, and M. D. Perry, ‘‘Laser-induced damage in dielectrics with nanosecond to sub-picosecond pulses,’’ Phys. Rev. Lett., 1995; 74, 2248–2251.

[7] S. Kuper and M. Stuke, ‘‘Ablation of polytetrafluoroethylene Teflon with femtosecond UV excimer laser pulses,’’ Appl. Phys. Lett. 1988; 54, 4–6,

[8] B. N. Chichkov, C. Momma, S. Nolte, F. von Alvensleben, and A. Tunnermann, ‘‘Femtosecond, picosecond, and nanosecond laser ablation of solids,’’ Appl. Phys. A: Solids Surf., 1996; 63, 109–115.

[9] P. P. Pronko, S. K. Dutta, J. Squier, J. V. Rudd, D. Du, and G. Mourou,, ‘‘Machining of sub-micron holes using a femtosecond

laser at 800 nm,'', Opt. Commun., 1995; 114, 106–110.
[10] Hase M., Ishioka, K., Demsar, J., Ushida, K., and Kitajima, M., Ultrafast dynamics of coherent optical phonons and nonequilibrium electrons in transition metals. Phys. Rev. B , 2005; 72: 189902.
[11] H. J. Zeiger, J. Vidal, T. K. Cheng, E. P. Ippen, G. Dresselhaus, and M. S. Dresselhaus, Phys. Rev. B 45, 768, 1992.
[12] S. Hunsche and H. Kurz, Appl. Phys. A: Mater. Sci. Process., 1997; 65, 221.
[13] K. S. Tinten, C. Blome, J. Blums, A. Cavalleri, C. Dietrich, A. Tarasevitch, I. Uschmann, E. Forster, M. Kammler, M. Horn-von-Hoegen, and D. Linde, Nature, 2003; 422, 287.
[14] Weiner, A.M., Femtosecond optical pulse shaping and processing. Prog, Quant, Electr, 1995; 19: 161-237.
[15] Saruwatari, M., Ultrafast optical pulse waveform measurement optical. Rev of Las Eng, 1991: 19: 8, 767-775.
[16] J. Diels, J. Fontaine, I. McMichael, and F. Simoni, "Control and measurement of ultrashort pulse shapes (in amplitude and phase) with femtosecond accuracy," Appl. Opt. 1985; 24:1270-1282
[17] A. M. Weiner, Femtosecond pulse shaping using spatial light modulators, Rev. Sci. Instrum. 2000; 71: 1929-1960

INVESTIGATION OF TOOLING EFFECTS, SLURRY COMPOSITION AND WORKPIECE MATERIALS IN VORTEX MACHINING

Jeffrey B. Hunt, Stephen C. Howard, Brigid A. Mullany and Stuart T. Smith
Center for Precision Metrology
The University of North Carolina at Charlotte
Charlotte, North Carolina, USA

INTRODUCTION

This abstract describes current research to investigate experimental parameters considered to influence the Vortex Machining process and machining of different materials. Multiple process parameters are currently being investigated: the effect of probe oscillation amplitude and its long-term stability on the material removal rate, the effect of slurry depth on probe dynamics, and probe wear as a function of time. This process has recently been applied to silicon, silica and tool steel. To date, tool wear was not observed with oscillating probes immersed in a slurry solution for periods of up to 94 hours.

BACKGROUND

Vortex Machining is a sub-aperture polishing process in which material is removed from a workpiece in a highly localized region. The process can be differentiated from other sub-aperture polishing techniques by the characteristic high aspect ratio tooling (herein called the *probe*) that consists of a 7 μm diameter fiber attached to one tine of a quartz tuning fork oscillator. Through electrical excitation of the tuning fork near its resonant frequency (~32 kHz), the fiber will produce a standing wave oscillation. Material removal is facilitated by inserting the oscillating fiber into a thin layer (~1 mm) of polishing slurry at a fixed distance above a workpiece surface. The standing wave oscillations induce vortices into the slurry close to the workpiece surface which causes material removal, see Figure 1.

Previous research into Vortex Machining focused on the development of an experimental platform. These efforts have resulted in a three-axis platform capable of sub-micrometer control of relative position between the probe mount and specimen with other controls implemented to maintain a constant slurry depth and stable probe dynamics [1]. With these developments, it is now possible to produce multiple footprints in a single testing cycle. While significant testing has been previously documented [1, 2], most tests were performed using a specific workpiece material (silicon <100>) and fixed experimental parameters. A major goal of these early studies was to assess process repeatability and to refine the experimental platform and controls. Current research is now focused on understanding the influence of different process parameters.

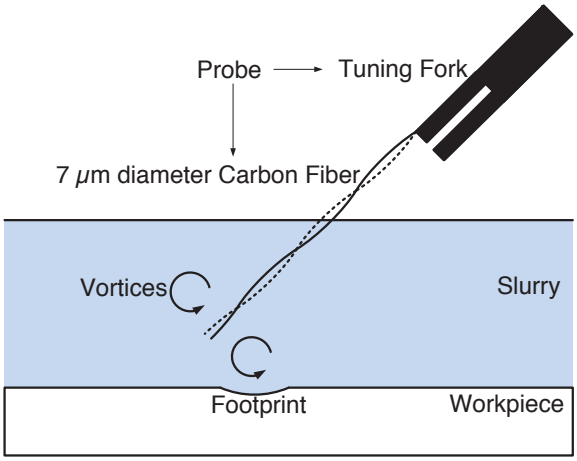

FIGURE 1. Schematic showing theory of operation in Vortex Machining.

PROCESS PARAMETER STUDIES

To date, findings on the effects of varying the parameters in this study have not been conclusive, but, from more recent studies, some general trends have been observed and are presented in the following sections.

Probe Wear and Contamination

Fiber wear and contamination are two major concerns for the long term stability of the tool.

To investigate tool (probe) wear, several probes were oscillated in alumina slurry for extended periods of time (24 and 94 hrs.) and observed, before and after, using a JEOL scanning electron microscope (SEM). During these long testing periods, precipitation of slurry

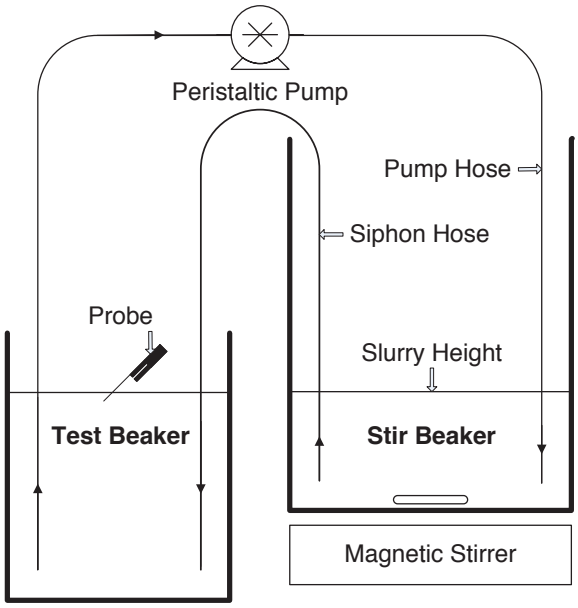

FIGURE 2. Tool wear experiment setup. Stirring and testing were conducted in separate slurry volumes to maintain an undisturbed slurry surface for testing while maintaining slurry particle suspension.

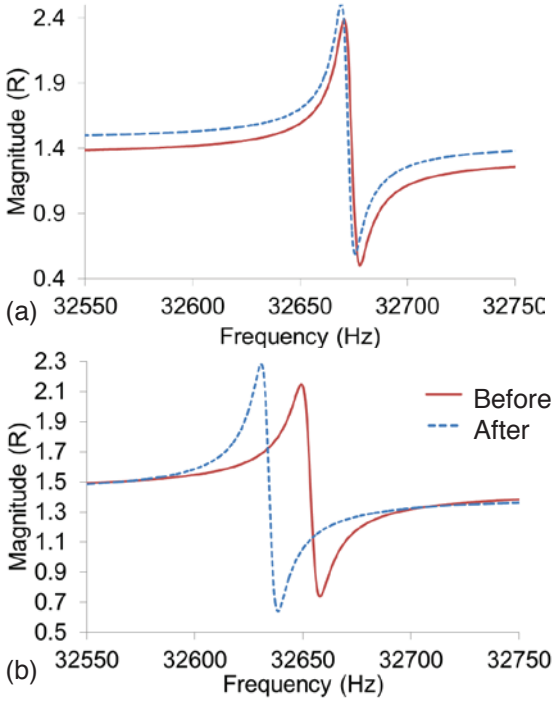

FIGURE 3. Frequency sweeps of probes before and after tool wear study of a probe vibrated for a) 94 hours and b) for 24 hours. Slurry accumulation on the fiber explains some of the small variation between before and after results.

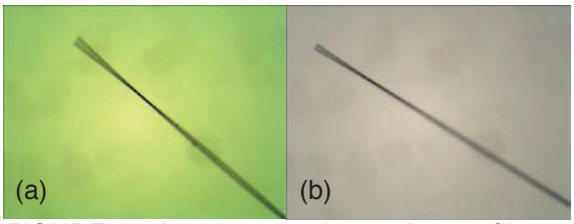

FIGURE 4. A representative tool-wear fiber a) before and b) after tool wear testing. Before tip-to-tip magnitude (maximum visual amplitude) was approximately 29 µm and after magnitude was approximately 20 µm. These images are of the probe vibrated in slurry for 24 hours and the 94 hour probe showed even less variation with a post testing decrease of only one micron.

particulates caused issues in the experiment. As a result, slurry circulation and mixing was implemented into the experimental apparatus to maintain slurry particle suspension and to provide an undisturbed slurry surface in which to submerge the fiber, see Figure 2. Electrical response and vibrating amplitude of the probes from before and after tool wear testing were compared, see Figure 3 and Figure 4. SEM images of the fiber tips before and after testing can be seen in Figure 5 with no visible wear.

In previous studies, a gradual accumulation of particles on the fiber was observed. After many testing cycles, significant attenuation of the oscillation amplitude was observed along with a subsequent reduction in material removal. It is still unclear if this attenuation is purely due to slurry accumulation, however in recent studies a tool maintenance protocol has been established. This protocol comprises measurement of the electrical response and vibration amplitude both before and after testing and, as necessary, a post-process cleaning operation using isopropyl alcohol. These phenomena are still being investigated, but post-process cleaning operations using alcohol-based solutions show promise for reducing slurry agglomeration over time, see Figure 6.

A possible, but not yet tested, source of tool wear is fiber-to-workpiece interactions. A long-term tool wear investigation is underway to validate previous results and gain a more complete understanding of tool wear by observing the carbon fibers under an SEM before and after multiple vortex machining tests as opposed to freely vibrating the fibers in slurry. While fiber-to-workpiece contact should not be

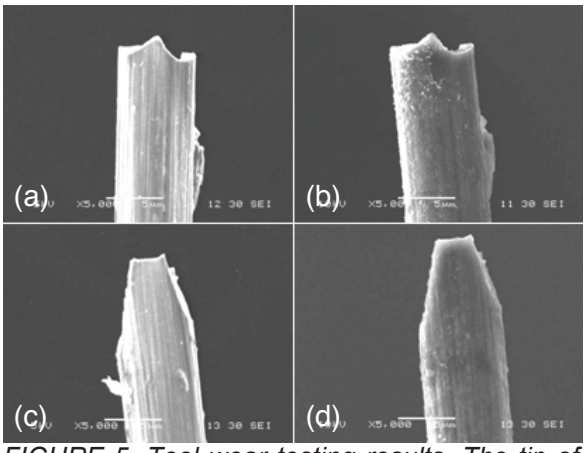

FIGURE 5. Tool wear testing results. The tip of two, 7 μm diameter, fibers used in probe wear testing are shown before (a,c) and after (b,d) testing with no observable wear. The probe in the top two images (a,b) was vibrated in slurry for 94 hours while the probe in the bottom two images (c,d) was vibrated in slurry for 24 hours. Note the slurry accumulation on the fiber walls in the after images on the right (b,d). All images are SEM images at 5000X.

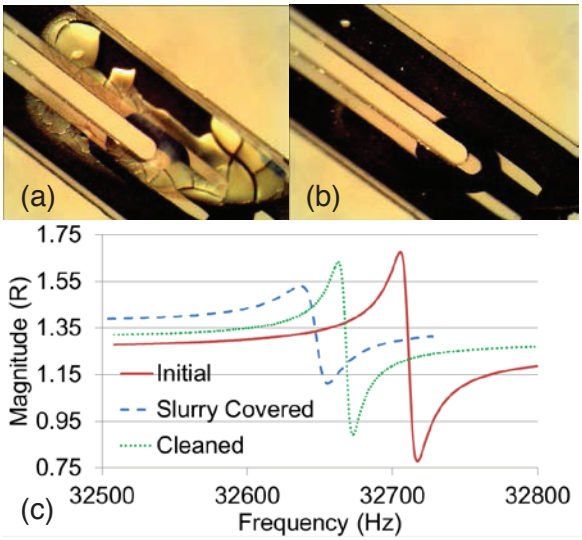

FIGURE 6. Tool cleaning results. a) A probe with an initial amplitude of 27 μm stopped vibrating after dried slurry accumulated. b) After cleaning, the probe vibrated again but the amplitude was too small to measure using current methods. c) This partial recovery due to cleaning can be seen in the frequency response. While the quartz fork is not typically submerged in slurry (only the attached carbon fiber is submerged), testing brings the fork into close proximity to the slurry surface and contamination of this kind occasionally occurs.

occurring during tests, it is a possibility and as such these studies will help to identify if this interaction is occurring and if it is a contributor to tool wear.

Slurry Depth

The location along the fiber of the slurry meniscus has been observed to effect probe dynamics, and consequently induced slurry flow energy [1, 2]. Further testing by observing the probe's peak-to-peak vibration amplitude at resonance as well as the electrical response as the fiber is lowered into water has now been completed. In this study, a probe was held in the same orientation as used in vortex machining and lowered into a clear-walled container full of water. A microscope and attached camera were used to observe the vibrating probe tip through the container wall. The probe's amplitude was measured in air and then lowered into the water in increments of 50 μm. Tip amplitude showed local fluctuations with an overall trend toward a reduction in amplitude with submersion depth. This experiment was repeated with a total of three probes, all of which showed similar characteristics. The in-air amplitude of the probes prior to testing (amplitudes of ~22, 42, 71 μm) decreased significantly (amplitudes of ~11, 17, 19 μm) as the probes came into initial contact with the slurry. At submersion depths near the standard machining depth of 1000 μm the vibrational amplitude of all three probes had further decreased to amplitudes barely larger than the 7 μm diameter fiber (amplitudes of ~ 9, 9, 11 μm). The modulating amplitude superposed on the steady decrease is undoubtedly influenced by the location of the water's meniscus along the fiber length (i.e. its intersection at a node or antinode). As an example, Figure 1 shows the slurry surface located at the fiber antinode. The probe's electrical response therefore correlates to the mode shape of the fiber as it interacts with the fluid surface.

While the effect of submersion depth on probe dynamics has been studied, the effect on the resulting footprint is still unclear. From analytical solutions previously formulated [3], increases in the probe's oscillation amplitude are predicted to induce higher energy flows, resulting in more slurry-workpiece interaction. Machining tests on silicon were conducted with different slurry depths ranging from 400 to 1600 μm. Note that in all cases the probe location above the workpiece remained at 20 μm. Multiple tests

support the theory that the material removal rate is dependent on the process energy (related to fiber amplitude). At slurry depths greater than 1000 μm, where there is little to no fiber oscillation, no material is removed from the workpiece. Other than that, no clear correlation was seen between slurry depth and volume removed or localization of footprints. This result is not surprising since, as already stated, the relationship between slurry submersion depth and probe dynamics is expected to vary depending on where the meniscus intersects the fiber length. Testing at the same machining depth intervals is being repeated with another probe to further corroborate these results.

Probe Stability

Throughout vortex machining studies, issues with probe stability are frequently encountered. Desirably, a stable probe will vibrate in one defined plane. In practice, numerous probes are observed to exhibit erratic behavior that is a function of probe manufacture and both excitation frequency and amplitude. This behavior typically manifests as either chaotic amplitude variations or, at larger amplitudes, a sporadic stopping and starting of the vibration. Non-planar oscillation of a probe fiber can be seen in Figure 7. Noting this behavior and observing subsequent machining footprints, it is generally found that more stable probes are correlated with more repeatable and localized machining footprints.

Workpiece Material

In addition to investigations of process parameters, studies are being undertaken on new workpiece materials such as fused silica and tool steels. Machined footprints have been observed on both materials.

To address some concerns about the passive corrosion of different workpiece materials by the slurry, studies of the effect of slurry chemistry on new materials have been conducted. While the alumina-based slurry has been successful for silicon workpieces [2], this is not optimal for other workpiece materials. In the case of tool steel, corrosive effects, mostly likely due to the slurry pH and prolonged immersion during machining, were observed to increase surface roughness to a point that the process footprint could not be distinguished using white light interferometry. To determine a non-corrosive steel-slurry combination, gage blocks from five

FIGURE 7. The tip of a vortex machining probe fiber viewed at a 45 degree angle (the tip being closer than the top) and showing an elliptical or circular path instead of the planar oscillation of the most simple model.

different companies (Webber, Ellstrom, Pratt and Whitney, Fonda and CEJ) were submerged in four slurries of various pH and observed before and after submersion for one and eighteen hours at 20 °C. Gage blocks from two of the five (CEJ and Fonda) had significant corrosion after both periods of submersion but only in the acidic slurries. The gage blocks from the three other manufacturers were un-corroded after both submersion intervals in the acidic as well as the basic slurries. Samples were selected from these three un-corroded specimens for testing of vortex machining on metals.

While results are limited, it has been noted that the resulting footprints are similar in shape when using either silicon, silica or steel workpieces. Early measurements suggest that the material removal rate is significantly higher on the silica and steel workpiece when compared to silicon. More experiments are required to quantify the differences in machining characteristics between these materials.

CONCLUSION

Improved repeatability has been obtained in the Vortex Machining process through advancements in position, slurry height and other controls. Due to these improvements, the current push in research is to characterize the sensitivity of the process to variations in key process parameters and to evaluate its ability to machine materials other than silicon.

Little to no wear was observed on probes after prolonged oscillation in slurry, thus indicating their stability over long periods of time. Probe amplitudes, and thus removal rates, were found to be sensitive to submersion depth in the slurry. Variations in the probe's oscillatory trajectory were observed between different probes and under different operating conditions. Both of these dynamic traits are still under investigation and are considered to be a source of process instability. Preliminary testing on silica and stainless steel successfully removed material and work is continuing in this area to better evaluate the material removal mechanisms and rates for the different materials.

ACKNOWLEDGMENTS

This work has been funded by the National Science Foundation (NSF) grant number 1030700. Any opinions, findings and conclusions or recommendations expressed in this material are those of the authors and do not necessarily reflect the views of the National Science Foundation.

The authors would like to thank Dewey Christy for contributing the gage blocks which were used for corrosion testing and as vortex machining workpieces.

REFERENCES

[1] Howard S, Chesna J W, Mullany B, and Smith S T. On the Development of an Experimental Testing Platform for the Vortex Machining Process. Journal of Manufacturing Science and Engineering, at press, 2013.

[2] Howard S, Chesna J W, Mullany B, and Smith S T. Observations During Vortex Machining Process Development. Journal of Manufacturing Science and Engineering, ISBN 978-0-7918-5499-0, 2013

[3] Holtsmark J, Johnsen I, Sikkeland T, and Skavlem S. Boundary Layer Flow Near a Cylindrical Obstacle in an Oscillating Incompressible Fluid. The Journal of the Acoustical Society of America, **26**, 26-39, 1954.

Relative Axis Error Modeling for Volumetric Errors of Machine Tools

Jooho Hwang[1], Chinh B. Bui[1], and Chun-Hong Park[1]
[1]Department of Ultra-Precision Machine and Systems
KIMM, Daejeon, Korea

INSTRUCTIONS

This research introduces a generalized modeling of volumetric errors for multi-axis machine tools in which the generalized modeling of coordinate system of all six axes is explained, followed by the simulation of volumetric errors after calculation. The theory of generalized modeling is evaluated by comparing with the reference made by conventional model. To point out the advantages of the generalized modeling, an application in early stage of the design process also is introduced in thesis as an example. The evaluation for generalized modeling in a 4-axis machine tool is presented, in which the data from ISO230-6 and R-test measurements are used to evaluate the estimated data from the generalized modeling of volumetric errors(V.E.).

GENERALIZED HTMS FOR V.E.

In assembly process, X-axis is attached to others in order to build the kinematic chains of machine tools. Therefore, to estimate the future motion behavior of a machine, the relative HTMs representing assembly parameters between two adjacent axes need to be defined. Moreover, to make the generalized modeling of volumetric errors for multi-axis machine tools, the generalized modeling of HTMs of assembly parameters for all six axes in the Cartesian coordinate system also need to be identified.

To build these generalized HTMs, it's possble to start from the general form of HTM in Equation 2. When the coordinate system O_1 moves to O_2, the general HTM is used to represent displacements a, b, c in X, Y, and Z direction, respectively, and angle ϕ_x, ϕ_y, ϕ_z to represent rotations around X, Y, and Z direction, respectively. Hence, this generalized HTM also can be applied to represent the coordinate relationship between two adjacent axes in a machine kinematic chain. In an axis kinematic chain, when an axis is attached to another axis, the assembly parameters encompass. In Equation 1, the assembly parameters include offset parameters and angular errors.

$$T_{rel} = \begin{bmatrix} 1 & 0 & 0 & O_x \\ 0 & 1 & 0 & O_y \\ 0 & 0 & 1 & O_z \\ 0 & 0 & 0 & 1 \end{bmatrix} \cdot \begin{bmatrix} 1 & 0 & 0 & 0 \\ 0 & \cos\gamma_x & -\sin\gamma_x & 0 \\ 0 & \sin\gamma_x & \cos\gamma_x & 0 \\ 0 & 0 & 0 & 1 \end{bmatrix} \cdot \begin{bmatrix} \cos\gamma_y & 0 & \sin\gamma_y & 0 \\ 0 & 1 & 0 & 0 \\ -\sin\gamma_y & 0 & \cos\gamma_y & 0 \\ 0 & 0 & 0 & 1 \end{bmatrix} \cdot \begin{bmatrix} \cos\gamma_z & -\sin\gamma_z & 0 & 0 \\ \sin\gamma_z & \cos\gamma_z & 0 & 0 \\ 0 & 0 & 1 & 0 \\ 0 & 0 & 0 & 1 \end{bmatrix} \quad (1)$$

The Figure 1 shows the case when X-axis is attached to another axis: the coordinate system of X-axis will offset $O_x(X)$, $O_y(X)$, and $O_z(X)$ compared with the coordinate system of previous axis in X, Y and Z direction, respectively. The assembly process will incur the perpendicular errors of X-axis with previous axes such as Y, B, Z, or C-axis.

The Figure 2 shows the case when A-axis is attached to other axes, the coordinate system of

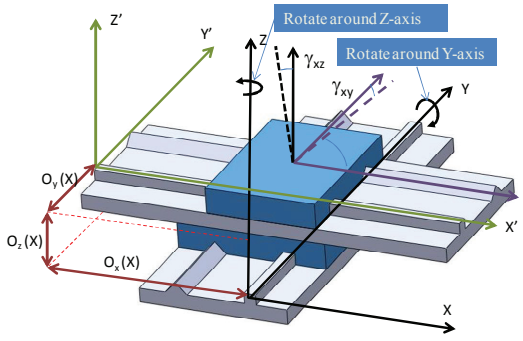

FIGURE 1. Assembly errors of X-axis

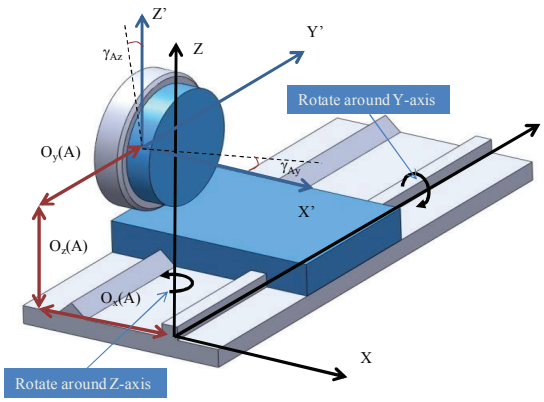

FIGURE 2. Assembly errors of A-axis

A-axis will offset $O_x(A)$, $O_y(A)$, and $O_z(A)$ compared with the coordinate system of previous axis in X, Y and Z direction, respectively. The assembly process will cause the perpendicular errors of A-axis with previous axes such as Y, B, Z, or C-axis.

In generalized HTM, A-axis is the first axis in the axis chain and the axis of movement of A-axis can play a role as X direction in the reference coordinate. Hence, there is no perpendicular error in the assembly HTM. When previous axis is Y-axis or Z-axis, there is only one perpendicular γ_{Ay} or γ_{Az}. In case of previous axis has the same axis of movement with Y-axis or Z-axis like B-axis or C-axis, the perpendicular errors γ_{AB} or γ_{AC} are orthogonal with axis of movement of B-axis or C-axis. Then the perpendicular errors γ_{Ay} or γ_{Az} in generalized HTM can be replaced by γ_{AB} or γ_{AC}, respectively.

Hence, the generalized HTM of A-axis can be calculated by multiplying the HTM of assembly parameters and the HTM of real motion illustrated in Equation 2

Hence, the generalized HTM of A-axis can be calculated by multiplying the HTM of assembly parameters and the HTM of real motion illustrated in Equation 2

$$T_A = \begin{bmatrix} 1 & -\gamma_{Ay} & \gamma_{Az} & O_x(A) \\ \gamma_{Ay} & 1 & 0 & O_y(A) \\ -\gamma_{Az} & 0 & 1 & O_z(A) \\ 0 & 0 & 0 & 1 \end{bmatrix}. \quad (2)$$

$$\begin{bmatrix} 1 & \varepsilon_y(A)\sin(\theta_A)-\varepsilon_z(A)\cos(\theta_A) & \varepsilon_y(A)\cos(\theta_A)+\varepsilon_z(A)\sin(\theta_A) & \delta_x(A) \\ \varepsilon_z(A) & \varepsilon_x(A)+\cos(\theta_A) & -\sin(\theta_A) & \delta_y(A) \\ -\varepsilon_y(A) & \sin(\theta_A) & \varepsilon_x(A)+\cos(\theta_A) & \delta_z(A) \\ 0 & 0 & 0 & 1 \end{bmatrix}$$

Simultaneously, in case when B-, C-axis are attached to other axes, the generalized HTMs of motion errors, offset parameters and perpendicular errors in assembly process can be represented by using the general form of HTMs in Equation 3 and 4.

$$T_B = \begin{bmatrix} 1 & -\gamma_{Bx} & 0 & O_x(B) \\ \gamma_{Bx} & 1 & -\gamma_{Bz} & O_y(B) \\ 0 & \gamma_{Bz} & 1 & O_z(B) \\ 0 & 0 & 0 & 1 \end{bmatrix}. \quad (3)$$

$$\begin{bmatrix} \varepsilon_y(B)+\cos(\theta_B) & -\varepsilon_z(B) & \sin(\theta_B) & \delta_x(B) \\ \varepsilon_x(B)\sin(\theta_B)+\varepsilon_z(B)\cos(\theta_B) & 1 & -\varepsilon_x(B)\cos(\theta_B)+\varepsilon_z(B)\sin(\theta_B) & \delta_y(B) \\ -\sin(\theta_B) & \varepsilon_x(B) & \varepsilon_y(B)+\cos(\theta_B) & \delta_z(B) \\ 0 & 0 & 0 & 1 \end{bmatrix}$$

$$T_C = \begin{bmatrix} 1 & 0 & \gamma_{Cx} & O_x(C) \\ 0 & 1 & -\gamma_{Cy} & O_y(C) \\ -\gamma_{Cx} & \gamma_{Cy} & 1 & O_z(C) \\ 0 & 0 & 0 & 1 \end{bmatrix}. \quad (4)$$

$$\begin{bmatrix} \varepsilon_z(C)+\cos(\theta_C) & -\sin(\theta_C) & \varepsilon_y(C) & \delta_x(C) \\ \sin(\theta_C) & \varepsilon_z(C)+\cos(\theta_C) & -\varepsilon_x(C) & \delta_y(C) \\ \varepsilon_x(C)\sin(\theta_C)-\varepsilon_y(C)\cos(\theta_C) & \varepsilon_x(C)\cos(\theta_C)+\varepsilon_y(C)\sin(\theta_C) & 1 & \delta_z(C) \\ 0 & 0 & 0 & 1 \end{bmatrix}$$

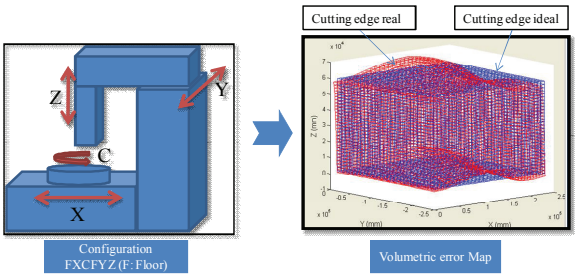

FIGURE 3. Simulation results of the volumetric error map

SIMULATION OF VOLUMETRIC ERRORS

The volumetric error is the translation of real cutting tool point in comparison with the ideal case on the workpiece surface. To estimate these errors, the generalized HTMs are used to calculate real position of cutting tool point in a chosen configuration of machine, then compare with the ideal ones to calculate volumetric error.

Figure 3 shows an example of 4-axis machine configuration, in which tool group include Y-axis, Z-axis and cutting tool and workpiece group include X and C-axis and workpiece. These two groups can be transformed to the reference frame in Equation 5 using generalized HTMs for kinematic chains.

$$\begin{aligned} {}^R T_{work} &= {}^R T_X T_C T_{work} \\ {}^R T_{tool} &= {}^R T_Y T_Z T_{tool} \end{aligned} \quad (5)$$

Where: ${}^R T_{work}$ and ${}^R T_{work}$ represent translation and orientation of workpiece group and cutting tool group in the respective reference coordinate,

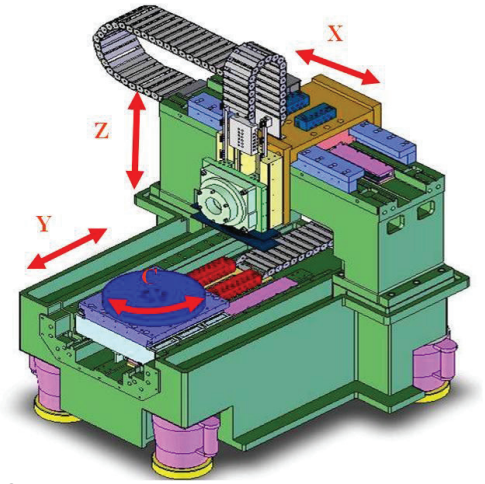

FIGURE 4. Four-axis machine tool with three linear and one rotary axis

respectively. ${}^{R}T_X$, T_Y, T_Z and T_C represent translation and orientation of X-axis, Y-axis, Z-axis and C-axis respective to following frame in their respective kinematic chains. T_{work} and T_{tool} represent translation and orientation of workpiece group and cutting group in their respective coordinate frames.

EVALUATION OF GENERIC KINEMATIC MODEL

A four-axis machine tool, shown in Figure 4, was chosen to evaluate the generic kinematic model approach for a specific case. The machine configuration can be divided into two groups: the cutting tool group (i.e., the X and Z axes), and the workpiece group (i.e., the Y and C axes). In practice, it is difficult to directly measure the deviation of the positioning errors of the cutting tool point when four axes move simultaneously. Hence, the machine evaluation process should be divided into two steps.

First, ISO230-6 was applied to determine the positioning accuracy on the body diagonals, which was then compared with estimations to evaluate the model. Thus, the three axes X, Y, and Z were evaluated.

Second, the R-test method was used to measure the deviation of the cutting tool points when the X, Y, and C axes moved simultaneously. The direct measurement was then compared with the estimation to evaluate the generalized model.

Evaluation for the X,Y, and Z axes

Figure 5 shows a schematic diagram of the three-face tests for the XY, YZ, and XZ planes using a master square mirror and three capacitive sensors to measure the six straightness errors. In Figure 6, a laser interferometer was used in the X, Y, and Z directions to measure the three linear motion errors.

The angular errors were calculated from the data of the three-point-probe measurement, shown in Figure 7. For the Y and Z axes, the three-point-probe measurement was used to calculate the roll and pitch of the Y-axis, as well as the squareness. The other angular errors can be calculated from the measured data of the XY and XZ planes setup. The perpendicular errors between X–Y, Y–Z, and X–Z were −57 μrad, 294 μrad, and 286 μrad, respectively. The resulting angular errors, including the roll, pitch, and yaw of the X, Y, and Z axes, are shown in Figure 8.

FIGURE 5. Three-point-probe measurement set-up

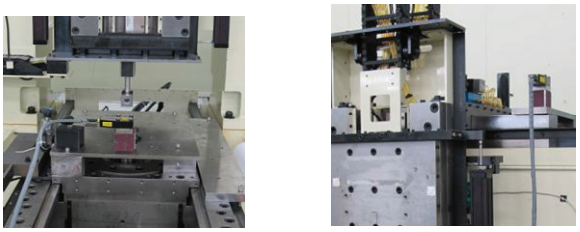

FIGURE 6. Three linear measurements

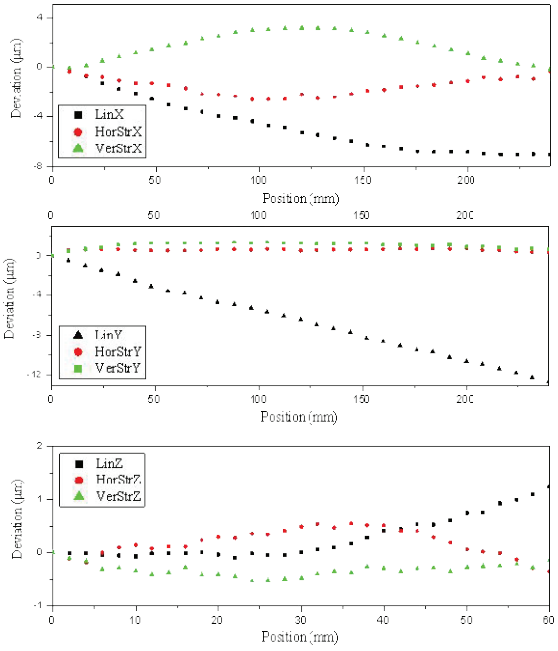

FIGURE 7. Linear and straightness errors

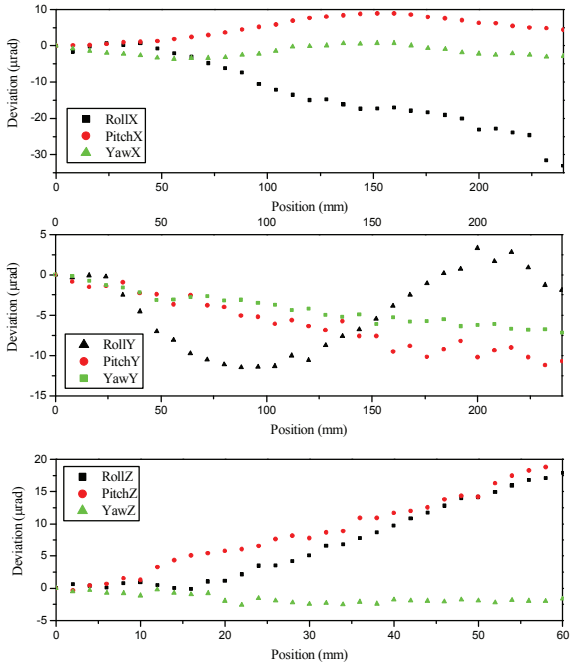

FIGURE 8. Angular errors for the X, Y, and Z axes

In a three-dimensional(3-D) workspace, ISO 230-6 standard is used for acceptance and verification of machine performance. Hence, body diagonal displacement tests can be used as a comparison index to evaluate the generalized model. The volumetric errors estimated by the generalized model were used to calculate the body diagonal displacements of the workspace. Accordingly, in this section, the procedure used to estimate the body diagonal displacements will be discussed.

By substituting the measured errors calculated from the previous sections into a generalized model, a volumetric error map of the workspace, $X \times Y \times Z$ = 240×240×60 mm, was simulated, as shown in Figure 9. In the figure, the ideal volume is represented by the red mesh and the error volume is represented by the blue mesh. The body diagonals *PPP*, *NPP*, *PNP*, and *PPN* following ISO230-6 were estimated from the volumetric error map.

Four body-diagonals (ISO230-6) were measured to determine the deviation of the cutting tool points (Figure 10). In these experiments, the laser beam was aligned with the four diagonal directions; the three axes *X*, *Y*, and *Z* were simultaneously moved to direct the mirror along the diagonal path.

To assess the accuracy of this procedure, directly measured ISO230-6 body diagonals

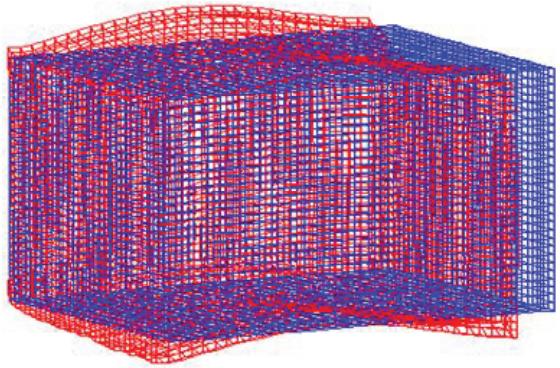

FIGURE 9. Volumetric error map

were compared with estimated values, as shown in Figure 10. The maximum difference between the estimated and measured diagonal positioning deviation was 17%; thus, the estimated errors from the generalized model were reliable.

CONCLUSIONS

This research applied HTM theory to build the generic kinematic model of volumetric errors for multi-axis machine tools, specifically, three-, four-, and five-axis tools. The model was evaluated for a four-axis machine tool by comparing the estimated data with measured data. The advantages of the generic kinematic model of volumetric errors compared with the application of conventional methods are simpler and faster estimation of volumetric error of any configuration. The research also provides machine tool designers with an effective generic kinematic model of volumetric errors for multi-axis machine tools to help determine the most suitable configuration in the very early stages of the design process.

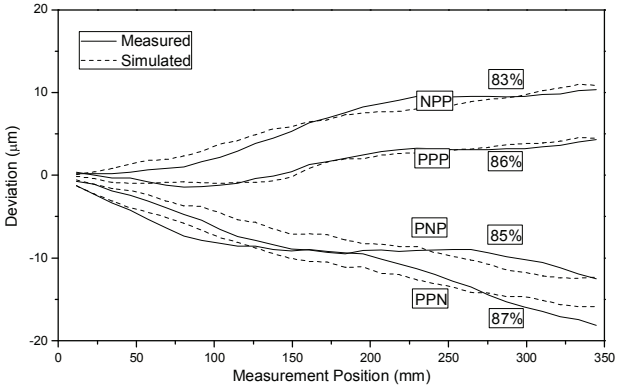

FIGURE 10. Comparisons of four body diagonals

Study on Releasability of Molded Resin from EDM Finished Surface with Metal Powder Mixed Fluid

Akira Okada[1], Ryoji Kitada[2], Shuhei Iwasaki[1] and Yasuhiro Okamoto [1]
[1]Graduate School of Natural Science and Technology
Okayama University
Okayama City, Okayama, Japan
[2] Bandoh Memorial Research Laboratory
TOWA Corporation, Japan
Kyoto City, Kyoto, Japan

INTRODUCTION

EDM technology has remarkably progressed, and very small surface roughness like a mirror can be obtained by controlling the discharge pulse energy or by using powder mixed working fluids, such as silicon powder mixed fluid or aluminum one [1-4]. Therefore, the finished surface by EDM is expected to be applied as a final metal mold surface in the near future. In this case, the life time of the metal mold and the molding performance depends mainly on the surface characteristics of EDMed surface. In general, the hardness of EDMed surface becomes higher than before machining because heat resolved carbon from kerosene type machining fluid is included into the surface.

One of the important surface characteristics for metal mold is releasability of molded resin from the metal mold surface. In the molding processes, small piece of resin material at times remains on the metal mold surface after releasing the product because of its strong adhesion of resin. Therefore, the metal mold surface has to be often cleaned to remove the remained adhesives, which makes the molding cycle time longer. Furthermore, the use of mold release agents or cleaning solution may deteriorate the metal mold surface and makes the life time of the metal mold shorter.

Therefore, the releasability of molded resin from the metal mold surface is important for long life of the metal mold. In order to evaluate the releasability of molded resin from the EDMed finished surface, the separation forces between molded epoxy resin and metal mold surface were measured by using a tensile tester in this study [5]. The releasability of molded epoxy resin from metal mold surfaces EDMed with powder mixed working fluids were tested and compared.

RELEASABILITY TEST

An alloy tool steel SKD11 was used as a workpiece. On the workpiece surface, a circular shallow cavity was machined by using NC die sinking EDM (Sodick EPOK3) with a cylindrical copper electrode of 25mm in diameter. Three types of working fluid, silicon powder mixed fluid (SPMF), aluminum powder mixed fluid (APMF), and normal kerosene type working fluid were used. They are widely used as working fluid in finishing EDM.

For evaluating the releasability of molded resin from EDMed surface, a separation force between molded resin and EDMed surface is measured by using a tensile tester, as shown in Fig.1. Initially, a thermosetting epoxy resin tablet is placed inside the jig mold set on the EDMed workpiece fixed on a heater table. In order to mold the resin and adhere it to EDMed surface, the workpiece and the jig are heated up by the heater. A compressive stress is loaded by a tungsten weight during the molding process. After the molding of resin, the hardened resin is pulled up together with the jig until the resin and the workpiece are separated. The test conditions are shown in Table 1 and they are based on the practical molding conditions.

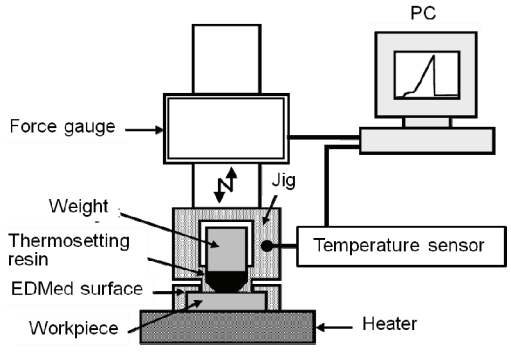

FIGURE 1. Releasability test equipment

Fig.2 shows the time variation of tensile force during the releasability test. It can be noticed that the tensile force increases with the time. Just before the molding resin and the EDMed surface are separated, the maximum load appears. The maximum force is regarded as a separation force in this study, and the releasability of resin from EDMed surface is evaluated by comparing these separation forces.

TABLE 1. Releasability test conditions

Mold resin	Epoxy resin
Compression load	1.13 N
Molding temperature	448 K
Cure time	10 min
Contacting area	154 mm^2
Release speed	10 mm/min

COMPARISON OF EDM SURFACES

The SEM images of EDMed surfaces using three types of working dielectric fluid are shown in Fig.3. In any cases, the surfaces were finished under small pulse energy conditions of the discharge current ie=0.4A. When the electrode polarity is negative, smoother surface can be formed on the surfaces finished with SPMF and APMF, compared with that in the kerosene fluid. When the electrode polarity is positive, the crater diameters in the any cases of dielectric fluid are smaller than those in the case of negative electrode polarity. By roughness curve measurements it was confirmed that the surface roughness values in the cases of SPMF and APMF were a little smaller than that in the case of kerosene, and the frequencies of surface undulation in the cases of powder mixed working fluids were lower than that in the case of kerosene.

DIFFERNCE IN SEPARATION FORCE

The influence of EDMed surface roughness on the releasability of molded resin was discussed. Fig.4 shows the relationship between separation force of molded resin and the surface roughness of EDMed surfaces. The EDM finished surfaces with different surface roughness were prepared by changing discharge pulse conditions. The separation force decreases almost linearly with an increase of surface roughness when kerosene type fluid is used. In general, it is thought that the separation force increases with an increase of the surface roughness because of anchor effect, but it decreases with surface roughness in this test. This is because the

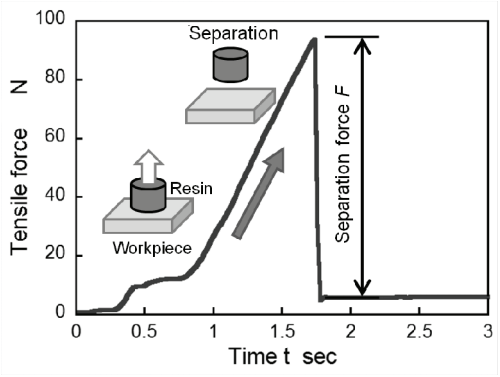

FIGURE 2. Time variation of tensile force

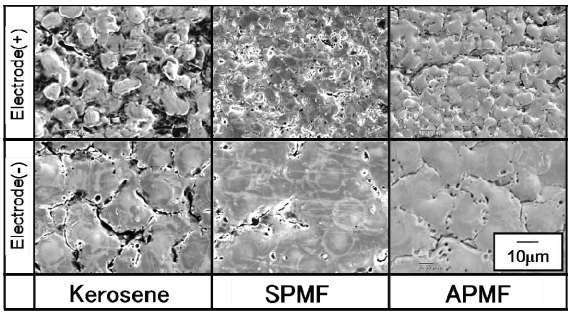

FIGURE 3. SEM images of EDM finished surface using different types of working dielectric fluid

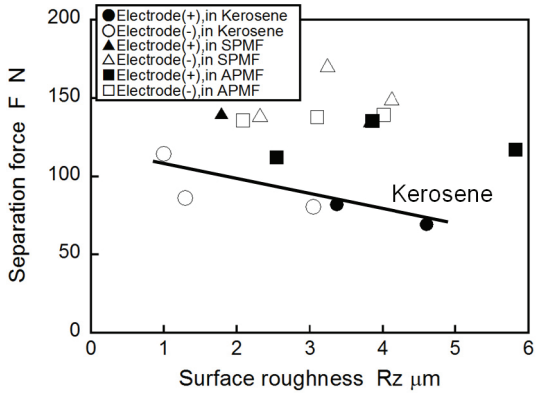

FIGURE 4. Variations of separation force with surface roughness for various types of working dielectric fluid

separation forces only in the direction perpendicular to the interface between resin and EDMed surface are measured in this study. Also the separation forces of molded resin from EDM finished surface using SPMF and APMF are higher than that using kerosene under any surface roughness. In particular, when the electrode polarity is negative, the separation force is higher. Therefore, EDM finished surface

with SPMF or APMF is not suitable for metal mold surface for epoxy resin molding.

FACTOR AFFECTING SEPARATION FORCE

The reasons of high separation forces in the cases of SPMF and APMF are discussed here. The adhesion force between two surfaces *F* is theoretically depends on the bonding force per unit area *f* and the real contacting area *S*. Thus, the separation force *F* is expressed with the following equation.

$$F \propto f \cdot S \quad (1)$$

The bonding force per unit area *f* is greatly affected by chemical components on the adhesive interface. On the other hand the real contact area *S* is affected by the real surface area of EDMed surface and the replication state of epoxy resin to the EDMed surface. The real length *L* on the surface profile curve of the EDMed surface which must reflect the real surface area on EDMed surface was measured, since it was difficult to measure the real contact area directly. Then the replicating ratio of molded epoxy resin to EDMed surface was evaluated by the ratio of surface roughness of epoxy resin to that of EDMed surface after separation test.

Figure 5 shows the measured result of real length *L* on the measured length of 10mm on the EDMed surface profile curve. As shown in the figure, the real length is almost the same regardless of the type of working fluid. Also Figure 6 shows the replication ratio of molded epoxy resin to the EDMed surface. It is confirmed that the replication ratios are nearly 100% in any cases of working fluid. Therefore, it can be concluded that the real contact area between molded epoxy resin and EDM finished surface is almost same regardless of type of working fluid.

The cross-sections of EDMed surface were observed by a transmission electron microscope in order to investigate the difference in surface structure with type of working fluid. The observation results are shown in Figure 7. White layers observed on the upper part of the images are carbon top coat layers for fabricating thin specimen with FIB, and the surfaces just below the coat layer are the EDMed outermost surfaces. In the case of EDMed surface using kerosene type working fluid, the surface structure with relatively small crystal grains can be observed in the resolidified layer. The

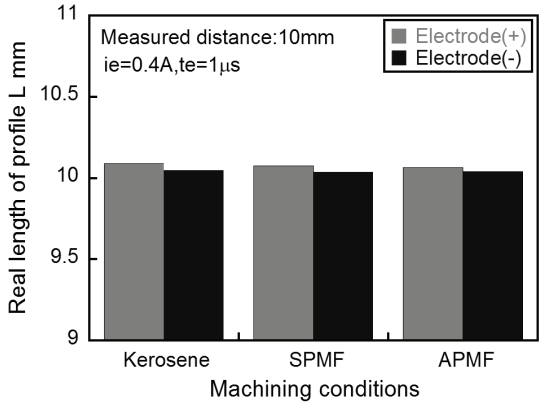

FIGURE 5. Difference in real surface length L on on EDM finished surface profile curve with type of working fluid

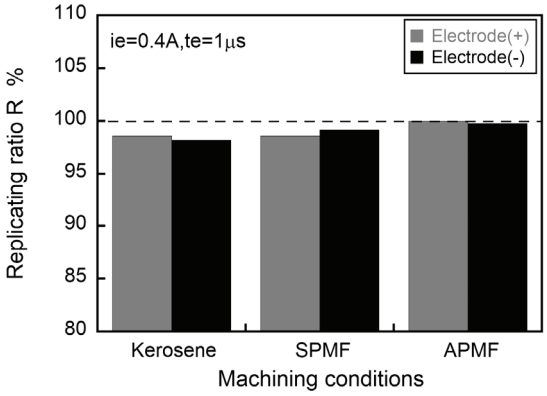

FIGURE 6. Difference in replication ratio of epoxy resin to EDM finished surface with type of working fluid

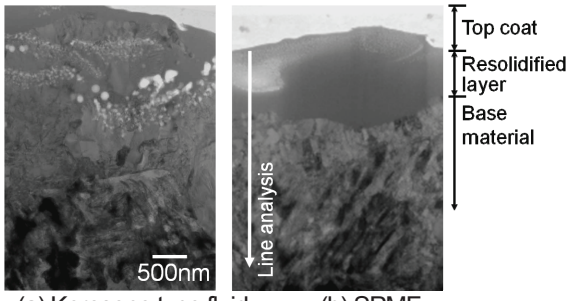

FIGURE 7. TEM images of resolidified layer

thickness seems to be 1-2μm. On the other hand, crystal grain structure cannot be confirmed in the resolidified layer at all under this magnification. This thickness is about 1μm and the base material structure can be observed underneath the layer. Therefore, it was clarified that the surface structure in the case of SPMF is

different from that in the case of kerosene type fluid [6]. In order to compare the chemical compositions of the surface, componential line analyses were carried out on the white line in the TEM image. The result is shown in Fig.8. As shown in the figure, much silicon can be detected on the surface. At the depth of 5μm or deeper, silicon content is under 0.4%, which corresponds to the original amount of silicon in the base material SKD11. Therefore, the silicon exists only in the resolidified layer, which means that silicon in SPMF was introduced into the resolidified layer during EDM. Epoxy resin has been widely used for packaging IC silicon chip, since the adhesion force between epoxy resin and silicon is generally high. Accordingly, the inclusion of much silicon into EDMed surface resulted in high separation force of molded epoxy resin from the EDMed surface.

Fig.9 shows component analysis result of EDMed surface using APMF. The aluminum content into EDMed surface is less than 0.3% under any EDM conditions. Also the component ratio was almost same as that using kerosene type working fluid. The cause of high separation ratio in the case of APMF might be very smoothed convex shape of the surface profile on EDMed surface as shown in Fig.3. Further discussion is needed for deep understanding of high separation force in the case of APMF.

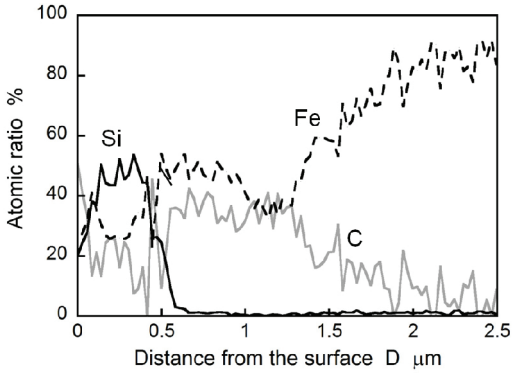

FIGURE 8. Line analysis results of cross section of EDM finished surface using SPMF

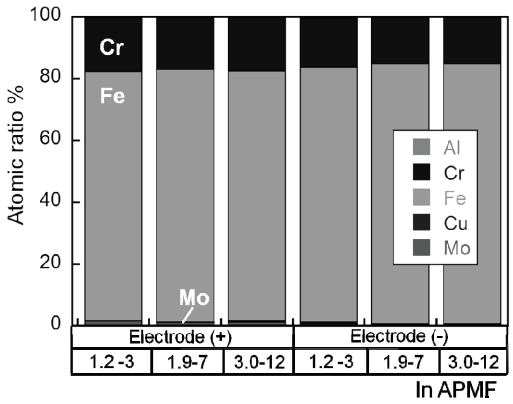

FIGURE 9.Component analysis result of EDM finished surface using APMF.

CONCLUSIONS

(1) The separation force of molded epoxy resin from the EDM finished surface with kerosene type working fluid decreases with an increase of the surface roughness.
(2) The separation forces of molded epoxy resin from the EDM finished surfaces with silicon powder mixed fluid and aluminium power mixed fluid are higher than that with kerosene type working fluid.
(3) Silicon content is included into the resolidified layer on EDM finished surface with silicon powder mixed fluid, which results in high separation force of molded epoxy resin, since the adhesion force between epoxy resin and silicon is generally high.

ACKNOWLEDGEMENTS

This research is financially supported by Adaptable and Seamless Technology transfer Program through targetdriven R&D, Japan Science and Technology Agency.

REFERENCES

[1] H. Narumiya et. al., *EDM by Powder Suspended Working Fluid*, Proc. of 9th ISEM, 5-8, 1989.
[2] N. Mohri, et. al., *A New Process of Finish Machining on Free Surface by EDM Methods*, Annals of the CIRP 40, 1 207-210, 1991.
[3] Y. Uno et. al., *Surface Generation Mechanism in Electrical Discharge Machining with Silicon Powder Mixed Fluid,* International Journal of Electrical Machining 2, 13-18, 1997.
[4] Y. Uno et. al., *Surface Modification of EDMed Surface with Powder Mixed Fluid*, Proc. of the 2nd Int. Conf. and Exhibition on Design and Production of Dies and Molds, CD-Rom, 2001.
[5] R. Kitada et. al., *Fundamental Study on Releasability of Resin from EDMed Surface* Proc. of the 9th International conference of euspen, 117-121, 2009.
[6] N. Sumi, et. al., *Study of Si-containing Amorphous Layer by Electrical Discharge Coating*, IJEM 16, 27-32, 2011.

MACHINING OF MICROFLUIDIC STRUCTURES FOR BIOTECHNOLOGICAL COMPONENTS

Eckart Uhlmann, Dirk Oberschmidt, Christoph Hein and Frederik Mahr

Department Micro Production Engineering
Fraunhofer-Institute Production Systems and Design Technology
Berlin, Germany

INTRUDUCTION

This work presents new approaches for the manufacturing of tailored microfluidic bioreactor chips, adapted to the requirements of innovative methods and to the evolutionary state of the process design. Taking a microfluidic bioreactor chip for cell-free protein synthesis as an example, this study describes in detail the advantages and disadvantages of different manufacturing procedures with regard to cost efficiency and process-related functionality. In this connection, different production processes for the manufacturing of prototypes, small and medium batches and for the manufacturing of mass-products are compared. Moreover, processing parameters were optimized in terms of the relevant technological characteristics such as surface roughness, planarity or structural resolution.

The qualitative assessment of the manufactured structures is made by production measurement technologies as well as an experimental study, based on the activity and yield of the cell-free expression of a fluorescent protein.

As a result of this work, a detailed procedure for the manufacturing of microfluidic chips is recommended, along with an assessment of the impact on the performance of a biological system in the microfluidic devices.

MOTIVATION

Important applications of microfluidic chips are small scale biochemical reactors, like they are used for the cell-free synthesis of proteins. Several technologies exist to process structures on those chips. Here appropriate production-technological processes for plastic chips are evaluated and discussed. Considering the general process capability of the used manufacturing technologies, a comparison regarding structural resolution, dimensional accuracy, shape stability, quality of the machined surfaces, and machining time is executed.

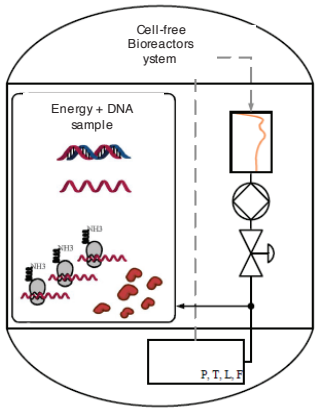

FIGURE 1. Schematic drawing of a bioreactor system for cell-free protein synthesis

Especially for the cell free protein synthesis, microfluidic bioreactor systems (Figure 1) are of particular relevance. Cell free protein synthesis abstains from living cells for the synthesis of product proteins. In contrast to conventional biotechnological methods, technical systems are used to reproduce the intracellular processes. Based on this emulation, protein synthesis is carried out. The resultant structural demands for novel biotechnological applications can be stated as follows:

- Microstructures with typical dimensions in the range of some 10 μm to some 100 µm for handling of volumes in μl range
- Reduction of volume to adapt biotechnological techniques and to improve the dynamic performance and accuracy of the control
- Machined channel surfaces that avoid the adsorption of biological components

The technological demands, with special regard to manufacturing technology, require a detailed analysis that is been done in the following.

EVALUATION OF APPROPRIATE MANUFACTURING METHODS

In particular pilot phases of the development of microfluidic bioreactors are often needed diverse structural variations [2]. Thus, a production chain is necessary that allows a fast evolutionary enhancement of the reactors. Laser ablation, micro milling, and injection molding meet the demands in different degree of fulfilment. In this investigation they are used for the manufacturing of a microfluidic example structure (Figure 2).

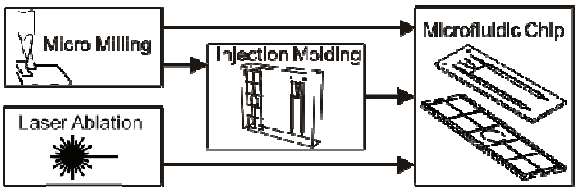

FIGURE 2. Schematic diagram of the evaluated process chain

The micro fluidic chip is a simple bioreactor system consisting of two reaction chambers and an additional channel network for fluid handling. The main dimensions of the bioreactor are represented in figure 3, a complete setup chip is shown in figure 4.

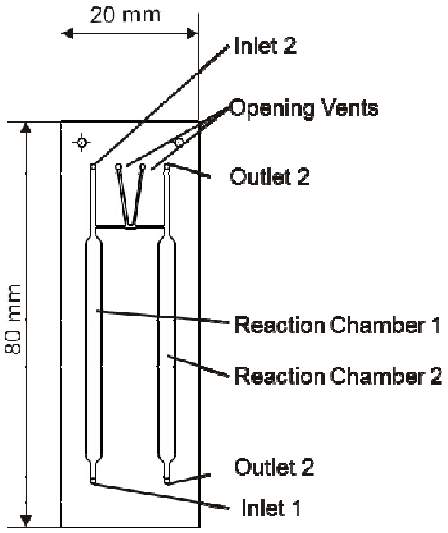

FIGURE 3: Schematic diagram of the evaluated structure

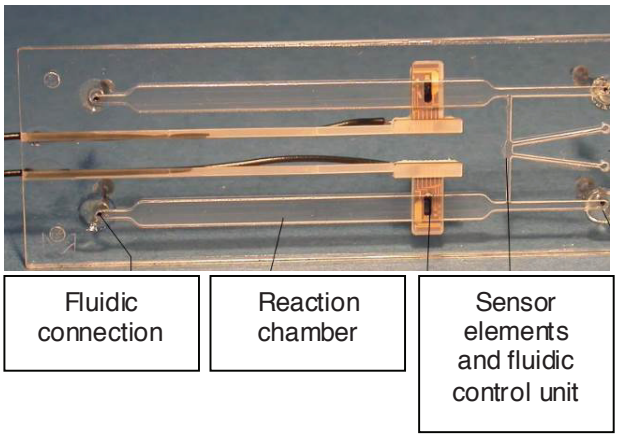

FIGURE 4: Schematic diagram of the evaluated structure

The manufacturing of microfluidic chips by laserablation was done with a 355 nm picosecond-laser-source with a mean power of 5 W, a pulse-duration of 15 ps and a repetition rate of up to 200 kHz. The positioning was done with an yx-Laserscanner and an ultra-precision machine tool Kugler MicroGantry Nano 5x. The structural resolution is limited by the focusing optic, beam quality, pulse length and repetition rate. The minimum producible structure size is 5 μm in which a feasible corner radius is 3 μm. The Micro-Milling was carried out using micro-cutting tools with a diameter between 50 μm and several millimeters and the machine tool Wissner Gamma 303. The minimum structure size is in the range of 50 μm and the minimum cutting tool corner radius correlates to the half of the tools diameter (see TABLE 1)

Injection molding was done with a Battenfeld Microsystem 50 micro injection molding machine. The resolution capacity of the process is directly depending on the injection molding tool. The manufacturing procedures, used for the production of the mold must therefore have equal or higher reproduction accuracy than the desired microfluidic chips. In this case study, replication was done with Topas 6013M-07.

For the manufacturing of the bioreactor system by laserablation ans micro milling, injection molded substrates of COC Topas 6013M-07 were used. For the injection molding, common granulate of the same material was used.

TABLE 1. Summarization of the used machine tool

manufacturing process	Machine Tool	Tools
Micro Milling	- Wissner Gamma 303 - Positioning accuracy < 2 μm - machine axes - 2 high frequency spindles: n_1 = 5,000 min^{-1} to 60,000 min^{-1} n_2 = 20,000 min^{-1} to 150,000 min^{-1}	- Cemented carbide End-Mills 0.05 mm ≤ D ≤ 3 mm - 2 fluted uncoated Tools - Measured runout < 2 μm - Application oriented cutting edge geometries
Laserablation	- Kugler MicrGantry Nano 5x - Aerostatic bearings - Positioning accuracy < 1 μm - 5 machine axes + 2 laser scanner axes	- Coherent Nd:YAG Picosecond Laser source - Mean power: 5W @ 355 nm - Pulse energy: 20 μJ - Pulse duration: 15 ps

MACHINING RESULTS

In order to evaluate surface qualities as an example for the whole study, each of the manufacturing procedures was evaluated for the manufacturing of the reference structure. Clear differences of surface qualities are obvious (Figure 5). The laser machined surfaces show a reflection of the laser pulses used for the processing (Figure 5a). Moreover, micro-pores occur on the channel surface. These pores constitute the reason for adsorption effects with a high probability.

The micro milled surfaces show a completely solid surface, in which processing marks of the used End-Mill are visible (Figure 5b). These have, in contrast to the micropores, a negligible influence on adsorption processes.

The injection molded surfaces show no detectable surface defects (Figure 5c). Therefore, injection molded bioreactor systems should show an outstanding performance in biotechnological evaluation.

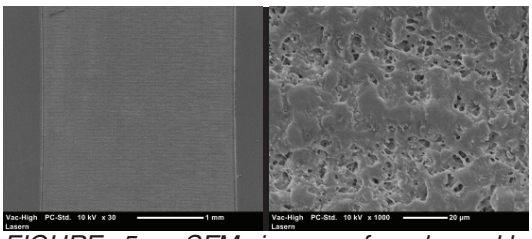

FIGURE 5a:. SEM image of a laserablated channel surface

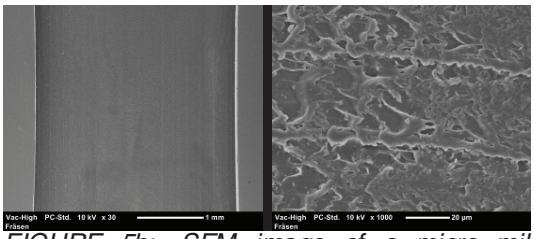

FIGURE 5b:. SEM image of a micro milled channel surface

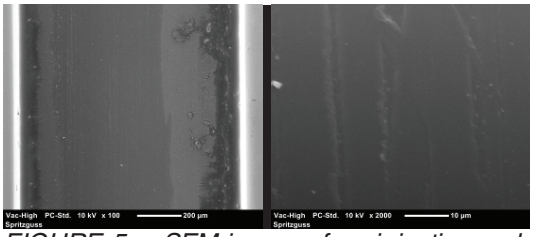

FIGURE 5c:. SEM image of an injection molded channel surface

The surface roughness of the laser machined surfaces is in the range of Ra = 0.8 μm. In contrast, the micro-milled surface shows significantly less machining marks and a surface roughness of Ra = 0.2 μm. The injection molded microfluidic chips have a substantially reduced surface roughness of Ra = 14 nm [3]. This is in confirmation with various publications. The reason is the behavior of the liquid polymer in contact with the wall of the mold.

The following FIGURE 6 shows AFM measurement results of the machined surfaces. The differences in the topography are obvious. It is astonishing that despite of the rough surface of the mold the molded surface is very smooth. It depends on the temperature regime during the injection process. Thus, it is possible to decrease the effort for the mold machining if only surface quality is required and no high quality regarding shape accuracy.

a

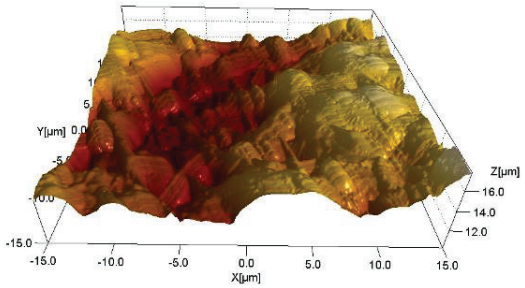

b

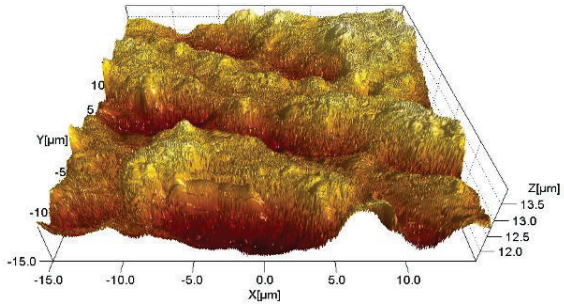

c

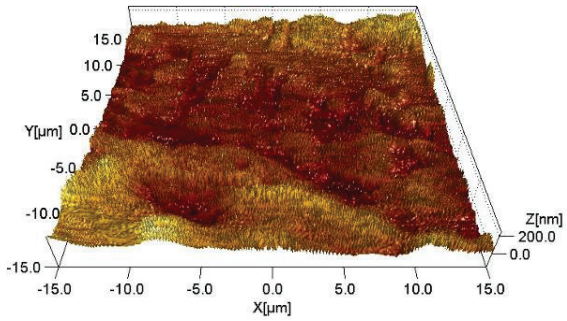

FIGURE 6: Micro surface analysis by atom force microscopy (AFM) of a laser machined surface (a), a micro milled surface (b) and an injection molded surface (c)

As Shown in figure 6, the visible surface defects (Figure 5) are also detectable by micro surface analysis.
Besides the manufacturing quality as a key parameter, it is necessary to take the manufacturing effort into account as a second evaluation parameter. The fabrication of the examined structures by injection molding, first of all a complex in injection molding tool is required. In this context, a careful evaluation of manufacturing quality and quality is essential for every stage in a development process.
In TABLE 2, the achieved results are summarized.

TABLE 2. Summarization of the manufacturing results

Production process	Production results	Example image
Micro Milling	- Ra, min: 0.2 µm - Minimal channel width: 50 µm - Minimal corner radius: 25 µm - Flatness of microfluidic chips (80 mm): 35 µm - Smooth, closed surface	
Laserablation	- Ra, min: 0.8 µm - Minimal channel width: < 10 µm - Minimal corner radius: < 5 µm - Flatness of microfluidic chips (80 mm): 85 µm - Porus surface	
Injection Molding	- Ra, min: < 50 nm - Minimal channel width: < 10 µm - Minimal corner radius: < 5 µm - Flatness of microfluidic chips (80 mm): < 20 µm	

BIOTECHNOLOGICAL EVALUATION

The biotechnological evaluation of the manufactured microfluidic chips was done by the synthesis of a green-fluorescent model protein (GFP) in the manufactured microfluidic reactor systems. As a fluidc interface a syringe pump system (Figure 7a; Cetoni GmbH, Germany) and a fluidic connection system (Figure 7b; dolomite, UK) was used. The microfluidic channels were filled with a solution containing all reagents needed for a cell-free synthesis reaction of GFP using a bacterial cell lysate.

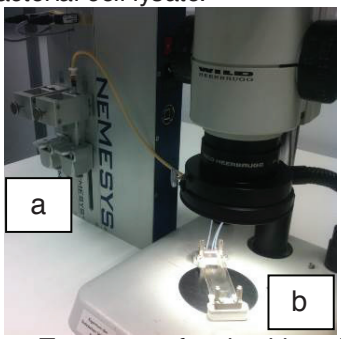

FIGURE 7: Test setup for the biotechnological evaluation

After one hour incubation at 37 °C, a qualitative analysis was carried out by fluorescent microscopy, furthermore the synthesized protein was visualized in a protein gel (Figure 8). Using an electrophoretic technique, proteins in a solution can be separated according to their weight. The investigation demonstrated a comparable rate of synthesis for all structures examined (Figure 8 b to d). However, in the laser machined channels agglomeration effects may be of influence be evident (Figure 8 b).

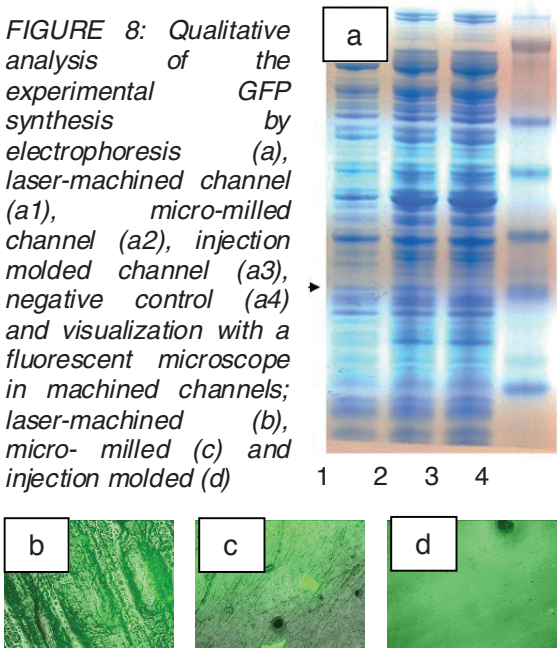

FIGURE 8: Qualitative analysis of the experimental GFP synthesis by electrophoresis (a), laser-machined channel (a1), micro-milled channel (a2), injection molded channel (a3), negative control (a4) and visualization with a fluorescent microscope in machined channels; laser-machined (b), micro- milled (c) and injection molded (d)

OUTLOOK AND CONCLUSION

Surface roughness, as a key parameter for the manufacturing of microfluidic chips, was presented in this case study as an example. The remaining parameters (Table 1) are under final investigation. The entire study will give a detailed and process based recommendation for the manufacturing of microfluidic chips.
Summarizing the exemplary manufacturing of microfluidic bioreactors, the extraordinary surface quality of injection molded reactor systems

REFERENCES

[1] Rötting O, Röpke W, Becker H, Gärtner C. Polymer microfabrication technologies. Microsystem Technologies 8. 2002, 32-36.
[2] Chantal G, Khan M. Laser processing for bio-microfluidics applications. Anal Bioanal Chem 385. 2006, 1351-1361.
[3] Attia Usama M.; Alcock Jeffrey R. Evaluating and controlling process variability in micro-injection moulding. Int J Adv Manuf Technol 52. 2008, 183 - 194
[4] Gärtner R.
[5] Analyse der Prozesskette zur Herstellung mikrostrukturierter Bauteile durch Spritzgießen, Dissertation, Aachen 2008
[6] Tosello G. Bissacco G. Tang, P. T. Hansen H. N. Nielsen, P. C. High aspect ratio micro tool manufacturing for polymer replication using µEDM of silicon, selective etching and electroforming. Microsyst Technol 14. 2008, 1757 -1764

HIGH SPEED MACHINING OF SEMI CONDUCTOR PRODUCTS

Pierre van den Hurk[1] and Luuk Berkelaar[1]
[1]Technology & Development
VDL Enabling Technologies Group
Eindhoven, the Netherlands

INTRODUCTION

Still many people talk about the fast emerging technology of High Speed Machining (HSM), but several definitions are used. One of the definitions for HSM is based on machining with a high spindle speed. But what is a high spindle speed? Is it 10,000 rpm? Is it 20,000 rpm? Or is it higher? Dependent on whom you ask, you will likely get different answers. Other HSM definitions are based on using material related cuttingspeeds [1] or to take a dynamic approach [2]. In order to fully understand, explore and utilize the possibilities of HSM, the VDL Enabling Technologies Group has defined it in the process approach: "HSM is achieving the shortest machining time by using a reliable low force machining process". A low force machining process has many advantages but seems contrary to achieve short machining times.

This paper describes the challenges VDL ETG has run into when implementing this HSM process in combining these two goals and looking at the four key process elements being: the workpiece, the process, the machine tool and the cuttingtools, see figure 1.

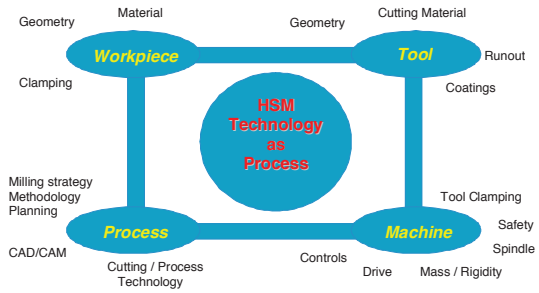

Figure 1. HSM process

WORKPIECE

A tendency in the High Tech Equipment market is the design of systems based on high accurate frames, parts and vacuum process chambers. The challenges in machining these products is to deal with on one hand the flexibility of these frame type products but on the other hand also the removal of high material volume in large and deep process chambers or when machining thin-walled light weight construction.

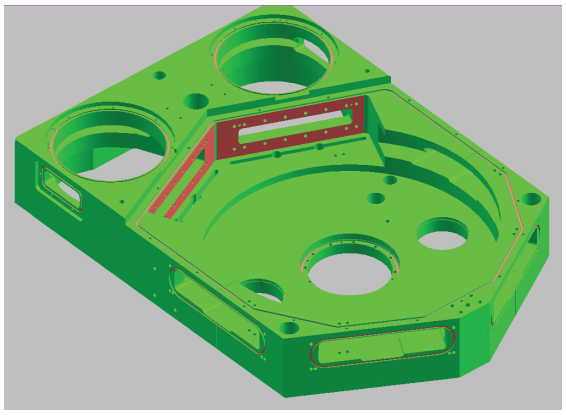

Figure 2. Example of a process chamber

PROCESS

The process aspects that do have a significant influence on the efficiency of HSM are:

Cutting strategy and methods

For pre-machining, the strategy is trying to use the available spindle power to an optimum in order to get the highest metal removal rate. At the same time, the amount of stresses brought into the material by the cutting process, is reduced to a minimum. For finishing, the feedrate is increased as much as possible. When finishing flexible parts or product features the approach is to keep the part stiff in the area to machine and let it become flexible where it is finished.

Knowledge on dynamic behavior

For a number of products it is required to use tools with a high ratio between length and diameter resulting in significant vibration problems. By measuring the dynamic behavior of these tools in combination with the product and feeding back the results to optimize the cutting process, significant improvements can be reached, see figure 3.

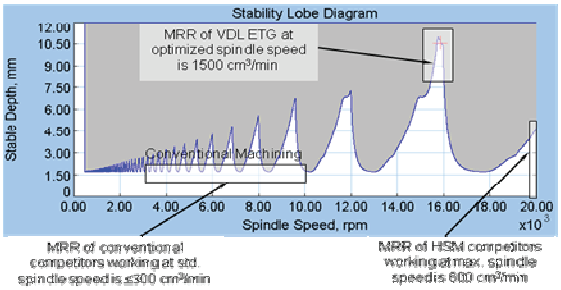
Stability Lobe Diagram
MRR of VDL ETG at optimized spindle speed is 1500 cm³/min
Conventional Machining
Stable Depth, mm
Spindle Speed, rpm
MRR of conventional competitors working at std. spindle speed is ≤300 cm³/min
MRR of HSM competitors working at max. spindle speed is 600 cm³/min

Figure 3. A stability lobe diagram showing the effect of knowledge on dynamic behavior.

MACHINE TOOL

For optimum performance it is very important to thoroughly know the machine tool. The most important elements of the machine tool are:

The spindle

Together with the tools and the tool clamping system, the spindle is the heart of the machine. In order to optimize the HSM process it is important to know the stability and power characteristics of the spindle. The results of several stability and power tests using different tool configurations for they are important feed backs for the CAM programmer to determine the optimum cutting strategy.

The behavior in travel motions

This behavior is determined both by the controller, the available acceleration / deceleration and positioning requirement. There can be significant difference between the programmed feeds and the actual feeds because of these factors. An assessment of this travel behavior by performing several basic tests contributed significantly to optimize NC-programs.

Other important machinetool features

The other two most important machine tool features are the temperature stability and chip removal for ensuring accuracy and process reliability.

CUTTINGTOOLS

Of course, the use of the right cuttingtools is essential. In order to find the right materials and geometry it is essential to perform sufficient tests with different configurations. The experience that we have gained during tests showed that a limited number of materials and geometries are suitable if you want to bring HSM to the outer limits.

Figure 4. Some cuttingtools

RESULTS

Using the HSM Process approach properly has lead to the following improvements:

1. Reduction in cutting forces resulting in less product distortion, a higher accuracy and improvement of the surface quality.
2. Use of less and smaller tools
3. The possibility to make more use of simple and lighter clamping methods.

Within our VDL ETG workshops we have found that just increasing spindle speed can lead to increased efficiency but the ETG HSM Process approach has lead to further cost reduction of over 30% with the proper machining strategy and cutting parameters. See figure 4 with result on individual tools.

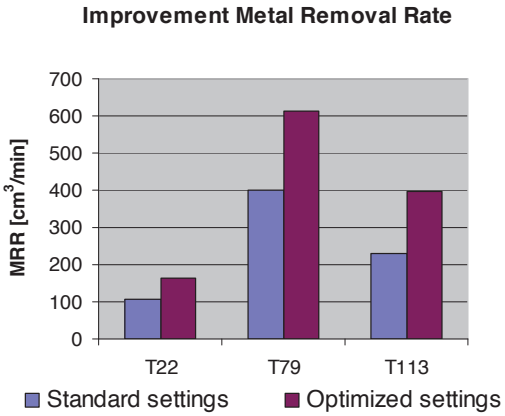

Figure 4. Improvement cuttingtool performance using the dynamic approach.

REFERENCES

[1] Schulz H., High-Speed Machining, ISBN 3-446-18796-0, 1996
[2] Smith S., University of Charlotte

Authors Index

Aarts, Ronald Godfried Karien Marie 166
Abolbashari, Mehrdad 98
Aguirre, Gorka 204
Ali, M. D. Hazrat 431
Alzaydi, Ammar Ayad 518
Anderson, Ben 157
Anton, Jayson 182
Aoyama, Hisayuki 282
Arneson, David A. 251, 318, 440, 445, 522
Assoufid, Lahsen 182
Astrelin, Andrey 121, 465
Awtar Sc.D., Shorya 172
Babaie, Gelareh 98
Badami, Vivek G. 133
Baer, Goran B. 82
Bauza, Marcin B. 68, 92, 127
Berkelaar, Luuk 563
Blackburn, Christopher 121, 465
Bosmans, Niels 109
Boyden, Edward S. 29
Brooks, Daniel R. 58
Brouwer, Dannis Michel 166
Brown, Nathan 483, 498
Brown, Nicolas S. 58
Bryan, Nick 318
Bui Ph.D., Chinh Ba 550
Bui, Pho Van 153
Cai, Zhonghou 182
Cao, Lei 295
Chalifoux, Brandon 78, 103
Chao, Leon Shih 209
Chen, Jianwei 290
Chen, Shih-Chi 290, 353
Chen, Zonghao 409
Cheng, Jiyi 353
Cherala, Anshu 144
Chesna, Jacob W. 74, 528
Cheung, Chi-Fai 532
Cho, Hee Keun 343
Cho, Hyun-Gwang 455
Choi, Byung-Jin 144
Chung Ph. D., Sung-Chong . . 295, 314, 327, 331, 455
Cilip, Christopher M. 68
Culpepper, Martin Luther 161, 176, 321, 347
Davis, Peter J. 299
DeFisher, Scott 92
DiBiasio Ph.D., Christopher M. 161
Dorsey-Palmateer, John W. 121, 465
Dow, Thomas A. 191, 231, 374
Drescher, Joseph D. 374
Du, Lucy 176
Dubetsky, Boris 299
Dumas, Paul R. 92
Eberhardt, Ramona 87
Echter, Michael A. 378
Edson, Stanley L. 299
Eisinger, Jamie 33
Elfizy, Amr 518
Elliott Ph.D., Kevin E. 498
Ellis, Jonathan D. 58, 364, 368, 378, 489, 493, 498, 504
Emmett, David H. 265
Engin, Serafettin 518
Enkrich, Christian 359
Erkorkmaz Ph.D., Kaan 518
Evans, Christopher J. 415
Fan, Aaron 29
Farahi, Faramarz 98
Farsad, Mahsa 415
Ferrucci, Massimiliano 121, 465
Fesperman Jr., Ronnie R. 498, 504, 512
Fitsos, Pete 299
Forest, Craig R. 29
Fritz, Matthias 269
Fukuta, Yusuke 540
Furushiro, Naomichi 385
Furutani, Katsushi 50
Ganguly, Vasishta 115

Gao, Jian 304
Garrard, Kenneth P. 191, 231, 374
Gebb, D. 191
Gebhardt, Andreas 87
Gerner, G. 465
Gettys, T. 191
Gillmer, Steven R. 364, 489
Glöss, Rainer Siegfried 359
Go, Jamison 29
Goch Prof. Dr.-Ing., Gert 415
Gorostiaga, Mikel 204
Grabowski, A. 498
Groothuijsen, Tim 33
Gunnink, Klaas-Jan 166
Guo, Jiang 536
Gweon, Dae-Gab 310
Haase, Thomas 359
Haber, Aleksandar 138
Hamaguchi, Tetsuya 243, 247, 256
Harder, Ross 182
Hayashi, Terutake 540
He, Peng 186
Heilmann, Ralf K. 78, 103
Hein, Christoph 558
Hesler, Gregory S. 191
Hill, Jim 265
Hiroi, Tetsumaro 339
Hirooka, Daisuke 385
Hiroshi, M. 431
Holst, Gregory L. 29
Hoogendijk, R. 33
Hopkins, Jonathan B. 214
Howard, Stephen Christopher 545
Huang, Peisen 304, 409, 421, 477
Huang, Wenyi 186
Hunt, Jeffrey B. 545
Hwang, Jooho 550
Ichinozuka, Asa 282
Iemata, Daichi 393
Ikeshima, Shota 256
Imai, Toru 448
Imkamp, Dietrich 127
Inubushi, Yuichi 239
Ishikawa, Tetsuya 239
Isohashi, Ai 153
Iwasa, Yasuhiro 385
Iwasaki, Shuhei 554
Jadhav, Raunak Dhanaji 427
Janitza, Dennis 269
Jared, Bradley H. 157
Jeon, Yongho 343
Johnson, Michael A. 299
Jones, Christopher W. 149
Kato, Taka 335
Katsuki, Akio 431
Kearney, Steven 182
Keene, Andrew D. 378
Keller, Eric E. 437
Kessing, Jonas 231
Khim, Gyungho 295
Kim, Hyunchang 310
Kim, Myeonghyeon 310
Kim, Myungjune 314
Kitada, Ryoji 554
Kiyono, Satoshi 393
Klar, Rainer 251
Knapp, Byron R. 251, 318, 437, 440, 445
Knox, Wayne H. 58
Kodandaramaiah, Suhasa B. 29
Kogusu, Shinichi 404
Kohn, Charlie M. 448
Kojima, Tatsuhiro 397, 404
Kolb, Ilya 29
Kong, Ling-Bao 532
Kretschmar, Mark 452
Krysinski, Adam 149
Kudenov, Michael W. 191
Kuroiwa, Megumu 397
Kurokawa, Syuhei 431
Kushnir, Emmanuil 273
Lai, Barry 182
Langmack, Malte 195
Laro, Dick A. H. 33
Leach, Richard K. 74, 149

Lee, James L. 186
Lee, Jihyun 54
Lee, Moon-Gu 343
Lee, Vincent 121, 465
Li, Chengzhang 222
Li, Lei 186
Li, Yan 368
Libby, Stephen B. 299
Liebers, Melvin J. 318, 445
Liu, Wenjun 182
Loftus, Tom 299
Lu, Chao 364
Lu, Coby 29
Lu, Xiaoming 144
Ludwick, Stephen J. 493, 498, 510
Maeda, Yukio 404
Mahr, Frederik 558
Mak, C. H. 532
Makinouchi, Susumu 448
Maneuf, B. Serge 498, 512
Marsh, Eric R. 437
Martin, Don L. 440, 452
Maser, Jorg 182
Mashrafi, Sheikh 44
Matloff, Laura 321
Matsuda, Shigetaka 385
Matsui, Shinsuke 218
Matsuyama, Satoshi 239
Matsuzawa, Ryo 20
Medicus, Kate M. 92
Michihata, Masaki. 540
Miller, Michele H. 222
Milligan, Spike. 121, 465
Min, Bok-Ki 314, 327, 331, 455
Miyakawa, Kodai. 20
Mohammadi, Hossein 228
Morita, S.. 536
Moroni, Giovanni 459
Morse, Edward P. 427
Mueller, Ulrich. 63
Mullany, Brigid A. 545
Munnig Schmidt, Robert-Han. 138
Muñoa, Jokin 204
Muralikrishnan, Bala 121, 465
Nagato, Keisuke 243, 247, 256
Nahata, Sudhanshu 471
Nakao, Masayuki 243, 247, 256
Nielson, Greg 157
Nishiguchi, Youichi 397
Nowak, W. John 231
Nyovanie, Prosper. 176
Oberschmidt, Dirk 195, 558
O'Connor, Brian P. 489, 498, 504, 512
Oh, Kwangje 331
Ohara, Tetsuo 448
Ohnishi, Osamu 431
Okada, Akira 554
Okamoto, Takeshi 153
Okamoto, Yasuhiro 554
Okandan, Murat 157
Okwudire, Chinedum E. 54
Ono, Manabu 335, 339
Ono, Takenori 235
Osaka, Taito 239
Oss, Daniel D. 318, 445
Osten, Wolfgang. 82
Otsubo, Tatsuki. 397
Ougiya, Yasuhiko 397, 404
Ozdoganlar, Osman Burak 471
Panas, Robert Matthew 161, 176, 214
Park, Chun-Hong. 295, 314, 331, 455, 550
Patten, John A. 24, 228
Petrò Ph.D., Stefano 459
Petrov, Peter 121, 465
Phillips, Steven D. 121, 465
Porchez, Thomas 204
Pratt, Daniel S. 68
Pratt, Jon R. 209
Preissner, Curt. 44
Pruss, Christof 82
Qian, Jun. 109
Qiang, Xuefeng 421
Qin, Zhang. 282
Ravindra, Deepak R. 24, 228

Reith, Jeremias 359
Ren, M. J. 532
Reynaerts, Dominiek 109
Risse, Stefan 87
Rivers, Ryan I. 528
Rojas, Folkers Eduardo 278
Roll, Christopher D. 378
Saathof, Rudolf 138
Saavedra, Michael P. 157
Sadakuni, Shun 153
Sain, John 476
Saito, Shunya 335
Sajima, Takao 431
Sakamoto, Makoto 335, 339
Sakata, Atsushi 50
Sakuragi, Yutaka 397
Salapaka, Srinivasa 44
Samara, Ayman M. 528
Sano, Yasushi 153, 239, 286
Satcher, Joe H. 476
Sato, Kaiji. 286
Sato, Takahiro 239
Sato, Toshimi 247
Savage, Daniel E. 58
Sawyer, Daniel S. 121, 465
Scattergood, Ronald O. 231
Schanne, Elizabeth 176
Schattenburg, Mark Lee 78, 103
Schimizu, Yuki 74
Schindler, Johannes 82
Schlamminger, Stephan 209
Schmitz, Tony L. 115, 200, 364
Selberg, Lars A. 133
Seugling, Richard M. 476
Sherlock, Ben 149
Shikazono, Naoki 243
Shimada, Shoichi 393
Shinagawa, Shunta 243
Shu, Deming 182
Slocum, Alexander H. 15, 278
Smith, Stuart T. 389, 528, 545
Soejima, Tsuyoshi 397
Sohn, Yong Woong 343
Sonnad, Vijay 299
Spronck, Jo W. 138
Sreenivasan, S. V. 144
Steinbuch, Maarten 33
Steinkopf, Ralf 87
Stoy, William 29
Suehiro, Daisuke 247
Sung, Edward 78, 103
Suzuki, Hirofumi Y. 536
Sweatt, William 157
Syam, Wahyudin Permana 459
Szklarzewski, Veronica 176
Takahashi, Ken 247
Takahashi, Satoru 20
Takamasu, Kiyoshi 20
Takasaki, Masahisa 448
Takaya, Yasuhiro 540
Tarbutton, Joshua 364
Taylor, John S. 299
Telleria, Maria Jose 321, 347
Terauchi, Shuntaro 385
Thomas, Marcel Adam Craig 161
Thompson, Daniel C. 299
Thousand, Jeffery D. 389
Tian, Kai 421
Tischier, Jonathan Z. 182
To, Suet Sandy 532
Tono, Kensuke 239
Toyoshima, Aya 282
Troutman, John 364
Trumper, David L. 39
Tyler, Christopher 200
Uda, Yutaka 393
Uehara, J. 536
Uhlmann, Eckart 195, 558
Umemura, Shigeru 218
van den Hurk, Pierre 563
van Eijk, Jan 33
Vasilescu, Denis 265
Verhaegen, Michel 138
Vogt, Stefan 182

Wang, Yuelai 286
Watanabe, Akihiro. 448
Weijun, Huang 282
Wenzel, Christian 251
Wesley, Alexander D. 133
Winkelmann, Ralf 251
Woody, Shane C. 498
Xiao, G. G. 532
Xu Ph.D, Ying 261
Xu, Huihua. 290
Xu, Lisen 58
Xu, Ruqing. 182
Yabashi, Makina 239
Yagi, Kenta 153
Yakovlev, Yuri. 121, 465
Yamagata, Yutaka 536
Yamaguchi, Tomomi 385
Yamauchi, Kazuto 153, 239
Yamauchi, Takuma 256
Yazawa, Takanori. 397, 404
Yen, Ying-Chieh 186
Yi, Allen Y. 186
Yoon, Jun Young 39
Young, Peter 476
Yu, Jianfeng 186
Yuan, Xin 404
Zhang, Junbin 477
Zhao, Huyue 44
Zhao, Ni. 290, 353
Zhou, Xi 353
Zhu, Minhao 368
Zimmerman, Kurt 359
Zou, Jing 261
Zwick, Susanne. 87

ISBN 978-1-887706-63-6